

## Acknowledgments

This collection of works was made possible by the dedication of many co-authors comprised of university colleagues, state and federal agency officials, graduate researchers, and various contributors from industry.

Aguilar, J.	Lewis, C.
Ashford, S.	Liby, L.
Berminham, P.	Meloy, N.
Brown, D.	Muchard, M.
Dapp, S.	Pai, N.
Deese, G.	Paikowski, S.
Dibb, E.	Patel, P.
Ealy, C.	Pierresaint, V.
Echelberger, W.	Race, R.
Engebretson, d.	Ranganath,
Fischer, J.	Robertson, D.
Garbin, E.	Rollins, K.
Gunaratne, M.	Salem, T.
Hajduk, E.	Schrader, A.
Hartley, A.	Sen, R.
Hourani, N.	Shahawy, M.
Issa, M.	Sosa, R.
Issa, M.	Spain, J.
Jacobsen, L	Stanley, B.
Johnson, K.	Stevens, K.
Jory, B.	Stinnette, P.
Justason, M.	Stokes, M.
Khouri, B.	Suh, K
Knight, W.	Thilikasiri, H.
Kranc, S.	Weinmann, T.
Kuo, C.	Winters, D.
Lane, D.	

## Table of Contents

Stevens, K., Jacobsen, L., Weinmann, T. and Mullins, G. (2009). "Improving Vibrating Wire Noise Immunity using Spectral Analysis," Conference Proceedings <i>Fatigue and Fracture in the Infrastructure - Bridges and Structures of the 21st Century</i> , July 26-29, Philadelphia.	6
Mullins, G. (2009). "I-35W Bridge Replacement, With an Ounce of Prevention," SPANS Quarterly Newsletter, Public Works Department, hillsboroughcounty.org, July.	14
Mullins, G., Sosa, R., Sen, R., and Issa, M. (2009). "Seal Slab Prestressed Pile Interface Bond from Full-Scale Testing," <i>Deep Marine Foundations, A Perspective on the Design and Construction of Deep Marine Foundations</i> , Deep Foundations Institute, ISBN: 978-0-9763229, pp.263-276.	15
Mullins, G., Sosa, R., Sen, R., and Issa, M. (2009). "Seal Slab / Steel Pile Interface Bond from Full-Scale Testing," <i>Deep Marine Foundations, A Perspective on the Design and Construction of Deep Marine Foundations</i> , Deep Foundations Institute, ISBN: 978-0-9763229, 277-288.	28
Stokes, M. and Mullins, G. (2009). "Concrete Stress Determination in Rapid Load Tests," Rapid Load Testing of Piles, Paul Holscher and Frits van Tol (eds), CRC Press / Taylor and Francis Group, London, ISBN: 978-0-415-48297-4, pp. 73-100.	39
Stokes, M., Mullins, G., Ealy, C., and Winters, D. (2008). "Statnamic Damping Coefficient: A Numerical Modeling Approach," <i>Journal of Geotechnical and GeoEnvironmental Engineering</i> , Vol. 134, No. 9, pp.1290-1298.	67
Suh, K.S., Sen, R, Mullins, G. and Winters, D. (2008). "Corrosion Monitoring of FRP Repaired Piles in Tidal Waters". <i>ACI SP-252</i> , pp. 137-156.	76
I. Winters, D., Mullins, G., Sen, R., Schrader, A. and Stokes, M. (2008). "Bond Enhancement for FRP Pile Repair in Tidal Waters". <i>ASCE, Journal of Composites for Construction</i> , Vol. 12, No. 3, pp. 334-343.	96
Mullins, G., Winters, D, and Dapp, S., (2008). "Closure to <i>Predicting End Bearing Capacity of Post Grouted Drilled Shafts in Cohesionless Soils</i> " <i>ASCE Journal of Geotechnical and GeoEnvironmental Engineering</i> , Vol. 134, No. 3, p. 413	106
Johnson, K. and Mullins, G. (2007). "Concrete Temperature Control via Voiding Drilled Shafts." <i>Contemporary Issues in Deep Foundations</i> , ASCE Geo Institute, GSP No.158, Vol. I, pp. 1-12	108
Sen, R. and Mullins, G. (2007). "New Developments in Underwater Pile Repair Using Fiber Reinforced Polymers". Proceedings, 5 <sup>th</sup> International Conference on Current and Future Trends in Bridge Design, Construction and Maintenance, Beijing, China, 234-241.	120
Sen, R., Mullins, G., Suh, K.S. and Winters, D. (2007). "Performance of FRP in Reducing Corrosion in Prestressed Elements". Proceedings of the 17 <sup>th</sup> International Offshore and Polar Engineering Conference, Lisbon, Portugal, July 1-6, Vol. 4, pp. 3504-3507	128
Suh, K.S., Mullins, G. Sen, R. and Winters, D. (2007). "Corrosion Monitoring of FRP Wrapped Piles", Proceedings, Third International Conference on Durability of Fibre Reinforced Polymer Composites for Construction, Quebec City, Canada, pp. 407-414.	132
Sen, R. and Mullins, G. (2007). "Application of FRP for Underwater Pile Repair" (invited). <i>Composites Part B</i> , Vol. 38, No. 5-6, pp. 751-758	140
Sen, R. and Mullins, G. (2007). "Further Developments in Underwater FRP Pile Repair". Proceedings, <i>COMPOSITES &amp; POLYCON 2007, American Composites Manufacturers Association, Educational Proceedings CDROM</i> , 5 pages	148
Kranc, S.C. and Mullins, G. (2007). "Inverse Method for the Detection of Voids in Drilled Shaft Concrete Piles from Longitudinal Temperature Scans," <i>Inverse Problems Design and Optimization Symposium</i> , Miami, FL, April 16-18, 2007	153
Meloy, N., Sen, R., Pai, N. and Mullins, G. (2007). " <i>Roof Damage in New Homes Caused by Hurricane Charley</i> ". <i>ASCE, Journal of Performance of Constructed Facilities</i> , Vol. 21, Mar/April, No 2, pp. 1-11	159
Sen, R. and Mullins, G. (2007). "Advances in Underwater Pile Repair Using FRP", 3 <sup>rd</sup> COBRAE Conference, Benefits of Composites in Civil Engineering, University of Stuttgart, March 28-30, Paper 19B, 10 pages.	170



Sen, R., Mullins, G. and Shahawy, M. (2007). "Fiber-Reinforced Polymer Repair and Strengthening of Structurally Deficient Piles". Transportation Research Record, No 2028, Design of Structures, pp. 221-230. <i>Nominated for Outstanding Paper Award</i>	180
Sen, R. and Mullins, G. (2007). "Developments in Underwater FRP Repair of Corroding Piles", Second International Conference on Recent Advances in Composite Materials, Bakht Symposium, New Delhi, India, Feb 20-23, 8 pages.	190
Suh, K., Mullins, G., Sen, R. and Winters, D (2007). "Effectiveness of Fiber-Reinforced Polymer in Reducing Corrosion in Marine Environment". ACI Structural Journal, Vol. 104, No. 1, 76-83.	198
Mullins, G. (2006). "In Situ Soil Testing," <i>Chapter 2, The Foundation Engineering Handbook</i> , Gunaratne, M. (ed), CRC Press, Taylor & Francis Group, Boca Raton, FL, ISBN 0-8493-1169-4, pp.47-86.	206
Mullins, G. (2006). "Design of Drilled Shafts," <i>Chapter 7, The Foundation Engineering Handbook</i> , Gunaratne, M. (ed), CRC Press, Taylor & Francis Group, Boca Raton, FL, ISBN 0-8493-1169-4, pp.299-326.	251
Mullins, G., Winters, D., and Dapp, S. (2006). "Predicting End Bearing Capacity of Post Grouted Drilled Shafts in Cohesionless Soils" ASCE Journal of Geotechnical and GeoEnvironmental Engineering, Vol. 132, No. 4. pp. 478-487 .	277
Mullins, G., Sen, R., Suh, K. and Winters, D. (2006). "A Demonstration of Underwater FRP Repair" <i>Concrete International</i> , Vol. 28, No. 1, pp. 70-73.	287
Deese, G. and Mullins, G. (2005). " Factors Affecting Concrete Flow in Drilled Shaft Construction," ADSC GEO3, GEO Construction Quality Assurance / Quality Control Conference Proceedings, Bruce, D.A. and Cadden, A. W. (eds) pp. 144-155, November.	291
Mullins, G., Sen, R., Suh, K and Winters, D. (2005). "Underwater Fiber-Reinforced Polymers Repair of Prestressed Piles in the Allen Creek Bridge". ASCE, <i>Journal of Composites for Construction</i> , Vol. 9, Issue 2, pp. 136-146.	303
Sen, R., Mullins, G., Suh, K. S. and Winters, D. (2005). "FRP Application in Underwater Repair of Corroded Piles". <i>ACI SP 230</i> , Vol. 2, pp. 1139-56.	314
Rollins, K., Lane, D., Dibb, E., Ashford, S., and Mullins, G. (2005). "Pore Pressure Measurement in Blast-Induced Liquefaction Experiments," Journal of the Transportation Research Board, No. 1936, Soil Mechanics, pp.210-220.	333
Garbin, E. and Mullins, G. (2004). "The Statnamic Analysis Workbook: A Tool for Automated Statnamic Data Analysis and Storage" <i>Journal of Engineering Technology</i> , ASEE, Washington, D.C., Fall, pp. 18-24.	344
Birmingham, P., Mullins, G., and Stokes, M. (2004). "Mobilization of Capacity During Rapid Axial Load Testing," Proceedings of the Seventh International Conference on the Application of Stresswave Theory to Piles 2004, Institute of Engineers, Malaysia, pp. 125-132.	351
Sen, R. and Mullins, G. (2004). "Developments in Underwater FRP Repair," Proceedings of ICFRC International Conference on Fibre Composites, High Performance Concretes and Smart Materials, Chennai, India, January 8-10, pp. 387-395.	358
Mullins, G., Muchard, M., and Khouri, B. (2003). "Post Grouted Drilled Shafts: A Case History of The PGA Boulevard Bridge Project," Proceedings of the Deep Foundations Institute 28 <sup>th</sup> Annual Conference on Deep Foundations, October 22-24, Miami, FL, pp. 57-71.	367
Mullins, G. (2003). "New Design Method Gives Drilled Shafts a Boost," Featured Technical Article, Deep Foundations Magazine, Deep Foundation Institute, Hawthorne, NJ.	382
Sen, R., Mullins, G. and Salem, T. (2003). Closure on paper "Durability of E-Glass/Vinylester Reinforcement in Alkaline Solution". <i>ACI Structural Journal</i> , Vol. 100, No. 2, Mar-April, pp. 265-266.	386
Mullins, G., Sen, R., Sosa, R. and Issa, M. (2003). "Full-Scale Testing of Seal Slab / Pile Interface Bond". <i>SP-211 ACI Large Scale Structural Testing</i> (Ed. M. Issa and Y.L. Mo). Farmington Hills, MI, pp 315-341	388
Mullins, G., Sosa, R., Sen, R., and Issa, M., (2002). "Seal Slab / Steel Pile Interface Bond from Full-Scale Testing," <i>ACI Structural Journal</i> , Vol 99, No. 6, pp. 757-763.	415
Dapp, S., and Mullins, G., (2002). "Pressure-Grouting Drilled Shaft Tips: Full-Scale Research Investigation for Silty and Shelly Sands," <i>Deep Foundations 2002: An International Perspective on Theory, Design, Construction, and Performance</i> , ASCE Geo Institute, GSP No.116, Vol. I, pp. 335-350.	422

Mullins, G., Lewis, C., and Justason, M., (2002). "Advancements in Statnamic Data Regression Techniques," <i>Deep Foundations 2002: An International Perspective on Theory, Design, Construction, and Performance</i> , ASCE Geo Institute, GSP No.116, Vol II, pp. 915-930.	438
Sen, R., Mullins, G., and Salem, T., (2002). "Durability of E-Glass/Vinylester Reinforcement in Alkaline Solution," <i>ACI Structural Journal</i> , Vol 99, No. 3, pp. 369-375.	454
Mullins, G., Sosa, R., and Sen, R., (2001). "Seal Slab Prestressed Pile Interface Bond from Full-scale Testing," <i>ACI Structural Journal</i> , Vol 98, No. 5, pp. 743-751.	461
Fischer, J., Mullins, G., Sen, R., Issa, M. (2001). "Studies on the Use of Powder Actuated Nails in Pile Repair," Proceedings of the Construction Institute Sessions ASCE Conference, Houston, TX, October 10-13, pp. 10-15.	470
Sen, R., Shahawy, M., Mullins, G. and Spain, J. (2001). "Effect of Environment on the Integrity of CFRP/Concrete Bond. Proceedings of the Eleventh International Offshore and Polar Engineering Conference, Stavanger, Norway, June17-22, (2001), Vol. 4, pp. 222-226.	476
Sen, R., Liby, L., and Mullins, G., (2001). "Strengthening Steel Bridge Sections using CFRP Laminates," <i>COMPOSITES Part B: Engineering International Journal</i> , Vol. 32, No. 4, pp. 309-322.	483
Thilakasiri, H., Gunaratne, M., Mullins, G., Stinnette, P. and Kuo, C., (2001). "Implementation Aid for Dynamic Replacement of Organic Soils with Sand," <i>Journal of Geotechnical and Geoenvironmental Engineering</i> , Vol. 127, No. 1, pp. 25-35.	497
Mullins, G., Dapp, S., and Lai, P., (2000). "Pressure Grouting Drilled Shaft Tips in Sand". <i>New Technological and Design Developments in Deep Foundations</i> , Dennis, N. D., et al. (ed.), ASCE, Geo Institute, GSP Vol. 100, pp 1-17.	508
Mullins, Gunaratne, Stinnette, and Thilakasiri, (2000). "Prediction of Dynamic Compaction Pounder Penetration," <i>Soils and Foundations</i> , Japanese Geotechnical Society, Vol. 40, No. 5, pp. 91-97.	525
Mullins, G., Hartley, A., Engebretson, D., and Sen, R. (2000). "Settlement Repair of Lightly Reinforced Concrete Block Walls Using CFRP," Proceedings of Second Conference of Seismic Repair & Rehabilitation of Structures (SRRS2), Mosallam, A. (ed), Fullerton, CA, March 21-22, pp. 171-180.	532
Sen, R., Shahawy, M., Mullins, G., and Spain, J., (1999). "Durability of Carbon Fiber-Reinforced Polymer/Epoxy/Concrete Bond in Marine Environment," <i>ACI Structural Journal</i> , Vol. 96, No. 6, pp. 906-914.	542
Mullins, G., Race, R. and Sen, R. (1999). "A New Device for In-Situ Testing of FRP/Concrete Adhesion". Fourth International Symposium, ACI SP-188 (Ed. C. Dolan, S. Rizkalla and A. Nanni), Farmington Hills, MI, pp. 383-391.	551
Muchard, M., Robertson, D., Mullins, G., and Stanley, B. (1998) "Statnamic and Dynamic Load Testing of an Instrumented Drilled Shaft at an I-35/I-80 Bridge in Des Moines, Iowa", <i>Second International Statnamic Seminar</i> , Tokyo, Japan, October 28-30 ISBN: 90-5809-13-17 pp. 83-98	560
Mullins, G., Garbin, E., Lewis, C., and Ealy, C. (1998) "Statnamic Testing: University of South Florida Research", <i>Second International Statnamic Seminar</i> , Tokyo, Japan, October 28-30, ISBN: 90-5809-13-17 pp. 117-132.	576
Hajduk, E., Paikowski, S., Mullins, G., Ealy, C., Lewis, C., and Hourani, N.M., (1998) "The Behavior of Piles in Clay During Statnamic, Dynamic, and different Static Load Testing Procedures", <i>Second International Statnamic Seminar</i> , Tokyo, Japan, October 28-30, ISBN: 90-5809-13-17, pp. 59-74.	592
Justason, M., Mullins, G., Robertson, D., and Knight, W. (1998) "A Comparison of Static and Statnamic Load Tests in Sand: A Case Study of the Bayou Chico Bridge in Pensacola, Florida," Presented to <i>The North American Deep Foundation Institute</i> , October 15-17, ISBN: 90-5809-13-17 pp. 43-54.	607
Robertson, D., Muchard, M., Mullins, G., and Brown, D. (1998) "Lateral Statnamic Load Testing: A new method for evaluating lateral load capacity", <i>Second International Statnamic Seminar</i> , Tokyo, Japan, October 28-30, ISBN: 90-5809-13-17 pp.	619
Mullins, G., Sen, R. and Spain, J. (1998). "Testing of CFRP/Concrete Bond," in "Fiber Composites in Infrastructure (Ed. H. Saadatmanesh and M. Ehsani)", Vol II, University of Arizona, Tucson, pp. 211-218.	629
Gunaratne, M., Stinnette, P., Mullins, G., Kuo, L., and Echelberger, W. Jr., (1998). "Compressibility Relations for Peat and Organic Soil," <i>Journal of Testing and Evaluation</i> , ASTM, Vol. 26, No. 1, pp. 1-9.	637

- Stinnette, P., Gunaratne, M., Mullins, G., and Thilakasiri, S., (1997). "A Quality Control Programme for Performance Evaluation of Dynamic Replacement of Organic Soil Deposits," *Geotechnical and Geological Engineering*, Vol.15, No. 4, pp. 283-302. 646
- Thilakasiri, S., Mullins, G., Stinnette, P., Gunaratne, M., and Jory, B., (1996). "Analytical and Experimental Investigation of Dynamic Compaction Induced Stresses." *International Journal of Numerical and Analytical Methods in Geomechanics*, Vol. 20, No. 10, pp. 753-767. 666
- Thilakasiri, H., Gunaratne, M., Mullins, G., Stinnette, P., and Jory, B., (1996). "Investigation of Impact Stresses Induced in Laboratory Dynamic Compaction of Soft Soils," *International Journal for Numerical and Analytical Methods in Geomechanics*, Vol. 20., pp.753-767. 681
- Thilakasari, S., Mullins, G., Stinnette, P., and Gunaratne, M., (1996). "Discussion of Impact of Weight Falling Onto the Ground," Paper No. 5957, *ASCE Journal of Geotechnical Engineering*, pp. 415-416. 696
- Gunaratne, Ranganath, Thilakasiri, Mullins, Stinnette, and Kuo, (1996). "Study of Pore Pressures Induced in Laboratory Dynamic Consolidation," *Computers and Geotechnics*, Vol 18., No. 2, pp.127-143. 698
- Sen, R., Rosas, J., Mullins, G., Liby, L., Sukumar, S. and Spillett, K. (1996) "Field Measurement of Transfer Length" in *Fiber Composites in Infrastructure ICCI'96*, First International Conference on Composites in Infrastructure (Ed. H. Saadatmash & M. Ehsani), Tucson, AZ, pp. 536-547. 715
- Engebretson, D., Sen, R., Mullins, G. and Hartley, A., (1996). "Strengthening Concrete Block Walls with Carbon Fiber". *Materials for the New Millennium, Proceedings of the Materials Engineering Conference Volume 2*, ASCE, New York, NY, pp. 1592-1600. 727
- Hartley, A., Mullins, G. and Sen, R. (1996) "Repair of Concrete Masonry Block Walls using Carbon Fiber", *Advanced Composite Materials in Bridges and Structures* (Editor M.El-Badry), Canadian Society of Civil Engineers, Montreal, P.Q. pp. 795-802. 736
- Sen, R., Liby, L., Mullins, G. and Spillett, K., (1996). "Strengthening Steel Composite Beams with CFRP Laminates". *Materials for the New Millennium, Proceedings of the Materials Engineering Conference Volume 2*, ASCE, New York, NY, pp. 1601-1607. 744

# Improving Vibrating-Wire Noise Immunity Using Spectral Analysis

Ken Stevens<sup>1</sup>, Larry Jacobsen<sup>2</sup>, Tom Weinmann<sup>3</sup>, Gray Mullins<sup>4</sup>

**Abstract:** Because vibrating-wire gages offer long-term stability, engineers often use them in static structural monitoring applications to measure strain and displacement. Vibrating-wire sensors are durable, stable, and accurate when making various measurements over extended periods of time. They have been used to measure strain, pressure, tilt, displacement, and load, and are found in structural, hydrological, and geotechnical applications. Traditional time-domain methods that read vibrating wire sensors suffer from susceptibility to external noise, sometimes rendering measurements unusable. This paper describes a new method using spectral analysis for vibrating-wire sensors, resulting in improved noise immunity. In a representative noise test, spectral analysis produced frequency errors of less than  $\pm 0.02$  percent of reading compared to errors exceeding 100 percent of reading using traditional methods. The new spectral analysis also improves measurement precision in the absence of external noise, achieving a precision of 0.001 Hz rms.

**Keywords:** vibrating wire, spectral analysis, noise immunity, time domain

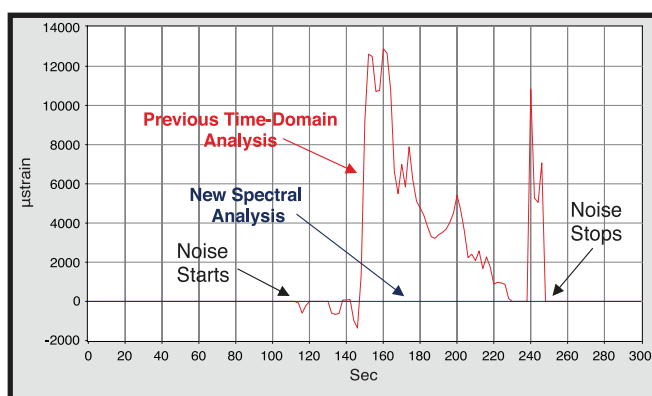


Fig. 1. Comparison of noise immunity of time-domain analysis with spectral analysis during a noise event

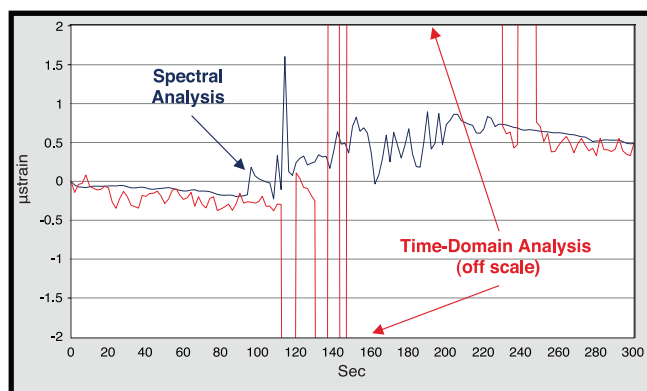


Fig. 2. Zoomed y-axis with the data in Fig. 1

## Introduction

Structural and geotechnical engineers often use vibrating-wire sensors to measure strain, pressure, tilt, displacement, and load. These sensors have a reputation for being accurate, stable, and durable—making them well-suited for long-term static monitoring. Despite their acceptance, vibrating-wire sensors are sometimes plagued by a susceptibility to external electromagnetic noise. This weakness can produce unusable data, requiring data analysts to devote considerable effort to qualifying their data. This susceptibility to external noise is especially difficult in real-time alarm systems where post-collection analysis is not possible.

This paper discusses a new frequency-domain approach that uses spectral analysis to read vibrating-wire sensors, which improves noise immunity when compared to traditional time-domain methods. Fig. 1 shows this improved noise immunity when a drill motor was turned on near a vibrating-wire strain gage.

Although the actual strain changed by only a few tenths of a  $\mu\text{strain}$  during the test, the time-domain analysis gave errors of 12,000  $\mu\text{strain}$ . As shown by Fig. 2, the spectral analysis gave errors of typically less than  $\pm 0.5$   $\mu\text{strain}$  during the same noise event.

<sup>1</sup> Industrial Group Manager, Campbell Scientific, Inc., 815 W 1800 N, Logan UT, 84321 Email: kstevens@campbellsci.com

<sup>2</sup> Vice President of Research, Campbell Scientific, Inc., 815 W 1800 N, Logan UT, 84321 Email: ljacobsen@campbellsci.com

<sup>3</sup> Principal and Group Manager, CTL Group, 5400 Old Orchard Road, Skokie, IL. Email: tweinmann@CTLGroup.com

<sup>4</sup> Associate Professor, University of South Florida, 4202 E. Fowler Ave., Tampa, FL. Email: gmullins@eng.usf.edu

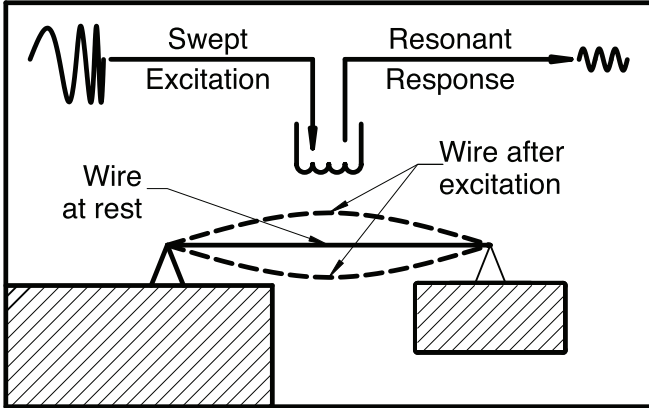


Fig. 3. Vibrating-wire measurement principles

This paper describes the old and new processing methods and describes two monitoring applications that use the new spectral analysis approach to reading vibrating-wire sensors.

### Vibrating-Wire Measurement Principle

A vibrating-wire sensor couples an external physical parameter, for example strain or displacement, to the tension of a taut wire within the gage. Because the tension in the wire is related to the wire’s fundamental resonant frequency (see Equation 1), measuring the resonant frequency of the wire measures the external physical parameter.

$$f = k \sigma^{1/2} \tag{1}$$

where  $f$  = fundamental resonant frequency  
 $k$  = combined wire constants  
 $\sigma$  = wire tension (force/area)

The taut wire in a vibrating-wire sensor is similar to a guitar string. By increasing the tension in the wire (or guitar string), the wire’s resonant frequency increases. While energy is coupled to a guitar string by plucking it, energy is coupled to the wire in a vibrating-wire sensor with a frequency-swept magnetic field that is included in the sensor (see Fig. 3). Once the wire is vibrating, data-acquisition equipment determines the resonant frequency of the wire and converts this resonant frequency into the desired engineering units. The following section describes the traditional time-domain approach used to determine the wire’s resonant frequency.

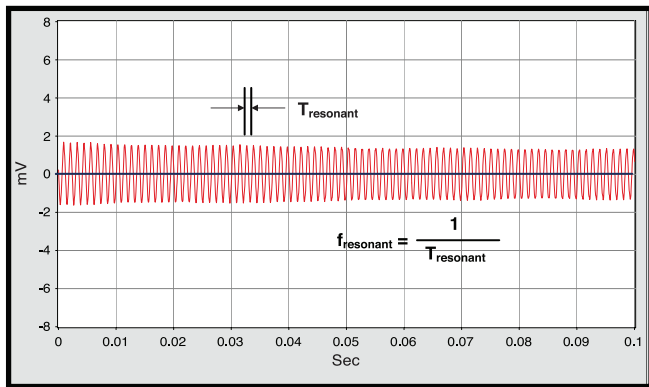


Fig. 4. Vibrating-wire time-domain response function

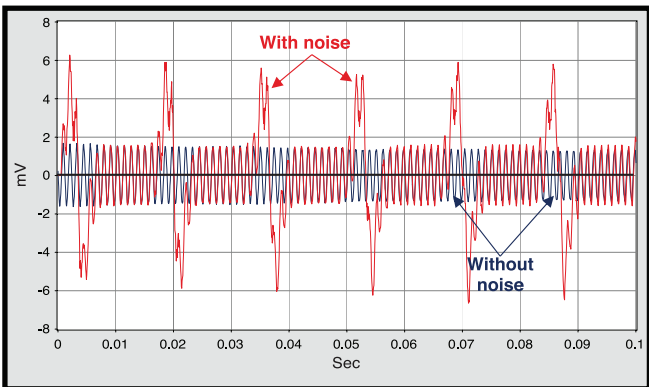
### Reading Vibrating-Wire Sensors: Time-Domain Analysis

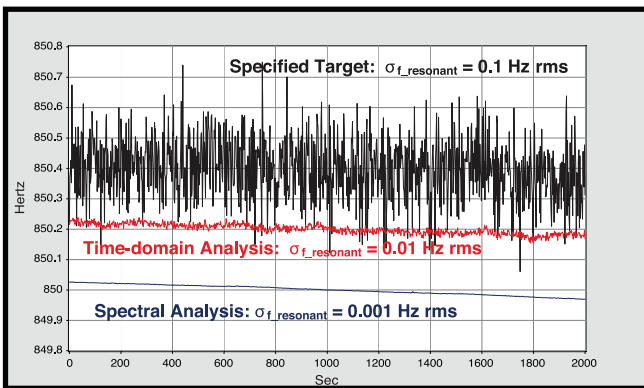
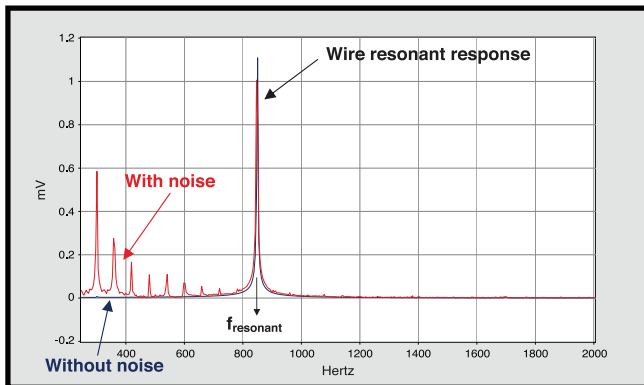
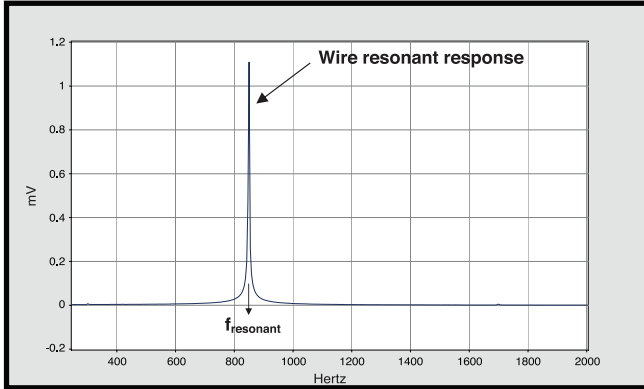
The traditional method for reading vibrating-wire sensors analyzes the response from a sensor as a

function of time using period averaging. This technique excites the wire and measures the average time between a predetermined number of positive-slope zero crossings in the wire’s response to give the wire’s resonant period. Fig. 4 demonstrates this process. The resonant frequency is the reciprocal of resonant period.

In a low-noise environment, this is an effective method of determining the resonant frequency of the wire. It has been successfully integrated into many data acquisition products that simplify its application with dedicated hardware modules, programming instructions, and software. This approach struggles, however, in noisy environments, as shown by the erroneous readings in Fig. 1.

Fig. 5 shows the problem of measuring zero crossings in the presence of external noise. The external noise disrupts the signal, erroneously removing zero crossings. In general, external noise may introduce errors by adding zero crossings to, or by removing zero crossings from, the uncorrupted signal.





Even with this difficulty, engineers are sometimes able to gather useful data in noisy environments. However, this requires extra effort to eliminate noise sources or schedule measurements around periods of increased noise. An alternative approach requires data analysts to identify and discard bad data by comparing measurement data before and after noise events.

Given these challenges, instrumentation engineers set out to find a method to determine the resonant frequency of vibrating-wire sensors with improved noise immunity. The following section describes this method.

## Reading Vibrating-Wire Sensors: Spectral Analysis

The spectral-analysis approach analyzes the response of the wire as a function of frequency. Because we are trying to determine the resonant frequency of a tensioned wire, then it makes sense to analyze the response of that wire as a function of frequency, rather than time. The approach applies a Fourier transform to the sampled response to move it from the time-domain to the frequency domain (see Fig. 6). By identifying the frequency of the peak response from the resulting spectrum, we have identified the resonant frequency of the wire.

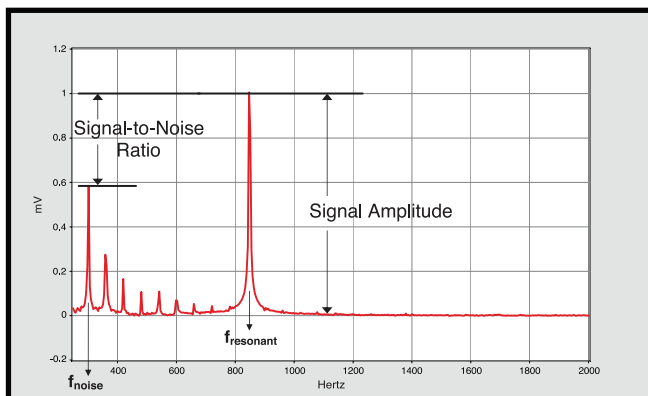
With the data converted to the frequency domain, the sensor's resonant frequency can be determined even in the presence of external noise. As shown in Fig. 7, spectral analysis allows us to distinguish the sensor's response from the noise.

Spectral analysis also provides improved measurement precision in the absence of external noise (Fig. 8). Vibrating-wire sensor manufacturers typically want to resolve changes in resonant frequency to 0.1 Hz. Time-domain analysis, in the absence of noise, can achieve measurement precision of 0.01 Hz rms. Spectral-analysis achieves measurement precision of 0.001 Hz rms, a significant improvement.

Transforming the sensor's response from the time domain into the frequency domain provides additional advantages—specifically, diagnostics that are not available with the time-domain approach. These include (see Fig. 9) signal amplitude, signal-to-noise ratio, and competing noise frequencies. These diagnostics are useful for a variety of purposes including validating measurements, understanding and identifying noise sources, and determining long-term sensor health.

In summary, the spectral-analysis approach provides noise immunity, improved measurement resolution, and useful diagnostics for reading vibrating-wire sensors—all significant improvements to those who rely on vibrating-wire sensors.





## Implementation of the Spectral Analysis Technique

The usefulness of spectral analysis to read vibrating-wire sensors depends on its suitability for field use. The device must be cost effective, rugged, low power, and easily integrated with existing data-acquisition equipment.

Campbell Scientific, a data-acquisition company based in Logan, Utah, previously developed time-domain methods to read vibrating-wire sensors. Armed with this experience, instrumentation engineers at Campbell Scientific developed a new vibrating-wire readout module that incorporates spectral analysis

(patent pending). This new module, the model AVW200, excites the sensor's wire, samples the response, applies the Fourier transform, and returns the measurement result and diagnostics to the datalogger—all within two seconds.

The AVW200 and its wireless counterpart, the AVW206, have been available since early in 2008. Since then, they have been successfully used in a number of applications. The following sections describe how the new technology benefited two large bridge projects: the widening of the Huey P. Long Bridge in Louisiana, and the reconstruction of the I-35 St. Anthony Falls Bridge in Minnesota.

### Case Study 1: Huey P. Long Bridge Widening Project



Fig. 10. Huey P. Long Bridge



Figure 11. Rendering of planned renovation

The four main spans of the Huey P. Long Bridge extend nearly 2400 feet over the Mississippi River in New Orleans, Louisiana. (Fig. 10) This cantilevered steel through-truss bridge opened to traffic in 1935 and is owned and operated by the New Orleans Public Belt Railroad. The bridge currently carries dual rail lines between the trusses and two lanes of vehicular traffic cantilevered to the exterior of each truss. Based on the need to improve vehicular traffic flow and constraints due to uninterrupted rail traffic, the Louisiana Department of Transportation and Development (LA DOTD) decided to widen the bridge rather than replace it.

The bridge widening will facilitate an increase in roadway width on each side of the bridge from its current width of 18 feet to 40 feet. The widening will entail the addition of upstream and downstream trusses parallel to the existing truss. The bridge piers are being modified with additional concrete encasements and steel frame to support the two new widening trusses (Fig. 11).

A structural health-monitoring program is included in the construction contract as a proactive measure to assess whether the anticipated amount of load is being transferred from the widening truss members to the existing truss members.

CTLGroup was awarded the contract to design and install the truss monitoring system according to the specifications for the Huey P. Long Bridge widening project. The truss monitoring specification required the following:

- Determination of initial dead-load stresses in existing eyebar members
- Installation of strain gages for measurement of construction-related stresses in 433 members
- Installation of strain gages for measurement of live-load stresses in 31 members
- Installation of biaxial tilt meters on each of the five existing bridge piers
- Monitoring system to read the gages, make comparisons with predicted values, and provide daily reports throughout the three-year construction process
- Performing load testing to calibrate the monitoring systems

A total of 433 existing truss members are monitored with an array of 827 static and dynamic strain gages designed to measure axial and bending load effects. In addition, tilt meters monitor the inclination of the piers. For the static system, CTLGroup chose vibrating-wire strain gages based on cost, built-in temperature compensation, and the ability to run long distances with lead wires.

The truss-monitoring data-acquisition system is composed of two separate monitoring systems: a static-load monitoring system and a live-load monitoring system (Fig. 12). The static system uses 23 track-side-mounted Nema enclosures that contain AM16/32 multiplexers to read 777 vibrating-wire sensors on 433 members. In addition, five piers were monitored using ten vibrating-wire tilt meters as well as ambient temperature, wind speed, and wind direction. Because of the need for wireless communication between multiplexers, dataloggers, and central computer, the system was configured using a combination of 24 AVW206 modules and RF401 spread spectrum radios. The multiplexers read the sensors, perform the signal processing, and transmit the data wirelessly to one of four CR1000 data loggers mounted on the track-side hand rail. These dataloggers then transmit the data wirelessly to the MTI office trailer approximately one-fourth mile from the bridge site.

The purpose of the system is to measure stresses (strains) in identified members and compare with predicted response during the bridge-widening construction process. This is accomplished by:

- Establishing limits for predicted response for staged construction
- Accounting for baseline fluctuations (traffic/locomotive loads and temperature effects)
- Comparing measured with predicted response
- Automated flagging of limits outside of predicted response

The system runs continuously and collects data approximately once every ten minutes. It posts the data to a password-protected website. The website visually flags (by color) data that are outside predetermined limits.

With hundreds of vibrating-wire sensors involved, this monitoring project provided an appropriate setting to apply the new spectral-analysis method. The outcome was very positive. Historically, an application with so many vibrating-wire measurements would require extra effort to validate measurements and identify noise-compromised data. Typically, some data would be lost due to noise interference. In this case, however, spectral analysis eliminated noise issues. No data were lost, and no extra effort was needed to identify noise-compromised data.

The diagnostics provided by the new method also proved to be beneficial, and they were used extensively throughout the project. CTLGroup reported that it could not have completed the monitoring project without the AVW206. Though they have previously used time-domain solutions, this experience has put them solidly behind the spectral analysis method.

The diagnostics provided by the new method also proved to be beneficial, and they were used extensively throughout the project. CTLGroup reported that it could not have completed the monitoring project without the AVW206. Though they have previously used time-domain solutions, this experience has put them solidly behind the spectral analysis method.



Fig. 12. Placement of gages



## Case Study 2: St. Anthony Falls Bridge Foundation Monitoring

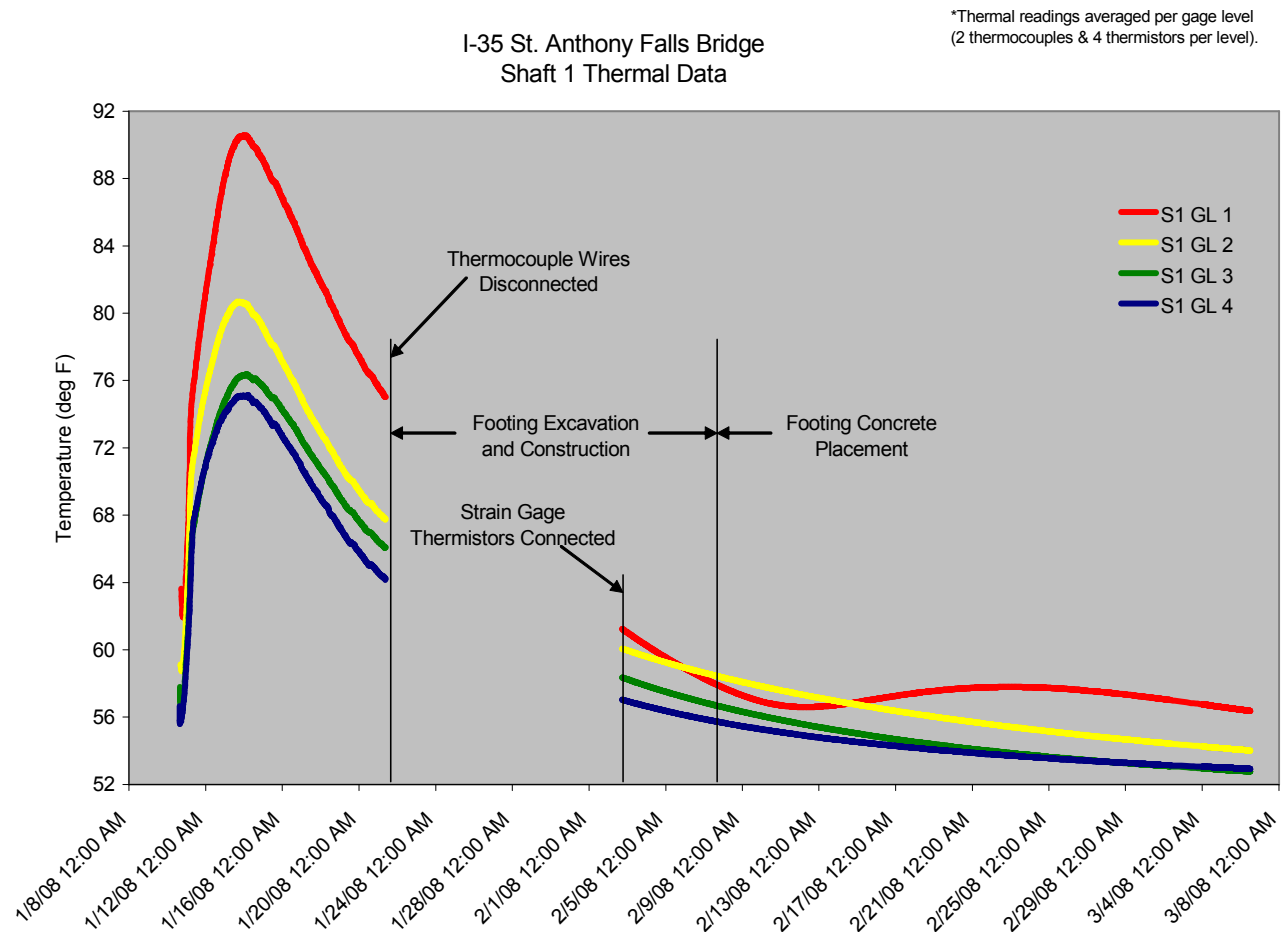
On August 1, 2007, the I35W St. Anthony Falls Bridge over the Mississippi River in Minneapolis, Minnesota, collapsed in the middle of rush hour. The collapse killed 13 people and opened the eyes of policymakers and engineers alike to the serious nature of America's failing infrastructure. A tremendously cooperative effort to quickly and safely replace the bridge resulted. It harnessed today's technologies and continues to provide insight into bridge performance and long-term health. To that end, a program was instituted to show how internal instrumentation could be used to increase quality assurance, monitor construction loads, and subsequently show traffic- and wind-load effects on the long-term pier performance.

This was the first part of a larger program involving the entire bridge, and pertained only to one of the three elevated piers, specifically the Southbound Pier 2 columns and foundations. Therein, two types of strain gages and thermometers were installed to monitor three phases of the bridge and foundation system: (1) internal concrete curing temperature of the foundation elements, (2) construction loads, and (3) long-term health.

Four levels of six strain gages each were installed in two of the eight 100-ft-deep drilled shaft foundation elements (48 gages total). Gage levels were designated to identify load-carrying contributions from various soil layers. These levels were at the top of shaft (ground surface), top of soft rock, top of competent rock, and bottom of shaft.

Each gage level consisted of four vibrating-wire strain gages positioned at quarter points around the circumference of the shaft cross section. Two of the four vibrating-wire gages at each level were coupled with a resistive strain gage situated at opposite sides of the shaft. This scheme provided long-term stability with the slower vibrating-wire gages along with fast measurements from the resistive gages during dynamic events.

In addition to the foundation measurements, two levels of four vibrating-wire strain gages were installed in



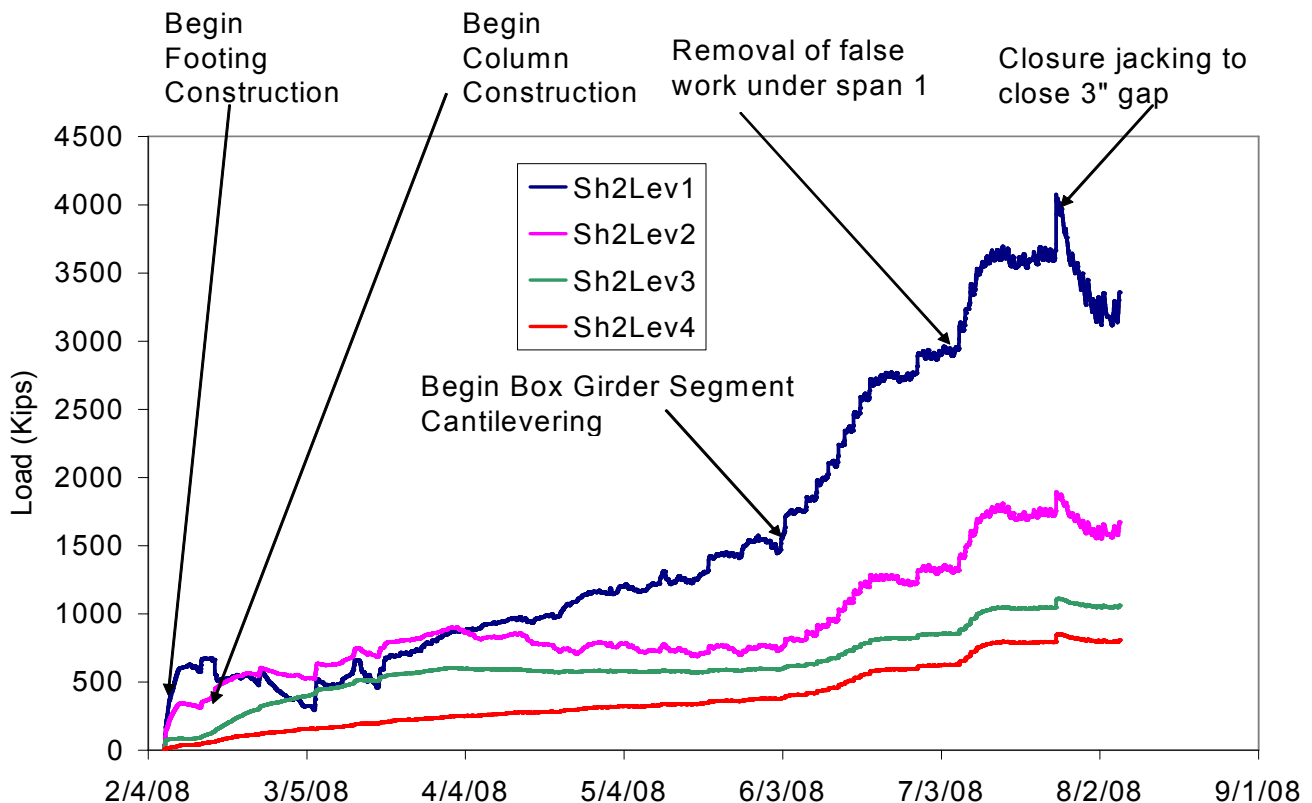
the two columns supporting the two southbound concrete box girders (16 total vibrating-wire gages). The first level was at the mid-height of the columns; the second was at the base of the column. Mid-level gages were duplicated with resistive strain gages for measuring short-duration transient events.

Two separate data acquisition systems were used to measure the vibrating-wire and resistive strain gages. The vibrating-wire gages were read with the AVW200 and recorded with a CR1000 datalogger, including the vibrating-wire internal thermistor recordings. The resistive gages were measured with Campbell Scientific's CR9000 high-speed data-acquisition system. Vibrating-wire gages were sampled every two minutes, and the sample period was later slowed to a 15-minute interval. Resistive gages were sampled at 100 Hz and the average, maximum, and minimum values were recorded every 15 minutes. Both systems were self-powered with solar panels and deep-cycle batteries, and each system uploaded data to a remote host server using cellular modems. This arrangement allowed the data acquisition systems to operate independently of on-site construction power and communications, and they did not interfere with day-to-day construction activities. Key aspects to both data acquisition systems were remote data monitoring, remote program downloading, and remote reconfiguration as the data acquisition requirements increased and decreased.

Phase 1 involved internal concrete temperature monitoring. The embedded thermistors internal to the vibrating-wire strain gages provided one means of assuring that concrete temperatures stayed within acceptable ranges. Fig. 13 shows the internal shaft temperature at each of the gage levels over the course of shaft and footing construction.

Phase 2 monitored increasing loads and how those loads were distributed down the length of the shafts as construction progressed. Fig. 14 shows the load on one of the shafts beneath the Pier 2 footing, along with construction milestones. This figure shows that almost 800 kips of the 3500-kip total shaft load was resisted in end bearing, and that about half the remaining load was carried by the rock layers side shear. Load steps are evident between May 29 and July 9, showing the placement of each of the 15 box-girder segments.

Phase 3 is ongoing. It uses the calibrations and correlations derived during Phase 2 to monitor the long-term health of the bridge. Variations in shaft and column loads can identify aberrant conditions, and alert officials to take appropriate actions.



This project, as with Case Study 1, was well-suited to demonstrate the benefits of the spectral analysis method for reading vibrating wire sensors. Not only did this project involve a large number of vibrating-wire sensors, but the setup was located 5 ft from a 1000-KW generator. As before, the outcome was very positive. Even with the large generator nearby, no data were lost due to noise, and no extra analyses were needed to determine if measurements had been compromised by noise. In fact, the raw data were posted automatically to a publicly-available website every 15 minutes, without review or qualification. Because of the success of the new method in this project, the program manager already has plans to make it a part of two future bridge-monitoring projects.

## **Conclusion**

This paper introduced spectral analysis as an improvement over the traditional time-domain approach to read vibrating-wire sensors. Spectral analysis improves immunity to external noise, provides better precision, and gives useful measurement diagnostics. These benefits have been validated in the field with the AVW200 vibrating wire spectrum analyzer. The new approach has been successfully applied in large and small monitoring projects, and it was key to the success of the two bridge projects described above—eliminating noise as a factor in vibrating wire measurements. As a field-proven technology with clear theoretical support, spectral analysis is a major step forward in vibrating-wire measurement technology and should replace the traditional time-domain approach.

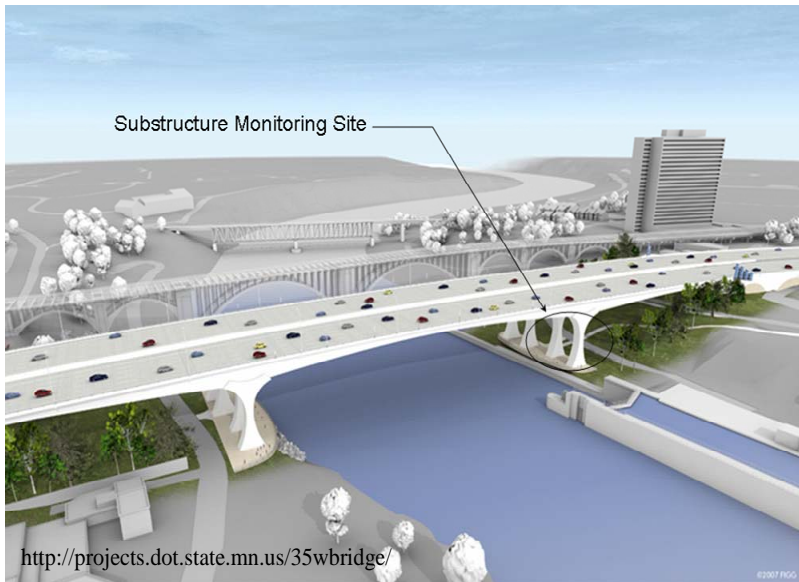
## **Acknowledgements**

We are grateful to the Louisiana Department of Transportation and Development, CTLGroup, the Minnesota Department of Transportation, and the University of South Florida for supporting the production of this paper.

## Guest Commentary

By: Gray Mullins

### I-35W Bridge Replacement, With an Ounce of Prevention



Interstate Highway I-35, through Minnesota, has a north-south orientation but I-35 W serves to tie together the easterly north leg and the westerly south leg as a connector, through the city of Minneapolis. This highway connector meets I-35, from the north, just north of the Mississippi River at St. Anthony Falls and turns west after crossing the river with the new, eight lane, highway bridge. Its predecessor collapsed on August 1, 2007 at the peak of the afternoon rush hour traffic. This collapse killed 13 people and opened the eyes of policy makers and engineers alike to the serious nature of America's failing infrastructure.

A tremendous cooperative effort ensued to quickly and safely replace the bridge. The urgency of this task opened minds and softened attitudes resulting in the harnessing of the latest technologies to build and monitor the long term performance of the structure. To that end, the goal of the Federal Highway Administration, through their consultants (the University of South Florida, Tampa and Foundation & Geotechnical Engineering, Plant City) determined how internal instrumentation could be utilized to increase quality assurance, monitor construction loading, and subsequently show traffic and wind loading effects for the long-term pier performance.

This was the first part of a larger program involving the entire bridge structure and included only the South Bound (SB) Pier 2 columns and foundations. Therein, two types of strain gages and thermocouples were installed to monitor three conditions of the bridge's foundation system: (1) the curing temperatures of the concrete foundation elements, (2) construction loading effects on these foundation elements, and (3) long-term monitoring of the structural elements as they continue to perform.

For the sake of brevity I will only focus on the construction load monitoring, item (2) above. Many of the design assumptions used by the engineer are based on probability and historical, codified data (Design Codes). However, with the new sensor technology and remote accessing it will be possible to view in real-time the structural responses to a wide range of loading conditions. With this knowledge one can determine the efficiency of the design and may be able to foresee areas that may be working close to their ultimate capacity so remedial measures can be put in place before an ultimate condition is encountered.

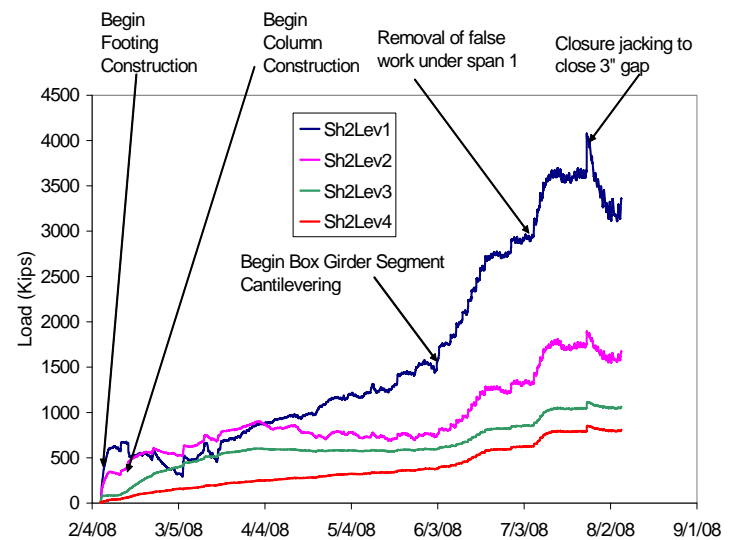
The traditional engineering design uses margins of error (safety factors) which will inflate the predicted loads, reduce the estimated capacity of the structure or include a combination of the two. The result is that the worst case scenarios, that control the design, may never occur and; hence, the structure's design is never fully verified and optimized. One way for the design engineer to confirm and safely optimize his design is to accurately determine the loading as it is applied and actually view the structures response to these loads.

The FHWA goal was to establish a prototypical, monitoring system (at Pier 2 South) for the expedited, I-35W bridge replacement program in order to develop a data-base that will more accurately describe the loading / structural response conditions during construction and for both short and long-term operational aspects for this type structure. The monitoring for the entire Bridge, including the prototypical work by USF/FGE at the SB, Pier 2, will be carried on by the Minnesota Department of Transportation in conjunction with the University of Minnesota.

The structure is founded on steel H sections at the south abutment and on drilled shafts at Piers 2, 3, and 4. The superstructure is a combination of cast-in-place (cip), concrete box-girders built on false-work at the two side spans. The main spans are pre-cast, segmental, concrete box-girders built in free cantilever. The main span piers are positioned on footings that are supported on drilled shafts. Instrumentation for two of the eight drilled shafts at SB, Pier 2 included four levels of 6 strain gauges in these 100' deep shafts. Gauge levels were designated so as to identify load carrying contributions of the various levels of rock formations along the shaft lengths. Gauge levels were at the top of shaft (ground level), top of soft rock, top of competent rock and at the bottom of the shaft.

Each gauge level consisted of 4 vibrating wire (VW) strain gauges positioned at quarter points around the circumference of the shaft cross section. Two of the four VW gauges at each level were coupled with resistance type strain gauges which were situated at opposite sides of the shaft. This scheme capitalized upon the long term stability associated with VW strain gauges and their capability to take instantaneous readings from dynamic loading events.

The attached graph (below) clearly charts the evolution of the construction loads and their accumulation onto the drilled shafts. Correspondingly, we can see how resistance to these loads is distributed: Sh2 Lev 1 (top of Drilled shaft) = 3200 kips; Sh2 Lev 2 = 1500 kips; Sh2 Lev 3 = 900 kips and Sh2 Lev 4 = 800 kips.



This newsletter was produced by:

#### Bridge Team

Design and Engineering Support Section  
Public Works Department  
601 E. Kennedy Blvd. 23<sup>rd</sup> Floor  
Tampa, FL 33601  
Phone number: (813) 272-5912  
<http://www.hillsboroughcounty.org/publicworks/resources/publications/home.cfm>

#### A Special Thanks to our Guest Commentator:

*Gray Mullins, Ph. D., P.E.*  
Associate Professor  
Department of Civil and  
Environmental Engineering,  
University of South Florida, Tampa  
Florida

#### Editor:

Nils Olsson, P.E., Bridge Team Leader  
Phone number: (813)-307-1844  
E-mail: [OlssonN@hillsboroughcounty.org](mailto:OlssonN@hillsboroughcounty.org)

#### Art/Technical Director:

An-Di Nguyen, Highway Design Team



## SEAL SLAB PRESTRESSED PILE INTERFACE BOND FROM FULL-SCALE TESTING

Gray Mullins, Ruben Sosa, Rajan Sen and Moussa Issa, University of South Florida, Tampa, FL, USA

This paper presents experimental results from a study to assess the interface bond between a cast-in-place concrete seal slab and prestressed concrete piles in cofferdams. Three different seal slab placement conditions - fresh water, salt water and bentonite slurry - were evaluated and the results compared against controls where no fluid had to be displaced by the concrete. Normal pile surfaces were investigated. Additionally, the situation of "soil caked" piles was also investigated. Both model and full-scale tests were conducted. In the model tests, twenty eight 15 cm square prestressed sections were used with the embedment depth varied between  $d-2d$ , where  $d$  is the width of the pile. In the full-scale tests, 16 specimens were tested. The prestressed piles were 36 cm square with the embedment varied between  $0.5d-2d$ . Four of the sixteen piles were cast with embedded gages located at the top, middle and bottom of the interface region.

The results showed that loads were transferred to the piles over an effective area, not the entire embedded depth. Significant bond stresses developed even for the worst placement condition. Recommendations are made for revising current values in specifications.

Keywords: seal slab, cofferdam, bond, concrete, bentonite, salt water, full-scale, prestressed, pile, foundation.

### INTRODUCTION

Seal slabs are unreinforced concrete slabs cast inside cofferdams to prevent the intrusion of water and provide a dry working surface for subsequent construction (see Figure 1). Concreting is typically carried out by displacing water (or natural slurry in cases where the cofferdam supports the sides of an excavation) using a *tremie*. A tremie is essentially a funnel with a long pipe that places concrete directly on the bottom of the cofferdam. Because the concrete does not fall through the water, cement is not washed away and there is no segregation of coarse and fine aggregates. A series of tremie pipes are used to limit the flow of concrete in the horizontal direction and to prevent the build-up of excessive laitance<sup>1</sup>.

As the function of the seal slab is primarily to provide a dry working surface, its design is relatively unsophisticated. The slab depth is selected so that its weight balances the maximum uplift forces. Thus, a 10 m unbalanced head would require a 4 m thick seal slab since concrete density is approximately two and a half times that of water. Such a calculation neglects the frictional resistance that develops at the interfaces between the seal slab and foundation elements such as piles or drilled shafts.

The Florida Department of Transportation (FDOT) requires<sup>2</sup> the seal slab to cure for at least 72 hours before the standing water (or slurry) inside the cofferdam can be pumped out. At that time, the seal slab experiences full uplift pressure due to imbalance in hydrostatic pressure inside and outside of the cofferdam. Rational design therefore requires information on the interface shear corresponding to the 72-hour concrete strength. Unfortunately, no published data is available even though the earliest work on interface shear between two concrete surfaces was reported as far back as 1914<sup>3</sup>.

In the absence of experimental data, specifications provide interface shear values that are of necessity conservative. For example, AASHTO<sup>4</sup> states that "*in seals, the bond between timber, steel or concrete piles and surrounding concrete may be assumed to be 10 psi*" (69 kPa). The 1998, Florida Design Guidelines<sup>5</sup> limited the interface bond between the

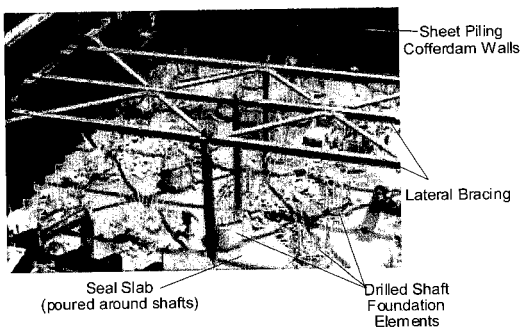


Figure 1: Seal Slab in Cofferdam Construction  
(Courtesy Georgia D.O.T.)

seal slab and concrete piles to 276 kPa though it was only set at 34 kPa for steel piles. The larger values permitted in Florida may be due to the local experience associated with the large number of bridges crossing waterways, a relatively high water table, and the predominance of highly pervious cohesionless (sandy) soils that result in excavations quickly filling with inflowing ground water.

Recognizing that the allowable values were too low, in 1997 the Florida Department of Transportation issued a request for proposals (RFP) to assess this bond from full-scale tests. In January 1998, the University of South Florida commenced a two-year research program to investigate this problem. Although the goal of the study was to evaluate bond on the basis of full-scale tests, a 1/3rd scale pilot study was initially carried out to evaluate critical parameters and to develop an efficient method of testing. Following completion of this study, a limited number of full-scale tests were conducted to assess the interface seal slab/pile bond characteristics for prestressed concrete and steel piles and to recommend suitable values for design. This paper presents results relating to the seal slab / concrete interface bond. A companion paper provides the corresponding results for steel piles<sup>6</sup>. The complete experimental results as well as the comparative finite element modeling may be found elsewhere<sup>7, 8</sup>.

### **RESEARCH SIGNIFICANCE**

No studies have previously been carried out to evaluate the seal slab/concrete interface bond for conditions that may be directly used in design specifications. This study provides the first such experimental data from full-scale tests. Results of the study have already led to changes in the latest specifications.<sup>9</sup> Therein, the allowable stresses are greater permitting thinner seal slabs and bringing about significant savings in construction costs.

### **OBJECTIVES**

The overall goal of the study was to recommend interface bond values for seal slab and piles that could be directly used in FDOT's design specifications. These values were to be based on full-scale tests on specimens prepared in accordance with current FDOT specifications for

commonly encountered conditions. Variables examined were the pile embedment depth, pile surface, pile material (steel or concrete), and the type of fluid displaced by the concrete.

### **EXPERIMENTAL PROGRAM**

A seal slab is subject to uplift pressures that are resisted in part by its weight and in part by shear resistance that develops at the pile/slab and sheetpile/slab interfaces as shown in Figure 2a. The same load transfer characteristics can be simulated by applying tensile loads to the pile and compressive loads to the seal slab (Figure 2b). In essence, the determination of the interface bond translated into conducting 'pull-out' tests on individual piles embedded in the seal slab; such an equivalent system was used in this study.

The reaction frame required to remove the piles from a seal slab had to meet multiple requirements of capacity, economy and portability. An adaptable design was also required to accommodate the differing connections for the steel and concrete pile specimens. Additionally, it needed to be integrated with electronic devices that permitted measurement of load and displacement.

A key parameter in the design of the test equipment was capacity. An upper limit could be determined on the basis of the ultimate tensile capacity of the prestressed pile. This depended on the pile size, concrete strength and the effective prestress. The greater the capacity, the larger and heavier the equipment, making testing that much more difficult (and expensive).

Uncertainties associated with bond strength predictions were addressed with a comprehensive pilot study using small-sized piles. A scale model study was carried out to develop an efficient testing method and also to identify critical parameters for the subsequent full-scale program. Brief details from both studies, a complete set of results, and their analysis are presented.

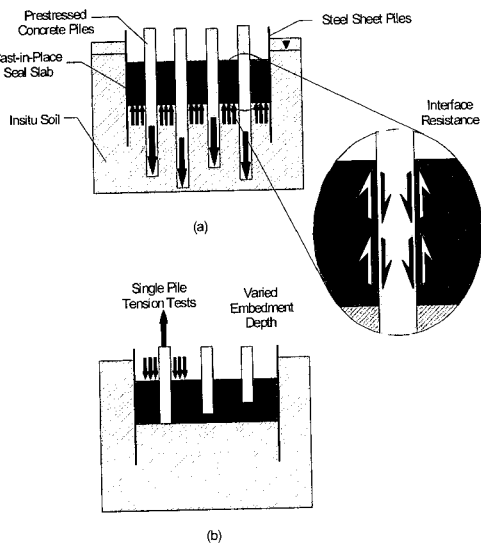


**Figure 2: (a) Field Loading, (b) Uplift Load Simulation**

**PILOT STUDY**

The pilot study simulated three different seal slab placement conditions involving (1) salt water (2) fresh water and (3) drilling fluid. Results were compared against the controls where no fluid was displaced by the concrete. One-third scale was selected since this allowed standard 45 cm prestressed piles to be exactly modeled<sup>10</sup>. Two different surface conditions - natural and soil-caked - were investigated.

Based on results of preliminary trials, the maximum interface bond between the two concrete surfaces was estimated to be about 1.7 MPa. This value was used to determine the maximum embedment depth that would not cause tension failure of the prestressed pile. As a result, three different embedment depths  $d$ ,  $1.5d$  and  $2d$  ( $d$  is the side of the pile) were investigated. For each embedment depth, two specimens were tested, i.e. 24 tests were conducted (4 conditions x 3 embedment depths x 2 specimens). In addition, four soil-caked specimens were tested - one for each placement condition - for an embedment depth of  $2d$ .

A total of 28 prestressed piles were tested. Square prestressed piles (1.22 m long, 15 cm wide) were fabricated at a commercial prestressing facility. During fabrication, 3.2 cm threaded Dywidag bars were embedded centroidally in the specimens to provide a convenient attachment for pulling the specimens (shown in Figures 3 and 4). Complete details may be found in the final report<sup>7</sup>.

**Cofferdam Simulation**

Four, 0.76 m high wood boxes with inside dimensions of 1.4 m x 1.4 m were fabricated to simulate the four excavation conditions. Plastic sheeting was used to make the boxes watertight. Wood templates were prepared so that the piles could be accurately positioned inside the form. The piles were spaced at 3 x pile size, i.e. the center to center distance was 0.45 m (3 x 0.15). The edge distance from the center line was  $1.5d$  or 0.23 m.

As all the specimens were the same length and the seal slab the same thickness, the three different embedment depths of  $d$ ,  $1.5d$  and  $2d$  were accommodated by varying the bonded and debonded lengths. For the 15 cm piles, this length varied between 15 ( $d$ ) to 30 cm ( $2d$ ). All bonded regions were at the bottom of the pile/seal slab. The debonded area was achieved by using bitumen covered with felt paper rapped in duct tape (Figure 3). A soil-caked surface was simulated by applying a paste consisting of a viscous mixture of the clay mineral kaolinite and water with a trowel. The clay had to be kept moist to prevent it from flaking off when it dried.

Three of the four simulated cofferdams were initially filled with either (1) fresh water, (2) 3% salt water, or (3) drilling fluid. The latter was made by mixing dry, high yield bentonite and fresh water to achieve slurry properties similar to those in the FDOT specifications. The final density achieved was 10 kN/m<sup>3</sup> with a pH of 8 and a viscosity of 37 seconds (Marsh Cone method). The fourth cofferdam was the control and was therefore not filled.

**Seal Slab Placement**

Class III seal concrete specified by FDOT<sup>2</sup> was used. This mix has 332 kg of cement/m<sup>3</sup>, a water cement ratio of 0.51, and a specified 28 day strength of 21 MPa. The concrete was purchased from a ready-mix plant and was pumped through a 7.6 cm diameter hose. It was placed from the bottom upwards keeping the hose tip below the rising level of concrete. This is similar in placement and identical in effect to the tremie method. Figure 3 shows the fresh water cofferdam just after concreting with several inches of free water still present.

**Pullout Frame**

The frame designed for the 1/3rd scale pilot study is shown in Figure 4. It consists of two telescopic sections that react against each other via a stiffened beam and a hydraulic jack as shown. A standard nut was used to connect the free end of the Dywidag



rod in the prestressed pile to the base of the tension assembly. Although Figure 4 conceptually depicts the device assembly, the test procedure was streamlined by leaving it partially assembled between tests. The entire device weighed over 2.2 kN fully assembled and required an overhead chain hoist to assemble and/or move.

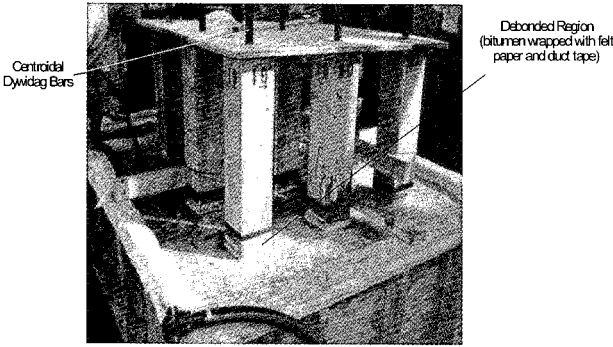


**Figure 3: Pilot Study Simulated Cofferdam**

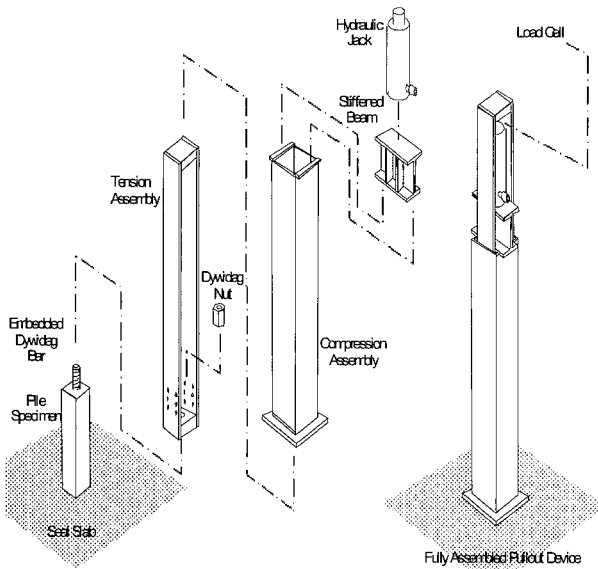


**Figure 4: Pullout Equipment in Pilot Tests**

Tension loads were measured using a load cell inserted between the top of the jack and the tension assembly. The stiffened beam transferred the load from the base of the jack to a built-up column section which in turn applied a uniform compressive stress to the seal slab.

**Leveling**

As the exposed surface of the seal slab was left uneven from the tremie placement method, a self-leveling grout pad had to be poured around each pile prior to testing. To further assist in the leveling process, a 12 mm steel bearing plate was placed on the grout immediately afterwards. Once the grout had time to cure (about 15 minutes), the tension assembly was connected to the pile and the compression assembly supported on the bearing plate.

**Instrumentation**

A Megadac data acquisition system by Optim Electronics Corporation was used for collecting and recording the test data generated. Loads were measured using a 100 tonne load cell and movement was monitored by two LVDTs. One of the LVDTs was magnetically attached to the compression assembly and positioned to record displacement with respect to an external reference beam. This registered any possible seal slab surface crushing or settlement occurring during testing. The other LVDT was attached to the tension assembly and referenced to the top of the compression assembly. This accounted for specimen movement, along with elastic deformation of the frame which was later accounted for in the data reduction.

**Test Procedure**

Tests were initiated after the seal slab had been cured for 72 hours. Concrete cylinders were periodically tested to monitor changes in compressive strength during the time it took to complete the tests. The frame was set in position and the pull-out test commenced. The tensile load was increased slowly using a manually operated toggle switch which intermittently engaged the power to a hydraulic pump. The load was increased slowly to reduce any possible dynamic stiffening of the system. Each specimen was displaced upward at least 2.5 cm.

**PILOT STUDY RESULTS**

A summary of the test results is presented in Table 1. This provides information from all 28 tests and contains details of the compressive strength, the failure load and the computed average bond stress. This was determined as the quotient of the measured failure load and the calculated surface area of the pile in contact with the seal slab. The following observations may be made:



1. Concrete strengths varied between 27-31 MPa over the duration of testing.
2. Significant bond stresses developed; the highest value obtained was 4.4 MPa (salt water/1.5d) and the lowest 0.2 MPa soil-caked control. Highest values were for salt water, followed closely by controls and fresh water.
3. Embedment depths above 1.5d led to lower average values (Table 1). This suggests that the bond stress distribution is non-uniform and instrumentation would be required to gain an understanding on the stress transfer.
4. Results for salt water and fresh water cofferdam conditions did not differ significantly.
5. The soil-caked condition did not affect interface bond except in the case of controls and bentonite slurry. For the salt water or fresh water condition, the soil caking was washed off by the water prior to the installation of the seal slab.

For the larger embedment depths, the prestressed concrete specimens cracked (see Figure 5).

This suggested that depths in excess of 1.5d may be inappropriate for the full-scale tests. Cracking of the seal slab was also observed during dismantling of the test set-up when the sides of the simulated cofferdam were removed. Figure 6 shows a load-slip plot obtained from the pilot study where the pullout capacity did not exceed the tensile capacity. Inspection of this plot indicates that there was continuous slip although minimal up to 50 kN (the elongation of the member was very small,  $L/AE=0.015$  mm/kN).

**Table 1: Summary of Pilot Test Results**

Type	Specimen	f <sub>c</sub> MPa	Bond Length	Pull out Load (kN)	Bond Stress (MPa)	Ave (MPa)
Control	C22	27	1d	377	3.9	3.8
	C23	27	1d	358	3.8	
	C24	27	1.5d	610	4.2	4.3
	C25	27	1.5d	632	4.3	
	C26	27	2d	630	3.3	3.3
	C27	27	2d	625	3.3	
	Salt Water	C8	29	1d	398	4.1
C9		29	1d	378	4.1	
C10		29	1.5d	631	4.4	4.2
C11		29	1.5d	591	4.1	
C12		29	2d	651	3.3	3.4
C13		29	2d	689	3.6	
Fresh Water		C15	29	1d	354	3.7
	C16	29	1d	417	4.3	
	C17	29	1.5d	620	4.3	4.1
	C18	29	1.5d	573	3.9	
	C19	29	2d	560	2.9	3.1
	C20	29	2d	622	3.2	
	Bentonite	C1	29	1d	141	1.5
C2		29	1d	149	1.5	
C3		29	1.5d	557**	3.9	2.8
C4		29	1.5d	237	1.6	
C5		29	2d	206	1.1	1.9
C6		29	2d	543**	2.8	
Soil-caked		Control	27	2d	39	0.2
	Salt Water	31	2d	521	2.7	
	Fresh Water	31	2d	397	2.0	
	Bentonite	31	2d	49	0.3	

(\*\* higher values are attributed to scouring action of the pumped concrete on piles closest to inflow)

**FULL SCALE STUDY**

The results of the pilot study were used to develop a program for full-scale tests. The principal changes were (1) elimination of the salt water condition (2) instrumentation of selected piles to allow evaluation of bond stress distribution with embedment depth and (3) restriction of the soil-caked surface to bentonite slurry placement. In view of the very high bond stresses that were obtained, the depth of embedment was limited to 1.5d excepting for bentonite where the maximum depth was increased to 2d. In addition, embedment depths of 0.5d were investigated for the control and fresh water placement conditions where the interface bond was expected to be very high.

With three different placement conditions (control, fresh water and bentonite), two different embedment depths (d, 1.5d or 2d) and two specimens per test, a total of 12 specimens were required. Four additional specimens were tested - one each for embedment depth of 0.5d (for the control and fresh water condition) and two for investigating the effect of soil caking for the bentonite slurry for an embedment depth of 1d. Thus, the controls and the fresh water condition each had five specimens with six specimens in the bentonite slurry condition.

The bond stresses obtained from the pilot study (Table 1) ranged from a low of 1.1 MPa (bentonite/2d) to a high of 4.3 MPa (control/1.5d). Because of these large values, 36 cm wide square prestressed piles were used in the full-scale tests. The length of each specimen was limited to 1.5 m.

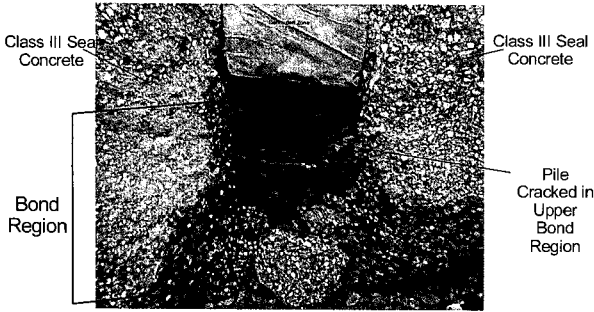


**Figure 5: Post-mortem Profile View of the Pilot Study Specimen During Dismantling**

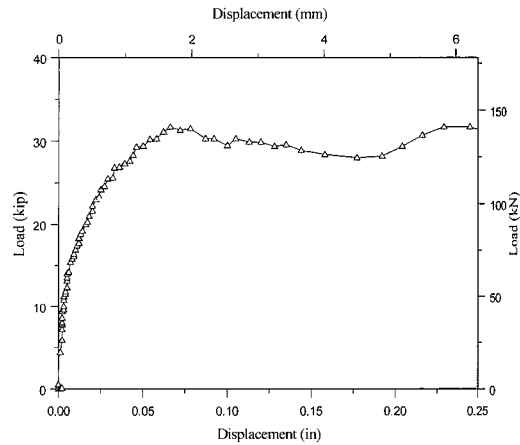


**Figure 6: Load vs. Displacement – Specimen C1 (1d, bentonite.)**

Unlike the pilot tests where a central Dywidag rod was integrally cast with the specimens, for the full-scale tests the strands were directly attached to the tension frame with prestressing chucks. To ensure that the piles would have a somewhat greater capacity, bigger 15mm strands were used instead of the standard 12.5 mm strands though they were stressed to provide the same effective prestress. The eight 15 mm strands gave an ultimate pulling capacity of  $260 \times 8 = 2.1$  MN that exceeded the expected pullout load of the pile. This provided a margin of safety against sudden, dangerous tensile failure of the strands.

A total of eighteen specimens were cast at the same commercial prestressing yard. The spacing of the specimens inside the prestressing bed was adjusted so that each specimen had a 0.6 m length of strand projecting from the pulling end that served as a connection point to the pull-out frame. Additionally, four specimens were instrumented with embedded sister bar-type strain gages to allow the distribution of bond stresses to be assessed. Figure 7 shows three sister-bar strain gages which consist of a resistive foil strain gage bonded to a short length of 13 mm rebar. These were located at the bottom, middle and top of the bonded length of 1d (three specimens) or 2d (1 specimen) (Figure 7). Complete fabrication details may be found in the final report<sup>7</sup>.

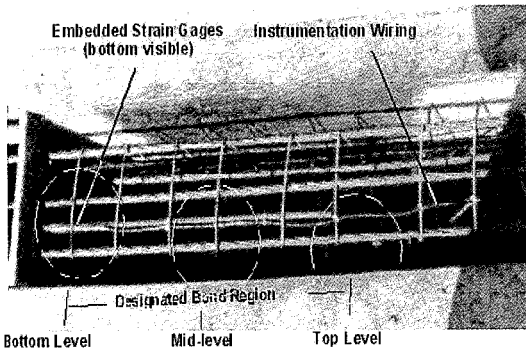


**Figure 7: Prestressing Bed for Casting 36 cm Instrumented Piles**

### Simulated Cofferdam

Three cofferdams had to be constructed for the three conditions investigated. The dimensions of the cofferdams were determined by the number of piles and a 3d pile spacing (1.07 m) as in the pilot study. Thus, two of the cofferdams - fresh water and control - were identical in size, but the bentonite slurry-filled cofferdam was larger as it had more specimens.

The cofferdams were constructed using rented steel reinforced plywood box forms made by Symons Corporation, Des Plaines, IL. The forms were connected to form each cofferdam using wedge pins provided by the manufacturer. They were also externally braced using wooden stakes and internally braced with a wooden template that maintained the pile positions. Additionally, each cofferdam was lined with 0.15 mm plastic sheeting. This allowed for the forms to be watertight, preventing the loss of any construction fluid (water or bentonite slurry).

### Specimen Support

Following the construction of the cofferdam, the specimens were accurately positioned on plywood pads to prevent damage to the plastic lining. Additionally, a polystyrene seal was placed between each concrete pile specimen and the wooden pad to prevent possible bonding between the cast-in-place seal concrete and the bottom of the pile. The specimens were vertically supported by a wooden framework that was secured to the Symons forms (Figure 8).

### Debonded Surface

As in the pilot study, differing lengths (0.5d, 1d, 1.5d and 2d) of the pile surface were bonded or debonded. Debonding was achieved in the identical manner. The bonded concrete surfaces were left in their natural state excepting for the two specimens that were tested for the soil-caked condition. For this case, an adhesive clay soil, typically used for clay models by artists was used because it bonded better than the kaolinite paste tested in the pilot study.

The debonded length extended from the boundary of the bonded region to approximately 15 cm above the intended elevation of the finished surface of the seal slab. This included an additional 36 cm depth determined from finite element analysis to ensure uniform distribution of compressive loads to the seal slab (Figure 2b).

The bentonite slurry was made by mixing dry, high yield bentonite and fresh water. The mixing was accomplished through the use of a shear pump. Enough bentonite clay was added to achieve slurry properties similar to FDOT specifications. The final density achieved was  $10.2 \text{ kN/m}^3$  with a viscosity of 40 seconds (Marsh Cone Method) and a pH of 8. Figure 8 shows the filling and completion of the bentonite slurry filled simulated cofferdam.



**Figure 8: Overview of Cofferdam During Concreting**

### Seal Slab Placement

Seal concrete was placed using a concrete pump truck. The concrete was pumped through a 15 cm diameter hose. It was placed from the bottom upwards keeping the hose tip below the rising level of concrete. This procedure is identical to the tremie method commonly used in construction practice.

## Testing Apparatus

Similar considerations of capacity, economy and portability dictated the design of the pullout frame. This design incorporated an available double-acting, 3 MN hydraulic jack, a 69 MPa hydraulic pump system, and could accommodate connections for both concrete and steel pile types. Additionally, it provided sufficient clearance for a 4MN loadcell as well as means to record pile displacement.

As with the pilot test, the reaction frame consisted of a tension and compression assembly. The tension assembly was connected directly to the pile using prestress chucks and supported by the hydraulic jack and load cell. The stiffened beam was integrated directly into the compression assembly which applied compressive loads to the seal slab. Fully assembled the device weighed 16 kN and was placed over each specimen with a straight mast industrial forklift (Figure 9). Additional information on the design and fabrication may be found elsewhere.<sup>7</sup>

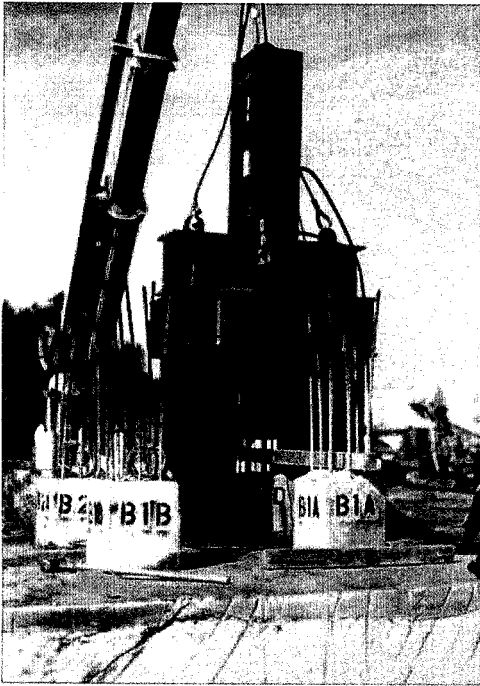


Figure 9: Full-Scale Pullout Device

## Test Setup

The test setup was similar to the pilot study and involved placement of a grout layer, assembly and connection of the hydraulic testing apparatus, attachment of the data acquisition system, and application of loading until failure. Given the requirement that testing be completed quickly following the 72 hour cure period, appropriate adjustments were made to expedite testing.

## Leveling Grout Pad

Since concrete vibration is not used in seal slab construction due to possible aggregate segregation in the submerged environment, various degrees of surface roughness developed depending on the pour condition. The bentonite pour condition had the greatest degree of unevenness; the control had the least. The uneven surfaces were leveled using a thin layer of high strength grout that was placed directly over the seal slab (Figure 9). The grout was poured and finished two days after the placement of the CIP seal slab. Since the debonded portion of each pile specimen extended well above the CIP slab, there were no difficulties with possible bonding of the grout to the piles.

## Frame Assembly

Although much heavier than the pilot study device, the full-scale pullout device was easier to use in that it could be left fully assembled between tests. This reduced the number of heavy lifts and expedited testing.

As the entire frame was lowered over the test specimen, the exposed prestressing strands were threaded through the holes in the base of the tension assembly. Standard prestressing chucks which incorporate wedge-type grips were secured on each strand. A 76 mm gap was maintained between the tension assembly and the top of the pile to permit removal of the prestressing chucks after testing. With the chucks in place, the frame was centered and the concrete pile tested.

## Data Acquisition

As with the pilot study, the Megadac data acquisition system by the Optim Electronics Corporation was used for collecting and recording the test data generated by the pull-out testing. Along with the Megadac, a load cell and two electronic displacement gages (LVDTs) were used to monitor each pile specimen as it was tested. The load cell had a capacity of 4 MN. The electronic displacement gages had a 50 mm range. Additionally, strains were monitored in selected piles

that had been cast with embedded resistance-type sister bar strain gages (Figure 7). For the concrete specimens, one LVDT was magnetically attached to the bottom of the tension assembly and positioned to register displacement with respect to an external reference beam. The other LVDT recorded relative displacement between the tension assembly and the top of the pile specimen. This accounted for any possible slippage of the prestressing chucks.

**Test Procedure**

Once the set-up procedure was completed, the pull-out testing could be conducted. The tensile load was increased slowly using a manually operated toggle switch which intermittently engaged the power to the hydraulic pump. The load was increased slowly to reduce any possible dynamic stiffening of the system. Each specimen was displaced upward at least 25 mm to ensure that the bond interface had been displaced.

**RESULTS**

A summary of the test results is presented in Table 2. This provides information from all 16 tests and contains details of the compressive strength, failure load, and the computed average bond stress. Inspection of Table 2 shows that the bond stresses were quite high ranging between 4.5 MPa for 0.5d embedment in the controls to the lowest value of 1.1 MPa for one of the soil-caked bentonite specimens. Trends observed in the pilot tests were repeated: the average bond stresses decreased with increased embedment depth. For example, the average bond stress reduces from 2.7 MPa to 2.0 MPa for fresh water specimens embedded 1.0d and 1.5d, respectively.

**Table 2: Summary of Full Scale Test Results**

Type	Specimen	f <sub>c</sub> MPa	Bond Lgth	Pull out Load (kN)	Bond Stress (MPa)	Ave (MPa)
Control	C0.5	27	0.5d	1151	4.5	3.2
	C1.0A	32	1d	1656	3.2	
	C1.0B	32	1d	1580	3.1	
	C1.5A	32	1.5d	1584	2.1	2.4
	C.15B	32	1.5d	2020	2.6	
Fresh Water	W0.5	27	0.5d	892	3.5	2.7
	W1.0A	27	1d	1358	2.7	
	W1.0B	27	1d	1336	2.6	
	W1.5A	27	1.5d	1591	2.1	2.0
	W1.5B	27	1.5d	1527	2.0	
Bentonite	B1B	23	1d	1338	2.6	2.5
	B1D	23	1d	1274	2.5	
	B2A	23	2d	1625	1.6	1.5
	B2B	23	2d	1438	1.4	
Bentonite (soil caked)	B1A	23	1d	931	1.8	1.5
	B1C	23	1d	570	1.1	

Variations in concrete strength over the duration of the test may also be noted. The lowest compressive strength was for the bentonite series (f<sub>c</sub> = 23 MPa) and the highest for the controls (32 MPa). This was in part due to increase in strength over the seven day period it took to complete the testing. A typical load vs slip variation plot is shown for each cofferdam condition in Figures 10-12. As before, the plots show continuous displacement with increasing load; initially elastic and then plastic. While measurements included the effect of elongation of the 1.5 m long prestressed pile, calculations show that length increases were minimal even after the pile had cracked. Figure 10 shows no evidence of cracking (bentonite) whereas Figures 11 and 12 indicate pile cracking at 1044 and 955 kN, respectively. The cracking load was consistently smaller than expected due to the shortened transfer length near the end of the pile and the associated inability to develop effective prestress in the concrete. This was due to the relatively short length of the test piles. In actual construction where longer piles are used this would not be the case. Additionally, variations in cracking force in nearly identical specimens was attributed to indiscernible alignment errors during testing.

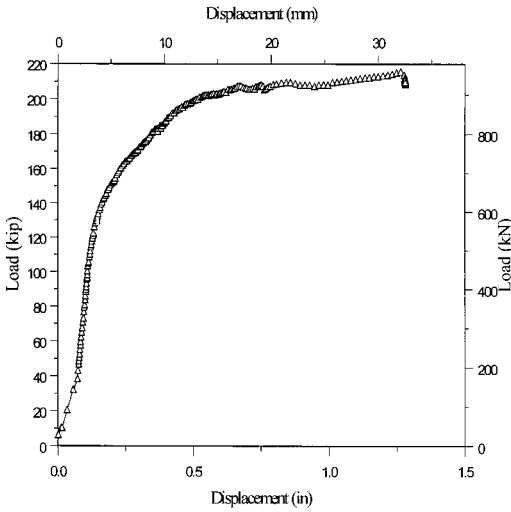


**Figure 10: Load vs. Displacement - Specimen B1A (1d, bentonite, soil-caked)**

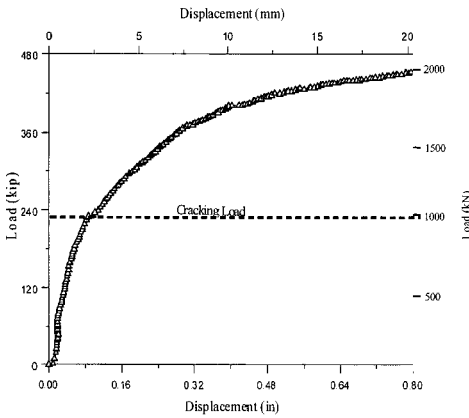


**Figure 11: Load vs. Displacement - Specimen W1.5B (1.5d, water)**

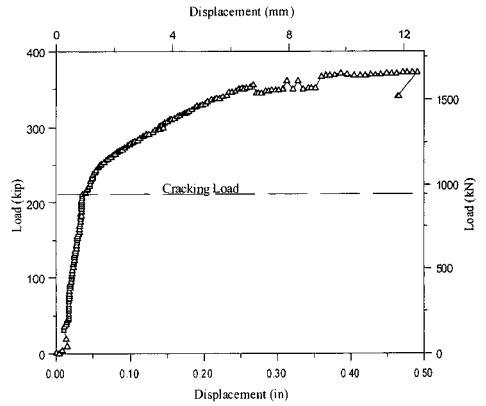


**Figure 12: Load vs. Displacement - Specimen C1.0A (1d, control)**

**Strain Variation**

The shear stress distribution within the bonded region of the pile was evaluated using embedded strain gages in four of the specimens: fresh water (1), control (1), and bentonite (2). The bond length was 1d for three of the specimens (one in each bed) and 2d for an additional specimen in the bentonite. The gages were located at the top, middle, and bottom of the bonded region. Figure 13 shows the axial strain at measured at three points along the bond interface during testing of one instrumented pile specimen. Additional results may be found in the final report<sup>7</sup>.

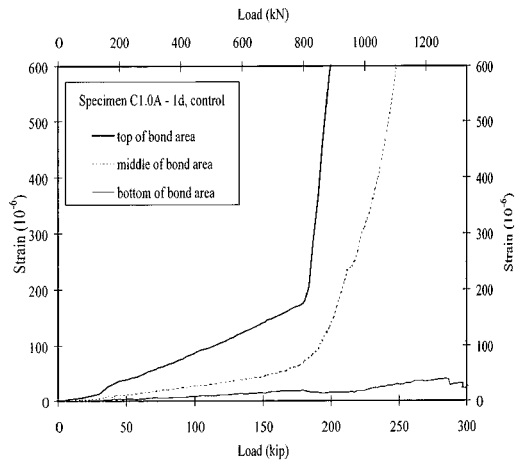


**Figure 13: Change in Strain with Respect to Load for Specimen C1.0A (control, 1d Embedment)**

The strains recorded at three levels (top, middle, and bottom of the bond interface) define two bonded layers (upper and lower) separated by the middle gage. The difference between the top and middle gage indicates the load carried by the upper layer. Likewise, the difference between the middle and bottom gage indicates the load carried by the lower bond layer. Inspection of this plot shows the load distribution stayed relatively constant up to the elastic limit of the upper bonded layer (2 MPa); at which time the load was gradually transferred to a lower layer. The top gage reading should linearly relate to the loadcell as there is no alternate load path between them. As expected, the gage at the bottom of the bond area registers near zero strains as no additional capacity can be developed below that level. The non-linear portion of the middle gage indicates the upper layer bond failing and transferring load to the lower layer. Sharp discontinuities are observed in the upper gages due to sudden cracking; whereas less severe strain changes are noticed in the middle gages as the cracked sections reach further into the seal slab.

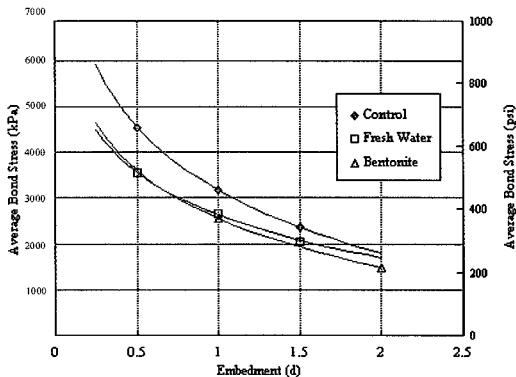


**Figure 14: Average Bond Stress Variation with Embedment from Full-Scale**

The load distribution as measured by the strain gages indicates that the full bond length contributed to its capacity. However, peak bond capacities occurred at different locations and time from top to bottom in that the amount of slippage required to develop peak shear strength is small with respect to elastic elongation. This can also be deduced by evaluating the average bond strengths from Table 2 with respect to embedment (e.g. Average Control Values: 0.5d, 4.5 MPa; 1.0d, 3.2 MPa; and 1.5d, 2.4 MPa). As embedment decreases, bond strength approaches an upper limit proportional to the concrete strength as shown in Figure 14.

As in the pilot study, cracking was observed in both the prestressed piles and in the seal slab. Figure 15 shows a transverse tension crack just above the seal slab. Figure 16 shows a crack that formed in the seal slab originating from the corner of a pullout specimen. These conditions need to be addressed in design.



**Figure 15: Pile Cracks During Loading**



Figure 16: Seal Slab Cracks During Testing

**CONCLUSIONS**

This study presents results from an experimental study that investigated the interface bond stress that developed between seal concrete and prestressed piles in cofferdams. Two series of tests were conducted. In the first series, one-third scale models were fabricated and tested. Three variables were investigated (1) displacement of fresh water, salt water and bentonite slurry, (2) different pile surface conditions, and (3) varied embedment depths expressed as multiples of the pile width (d). In the second series, full-scale tests were conducted for only two conditions (fresh water and bentonite slurry) as well as varied embedment depths. In all cases, results were compared against controls where no fluid was displaced. Seal slabs were cast using concrete delivered by ready-mix plants that conformed to Class III concrete in current FDOT specifications<sup>2</sup>. The concrete was allowed to cure for 72 hours prior to testing as permitted by existing specifications.

The following conclusions may be drawn:

Bond stresses determined experimentally were significantly higher than set in current specifications. Average values obtained from the full-scale tests

varied between 2.0-2.7 MPA for fresh water displacement and from 1.5-2.5 MPA for bentonite displacement. The lowest value obtained was 1.1 MPA for piles caked in soil and embedded in bentonite to a depth d.

Bond stress values from the full-scale tests were generally smaller than those for the model tests excepting for bentonite slurry (Tables 1 and 2). Strain data indicated that regardless of the embedment depth, loads were transferred to the pile over an effective depth. For the specimens tested, this depth was the same as the size of the pile (d). The bond between seal slab and piles caked with mud was largely unaffected when fresh water or salt water was displaced. These effects became important in controls or when bentonite slurry was displaced. This was because the caked soil was washed away by water currents that developed during concreting.

Prestressed piles and seal slabs developed cracks before the full pullout load was developed. Thus, structural failure of the seal slab and/or the piles themselves should be considered in any rational design process.

**RECOMMENDATIONS**

The buoyancy force generated at the base of a seal slab can be withstood using a combination of both the bond strength formed between the pile and the cast-in-place concrete as well as its self weight. While using this bond to offset a portion of the upward load, the tensile force developed in the pile cannot be permitted to exceed its cracking strength. The bond capacity developed by an individual pile may be determined using the allowable bond stress,  $f_b$ , listed in Table 3.

Table 3: Allowable Bond Stresses for Square Piles

Material	Condition	$f_b$ (MPa)
Concrete	Salt or Fresh	2.1
	Water	
	Bentonite	0.7

This stress ( $f_b$ ) may be assumed to act uniformly over an effective surface area,  $A_e$  given by:

$$A_e = pD \quad \text{if} \quad D < d, \text{ or}$$

$$A_e = pd \quad \text{if} \quad D > d$$

given the pile width  $d$ , pile perimeter  $p$ , and the seal slab thickness  $D$ . This limits the effective bond length to  $1.0d$  of the pile. Hence, the uplift capacity of the pile ( $P$ ) is the lesser of the allowable bond



capacity (P sub a ~ f sub b A sub e), or the pile tensile strength (e.g. AASHTO (5.6.3.4.1-1)).

In the latest Florida Design Guidelines<sup>9</sup>, allowable bond stress values have been increased from 40 psi (0.3 MPA) to 250 psi (1.7 MPA) based on the results that are presented in this paper.

**ACKNOWLEDGMENTS**

This investigation was carried out with the financial support of the Florida Department of Transportation. The authors especially acknowledge the contribution of Hayward Baker Inc. Tampa, FL in the full-scale testing as well as Rudy. Additional thanks are extended to Mr. Paul V. Liles, Jr. and the Georgia Department of Transportation for providing Figure 1. The opinions, findings and conclusions expressed in this publication are those of the writers and not necessarily those of the Florida Department of Transportation.

**REFERENCES**

1. Tomlinson, M.J. (1986). Foundation Design and Construction, 5<sup>th</sup> ed., Longman Scientific and Technical, Essex, England.
2. Standard Specifications for Road and Bridge Construction (1999). Florida Department of Transportation, State Specifications Office, Tallahassee, FL.

3. Johnson, L.J. and Nichols, J.R. (1914). "Shearing Strength of Construction Joints in Stems of Reinforced Concrete T-Beams as Shown by Tests," Transactions of the American Society of Civil Engineers, Dec., pp. 1499-1522
4. Standard Specifications for Highway Bridges 13<sup>th</sup> Edition (1983). American Association of State Highway and Transportation Officials, Washington, D.C., Section 4.3.4.6.2.
5. Structural Design Guidelines (1998). Florida Department of Transportation, Section 4.18, Topic No: 625-020-150c, July, p. 4-12, Tallahassee, FL.
6. Mullins, G., Sosa, R., Sen, R. and Issa, M. (2001). "Seal Slab/Steel Pile Interface Bond from Full-Scale Tests," Paper in preparation.
7. Mullins, G., Sosa, R. and Sen, R. (2000). "Seal Slab/Pile Interface Bond", *Final Report* submitted to Florida Department of Transportation, June, pp. 151.
8. Wu, Z (1999). "Studies of Bond of Cast-in-Place Concrete to Other Surfaces," MSCE Thesis, Department of Civil and Environmental Engineering, University of South Florida, Tampa, FL, August.
9. Structural Design Guidelines (2000). Florida Department of Transportation, Table 5.3, Tallahassee, FL.
10. Fischer, J., Mullins, G. and Sen, R. (2000). "Strength of Repaired Piles." *Final Report* submitted to Florida Department of Transportation.

## SEAL SLAB / STEEL PILE INTERFACE BOND FROM FULL-SCALE TESTING

Gray Mullins, Ruben Sosa, Rajan Sen and Moussa Issa, University of South Florida, Tampa, FL, USA

This paper presents results from model and full-scale tests to assess the interface bond between a cast-in-place concrete seal slab and steel H-piles in cofferdams. Three different seal slab placement conditions - fresh water, salt water and bentonite slurry - were evaluated and the results compared against controls where no fluid was displaced by the concrete. Normal pile surfaces were investigated. Additionally, the situation of "soil caked" piles was also tested.

In the model tests, eight 15 cm deep, W6 x 15 sections were used for two different embedment depths of 1.5d and 2d, d being the depth of the section. In the full-scale tests, 16 specimens 35 cm deep (W14 x 90 sections) were tested with the embedment varied between 0.5d-2d. The results show that significant bond stresses developed even in the worst placement condition. Recommendations made for revising current values in specifications have already been implemented by the Florida Department of Transportation.

### INTRODUCTION

Cofferdams are usually required in the construction of bridge foundations over waterways. Typically, a sheet pile enclosure is constructed in water and piles are driven as shown in Figure 1. A tremie concrete seal is then poured. When the seal has sufficiently cured, the cofferdam is dewatered and internal bracing installed. Thus, the seal allows the construction of the pier to be carried out under dry conditions.

As the function of the unreinforced seal slab is primarily to provide dry working conditions its design is quite simple. The seal thickness is essentially determined so that its weight balances the maximum uplift pressure since the allowable interface shear stresses are very small. Earlier AASHTO specifications<sup>1</sup> permitted interface shear stress values of 69 kPa (10 psi). However, these values were reduced to 34.5 kPa (5 psi) for steel interfaces in the Florida Design Guidelines<sup>2</sup>. Neither values are based on test data.

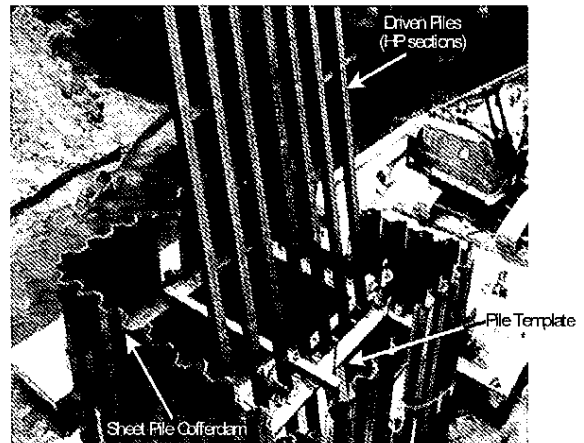


**Figure 1: Sheet pile cofferdam with pile driving template. (Courtesy of Applied Foundation Testing)**

In 1997 the Florida Department of Transportation funded a study to evaluate interface bond from full-scale tests. This paper presents results relating to the seal slab /steel pile interface bond. A companion paper provides the corresponding results for prestressed piles<sup>3</sup>. The complete results from this study including finite element modeling may be found elsewhere<sup>4,5</sup>.

## RESEARCH SIGNIFICANCE

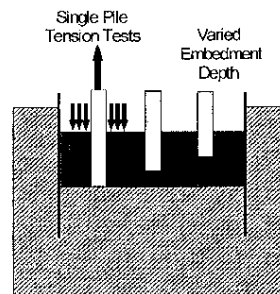
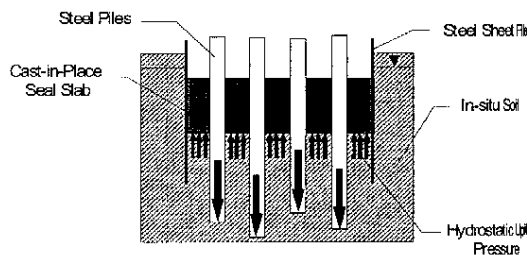
This study provides the first set of experimental results on the interface shear between steel piles and seal concrete slabs cast in accordance with construction specifications<sup>6</sup>. The results obtained have already led to increased allowable interface shear in the latest specifications.<sup>7</sup> This should result in reduced construction costs.

## OBJECTIVES

The overall goal of the study was to recommend interface shear stress values for seal slab and piles that could be directly used in FDOT's design specifications. These values were to be based on full-scale tests conducted on specimens that had been prepared in accordance with current FDOT specifications<sup>6</sup> for conditions that were commonly encountered. Variables examined were the pile embedment depth, effect of pile surface, effect of the pile material (steel or concrete) and the type of fluid that was displaced by the concrete.

## EXPERIMENTAL PROGRAM

The load transfer characteristics in seal slabs can be simulated by conducting pullout tests as illustrated in Figure 2 in which compressive loads are applied to the seal slab and tensile loads to the steel piles. Careful attention had to be paid to the experimental set-up so that tests could be carried out under field conditions. Small-scale bond tests were conducted to identify the maximum pullout lengths for a 1/3 scale pilot study. Results of the pilot study were used to subsequently refine the apparatus and procedures for the full-scale testing.



Profile View

Figure 2: Simulation of loads

## PILOT STUDY

The pilot study simulated three different seal slab placement conditions involving: (1) salt water, (2) fresh water, and (3) drilling fluid. These results were compared against controls where no fluid had to be displaced by the concrete. The 15 cm deep, wide flange sections were tested for two different embedment depths, 1.5d and 2d (d is the nominal pile size). Thereby a total of 8 model scale tests were conducted (4 conditions x 2 embedment depths).

The steel pile specimens were fabricated using a W 6 x 15 beam section made from A36 structural steel. Each steel pile was 0.91 m (36 inches) in length. On each pile, a line of three, 23.8 mm (15/16 inch) diameter holes were drilled into each flange to facilitate the twelve, 22 mm (7/8 inch) bolts required to provide the connection to a pullout apparatus.

## Cofferdam Simulation

Four, 0.76 m high wood boxes with inside dimensions of 1.4 m x 1.4 m were fabricated to simulate the four placement conditions. Plastic sheeting was used to line and seal the boxes. Wood templates were used to properly position each pile within the simulated cofferdams. The piles were spaced at 3 x pile size, i.e. the center to center distance was 45 cm. The edge spacing from the center line to the box edge was 1.5d or 22.5 cm.

All piles were identical in length and tip elevation; however, the two different embedment depths of 1.5d and 2d were accommodated by varying the bonded and debonded lengths within the concrete. The bonded region (steel to seal slab) was provided at the bottom of the simulated cofferdam in all the specimens. For the 15 cm piles, the bonded length was either 22.5 cm (1.5d) or 30 cm (2d). Above this bonded length, the piles were debonded using a thick layer of bitumen (Figure 3) applied up to a height sufficiently above the anticipated upper surface of the seal slab. The overall slab thickness and debonded region was set such that the bitumen extended at least 1d below the upper seal slab surface for all specimens. This minimum debond length was intended to eliminate bearing stress concentrations based on finite element modeling.

Three of the four boxes were filled with either fresh water, 3% salt water or bentonite slurry (Figure 3). The latter was made by mixing dry, high yield bentonite and fresh water to achieve slurry properties similar to those in the FDOT specifications<sup>6</sup>. The final density achieved was 10 kN/m<sup>3</sup> (64 pcf) with a pH of 8 and a viscosity of 37 seconds (Marsh Cone method). The fourth box served as a control and was therefore not filled.



**Figure 3: Drilling fluid pumped into simulated cofferdam**

## Seal Slab Placement

Class III seal concrete specified by FDOT<sup>6</sup> was used. The specified 28 day strength of the seal slab was 21MPa (3000 psi). This mix has 330 kg of cement / m<sup>3</sup> (560 lb of cement/cy) and a water cement ratio of 0.51. The concrete was purchased from a Readi-Mix plant and was pumped through a 76 mm (3 inch) diameter hose. The concrete was placed from the bottom upwards keeping the hose tip below the rising level of concrete. This is similar in placement and identical in effect to using a tremie pipe.

## Pullout Frame

The pullout frame used is shown in Figure 4. It consists of two telescopic sections that react against each other via a stiffened beam and a hydraulic jack. The pile specimen was bolted to the tension assembly. The pullout frame weighed 2.2 kN fully assembled and required an overhead chain hoist to assemble and/or move. Tension loads were measured using a load cell positioned between the top of the jack and the tension assembly. The stiffened beam transferred load from the base of the jack to a built-up column section which in turn applied uniform compressive stress to the seal slab.

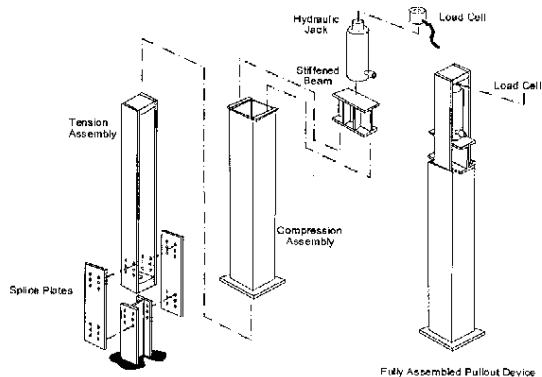


**Figure 4: Model scale pullout equipment**

**Leveling**

Before the pullout frame was installed, a grout pad was poured around each pile specimen using a high strength, fast curing, self-leveling grout. To further assist in this alignment process, a steel bearing plate was placed in the fresh grout and squared with respect to the longitudinal axis of the pile.

**Instrumentation**

A MEGADAC data acquisition system by Optim Electronics Corporation was used for monitoring and recording the test data generated. Loads were measured using a load cell and slip was monitored by two LVDTs. One of the LVDTs was magnetically attached to the compression assembly and positioned to record displacement with respect to an external reference beam. This registered any possible seal slab surface crushing or settlement that might occur during testing. The other LVDT was attached to the tension assembly and referenced to the top of the compression assembly. This recorded specimen movement as well as the compliance of the frame which was later accounted for in the data reduction.

**Test Procedure**

Pullout tests were commenced after the seal slab had been cured for 72 hours in accordance with FDOT requirements. Concrete cylinders were tested at periodic intervals to monitor the change in compressive strength. The tension

assembly was bolted to the piles using 22 mm (7/8 inch) diameter bolts. Once the grout had time to cure (about 15 minutes), the compression assembly was lowered on to the bearing plate. The stiffened beam, along with the hydraulic jack, was then positioned between the compression section and the upper end of the tension assembly as shown in Figure 4.

With the specimens set-up, the pull-out test commenced. The tensile load was increased slowly using a manually operated toggle switch which intermittently engaged the power to the hydraulic pump. The load was increased slowly to reduce any possible dynamic stiffening of the system. Each specimen was displaced at least 25 mm.

**RESULTS**

A summary of the test results is presented in Table 1. This provides information from the 8 tests and contains details of the compressive strength, the failure load and the average bond stress. Over the duration of the tests, there was no change in the compressive strength.

**Table 1: Summary of pilot test results**

Type	Specimen	f <sub>c</sub> MPa	Bond Lgth	Bond Area (m <sup>2</sup> )	Pull out Load (kN)	Bond Stress (MPa)
Control	H41	31	1.5d	0.206	611	3.01
	H42	31	2d	0.274	720	2.66
Salt Water	H21	31	1.5d	0.206	744	3.66
	H22	31	2d	0.274	563	2.08
Fresh Water	H31	31	1.5d	0.206	336	1.66
	H32	31	2d	0.274	620	2.29
Ben-tonite	H11	31	1.5d	0.206	320	1.58
	H12	31	2d	0.274	344	1.27

The following observations may be made:

Significant bond stresses were developed; the highest value obtained was 3.66 MPa (salt water/1.5d) and the lowest 1.27 MPa (bentonite/2d). Highest values varied with embedment depth. For 1.5d embedment, the highest was for salt water followed by controls and fresh water. For 2d, control values were highest followed by fresh water then salt water. The magnitude of the bond stress decreased with an increase in embedment depth. This suggests that the distribution of bond stress is non-uniform.

The results for bentonite slurry were surprisingly good. Indeed, for embedment depth of 1.5d, values obtained were comparable to that for fresh water.

Values for salt and fresh water are similar.

### **FULL SCALE STUDY**

The pilot study provided important information on the magnitude of the interface steel/seal bond that could develop. The significant scatter in the results indicated the need to conduct additional tests. These findings led to refinements in the full-scale test program. The principal changes were: (1) elimination of the salt water condition - this was based on the results of more extensive tests carried out on prestressed piles<sup>3</sup>, (2) consideration of the effect of soil-caked surface, and (3) increase in the number of specimens.

In view of the very high bond stresses that were obtained, the depth of embedment was limited to 1.5d excepting for bentonite where the maximum depth was increased to 2d. In addition, embedment depths of 0.5d were investigated for the control and fresh water placement conditions.

With three different placement conditions (control, fresh water and bentonite), two different embedment depths (d, 1.5d or 2d) and two specimens per test, a total of 12 specimens were required. Four additional specimens were tested - one each for embedment depth of 0.5d (for the control and fresh water condition) and two for investigating the effect of soil caking for the bentonite slurry for an embedment depth of 1d. Thus, the controls and the fresh water condition each had five specimens with six

specimens for the bentonite slurry condition. These were identical to the conditions investigated for prestressed piles<sup>3</sup>.

The depth (35 cm) and length of the steel piles was kept the same as that for the prestressed piles. As a result, 1.52 m long W14 x 90 sections made from A36 steel were used. Holes for 28.6 mm (1-1/8 inch) diameter bolts were drilled in each flange to connect the pile specimens to the tension assembly frame (Figure 5).

### **Simulated Cofferdam**

Three cofferdams had to be constructed for the three conditions that were investigated. Two of these - fresh water and control - were identical in size. The bentonite slurry condition with the larger number of specimens was larger. The dimensions of the cofferdam were determined by specimens and edge distances that were kept the same 3d (1.06 m) as in the pilot study.

The cofferdams were constructed using rented steel reinforced plywood box forms connected to each other using wedge pins provided by the manufacturer. They were also externally braced using wooden stakes and a two-by-four framework. Additionally, each cofferdam was lined with 0.2mm (6 mil) plastic sheeting. This provided a water-tight barrier, preventing the loss of any construction fluid (water or bentonite slurry). Figure 5 shows one of the cofferdams just prior to filling with fluid.

### **Specimen Support**

Following the construction of the cofferdam, the specimens were accurately positioned on plywood pads to prevent damage to the plastic lining. The specimens were vertically supported with a wooden two-by-four framework that was secured to the box forms (Figure 5).

### **Debonded Surface**

As in the pilot study, differing lengths (0.5d, 1d, 1.5d and 2d) of the pile surface were bonded or debonded. Debonding was achieved in the identical manner as in the pilot study. The bonded steel surfaces were left in their natural state excepting for the two specimens that were tested for the soil-caked condition. For this case, an adhesive clay soil, typically used for clay models by artists was used because it bonded better than the kaolinite paste tested in

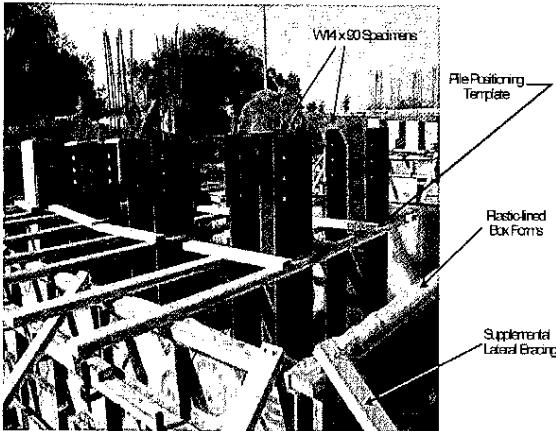


**Figure 5: Steel Piles in simulated cofferdam (Prestressed piles were also tested in the same bed.)**

the pilot study<sup>3</sup>. The debonded length extended from the boundary of the bonded region to approximately 15 cm above the intended elevation of the finished surface of the seal slab. This included an additional 35 cm length determined as needed by finite element analysis to ensure uniform distribution of compressive loads to the seal slab surrounding the bonded region.

**Placement Conditions**

One cofferdam was left dry prior to concrete placement (control); the second was filled with fresh water from a nearby potable source. The third was filled with bentonite slurry which was made by mixing dry, high yield bentonite and fresh water. The mixing was accomplished through the use of a shear pump. Enough bentonite clay was added to achieve slurry properties similar to FDOT specifications. The final density achieved was 10 kN/m<sup>3</sup> (65 pcf) with a viscosity of 40 seconds (Marsh Cone Method) and a pH of 8.

**Seal Slab Placement**

Seal concrete was placed using a concrete pump truck. The concrete was pumped through a 15 cm (6 in) diameter hose and was placed from the bottom upwards keeping the hose tip below the rising level of concrete. This is similar in placement and identical in effect to the tremie method.

**Testing Apparatus**

Identical considerations of capacity, economy and portability dictated the design of the pullout equipment. A steel reaction frame was designed to take advantage of an available double-acting, 2670 kN (300 ton) hydraulic jack which would be operated with a portable 69 MPa (10 ksi) hydraulic pump system. The frame required connection designs for both concrete and steel pile types. Additionally, the frame would need to be integrated with electronic devices to measure load and displacement.

As for the pilot test, the reaction frame consisted of a tension and compression assembly. The tension assembly was connected directly to the pile with two splice plates and housed the hydraulic jack and load cell. The compression assembly applied compressive loads to the seal slab. Figure 6 shows a photograph of the complete assembly being placed over a pile specimen. Additional information on the design and fabrication may be found elsewhere<sup>4</sup>.

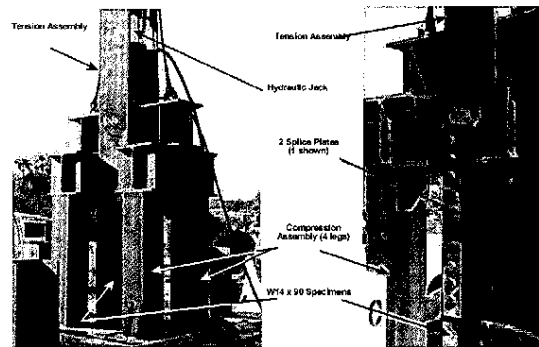


**Figure 6: Full scale test apparatus**

**Test Procedure**

The test setup and procedure was similar to the pilot study involving placing a grout layer, connecting the tension assembly to the pile, lowering the compression assembly on to the leveled grout surface, attach the appropriate instrumentation, and extract the specimens. However, some variations were adopted to expedite the testing procedure so less variation in concrete strength would be observed after the 72 hour FDOT curing period.

Since no concrete vibration or finishing is used in seal slab construction, various degrees of surface roughness developed in the submerged conditions. Instead of leveling the base of each pile individually, all cofferdams were leveled at the same time with a skim coat of grout batched from a single truck. The grout was poured and finished two days after the placement of the CIP seal slab without adding significant delay before testing could commence. The bentonite pour condition had the greatest degree of unevenness, whereas the control was more uniformly placed due to the visual input during its placement (although unfinished). Since the debonded portion of each pile specimen extended well above the CIP slab, there were no difficulties with possible bonding of the grout to the piles (Figure 7).

Although much larger than the model scale device, the pullout apparatus could be attached more quickly due to easy access of the splice plate bolts. It was also left fully assembled between tests. Instrumentation and data acquisition attached to the device was again similar to the model scale tests with the exception of the load cell capacity (2670 kN) which was sized to accommodate the increased loads. One of two displacement gages was magnetically attached to the pile and referenced to the top of the slab. The other gage was magnetically attached to the pile and referenced to an external reference beam to monitor global movements.

The tensile load was increased slowly using a manually operated toggle switch which intermittently engaged the power to the hydraulic pump. The load was increased slowly to reduce any possible dynamic stiffening of the system. Each specimen was displaced upward at least 25 mm to ensure that the bond capacity had been fully developed.

## RESULTS

A summary of the test results is presented in Table 2. This provides information from all 16 tests and contains details of the compressive strength, the failure load, and the average bond stress. Inspection of Table 2 shows that the bond stresses were quite low compared to the pilot study. The highest value was 1.63 MPa (control/0.5d) and the lowest 0.50 MPa (bentonite/2d). However, trends observed in the pilot tests were repeated; the average bond stresses declined with increased embedment depth. For example, the average bond stress reduces from 1.31 MPa to 1.07 MPa for a fresh water embedment depth increase from  $d$  to  $1.5d$ .

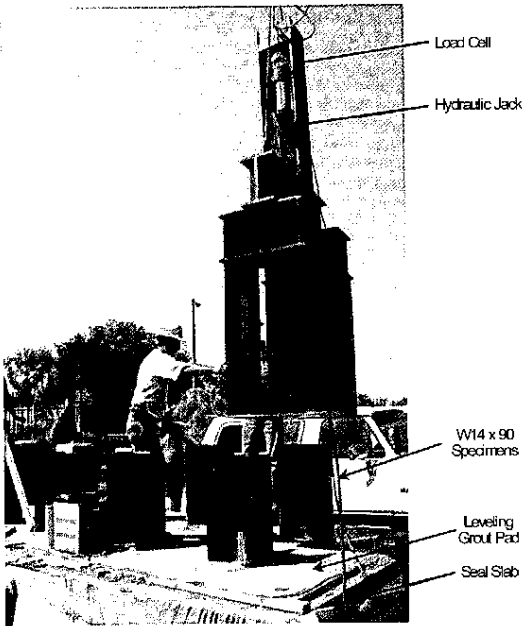


Figure 7: Full Scale pullout device suspended over test specimen



**Table 2: Summary of full scale test results**

Type (w)	Spec. (w)	f <sub>c</sub> MPa	Bond Lgth (w)	Pull out Load kN	Bond Stress MPa	Ave MPa	Normalized MPa
Control	SC0.5	32	0.5d	618	1.63		
	SC1.0A	32	1d	1018	1.34	1.40	1.20
	SC1.0B	32	1d	1100	1.45		
	SC1.5A	32	1.5d	1140	1.00	1.02	0.88
	SC.15B	32	1.5d	1187	1.04		
Fresh Water	SW0.5	27.5	0.5d	438	1.15		
	SW1.0A	27.5	1d	1105	1.33	1.31	1.21
	SW1.0B	27.5	1d	975	1.29		
	SW1.5A	27.5	1.5d	1317	1.16	1.07	0.99
	SW1.5B	27.5	1.5d	1116	0.98		
Bentonite	SB1B	23.5	1d	874	1.15	0.88	0.88
	SB1D	23.5	1d	466	0.62		
	SB2A	23.5	2d	827	0.55	0.52	0.52
	SB2B	23.5	2d	767	0.50		
Bentonite (soil-caked)	SB1A	23.5	1d	629	0.83	0.91	0.91
	SB1C	23.5	1d	753	0.99		

Variations in concrete strength over the duration of the test may also be noted. The lowest compressive strength was for the bentonite series (f<sub>c</sub> = 23.5 MPa) and the highest for the controls (32 MPa). The bond strength is normalized to a 23.5 MPa concrete strength in Table 2 by dividing the measured values by the percent increase in the square root of the concrete strength. For example the control values were normalized as follows:

$$1.20MPa = 1.40MPa \frac{\sqrt{23.5}}{\sqrt{32}}$$

Representative load vs displacement plots are shown for each of the simulated cofferdam conditions in Figures 8-10. Each graph also shows the effect of embedment depth on the pullout response for the various conditions. The control and freshwater environments showed similar results for normalized bond values of 1.20 MPa and 1.21 MPa, respectively. Likewise, the trends associated with the effects of embedment were comparable (Figures 8 and 9). The pullout capacity increased somewhat linearly with embedment depth up to 1d. This can be noted in both peak and residual values when comparing the 0.5d and 1d test results. With longer embedment depths (1.5d) little increase in average capacity was observed (10% in controls and 17% in water). This was also noted in Table 2 where average bond strengths decreased 18% (1.31 to 1.07 MPa) and 27% (1.40 to 1.02 MPa) in the water and control specimens, respectively for the same increased embedment depths. Figure 10 shows the pullout response of the piles cast in the bentonite slurry-filled cofferdam. Therein, several differences were introduced due to anticipated decreases in bond strength: (1) 0.5d embedment was not used, (2) the 1.5d was increased to 2d, and (3) soil caking was applied to some 1d specimens. The effects of embedment were similar in this set of tests as no significant additional pullout capacity was realized with the additional bond area from 1d to 2d embedment. This is supported by the moderate 19% average increase in pullout with a 100% increase in embedment (670 kN to 797kN). This decreased bond efficiency is further illustrated by the 41% decrease in the average bond strength in Table 2 (0.88 MPa to 0.52 MPa). The effect of soil caking was less significant than that of the embedment depth most probably due to the scouring action during the seal slab placement. In general, the bentonite condition produced larger variations in the measured bond values. However, the overall findings indicate that the bond between steel and seal slabs is significantly higher than specified in design codes.

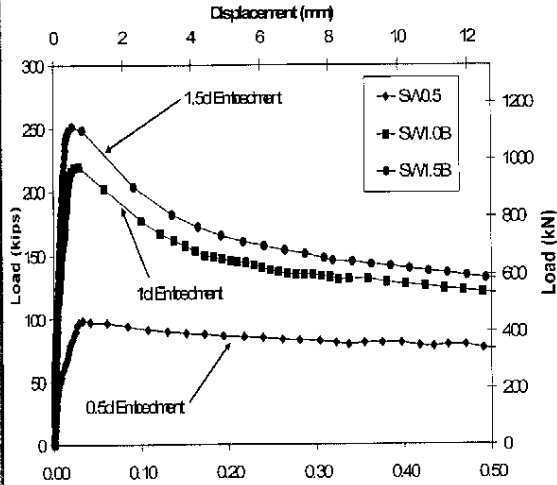


Figure 8: Water-filled cofferdam test results

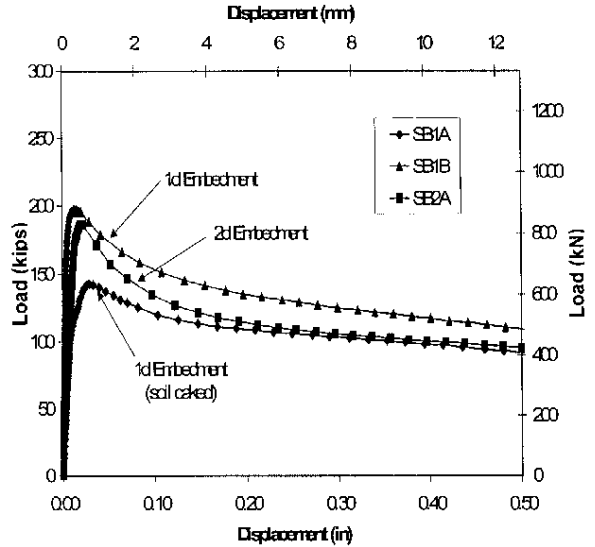


Figure 10: Bentonite slurry-filled cofferdam test result

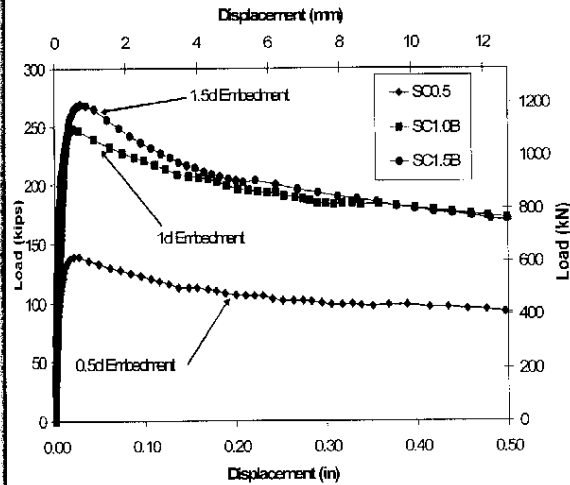


Figure 9: Control cofferdam test result

**DISCUSSION**

The goal of the study was to determine the interface bond between steel piles and seal slabs that had been cast in accordance with existing construction specifications (concrete piles were also tested). As the FDOT specifications allow a 72 hour cure period for the seal slab, the need to develop a scheme that met the requirement for rapid testing without compromising the results was of critical importance. Pullout testing was used and several innovative measures adopted to expedite the testing process.

In the model study, 36 tests (28 concrete and 8 steel) were completed within 8 hours following the 72 hour cure period. During this time, no changes in concrete strength were observed. In the full-scale tests, greater time was required to complete the testing. An important constraint was access to heavy lifting equipment (and an operator) to move the pullout frame after every test. However, all 32 tests (16 concrete and 16 steel) were completed within 10 days of the casting of the seal slab. As concrete strengths

were evaluated throughout the test period, the relationship between the interface bond and concrete strength was used to normalize the bond values. Taking into consideration the totality of the study, the model and full-scale results provide a good indication of the magnitude of the interface bond that develops between the seal concrete and piles.

The results from the model tests gave higher bond values than those from the full-scale tests (see Tables 1 and 2). Similar trends were observed in the tests on the prestressed piles<sup>3</sup> though the differences were much smaller. This is most likely because the surfaces of the steel piles in the full-scale tests were smoother compared to those used in the model tests. In contrast, the concrete surfaces in both model and full-scale tests were similar.

As with prestressed piles, the results clearly indicate that the variation in the interface bond is non-linear since the pullout load was not proportional to the embedment depth. Unfortunately, this distribution could not be measured without introducing surficial anomalies due to instrumentation. However, in the concrete piles where strain gages could be embedded during casting this relationship could be ascertained<sup>3</sup>. The non-linearity in the interface shear distribution was indirectly incorporated in the proposed recommendation by defining an effective "embedment depth." Embedment in excess of this effective depth did not contribute significantly towards the total resistance (Figures 8 - 10).

## CONCLUSIONS

This study presents results from an experimental study that attempted to determine the interface bond stress that developed between seal concrete and steel piles. Two series of tests were conducted. In the first series, a one-third scale model was fabricated and tested. Three different placement conditions were investigated - displacement of fresh water, salt water, and bentonite slurry for two different embedment depths. In the second series, full-scale tests were conducted for two different conditions - fresh water and bentonite slurry. In all cases, results were compared against controls where no fluid was displaced. Seal slabs were cast using concrete delivered by ready-mix plants and conformed to Class III concrete in current FDOT specifications. The concrete was allowed

to cure for at least 72 hours prior to testing as permitted by existing specifications. The following conclusions may be drawn:

Bond stresses determined experimentally were significantly higher than set in current specifications. Average values obtained from the full-scale tests varied between 1.1-1.3 MPa for fresh water displacement and 0.5-0.9 MPa for bentonite displacement. The lowest value obtained was for piles embedded in bentonite cofferdam a depth 2d.

Bond strength varied with embedment depth as indicated by both the model and full scale test results. This implies that thicker seal slabs cannot develop full bond capacity simultaneously along the entire bonded area beyond a maximum length. Instead, they develop full capacity over shorter bonded lengths dependent on the concrete shear strain limit value with respect to the elongation of the pile. In this case it was shown that embedment depths in excess of 1d were ineffective in supplying additional pullout capacity.

The results of the study confirm the poorer interface bond for steel surfaces compared to concrete where 1d average values for water and bentonite conditions were 2.7 MPa and 2.5 MPa, respectively<sup>4</sup>.

Variations between the model-scale and full-scale test results can be in part attributed to the surface roughness of the as-delivered steel piles. The model piles were partially oxidized, whereas the full-scale piles had never been exposed to an outdoor environment prior to placement. The recommended values are based on the full-scale test results which are therefore conservative.

## RECOMMENDATIONS

Loads supported by the bond between seal concrete and steel piles (*section depth d, perimeter p, embedded depth D in seal slab*) may be determined from the allowable bond stress,  $F_b$ , listed in Table 3. This stress may be assumed to be uniform over an effective area  $A_e$  given by:

$$A_e = pD \quad \text{if } D < d$$
$$A_e = pd \quad \text{if } D > d$$

**Table 3 Allowable Bond Stresses:**

Material	Condition	$F_b$ (kPa)
Steel	Salt/Fresh Water	1000
	Bentonite	350

In the latest Florida Design Guidelines<sup>7</sup>, allowable interface shear values have been greatly increased based on the findings presented in this paper.

**ACKNOWLEDGMENTS**

This investigation was carried out with the financial support of the Florida Department of Transportation. The authors especially acknowledge the contribution of Hayward Baker Inc. Tampa, FL in the full-scale testing as well as Rudy. However, the opinions, findings and conclusions expressed in this publication are those of the writers and not necessarily those of the Florida Department of Transportation.

**REFERENCES**

1. Standard Specifications for Highway Bridges 13<sup>th</sup> Edition, American Association of State Highway and Transportation Officials, Washington, D.C., 1983.
2. Structural Design Guidelines, Florida Department of Transportation, Section 4.18, Topic No: 625-020-150c, July, p. 4-12, Tallahassee, FL, 1998.
3. Mullins, G., Sosa, R., Sen, R. and Issa, M., "Seal Slab Prestressed Pile Interface Bond from Full-Scale Tests," ACI Structural Journal, Vol 98, No.5 Sept.- Oct., 2001, pp.743-751.
4. Mullins, G., Sosa, R. and Sen, R., "Seal Slab/Pile Interface Bond", *Final Report* submitted to Florida Department of Transportation, June, 2000, pp. 151.
5. Wu, Z., "Studies of Bond of Cast-in-Place Concrete to Other Surfaces," Master's Thesis, Department of Civil and Environmental Engineering, University of South Florida, Tampa, FL, August, 1999.
6. Standard Specifications for Road and Bridge Construction, Florida Department of Transportation, State Specifications Office, Tallahassee, FL, 1999.
7. Structural Design Guidelines, Florida Department of Transportation, Table 5.3, Tallahassee, FL, 2000.

## Chapter 6

---

# Concrete stress determination in Rapid Load Tests

*Michael Stokes and Gray Mullins*

*University of South Florida, Tampa, FL, USA*

---

### INTRODUCTION

The effects of loading rate on concrete strength and elastic modulus have long been recognized with regards to seismic and/or dynamic loading events. In such cases an increase in strength is reported to show up to 15 percent higher values. Rapid load tests of deep concrete foundation elements use the concrete modulus determined from field calibration via strain gages directly under the applied (known) load. Therein, rate-dependent effects can be directly incorporated into the determination of load from strain measurements elsewhere in the foundation element. However, in many cases the strain rate at various strain gage levels throughout the foundation may differ and the magnitude of strain may or may not lend itself to linearly approximated stress-strain relationships.

Hence, the modulus selected to determine the load sensed at these levels can produce erroneous results if a single value is assumed. This article presents the findings of an experimental program designed to quantify the relationship between concrete stress, strain, and strain rate. Developed equations are used to show the effect of various stress evaluation methods on rapid load test results.

### GENERAL REVIEW OF THE RESEARCH

In long test piles that exhibit a significant amount of side shear, multiple strain gages are often embedded at different levels so as to better understand the distribution of forces along the length of the pile (Figure 1). Strains recorded at these gage locations lend insight into the amount of load transferred to the surrounding soil. In order to perform these computations, the cross-sectional area and elastic modulus at each gage location are typically used to estimate the load at that level. In the case of the cross-sectional area, it can be accurately measured prior to driving (driven piles) or legitimately assumed based on the borehole diameter (drilled shaft). The modulus at each gage location is taken as a composite modulus based on the modular ratio and the proportions of steel and concrete. Where the elastic modulus of steel is well documented and remains relatively constant regardless of its grade (200 GPa or 29000 ksi), information gathered from a concrete compression test (ASTM C39) on a sample of the mix and empirical equations are often used to estimate the elastic modulus of concrete. The following equations from the American Concrete Institute (ACI) are based on a secant modulus of approximately  $0.45 f'_c$  (Eqns. 1 and 2).

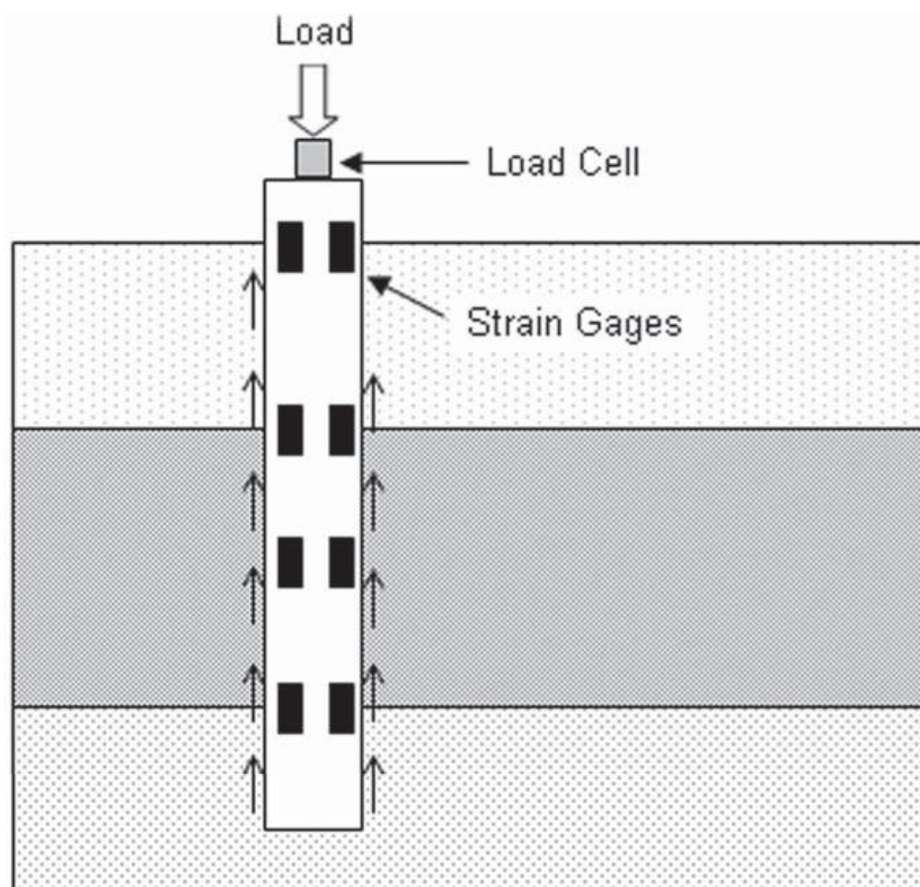


Figure 1 Instrumentation scheme in a long pile.

$$E_c = 33w_c^{1.5}\sqrt{f'_c} \quad (w_c \text{ in pcf and } f'_c \text{ in psi}) \quad (1)$$

$$E_c = 57000\sqrt{f'_c} \quad (\text{for normal weight concrete}) \quad (2)$$

Alternately, the composite modulus can be calculated directly by calibrating the measured load at the top of the pile with near-surface strain or modulus gages. This process of “matching” the top level strain to the load eliminates the need to determine the individual contribution of the steel and concrete, for the calibration inherently accounts for the composite cross-section. Adjustments are then made depending on the reinforcement ratio throughout the length of the pile. If the measured load and strain are used to back-calculate a composite modulus as a function of time, it becomes apparent that the modulus changes significantly throughout the test (Figure 2).

Whether using empirical equations or near-surface gages, the composite modulus is assumed to remain constant throughout the duration of the load test, and a simple

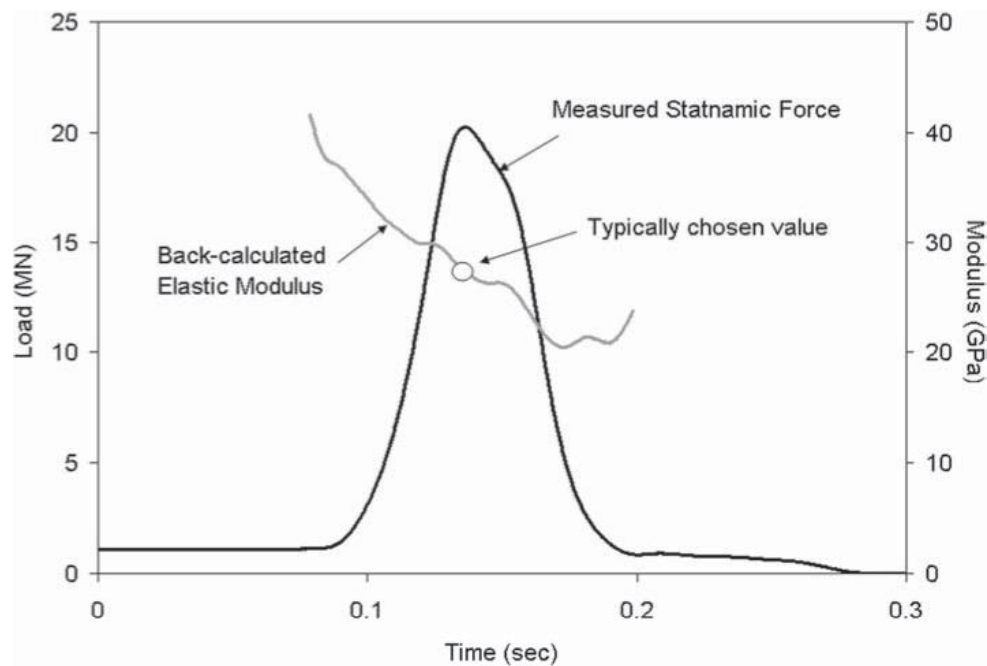


Figure 2 Back-calculated (field calibrated) elastic modulus from near-surface or modulus gages.

linear relationship (Hooke's Law) is used to relate the measured strain to the stress at a particular gage level (Figure 3). This relationship may be valid as it applies to the steel, but the nonlinear behavior of concrete can lead to grossly inaccurate estimations of stress within the concrete portion of the composite section. A more representative estimation of stress can be computed with the implementation of a nonlinear model where the concrete modulus varies as a function of the level of strain.

Recently, consideration has been given to the use of a variable strain-dependent modulus in the regression of static load test data (Fellenius 2001). In this particular case study, static load test data on a 20 m monotube pile was evaluated using both a strain-dependent modulus and a constant, average modulus. Results from the evaluation indicated that the mid-level pile stresses were lower than what was computed using a constant modulus, and lower level stresses were higher. It was concluded that if the constant modulus were used, the "resistance acting between the two levels would have been determined with an about 10 percent to 20 percent error."

The Hognestad model is one of the more popular parabolic stress-strain relationships whose first derivative, or modulus, varies as a function of strain. It expresses a stress-strain curve that is only dependent on the compressive strength and the corresponding ultimate strain (Eqns. 3 and 4). Though the use of a nonlinear stress-strain model may account for a strain-dependent modulus, it does not address unloading stresses or compensate for load rate effects that occur during rapid and/or dynamic load tests.

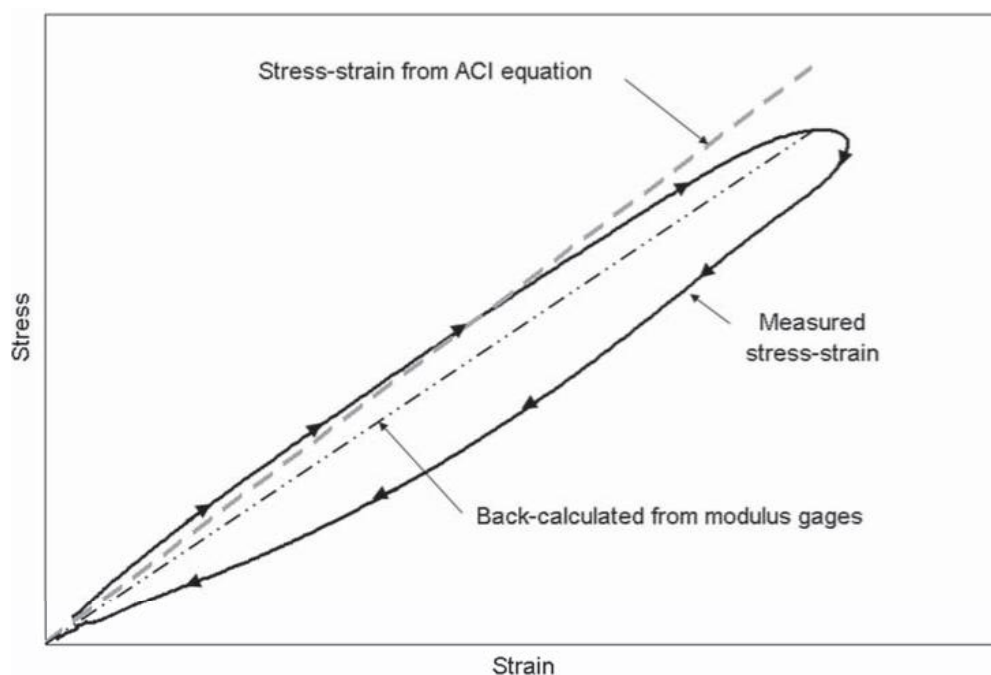


Figure 3 Assumed linear stress-strain relationship vs. measured response.

$$f_c = f'_c \left[ \frac{2\varepsilon_c}{\varepsilon_o} - \left( \frac{\varepsilon_c}{\varepsilon_o} \right)^2 \right] \quad \text{or} \quad (3)$$

$$f_c = -\frac{f'_c}{\varepsilon_o^2} \varepsilon_o^2 + \frac{2f'_c}{\varepsilon_o} \varepsilon_c \quad (4)$$

The effect of increased load rates on the compressive strength of concrete has long been realized. Takeda and Tachikawa (1971) proposed a relationship between stress, strain, and strain rate from test results of 14 different batch mixes with varying aggregate sizes subjected to strain rates ranging from 1 me/s to 1 e/s (Figure 4). Despite the different mix designs and concrete properties, all specimens produced geometric similarities in their stress-strain-strain rate relationships. Most researchers agree that the compressive strength of concrete increases as much as 15% at strain rates of 0.02 e/s, although the increase in modulus is more moderate (Fu *et al.* 1991). Some signal matching algorithms for dynamic wave analyses recognize these rate effects and compensate by varying the concrete modulus throughout the length of the pile. However, the modulus assigned to each level is again assumed constant and Hooke's Law used to determine the stress.

Strain values in a pile exhibiting either elastic behavior or large amounts of side shear can vary significantly throughout the length of the foundation (location) as well



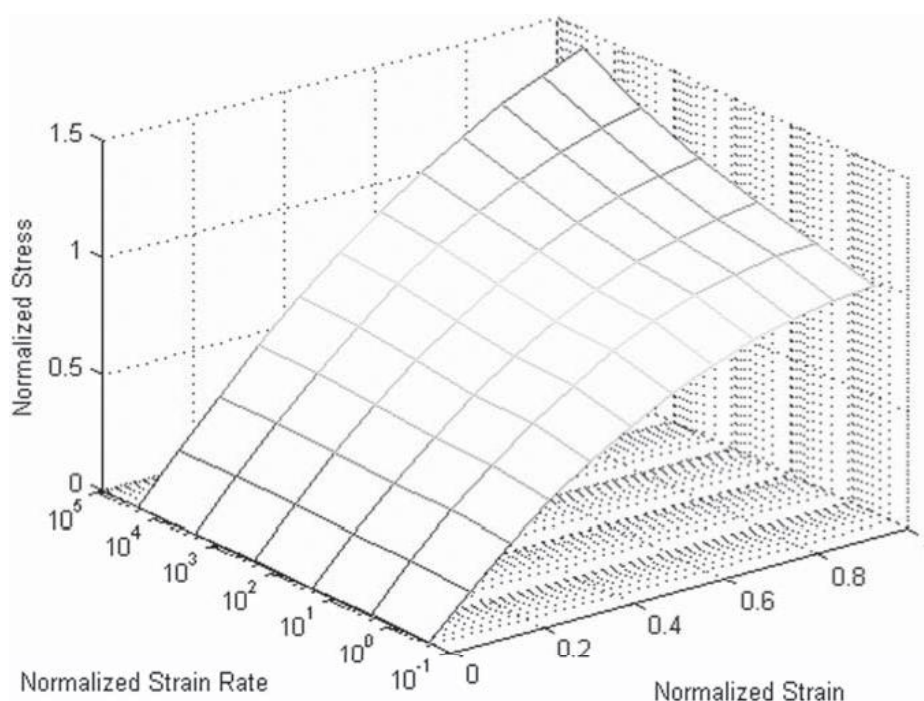


Figure 4 Normalized concrete stress-strain-strain rate relationship (adapted from Takeda and Tachikawa (1971)).

as throughout the loading event (time). During rapid and dynamic tests, these strain measurements are almost never in phase and therefore add a degree of difficulty when determining the ultimate capacity. Consider the strain at multiple levels throughout the drilled shaft in Figure 5. Not only is it evident that the upper level gages experience higher strains, but they undergo much larger strain rates than the lower level gages. Also prominent is a delay of maximum strain, or phase shift, at each level. Had the maximum strains occurred simultaneously at each gage level, then perhaps compensation for strain rate effects may not prove to be worthwhile when calculating the ultimate capacity, since the strain rate at maximum strain is zero. However, the ultimate capacity in rapid and dynamic tests usually occurs at a point in time between the maximum strains of the upper and lower levels. Because of this, strain rate effects must be considered, and unloading stresses must be accurate.

### CONSEQUENCES OF THE RESULTS FOR THE STANDARD AND THE GUIDELINES

The nonlinear hysteretic behavior of concrete coupled with its sensitivity to increased loading rates suggests that the use of a constant concrete modulus and a linear stress-strain relationship may be inappropriate for certain load tests that exhibit a wide range of strains and strain rates throughout a pile. Previous research on static load

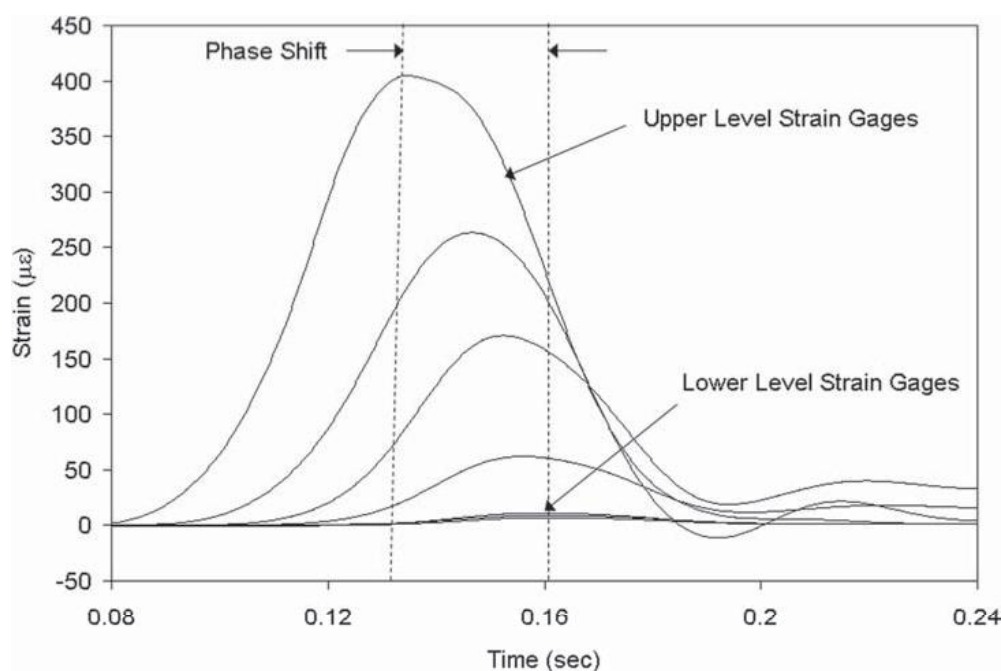


Figure 5 Strain distribution throughout a pile during a rapid load test.

test results has shown that the use of a constant concrete modulus in determining gage level stresses from measured strains can substantially over-predict stresses near the top and under-predict stresses near the bottom of a pile. With this in mind, strain rate effects introduced during rapid load tests only compound the complexity. Regardless of the type of load test used or analysis procedure performed, provisions for a variable modulus and/or nonlinear hysteretic stress-strain-strain rate model may prove to refine the test results and ultimately yield a more accurate interpretation of the foundation performance. A suitable solution is provided herein.

## DESCRIPTION AND RESULTS OF THE RESEARCH

In order to confirm the results of previous researchers and identify the strain rate effects indicative of rapid load tests, thirty 50 mm × 100 mm (2 in × 4 in) cylindrical mortar specimens were cast and tested at various loading rates using a MTS 809 Axial/Torsional Test System and a 180 kN (20 T) laboratory-scale rapid load testing device (Stokes 2004). Due to the limitations of the rapid load testing device, smaller diameter mortar cylinders were chosen as test specimens to ensure that failure was achievable, especially with an anticipated rate-dependent strength increase of 15%. Though aggregate scaling issues existed between the mortar specimens and published concrete data, results of Takeda and Tachikawa indicate that their behaviors should be similar.

Table 1 contains the mix design for the batch of specimens. Each specimen was instrumented with 2–10 mm resistive type strain gages located at mid-height and

Table 1 Specimen mix design.

Batch volume	0.014 m <sup>3</sup>
w/c ratio	0.485
Mini-slump pat	
Diameter	63.61 cm <sup>2</sup>

Table 2 Specimen load rates.

Number of specimens	Load rate (kN/sec)
4	0.7
2	2.4
2	7.7
3	25.4
3	82.3
3	266.3
3	861.6
3	2788.1

180 degrees apart. Data was collected using a data acquisition device at various sampling rates appropriate for the loading rate of each specimen.

*Phase 1 testing* The first 23 cylinders were tested to failure using the MTS compression device at load rates that ranged from 0.7 to 2788 kN/sec (Table 2). A minimum of two cylinders were tested at a given load rate as is customary with ASTM standards. Scaled testing caps were made to replicate those used in larger cylinder tests and reduce the frictional restraining forces between the ends of the specimens and the testing platens.

*Phase 2 testing* The remaining 7 cylinders were tested using the laboratory-scale rapid load testing device. This device was used to achieve representative rapid load test strain rates that were beyond the limitations of the MTS device. Though the intent was to load each cylinder to failure, 3 of the tests did not provide adequate force to break the cylinders, therefore unload data was inadvertently obtained. This mishap proved fortunate in the later developmental stages of the stress-strain model.

### Model formulation

Results from the first testing phase and the cylinder breaks from the second testing phase showed that the stress and modulus at any given strain increased with increasing load rate (Figure 6). Though the strength exhibited a distinct increase, any trend in the ultimate strain was indiscernible. If assumed that the strain rate remains constant throughout the test as is loading rate, then the individual tests can be plotted in a 3-dimensional space as seen in Figure 7. In order to determine the best-fit surface through these data points, the Hognestad parabolic stress-strain model was used to

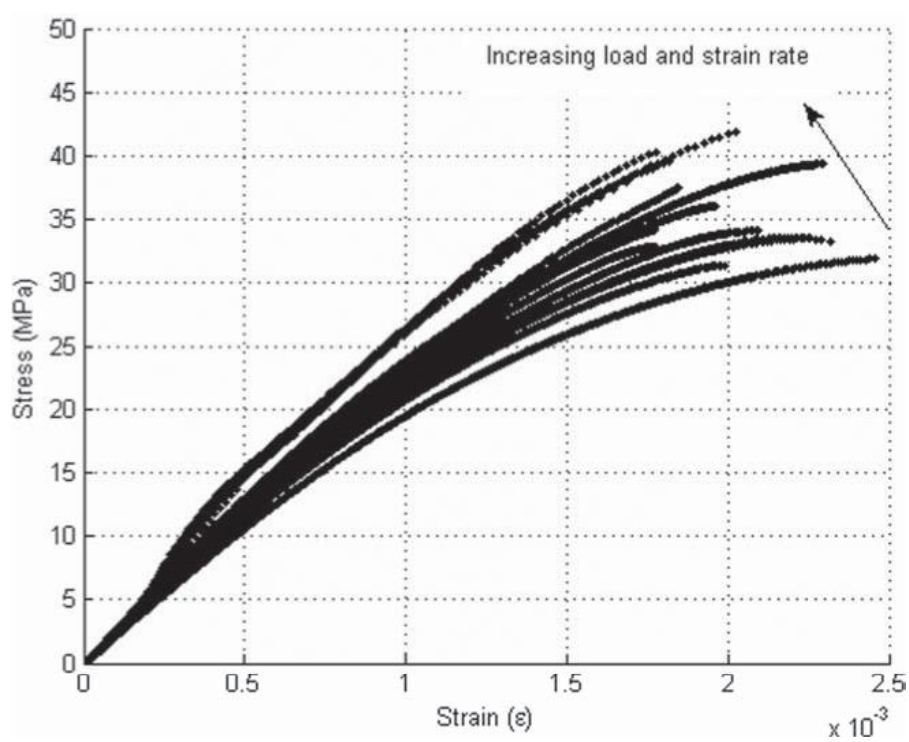


Figure 6 Stress-strain relationship from first and second phase laboratory tests.

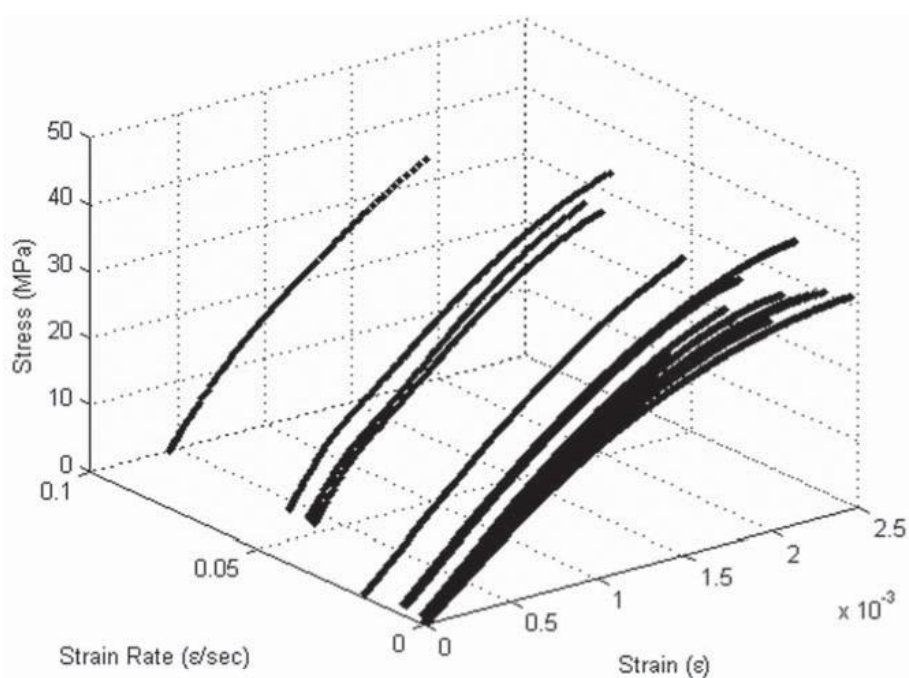


Figure 7 Stress-strain-strain rate relationship assuming constant strain rates.

fit the two tests run at the upper ASTM loading rate limit (0.7 kN/sec). This well-accepted parabolic relationship proved to be a relatively simple but reliable model for fitting the ASTM load rate data (Figure 8).

To better understand the strain rate effects and to expand the Hognestad relationship into the strain rate dimension, all data falling within constant values of strain (strain bands) were plotted in the stress-strain rate plane (Figure 9). From this, a cubic relationship for each constant-strain band was determined and applied to the base Hognestad model such that a best-fit surface could be created through the data (Figure 10). A more familiar surface appears when the strain rate is converted to log-scale as is traditionally published (Figure 11).

This model was developed with the assumption that both the strain rate and load rate remained constant throughout each test. However, examination of the data as a function of time revealed that they varied significantly. Variations in the loading rate are largely due to the logic statements in the computer code and feedback controls attempting to hone the testing device on a specified loading rate. Although variations in the strain rate are partly a result of the load rate control, they are mostly the result of the nonlinear behavior of the mortar. As previously discussed, a simple linear stress-strain model does not adequately describe the nonlinear stress-strain response of concrete and/or mortar, therefore it should not be expected that the time derivatives be directly proportional.

$$f_c \propto \varepsilon_c \therefore \dot{f}_c \propto \dot{\varepsilon}_c \quad (5)$$

If an instantaneous strain rate is calculated for each test instead of assuming that the strain rate remains constant, a slightly different plot emerges (Figure 12). After performing the same procedure described above for determining the best-fit surface, a model was developed which exhibits a similar shape but more subtle increase in ultimate strength with increasing strain rate (Figure 13).

$$f_c = -\frac{f'_c}{\varepsilon_o^2} \varepsilon_c^2 + \frac{f'_c}{\varepsilon_o} \varepsilon_c \left[ \frac{5}{4} (\dot{\varepsilon}_c - \dot{\varepsilon}_o)^{\frac{1}{3}} + 2 \right] \quad (6)$$

Upon close examination, it can be seen that the above equation is a modified version of the published Hognestad relationship. The modification is in the form of a strain rate multiplier applied only to the "B" coefficient of the base parabolic equation. As a result of the data analysis, it was determined that modifications to the "A" coefficient led to no sizeable effects that could not be accounted for entirely in the "B" coefficient. A statistical analysis was performed against the raw data and their corresponding modeled values which yielded a coefficient of determination of 0.993. Again, the modeled surface displays a familiar geometric shape when the strain rate axis is plotted in log-scale (Figure 14).

Another attempt at developing a modeled surface was made; however, this model was based on a logarithmically increasing stress as a function of strain rate (Eqn. 7). Though the logarithmic-based multiplier promised a better fit at lower strain rates, it did not represent the increase in stress beyond 0.2 e/sec well. Despite this downfall,

## 82 Rapid Load Testing on Piles

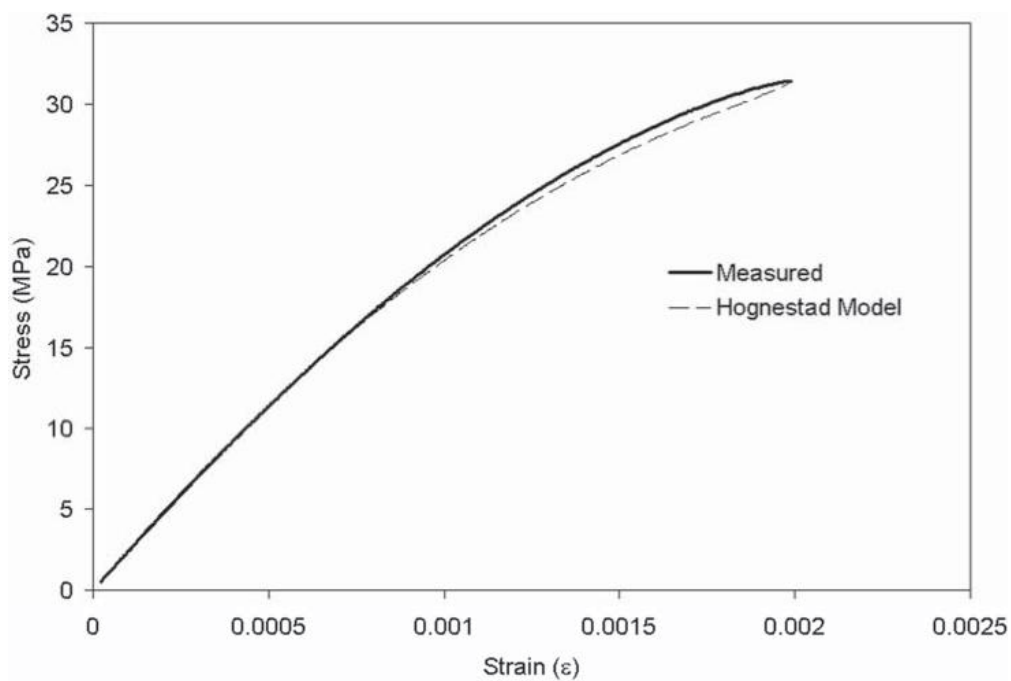


Figure 8 Hognestad modeled stress-strain relationship for ASTM strain rate data.

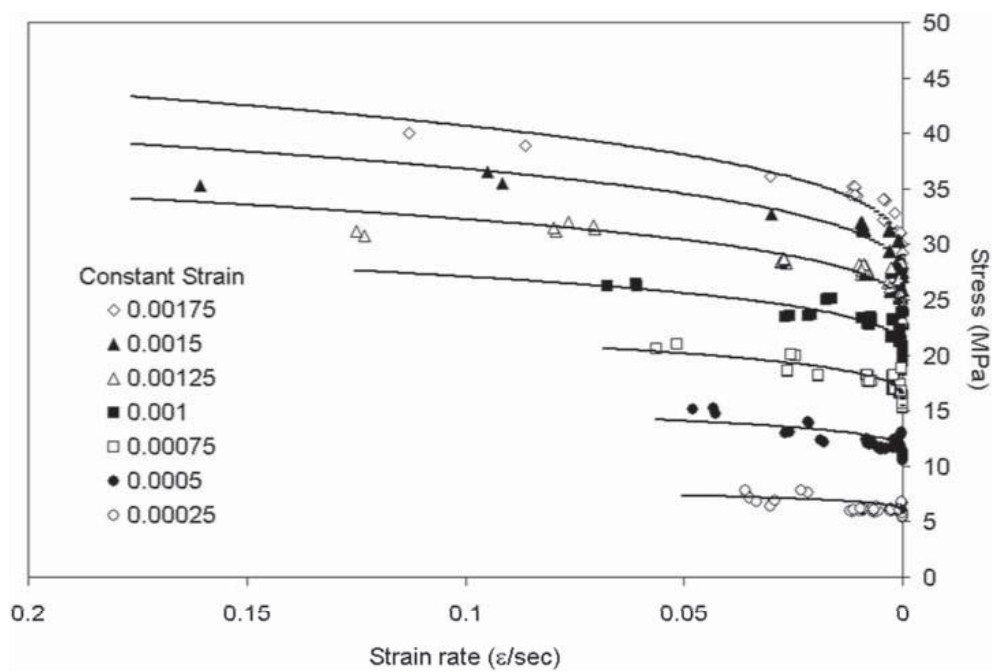


Figure 9 Stress-strain rate relationship plotted for incremental constant values of strain.



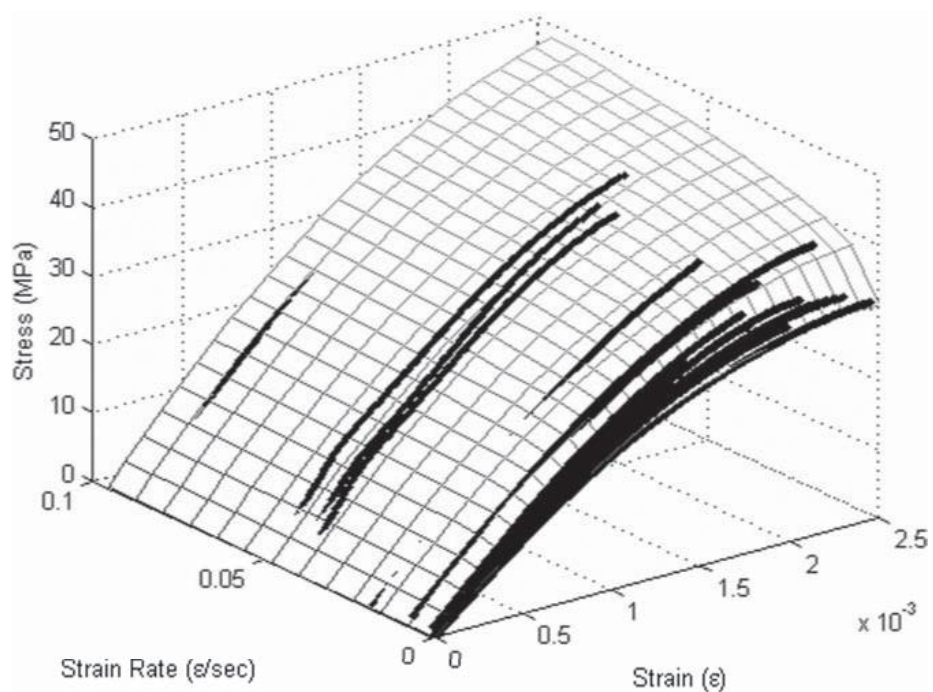


Figure 10 Best-fit surface for assumed constant strain rate data.

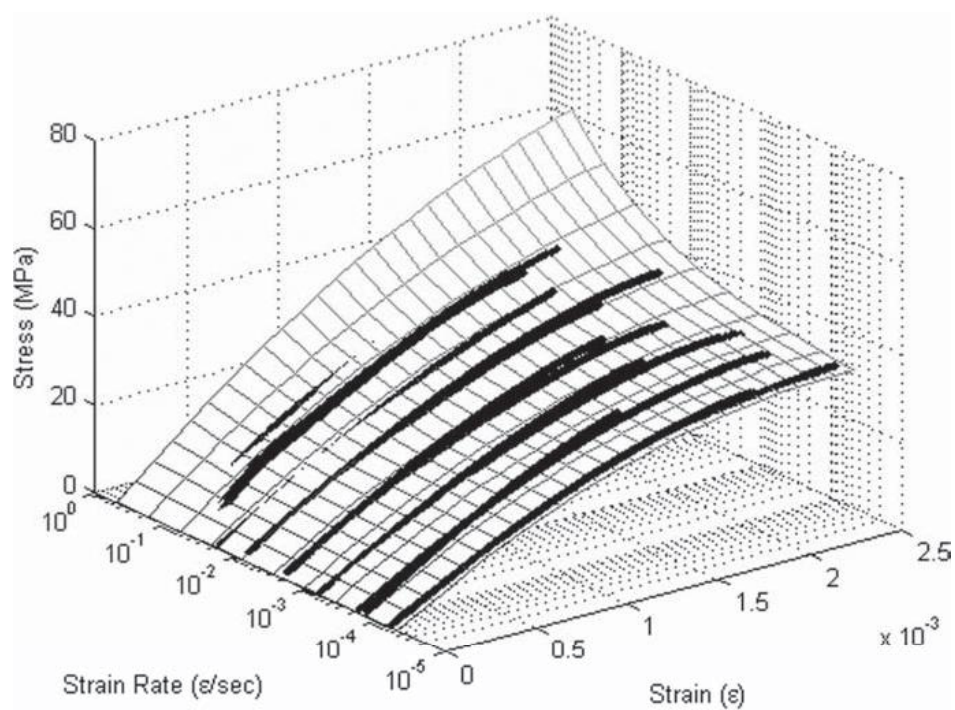


Figure 11 Best-fit surface for assumed constant strain rate plotted in log scale.

## 84 Rapid Load Testing on Piles

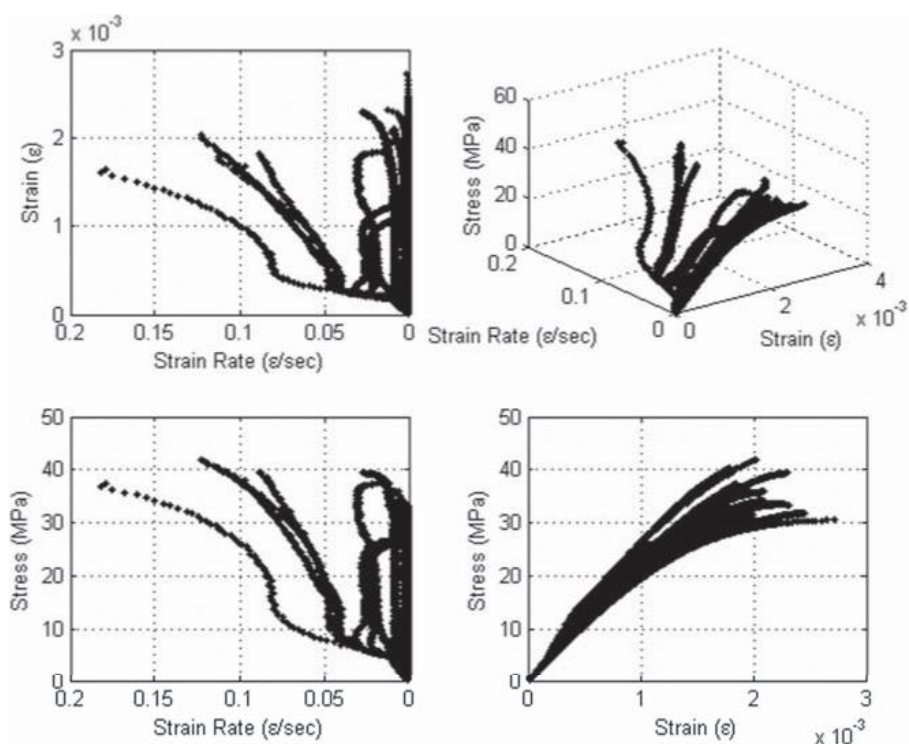


Figure 12 Data plotted using instantaneous strain rate instead of assumed constant strain rate.

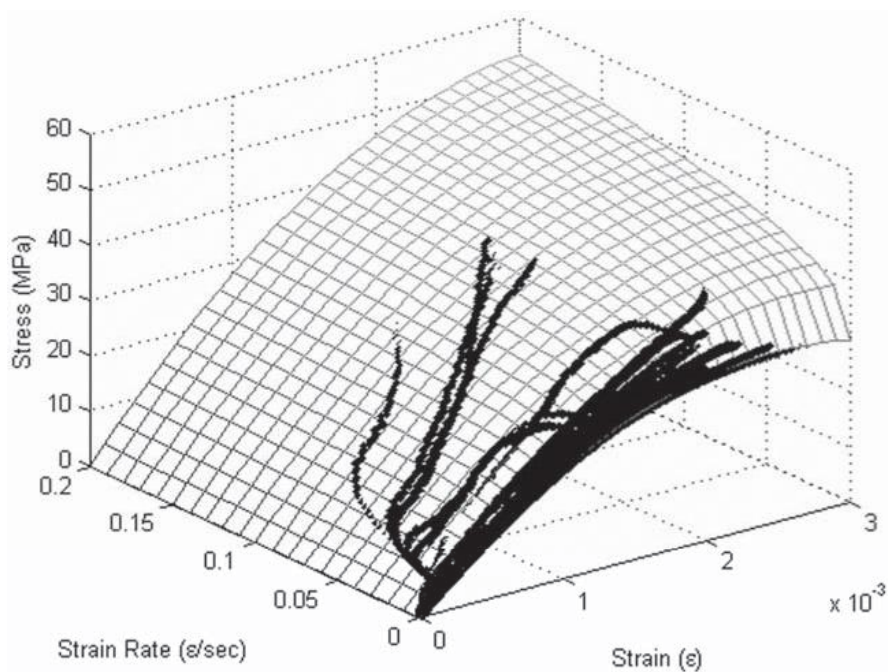


Figure 13 Best-fit surface for data using instantaneous strain rate.



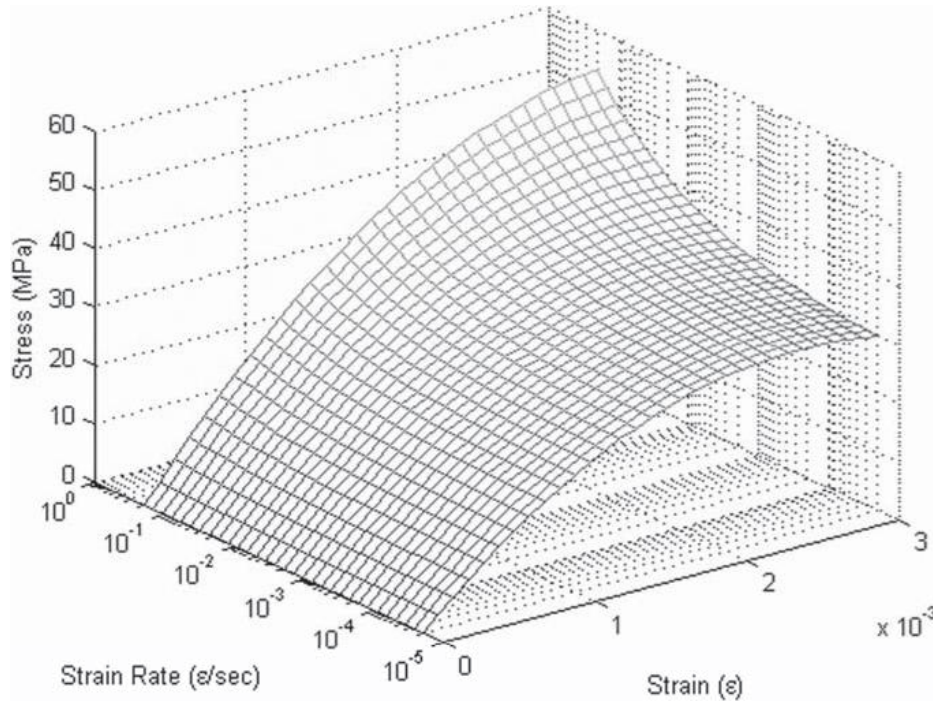


Figure 14 Best-fit surface for data using instantaneous strain rate (log scale).

the logarithmic model yielded a coefficient of determination of 0.992, and although both models seemed to match well, the cubic model was chosen due to its consistency with published results.

$$f_c = -\frac{f'_c}{\epsilon_o^2} \epsilon_o^2 + \frac{f'_c}{\epsilon_o} \epsilon_c \left[ \frac{1}{17} \ln \left( \frac{\dot{\epsilon}_c}{\dot{\epsilon}_o} \right) + 2 \right] \quad (7)$$

In an attempt to apply the model toward all concrete/mortar types, the base Hog-nestad model and the strain-rate compensating multiplier were normalized to all three input parameters: the ultimate strength ( $f'_c$ ), the strain at ultimate strength ( $\epsilon_o$ ), and the strain rate at which the ultimate strength and strain were determined ( $\dot{\epsilon}_o$ ). All values can be determined from a standard concrete cylinder compression test (e.g. ASTM C39). Though it has been noted that the strain rate and load rate do not remain constant throughout a compression test, the ASTM standard makes provisions for this variability by stating that “the designated rate of movement shall be maintained at least during the latter half of the anticipated loading phase of the testing cycle.” For the purposes of normalization, the strain rate is taken near the latter half of the testing cycle where it remains fairly constant.

$$f_N = 2\epsilon_N \left[ \frac{1}{50} (\dot{\epsilon}_N - 1)^{\frac{1}{3}} + 1 \right] - \epsilon_N^2 \quad (8)$$

When plotting a single test where failure occurred, the stress path can be seen as it maneuvers closely along the modeled surface (Figure 15). However, in a test specimen where failure did not occur, the stress path deviates from the surface as the strain rate decreases (Figure 16). Once the strain rate decreases to within ASTM rates, the stress does not decrease as the model predicts, but remains higher. This led to the presumption that the model was only valid for specimens that were loaded to failure where the strain rate was in a continually increasing state. For tests that did not experience failure but underwent a load cycle, the model sufficiently predicts the stress up to the point of maximum strain rate; but afterwards, the measured stress follows a different path.

By plotting the test data from the Phase 2 specimens that underwent a load cycle, it was determined that beyond the point of maximum strain rate (hereafter referred to as the transition point), constant strain bands decreased linearly (Figure 17).

A second surface was fit to model these data beyond the transition point (Figure 18). It is important to note that the origin for the linear decrease of the second model is entirely based on the stress-strain relationship defined at the location of the transition point. Depending on the magnitude of loading, the stress-strain relationship diverges from a common loading surface beyond the transition point (Figure 19). Prior to reaching the transition point, the A and B coefficients of the parabolic stress-strain curve are changing based on the cubic model (equation 8). When the transition point is reached, the strain rate multiplier on the B coefficient remains constant for the remaining portion of the test, and a linearly decreasing offset is applied to the entire relationship (equation 9). This offset is a function of strain-rate and was derived using only data in the decreasing strain-rate portion of the test. Despite a second inflection in strain rate near the end of the loading cycle (Figure 20), this linearly offset model sufficiently predicts the end-of-test stresses.

$$f_N = 2\varepsilon_N \left[ \frac{1}{50} (\dot{\varepsilon}_{N-tp} - 1)^{\frac{1}{3}} + 1 \right] - \varepsilon_N^2 - 0.00012 (\dot{\varepsilon}_{N-tp} - \dot{\varepsilon}_N) \quad (9)$$

Figures 21 and 22 offer a three-dimensional outlook on the normalized stress path taken by one of the specimens (STN 6) and the modeled stress as determined by the pre-transitional cubic model and the post-transitional linear model (Figure 23). The coefficient of determination is 0.997, thereby showing that there is good agreement between the measured and modeled stress.

### Case studies

During the development stage of the model, input values were normalized with respect to the ultimate compressive strength, the strain at ultimate strength, and the strain rate at which these values were determined. The intent was to define a model that could be applied to the regression of concrete pile load test data despite the many possible variations in the concrete mix design. In order to test the viability of the model, two case studies were examined where stress, strain, and strain rate information were available. These case studies were selected due to the presence of modulus gages and concrete strength information. In both cases, the upper level strain gages were located

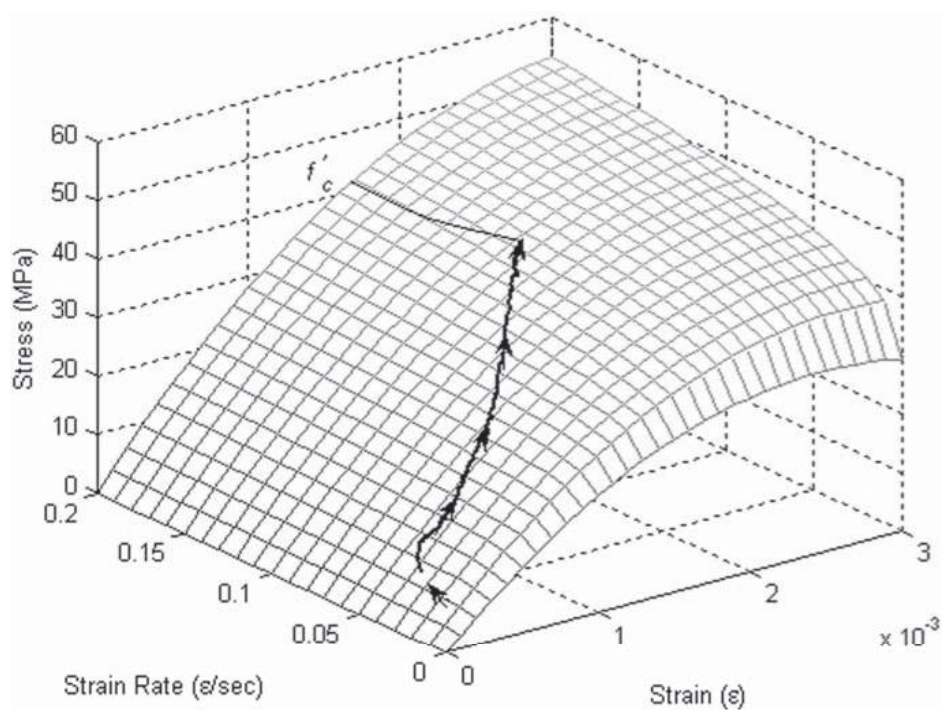


Figure 15 Stress path of a specimen taken to failure.

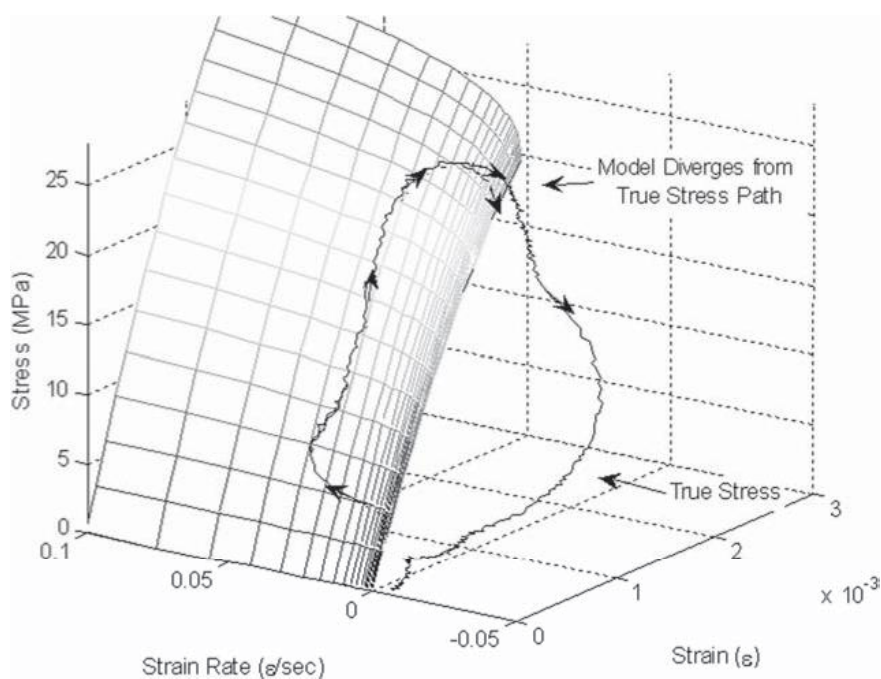


Figure 16 Stress path of a specimen that underwent a load cycle and divergence from original surface.

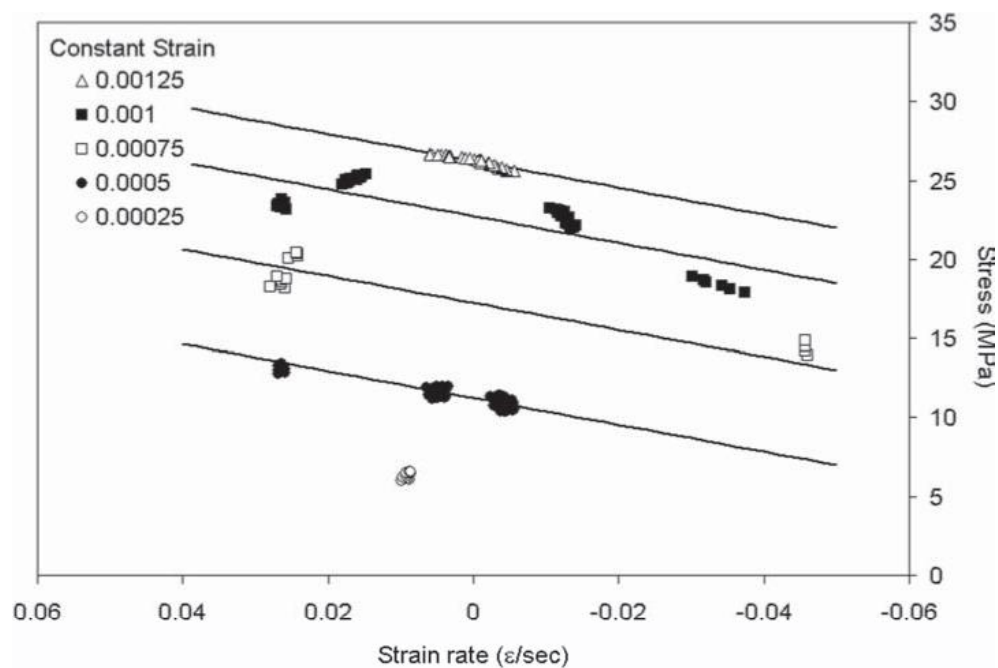


Figure 17 Constant strain bands for load cycle specimens.

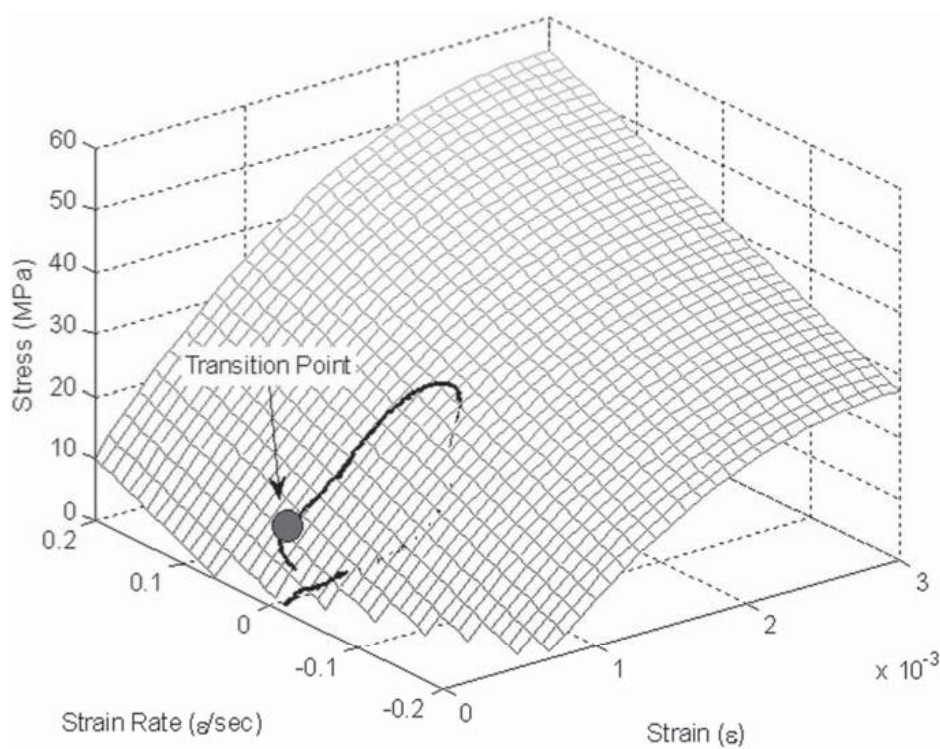


Figure 18 Linearly decreasing best-fit surface beyond transition point.

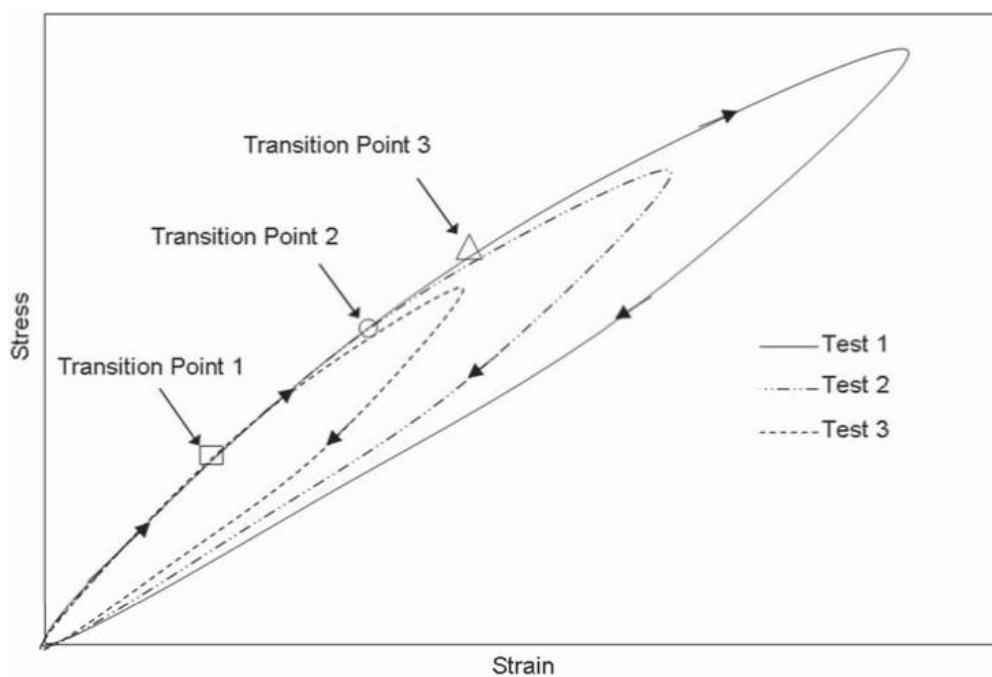


Figure 19 Dependence of unloading response on degree of loading.

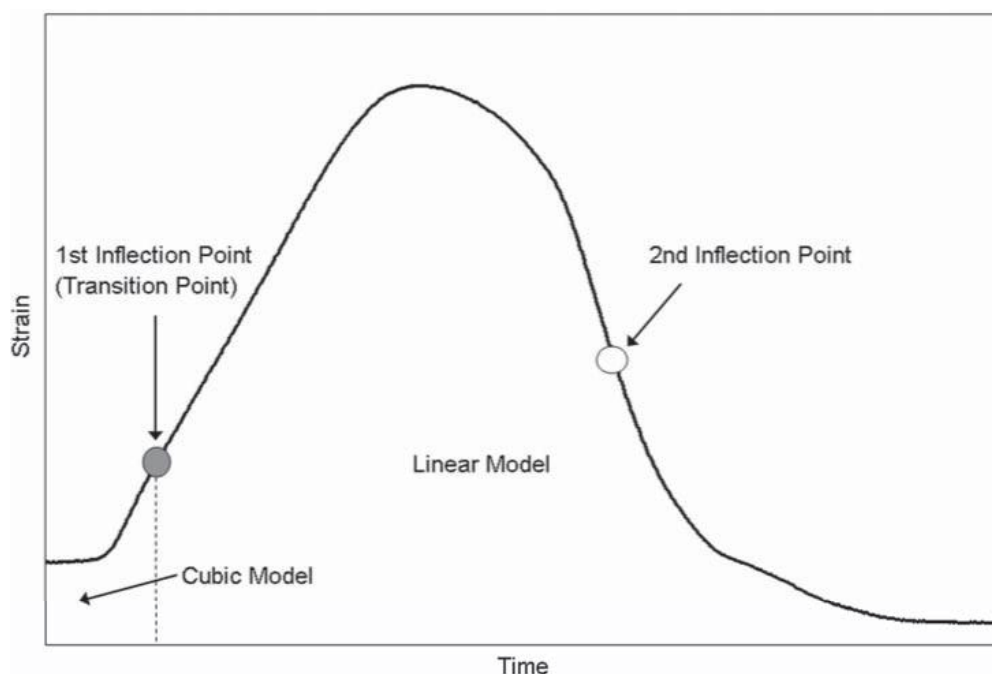


Figure 20 Regions of model application and locations of strain inflections.



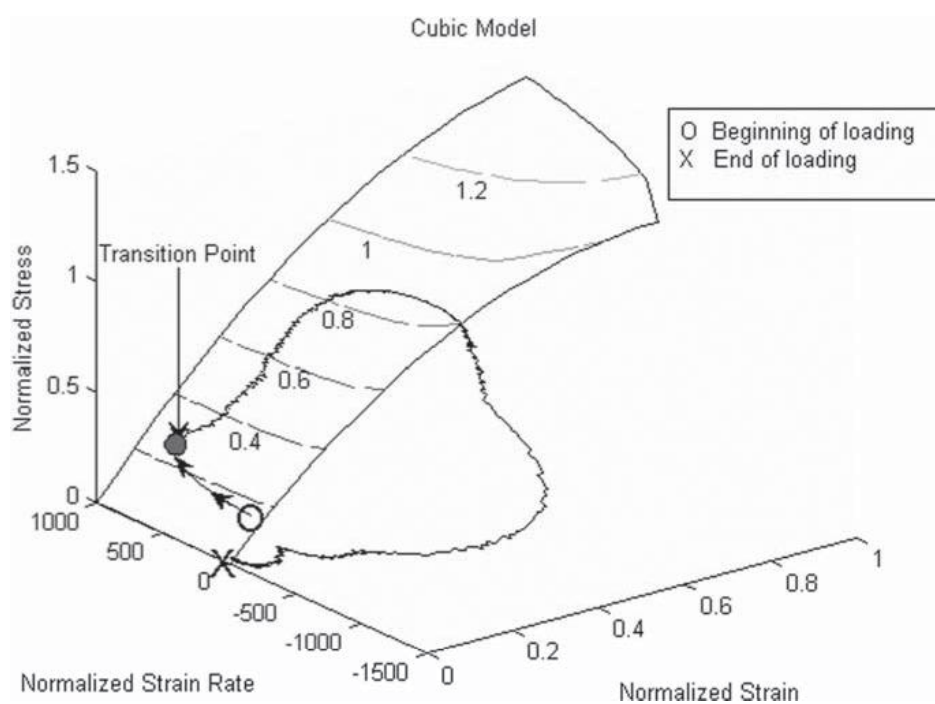


Figure 21 Normalized pre-transitional cubic model.

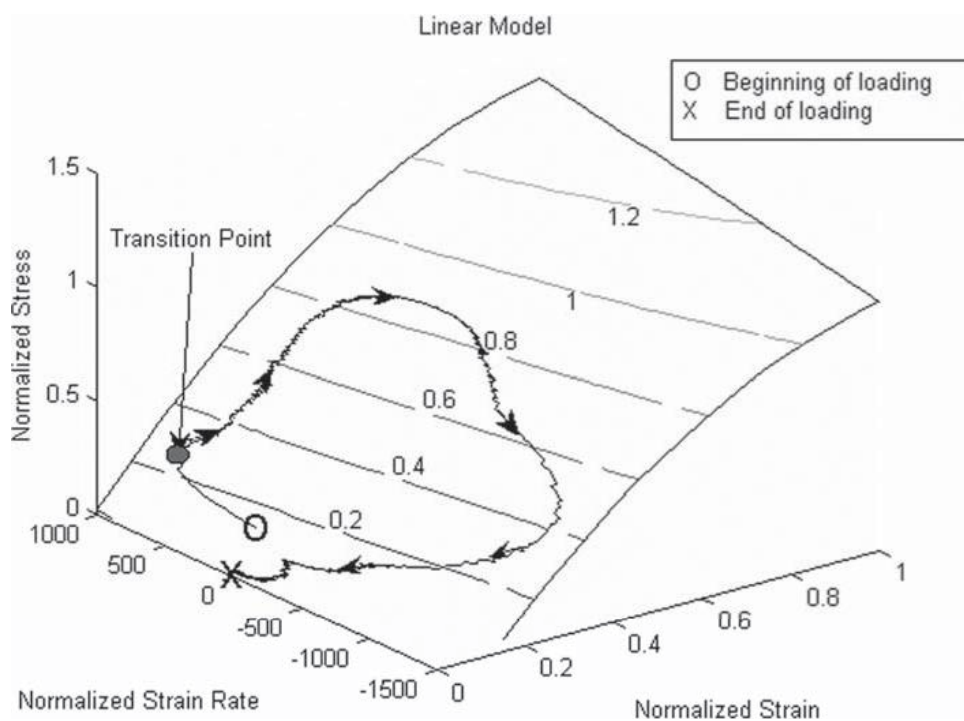


Figure 22 Normalized post-transitional linear model.

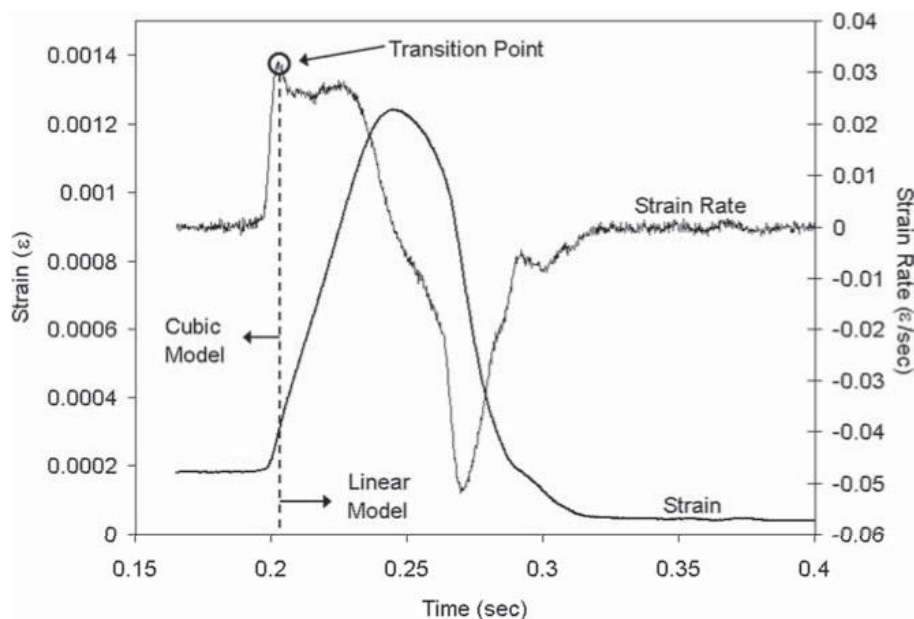


Figure 23 Transition point defining the application of the cubic and linear models.

such that there was no appreciable loss of load due to load shed. This ensured that the true axial stress at the gage location could be reasonably computed and provide a means for comparison.

*Houston Shaft S-1* As part of a collaborative effort between the University of South Florida (USF) and the University of Houston (UH) to demonstrate the effectiveness of post grouting, four drilled shafts were constructed then tested using a 16 MN static load testing device (Mullins and O'Neill 2003). Two of the 1.2 m (4 ft) diameter drilled shafts were embedded in sand, and the other two were embedded in clay. One shaft from each set served as a control (ungROUTED), while the other was post grouted prior to load testing. For the purposes of this article, the particular shaft of interest is the ungrouted control embedded in sand (Shaft S-1).

Shaft S-1 was constructed to 6.4 m (21 ft) using 18-#9 reinforcing bars with #4 ties on 15 cm (6 in) centers. Strain gages were placed on the reinforcing cage so as to correspond to changes in the soil strata at 1.2 m (4 ft), 2.1 m (7 ft), and 6.1 m (20 ft). Each strain gage level consisted of four resistive-type electrical strain gages positioned 90 degrees apart.

Since the upper level strain gages were located close enough to the ground surface to reasonably assume no losses due to load shed, the measured static force was used to determine the concrete stress at the upper level gage location.

Because the force was being applied to a composite cross-section, a portion of the load had to be discounted due to the presence of the reinforcing steel. This was accomplished by using the measured strain, known cross-sectional area of steel, and Hooke's Law to determine the force in the steel. Also, inertial effects were considered

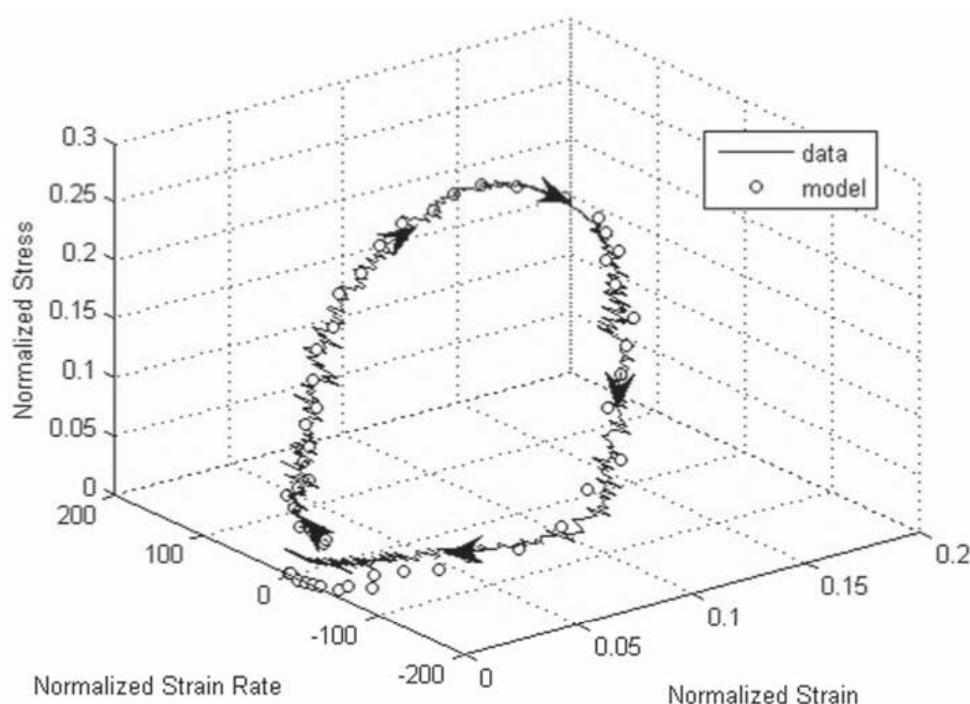


Figure 24 Modeled stress path vs. true measured stress path for Shaft S-1.

since the load cell and the strain gages were separated by a 3518 kg mass of concrete and steel. After these adjustments were made, the corrected force was divided by the cross-sectional area of concrete to obtain the stress at the upper gage level.

Using the information from the concrete cylinder compression tests, the ultimate strength (26.2 MPa or 3.8 ksi), ultimate strain (0.001862 e), and strain rate (40 me/sec) were determined and the data normalized. Figure 24 shows the normalized data plotted with the modeled response.

Good agreement was found between the data and the model despite the differences in the mix design between the concrete drilled shaft from which the data was taken and the mortar cylinders from which the model was developed (coefficient of determination of 0.980).

**Bayou Chico Pier 15** The Bayou Chico bridge project involved the replacement of an existing drawbridge in Pensacola, Florida with a newer high-rise bridge. One of the 600 mm square prestressed piles located at Pier 15 of the new bridge became part of an extensive load test program implemented by the Florida Department of Transportation (FDOT) that compared cycles of static, statnamic, and dynamic load tests (Lewis 1999). Prior to casting, vibrating wire and resistive type strain gages were mounted 180 degrees apart at five levels throughout the pile: 0.71, 2.57, 4.55, 6.6, and 8.53 m from the toe. The pile was driven to a depth of 8.4 m which resulted in the uppermost gages being positioned above ground surface.

A dynamic test was recorded on the pile during the last blow of installation, after which three consecutive static load cycles were performed. Nearly two months later,



a statnamic test was completed using a 14 MN device. For the purposes of this paper, only results from the statnamic test are considered.

An inertial correction was applied to determine the stress at the upper level strain gages and similar calculations performed as outlined in the previous case study; however, no correction was made on behalf of the prestressing strands. Since the strands remain in tension throughout the load test, any compressive stresses imparted by the device are taken entirely by the cross-sectional area of concrete. The only compensation for prestressing was applied as an initial compressive offset at strand release of 7.6 MPa.

No concrete cylinder compression test information was readily available for this particular case study, therefore information from previous data regressions was used to determine the ultimate strength (49.3 MPa or 7.15 ksi). The ultimate strain ( $0.0027\epsilon$ ) and strain rate ( $40 \mu\epsilon/\text{sec}$ ) were assumed based on cylinder compression test results of similar piles. Figure 25 shows the normalized data plotted with the modeled response. Again, good agreement is notable between the data and the model (coefficient of determination of 0.979).

When plotting the normalized results of both case studies, the difference in pile type is accentuated by the prestressing offset visible in the Bayou Chico pile (Figure 26).

### Model application

Since the results from the case studies indicate that the model provides a reasonably accurate prediction of upper level gage stresses in both the cast-in-situ drilled shaft and the precast driven pile, the model was applied to a load test scenario to determine the effect on the regressed data. The scenario involves a relatively long drilled shaft (length to diameter ratio of 49) tipped in soft soil but which exhibits a significant amount of side shear when rapidly loaded to geotechnical failure. These conditions highlight the need to address variations in strain magnitude and rate throughout a given test shaft.

The hypothetical shaft is 1.22 m (4 ft) in diameter and 61 m (200 ft) in length with strain gages located at ground surface and depths of 15 m (49 ft), 30 m (98 ft), 55 m (180 ft), and 60 m (197 ft). Longitudinal reinforcement is continuous throughout the length of the shaft such that the cross-sectional area of steel and concrete at all gage levels is  $117 \text{ cm}^2$  ( $18 \text{ in}^2$ ) and  $1.156 \text{ m}^2$  ( $12.44 \text{ ft}^2$ ) respectively. The concrete strength ( $f'_c$ ), ultimate strain ( $\epsilon_o$ ), and strain rate at which the compression test was performed ( $\dot{\epsilon}_o$ ) is 27.58 MPa,  $0.0027 \epsilon$ , and  $40 \mu\epsilon/\text{sec}$ .

The measured load test data is presented in Figure 27. Variations between the strains at each gage level implies that a large portion of the applied load is taken by side shear. Also predominant is the characteristic phase lag between peak strain values seen in rapidly loaded piles. Both phenomena lend the data to a segmental analysis (Mullins *et al.* 2002). However, to perform the analysis, it is necessary to determine the force or stress applied at each gage level.

The stress at each gage location within the shaft is computed using three methods: (1) a linear elastic stress-strain relationship based on an ACI modulus, (2) a linear elastic stress-strain relationship based on a back-calculated modulus from the top gages, and (3) a nonlinear hysteretic stress-strain relationship based on the proposed model. The ACI equation produces a concrete modulus of 24.68 GPa

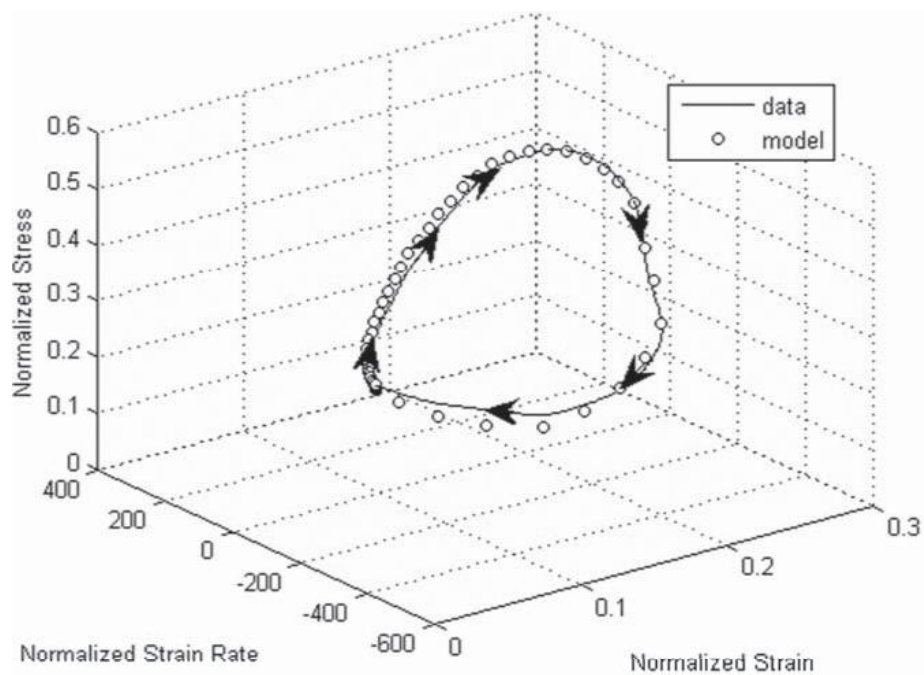


Figure 25 Modeled stress path vs. true measured stress path for Bayou Chico Pier 15.

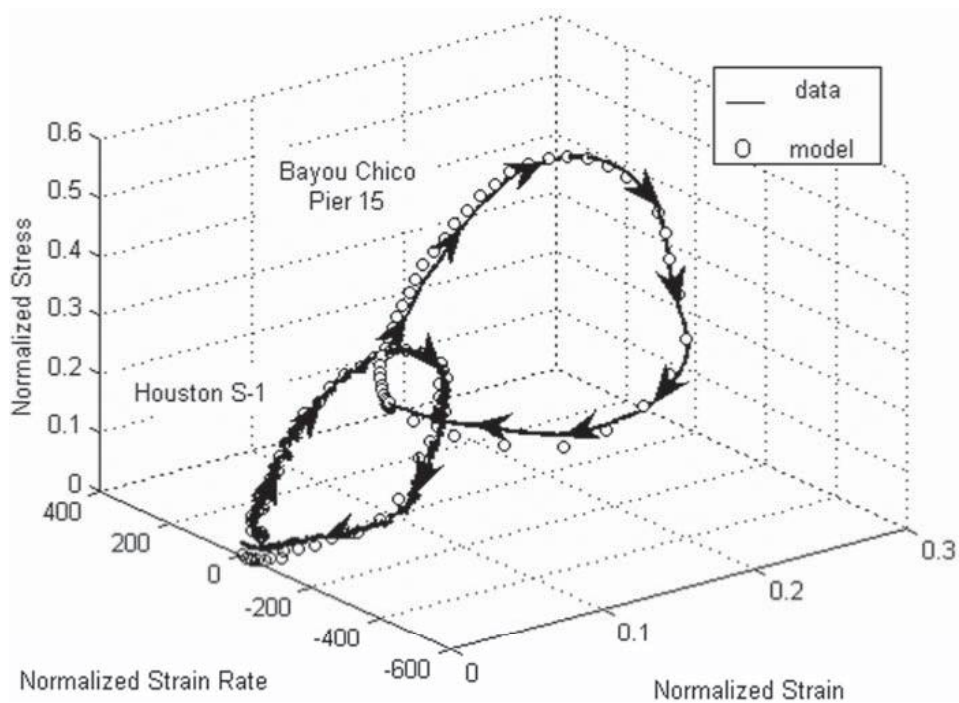


Figure 26 Individual Houston S-1 and Bayou Chico stress paths showing the stress offset due to prestressing.

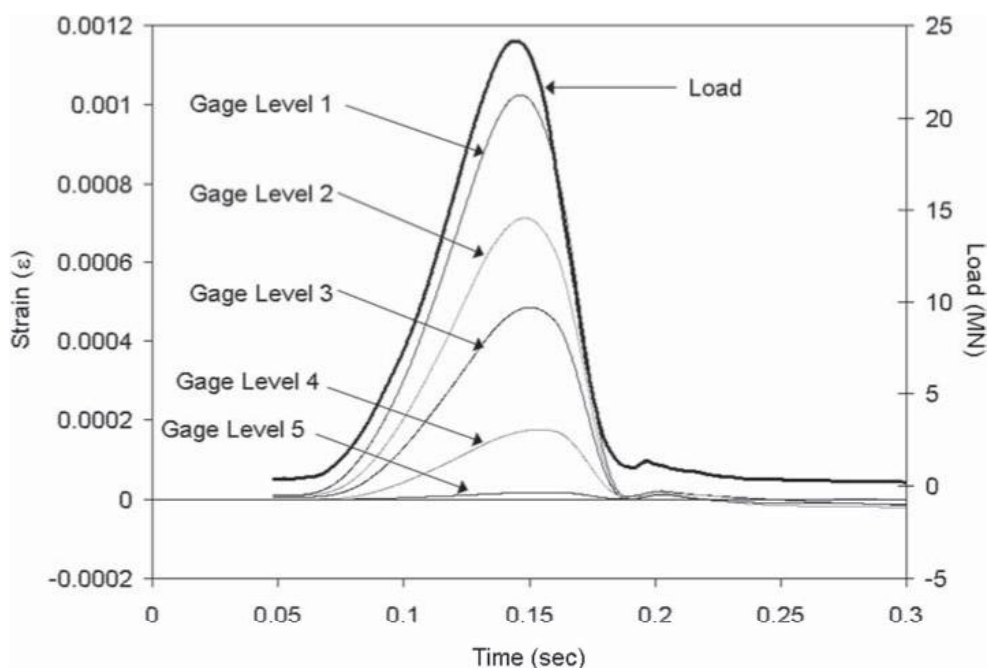


Figure 27 Hypothetical rapid load test data.

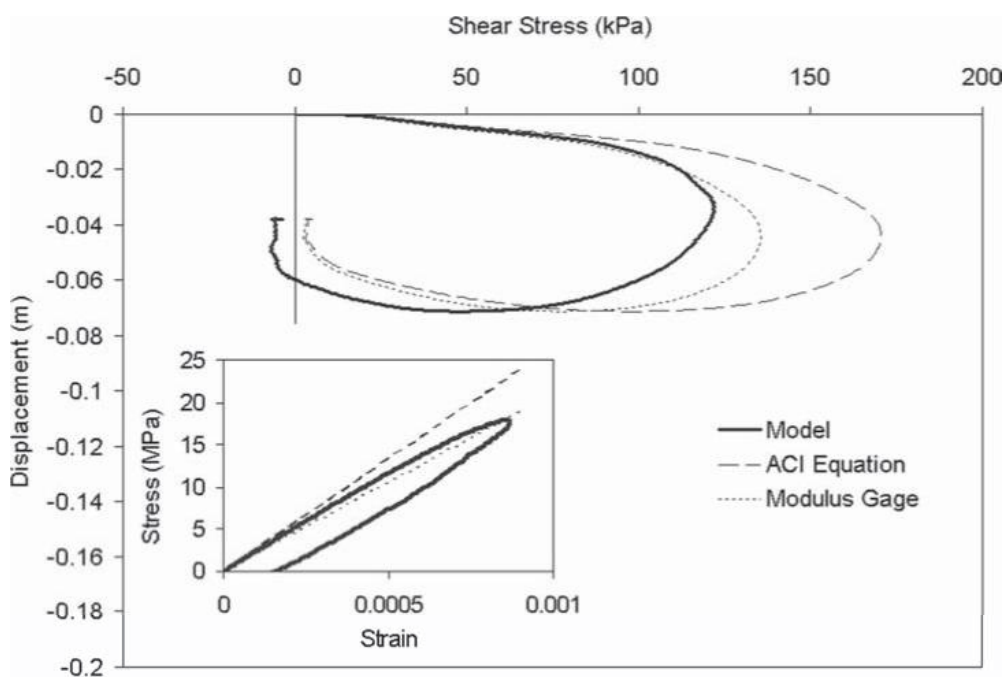


Figure 28 Segment I dynamic t-z curves and accompanying stress-strain model.

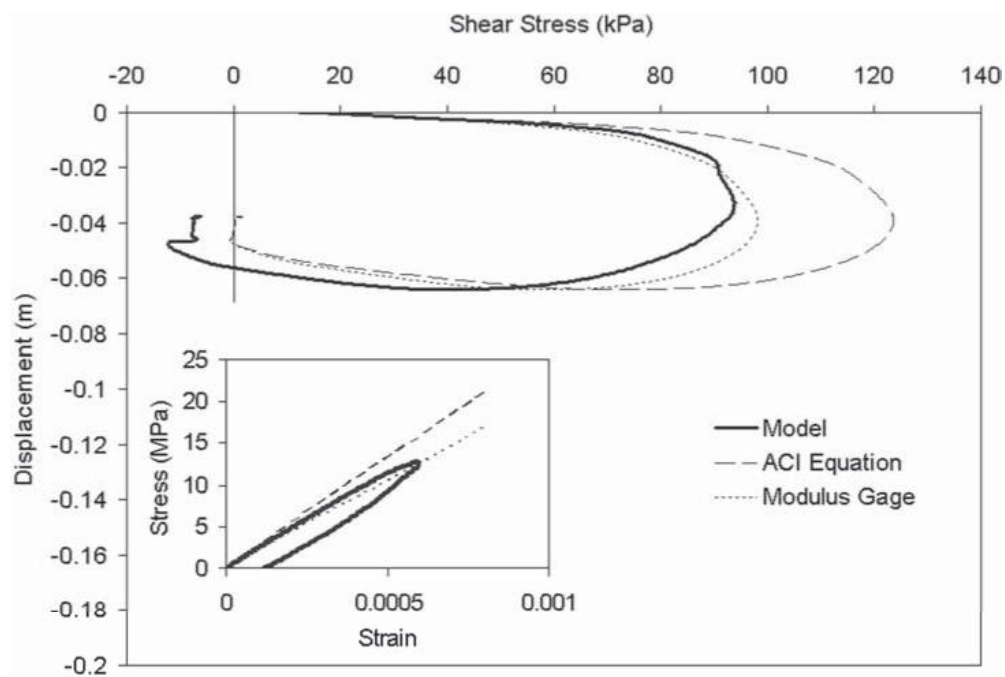


Figure 29 Segment 2 dynamic t-z curves and accompanying stress-strain model.

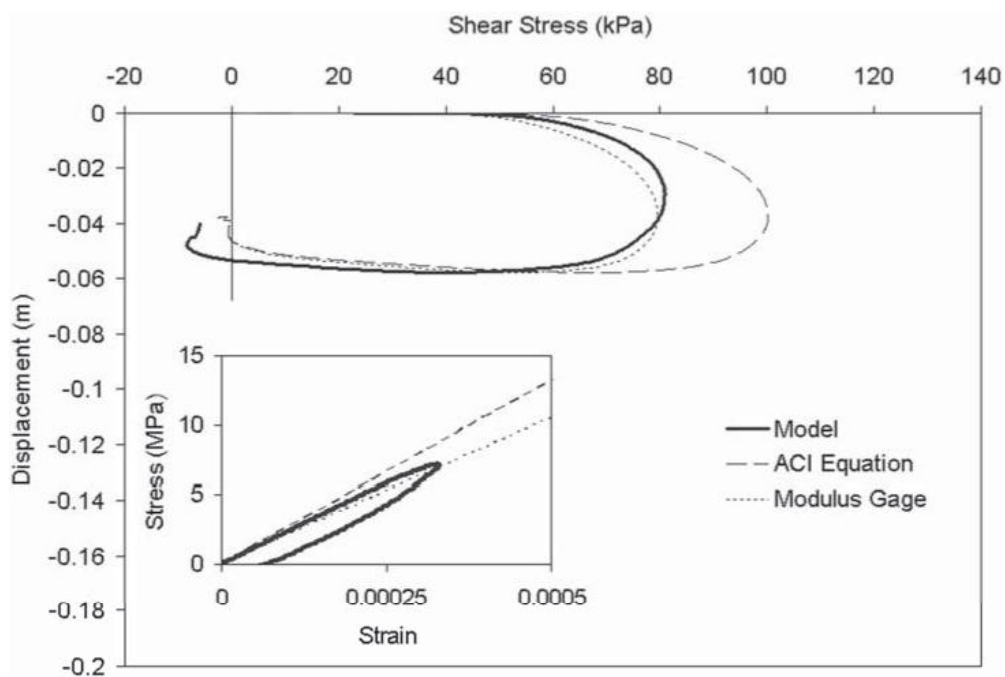


Figure 30 Segment 3 dynamic t-z curves and accompanying stress-strain model.

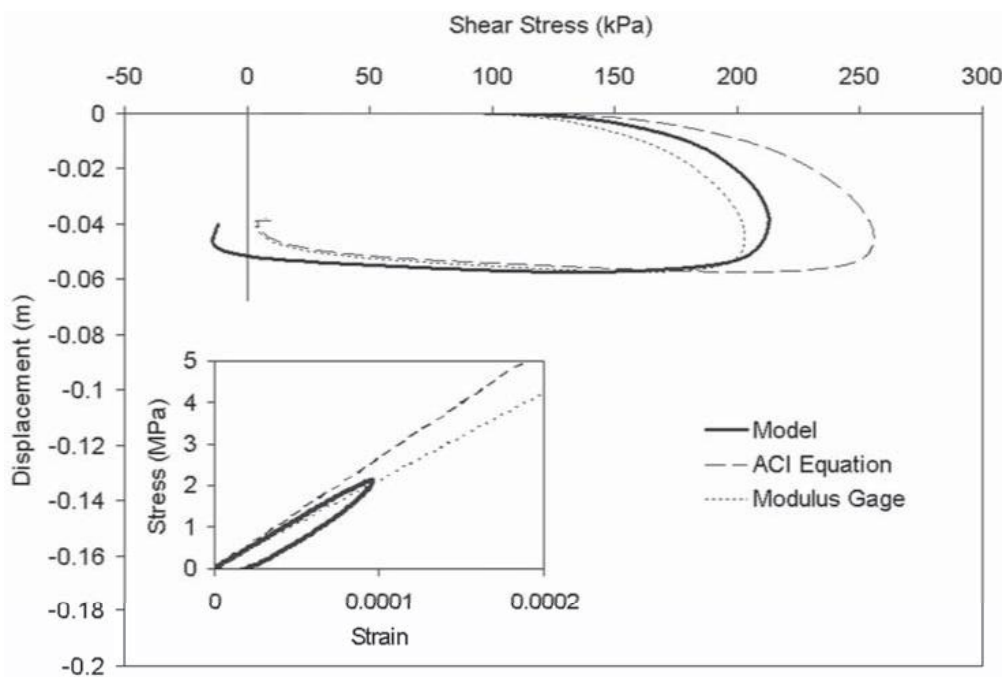


Figure 31 Segment 4 dynamic t-z curves and accompanying stress-strain model.

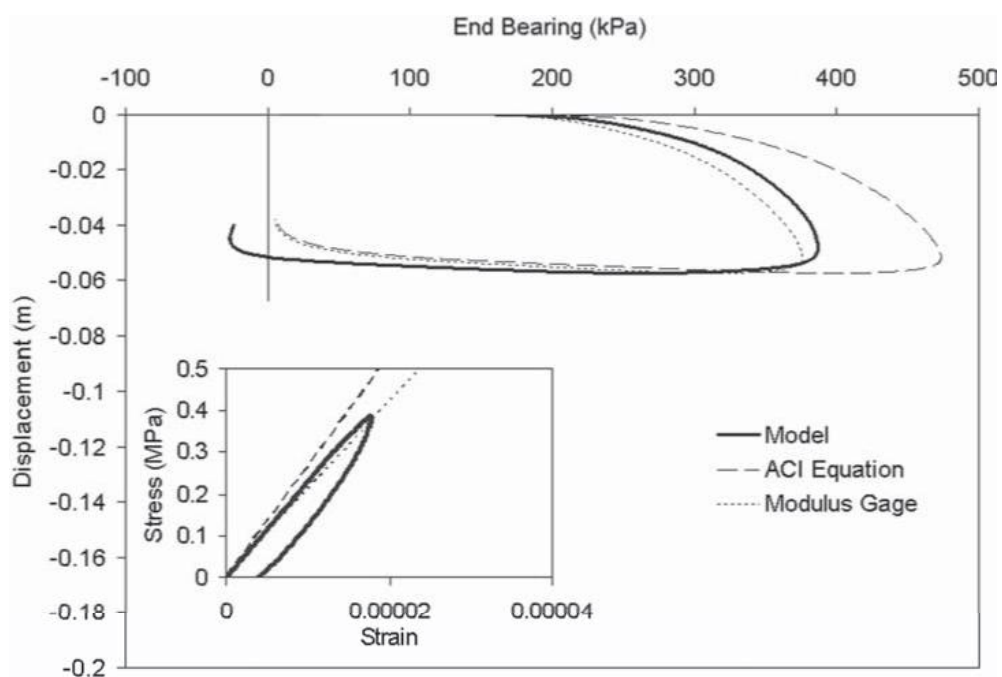


Figure 32 Dynamic end bearing response and accompanying stress-strain model.

(3580 ksi), that when weighed with a steel modulus of 200 GPa (29000 ksi), yields a composite modulus of 26.44 GPa (3834 ksi). The calibrated composite modulus as determined by the ground surface gage level (back-calculated modulus) is 21 GPa (3046 ksi).

Once the stress/load at each gage level is computed, the difference in load between gage levels is divided by its corresponding segment surface area to obtain dynamic t-z curves which are uncorrected for inertia and damping effects (Figures 28 through 32). Segment 1, the portion of the shaft between gage level 1 and 2, shows a 21% reduction in maximum stress when the back-calculated modulus is used instead of the ACI modulus.

All other segments, including the toe of the shaft, show the same reduction. This constant reduction in load is a direct result of a 21% reduction between the back-calculated and the ACI calculated composite moduli.

When considering the segment loading based on the modeled stress, a distinct shift in the distribution of load along the length of the shaft becomes noticeable. The upper level segments (1 and 2) do not distribute as much load as the back-calculated modulus curve suggests, whereas the lower level segments (3 and 4) distribute more.

This occurrence can be explained using the segment stress-strain plots located within each figure (Figures 28–32).

When observing the stress-strain relationship of segment 1 (Figure 28), although barely distinguishable, the linear modulus gage relationship intersects the modeled relationship slightly above the point of maximum stress. As the magnitude of strain and strain rate decreases (moving downward through the shaft), the point of intersection begins to fall below the point of maximum stress on the model (Figures 29–32). This is again a by-product of the nonlinearity of the concrete material and results in the overestimation of stresses in the upper segments and underestimation of stresses in the lower segments.

At this point, a segmental unloading point analysis (SUP) could be performed on the data to obtain the equivalent static response of each segment (see Lewis 1999; Winters 2002, and Mullins *et al.* 2002). However, it is not the intent of this paper to promote a particular analysis procedure or execute a complete analysis but to merely highlight the possible variations in deep foundation segmental load distribution as a result of modulus selection, or rather the selection of a particular stress-strain-strain rate relationship.

## CONCLUSION

Long piles subjected to significant amounts of side shear are often constructed with embedded strain gages positioned at strategic locations throughout the pile so as to better distinguish the load contributing components (end bearing *vs.* side shear) and develop the side shear load distribution. In load tests that produce low concrete strains and/or strain rates, an approximated linear stress-strain relationship and constant modulus may prove to be sufficient for determining the stress at strain gage locations. Tests exhibiting low strain rates but high strains are best evaluated using a non-linear, parabolic stress strain relationship. However, in tests that produce both high strains and strain rates, the evaluation of the true concrete stress requires more sophisticated

analysis. The presented approach incorporates the effects of strain magnitude, strain rate, and the rate of change of strain rate. As a result, the concept of a linear elastic modulus in concrete is virtually unusable.

Based on the results of the nonlinear hysteretic model developed herein, certain conclusions can be drawn:

- A linear stress-strain relationship (constant modulus) at best slightly over predicts stresses at upper gage levels and under predicts stresses at lower gage levels; in the worst case it misrepresents all gage levels.
- Since the use of ACI and modulus gage values are constant modulus assumptions, the segment t-z curves will show similar geometric shapes, but differ in value by the same degree as the difference in assumed moduli. But, neither accounts for the true nonlinearity or strain rate dependency.
- Since most foundations are not loaded to structural failure, a concrete stress-strain-strain rate relationship purely based on concrete break data is inadequate in describing load/unload cycles found in load tests.
- In all concrete specimens that undergo a load cycle, the stress follows a common surface up to the point of strain inflection or maximum strain rate (herein referred to as the transition point). However, each specimen returns along a different path defined by the strain rate at the transition point which can vary depending on the rate and magnitude of loading.

In order to implement the proposed model toward the regression of load test data, the following procedures are recommended:

- Concrete cylinder compression tests should be performed in accordance with ASTM C39 on specimens from each pile to identify the ultimate compressive strength ( $f'_c$ ), the strain at ultimate strength ( $\epsilon_o$ ), and the strain rate at which the ultimate strength and strain were determined ( $\dot{\epsilon}_o$ ). If analyzing static load test data, the Hognestad formula is sufficient.
- Strain gages should be placed at or near ground surface such that the measured load can be used to define the concrete stress-strain relationship prior to the occurrence of load shed. This measured load should be inertia-corrected and discounted depending on the reinforcement. Although it is ideal to place the gages above the ground surface, some piles and shafts do not extend above the ground. In these circumstances, the gages should be placed reasonably shallow.
- Using the values from the concrete cylinder compression tests, normalize the stress, strain, and strain rate (if necessary) at the upper gage level. Plot the results against the modeled response to determine whether the model sufficiently predicts the stress path.
- If the model sufficiently predicts the stress at the upper gage level, then apply the model to all gage levels.
- If performing a rapid load test, further regress the data to obtain the equivalent static response.



**NOTATION**

- $E_c$  = Young's modulus or elastic modulus;  
 $f_c$  = stress at a particular strain;  
 $f'_c$  = compressive strength or ultimate strength;  
 $f'_N$  = stress normalized with respect to compressive strength;  
 $w_c$  = unit weight of concrete;  
 $\epsilon_c$  = concrete strain;  
 $\epsilon_N$  = strain normalized with respect to  $\epsilon_o$ ;  
 $\epsilon_o$  = concrete strain at  $f'_c$ ;  
 $\dot{\epsilon}_c$  = instantaneous concrete strain rate;  
 $\dot{\epsilon}_o$  = concrete strain rate normalized to  $\dot{\epsilon}_o$ ;  
 $\dot{\epsilon}_{N-tp}$  = normalized concrete strain rate at the transition point; and  
 $\dot{\epsilon}_o$  = concrete strain rate corresponding to ASTM loading rate.

**REFERENCES**

- ASTM C 39-01. "Standard Test Method for Compressive Strength of Cylindrical Concrete Specimens." American Society for Testing and Materials, West Conshohocken, PA.
- Fellenius, B. (2001). "From Strain Measurements to Load in an Instrumented Pile." *Geotechnical News*, March, 35–38.
- Fu, H.C., Erki, M.A. and Seckin, M. (1991). "Review of Effects of Loading Rate on Reinforced Concrete," *Journal of Structural Engineering*, Vol. 117, No. 12, December, 3660–3679.
- Lewis, C. (1999). *Analysis of Axial Statnamic Testing by the Segmental Unloading Point Method*, Master's Thesis, University of South Florida, Florida.
- Mullins, G., Lewis, C. and Justason, M. (2002). "Advancements in Statnamic Data Regression Techniques." *Deep Foundations 2002: An International Perspective on Theory, Design, Construction, and Performance*, ASCE Geo Institute, GSP# 116, Vol. II, 915–930.
- Mullins, G. and O'Neill, M. (2003). *Pressure Grouting Drilled Shaft Tips: A Full-Scale Load Test Program*, May.
- Stokes, M. (2004). *Laboratory Statnamic Testing*, Master's Thesis, University of South Florida, Florida.
- Takeda, J. and Tachikawa, H. (1971). "Deformation and Fracture of Concrete Subjected to Dynamic Load." *Proceedings of International Conference on Mechanical Behavior of Materials*. Kyoto, Japan, 267–77.



# Statnamic Damping Coefficient: Numerical Modeling Approach

Michael Stokes, S.M.ASCE<sup>1</sup>; Gray Mullins, M.ASCE<sup>2</sup>; Carl Ealy, M.ASCE<sup>3</sup>; and Danny Winters<sup>4</sup>

**Abstract:** The damping associated with dynamic or statnamic tests has typically been over simplified to provide a “catch-all” factor for those responses that could not be fully accounted for using present analyses. This factor has historically been considered constant for a given pile–soil system, but recent investigations as well as previous case studies show the plausibility of another explanation. This study hypothesizes that damping is more closely associated with the increase in strain and not the total strain. Therein, the change in the volumetric strain is being scrutinized to investigate its relationship to damping. To validate this assumption, a numerical model is created which simulates the testing of a full-scale drilled shaft and results analyzed to determine the extent of the zone of influence and volumetric contribution to damping.

**DOI:** 10.1061/(ASCE)1090-0241(2008)134:9(1290)

**CE Database subject headings:** Cohesionless soils; Damping; Pile load tests; Load tests; Soil-pile interaction.

## Introduction

In the area of quality assurance of foundations, numerous factors play into providing safe, reliable structures. These include, but are not limited to, preconstruction soil investigations, structural material properties, construction methods, inspection methods, and postconstruction verification load testing. In actuality the latter provides proof that all the rest were perhaps adequately addressed. Rapid load testing (such as statnamic) is one such method that assures a foundation can adequately support the anticipated design loads.

Rapid load tests (ASTM 2006) are categorized as being faster than static testing (ASTM 1981) while being longer in duration than dynamic testing (ASTM 2000). The significance lies in the analysis of the foundation response to such a loading. The rapid nature of the test induces foundation acceleration, but the relatively long duration when compared to dynamic tests simplifies the regression as no wave mechanics analyses are necessary. To date, single degree of freedom systems have adequately modeled the foundation response so as to ascertain a predicted ultimate

static equivalent. Refinements to these methods continue to evolve that further the understanding of all rapid loading events as well as similarly modeled dynamic events. One such refinement is presented herein.

## Background

The impulsive nature of a statnamic test introduces rate-dependent components to the static response of a foundation. Assuming a single degree of freedom, lumped mass system, the equation of motion describing a statnamic event is

$$F_{\text{statnamic}} = kx + ma + cv \quad (1)$$

where  $F_{\text{statnamic}}$  = applied force;  $kx$  = desired equivalent static response (theoretical spring force);  $m$  = mass of foundation and soil contributing to inertial effects;  $a$  and  $v$  = acceleration and velocity of the foundation, respectively; and  $c$  = damping coefficient. In almost all geotechnical applications, the damping force ( $cv$ ) attributed by soil is regarded as viscous in nature. All values required for solving the equivalent static response are either recorded or can be easily found save two, the spring constant ( $k$ ) and the damping coefficient ( $c$ ). As the foundation response is nonlinear, the  $kx$  term (which is the equivalent static response) remains coupled as a single unknown. This leaves two unknowns and one equation.

One of the most common methods to solve Eq. (1) from statnamic test data is the Unloading Point Method, [UPM, Middendorp et al. 1992] or some variations such as the Modified Unloading Point, or Segmental Unloading Point (Mullins et al. 2002). These methods make two critical assumptions regarding  $kx$  and  $c$ : the static capacity of the pile or pile segment is constant while plunging and the damping coefficient is constant throughout the test. With these two assumptions in place, it is possible to determine the damping coefficient, and thus the equivalent static response.

Two points on the statnamic load–displacement curve are of particular interest when performing these procedures (Fig. 1): the point of maximum statnamic force (1) and the point of maximum

<sup>1</sup>Postdoctoral Researcher, Dept. of Civil and Environmental Engineering, Univ. of South Florida, 4202 E. Fowler Ave., ENB 118, Tampa, FL 33620. E-mail: mjstoke2@eng.usf.edu

<sup>2</sup>Associate Professor, Dept. of Civil and Environmental Engineering, Univ. of South Florida, 4202 E. Fowler Ave., ENB 118, Tampa, FL 33620. E-mail: gmullins@eng.usf.edu

<sup>3</sup>Senior Research Engineer, Federal Highway Administration, Turner-Fairbanks Highway Research Center, 6300 Georgetown Pike, McLean, VA 22101-2296. E-mail: carl.ealy@fhwa.dot.gov

<sup>4</sup>Research Associate, Dept. of Civil and Environmental Engineering, Univ. of South Florida, 4202 E. Fowler Ave., ENB 118, Tampa, FL 33620. E-mail: dwinters@eng.usf.edu

Note. Discussion open until February 1, 2009. Separate discussions must be submitted for individual papers. The manuscript for this paper was submitted for review and possible publication on April 3, 2006; approved on January 18, 2008. This paper is part of the *Journal of Geotechnical and Geoenvironmental Engineering*, Vol. 134, No. 9, September 1, 2008. ©ASCE, ISSN 1090-0241/2008/9-1290-1298/\$25.00.

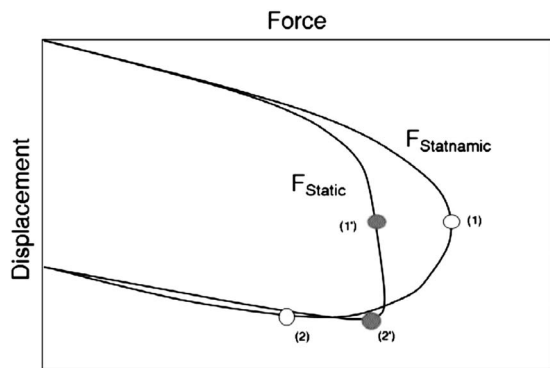


Fig. 1. UPM time window for  $c$  determination (adapted from Transportation Research Board 2003)

displacement (2), where the velocity of the foundation and resulting damping force ( $cv$ ) equals zero. This first point corresponds to a point of yield (or postyield) on a theoretical static curve (1'); the second corresponds to the point of maximum displacement (2') and is referred to as the unloading point. At that instant, the static capacity can be determined using

$$F_{\text{static}} = kx = F_{\text{statnamic}} - ma \quad (2)$$

The value of  $kx$  is determined and assumed constant from Points (1) to (2). This enables the damping coefficient to be calculated within this range. Typically, either the average or median value of  $c$  is taken, but reviewing the overall trend may lead to a more appropriate value (Transportation Research Board 2003) (Fig. 2).

As the UPM determines the damping coefficient between Points (1) and (2), it effectively determines the ultimate capacity. However, it has been shown that at smaller displacements, in the more elastically responding regions of the loading, that same damping coefficient is not appropriate. Therein, the damping coefficient may not actually be constant throughout the entire loading event when plastic deformation is achieved. This is likely to be a by-product of the size of the zone of influence engaged by the pile at a given degree of loading; this concept forms the basis of this paper.

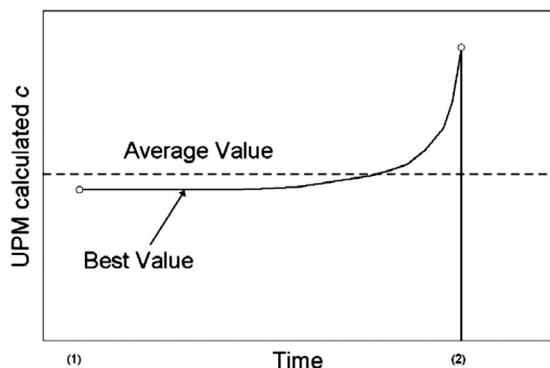


Fig. 2. Variation in  $c$  between times (1) and (2) (adapted from Transportation Research Board 2003)

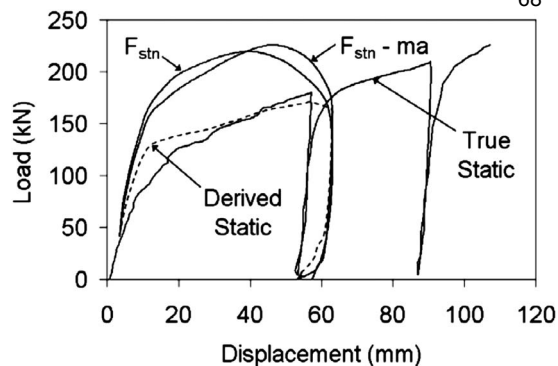


Fig. 3. Static/derived static comparison (adapted from Mullins et al. 2000)

## Case Studies

Previous studies have shown that the statnamic damping coefficient as defined by Eq. (1) is not constant throughout the entire load test, but decreases from a higher, preyield value. These conclusions were based on the rationale that the damping force,  $cv$ , accounts for all differences between the inertia-corrected statnamic force and the observed static capacity as shown in the rearranged configuration of Eq. (1)

$$cv = (F_{\text{statnamic}} - ma) - F_{\text{static}} \quad (3)$$

Case 1: Shallow Foundations. The first of these studies (1997) involved a series of static load tests (SLT) and statnamic (STN) tests conducted at the Turner-Fairbanks Highway Research Center (TFHRC) in McClean, Va. (Mullins et al. 2000). Therein, three side-by-side footings founded in sand were tested. The first (Test 1) of the three was loaded statnamicly with four incrementally increasing load cycles up to and beyond the bearing capacity (two cycles under-yield and two beyond-yield). The second footing (Test 2) was tested statically to a displacement that fully defined failure. The third (Test 3) was loaded with a single statnamic load cycle that again reached bearing capacity.

When comparing the true static capacity measured from Test 2 and the UPM-derived static capacity from Test 3, good agreement was found for the ultimate capacity but a significant variation was noted in the response prior to yield (Fig. 3).

The difference between the inertia-corrected load of Test 3 and the static capacity of Test 2 was then determined at each displacement and used to backcalculate the damping coefficient that satisfied Eqs. (1) and (3) for the corresponding velocity. Fig. 4 shows the inertia-corrected statnamic load response and the true static as well as the damping coefficient backcalculated from the two tests. The reported results indicated that the damping coefficient decreased in value by more than 50% after shear failure occurred.

Similarly, the UPM-derived damping coefficients for each of the four cycles of Test 1 (denoted in Fig. 4 by Test 1-1, Test 1-2, Test 1-3, and Test 1-4) showed similar values for like displacements or degrees of loading when compared to the backcalculated. The failure envelope defined by Test 1 was slightly higher than the static envelope defined by Test 2. This deviation was attributed to slight densification caused by the four progressive load cycles.

Case 2: Pile Group Tests. A second case study showing discrepancies in the assumed constant damping coefficient was also conducted at the TFHRC but by Ealy and Justason in 1996 on a

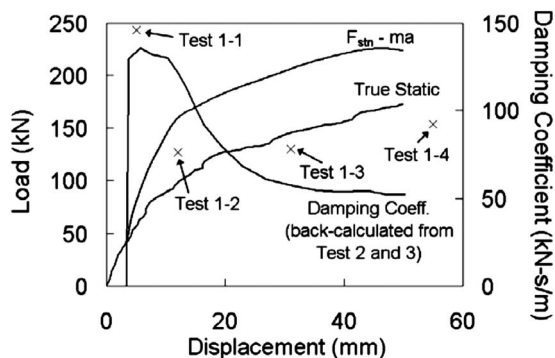


Fig. 4. Backcalculated damping coefficient from plate load tests (adapted from Mullins et al. 2000)

small scale driven pile group (Ealy and Justason 2000). The group consisted of nine, 75 mm diameter, 3.6 m long piles arranged in a  $3 \times 3$  configuration. Test procedures included: static quick test, constant rate of penetration, and statnamic. The purpose of the study was to show the similarities and/or differences in the load-settlement response when subjected to a range of loading rates.

With regards to the effects of damping coefficient selection, coefficients ranging from zero to twice the UPM-derived value were input to illustrate the variations in the derived static capacity. In general, very little difference could be noted in the elastic regions of the curves with more pronounced variations at post-yield displacements (Fig. 5). These findings highlighted the sensitivity of the derived static response to selection of a damping coefficient when compared to an inertia-corrected statnamic response where no damping is subtracted (curve corresponding to  $c=0$ ). When compared to the findings of the static test, a damping coefficient value of approximately 30 kN s/m was found to match most closely (Fig. 6). The authors concluded that even though the UPM-derived static response was reasonable when compared to the static, the overall shape of the curves did not follow the static or the CRP test results exactly. They continued by stating that perhaps a more sophisticated damping coefficient may be appropriate to more closely match the true static response. Fig. 6 shows similar results to that observed in Case 1 whereby the authors performed the same type of backcalculation to develop a trend of actual damping versus displacement.

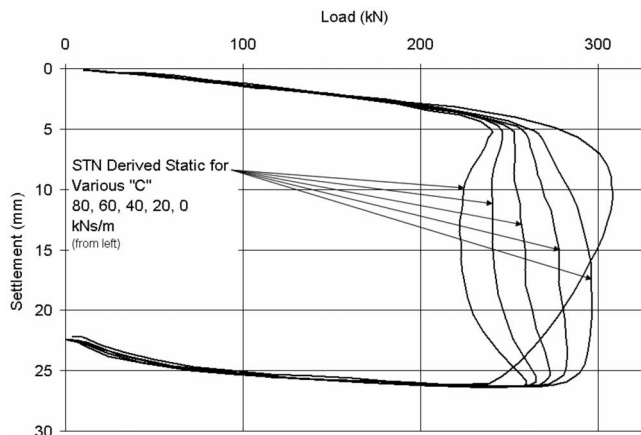


Fig. 5. Sensitivity of derived static curve (from statnamic) to values of damping constant  $c$  (adapted from Ealy and Justason 2000)

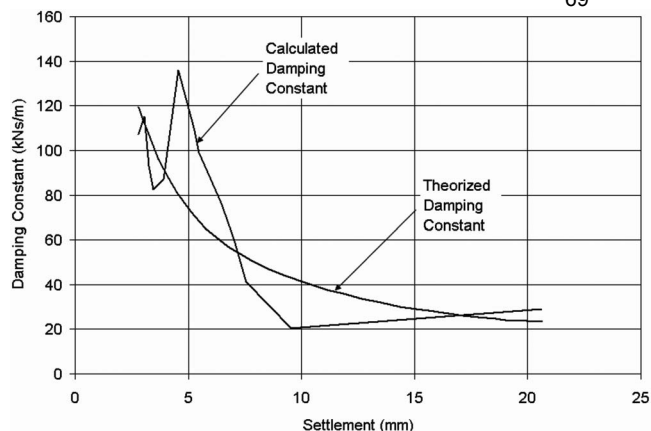


Fig. 6. Theorized variation in damping versus settlement (adapted from Ealy and Justason 2000)

Case 3. Small scale drilled shafts. This study involved the static and statnamic testing of 3 m long, 11.4 cm diameter shafts cast in the TFHRC test pits in 2004. Therein, 8 shafts were constructed using full length temporary casing and duplex drilling (drilling and casing advancement together) through sand. The use of full length temporary casing ruled out variations in side shear from slurry properties and/or their effects. The water table was maintained below the tip of the shafts during installation and the concrete was placed by free fall into the cased hole. A single 12 mm reinforcing bar was centrally located, which was instrumented with strain gauges for end-bearing delineation. All shafts were tested statically and statnamicly, but in various orders depending on location. Most shafts were tested with three cycles, either STN/SLT/STN or SLT/STN/SLT. This allowed subtle changes in the strength envelope to be identified when trying to compare two consecutive tests that should have been identical. However, in this loose sandy soil, all tests after the initial load cycle appeared to fail at the same load and displacement with a similar response. Fig. 7 shows the comparison of the static and statnamic testing along with the UPM-derived and backcalculated values for the damping coefficient.

In all the cases cited, two apparent damping responses appear to have existed: a preyield or preshearing value and a lesser post-yield value linked by a rapid transitional period. It is at this transitional point that the radius of the zone of influence is

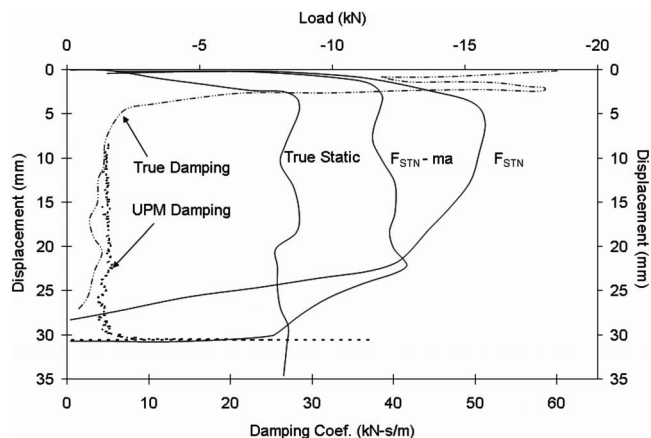


Fig. 7. Comparison of true damping and UPM damping

thought to collapse such that only the soil remaining within close proximity of the shear interface contributes to damping. Numerical modeling which is presented later was undertaken to shed some insight. Full details regarding each case study can be found in Mullins et al. (2000), Ealy and Justason (2000), and Mullins and Stokes (2007), respectively.

As damping is caused by energy loss due to soil-particle interaction as well as the rate at which they interact, the size or volume of the soil affected by the loading event should be directly related to damping. The energy associated with damping is lost and not stored, therefore it is dependent on soil undergoing active strain at a particular instant and not the cumulative amount of strain experienced throughout the entire loading event. It is hypothesized, herein, that the damping coefficient at a given displacement is closely related to the instantaneous volume change of the soil surrounding the foundation. Up to the point of shear failure around a pile, the radius of the affected soil and the straining volume increases; upon shearing, the more distal soils no longer continue to strain, and the radius of the zone and the volume of actively straining soil decreases. The changing volume of strained soil signifies a change in the energy absorbing potential of the soil matrix (the damping coefficient,  $c$ ).

## Impulse Response

A side issue relevant to the idea of a higher preyield value of the statnamic damping coefficient, but nonrelated to the changing volume of strained soil, is the investigation into the “impulse response” of a statnamic test. The term is used to describe the foundation response due to the applied force over time, or impulse, and is not to be confused with the low-strain, nondestructive test used in the evaluation of deep foundations. It is introduced here only as additional support to the hypothesis and does not intend to offer an alternative analysis procedure but to merely serve as an indicator of damping variability. The previous discussion defines damping as an energy-related phenomenon; however, an indication of the variability of damping becomes evident when considering the statnamic event in the time domain.

Load tests are typically conceived in terms of work-energy principles (i.e., load-displacement graphs). However, accelerations inherent to dynamic events allow for exploration using principles of impulse and momentum. If Eq. (1) is rearranged and the integral taken with respect to time, the impulse imparted by the inertia-corrected statnamic force can be characterized

$$\int (F_{\text{statnamic}} - ma)dt = \int (kx)dt + \int (cv)dt \quad (4)$$

As the applied statnamic force and foundation acceleration are measured and the system mass is assumed to remain constant throughout the event, the inertia-corrected impulse on the left-hand side of Eq. (4) can be easily calculated, at least in its discrete or measured form. Taking the derivative of Eq. (4) with respect to top of shaft displacement lends insight into how the impulse changes throughout the loading event

$$d/dx \int (F_{\text{statnamic}} - ma)dt - d/dx \int (kx)dt = d/dx \int (cv)dt \quad (5)$$

In this form, Eq. (5) is particularly difficult to evaluate any further. As it is hypothesized that the term  $c$  is not constant and

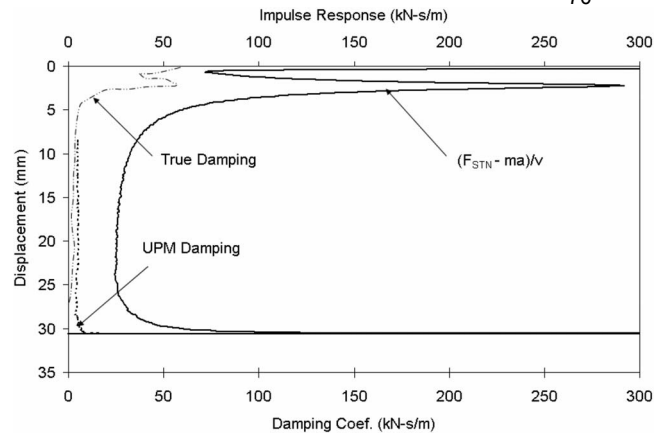


**Fig. 8.** Comparison of true damping and UPM damping to the impulse response of the inertia-corrected statnamic pulse

likely a function of time or displacement, the damping force  $cv$  cannot be legitimately uncoupled. However, the discrete form of the equation at a given time step proves to be more manageable

$$(F_{\text{statnamic}} - ma)\Delta t/\Delta x = (kx)\Delta t/\Delta x + (cv)\Delta t/\Delta x \quad (6)$$

or

$$(F_{\text{statnamic}} - ma)/v = kx/v + c \quad (7)$$

where  $c$ ,  $v$ ,  $a$ ,  $F_{\text{statnamic}}$ , and  $F_{\text{static}}$  are all functions of time and  $m$  is assumed constant.

In this form [Eq. (7)], it is apparent that the derivative of the inertia-corrected impulse (hereafter referred to as the impulse response) is composed of two distinct terms, one of which is the damping coefficient. The other term,  $(kx)/v$ , can be thought of as a “mock” impedance, similar to what is used in pile driving analysis. Though Eq. (7) could have been quickly reached by rearranging Eq. (1) and dividing by  $v$ , the relevance of the process comes from viewing the loading event in terms of an imparted impulse or area under the load pulse curve. When plotted, the usefulness of this method becomes more transparent (Fig. 8).

Fig. 8 represents the impulse response of the third case study previously discussed as compared to the true and UPM calculated damping coefficients. It offers an alternative to viewing the statnamic event as a load-displacement curve and represents the graphical interpretation of Eq. (7) where the difference between the impulse response and damping curves is attributed to the equivalent static component,  $(kx)/v$ , or impedance. Though the static component remains unknown, the predominant advantage of viewing the event in this manner is the ability to clearly indicate the transition between preyield and postyield conditions without knowledge of the actual static capacity. Noting the similarities between the impulse response and the true damping reinforces the hypothesis of a higher preyield damping coefficient.

## Numerical Model

In order to test the hypothesized damping variation, a numerically modeled shaft was generated and subjected to different simulated loading scenarios. The purpose of the modeling was to isolate the zone of influence around a loaded pile by determining both the radial extent and the degree of volumetric change experienced in these zones. Therein closer soils would experience more strain and more distal soils less. The total cumulation of the volume



change within each soil element provides an indication of the strain energy potential. Modeling of the zone of influence and the soil parameters that affect this zone (e.g., soil type, soil strength, and relative stiffness between the pile and the soil) were initially conducted under static conditions in order to shed light on this phenomenon without compounding the complexity from inertial or damping forces. Parameters other than those directly related to the surrounding soil matrix, such as pile diameter and length, were held constant to eliminate the vast complexity of the system and focus on a general understanding of the system response. Though it is intuitive that the pile geometry largely influences the size of the affected region of soil, it was the objective of the modeling to merely identify the aforementioned phenomenon and not to stage the development of correlations. Once a clear understanding of the soil/shaft interaction was obtained, complexity was progressively added to the model.

The computer program chosen to perform the numerical modeling was Fast Lagrangian Analysis Continuum (FLAC). FLAC is a two-dimensional explicit finite-difference program that proves particularly useful in simulating the plastic flow of materials (e.g., soil, rock, and concrete) upon yielding. The materials are represented as elements that form an interlocking mesh. Once material properties are assigned to each element, various loading conditions can be applied to the matrix and the response of each element recorded (Itasca Consulting Group, Inc. 2002).

During the initial stages of development, several models were investigated in order to determine the most appropriate model size, model type, boundary conditions, and constitutive models. An axisymmetric mesh containing nearly 1,800 elements ultimately defined the 1 m diameter  $\times$  10 m long shaft and the zone of influence to a radial distance of  $12D$  ( $12 \times$  shaft diameter) and depth below the toe of  $\frac{1}{2}L$  ( $\frac{1}{2} \times$  shaft length). The axisymmetric model proved most appropriate for the modeling of a cylindrical shaft in a semi-infinite medium. Such an extreme radial boundary was chosen as to ensure total inclusion of the entire zone of influence. Though negligible effects were noted at the boundary, the large model size was retained as a high-speed computer was available to perform the finite-difference calculations effortlessly. Velocities in the horizontal direction were fixed at the boundary ( $12D$ ), thereby impeding horizontal displacements, although the soil was allowed to undertake vertical displacements. This ensured that the soil was in no way forced to a preconceived vertical displacement. The matrix was discretized into small regions within close proximity to the soil/shaft interface that increased geometrically in size with increasing radial distance. This refinement ensured the capture of crucial information near the shaft/soil interface that would otherwise go undetected with large elements.

Preliminary models were fraught with an overly elastic soil behavior when using a linear-elastic, perfectly plastic material with Mohr–Coloumb failure criteria. As more information was required than a simple failure or no-failure scenario, it was necessary to implement a more sophisticated model that could closely represent the nonlinear behavior of soil. The soil was eventually modeled as a nonlinear elastoplastic (hyperbolic Duncan–Chang constitutive model), homogeneous sand matrix with properties corresponding to Standard Penetration Test (SPT) correlations (Gunaratne 2006).

An interface was defined to delineate the side of the shaft from the adjacent soil. This interface was assigned stiffness values that would eventually allow slippage along the boundary. However, the interface was given properties synonymous with those assigned to the soil. Therefore, the strength of the shear interface was the same as the strength of the surrounding soil (soil/soil

**Table 1.** Model Soil Properties Corresponding to Standard Penetration Test  $N$  Values

Soil properties	Standard penetration test $N$ values		
	20	30	40
$\rho^a$ (kg/m <sup>3</sup> )	1.7	1.8	1.9
$E_i^a$ (MPa)	19.2	28.8	38.3
$G_i$ (MPa)	7.4	11.1	14.7
$K_i$ (MPa)	16.0	24.0	32.0
$\phi$ (degrees)	30.0	32.0	33.0
$\nu$	0.3	0.3	0.3

<sup>a</sup>From Shaft 1-2-3 (Mullins and Winters 2004).

interface instead of a concrete/soil interface). This assumption neglects reduced interface friction that can potentially happen during wet construction of a drilled shaft when a slurry-cake lines the insides of a borehole. The values assigned to the interface are much more representative of a drilled shaft with rough sides constructed under dry conditions. It was also assumed that the introduction of the shaft did not significantly alter the ground stresses from their initial state.

Though all other parameters (soil type, shaft length, shaft diameter) remained constant, successive models entertained SPT  $N$  values of 20, 30, and 40 (Table 1). This allowed for insight into the effect of differing soil properties without individually varying each soil property. It was envisioned that this approach may prove more useful in identifying trends as there exists a high probability that any future correlations developed from full-scale load tests would likely be based on SPT results. Also, varying the in situ soil conditions based on SPT  $N$  values allowed for a more manageable testing matrix.

## Statically Loaded Model and Results

Once the in situ soil conditions for the model were established, a static load test was performed to a displacement in excess of 0.05 m (5% of the shaft diameter) to ensure full mobilization. Load was applied to the top of the shaft in increasing 20 kN increments with intermittent convergence criteria set to within 1 N. Fig. 9 shows the load–displacement curves for the three different SPT  $N$  values. In order to ensure that the load–displacement responses are reasonable, an envelope showing the output from a drilled shaft design program (Shaft 1-2-3) (Mullins and Winters 2004) is plotted with and sufficiently bounds the computer-generated data.

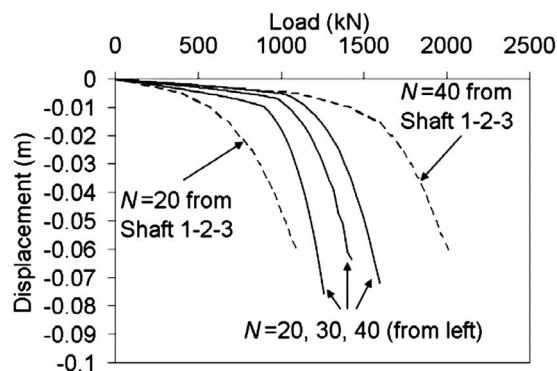


**Fig. 9.** Computer-generated static load–displacement curves

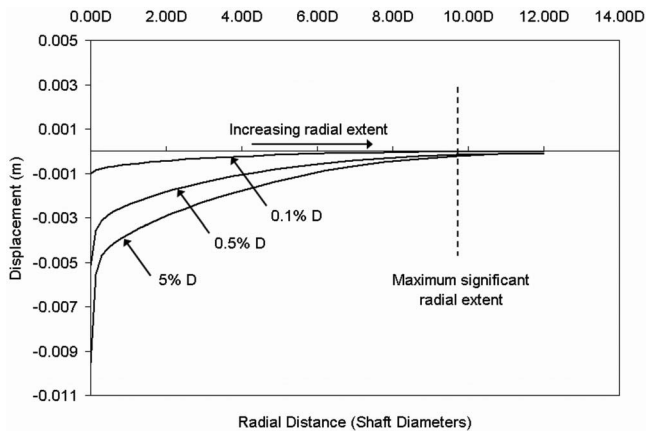


**Fig. 10.** Ground displacement profiles during a static load test ( $N=20$ )

Results from the static model show trends that are congruous to the hypothesized soil behavior (Fig. 10). It is apparent by observing the ground surface displacement profiles that the volume of strained soil increases radially from the shaft to a point of maximum volume prior to shear failure. Once shear failure is reached, only the soil immediately surrounding the shaft significantly displaces, thereby decreasing the actively affected zone, or the zone of influence. For the purposes of this paper, the maximum significant radial extent of the zone of influence is determined by an arbitrarily chosen vertical displacement value of 0.0001 m. Displacements less than this limit were considered insignificant.

Interestingly, the change in the cumulative volume (total volume lost due to the straining soil mass) throughout the static loading (Fig. 11) mimics the trend in the load–displacement curve. Further, by taking the displacement-dependent derivative of the cumulative volume (derivative of cumulative volume with respect to top of shaft displacement), a trend appears which closely resembles the damping noted by the aforementioned case studies (Fig. 12). In agreement with the backcalculated damping coefficient from previous figures is the decreasing trend in  $dV/dx$  or  $\Delta V/\Delta x$ , hereafter referred to as the displacement-dependent volume change (DDVC). Near the beginning of the load test, there is a large change in volume. Shortly into the loading cycle, the DDVC rapidly decays through a transition until ultimately diminishing to a near constant value well into shear failure.

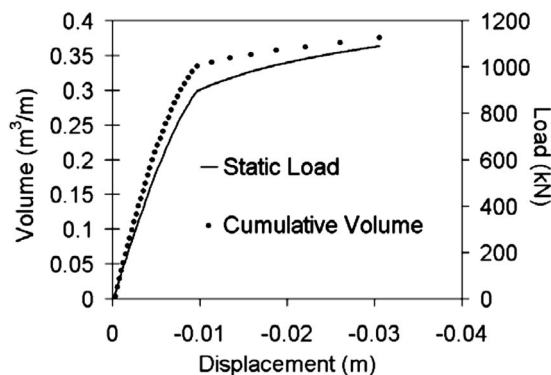


**Fig. 11.** Cumulative volume change ( $N=20$ )

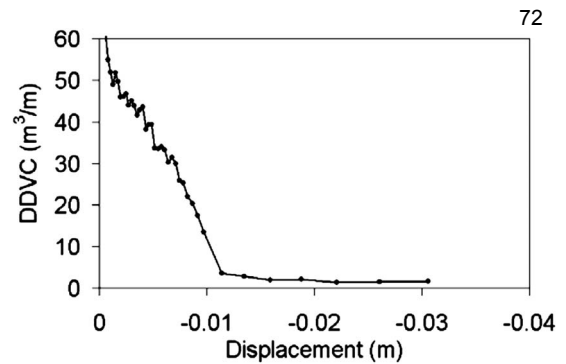


**Fig. 12.** Displacement-dependent volume change ( $N=20$ )

Though the trends noted in the numerical model are useful in that the geometric shape of the curve provides insight into the occurrence of significantly sizable events (point of failure denoted by sudden stability of the DDVC) throughout the loading, it is impractical, if not impossible, to capture soil displacement information at every location within the zone of influence (especially at depth). If the numerical solution is to be useful, the model data must be recorded in the same fashion as is plausible in the field. For this reason, it is necessary to investigate alternative methods of arriving at the displacement-dependent volumetric change.

An alternative method for calculating the DDVC involves recording the ground surface profile (Fig. 13) of the surrounding soil and determining the incremental loss of soil volume associated with the depressed surface. With the aid of current data acquisition devices and displacement transducers, this method becomes an attractive option for verifying this soil behavior during shaft loading. Given an initial soil volume where the boundaries are located a sufficient distance away from the shafts as not to experience any effects from the loading event (Fig. 14), it is reasonable to conclude that the incremental loss of volume at the ground surface is the change in volume experienced by the system. Indeed, a comparison of the DDVC calculated using both methods shows the similarities (Fig. 15) and reinforces the validity and practicality of using soil surface measurements to indicate total change in soil volume. This approach was then used for all subsequent models with an understanding of the limitations of the Duncan–Chang model. Though the model is able to address the small strain nonlinearity necessary for determining the ground surface profile, it does not address volumetric changes due to dilation that may be present in stiffer soils.

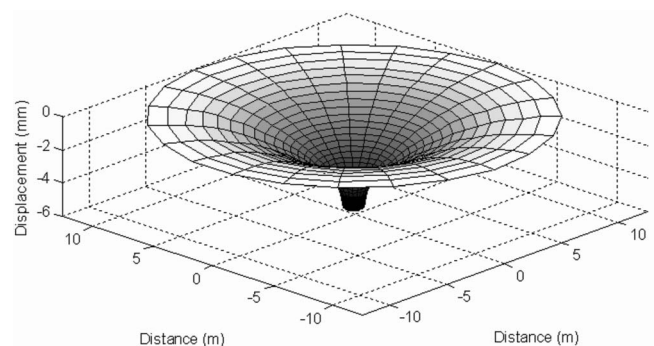


**Fig. 13.** Modeled ground surface profile from a static load test

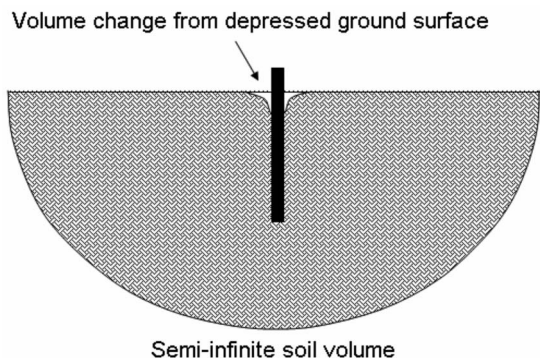


**Fig. 14.** Method of calculating the change in volume using the ground surface profile

### Dynamically Loaded Model and Results

Once confidence was obtained in the results of the statically loaded model, a more complex loading condition was applied to the in situ conditions already established. Doing so provided a means of comparing static and statnamic load test results on two shafts of identical in situ conditions, a luxury not available during full-scale piles load tests. Dynamic effects were introduced into the computations by applying a simulated statnamic load pulse, initially in the form of a sinusoidal function, then later as an actual statnamic load pulse recorded during a typical load test. This also required a modest modification to the model. In order to minimize wave reflections, it was necessary to remove the previously fixed boundary conditions and apply normal and shear quiet (viscous) boundary conditions to both the extreme radial and bottom boundaries.

Data from the numerical run were recorded and analyzed using the UPM (Fig. 16). Similar to the previously mentioned research results, the UPM satisfactorily predicted the static capacity near the unloading point, but significant variation existed throughout most of the test.

The large zone bounded by the maximum statnamic force and maximum displacement afforded the opportunity to calculate the UPM damping coefficient over a large percentage of the test. This occurrence, coupled with the backcalculated damping coefficient, allowed for a representative plot of the preyield, transitional, and postyield statnamic damping coefficient (Fig. 17). The overlapping region between the true damping and UPM damping curves shows agreement between the calculations and ultimately offers a

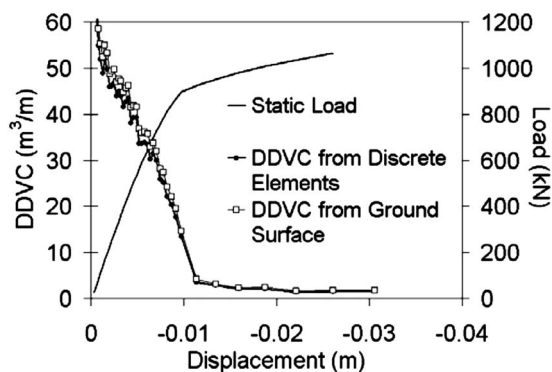


**Fig. 15.** Comparison of DDVC calculation methods for a static load test ( $N=20$ )

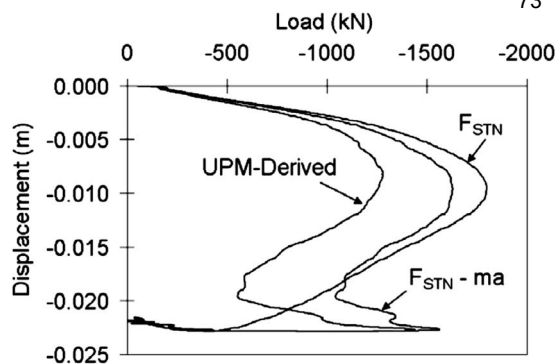


**Fig. 16.** UPM-derived static response for a statnamic load test ( $N=20$ )

reasonable plot of a variable damping coefficient. Equipped with this plot, it was desirable to determine the cumulative volume change and its relationship to damping.

As it was predetermined from the static test results that an idealized zone of influence could be described from the ground surface profile alone, only nodal locations along the ground surface of the model were monitored and analyzed to compute the DDVC. As before, the cumulative loss in volume resulting from the depressed ground surface profile was calculated. When taking the change in the total volume with respect to top of shaft displacement, the trend displayed notable geometric similarities to the plot of the damping coefficient (Fig. 18).

As with the results from the static model, the DDVC from the dynamic model is large prior to yielding but decreases with the damping coefficient. Near the end of the test, both the DDVC and the damping coefficient increase rapidly to a very large value. Similar calculations were conducted for the other specified soil conditions (SPT  $N$  values corresponding to 30 and 40). The same trends were noted in all three in situ conditions (Fig. 19). When plotted with the DDVC from the accompanying static tests, it becomes apparent that the loading rate has an effect on the magnitude of the DDVC. Although the magnitude of the volume change between the static and dynamic models is quite different, it is reasonable when considering that inertial resistance introduced by the soil during dynamic loading decreases the magnitude of the ground displacement. This rationale begs the validity

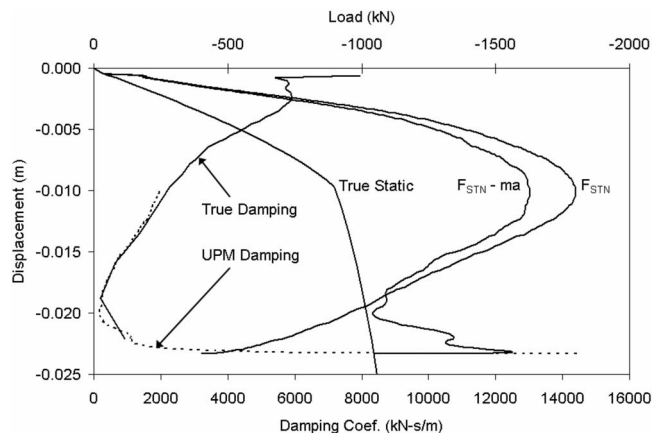


**Fig. 17.** Comparison of true damping and UPM damping using numerically modeled results ( $N=20$ )



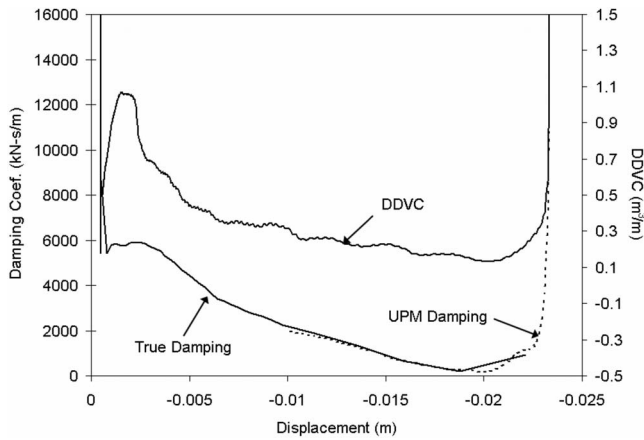


**Fig. 18.** Relationship between the DDVC and the true and UPM damping coefficients ( $N=20$ )

of assuming a constant system mass throughout the test. Perhaps the system mass as well as the damping coefficient is variable.

Also evident in Fig. 19 is the increase in the peak value of the static DDVC with increasing SPT  $N$  values. After shear failure, denoted by the drastic change in the corresponding static DDVC curve, the static DDVC for all three tests seemingly converges asymptotically to a like value, similar to the true damping as seen in Fig. 20. Considering the relationship noted between the DDVC and the true and UPM damping coefficients, it is presumable that the preyield value of the damping coefficient increases in a similar manner with increasing soil strength (SPT  $N$  value).

## Conclusions

The current, most widely accepted method for analyzing static data is the Unloading Point Method (UPM), or some variation thereof. There are two assumptions upon which the method is based: the static capacity of the pile is constant while plunging and the damping coefficient is constant throughout the test. The damping coefficient is calculated over a region near the end of the test; therefore, the calculated value of the damping coefficient is only valid over this region. When a pile exhibits a purely elastic

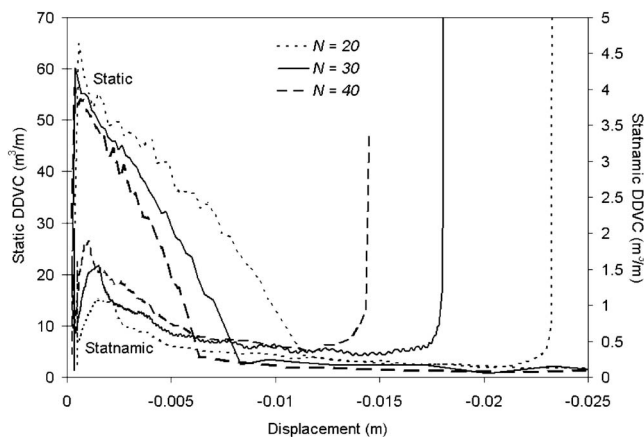


**Fig. 19.** DDVC values for various in situ conditions calculated from modeled static and statnamic tests

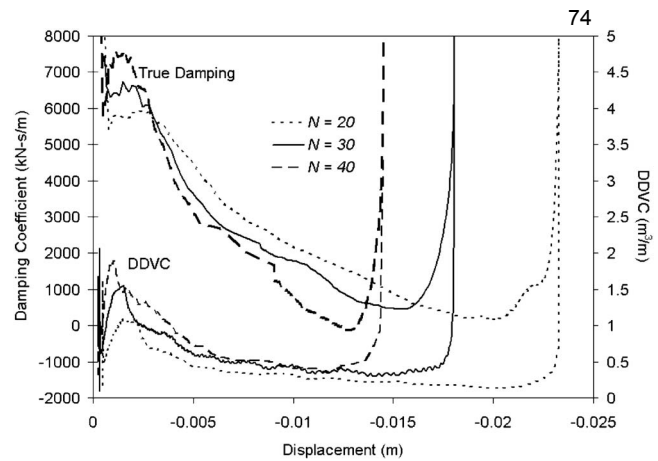


**Fig. 20.** DDVC values for various in situ conditions compared to their corresponding true damping curves

behavior, the associated damping coefficient is valid over the entire test. However, when a pile surpasses elastic behavior and begins yielding, the calculated damping coefficient is no longer valid within the elastic region but only within the yielding region. Since application of the UPM, previous case studies have noted that the derived damping coefficient:

- Is valid over much of the load cycle for piles that exhibit purely elastic behavior;
- Provides a good estimate of the ultimate static capacity when yielding is observed; but
- Does not serve as a good estimate of the static capacity within the elastic region of piles which exhibit yielding.

The intent of this study was to entertain the hypothesis that damping is more closely associated with the actively straining soil not necessarily constant for a given foundation/soil system. Though the numerical model was not created to predict specific numerical values, the computer-generated data reinforce the results of previous case studies by offering a plot of the static damping coefficient which was backcalculated from modeled static and statnamic tests on shafts of identical in situ conditions. The plot of this “true” static damping coefficient shows values that are initially higher prior to yielding which then asymptotically degrade through a transitional stage, where they coincide with the UPM-calculated damping coefficient. The similarity in shape of the UPM-calculated damping coefficient and the displacement-dependent volume change (herein referred to as the DDVC) strongly suggest that such a relationship exists. This is further reinforced by the similarity in shape with the backcalculated damping coefficient, at least at small strains (prior to and just after yielding).

Differences between the magnitude of the static and dynamic DDVC are suspected to be a result of inertial contributions from the soil mass. This brings to surface an important question as to whether the assumption of a constant system mass is just as invalid as a constant static damping coefficient. Perhaps the catch-all static damping coefficient is largely comprised of variations in the system mass.

Though tempting, the writers strongly discourage the practice of developing empirical correlations from numerically modeled results. Therefore, any future correlations will be reserved for full-scale load tests. These tests could provide an arsenal of data with which to establish a quantifiable relationship between an experimentally measured DDVC and the static damping coefficient. If estimations of the static damping coefficient can



eventually be established using DDVC measurements, then perhaps an analysis procedure can be adopted that will provide the reliability of the UPM at ultimate capacity as well as an accurate prediction of static capacity at small displacements. If it can be determined that the DDVC measured during a load test is proportional to damping, then one simple procedure could involve signal matching the measured DDVC curve to the UPM-calculated damping value. Once matched, this altered DDVC curve could then be applied as a template for the damping coefficient throughout the entire test. Alternatively, the ratio of the peak measured DDVC (at the brink of yielding) to the minimum measured DDVC value can be calculated and applied to the UPM-calculated damping value to obtain a peak damping coefficient prior to yield. The impulse response can aid in delineating preyield and postyield conditions, and an appropriate transition applied between the two damping values. As both procedures involve the measurement of DDVC during the load test, they would prove advantageous in that the measurements would encompass the specific characteristics of the foundation, thereby including effects from size, length, soil type, etc.

Researchers at the Univ. of South Florida are currently analyzing experimentally measured DDVC data taken from both model-scale and full-scale load tests where the backcalculated damping coefficient is available to verify the legitimacy of the aforementioned procedures.

## Acknowledgments

The writers would like to acknowledge and thank the Federal Highway Administration for funding this study; Dr. Alaa Ashmawy, M.ASCE for his technical assistance; Bermingham Foundation Solutions, Ontario; and Foundations and Geotechnical Engineering (FGE) for their continual support.

## Notation

The following symbols are used in this paper:

$a$	= acceleration;
$c$	= damping coefficient;
$D$	= modeled shaft diameter;
$E_i$	= initial Young's modulus;
$F_{\text{static}}$	= equivalent static force;
$F_{\text{statnamic}}$	= measured statnamic force;
$F_{\text{stn}}$	= measured statnamic force;
$G_i$	= initial shear modulus;
$K_i$	= initial bulk modulus;

$k$	= equivalent spring constant;
$L$	= modeled shaft length;
$m$	= mass;
$t$	= time;
$V$	= volume of soil mass;
$v$	= velocity;
$x$	= displacement;
$\Delta$	= change as it pertains to the surrounding soil mass;
$\nu$	= Poisson's ratio;
$\rho$	= density; and
$\phi$	= internal friction angle.

## References

- ASTM. (1981). "Standard test method for piles under static axial compressive load (Withdrawn 2006)." *ASTM D 1143*, Philadelphia.
- ASTM. (2000). "Standard test method for high-strain dynamic testing of piles." *ASTM D 4945*, Philadelphia.
- ASTM. (2006). "Standard test method for a pile under an axial compressive force pulse." *ASTM WK 7120*, Philadelphia (under development).
- Ealy, C. D., and Justason, M. D. (2000). "STATNOMIC and static load testing of a model pile group in sand." *Proc., 2nd Int. Statnamic Seminar*, Tokyo, Balkema, Rotterdam, The Netherlands, 169–177.
- Gunaratne, M. (2006). *The foundation engineering handbook*, CRC Press, Boca Raton, Fla., 306–307.
- Itasca Consulting Group, Inc. (2002). *FLAC user's guide*, Mill Place, Minneapolis.
- Middendorp, P., Bermingham, P., and Kuiper, B. (1992). "Statnamic load testing of foundation piles." *Proc., 4th Int. Conf. on Application of Stress-Wave Theory of Piles*, The Hague, Balkema, Rotterdam, The Netherlands, 581–588.
- Mullins, G., Garbin, E. J., and Lewis, C. (2000). "STATNOMIC testing: University of South Florida research." *Proc., 2nd Int. Statnamic Seminar*, Tokyo, Balkema, Rotterdam, The Netherlands, 117–132.
- Mullins, G., Lewis, C., and Justason, M. (2002). "Advancements in statnamic data regression techniques." *Deep foundations 2002: An international perspective on theory, design, construction, and performance*, Vol. II, GSP No. 116, ASCE Geo Institute, Orlando, Fla., 915–930.
- Mullins, G., and Stokes, M. (2007). "Statnamic damping." *Proc., Rapid Load Test Seminar*, GeoDelft, Delft, The Netherlands.
- Mullins, G., and Winters, D. (2004). "Post grouting drilled shaft tips—Phase II final report." *Final Rep., Submitted to Florida Dept. of Transportation*, Tallahassee, Fla.
- Transportation Research Board of the National Academies. (2003). "Prefabricated bridge elements and systems to limit traffic disruption during construction: A synthesis of highway practice." *National Cooperative Highway Research Program Synthesis No. 324*, Washington, D.C.

SP-252—9

## **Corrosion Monitoring of FRP Repaired Piles in Tidal Waters**

**by K. Suh, R. Sen, G. Mullins, and D. Winters**

Synopsis: This paper provides an overview of three different instrumentation schemes used to monitor long term performance of FRP repaired piles in tidal waters. These schemes were evaluated in four demonstration projects extending nearly five years. Two of these used linear polarization to estimate the corrosion rate while the third focused on the variation in the corrosion current. Problems associated with selection, installation and monitoring are described and representative results presented from all three systems. The results suggest data from linear polarization is more consistent. Findings indicate FRP wrapping lowers the prevailing corrosion rate.

Keywords: corrosion; FRP; galvanic current; linear polarization; piles; tidal waters

## 138 Suh et al.

Kwangsuk Suh is a senior engineer at PB Tampa FL. He completed his Ph.D at the University of South Florida, Tampa, FL. His major interest is on evaluation and repair of corrosion damaged bridge piles exposed to marine environments.

Rajan Sen is a professor of structural engineering at the University of South Florida, Tampa, FL. He is a fellow of both ACI and ASCE and held the Samuel and Julia Flom Chair. Dr. Sen is active in FRP research and serves on ACI Committees 215, Fatigue of Concrete; 440, Fiber Reinforced Polymer Reinforcement and 444, Experimental Analysis for Concrete Structures.

Gray Mullins is an associate professor in structural engineering at the University of South Florida, Tampa, FL. His primary research interest is in the area of full-scale testing and instrumentation of structures and foundations. Dr. Mullins has authored numerous publications and holds two US patents.

Danny Winters is a research associate and a Ph.D. student in the Department of Civil and Environmental Engineering at the University of South Florida, Tampa, FL. His research interest is in full-scale testing of foundations.

### INTRODUCTION

The high cost of repairing corrosion damage has led highway authorities to explore the possible use of fiber reinforced polymers (FRP). In the past decade, several demonstration projects were completed that largely focused on repairs to columns and bents damaged by salt water run-off<sup>1</sup>. More recently, with the availability of resins that can cure in water, there has been increased interest in using FRP for repairing piles in tidal waters<sup>2-3</sup>.

Unlike damage caused by salt-water run-off, corrosion damage in piles in tidal waters is limited to a region close to the water surface (“the splash zone”) that is subjected to periodic wetting and drying due to tide change. In the fully submerged region, there is little corrosion because of the much lower solubility of oxygen in water. Moreover, marine growth on the pile surface (see Fig. 1) also slows down the corrosion rate<sup>4</sup>.

Independent laboratory studies have conclusively demonstrated that the corrosion rate is lowered when a corroded region is FRP wrapped<sup>1</sup>. However, in all the tests, wrapping was carried out under optimal, dry conditions. Since conditions for wrapping partially submerged elements in field repairs are less controlled, laboratory outcomes may not necessarily apply. For this reason, it is crucially important to develop instrumentation and measurement techniques for monitoring the performance of the FRP wrapped piles in field applications.

Typically, piles are instrumented when cathodically protected<sup>5,6</sup>. The instrumentation is primarily intended to monitor the protective current that polarizes the steel (makes it more negative than its original potential). The measurement of this protective current and the shift in its potential in the depolarized state (when the current is temporarily stopped) are used to assess the effectiveness of the cathodic protection system. Such systems are not suitable for monitoring the performance of FRP wrapped piles where information on corrosion rates before and after wrapping is relevant. Not surprisingly, none of the earlier FRP repaired piles were instrumented<sup>2-3</sup>.

This paper provides an overview of systems developed for monitoring the performance of FRP in corrosion repairs conducted over the past five years. Linear polarization and galvanic current measurements techniques were used and three different instrumentation schemes evaluated. Corrosion measurements were taken regularly until the completion of the projects and sporadically subsequently.

### RESEARCH SIGNIFICANCE

Piles driven in tidal waters are difficult to instrument for corrosion rate monitoring. This paper provides an overview of three different instrumentation schemes that were used in four field demonstration projects to repair piles. As such, it provides unique information that is of value to researchers and highway agencies alike.

## Health Monitoring Systems and Sensors for Assessing Concrete 139

### BACKGROUND

Corrosion is an electrochemical process consisting of simultaneous oxidation / reduction reactions on the surface of the corroding steel. Oxidation is an anodic process in which electrons are released by the steel resulting in metal loss. Reduction is a cathodic process in which electrons are consumed. The anodic and cathodic sites in a corroding bar may be adjacent to each other to form a micro-cell or distant from each other (as in different layers of steel) to form a macro-cell.

The passage of electrons along the metal from the anode to the cathode creates a circuit that is completed by ionic transport of current within the concrete through the pore solution. The corrosion rate is determined by the equilibrium of these opposing anodic and cathodic reactions. If the instantaneous corrosion rate can be measured, it can be used to calculate metal loss and estimate remaining life of the structure using Faraday's law.

#### Linear Polarization

It would seem that measurement of the corrosion current would be a simple matter of attaching an ammeter to the corroding metal and taking a reading. Unfortunately, such a connection is equivalent to internal shorting because the electrical resistance of the reinforcement is negligible compared to that of the concrete<sup>7</sup>. For this reason, the corrosion current cannot be measured by direct means and alternative indirect means must be used.

Two indirect methods are widely used to estimate the corrosion current. These are known as linear polarization resistance (LPR) and electrochemical impedance spectroscopy (EIS). Both are based on the original empirical observation made by Tafel in 1905 relating current density (corrosion current divided by the reacting surface area of the bar) to the "over-potential". The "over-potential" is the result of the application of an external current or potential that shifts the potential of the metal away from its equilibrium potential. In case of EIS, this shift is investigated over a wide frequency range typically from 0.1 Hz to 100 kHz. In LPR, only a single frequency is used. EIS therefore takes a longer time. For this reason, LPR was used in the testing.

In LPR, because the over-potential is restricted to be very close to the equilibrium potential, the slope  $\Delta E/\Delta I$  ( $\Delta E$  = shift in potential,  $\Delta I$  = resulting current) is linear and is defined as the polarization resistance,  $R_p$ . The corrosion current,  $i_{corr}$ , is inversely related to the polarization resistance through the Stern-Geary constant. Thus, the lower the polarization resistance, the greater the corrosion rate and vice versa.

Several portable devices are available that can be used to make the LPR measurements. The demonstration projects reported in this paper use a PR-Monitor Model 4500 manufactured by Cortest International System, Inc.

#### Galvanic current

As stated earlier, corrosion involves ionic transport of current through the wet concrete that serves as the electrolyte. In galvanic current measurements, sensors made of the same or different steel are embedded at different depths in the concrete close to the reinforcement. The small galvanic or macro-cell currents set up by the corrosion process between these sensors are measured typically using a zero resistance ammeter through an external connection.

The variation in the pre-wrap potential of the steel in piles supporting the Gandy Bridge is shown in Fig. 2. As potentials are more negative at a greater depth, they serve as anodic sites. The less negative locations closer to the pile cap serve as cathodic sites. Thus, prior to wrap, electrons will travel upward along the rebar from the anodic to the cathodic sites. The corresponding ionic current through the wet concrete is in the opposite direction as shown in Fig. 3. As the FRP wrap is a barrier, over time it may be expected to slow down access of oxygen and moisture. As a result, anodic sites become less anodic resulting in a reduction in the measured current and a possible reversal in its direction.

Galvanic current data can therefore serve as a qualitative indicator of the effectiveness of the FRP in slowing down corrosion. An essential requirement is for the embedded probes to be parallel and close to the corroding steel for this technique to be effective. Since installation of the probe disturbs the electro-chemistry of the concrete that is replaced, meaningful results may not be immediately realizable.

### PROBLEM STATEMENT

The issues relating to access, logistics, installation of probes and taking measurements are common to all field instrumentation efforts. More recently, consideration must also be given to counteract the potential for damage by vandalism particularly in urban areas.

These issues are compounded when instrumenting piles in tidal waters because of the lack of ready access to support services. Environmental conditions can result in unpredictable consequences. Particular attention needs to be paid to ensure that electrical connections do not corrode and are protected against the elements. Safety is of paramount importance and must be factored in all operations. Meticulous planning and coordination is required to prepare for unexpected situations. Brief descriptions of some of the relevant parameters are presented below:

#### Probe size

All probes that can be used have to fit in the 75 mm (3 in) concrete cover in piles. Size is therefore a critical consideration. Moreover, the larger the probe, the greater the effort required for installation and the greater the disturbed concrete region.

#### Patching material

The ideal patching material should be electro-chemically compatible with the existing concrete, e.g. similar chloride content and oxygen diffusivity. As with any concrete repair material, it should be a low shrinkage, high tensile strength material with the same coefficient of thermal expansion to minimize cracking.

#### Corrosion protection

Special care must be taken to ensure that materials used are corrosion / weather resistant. Specifically, stainless steel rods must be used for making connections to the steel reinforcement. Special weather proof PVC boxes are required to house the connections. Junction boxes have to be made inaccessible or unobtrusive so as to avoid unwanted attention.

#### Environmental

Low tide, and low winds are ideal but may not always be possible. As the corrosion rate fluctuates with temperature, readings should be taken at similar times at the designated intervals. As this too may not always be possible, temperature records should also be kept.

### DESCRIPTION OF DEMONSTRATION STUDIES

Four field demonstration studies were conducted at two contrasting sites. The first, Allen Creek Bridge, located in Clearwater Florida, exhibits shallow and relatively calm waters. The remaining three studies were carried out on piles supporting Gandy Boulevard bridges spanning Tampa Bay, Florida's largest estuary. These bridges – the Friendship Trails Bridge and the Gandy Bridge are adjacent to each other. Fig. 4 shows their relative location. In all the studies, selected piles were wrapped using fiber reinforced polymers. Details may be found elsewhere<sup>8-11</sup>.

Whereas the piles for both the Allen Creek and the Gandy Bridge were prestressed concrete, those supporting the Friendship Trails Bridge were made of reinforced concrete. However, the procedures for instrumenting and monitoring were virtually identical.

### STEEL CONNECTION

Before any corrosion measurements can be made to assess the pre or post wrap state, an electrical connection has to be made to the reinforcing steel or the prestressing strands. This steel serves as the 'working' electrode in the electro-chemical measurements. The steel connections were deliberately made very close to the pile cap to make them inaccessible. More importantly, in case of prestressed strands, stresses are lower because they are located well within the transfer length (50 x strand diameter).

## Health Monitoring Systems and Sensors for Assessing Concrete 141

In the initial studies, connections were made to reinforcement on all four faces of the pile. This was found to be unnecessary and therefore in later studies only a single connection was made. The targeted reinforcement was at the center of the pile face that could be easily located without the need for a rebar locator (pachometer).

To make the connection, a 50 mm (2 in) diameter, 75 mm (3 in) deep hole was drilled into the pile close to the underside of the pile cap and a 100 mm (3.9 in) long, 5 mm (0.2 in) diameter stainless rod connected to the prestressing strand by brazing. In case of reinforcement, a hole was drilled in the bar and tapped to allow a stainless threaded rod to be screwed to it. In the Allen Creek Bridge where the steel connection was left exposed, 316 grade stainless steel was selected because of its superior corrosion resistance compared to the less expensive 304 grade. Where the connection was protected, the less expensive stainless steel was used.

The 75 mm (3 in) deep hole was filled with mortar leaving a 25 mm (1 in) section of the 100 mm (3.9 in) stainless rod protruding. Before any pre-wrap readings were taken all marine growth covering the pile surface below the high water line was scraped off and removed. Potential readings were taken by connecting a standard copper-copper sulfate half cell to the negative terminal of a high impedance voltmeter while attaching the positive terminal to the steel strand via the stainless steel rods protruding from each face. A special template with holes punched on a 15 cm grid was prepared to ensure readings were consistently taken at the same locations relative to the position of the steel connection. In other applications, the grid locations where readings were to be taken were marked off on the pile and readings taken accordingly.

### CHLORIDE ANALYSIS

Several concrete cores were taken to determine the chloride variation in the cover. The total chloride was determined every 25 mm (1 in) down to the level of the steel using the Florida Method<sup>12</sup>. Table 1 summarizes typical results obtained for four piles P1 to P4 in the Gandy Bridge. The chloride level varied between 2.6-24.2 kg/m<sup>3</sup> (0.16-1.51 lbs/ft<sup>3</sup>). As expected, they greatly exceeded the 0.6-1.2 kg/m<sup>3</sup> (0.04-0.07 lbs/ft<sup>3</sup>) chloride threshold<sup>13</sup>. Values were highest in the first 25 mm (1 in) of cover and were lowest for concrete closest to the steel as can be expected. The highest chloride content was 310 mm (12.2 in) above the high water level.

### PROBE DETAILS

Three different types of probes were used to monitor corrosion performance – two for determining the corrosion rate using LPR and the other for measuring the galvanic current (Table 2). Of these, one was a commercial probe, one an in-house probe and third developed by the Florida Department of Transportation. Photographs of these probes are shown in Fig. 5.

#### USF

The USF sensor makes use of the fact that linear polarization is based on perturbation of the corrosion potential rather than its absolute value. Therefore, any corrosion resistant metal with a stable potential can be used for obtaining the polarization resistance. The USF sensor was developed<sup>8</sup> to address possible vandalism concerns for an exposed site on the busy US 19 highway where accessible junction boxes could attract unwelcome attention. The intent was to use a system that eliminated the need for wiring and junction boxes.

This sensor consisted of a 1.07 m (3.5 ft) long, 5 mm (0.2 in) diameter Grade 316 stainless rod with a 90° hook at one end (Fig. 6). It was embedded in the middle of each of the four pile surfaces, 19 mm (0.75 in) from the concrete surface. The 90° hook protruded from the concrete surface at the top so that alligator clips could be used to make the necessary electrical connections.

Measurements were initially made by successively treating each of the four stainless rods as the reference or counter electrode, i.e. four sets of readings were taken. An analysis of the results indicated that a single reading was adequate and this was subsequently adopted.



## 142 Suh et al.

### FDOT

The Florida Department of Transportation developed reinforcing steel sensors that were used to monitor the effectiveness of sprayed-zinc sacrificial anodes<sup>14</sup>. The sensors are #4 bars cut to 45 mm (1.8 in) length with an exposed surface area of 1300 mm<sup>2</sup> (2 in<sup>2</sup>). One end of the sensor has a length of insulated copper wire that is connected to the reinforcement in the pile. The sensor is inserted lengthwise, i.e. parallel to the reinforcement and 25 mm (1 in) away from it in a 50 mm (2 in) diameter hole drilled into the concrete. The hole is filled with mortar consisting of approximately 50% fresh water and 50% bay water.

### Commercial

A commercial sensor was used for the linear polarization measurement. It uses a modified graphite reference electrode and a titanium ribbon counter electrode which are encased in a mortar block. Its overall dimensions are 60 mm x 60 mm x 125 mm (2.4 in x 2.4 in x 4.7 in). The sensor has two cables for direct connection to the steel working electrode and to the PR monitor used for making the measurements.

### INSTALLATION

The sensors were embedded inside the concrete cover, so the ease of installation depended on its size. The USF sensor was the simplest to install because of its small diameter and shallow embedment depth of 19 mm (0.75 in). More importantly, no external wiring was required. A concrete saw with a pre-set depth was used to create slotted openings on each of the four faces of the pile and the sensor installed (Fig. 6).

The relatively small size of the rebar sensor also made it relatively simple to install. However, because the embedment depth was greater (50 mm), it was necessary to use a 50 mm (2 in.) diameter core drill to create a 50 mm (2 in) deep hole perpendicular to the concrete surface in which the rebar probe was positioned parallel to the main steel 25 mm (1 in.) away. Additionally, shallow slots had to be cut to route the wiring to the junction box where it was permanently connected to the steel (Fig. 7).

The commercial probe was the largest and therefore required the greatest effort for installation. To accommodate this large sensor, multiple side-by-side cored holes were needed. Additionally, as the leads were thicker, deeper slots had to be cut on the pile surface to route to the junction box.

As mentioned earlier, the openings made to install the sensors have to be filled with mortar. Since the chloride content around the reinforcement affects the corrosion condition of the steel being monitored, changes in chloride level can affect its corrosion state. For this reason, the mortar was made to match the chloride content of the surrounding concrete in the USF and the FDOT probes by using appropriate quantity of salt water. This was approximately achieved by making the mortar using about 50% fresh water and 50% bay water.

### Junction Boxes

Except for the USF sensor, junction boxes were required to protect the wiring from corrosion and also to allow data measurements to be performed easily. An electrical connection was first made to the reinforcing or prestressing steel used in the pile. The wires coming out from the rebar sensors were connected to a stainless steel rod inside the junction box. The two cables from the commercial probe were similarly brought into this box. All exposed wiring and cables were inserted in grooves cut on the surface and sealed with hydraulic cement and or epoxy (Fig. 8).

### PROCEDURE FOR MEASUREMENT

Before any measurements were made, the PR monitor was calibrated against a Gamry Corrosion Measurement System. Polarization resistance values obtained from the two systems were almost identical. Similar agreement was also obtained for solution resistance readings from the PR monitor and a Nilsson 400 soil resistance meter.

Since the piles were located in tidal waters, it was necessary to use a boat for access. The PR Monitor was used to take the linear polarization measurements for both the commercial and the USF sensors. The latter required appropriate connections to the working, reference and counter electrodes using alligator clips.



## Health Monitoring Systems and Sensors for Assessing Concrete 143

The PR monitor was set up so that the linear polarization test would be initiated when the potential drift between the working and reference electrode was within 2 mV. For both systems, results were obtained from five potential scans with a 3mV step size and a step duration of around 50 seconds.

Stabilization took much longer for the USF probe since measurements were made for all the strands in the pile. This was compounded by the fact that the water level in Allen Creek rose rapidly as the tide came in because of its relatively narrow width. Thus, it was not possible to take readings for all six piles under the same low tide condition.

The rebar sensors were used to measure the corrosion current. This requires a zero resistance ammeter. As mentioned earlier, the sensors were permanently connected to the pile reinforcing steel inside the junction box.

Three sets of measurements were made; in each case the connection of the sensor to the pile reinforcing steel was temporarily disconnected. The first two sets of measurement were made to obtain a measure of the corrosion current in the pile. The current measurement required the ammeter to be connected between the reinforcing steel and each of the two rebar sensors. In the third set, the current flow between the two sensors was measured by connecting the ammeter between the two probes.

The measurements were made by connecting the negative terminal of the ammeter to the lower probe and the positive terminal to the upper probe. For this set up, negative readings signify that the conventional current flows from the bottom to the top. The movement of electrons is in the opposite direction, i.e. from top to bottom signifying the lower probe is less anodic than the upper probe.

### RESULTS

Representative results from the demonstration projects are summarized in Tables 3-6. The results from the linear polarization tests are given in Tables 3 and 4 while those for galvanic current measurements in Tables 5 and 6. Corrosion rates in Tables 3 and 4 are classified as 'very high' (VH), 'high' (H), 'intermediate' (I), 'moderate' (M) or 'low' (L) in accordance with the classification described in Ref. 7. The definition of this classification is provided as a footnote to these tables.

#### Linear Polarization Resistance

The results obtained using the commercial probe for the GFRP wrapped piles P1, P2, P3 and the (unwrapped) control P4 are listed in Table 3. For each wrapped pile, three sets of data corresponding to readings taken in November 2004, June 2005 and July 2007 are provided. For the control P4, three sets of data are also provided excepting that the last set is from August 2007.

The corrosion current,  $I_{corr}$ , was obtained from the measured linear polarization resistance  $R_p$  taking the Stern-Geary constant for the actively corroding steel as 26 mV. The polarized area ( $6800 \text{ mm}^2$ ) was assumed to be that for a single strand with the same length as the probe. The entire circumference was assumed to be polarized as shown in Fig. 9. The corresponding corrosion rate ( $\mu\text{m}/\text{yr}$ ) was calculated using Faraday's law given by Eq. 1

$$M = \frac{WI_{corr}t}{nF} \quad (1)$$

In Eq. 1,  $M$  is the mass loss of steel,  $W$  the atomic weight of steel (55.85g),  $I_{corr}$  the current in amperes obtained from linear polarization,  $t$  the time in seconds,  $n$  the ionic charge (two for  $\text{Fe} \rightarrow \text{Fe}^{2+} + 2e^-$ ) and  $F$  is Faraday's constant (96,500A).

Of the piles wrapped, pile P1 was the most severely corroded (Fig. 10). The corrosion rate 31 cm below the high water line was  $194 \mu\text{m}/\text{yr}$  in November 2004 but reduced to  $10.2 \mu\text{m}/\text{yr}$  by July 2007 (Table 3). Similar trends can also be discerned in piles P2 (from 84 to  $34 \mu\text{m}/\text{yr}$ ) and P3 (from 103.8 to  $47 \mu\text{m}/\text{yr}$ ). Unfortunately, the control (P4) was in much better shape originally (see Fig. 10) and was selected only because it was in the same bent. Its corrosion rate fluctuated between 49.6 and  $38.5 \mu\text{m}/\text{yr}$  at the same location over the same time frame. The intermediate reading for both the control and P3 was lower than the final reading. This could be because of the higher ambient temperature.

## 144 Suh et al.

The results from the USF probe for six piles including two controls and four FRP wrapped piles using both carbon and glass are summarized in Table 4. Two of the piles were wrapped under ideal conditions using a cofferdam (C1 and D1). Four sets of readings corresponding to June 2003, June 2004, June 2005 and June 2007 are presented. Inspection of Table 4 shows that barring the initial readings for control B2, all rates are low (L).

This was the first attempt by the research team to repair piles using FRP. Although the site was selected by FDOT, none of the wrapped piles including the controls had visible signs of corrosion. The corrosion rates were small to begin with and fluctuated only slightly over the four year period when measurements were made.

Given the low corrosion rates, it is not possible to draw definitive conclusions. The corrosion rates for the coffer dam wrapped (C1, D1) and the water wrapped piles (F1, E2) have remained low throughout the four year monitoring period. The performance of the GFRP (E2) and the CFRP wrapped piles (C1, D1, F1) are comparable. Though the rates in the controls show reductions, this could be because of the rapid change in water level due to tide; this meant that not all readings were taken under the same low tide conditions.

### Galvanic Current

Table 5 and 6 summarize the results of the galvanic probe measurements from the Friendship Trails and the Gandy Bridges. These show the current flow between probes placed at two levels identified here as ‘top’ and ‘bottom’ illustrated in Fig. 3.

The initial current flow measurements for the Friendship Trails Bridge in Table 5 (Aug 2003) in both controls (99-S, 99-N) and two of the wrapped piles (100-N, 101-N) were positive, i.e. bottom probe was anodic. For the other wrapped pile, 100-S, the reading was negative signifying that the top probe was anodic. Over the next four years, the trend in the wrapped piles was to reduce [100-S (-21 to 0.1 $\mu$ A), 101-N (17 to 0.9 $\mu$ A)] or remain about the same [100-N (12 to 13.3 $\mu$ A)]. A similar trend was also indicated for the controls, e.g. 99-S changed from 1 to 3.5 $\mu$ A while 99-N reversed from 4 to -11.4 $\mu$ A.

No similar trends can be discerned in the results for piles P1 to P4 for the Gandy Bridge summarized in Table 6. For the control P4, the current became negative and then assumed a positive value. For all three wrapped piles P1, P2 and P3, the readings reverted to their initial readings after three years.

Overall, the data from the galvanic current measurement data is confusing. This may be because of the difficulty in accurately measuring very small currents.

## DISCUSSION

The results obtained highlight some of the inconsistencies and difficulties associated with corrosion monitoring. Numerous factors affect corrosion that cannot be isolated. Field installation disturbs the electro-chemistry and this can affect measurements particularly for galvanic current measurement. Not surprisingly, results for the galvanic current measurements (Table 5 and 6) were found to be inconclusive.

Linear polarization yielded more consistent results but here again measurements were influenced by tide change. This particularly affected readings from the USF probe where reaching a steady state took as long as 30 minutes. Taking readings for six piles sometimes took 6 hours during which time the water level changed.

Aside from tidal effects, uncertainty regarding the polarized area is well documented. In this study, the polarized area was calculated on the basis of the entire circumference as shown in Fig. 9. This may be valid where the concrete is moist and its conductivity high. In dry concrete resistivity is high and therefore only a portion of the circumference facing the electrode is polarized<sup>15</sup>. For this condition, the polarized area is about half the circumference and therefore the calculated corrosion current is doubled. Furthermore, if cracks and voids are present in the concrete, the polarizing current cannot be distributed. Therefore, readings will be erroneous. Moreover, rates are strongly affected by environmental conditions such as temperature and humidity. Collectively, these factors account for the large fluctuations observed.

## Health Monitoring Systems and Sensors for Assessing Concrete 145

Results were also inconclusive because several instrumented piles had low corrosion rates at the onset of the project. This was the case for the piles supporting Allen Creek Bridge (Table 4). Given the uncertainty associated with corrosion data, definitive conclusions cannot be drawn for this case.

The most severely corroding pile wrapped was pile P1 (Fig. 10). For this pile, there was significant reduction in the corrosion rate following wrapping: it reduced from 194 to 10.2 $\mu\text{m}/\text{yr}$  over three years. This result is consistent with data obtained from laboratory testing which shows that FRP wrapping slows down but does not stop corrosion<sup>1</sup>. This trend is reflected to a lesser extent in piles P2 and P3 where the original corrosion rates were lower. It may be reasonable to conclude from this data that FRP wrapping slows down the corrosion rate in piles.

### CONCLUSIONS

This paper provides an overview of techniques used to monitor the corrosion performance of wrapped piles. Based on the results presented the following conclusions may be drawn:

1. Data obtained using rebar sensors was inconclusive (Table 5 and 6). Difficulties in measuring small currents make them less useful for monitoring the performance of FRP wrapped piles.
2. Linear polarization results using the commercial probe were more consistent. Measurements over three years indicated a significant reduction in the corrosion rate in pile P1 (Fig. 10, Table 3) which was most heavily corroded prior to the wrap. Similar reductions were also observed in piles P2, P3. All these piles were wrapped using GFRP.
3. The USF probe (Fig. 6) worked well. It needs to be evaluated at another site where the impact of tide change is not as drastic. Results would have been more conclusive using these probes had the prevailing corrosion rates in the piles been higher initially.

### ACKNOWLEDGMENTS

The studies reported were performed in cooperation and funding from the State of Florida and US Department of Transportation and Hillsborough County. The assistance and guidance of Mr. Jose Garcia and Mr. Steve Womble (both FDOT) is gratefully acknowledged. We also thank Mr. Nils Olsson and Ms Mara Nelson (Hillsborough County) for their support. The opinions findings and conclusions expressed in this publication are those of the authors and not necessarily those of the Florida or US Department of Transportation.

### REFERENCES

1. Sen, R. 'Advances in the application of FRP for repairing corrosion damage', *Progress in Structural Engineering and Materials*, **5** (2), 2003, 99-113.
2. Bazinet, S., Cercone, L. and Worth, L. *SAMPE Journal*, **39** (3), 2003, 8-16.
3. Watson, R.J. 'The use of composites in the rehabilitation of civil engineering structures', *ACI SP 215* (Ed. S. Rizkalla and A. Nanni), ACI, Farmington Hills, MI, 2003, 291-302.
4. Gjorv, O.E., Vennedland, O. and El-Busaidy, A.H. (1987). Diffusion of dissolved oxygen through concrete", *Material Performance*, Vol. 25, No. 2, 1987, pp. 39-44.
5. R.J. Kessler, R.G. Powers and I.R. Lasa "Update on sacrificial anode cathodic protection on steel reinforced concrete structures in seawater," *CORROSION/95*, 1995, Paper no 516.
6. Leng, D.L. (2000). "Zinc mesh cathodic protection systems," *Materials Performance*, Vol. 41, No. 8, 2000, pp. 28-33.
7. Bertolini, L., Elsener, B., Pedferri, P. and Polder, R. (2004). *Corrosion of Steel in Concrete*, Wiley-Vch Verlag GmbH & Co. KGaA, Weinheim, Germany.
8. Mullins, G., Sen, R., Suh, K and Winters, D. 'Underwater FRP repair of prestressed piles in the Allen Creek Bridge'. *ASCE, Journal of Composites for Construction*, **9** (2), 2005, 136-146.
9. Sen, R., Mullins, G., Suh, K. and Winters, D. 'FRP application in underwater repair of corroded piles'. *ACI SP 230* (Eds. C. Shield, J. Busel, S. Walkup, D. Gremel), Vol. 2, 2005, 1139-1156.
10. Mullins, G., Sen, R., Suh, K. and Winters, D. 'A demonstration of underwater FRP repair', *Concrete International*, **28** (1), 2006, 1-4.
11. Mullins, G., Sen, R., Winters, D. and Schrader, A. 'Innovative pile repair'. Final report submitted to Hillsborough County, 2007, 40 pp.

## 146 Suh et al.

12. FDOT. Florida method of test for determining low-levels of chloride in concrete and raw materials, designation: FM 5-516, 2000.
13. Mindess, S., Young, J. and Darwin, D. *Concrete*, Prentice-Hall, Englewood Cliffs, NJ, 2003.
14. Sagues, A. and Powers, R. 'Field experience with rebar probes to monitor performance of sprayed zinc galvanic anodes on concrete', in *Techniques to Assess the Corrosion Activity of Steel Reinforced Concrete Structures* (Neal Berke, Edward Escalante, Charles Nmai and David Whiting, Eds.), ASTM, 1996, 173-814.
15. SHRP-S-324 Condition evaluation of concrete bridges relative to reinforcement corrosion, Vol. 2, "Method of measuring the corrosion rate of reinforcing steel", Strategic Highway Research Program, National Research Council, Washington, DC.

**Table 1** -- Result of Chloride Content Analysis in Gandy Bridge

Pile Name	Location*	0 - 25 mm (kg/m <sup>3</sup> )	25 - 50 mm (kg/m <sup>3</sup> )	50 - 75 mm (kg/m <sup>3</sup> )
P4 (Control)	A: 76 cm	8.9	5.4	2.6
	B: 61 cm	10.6	7.1	4.4
	C: 53 cm	10.9	8.3	4.7
	D: 31 cm	17.6	12.0	7.6
P1 (GFRP)	A: 76 cm	7.3	18.6	11.2
	B: 61 cm	10.2	11.2	9.1
	C: 53 cm	13.2	12.9	N/A
	D: 31 cm	14.0	15.1	14.4
P2 (GFRP)	A: 76 cm	7.4	5.4	2.7
	B: 61 cm	8.8	5.4	3.5
	C: 53 cm	9.3	7.7	4.5
	D: 31 cm	24.2	16.0	9.9
P3 (GFRP)	A: 76 cm	9.1	9.9	8.4
	B: 61 cm	9.9	9.7	7.1
	C: 53 cm	10.6	9.3	6.2
	D: 31 cm	19.6	11.2	7.9

\*Dimensions are above High Water Level

## Health Monitoring Systems and Sensors for Assessing Concrete 147

**Table 2 -- Sensors Used in Demonstration Projects<sup>8-11</sup>**

Site	Sensor	Size	System
Allen Creek Bridge, Clearwater (2003)	USF	5mm diameter x 1.07m Grade 316 stainless steel rod	LPR
Gandy Bridge, Tampa Bay (2004)	Commercial	60mm x 60mm x 125mm	LPR
	FDOT	45mm long # 4 bar with 1300mm <sup>2</sup> surface area	GC
Friendship Trails Bridge, Tampa Bay (2004)	FDOT	45mm long # 4 bar with 1300mm <sup>2</sup> surface area	GC
Friendship Trails Bridge, Tampa Bay (2006)	FDOT	45mm long # 4 bar with 1300mm <sup>2</sup> surface area	GC

LPR – Linear Polarization Resistance; GC – galvanic current

**Table 3 -- Linear Polarization Data – Commercial Probe**

Probe ID #	Date	$I_{corr}^*$ ( $\mu\text{A}/\text{cm}^2$ )	Rate ( $\mu\text{m}/\text{yr}$ )	Classification	Temp ( $^{\circ}\text{C}$ )
P4 (Control) – 910 mm Above HWL	Nov 2004	0.723	8.39	M	27.4
	Jun 2005	0.584	6.77	M	27.5
	Aug 2007	0.815	9.46	M	31.4
P4 (Control) – 310 mm Below HWL	Nov 2004	4.276	49.6	I	27.4
	Jun 2005	1.765	20.48	I	27.5
	Aug 2007	3.318	38.48	I	31.4
P1 (GFRP) – 910 mm Above HWL**	Nov 2004	1.597	18.52	I	27.4
	Jun 2005	0.633	7.34	M	27.5
	July 2007	0.496	5.75	M	31.1
P1 (GFRP) – 310 mm Below HWL	Nov 2004	16.732	194.09	VH	27.4
	Jun 2005	3.346	38.82	I	27.5
	July 2007	0.879	10.19	I	31.1
P2 (GFRP) – 910 mm Above HWL	Nov 2004	0.726	8.42	M	27.4
	Jun 2005	0.524	6.08	M	27.5
	July 2007	0.274	3.18	L	31.1
P2 (GFRP) – 310 mm Below HWL	Nov 2004	7.261	84.23	H	27.4
	Jun 2005	4.009	46.50	I	27.5
	July 2007	2.960	34.34	I	31.1
P3 (GFRP) – 910 mm Above HWL	Nov 2004	1.015	11.78	I	27.4
	Jun 2005	0.588	6.82	M	27.5
	July 2007	0.686	7.96	M	31.1
P3 (GFRP) – 310 mm Below HWL	Nov 2004	8.95	103.82	VH	27.4
	Jun 2005	2.291	26.57	I	27.5
	July 2007	4.051	46.99	I	31.1

\*Assumed polarized area = 6800 mm<sup>2</sup>

\*\*HWL = High Water Level

VH = very high (>100  $\mu\text{m}/\text{yr}$ ); H = high (50-100  $\mu\text{m}/\text{yr}$ ); I = intermediate (10-50  $\mu\text{m}/\text{yr}$ );

M = moderate (5-10  $\mu\text{m}/\text{yr}$ ); L = low (2-5  $\mu\text{m}/\text{yr}$ )<sup>7</sup>

Table 4 -- Linear Polarization Data – USF Probe

Probe ID #	Date	$I_{\text{corr}}^*$ ( $\mu\text{A}/\text{cm}^2$ )	Rate ( $\mu\text{m}/\text{yr}$ )	Classification
B2 (Control)	June 2003	0.837	9.713	M
	June 2004	0.302	3.501	L
	June 2005	0.956	11.08	I
	June 2007	0.179	2.079	L
G1 (Control)	June 2003	0.401	4.655	L
	June 2004	0.229	2.661	L
	June 2005	0.226	2.624	L
	June 2007	0.147	1.706	L
C1 (CFRP) Cofferdam Dry Wrap	June 2003	0.078	0.903	L
	June 2004	0.165	1.911	L
	June 2005	0.084	0.978	L
	June 2007	0.174	2.016	L
D1 (CFRP) Cofferdam Dry Wrap	June 2003	0.095	1.103	L
	June 2004	0.164	1.900	L
	June 2005	0.081	0.937	L
	June 2007	0.191	2.217	L
F1 (CFRP)	June 2003	0.116	1.341	L
	June 2004	0.039	0.453	L
	June 2005	0.087	1.008	L
	June 2007	0.122	1.415	L
E2 (GFRP)	June 2003	0.302	3.500	L
	June 2004	0.198	2.294	L
	June 2005	0.205	2.376	L
	June 2007	0.319	3.695	L

\*Assumed polarized area =  $0.4534 \text{ m}^2$

I = intermediate ( $10\text{-}50 \mu\text{m}/\text{yr}$ ); L = low ( $2\text{-}5 \mu\text{m}/\text{yr}$ ); M = moderate ( $5\text{-}10 \mu\text{m}/\text{yr}$ )<sup>7</sup>

## Health Monitoring Systems and Sensors for Assessing Concrete 149

**Table 5 -- Current Data – Rebar Probe Friendship Trails Bridge**

Pile ID #	Date	<i>I</i> * ( $\mu$ A)	Temp ( $^{\circ}$ C)
99-S (Control)	Aug 2003	1.0	30.7
	June 2004	-0.3	28.5
	June 2005	7.4	27.5
	July 2007	3.5	31.1
99-N (Control)	Aug 2003	4.0	30.7
	June 2004	-29.1	28.5
	June 2005	-22.7	27.5
	July 2007	-11.4	31.1
100-S (GFRP)	Aug 2003	-21.0	30.7
	June 2004	0.6	28.5
	June 2005	0.2	27.5
	July 2007	0.1	31.1
100-N (CFRP)	Aug 2003	12.0	30.7
	June 2004	8.0	28.5
	June 2005	6.8	27.5
	July 2007	13.3	31.1
101-N (GFRP)	Aug 2003	17.0	30.7
	June 2004	23.1	28.5
	June 2005	10.1	27.5
	July 2007	0.9	31.1

\*Current readings taken between top and bottom probes.

**Table 6 -- Current Data – Rebar Probe Gandy Bridge**

Pile ID #	Date	<i>I</i> * ( $\mu$ A)	Temp ( $^{\circ}$ C)
P4 (Control)	Oct 2004	0.0	28.1
	June 2005	-19.0	27.5
	July 2007	4.4	31.1
P1 (GFRP)	Oct 2004	-24.5	28.1
	June 2005	-42.1	27.5
	July 2007	-23.0	31.1
P2 (GFRP)	Oct 2004	-21.1	28.1
	June 2005	-97.6	27.5
	July 2007	-21.2	31.1
P3 (GFRP)	Oct 2004	27.5	28.1
	June 2005	7.0	27.5
	July 2007	26.3	31.1

\*Current readings taken between top and bottom probes.





Figure 1 – Marine Growth.

	P1			P2			P3			P4		
1.4m	-346	-352	-348	-248	-226	-216						
1.5m	-369	-371	-371	-234	-230	-237	-269	-271	-269	-263	-257	-282
1.7m	-398	-396	-396	-297	-285	-301	-282	-284	-289	-267	-283	-292
1.8m	-426	-415	-422	-312	-310	-289	-296	-283	-299	-308	-311	-321
2.0m	-436	-436	-448	-341	-353	-346	-328	-308	-318	-321	-337	-345
2.1m	-471	-474	-498	-343	-348	-375	-324	-318	-327	-368	-386	-377
2.3m	-507	-529	-502	-379	-384	-387	-346	-342	-347	-374	-409	-401
2.4m	-517	-534	-553	-414	-429	-431	-379	-360	-376	-425	-414	-414
2.6m	-531	-553	-573	-459	-462	-478	-396	-405	-405	-464	-462	-461
2.7m	-563	-568	-596	-487	-483	-488	-480	-456	-434	-522	-514	-513

Tidal Range

Figure 2 -- Pre-wrap corrosion potential measurement (mV).

# Health Monitoring Systems and Sensors for Assessing Concrete 151

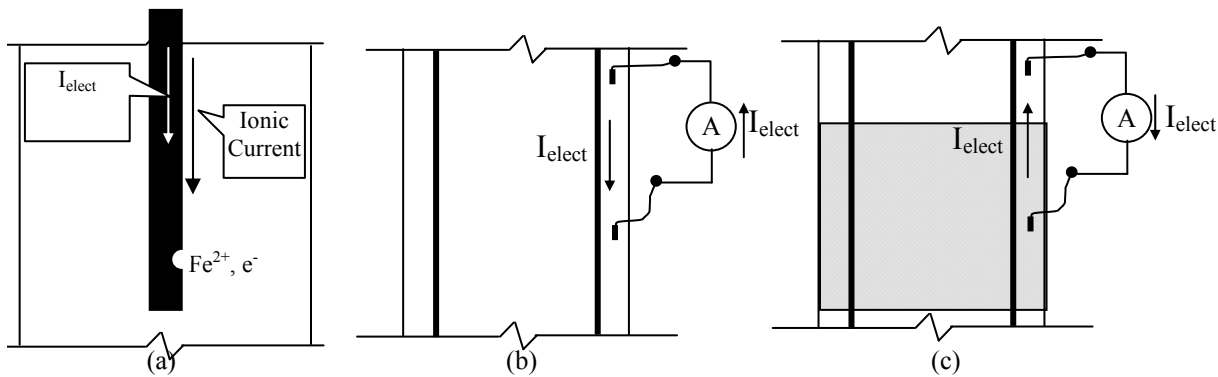


Figure 3 -- (a) Current flow in corroded steel; (b) Current flow between two rebar probes in unwrapped pile; (c) Likely current flow between same two probes in wrapped pile.

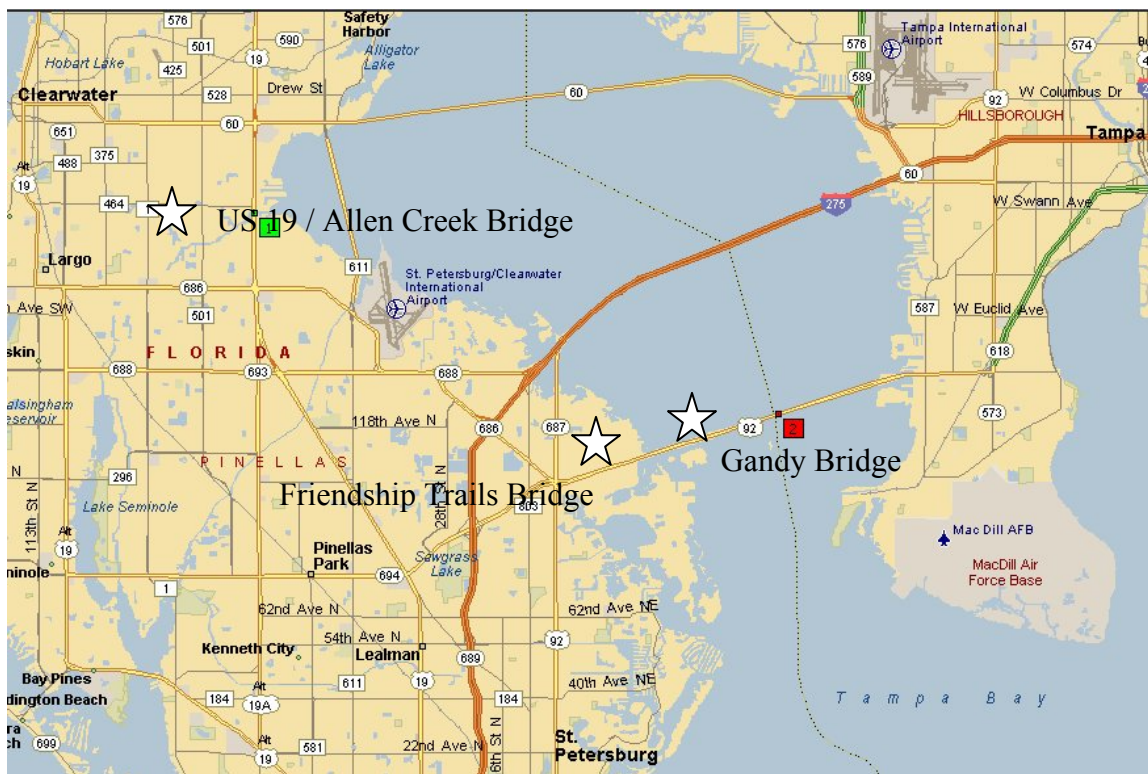
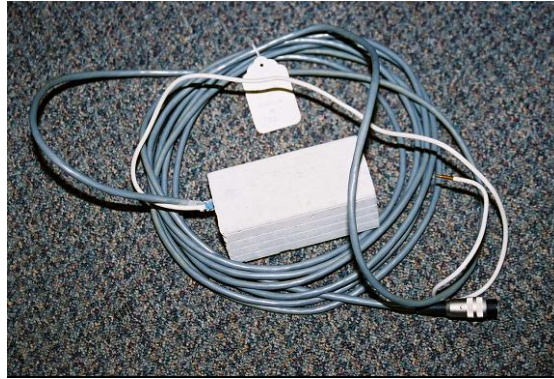


Figure 4 – Location of sites for pile repair.



(a)



(b)



(c)

Figure 5 -- (a) FDOT rebar probe; (b) Commercial probe; and (c) USF probe.

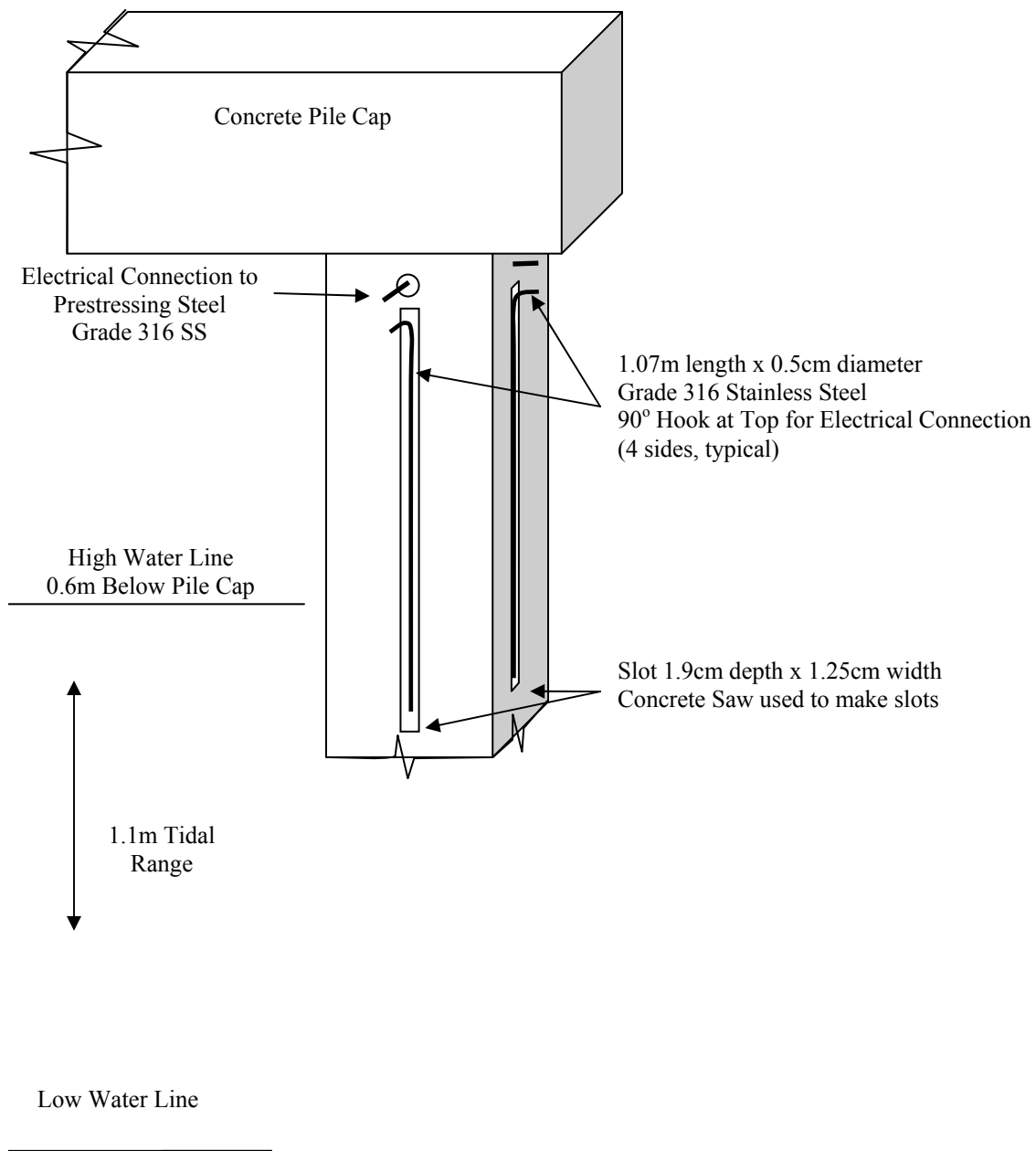
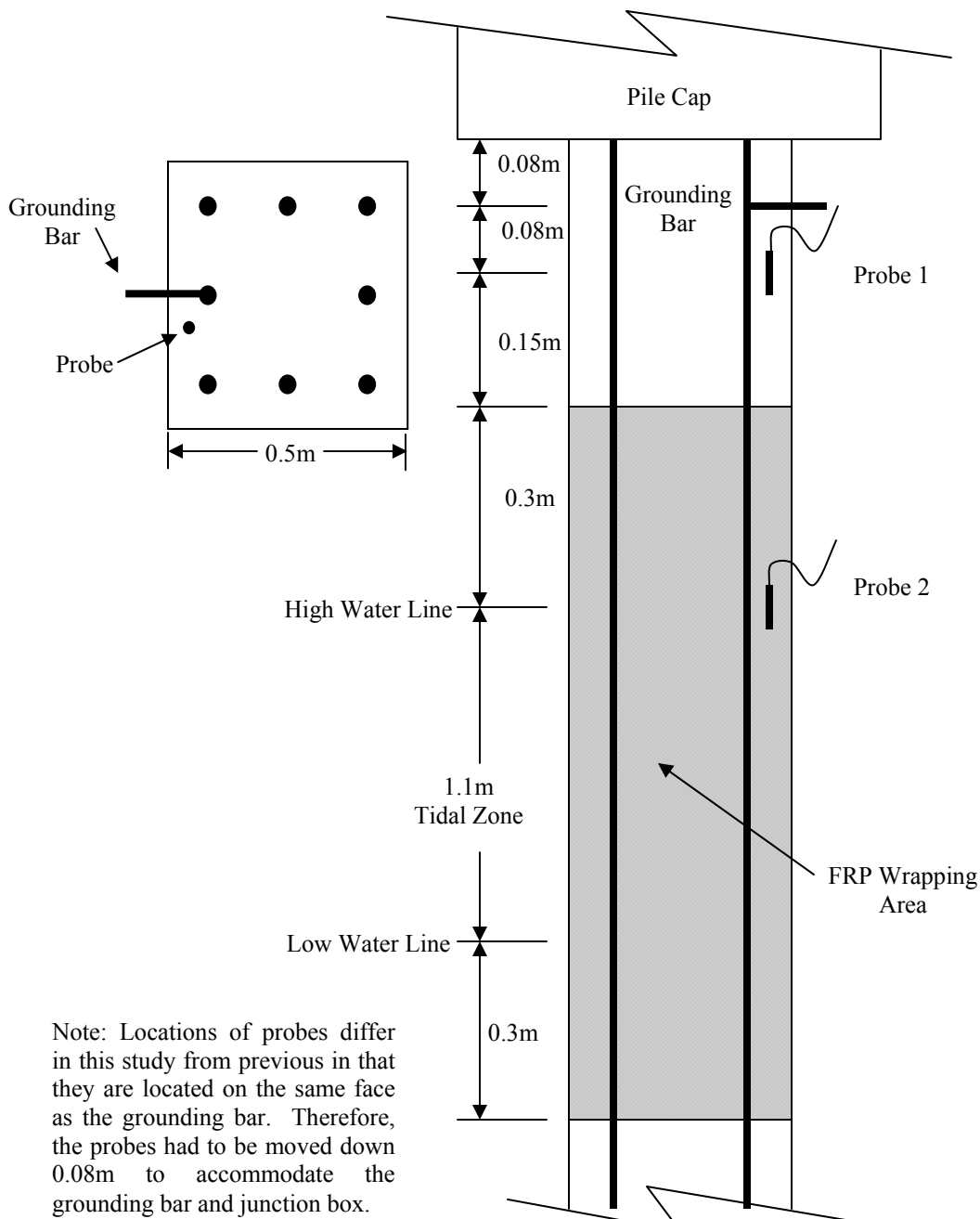


Figure 6 -- USF sensor installation schematic.



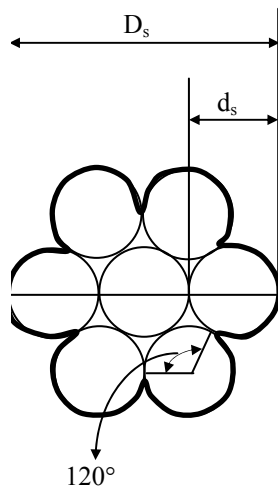
Note: Locations of probes differ in this study from previous in that they are located on the same face as the grounding bar. Therefore, the probes had to be moved down 0.08m to accommodate the grounding bar and junction box.

Figure 7. FDOT probe installation schematic.





Figure 8 – Installing junction box and wiring.



$D_s$  = diameter of a strand

$d_s$  = diameter of one wire (=  $D_s/3$ )

$P_s$  = perimeter of one strand (=  $\pi * d_s * 6 \text{wires} * (240/360)$ )

$L_s$  = polarized strand length (= the length of the counter electrode)

Polarized Surface Area of Strand =  $P_s * L_s$

Figure 9 – Calculation of polarized area.

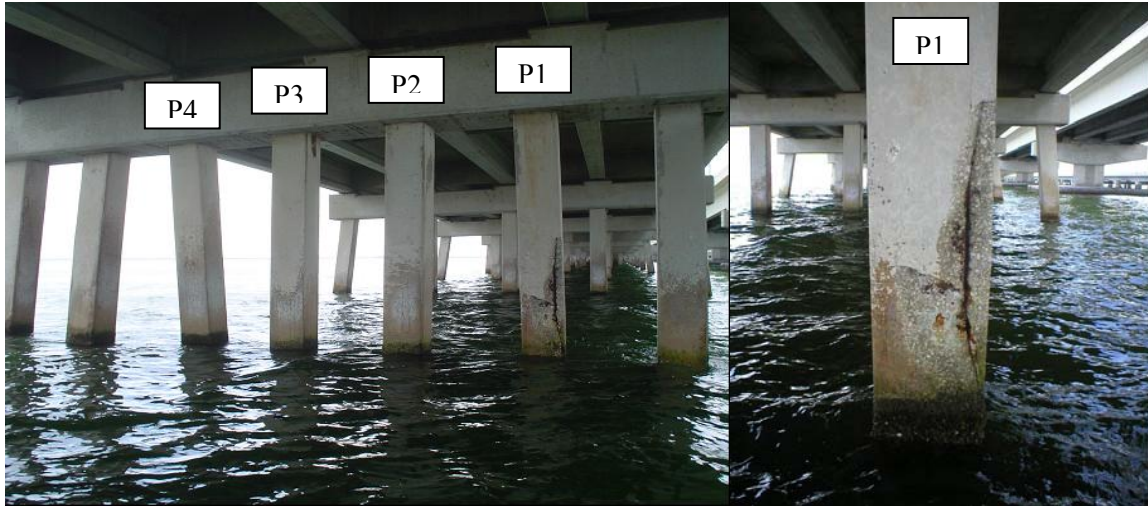


Figure 10 – Gandy bridge piles. P1 was the most corroded. P4 was the control.



# Bond Enhancement for FRP Pile Repair in Tidal Waters

Danny Winters<sup>1</sup>; Gray Mullins, M.ASCE<sup>2</sup>; Rajan Sen, F.ASCE<sup>3</sup>; Andy Schrader, A.M.ASCE<sup>4</sup>; and Michael Stokes, S.M.ASCE<sup>5</sup>

**Abstract:** Vacuum bagging and pressure bagging are established techniques used by the composites industry for fabricating components. This paper describes a study that explored the adaptation of these techniques for improving the FRP-concrete bond in the repair of partially submerged piles. Prototype vacuum bagging and pressure bagging systems were developed and bond improvement assessed from results of pullout tests on full size piles repaired under simulated tide in the laboratory. Pressure bagging gave better bond and was found to be simpler because it did not require an airtight seal. A field demonstration project was conducted in which pressure bagging was used in combination with two different GFRP systems to repair two corroding piles supporting the Friendship Trails Bridge across Tampa Bay. Inspection of the postcured wrap showed no evidence of air voids. The study demonstrates that techniques developed by the composites industry may be readily adapted to provide effective and inexpensive means for improving FRP-concrete bond.

**DOI:** 10.1061/(ASCE)1090-0268(2008)12:3(334)

**CE Database subject headings:** Fiber reinforced polymers; Field tests; Corrosion; Rehabilitation; Tidal currents; Piles.

## Introduction

Recent advances in resin technology have made it possible to use FRP for the corrosion repair of partially submerged piles (Bazinet et al. 2003; Watson 2003; Mullins et al. 2005, 2006, 2007). In all the applications, the FRP was directly applied over the corroding region in the “splash zone” (subjected to diurnal wet/dry cycles) without removal of the chloride-contaminated concrete.

Several investigators, e.g., Sheikh et al. (1997), Bonacci (2000), Debaiky et al. (2002), Wheat (2002), Wootton et al. (2003), and Suh et al. (2007) have independently demonstrated that while FRP cannot stop corrosion, it can significantly reduce the corrosion rate. However, the extent of the reduction depends on the integrity of the FRP-concrete bond. Thus, Michigan State University researchers Baiyasi and Harichandran (2001) reported that metal loss was lower where FRP was bonded compared to its unbonded counterpart. Similarly, a study sponsored by Texas DOT found that in locations where the FRP had debonded, there was increased localized corrosion under simulated tidal cycles (Berver et al. 2001). Thus, good FRP-concrete bond over the entire wrapped region is essential for successful performance.

The authors recently conducted on-site pullout tests on FRP

repaired piles at both above and below high water locations (Sen and Mullins 2007). Fig. 1 shows a plot of the residual bond stress obtained for two different systems, a prepreg and a wet layup. Inspection of Fig. 1 shows considerable variability in the bond. It ranges from 0.7 to 1 MPa in the dry region of the pile and from 0.4 to 1.8 MPa in the critical wet/dry region. In another demonstration project, the FRP was found to have completely debonded from the concrete (Suh et al. 2005). Research suggests that if the on-site FRP bond were improved by making it less variable, service life of the FRP repair would be extended, making it more cost effective.

## Why Bond Is Variable

FRP pile repair typically uses hand layup techniques to impregnate the fibers. In this case, the weight of the wet FRP material acting downwards has a tendency to make it slide down the pile surface. Moreover, as the vertical surface is seldom absolutely true, the FRP is not necessarily in continuous contact with the concrete over the entire length as the resin cures.

To counteract these tendencies, a plastic sheet called shrink wrap is tightly wound around the wet FRP over its entire length. Unfortunately, because of buoyancy effects and difficulty in wrapping tightly above shoulder height, the applied pressure is not uniform.

Uniform pressure is widely used to improve adhesion in bonded connections. For example, in segmental construction, a minimum compressive pressure of 276 kPa (40 psi) is applied to join epoxied match-cast units (AASHTO 1999). If uniform (gage) pressure can be maintained on the FRP wrap while the resin cures, the FRP concrete bond may be similarly expected to improve.

## Techniques for Applying Uniform Pressure

Uniform pressure, through vacuum or pressure bagging, has long been used by the aerospace and automotive industry for fabricat-

<sup>1</sup>Dept. of Civil and Environmental Engineering, Univ. of South Florida, Tampa, FL 33620.

<sup>2</sup>Dept. of Civil and Environmental Engineering, Univ. of South Florida, Tampa, FL 33620.

<sup>3</sup>Dept. of Civil and Environmental Engineering, Univ. of South Florida, Tampa, FL 33620.

<sup>4</sup>Karins Engineering Group Inc., St. Petersburg, FL 33713.

<sup>5</sup>Dept. of Civil and Environmental Engineering, Univ. of South Florida, Tampa, FL 33620.

Note. Discussion open until November 1, 2008. Separate discussions must be submitted for individual papers. To extend the closing date by one month, a written request must be filed with the ASCE Managing Editor. The manuscript for this paper was submitted for review and possible publication on May 14, 2007; approved on August 17, 2007. This paper is part of the *Journal of Composites for Construction*, Vol. 12, No. 3, June 1, 2008. ©ASCE, ISSN 1090-0268/2008/3-334-343/\$25.00.

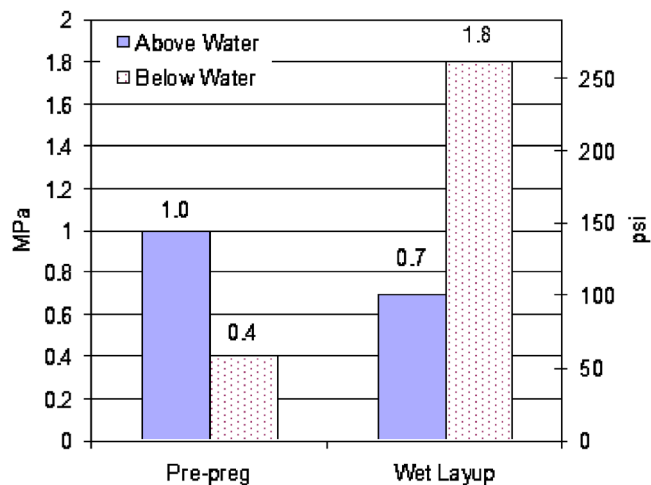


Fig. 1. Residual bond stress from field study

ing FRP components. Vacuum bagging has occasionally been used in infrastructure applications, e.g., Stallings et al. (2000) and Nazier et al. (2005). However, no similar reference relating to the application of pressure bagging was found in the literature.

## Objectives

The overall goal of the research project was to explore the feasibility of adapting vacuum bagging or pressure bagging for improving FRP-concrete bond in the field repair of corroding piles in tidal waters. In order to meet this objective, it was necessary to:

1. Develop prototype vacuum bagging and pressure bagging techniques appropriate for FRP repair of partially submerged piles.
2. Evaluate improvement in bond through pullout testing.
3. Implement the system developed through a field demonstration.

## Background

### Vacuum Bagging

Vacuum bagging applies pressure by creating a vacuum (limited to a maximum of 1 atm—760 mm of Hg). The essential components of a vacuum bagging system are (1) a vacuum bag; and (2) a vacuum pump capable of creating a significant vacuum. Stallings et al. (2000) used a vacuum pressure of 0.034 MPa during a 6 h curing period for repairing a bridge girder. Nazier et al. (2005) did not state the vacuum pressure used, but their pump had the facility to achieve 25  $\mu\text{m}$  of vacuum (1 atm = 760,000  $\mu\text{m}$  Hg).

Since vacuum is only sustained with an airtight seal around the perimeter of the wrapped region, surface smoothness at the perimeter is a critical consideration. Additionally, there needs to be a method for soaking up expelled resin and its subsequent removal after the FRP has cured, so that its external appearance is not marred.

Fig. 2 shows a schematic of the vacuum bagging system used in the study. In this figure, a porous, thin, nonstick film is referred to as the “release” and a thicker layer of absorbent material, called a “breather”.

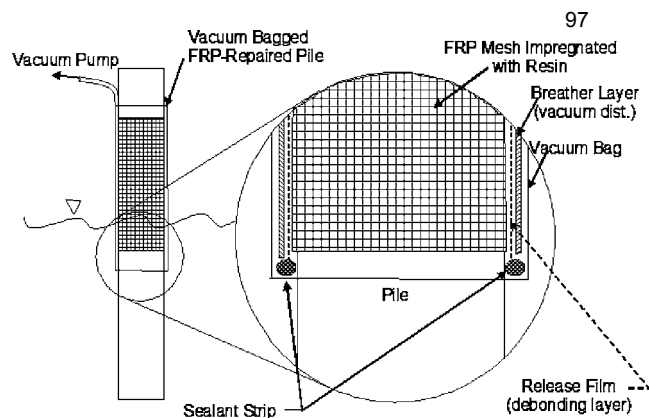


Fig. 2. Vacuum bagging schematic

The release is a nonstick plastic stretch wrap material. The breather material was a thick burlap cloth that allows air to be extracted from inside the bag. The bag is sealed at its ends so that there are no leaks.

### Pressure Bagging

Pressure bagging makes use of a pressure bladder that surrounds a pile (or a column in above water applications) similar to a blood pressure cuff. In essence, it incorporates an air-tight bladder inside an outer restraining structure that can be rigid or flexible. Flexible restraints are more suitable as they can be fitted and adapted as necessary to accommodate different pile sizes.

Fig. 3 shows a schematic of the pressure bag system developed. It secures to itself using a set of 21 toggles. The air bladder is inside this bag and is connected to a source of compressed air. The material of the bladder needs to be able to withstand tensile stresses that develop as it is inflated. Fig. 4 shows the components of the prototype used in the laboratory testing.

## Experimental Program

The intent of the laboratory testing was to develop and evaluate a prototype system that could be used in a field demonstration study. Since the literature was dismissive regarding the suitability of pressure bagging, e.g., Nazier et al. (2005), only vacuum bagging was considered initially. However, because of problems encountered in establishing a vacuum, pressure bagging was included and the original test program modified. In the text, tests relating to vacuum bagging are referred to as the “first series” while those for pressure bagging as the “second series”.

### Material Properties

The FRP systems selected for the laboratory study were identical to that used in previous demonstration studies (Mullins et al. 2005, 2006, 2007). These were a prepreg system developed by Air Logistics Corporation (2002) and a wet layup system developed by Fyfe (2002). Since the goal of the study was to improve bond, only the lower cost fiberglass was tested.

### Prepreg System

The prepreg system uses a unique water-activated urethane resin in conjunction with a custom woven fabric. Because it is water activated, the FRP material is preimpregnated with resin and sent

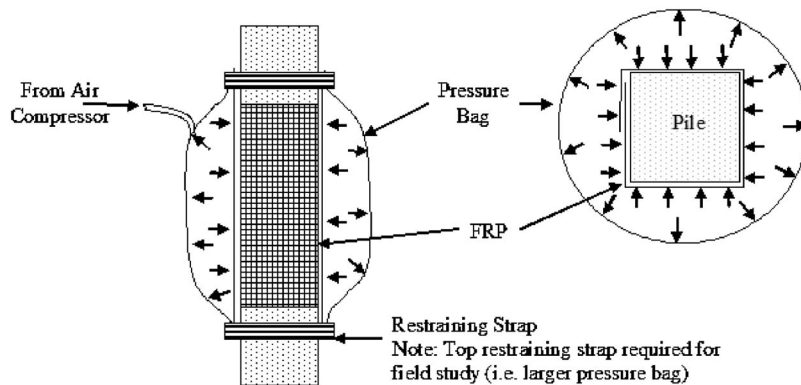


Fig. 3. Pressure bagging schematic

to the site in hermetically sealed foil pouches. The pouches are opened just prior to application to prevent premature curing from moisture present in the atmosphere. The properties of the unidirectional fibers as provided by the manufacturer are summarized in Table 1.

#### Wet Layup System

Fyfe's Tyfo (San Diego, CA) SEH-51A was the wet layup system used. It is a custom weave, unidirectional glass fabric that is usually used with Tyfo-S epoxy. However, for underwater application, Tyfo SW-1 underwater epoxy is used instead. The FRP fabric must be impregnated on site just prior to use. Properties of the materials as provided by the manufacturer are summarized in Table 2.

#### Specimen Details

A total of eight, 1.52 m (5 ft) long  $\times$  0.305 m (12 in.) wide square prestressed piles were used in the study. These were obtained by cutting two 6.1 m (20 ft) length piles donated by a local precaster. The piles were prestressed by eight 12.7 mm (0.5 in.) diam Grade 270 (1,861 MPa) strands. The average compressive strength was estimated to be 27.6 MPa (4,000 psi) using a Schmidt hammer.

The eight specimens were originally labeled A1 to A4 or F1 to F4 depending on whether the prepreg or the wet layup systems was used. However, because of changes made to incorporate pressure bagging, one of the originally designated wet layup specimens F4, was used with the prepreg system (relabelled A5). Thus, five prepreg specimens (A1–A5) and three wet layup specimens (F1–F3) were tested.

#### Underwater Setup

Wrapping was conducted inside a  $3.05 \times 1.83 \times 1.22$  m deep tank filled with fresh water to a depth of 0.914 m (3 ft) to simulate field repair conditions (Fig. 5). This ensured that exactly half the wrapped length (0.457 m) was under water and half above. To encourage marine type growth on the pile surface, specimens were left in standing water for 3 months prior to wrapping.

#### Surface Preparation

The corners of the piles were rounded to a 12.7 mm (1/2 in.) radius and all surface irregularities in the region to be wrapped were patched and filled with hydraulic cement. Water pressure was used to clean the pile surface. In the first test series, a 20.7 MPa (3 ksi) water pressure was used (vacuum bagging). A

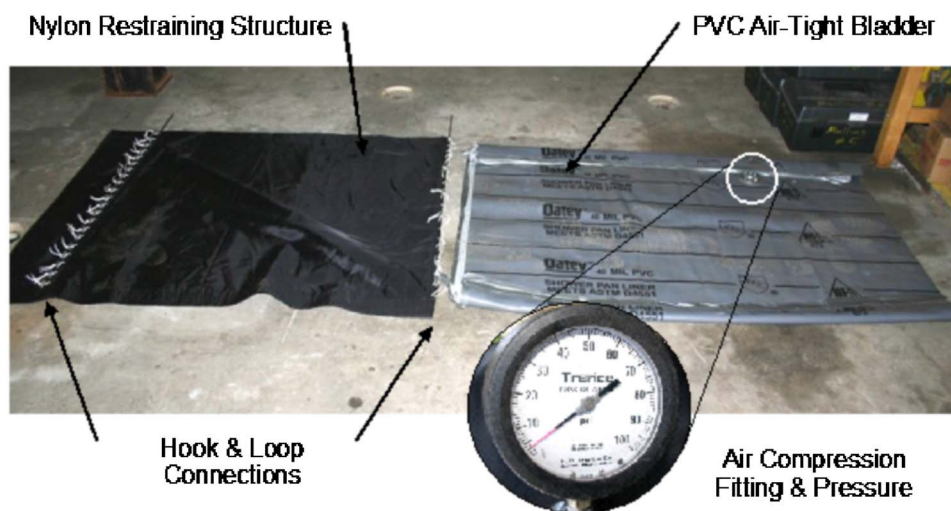


Fig. 4. Pressure bagging components



**Table 1.** Properties of Aquawrap Glass Fabrics (Azusa, Calif.)<sup>a</sup>

Fibers	Tensile strength (MPa)	Tensile modulus (GPa)	Load per ply (kN/m)
Type G-05 bidirectional fabric	6.8	22	5.7
Type G-06 unidirectional fabric	12.0	35	10.0

<sup>a</sup>Data derived from coupons prepared and tested in accordance with ASTM D3039.

higher pressure, 68.9 MPa (10 ksi) was used in the second series (pressure bagging) for which equipment had to be rented. This is the pressure recommended by the *ACI Guide for Underwater Repair* (ACI 546.2R-98) (ACI 1998). Fig. 6 shows pressure washing of the test piles at 68.9 MPa (10 ksi).

### Test Program

As mentioned earlier, four piles were originally designated for testing using vacuum bagging for each of the two FRP systems. In each set, there was one control, i.e., external pressure applied using a shrink wrap, and three other piles in which the pressure was kept at  $-14.5$  kPa ( $-2.1$  psi),  $-34.5$  kPa ( $-5$  psi), and  $-68.9$  kPa ( $-10$  psi). These pressures were selected because they could be readily provided by ordinary vacuum pumps.

Vacuum bagging posed problems not only because of the difficulty in maintaining an airtight seal along the perimeter of the wrap, but more importantly air could infiltrate through cracks in the concrete outside the wrapped region. For this reason, vacuum bagging was abandoned after initial tests and pressure bagging evaluated with the remaining specimens. In all, two piles, A3 and A4 (both prepreg) were tested under vacuum pressure of  $-68.9$  kPa ( $-10$  psi). Three others, F1, F2 (both wet layup), and A5 (prepreg originally labeled F4) were tested using pressure bagging. These were tested under three different pressures of 14.5 kPa (2.1 psi), 34.5 kPa (5 psi), and 68.9 kPa (10 psi). One specimen, A2 could not be tested because an experimental surface coating peeled off. Table 3 summarizes the revised test matrix.

The FRP wrapped region extending 0.457 m (18 in.) above and 0.457 m (18 in.) below the water line is shown in Fig. 7. As stated earlier, the pressure provided by the hand-applied stretch film (deemed as zero applied pressure) was taken as the control. The prepreg piles were tested using both the vacuum bag and pressure bag systems, while the wet layup piles were only tested with the pressure bag system.

### FRP Wrapping

The wrapping scheme used by both systems consisted of three glass layers—one unidirectional layer in the longitudinal direction and two unidirectional layers in the transverse direction. The

**Table 2.** Dry Fiber Properties of Tyfo (San Diego, CA) SEH-51A (Fyfe 2002)

Properties	Quantities
Tensile strength	3.24 GPa
Tensile modulus	72.4 GPa
Ultimate elongation	4.5%
Weight	915 g/m <sup>2</sup>

**Fig. 5.** View of partially submerged full-size test piles

prepreg system had an additional veil layer. This was consistent with layouts used in earlier demonstration studies.

The longitudinal layer consisted of four  $0.914 \times 0.305$  m wide individual pieces. The dimensions of the transverse pieces differed for the two systems: For the prepreg, it was a single  $0.203 \times 15.85$  m long piece, whereas for the wet layup, it consisted of two  $0.305 \times 1.27$  m pieces.

### Vacuum Bagging

In the prepreg system, a base resin coating is applied to the concrete surface prior to wrapping to improve the FRP-concrete bond. The opportunity was taken to evaluate two different resins: (1) Aquawrap Base Primer No. 4; and (2) Bio-Dur 563, a heavy-duty epoxy. These were each applied to two of the four pile surfaces.

Test piles A1 and A4 were wrapped on the first day with A1 as the control pile and A4 with vacuum pressure ( $-68.9$  kPa). Test pile A4 encountered problems with the sealing of the vacuum bag to the concrete surface above and below the FRP area. Extensive cracking above the FRP repair area allowed air to breach the vacuum bag, not allowing formation of an airtight seal. The air leaks were contained by filling in the cracks with epoxy, and a vacuum seal was obtained 45 min after the FRP was applied (Fig. 8).

Test piles A2 and A3 were repaired next with the base resin applied to the entire pile beyond the repair areas so as to seal the

**Fig. 6.** Pressure washing test piles with 68.9 MPa water pressure

**Table 3.** Test Matrix

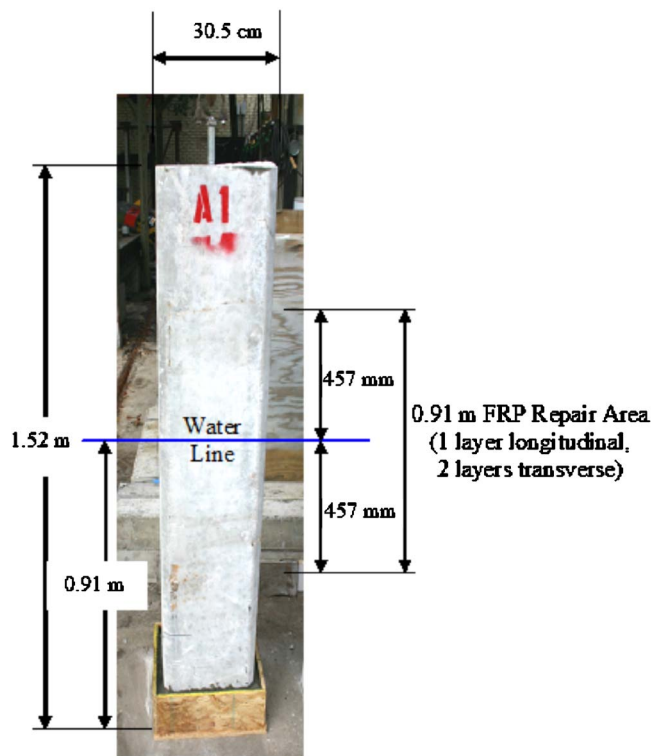
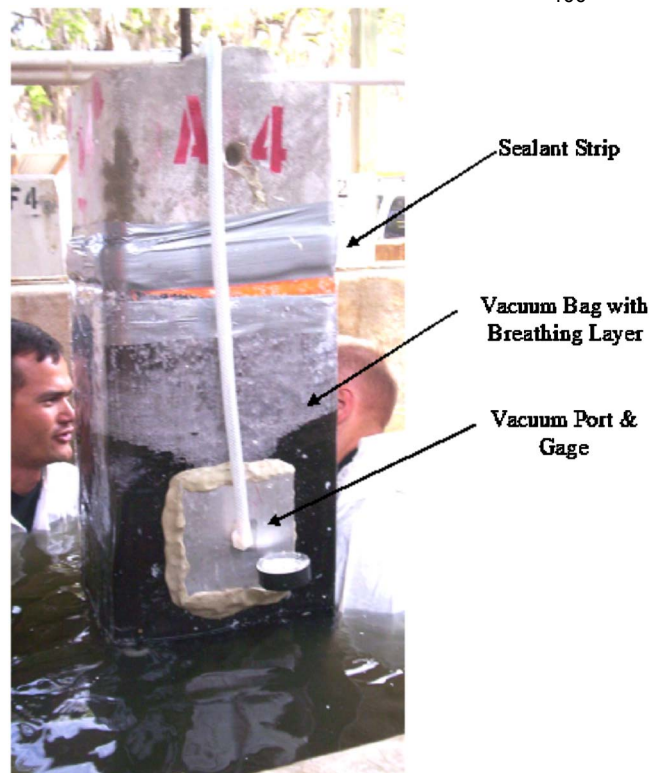
Test pile	Wrapping system	Confinement system	Applied pressure (kPa)
A1	Air Logistics	Control	0
A2 <sup>a</sup>	One longitudinal layer, four pieces—0.914 m × 0.305 m	(stretch wrap)	N/A
A3	Two transverse layers, one piece—0.203 m × 15.8 m	Vacuum bag	68.9
A4		Vacuum bag	68.9
A5		Pressure bag	68.9
F1	Tyfo SEH-51A	Pressure bag	34.5
F2	One longitudinal layer, four pieces—0.914 m × 0.305 m	Pressure bag	14.5
F3	Two transverse layers, two pieces—0.914 m × 1.27 m	Control (stretch wrap)	0

<sup>a</sup>Pile A2 was abandoned and not used for pressure bag tests.

cracked concrete surface. As before, two surfaces used Aquawrap Base Primer No. 4 resin and the other two used Bio-Dur 563 epoxy.

The FRP material was immediately installed on pile A3 following the application of the base resin. Again, the vacuum bag had difficulties sealing despite the coating of the uncured resin on the pile. Once an airtight seal was obtained, a  $-68.9$  kPa ( $-10$  psi) vacuum pressure was readily achieved.

The base resin applied to pile A2 was allowed to cure 24 h prior to the application of the FRP material. After 24 h, the resin precoat was inspected and it was found that no significant bond was achieved below the water line between the resin base layer and the concrete substrate. As a result, no FRP was subsequently applied to the pile.

**Fig. 7.** Test pile repair schematic**Fig. 8.** Vacuum bag applied to prepreg system

The researchers concluded that vacuum bagging was only effective for undamaged piles where an air-tight seal could be obtained. There was no similar need for air-tight seals if only an external pressure had to be maintained. As piles in need of repair were likely to be cracked, vacuum bagging was likely to be problematic in field repairs.

### Pressure Bagging

Unlike vacuum bagging where a vacuum pump was needed, pressure bagging only needed compressed air. However, a suitable pressure bag had to be designed and fabricated for the testing. Consideration had to be given to the material used for the bladder so that it could withstand tensile hoop stresses that developed from pressurization.

The two components of the pressure bag are the inner bladder and the restraining bag (Fig. 4). The inner bladder was constructed of PVC shower liner material and the restraining bag made out of nylon rip-stop material. The nylon rip-stop material was selected to withstand the tensile hoop stresses.

**Prepreg System.** The pressure bag was designed to resist the maximum 68.9 kPa (10 psi) pressure applied to the FRP repair area during curing. Pile A5 was repaired using the pressure bag system. Fig. 9 shows the inflated pressure bag around the test pile. No major difficulties were encountered. However, gas bubbles generated during the curing phase of the urethane resin were seen escaping from between the pile and bag below the water line.

**Wet Layup System.** The wet layup system was only tested using the pressure bag system on piles F1 and F2 with F3 serving as a control pile. The applied pressure was 34.5 kPa (5 psi) and 14.5 kPa (2.1 psi) on test piles F1 and F2, respectively.





Fig. 9. Pressure bag applied to prepreg system

Results

The FRP-concrete bond was evaluated both nondestructively via acoustic and thermal imaging tests and destructively from pullout tests. Only the results of the destructive testing are reported here. Results of the nondestructive testing may be found elsewhere (Mullins et al. 2007; Schrader 2007).

The bond between FRP and concrete was determined from pullout tests carried out in accordance with ASTM D 4541 (ASTM 2002) using an Elcometer 106 Adhesion Tester. The tester used 3.6 cm (1.456 in.) diam aluminum dollies. A 0.1×0.1 m grid was drawn on all four wrapped surfaces and destructive tests conducted at selected intersections in all the test specimens. A total of 151 pullout tests were conducted. Of these, 83 were conducted above the water line and 68 below the water line. Fewer tests were conducted below the original water line because regions where the bond was poor were not smooth (Schrader 2007).

A summary of relevant results is shown in Fig. 10. The “above water” and “below water” results are shown separately. These compare the average bond for both the prepreg and the wet layup systems.

Inspection of Fig. 10 shows that vacuum bagging (used only with the prepreg system) did not lead to any improvement in bond. Pressure bagging, on the other hand, led to significant improvement in bond both above (from 0.94 to 1.57 MPa) and below the water line (from 0.16 to 1.17 MPa). In contrast, the results for the wet layup system were mixed. It reduced marginally from 2.01 to 1.95 MPa above water but increased from 1.65 to 1.77 MPa below water.

FRP pile repair is part bond critical, part contact critical since the wrap must withstand expansive forces due to corrosion. For bond-critical applications, ACI 440 (ACI 2002) guidelines specify 1.38 MPa (200 psi) as a minimum pull-off strength if FRP is to be used. This limit was used as a filter to distinguish between satisfactory and unsatisfactory bond.

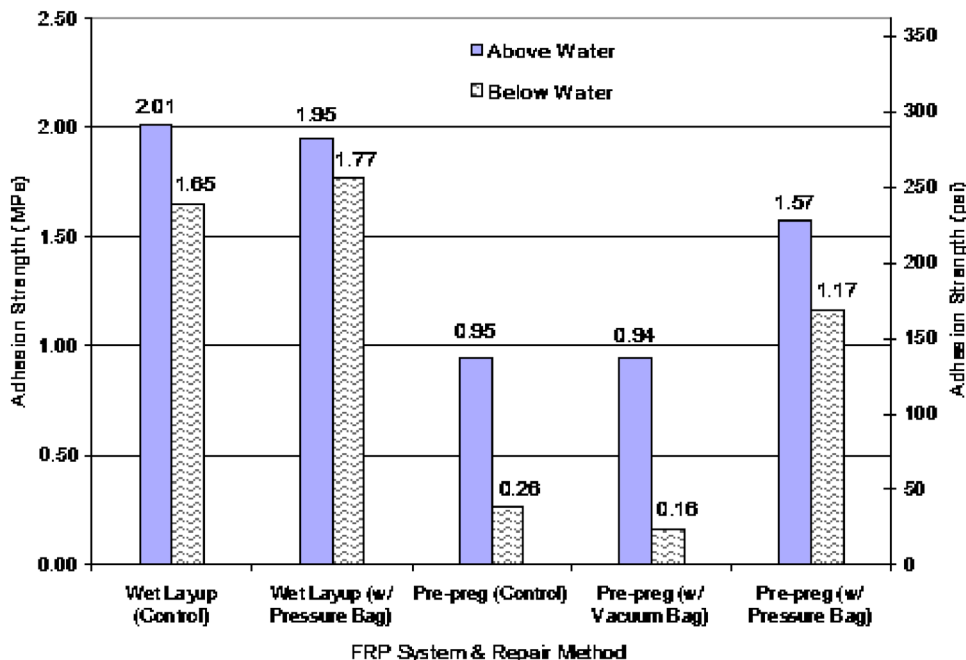


Fig. 10. Pullout test results for two systems

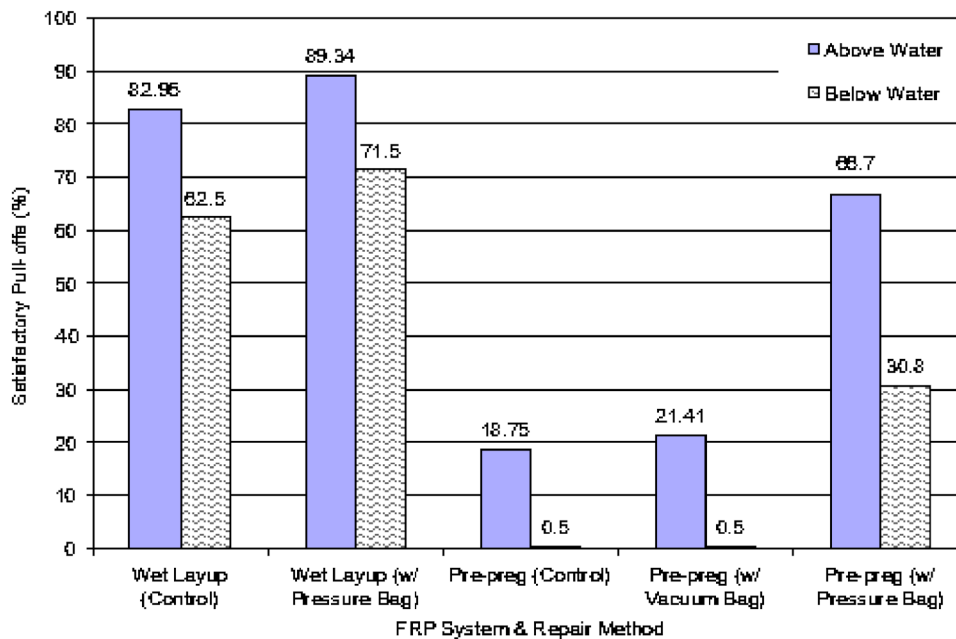


Fig. 11. Percentage of satisfactory pullout results using 1.38 MPa cut off

Fig. 11 plots the percentage of pullout results that exceeded the ACI 1.38 MPa threshold from all the tests. Inspection of this figure shows that pressure bagging benefited both the wet layup and the prepreg systems. In case of wet layup, the increase in satisfactory bond ranged from around 83 to 89% above water and from around 63 to over 72% below water. For the prepreg system, the corresponding increase was from 19 to about 67% (above water) and from 0.5 to over 30% below water. The percentage improvement was more noticeable for the prepreg system due to low initial baseline values (see Fig. 1).

## Field Study

A demonstration project was conducted to implement the pressure bag system developed. The site for the repair was the Tampa side of the Friendship Trails Bridge that is under the jurisdiction of Hillsborough County.

The Friendship Trails Bridge no longer carries vehicular traffic, but is now the world's longest over-the-water recreation trail. The 4.18 km (2.6 mile) bridge is supported on 254 piers and 22 columns numbered 1–276 extending east from St. Petersburg to Tampa. Seventy-seven percent of the 254 piers have needed to be repaired, indicating that the environment is very aggressive.

In a previous study (Mullins et al. 2006), Piers 99–101 on the Tampa side of the Friendship Trails Bridge were considered to be the most suitable because all the piles were in a similar state of disrepair. For this reason, two remaining unwrapped reinforced concrete piles in Pier 101 were selected for the field demonstration in this study. The 0.508 × 0.508 m (20 × 20 in.) piles were reinforced by eight No. 8 (25.4 mm diam) bars.

Details of the two piles selected are summarized in Table 4. The table also includes information on the two instrumented controls in pier 99 from the previous study. The relative positions of the test piles in the pier are shown in Fig. 12. Instrumentation consisting of rebar probes developed by the Florida Department of Transportation was the same as used in the earlier study. As before, they were installed at two different depths along a pile to

allow measurement of the corrosion current between the probes after the system had stabilized.

## Pressure Bag

The prototype built for the laboratory testing was scaled up to match the dimensions of the larger field piles. However, some changes were made to the original design, namely (1) a cinch strap was introduced to tie the bag at the top to prevent upward movement (due to buoyancy effects) after the bladder had been inflated; (2) the toggle connections of the two ends (Fig. 4) were replaced by snap-on hooks. In addition, a burlap breather layer was added to the prepreg system to allow gases generated during curing to exit. It was believed bond had been adversely affected for the prepreg system by the outward pressures exerted by escaping gases that formed during curing.

## Surface Preparation

Previous procedures were followed except for a change in the water pressure used for the final cleaning. A scraper was used to remove all marine growth from the region to be wrapped. Projecting parts of the concrete surface were chipped using a hammer

Table 4. Test Pile Details

Pier no.	Repair system	Specimen type	Pile name	Instrumentation
Pier 99	N/A	Control	99-N	Yes
	N/A	Control	99-S	Yes
Pier 101	Prepreg	Glass 1+1 layers <sup>a</sup>	101-I.N.	Yes
	Wet layup	Glass 1+1 layers <sup>a</sup>	101-I.S.	Yes

<sup>a</sup>Signifies number of layers in the longitudinal and transverse direction, respectively.



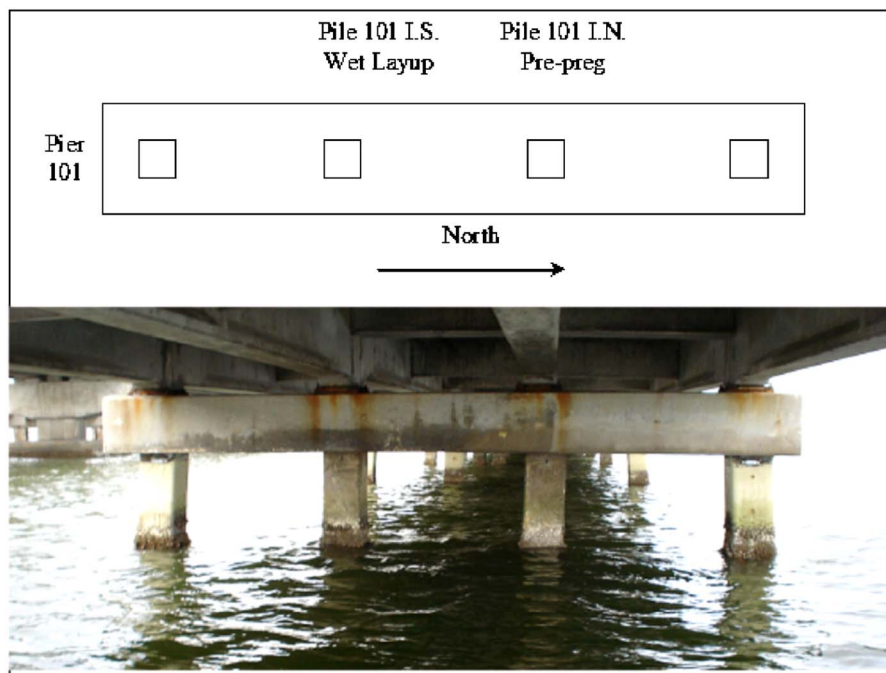


Fig. 12. Pier 101 layout



(a)



(b)



(c)



(d)

Fig. 13. (a) Scraping large deposits off the surface of the piles; (b) grinding the surface and corners; (c) pressure washing with 68.9 MPa water pressure; and (d) pressure washing with 20.7 MPa water pressure

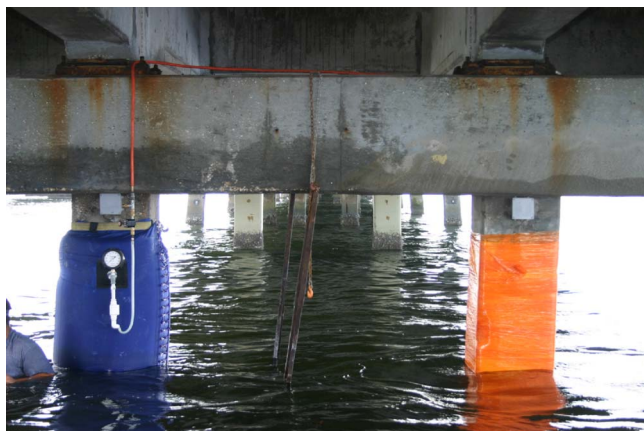


**Fig. 14.** Pressure bag applied to the wet layup pile at 14.5 kPa

and chisel. All four corners were chamfered and were ground to a 19 mm (3/4 in.) radius using a grinder. Finally, all surfaces were ground and pressure washed using fresh water to remove all dust, debris, and remaining marine growth just prior to wrapping.

Fig. 13 shows the test piles prior to FRP application. Pressure washing was attempted with the same 68.9 MPa (10 ksi) unit used in the laboratory study. However, because of the large water supply demand and lack of ready availability of fresh-water at the site, the 20.7 MPa (3 ksi) pressure washer was used instead.

### Wrapping

#### Prepreg

The prepreg system was used to wrap the interior north pile in Pier 101. It was wrapped using one unidirectional glass fiber layer in both the longitudinal and transverse directions. Wrapping commenced from the pile top 0.3048 m (12 in.) below the underside of the pile cap to accommodate the presence of the junction box used for corrosion measurements. The procedure for applying the glass fiber used earlier was followed (Mullins et al. 2006). However, a new device (resembling a miniature bed of nails) was used to puncture the entire surface of the stretch wrap with tiny holes to allow curing gases to escape.

A burlap breathing layer was now placed over the punctured stretch wrap. This ensured that gases generated during curing of the urethane resin could escape without compromising bond. Next, the pressure bag was carefully positioned so that the two ends were joined over the middle of the pile. The cinch straps were tightened at the top and bottom to prevent the bag from moving upwards once the bladder inside the bag had been inflated. A constant pressure of 14.5 kPa (2.1 psi) was applied to the wrap during curing for a period of 3 h (initial set). The pressure bag was then removed. The wrap was subsequently allowed to cure for one week. After removing the plastic stretch film, the pile was painted with the same base primer for UV protection.

#### Wet Layup System

The interior south pile in Pier 101 was wrapped using the wet layup system. The fibers were impregnated with resin on site by hand using a roller to distribute the epoxy evenly over the fabric. The usual procedure for wrapping was followed (Mullins et al.



**Fig. 15.** Piles after FRP repair with UV coating

2006). Since no gases are given off during curing, the burlap breathing layer was not required. The pressure bag was directly placed over the plastic stretch film that covered the entire wrapped region. As before, the ends of the pressure bag were positioned over the middle face of the pile and cinch straps at the top and bottom tightened to prevent the bag from moving when it was inflated. A constant pressure of 14.5 kPa (2.1 psi) was applied to the wrap during curing for a period of 16 h. This was significantly longer than the time used for the prepreg system because the initial set time was longer. Fig. 14 shows the pressure bag applied to the wet layup pile. Fig. 15 shows the FRP repaired piles with the UV protection applied.

### Discussion

This study described the adaptation of techniques widely used by the composite industry to improve FRP-concrete bond. Both vacuum bagging and pressure bagging were successfully implemented.

The advantage of the vacuum bag system is that there are no strength requirements, since pressure is applied by evacuating air. However, it requires air tight seals around the perimeter that may be difficult to achieve, especially if the pile is cracked. The pressure bag system does not require air tight seals, but the material of the air bladder must be strong enough to withstand tensile hoop stresses that develop.

In the study, vacuum bagging was only tested for the prepreg system where it was found to be ineffective, possibly because of the short setting time of the urethane resin. The time taken to resolve leaks in the seal coupled with gases generated during curing may have been responsible for this unanticipated result. However, as the chemistry for epoxy resin is different, it would be unwise to extrapolate the findings for the urethane resin. Unfortunately, tight deadlines did not permit further investigation.

Destructive pullout tests showed that pressure bagging led to improved bond. This is most probably because uniform pressure ensured the FRP was in continuous contact with the concrete surface as it cured. This automatically enhanced the chemical adhesion between concrete surface and FRP. Additionally, bond was enhanced by forcing resin into the concrete pore structure.



Pressure also made the FRP denser by squeezing out excess resin, thereby improving the mechanical and corrosion resistant properties of the system.

## Conclusions

This study was undertaken to improve the integrity of the FRP-concrete bonding that was achievable under water. Previous tests had found this to be variable (Fig. 1). It was believed that if constant pressure were maintained as the resin cured, bond would be improved because of increased frictional resistance.

Two disparate approaches were tested in the laboratory—vacuum bagging and pressure bagging. Both systems were made to work. However, inherent sealing problems associated with vacuum bagging made it a less attractive solution, particularly for repairs of damaged piles. Pressure bagging had no similar requirement and was found to be more effective, particularly for the wet layup system.

The pressure bagging system developed was implemented without incident in the repair of two piles on pier 101 of the Friendship Trails Bridge. Visual and tactile inspection indicated that the FRP-concrete bond obtained was better than in earlier projects.

The study is indicative of the relative ease with which technologies developed by the composites industry can be used in infrastructure applications. While the application focused on pile repair, the systems developed are versatile and can also be used for repairs of columns and bents under dry conditions.

## Acknowledgments

This study was supported by Hillsborough County Public Works Department. The assistance and guidance of Mr. Nils Olsson, P.E. from Hillsborough County is gratefully acknowledged. The writers are indebted to Mr. Ed Fyfe, Fyfe & Co, LLC and Mr. Franz Worth, Air Logistics, for providing materials used in the testing. The writers also thank FDOT for their contribution.

## References

- AASHTO. (1999). "Guide specifications for design and construction of segmental concrete bridges." *Section 28.3.2*, Washington, D.C.
- ACI. (1998). "Guide to underwater repair of concrete." *ACI 546.2R-98*, ACI, Farmington Hills, Mich.
- ACI. (2002). "Guide for the design and construction of externally bonded FRP systems for strengthening concrete structures." *ACI 440.2R-02*, ACI, Farmington Hills, Mich.
- Air Logistics Corporation. (2002). Aquawrap Repair System, Pasadena, Calif.
- ASTM. (2002). "Test method for pull off strength of coatings using portable adhesive tester." *ASTM D4541*.
- Baiyasi, M., and Harichandran, R. (2001). "Corrosion and wrap strains in concrete bridge columns repaired with FRP wraps." *Proc., 80th Annual Meeting*, Transportation Research Board, Washington, D.C., Paper No. 01-2609.
- Bazinet, S., Cereone, L., and Worth, F. (2003). "Composite FRP moves into underwater application." *SAMPE J.*, 39(3), 8–16.
- Berver, E., Jirsa, J., Fowler, D., Wheat, H., and Moon, T. (2001). "Effects of wrapping chloride contaminated concrete with fiber reinforced plastics." *FHWA/TX-03/1774-2*, Univ. of Texas, Austin, Tex.
- Bonacci, J. (2000). "Rehabilitation of corrosion-damaged RC infrastructure using externally bonded FRP." *Proc., ACMBMS 2000*, CSCE, Montreal, 561–568.
- Debaiky, A., Green, M., and Hope, B. (2002). "Carbon fiber-reinforced polymer wraps for corrosion control and rehabilitation of reinforced concrete columns." *ACI Mater. J.*, 99(2), 129–137.
- Fyfe Co. LLC. (2002). "Tyfo® SEH-51A composite using Tyfo® S epoxy." (<http://www.fyfeco.com/products/compositesystems/pdf/seh-51a.pdf>) (August 24, 2007).
- Mullins, G., Sen, R., Suh, K., and Winters, D. (2005). "Underwater FRP repair of prestressed piles in the Allen Creek Bridge." *J. Compos. Constr.*, 9(2), 136–146.
- Mullins, G., Sen, R., Suh, K., and Winters, D. (2006). "A demonstration of underwater FRP repair." *Concr. Int.*, 28(1), 1–4.
- Mullins, G., Sen, R., Winters, D., and Schrader, A. (2007). "Innovative pile repair." *Final Rep. submitted to Hillsborough County*, Fla.
- Nazier, M., Giancaspro, J., and Balaguru, P. (2005). "Composite jackets for rehabilitation of damaged reinforced concrete pier caps." *Proc., SAMPE '05*, Vol. 50, Long Beach, Calif., 1011–1024.
- Schrader, A. (2007). "Methods to improve bond on FRP wrapped piles." M.S. thesis, Dept. of Civil and Environmental Engineering, Univ. of South Florida, Tampa, Fla.
- Sen, R., and Mullins, G. (2007). "Application of FRP for underwater pile repair." *Composites, Part B*, 38(5–6), 751–758.
- Sheikh, S., Pantazoupoulou, S., Bonacci, J., Thomas, M., and Hearn, N. (1997). "Repair of delaminated circular pier columns with advanced composite materials." *Ontario Joint Transportation Research Rep. No. 31902*, Ministry of Transportation of Ontario, Canada.
- Stallings, J., Tedesco, J., El-Mihilmy, M., and McCauley, M. (2000). "Field performance of FRP bridge repairs." *J. Bridge Eng.*, 5(2), 107–113.
- Suh, K. S., Mullins, G., Sen, R., and Winters, D. (2005). "Use of FRP for corrosion strengthening applications in a marine environment." *Final Rep. submitted to Florida/U.S. Dept. of Transportation*, Tallahassee, Fla.
- Suh, K. S., Mullins, G., Sen, R., and Winters, D. (2007). "Effectiveness of FRP in reducing corrosion in a marine environment." *ACI Struct. J.*, 104(1), 76–83.
- Watson, R. J. (2003). "The use of composites in the rehabilitation of civil engineering structures." *ACI SP-215*, S. Rizkalla and A. Nanni, eds., Farmington Hills, Mich., 291–302.
- Wheat, H. G. (2002). "Using polymers to minimize corrosion of steel in concrete." *Cem. Concr. Compos.*, 24, 119–126.
- Wootton, I., Spainhour, L., and Yazdani, N. (2003). "Corrosion of steel reinforcement in CFRP wrapped concrete cylinders." *J. Compos. Constr.*, 7(4), 339–347.

## Discussion of “Predicting End Bearing Capacity of Post-Grouted Drilled Shaft in Cohesionless Soils” by Gray Mullins, Danny Winters, and Steven Dapp

April 2006, Vol. 132, No. 4, pp. 478–487.

DOI: 10.1061/(ASCE)1090-0241(2006)132:4(478)

Miguel Ruiz<sup>1</sup> and Miguel Pando, M.ASCE<sup>2</sup>

<sup>1</sup>Assistant Professor, National University of Cordoba, C.C. 916, X5000ZAA, Cordoba, Argentina. E-mail: mruiz@efn.uncor.edu

<sup>2</sup>Associate Professor, Dept. Civil Engineering, Univ. of Puerto Rico, PO Box 9041, Mayaguez 00681, Puerto Rico. E-mail: mpando@uprm.edu

The authors have presented a very interesting paper on post-grouted drilled shafts (PGDS), a deep foundation system that is relatively new to North American geotechnical practice. A clear strength of the paper is the documentation of full-scale field test data for five test sites, particularly given the scarcity of these types of data on deep foundation systems. In the opinion of the discussers, however, the paper does not provide important information regarding procedures and data reduction of the field tests conducted. This lacking information is important so that readers can have a complete story. However, the discussers believe this paper is a very useful contribution toward establishing a reliable design rationale and methodology for PGDS in different types of soils.

Review of the references cited in the paper shows that the case histories involved load tests carried out using the Statnamic device, which typically involves test durations of less than a second. This is important information that should be mentioned explicitly in the paper. Although Statnamic testing has been used for quite some time and its usefulness is not questioned, it is important that this aspect be mentioned in the paper and any associated assumptions involved in the field data reduction should be stated and discussed. Furthermore, some important details on the full-scale load tests were not found in the references cited for each case history, and it would be helpful to the geotechnical community's understanding of the use of postgrouted drill shafts if some additional information is provided by the authors.

This is particularly important in North America, where this deep foundation system is relatively new. Specifically, the following design issues should be specified for each case history presented: (1) whether grout pressure was locked in or not; (2) how end bearing load versus tip displacement was measured or back-calculated during each Statnamic test; and (3) whether the end bearing versus tip displacement results presented were corrected for possible damping and load rate effects that can be associated to the Statnamic testing procedure.

In closing, the authors have provided a very valuable paper that illustrates the promise of this new deep foundation system and improves our knowledge of the design issues involved with postgrouted drilled shafts. As our knowledge and understanding of some of the pending technical and design issues related to the use of postgrouted drilled shafts increase, we will likely find that

this foundation system becomes more mainstream in North America.

## Closure to “Predicting End Bearing Capacity of Post-Grouted Drilled Shaft in Cohesionless Soils” by Gray Mullins, Danny Winters, and Steven Dapp

April 2006, Vol. 132, No. 4, pp. 478–487.

DOI: 10.1061/(ASCE)1090-0241(2006)132:4(478)

Gray Mullins<sup>1</sup>; Danny Winters<sup>2</sup>; and Steven Dapp<sup>3</sup>

<sup>1</sup>Associate Professor, Dept. of Civil and Environmental Engineering, Univ. of South Florida, 4202 E. Fowler Ave., ENB 118, Tampa, FL 33620 (corresponding author). E-mail: gmullins@eng.usf.edu

<sup>2</sup>Research Associate, Dept. of Civil and Environmental Engineering, Univ. of South Florida, 4202 E. Fowler Ave., ENB 118, Tampa, FL 33620. E-mail: dwinters@eng.usf.edu

<sup>3</sup>Principal, Dan Brown & Associates, 300 Woodland Rd., Sequatchie, TN 37374. E-mail: sdapp@danbrownandassociates.com

The authors appreciate the discussers' interest in this topic and the time taken to submit a discussion. Therein, the use of rapid load testing and the various analysis methods were of interest to the discussers, along with the pressure state of grout while it cured. Although some of these points can be gleaned from the paper, procedures and “how-to” knowledge could not be adequately addressed without detracting from the intended design emphasis.

Rapid load tests were used on all shafts in the original studies whereby both inertia and damping corrections were applied, which became standard ca. 1995 (Middendorp 1995). This included both the grouted and ungrouted shafts. Methods for establishing the shear stress and displacement distribution throughout the shaft are commonly applied using the *segmental unloading point method* (Lewis 1999; Mullins et al. 2002). Thereby, toe displacements are computed from the measured strain distribution and the top of shaft movement for each measured time interval. In most of the test shafts used in the presented study, toe accelerometers were also used to corroborate the computed values.

No appreciable effect on load-carrying capacity has been noted by using either a “locked-in” or “unlocked” grout pressure state in shafts tipped in cohesionless soils. In brittle bearing strata, however, that may not be the case. Locking in the applied grout pressure forces the side shear to react with a downward force to balance the upward grout pressure. Upon subsequent structural loading, all loads are transferred directly to the tip until sufficient displacement is experienced to reverse the side shear force direction. If the end bearing strata cannot tolerate additional load or brittle fracture occurs beneath the tip, all load will be quickly transferred to the side shear whereby it will be forced to solely support the structural load. Under these conditions, relying on additional strain tolerance could be catastrophic and may cause the two capacity components (side shear and end bearing) to act

independently instead of in concert. For the case studies cited, five shafts were locked in and three unlocked.

## References

- Lewis, C. L. (1999). "Analysis of axial Statnamic testing by the segmental unloading point method." Master's thesis, Univ. of South Florida, Tampa, Fla.
- Middendorp, P., and Bielefeld, M. W. (1995). "Statnamic load testing and the influence of stress wave phenomena." *Proc., 1st Int. Statnamic Seminar*, Vancouver, Canada, 207–220.
- Mullins, G., Lewis, C., and Justason, M. (2002). "Advancements in Statnamic Data Regression Techniques." *Deep foundations 2002: An int. perspective on theory, design, construction, and performance*, M. W. O'Neill and F. C. Toursend, eds., ASCE, Reston, Va., 915–930.

## Concrete Temperature Reduction via Voided Drilled Shafts

K. Johnson<sup>1</sup>, G. Mullins, M ASCE<sup>2</sup> and D. Winters, M ASCE<sup>3</sup>

<sup>1</sup> Doctoral Candidate, Department of Civil and Environmental Engineering, University of South Florida, 4202 E. Fowler Ave, ENB 118, Tampa, FL 33620, PH (813) 974-2110, email [kmjohns6@eng.usf.edu](mailto:kmjohns6@eng.usf.edu)

<sup>2</sup> Associate Professor, Department of Civil and Environmental Engineering, University of South Florida, 4202 E. Fowler Ave, ENB 118, Tampa, FL 33620, PH (813) 974-5845, email [gmullins@eng.usf.edu](mailto:gmullins@eng.usf.edu)

<sup>3</sup> Research Associate, Department of Civil and Environmental Engineering, University of South Florida, 4202 E. Fowler Ave, ENB 118, Tampa, FL 33620, PH (813) 974-5830, email [d winters@eng.usf.edu](mailto:d winters@eng.usf.edu)

### ABSTRACT

As the concrete in drilled shafts cures, extremely high internal temperatures can be generated (even when relatively small in diameter) giving rise to mass concrete conditions. When the concrete temperature exceeds safe limits, the concrete may not cure correctly and can ultimately degrade via delayed ettringite formation. Minimizing the peak temperature (and the associated defects) can be undertaken by casting the shafts without concrete in the core thereby removing a large amount of the energy producing material in a region that is least likely to benefit the structural capacity and that is less able to dissipate the associated core temperatures due to the presence of the more peripheral concrete. This paper presents the field temperature results of shafts cast under normal conditions and the surprisingly alarming findings. A numerical model was subsequently calibrated and used to show the tremendous potential for voiding shafts. Finally, construction issues that are likely to be encountered are summarized with possible solutions.

### INTRODUCTION

Drilled shafts are large-diameter cast-in-place concrete structures that can develop enormous axial and lateral capacity and consequently, are the foundation of choice for many large bridges subject to extreme event loads such as vessel collisions. In some cases these foundation elements have been constructed without considering mass concrete effects and the possible long-term implications of the concrete integrity. Such considerations address the extremely high internal temperatures that can be

generated during the concrete hydration/curing phase. This can be detrimental to the shaft durability and/or integrity in two ways: (1) short-term differential temperature-induced stresses that crack the concrete and (2) long-term degradation via prolonged excessively high temperatures while curing.

Mass concrete is generally considered to be any concrete element that develops differential temperatures between the innermost core and the outer surface that in turn can develop tension cracks. Some state DOTs have defined geometric guidelines that identify potential mass concrete conditions as well as limits on the differential temperature experienced. For instance, the Florida DOT designated any concrete element with minimum dimension exceeding 0.91m (3 ft) and a volume to surface area ratio greater than  $0.3\text{m}^3/\text{m}^2$  will require precautionary measures to control temperature-induced cracking (FDOT, 2006). The same specifications set the maximum differential temperature to be 20C (35F) to control the potential for cracking. For drilled shafts, however, any element with diameter greater than 1.83m (6 ft) is considered a mass concrete element despite the relatively high volume to area ratio.

The latter of the two integrity issues, *i.e.*, excess high temperature, is presently under investigation at a number of institutions. When concrete temperature exceeds safe limits on the order of 65C (150F), the concrete may not cure correctly and can ultimately degrade via latent expansive reactions termed delayed ettringite formation (DEF). This reaction may lay dormant for several years before occurring; or the expansion may not occur as it depends on numerous variables involving the concrete constituent properties and environment. Concrete mixes with low pozzolans have lower threshold temperatures whereas higher pozzolan content concretes may not exhibit adverse effects up to 85C (185F). At present, a definitive upper temperature limit is not available (Whitfield, 2006). What is known is that staying below 65C appears to prevent temperature-related long-term detrimental effects.

## CASE STUDIES

Numerous case studies have documented the effects of hydrating cement in mass concrete structures. The most famous of which is perhaps the Hoover Dam project constructed during the depression from 1932 to 1935 where over 4 million cubic meters of concrete were used. At that time it was understood that staged construction and a cooling system would be required to help control elevated temperatures. The primary concern was concrete cracking from differential temperature. Without these considerations, temperature dissipation was estimated to take over 100 years and temperature-induced cracking would have severely compromised its structural integrity and its ability to prevent fluid ingress (DOI, 2004). Preventing microcracking and fluid ingress are important to warding off DEF (Collepari, 2003) and sulfate attack generally (Stark and Bollman, 1998).

**Ringling Causeway Bridge.** A relatively recent structure which started to shed light on drilled shafts as mass concrete was the Ringling Causeway Bridge spanning across Sarasota Bay, Florida. This segmental, post-tensioned concrete box girder bridge is supported by single column piers founded on two 2.75m (9 ft) diameter drilled shafts. The concrete mix was a type I/II with 20% cement replacement with fly ash (probably



class F). In spite of relatively cool weather (for Florida) and that it was bathed in cool bay water, the core temperature of the shafts reached 69C (157F). Figure 1 shows temperature traces over a 9 day period for the shaft center and edge as well as in the surrounding water and air. The bay water temperature averaged 17C (63F) while the air temperature dipped as low as 3C (37F). A maximum differential temperature of 37C (67F) was recorded shortly after the coldest spell.

These results were used to calibrate a 3-D numerical model whereby other size shafts could be evaluated under similar pour conditions with a similar concrete mix (same energy production per cubic volume of cement). The finite difference model incorporated a temperature time series as a boundary condition, and specified initial conditions for concrete, water (or soil) and atmosphere. A water diffusion rind of 0.37m (1.2ft) was placed between the concrete shaft and the imposed boundary.

Figures 2 and 3 show the peak and differential temperatures, respectively, for four modeled shaft diameters; the 2.75m shaft closely matched that observed (model calibration). Under these relatively cool conditions, the differential temperature predictions show shafts as small as 1m can exceed the recommended limit; the generated peak temperatures in general did not.

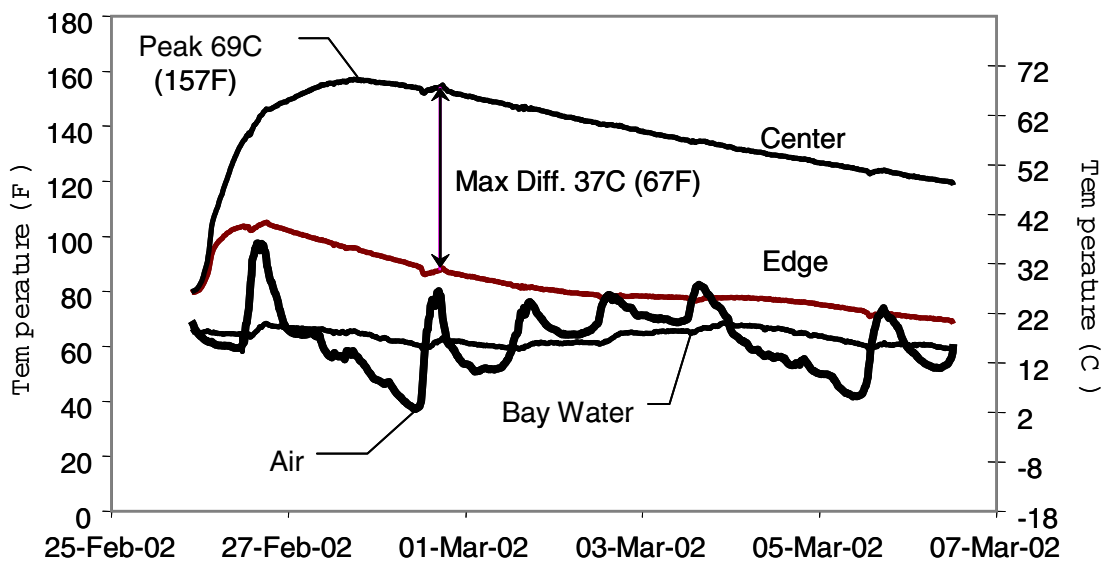


Figure 1. Temperature traces from the Ringling Causeway Bridge.

**Clearwater Test Site.** The large diameter shafts used in the Ringling project were predicted to behave as mass concrete. However, more commonly used shaft sizes like 1.22m shafts have been installed without concern for years. A recent study in Clearwater, Florida was conducted whereby a 7.6m deep, 1.22m diameter shaft was cast in saturated sandy to silty sandy soil complete with thermocouple and strain gage instrumentation. The full scope of the study involved anomaly detection, shaft integrity test method evaluations, and temperature development in a commonly used shaft size. Only the peak and differential temperature results are presented herein. Full details of the entire study will be available upon completion of the project (FDOT).

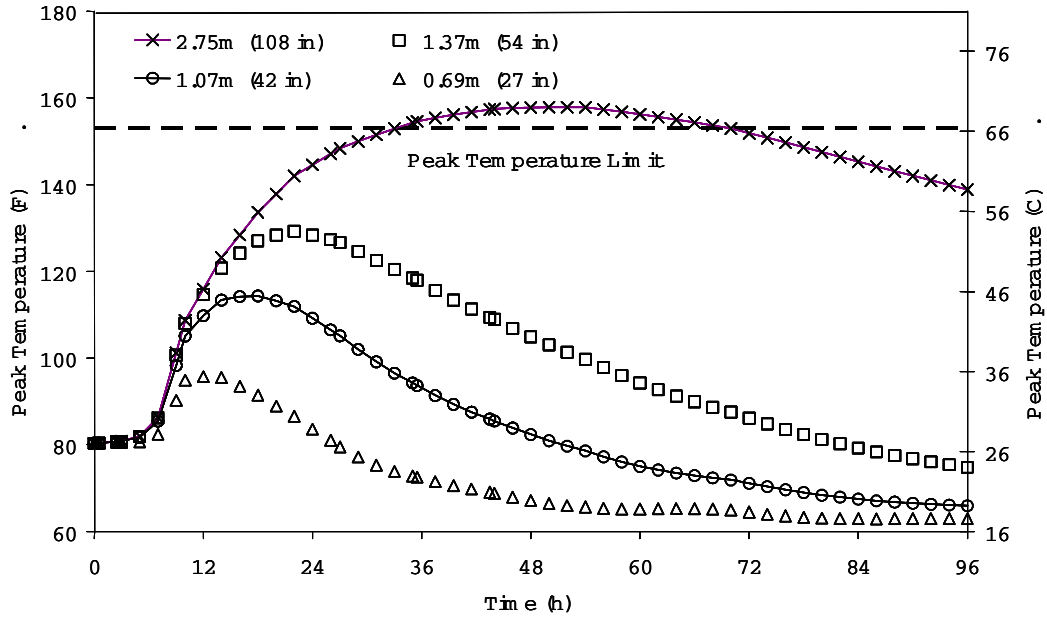


Figure 2. Modeled peak temperature traces for various shaft sizes, based on “Ringling” shaft mix design and conditions.

Using the measured temperature response, the same numerical model was applied to this site’s conditions which were significantly different from the Ringling site. Specifically, the ambient temperature was much higher, the surrounding heat diffusing materials were non-convective with no flowing water, and the mix design contained little to no pozzolans. Figure 4 shows the measured and modeled results superimposed with no recognizable differences aside from the diurnal temperature fluctuations on one thermocouple channel. A peak temperature of 84C (183F) was observed with a maximum differential temperature of 32C (57F).

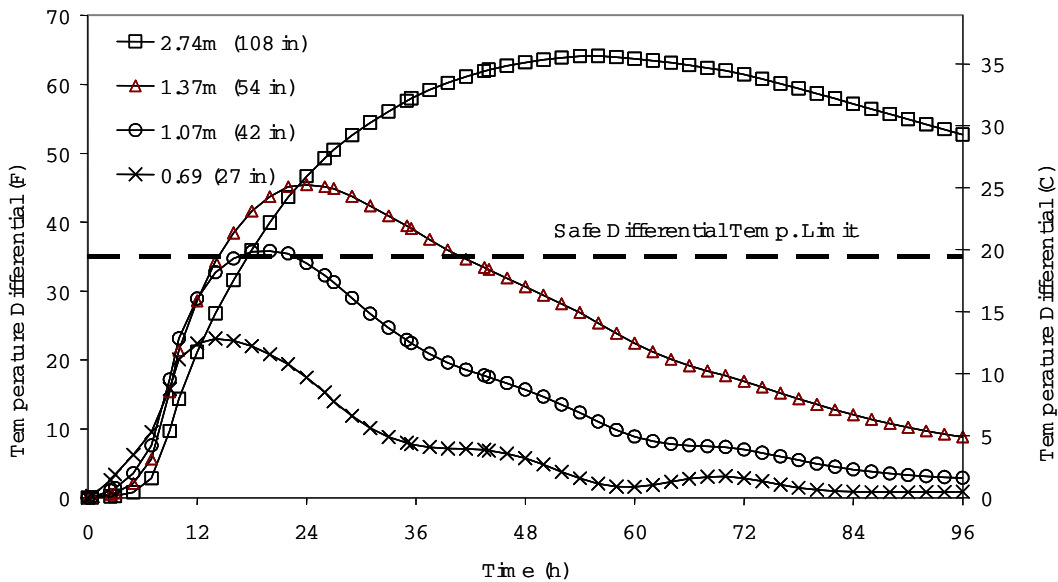


Figure 3. Modeled differential temperatures for “Ringling” shaft mix.

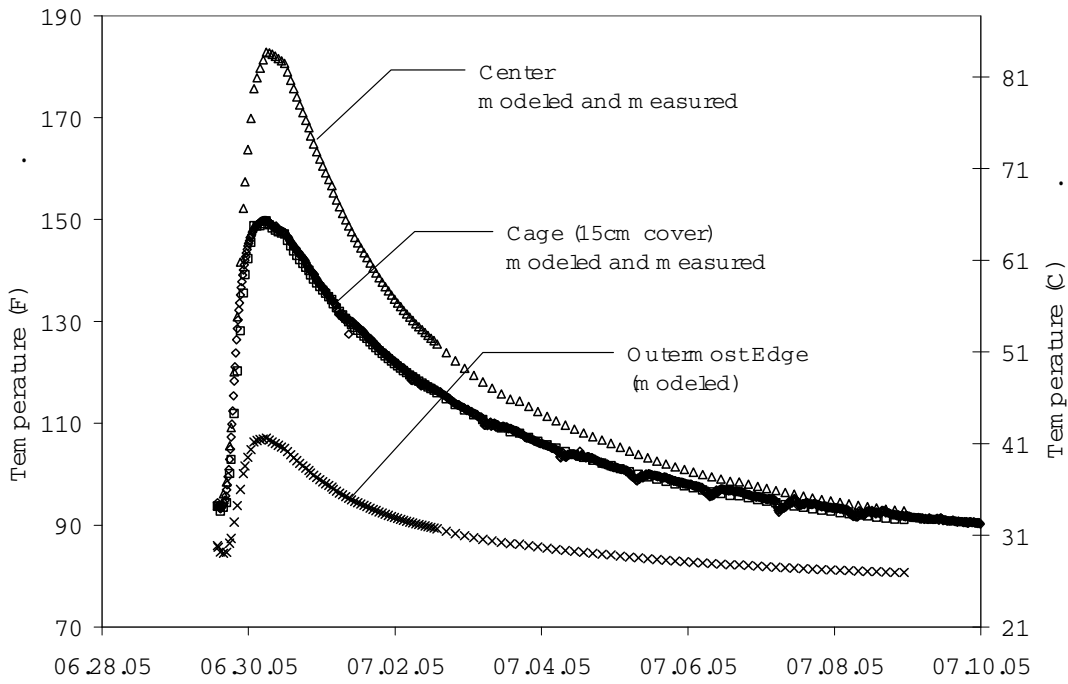


Figure 4. Temperature traces for the 1.22m Clearwater shaft (modeled and observed).

Using the same Clearwater conditions, the numerical model was extended to simulated smaller shaft sizes (Figure 5). The results showed that even the smallest of constructible shafts (0.6m) would exhibit mass concrete under these highly adverse conditions.

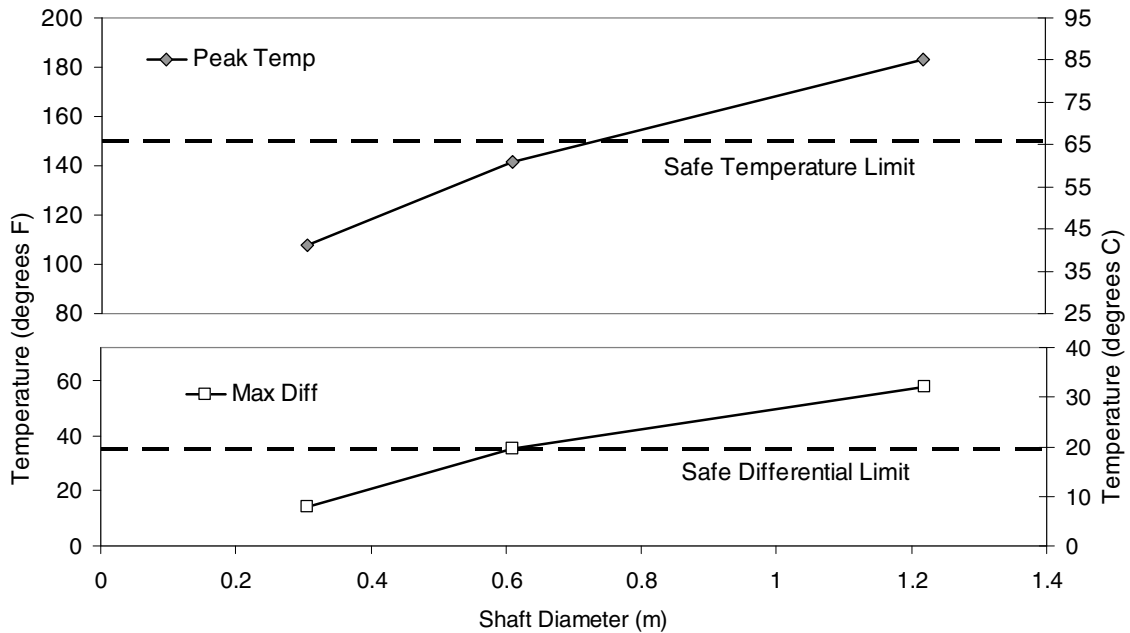


Figure 5. Modeled temperature generation versus shaft diameter.

Minimizing the peak and differential temperature (and the associated defects) can be undertaken by casting shafts with a full length centroidal void. This removes a large amount of the energy producing material in a region that is least likely to benefit the structural capacity and that is less able to dissipate the associated core temperatures due to the presence of the more peripheral concrete. An overview of this concept forms the basis of this article.

## VOIDED SHAFTS

Large prestressed piles (0.6 – 0.9m) are often cast with a cylindrical void aligned with the longitudinal axis of the pile to minimize construction weight while also reducing concrete cost. Larger diameter post-tensioned cylinder piles (0.9 – 1.8m) develop enormous axial and bending capacity with only a 15 to 20cm thick annular ring of concrete (concrete pipe pile). An even larger version is plausible in the form of a voided drilled shaft. Aside from obvious constructability issues, benefits include reducing concrete volume and pouring time which in turn would relax concrete supplier issues as well as reducing hydration heat generation.

**Construction Considerations.** Construction of drilled shafts, simply stated, involves excavating a hole deep in the ground with rotary type augers (hence the name drilled), inserting reinforcing steel into the excavation in the form of a cylindrical cage, and filling the hole with wet/liquid concrete which occupies the space from which the soil was excavated. To construct a shaft with a central void would involve normal excavation of the shaft's outer diameter followed by the insertion of a centralized steel casing (or similar) that can adequately maintain its position during the concreting of the annular volume. This may require that additional excavation of the smaller diameter to allow the inner casing to adequately seal below the bottom of the outer shaft diameter (Figure 6).

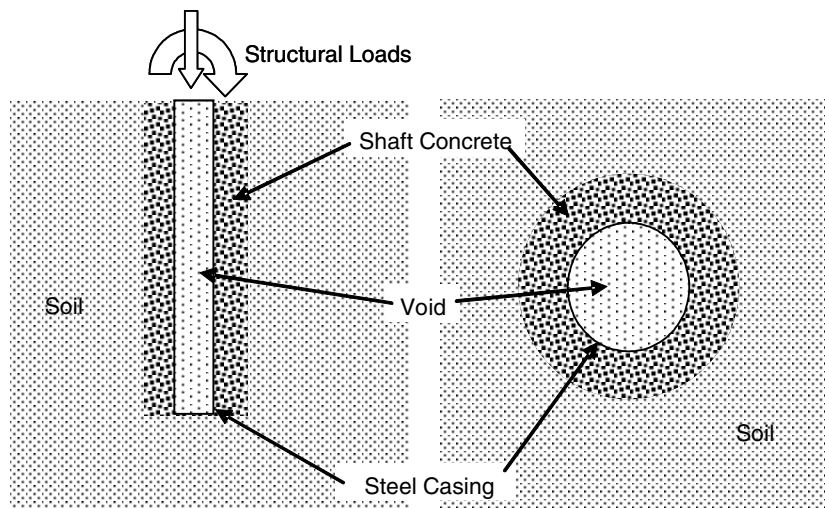


Figure 6. Conceptual schematic of a voided drilled shaft, in profile view (left) and plan view (right).

Concrete placement can be carried out with any method (full length pump truck hose or tremie) provided it can be easily moved during concreting to unify the concrete flow levels around the inner casing. Use of new high performance shaft concrete would certainly be advantageous.

Inner casing installation, alignment, and overcoming potential buoyancy forces are perhaps the most significant obstacles to constructing voided shafts. The physics of buoyancy forces only provide a problem if the concrete can form a pressure face beneath the casing causing an upward force (Figure 7). Lateral concrete pressure will not induce buoyancy but rather will require sufficient casing stiffness such that it will not collapse. As there is little surface area on which upward pressure could act (open ended casing), the real issue is assuring concrete will not flow underneath and fill the inner casing. Therefore, the casing must form a seal with the bottom of the excavation in spite the upward drag force that accompanies concreting.

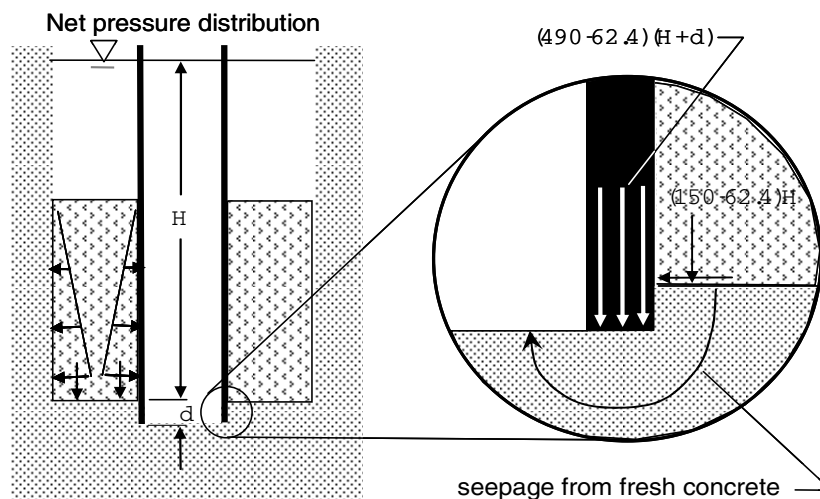


Figure 7. Net hydrostatic pressure distribution during construction.

One method of sealing the casing is socketing it beneath the toe of the voided shaft. This socket is not required to develop significant side shear with the inner casing but must provide a reasonable seal. Advancing the inner casing into the underlying strata could be performed by duplex drilling (drilling beneath the casing while advancing), vibratory, or oscillatory installation. When slurry stabilization is to be used, duplex drilling would likely be preferred as vibratory installation could disrupt the integrity of the excavation walls. In most cases, cuttings would not need to be removed (or at least not completely) from the inner casing during its installation, nor would it be necessary to perform clean-out processes within the inner casing. When full length temporary casing is employed to stabilize the hole, duplex, vibratory, oscillatory, or a combination installation method would suffice to install the inner casing.

An alternate method of providing a seal between the inner casing and the excavation bottom might include a flange at the base of the casing (rigid, flexible, or combination thereof) that would both center the casing at the toe and provide a flat surface on which the self weight of the shaft concrete would secure the seal (Figure 8). A combination of flange and socketing may be found most suitable in certain circumstances.

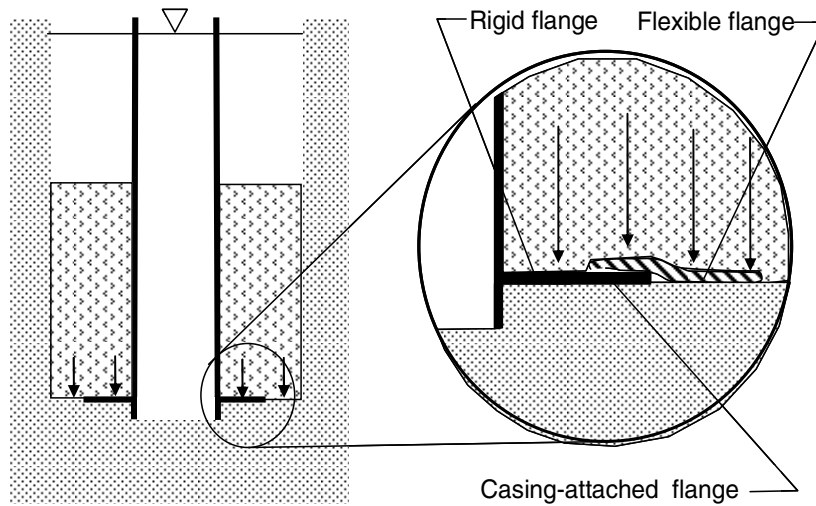


Figure 8. Rigid and flexible combination sealing flange is attached to the void casing, and engaged by the slurry and concrete load.

Centering the inner casing as well as the reinforcement cage is also important and can be achieved by attaching a simple frame work to the inner casing. If a flange assembly is used, the frame work is extended from and/or incorporated into the flange. Struts attached to this frame to provide the necessary stiffness serve dual purpose by providing cage centering via properly dimensioning their connection locations (Figure 9). This provides better assurance of the cage placement than the presently used plastic spacers which often are found floating to the top during concreting.

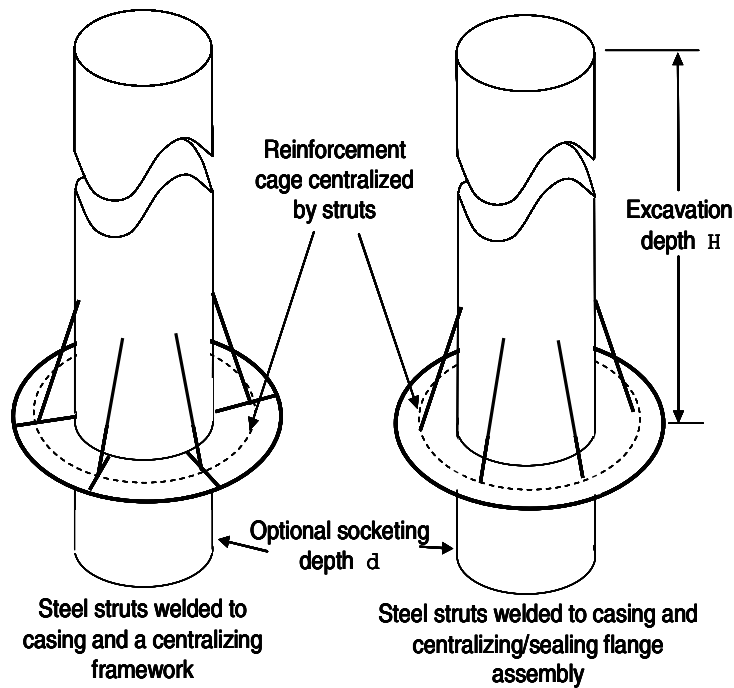


Figure 9. Void (inner) casing and reinforcement cage piloting framework.

**Strength Considerations.** Strength reduction caused by the reduced cross-sectional area has little effect on the structural performance of the foundation element in that the soil resistance is typically the limiting parameter. Therein, the geotechnical capacity is only affected by the reduction in end bearing area which is not typically considered a significant capacity contributor in large diameter shafts. However, if the inner casing was initially plugged or plated this capacity could be regained.

Structurally, a centrally voided shaft would exhibit a reduction in axial capacity roughly proportional to the loss in cross-sectional area. In general, load cases involving lateral loads and overturning moments produce far more severe stresses but would only be mildly affected by the presence of the void. For example, a 2.75m (9 ft) diameter shaft with a 1.22m (4ft) diameter void, 1% 410MPa (60ksi) steel, and  $f'_c$  of 34MPa (5ksi) would result in a axial capacity reduction in the range of 17% whereas the bending capacity would be reduced less than 1%. This is due to the minimal contribution to the moment of inertia and the associated bending strength provided by the more centrally located concrete material. Further, the 1% reduction does not consider the gain in bending capacity associated with the inner steel casing if permanent. If the axial capacity must be maintained slightly increasing  $f'_c$  to 41MPa (6ksi) would suffice. Figure 10 shows the interaction diagram for the above example shafts as well as the 41MPa voided option.

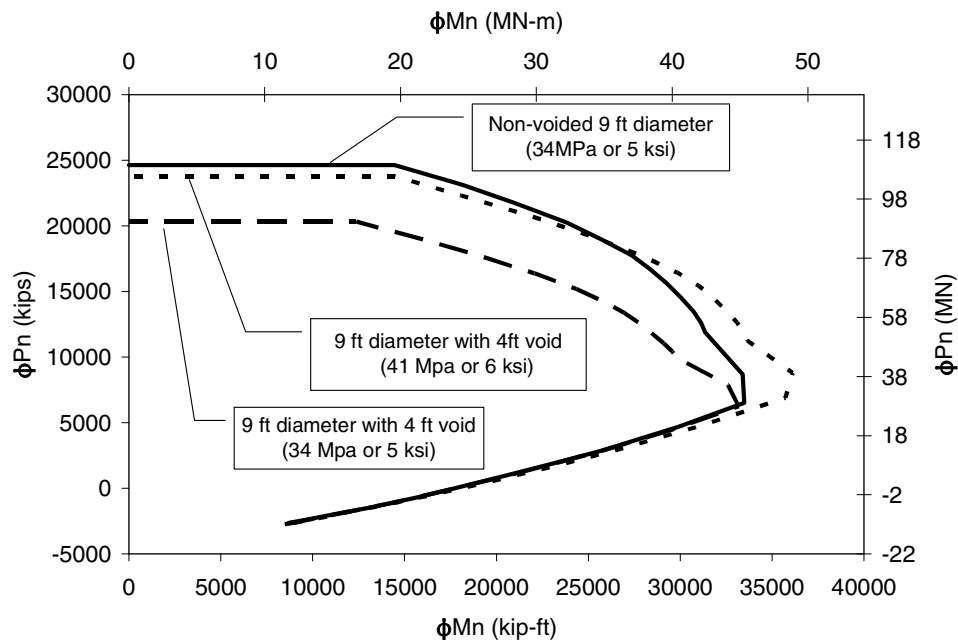


Figure 10. Interaction diagram of 2.75m diameter voided and un-voided shafts.

**Curing Temperature Maintenance.** The numerically modeled temperature responses of a 2.75m (9ft) diameter shaft with and without a 1.22m (4 ft) diameter void are shown in Figure 11. The model parameters simulated summer ambient conditions (changing winter to summer) but used concrete heat parameters similar to the Ringling Causeway Bridge. Note that under those conditions the peak temperature increase in the un-voided shaft (Figure 2 and 11) is related to the difference in ambient temperature and the lack of thermal convection in saturated soil.



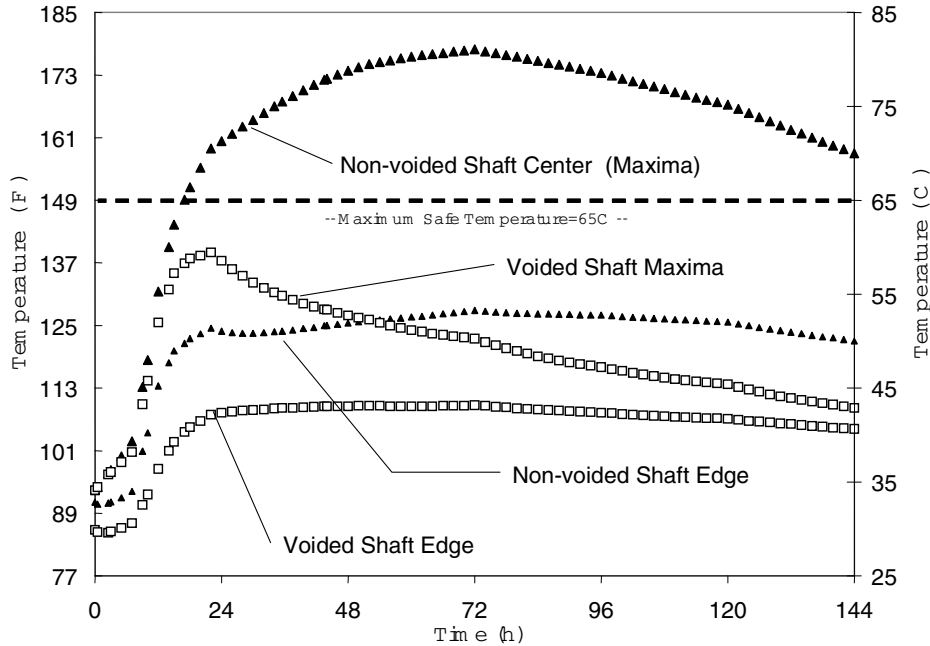


Figure 11. Calculated temperatures for 2.75m voided and non-voided drilled shafts in saturated sands, with summer installation (“Clearwater” type).

The voided shaft was modeled with the void (center of casing) filled with slurry which in turn attained the same peak temperature. This was well less than the recommended safe temperature, and temperature differentials momentarily approach but do not exceed 20C. Recent unpublished results, using published cement heat parameters, also indicate that supplanting 50% cement with ground granulated blast furnace slag does not diminish either peak or differential temperatures in large diameter shafts, but increases the centroidal peak time lag.

Although the accuracy of the model has been verified with field data that supports the un-voided shaft temperature response, a voided shaft has not been constructed and therefore has not been verified at this time. The FDOT is presently planning the construction of a demonstration voided shaft completely instrumented to verify temperature consideration while also addressing the constructability issues.

**Cost Effectiveness.** Preliminary cost comparisons between the permanent steel casing required to maintain the void during concreting and the central concrete that would be displaced (not required) showed the concept to be cost effective even without the savings associated with the now un-necessary cooling system. Figure 12 shows that for void diameters greater than about 1.3m (4.3ft) the cost savings from concrete not used offsets the cost of the steel casing. This assumes that the casing is permanent and no innovative method of inner form-work extraction has been devised.

For 2.75m shafts, voids larger than 1.2 to 1.5m are not likely to be considered as an annular thickness of 0.75m is envisioned to be the practical lower limit for construction. This leaves approximately 0.6m between the inner casing and the reinforcement cage for a pump truck hose or tremie to negotiate the concrete placement process. As a result, the Figure 13 results show a break even cost for 1.3m voids which would be reasonable for 2.75m shafts. For larger diameter voids (larger

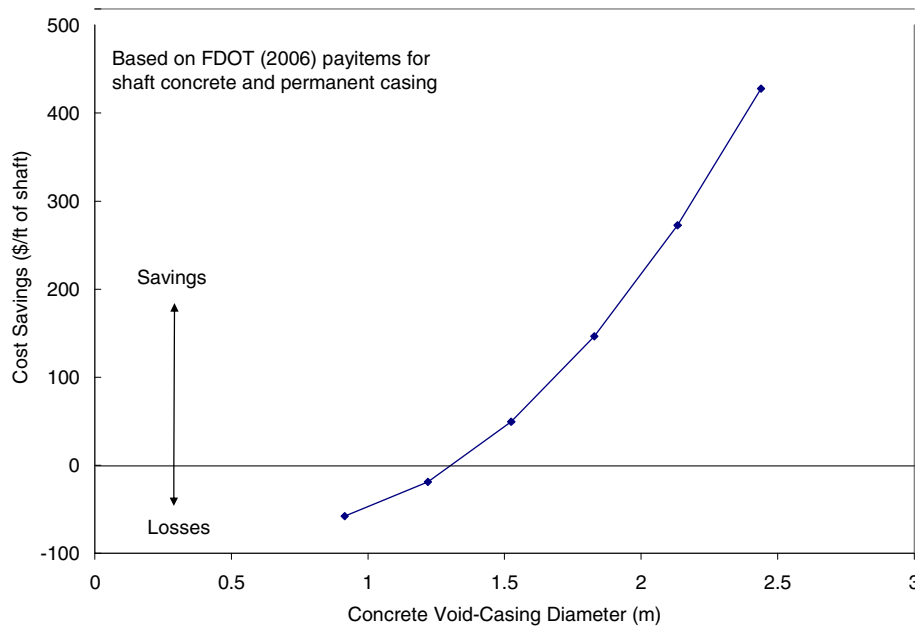


Figure 12. Cost savings per ft from unused concrete, including the inner casing, which is assumed permanent.

shafts) cost savings can be realized with additional savings from no required cooling system. Further benefits accompany voiding shafts in the assurance of long-term durability.

## SUMMARY

It has long been understood that heat generation from curing concrete leading to differential temperatures can induce cracking stresses that may render the final structure unsound. To combat the potential problem, limiting temperature differentials have been implemented with successful results. In the last several years, however, an awareness concerning the effects of elevated temperatures on concrete durability has arisen as it pertains to the developed peak temperature as well as differential. This is of particular interest in the wake of higher and higher strength concrete mixes with more energy producing constituents. Upper temperature limits are now being investigated to prevent the latent expansive reactions that result (years later) from severely elevated temperatures while curing. Further, as the use of larger diameter drilled shafts has heightened to accommodate extreme event limit states for longer span bridges, drilled shafts are now being viewed as mass concrete elements that require special attention.

Case studies were presented where mass concrete effects were encountered in both large and small diameter shafts. Although it was predicted in the larger (2.75m) shafts, the occurrence in the smaller 1.22m shaft was somewhat surprising. The second case admittedly involved severe conditions with poor dissipation to surroundings and high ambient temperature. However, had the first case with 2.75m shafts been constructed in the conditions of the latter, a far more detrimental scenario would have arisen. It is this potentially harmful condition that gives merit to the casting drilled shafts with a full-length central void.

Model predictions of temperature generations were introduced that clearly show that internal peak temperatures can be minimized by cast shafts with voids. Construction and strength considerations were discussed which further outlined the feasibility. Finally, cost savings were discussed; although no present values can be assigned to the increase in contractor duties, the values used to estimate savings were based on state pay item material costs that typically include contractor efforts.

In closing, the Florida Department of Transportation is seriously considering a demonstration project in the near future to flesh out the feasibility and potential benefits.

## ACKNOWLEDGMENTS

This article stemmed from research funded by the Florida Department of Transportation for which the authors are grateful. The input from the State Materials Office from Michael Bergin, David Horhota, and Charles Ishee has been invaluable. In addition, the authors would like acknowledge R.W. Harris, Inc. for providing the Clearwater test site as well as all the shaft construction services at that site. Specifically, the authors are indebted to both Ron Harris and Chris Harris. Finally, the oversight from Rudy, Ltd. is always appreciated.

## REFERENCES

Collepari, M., (2003), "A State-of-the-Art Review on Delayed Ettringite Attack on Concrete", *Cem. Conc. Res.*, v. 25, p.401-407.

FDOT. (2006). "Structures Design Guidelines." *Section 3.9, Mass Concrete* <http://www.dot.state.fl.us/structures/StructuresManual/CurrentRelease/FDOTBridgeManual.htm>.

FDOT. (2000). "Standard Specifications for Road and Bridge Construction 2000." Florida Department of Transportation, Tallahassee, FL.

FDOT. (2006). "Payitems History Reports & Estimates." State Estimates Office, <http://www.dot.state.fl.us/estimates/Main/BOEpayitems.htm>

Stark, J., and Bollman, K., (1998), "Delayed Ettringite Formation in Concrete", *Nordic Concrete Research*, v. 23-2, <http://www.itn.is/ncr/publications/pub-23.pdf>.

U.S. Department of the Interior. (2004). "Story of Hoover Dam; Concrete," Bureau of Reclamation, <http://www.usbr.gov/lc/hooverdam/History/essays/concrete.html>.

Wagner, R.V. (2006). "Temperature Rise in Concrete." *Master's Thesis*, University of South Florida, Tampa, FL. pp.182.

Whitfield, T. T. (2006). "Effect of C<sub>3</sub>S Content on Expansion Due to Ettringite Formation." *Master's Thesis*, University of South Florida, Tampa, FL (August).

# New Developments in Underwater Pile Repair Using Fiber Reinforced Polymers

**Dr. Rajan Sen**, Dept. of Civil & Environmental Engineering, USF, Tampa USA  
**Dr. Gray Mullins**, Dept. of Civil & Environmental Engineering, USF, Tampa USA

## Abstract

The development of resins that can cure in water has led to interest in the possible application of fiber reinforced polymers (FRP) for the underwater repair of corrosion-damaged piles. Over the past four years, USF have completed four demonstration projects in which FRP was used to repair corroding piles. The FRP material was directly applied to the submerged, partially wet or dry concrete surface. Fiberglass and carbon were both used in conjunction with two types of resin - a water-activated urethane resin and an epoxy resin. In all the projects, selected piles were instrumented to allow evaluation of the post-wrap FRP corrosion mitigation performance. No particular problems were encountered in wrapping the partially submerged piles. Linear polarization measurements indicated lower corrosion rates in the FRP wrapped specimens in comparison to their unwrapped counterpart. This paper provides an overview of the studies and highlights some of the important lessons that were learned.

## Introduction

Corrosion of reinforced or prestressed piles in tidal waters in sub-tropical environments is a world-wide problem. The combination of wet/dry cycles in a marine environment and high temperature/high humidity can be lethal since it allows chloride ions to readily penetrate the concrete cover and destroy the passive layer that normally protects steel in concrete's alkaline environment. Subsequent electrochemical reactions can cause steel to corrode rapidly, sometimes within eighteen months of service.

Traditionally, corroded piles are repaired using methods such as '*chip and patch*', '*shotcreting*', '*epoxy injection*' and '*pile jacketing*' (Fig. 1). Typically, chloride-free concrete is placed directly adjacent to chloride contaminated concrete. This sets up new corrosion cells that lead to more corrosion. The wisdom of following procedures that result in costly re-repair is increasingly under question.

Over the past decade, several highway authorities in Canada and US have explored the possibility of using FRP for corrosion repair<sup>1</sup>. In most applications no attempt was made to remove the chloride contaminated concrete and the wrapping was conducted under dry conditions. The availability of new resins that cure under wet conditions has spurred interest in extending FRP repair to partially submerged piles. Some full-scale FRP pile repairs were recently reported<sup>2,3</sup>. However, as the piles were not instrumented the performance of the FRP in reducing corrosion cannot be quantitatively assessed from these studies.



Figure 1. Jacketed pile repair (left) and view with jacket removed (right)

The University of South Florida (USF) have completed four demonstration projects in which corroding reinforced and prestressed piles were repaired using FRP. These projects were the culmination of several research studies that investigated the role of FRP in corrosion mitigation applications<sup>4-6</sup>. Several of the wrapped and unwrapped piles were instrumented to allow assessment of long term performance (these results are, however, not included in this paper). Moreover, as the sites for the repairs differed, alternative instrumentation approaches had to be explored. This paper provides a brief overview of the projects. Complete descriptions may be found elsewhere<sup>7-9</sup>.

## Background

The external bonding of FRP in underwater applications is more involved than similar repairs carried out under dry conditions. Changing tides, winds, wave action create unfavorable conditions that need careful attention. For this reason, existing application methods developed for repair under dry conditions have to be modified and new techniques developed to minimize the impact of the potentially adverse conditions.

As repair involves restoration of strength, bond is an important consideration. As with any bonded application, surface preparation is critical; good bond requires the substrate to have an open pore structure to ensure capillary suction of the epoxy<sup>10</sup>. In underwater application, however, pores will be saturated with water or small marine organisms or algae that are likely to adversely impact bond. New surface preparation techniques and new measures, e.g. bonding agents, may be required to ensure satisfactory performance.

FRP will only be used for repair if it leads to lower initial costs and better performance in comparison to traditional repairs. Thus, pile repairs need to be properly engineered so that FRP use is optimized. This requires reliable information not only on the capacity that must be restored but also on the relationship between corrosion and expansion. Available experimental data obtained from accelerated corrosion tests may not be applicable. Whereas laboratory studies result in symmetrical cracking, the combined action of wind and waves result in uneven chloride penetration and asymmetric cracking in piles. More importantly, the solubility of corrosion products from accelerated testing may differ from that under field conditions. Lack of information on expansion introduces uncertainty in design.

Finally, constructability and safety are of prime importance. The most careful attention has to be paid to all details so that the wrap is carried out safely and expeditiously.

## Designing FRP Repairs

The design of the FRP wrap requires the same information needed for conventional repair, namely, an estimate of the capacity loss that has to be recovered. Additionally, information is required on corrosion expansion that has to be accommodated by the FRP; several researchers have independently demonstrated<sup>1</sup> that corrosion continues as long as the ingredients required for the electro-chemical reactions remain inside the wrap. Thus, the FRP material simply serves as a barrier element reducing future ingress of deleterious materials such as chlorides and moisture.

The role of FRP in pile repair is therefore twofold: first to restore lost flexural capacity due to corrosion of steel; second to provide resistance to withstand expansive forces caused by corrosion products. The former requires fibers to be oriented parallel to the direction of the reinforcing or prestressing steel, i.e. along the length, while the latter requires fibers in the transverse or hoop direction, i.e. perpendicular to the steel. This can be met either by using two different sets of uni-directional fibers - one for each direction or preferably, by using bi-directional FRP material.

Research has shown that there is no simple relationship between metal loss and strength. This uncertainty stems from its dependence on other factors such as the bond between steel and concrete, the confinement provided by the ties and ductility reduction in steel due to corrosion. Given this uncertainty, it may be prudent to assume a safe, conservative value. This was the case in the demonstration projects where capacity loss was taken as 20%.

As noted already, at the present time there is a lack of reliable information on transverse expansion caused by corrosion. In view of this, a simplified procedure<sup>8,11</sup> was developed. For design, the expansion strain was assumed as 0.1% (approximately 3 times the ultimate concrete tensile strain assumed to be 10% of the ultimate concrete failure strain).

A simplified two step design procedure was developed in which the requirements for strength and corrosion expansion were uncoupled. The strength requirements were first met by strain compatibility analysis in which the contribution of the FRP to the tensile (but not compressive) capacity were determined through interaction diagrams for the assumed shortfall in strength. The confining lateral strain provided by this strengthening was then checked to ensure that it satisfied the maximum assumed expansion of 0.1%.

Results obtained were found to be reasonable when compared to solutions from competing methods developed for seismic retrofit<sup>8,11</sup>. For bi-directional carbon fiber, only two FRP layers were required. Twice as many layers were required for fiberglass because of its lower strength and stiffness.

## FRP Materials

Two types of materials were used. One was a pre-preg, the other a wet lay up. The pre-preg system was from Air Logistics in which all the FRP material was cut to size, resin-saturated in the factory and sent to the site in hermetically sealed pouches. The wet lay up system required on-site impregnation and was from Fyfe excepting for the Allen Creek Bridge where an alternative system was used. As this repair was carried out under dry conditions inside a coffer dam<sup>8</sup> it is not included here. Both carbon and fiberglass were used. Details of the properties of the fiber and the resin as provided by the suppliers are summarized in Tables 1-2<sup>12-13</sup>.



Table 1. Properties of Pre-Preg System<sup>12</sup>

<b>Fibers</b>	<b>Tensile Strength (MPa)</b>	<b>Tensile Modulus (GPa)</b>	<b>Load per Ply (kN/m)</b>
Uni-directional (GFRP)	590	36	420
Bi-directional (GFRP)	320	21	210
Uni-directional (CFRP)	830	76	596
Bi-directional (CFRP)	590	22	420

Table 2. Properties of Wet Layup System<sup>13</sup>

<b>Properties</b>	<b>Quantities</b>
Tensile Strength	3.24 GPa
Tensile Modulus	72.4 GPa
Ultimate Elongation	4.5 %
Laminate Thickness	0.127 cm
Dry fiber weight per sq. yd.	915 g/m <sup>2</sup>
Dry fiber thickness	0.038 cm

## Field Demonstration

Four field demonstration studies were conducted at two contrasting sites. The first site, Allen Creek Bridge, Clearwater, FL is located in shallow, relatively calm waters; the subsequent repairs were carried out on piles supporting the Friendship Trails Bridge and the Gandy Bridge that span Tampa Bay, Florida's largest estuary that flows into the Gulf of Mexico. The procedure for wrapping under water was identical to that above water. Usually, wrapping was scheduled for low tide when the submerged region could be readily accessed. On rare occasions when the water level was higher, diving masks were used.

### Allen Creek Bridge

Allen Creek Bridge is located on the busy US 19 highway connecting Clearwater and St. Petersburg, FL. The original bridge built in 1950 was supported on reinforced concrete piles driven into Allen Creek. In 1982, the bridge was widened and the widened section was supported on 35 cm square prestressed piles.

The waters from Allen Creek flow east into Old Tampa Bay that in turn joins the Gulf of Mexico to the south. The environment is very aggressive; all the reinforced concrete piles from the original construction had been rehabilitated several times. At low tide, the water level in the deepest portion of the creek is about 0.8m. At maximum high tide it is about 1.9m. This shallow depth meant that the underwater wrap did not require divers and could be carried out on a ladder.

Instrumentation was installed to allow linear polarization and corrosion potential measurements to be made<sup>4</sup> without junction boxes and wiring. Cores were taken from various locations to determine the chloride content at the level of the prestressing strands. Results indicated that the strands were corroding though there were no visible signs of corrosion.

## Surface Preparation

Pile surfaces were covered with marine growth that had to be scraped off. Additionally, two of the four corners that were not rounded but chamfered had to be ground using an air-powered grinder. This was a difficult operation particularly for sections that were below the water line. Quick-setting hydraulic cement was used to fill any depression, discontinuities and to provide a smooth surface. The entire surface was pressure washed using freshwater to remove all dust, marine algae just prior to wrapping.



Figure 2. Patching damage (left) and grinding surface (right).

## FRP Wrap

Two different schemes using two different materials were evaluated. In each scheme four piles were wrapped with two other instrumented piles serving as controls. In the first scheme, cofferdam construction was used and the piles wrapped using a bi-directional FRP in wet layup under dry conditions. Complete details may be found in Ref. 8. As this was wrapped under ‘perfect’ conditions, its performance provided a means for evaluating piles that were directly wrapped in water using the water activated urethane resin.

Post-wrap corrosion measurements showed that the corrosion rate was smaller for the wrapped piles compared to the unwrapped controls<sup>4,8</sup>. However, rates are still small.

## Tampa Bay Bridges

The Friendship Trails Bridge and the Gandy Bridge are two of four bridges that cross Tampa Bay. When it was first opened to traffic in the 1920’s it was the longest bridge in the United States reducing the distance between Tampa and St. Petersburg by 72 km. The environment is very corrosive and the majority of the piles supporting these bridges have sustained severe corrosion damage and needed to be repaired. Three demonstration studies were carried out on these piles over the period 2004-06.

All piles repaired were 50 cm x 50 cm either reinforced or prestressed concrete piles. They were all located in waters that are approximately 4.9 m deep. This meant that ladders could no longer be used in this situation. An innovative scaffolding system (Fig. 2) was designed and fabricated for the study. It was lightweight, modular yet sufficiently rigid when assembled to support 4-6 people. The scaffolding was suspended from the pile cap and extended 2.74 m below the pile cap. Its mesh flooring provided a secure platform around the pile that allowed the wrap to be carried out unimpeded in knee deep waters without the need for diving gear.

Two different FRP systems were used. One was the water-activated, pre-preg urethane resin system used in the Allen Creek Bridge. The other system used a special epoxy that could cure in water. The first system was used to wrap four piles – two using carbon and two using glass. In the second system, the FRP material had to be pre-impregnated on site prior to the wrap. Two piles were wrapped with fiberglass using this system. Of the two, one was an experimental FRP system that combined wrapping with a sacrificial cathodic protection system. Two other unwrapped piles in a similar initial state of disrepair were used as controls to evaluate the performance of the wrapped piles.



Figure 3. Installation vertical (left) transverse layer (right) typically at low tide

As for the piles in the Allen Creek Bridge, several piles were instrumented but using a special rebar probe developed by the Florida Department of Transportation<sup>7</sup>. This allowed measurement of the corrosion current between the locations where they were located. Reductions in current compared to the controls were expected to provide a measure of the efficacy of the FRP wrap. Unlike, Allen Creek Bridge, junction boxes and wiring were required to allow readings to be taken. Preliminary corrosion measurements were however inconclusive because the system had not yet stabilized following the installation of the probes.

The FRP material for the first system was identical to that used in Allen Creek Bridge, i.e. unidirectional longitudinal layer followed by transverse bi-directional material. For the second system, all material was uni-directional. The scaffolding system enabled the wrapping to be carried out with relative ease.

On average, it took between 30 minutes and 45 minutes to wrap a pile depending on the number of FRP layers. For the wet-lay-up system, it took additional time to impregnate the FRP material and transport it to the pile site. The total time taken averaged about 90 minutes in this case.

Fig. 3 shows the installation of the longitudinal layer at the corners followed by the transverse layer that was applied spirally with no overlap. Fig. 4 shows a view of the wrapped piles and a close-up view more than two years later showing marine deposition on the wrap.





Figure 4. View of FRP wrapped piles when new (left) and after 2 years (right)

### New Developments

The results from the initial repairs carried out on the piles supporting Allen Creek Bridge and the Tampa Bay bridges showed that it was feasible to wrap corroding piles under typical field conditions. Corrosion rate measurements also indicated that the FRP wrapping led to a reduction in the corrosion rate. However, the FRP-concrete bond was found to be poorer when compared to the bond that was obtained under laboratory conditions<sup>8,14</sup>.

Laboratory studies were undertaken over the past year to evaluate alternative strategies used by the aerospace industry to improve the underwater FRP-concrete bond. Two candidate techniques widely used in aerospace (1) vacuum bagging and (2) pressure bagging were evaluated. Prototype systems were developed and the bond evaluated both non-destructively and destructively<sup>9</sup>. Both techniques worked but in the subsequent field demonstration, pressure bagging was used. Qualitatively, the bond appeared to be much improved though no on-site destructive bonds have yet been conducted. Such tests are planned in the future.

The USF research team has just received funding for implementing a pilot sacrificial cathodic protection system. This is expected to be implemented over the next several months at the same Friendship Trails Bridge site.

### Conclusions

This paper provides a brief overview of demonstration projects in which instrumented reinforced and prestressed piles were wrapped using different FRP systems. Initially, wrapping was carried out directly under water using ladders. Subsequently, a lightweight scaffolding system was developed that could be suspended from the pile cap. With all-around access, FRP wrapping was conducted with ease.

Based on our experience, it is clear that it is feasible to use FRP for underwater corrosion repair. The performance of the FRP in slowing down the corrosion rate appears to be comparable to that determined from laboratory testing. Visual inspection suggests that the repairs have held up well with the longest over four years old at this time. More detailed examination may be possible in the future when the Allen Bridge is replaced. However, on-site pull-out tests on several piles repaired in the initial phase have shown that the FRP-concrete bond was poorer than that obtained under dry laboratory conditions.

A pressure bagging technique was developed and successfully implemented last year to address this variability in bond. While no on-site pullout tests have yet been conducted, visual examination suggests that the bond was better. Efforts are currently underway to incorporate a sacrificial cathodic protection (CP) system within the wrap that can stop corrosion. With all the development work carried out, the prospects of FRP emerging as an alternative cost effective pile repair system appear bright.

## Acknowledgements

The demonstration studies reported were funded by the Florida/US Department of Transportation and Hillsborough County. The support and guidance of Mr. Pepe Garcia and Mr. Steve Womble, both from Florida Department of Transportation are gratefully acknowledged. We thank Ms. Mara Nelson, and Mr. Nils Olsson, both from Hillsborough County, and SDR Engineering, Tallahassee for their contribution. We thank Mr. Franz Worth of Air Logistics and Mr. Ed Fyfe, President, Fyfe for their support. This work could not have been carried out without the tireless effort of current and former graduate students Dr. K S Suh, Dr M. Stokes, Mr. I Gualtera, Mr. D. Winters, Mr. Julio Aguilar and Mr. Andy Schrader.

## References

1. Sen, R. "Advances in the Application of FRP for Repairing Corrosion Damage", *Progress in Structural Engineering and Materials*, 2003, Vol. 5, No 2, pp. 99-113.
2. Bazinet, S., Cercone, L. and Worth, F. "Composite FRP Moves into Underwater Repair Applications", *SAMPE Journal*, 2003, Vol. 39, No. 3, pp. 8-16.
3. Watson, R.J. "The Use of Composites in the Rehabilitation of Civil Engineering Structures", *ACI SP 215* (Ed. S. Rizkalla and A. Nanni), ACI, Farmington Hills, MI, 2003, pp. 291-302.
4. Mullins, G., Sen, R., Suh, K and Winters, D. "Underwater FRP Repair of Prestressed Piles in the Allen Creek Bridge", *ASCE, Journal of Composites for Construction*, 2005, Vol. 9, No. 2, pp.136-146.
5. Mullins, G., Sen, R., Suh, K. and Winters, D. "A Demonstration of Underwater FRP Repair", *Concrete International*, 2006, Vol. 28, No. 1, pp. 1-4.
6. Sen, R., Mullins, G., Suh, K. S. and Winters, D. "FRP Application in Underwater Repair of Corroded Piles". *ACI SP 230* (Eds. C. Shield, J. Busel, S. Walkup, D. Gremel), 2005, Vol. 2, pp 1139-1156.
7. Mullins, G., Sen, R., Suh, K and Winters, D. "Underwater Pile Wrap of the Friendship Trails Bridge", *Final Report, Hillsborough County*, June 2004, 32 pp.
8. Mullins, G., Sen, R., Suh, K.S. and Winters, D. "Use of FRP for Corrosion Mitigation Applications in a Marine Environment", *Final Report submitted to Florida / US Department of Transportation, Tallahassee, FL* October 2005, 406 pp.
9. Mullins, G., Sen, R., Winters, D. and Schrader, "Innovative Pile Repair", *Final Report submitted to Hillsborough County, FL*, January 2007, 40 pp.
10. Emmons, P. Means, P. *Concrete Repair and Maintenance Illustrated*, RS Means, Kingston, MA, 1993.
11. Sen, R., Mullins, G. and Shahawy, M. (2007). "FRP Repair and Strengthening of Structurally Deficient Piles". To appear in *Journal of Transportation Research Board*.
12. Air Logistics Corporation. *Aquawrap Repair System*, Pasadena, CA.
13. Fyfo Co. LLC, <http://www.fyfeco.com/>
14. Sen, R. and Mullins, G. "Application of FRP for Underwater Pile Repair", *Composites Part B*, 2007, Vol. 38, No. 5-6, 751-758.

## Performance of FRP in Reducing Corrosion in Prestressed Elements

*Rajan Sen, Gray Mullins, Danny Winters*

Department of Civil and Environmental Engineering, University of South Florida, Tampa, FL, USA

*Kwangsuk Suh*

PB Americas, Inc., Tampa, FL, USA

### ABSTRACT

This paper provides an overview of a multi-year laboratory study to evaluate the role of fiber reinforced polymers (FRP) in reducing the corrosion rate in a marine environment. Twenty two, one-third scale prestressed piles were cast with built-in chloride. Titanium reference electrodes and thermocouples were placed inside the specimens at the time of casting. Sixteen of the specimens were wrapped after 28 days using CFRP or GFRP. The remaining six unwrapped specimens served as controls. The specimens were exposed to simulated tidal cycles under outdoor ambient conditions for nearly three years. Linear polarization measurements were taken throughout the exposure period to monitor the corrosion rate of the steel. At the end of the exposure period, gravimetric tests were conducted to measure the metal loss in both wrapped and unwrapped specimens. The trends predicted by the linear polarization measurements were confirmed by gravimetric results. Corrosion rates in wrapped specimens were significantly lower than that in identically exposed controls.

**KEY WORDS:** corrosion; underwater; FRP; prestress; repair

### INTRODUCTION

Over the past decade a number of field demonstration projects have been completed in which FRP was used for repair and strengthening corroded structures. The majority of these applications related to above ground elements such as bridge columns or bents. More recently, the availability of resins that can cure in water has led to similar demonstration projects for repairing corroded substructure concrete piles in tidal waters.

Unlike cathodic protection that can stop the electrochemical reactions responsible for corrosion, FRP only serves as a barrier element that slows down the ingress of deleterious elements responsible for corrosion. In the circumstance, information on corrosion rates in FRP wrapped elements is of great interest to highway authorities since it can be used to assess the life of the repair and provide a realistic estimate of its cost.

A number of studies have been conducted in which the performance of

FRP wrapped concrete members was experimentally determined. Details may be found in a recent state-of-the-art review paper, Sen 2003.

The majority of these studies were for reinforced concrete elements; information on prestressed elements is more limited (Mullins et al. 2001). This paper provides an overview of an experimental study in which instrumented FRP wrapped and unwrapped corroding prestressed specimens were exposed to simulated tidal cycles under ambient outdoor conditions. Their performance was evaluated both non-destructively and by destructive gravimetric testing. The study was part of an overall research effort to assess the feasibility of using FRP for corrosion repair of prestressed piles in Florida's tidal waters. Complete details of this study may be found elsewhere (Suh et al. 2005, Suh et al. 2007).

### BACKGROUND

Concrete's alkaline environment normally protects steel by forming a passive layer that limits access of oxygen, moisture and other aggressive species. This protective layer can be destroyed if the pH drops below 11.5 or at high alkalinities if chloride ions penetrate the concrete. In Florida's tidal waters, the high concentration of chloride ions combined with high humidity and temperature allow chloride ions to reach the level of the reinforcement even for high quality concrete.

The chloride profile in piles varies depending on its location relative to the mean sea level. It is highest closest to the surface in the "splash zone" (0.6-1.8m of the mean sea level) because of the cumulative effect of evaporation of salt water from the pile surface. However, these high chloride levels are localized near the surface. In contrast, in the submerged region, chloride concentrations are lower but penetrate deeper.

Corrosion is generally assumed to be initiated when the chloride ion concentration reaches a critical threshold value of 1.2 kg Cl/m<sup>3</sup> (Mindess et. al. 2003). This threshold depends on many factors, the principal being the oxygen supply at the surface of the reinforcing steel. Since oxygen's solubility in water is very small, if the concrete pores are saturated with water (as is the case for piles in tidal waters), the chloride threshold for corrosion initiation can be one order of



magnitude greater than that exposed to the atmosphere (Bertolini et. al. 2004). Because concrete cover in marine applications is larger, chloride ions take longer to reach the steel surface than under atmospheric exposure. Given that the concrete pores in the splash zone and in the submerged region of the pile are saturated with moisture, the chloride threshold for corrosion is higher. Collectively this means that high levels of chloride are present over larger areas making pitting corrosion less likely. Pitting corrosion is likely in piles that cracked while they were being driven into the ground.

## EXPERIMENTAL PROGRAM

Surveys of corrosion-damaged piles conducted by the research team identified corrosion damage to be most prevalent in 45 cm square prestressed piles. For this reason, a 1/3rd scale model of these piles was selected for the laboratory investigation.

The test specimens were 15 cm. x 15 cm with a 25 mm cover. Prestressing was provided using four 7.9 mm, 1860 MPa strands. A fifth unstressed strand was provided to accelerate corrosion using a constant current system in another study.

When stressed to code specified limits, the effective prestress in the specimens exactly matched that of the 45 cm prototype. The specimen length was set as 1.52 m. This ensured that their weight (under 900 N) was such that it could be moved without requiring lifting equipment.

To initiate the corrosion process, chloride was mixed with the concrete during fabrication. The chloride was confined to a symmetric 55 cm region that corresponded to 1.65 m splash zone in the prototype. The chloride ion content was kept at 3% by weight of the cementitious material that corresponded to a 15.1 kg/m<sup>3</sup>. This is an order of magnitude higher than the threshold for initiating corrosion under atmospheric exposure.

To ensure all specimens were identical they were cast simultaneously in a specially adapted prestressing bed at a commercial prestressing facility. To facilitate wrapping, wood inserts with the appropriate radii were placed at the corners of the form. Similarly, special trowels were used to finish the top surface so that they were also curved. These simple measures greatly simplified the preparation work needed for subsequent wrapping. Activated titanium reference electrodes and thermocouples were installed prior to casting of concrete to allow the post-wrap performance to be non-destructively monitored (Fig. 1).

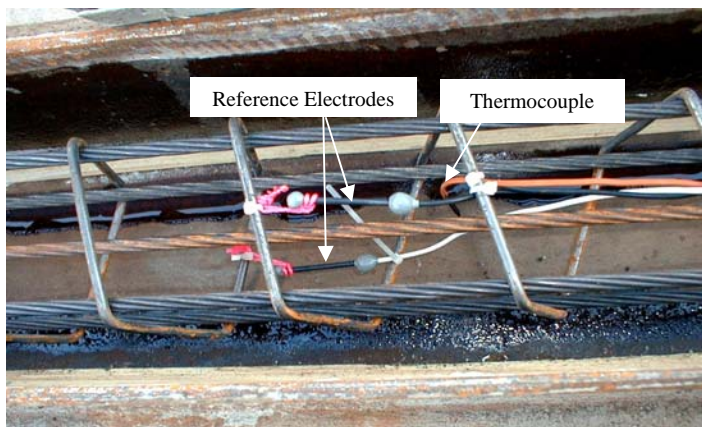


Fig. 1 View of titanium reference electrode and thermocouple

## Wrapping

Of the 22 specimens used in the study, 16 were wrapped using commercially available CFRP and GFRP material. Wrapping was carried after the concrete had reached its 28 day strength. The number of layers was varied from 1 to 4 to allow its effect on the corrosion rate to be assessed.

The wrap was applied over a 90 cm length symmetric with respect to the specimen. This meant that it extended 17.5 cm. symmetrically beyond the 55 cm chloride contaminated region. Since the specimen was 1.5 m in length, 30 cm concrete sections were not wrapped at the top and bottom. Details of the material properties of the FRP material and their manner of installation may be found in the final report, Suh et al 2005.

## Exposure

Of the 22 specimens, 20 specimens were placed upright in a 1.82m wide x 3.05m long x 1.22m deep containing 3.5% saltwater to allow tidal cycles to be simulated. Two other controls were placed upright in a similar environment, but indoors.

The water level at high tide was 80 cm from the bottom and 35 cm at low tide. The change in the water level reflected tide changes in the Tampa Bay area. The water level was automatically changed every six hours (see Fig. 2) so that two exposure cycles were completed every day. It may be noted that at low tide the water level was 35 cm or 5 cm above lowest point wrap. Thus, the exposure ensured that a portion of the wrap was always submerged; a part was subjected to wetting and drying conditions while the part at the top was always dry. The two other unwrapped controls kept indoors were similarly exposed to twice daily tidal cycles.

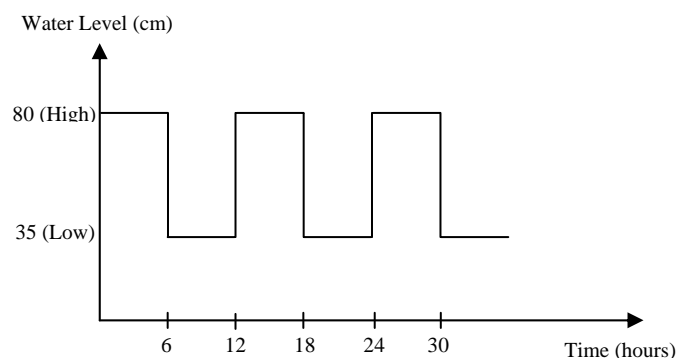


Fig. 2 Schematic of exposure cycle

## Non Destructive Monitoring

Throughout the exposure period, a data logger was used to record the temperature inside each of the specimens. Additionally, half-cell and linear polarization measurements were taken at periodic intervals using a PR monitor. These measurements were carried out both before and after wrapping. All measurements for all specimens were carried out at low tide.

Typical results from the non-destructive monitoring are shown in Figs. 3 and 4 that compare the variation in the half-cell potential (with respect to a copper-copper sulfate reference electrode) and the

corrosion rate for unwrapped (controls) and wrapped specimens. Only results for the 2 layer CFRP and GFRP specimen are presented. However, the readings were similar for other layers.

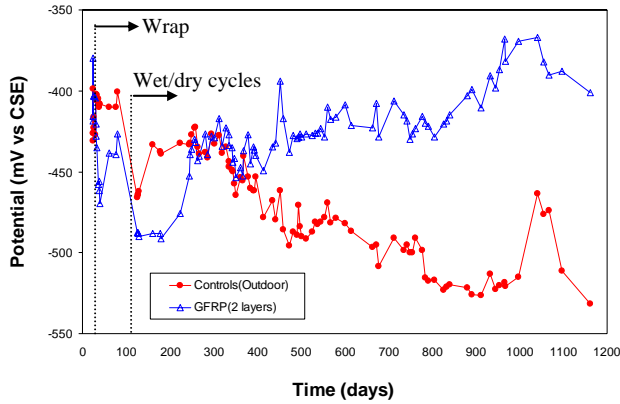


Fig. 3 Potential variation for control and GFRP wrap

The half-cell potential readings at mid-height in Fig. 3 show that readings for the controls and the wrapped specimens were comparable for the about the first 350 days. This coincided with the appearance of visible cracks in the splash zone in the controls (Fig. 5). Following this period, the readings for the wrapped specimen became less negative while that for the unwrapped specimens became more negative. However, all readings were more negative than -350mV signifying that the probability of corrosion in all the specimens exceeded 90%.

The results for the corrosion rate measurements obtained from linear polarization are shown in Fig. 4. These readings correspond to the reference electrode located at the middle of the specimen.

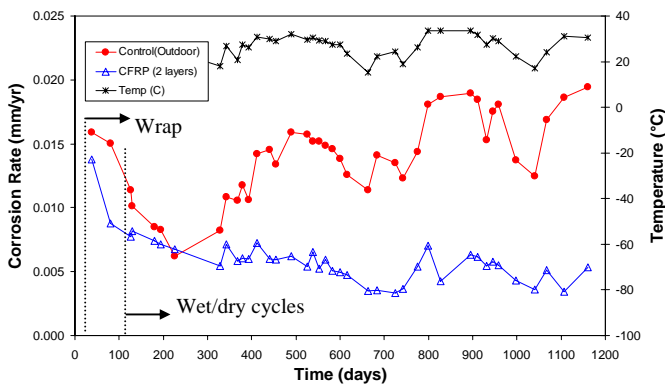


Fig. 4 Corrosion rate variation for control and CFRP wrap

The trend in the corrosion rate mirrors that of the half-cell potential readings shown in Fig. 3. After an initial period of about 350 days when there is little difference in the corrosion rates in the wrapped and unwrapped specimens, the rates for unwrapped controls increase while those of the wrapped specimens decrease.

Only results for the CFRP wrap with two layers is shown for clarity. However, averaged results for all the layers showed similar trends.

More plots may be found in the final report, Suh et al. 2005

At the end of the exposure period of nearly 3 years, the average corrosion rate in the controls was 0.018 mm/year but only 0.0055 mm/year, or nearly a third in the wrapped specimens. These rates are commensurate with corrosion where visible damage can be expected within 2 to 10 years. This contrasts with the controls where visible corrosion was observed within 1 year.



Fig. 5 Cracked control (L) vs uncracked FRP wrapped specimen (R)

Following the completion of the exposure period, the actual metal loss was determined from destructive gravimetric testing. In the tests, the strands were carefully retrieved from the specimens, cleaned and carefully weighed to measure the actual metal loss. Results are summarized in Table 1. It may be seen from Table 1 that the metal loss in strands for the controls (6.6%) was about twice (3.3-3.4%) that in the wrapped specimens. The performance of CFRP and GFRP were also comparable. There was no improvement in performance for specimens wrapped with more than two FRP layers.

Table 1 Averaged Metal Loss (%)

Type	Strand		Tie	
	Average	Range	Average	Range
Controls	6.6	3.7-12.6	9.5	7.9-11.7
GFRP	3.4	2.7-3.9	6.3	5.4-6.9
CFRP	3.3	2.6-4.3	6.6	5.2-7.7

## DISCUSSION

The goal of the study was to determine the extent to which FRP material slowed down the corrosion rate in specimens in which the threshold for corrosion had been exceeded.

The results from both non destructive corrosion monitoring and the gravimetric testing clearly indicated that the FRP material was effective in slowing down but not stopping corrosion. Total metal loss in the strands in the wrapped specimens was about half that in the unwrapped controls. Additionally, control specimens developed cracks along the strand line after about 1 year of exposure.

Aside from the total metal loss, it was found that there were 30 wire breaks in the six control specimens. In contrast there was similar breakage in only 1 of the 16 wrapped specimens. This breakage of wires was most likely the result of pitting corrosion facilitated by

cracking. Thus FRP wrapping led to significantly improved performance.

A concern among DOT officials is the possible upward movement of the corrosion cells from the wrapped region as has been observed in jacketed piles. However, no similar movement could be discerned in the gravimetric testing. This could be because the wrap extended 17.5 cm above the chloride contaminated region. Also, there was no localized corrosion in the always submerged region as had been observed in a study supported by Texas DOT (Berver et al. 2001).

## CONCLUSIONS

This paper presents a brief overview of a multi-year study to evaluate the role of FRP in corrosion mitigation application. The specimens tested were cast with high built in chlorides comparable to that observed in field studies (Mullins et al. 2005). Exposure was limited to two daily wet/dry cycles under outdoor ambient conditions. Other than the chloride cast at the time of fabrication to initiate corrosion, the study therefore accurately modeled field conditions for piles in a marine environment. The results presented provide a realistic measure of the likely performance of FRP in mitigating corrosion in a marine environment after chloride ingress had led to a destruction of the protective passive layer.

The results from the test (Figs. 3-5 and Table 1) conclusively show that if the wrap is properly applied corrosion performance is significantly improved not only in terms of overall metal loss but by the absence of wire breaks. The wire breaks in the controls were likely the result of pitting corrosion. Given the uniform cast-in-chloride, the anodic region was large and corrosion should have been uniform. However, cracking of the controls (Fig. 5) provided increased oxygen supply and changes in chloride level at selected locations along the length of the pile. Such changes facilitated the formation of micro-cells and pitting corrosion leading to breakages in 30 wires in the controls. In contrast, there was similar breakage in only one wrapped specimen. Thus, wrapping protects the pile by greatly diminishing the extent of pitting corrosion in the most vulnerable region of the splash zone.

A surprising finding was that two FRP layers provided optimal protection. The precise reason for this is not known. However, it could be because the additional layers were not sufficiently saturated with resin. Alternatively, it could also signify that the role of the FRP as a barrier element was not improved when additional layers were provided. Oxygen and moisture already present in the specimens allowed the electrochemical reactions to continue regardless.

In the study, the specimens were wrapped after chloride contamination. Had piles been wrapped immediately after installation, the ingress of chlorides would be stopped and the performance would be even better. In any event since the FRP material also provides strengthening, it can help restore lost capacity.

It should be noted that the FRP wrapping was carried out under dry conditions where the FRP-concrete bond was excellent. Tests on field repairs have shown that the FRP-concrete bond can be variable depending on the resin system used. Thus, the results presented in the paper are valid for situations where bond is good over the entire length of the wrap. However, recent advances by the USF research team suggest that it is possible to ensure excellent bond even in field situations (Mullins et al 2007).

## ACKNOWLEDGEMENTS

This study was funded in part by the Florida Department of Transportation. This support is gratefully acknowledged. The opinions findings and conclusions expressed in this publication are those of the writers and not necessarily those of the Florida Department of Transportation.

## REFERENCES

- Bertolini, L., Elsener, B., Pedferri, P. and Polder, R. (2004). *Corrosion of steel in concrete*, Wiley-VCH, Verlag GmbH & Co. KGaA, Weinheim, Germany.
- Berver, E., Jirsa, J., Fowler, D., Wheat, H. and Moon, T. (2001). "Effects of wrapping chloride contaminated concrete with fiber reinforced plastics", FHWA/TX-03/1774-2, University of Texas, Austin.
- Mindess, S., Young, J. and Darwin, D. (2003). *Concrete*, Prentice-Hall, Englewood Cliffs, NJ, pp. 496-497.
- Mullins, G., Sen, R., Suh, K., and Torres-Acosta, A. (2001). "CFRP wrap for repairing corrosion damage". Part 2 of final report entitled "Lateral Capacity of Corroded Pile Bents" submitted to Florida Department of Transportation, Tallahassee, FL
- Mullins, G., Sen, R., Suh, K and Winters, D. (2005). "Underwater FRP repair of prestressed piles in the Allen Creek Bridge". ASCE, *Journal of Composites for Construction*, Vol. 9, Issue 2, pp. 136-146.
- Mullins, G., Sen, R., Winters, D. and Schrader, A. (2007). "Innovative underwater pile repair". Final report submitted to Hillsborough County, Tampa FL, January.
- Sen, R. (2003). "Advances in the application of FRP for repairing corrosion damage" *Progress in Structural Engineering and Materials*, Vol. 5, No 2, pp. 99-113.
- Suh, K., Mullins, G., Sen, R., and Winters, D. (2005). "Use of FRP for corrosion strengthening applications in a marine environment. Final Report submitted to Florida / US Department of Transportation, Tallahassee, FL, Oct., 406 pp.
- Suh, K., Mullins, G., Sen, R., and Winters, D. (2007). "Effectiveness of fiber-reinforced polymer in reducing corrosion in marine environment", *ACI Structural Journal*, Vol. 104, No 1, pp. 76-83.

## **CORROSION MONITORING OF FRP WRAPPED PILES**

K. Suh <sup>1</sup>, G. Mullins <sup>2</sup>, R. Sen <sup>2</sup> and D. Winters <sup>2</sup>

<sup>1</sup> PB Americas, Inc., Tampa FL, USA

<sup>2</sup> Department of Civil and Environmental Engineering, USF, Tampa FL, USA

### **ABSTRACT**

Fiber reinforced polymers (FRP) are now widely used especially for the repair and rehabilitation of concrete structures. Over the past decade there has been increasing interest in extending their application for repairing corrosion-damaged sub-structure elements. This was made possible by the availability of resins that cure in water so that repairs could be carried out without resorting to coffer dam construction. The USF research team has pioneered the FRP repair of piles in tidal waters. In the applications, different instrumentation schemes for monitoring long term performance were explored. These included commercially available sensors and others that were developed in-house either by the research team or the Florida Department of Transportation. This paper provides an overview of the different systems, their implementation for long term monitoring of corrosion rate in piles and an assessment of their relative performance from several field applications.

### **1. INTRODUCTION**

Over the past decade, numerous demonstration projects were conducted to evaluate the effectiveness of fiber reinforced polymers in corrosion repair. The majority of these applications related to the repair of corroding columns and bents where the FRP was applied to dry surfaces [1]. With the availability of resins that can cure under wet conditions, similar applications have extended to the repair of partially submerged corroding piles [2, 3].

In the recent past, the University of South Florida (USF) have completed four demonstration projects involving the FRP repair of piles in tidal waters [4-7]. A unique feature of each of these studies was that piles were instrumented to allow the long term

effectiveness of the FRP material to be evaluated. For various reasons, it was not always possible to use the same instrumentation scheme in each of these repairs. This paper provides a critical overview of the different systems.

## 2. BACKGROUND

Corrosion monitoring uses non-destructive electrochemical methods that take advantage of the electrochemical nature of corrosion. Available methods include measurement of concrete resistance and resistivity, half-cell potential and corrosion current. However, in the case of FRP wrapped elements where the concrete surface is inaccessible, sensors have to be embedded inside the concrete. For applications involving piles, the size of the sensor is critical since it must be small enough to be accommodated within the available 75 mm concrete cover.

Embedded sensors may be used to evaluate the corrosion state in wrapped piles using (1) linear polarization and (2) galvanic current measurement. Linear polarization is an established technique for measuring the corrosion rate of steel in concrete structures. It relies on the linear relationship between corrosion current and its potential when the equilibrium potential is perturbed by the application of an incremental current ("galvanostatic") or incremental voltage ("potentiostatic"). Several portable devices are available that can be used to make the measurement. In the demonstration projects, a PR - Monitor Model 4500 manufactured by Cortest Instrument Systems, Inc. was used.

In galvanic current measurements, sensors made of the same or different steel are embedded at different depths in the concrete. The small galvanic or macro-cell currents set up by the corrosion process between these sensors are measured typically using a zero resistance ammeter through an external connection. Both systems were used in the studies.

## 3. SENSOR DETAILS

Table 1 summarizes information on the type of sensors used in the four demonstration projects. Three different types of sensors were used. These included one developed by USF researchers, a commercially available one developed by Concorr Inc. and a 'rebar' sensor used by the Florida Department of Transportation (FDOT).

Table 1: Sensors used in demonstration projects [4-7]

Site	Monitoring System	Sensor
Allen Creek Bridge, Clearwater (2003)	Linear polarization	USF
Friendship Trails Bridge, Tampa Bay (2004)	Galvanic current	FDOT
Friendship Trails Bridge, Tampa Bay (2006)	Galvanic current	FDOT
Gandy Bridge, Tampa Bay (2004)	Linear polarization Galvanic current	Commercial FDOT

### 3.1 USF

The USF sensor makes use of the fact that linear polarization is based on perturbation of the corrosion potential rather than its absolute value. Therefore, corrosion resistant metal rods with stable potentials can be used for this purpose. This type of sensor was developed [4] to address possible vandalism concerns for an exposed site on the busy US 19 highway where accessible junction boxes could attract unwelcome attention. The intent was to use a system that eliminated the need for wiring and junction boxes.

This sensor consisted of a length of 0.5 cm diameter Grade 316 stainless rod with a 90° hook at one end. It was embedded in the middle of each of the four pile surfaces, 1.9 cm from the concrete surface. The 90° hook protruded from the concrete surface at the top so that alligator clips could be used to make the necessary electrical connections.

Measurements were initially made by successively treating each of the four stainless rods as the reference or counter electrode, i.e. four sets of readings were taken. An analysis of the results indicated that a single reading was adequate and this was subsequently adopted.

### 3.2 FDOT

The Florida Department of Transportation developed reinforcing steel sensors that were used to monitor the effectiveness of sprayed-zinc sacrificial anodes [8]. The sensors are 5 cm long with an exposed surface area of 13 cm<sup>2</sup>. One end of the sensor has a length of insulated copper wire that is connected to the reinforcement in the pile. The sensor is inserted lengthwise, i.e. parallel to the reinforcement in a 5 cm diameter hole drilled on the concrete surface. The hole is filled with mortar consisting of approximately 50% fresh water and 50% bay water to match the chloride content of the surrounding concrete.

### 3.3 Commercial

A commercial sensor was used for the linear polarization measurement. It uses a modified graphite reference electrode, and a titanium ribbon counter electrode that are encased in a mortar block. It is 6 cm x 6 cm. x 12.5 cm in size. The sensor has cables for direct connection to the steel working electrode and to the PR monitor used for making the measurements.

## 4. INSTALLATION

The sensors were embedded inside the concrete cover, so the ease of installation depended on its size. The USF sensor was the simplest to install because of its small diameter and shallow embedment depth of 1.9 cm. More importantly, no external wiring was required. A grinder was used to create slotted openings on each of the four faces of the pile and the sensor installed (Fig. 1).

The relatively small size of the rebar sensor also made it relatively simple to install. However, because the embedment depth was greater (5 cm), it was necessary to use a hollow core drill to create a 5 cm hole perpendicular to the concrete surface to allow the rebar to be positioned parallel to the main steel and 2.5 cm away from it. Moreover, slots



had to be cut to route the wiring to the junction box where it was permanently connected to the reinforcing steel (Fig. 2).

The commercial probe was the largest and therefore required the greatest effort for installation. To accommodate the large sensor, multiple cored holes were needed (Fig. 2). Additionally, thicker leads meant that deeper slots had to be cut on the pile surface to route it to the junction box.

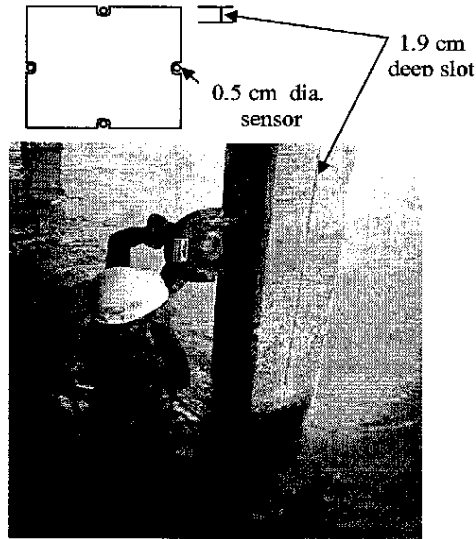


Fig. 1: 1.9 cm deep saw cut for USF sensor.

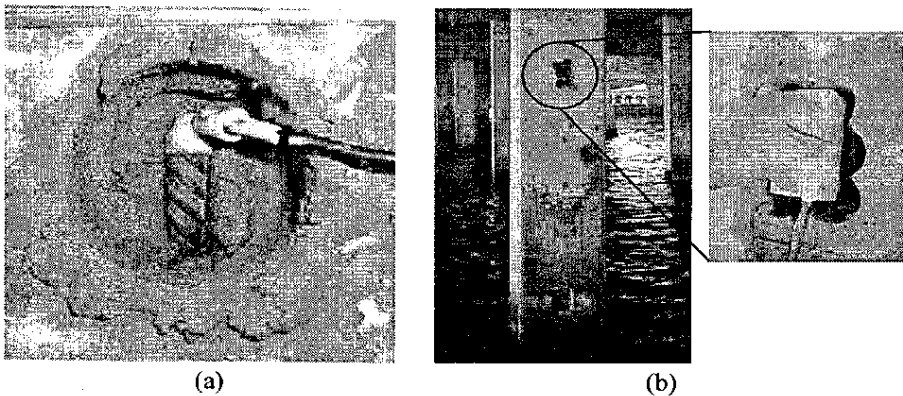


Fig. 2: (a) 5 cm core hole with FDOT rebar sensor; (b) Multiple core holes to accommodate commercial sensor.

As mentioned earlier, the openings made to install the sensors have to be filled with mortar. Since the chloride content around the reinforcement affects the corrosion condition of the steel being monitored, changes in chloride level can affect its corrosion state. For this reason, the mortar was made to match the chloride content of the surrounding concrete by using appropriate quantity of salt water.

#### 4.1 Junction Boxes

Excepting for the USF sensor, junction boxes were required to protect the wiring from corrosion and also to allow data measurements to be performed easily. An electrical connection was first made to the reinforcing or prestressing steel used in the pile. The wires coming out from the rebar sensors were connected to this stainless steel rod inside the junction box. The two cables from the commercial probe were similarly brought into this box. All exposed wiring and cables were inserted in grooves cut on the surface by an electric saw and sealed with hydraulic cement (leak stopper) and epoxy.

### 5. PROCEDURE FOR MEASUREMENT

Since the piles were located in tidal waters, it was necessary to use a boat for access. The PR Monitor was used to take the linear polarization measurements for both the commercial and the USF sensor. The latter required appropriate connections to the working reference and counter electrodes shown schematically in Fig. 3.

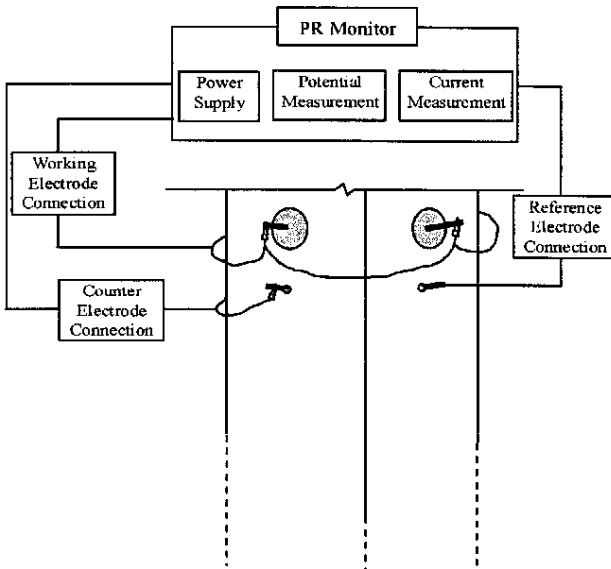


Fig. 3: Schematic drawing showing connections to USF sensor.

The rebar sensors were used to measure the corrosion current. As mentioned earlier, these were permanently connected to the pile reinforcing steel inside the junction box. Two sets of measurements were made; in each case the connection of the sensor to the pile reinforcing steel was temporarily disconnected. The first was made to obtain a measure of the corrosion current in the pile steel. In the second set, the current flow between the two sensors was measured.

## 6. RESULTS

Typical results of the post-wrap corrosion obtained from linear polarization using the USF sensor and the commercial sensor are shown in Fig. 4. Results from the USF sensor (Fig. 4a) indicate that after 900 days the corrosion rates are lower in the wrapped specimens compared to the controls. The performance of carbon and glass were comparable. A similar trend is shown for the commercial sensor though the data is for a shorter time frame. No results for the rebar sensors are included since the measurements indicated that the system had not yet stabilized.

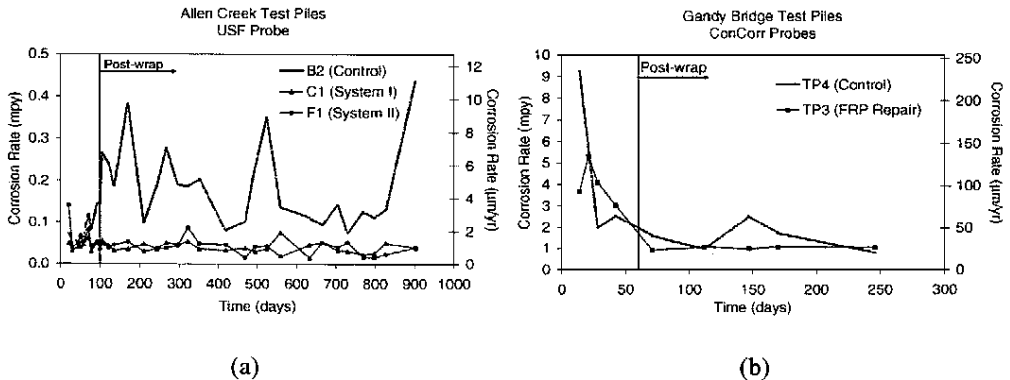


Fig. 4: Representative data for (a) USF corrosion probe, (b) commercial probe.

## 7. DISCUSSION

This paper presents an overview of different types of sensors used to monitor the effectiveness of FRP in corrosion repair of partially submerged piles. From the standpoint of installation, the USF and the FDOT sensors required the least amount of work. The commercial sensor was more difficult to install because of its relatively larger size (Fig. 2). Readings from linear polarization generally take longer. The results from the rebar sensor were inconclusive. However, it has proven effective in other applications [8].

Since calculated corrosion rates are based on an assumed polarized steel area, they may not accurately reflect the true corrosion rate. Moreover, measurements are sensitive to environmental conditions such as temperature and humidity. This may account for the large fluctuations between readings (Fig. 4). Nonetheless, long term trends are discernible that

clearly indicate that the corrosion rate in wrapped piles is lower than that in unwrapped controls and that the performance of carbon and glass were comparable.

## 8. CONCLUSIONS

Long term monitoring of the corrosion performance of piles in aggressive environments poses many problems both in installing the sensors and subsequently in taking the measurements. This paper describes three different sensors (Table 1) that were used to evaluate the post-wrap performance of corroding piles. Linear polarization and galvanic current pre- and post-wrap measurements were taken.

Results from the linear polarization measurements (Fig. 4) indicate that the corrosion rate in wrapped piles is lower than that in unwrapped controls originally in a similar state of disrepair. The results using the rebar sensor were inconclusive. This is most probably because the installation equilibrium state disturbed by the installation of the rebar had not yet been restored.

No further readings are currently being taken because the supporting grants have ended. However, the system is working and it will be possible to resume measurements at a future date when such support is received.

## 9. ACKNOWLEDGMENTS

The studies reported were performed in cooperation and funding from the State of Florida and US Department of Transportation and Hillsborough County. The assistance and guidance of Mr. Jose Garcia and Mr. Steve Womble (both FDOT) is gratefully acknowledged. We thank Mr. Nils Olsson and Ms Mara Nelson (Hillsborough County). The opinions findings and conclusions expressed in this publication are those of the authors and not necessarily those of the Florida or US Department of Transportation.

## 10. REFERENCES

1. Sen, R. 'Advances in the Application of FRP for Repairing Corrosion Damage', *Progress in Structural Engineering and Materials*, **5** (2), 2003, 99-113.
2. Bazinet, S., Cercone, L. and Worth, L. *SAMPE Journal*, **39** (3), 2003, 8-16.
3. Watson, R.J. 'The Use of Composites in the Rehabilitation of Civil Engineering Structures', *ACI SP 215* (Ed. S. Rizkalla and A. Nanni), ACI, Farmington Hills, MI, 2003, 291-302.
4. Mullins, G., Sen, R., Suh, K and Winters, D. 'Underwater FRP Repair of Prestressed Piles in the Allen Creek Bridge'. ASCE, *Journal of Composites for Construction*, **9** (2), 2005, 136-146.
5. Sen, R., Mullins, G., Suh, K. and Winters, D. 'FRP Application in Underwater Repair of Corroded Piles'. *ACI SP 230* (Eds. C. Shield, J. Busel, S. Walkup, D. Gremel), Vol. 2, 2005, 1139-1156.
6. Mullins, G., Sen, R., Suh, K. and Winters, D. 'A Demonstration of Underwater FRP Repair', *Concrete International*, **28** (1), 2006, 1-4.

7. Mullins, G., Sen, R., Winters, D. and Schrader, A. 'Innovative Pile Repair'. Final report submitted to Hillsborough County, 2007, 40 pp.
8. Sagues, A. and Powers, R. 'Field Experience with Rebar Probes to Monitor Performance of Sprayed Zinc Galvanic Anodes on Concrete', in *Techniques to Assess the Corrosion Activity of Steel Reinforced Concrete Structures* (Neal Berke, Edward Escalante, Charles Nmai and David Whiting, Eds.), ASTM, 1996, 173-814.



# Application of FRP composites for underwater piles repair

Rajan Sen <sup>\*</sup>, Gray Mullins

*Department of Civil and Environmental Engineering, University of South Florida Tampa, FL 33620, USA*

Received 15 March 2006; accepted 16 July 2006

Available online 2 February 2007

---

## Abstract

The lightweight, high strength and corrosion resistance of fiber reinforced polymers (FRP) make them ideally suited for quick and effective structural repairs. As a result, they have been favoured for conducting emergency bridge repairs where speed is of essence. The availability of resins that can cure under water has made it possible to similarly extend its application to substructure elements such as partially submerged damaged piles. Such repairs can be carried out using the same strategies that were successfully used in recent demonstration projects in which FRP was used to repair and rehabilitate corrosion-damaged piles. In the projects two disparate FRP systems – a pre-preg and a wet layup – were used and both carbon and glass evaluated. Access to the piles in the deep waters was provided by a custom-designed, lightweight modular scaffolding system that was assembled around the piles. An overview of the project is provided with particular emphasis on changes that would allow its adoption for emergency repairs.

© 2006 Elsevier Ltd. All rights reserved.

*Keywords:* A. Carbon fibre; A. Glass fibres; A. Prepreg; B. Strength

---

## 1. Introduction

Fiber reinforced polymers (FRP) have long been used for the repair and retrofit of concrete structural elements. Their lightweight, high strength and resistance to chemicals offer obvious benefits. In fabric form, they provide unparalleled flexibility. Moreover, as fibers can be oriented in any direction, their use can be optimized. This makes FRP particularly suited for emergency repairs (Fig. 1) where damage can be multi-directional and speed of strength restoration critically important.

The emergence of new adhesives [1] that allow FRP to be bonded to wet concrete surfaces makes it possible to economically conduct emergency repairs on sub-structure elements. Fig. 2 shows impact damage that led to both cross-section loss and breakage of the spiral ties. Conventional repairs will require the cross-section to be enlarged to accommodate new ties. If instead, FRP were used it

would only be necessary to re-form the cross-section and apply bi-directional layers that could restore lost tensile capacity while providing equivalent lateral support to the longitudinal steel. Moreover, the application of a protective UV (ultra-violet) coating on the wrap of the right color will render the repaired pile indistinguishable from other undamaged piles. The aesthetics of FRP repair is one of its unheralded benefits.

The techniques developed recently for underwater FRP corrosion repair of piles [2–4] are equally applicable for repairing other types of damage. This paper distils relevant information from recently completed demonstration projects [5,6] in which two disparate FRP systems were used for repairing corroding reinforced concrete piles. In the projects both carbon and glass were used and the piles instrumented to monitor performance. Additionally, bond tests were carried out after two years to evaluate the residual bond. An overview of the studies is presented with particular emphasis on changes that will be needed for emergency repairs. Recommendations are also made regarding strategies that were found to be the most effective.

---

<sup>\*</sup> Corresponding author. Fax: +1 813 974 2957.

E-mail address: [sen@eng.usf.edu](mailto:sen@eng.usf.edu) (R. Sen).





Fig. 1. Damage to prestressed girder due to vehicular collision (Courtesy A. Alvi).

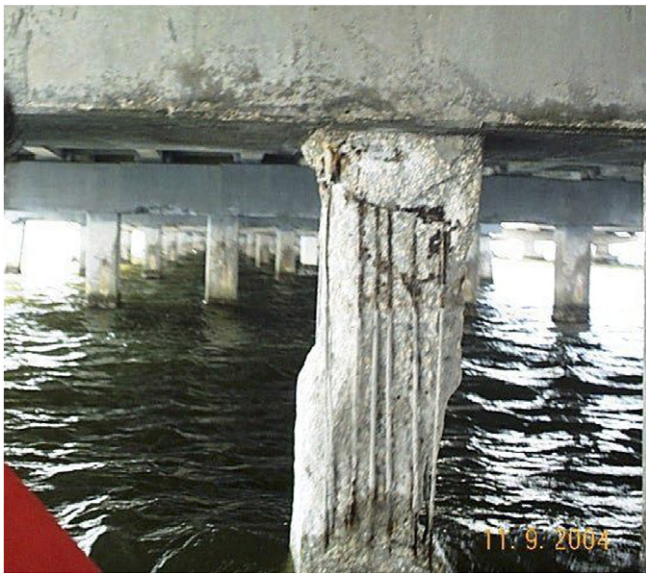


Fig. 2. Damage to pile requiring emergency repair (Courtesy FDOT).

## 2. Problem statement

The application of FRP wrap for underwater repair and rehabilitation of piles is problematic for the following reasons:

1. Surface preparation suitable for dry conditions cannot be directly used for wrapping partially submerged elements. New methods and equipment may be required.
2. All round access to the pile in deep waters poses many logistic problems. Meticulous planning is required and safety issues must be carefully addressed.

Moreover, even if the application is perfect, there may be unexpected bond problems. For example, since the FRP material is a barrier element it can trap moisture that is already inside the pile. Evaporation of this water by heat generated during curing may trigger localized debonding.

While bond is not as critical for applications where the FRP material is wrapped completely around the pile, it can accelerate corrosion in the debonded region.

It is however unrealistic to expect satisfactory resolution of all potential problems given the limited number of field studies that have been completed to date. Some of the solutions that have evolved are described with particular reference to a recently completed field study [5].

## 3. Field demonstration project

The friendship trails bridge, formerly the “old” Gandy Bridge, is one of four bridges spanning Tampa Bay, the most famous being the Sunshine Skyway Bridge. Originally built in 1956, it was scheduled for demolition in 1997 following the construction of the new Gandy Bridge. Instead, it was rehabilitated and converted into a recreational trail that is closed to vehicular traffic.

The 4.2 km (2.6 mile) bridge is supported by 254 piers and 22 columns numbered 1–276 extending east from St. Petersburg in Pinellas County to Tampa in Hillsborough County. Seventy seven percent of the 254 piers have needed to be repaired indicative of a very aggressive environment. As a result, the site provides a rich history of the various attempts made over the years to repair piles.

The piles selected for this study were identified following a detailed survey of the site. Its aim was to locate piles on the Hillsborough side of Tampa Bay (Hillsborough County funded the study) that were in the same general state of disrepair. Piers 99, 100, and 101 were found suitable for this purpose. Pier 99 was a six pile bent while piers 100 and 101 were both four pile bents.

Details of the eight piles selected for the study are summarized in Table 1. Piles are identified by the Pier Number followed by the letter N or S signifying ‘north’ or ‘south’. Six of the eight piles were instrumented. Instrumentation consisted of special rebar probes developed by the Florida Department of Transportation that were installed at two locations along a pile length to provide a measure of the corrosion current. Details on the performance of these probes and results obtained may be found elsewhere [5].

The four piles in Pier 100 were wrapped using a pre-preg system developed by Air Logistics referred to subsequently as System A [7]. Two were wrapped with carbon and two others with glass. The glass wrap required a greater number of layers to compensate for its lower strength. The two piles in Pier 101 were wrapped with a wet layup system developed by Fyfe referred to subsequently as System B [8]. Both piles were wrapped using glass. One of the piles used an experimental zinc mesh sacrificial cathodic protection system. The other was a regular glass wrap.

The wrap length extended to the underside of the pile cap excepting for instrumented piles that were 15 cm (6 in.) shorter to accommodate junction boxes needed for measuring the corrosion current. It extended 45 cm (18 in.) above the high water line and 15 cm (6 in.) below the low water line. The wrap length in non-instrumented

Table 1  
Test pile details

Pier number	Repair system	Specimen type	Pile name	Instrumentation
Pier 99	None	Control	99-N	Yes
	None	Control	99-S	Yes
Pier 100	Aquawrap®	Carbon 1 + 2 layers <sup>a</sup>	100-N	Yes
		Carbon 1 + 2 layers	100-N*	No
		Glass 2 + 4 layers	100-S*	No
		Glass 2 + 4 layers	100-S	Yes
Pier 101	Tyfo® SEH-51A	Glass 2 + 4 layers	101-N	Yes
	Tyfo Zinc Cathodic Protection	Glass 2 + 4 layers	101-S	Yes

<sup>a</sup> Signifies number of layers in the longitudinal and transverse directions respectively.

piles was 1.83 m (6 ft) long. It was 1.68 m (5 ft 6 in.) in instrumented piles.

#### 4. Material properties

**System A:** The Aquawrap® Repair system [7] uses a unique water-activated urethane resin in conjunction with custom woven FRP fabric that can be wrapped around the pile. Because it is water-activated, the FRP material must be pre-impregnated with the resin and sent to the site in hermetically sealed foil pouches. The pouches are opened just prior to application to prevent premature curing by atmospheric moisture. Properties of the uni-directional and bi-directional fibers used as reported by the manufacturer are summarized in Table 2. Note the higher capacity of carbon compared to glass.

**System B:** System B used Tyfo® SEH-51A [8] and was used to wrap two piles in Pier 101. Tyfo® SEH-51A is a custom weave, uni-directional glass fabric that is normally used with Tyfo-S Epoxy. However, for the underwater application, Tyfo® SW-1 underwater epoxy was used. The epoxy was mixed at the site and the FRP fabric impregnated just prior to use. Properties of materials as provided by the manufacturer are summarized in Table 3.

Table 2  
Properties of Aquawrap® fabrics [7]

Fibers	Tensile strength (ksi)	Tensile modulus (ksi)	Load per ply (lb/in.)
Uni-directional glass fiber	85	5200	2400
Bi-directional glass fiber	47	3000	1200
Uni-directional carbon fiber	120	11,000	3400
Bi-directional carbon fiber	85	3200	2400

1 ksi = 6.895 MPa; 1 lb/in. = 1.75 N/cm.

Table 3  
Properties of Tyfo® SEH-51 composite [8]

Properties	Quantities
Tensile strength	3.3 k/in.
Tensile modulus	3030 ksi

1 ksi = 6.895 MPa; 1 lb/in. = 1.75 N/cm.

#### 5. Composite jacket design

The FRP wrap must restore the lost axial, bending and shear capacity due to damage, e.g. corrosion, impact, fire etc. Available ACI [9] and ISIS [10] guidelines provide design equations and worked out numerical examples. Design manuals for specific systems are also available, e.g. Fyfe Co., [11]. The provisions in all the guides are comparable though equations are more simplified for the proprietary systems. However, axial, flexural and shear strengthening are considered independently; their interaction, necessary for designing pile wraps, is not considered.

The low strain capacity of the FRP makes the maximum permissible strain, the critical parameter in design. For strengthening applications, ACI 440 guidelines [9] specifies strain limits for both “contact-critical” (FRP in intimate contact with the substrate with no specific adhesion requirement) and “bond-critical” (minimum adhesion required since load transfer is by bond) applications. For piles, the limit for contact-critical application applies as the FRP material is wrapped completely around the circumference. This is set as the lower of 0.4% or 75% of the FRP design rupture strain. The latter limit was established from tests to avoid loss of aggregate interlock that can occur at strains below the ultimate fiber strain.

As piles corrode, they expand in the lateral direction since the volume of the corrosion products can be as much 600% of the original steel [12]. To accommodate such a large potentially uniform increase, a lower maximum strain limit may be appropriate. This can be based on experimental data [13] or from other considerations.

A strain limit of 0.1% – approximately three times the maximum tensile strain leading to cracking – was selected for designing the FRP to withstand corrosion expansion [5,6]. This value was used since reported experimental strains, calculated from the total circumferential increase,

tend to be on the high side because it includes unrestrained movement of the crack.

Interaction diagrams can be developed for FRP strengthening, as for reinforced concrete columns, by using strain compatibility analysis [14]. The only difference is that the equations incorporate the contribution of the FRP. Since FRP wrapping can provide increased tensile but limited compressive strength increase, only the tensile contribution was incorporated in the analysis. Also, as the confinement effect of concrete leads to modest increases in the ultimate axial capacity in non-circular sections, it was ignored. As with most strengthening applications, the role of the FRP is passive. That is, the FRP is unstressed except for additional load applied to the structure after it has been retrofitted.

Fig. 3 shows a typical interaction diagram for the design of the wrap used for underwater corrosion repair. In the applications, capacity loss was estimated to be 20%. It

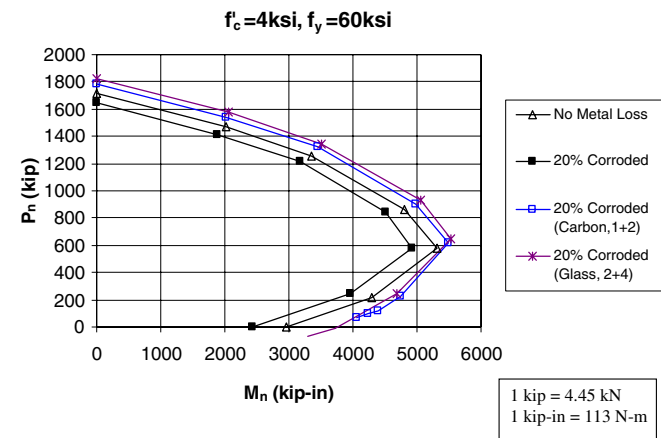


Fig. 3. Interaction diagram for corrosion repair of piles.

was found that this could be restored by using two transverse and one longitudinal carbon layer for the material properties outlined in Table 2. For the weaker glass, two longitudinal and four transverse layers were required to restore full capacity [6].

## 6. Access to piles

All around access to the pile is needed to allow the FRP material to be wrapped around the circumference expeditiously. In shallow waters, access is not a problem and ladders can be used. For deeper waters, a boat may be used to wrap the pile above water while divers can wrap the submerged region (Fig. 4). This solution can be economical where repairs are to be carried out on a single isolated pile.

In the field demonstration study however, several piles in the same bent were wrapped. For this case, a scaffolding system was more suitable since it allowed ready access to all the piles. The scaffold was built using 19 mm (3/4 in.) #9 expanded steel mesh on a 5 cm × 5 cm × 0.6 cm (2 in. × 2 in. × 1/4 in.) steel angle framework. The stiff but lightweight mesh helped minimize the forces from wave action while providing a secure working surface. Its modular design meant it could be placed around one or more piles depending on the application. Each framework consisted of two half-sections with cut-outs sized for the specific pile.

The four-part platform was 10 m (33 ft) long and 2.13 m (7 ft) wide when fully assembled. Advantage was taken of the overhead pile cap to suspend the scaffold at an appropriate elevation. In this case it was 2.74 m (9 ft) from the pile cap to allow piles to be wrapped over a 1.83 m (6 ft) length starting from the underside of the cap. Wood railing



Fig. 4. Underwater repair using a boat and divers (Courtesy: Air Logistics).



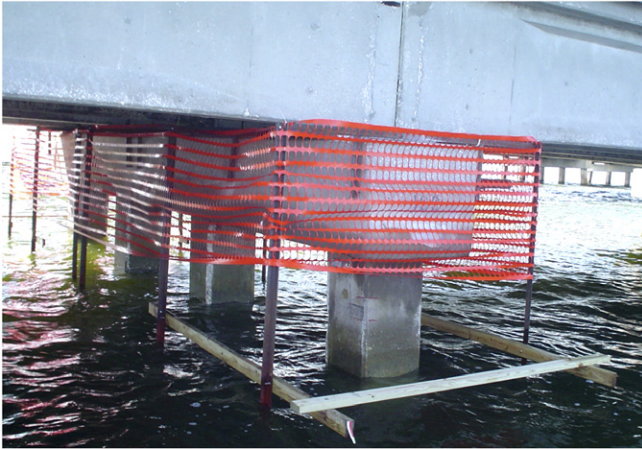


Fig. 5. Scaffolding system suspended from pile cap.

was bolted to the steel angles to delineate the extent of the underwater platform (Fig. 5).

### 7. Surface preparation

Surface preparation for contact-critical applications is defined as providing “continuous, intimate contact” [9] between the concrete substrate and the FRP material. In a marine environment this implies removal of all marine growth. As for dry conditions, depressions and voids on the concrete surface have to be patched using suitable material that is compatible with the concrete substrate. If there are corners, they need to be ground to a minimum of 19 mm (3/4 in.) [9] radius to avoid stress concentration in the wrapping material.

In case of emergency repairs, it may be necessary to reform the concrete section. Advantage should be taken to insert appropriate cut-outs with the required radius inside the form so that the corners of the formed surface are automatically rounded. Otherwise, the sharp corners would have to be ground to the required 19 mm (3/4 in.) radius. This approach was successfully used in a recently completed study [6] that investigated the effectiveness of FRP in corrosion mitigation application for new specimens. Fig. 6 shows one of the wood trim cut-outs placed inside the form of the prestressing bed prior to concreting.

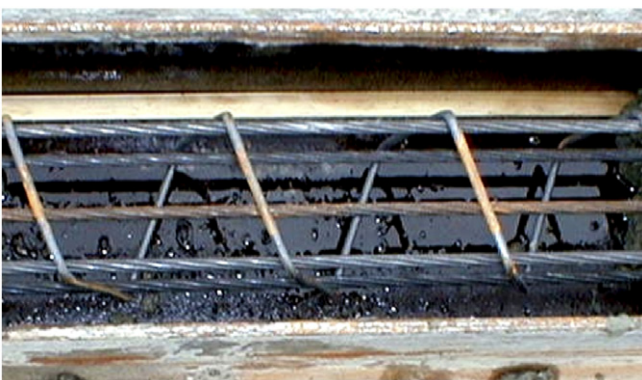


Fig. 6. Curved wood trim inserts at corners.

In the demonstration project, there was significant marine growth at the water line that was removed with a scraper prior to wrapping. Projecting parts of the concrete surface were chipped using a hammer and chisel. All four corners were chamfered and ground to a 19 mm (3/4 in.) radius using an underwater pneumatic grinder. To provide a smooth surface, quick setting hydraulic cement was used to fill surface voids. Finally, all surfaces were pressure washed using fresh water to remove all dust, debris, and remaining marine growth just prior to wrapping.

### 8. Pre-preg system

The pre-preg system was used for wrapping four piles in Pier 100. The two piles at the north end were wrapped using one layer of unidirectional carbon fiber and two layers of bi-directional carbon fibers. The two piles in the south end of the same pier were wrapped using two layers of unidirectional glass fibers and four layers of bi-directional glass fibers. As this was a pre-preg, all FRP material was pre-saturated in a factory and sent to the site in hermetically sealed pouches. The FRP material was removed from the packet just prior to the wrap, unrolled and was ready to be applied to the prepared surface.

Wrapping commenced from the pile top or 15 cm (6 in.) below the underside of the pile cap for the instrumented piles located in the north and south ends because of the presence of the junction box. The longitudinal layer was placed vertically followed by two transverse layers that were spirally wrapped around the pile without overlap (Fig. 7). In case of glass, this sequence was repeated since two longitudinal layers and four transverse layers were needed to provide the same strength.

A 25 cm (10 in.) wide glass fiber veil with a 5 cm (2 in.) overlap was used to consolidate the wrap and provide a better finish. This was covered by plastic stretch film to keep the wrap in place as it cured. On an average it took less than one hour to wrap a pile.

The FRP was allowed to cure for one day. After removal of the stretch film, all wrapped piles were painted



Fig. 7. Applying second transverse CFRP layer.

over the veil using the same base primer to provide protection against UV radiation.

**9. Wet layup system**

The Tyfo® SEH-51A composite system was used to wrap piles 101N and 101S. The original plan was to use two different epoxies one for the submerged region and the other for the dry region in the pile. This scheme was tried on pile 101N. However, because of wave action, the dry region was not dry and resulted in observable poor bond between the FRP and the pile. This wrap was later removed. As a result, the same underwater epoxy Tyfo® SW-1 was used for both piles along with Tyfo® SEH-51A fiberglass fabric.

Unlike System A that was a ‘pre-preg’, in System B the fibers had to be impregnated with resin on-site. This gave greater flexibility since wrap lengths could be adjusted but posed greater logistic problems since impregnation had to be done on-site in a timely manner. This required careful planning and system redundancies to avoid unexpected problems arising from equipment malfunction.

The FRP fabric for pile 101S was impregnated by hand. For pile 101N re-wrapped three months later, a resin impregnator was used (Fig. 8). Following the saturation of the FRP, the wrapping procedure was identical to that for System A. Complete details may be found in the final report [5].



Fig. 8. On-site saturation of fiberglass fabric.

**10. Bond tests**

For contact-critical applications there is a requirement for intimate contact but no specific requirement for adhesion of the FRP to the concrete substrate [9]. Nonetheless, on-site pullout tests were conducted to evaluate the FRP-concrete bond two years after the wrapping had been completed. An Elcometer106 adhesion tester and a 3.7 cm (1.456 in.) diameter dolly was used to evaluate the FRP/concrete bond. Two System A wrapped piles 100-N\* (carbon) and 100-S\* (glass), and one System B wrapped pile 101-N were selected. The tests were conducted on two faces per pile at two different levels – in the dry and the tidal region.

FRP witness panels created during the wrap on the east and west faces of the piles were used in the testing. Bond tests were carried out in accordance with established procedure. The FRP surface was scored using a 4.4 cm (1 3/4 in.) diameter diamond core drill. The surfaces of the scored FRP were cleaned using coarse sand paper and dust removed. Fast curing epoxy (Power-Fast+) manufactured by Powers Fasteners, Inc. was used for bonding the dollies to the FRP. This took 15 min to dry and cured in 24 h. It can provide maximum bond strength of 20 MPa (3000 psi.).

Table 4 and Fig. 9 summarize the results of the pullout tests. The bond of FRP to the concrete substrate was found to be poor. Most of the wet layup wrapped piles showed epoxy failures where the dolly separated from the concrete at its interface (Fig. 10). All tests conducted on the pre-preg system were inter-layer failures (Fig. 11) indicating that the bond between the FRP layers was poorer than its bond to concrete.

Inspection of Table 4 shows that the bond from System B performed better in the wet region while System A was better for the dry region. Similar differences were not observed on laboratory specimens tested [6]. Therefore, the problem with bond can be attributed to the field techniques used for wrapping. On-going research is developing a new protocol to prevent such inconsistency.

Table 4  
Summary of bond test result (unit: psi)

Name	Type	Face	Top	Bottom
#100-N*	Carbon AirLogistics	East	145.0 (layer)	58.0 (layer)
		West	116.0 (layer)	0.0 (layer)
		Average	130.5	29.0
#100-S*	Glass AirLogistics	East	0.0 (layer)	0.0 (layer)
		West	0.0 (layer)	0.0 (layer)
		Average	0.0	0.0
#101-N	Glass Fyfe	East	101.5 (epoxy)	58.0 (epoxy)
		West	29.0 (epoxy)	260.9 (concrete)
		Average	65.2	159.5

1 MPa = 145 psi.



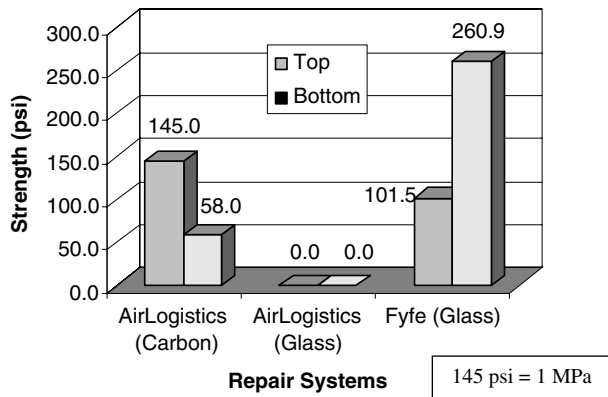


Fig. 9. Maximum residual bond strength after 2 years.

## 11. Discussion

This paper provides an overview of a demonstration project that explored the feasibility of using FRP to repair corroded reinforced piles in the tidal waters of Tampa Bay. In the study, two contrasting FRP systems were used and two different materials evaluated. Additionally, long term bond was also evaluated from on-site bond tests that were conducted two years after the wrap had been applied.

Of the two systems, the pre-preg was unquestionably the easier to use. The alternative wet layup system offered greater flexibility but required on-site saturation of the resin that requires much greater preparation. Though bond

is not a requirement for contact-critical applications, the results from the bond tests showed that the wet layup system performed better particularly in the partially wet and submerged regions. The water-activated pre-preg system performed better in the dry regions.

While the demonstration project was for corrosion repair, the FRP system can be readily adapted for emergency repair. A combination of a boat and divers would allow the wrap to be easily conducted in both the dry and the submerged regions. However, a customized scaffolding system may be better since it can eliminate uncertainty associated with underwater currents and changing weather conditions that can complicate the wrapping operation. The light weight modular scaffolding systems used in the demonstration project can be readily and inexpensively fabricated. They were assembled around the pile and conveniently suspended from the pile cap. Its height was adjusted so that the walk way was below the lowest wrapping depth. In a second demonstration study, steel chains rather than angles were used to support the scaffold from the pile cap since it was deemed to be more convenient for the application [6].

The wrapping operation for the corrosion repairs was carried out at low tide. In case of emergency repairs, an adjustable scaffolding system can be designed to accommodate changing tides. Should repairs be carried out much below the water line, divers would also be needed. The economics of wrapping will require contractors to devise

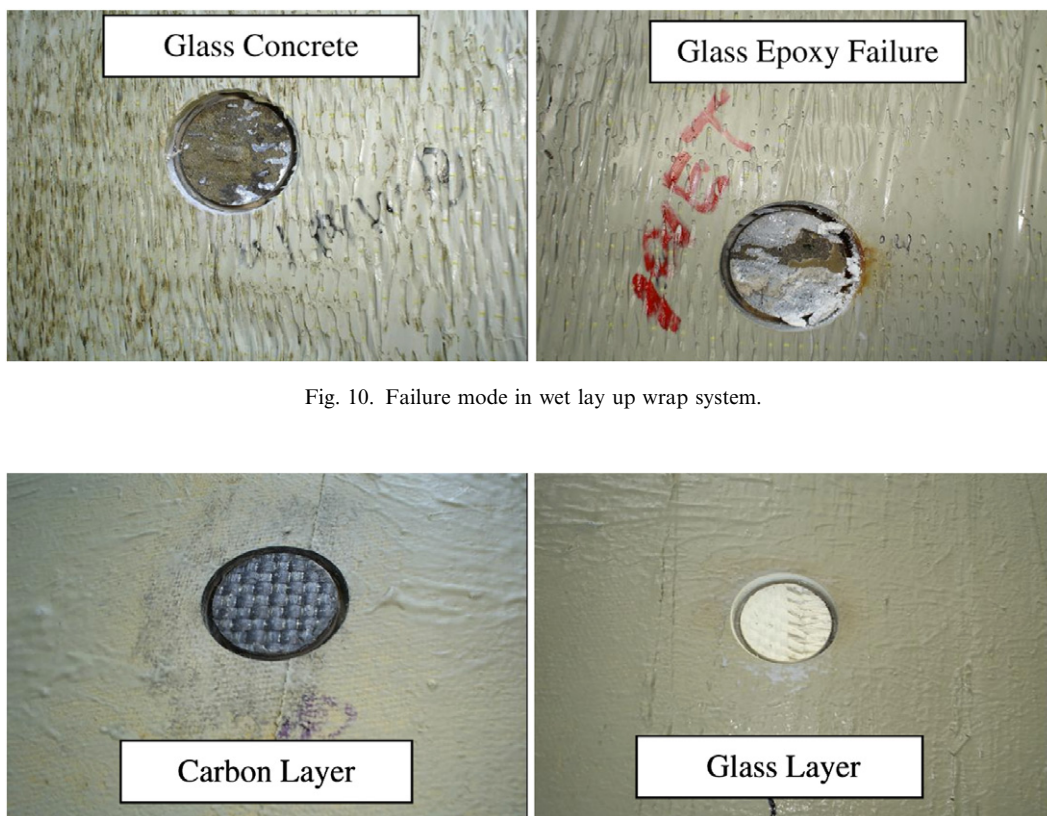


Fig. 10. Failure mode in wet lay up wrap system.

Fig. 11. Failure mode in pre-preg wrap system.



appropriate re-usable, modular, systems that can be used in a number of alternative applications.

The damage to the section needs to be repaired using low shrinkage materials compatible with concrete. Should the section be reformed, appropriate inserts should be used at the corners (Fig. 6). This will greatly reduce the surface preparation work needed to round the edges since sharp corners introduce stress concentrations that cannot be taken by thin FRP material.

Estimate of material cost for wrapping the piles was provided for both systems. This did not include the cost of mobilization or installing the system. Costs expressed per linear m (ft) of the 50 cm (20 in.) square piles ranged from \$670/m (\$204/ft) for glass to \$885/m (\$270/ft) for carbon. These costs compare favourably with alternative repair systems [5,6].

## 12. Conclusions

The use of FRP for repairing partially submerged concrete elements is relatively new. All applications reported to date relate to corrosion repair. However, given the lightweight, high strength and corrosion resistance of the FRP it is just as suitable for conducting cost-effective emergency repairs. The procedures described in this paper that were used for corrosion repair can be readily adapted for repair of piles damaged otherwise.

Based on the experience gained from the demonstration studies, the following recommendations are made:

1. Speed is of essence in emergency repairs. All around access to piles needed for the wrapping operation is best provided by using scaffolding systems that can be suspended from the pile cap. Should repairs be required significantly below the water line, divers may be needed for wrapping below the water line. If possible, operations should be scheduled for low tide.
2. The FRP wrap should be engineered to provide the required strength. Interaction diagrams need to be developed to allow the combined effect of axial and bending capacity to be considered. The design should seek to keep the number of FRP layers to a minimum. For this reason, bi-directional material should be preferred over uni-directional material and carbon over glass.
3. Both pre-pregs and on-site saturated FRP systems can be used. However, if repairs have to be carried out at very short notice, on-site saturation systems may be the more suitable.
4. If the section is to be re-formed, styrofoam or wood inserts with a curved profile should be placed in the corners so that surface preparation work is minimized and overall costs reduced.

The methods described in the paper were refined and improved with each new application. This will undoubtedly be the case for emergency repairs where similar improvements may be expected. The possibility of using FRP may provide highway authorities with a cost-effective alternative to conventional repair of damaged piles.

## Acknowledgements

The authors gratefully acknowledge the financial support of Hillsborough County who funded the study. The cooperation of the Florida Department of Transportation, State Materials Office, Air Logistics and Fyfe are likewise acknowledged. Special thanks to graduate students K.S. Suh and D. Winters for their contribution in the studies.

## References

- [1] Bazinet S, Cereone L, Worth F. Composite FRP moves into underwater repair applications. *SAMPE J* 2003;39(3):8–16.
- [2] Mullins G, Sen R, Suh K, Winters D. Underwater FRP repair of prestressed piles in the Allen Creek Bridge in the city of clearwater. *ASCE, J Composites Constr* 2005;9(2):136–46.
- [3] Sen R, Mullins G, Suh KS, Winters D. FRP application in underwater repair of corroded piles. In: Shield C, Busel J, Walkup S, Gremel D, editors. *ACI SP 230*, vol. 2. p. 1139–56.
- [4] Mullins G, Sen R, Suh K, Winters D. A demonstration of underwater FRP repair. *Concrete Inter* 2006;28(1):1–4.
- [5] Mullins G, Sen R, Suh KS, Winters D. Underwater FRP pile wrap of the friendship trails bridge, final report submitted to Hillsborough County, FL, June, 2004. p. 32.
- [6] Suh KS, Mullins G, Sen R, Winters D. Use of FRP for corrosion strengthening applications in a marine environment, final report submitted to Florida Department of Transportation, Tallahassee, FL, October 2005, p. 406.
- [7] Air Logistics Corporation. (no date) Aquawrap Repair System, Pasadena, CA.
- [8] Fyfe Co. LLC, <http://www.fyfeco.com/>.
- [9] ACI 440.2R-02. Guide for the design and construction of externally bonded FRP systems for strengthening concrete structures. ACI, Farmington Hills, MI, 2002.
- [10] ISIS Canada. Strengthening reinforced concrete structures with externally-bonded fibre reinforced polymers, *Design Manual*, 2001.
- [11] Fyfe Co. LLC. Design manual for the Tyfo fiberwrap systems, San Diego, CA, 2005.
- [12] Mehta P, Monteiro P. *Concrete*. 2nd ed. Englewood Cliffs, NJ: Prentice-Hall; 1993, p. 162.
- [13] Mullins G, Sen R, Suh KS, Goulsh A, Torres-Acosta A. Evaluation of transverse strain in corroding square prestressed concrete elements. In: *Proceedings of the 47th international SAMPE symposium and exhibition-science of advanced materials and process engineering series*, vol. 47, Long Beach, CA, May 12–16. Society for the Advancement of Material and Process Engineering, p. 955–63, 2002.
- [14] MacGregor J, Wight J. *Reinforced concrete: mechanics and design*. 4th ed. Upper Saddle River, NJ: Prentice-Hall; 2005.

*COMPOSITES & POLYCON 2007*  
*American Composites Manufacturers Association*  
*October 17-19, 2007*  
*Tampa, FL*

## **Further Developments in Underwater FRP Pile Repair**

Rajan Sen and Gray Mullins  
 Department of Civil and Environmental Engineering  
 USF Tampa FL 33620-5350

### **Abstract**

Over the past five years, the University of South Florida (USF) has completed several field demonstration projects in which corroding piles in tidal waters were repaired using FRP without cofferdam construction. The goal of the research has been to develop an alternative cost effective FRP pile repair system. This paper provides a brief overview of the advances made in this direction with particular reference to four completed projects and an on-going study.

### **Introduction**

Fiber reinforced polymers (FRP) have been used for the repair and rehabilitation of highway structures as far back as 1977<sup>1</sup>. In a majority of the applications, the FRP material was applied to dry surfaces under dry conditions. However, recent advances in resin technology have made it possible to use FRP for underwater repair. This has led to demonstration studies in which FRP was used to repair partially submerged piles in tidal waters<sup>2</sup>.

The lightweight, high strength and corrosion resistance of FRP offer obvious advantages for infrastructure repair. These advantages also apply to underwater repair where FRP may be expected to be equally effective in the future. But this will require development of new techniques and equipment to simplify construction and expedite the repair process.

USF has been exploring the application of FRP for corrosion repair for several years. Initially, laboratory studies were conducted to evaluate the role of FRP in corrosion repair<sup>3,4</sup> of piles in tidal waters. Subsequently, field demonstration projects were conducted at contrasting sites<sup>5-7</sup>. These locations were specially selected by the Florida Department of Transportation because of the aggressiveness of the environment. This was subsequently confirmed by chloride analysis of

concrete cores taken from several repaired piles. In general, the chloride content at the level of the reinforcement exceeded the threshold required for corrosion initiation.

The field demonstration projects undertaken may be conveniently classified as belonging to three distinct phases. In the first phase, completed in 2005, the focus was primarily on the feasibility of repairing partially submerged piles with FRP. The second phase, completed the following year, focused on improving the FRP-concrete bond by adapting vacuum bagging and pressure bagging techniques widely used by the composites industry. The third phase is on-going and is intended to develop an economical sacrificial cathodic protection system that can be integrated within the wrap. If the proposed system is proven to be effective, highway authorities will have access to a cost competitive alternative to available jacketing repair methods.

### **Materials**

Two types of materials were used in all the repairs. One was a pre-preg, the other a wet lay up. The former uses a special, water-activated urethane resin. For this reason, the FRP material is cut to size, resin-saturated in the factory and shipped to the site in hermetically sealed pouches where it is opened just prior to the application. The wet lay up system is epoxy based and requires on-site impregnation. An additional wet lay up system was also used but this repair was carried out under dry conditions inside a cofferdam. For this reason, it is not discussed in here. Both carbon and fiberglass were used which resulted in similar corrosion rate reductions. Material properties of the fiber and resin as provided by the suppliers are summarized in Tables 1-2<sup>8,9</sup>.

### **Phase I - Technology Transfer**

The first phase commenced in late 2002 when preparations were made to conduct the first pile repair. The site for this demonstration was Allen Creek Bridge, Clearwater, FL (Fig. 1). Located on the busy US 19, it was selected primarily because it is in shallow, relatively calm waters. The remaining two studies conducted in this phase were on piles supporting Gandy Boulevard bridges spanning Tampa Bay, the largest estuary in Florida. The first of these two bridges is the Friendship Trails Bridge, now a recreational trail for pedestrians and cyclists. The second is the Gandy Bridge that is adjacent to the Friendship Trails Bridge. These bridges vary in age from 20 to 50 years old and consequently have different levels of distress. The oldest has over 90% of the 275 piers with either repairs or need of repairs. The newer, has less than 10% incidence of distressed piers. The waters of Tampa Bay in that area are deeper and more turbulent than those of Allen Creek Bridge and the site is

more representative of conditions where pile repairs are carried out in practice.

No particular difficulties were associated with any of the repairs. In all cases, selected piles were instrumented to allow long term performance of the FRP wrap to be monitored. Detailed descriptions of these repairs are given elsewhere<sup>5-7</sup>. The field application clearly demonstrated the feasibility of conducting repairs on corroding piles without the use of cofferdam construction.

The main contributions from this phase were in three areas (1) instrumentation (2) design and (3) access systems. These are briefly described below:

### Instrumentation

A new linear polarization based instrumentation system was developed which eliminated the need for wiring and junction boxes. The system used stainless steel rods that were embedded close to the pile surface on each face (Fig. 2). These rods served successively as the reference and counter electrodes in the linear polarization measurements. Because the rods had 90 degree protruding hooks at one end, there was no need for wiring. Alligator clips could be used to make the necessary connections to the steel bars (reference and counter electrodes) and also to the working electrodes (steel reinforcement in concrete) as shown in Fig. 3. This system is inexpensive and can be used with available systems to monitor long term performance. Field measurements confirmed laboratory findings and showed that corrosion rates were lower in wrapped piles compared to unwrapped controls that were in a similar state of disrepair originally. Performance of carbon and glass were comparable.

### Design

For an FRP system to be cost effective, it must be engineered so that factors of safety are consistent with those used in traditional engineering practice. Design determines the fiber architecture in the longitudinal (for strength) and transverse (for confinement) directions and the number of layers needed.

A simple design method was developed in which the disparate requirements for strength and expansion were uncoupled. In essence, FRP was designed for strength from strain compatibility considerations using interaction diagrams (as in column design). The lateral expansion capacity of the strengthening provided was then checked to ensure that it could accommodate a lateral expansion set at 0.1%. Comparison with alternative design procedures showed that the proposed

method was more economical and resulted in fewer FRP layers<sup>10</sup>.

### Access

All-around access to piles is crucial during wrapping. In the first demonstration project in shallow waters, ladders were sufficient. But in all subsequent repairs conducted in the middle of Tampa Bay, access was provided by scaffolding. A lightweight, modular scaffolding system was designed that was assembled around the pile and suspended from the pile cap using angles or chains. The lightweight permitted the scaffolding to be readily moved between piles within a group (Fig. 4).

## Phase II – Improving FRP-Concrete Bond

Laboratory studies have shown that the success of FRP in slowing down corrosion rates is contingent on the integrity of the FRP-concrete bond<sup>11-12</sup>. Where bond was intact, good performance is assured. Where bond was poor, there was evidence of localized corrosion.

In-situ pullout tests were conducted in accordance with ASTM D4541 to assess the FRP-concrete bond in selected specimens that were repaired in Phase I. Fig. 5 shows results from the bond test. Inspection of Fig. 5 shows that the bond was variable even though the same surface preparation and application method was used for the two systems. For the water-activated resin system, bond was poorer in the wet (bottom) locations; for the epoxy systems it was poorer in the dry (top) regions.

Usually, poor bond is attributed to improper surface preparation. But since surface preparation was not a factor, this variability is believed to be due to the adverse effect of self-weight of the saturated FRP in a vertical configuration. In this situation, the self weight of the wet wrap tends to make it pull away and/or slide down the pile surface. This is prevented by a plastic wrap that is wound tightly around the pile. The variability in the measured pullout resistance indicates that the effective pressure applied was not only variable (due to buoyancy and other effects) but also insufficient to generate adequate frictional resistance to counteract self-weight.

To solve this problem, laboratory studies were undertaken using full-size pile specimens in which vacuum bagging and pressure bagging systems were evaluated<sup>13</sup>. Both systems were made to work. However, vacuum bagging proved to be more problematic because of the difficulty in ensuring an airtight seal along the wrap boundary in cracked piles. Pressure bagging did not

pose a similar problem and was therefore selected for the field application.

A prototype pressure bagging system was developed and was implemented in the most recent field trials that were completed in late 2006. In the application, two piles using the two different resin systems were wrapped. Fig. 6 shows a photograph of one of the repaired piles with the inflated pressure bag in place. The air pressure was kept at 14.5 kPa (300 psf). This was determined from the laboratory tests conducted. While no pullout tests have yet been carried out, results based on visual inspection and acoustic testing suggest that the FRP-concrete bond was excellent.

### Phase III – Incorporating Cathodic Protection

The first two phases helped ensure that the quality of the FRP repair was consistent with that achievable in the laboratory. Nonetheless, as FRP serves simply as a barrier element it cannot stop electrochemical reactions caused by deleterious elements such as chlorides, moisture and oxygen present inside the wrap from continuing. Cathodic protection is the only proven method for stopping corrosion.

A new study that was just funded will explore the possibility of integrating a sacrificial cathodic protection system within the FRP wrap. The study is in its preliminary phase but the design of the system is expected to be completed by the end of the year. Field implementation will be carried out the following year. The performance of the cathodic protection will be monitored over the next several months.

### Discussion

Steady progress has been made in advancing the state-of-the-art for FRP underwater pile repair. The demonstration projects completed to date have identified and solved several of the technical and logistic problems encountered or anticipated for the field wrap. These have been in these four areas: (1) instrumentation and monitoring (2) design (3) access and (4) new techniques for improving the underwater FRP-concrete bond.

Progress to date clearly shows that FRP systems are viable and can be used for repairing piles in tidal waters. On-going research on a sacrificial cathodic protection system will further strengthen the case for using FRP.

### Conclusions

The extension of FRP for the repair of corroding pile in tidal waters has proven to be simpler than was anticipated. After four demonstration projects, the major

ingredients for successful technology transfer are in place: a design method that allows an economical fiber layout to be selected; a pressure bagging system that ensures consistent bond between FRP and concrete; a modular scaffolding system that allows all-around access to piles. Other developments will allow steel to be cathodically protected thereby reducing the demand for the more expensive FRP material and extending the life of the repair.

Based on our experience, it is clear that it is feasible to use FRP for underwater corrosion repair. The performance of the FRP in slowing down the corrosion rate appears to be comparable to that determined from laboratory testing. The repairs have held up well with the longest over four years at this time.

Overall, the portents are promising and hopefully will culminate in the availability of a cost effective long-term or short-term solution for repairing piles that is acceptable to highway authorities worldwide.

### Acknowledgements

The demonstration studies reported were funded by the Florida/US Department of Transportation and Hillsborough County. The support and guidance of Mr. Pepe Garcia and Mr. Steve Womble, both from Florida Department of Transportation are gratefully acknowledged. We thank Ms. Mara Nelson, and Mr. Nils Olsson of Hillsborough County for their contribution. FRP materials used were donated by Air Logistics, Corporation and Fyfe & Co LLC. We are also indebted to SDR Engineering, Tallahassee for their contribution to this research. This study could not have been accomplished without the assistance of numerous former and current graduate students at USF.

### References

1. Ohta, T., Sakai, K., Obi, M. & Ono, S. (1992). Deterioration in a rehabilitated prestressed concrete bridge. *ACI Materials Journal*, 1992:89(4):328-336.
2. Sen, R. (2003). "Advances in the application of FRP for repairing corrosion damage", *Progress in Structural Engineering and Materials*, Vol. 5, No 2, pp. 99-113.
3. Mullins, G., Sen, R., Torres-Acosta, Goulis, A., Suh, K., Pai, N. and Mehrani, A. (2001). Load capacity of corroded pile bents. Final report submitted to the Florida Department of Transportation, September, 327 pp.
4. Mullins, G., Sen, R., Suh, K.S. and Winters, D. (2005). "Use of FRP for corrosion mitigation application in a marine environment". Final report

submitted to Florida / US Department of Transportation, Tallahassee, FL, Oct., 406 pp.

5. Mullins, G., Sen, R., Suh, K. and Winters, D. (2006). "A demonstration of underwater FRP repair" *Concrete International*, Vol. 28, No. 1, pp1-4.
6. Mullins, G., Sen, R., Suh, K and Winters, D. (2005). "Underwater FRP repair of prestressed piles in the Allen Creek Bridge". ASCE, *Journal of Composites for Construction*, Vol. 9, Issue 2, pp. 136-146.
7. Sen, R., Mullins, G., Suh, K. S. and Winters, D. (2005). "FRP application in underwater repair of corroded piles". ACI SP 230 (Eds. C. Shield, J. Busel, S. Walkup, D. Gremel), Vol. 2, pp 1139-1156.
8. Air Logistics Corporation (2002). Aquawrap Repair System, Pasadena, CA.
9. Fyfo Co. LLC, <http://www.fyfeco.com/>
10. Sen, R., Mullins, G. and Shahawy, M. (2007). "FRP repair and strengthening of structurally deficient piles". To appear in *Journal of Transportation Research Board*.
11. Baiyasi, M. & Harichandran, R. (2001). Corrosion and wrap strains in concrete bridge columns repaired with FRP wraps. Paper No 01-2609, 80<sup>th</sup> Annual Meeting, Transportation Research Board, Washington, DC.
12. Berver, E., Jirsa, J., Fowler, D., Wheat, H. and Moon, T. (2001). "Effects of wrapping chloride contaminated concrete with fiber reinforced plastics", FHWA/TX-03/1774-2, University of Texas, Austin, October.
13. Mullins, G., Sen, R., Winters, D. and Schrader, A. (2007). 'Innovative pile repair', Final report, Hillsborough County, pp. 40.

**Table - 1** Properties of Pre-Preg Fabrics

Fibers	Tensile Strength (MPa)	Tensile Modulus (GPa)	Load per Ply (kN/m)
Uni-directional (GFRP)	590	36	420
Bi-directional (GFRP)	320	21	210
Uni-directional (CFRP)	830	76	596
Bi-directional (CFRP)	590	22	420

**Table - 2.** Properties of Wet lay Up Composite

Properties	Quantities
Tensile Strength	3.24 GPa
Tensile Modulus	72.4 GPa
Ultimate Elongation	4.5 %
Laminate Thickness	0.127 cm
Dry fiber weight per sq. yd.	915 g/m <sup>2</sup>
Dry fiber thickness	0.038 cm



**Figure – 1.** Allen Creek Bridge piles



**Figure – 2.** Embedded stainless steel electrode





Figure – 3. Linear polarization connections



Figure - 6. Pressure bag securing FRP while curing



Figure – 4. Scaffold system for deep water access

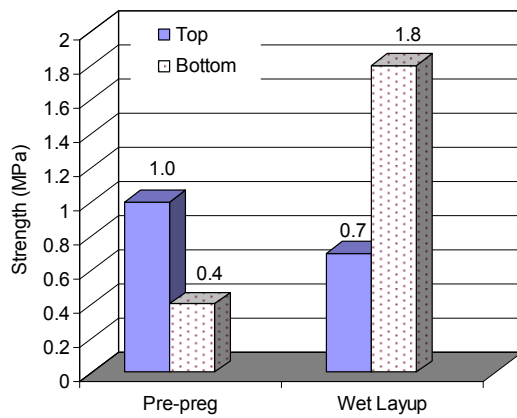


Figure – 5. Variability in bond



## INVERSE METHOD FOR THE DETECTION OF VOIDS IN DRILLED-SHAFT CONCRETE PILES FROM LONGITUDINAL TEMPERATURE SCANS

**S. C. Kranc**

*Department of Civil and Environmental  
 Engineering  
 University of South Florida  
 Tampa, Florida, USA  
 kranc@eng.usf.edu*

**Austin Gray Mullins**

*Department of Civil and Environmental  
 Engineering  
 University of South Florida  
 Tampa, Florida, USA  
 gmullins@eng.usf.edu*

### ABSTRACT

Pilings cast with concrete in drilled shafts are prone to develop void regions during the pouring operation, compromising structural integrity. A technique for detecting problem areas in the shaft shortly after the concrete has begun to set has been developed, based on temperature rise resulting from the hydration of cement. This paper is concerned with the development of an inverse modeling technique using measured temperature profiles along the shaft in an attempt to reconstruct the position and size of any suspected anomaly. The strategy adopted is to model the column, allowing for a possible void, and then minimizing error between the model and the observational data when the shape and position of the void are allowed to vary. Results for numerical experiments were successful but in practice the method is complicated by uncertain soil conditions, rate of heat generation, and boundary conditions at the site of the anomaly.

### NOMENCLATURE

$k$	– thermal conductivity (W/m <sup>2</sup> °K)
$L_0$	– length of column sector (m)
$R$	– column radial position(m)
$R_0$	– column radius (m)
$q^*$	– volumetric heating rate (W/m <sup>3</sup> )
$r$	– radial coordinate
$T$	– temperature (°K)
$T_{amb}$	– ambient temperature (°K)
$t$	– time
$Z$	– vertical position (m)
$Z_0$	– length of column (m)
$z$	– vertical coordinate

### Greek

$\alpha$	– thermal diffusivity (m <sup>2</sup> /s)
$\theta$	– azimuthal coordinate, position

### INTRODUCTION

During the construction of subterranean drilled-shaft pilings, sections of the earth wall may collapse into the concrete as it is poured. Alternatively, it is possible that a spontaneous void or pocket may develop during the process (Fig. 1). In either case, the concrete cover will be reduced or absent altogether, leaving the steel reinforcing cage exposed to accelerated corrosion, especially in salty soils. Ultimately, the structural strength of the column may be impaired, making repair of such conditions a high priority.

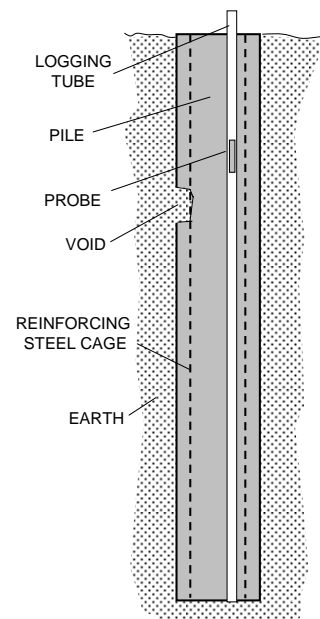


Fig. 1: Illustration of drilled shaft piling. Cutaway view shows void exposing reinforcing steel.

A technique for detecting voids in the shaft shortly after the concrete has begun to harden has been developed [1]. The basis of this test procedure is the fact that the temperature of the pile increases for a period of time as a result of the hydration of the cement binder. Normally, within a sound column a relatively uniform, symmetric temperature profile develops, however in situations where a void occurs during construction, the local temperature in this region will be altered. After some time has elapsed information from this thermal disturbance will diffuse for some distance from the original void.

This paper is concerned with the development of inverse modeling techniques utilizing measurements of temperature distribution along the shaft in an attempt to recreate the position and size of any possible void. The ultimate goal of this approach is to recover information concerning both the size and position of possible voids, utilizing the logging measurements plus any additional information available. While any temperature anomaly detected is suspect, obtaining an improved image of the condition of the pile integrity would be quite valuable since it is possible that if a flaw is detected with sufficient spatial accuracy (and timeliness), remedial actions (such as concrete injection near a void) could be attempted.

### DETECTION OF VOIDS

Small vertical logging tubes cast inside the concrete piling during construction make possible observations of the longitudinal temperature profiles at several locations by means of a probe fitted with infrared sensors and lowered into the tube, as illustrated in Figs. 1 and 2. These measurements can be made at various times as the hydration reaction continues. Fig. 3 contains an example of the type of observations being made currently. In this particular instance, the pile was fitted with three logging tubes attached to the rebar cage at approximately  $120^\circ$  intervals around the periphery. Bags of sand were attached to the cage (as shown in the figure) to simulate the type of concrete voids caused by cave-in, the situation of interest here. The shaft was 8.4 m in length and 1.2 m in diameter. Two small bags approximately 0.13 m deep, 0.46 m high and 0.9 m long were centered at about  $80^\circ$  and  $120^\circ$  from tube, at the depth shown in the figure. The lower bag was twice that size and centered on the tube.

A thermal disturbance due to the sandbag was easily detected, and the approximate position can

be estimated both vertically and in relation to the logging tubes around the circumference. Experiments are difficult (due to environmental conditions) and expensive to conduct.

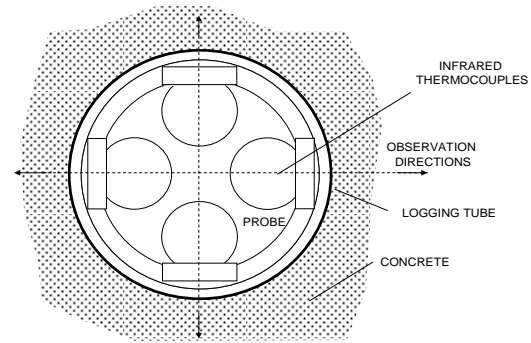


Fig. 2: Illustrating the probe with four thermocouple sensors inserted in logging tube.

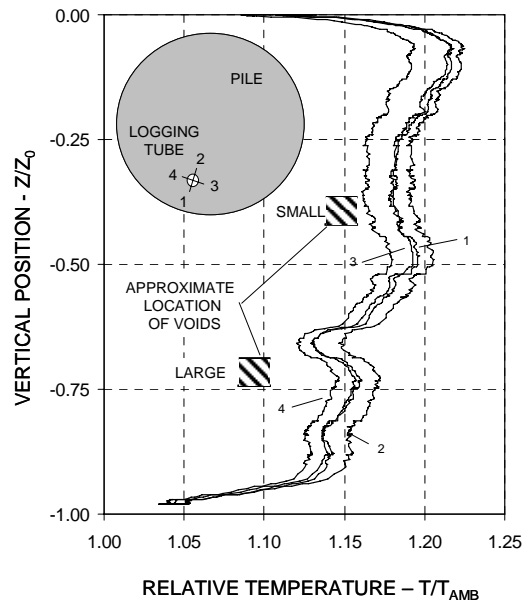


Fig. 3: Data obtained from typical experiment at 14 hours. Temperature data is normalized to the ambient conditions at start of test.

Although preliminary, these measurements clearly indicate the presence of a void and provide an indication of approximate location. Anticipating improvement in signal quality with further experience, the purpose of the investigation presented here is to determine whether inverse modeling techniques can be

utilized to refine estimates of the position and size of any suspected voids. It is noted that others have made similar temperature measurements [2] and have reported apparent anomalies, believed to be due to outward bulging of the column wall.

**THERMAL BEHAVIOR NEAR VOID**

Numerical experiments were conducted utilizing simulated data, since no reliable experimental data is currently available. Data sets were synthesized by modeling of the column at various times during the hydration period to obtain temperature profiles in the logging tubes. Beginning with the conventional time-dependent heat transfer equation, including heat generation, in cylindrical coordinates (Eq. 1), a finite difference model for the temperature, T, was constructed for a cylindrical section of the column,

$$\frac{1}{\alpha} \frac{\partial T}{\partial t} = \frac{\partial^2 T}{\partial r^2} + \frac{1}{r} \frac{\partial T}{\partial r} + \frac{1}{r^2} \frac{\partial^2 T}{\partial \theta^2} + \frac{\partial^2 T}{\partial z^2} + \frac{q^*}{k} \quad (1)$$

where k is the thermal conductivity and q\* is the volumetric rate of heat generation. The following assumptions were made:

1. The dimensions of the column section were R<sub>0</sub>=.65 m, L<sub>0</sub>= 1 m.
2. The thermal diffusivity, α, of concrete was taken to be 4.18x10<sup>-7</sup> m<sup>2</sup>/s.
3. An insulated boundary at the cylinder ends (away from any disturbance) was imposed.
4. The generation term, q\*/k, was given as a function of time (Fig. 4).
5. Two logging tubes were located at 90° intervals (Fig. 5).

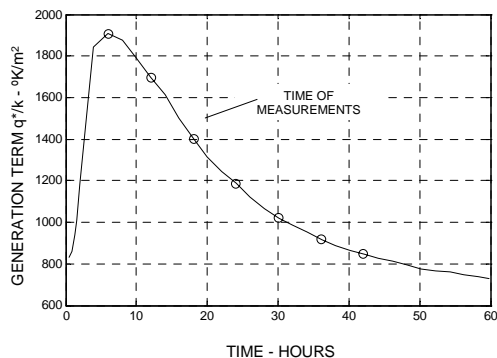


Fig. 4: Heat generation function employed for simulated data and numerical experiments.

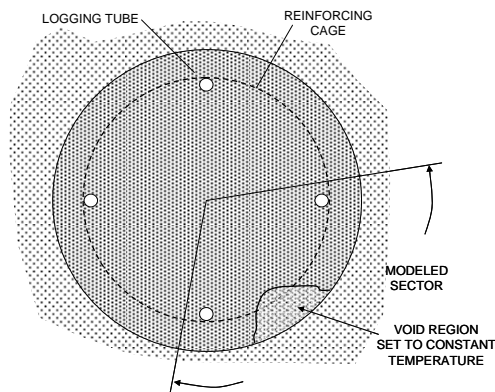


Fig. 5: Test configuration and region of computations for work reported here.

Synthesized data were calculated at 18 hours from the beginning of pouring. The probe is currently constructed to permit observation of temperature in four directions and (if stabilized against rotation in the tube) can be oriented so that observations are made in the radial and azimuthal directions (Fig. 3). Because the computational grid is relatively coarse (14x18x20 nodes), conditions at the logging tubes were constructed numerically in the following manner. In each of the four directions a three point estimate of the derivative was constructed for the point half way between the node representing the tube center and the next node outward (Fig. 6).

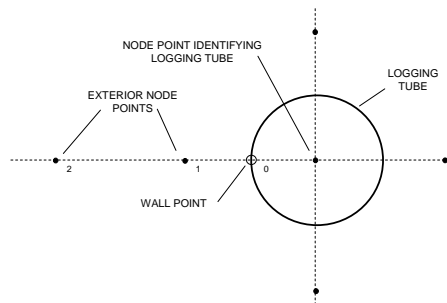


Fig. 6: Computational grid in vicinity of logging tube showing the extra point (labeled 0) used to calculate the temperature along the tube facing one direction.

Imposing an insulated condition at the wall implies that the derivative is zero, permitting a solution to the tube wall temperature in each direction [3]. The quadrant modeled included three sets of nodes beyond the logging tubes to permit this computation (Fig. 5). At each time step the node at the center of the tube was replaced with the average of the wall temperatures.

A test void (0.2 m deep x 0.17 m high x 0.17 m wide) was utilized for numerical experiments. The cylindrical test section containing the void is depicted in Fig. 7.

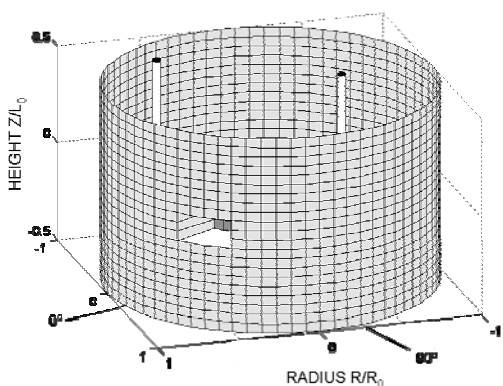


Fig. 7: Representation of the surface of the column section for trial data set. Depth of void is  $0.7 R_0$ . Logging tubes shown for clarity.

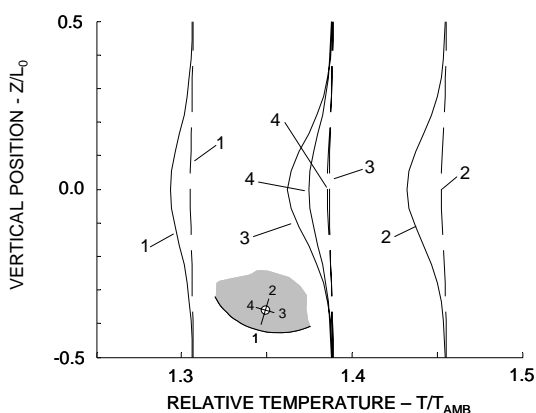


Fig. 8: Calculated temperature profiles at logging tubes at 18 hours, used for trial data. Inset indicates probe measurement directions; dashed lines indicate logging tube most distant from void.

Fig. 8 contains the temperature profiles that would be measured by a probe, obtained by direct computation of the temperature distribution for the column shown in Fig. 7 (employing the assumed hydration function). While the signal observed at the logging tube nearest the void is substantial, the other tube shows a very limited temperature change.

These results (functions of time and depth) were utilized as trial data for the inverse modeling strategies examined here. To remove the dependence on grid spacing, results for the wall temperatures in the logging tubes were interpolated by a cubic spline at desired locations to simulate a hypothetical data set.

**INVERSE METHODS**

Two inverse strategies for recovering the position and size of the void were investigated. The first of these, intended to utilize the data to identify just the azimuthal position of a suspected void, was developed as follows. A two-dimensional  $(r, \theta)$  finite difference, time dependent heat transfer model (with heat generation) was constructed for a concrete disk, in a manner similar to that used to produce the original data (but with different grid spacing). Again, the outer surface of the concrete was assumed to be at ground temperature,  $T_{amb}$ . This model was formulated as a function of a nine element vector which determined the extent of the void.

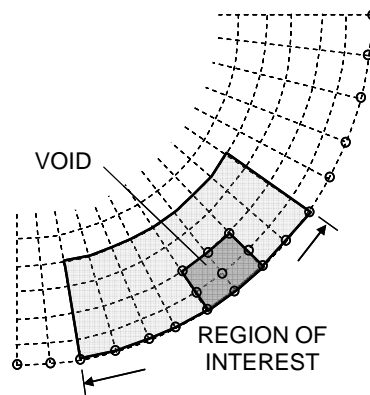


Fig. 9: Region of interest within the computational grid. The radial position held at  $T_{amb}$  forms a nine vector composed of integer elements. In the example shown all circled nodes are set to  $T_{amb}$ .

As can be seen in Fig. 9, the void was formed by also setting some additional nodes to  $T_{amb}$ , inwards from the outer surface as determined by the vector parameter. The vector represented the integer values of the nodes forming the radial position of the void or if not part of the void, the outer surface. The nodes in the region of interest and thus affected by the value of the nine vector were centered near the position of the suspected void.

This model was then used as an objective function, in a scheme which attempted to minimize the square error (at the time of observation) between the model results and the observed temperature at the logging tube when the shape and position of the void are allowed to vary. The MATLAB<sup>®</sup> constrained optimization function (*fmincon*) was employed to minimize the least square error between the model output and the simulated data set while varying the nine vector parameter. Since this routine does not handle integer parameters, the nine-vector was developed as a fraction of the radius, multiplied by the number of radial elements and rounded to an integer within the objective function. The step size in the minimization routine was set to be consistent with integer intervals.

The results of a numerical experiment utilizing the two-dimensional model are shown in Fig. 10.

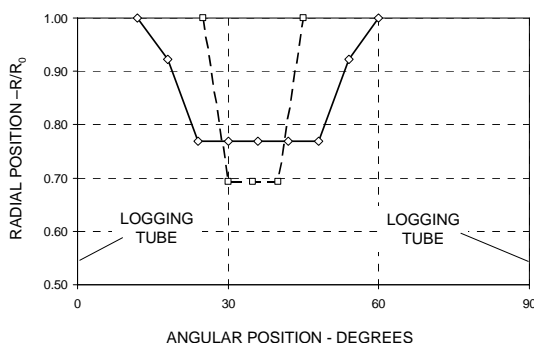


Fig. 10: Void location and depth recovered from trial data by two dimensional inverse method.

The computed void appears to match the actual conditions reasonably well but the shape is somewhat broadened. This method indicates the approximate location of the center of the void and moving the midpoint of the nine-vector gave

similar results, although not necessarily as close a match. The use of one more step in time forward or back gave little change, nor did utilizing data from several time steps simultaneously. It should be noted that in practice it is not always feasible to wait for more extensive tests if repairs are to be made.

The second strategy consisted of an attempt to reconstruct the void position and volume using a three-dimensional model. This model was formulated much like the first but as a function of a 5X5 array, which was again used to determine which nodes were set to  $T_{amb}$ . In this case however a more realistic image of a void is obtained (as can be seen in Fig. 11), since the vertical variation in logging tube data is additionally utilized to produce a three dimensional image. An initial guess concerning the location of the void center can be obtained from the first method and the vertical characteristics of the data. The location of the void has been determined reasonably well. For comparative purposes, the volume of the computed void is about 1.5 times that of the original.

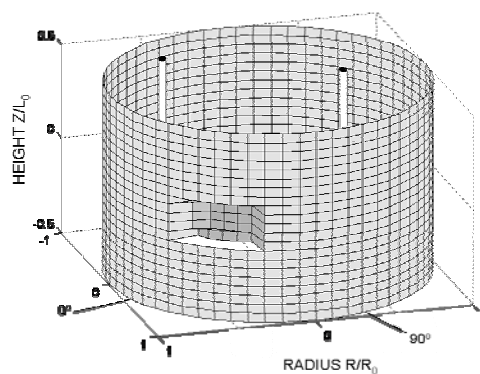


Fig. 11: Representation of the cylindrical section of the pile containing the void as reconstructed by the three-dimensional modeling technique.

## CONCLUSIONS AND FUTURE DIRECTIONS

Two inverse techniques for spatially resolving voids in drilled shaft concrete piles have been developed and successfully tested with synthesized data, representing temperature information available from inside the shaft. It is expected that these concepts can eventually be used. Unfortunately, the quality of the experimental measurements is not yet at the level

suitable for further analysis such as that proposed here.

The experimental method is complicated by uncertain soil conditions, rate of heat generation, and boundary conditions at the site of the anomaly. At present the analysis relies on several ad hoc assumptions regarding the ambient temperature and conditions at the wall. Eventually it may be possible to use data from regions without voids to deduce these conditions as well as the rate of heat generation, also by inverse techniques.

#### **REFERENCES**

1. A. G. Mullins and S. C. Kranc, "Method for Testing Integrity of Concrete Shafts", Patent #6,783,273 B1, Aug 31, 2004,
2. FHWA PAPER
3. Burden Faires



# Roof Damage in New Homes Caused by Hurricane Charley

Nick Meloy<sup>1</sup>; Rajan Sen, F.ASCE<sup>2</sup>; Niranjan Pai<sup>3</sup>; and Gray Mullins, M.ASCE<sup>4</sup>

**Abstract:** Hurricane Charley was the first Category 4 hurricane to strike Florida after 1992. This paper presents results of a study to investigate the performance of 425 of 747 roofs of new homes in Punta Gorda Isles, a subdivision of Punta Gorda that was directly in the path of Hurricane Charley shortly after it made landfall. The homes examined were larger, concrete/clay tiled roof homes having irregular floor plans and complex roof configurations not explicitly addressed by prevailing wind load codes. Roof damage was evaluated using images from aerial photographs taken at an elevation of approximately 762 m (2,500 ft.) Specialized software was used to quantify damage. Damage was classified based on tile loss area. The study showed that the vast majority of the roofs were either undamaged or sustained minor damage. Fewer than 14% were classified as damaged. The most common observed tile loss was along ridges, corners, or in the hip zone where negative uplift pressures are recognized to be the highest. Given the modest observed damage, prevailing methods for estimating wind loads for irregular buildings specified in codes may be adequate. Problems encountered may be best resolved through new details for attaching tiles on ridges, corners, and hip zone.

**DOI:** 10.1061/(ASCE)0887-3828(2007)21:2(97)

**CE Database subject headings:** Hurricanes; Buildings, residential; Wind pressure; Roof failures; Damage assessment; Building design; Florida.

## Introduction

The 2004 hurricane season was devastating for Florida. For the first time in 153 years of record keeping, the state was struck by four hurricanes. Of these, the first, Hurricane Charley, a Category 4 storm was the most severe and caused the most destruction. Charley made landfall in the barrier islands in Lee County, Fla., on August 13, 2004 causing 33 deaths and an estimated \$14 billion of insured loss. This made it the second costliest hurricane in the state since Hurricane Andrew struck South Florida in 1992 (National Climatic Data Center 2005).

Unlike buildings with steep roof slopes characteristic of cold regions, buildings with moderate roof slopes common in the southeast, are subjected to large uplift forces. These uplift forces can cause the lightweight roofs to sustain significant damage unless they are properly engineered. Indeed, 90% of all homes in the path of Hurricane Andrew experienced roof damage with 33% sustaining severe damage. Typical damage resulting from these forces include separation of roof components, buckling of roof

trusses, pullout of anchorage and collapse of structural support (Bradford and Sen 2004).

The problems identified by damage caused by Hurricane Andrew in 1992 (Cook and Soltani 1994) led to changes in code requirements to rectify shortfalls in design, detailing, and inspection. In 1993, the Standard Building Code (SBC) issued a deemed to comply publication "Standard for Hurricane Resistant Residential Construction (SSTD 10)" also referred to as SSTD 10 (SBC 1993). This was subsequently updated in 1999 (SBC 1999). SSTD 10 provides a prescriptive method for building one-, two-, and three-story residential buildings to withstand high winds.

In 1998, the Florida legislature passed a law to create a new statewide code that replaced the 470 local codes that were in force. This new code published in 2001 was adopted in 2002 (Florida Building Code 2001). It is modeled after the 1999 SBC code and the South Florida code and retained many of its provisions (FEMA 2005).

The damage caused by Hurricane Andrew was also repeated by Hurricane Charley in older homes designed and built to pre-Andrew codes. For example, Charley damaged 11,615 homes in Charlotte County (St. Petersburg Times 2005). These failures were due to well documented deficiencies rectified in the newer codes and are therefore outside the scope of this paper.

## Objectives and Scope

The aim of the study was to evaluate the performance of roof coverings of newer homes in Punta Gorda Isles (PGI), a subdivision of Punta Gorda, built to post-Andrew codes that were subjected to Charley's strongest sustained winds. For this reason, homes were limited to those built in the past ten years. This allowed the performance of the newer SSTD 10 and the Florida Building Code to be assessed. As all homes in PGI were required to have concrete or clay tiled roofs (this ordinance was changed

<sup>1</sup>Project Engineer, Universal Engineering Sciences, Orlando, FL 32811; formerly, Undergraduate Student, Univ. of South Florida, Tampa, FL, 33620.

<sup>2</sup>Professor, Dept. of Civil and Environmental Engineering, Univ. of South Florida, Tampa, FL 33620.

<sup>3</sup>Research Associate, Dept. of Civil and Environmental Engineering, Univ. of South Florida, Tampa, FL 33620.

<sup>4</sup>Associate Professor, Dept. of Civil and Environmental Engineering, Univ. of South Florida, Tampa, FL 33620.

Note. Discussion open until September 1, 2007. Separate discussions must be submitted for individual papers. To extend the closing date by one month, a written request must be filed with the ASCE Managing Editor. The manuscript for this paper was submitted for review and possible publication on September 12, 2005; approved on May 8, 2006. This paper is part of the *Journal of Performance of Constructed Facilities*, Vol. 21, No. 2, April 1, 2007. ©ASCE, ISSN 0887-3828/2007/2-97-107/\$25.00.

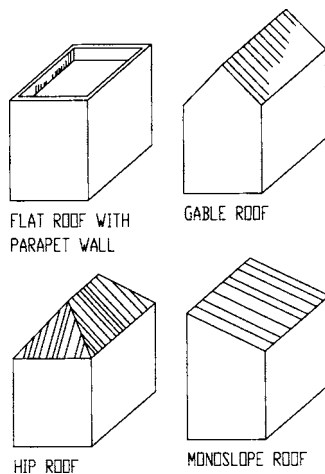


**Fig. 1.** Types of roofs addressed in codes and standards

following Charley), conclusions from this study are limited to houses with concrete or clay tiled roofs.

An equally important objective was to evaluate the performance of homes with irregular floor plans and complex roof configurations since these are outside the scope of prevailing standards (Stathopoulos 2003). As illustrated in Fig. 1, the roof types covered in the prevailing standards are flat roof with parapet wall, gable roof, hip roof, and monoslope roof with overall rectangular layouts. Most modern homes have a combination of gable and hip roofs on nonrectangular layouts.

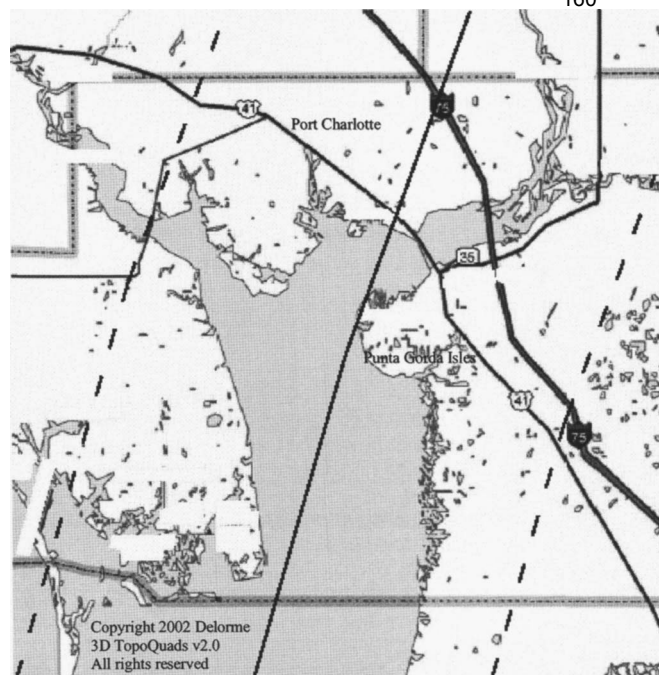
### Path of Hurricane Charley

Fig. 2 shows the path of Hurricane Charley as it made landfall in Florida. This fast moving, intense, narrow [hurricane force winds extended approximately 11.3 km (7 mi) from the center] first made landfall in Cayo Costa, Fla. Subsequently it crossed Charlotte Harbor moving inland first towards Punta Gorda, then Port Charlotte, and Arcadia. The highest wind speeds were not measured. However, model-based assessment of Charley's maximum wind speeds estimated it to be between 201.2 and 225.3 km/h (125 and 140 mi/hr) (for downtown Punta Gorda—Exposure B, 3-second peak gust). The corresponding maximum speed for Exposure C was estimated to be between 225.3 and 257.5 km/h (140 and 160 mi/h). These speeds exceeded the design speed of 183.5 to 209.2 km/h (114 to 130 mi/h) for Charlotte County (FEMA 2005).

### Survey Site

PGI, a new subdivision of Punta Gorda, was selected for the survey as it met all the requirements for this study. As it was directly in the path of Hurricane Charley shortly after it made landfall, all buildings in the subdivision were subjected to the strongest sustained winds. Equally importantly, it had a significant number of homes built to new codes. These homes were all large [325 m<sup>2</sup> (3,500 ft<sup>2</sup>) average] having irregular floor plans and complex roofs. PGI was also a deed restricted community that required all homes to have tiled roofs.

Development of PGI started in 1957 and different areas were opened over the years. There are 18,794 parcels in PGI of which



**Fig. 2.** Path of Hurricane Charley. The dark line cutting through Charlotte Harbor represents the centerline of Charley's path (2002 DeLorme (www.delorme.com) 3-D TopoQuads).

17,598 have been built upon. PGI has 747 homes built from 1996 to 2003. Of these, 425 were evaluated in this study (57%). With the exception of a few homes located on a golf course, all homes in PGI are on wide canals with access to Charlotte Harbor and the Gulf of Mexico (The Andrea Group 1997–2003).

### Approach

A systematic study was conducted in which post-Charley aerial photographs of 425 of the 747 new homes constructed in PGI were reviewed. Aerial photographs were obtained from Pictometry International Corp. (Rochester, N.Y.), who photographed the storm-affected areas shortly after Hurricane Charley moved through the area.

Most images were taken on August 21, 2004, with a small portion taken between August 27 and 28, 2004. All images were high resolution [12.2 cm (0.4 ft) per pixel] and in digital format. Special software provided by Pictometry allowed buildings to be identified by their address. With information provided by the Charlotte County Geographical Information Systems Department (Charlotte County, Florida 1997–2004) and the Charlotte County Property Appraiser (Charlotte County Property Appraiser 1997–2004), buildings could be identified very efficiently.

Other providers of aerial photography were also considered. These included Keyhole, Applied Geotechnologies, M7 Visual Intelligence, and Digital Globe. Pictometry was chosen for their coverage of the area of interest after the storm, their willingness to assist in this research, and the quality of their product including pictures and software.

Additionally, site visits were made to the homes classified as “damaged” (see the section entitled “Damage Classification” for further explanation). The purpose of the site visit was to attempt to verify the mode of damage seen in aerial photographs. Details such as contractor and attachment method were also included in



**Fig. 3.** Example neighborhood oblique image. Four views allow for damage on all sides to be clearly seen and estimated: (a) south; (b) north; (c) west; and (d) east views of a damaged house (Reprinted with permission, Pictometry International Corp. 2006).

the inquiry. Unfortunately not all of the homeowners were available during site visits and several of the homes had been repaired or were under repair. Therefore, tile material type and contractor information could not be quantified.

### **Aerial Photographs**

Traditionally aerial images are taken orthogonally or straight down. Pictometry markets a unique product in that they provide images taken at an angle. These oblique images were used in this study so that features could be easily seen in their entirety. All aerial images used in the study were supplied by Pictometry International.

Oblique pictures (at an angle of 40–45°) were taken from different directions at two elevations for the *neighborhood* [approximately 762 m (2,500 ft)] and the *community* [approximately 1,530–1,830 m (5,000–6,000 ft)]. This made it possible to view and analyze any house or building feature in PGI from all cardinal directions [see Figs. 3(a–d)]. Having four views of each property provided a more complete image of the damage, although details such as tile material (i.e., concrete or clay) or tile pattern could not be definitively identified from the photographs.

Pictometry has a unique patented information system that combines aerial imaging with a state of the art software system that includes tools useful in analysis of aerial images called Electronic Field Study (EFS) (Pictometry International 2002). Distances, heights, and areas can all be estimated using this software.

### **Quantification of Damage**

EFS permits areas to be measured simply by drawing a line around the target region with an “area tool.” The program then calculates the enclosed area (Fig. 4). Other tools allow dimensions to be estimated, e.g., roof height or photographs to be annotated to show the wind direction.

The specific area tool used for this research did not take the pitch of the roof into consideration, and as such, the measurements obtained had a range of accuracy. The accuracy could be improved by using newer EFS tools that allow the user to take the roof pitch into account or by incorporating better elevation models. Regardless of which tool is used, the final measurement accuracy is affected by how accurately the user draws the height



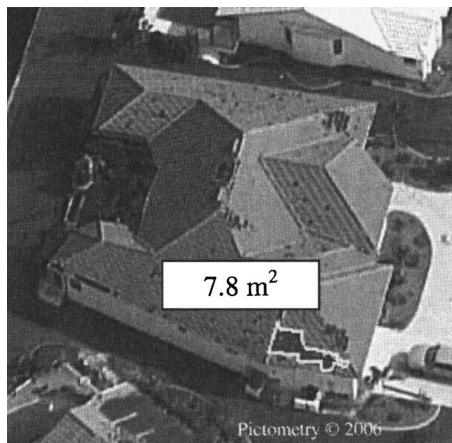


**Fig. 4.** Pictometry area tool. Area is estimated at 24.68 m<sup>2</sup> (84 ft<sup>2</sup>). (Reprinted with permission, Pictometry International Corp. 2006).

lines and area boundaries with a mouse. Nonetheless, since the same method was used for all the buildings, it provides valuable comparative data.

### Damage Classification

Property data were plotted using mapping software to give a visual representation of the location of homes relative to the path of Hurricane Charley (Fig. 5). Homes were chosen randomly from this plot and analyzed in EFS. Four views, one from each cardinal direction (Fig. 3), of each home were saved and the estimated area of missing tiles was recorded in a database along with property information.

### Damage Home

A home designated as damaged would have large areas of missing tiles or at least 9.29 m<sup>2</sup> (100 ft<sup>2</sup>) of missing tile. See Fig. 6.

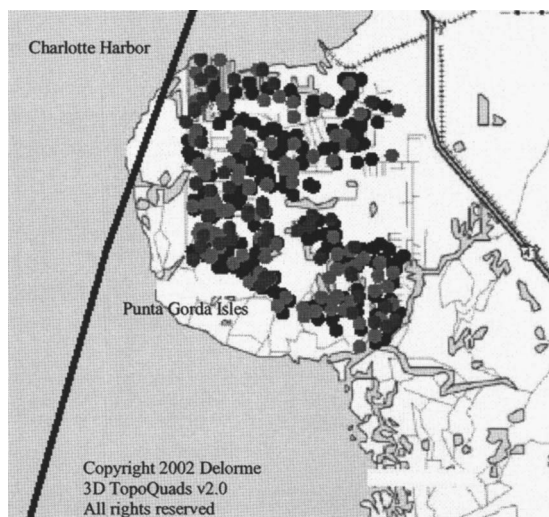


**Fig. 5.** Plot of PGI properties. Damaged (57 homes), minor damage (158 homes), and no damage (210 homes) (2002 DeLorme (www.delorme.com) 3D TopoQuads).

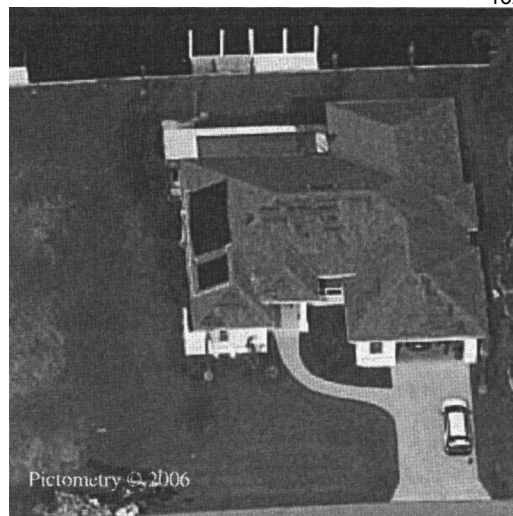


**Fig. 6.** Damaged home. Large areas or more than 9.29 m<sup>2</sup> (100 ft<sup>2</sup>) of missing tiles/shingles (Reprinted with permission, Pictometry International Corp. 2006).

### Minor Damage

If the area of missing tiles was between 0.46 and 9.29 m<sup>2</sup> (5 and 100 ft<sup>2</sup>) or there were no large areas of missing tiles damage was classified as minor. See Fig. 7.

### No Damage

A home with less than 0.46 m<sup>2</sup> (5 ft<sup>2</sup>) of missing tiles was considered to have no damage. See Fig. 8.

### Location of Homes

After property damage had been categorized based on measured damage from the aerial photographs, markers identifying the location of these properties were placed on a map of PGI (see Fig. 5).



**Fig. 7.** Home with minor damage. 0.46–9.29 m<sup>2</sup> (5–100 ft<sup>2</sup>) of missing tiles (Reprinted with permission, Pictometry International Corp. 2006).

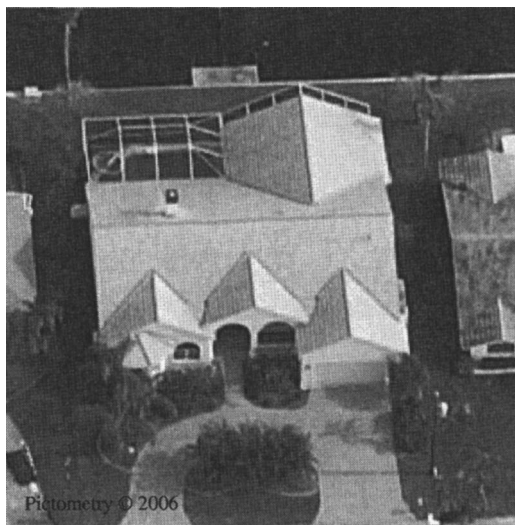


**Fig. 8.** Home with no damage. Less than  $0.46 \text{ m}^2$  ( $5 \text{ ft}^2$ ) of missing tiles/shingles (Reprinted with permission, Pictometry International Corp. 2006).

The locations of these homes relative to the eye of the Hurricane are shown in Fig. 9 for damaged homes, in Fig. 10 for homes with minor damage and in Fig. 11 for those with no damage. It may be seen that damaged homes are concentrated in the southern and western part of PGI, whereas the others are more evenly distributed over the region. A complete photographic record of damaged homes compiled in this study is included in the final report (Meloy et al. 2005).

### Analysis of Data

Table 1 provides a year-wise breakdown of the 425 homes studied which accounts for 57% of the 747 homes built in Punta Gorda Isles from 1996 to 2003. In numerical terms, the largest number

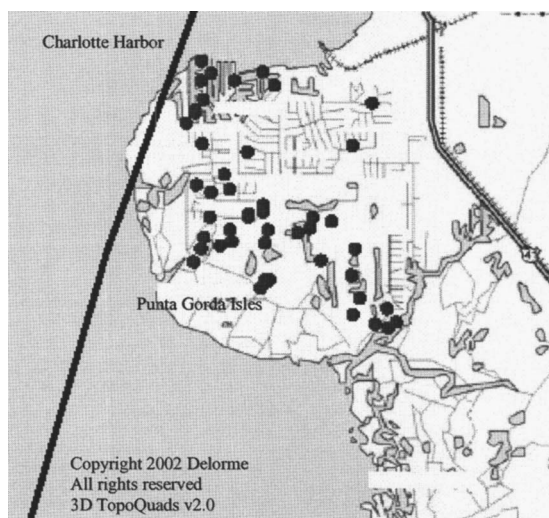


**Fig. 9.** Damaged homes. Notice the distribution of damaged and minor damaged homes. Damaged homes are concentrated in the southern and western sides of Punta Gorda Isles (2002 (www.delorme.com) DeLorme 3D TopoQuads).

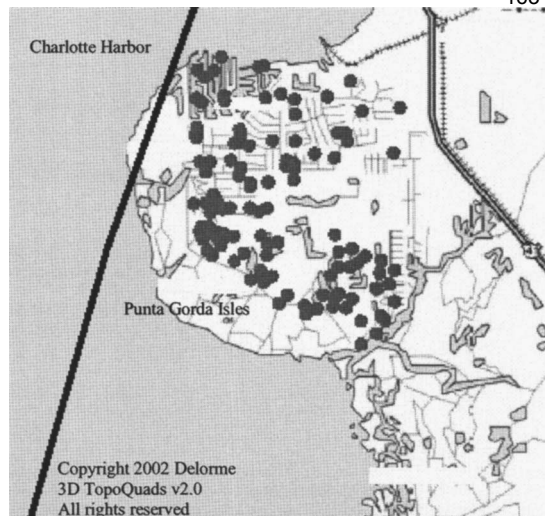


**Fig. 10.** Homes with minor damage. Minor damaged homes have a more uniform distribution (2002 (www.delorme.com) DeLorme 3D TopoQuads).

of homes were those built in 2000 (76), whereas the fewest was for 2003 (31). Table 1 also shows that the sample size relative to the number of houses built was over 50% for homes built in 1996 (52%) and 1997 (51%) and in the mid-40% range for the remaining years.

From the data presented in Table 1, it may be seen that, in terms of average damage per home, the least damage was in homes built in 1996 [ $1.8 \text{ m}^2$  ( $19.4 \text{ ft}^2$ )], 1998 [ $2.1 \text{ m}^2$  ( $23 \text{ ft}^2$ )], and 2001 [ $3.2 \text{ m}^2$  ( $34.2 \text{ ft}^2$ )]. The greatest damage was for homes built in 1999 [ $7.8 \text{ m}^2$  ( $83.5 \text{ ft}^2$ )] and in 2003 [ $13.9 \text{ m}^2$  ( $149.2 \text{ ft}^2$ )]. The damage for 2003 included two houses that contributed 58.7% of the total damage for that year. These two homes did not have any attribute, such as geographic position or floorplan, which could explain the large amount of damage. Poor construction is the most probable reason for these outliers. If these two houses are omitted, the average damage for homes built in 2003 is much smaller ( $6.1 \text{ m}^2$  or  $65.9 \text{ ft}^2$ ).

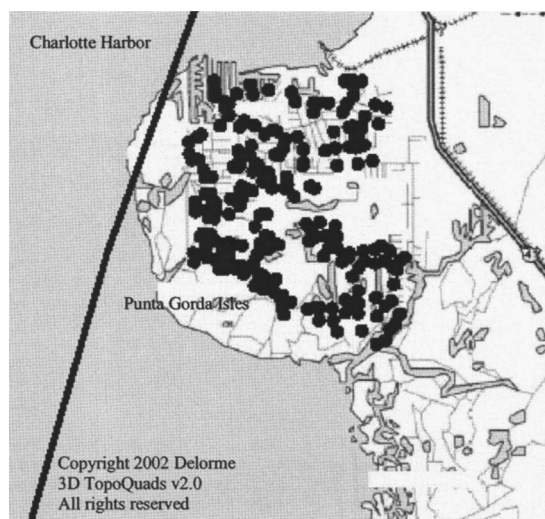


**Fig. 11.** Homes with no damage. Homes with no damage are evenly distributed throughout the area (2002 (www.delorme.com) DeLorme 3D TopoQuads).



**Table 1.** Damage Breakdown by Year

Year	Number of homes studied	Number of homes built	Percent of homes studied	Total damage (m <sup>2</sup> )	Average damage (m <sup>2</sup> )	Average appraised value (\$)	Average total building area (m <sup>2</sup> )
1996	37	71	52	67	1.8	427,525	309
1997	46	90	51	226	4.9	398,507	311
1998	59	122	48	122	2.1	412,658	316
1999	68	152	45	528	7.8	439,755	324
2000	76	163	47	375	4.9	440,632	325
2001	62	139	45	197	3.2	435,457	323
2002	46	129	36	182	4.0	467,482	330
2003 (without extreme cases)	29	66	44	178	6.1	526,805	343
2003 (with extreme cases)	31	66	47	430	13.9	524,598	366
Annual average <sup>a</sup>	53	124	43	234	4.3	443,603	323
Annual average <sup>b</sup>	53	124	43	2,942	5.4	443,327	327
Total <sup>a</sup>	423	745	57	1,875	—	—	—
Total <sup>b</sup>	425	747	57	2,127	—	—	—

<sup>a</sup>Without extreme cases.<sup>b</sup>With extreme cases.

A damage-wise breakdown of the same data is given in Table 2. Of the 425 homes studied, the roofs of 210 (49%) suffered no damage, whereas 158 others (37%) had minor damage. This means that only a small fraction of the homes (14%) were classified as damaged. Given the large sample size, it is reasonable to conclude for tiled roofs used in these large homes current methods for calculating design wind speeds for irregular roofs are adequate.

Table 3 compares the relative performance of homes built to the Standard Building Code and the Florida Building Code. Based on the measured tile loss, the overall performance of the buildings designed to the SBC (1996–2001) or the Florida Building Code (2002–2003) are quite comparable. Average tile losses were

**Table 2.** Damage Breakdown by Category

Damage	Number of homes sited	Total damage (m <sup>2</sup> )	Average damage (m <sup>2</sup> )	Average appraised value (\$)
With extreme cases	57	5,268	90	456,570
Without extreme cases	55	4,441	78	455,743
Minor	158	1,709	11	440,759
No	210	0	0	433,478
<b>Total with extreme cases</b>	<b>425</b>	<b>6,977</b>	<b>16</b>	<b>—</b>
<b>Total without extreme cases</b>	<b>423</b>	<b>6,150</b>	<b>15</b>	<b>—</b>

**Table 3.** Code Comparison with Estimated Damage

Year range	Building code	Total damage (m <sup>2</sup> )	Average damage (m <sup>2</sup> )
1996–2001	Southern	1,594.000	4.550
2002–2003 <sup>a</sup>	Florida	610.100	7.900
2002–2003 <sup>b</sup>		358.000	4.650

<sup>a</sup>With extreme cases.<sup>b</sup>Without extreme cases.**Table 4.** Damage Breakdown (Category, Year Built, and Value)

Year	Damaged				Average appraised value (\$)
	Damaged area (m <sup>2</sup> )	Number of homes studied	Number of homes in category	Percent of total	
1996	25	37	2	5	425,833
1997	178	46	9	20	418,692
1998	48	59	3	5	400,234
1999	439	68	14	21	422,249
2000	252	76	8	11	430,761
2001	135	62	7	11	437,187
2002	118	46	6	13	502,224
2003	412	31	8	26	615,383
<b>Total</b>		<b>425</b>	<b>57</b>	<b>13</b>	<b>456,570</b>
	<b>Minor damage</b>				
1996	42	37	14	38	435,102
1997	48	46	17	37	403,619
1998	75	59	25	42	427,516
1999	89	68	24	35	432,176
2000	123	76	34	45	440,038
2001	63	62	20	32	436,852
2002	64	46	19	41	496,209
2003	17	31	5	16	454,564
<b>Total</b>		<b>425</b>	<b>158</b>	<b>37</b>	<b>440,759</b>
	<b>No damage</b>				
1996	0	37	21	57	421,640
1997	0	46	20	43	373,211
1998	0	59	31	53	410,226
1999	0	68	30	44	464,839
2000	0	76	34	45	451,099
2001	0	62	35	56	432,330
2002	0	46	21	46	404,012
2003	0	31	18	58	510,467
<b>Total</b>		<b>425</b>	<b>210</b>	<b>49</b>	<b>433,478</b>



**Table 5.** Damage Distribution

Year	Number of homes studied	Number of damaged homes		Damage (m <sup>2</sup> )				
				North	East	South	West	Total
1996	37	2	Total	2.60	8.18	13.47	0.74	25
			Average	1.30	4.09	6.78	0.37	—
1997	46	9	Total	19.70	130.90	18.12	9.66	178
			Average	2.23	14.59	2.04	1.11	—
1998	59	3	Total	4.46	26.85	15.89	0.37	48
			Average	1.49	8.92	5.30	0.09	—
1999	68	14	Total	114.27	166.02	61.59	96.62	439
			Average	8.18	11.89	4.37	6.87	—
2000	76	8	Total	58.62	143.35	30.29	19.51	252
			Average	7.34	17.93	3.81	2.42	—
2001	62	7	Total	17.09	93.83	16.07	7.62	135
			Average	2.42	13.38	2.32	1.11	—
2002	46	6	Total	13.01	75.62	20.07	8.83	118
			Average	2.14	12.63	3.34	1.49	—
2003	31	8	Total	68.28	177.91	108.70	57.51	412
			Average	8.55	22.20	13.56	7.15	—
<b>Total 1996–2003</b>				<b>298</b>	<b>823</b>	<b>284</b>	<b>201</b>	
<b>Average 1996–2003</b>				<b>142</b>	<b>243</b>	<b>194</b>	<b>101</b>	

Note: The values indicate damage on respective side of roof.

4.55 m<sup>2</sup> (49 ft<sup>2</sup>) for those built to the SBC versus 4.65 m<sup>2</sup> (50 ft<sup>2</sup>) to the Florida Building Code if the two houses that contributed significantly are omitted.

Table 4 provides data on the relationship between damage and year of construction. As noted earlier, overall only 14% of the 425 homes were damaged. However, homes built in 1997 (20%), 1999 (21%), and 2003 (26%) suffered greater damage while those built in 1996 or 1998 (both 5%) suffered the least damage. In terms of undamaged homes, homes built in 1996 (57%), 2001 (56%), and 2003 (58%) fared the best. It is interesting to note that homes built in 2003 have the largest percentage of undamaged homes and also the largest percentage of damaged homes. Only 16% of homes built in 2003 had minor damage compared to a range of 32–45% for the other years. The exact cause of the large disparity

in behavior of homes built in 2003 is not clear, but it may be due to combination of the relatively small sample size and some cases of poor construction and unfavorable location.

Table 5 provides a year-wise breakdown of the damage to the roof in the cardinal directions. With the exception of homes built

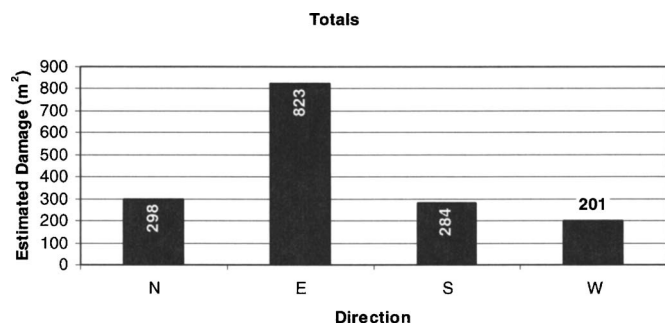
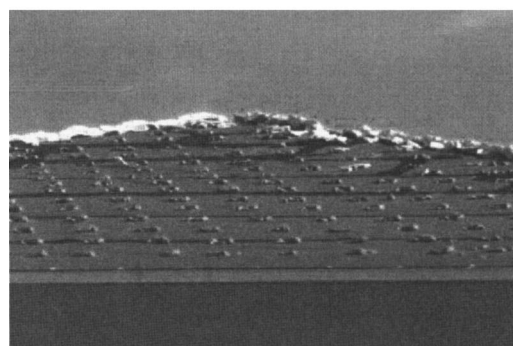


**Fig. 12.** Damage distribution totals. Wind direction indicates which direction the wind is from (i.e., wind direction=E, wind is from the east). Homes suffered the greatest damage on the east side possibly indicating damage was done by debris. Winds were initially from the east. Assuming most damage was done by the first and strongest winds, this may show that much of the damage was caused by debris as tiles are more commonly lost on the negative pressure or downwind side. Airborne debris would be traveling westward and impacting homes on the east side.

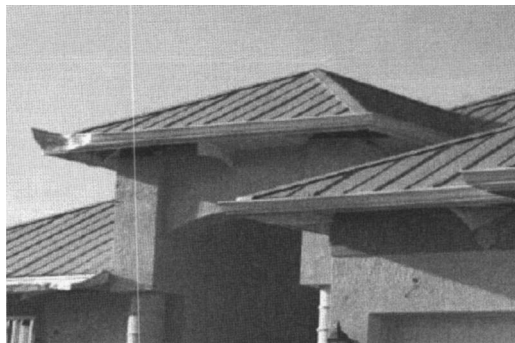


(a)



(b)

**Fig. 13.** Examples of roof damage due to poor workmanship: (a) insufficient mortar; (b) insufficient adhesive



(a)



(b)

**Fig. 14.** (a) Roof damage due to impact near gutter note damage to soffit; (b) tile damage due to windborne debris (Courtesy of homeowner)

in 1996 where more damage was sustained in the south face, by and large, damage on the eastern side is much greater. This is evident from the cumulative damage listed in the last line of the table that is also plotted in Fig. 12. This is to be expected as initial winds were from the east and would have been the strongest.

### Damage Characterization

As in previous surveys of damage caused by other hurricanes, such as Andrew (Cook and Sotani 1994) and Hugo (Sell and Sparks 1991) there was damage due to poor workmanship and due to windborne debris. This needs to be separated in order to evaluate the role of high winds on the performance of new roof construction.

#### Damage due to Poor Construction

The Florida Roofing, Sheet Metal and Air Conditioning Contractors Association have developed consensus standards (updated or reaffirmed every three years) for the installation of concrete and clay roof tiles. Several alternate approved systems for installing tiles are permitted, e.g., using mechanical fasteners, mortar set, or adhesive.

Roof damage observed in the field region of the roof, i.e., excluding the high suction regions such as corners, perimeter or ridges, could be due to improper attachment of the tiles. An example of such damage is shown in Fig. 13(a) where the mortar-set attachment method was used. Here the damage extends to the field region beyond the ridge. The mortar-set installation was identified as more susceptible to damage by the Federal Emer-

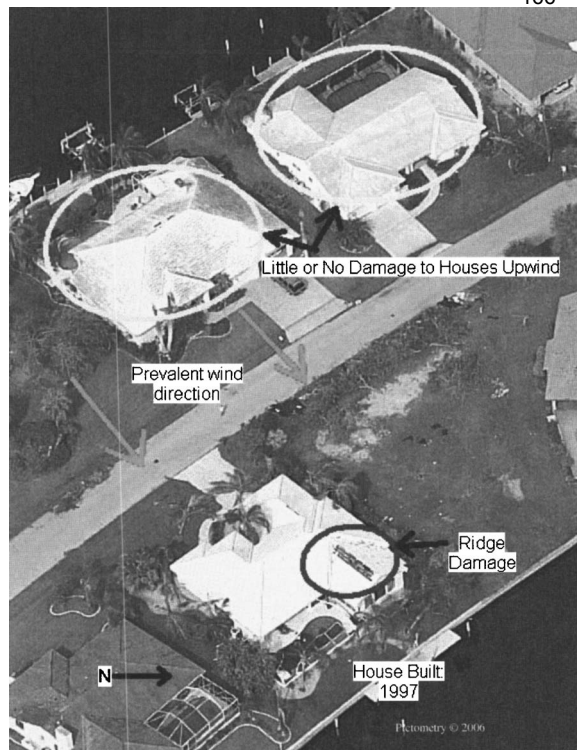


**Fig. 15.** Damage due to high wind in roof ridge. Note also damage to the ridge on the east side and missing tiles at the northeast corner (Reprinted with permission, Pictometry International Corp. 2006).

gency Management Association (FEMA 2004). There was also widespread damage to building soffits (vents under the roof overhang that allow the attic to breathe) because it had not been properly attached [see Fig. 14(a)].

#### Damage due to Flying Debris

The new codes require houses built in close proximity to the coast to protect openings by providing damage resistant glass or protective shutters. However, tile roofs are vulnerable to damage by flying debris. This type of damage was reported by home owners who responded to the contact letter sent out by the University of South Florida (USF) or in discussions with the USF research team during site visits. An example of such roof damage provided by a homeowner is shown in Fig. 14(b). Such impact damage was distinguished by remnants of smashed tiles/shingles that were left behind.

#### Damage due to Wind

Five examples of characteristic damage due to high wind are shown in Figs. 15–19. In each case, the area surrounding the damaged home is shown along with information on the year the house was built and nearby homes to provide a measure of the damage sustained in the neighborhood. Figs. 15–19 were specially selected because neighboring homes sustained little damage. Tile loss cannot therefore be attributed to flying debris but due to the intensity of the wind and its interaction with the building. The direction of the prevailing wind is also shown in some cases. This of course reverses as the eye of the hurricane crosses a region.

Inspection of these photos shows that damage was typically





**Fig. 16.** Damage along ridges. Houses upwind show little damage (Reprinted with permission, Pictometry International Corp. 2006).

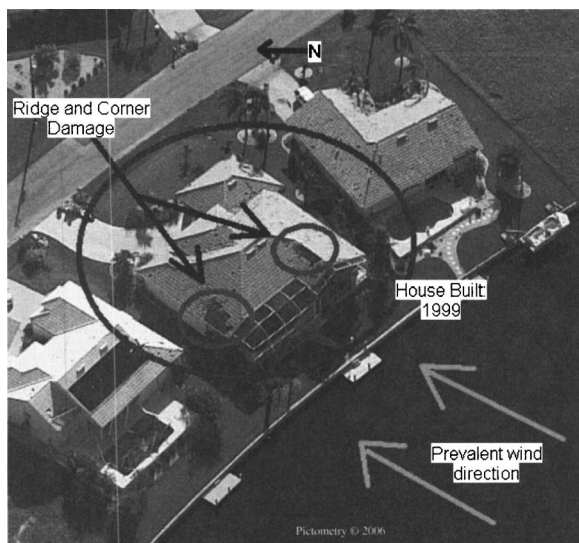


**Fig. 17.** Damage due to wind along ridges and corners (Reprinted with permission, Pictometry International Corp. 2006)



**Fig. 18.** Damage due to wind along ridges (Reprinted with permission, Pictometry International Corp. 2006)

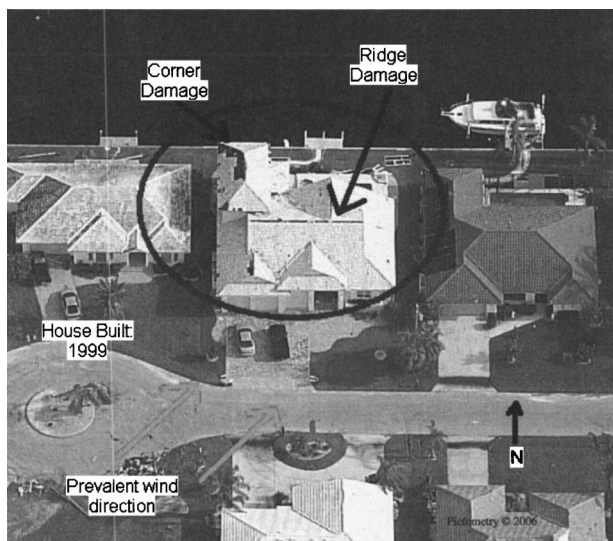


**Fig. 19.** Damage due to wind along ridges and the hip zone (Reprinted with permission, Pictometry International Corp. 2006)

along the ridges (Figs. 15–19), corners (Figs. 15, 17, and 19), the hip zone (Fig. 16 and 19), and eaves (Fig. 19). These occurred at locations of high suction forces that are well recognized by codes though in this case sustained winds exceeded the basic design wind speed for Punta Gorda (ASCE 2003).

It may be seen that all five homes in Figs. 15–19 have complex roof configurations that are not strictly catered to by codes. Nonetheless, a large number of homes in the neighborhood of the damaged home sustained no damage (see Figs. 15–17 and 19). This could be related to local variation in wind velocity, its direction relative to the house or the method by which the tiles were attached.

Fig. 20(a) shows a close-up view of damage to ridge tiles provided by a home owner. Fig. 20(b) shows a photo of similar damage taken by the research team. As with Figs. 15–19, damage was in the zone of high negative pressure. The absence of evidence of flying debris from neighboring houses clearly indicates that damage was due to the intensity of the wind and its interaction with the structure, not poor workmanship as was the case in Fig. 16.

## Discussion

This paper provides a brief overview of the type of damage occurring in an upscale neighborhood consisting of large, expensive, waterfront homes that bore the brunt of Hurricane Charley. 57% of all homes built in PGI from 1996 to 2003 were examined in the study but damage was found to be limited even in houses that were located close to the eye of the hurricane. This was most probably because the hurricane was compact and the entire PGI region was subjected to similar sustained winds that were estimated to be above the design wind speed.

This excellent performance of the new homes indicates that current specifications for the type of buildings examined (irregular with clay or concrete tiled roofs) are generally adequate. Wind damage was sustained along ridges, corners, in the hip zone, and eaves regions that are known to be subject to high suction forces. Given that the roofs of a majority of homes were undamaged, there is no compelling reason for making any significant changes.



(a)



(b)

**Fig. 20.** Views of wind damage along: (a) ridges; (b) ridge

However, specifications for attaching tiles along ridges, hip zones should be tightened to ensure that damage observed is not encountered under a similar wind event in the future.

These findings may be relevant for the entire northeastern United States that can also be subject to hurricane force winds. Over the last 30 years, the average U.S. home has significantly increased by 40% from 154 m<sup>2</sup> (1,660 ft<sup>2</sup>) in 1973, to (216 m<sup>2</sup>) 2,330 ft<sup>2</sup> in 2003 (U.S. Census Bureau 2003). Larger homes are characterized by irregular floor and complex roof configurations. The homes examined in this project were much larger [325 m<sup>2</sup> (3,500 ft<sup>2</sup>)] with more complex roof configurations and the good performance observed in this study will be reassuring to those living in these new homes.

## Summary and Conclusions

This paper presents an analysis of the roof damage in newer, larger, irregular homes caused by Hurricane Charley. The site for the study was Punta Gorda Isles, a new subdivision of Punta Gorda and only homes built from 1996 to 2003 were examined. Aerial photographs were used for the study and damage was



quantified using specialized software. Homes were characterized as damaged, undamaged or moderately damaged based on area of tile loss (see Figs. 6–8). From the findings presented, the following conclusions may be drawn.

1. Despite being subjected to winds in excess of the design speed, there was relatively little roof damage in terms of missing tiles. Of the 425 homes examined, there was no roof damage in 210 homes (49%). There was minor damage in 158 homes (37%). Only 57 homes (14%) sustained significant damage. This suggests that existing code methods for calculating wind pressures in irregular structures or deemed to satisfy details for one- and two-story buildings in the Standard Building Code and Florida Building Code are adequate (see Table 2).
2. The buildings that sustained damage were located in the southern and western sides of Punta Gorda Isles (Fig. 9). Homes that were undamaged or moderately damaged were distributed more evenly (Figs. 10 and 11).
3. There was some evidence of damage due to poor tile installation. Impact from windborne debris also caused damage in some cases. Site visits revealed that in many cases windborne debris consisted of roof tiles from neighboring homes [Fig. 14(b)].
4. Damage was nearly twice as much on the eastern side of buildings compared to other sides (Table 5 and Fig. 12). This can be expected as primary sustained winds came from the east in the first part of the storm. These winds would have been stronger than the west winds produced as the storm passed over land and weakened. Also homes in disrepair or insufficiently secured roof tiles can be expected to have lost tiles during the first part of the storm. Any airborne debris would be traveling westward and impacting buildings on the eastern side.
5. Proximity to the eye of the hurricane did not necessarily result in greater damage.
6. Wind damage was concentrated to corners, ridges, hip zones, and eaves where negative pressures can be highest. It is possible that wind pressure coefficients in the complex roofs examined in these locations were underestimated. This problem can be most readily rectified by strengthening requirements for fastening tiles in these locations and ensuring that these measures are enforced through rigorous inspection.

It should be noted that all buildings in PGI were deed restricted to have tiled roofs. Therefore, these conclusions are valid for homes with concrete or clay tiled roofs.

## Acknowledgments

This study was funded by an exploratory grant (No. CMS-0456569) from the National Science Foundation. This funding is

gratefully acknowledged. However, the opinions, findings reported are those of the writers and not those of the National Science Foundation. The writers are indebted to Pictometry International for making available aerial photographs of damage used in this paper.

## References

- ASCE. (2003). *7-02 minimum design loads for buildings and other structures*, New York.
- Bradford, N. M., and Sen, R. (2004). "Gable end-wall stability in Florida hurricane regions, 10-year review: Post-Hurricane Andrew (1992) to Florida Building Code (2002)." *J. Archit. Eng.*, 10(2), 45–52.
- Charlotte County Florida. (1997–2004). "Charlotte County Florida geographical information systems." ([www.ccgis.com](http://www.ccgis.com)) (April 28, 2005).
- Charlotte County Property Appraiser. (1997–2004). "Record search." ([http://www.ccappraiser.com/rp\\_real\\_search.asp](http://www.ccappraiser.com/rp_real_search.asp)). (March 8, 2005).
- Cook, R., and Sotani, M., eds. (1994). *Hurricanes of 1992: Lessons Learned and Implications for the Future, Proc., Conf.*, ASCE, Miami, Fla., Dec. 1–3, 1993.
- FEMA. (2004). "Tile roofing for hurricane prone areas, recovery advisory No. 3." ([www.fema.com](http://www.fema.com)) (June 21, 2005).
- FEMA. (2005). "Hurricane Charley in Florida." Washington, D.C.
- Florida Building Code. (2001). ([www.floridabuilding.org/bc/default.asp](http://www.floridabuilding.org/bc/default.asp)), Dept. of Community Affairs, Tallahassee, Fla., (May 11, 2005).
- Meloy, N., Pai, N., Sen, R., and Mullins, G. (2005). "Impact of Hurricane Charley on residential and commercial construction." *Final Rep. to the National Science Foundation, CMS-0456569*.
- National Climatic Data Center. (2005). "Climate of 2004 Atlantic hurricane season." (<http://www.ncdc.noaa.gov/oa/climate/research/2004/hurricanes04.html#charley>) (June 17, 2005).
- Pictometry International. (2002). *User guide: Electronic field study version 2.4*, Pictometry International, Rochester, N.Y.
- Southern Building Code Congress International (SBC). (1993). "Standard for hurricane resistant residential construction." *SSTD 10-93*, Southern Building Code Congress, Birmingham, Ala.
- Southern Building Code Congress International. (1999). "Standard for hurricane resistant residential construction." *SSTD 10-99*, Southern Building Code Congress, Birmingham, Ala.
- Stathopoulos, T. (2003). "Wind loads on low buildings: In the wake of Alan Davenport's contributions." *J. Wind. Eng. Ind. Aerodyn.*, 91(12–15), 1565–1585.
- Sell, B. L., and Sparks, P. R., eds. (1991). *Hurricane Hugo one year later*, ASCE, New York.
- St. Petersburg Times. (2005). "FEMA: Costly repairs worth it." June 3, 1A.
- The Andreae Group. (1997–2003). "Punta Gorda waterfront real estate." ([www.liveonthewater.com/punta-gorda-isles.htm](http://www.liveonthewater.com/punta-gorda-isles.htm)) (May 26, 2005).
- U.S. Census Bureau. (2003). "Median and average square feet of floor area in new one-family houses completed by location." (<http://www.census.gov/const/C25Ann/sfttotalmedavgsgft.pdf>) (June 18, 2003).

## ADVANCES IN UNDERWATER PILE REPAIR USING FRP

### **Authors:**

*Rajan Sen and Gray Mullins*

Department of Civil and Environmental Engineering  
USF  
Tampa FL 33620  
USA

Phone: (01) 813- 974 5820

Fax: (01) 813- 974 2957

Email: sen@eng.usf.edu



### **About the Author: (12 pt. Bold underscore)**

Rajan Sen is a professor of structural engineering at the University of South Florida, Tampa, FL, where he held the Samuel and Julia Flom Endowed Chair. He is a fellow of both ACI and ASCE and on the editorial board of ASCE's Journal of Composites for Construction. Dr. Sen is active in FRP research and is a member of ACI 440, TRB's AFF80 and RILEM's FRP Bond Committee.

Gray Mullins is an associate professor in structural engineering at the University of South Florida, Tampa, FL. His primary research interest is in the area of full-scale testing and instrumentation of structures and foundations. Dr. Mullins has authored numerous publications and holds two US patents.

### **Abstract: (12 pt. Bold underscore)**

The availability of resins that can cure in water has made it possible to explore the use of FRP for the corrosion repair of piles. Over the past three years, USF has completed four such demonstration projects. Three of these were conducted in the tidal waters of Tampa Bay, Florida's largest estuary connecting Tampa Bay to the Gulf of Mexico. In each case selected piles were instrumented to allow long term monitoring of FRP's performance in mitigating corrosion. This paper presents an overview on the lessons learnt and future developments planned with particular reference to the completed field demonstration projects.



## 1. INTRODUCTION

Fiber reinforced polymers (FRP) have been used for the repair and retrofit of concrete structural elements for over two decades. Their lightweight, high strength and resistance to chemicals offer obvious advantages. In fabric form, they provide unprecedented flexibility since fibers can be oriented to provide strength in any desired direction.

More recently, FRP has also been used for corrosion repair. This application is somewhat controversial because of uncertainty regarding the consequences of continuing corrosion inside the wrap. Nonetheless, several demonstration projects have been completed though the majority of such repairs were carried out in dry conditions<sup>1</sup>.

Underwater FRP repair became a possibility following the availability of resins that can cure under wet conditions. This paper provides an overview of the progress made over the last four years in exploring the use of FRP for repairing corroding piles in Florida's tidal waters.

## 2. BACKGROUND

Among contiguous states in the United States, Florida has the longest coast line. Its sub-tropical climate, combined with the high salinity characteristic of Atlantic waters in the 20-30° latitude has made concrete piles in marine environments very susceptible to corrosion. The process starts by ingress of chlorides through the concrete cover that result in the destruction of the protective passive oxide film on the steel surface. Oxygen from the air or dissolved oxygen from the water coupled with moisture present in the concrete then oxidizes the steel leading to the formation of rust that occupies a much greater volume than the original steel. The resulting tensile stresses cause cracking and spalling that are symptomatic of corrosion damage.

Minor corrosion repairs are carried out using 'chip and patch' repair techniques. Greater damage is commonly repaired by encapsulating the corroded area in the "splash zone" (a region subjected to wet-dry tidal cycles) in a jacket (Fig. 1), usually made of fiberglass because of its light weight. The jacket does not contribute to the repair strength but merely serves as a stay-in-place form for the concrete that is poured in the annular space between the pile and the inside surface of the jacket. Since the fiberglass jacket is opaque the repaired region is hidden making it impossible for inspectors to assess its state of repair unless corrosion has progressed to the extent that external rust stains become visible.



Fig. 1. View of jacketed piles (left) and view of underlying corrosion with the jacket removed (right)

As a general principle, repairs are only durable if the conditions responsible for the original damage are removed. For corrosion damage, this requires removal of all the chloride-contaminated concrete and its replacement by sound concrete. This is a daunting task even when the repair is carried out under dry conditions. For piles that are half-submerged in salt water, the cost of such preparation is prohibitive. As a result, pile repairs are not durable unless they are used in combination with a cathodic protection system. Otherwise, it is only a matter of time before the repaired region corrodes again. Fig. 1 shows the state of corrosion in a pile revealed by removing the pile jacket. Such recurring damage makes repairs costly over the lifetime of the structure.

It should be noted that as FRPs are simply barrier elements they cannot stop the electro-chemical reactions responsible for corrosion. However, if the FRP system can be optimized, repairs may prove more durable and thereby offer a cost effective alternative to highway authorities. This is one of the motivating factors for continued research and development on this application.

### 3. ISSUES RELATING TO UNDERWATER FRP REPAIR

The critical issues relating to underwater FRP repair are in many respects similar to those for repairs carried out under dry conditions. For example, it requires the same attention to surface preparation, material placement and cure. It is therefore not unreasonable to expect underwater FRP repair to enjoy similar dominance in the repair market if overall costs are lower and the repair more durable than current jacketing methods (Fig. 1). Some of the issues relating to underwater repair are addressed briefly below:

*Surface Preparation* – as FRP pile repairs are part contact-critical (to withstand expansion due to corrosion) and part bond-critical (to allow flexural strengthening), surface preparation is crucially important. Unlike repairs above ground, pile repair necessitates removal of marine growth that forms at the water line (Fig. 2). This is best removed by using air-driven needle scalers, grinders or simply by chipping. Following removal of this growth, the surface needs to be cleaned and made smooth again. High pressure washing using fresh water is the most effective technique for cleaning. *ACI's Guide to Underwater Repair*<sup>2</sup> recommends a pressure of 68.5 MPa (10,000 psi) with a standoff distance of 10 to 80 mm (0.5 to 3 in.) and an impingement angle of 40-90° for best results. With a flow rate of 100L/min (26 gal/min), cleaning rates of 0.35 to 0.65 m<sup>2</sup>/min (4 to 7 ft<sup>2</sup>/min) are attainable.

*Cleaning Corroded Steel* – the International Concrete Repair Institute provides guidelines for the repair of deteriorated concrete resulting from steel corrosion (Guideline No. 03730<sup>3</sup>). This requires undercutting of all exposed corroded bars to provide access for under bar cleaning of the full circumference of the bar. Additionally, delaminated concrete must be removed to provide minimum thickness for the repair material. At edge locations, right angle cuts are required so that there is no 'feather edge', i.e. the depth of the cut is not reduced at the edges. However, in most demonstration projects reported in the literature<sup>1</sup> no particular attempt was made to comply with these guidelines because of the cost and potential danger to the structure. Instead, the wrap was designed to account for a greater steel loss.

*Access to Piles* – the success of the repair requires easy access to the entire region to be wrapped. Cofferdam construction (Fig. 3) permits ready access; however, it is likely to be costly. Customized scaffolding systems offer a cost effective solution and were used in the demonstration projects in deep waters. In essence it consists of a lightweight horizontal platform constructed of two expanded steel mesh sections that can be bolted in place around the piles. The assembly can be suspended from the pile cap by steel angles or chains.



Fig. 2. Marine growth

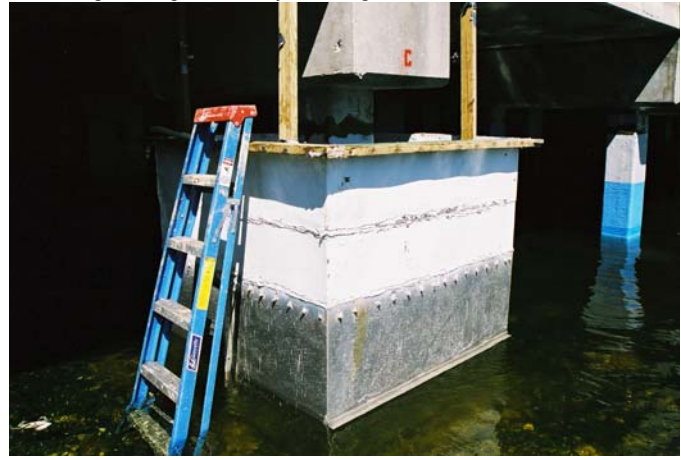


Fig. 3. Cofferdam construction

*Environmental conditions* – temperature, wind and tide conditions interfere with placement of the wrap and can adversely affect the quality of the repair. Strong winds and high tides are best avoided. Ideal conditions are low tide with light winds.

*Repair region* - Corrosion is particularly prevalent in elements that are exposed to the 'splash zone', i.e. within 0.6-1.8 m of the water line. The combination of deposition of salt on the pile surface and alternate dry/wet cycles due to tide change provide ideal conditions for corrosion in steel. This is the region that has to be repaired. There are, however, concerns that wrapping may result in migration of corrosion cells to locations above the FRP wrap as observed in conventional jacketed repairs. Laboratory tests<sup>4,5</sup> show that this can be avoided if the wrap is extended beyond the chloride contaminated part.

#### 4. DESIGN OF FRP WRAP

The economics of underwater FRP repair require that the wrap be engineered. The right FRP material with the optimal fiber layout should be selected to simplify field placement. This requires information on (1) the capacity loss that has to be restored and (2) the post-wrap expansion that has to be accommodated. Capacity loss is restored by orienting fibers parallel to the steel, i.e. length-wise. Expansion requires fibers in the transverse or hoop direction, i.e. perpendicular to the main steel. Both requirements are met by using bi-directional FRP material.

*Estimation of Strength Loss* – The problems posed in estimating strength loss are no different than that for repairs conducted under dry conditions. The first step is the estimation of metal loss. This depends on whether the corrosion is uniform or there is localized pitting corrosion. Estimation will be reliable if corrosion is so severe that the entire bar is fully exposed. Unfortunately, even if the steel loss were known, there is no simple relationship between metal loss and resulting ultimate capacity reduction since it depends on a number of factors such as the bond between steel and concrete, the confinement provided by the ties and ductility reduction in steel due to corrosion. Emmons<sup>6</sup> mentions that capacity reduces for steel if corrosion exceeds 1.5%; data he quoted stated that at 4.5% corrosion the ultimate load reduced by 12%. This suggests that it would be foolhardy to assume a linear relationship between metal loss and capacity even when losses are quite modest. In our demonstration studies, the metal loss was conservatively assumed to be 20%.

*Corrosion Expansion* – Although several experimental studies have been conducted to measure transverse strain due to corrosion expansion<sup>1</sup>, the results inevitably incorporate strains resulting from

*unrestrained* crack opening. CALTRANS<sup>6</sup> have a method for determining the number of FRP layers required to withstand lateral expansion during earthquakes. Though intended for circular sections, factors are provided that allow rectangular sections of certain proportions to be designed. After careful analysis, a strain limit of 0.1% - approximately three times the maximum tensile strain leading to cracking – was selected and was used in design<sup>5</sup>.

*Analysis* –An interaction diagram-based method was developed for designing the wrap for restoring capacity lost by corrosion. In the analysis only the FRP contribution to tensile strength was considered. The confinement effect of concrete was disregarded since it leads to modest increases in the ultimate axial capacity in non-circular sections. It was found that the assumed 20% strength loss was restored by using two transverse and one longitudinal carbon layer for the material properties outlined in Tables 1-2. For the weaker glass, two longitudinal and four transverse layers were required to attain the same objective. The wrap selected was checked to ensure that it had a transverse strain capacity of 0.1% to accommodate the expected transverse expansion.

## 5. FRP MATERIALS

Two types of materials were used in all the repairs. One was a pre-preg, the other a wet lay up. The pre-preg system was from Air Logistics in which all the FRP material was cut to size, resin-saturated in the factory and sent to the site in hermetically sealed pouches. The wet lay up system required on-site impregnation and was from Fyfe. An additional wet lay up system was also used but this repair was carried out under dry conditions inside a coffer dam<sup>5</sup>. For this reason, it is not discussed in this paper. Both carbon and fiberglass were used. Details of the properties of the fiber and the resin as provided by the suppliers are summarized in Tables 1 to 2<sup>7,8</sup>.

**Table 1.** Properties of Aquawrap® Fabrics<sup>7</sup>

<b>Fibers</b>	<b>Tensile Strength (MPa)</b>	<b>Tensile Modulus (GPa)</b>	<b>Load per Ply (kN/m)</b>
Uni-directional (GFRP)	590	36	420
Bi-directional (GFRP)	320	21	210
Uni-directional (CFRP)	830	76	596
Bi-directional (CFRP)	590	22	420

**Table 2.** Properties of Tyfo® SEH-51 Composite<sup>8</sup>

<b>Properties</b>	<b>Quantities</b>
Tensile Strength	3.24 GPa
Tensile Modulus	72.4 GPa
Ultimate Elongation	4.5 %
Laminate Thickness	0.127 cm
Dry fiber weight per sq. yd.	915 g/m <sup>2</sup>
Dry fiber thickness	0.038 cm

## 6. FIELD WRAP

The field demonstration projects were conducted in two phases. The first phase (completed in 2005) focused primarily on the feasibility of conducting an FRP repair of partially submerged pile. The



second phase (on-going) is intended to refine and improve the application to make underwater FRP repairs competitive in the market place.

The sites for all the demonstration projects were identified by the Florida Department of Transportation because of the aggressiveness of the environment. This was confirmed from chloride content analysis of concrete cores taken from several piles. The chloride content at the level of the reinforcement generally exceeded the threshold required for corrosion to be initiated.

The first demonstration project was carried out on piles supporting the Allen Creek Bridge, Clearwater, FL. It was selected because it is in shallow, relatively calm waters. The remaining studies were carried out on piles supporting Gandy Boulevard bridges spanning Tampa Bay, the largest estuary in Florida. The first of these two bridges is the Friendship Trails Bridge, now a recreational trail for pedestrians and cyclists. The second is the Gandy Bridge that is adjacent to the Friendship Trails Bridge. The waters of Tampa Bay are deeper and more turbulent than those of Allen Creek Bridge and the site is more representative of conditions where actual pile repairs are carried out.

### 6.1 Surface preparation

Good bond requires the substrate to have an open pore structure to ensure capillary suction of the resin<sup>6</sup>. In underwater repair, however, pores are saturated with water, small marine organisms or algae. As mentioned earlier, marine growth at the water line (Fig. 2) needs to be scraped off first. Additionally, sharp corners have to be ground to an acceptable radius using an air-powered grinder. This is a difficult operation particularly for sections that are below the water line. Quick-setting hydraulic cement was used to fill any depression, discontinuities and provide a smooth surface for wrapping. Just prior to the wrap, the entire surface must be pressure-washed using fresh water to remove all traces of dust, marine organisms and new algae growth.



Fig. 4. Scaffolding used for repair

### 6.2 Scaffolding

Excepting for the Allen Creek Bridge that was located in shallow waters, the remaining two bridges were in deeper waters in the middle of Tampa Bay. Whereas ladders were suitable for the Allen Creek Bridge site, a customized scaffolding system had to be designed, fabricated and installed for the other applications. Fig. 4 shows the scaffolding used in the Friendship Trails Bridge. This was developed for



a project in which all piles in a bent had to be wrapped. Thus, the scaffolding extended over the entire length of the pile cap. In subsequent studies, only 1 or 2 piles in a bent were wrapped and the scaffolding was re-designed for the smaller number of piles. This resulted in a lighter scaffold catering to individual piles. It was supported by steel chains so that it could be readily moved to provide access to other piles in the same bent that were to be repaired.

### 6.3 Impregnating FRP

As mentioned earlier, two different systems – a pre-preg and a wet layup were used. In the pre-preg system, the FRP was saturated with resin in a factory and sent to the site in hermetically sealed packages that were opened just prior to the wrap. In contrast, the wet layup system required on-site impregnation. This meant that the FRP fabric had to be pre-cut to size and then saturated with resin on-site (Fig. 5). In the initial application, an impregnating machine was built but this was abandoned in favor of manual application. In the latter, the two parts of the resin were mixed and then applied over the surface of the FRP fabric with a roller. The fabric was then flipped over and the other surface similarly saturated. The saturated elements were made into a roll for easy transportation.



Fig. 5. Saturating FRP on site



Fig. 6. Applying transverse wrap

### 6.4 FRP wrap

For the pre-preg system, a layer of the same urethane resin was first applied to the pile surface to improve the FRP-concrete bond. Subsequently, the longitudinal layers were placed on each face. The transverse piece was wrapped around it (Fig. 6) in a spiral fashion (excepting at the top and bottom locations) with no overlap. This sequence was repeated for multiple layers. A fiberglass veil material was also used to wrap transversely around the pile to provide a smooth finish.

For the wet lay up epoxy system, the saturated FRP material was directly wrapped on the concrete surface in the same manner – first longitudinal then transverse. Following completion of the wrap, a plastic shrink material was wound tightly around the pile to hold it in place while the resin cured. For the pre-preg, the surface of the plastic was punctured so that gases generated when the urethane resin cured could escape. After 24 hours, the plastic wrap was removed and a protective UV layer applied on the wrapped surface.

In each of the applications, a 1.5-1.8 m depth of the pile was wrapped using the appropriate number of longitudinal and transverse FRP layers. The wrapping operation generally took less than an hour.

## 6.5 Post wrap performance

The majority of the piles wrapped were instrumented to provide information on long term performance. Different instrumentation schemes were used so that the corrosion current or the corrosion rate could be determined. In general, corrosion performance of the FRP was monitored until the official end date for the project. This was longest for the Allen Creek Bridge where monitoring continued for over two and a half years. Results indicated that the performance of carbon and glass were comparable and were superior to that of the unwrapped control. Thus, these results replicated laboratory findings. More details may be found elsewhere<sup>4,5</sup>.

In addition to corrosion monitoring, the integrity of the FRP-concrete bond was evaluated destructively from on-site pullout tests. The results indicated that the bond was variable. For the epoxy system, the bond was found to be poorer in the dry part of the pile. For the pre-preg system it was worse for the wet region. Analysis of the results suggested that this was partly because of the difficulty in tightly wrapping material above shoulder height and also because of gases released by the pre-preg system during curing.

## 7. NEW DEVELOPMENTS

The results from the first phase were promising because it demonstrated that it was feasible to wrap corroding piles under typical field conditions. Moreover, corrosion rate measurements offered assurance that the FRP material was behaving in the same manner as in the laboratory. However, field bond performance was inferior compared to laboratory conditions.

The second phase was initiated in late 2005 to refine and improve the technology. Its goal is twofold: first to develop techniques that would result in less variability in the FRP-concrete bond. The second is to explore the possibility of incorporating a sacrificial cathodic protection system within the wrap.

Laboratory studies were made during 2005-2006 to evaluate alternative methods for improving the underwater FRP-concrete bond. In the tests, full-sized piles were used. Two candidate techniques widely used in aerospace were identified and adapted for pile repair. These were (1) vacuum bagging and (2) pressure bagging. Prototype systems were developed and the bond evaluated both non-destructively and destructively. Both techniques worked but from the practical standpoint it was concluded that pressure bagging was simpler to implement in the field.

Pressure bagging was successfully used in field repairs on piles supporting the Friendship Trails Bridge<sup>10</sup>. Qualitatively, the bond appeared to be improved though no on-site destructive bonds have yet been conducted. Such tests are planned in the future. Funding was recently received for implementing a pilot sacrificial cathodic protection system. This is expected to be implemented over the next 6-9 months at the same Friendship Trails Bridge site.

## 8. DISCUSSION

Over the past four years, steady progress has been made in advancing the state-of-the-art for FRP underwater pile repair. The demonstration projects completed to date have identified and solved several of the technical and logistic problems encountered or anticipated for the field wrap. These have been in these four areas: (1) instrumentation and monitoring (2) design (3) scaffolding and (4) new techniques for improving the underwater FRP-concrete bond.

Currently, the research team is looking at (1) developing a low-cost prototype for non-destructive field evaluation of the FRP concrete bond and (2) implementation of a sacrificial cathodic protection system. Additionally, consideration will be given towards implementing instrumentation that will allow remote monitoring and further refinement of the design procedure. The overall goal is to develop a cost effective, underwater FRP wrap system.

## 9. CONCLUSIONS

This paper provides a brief overview of FRP systems used in demonstration projects to repair corroding piles. Over the years, techniques have evolved to make the wrapping more cost effective. Initially, wrapping was carried out directly in water using ladders and later using a custom-designed scaffolding system. Two different FRP systems, a pre-preg and a wet layup, were evaluated and both carbon and glass tested. In each case, piles were instrumented to allow the long term performance of the FRP material to be assessed.

Based on our experience, it is clear that it is feasible to use FRP for underwater corrosion repair. The performance of the FRP in slowing down the corrosion rate appears to be comparable to that determined from laboratory testing. The repairs have held up well with the longest nearly four years old at this time. The FRP-concrete bond however was found to be poorer than that obtained under laboratory conditions.

Work is continuing to further improve the FRP system. A pressure bagging technique was developed last year to improve bond and the feasibility of incorporating a cathodic protection (CP) system within the wrap is currently being examined. Overall, the portents are promising and hopefully will culminate in the availability of a cost effective solution for repairing piles that is accepted by highway authorities.

## Acknowledgements

The demonstration studies reported were funded by the Florida/US Department of Transportation and Hillsborough County. The support and guidance of Mr. Pepe Garcia and Mr. Steve Womble, both of Florida Department of Transportation are gratefully acknowledged. We thank Ms. Mara Nelson, and Mr. Nils Olsson of Hillsborough County for their contribution. FRP materials used were donated by Air Logistics, Corporation and Fyfe & Co LLC. We thank Mr. Franz Worth of Air Logistics and Mr. Ed Fyfe, President, Fyfe for this support. We are also indebted to SDR Engineering, Tallahassee for their contribution in this research study. This study could not have been accomplished without the assistance of numerous former and current graduate students at USF.

## References

1. Sen, R. (2003). "Advances in the Application of FRP for Repairing Corrosion Damage", *Progress in Structural Engineering and Materials*, Vol. 5, No 2, pp. 99-113.
2. 546.2R-98 (1998). "Guide to Underwater Repair of Concrete", ACI, Farmington Hills, MI.
3. Concrete Repair Manual (2003). Second Edition, Vol. 1, p. 915-924, ACI, Farmington Hills, MI.
4. Suh, K., Mullins, G., Sen, R. and Winters, D (2007). "Effectiveness of FRP in Reducing Corrosion in a Marine Environment". *ACI Structural Journal*, Vol.104, No. 1, pp. 76-83

5. Mullins, G., Sen, R., Suh, K.S. and Winters, D. (2005). "Use of FRP for Corrosion Mitigation Application in a Marine Environment". Final Report submitted to Florida / US Department of Transportation, Tallahassee, FL, Oct., 406 pp.
6. Emmons, P.H. (1993). *Concrete Repair and Maintenance Illustrated*, R S Means, Kingston, MA.
7. CALTRANS (2000). Memo To Designers 20-4 Attachment B.
8. Air Logistics Corporation (2002). Aquawrap Repair System, Pasadena, CA.
9. Fyfo Co. LLC, <http://www.fyfeco.com/>
10. Mullins, G., Sen, R., Winters, D. and Schrader, A. (2007). 'Innovative Pile Repair', Final report, Hillsborough County, pp. 40.

# Fiber-Reinforced Polymer Repair and Strengthening of Structurally Deficient Piles

Rajan Sen, Gray Mullins, and Mohsen Shahawy

The poor durability of conventional repairs has led to increased interest in the application of fiber-reinforced polymers (FRP) for repairing corroded concrete structures. The availability of resins that can cure under wet conditions has made it possible to consider FRP for repairing partially submerged piles. An overview is provided of a recently completed multiyear study that investigated this problem. In the project, laboratory studies were conducted to determine the effectiveness of FRP in corrosion repair, and two field demonstration projects were completed. A simple, new design method was developed and used for the design of the FRP wrap in the demonstration projects. Some of the issues related to pile repair are addressed, with particular attention to the newly developed design method.

Fiber-reinforced polymers (FRP) have been used for the repair and retrofit of concrete structural elements for more than two decades. Their light weight, high strength, and resistance to chemicals offer obvious advantages. In fabric form, they provide unprecedented flexibility since fibers can be oriented to provide strength in any desired direction.

More recently FRP also has been used for corrosion repair. This application is somewhat controversial because of uncertainty regarding the consequences of continuing corrosion inside the wrap. Nonetheless, several demonstration projects have been completed, most carried out under dry conditions (1).

The problems associated with conducting FRP repairs on partially submerged elements were greatly reduced following the availability of resins that can cure under wet conditions. This development, along with the proposed, rational FRP design method, has the potential to make FRP competitive in the market place.

This paper provides an overview of a recently completed research project. It contains information on a long-term exposure study to evaluate the effectiveness of FRP in corrosion repair and also addresses general issues relating to FRP repair of structurally deficient piles. A detailed description of the design method is included, along with a brief summary on the field demonstration projects. Complete details on the entire study may be found in the final report (2).

R. Sen and G. Mullins, Department of Civil and Environmental Engineering, University of South Florida, 4202 East Fowler Avenue, Tampa, FL 33620. M. Shahawy, SDR Engineering Consultants, Inc., 2434 Oakdale Street, Tallahassee, FL 32308. Corresponding author: R. Sen, sen@eng.usf.edu.

*Transportation Research Record: Journal of the Transportation Research Board*, No. 2028, Transportation Research Board of the National Academies, Washington, D.C., 2007, pp. 221–230.  
DOI: 10.3141/2028-24

## LABORATORY INVESTIGATION

Laboratory studies were undertaken to quantify the role of FRP in corrosion repair (2, 3). In the study, 22 one-third-scale pile specimens  $15 \times 15$  cm in cross section were fabricated with 3% by weight cementitious material (corresponding to  $15.1 \text{ kg/m}^3$  chloride ions) so that the passive layer protecting steel was immediately destroyed. Of these, 16 were wrapped by using carbon (eight specimens) and glass (eight specimens) FRPs at 28 days' strength. The remaining six unwrapped specimens were used as controls. Embedded activated titanium reference electrodes and thermocouples were used to instrument the specimens so that the performance of the FRP material could be evaluated nondestructively from half cell readings and linear polarization measurements.

A total of 20 specimens—16 wrapped and four unwrapped controls—were exposed to simulated tidal cycles in 3% saltwater in an outdoor environment for more than 3 years. Two other unwrapped controls were exposed to the same environment indoors over the same period. Within 1 year, there were cracking and rust stains in the unwrapped controls. No similar visible signs of corrosion were detected in the wrapped specimens exposed to the identical environment.

The corrosion state of the specimens was monitored throughout the exposure period. Linear polarization measurements indicated that the average corrosion rate in the controls was 0.018 mm/year compared to only 0.0055 mm/year in the wrapped specimens. These rates are commensurate with corrosion where visible damage can be expected within 2 to 10 years. Since the controls cracked within the first year, the measured uniform corrosion rates underpredicted the true corrosion state in the controls.

After more than 3 years of exposure, the specimens were removed from the tanks and cut open to retrieve the strands and ties from all the wrapped and unwrapped specimens. The metal loss was determined in accordance with established gravimetric procedures outlined in ASTM G1-90.

A summary of the results of the measured metal loss is given in Figure 1, which shows that the metal loss in the strands in FRP-wrapped specimens (ranging from 3.4% to 4.4%) was considerably smaller than that in the controls (12.6%). These results corroborated well with measured corrosion rates from the linear polarization mentioned earlier. The results also suggested that an increased number of layers did not necessarily lead to improved performance. The best results were obtained by using two layers. It is not evident why results with a greater number of layers were inferior, although a similar finding had been reported earlier (1).

The results from the gravimetric measurements are somewhat misleading because they reflect average values. This does not account for breaks in individual wires in the strands that were discovered. There



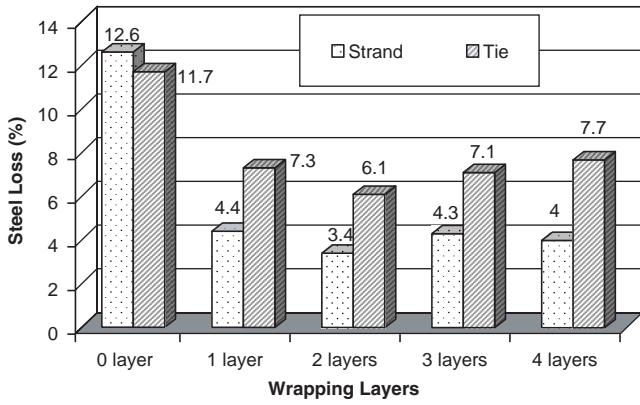


FIGURE 1 Measured steel loss in unwrapped (0 layer) and wrapped specimens after 3 years of identical exposure in wet-dry saltwater cycles under ambient conditions.

were 30 total wire breaks in the six unwrapped control specimens. Figure 2 shows such a wire break in a strand. In contrast, the strands in the FRP-wrapped specimens showed no similar damage (Figure 2b)—in fact, there was only one wire break of 64 strands in the 16 wrapped specimens. The wire breaks most likely were the result of localized pitting corrosion that may have occurred at a section that was cracked. Taking the wire breaks into consideration, FRP wrapping led to significantly improved performance.

Although some of the metal loss in the FRP-wrapped specimens may have occurred in the 28 days before the specimens were wrapped, the results clearly indicate that FRP material cannot stop corrosion, although it can slow it significantly. Thus, service life is extended. This increase in service life is shown schematically by using Tuutti’s model in Figure 3 (4). With the destruction of the passive layer, corrosion was initiated at the same time in both the controls and the wrapped specimens. However, the much lower corrosion rate in the wrapped specimens implies that the specimens took longer to crack and to subsequently deteriorate. If the FRP repair can extend the life of a repair by, say, 5 to 10 years, it may well prove to be a cost-



FIGURE 2 Retrieved strands after 38 months of exposure to outdoor simulated tidal cycles in 3% saltwater: unwrapped (top) and FRP wrapped (bottom).

effective alternative to repairs in which the piles repairs are carried out in conjunction with cathodic protection.

### ISSUES RELATING TO UNDERWATER FRP REPAIR

The critical issues relating to underwater FRP repair of partially submerged piles are in many respects similar to those for repairs carried out under dry conditions. Some of these are addressed briefly here.

#### Repair Region

Corrosion is particularly prevalent in elements that are exposed to the splash zone, that is, within 0.6 to 1.8 m of the water line. The combi-

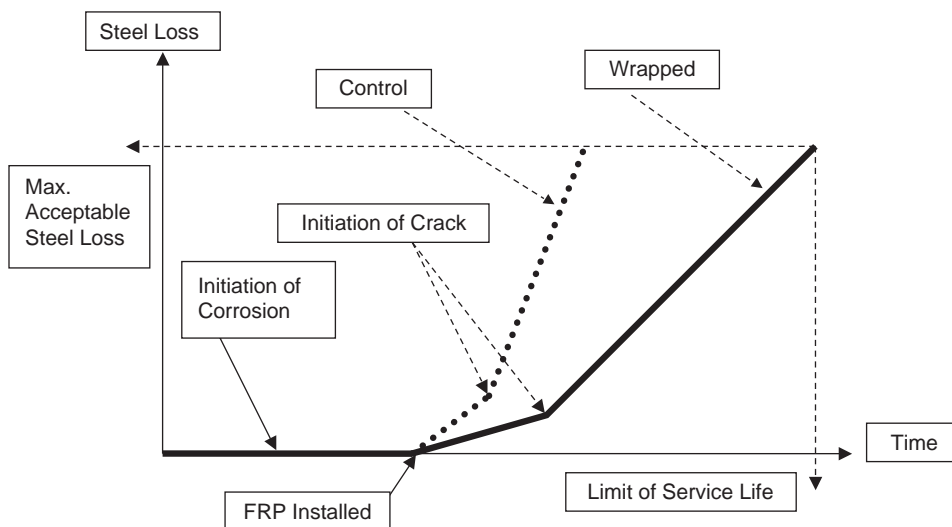


FIGURE 3 Extended service life in wrapped piles.

nation of deposition of salt on the pile surface and alternate dry–wet cycles caused by tide change provides ideal conditions for corrosion in steel. This is the region that has to be repaired. There are concerns, however, that wrapping may result in migration of corrosion cells to locations above the FRP wrap, as observed in conventional jacketed repairs. Laboratory tests, however, showed that this can be avoided if the wrap is extended beyond the chloride contaminated region (2, 3).

### Access

Repair requires easy access to the entire region to be wrapped. Cofferdam construction permits such access; however, it is likely to be costly. Customized scaffolding systems offer a cost-effective solution and were used in the demonstration projects in deep waters. In essence, a lightweight horizontal platform was constructed of two expanded steel mesh sections that were bolted in place around the piles. The assembly was suspended from the pile cap by steel angles or chains (2).

### Environment

Temperature, wind, and tide conditions interfere with the proper placement of the wrap and can adversely affect the quality of the repair. Strong winds and high tides are best avoided. Ideal conditions are low tide and light winds.

### Cleaning Steel

The International Concrete Repair Institute provides guidelines on the repair of deteriorated concrete resulting from steel corrosion (5, pp. 915–924). This requires undercutting of all exposed corroded bars to provide access for cleaning the full circumference of the bar. Additionally, delaminated concrete must be removed to provide minimum thickness of the repair material. At edge locations, right angle cuts are required so that there is no feather edge, that is, so the depth of the cut is not reduced at the edges. However, in most demonstration projects reported in the literature, no particular attempt was made to comply with these guidelines because of the cost and potential danger to the structure. Instead, the wrap was designed to account for a greater steel loss.

### Surface Preparation

As FRP pile repairs are in part contact critical (to withstand expansion due to corrosion) and in part bond critical (to allow flexural strengthening), surface preparation is crucially important. Unlike repairs above ground, pile repair necessitates removal of marine growth that forms at the water line. This is best removed by using air-driven needle scalers or grinders or simply by chipping. Following removal of this growth, the surface needs to be cleaned and made smooth again. High-pressure washing using fresh water is the most effective technique for cleaning. The American Concrete Institute's *Guide to Underwater Repair* recommends a pressure of 68.5 MPa (10,000 psi) with a standoff distance of 10 to 80 mm (0.5 to 3 in.) and an impingement angle of 40° to 90° for best results (6). With a flow rate of 100 L/min (26 gal/min), cleaning rates of 0.35 to 0.65 m<sup>2</sup>/min (4 to 7 ft<sup>2</sup>/min) are attainable.

## DESIGN OF FRP WRAP

The economics of underwater FRP repair require that the wrap be properly engineered. The right FRP material with the optimal fiber layout should be selected to simplify field placement. This requires information on (a) the capacity loss that has to be restored and (b) the postwrap expansion that has to be accommodated. Capacity loss is restored by orienting fibers parallel to the steel, that is, lengthwise. Expansion requires fibers in the transverse or hoop direction, that is, perpendicular to the main steel. Both requirements are readily met by using bidirectional FRP material.

### Estimation of Strength Loss

The problems posed in estimating strength loss are no different from those for repairs conducted under dry conditions. The first step is the estimation of metal loss. This depends on if the corrosion is uniform or if there is localized pitting corrosion. Estimation may be reliable if corrosion is so severe that the entire bar is fully exposed. Unfortunately, even if the steel loss were known, there is no simple relationship between metal loss and resulting ultimate capacity reduction since it depends on other factors, such as the bond between steel and concrete, the confinement provided by the ties, and ductility reduction in steel because of corrosion. Emmons mentioned that capacity reduces for steel if corrosion exceeds 1.5% (7); data he quoted stated that at 4.5% corrosion, the ultimate load reduced by 12%. This suggests that it would be foolhardy to assume a linear relationship between metal loss and capacity even when losses are quite modest. In the present demonstration studies, the metal loss was conservatively assumed to be 20%.

### Corrosion Expansion

Although several experimental studies have been conducted to measure transverse strain caused by corrosion expansion (2, 7–9), the results inevitably incorporate strains resulting from unrestrained crack opening (see Table 1). The California Department of Transportation (Caltrans) has a method for determining the number of FRP layers required to withstand lateral expansion during earthquakes (10). Although intended for circular sections, factors are provided that allow rectangular sections of certain proportions to be designed.

## ASSUMPTIONS

Several simplifying assumptions were used in the analysis because of lack of information. Some of the more important ones are as follows:

1. The loss of prestressing steel was conservatively taken as 20%.
2. The increase in concrete strength because of the confining effect of the FRP material was disregarded (11, 12).
3. The postwrap expansion strain is based on the ultimate tensile strain. For simplicity this was assumed to be 10% of the ultimate compressive strain of 0.003. In piles, corrosion is rarely uniform but usually starts at a corner, from which corrosion can proceed in two directions. In view of this, a factor of safety of 3 was assumed to account for this nonuniformity. Thus, the design tensile strain was taken as 0.001.

TABLE 1 Measured Expansion Strain

Author	Specimen and Test Details	Steel Loss	Transverse Strain (%)	Comments
Lee et al. (8)	Circular section 305 dia × 1,016 height reinforced by six 15-m bars and D5 spirals at 44 mm	6.7%	0.18	Measured by mechanical collars Steel loss estimated from corrosion, Faraday's laws
		7.8%	0.18	
		9.5%	0.16	
Pantazopoulou et al. (9)	Circular section 150 dia and 300 high reinforced by three 10-mm dia bars. With spirals – 3 mm at 25-mm pitch and without spirals	110–170 g 155–440 g	1.4–2.0 2.0–4.0	Spirals No spirals
Mullins et al. (10)	Square section 150 × 150 × 1,000 mm prestressed by four 8-mm strands and 5.3-mm spirals at 11.4-cm pitch	11.5%	0.20	Measured using crack gauges; losses from gravimetric analysis
		21.6%	0.32	
Mullins et al. (2)	Square section 150 × 150 × 1,000 mm prestressed by four 8-mm strands and 5.3-mm spirals at 11.4-cm pitch	12.85%	0.4	Measured by circumferential strain wires; losses from gravimetric analysis
		19.54%	1.11	

4. The bond between the FRP and the concrete is assumed to be perfect. As a cofferdam was used, and the wrap was conducted under a dry environment, this was a reasonable assumption.

5. Only the carbon fiber–reinforced polymer (CFRP) material on the tension face of the column is considered.

6. The distance from the extreme compression or tension fiber to the centroid of the prestressing strands was taken as 3 in. (75 mm).

7. The prestressing strands in the demonstration piles were assumed to be stress relieved, and their effective prestress was taken as 135 ksi (930 MPa).

## MATERIAL PROPERTIES

The CFRP material used was a bidirectional fabric wrap using Amaco fibers. Its properties are summarized in Table 2. The epoxy used is a specially formulated resin marketed as the MAS2000 repair system. Its basic properties are shown in Table 3. Carbon properties relate to the individual yarns, which make up the larger weave. These yarns are produced from a continuous-length, high-strength, high-modulus fiber consisting of 12,000 filaments. The 12,000 filaments produce one strand with a total cross-sectional area of 0.45 mm<sup>2</sup> (70 × 10<sup>-5</sup> in.<sup>2</sup>) and a tensile strength of 3,654 MPa (530 ksi). The tensile strength per unit length is 4.34 kN/cm (2.48 kips/in.).

TABLE 2 Material Properties for Carbon Wrap System, Carbon Fabric

Description	Manufacturer's Data <sup>a</sup>
Tensile strength	530 ksi (3.65 GPa)
Tensile modulus of elasticity	33,500 ksi (231 GPa)
Ultimate tensile elongation	1.4%
Filament diameter	7 μm
Number of filaments per yarn	12,000
Number of yarns (X/Y) per inch	6.7/6.7
Density	12 oz/yd <sup>2</sup>
Equivalent thickness per layer	0.0048 in.
Section area per yarn	70 × 10 <sup>-5</sup> in. <sup>2</sup> /yarn

<sup>a</sup>Reported for carbon fabric only.

## RESTORING CAPACITY LOSS

For the assumptions made, the well-known strain compatibility analysis may be extended to apply to cross sections strengthened by using FRP. With this analysis, a parametric study was carried out to determine the effect of prestress loss on the tension face or the compression face strands in the  $M_n$ – $P_n$  interaction diagram. Three levels of prestress loss, namely, 0%, 10%, and 20%, were considered. The study showed that the differences between the  $M_n$ – $P_n$  diagrams relating to uniform loss (i.e., distributed in all faces of the column) and loss on strands located on the tension face only, on one hand, and on compression face only, on the other hand, were negligible for 0% to 20% loss and did not affect the design. For this reason, the results reported are for uniform loss on all four faces.

## M–P DIAGRAMS

Figure 4 shows the  $M_n$ – $P_n$  interaction diagrams for the 14 × 14 in. (355 × 355 mm) piles corresponding to a uniform prestress loss of 0% and 20%. It may be seen that the compression-controlled part of the diagram does not change with prestress loss due to corrosion. However, the flexure-controlled portion is substantially affected by the loss. A 20% loss resulted in an approximate 15% decrease in the moment capacity for typical axial service loads. Also shown in Figure 4 are the results from strengthening with two and three layers of carbon wraps. It may be concluded that for an assumed concrete compressive strength of 4 ksi (27.6 MPa), two layers of CFRP are sufficient to compensate for 20% loss in prestressing reinforcement and to restore the initial capacity of the pile.

Figure 5 shows the effect of compressive concrete strength on the overall performance. The variation of concrete strength generally influences the axial load capacity and, to a lesser magnitude, the moment capacity. The figure shows that use of two layers of CFRP is sufficient to establish the original load-carrying capacity regardless of the assumed compressive concrete strength.

## CORROSION EXPANSION DURING SERVICE LIFE

The strengthening solution outlined uses only the longitudinal fibers of the FRP wrap. In other words, the confinement effect of the lateral CFRP fibers in the case of a bidirectional wrap on the compressive

**TABLE 3 Material Properties for Carbon Wrap System, Material Properties for Epoxy**

Description	Values	Test Method
Mix ratio		
By weight	100 : 27	Manufacturer
By volume	3 to 1	
Color	Light amber	Visual
Mixed viscosity, centipoise, @ 77°F	900–950 cps	ASTM D2393
Pot life, 4 fluid ounces mass	1 h	ASTM D2471
Cured hardness, shore D	88D	ASTM D2240
Specific gravity, gm/cc	1.11	ASTM D1475
Density		
lb/cu.in.	0.0401	ASTM D792
lb/gal	9.26	
Specific volume, cu. in./lb	25	ASTM D792
Tensile strength, psi	45,170 psi	ASTM D638
Elongation <sup>(1)</sup>	1.96%	ASTM D638
Tensile modulus, psi	$2.62 \times 10^6$ psi	ASTM D638
Flexural strength, psi	62,285 psi	ASTM D790
Flexural modulus, psi	$2.56 \times 10^6$ psi	ASTM D790
Glass transition temperature ( $T_g$ )	196°F	TMA
Coefficient of thermal expansion	$4.3 \times 10^{-5}$ in./in./°F	ASTM D696
Range: 100°F – 150°F		

concrete strength was not considered in the proposed solution, which is conservative since such a confinement would lead to yet a greater resistance of the column, ranging from 2.3% for one layer to 9.4% for four layers for the materials used in the study (11). This confinement effect provided by the FRP wrap in the transverse direction can also be used to mitigate corrosion by containing the expansion of the concrete that develops as steel corrodes during the service life of the pile.

The number of layers of FRP wrap needed to contain corrosion expansion is an important element that must be examined. In the following calculations, three methods are used to address the problem. These methods are based on (a) Caltrans recommendations (13), (b) ISIS recommendations (14), and (c) the model proposed

by Chaallal et al. (12). However, note that the Caltrans recommendations, particularly those for the column hinge zones, are severe since they are intended for bridges located in seismic regions, such as California. Therefore, they must be adapted for reality in Florida. All notations used are those of the source publications; however, they are redefined here for convenience.

**Caltrans Model**

According to Caltrans, the analysis to be performed is for circular columns, with the resulting number of layers arbitrarily multiplied by a factor of 1.5 to give the correct layer setup for a rectangular

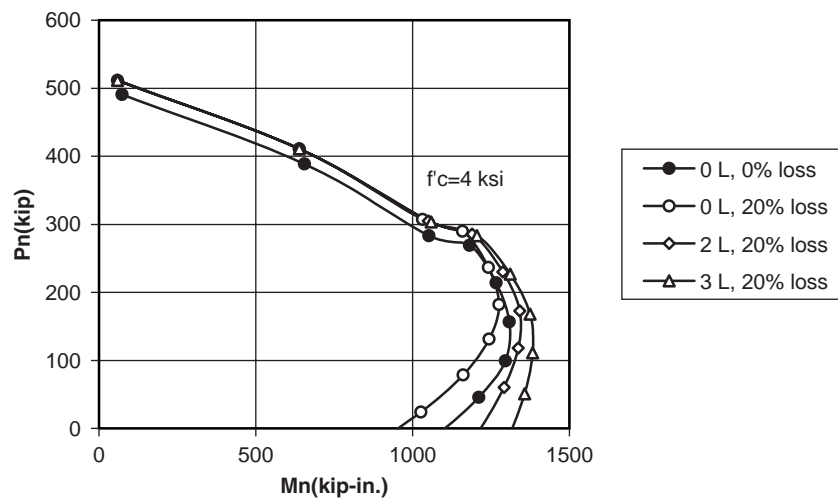


**FIGURE 4 Effect of uniform 20% loss of prestressing strands.**

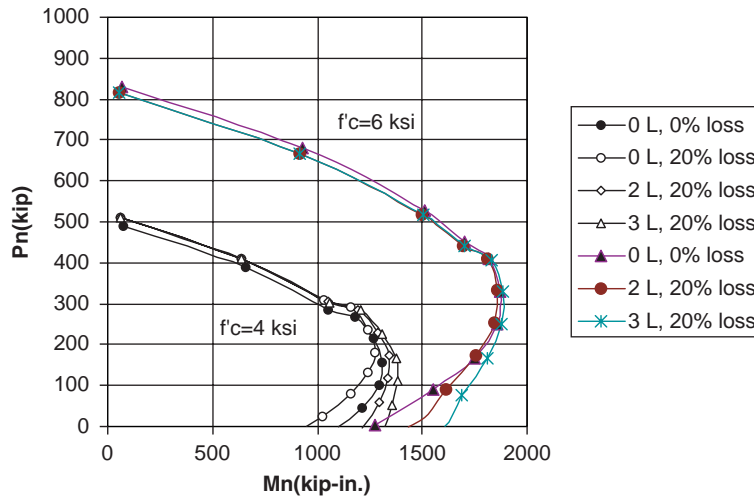


FIGURE 5 Effect of concrete strength.

column. Based on the cross-sectional area of concrete, the square pile 14 × 14 in. is equivalent to a circular pile with a diameter *D* of 15.8 in. (400 mm).

Caltrans recommends a confining stress of 300 psi (2,068 kPa) at a strain of 0.004 in the hinge region and 150 psi (1,034 kPa) at a strain of 0.004 in other regions. Following Figure 6 the thickness of the FRP can be calculated by using the well-known expression for hoop stress given by Equation 1 as

$$2(t)(\epsilon_j)(E_j) = (f_i)(D) \tag{1}$$

where

- t* = dry fiber thickness,
- D* = equivalent column diameter,
- f<sub>i</sub>* = confining stress,
- E<sub>j</sub>* = Young's modulus of the jacket material multiplied by a reduction factor of 0.9, and
- $\epsilon_j$  = dilating strain in the FRP material.

The numerical applications are as follows:

1. Hinge region:

$$2(t)(E_j)(0.9)(0.004) = (300 \text{ psi})(D)$$

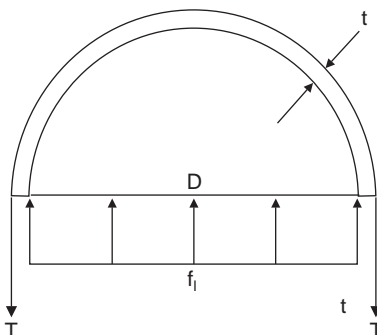


FIGURE 6 Hoop stress in FRP wrap.

where 0.9 is a reduction factor for modulus of elasticity of FRP;

$$2(t)(33,500,000)(0.9)(0.004) = (300 \text{ psi})(15.8) = 4,740$$

resulting in *t* = 0.02 in. (0.51 mm);

- Carbon layer thickness, *t* (1 layer) = 0.0048 in. (0.122 mm);
- Number of layers = 0.02/0.0048 = 4.16;
- Rectangular section needs 1.5 × 4.16 = 6.24 (say, seven layers).

2. Other region:

$$2(t)(E_j)(0.9)(0.004) = (150 \text{ psi})(D)$$

where 0.9 is a reduction factor for modulus of elasticity of FRP;

$$2(t)(33,500,000)(0.9)(0.004) = (150)(15.8) = 2,370$$

resulting in *t* = 0.0098 in. (0.25 mm);

- Number of layers = 0.0098/0.0048 = 2.04;
- Rectangular column would require 1.5 × 2.04 = 3.06 (say, four layers).

3. Application to Florida. As mentioned earlier, expansion just before cracking (the ultimate tensile strain) is roughly 10% of the ultimate compressive strain (0.1)(0.003) = 0.0003 and provides a lower bound on the expansion strain. It is believed that a strain value of 0.001 (that is, a safety factor of 3) is appropriate for this case. In this case, the confining stress for three layers of CFRP lateral confinement (*t* = 3 × 0.0048 = 0.0144 in.) can be calculated as follows by using the Caltrans equation:

$$2(t)(E_j)(0.9)(0.001) = (f_i)(D)$$

where  $f_i = 2(0.0144)(33,500,000)(0.9)(0.001)/(15.8)$  or  $f_i = 55$  psi for a circular section. That is, 1.5 × 55 = 83 psi for a rectangular column.

With the Caltrans equation and for a confining stress of 150 psi and a strain of 0.001, 4 × 2.04 = 8.2 layers of CFRP wrap would be needed for a circular column and 8.2 × 1.5 = 12.3 layers for rectangular columns. Table 4 gives the number of CFRP layers for different confinement strains and stresses following the Caltrans recommendations.



**TABLE 4 CFRP Layers for Confinement Strain and Stress per Caltrans Model for Circular Column**

Confinement <sup>a</sup>		Number of CFRP Layers <sup>b</sup>		Comments
Strain	Stress (psi)	Circular	Rectangular <sup>c</sup>	
0.004	300	4.1	6.2	300 psi for hinge location in seismic areas
0.004	150	2.1	3.1	150 psi for nonhinge location in seismic areas
0.002	150	4.1	6.2	
0.001	150	8.2	12.3	
0.001	55	3	4.5	Values for 3 layers

<sup>a</sup>For circular column.  
<sup>b</sup>Based on thickness/layer = 0.0048 in.  
<sup>c</sup>Value of circular times 1.5.

**ISIS Model**

ISIS Canada limits the lateral strain in FRP wraps for rectangular columns to 0.002, which is twice the representative value for corrosion assumed to be 0.001 in this paper. The lateral stress  $f_{l,frp}$  is given by the following equation:

$$f_{l,frp} = \frac{2N_b \phi_{frp} E_{frp} \epsilon_{frp} t_{frp} (b + h)}{bh} \tag{2}$$

where

- $b$  = width of the concrete cross section,
- $E_{frp}$  = modulus of elasticity of FRP,
- $f_{l,frp}$  = lateral stress of FRP,
- $h$  = height of the concrete cross section,
- $N_b$  = number of FRP layers,
- $t_{frp}$  = thickness of one FRP layer,
- $\epsilon_{frp}$  = strain of FRP, and
- $\phi_{frp}$  = capacity reduction factor.

Given that the number of layers recommended for a 20% loss is 2, the lateral stress corresponding to the same number of layers is calculated, that is,  $N_b = 2$ . By using the above equation, it follows that

$$f_{l,frp} = \frac{2 \times 2 \times 0.75 \times 33,500,000 \times 0.002 \times 0.0048}{(14 + 14)(14 \times 14)} = 138 \text{ psi}$$

For a confining stress of 138 psi and a strain of 0.002, two layers of FRP are required. It follows that for a 300-psi confinement, as recommended by Caltrans for plastic hinge zones, and a strain of 0.002,  $300/138 \times 2 = 4.3$  layers will be required.

Table 5 gives the number of CFRP layers for different confinement strains and stresses following the ISIS recommendations.

**Model of Chaallal et al.**

On the basis of an expansion strain of 0.001 (that is, the strain at cracking multiplied by a safety factor of 3), the ultimate lateral strain,  $\epsilon_{cc,t}$  for a given confinement coefficient  $k$  (provided by two layers of CFRP) and an unconfined concrete strength  $f_{co}$ , is calculated according to the model for rectangular columns as follows:

$$\epsilon_{cc,t} = \left[ 4.2 + 4,000 k - 320,000 k^2 \right] / f_{co} \tag{3}$$

where  $f_{co}$  is 4,000 psi, and  $k$ , the stiffness factor, is given by

$$k = E_{frp} A_{frp} / E_{co} A_{co} \tag{4}$$

That is,

$$k = 33,500 \times 2 \times 0.0048 / (3,605 \times 14 \times 14) = 0.0005$$

It follows that  $\epsilon_{cc,t} = 0.0015$ .

The two CFRP confinement layers provided will therefore provide a lateral strain capacity of 0.0015. This strain value is of the same order as the representative strain corresponding to crack strain (0.001) times a safety factor of 3.

Using this model and assuming that  $\epsilon_{cc,t} = 0.002$  will require approximately 4.4 layers of CFRP.

Table 6 gives the number of CFRP layers for different confinement strains based on this model. It may be seen that for prestress steel loss of up to 20%, two layers of CFRP wrapping can be used to restore the initial capacity of the piles, while simultaneously accommodating

**TABLE 5 CFRP Layers for Confinement Strain and Stress per ISIS Model for Rectangular Columns**

Confinement <sup>a</sup>		Number of CFRP Layers <sup>b,c</sup>
Strain	Stress (psi)	
0.002	138	2.0
0.002	300	4.3
0.001	138	4.0
0.001	83 <sup>d</sup>	2.4 <sup>e</sup>

<sup>a</sup>For rectangular column.  
<sup>b</sup>Based on a thickness per layer of 0.0048 in.

$$N_b = \frac{f_L (b \times h)}{2 \phi_{frp} E_{frp} \epsilon_{frp} t_{frp} (b \times h)}$$

<sup>d</sup>Compare with 55 psi in Table 3, Confinement Stress, circular column.  
<sup>e</sup>Compare with 4.5 CFRP layers in Table 3, rectangular column.

**TABLE 6 CFRP Layers for Confinement Strain per Author Model for Rectangular Columns**

Confinement Strain <sup>a</sup>	Number of Layers
0.0015	2.0
0.002	4.4
0.003	10.6
0.004	20.9

<sup>a</sup>For a concrete strength of 4,000 psi.

a transverse expansion strain of 0.0015. This gives fewer layers compared with the Caltrans (4.5) and ISIS (2.4) models, appearing as the last line in Tables 4 and 5, respectively.

## FIELD WRAP

Two field demonstration projects were conducted. The sites for the demonstration project were identified by the Florida Department of Transportation because of the aggressiveness of the environment. This was confirmed from chloride analysis of concrete cores taken from several piles. The chloride content at the level of the reinforcement generally exceeded the threshold required for corrosion to be initiated.

The first demonstration project was carried out on piles supporting the Allen Creek Bridge in Clearwater, Florida. It was selected because it is in shallow, relatively calm waters. The second was carried out on piles supporting Gandy Boulevard bridges spanning Tampa Bay, the largest estuary in Florida.

## Surface Preparation

Good bond requires the substrate to have an open pore structure to ensure capillary suction of the resin. In underwater repair, however, pores are saturated with water, small marine organisms, or algae. As mentioned, marine growth at the water line needs to be scraped off first. Additionally, sharp corners have to be ground to an acceptable radius by using an air-powered grinder. This is a difficult operation, particularly for sections that are below the water line. Quick-setting hydraulic cement was used to fill any depressions and discontinuities and to provide a smooth surface for wrapping. Just before the wrap, the entire surface must be pressure washed by using fresh water to remove all traces of dust, marine organisms, and new algae growth.

## Scaffolding

Scaffolding was needed to access the piles supporting the Gandy Bridge that spans Tampa Bay. A customized scaffolding system with modular elements was designed, fabricated, and installed to provide such access.

## Impregnating FRP

Two different systems—a pre-preg and a wet layup—were used. In the pre-preg system, the FRP was saturated with resin in a factory and sent to the site in hermetically sealed packages that were opened just before the wrap. In contrast, the wet layup system required on-site impregnation. This meant that the FRP fabric had to be precut

to size and then saturated with resin on site. In the initial application, an impregnating machine was built, but this was abandoned in favor of manual application. In the latter, the resin was mixed and applied over the surface of the FRP fabric with a roller. The fabric was then flipped over and the other surface similarly saturated. The saturated elements were made into a roll for easy transportation.

## FRP Wrap

For the pre-preg system, a layer of the same urethane resin was first applied to the pile surface to improve the FRP–concrete bond. Subsequently, the longitudinal layers were placed on each face. The transverse piece was wrapped around it in a spiral fashion (excepting at the top and bottom locations) with no overlap. This sequence was repeated for multiple layers. A fiberglass veil material was also used to wrap transversely around the pile to provide a smooth finish.

For the wet layup epoxy system, the saturated FRP material was directly wrapped on the concrete surface in the same manner—first longitudinal, then transverse. Following completion of the wrap, a plastic shrink material was wound tightly around the pile to hold it in place while the resin cured (Figure 7). For the pre-preg system, the surface of the plastic was punctured so that gases generated when the urethane resin cured could escape. After 24 h, the plastic wrap was removed and a protective UV layer applied to the wrapped surface.

In each of the applications, a 1.5- to 1.8-m depth of the pile was wrapped by using the appropriate number of longitudinal and transverse FRP layers. The wrapping operation generally took less than an hour.

## Postwrap Performance

Most of the piles wrapped were instrumented to provide information on long-term performance. Different instrumentation schemes



**FIGURE 7** View of shrink-wrapped FRP repaired piles, Gandy Bridge, Tampa Bay.

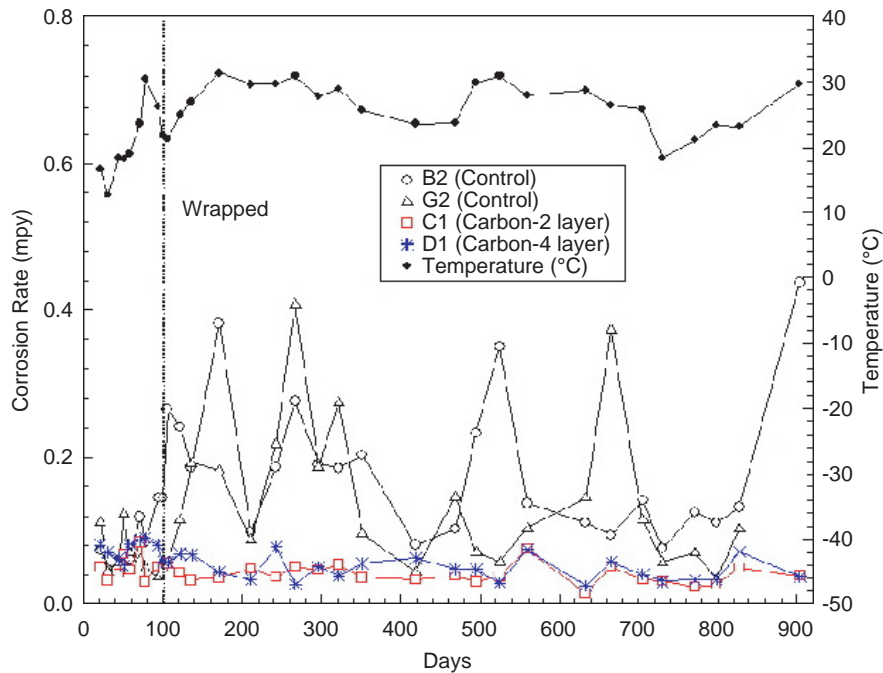


FIGURE 8 Corrosion rates in wrapped and unwrapped piles, Allen Creek Bridge, Clearwater.

were used so that the corrosion current or the corrosion rate could be determined. In general, corrosion performance of the FRP was monitored until the official end date for the project. This was longest for the Allen Creek Bridge, where monitoring continued for more than two and a half years.

Results shown in Figure 8 indicate that the corrosion rate in the wrapped piles was lower than that in the unwrapped controls. Thus, these results replicated laboratory findings. Details are available elsewhere (2, 15).

In addition to corrosion monitoring, the integrity of the FRP–concrete bond was evaluated destructively from on-site pullout tests (2). The results indicated that the bond was variable. For the epoxy system, the bond was found to be poorer in the dry part of the pile. For the pre-preg system, it was worse for the wet region. Analysis of the results suggested that this was partly because of the difficulty in tightly wrapping material above shoulder height and also because of gases released by the pre-preg system during curing.

## CONCLUSIONS

This paper provided a brief overview of a multiyear research study to evaluate the role of FRP in corrosion repair and also to explore the feasibility of conducting field repairs by using this technology. The laboratory studies that were carried out outdoors by using simulated tidal cycles showed that FRP can significantly reduce the corrosion rate (Figure 1). Retrieved strands were in far better condition (Figure 2). Thus, long-term service is likely to be significantly extended (Figure 3).

All-around pile access was the main problem in the field repair. However, a customized scaffolding system easily solved this problem. Surface preparation requires more work because the edges have to be rounded under water. Of the two systems investigated, the pre-preg was easier to use, but its bond with concrete was

somewhat poorer particularly in the submerged regions. Long-term monitoring of the corrosion rate shows that the performance of the wrapped piles (Figure 8) was similar to that observed in laboratory studies.

On the basis of this experience, it is clear that it is feasible to use FRP for underwater corrosion repair. The repairs have held up well, and the oldest is nearly 4 years old. Work is continuing to improve the FRP system. Overall, the portents are promising and, it is hoped, will culminate in the availability of a cost-effective solution for repairing piles that is accepted by highway authorities.

## ACKNOWLEDGMENTS

The demonstration studies reported were funded by the Florida and U.S. Departments of Transportation and by Hillsborough County. The support and guidance of Pepe Garcia and Steve Womble, of the Florida Department of Transportation, are acknowledged. The authors thank Mara Nelson and Nils Olsson, of Hillsborough County, for their contributions. FRP materials used were donated by Air Logistics Corporation and Fyfe & Co. LLC; the authors thank Franz Worth, of Air Logistics, and Ed Fyfe, of Fyfe & Co., for this support. The authors acknowledge the assistance of numerous former and current graduate students of the University of South Florida.

## REFERENCES

1. Sen, R. Advances in the Application of FRP for Repairing Corrosion Damage. *Progress in Structural Engineering and Materials*, Vol. 5, No. 2, 2003, pp. 99–113.
2. Mullins, G., R. Sen, K. S. Suh, and D. Winters. *Use of FRP for Corrosion Mitigation Application in a Marine Environment*. Florida Department of Transportation, Tallahassee, 2005.

3. Suh, K., G. Mullins, R. Sen, and D. Winters. Effectiveness of Fiber-Reinforced Polymer in Reducing Corrosion in Marine Environment. *ACI Structural Journal*, Vol. 104, No 1, 2007, pp. 76–83.
4. Tuutti, K. *Corrosion of Steel in Concrete*. Swedish Foundation for Concrete Research, Stockholm, 1982.
5. *Concrete Repair Manual*, 2nd ed., Vol. 1. American Concrete Institute, Farmington Hills, Mich., 2003.
6. *Guide to Underwater Repair of Concrete*. American Concrete Institute, Farmington Hills, Mich., 1998.
7. Emmons, P. H. *Concrete Repair and Maintenance Illustrated*. R. S. Means Co., Kingston, Mass., 1993.
8. Lee, C., M. Bonacci, M. Thomas, M. Maalej, S. Khajehpour, N. Hearn, S. Pantazopoulou, and S. Sheikh. Accelerated Corrosion and Repair of Reinforced Concrete Columns Using Carbon Fibre Reinforced Polymer Sheets. *Canadian Journal of Civil Engineering*, Vol. 27, 2000, pp. 941–948.
9. Pantazopoulou, S., J. Bonacci, S. Sheikh, M. Thomas, and N. Hearn. Repair of Corrosion-Damaged Columns with FRP Wraps. *Journal of Composites for Construction*, Vol. 5, No. 1, 2001, pp. 3–11.
10. Mullins, G., R. Sen, K. S. Suh, A. Goulish, and A. Torres-Acosta. Evaluation of Transverse Strain in Corroding Square Prestressed Concrete Elements. *Proc., 47th International SAMPE Conference*, 2002, pp. 955–963.
11. Shahawy, M., and O. Chaallal. Performance of Fiber-Reinforced Polymer-Wrapped Reinforced Concrete Column Under Combined Axial-Flexural Loading. *ACI Structural Journal*, Vol. 97, No. 4, 1999, pp. 659–668.
12. Chaallal, O., M. Shahawy, and M. Hassan. Confinement Model for Axially Loaded Short Rectangular Columns Strengthened with FRP Wrapping. *ACI Structural Journal*, Vol. 100, No. 2, 2003, pp. 215–221.
13. *Caltrans Memo To Designers 20-4 Attachment B*. California Department of Transportation, Sacramento, Nov. 2000.
14. *Strengthening Reinforced Concrete Structures with Externally-Bonded Fibre Reinforced Polymers (FRPs)*, Design Manuel No. 4. ISIS Canada, Winnipeg, Manitoba, Canada, 2001.
15. Mullins, G., R. Sen, K. Suh, and D. Winters. Underwater FRP Repair of Prestressed Piles in the Allen Creek Bridge. *Journal of Composites for Construction*, Vol. 9, No. 2, 2005, pp. 136–146.

---

*The Structural Fiber-Reinforced Polymers Committee sponsored publication of this paper.*

## DEVELOPMENTS IN UNDERWATER FRP REPAIR OF CORRODING PILES

Rajan Sen and Gray Mullins  
Department of Civil and Environmental Engineering  
University of South Florida  
Tampa, FL 33620  
Email: [sen@eng.usf.edu](mailto:sen@eng.usf.edu)

**Abstract.** The poor durability of conventional repairs has led to increased interest in the application of fiber reinforced polymers (FRP) for repairing corroded concrete structures. Over the past decade, several highway agencies in Canada and US have conducted demonstration projects to evaluate the application of FRP for repairing corrosion damage. In most instances, repairs were limited to dry bridge elements that had corroded due to salt water runoff from faulty expansion joints or salt spray from passing vehicular traffic. These FRP repairs have held up well and show little sign of deterioration. The development of resins that can cure in water has led to interest in the possible application of FRP for the underwater repair of corrosion damaged piles. Over the past 4 years, USF completed several demonstration projects in which corroding reinforced and prestressed piles were repaired using FRP. Several of the piles were instrumented to allow long term monitoring of corrosion performance. This paper discusses issues that are relevant for underwater FRP repair with particular reference to the completed field demonstration projects.

### 1. INTRODUCTION

Florida's long coastline and sub-tropical climate makes reinforcing and prestressing steel vulnerable to corrosion. Over the last seventy five years measures adopted to control it, such as increasing the cover, reducing permeability, using epoxy coating, have not always proven effective. Indeed, a random survey of fifteen Florida bridges [1] indicated that on an average, visible corrosion was evident, within 11.5 years of construction.

Corrosion is particularly prevalent in elements that are exposed to the 'splash zone', i.e. within 0.6-1.8 m of the water line. The combination of deposition of salt on the pile surface and alternate dry/wet cycles due to tidal changes provide ideal conditions for corrosion in steel. Its inevitability is even factored in current Florida Department of Transportation Structures Design Guidelines [2]. This requires prestressed piles located in 'extremely aggressive' salt water sites to be at least 60 cm x 60 cm *regardless of loading*. The rationale is that in time spalling of the concrete cover will reduce the cross-section so that if a 60 cm square pile were used originally, a central core of 45 cm square would remain.

Two types of repairs are typically conducted. For minor damage a 'chip and patch' repair is carried out in which the concrete in the corroding region is chipped and replaced by new patch material. Where damage is more severe, a pile jacket is used to encapsulate the damaged region with the annular space between the pile and the jacket filled with cementitious repair material. Since such repairs fail to address the electrochemical nature, corrosion continues unabated. In view of this, jackets nowadays incorporate a cathodic protection system [3]. While this system has proven to be effective, it may not always be affordable. Thus, there is a need for an alternative repair system that is more cost effective than the chip and patch repair yet not as expensive as jacket systems incorporating cathodic protection. Fiber reinforced polymers (FRP) offer the prospect of being such a system. This paper describes the application of FRP in pile repair.



## 2. BACKGROUND

Fiber reinforced polymers have long been used for the repair and retrofit of concrete structural elements. Their lightweight, high strength and resistance to chemicals offer obvious advantages. In fabric form, they provide unprecedented flexibility in construction. Moreover, as fibers can be oriented as required they can provide strength in any desired direction. This versatility has led to several research studies to investigate whether FRP's strength and durability can be harnessed to successfully repair corrosion damage [4].

Since 2003, the University of South Florida (USF) have completed four demonstration projects in which FRP was used to repair piles at two contrasting sites. The first was at a shallow site where repairs could be carried out using ladders. The subsequent three repairs were undertaken in the deeper and more turbulent waters of Tampa Bay, Florida's largest estuary where the waters of Tampa Bay join with those of the Gulf of Mexico. Here the piles repaired were those supporting the 4.2 km long Gandy and the Friendship Trails Bridges that connect Tampa and St. Petersburg. At the time the bridge was first opened to traffic in 1924, it was the longest bridge in the United States.

### 2.1 FRP materials

Two types of materials were used in all the repairs. One was a pre-preg, the other a wet lay up. The pre-preg system was from Air Logistics in which all the FRP material were cut to size, resin saturated in the factory and sent to the site in hermetically sealed pouches. The wet lay up system required on-site impregnation and was from Fyfe. An additional wet lay up system was also used but this was carried out under dry conditions inside a coffer dam [5]. For this reason, it is not discussed in this paper. Both carbon and fiberglass were used. Details of the properties of the fiber and the resin as provided by the suppliers are summarized in Tables 1 to 2 [6, 7].

**Table 1.** Properties of Aquawrap® Fabrics [6]

<b>Fibers</b>	<b>Tensile Strength (MPa)</b>	<b>Tensile Modulus (GPa)</b>	<b>Load per Ply (kN/m)</b>
Uni-directional (GFRP)	590	36	420
Bi-directional (GFRP)	320	21	210
Uni-directional (CFRP)	830	76	596
Bi-directional (CFRP)	590	22	420

**Table 2.** Properties of Tyfo® SEH-51 Composite [7]

<b>Properties</b>	<b>Quantities</b>
Tensile Strength	3.24 GPa
Tensile Modulus	72.4 GPa
Ultimate Elongation	4.5 %
Laminate Thickness	0.127 cm
Dry fiber weight per sq. yd.	915 g/m <sup>2</sup>
Dry fiber thickness	0.038 cm

## 2.2 Wrap design

The FRP wrap has two primary functions: first, to restore lost structural capacity; second, to ensure that it has sufficient capacity to withstand the expansive forces caused by corrosion of steel. The former requires fibers to be oriented parallel to the steel, i.e. along the length; the latter requires fibers in the transverse or hoop direction, i.e. perpendicular to the strands. This can be most conveniently accommodated by using bi-directional FRP material. However, in the demonstration projects both uni-directional and bi-directional materials were used.

Available ACI [8] and ISIS [9] guidelines provide design equations and worked out numerical examples. Design manuals for specific systems are also available, e.g. Fyfe Co [10]. Their provisions are comparable though equations are simplified. It should be noted that in all the guides mentioned, axial, flexural and shear strengthening are considered separately. Their interaction necessary for designing wraps for piles is not considered.

The low strain capacity of the FRP makes the maximum permissible strain, the critical parameter in design. For strengthening applications, ACI 440 guidelines [8] specifies strain limits for both “contact-critical” (FRP in intimate contact with the substrate with no specific adhesion requirement) and “bond-critical” (minimum adhesion required since load transfer is by bond) applications. For piles, the limit for contact-critical application applies as the FRP material is wrapped completely around the circumference. This is set as the lower of 0.4% or 75% of the FRP design rupture strain. The latter limit was established from tests to avoid loss of aggregate interlock that can occur at strains below the ultimate fiber strain.

As piles corrode, they expand in the lateral direction since the volume of the corrosion products can be as much 600% of the original steel [11]. To accommodate such a large potentially uniform increase, a lower maximum strain limit may be appropriate. This can be based on experimental data [12] or from other considerations.

A strain limit of 0.1% - approximately three times the maximum tensile strain leading to cracking – was used for designing the FRP to withstand corrosion expansion [5]. This value was used since reported experimental strains, calculated from the total circumferential increase, tend to be on the high side as it includes unrestrained movement of the crack.

Interaction diagrams can be developed for FRP strengthening as for reinforced concrete columns by using strain compatibility analysis [5]. The only difference is that the equations incorporate the contribution of the FRP. Since FRP wrapping can provide increased tensile but not increased compressive strength, only the tensile contribution should be considered in the analysis. Also, as the confinement effect of concrete leads to modest increases in the ultimate axial capacity in non-circular sections, it is best ignored. As with most strengthening applications, the role of the FRP is passive. That is, the FRP is unstressed except for additional load applied to the structure after it has been retrofitted.

In the applications, capacity loss was estimated to be 20%. It was found that this could be restored by using two transverse and one longitudinal carbon layer for the material properties outlined in Tables 1-2. For the weaker glass, two longitudinal and four transverse layers were required to restore capacity.

## 2.3 Instrumentation

Corrosion monitoring uses non-destructive electrochemical methods that take advantage of the electrochemical nature of corrosion. Available methods include measurement of concrete resistance and resistivity, half-cell potential and corrosion current. However, in the case of FRP wrapped elements where the concrete surface is inaccessible, sensors have to be embedded inside the concrete. For applications involving piles, the size of the sensor is critical since it must be small enough to be accommodated within the available 75 mm concrete cover.

Embedded sensors may be used to evaluate the corrosion state in wrapped piles using (1) linear polarization and (2) galvanic current measurement. Linear polarization is an established technique for measuring the corrosion rate of steel in concrete structures. It relies on the linear relationship between corrosion current and its potential when the equilibrium potential is perturbed by the application of an incremental current (“galvanostatic”) or incremental voltage (“potentiostatic”). Several portable devices are available that can be used to make the measurement. In the demonstration projects, a PR - Monitor Model 4500 manufactured by Cortest Instrument Systems, Inc. was used.

In galvanic current measurements, sensors made of the same or different steel are embedded at different depths in the concrete. The small galvanic or macro-cell currents set up by the corrosion process between these sensors are measured typically using a zero resistance ammeter through an external connection. Both systems were used in the studies.

## 2.4 Sensor details

Table 3 summarizes information on the type of sensors used in the four demonstration projects. Three different types of sensors were used. These included one developed by USF researchers, a commercially available one developed by Concorr Inc. and a ‘rebar’ sensor used by the Florida Department of Transportation (FDOT).

**Table 3.** Sensors used in demonstration projects

Site	Monitoring System	Sensor
Allen Creek Bridge, Clearwater (2003)	Linear polarization	USF
Friendship Trails Bridge, Tampa Bay (2004)	Galvanic current	FDOT
Friendship Trails Bridge, Tampa Bay (2006)	Galvanic current	FDOT
Gandy Bridge, Tampa Bay (2004)	Linear polarization	Commercial
	Galvanic current	FDOT

## 3. FIELD WRAP

### 3.1 Surface preparation

The application of FRP for repair and strengthening of piles is part bond-critical and part contact-critical since the FRP material provides both strengthening and confinement. As with any bonded

application, surface preparation is critical; good bond requires the substrate to have an open pore structure to ensure capillary suction of the epoxy [13]. In underwater application, however, pores will be saturated with water or small marine organisms or algae.

In all cases, the pile surfaces were covered with marine growth (Fig. 1) that had to be scraped off. Additionally, corners that were not rounded had to be ground using an air-powered grinder. This was a difficult operation particularly for sections that were below the water line. A quick-setting hydraulic cement was used to fill any depression, discontinuities and provide a smooth surface. The entire surface was pressure washed just prior to wrapping using fresh water to remove all dust, marine algae.



**Figure 1.** Marine growth



**Figure 2.** Scaffolding used for repair

### 3.2 Scaffolding

Excepting for the Allen Creek Bridge that was located in shallow waters, the remaining three bridges were located in the middle of Tampa Bay where a scaffolding system had to be set up for safety and also to provide all around access to the piles. Fig. 2 shows the scaffolding used in the Friendship Trails Bridge. This was developed for a project in which all piles in a bent had to be wrapped. In subsequent studies, only 1 or 2 piles in the bent were wrapped and therefore the scaffolding was re-designed to cater to a single pile. This resulted in a lighter system that could be readily moved over to provide access to other piles.

### 3.3 Impregnating FRP

As mentioned earlier, two different systems – a pre-preg and a wet layup were used. In the pre-preg system, the FRP was saturated with resin in a factory and sent to the site in hermetically sealed packages that were opened just prior to the wrap. The wet layup system required on-site impregnation. This meant that the FRP fabric had to be pre-cut to size and then saturated with resin. In the initial application, an impregnating machine was built but this was abandoned in favor of

manual application. In the latter, the two parts of the resin were mixed and then applied over the surface of the fabric that was placed on a plastic sheet. The resin was then impregnated on one surface using a roller, flipped over and the other surface similarly saturated. The saturated element was then made into a roll for easy transportation (Fig. 3).



Figure 3. Saturating FRP on site



Figure 4. Applying transverse wrap

### 3.4 FRP wrap

For the pre-preg system, a layer of the same urethane resin was first applied to the pile surface. Subsequently, the longitudinal layers were placed on each face starting at the corners. The transverse piece was wrapped around it (Fig. 4). This process was repeated for additional layers. For the pre-preg system, a fiberglass veil material was also used to wrap transversely around the pile to provide a smooth surface. For the wet lay up epoxy system, the saturated FRP material was directly wrapped on the concrete surface. Following completion of the wrap, a plastic shrink material was wound tightly around the pile to hold it in place while the resin cured. For the pre-preg, the surface of the plastic was punctured so that gases generated when the resin cured could escape. After 24 hours, the plastic wrap was removed. A protective UV layer was applied on the wrapped surface. In each of the applications, a 1.5-1.8 m depth of the pile was wrapped using up to 4 layers. The wrapping operation generally took less than an hour to complete.

#### Post wrap performance

The corrosion performance of the FRP was monitored until the end of the project. This was longest for the Allen Creek Bridge where monitoring was continued for over two and a half years. Results indicated that the performance of carbon and glass were comparable and were superior to that of the unwrapped control. More details may be found elsewhere [5].

#### FRP bond

The FRP bond with concrete was evaluated in several cases using pullout tests. The results indicated that the bond was variable. For the epoxy system, the bond was found to be poorer in the dry part of the pile. For the pre-preg system it was worse for the wet region. Analysis of the results suggested that this could be because the pressure impressed by the shrink wrap on the FRP as it cured was insufficient to overcome the weight of the fabric. Laboratory tests were conducted to investigate



alternative systems that could be used to overcome this problem. Two promising techniques have been developed one which was implemented in the latest repair conducted on the Friendship Trails Bridge [14].

#### Future developments

FRP slows down the corrosion rate by serving as a barrier element to the ingress of deleterious materials such as chlorides, moisture and oxygen. However, results from laboratory tests that show that corrosion continues inside the wrap indicating that there is sufficient oxygen and moisture trapped inside the wrap to allow corrosion to continue. This can be prevented by incorporating a cathodic protection system within the FRP wrap. Development work is currently being undertaken to examine how such a system can be implemented. The USF research team plan to complete such a demonstration study in 2007.

## CONCLUSIONS

This paper provides a brief overview of FRP systems used in demonstration projects to repair corroding piles. Wrapping was carried out directly in water using ladders where the depth was shallow and using a custom designed scaffolding system where the depth was greater. Two different systems were evaluated and both carbon and glass tested. In each case, piles were instrumented to allow the long term performance of the FRP material to be assessed.

Based on the experience it is clear that it is feasible to use FRP for repairing corrosion damage. Results of long term monitoring indicate that wrapped specimens have lower corrosion rates. Repairs have held up well with the longest repair now nearly four years old.

Work is continuing to further improve this application. Two areas that the research team are currently exploring are enhancing the FRP-concrete bond and secondly the feasibility of incorporating a cathodic protection (CP) system within the wrap. A project was recently completed [14] in which a new system to improve bond was used. The bond appears to be better. Tests will be carried out next year to quantify the bond. The FRP-CP system is expected to be also developed within the next few months.

Results obtained relating to corrosion performance are promising. The new techniques that are currently under development will significantly improve performance. Highway agencies will have access to another method of pile repair that may be economical in some situations.

## Acknowledgements

The demonstration studies reported were funded by the Florida/US Department of Transportation and Hillsborough County. The support and guidance of Mr. Pepe Garcia and Mr. Steve Womble, both of Florida Department of Transportation are gratefully acknowledged. We thank Ms. Mara Nelson, Hillsborough County for her contribution. FRP materials used were donated by Air Logistics, Corporation and Fyfe & Co LLC. We thank Mr. Franz Worth of Air Logistics and Mr. Ed Fyfe, President, Fyfe for this support. We are also indebted to SDR Engineering, Tallahassee for

their contribution in this research study. We gratefully acknowledge the assistance of graduate students Dr. K S Suh and doctoral student Mr. Danny Winters in these projects.

## References

- [1] Powers, R. Florida Department of Transportation, Private Communication (1988).
- [2] Structures Design Guidelines, Florida Department of Transportation, Tallahassee, FL, (2006) Vol. 1, Section 3.5.1F.
- [3] Leng, D. 'Zinc Mesh Cathodic Protection Systems', *Materials Performance*, (2002), V. 41, No. 8, Aug., pp. 28-33.
- [4] Sen, R. "Advances in the Application of FRP for Repairing Corrosion Damage", *Progress in Structural Engineering and Materials* (2003), Vol. 5, No 2, pp. 99-113.
- [5] Mullins, G., Sen, R., Suh, K.S. and Winters, D. Use of FRP for Corrosion Mitigation Application in a Marine Environment. Final Report submitted to Florida / US Department of Transportation, Tallahassee, FL (2005), Oct., 406 pp.
- [6] Air Logistics Corporation (2002). Aquawrap Repair System, Pasadena, CA.
- [7] Fyfo Co. LLC, <http://www.fyfeco.com/>
- [8] ACI 440.2R-02. Guide for the Design and Construction of Externally Bonded FRP Systems for Strengthening Concrete Structures. ACI , (2002), Farmington Hills, MI..
- [9] ISIS Canada. Strengthening Reinforced Concrete Structures with Externally-Bonded Fibre Reinforced Polymers, Design Manual (2001).
- [10] Fyfe Co. LLC. Design Manual for the Tyfo Fibrwrap Systems (2005), San Diego, CA.
- [11] Mehta, P. and Monteiro, P. Concrete, p. 162, Second Edition, Prentice-Hall, Englewood Cliffs, NJ, (1993).
- [12] Mullins, G., Sen, R., Suh, K.S., Goulsh, A. and Torres-Acosta, A.. "Evaluation of Transverse Strain in Corroding Square Prestressed Concrete Elements". Proceedings of the 47<sup>th</sup> International SAMPE Symposium and Exhibition-Science of Advanced Materials and Process Engineering Series, Vol 47, Long Beach, CA, May 12-16. Society for the Advancement of Material and Process Engineering, (2002), pp. 955-963.
- [13] Emmons, P.H., *Concrete Repair and Maintenance Illustrated*, R S Means, Kingston, (1993), MA.
- [14] Mullins, G., Sen, R., Winters, D. and Schrader, A. 'Innovative Pile Repair', Final report submitted to Hillsborough County, (2006).

Title no. 104-S09

# Effectiveness of Fiber-Reinforced Polymer in Reducing Corrosion in Marine Environment

by Kwangsuk Suh, Gray Mullins, Rajan Sen, and Danny Winters

*This paper presents results from a long-term study that evaluated the role of fiber-reinforced polymer (FRP) in reducing the corrosion rate in a marine environment. Twenty-two 1/3-scale models of prestressed piles cast with built-in chloride were exposed to simulated tidal cycles under outdoor ambient conditions for nearly 3 years. These included eight carbon FRP (CFRP), eight glass FRP (GFRP)-wrapped specimens, and six controls. Embedded titanium reference electrodes and thermocouples were used to monitor the corrosion performance inside the wrapped region throughout the exposure period. The performance of the FRP was evaluated on the basis of bond and gravimetric tests conducted at the end of the exposure period. The results showed that the FRP-concrete bond was largely unaffected by exposure and both CFRP and GFRP-repaired specimens significantly outperformed the controls. The underlying trend in corrosion rate measurements showed increases for the controls and reductions for the wrapped specimens. This was reflected by much lower metal losses in wrapped specimens compared with controls. Overall, the study showed that FRP is effective in mitigating corrosion in a marine environment.*

**Keywords:** bond; corrosion; prestress; reinforcement; test.

## INTRODUCTION

The poor performance of conventional repairs has led to renewed interest in the application of fiber-reinforced polymer (FRP) materials for rehabilitating corroded concrete structures. Despite higher material costs, FRP repairs may be more economical if they result in a reduction in re-repairs that is often the reality for corrosion repair. Several highway agencies have explored this option over the past decade. In 1994, the Vermont Transportation Agency opted to use FRP over conventional methods for repairing corrosion-damaged columns because it resulted in 35% cost savings.<sup>1</sup> For the same reason, the New York State Department of Transportation (NYDOT) chose FRP for repairing corrosion-damaged columns.<sup>2</sup> More examples may be found in a recent state-of-the-art paper.<sup>3</sup>

The role of FRP in mitigating corrosion has been the subject of several investigations.<sup>3</sup> The majority of the studies<sup>4-8</sup> focused on applications relating to corrosion damage in reinforced concrete elements in cold regions caused by salt water run-off from faulty expansion joints. There have been fewer studies relating to corrosion mitigation in tidal waters under hot, humid conditions<sup>9-12</sup> where corrosion rates are significantly higher. Such applications have only become possible<sup>13-16</sup> because of the availability of new resins that can cure in water.

In 2001, the Florida and U.S. Department of Transportation funded a 44-month study to investigate the use of FRP for the underwater repair of prestressed piles. The study included both laboratory testing and field demonstrations. This paper provides details of a long-term exposure study

conducted to assess the role of FRP in mitigating corrosion. In the study, instrumented, 1/3-scale models of carbon FRP (CFRP) and glass FRP (GFRP) wrapped prestressed piles were exposed to simulated tidal cycles under outdoor ambient conditions for nearly 3 years. The performance of the FRP was assessed in comparison to identical unwrapped specimens that were placed in the same environment through gravimetric testing. Complete details may be found in the final report.<sup>12</sup>

## RESEARCH SIGNIFICANCE

This paper provides quantitative data on the performance of FRP in reducing corrosion under exposure comparable to natural conditions. The use of embedded reference electrodes permitted the corrosion performance of the FRP wrapped region to be monitored throughout the exposure. Comparative data on the actual metal loss in identically exposed wrapped and unwrapped specimens is helpful for highway agencies in assessing the efficacy of FRP in corrosion mitigation applications.

## OBJECTIVES

The overall goal of the research project was to evaluate the effectiveness of FRP in slowing down corrosion in heavily chloride-contaminated prestressed concrete elements that are characteristic of a marine environment. Both carbon and fiberglass were tested and the role of number of fiber layers investigated. Effectiveness was evaluated by monitoring corrosion rate and by gravimetric testing in which the actual metal loss in strands and ties retrieved from exposed specimens was determined.

## EXPERIMENTAL PROGRAM

As corrosion is a slow process, two broad strategies have been used for accelerating corrosion. In the first method, electrochemical reactions responsible for corrosion are simulated by applying appropriate corrosion currents using either a constant voltage or a constant current system. In the second method, acceleration is achieved by using permeable, high water-cement mixtures, heat, or by casting specimens with chlorides. Specimens are subsequently exposed to simulated tidal cycles and subjected to alternate drying and wetting. Acceleration may be achieved by manipulating the relative lengths of the dry and wet cycles. By making the dry cycle longer, accessibility of oxygen is enhanced that can

*ACI Structural Journal*, V. 104, No. 1, January-February 2007.

MS No. S-2006-110 received March 14, 2006, and reviewed under Institute publication policies. Copyright © 2007, American Concrete Institute. All rights reserved, including the making of copies unless permission is obtained from the copyright proprietors. Pertinent discussion including author's closure, if any, will be published in the November-December 2007 *ACI Structural Journal* if the discussion is received by July 1, 2007.

ACI member **Kwangsook Suh** is a Structural Engineer at Parsons Brinckerhoff Quade and Douglas, Inc., Tampa, Fla. He received his PhD from the Department of Civil and Environmental Engineering at the University of South Florida, Tampa, Fla.

**Gray Mullins** is an Associate Professor of structural engineering at the University of South Florida. His research interests include full-scale testing and instrumentation of structures and foundations.

**Rajan Sen**, F.ACI, is a Professor of structural engineering at the University of South Florida. He is a member of ACI Committees 215, Fatigue of Concrete; 440, Fiber Reinforced Polymer Reinforcement; and 444, Experimental Analysis for Concrete Structures. His research interests include fiber-reinforced polymers.

**Danny Winters** is a Research Associate and a PhD student in the Department of Civil and Environmental Engineering at the University of South Florida. His research interests include full-scale testing of foundations.

accelerate the corrosion process. The first approach yields results more quickly. The second is slower, but corrosion products and processes are more representative of naturally occurring corrosion.

In this study, the second approach was adopted in which specimens were exposed to simulated tidal cycles under outdoor ambient conditions. The wet-dry cycles were kept the same but the exposure period made sufficiently long so that the difference in the performance of wrapped and unwrapped specimens would become apparent.

### Specimen details

The specimens used in the study were 1/3-scale model of 45 cm (18 in.) square prestressed piles that had been identified in earlier studies as being the most common and, therefore, most commonly found to have exhibited corrosion damage. The 15 x 15 x 152 cm (6 in. x 6 in. x 5 ft) long specimens were prestressed by four 8 mm (5/16 in.), seven-wire, low relaxation 1860 MPa (Grade 270) strands (Fig. 1). This configuration ensured that the effective prestress in the model piles exactly matched that in the prototype when stressed to code-specified stressing levels. The central fifth strand shown in Fig. 1 was unstressed and served as a counter electrode for linear polarization tests that were used to monitor the corrosion rate in the steel.

A 55 cm (22 in.) length corresponding to 1.67 m (66 in.) splash zone in the prototype was fabricated with 3% of chloride ion by weight of cementitious material. This left 48 cm (19 in.) of regular concrete both above and below that was sufficient for full prestress force transfer ( $50d_b = 39.6$  cm [15.6 in.]).

Specimens were cast all at once in a single line in a specially adapted prestressing bed at a commercial facility. As a result, the prestressing forces and concrete mixtures were identical for all specimens. Wood trims with a radius of 13 mm (1/2 in.) were inserted along the bottom corners of the form to ensure that there no sharp corners at these locations. The edges at the top were finished using a 7.5 cm (3 in.) wide edging trowel so that these edges were also curved. This greatly reduced the preparation work required in subsequent wrapping.

### Instrumentation

The prestressing forces at the live and dead ends were monitored during fabrication of the specimen to ensure that the final effective stresses were consistent with those in the prototype pile. Embedded activated titanium reference electrodes and thermocouples were installed at pre-designated locations as shown in Fig. 1.

Embedded reference electrodes ensured greater reliability of the corrosion measurements (when compared with surface

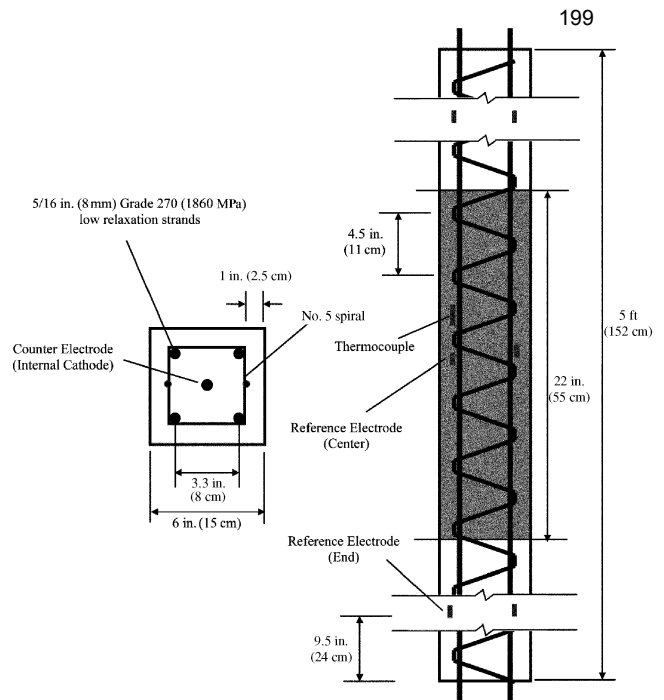


Fig. 1—Specimen geometry.

measurements) by eliminating environmental effects due to changes in the temperature and humidity of the surface. More importantly, it allowed potential measurements inside the wrapped region to be readily made without the need for cutting through the wrap to expose the concrete surface. Thermocouples enabled changes in corrosion rate with temperature to be assessed.

### Concreting

The concrete placement was conducted in two phases: a regular FDOT Class V special mixture was first placed, vibrated, and finished followed by a second batch in which a measured amount of the chloride admixture<sup>12</sup> was added to the concrete mixer, rotated, and placed between sheet metal barriers (dams) that were removed subsequently. The specimens were covered by a plastic sheet and allowed to cure. The average compressive strength at the time of release was 41.7 MPa (6.05 ksi) for the regular concrete and 34.3 MPa (4.98 ksi) for the chloride contaminated concrete.

### Wrap details

The goal of the study was to evaluate the performance of FRP in specimens where the chloride threshold had been exceeded, but there was no visible sign of corrosion. For this reason, 16 specimens were wrapped when the concrete was 28 days old. FRP was applied over a 0.91 m (36 in.) length in the central region of the specimen. This meant that it extended 17.5 cm (7 in.) above and below the boundary of the 55 cm (22 in.) chloride contaminated region (Fig. 1). Eight specimens were wrapped with bidirectional CFRP using bidirectional CFRP system. Eight others were wrapped using a bidirectional GFRP and epoxy.

Material properties of the epoxies and the FRP provided by the manufacturers are summarized in Table 1 and 2. The number of FRP layers varied from 1 to 4 and the recommended lap length was provided. This was 5 cm (2 in.) for CFRP and 15 cm (6 in.) for GFRP. To protect the FRP wrap



Fig. 2—Outdoor exposure specimens.

**Table 1—Material properties of epoxies**

Properties	CFRP (MAS 2000)	GFRP (Tyfo® S)
Tensile strength, ksi (MPa)	45.2 (312)	10.5 (72)
Tensile modulus, ksi (MPa)	2620 (18,064)	461 (3178)
Flexural strength, ksi (MPa)	62.3 (430)	11.5 (79)
Flexural modulus, ksi (MPa)	2560 (17,651)	400 (2758)
Elongation, %	1.96	5

**Table 2—Material properties of FRP**

Property	Values	
	CFRP	Tyfo® Web
Tensile strength, ksi (MPa)	90 (621)	44.8 (309)
Modulus of elasticity, ksi (MPa)	10,600 (73,084)	2800 (19,305)
Elongation at break, %	1.2	1.6
Thickness, in. (mm)	0.020 (0.508)	0.01 (0.254)

**Table 3—Details of test specimens**

Specimen type	Specimen ID	Wrap layers	Reference electrodes	
Outdoor control	No. 38, 39, 40	0	2	
	No. 41		6	
Indoor control	No. 42		2	
	No. 43		6	
CFRP wrap	No. 52, 56		1	2
	No. 53		2	
	No. 54, 58	3		
	No. 55	4	6	
	No. 57	2		
No. 59	4			
GFRP wrap	No. 44, 48	1	2	
	No. 45	2		
	No. 46, 50	3		
	No. 47	4	6	
	No. 49	2		
	No. 51	4		

from ultraviolet radiation, two coats of external latex paint were applied over the wrapped area.

### TIDAL SIMULATION SETUP

Twenty specimens (16 wrapped and four unwrapped controls) were placed upright inside a 1.82 x 3.04 x 1.22 m (6 x 10 x 4 ft) tank, which was kept outdoors (Fig. 2). Two unwrapped specimens were placed in an indoor tank in a

controlled environment and served as indoor controls. Details are summarized in Table 3.

All outdoor and indoor specimens were subjected to simulated tidal cycles in 3.5% salt water (Fig. 2). The variation in water depth was modeled for the Tampa Bay region where the difference between high and low tide is approximately 45 cm (18 in.). The water level at high tide was 80 cm (32 in.) from the bottom. It was 35 cm (14 in.) at low tide. The tide was changed every 6 hours and was controlled by a water pump and floating switch. This ensured that a 5 cm (2 in.) length of the wrap was permanently submerged in water. This type of exposure had the maximum chance of trapping moisture within the wrap. Such entrapment of moisture had been observed in a study conducted by the University of Texas at Austin.<sup>17</sup>

Specimens were exposed to this environment for nearly 3 years at which time they were removed for detailed examination and analysis that included measurement of metal loss in wrapped and unwrapped specimens by gravimetric testing.

### CORROSION MONITORING

Half-cell potential measurements were taken using a high impedance voltmeter. The embedded titanium reference electrodes were calibrated against a copper-copper sulfate reference electrode (CSE) and all results reported are with respect to these electrodes. Potential measurements were regularly made with the first reading taken 24 days after the specimens had been cast. Initially, measurements were taken weekly but became less frequent as readings stabilized following prolonged exposure.

Linear polarization measurements were made using a PR monitor. This has a three-electrode probe comprising a reference, working, and counter electrode. The central strand provided in the specimen (Fig. 1) served as the counter electrode. The PR monitor measures the polarization resistance that is inversely proportional to the corrosion rate in the steel. In the calculations, the polarized area was assumed to be the same as the chloride-contaminated area (55 cm [22 in.] length). Concrete resistivity was measured using a soil-resistance meter.

All thermocouples embedded in the concrete were hooked to a data acquisition system. Temperature data was measured and recorded every hour. Connections to the steel and the titanium reference electrodes for the corrosion measurements were placed inside a weatherproof box (Fig. 3) that allowed readings to be readily taken.

### RESULTS

#### Half-cell potentials

Figure 4 provides an overview of the variation in the averaged half-cell potential (relative to copper-copper sulfate) measured at midheight, that is, at the center of the wrapped region for all the controls (four outdoors and two indoors) and the wrapped specimens (eight CFRP and eight GFRP). Wrapping was conducted on the 28th day and wet-dry cycles started on the 111th day after casting when the simulated tidal setup became operational.

All readings were more negative than -350 mV indicating that there was a 90% probability of corrosion. The readings became much more negative immediately after the start of wet-dry cycles possibly because of the availability of water. For the specimens kept outdoors, potential changes were broadly similar for the first 350 days. After this time period, however, there was a divergence in the potential values with





Fig. 3—Weatherproof measurement box.

the unwrapped control specimens becoming more negative and the FRP wrapped specimens becoming less negative. This change in readings coincided with the appearance of cracks along the strand line and the formation of corrosion products around cracks on the surface of the unwrapped control specimens (Fig. 5). There was no similar evidence of damage in any of the wrapped specimens. Nor were the readings for CFRP and GFRP significantly different. Additional results<sup>12</sup> showed that the number of FRP layers had a relatively minor effect on the potential readings.

### Corrosion rate results

Linear polarization measurements were taken at midheight where corrosion rates were expected to be the highest. Figure 6 provides an overview of all the results as well as the temperature variation. Each corrosion rate data point represents the average for that type of specimen (for example, eight CFRP, eight GFRP, two indoor controls, or four outdoor controls). Additional plots showing individual results may be found in the final report.<sup>12</sup>

The corrosion rate in Fig. 6 is expressed in mm/year. Inspection of Fig. 6 shows that while corrosion rates in all specimens declined during the period between wrapping and exposure to the simulated tidal cycles, the underlying trend in the subsequent results was an increase in the corrosion rate in the controls and a decrease in the rate in the wrapped specimens. Undulations in the corrosion rate were largely due to variations in the ambient temperature at the time the reading was taken (always at low tide) and were more prominent in the outdoor controls when compared to the indoor specimens. The temperature of the indoor controls was unfortunately not constant, but rather maintained for laboratory occupant comfort (near 25 °C [77 °F]) and would have fluctuated somewhat with the outdoor conditions. There was little difference between the corrosion rates in the CFRP and GFRP wrapped specimens; temperature-induced changes in corrosion rate were likewise apparent. Such temperature-induced corrosion rate variations are not surprising given the electrochemical nature of the corrosion process.

The average corrosion rate in the controls was 0.018 mm/year at the end of the exposure period. The wrapped specimens show approximately 1/3 of this magnitude at 0.0055 mm/year. These values are commensurate with corrosion rates where visible damage can be expected in 2 to 10 years.<sup>18</sup>

### EFFECT OF EXPOSURE ON BOND

Following conclusion of the exposure, test specimens were removed from the tanks for further evaluation and

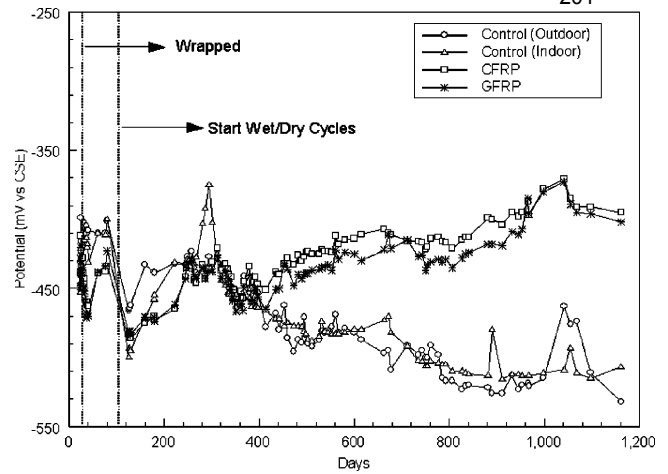


Fig. 4—Result of half-cell potential measurements.



Fig. 5—Surface cracks on unwrapped specimens.

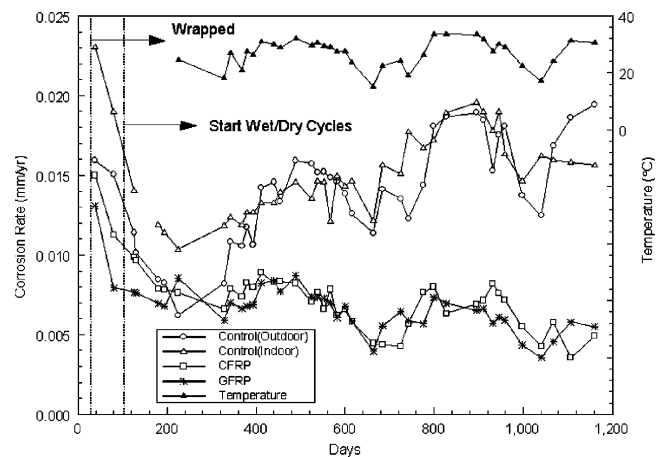


Fig. 6—Result of linear polarization tests.

testing. This included bond tests on the wrapped specimens, crack mapping of the controls, and gravimetric testing to quantify metal loss.

The bond between FRP and concrete was determined from pull-out tests carried out in accordance with ASTM D 4541<sup>19</sup> using an adhesion tester. The tester used 3.6 cm (1.456 in.) diameter aluminum dollies. A total of eight wrapped specimens were tested: four CFRP specimens (No. 54, No. 55, No. 56, and No. 57) and four GFRP (No. 47, No. 48, No. 50, and No. 51) with one, two, three, or four FRP layers.

The tests were performed on two faces of each specimen and at three locations per face (Fig. 7). The three levels



Fig. 7—Bond test.

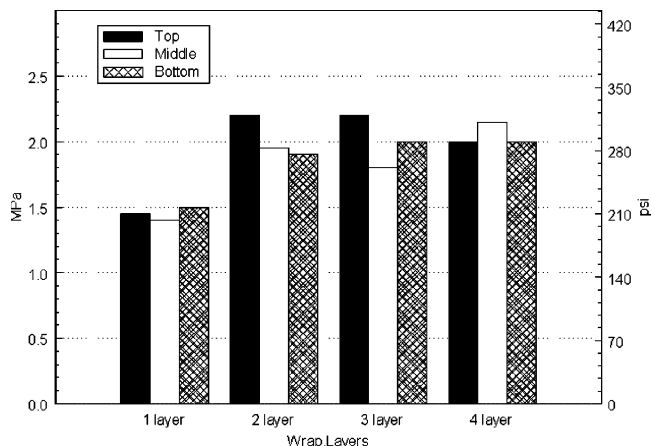


Fig. 8—Bond test results for CFRP wrap.

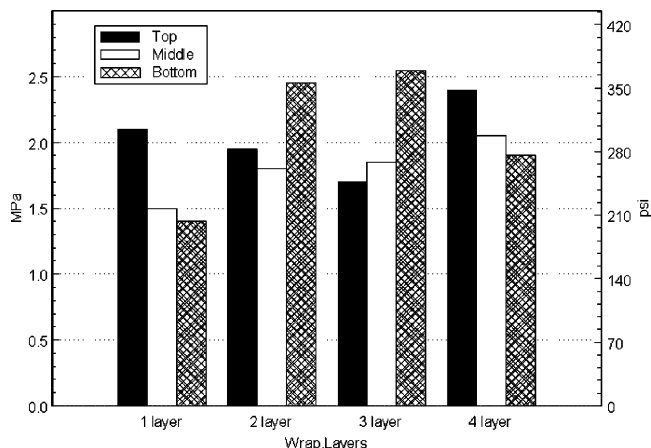


Fig. 9—Bond test results for GFRP wrap.

selected were the dry zone (top), tidal zone (middle), and the submerged zone (bottom).

The results of the bond tests for the CFRP- and GFRP-wrapped specimens are summarized in Fig. 8 and 9, respectively. The bond strength of CFRP specimens varied from 1.4 to 2.2 MPa (203 to 319 psi) and those for the GFRP specimens from 1.4 to 2.6 MPa (203 to 370 psi). Most of the bond failures in the top and middle locations occurred in the concrete indicating that the bond was good. In the submerged zones, however, failure occurred in the epoxy.

The average bond strength at these three levels considering all the specimens varied from 1.8 to 2.0 MPa (265 to 285 psi) in CFRP specimens and from 1.8 to 2.1 MPa (261 to 301 psi) in GFRP specimens. Thus, the average bond strength was marginally higher in the glass-fiber specimens in comparison to the carbon fiber specimens.

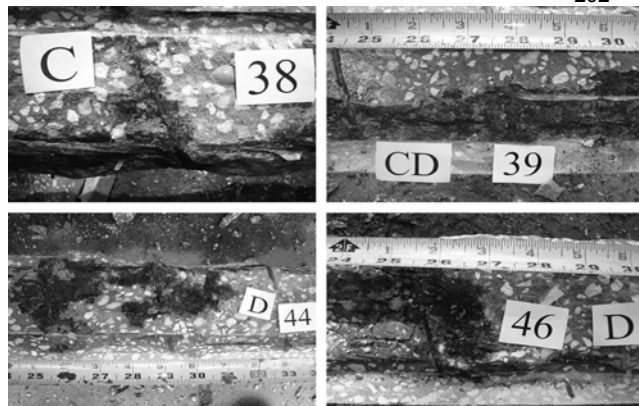


Fig. 10—Exposed steel of unwrapped specimens.

Although epoxy failure was the most commonly occurring mode in the submerged region, the measured ultimate bond stress was not significantly higher even where there was failure in the concrete. The bond strength was also unaffected by the number of FRP layers indicating that the inter-layer bond was good and the material was properly bonded in the first place. The somewhat poorer performance in the submerged region is not a result of the installation method as all specimens were dry-wrapped but rather is more likely a consequence of ingress of moisture into the resin over time.

### GRAVIMETRIC TESTING

All 22 specimens were gravimetrically tested to determine the actual steel loss at the end of the 1160-day exposure period. As noted previously, the Texas study<sup>17</sup> reported that the FRP wrap had entrapped water that had led to increased corrosion inside the wrap. No similar entrapment was found in this study and no similar localized corrosion was observed.

The strands and ties were extracted by making longitudinal cuts on the concrete surface with an electric saw and subsequently carefully chipping the cover off to expose the steel (Fig. 10 and 11). Inspection of these figures shows that there was much greater corrosion in the unwrapped controls than in the wrapped specimens. In the wrapped specimens, there was no evidence of corrosion products in some specimens unlike that in the unwrapped controls where corrosion products were always present.

The prestressing strands and ties were carefully extracted from all the specimens. The central-most section of the strands were cut to 0.91 m (36 in.) lengths, labeled, and numbered. The strands and ties were stored in sealed bags for subsequent cleaning. In the cleaning process, the strands were disassembled into seven separate wires to ensure there was no trapped rust.

A summary of the measured steel loss from all the results is shown in Table 4. Because the target area contaminated with chloride was 55 cm long (22 in.), located in the central portion of the specimen (Fig. 1), the steel loss was assumed to have occurred only in the chloride-contaminated region. The total loss in all four strands and ties was averaged for each specimen and compared with the controls.

It may be seen from Table 4 that the average steel loss in strands and ties in outdoor and indoor unwrapped specimens were similar (6.6 and 10.1% versus 6.6 and 8.9%). This suggests that temperature and humidity variation did not make as much a difference. Thus, corrosion gains made in the outdoor specimens during summer and fall were offset

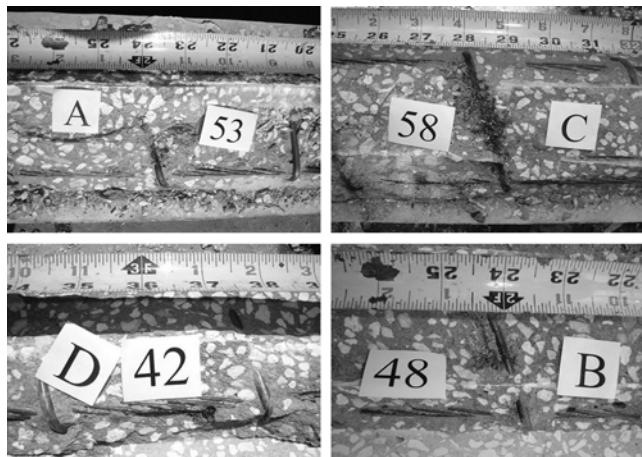


Fig. 11—Exposed steel of wrapped specimens.

Table 4—Averaged metal loss

Specimen type	Layer	Metal loss, %	
		Strand	Tie
Outdoor	0	6.6	10.1
Indoor	0	6.6	8.9
CFRP	1	3.5	7.1
	2	3.1	5.7
	3	3.4	6.9
	4	3.3	6.9
	Average	3.3	6.6
GFRP	1	3.6	6.7
	2	3.3	6.2
	3	3.5	5.9
	4	3.3	6.5
	Average	3.4	6.3

by lower corrosion rates in winter and spring. In contrast, the fluctuations in the corrosion rate in specimens kept inside the laboratory were smaller.

The performance of the wrapped specimens was much better as is evident from Fig. 10 and 11. The average metal loss in strands was 3.3% for CFRP and 3.4% for GFRP, approximately half that of the 6.6% in the controls. For the ties, average metal loss was 6.6% for carbon and 6.3% for glass compared with 10.1% for the outdoor controls (Table 4).

Aside from the difference in metal loss, there were 30 breaks in individual wires making up the strands in the six unwrapped specimens (average five breaks per pile) indicative of localized pitting corrosion. In contrast, there was only one instance of breakage in the 16 wrapped specimens (0.0625 breaks per pile). Thus, the averaged readings do not completely reflect the actual performance of the unwrapped specimens compared with the wrapped ones.

A more detailed breakdown of the gravimetric results showing the relationship between metal loss and number of FRP layers is given in Table 5. It may be seen from this table that the performance of the FRP did not necessarily improve as the number of layers increased. Overall, the results for carbon and glass were comparable.

## DISCUSSION

The goal of this study was to evaluate the effectiveness of the FRP in slowing down the corrosion rate in specimens in which the chloride threshold for corrosion initiation had been

Table 5—Summary of gravimetric results

Specimen type	Specimen ID	Metal loss, %			
		Strand	Tie		
Outdoor control	No. 38	6.3	11.7		
	No. 44	7.6	9.8		
	No. 45	6.4	9.7		
	No. 46	5.9	9.1		
	Average	6.6	10.1		
Indoor control	No. 39	6.5	10.0		
	No. 49	6.6	7.9		
	Average	6.6	8.9		
Carbon	1 layer	No. 54	3.4	6.8	
		No. 58	3.6	7.3	
		Average	3.5	7.1	
	2 layers	No. 55	3.1	6.1	
		No. 42	3.1	5.2	
		Average	3.1	5.7	
	3 layers	No. 56	3.3	6.7	
		No. 59	3.5	7.1	
		Average	3.4	6.9	
	4 layers	No. 57	3.4	7.7	
		No. 43	3.2	6.1	
		Average	3.3	6.9	
	Carbon average		3.3	6.6	
	Glass	1 layer	No. 48	3.5	6.4
			No. 52	3.6	6.9
			Average	3.6	6.7
		2 layers	No. 47	3.4	6.0
			No. 40	3.3	6.3
			Average	3.3	6.2
		3 layers	No. 50	3.7	6.4
No. 53			3.3	5.4	
Average			3.5	5.9	
4 layers		No. 51	3.7	6.4	
		No. 41	3.0	6.6	
		Average	3.3	6.5	
Glass average		3.4	6.3		

exceeded prior to wrapping. Here, the passive layer protecting steel is destroyed; but there is no visible sign of corrosion. This condition is not uncommon and was encountered in recent field applications<sup>14-16</sup> where chloride levels in the cover were comparable to those used in the test specimens.

The outdoor exposure setup and the simulated tidal cycles were very similar to natural conditions under which corrosion occurs in a marine environment. By using multiple embedded reference electrodes, both corrosion potential and linear polarization rates could be readily measured at the critical midheight without compromising the integrity and continuity of the wrap. These measurements indicated that FRP slowed down but did not stop the corrosion rate. The performance of the CFRP and GFRP were comparable and largely independent of the number of wrapping layers. These findings were confirmed through destructive gravimetric testing where metal losses in wrapped specimens were measured to be significantly lower than its identical unwrapped counterpart.

The fact that FRP was unable to stop the corrosion process is not particularly surprising given that oxygen and moisture present inside the concrete prior to wrap were sufficient to sustain the electrochemical reaction. Given that there are

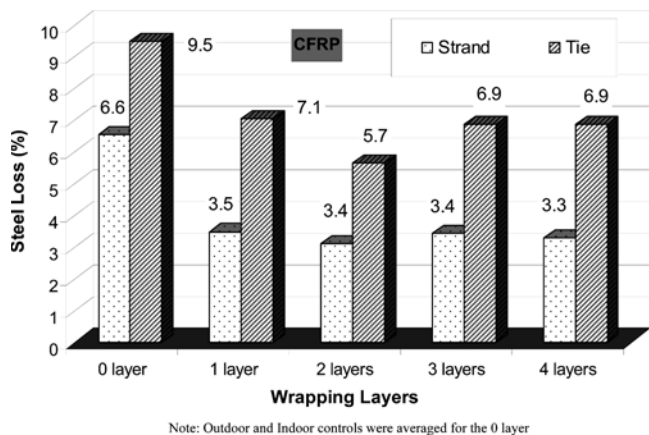


Fig. 12—Effect of CFRP wrap on maximum steel loss.

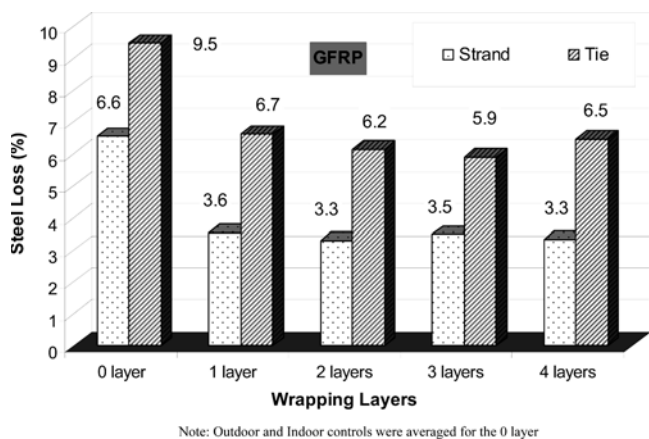


Fig. 13—Effect of GFRP wrap on maximum steel loss.

multiple pathways for transporting both these deleterious materials (from regions outside the wrapped area) through the pores in hardened concrete, it is unlikely that the corrosion can be stopped. As the FRP also confines the concrete, however, the confining pressures can compress the corrosion products and change the underlying electrochemical reactions. This may explain why trends in the corrosion rate measurements showed reductions in the corrosion rate over time (Fig. 6).

The surprising result was that two FRP layers were optimal regardless of the material (Table 5). Providing a larger number of layers provided increased strength but did not help corrosion mitigation. It provides further evidence that oxygen and moisture inside the wrap dictate the corrosion process. As results for one FRP layer were poorer, however, a minimum of two layers should be used in FRP corrosion mitigation applications.

A detailed examination of the profile of the corroded strand has not yet been made. Development work is currently underway to construct an automated system that can electronically record the profile of the strands. Once this has been completed, tests will be conducted to determine the stress-strain characteristics of the corroded strands. These findings will be reported at a future date.

## CONCLUSIONS

Based on the results presented, the following conclusions may be drawn:

1. The measured metal loss in wrapped specimens was significantly lower than that in identical unwrapped controls exposed to the same environment. Both CFRP and GFRP were equally effective in drastically reducing the rate of corrosion but were nonetheless unable to stop corrosion even when four layers were used (Fig. 12 and 13);

2. The performance of CFRP and GFRP in slowing down the corrosion rate was comparable (Table 4). The linear polarization measurements correctly predicted this and also the underlying trends in the metal loss in wrapped and unwrapped specimens (Fig. 5);

3. The level of corrosion protection afforded by FRP does not increase with the number of FRP layers. In this study, two layers were found to be the optimal number based on gravimetric testing (Table 5 and Fig. 12 and 13);

4. The gravimetric testing method used to determine metal loss is not fully indicative of the severity of the structural impact of the damage as the metal losses. Localized corrosion led to breakages in 30 wires in the six unwrapped controls. Such breakage was only observed in one wire from among all the 16 wrapped specimens; and

5. The average residual bond for the CFRP and GFRP were similar and largely unaffected by exposure. Adhesives used by both systems were durable.

In practice, if piles were wrapped at the time of installation, their performance would be vastly superior because the FRP would serve as a barrier to the ingress of chloride and significantly delay the onset of corrosion. Electrochemical measurements clearly indicate, however, that there are sufficient oxygen and moisture within the wrapped region to sustain the corrosion inside the wrap. This can be remedied by integrating a cathodic protection system within the wrap. Such development work is currently underway.

## ACKNOWLEDGMENTS

This study was performed in cooperation and funding from the State of Florida and the U.S. Department of Transportation. This support is gratefully acknowledged. The assistance and guidance of J. Garcia and S. Womble from the FDOT are gratefully acknowledged. The authors are indebted to E. Fyfe, Fyfe & Co, LLC, for providing materials used in the testing. The authors also thank SDR Engineering, Tallahassee, Fla., for its contribution.

## REFERENCES

- Tarricone, P., "Composite Sketch," *Civil Engineering*, ASCE, May 1995, pp. 52-55.
- Alampalli, S., "Reinforced Polymers for Rehabilitation of Bridge Columns," *Proceedings of the 5th National Workshop on Bridge Research in Progress*, Oct. 2001, pp. 39-41.
- Sen, R., "Advances in the Application of FRP for Repairing Corrosion Damage," *Progress in Structural Engineering and Materials*, V. 5, No. 2, 2003, pp. 99-113.
- Sheikh, S.; Pantazoupoulou, S.; Bonacci, J.; Thomas, M.; and Hearn, N., "Repair of Delaminated Circular Pier Columns with Advanced Composite Materials," *Ontario Joint Transportation Research Report No. 31902*, Ministry of Transportation of Ontario, Aug. 1997, 75 pp.
- Neale, K. W., and Labossiere, P., "Fiber Composite Sheets in Cold Climate Rehab," *Concrete International*, V. 20, No. 6, June 1998, pp. 22-24.
- Bonacci, J., "Rehabilitation of Corrosion-Damaged RC Infrastructure Using Externally Bonded FRP," *Proceedings of ACMB 2000*, CSCE, Montreal, Quebec, Canada, 2000, pp. 561-568.
- Baiyasi, M., and Harichandran, R., "Corrosion and Wrap Strains in Concrete Bridge Columns Repaired with FRP Wraps," *Paper No. 01-2609*, 80th Annual Meeting, Transportation Research Board, Washington, D.C., 2001.
- Debaiky, A.; Green, M.; and Hope, B., "Carbon Fiber-Reinforced Polymer Wraps for Corrosion Control and Rehabilitation of Reinforced Concrete Columns," *ACI Materials Journal*, V. 99, No. 2, Mar.-Apr. 2002, pp. 129-137.
- Wootton, I.; Spainhour, L.; and Yazdani, N., "Corrosion of Steel Reinforcement in CFRP Wrapped Concrete Cylinders," *Journal of Composites for Construction*, V. 7, No. 4, 2003, pp. 339-347.

10. Wheat, H. G.; Jirsa, J. O.; and Fowler, D. W., "Monitoring Corrosion Protection Provided by Fibre Reinforced Composites," *International Journal of Materials and Product Technology*, V. 23, No. 3/4, 2005, pp. 372-388.
11. Mullins, G.; Sen, R.; Torres-Acosta, A.; Goulis, A.; Suh, K.; Pai, N.; and Mehrani, A., "Load Capacity of Corroded Pile Bents," *Final Report* submitted to the Florida Department of Transportation, Sept. 2001, 327 pp.
12. Suh, K. S.; Mullins, G.; Sen, R.; and Winters, D., "Use of FRP for Corrosion Strengthening Applications in a Marine Environment," *Final Report* submitted to Florida/U.S. Department of Transportation, Tallahassee, Fla., Oct. 2005, 406 pp.
13. Bazinet, S.; Cereone, L.; and Worth, F., "Composite FRP Moves into Underwater Repair Applications," *SAMPE Journal*, V. 39, No. 3, May-June 2003, pp. 8-16.
14. Mullins, G.; Sen, R.; Suh, K.; and Winters, D., "Underwater FRP Repair of Prestressed Piles in the Allen Creek Bridge," *Journal of Composites for Construction*, ASCE, V. 9, No. 2, 2005, pp. 136-146.
15. Sen, R.; Mullins, G.; Suh, K. S.; and Winters, D., "FRP Application in Underwater Repair of Corroded Piles," *7th International Symposium on Fiber-Reinforced (FRP) Polymer Reinforcement for Concrete Structures*, SP-230, C. Shield, J. Busel, S. Walkup, and D. Gremel, eds., V. 2, American Concrete Institute, Farmington Hills, Mich., 2005, pp. 1139-1156.
16. Mullins, G.; Sen, R.; Suh, K.; and Winters, D., "A Demonstration of Underwater FRP Repair," *Concrete International*, V. 28, No. 1, Jan. 2006, pp. 70-73.
17. Berver, E.; Jirsa, J.; Fowler, D.; Wheat, H.; and Moon, T., "Effects of Wrapping Chloride Contaminated Concrete with Fiber-Reinforced Plastics," FHWA/TX-03/1774-2, University of Texas at Austin, Austin, Tex., Oct. 2001, 112 pp.
18. *Concrete Repair Manual*, 2nd Edition, V. 1, American Concrete Institute, Farmington Hills, Mich., 2003, p. 464.
19. ASTM D 4541, "Standard Test Method for Pull-Off Strength of Coatings Using Portable Adhesion Testers," ASTM International, West Conshohocken, Pa., 2002, 13 pp.



# Insitu Testing

## *Introduction*

In terms of foundation engineering, insitu (or in place) testing refers to those methods that evaluate the performance of a geotechnical structure or the properties of the soils or rock used to support that structure. This testing can range from a soil boring at a surveyed location to monitoring the response of a fully loaded bridge pier, dam, or other foundation element. The reliability of a given structure to function as designed is directly dependent on the quality of the information obtained from such testing. Therein, it is imperative that the design engineer be familiar with the types of tests and the procedures for proper execution as well as the associated advantages and disadvantages.

Methods of insitu evaluation can be invasive or noninvasive, destructive or nondestructive, and may or may not recover a specimen for visual confirmation or laboratory testing. Invasive tests (e.g. soil borings or penetration tests) tend to be more time consuming, costly, and precise; whereas, noninvasive tests (e.g. GPR or seismic refraction) provide a large amount of information in a short period of time that is typically less quantifiable. However, when used collectively, the two methods can complement each other by: (1) defining areas of concern from noninvasive techniques, and (2) determining the foundation design parameter from invasive techniques. This is particularly advantageous on large sites where extreme variations in soil strata may exist.

## *Site Exploration Plan*

The subsurface investigation program for a given site should account for the type, size, and importance of the proposed structure. These parameters help focus the design of the site exploration program by determining the quantity and depth of soil soundings (or borings) required. Planning for a site investigation should also include the location of underground utilities (i.e. phone, power, gas, etc.). As such, a local "call before you dig" service should be notified several days prior to the anticipated investigation. These services are usually subsidized by the various local utilities and have no associated cost.

The quantity of borings is largely dependent on the overall acreage of the project, the number of foundations, or the intended use of the site. For foundations, the depth of borings depends on the zone of soil influenced by the foundation geometry and the given loading. For instance, a proposed roadway alignment typically requires a hand-auger investigation every 100 feet along the centerline to a depth of 5 feet to define uniformity of the subgrade material as well as spatial variability. Therein, the importance of the structure, in the form of causal effects should a failure occur, is somewhat minimal. Further, if undesirable soils conditions were identified, a followup investigation could be requested. In contrast, preliminary borings along the alignment of a proposed bridge foundation can be more frequent and are much deeper depending on the depth to a suitable bearing strata. At a minimum, one boring should be performed at each pier location to a depth 3 - 5 foundation diameters below the anticipated foundation. Likewise, buildings with large column loads

often require a boring at each column location unless the soil shows extremely consistent behavior. For extremely important structures the designer and/or client not only require more scrutiny from the subsurface investigation, but also require an amplification factor (or importance factor) be applied to the load to assure a low probability of failure (AASHTO, 1997).

In virtually all cases, the additional cost of more thorough subsurface investigation can be reconciled with a more cost effective foundation design. Uncertainty in subsurface conditions in most instances promotes needless over-design. Depending on the type of design to be considered, the designer must recognize the effect of site variability as well as the type of testing that can be conducted to increase confidence and reduce the probability of failure.

## ***Geophysical Testing Methods***

### **Ground Penetrating Radar**

Ground Penetrating Radar (GPR) is a geophysical exploration tool used to provide a graphical cross-section of subsurface conditions. This cross-sectional view is created from the reflections of repeated short-duration electromagnetic (EM) waves which are generated by an antenna in contact with the ground surface as the antenna traverses across the ground surface. The reflections occur at the interfaces between materials with differing electrical properties. The electrical property from which variations cause these reflections is the dielectric permittivity, which is directly related to the electrical conductivity of the material. GPR is commonly used to identify underground utilities, underground storage tanks, buried debris, or geological features. The information from GPR can be used to make recommendations for more invasive techniques such as borings. Figure 1 shows a ground launch GPR system being pushed along a predetermined transect line.



**Figure 1** GPR field device (Courtesy of Universal Engineering, Inc.).

The greater the electrical contrast between the surrounding earth materials and the target of interest, the greater the amplitude of the reflected return signal. Unless the buried object/target of interest is highly conductive, only part of the signal energy is reflected back to the antenna located on the ground surface with the remaining portion of the signal continuing to propagate downward to be reflected by deeper features. If there is little or no electrical contrast between the target of interest and the surrounding earth materials, it would be very difficult if not impossible to identify the object using GPR.

The GPR unit consists of a set of integrated electronic components which transmits high frequency (100 to 1500 megahertz [MHz]) electromagnetic waves into the ground and records the energy reflected back to the ground surface. The GPR system is comprised of an antenna, which serves as both a transmitter and receiver, and a profiling recorder that both processes the data and provides a graphical display of the data.

The depth of penetration of the GPR is very site specific and is controlled by two primary factors: subsurface soil conditions and antenna frequency. The GPR signal is attenuated (absorbed) as it passes through earth materials. As the energy of the GPR signal is diminished due to attenuation, the energy of the reflected waves is reduced, eventually to a level where the reflections can no longer be detected. In general, the more conductive the earth materials, the greater the GPR signal attenuation. In Florida, typical soil conditions which severely limit the GPR signal penetration are near-surface clays, organic materials, and the presence of sea water in the soil pore water space.

A GPR survey is conducted along survey lines (transects) which are measured paths along which the GPR antenna is moved. Known reference points (i.e., building corners, driveways, etc.) are placed on a master map, which includes traces of the GPR transects overlying the survey geometry. This survey map allows for correlation between the GPR data and the position of the GPR antenna on the ground.

For geological characterization surveys, the GPR survey is conducted along a set of perpendicularly oriented transects. The survey is conducted in two directions because subsurface features are often asymmetric for residential surveys. Spacing between the survey lines is initially set at 10 feet. More closely spaced grids may be used to further characterize a recorded anomaly.

The features observed on the GPR data that are most commonly associated with potential sinkhole activity are:

A down-warping of GPR reflector sets, that are associated with suspected lithological contacts, towards a common center. Such features typically have a bowl or funnel shaped configuration and are often associated with deflection of overlying sediment horizons caused by the migration of sediments into voids in the underlying limestone (Figure 2). In addition, buried depressions caused by differential subsidence over buried organic deposits and debris may also cause these observed features.

A localized significant increase in the depth of penetration and/or amplitude of the GPR signal response. The increase in GPR signal penetration depth or amplitude is often associated with a localized increase in sand content at depth.

An apparent discontinuity in GPR reflector sets that are associated with suspected lithological contacts. The apparent discontinuities and/or disruption of the GPR reflector sets may be associated with the downward migration of sediments.

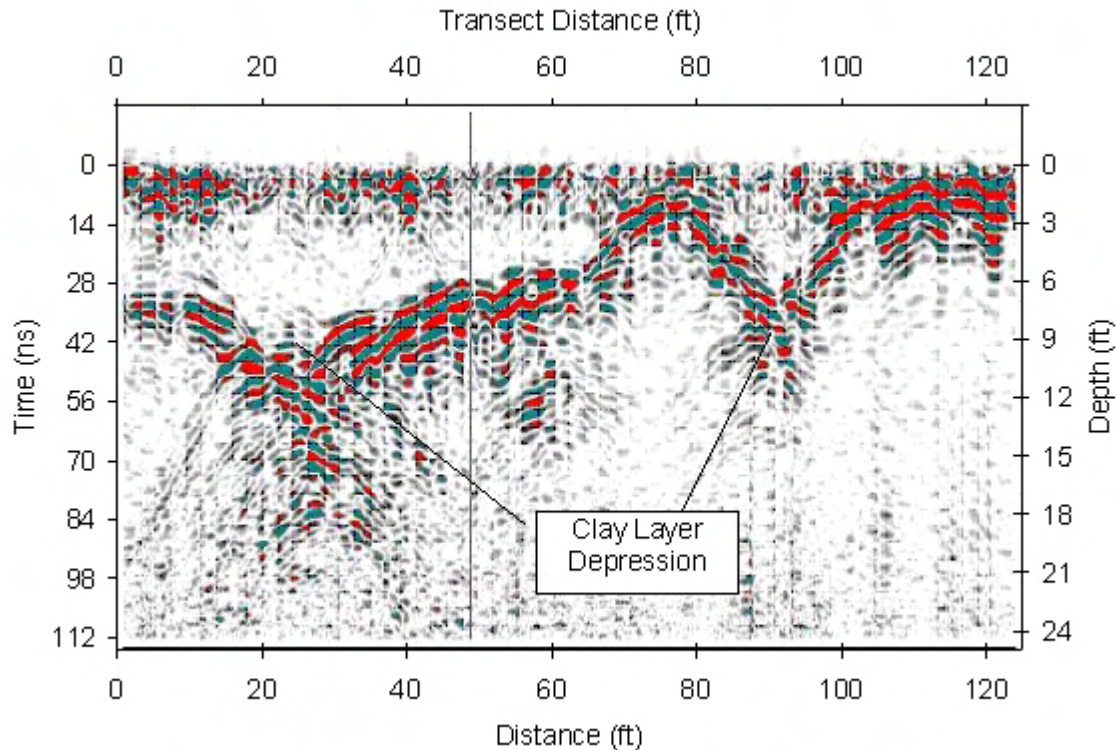


**Figure 2** GPR image (courtesy of Universal Engineering, Inc).

The greater the severity of the above features or a combination of these features, the greater the likelihood that the identified feature is related to past or present sinkhole activity.

Depth estimates to the top of the lithological contacts or targets of interest are derived by dividing the time of travel of the GPR signal from the ground surface to the top of the feature by the velocity of the GPR signal. The velocity of the GPR signal is usually obtained for a given geographic area and earth material from published sources. In general, the accuracy of the GPR-derived depth estimates ranges from  $\pm 25$  percent of the total depth.

Although the GPR is very useful in locating significant lithologic soil changes, strata thickness, and inferred subsurface anomalies, the GPR cannot identify the nature of earth materials nor their condition (i.e., loose vs. dense sand, soft vs. stiff clay). The GPR data is best used in conjunction with other geotechnical and physical tests to constrain the interpretation of the virtual cross-section profiles.

## Resistivity Tests

Electrical Resistivity Imaging (ERI) is a geophysical method that maps the differences in the electrical properties of geologic materials. These changes in electrical properties can result from variations in lithology, water content, pore-water chemistry, and the presence of buried debris. The method involves transmitting an electric current into the ground between two electrodes and measuring the voltage between two other electrodes. The direct measurement is an apparent resistivity of the area beneath the electrodes that includes deeper layers as the electrode spacing is increased. The spacing of electrodes can be increased about a central point, resulting in a vertical electric sounding (VES) that is modeled to create a 1-D geoelectric cross-section. Recent advances in technology allow for rapid collection of adjacent multiple soundings along a transect that are modeled to create a 2-D geoelectric *pseudo* cross-section. The cross-section is useful for mapping both the vertical and horizontal variations in the subsurface (see Figure 3).

Although the result from this method are not absolute, the resistivity trends obtained are useful for mapping stratigraphy such as aquatards, bedrock, faults and or fractures. It can delineate anomalous formations or voids in karstic material, the presence of salt water intrusion in coastal regions, and detect leaks in dams as well as other applications. It is most successful in large cleared areas without severe changes in topography; not recommended for small congested or urban sites. Buried utilities or other highly conductive anomalies can adversely affect the results.

This method is fast, non-invasive, and relatively inexpensive when compared to drilling. When compared to electromagnetic methods, is it less susceptible to interference from overhead power lines. It is easily calibrated to existing boreholes to allow for correlations between measured resistivity and estimated soil properties. As with other geophysical test methods, it is best suited for environmental or water resources disciplines that require stratigraphy or soil property mapping of large land parcels.

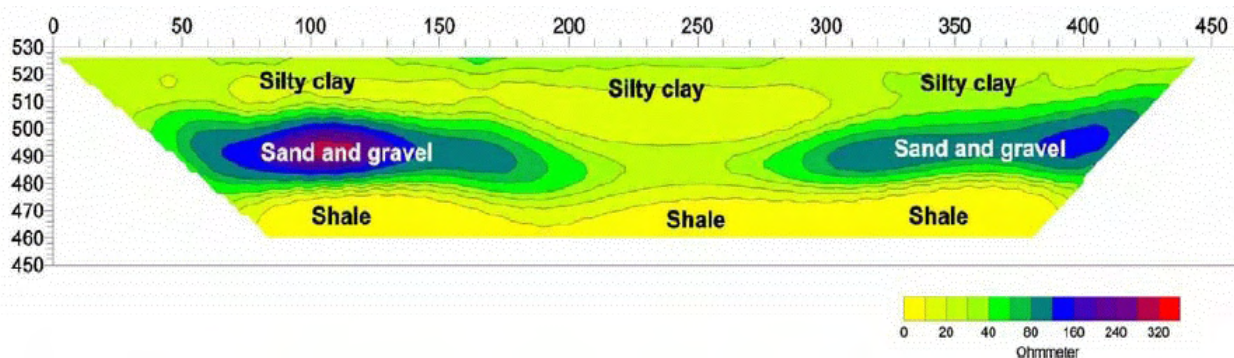


**Figure 3** Rendering of soil cross section from ERI output (courtesy of Universal Engineering, Inc.)



## Seismic Refraction

The seismic refraction technique measures the seismic velocity of subsurface materials and models the depth to interfaces with a velocity increase. Soil conditions and geologic structure are inferred from the results, since changes in material type, or soil conditions, are often associated with changes in seismic velocity. Seismic energy, which is introduced into the subsurface using a drop weight or explosive source, propagates through the earth as a wave front that is refracted by the material through which it passes. As illustrated in Figure 4, the wave front intersects a high-velocity interface, creating a "head wave" that travels in the higher velocity material nearly parallel to the interface. The energy in this head wave leaves the interface and passes back through the low velocity material to the surface. Geophones placed at selected intervals along the ground surface detect the ground motion and send an electrical signal, via a cable, to a recording seismograph. The objective is to determine the arrival times of these refracted waves in order to calculate the velocity of the material and model the depth to various interfaces.

This test is used to determine stratigraphy such as the depth to bedrock. It is best suited for stratigraphy that increases in density (or seismic velocity) with depth. In such cases it can estimate the depth of borrow materials, aid in mapping faults and fractured rock zones, locate the water table, estimate material elastic properties such as shear modulus and Poisson's ratio. The depth of exploration is limited by the energy source and the maximum length of geophone spacing. The test is less expensive most soil exploration methods as well as other comparable seismic reflection methods. The vertical resolution is usually better than electrical, magnetic or gravity methods of site investigation.

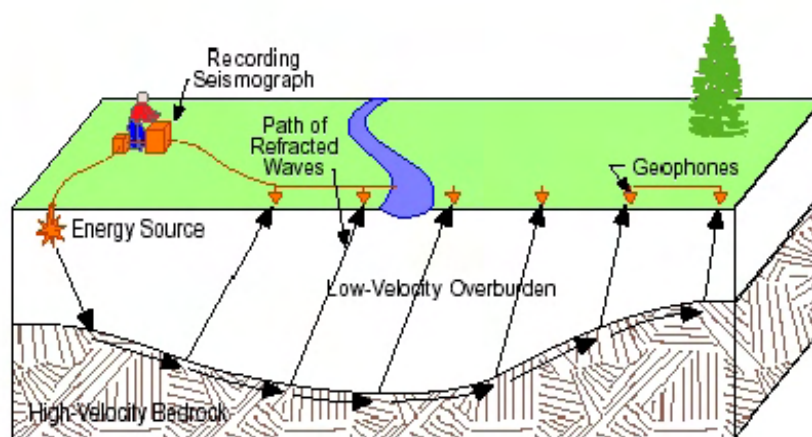


**Figure 4** Conceptual sketch of seismic refraction layout and wave paths  
(Courtesy of Universal Engineering, Inc.).

## ***Physical Sampling and Penetration Tests***

### **Standard Penetration Test**

The standard penetration test (SPT) is undoubtedly the most common method of soil exploration for foundation design. It is an invasive test that not only provides information from which soil strength can be estimated, but also it provides a physical sample that can be visually inspected or used for laboratory classification. Although the test method has undergone several iterations with respect to upgrading equipment, it is sensitive to operator and equipment variability. Regardless, the general concept of penetration resistance and the hands on soil sample recovery make it the choice of many designers.

The SPT is described by the American Society for Testing and Materials (ASTM) as test number D-1586, entitled "Standard Method for Penetration Test and Split-Barrel Sampling of Soils." This standard defines the appropriate manner in which the test should be conducted which involves drilling techniques, penetration and sampling methods, proper equipment, and the reporting of results. In general, a 2" O.D. split spoon sampler is driven into the ground with a 140 lb drop hammer dropped 30 inches repeatedly until a penetration of 18 inches is achieved. The number of blows of the hammer is recorded for each of three 6" intervals (totaling 18 inches). The number of blows required to advance the sampler the last 12 inches (2<sup>nd</sup> and 3<sup>rd</sup> interval) is defined as the SPT N-value. Upon extraction of the sampler, the soil retrieved is visually inspected, documented, and placed in jars for more elaborate testing (if so determined by the engineer). At best, continuous sampling produces a single SPT N-value every 1.5 ft. At minimum, a sample should be taken every 5 feet of depth.

Between each penetration test, a boring should be advanced to permit the next sample without interference from side shear resistance along the length of the drill rod. Several boring techniques are acceptable: one-hole rotary drilling, continuous flight hollow stem augering, wash boring, or continuous flight solid stem augering. However, under no circumstances should the soil beneath the advanced borehole be disturbed by jetting or suction action caused by improper drilling techniques. For instance, extracting a continuous flight auger from submerged soils will reduce the insitu stresses and produce lower N-values.

The hammer used to drive the sampler can either be manual or automatic. Numerous configurations of both hammer types have been manufactured. The safety type is the most common manual hammer as it is equally suited to both drive and extract the split spoon. This type of hammer is lifted by the friction developed between a rope and a spinning cathead power take-off. The number of wraps around the cathead as well as the diameter of cathead are specified as well as the condition of the rope and cathead surface (Figure 5). Due to the incomplete release of the drop weight from the cathead, the total potential energy of the drop is not available to advance the sampler. A recent study showed that manual hammers transfer anywhere between 39 and 93% of the energy (average 66%), while automatic hammers ranged between 52 and 98% (average 79%). Although the reproducibility of a automatic hammer is better than manual hammers, the variation in energy efficiency cited is dependent on the upward velocity of the hammer as controlled by the revolutions per minute of the drive chain motor (Figure 6). To this end, a given machine should be calibrated to produce an exact 30 inch drop height and the rpms required to produce that drop recorded and maintained.



**Figure 5** Manual hammer SPT apparatus.



**Figure 6** Truck-mount drill rig (left), chain driven automatic SPT hammer (right).

Aside from the visual and physical classification that can be obtained from a standard penetration test, correlations have been established that provide estimates of insitu soil properties based on the soil type and blow count. These correlations can be based on the corrected or uncorrected SPT blow count  $N'$  or  $N$ , respectively.

Corrected blow counts provide a method of accounting for the insitu state of stress surrounding a soil sample while it was being tested. For instance, sands with identical structure with appear stronger (higher blow counts) at greater depths than when at shallower depths. As such, soil properties such as unit weight may be better estimated if overburden effects are removed or normalized. However, soil properties such as shear strength or available end bearing are enhanced by greater insitu stresses and are generally correlated to uncorrected blow counts. The following expression is used to correct SPT  $N$ -values by normalizing it to a 1 tsf overburden insitu state.

Tables SPT-1 and SPT-2 provide estimated values for corrected and uncorrected blow counts, respectively.

Table SPT-1 (FHWA, 1993)

Corrected SPT- $N'$	Description	$\gamma_{\text{moist}}$		$\phi$
		(pcf)	(kN/m <sup>3</sup> )	(deg)
SANDS				
0	Very Loose	70 - 100	11.0 - 15.7	25-30
4	Loose	90 - 115	14.1 - 18.1	27-32
10	Medium	110 - 130	17.3 - 20.4	30-35
30	Dense	120 - 140	18.8 - 22.0	35-40
50	Very Dense	130 - 150	20.4 - 23.6	38-43
CLAY				qu, ksf
0	Very Soft	100 - 120	15.7 - 18.8	0
2	Soft			0.5
4	Medium	110 - 130	17.3 - 20.4	1.0
8	Stiff			2.0
16	Very Stiff	120 - 140	18.8 - 22.0	4.0
32	Hard			8.0

Table SPT-2 (Kulhawy and Mayne, 1990)

SPT-N	$\gamma_{sat}$		$\gamma_{sub}$		$\phi$ (deg)
	(pcf)	(kN/m <sup>3</sup> )	(pcf)	(kN/m <sup>3</sup> )	
SANDS					
0-2	100	15.7	37.6	5.9	26
3-4	100	15.7	37.6	5.9	28
4-10	105	16.5	42.6	6.7	29
10-20	110	17.3	47.6	7.5	30
20-30	115	18.1	52.6	8.3	32
30-40	120	18.9	57.6	9.1	33
>40	125	19.6	62.6	9.8	34
CLAY					
0-2	105	16.5	42.6	6.7	0
2-4	110	17.3	47.6	7.5	0
4-8	115	18.1	52.6	8.3	0
8-15	120	18.9	57.6	9.1	0
15-30	125	19.6	62.6	9.8	0
>30	125	19.6	62.6	9.8	0
<p><i>Clay Shear Strength <math>C = N / T_i</math> in psf, where <math>T_i</math> is the soil type factor</i>  <math>T_i = 8</math> for most clay  <math>T_i = 10</math> for low plasticity or SC  <math>T_i = 12</math> for peat</p>					
LIMESTONE					
SPT - N	Shear Strength		$\gamma_{sat} = 135$ pcf (21.2 kN/m <sup>3</sup> ) $\gamma_{sub} = 72.6$ pcf (11.4 kN/m <sup>3</sup> ) $\phi = 0$ deg $K_a = 1.0$ $K_p = 1.0$		
	pcf	kN/m <sup>2</sup>			
10-20	4000	190			
20-50	8000	380			
50-100	15000	720			

## Insitu Rock Testing

The design of rock-socketed drilled shafts is highly dependent on the integrity of the rock core samples obtained from field investigation. When sufficient samples are recovered, laboratory tests can be conducted to determine the splitting tensile strength,  $q_t$ , (ASTM D 3967) and the unconfined compressive strength,  $q_u$ , (ASTM D 2938). The shear strength of the shaft/limestone interface,  $f_{su}$ , is then expressed as a function of  $q_t$  and  $q_u$  (McVay et al., 1992). This value is typically adjusted by rock quality indicators such as the Rock Quality Designation,  $RQD$ , (ASTM D 6032) and/or the percent recovery,  $REC$ . For example, the State of Florida outlines a method using the percent recovery to offset the highly variable strength properties of the Florida limestone formation. Therein, a design value,  $(f_{su})_{DESIGN}$ , is expressed as  $REC * f_{su}$  (Lai, 1999). These methods work well in consistent, competent rock but are subject to coring techniques, available equipment, and driller experience. Sampling problems are compounded in low quality rock formations as evidenced by the occurrence of zero  $RQD$  and low  $REC$  values.

**Timed Drilling.** To counter poor quality samples (or no sample at all) some designers with extensive local experience use timed drilling techniques to estimate rock quality and shaft design values in addition to, or in lieu of, the previous methods. With this technique, the driller must record the time to advance a wash boring through a bearing strata while maintaining a constant "crowd" pressure, fluid flow, and rotational bit speed. Advance times would typically need to be greater than 2 - 3 minutes per foot to be useful. Lower advance times are common in weaker soils which are more effectively tested by Standard Penetration Testing. Like SPT and CPT, the equipment should maintain reasonably consistent physical dimensions (i.e. the bit should stay in good working condition). Although this method is very simple, it is highly empirical and largely dependent on the uniformity of the drilling techniques. Additionally, the designer must have developed a large enough database (with load test calibration) to design with confidence. Such databases exist, but are proprietary and not common knowledge.

**Coring Methods.** When designing from rock core samples it is important to consider the factors affecting sample retrieval and hence their quality. The recovered samples can range in diameter from 0.845" to 6" where larger samples are preferred in soft limestone. The State of Florida requires a minimum core diameter of 2.4" but recommends 4". The drill core samples can be obtained from three different types of core barrels: single tube, double tube, and triple tube. The simplest is the single tube in which the drill core and flushing fluid occupy the same space and consequently can lead to erosion of low strength or fragmented rock samples. As a result, this type of core barrel is not permitted for use with Florida limestone (FDOT, 1999).



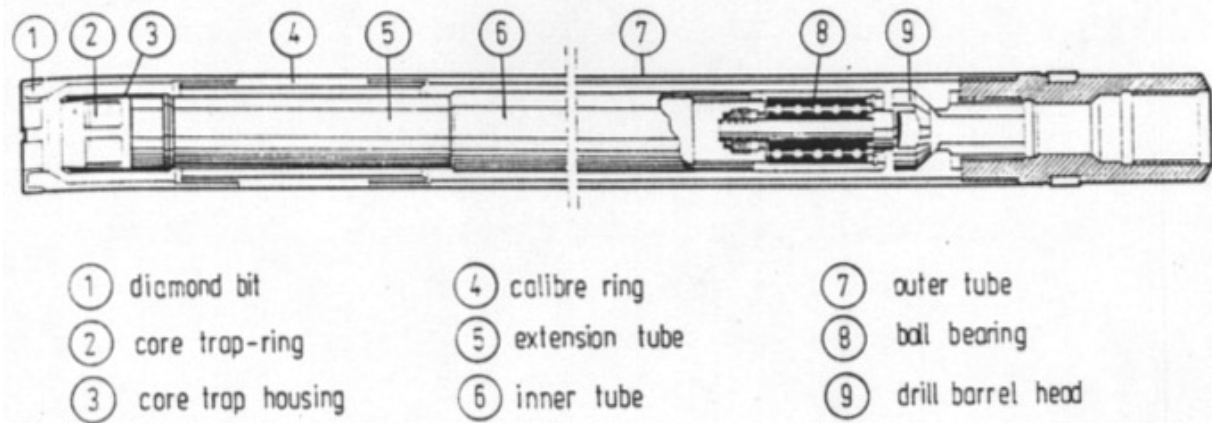


**Figure 7** Double tube core barrel schematic (after Wittke, 1990).

Double tube core barrels differ from single tube by essentially isolating the drill core from the flushing fluid (see Figure 7). Simple versions of this type of core barrel use a rotating inner tube which requires a small fraction (approx. 10%) of the drilling fluid to circulate around the drill core to prevent binding and direct contact of the sample with the tube. Most double tube systems now use a fixed inner tube which requires no flush fluid around the drill core and thus causes less disturbance to the sample. During extraction of the entire barrel assembly, a core trap-ring at the leading edge of the inner barrel snares the drill core preventing its loss (see Figure 8). Recovering the sample from the inner tube without disturbing it is difficult in soft, fragmented, or inter-layered rock deposits. Both fixed and rotating inner core barrels are permitted by FDOT but significant variations in recovery values should be expected.

The triple tube core barrel, in concept, is essentially the same as the double tube (with the fixed

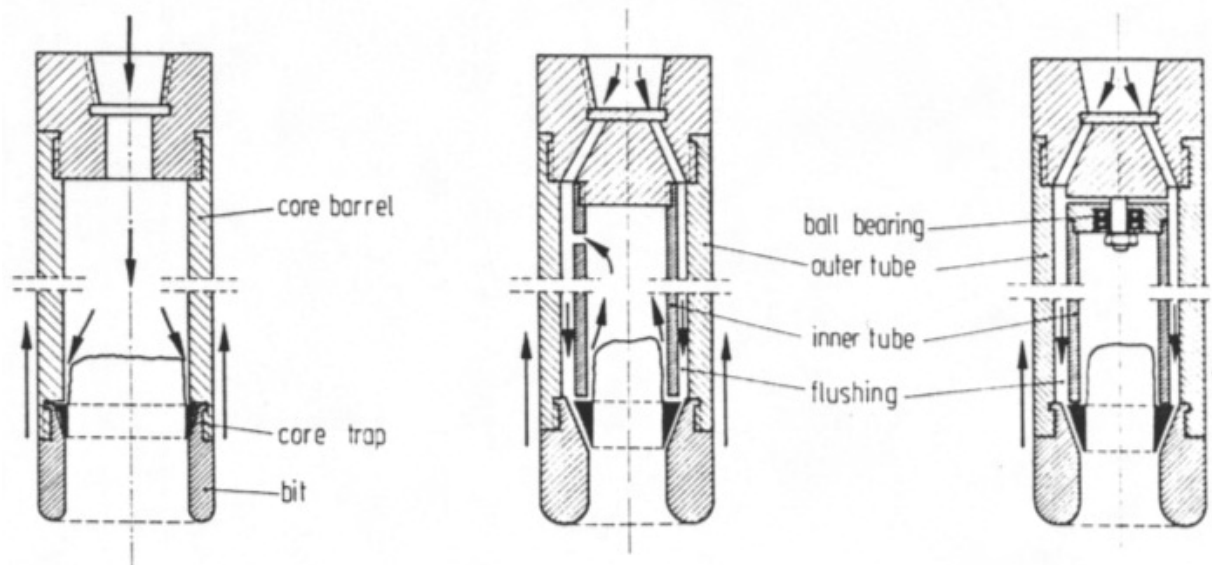


**Figure 8** Single tube (left), double tube w/rotating inner tube (center), and double tube w/fixed inner tube (right), after Wittke, 1990 .

inner tube). It differs in the way the specimen is recovered in that the inner tube is fitted with yet a third sleeve or split tubes in which the drill core is housed. The entire sleeve or split tube is extruded from the inner barrel using a plunger and pressure fitting that pushes directly on the split tubes. The extrusion process is similar to that of Shelby tube samples except the sample is not stressed. In this manner, the sample is not compressed or shaken loose. Figures 9-12 show the components of the triple tube core barrel and sample extruder.



**Figure 9** Triple tube core barrel components.



**Figure 10** Sample extruder.



**Figure 11** Cutting bits used by FDOT District I.

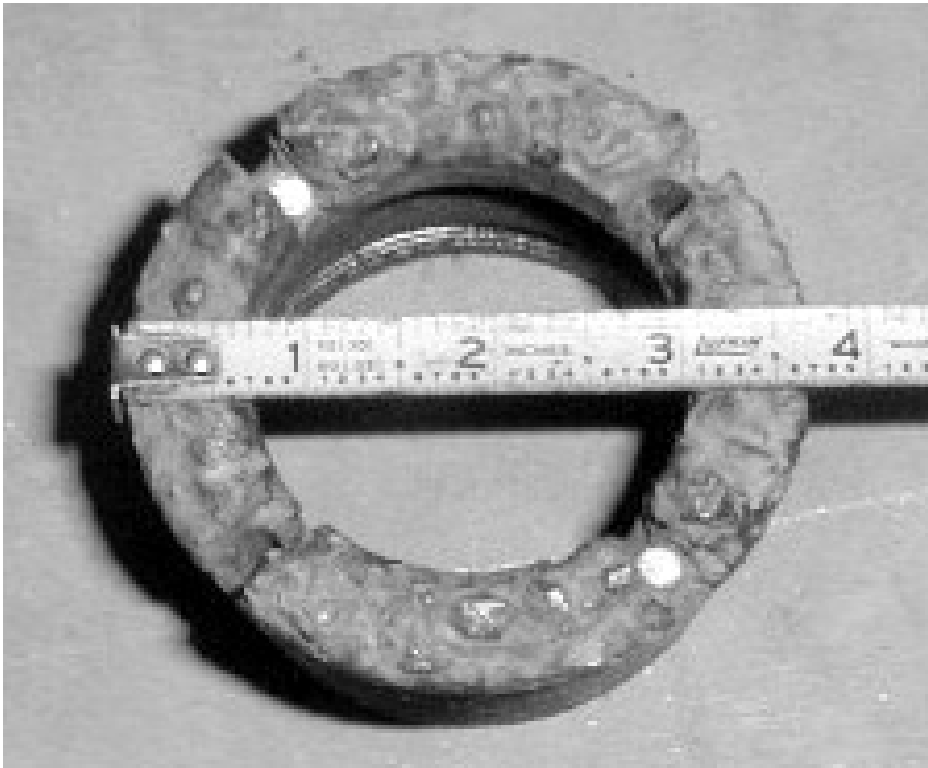


**Figure 12** HQ3 triple tube cutting tip, "Devil's Nightmare," 3.78" O.D.

Further variables affecting core drilling results include: the type of drill bit, the flow rate of the flushing fluid, the end gap between the inner and outer barrels, the crowd pressure, and the advance rate through softer inter-layered deposits. With so many variables controlling sample recovery, methods of investigating the remaining borehole for the insitu limestone characteristics could have significant merit.

**Insitu Rock Strength Tests.** Direct measurements of the insitu bond/shear strength of the drilled shaft-to-rock interface can be obtained through small-scale anchor pull-out tests or full-scale load tests. Anchor pull-out tests are purported to have produced reasonable correlations with full-scale results (Bloomquist et al., 1991). The test method involves simply grouting a high strength post tensioning rod into a borehole, and measuring the load required to pull the grout plug free (*Note: load is directly applied to the base of the plug to produce compression and the associated Poisson expansion in the specimen*). Attention must be given to the surface area formed by the volume of grout actually placed. This test is an attractive option in that it is relatively inexpensive, requires minimal equipment mobilization, and can be conducted at numerous locations throughout a site. However, it has received little attention as a whole and remains comparatively unused.

Design-phase, full-scale, insitu testing of the shaft/limestone interface is by far the surest method to determine the design parameters of a drilled shaft. This can be accomplished by several means: top down static loading, bi-directional static loading, static loading, or drop-hammer dynamic loading (discussed later). However, due to the associated costs, only a small fraction of rock sockets are tested in this fashion, and rarely at the design phase. Additionally, a single test may not adequately account for the spatial variability of rock formations without correlation to standard site investigation methods. As such, a host of insitu borehole devices have been developed to aid in estimating soil and rock strength parameters.

In situ borehole modulus devices are classified into two categories based on their loading apparatus: (1) rotationally symmetric borehole loading devices, and (2) diametrically arranged lateral loading plates (Wittke, 1990). Figure 13 shows the loading scheme of the two conceptual mechanisms.

Type (1) probes apply load via a rubber diaphragm which is pressurized by either gas or liquid. In general, measurements of displacement are made directly when using gas pressure, and indirectly through change in volume when using fluid pressure. Table 1 lists Type (1) devices that have been developed by various manufacturers.

Type (2) probes use two semi-cylindrical thrust plates diametrically aligned to apply loads to the arc of the borehole. Measurements of displacement are obtained directly at a minimum of two locations along the longitudinal axis of the plates. Whereas Type (1) devices produce uniformly distributed radial stresses in the borehole, the stress distribution in Type (2) devices is dependent on the relative

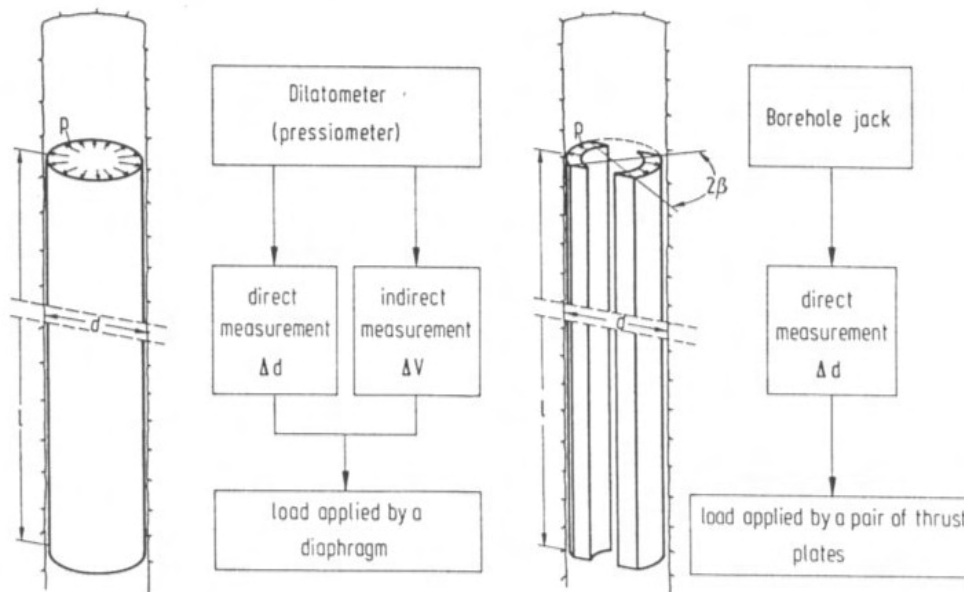


**Figure 13** Loading scheme of the two types of modulus devices.

stiffness of the rock and the plate. Table 2 lists Type (2) devices that have been developed by various manufacturers.

Table 1 List of Type (1) Borehole Devices (after Wittke, 1990)

Name	Method of Measuring	Number of Measuring Devices	Max. Applied Pressure $P_{max}$ [MN/m <sup>2</sup> ]	Borehole Diameter d[mm]	Test length l [mm]	l/d
Menard pressiometer	indirect ( $\Delta v$ )	-	10	34-140	502-910	$\geq 65$
CSM cell	indirect ( $\Delta v$ )	-	70	38	165	4.3
Janod Mermin probe	direct ( $\Delta d$ )	3	15	168	770	4.6
Sounding dilatometer	direct ( $\Delta d$ )	2	4/7.5	200/300	1000/1200	5/4
Comes probe	direct ( $\Delta d$ )	3	15	160	1600	10
LNEC dilatometer	direct ( $\Delta d$ )	4	15	76	540	7.1
Tube deformer	direct ( $\Delta d$ )	4	4	297	1300	4.4
Prigozhin pressiometer	direct ( $\Delta d$ )	2	20	46	680	14.8
Atlas dilatometer	direct ( $\Delta d$ )	8	10	144	890	6.2
BGR dilatometer	direct ( $\Delta d$ )	4	40	86	1000	11.6
Dilatometer 95	direct ( $\Delta d$ )	3	12	100	1000	10
Dilatometer 112	direct ( $\Delta d$ )	3	12	116	1000	8.6
Elastometer 100	direct ( $\Delta d$ )	2	10	62	520	8.4
Elastometer 200	direct ( $\Delta d$ )	3	20	62	520	8.4

Table 2 List of Type (2) Borehole Devices (after Wittke, 1990)

Name	Thrust plates' angle of opening	Max. applied pressure $P_{max}$ [MN/m <sup>2</sup> ]	Borehole diameter d [mm]	Test length l [mm]	l/d
Geoextensometer	$2\beta = 143^\circ$	34	76	306	4.0
Goodman jack	$2\beta = 90^\circ$	64	74-80	204	2.6-2.8
CSIRO pressiometer	$2\beta = 120^\circ$	35	76	280	3.7

Another mechanism (not originally intended for rock) that has interesting features in respect to weak rock is the Iowa borehole shear device. The test scheme for this device is a combination of both the anchor pull-out test and the borehole modulus test. The device is expanded into the walls of the borehole and is then pulled to determine the shear strength of the soil. Typically, several lateral pressures are investigated (Demartinecourt, 1985).



## Cone Penetration Test

The cone penetration test (CPT) is an invasive soil test that defines soil strata type, soil properties, and strength parameters. It is highly repeatable, insensitive to operators, and best suited for uncemented soils, sands, or clay. Although this test retrieves no sample for laboratory testing or visual inspection, it has the capability of producing enormous amounts of physical information based on correlations with side-by-side tests with other test methods such as SPT. Further, as the test provides direct measurements of ultimate end bearing and side shear, it is directly applicable for design of foundations of all kinds.

The CPT is described in ASTM test number D-3441, entitled "Standard Test Method for Deep, Quasi-Static, Cone and Friction-Cone Penetration Tests of Soil." This is to include cone penetration type tests that use mechanical or electronic load detection, tip or tip and friction stress delineation, and those tests where the penetration into the soil is slow and steady in a vertically aligned orientation. Those tests conducted with mechanical load detection are typically denoted as *Dutch Cone Tests* and those using electronic detection are simply called *Cone Penetration Tests*. The term "quasi-static" refers to a steady rate of penetration where the acceleration is zero, but the velocity of penetration is constant (1 - 2 cm/sec  $\pm$  25%).

The test apparatus consists of a 60 degree conical tip of known cross-sectional area that is thrust into the soil at a near constant rate. Behind the cone tip, a friction sleeve of known surface area is also included that is used to detect the side shear or adhesion between the steel sleeve and the surrounding soil. The force required to advance the tip through the soil is divided by the cross-sectional area to determine the tip stress,  $q_c$ . Similarly, the force required to advance the friction sleeve is divided by the sleeve surface area to produce the local friction value,  $f_s$ . The tip area and sleeve area vary from device to device but the most common areas are 10 cm<sup>2</sup> and 150 cm<sup>2</sup>, respectively.

The tip area (diameter) can influence the magnitude of the resulting  $q_c$  value similar to the effects of foundation diameter on capacity. This is due to the increased zone of influence beneath the tip as the cone diameter increases for various devices. Therefore, in relative uniform soils, the tip diameter has little effect. In layered or more heterogeneous strata, a smaller tip diameter will better register the minute changes in soil type and strength. Larger diameter cones physically average the effects of thin layers. Figure 14 shows two different-sized cone tip and sleeve assemblies.

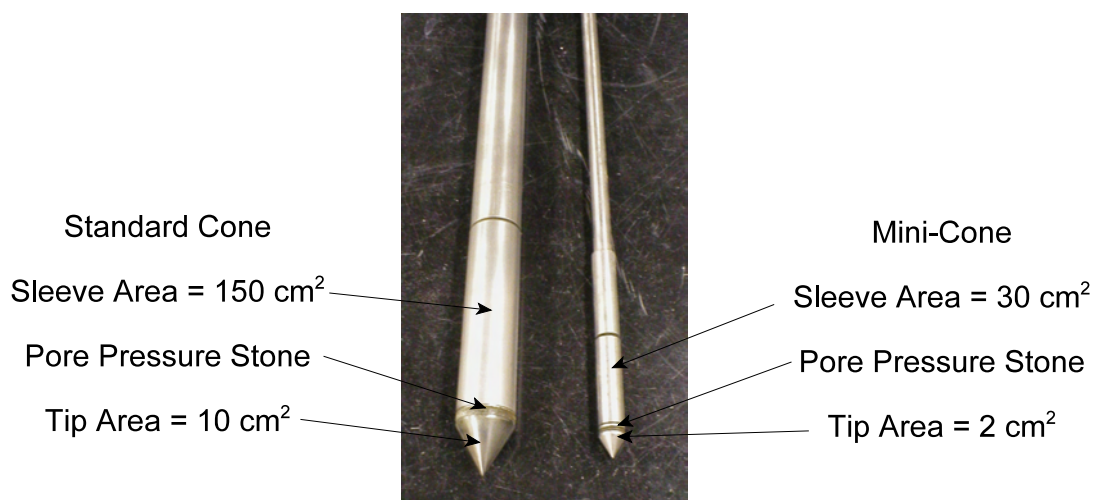


**Figure 14** Two cone tip and sleeve assemblies of different sizes.

Another feature that CPT equipment usually incorporate is the capability of monitoring the pore water pressure while advancing the cone/sleeve assembly. There can be a significant amount of excess pore pressure developed by forcing the volume of the cone into a somewhat fixed volume of a poorly draining material. In contrast, in dense fine-grained soils, the cavity expansion can cause a decrease pore pressure. The assemblies shown in Figure 14 have a pressure transducer within the tip body that registers the pore pressure directly behind the tip (between the tip and sleeve). This information can be used to convert the total stress registered by the tip to effective stress similar to a consolidated undrained triaxial compression test. When pore pressure measurements are taken the test is denoted as CPTU. Smaller cones tend to induce less cavity expansion and therefore less effects on total stress.

The thrust required to advance the cone assembly is dependent on the strength of the soil as well as the size of the tip. Given the disparity between the cone sizes in Figure 14, it is not surprising that the size of the equipment required to advance these cones is also disparate. Figure 15 shows the associated truck mounted CPT rigs that use these devices. The larger diameter cone requires a 20 ton thrust mechanism and can reach depths of 100 meters; the mini-cone requires about 1/5 the thrust and can be mounted on the front of a standard truck or utility vehicle. Mini-CPTs are limited to a practical maximum depth 20 meters.



**Figure 15** Standard 20 ton cone truck (left); 4 ton mini-cone vehicle (right).

The thrust mechanisms also vary between the two systems in Figure 15. The standard CPT system uses 1 meter segmental rods to advance the cone tip/sleeve assembly. The thrusting ram is designed to grip, thrust downward 1 meter, release and stroke upward 1 meter, re-grip and repeat. At a penetration rate of 2 cm / sec, the process progresses at an average advance rate of 1 cm / sec to account for the re-gripping. An average sounding to 30 meters should take on the order of 1.5 - 2 hours (in and out). A SPT to a similar depth could take multiple days. The mini-cone uses a more time efficient method of advancing the cone. It uses a contiguous length of mild stainless steel tubing (10 - 20 meters long) that is continuously feed at a constant rate without having to re-stroke and re-grip. Therein, the tubing is straightened from a large diameter coil as it is continuously gripped by side-by-side opposing chains specially designed to mate to the coil diameter. Figure 16 shows both thrust mechanisms.

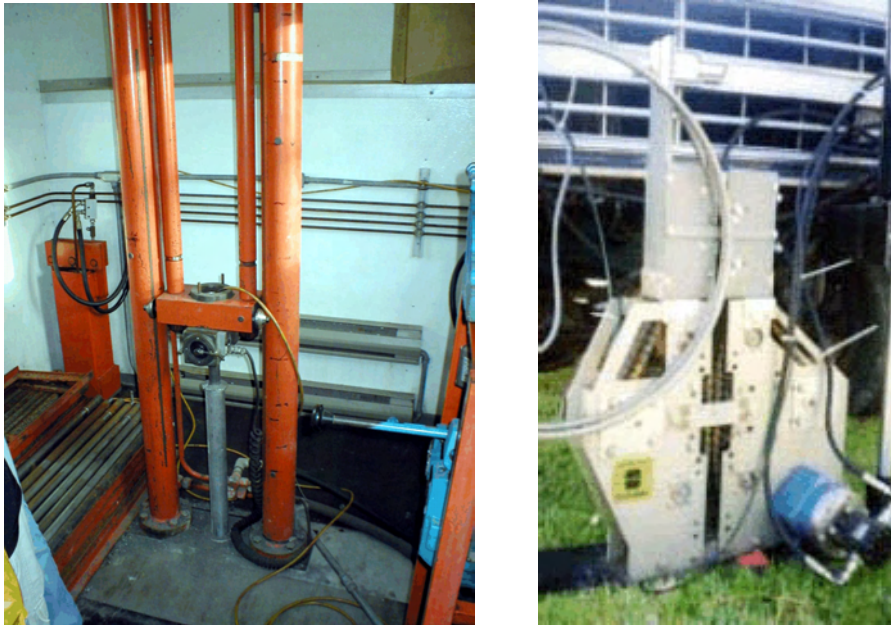


**Figure 16** Twin 10 ton rams used to thrust standard cone rod (left); continuous feed chain drive used to thrust mini cone (right).

The data collection during cone penetration testing is typically taken at 5 cm intervals but can be taken as frequent as permitted by the data acquisition system. This gives a virtually continuous sounding of tip and sleeve stresses. As both of these devices use strain gage based load cells, the instrumentation leads are routed through the center of the thrusting rod / tube. The data are processed to produce the soil type as well as other parameters in real time. The basis for the data regression is based on correlations developed by Robertson and Campanella, (1983). Although many correlations exist, the most significant uses a calculated parameter that defines the ratio of measured side to the measured tip stress. This ratio is defined as the friction ratio,  $R_f$ . To aid in classifying various soils, twelve soil types were defined that could be readily identified given the cone bearing stress,  $q_c$ , and the friction ratio,  $R_f$ . Figure 17 shows the classification chart used to identify soils from CPT data. Further, correlations from CPT to SPT test data were developed to elevate the comfort of designers more familiar with SPT data. Therein, the  $q_c/N$  ratio was defined for each of the twelve soil types (also shown in Figure CPT 7).

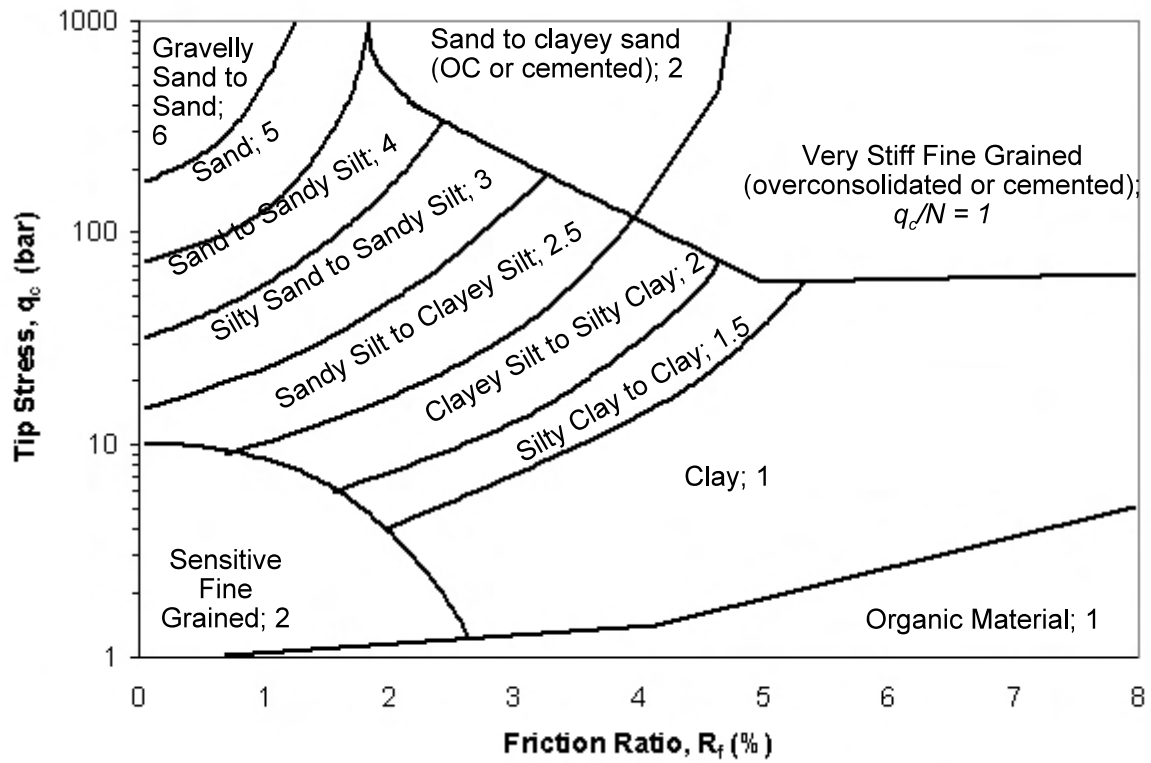


**Figure 17** CPT data correlated to soil type and equivalent SPT-N (after Robertson and Campanella, 1983).



## ***Quality Assurance Test Methods***

The construction of foundation is plagued with unknowns associated with the integrity of the as-built structure. This is particularly problematic with deep foundations that are installed without visual certainty of the actual conditions or configuration. This section will discuss several methods used to raise the confidence of the design with regards to concrete quality or capacity verification.

### **Shaft Inspection Device (SID)**

The inspection device is a visual inspection system for evaluating bottom cleanliness of drilled shaft excavations. A special video camera contained in a weighted, trapped-air bell housing is lowered into the shaft excavation prior to concreting to record the condition of the bottom. This is particularly helpful in slurry excavations where quality assurance is difficult to maintain. The bell housing is outfitted with gages in clear sight of the video camera that are capable of registering the thickness of accumulated debris or sediment at the shaft excavation. The system is capable of testing shafts with depths in excess of 200 feet. Several generations of this device exist that range in size from less than a foot in diameter to over 3 feet in diameter. The inspection is viewed in realtime on a color video monitor and recorded on a standard VHS tape. Voice annotations are recorded simultaneously during the inspection process similar to standard camcorders.



**Figure 18** Miniature shaft inspection device (Courtesy of Applied Foundation Testing, Inc.)

### **Crosshole Sonic Logging (CSL)**

Crosshole sonic logging is a geophysical test method used to determine the compression wave velocity between two parallel, water-filled tubes or slurry filled boreholes. By using two geophones (one emitting and one receiving) the sound wave arrival times can be logged at various depths within

the tubes. From this information the insitu properties of the materials between the tubes can be inferred thus identifying various strata. More recently, this test has become a non-destructive method for evaluating the quality of newly placed drilled shaft concrete. Therein, the arrival times are measured between logging tubes attached peripherally to the reinforcing cage allowing concrete quality between the tubes to be assessed. As only the concrete in a direct line between the tubes can be tested, multiple access tubes can be installed. Typically, one tube for every foot of diameter is required to satisfactorily survey a representative portion of the shaft concrete. Data is viewed in the field on a special data acquisition system.



**Figure 19** Cross-hole sonic logging of 4 ft diameter shaft  
(Courtesy of Applied Foundation Testing, Inc.).

### **Shaft Integrity Test (SIT) or Pile Integrity Test (PIT)**

The shaft/pile integrity test is an impact echo test that uses the reflections of anomalous cross sectional shaft or pile dimensions to determine the quality of a drilled shaft, auger-cast-in-situ or driven pile. The reflected sound waves from within the concrete are plotted as a function of arrival times which can then be correlated to the depth from which the reflection emanated. Figures SIT-1 and 2 shows the equipment used to conduct the test as well as the outputted results.

This test is well-suited for determining the depth of the foundation as well as the depth to anomalous features. However, it can not determine the magnitude of anomalous features, it requires access to the pile top to minimize confounding signals, and it is generally limited to depths on the order of 50 times the pile diameter.





**Figure 20** Equipment used for sonic echo test (left), impact hammer struck on shaft head (right).  
(Courtesy of Applied Foundation Testing, Inc.)

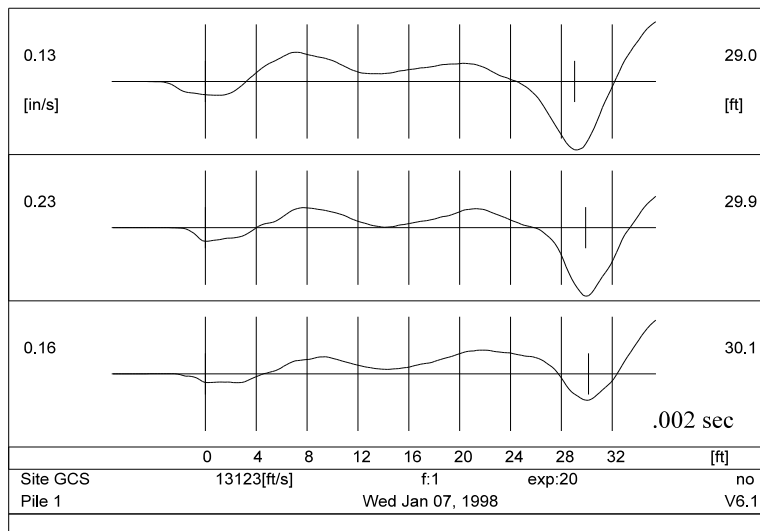


**Figure 21** Sonic echos from three consecutive hammer impacts.

### Pile Driving Analyzer (PDA)

During pile driving, the stresses and accelerations imparted to the pile can be monitored and recorded to assess the quality of the installation. Although this information is also used to ascertain the load carrying capability of the pile, the quality assurance associated with type of equipment is perhaps its greatest contribution. Therein, the tensile and compressive stresses in piles can be monitored via strain gage instrumentation to prevent unnecessary damage while adjusting pile driving hammer energy to maximize production rates. The movement is also monitored using integrated accelerometer data. Figure 22 shows the instrumentation and its position during pile driving.

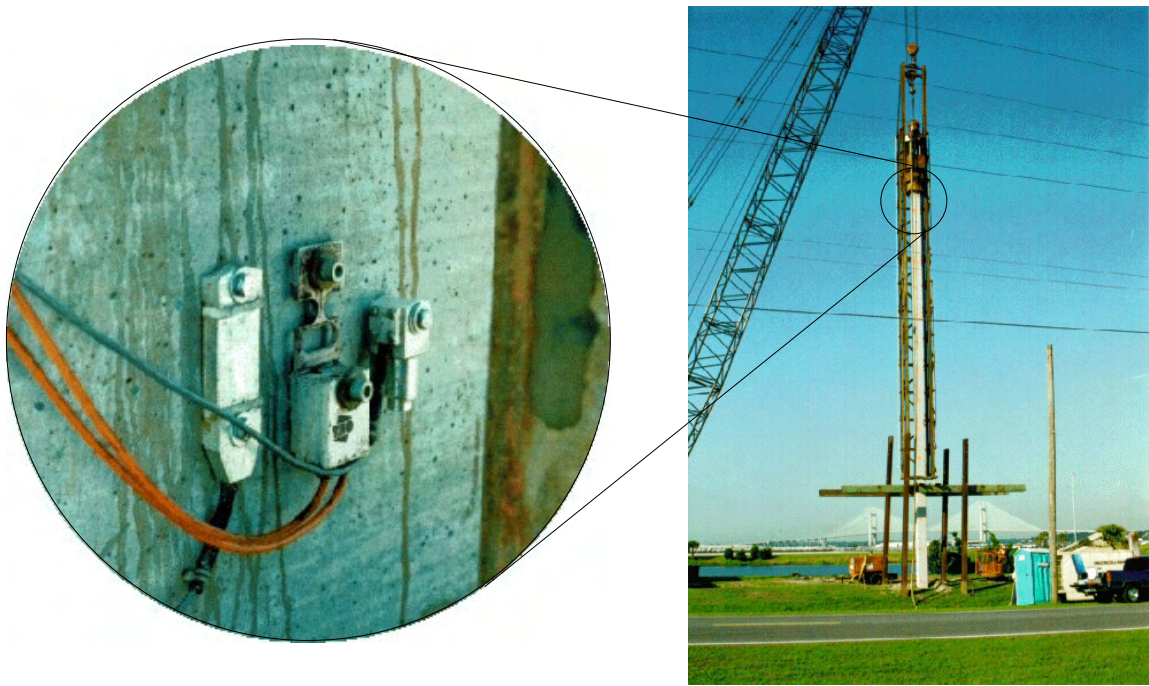


**Figure 22** Strain gages and accelerometers attached to pile during pile driving.  
(Courtesy of Applied Foundation Testing, Inc.)

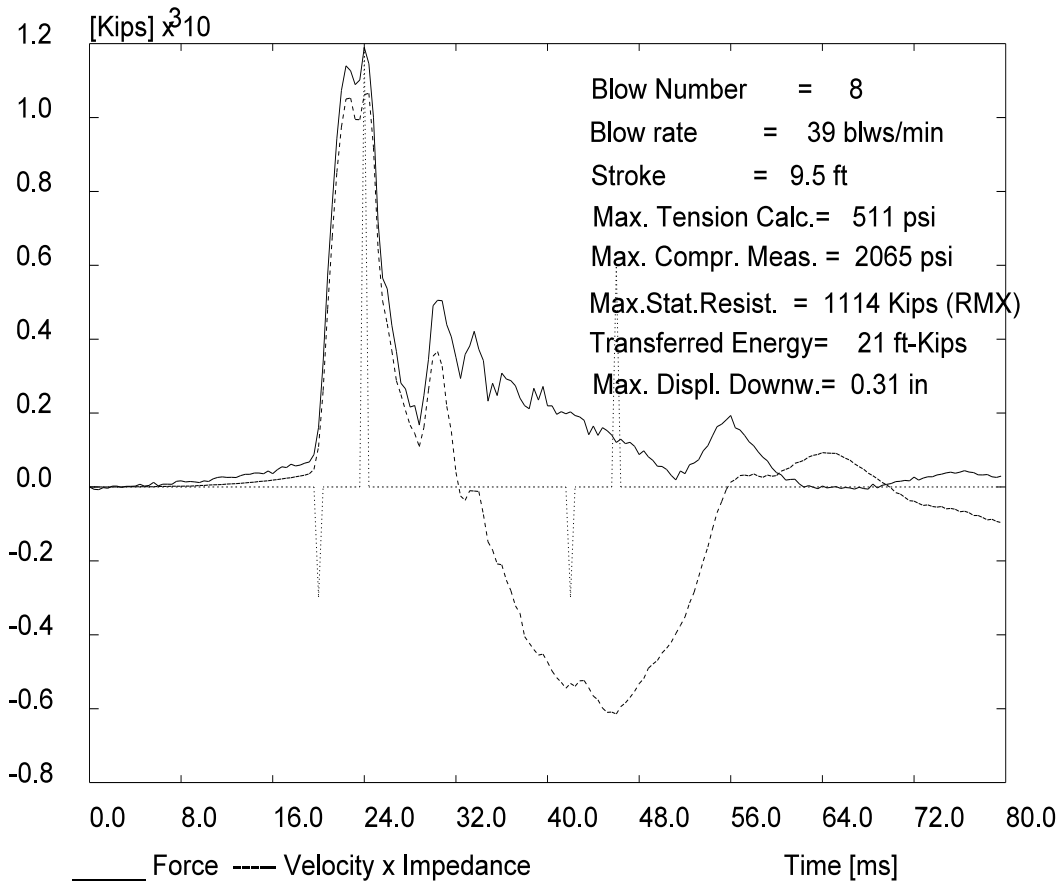


**Figure 23** Field data showing pile driving performance (Courtesy of Applied Foundation Testing, Inc.).

## Post Grout Test

The post grout test is a bi-product of an end bearing enhancement technique used during the construction of drilled shafts. This test is relatively simple in concept yet confirms the performance of every grouted shaft up to a lower limit of shaft capacity. During the process of tip grouting, the upward displacement, grout pressure, and grout volume are recorded. This information provides the design engineer the response of the shaft to loading. Therein, the side shear as well as the end bearing of the shaft are verified up to the level of the applied grout pressure. The product of the grout pressure and tip area produce the tip load; this preloading is afforded by an equivalent reaction from the side shear component. Therefore, the proven capacity of the shaft is established as twice the tip load. The upper limit of capacity can be shown to be on the order of 2 to 3 times the proven capacity when verified by downward load testing. The design of post grouted shafts is discussed in a later chapter. Figure PG1-2 show the standard field data obtained from every grouted shaft. Figure PG3 shows the performance for each of 76 shafts grouted on a bridge project in West Palm Beach, Florida.

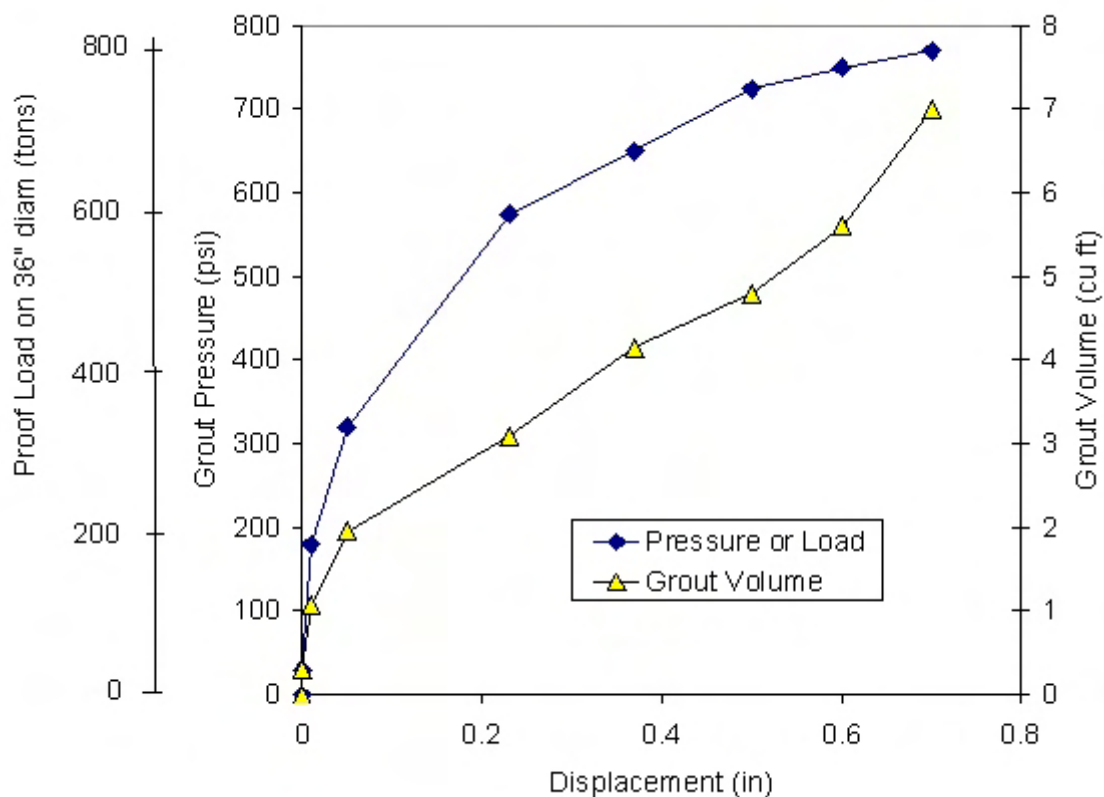


**Figure 24** Field data used to confirm shaft performance.

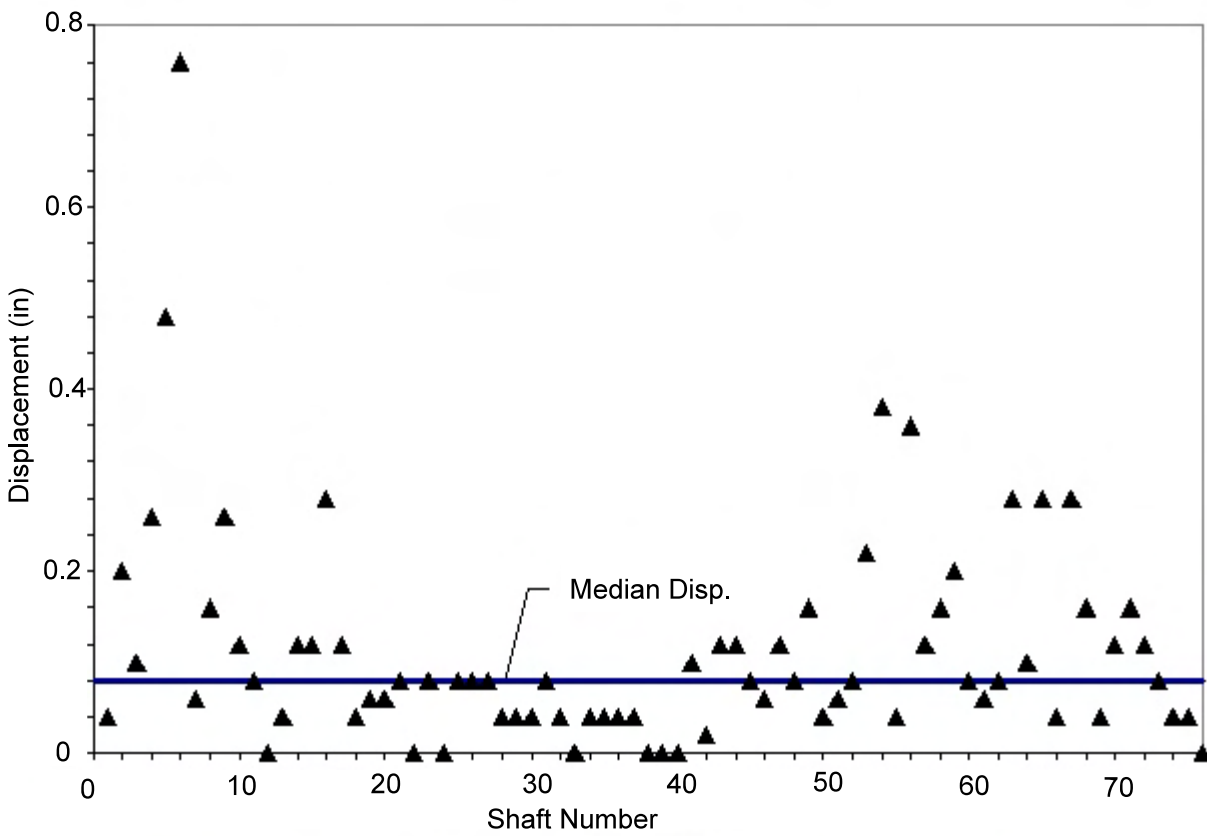


**Figure 25** The displacement observed for every shaft on a project at design pressure.

## ***Load Testing***

Load testing is considered to be the best measure of foundation suitability to resist anticipated design loads. These tests involve the application of a load capable of displacing the foundation and determining its capacity from its response. Various approaches have been devised to obtain this information. When comparing these approaches, they can be sorted from simplest to most complex in the following order: static load test, rapid load test, and the dynamic load test. These categories can be delineated by comparing the duration of the loading event with respect to the axial natural period of the foundation ( $2L/C$ ), where  $L$  represents the foundation length and  $C$  represents the strain wave velocity. Test durations longer than  $1000 L/C$  are considered static loadings and those shorter than  $10 L/C$  are considered dynamic (Janes et al., 2000; Kusakabe et.al, 2000). Tests with a duration between  $10L/C$  and  $1000 L/C$  are denoted as rapid load tests. The static and rapid load test will be discussed in this chapter. The dynamic load test is discussed in the pile driving and analysis chapter.

### **Static Load Test**

Static load testing encompasses all test methods that systematically apply an increasing load to a foundation in multiple loading increments at such a rate so as to produce no dynamic movements as stated above. These tests include many applications (i.e. deep foundations or shallow foundations, tension or compression loads) with numerous loading configurations. With regard to full-scale insitu load tests, several test procedures are most prominent: plate load test (ASTM D 1195), pile load test in compression (ASTM D 1143), pile load test in tension (ASTM D 3689), and the Osterberg load test.

**Kentledge Load Test.** The load from structures to the foundations can be compression (downward), tension (upward), or lateral (sideways). The downward load carrying resistance of a foundation encompasses most of the load conditions considered. In order to replicate these often enormous loads, several methodologies have been devised. The simplest form of a load test is the dead load or Kentledge method. This requires that the full test load be supplied in the form of dead weight stacked above the foundation on some framework. The framework must be capable of supporting the entire load at a single location where a hydraulic ram / jack can progressively transfer the load to the top of the foundation (Figure 26). This type of test accurately predicts the foundation response at full Kentledge load, but over estimates the stiffness of the foundation at lower loads due to the presence of the dead load overburden pressure applied to the ground surface. The practical upper limit of these tests is approximately 400 tons although physical site constraints may extend or restrict this limit drastically. Further, these tests are the most expensive and time consuming to perform from the standpoint of setup requirements. As with all static load tests, these tests are typically run in compliance with ASTM D-1143 or similar standard.

**Anchored Load Tests.** Static load tests with anchored reaction systems are the most common of the static load tests. These tests supply the full load to the foundation via a series of tension anchors (or adjacent deep foundations) in conjunction with a beam or truss (Figure 27). The beam must resist the load applied to the foundation by transferring it the reaction anchors which are preferably no closer than 5 diameters of the foundation (center to center spacing). The reaction anchors must not displace significantly while developing the required load. Excessive upward movement from these anchors can alter the stress field surrounding the foundation being tested and decrease the resultant



ultimate capacity. Due to the constraints in designing such a reaction system, rarely does an anchored static load test exceed 1500 tons. However, anchored tests as large as 3500 tons are commonplace in some parts of the world.

The analysis of static load testing requires no more than plotting the load versus displacement response. As every foundation application can have a unique failure criteria, the design engineer must decide at what displacement the foundation capacity should be determined. In some instances this is based on a given fraction of ultimate load. In other cases, it may be based upon the some displacement offset method such as the Davisson Method or the FHWA method. With LRFD-type approaches, a fraction of the ultimate capacity is compared to the factored design load in a strength limit state, and displacement is considered separately in a service limit state. Figure 28 shows typical static load test results and three common approaches to determining capacity (a) a maximum permissible displacement usually set by structural sensitivity, (b) displacement offset method, and (c) the load at which additional displacement is obtained without increase in load.



**Figure 26** Kentledge load test setup; 400 ton (Courtesy of Bermingham Construction, Ltd).





**Figure 27** Static load test using 8, H-type reaction piles; 1200 ton.

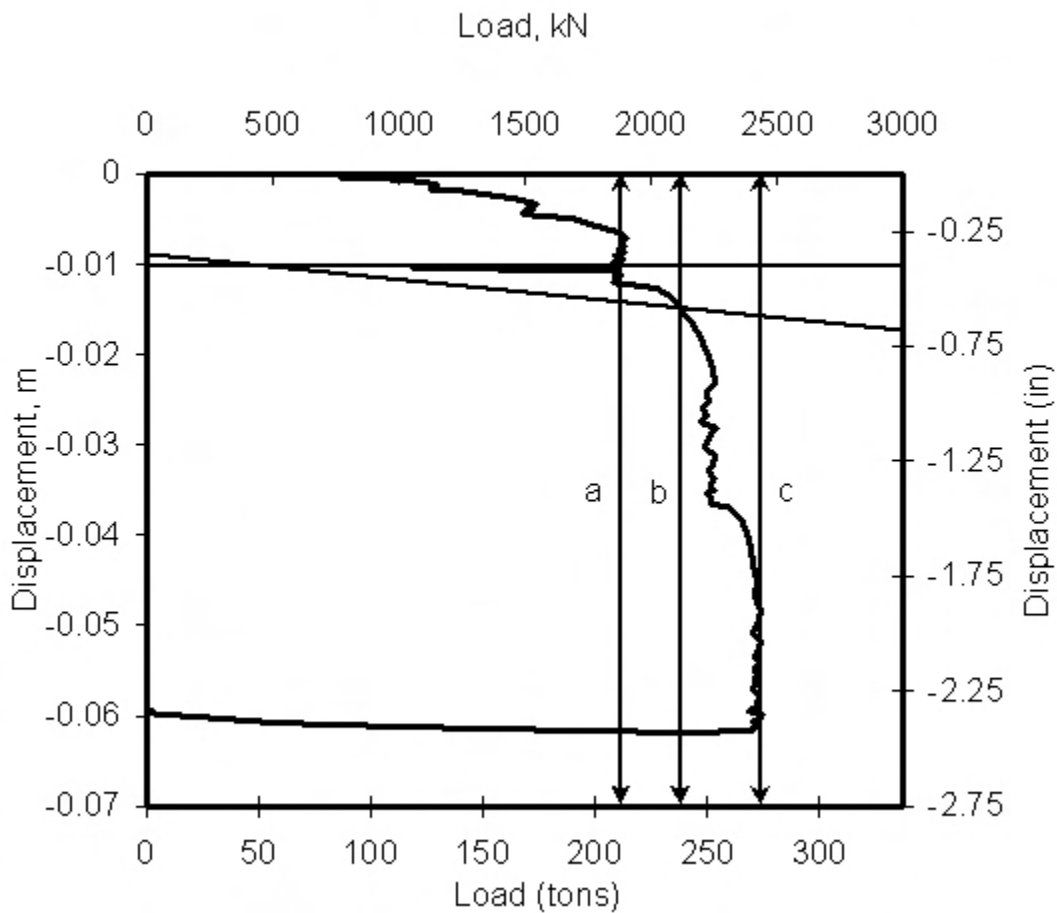


**Figure 28** Static load test results showing 3 different failure criteria capacities (a) a 10mm permissible disp, (b) offset method, and (c) ultimate capacity.

**Bidirectional Static Load Test.** The Osterberg Cell (O-cell<sup>®</sup>) Test provides a simple, efficient and economical method of performing a static load test on a deep foundation. The O-cell is a sacrificial jack which the Engineer installs at the bottom of a pile or drilled shaft. It provides a static load and requires no overhead load frame or other external reaction system (Figure 29). The O-cell is easily installed in drilled shafts using common construction equipment and is attached to the tip of a driven pile before driving.

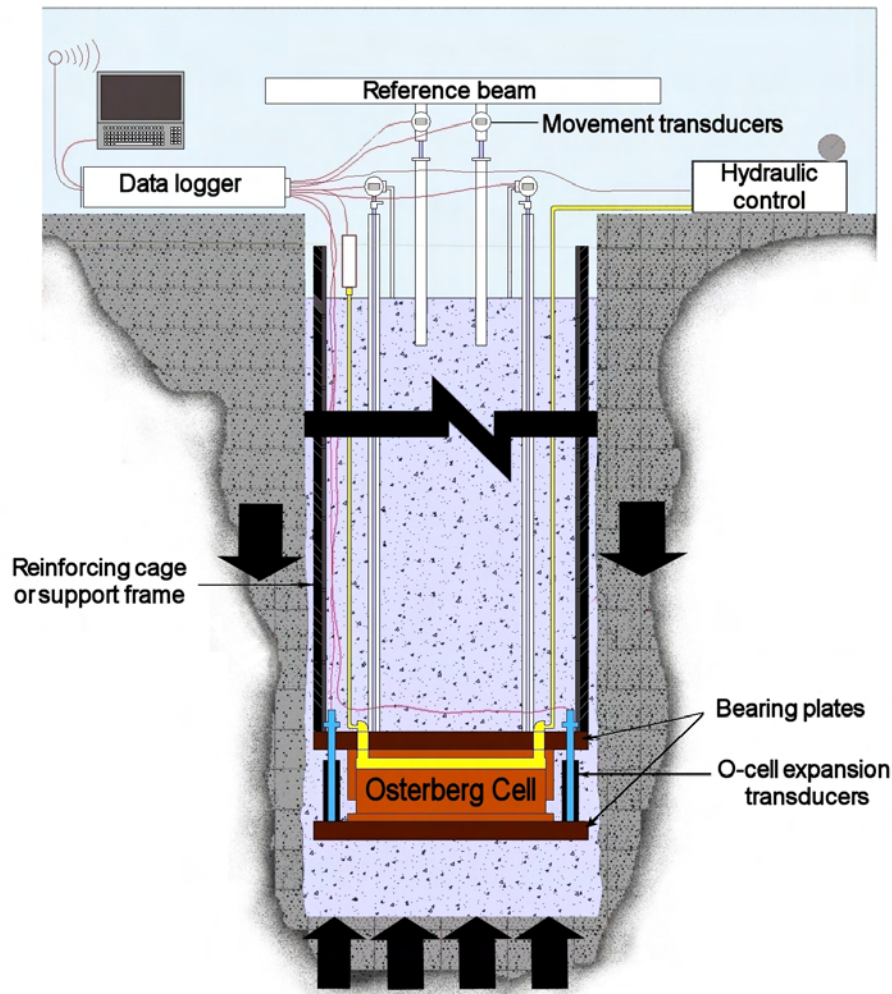


**Figure 29** Section view of the bidirectional loading scheme of an O Cell  
(Courtesy of LoadTest, Inc).

Installation methods on a drilled shaft can vary, but the following procedures are typical. An O-cell or O-cells are attached to a top and bottom steel plate, which is then placed near or at the bottom of a shaft as part of the reinforcing cage or carrying frame (Figure 30). Strain gage instruments are also attached to the assembly and all wires are channeled to the surface via the cage or beam. The complete assembly is then lifted and set into the open shaft prior to the concreting process. In the case of multi-level O-cell assemblies, or placement of the O-cell off the bottom of the shaft, a tremie pipe is fed through a prefabricated hole in the steel plates to ensure proper cementation below the O-cells.



**Figure 30** O Cell and cage lifted for installation  
(Courtesy of LoadTest, Inc.).

Once the concrete has reached required strength the O-cell is pressurized. The O-cell uses the soil system for reaction, eliminating the need for overhead or external reaction systems. The O-cell is expanded until the expansion force is some desired proof multiple of the design loading, or one of the two components, side friction or end bearing, reaches some defined failure condition, or the cell reaches its maximum expansion.

Depending on the shaft diameter, O-cells can be grouped together on a single plane to increase the effective load. Testing is typically performed following the ASTM Quick Test Method D1143 (ASTM, 1993). Instrumentation used to measure load and deflection is similar to instrumentation used for conventional load tests. At the completion of the test the cell can be filled with grout to reestablish its integrity and permit the test shaft or pile to become a production shaft or pile.

The O-cell loads the test pile in compression similar to a conventional static load test. Data from an O-cell test is therefore analyzed much the same way as conventional static test data. The only significant difference is that the O-cell provides two load-versus-movement curves, one for shaft

resistance and one for toe resistance (Figure 31). The failure load for each component may be determined from these curves using a failure criteria similar to that recommended for conventional load tests. To determine the shaft resistance capacity, the buoyant weight of the pile should be subtracted from the upward O-cell load. Analysis for the toe resistance should not include elastic deformation since the load is applied directly.

The engineer may further utilize the component curves to construct an equivalent pile head load-deflection curve and investigate the overall pile capacity. If the pile is then assumed rigid, the pile head and toe move together and have the same deflection at this load. By adding the shaft resistance to the mobilized toe resistance at the chosen deflection, a single point on the equivalent pile head load curve is determined. Additional points may then be calculated to develop the curve up to the maximum deflection (or maximum extrapolated deflection) of the component that did not fail. Points beyond the maximum deflection of the non-failing component may also be obtained by conservatively assuming that at greater deflections it remains constant at the maximum applied load.

An O-cell test can be performed on types of shafts and piles, including; pre-cast, open-ended pipe piles, mandrel driven piles, and has been used on large diameter drilled shafts. O-cells can be used to test deep foundations over water or confined areas because the O-cell test does not require an overhead reaction system. An O-cell test may be applied in many situations due to the systems flexibility, e.g. placement of the O-cell within the shaft may be altered, or additional layers of O-cells may be used to isolate significant soil zones.

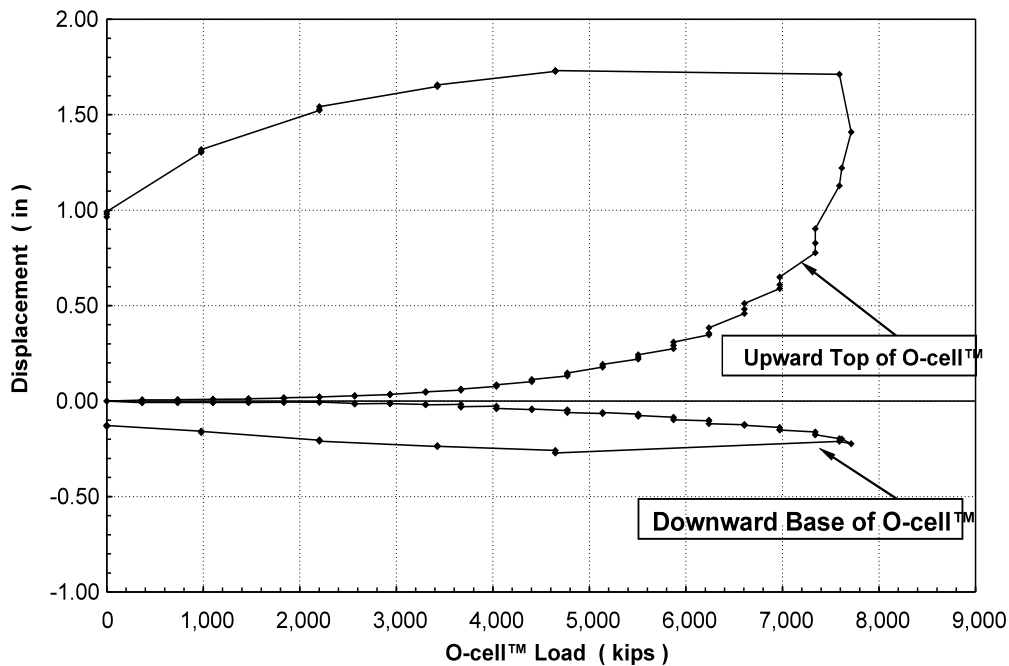


**Figure 31** Typical output showing upward and downward foundation response.  
(Courtesy of Load Test, Inc.)



## Rapid Load Test

Since its inception in 1988, the inertia loading technology called Statnamic testing has gained popularity with many designers largely due to its time efficiency, cost effectiveness, data quality, and flexibility in testing existing foundations. Where large capacity static tests may take up to a week to set up and conduct, the largest of Statnamic tests (3500 tons) typically takes no more than a few days. Further, multiple smaller-capacity tests (up to 2000 tons) can easily be completed within a day. The direct benefit of this time efficiency is the cost savings to the client and the ability to conduct more tests within a given budget. Additionally, this test method has boosted quality assurance by giving the contractor the ability to test foundations thought to have been compromised by construction difficulties without significantly affecting production and without requiring previous planning for its testing.

Statnamic testing is designated as a rapid load test that uses the inertia of a relatively small reaction mass instead of a reaction structure to produce large forces. The duration of the Statnamic test is typically 100 to 120 milliseconds, but is dependant on the ratio of the applied force to the weight of the reaction mass. Longer duration tests of up to 500 milliseconds are possible but require more reaction mass.

The Statnamic force is produced by quickly-formed high pressure gases that in turn launch a reaction mass upward at up to twenty times the acceleration of gravity. The equal and opposite force exerted on the foundation is simply the product of the mass and acceleration of the reaction mass. It should be noted that the acceleration of the reaction mass is not significant in the analysis of the foundation; it is simply a by-product of the test. Secondly, the load produced is not an impact in that the mass is in contact prior to the test. Further, the test is over long before the masses reach the top of their flight. The parameters of interest are only those associated with the movement of the foundation (i.e. force, displacement, and acceleration). Figure 32 shows the setup for both an axial compression and lateral statnamic test setup.



**Figure 32** Axial statnamic test setup (left), lateral statnamic test in progress (right).

**Analysis Procedures.** Typical analysis of Statnamic data relies on measured values of force, displacement and acceleration. A soil model is not required, hence, the results are not highly user dependent. The Statnamic forcing event induces foundation motion in a relatively short period of time and hence acceleration and velocities will be present. The accelerations are typically small(1-2 g's), however the enormous mass of the foundation when accelerated resists movement due to inertia and as such the fundamental equation of motion applies, Equation 1.

$$F = ma + cv + kx \quad (1)$$

where, F = forcing event  
m = mass of the foundation  
a = acceleration of the displacing body  
v = velocity of the displacing body  
c = viscous damping coefficient  
k = spring constant of the displacing system  
x = displacement of the body

The equation of motion is generally described using four terms: forcing, inertial, viscous damping, and stiffness. The forcing term ( $F$ ) denotes the load application which varies with time and is equated to the sum of remaining three terms. The inertial term ( $ma$ ) is the force which is generated from the tendency of a body to resist motion, or to keep moving once it is set in motion (Young, 1992). The viscous damping term ( $cv$ ) is best described as the velocity dependant resistance to movement. The final term ( $kx$ ), represents the classic system stiffness, which is the static soil resistance.

When this equation is applied to a pile/soil system the terms can be redefined to more accurately describe the system. This is done by including both measured and calculated terms. The revised equation is displayed below:

$$F_{Statnamic} = (ma)_{Foundation} + (cv)_{Foundation} + F_{Static} \quad (2)$$

where,  $F_{Statnamic}$  is the measured Statnamic force,  $m$  is the calculated mass of the foundation,  $a$  is the measured acceleration of the foundation,  $c$  is the viscous damping coefficient,  $v$  is the calculated velocity, and  $F_{static}$  is the derived pile/soil static response.

There are two unknowns in the revised equation  $F_{static}$  and  $c$ , thus the equation is under specified.  $F_{static}$  is the desired value, so the variable  $c$  must be obtained to solve the equation. Middendorp (1992) presented a method to calculate the damping coefficient referred to as the Unloading Point Method (UP). With the value of  $c$  known, the static force can be calculated. This force, termed "Derived Static," represents an equivalent soil response similar to that produced by a traditional static load test.

**Unloading Point Method.** The UP is a simple method by which the damping coefficient can be determined from the measured Statnamic data. It uses a simple single degree of freedom model to represent the foundation/soil system as a rigid body supported by a non-linear spring and a linear dashpot in parallel (see Figure 32). The spring represents the static soil response ( $F_{Static}$ )



which includes the elastic response of the foundation as well as the foundation/soil interface and surrounding soil response. The dashpot is used to represent the dynamic resistance which depends on the rate of pile penetration (Nishimura, 1995).

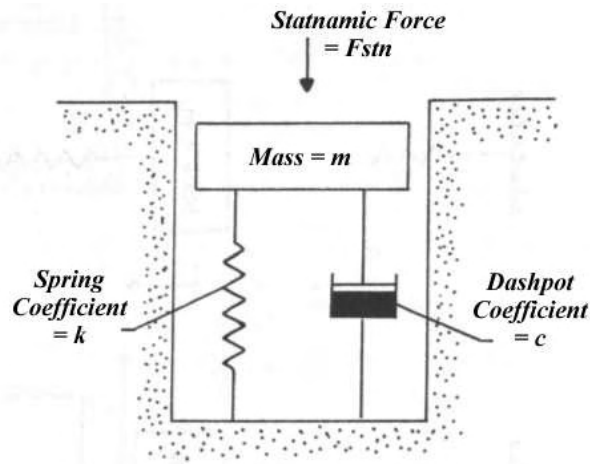


**Figure 33** Single D.O.F. Model

The UP makes two primary assumptions in its determination of “c.” The first is the static capacity of the pile is constant when it plunges as a rigid body. The second is that the damping coefficient is constant throughout the test. By doing so a time window is defined in which to calculate the damping coefficient as shown in Figure 33. This figure shows a typical Statnamic load-displacement curve which denotes points (1) and (2).

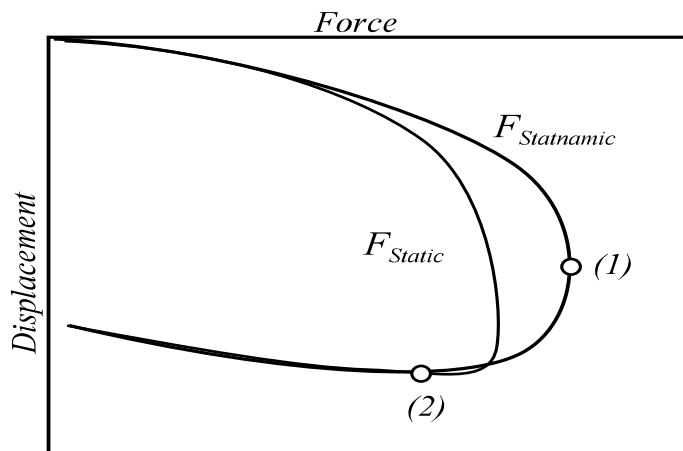


**Figure 34** UP time window for  $c$  determination.

The first point of interest (1) is that of maximum Statnamic Force. At this point the static resistance is assumed to have become steady state, for the purpose of calculating “c”. Thus, any extra resistance is attributed to that of the dynamic forces ( $ma$  and  $cv$ ). The next point of interest (2) is that of zero velocity which has been termed the “Unloading Point.” At this point the

foundation is no longer moving and the resistance due to damping is zero. The static resistance, used to calculate "c" from point (1) to (2), can then be calculated by the following equation:

$$F_{Static_{UP}} = F_{Statnamic} - (ma)_{Foundation} \quad (3)$$

Where,  $F_{Statnamic}$ ,  $m$ , and  $a$  are all known parameters;  $F_{Static_{UP}}$  is the static force calculated at (2) and assumed constant from (1) to (2).

Next, the damping coefficient can be calculated throughout this range, from maximum force (1) to zero velocity (2). The following equation is used to calculate  $c$ :

$$c = \frac{F_{Statnamic} - F_{Static_{UP}} - (ma)_{Foundation}}{v_{Foundation}} \quad (4)$$

Damping values over this range should be fairly constant. Often the average value is taken as the damping constant, but if a constant value occurs over a long period of time it should be used (see Figure 34).

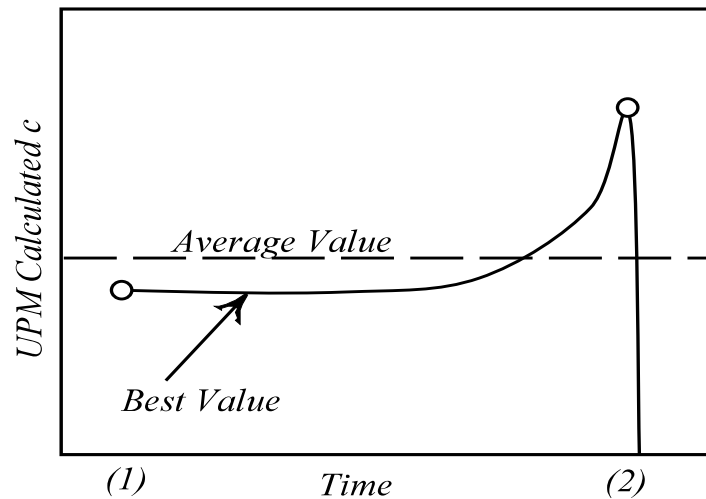


**Figure 35** Variation in  $c$  between times (1) and (2).

Note that as  $v$  approaches zero at point (2), values of  $c$  can be different from that of the most representative value and therefore the entire trend should be reviewed. Finally the derived static response can be calculated as follows:

$$F_{Static} = F_{Statnamic} - (ma)_{Foundation} - (cv)_{Foundation} \quad (5)$$

Currently software is available to the public that can be used in conjunction with Statnamic test data to calculate the derived static pile capacity using the UP Method (Garbin, 1999). This software was developed by the University of South Florida and the Federal Highway

Administration and can be downloaded from [www.eng.usf.edu/~gmullins](http://www.eng.usf.edu/~gmullins) under the Statnamic Analysis Workbook (SAW™) heading.

The UP has proven to be a valuable tool in predicting damping values when the foundation acts as a rigid body. However, as the pile length increases an appreciable delay can be introduced between the movement of the pile top and toe, hence negating the rigid body assumption. This occurrence also becomes prevalent when an end bearing condition exists; in this case the lower portion of the foundation is prevented from moving jointly with the top of the foundation.

Middendorp (1995) defines the "Wave Number" ( $N_w$ ) to quantify the applicability of the UP. The wave number is calculated by dividing the wave length (D) by the foundation depth (L). D is obtained by multiplying the wave speed c in length per second by the load duration (T) in seconds. Thus, the wave number is calculated by the following equation:

$$N_w = \frac{D}{L} = \frac{cT}{L} \quad (6)$$

Through empirical studies Middendorp determined that the UP would predict accurately the static capacity from Statnamic data, if the wave number was greater than 12. Nishimura (1995) established a similar threshold at a wave number of 10. Using wave speeds of 5000 m/s and 4000 m/s for steel and concrete respectively and a typical Statnamic load duration, the UP is limited to piles shorter than 50 m (steel) and 40 m (concrete). Wave number analysis can be used to determine if stress waves will develop in the pile. However, this does not necessarily satisfy the rigid body requirement of the UP.

Statnamic tests cannot always produce wave numbers greater than 10, and as such there have been several methods suggested to accommodate stress wave phenomena in Statnamicly tested long piles (Middendorp, 1995). Due to limitations on paper length these methods are not presented.

**Modified Unloading Point Method.** Given the limitations of the UP, users of Statnamic testing have developed a remedy for the problematic condition that arises most commonly. The scenario involves relatively short piles ( $N_w > 10$ ) that do not exhibit rigid body motion, but rather elastically shorten within the same magnitude as the permanent set. This is typical of rock-socketed drilled shafts or piles driven to dense bearing strata that are not fully mobilized during testing. The consequence is that the top of pile response (i.e. acceleration, velocity, and displacement) is significantly different from that of the toe. The most drastic subset of these test results show zero movement at the toe while the top of pile elastically displaces in excess of the surficial yield limit (e.g. upwards of 25 mm). Whereas with plunging piles (rigid body motion) the difference in movement (top to toe) is minimal and the average acceleration is essentially the same as the top of pile acceleration; tip restrained piles will exhibit an inertial term that is twice as large when using top of pile movement measurements to represent the entire pile.

The Modified Unloading Point Method (MUP), developed by Justason (1997), makes use of an additional toe accelerometer that measures the toe response. The entire pile is still assumed to be a single mass, m, but the acceleration of the mass is now defined by the average of the top and toe movements. A standard UP is then conducted using the applied top of pile Statnamic force and

the average accelerations and velocities. The derived static force is then plotted versus the top of pile displacement as before. This simple extension of the UP has successfully overcome most problematic data sets. Plunging piles instrumented with both top and toe accelerometers have shown little analytical difference between the UP and the MUP. However, MUP analyses are now recommended whenever both top and toe information is available.

Although the MUP provided a more refined approach to some of the problems associated with UP conditions, there still exists a scenario where it is difficult to interpret Statnamic data with present methods. This is when the wave number is less than ten (relatively long piles). In these cases the pile may still only experience compression (no tension waves) but the delay between top and toe movements causes a phase lag. Hence an average of top and toe movements does not adequately represent the pile.

**SUP Method.** The fundamental concept of the Segmental Unloading Point (SUP) method is that the acceleration, velocity, displacement, and force from each segment of a pile can be determined using strain gage measurements along the length of the pile (Mullins, et al., 2002). Individual pile segment displacements are determined using the relative displacement as calculated from strain gage measurements and an upper or lower measured displacement. The velocity and acceleration of each segment are then determined by numerically differentiating displacement then velocity with respect to time. The segmental forces are determined by calculating the difference in force from two strain gage levels.

Typically the maximum number of segments is dependent on the available number of strain gage layers. However, strain gage placement does not necessitate assignment of segmental boundaries; as long as the wave number of a given segment is greater than 10, the segment can include several strain gage levels within its boundaries. The number and the elevation of strain gage levels are usually determined based on soil stratification; as such, it can be useful to conduct an individual segmental analysis to produce the shear strength parameters for each soil strata. A reasonable upper limit on the number of segments should be adopted because of the large number of mathematical computations required to complete each analysis. Figure 36 is a sketch of the SUP pile discretization.

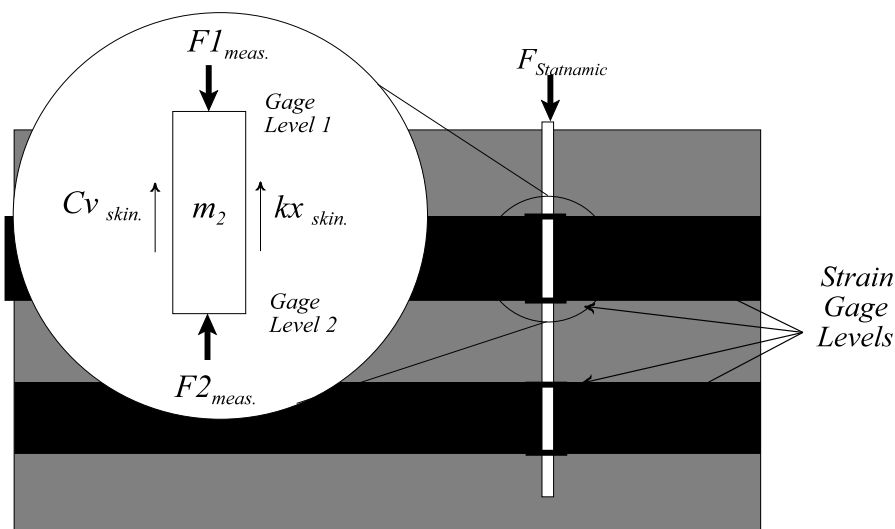


**Figure 36** Segmental Free Body Diagram

The notation used for the general SUP case defines the pile as having  $m$  levels of strain gages and  $m+1$  segments. Strain gage locations are labeled using positive integers starting from 1 and continuing through  $m$ . The first gage level below the top of the foundation is denoted as  $GL^1$  where the superscript defines the gage level. Although there are no strain gages at the top of foundation, this elevation is denoted as  $GL^0$ . Segments are numbered using positive integers from 1 to  $m+1$ , where segment 1 is bounded by the top of foundation ( $GL^0$ ) and  $GL^1$ . Any general segment is denoted as segment  $n$  and lies between  $GL^{n-1}$  and  $GL^n$ . Finally, the bottom segment is denoted as segment  $m+1$  and lies between  $GL^m$  and the foundation toe.

**Calculation Of Segmental Motion Parameters.** The SUP analysis defines average acceleration, velocity, and displacement traces that are specific to each segment. In doing so, strain measurements from the top and bottom of each segment and a boundary displacement are required. Boundary displacement may come from the Statnamic laser reference system (top), top of pile acceleration data, or from embedded toe accelerometer data.

The displacement is calculated at each gage level using the change in recorded strain with respect to an initial time zero using Equation 7. Because a linearly-varying strain distribution is assumed between gage levels, the average strain is used to calculate the elastic shortening in each segment.

Level displacements

$$x_n = x_{n-1} - \Delta\epsilon_{\text{average seg } n} L_{\text{seg } n} \quad (7)$$

where

$$\begin{aligned} x_n &= \text{the displacement at the } n\text{th gage level} \\ \Delta\epsilon_{\text{average seg } n} &= \text{the average change in strain in segment } n \\ L_{\text{seg } n} &= \text{the length of the } n\text{th segment} \end{aligned}$$

To perform an unloading point analysis, only the top-of-segment motion needs to be defined. However, the MUP analysis, which is now recommended, requires both top and bottom parameters. The SUP lends itself naturally to providing this information. Therefore, the average segment movement is used rather than the top-of-segment; hence, the SUP actually performs multiple MUP analyses rather than standard UP. The segmental displacement is then determined using the average of the gage level displacements from each end of the segment as shown in the following equation:

$$x_{\text{seg } n} = \frac{x_{n-1} + x_n}{2} \quad (8)$$

where  $x_{\text{seg } n}$  is the average displacement consistent with that of the segment centroid.

The velocity and acceleration, as required for MUP, are then determined from the average displacement trace through numerical differentiation using Equations 9 and 10, respectively:

$$v_n = \frac{x_{n_t} - x_{n_{t+1}}}{\Delta t} \quad (9)$$

$$a_n = \frac{v_{n_t} - v_{n_{t+1}}}{\Delta t} \quad (10)$$

where  $v_n$  = the velocity of segment  $n$   
 $a_n$  = the acceleration of segment  $n$   
 $\Delta t$  = the time step from time  $t$  to  $t+1$

It should be noted that all measured values of laser displacement, strain, and force are time dependent parameters that are field recorded using high speed data acquisition computers. Hence the time step,  $\Delta t$ , used to calculate velocity and acceleration is a uniform value that can be as small as 0.0002 seconds. Therefore, some consideration should be given when selecting the time step to be used for numerical differentiation.

The average motion parameters ( $x$ ,  $v$ , and  $a$ ) for segment  $m+1$  can not be ascertained from measured data, but the displacement at  $GL^m$  can be differentiated directly providing the velocity and acceleration. Therefore, the toe segment is evaluated using the standard UP. These segments typically are extremely short (1 - 2 m) producing little to no differential movement along its length.

**Segmental Statnamic and Derived Static Forces.** Each segment in the shaft is subjected to a forcing event which causes movement and reaction forces. This segmental force is calculated by subtracting the force at the top of the segment from the force at the bottom. The difference is due to side friction, inertia, and damping for all segments except the bottom segment. This segment has only one forcing function from  $GL^m$  and the side friction is coupled with the tip bearing component. The force on segment  $n$  is defined as:

$$S_n = A_{(n-1)} E_{(n-1)} \epsilon_{(n-1)} - A_n E_n \epsilon_n \quad (11)$$

where  $S_n$  = the applied segment force from strain measurements  
 $E_n$  = the composite elastic modulus at level  $n$   
 $A_n$  = the cross sectional area at level  $n$   
 $\epsilon_n$  = the measured strain at level  $n$

Once the motion and forces are defined along the length of the pile, an unloading point analysis on each segment is conducted. The segment force defined above is now used in place of the Statnamic force in Equation 2. Equation 12 redefines the fundamental equation of motion for a segment analysis:

$$S_n = m_n a_n + c_n v_n + S_n^{Static} \quad (12)$$

where,  $S_n^{Static}$  = the derive static response of segment  $n$   
 $m_n$  = the calculated mass of segment  $n$   
 $c_n$  = the damping constant of segment  $n$

The damping constant (in Equation 13) and the derived static response (Equation 14) of the segment are computed consistent with standard UP analyses:

$$c_n = \frac{S_n - S_n^{Static}}{v_n} \quad (13)$$



$$S_{n \text{ Static}} = S_n - m_n a_n - c_n v_n \quad (14)$$

Finally the top-of-foundation derived static response can be calculated by summing the derived static response of the individual segments as displayed in the following equation:

$$F_{\text{Static}} = \sum_{n=1}^{m+1} S_{n \text{ Static}} \quad (15)$$

Software capable of performing SUP analyses (SUPERSAW™) has been developed at the University of South Florida in cooperation with the Federal Highway Administration (Winters, 2002). It can be downloaded from [www.eng.usf.edu/~gmullins](http://www.eng.usf.edu/~gmullins) under the Statnamic Analysis Software heading.

## ***General References***

ASTM, 1998, "Soil and Rock," *Annual Book of ASTM Standards*, Volume 4.08, West Conshohocken, PA.

Bloomquist, David and Townsend, Frank C., 1991, Development of Insitu Equipment for Capacity Determinations of Deep Foundations in Florida Limestone," Florida Department of Transportation Funded Research, Project #23385-001, March.

Birmingham, P., and White, J., (1995), "Pyrotechnics and the Accurate of Prediction of Statnamic Peak Loading and Fuel Charge Size", First International Statnamic Seminar, 1995, Vancouver, British Columbia Canada

Dapp, S., and Mullins, G., (2002). "Pressure-Grouting Drilled Shaft Tips: Full-Scale Research Investigation for Silty and Shelly Sands," *Deep Foundations 2002: An International Perspective on Theory, Design, Construction, and Performance*, ASCE Geo Institute, GSP No.116, Vol. I, pp. 335-350.

FDOT, 1999, *Soils and Foundations Manual*, State Materials Office, Gainesville, FL.

FHWA, 1993, *Soils and Foundations, Workshop Manual - Second Edition*, FHWA HI-88-009, National Highway Institute, NHI Course No. 13212, Revised July.

Garbin, E. J., (1999), "Data Interpretation for Axial Statnamic Testing and the Development of the Statnamic Analysis Workbook," Master's Thesis, University of South Florida, Tampa, FL.

Goodman, Richard E., 1989, "Rock Mechanics," 2<sup>nd</sup> ed., John Wiley and Sons, New York.

Janes, M.C., Justason, M.D., Brown, D.A., (2000), "Long period dynamic load testing ASTM standard draft," *Proceedings of the Second International Statnamic Seminar*, Tokyo, October, 1998, pp. 199-218.

Justason, M.D., (1997), "Report of Load Testing at the Taipei Municipal Incinerator Expansion Project," Taipei City, Taipei.

Kulhawy, F. H. and Mayne, P. W., (1990), " manual on Estimating Soil Properties for Foundation Design," EPRI EL - 6800 Research Project 1493-6, Electric Power Research Institute, August.

Kusakabe, Kuwabara, and Matsumoto (eds), (2000), "Statnamic Load Test," Draft of 'method for rapid load test of single piles (JGS 1815-2000),' *Proceedings of the Second International Statnamic Seminar*, Tokyo, October 1998 pp. 237-242.

Lai, P.W., 1999, "Determination of Design Skin Friction for Drilled Shafts Socketed in the Florida Limestone," *Soils and Foundations Manual*, State Materials Office, Gainesville, FL.

Lewis, C.L., (1999), "Analysis of Axial Statnamic Testing by the Segmental Unloading Point

Method," Master's Thesis, University of South Florida, Tampa, FL.

McVay, M.C., Townsend, F.C., and Williams, R.C., 1992, "Design of Socketed Drilled Shafts in Limestone," *Journal of Geotechnical Engineering*, Vol. 118, No 10, October.

Middendorp, P. and Bielefeld, M.W., (1995), "Statnamic Load Testing and the Influence of Stress Wave Phenomena," *Proceedings of the First International Statnamic Seminar*, Vancouver, Canada, pp. 207-220.

Middendorp, P., Bermingham, P., and Kuiper, B. , (1992), "Statnamic Load Testing Of Foundation Pile." Proceedings, 4<sup>th</sup> International Conference On Application Of Stress-Wave Theory To Piles, The Hague, pp. 581-588.

Mullins, G., Dapp, S., and Lai, P., (2000). "Pressure Grouting Drilled Shaft Tips in Sand". *New Technological and Design Developments in Deep Foundations*, Dennis, N. D., et al. (ed.), ASCE, Geo Institute, Vol. 100, pp 1-17.

Mullins, G., Lewis, C., and Justason, M., (2002). "Advancements in Statnamic Data Regression Techniques," *Deep Foundations 2002: An International Perspective on Theory, Design, Construction, and Performance*, ASCE Geo Institute, GSP No.116, Vol II, pp. 915-930.

Mullins, G. and O'Neill, M. W., (2003). "Pressure Grouted Drilled Shafts," Report submitted to A.H. Beck Foundation, Inc., June, 299 pgs.

Nishimura, S., and Matsumoto, T., (1995), "Wave Propagation Analysis During Statnamic Loading of a Steel Pipe Pile," *Proceedings of the First International Statnamic Seminar*, Vancouver, Canada, September.

Osterberg, J.O. (1994) *Recent Advances in Load Testing Driven Piles and Drilled Shafts using the Osterberg Load Cell Method*. Geotechnical Lecture Series, Geotechnical Division of the Illinois Section, ASCE, Chicago IL.

Winters, D. (2002), "SUPERSAW Statnamic Analysis Software," Master's Thesis, University of South Florida, Tampa, FL, May.

Wittke, Walter, 1990, "Rock Mechanics, Theory and Application with Case Histories," Springer-Verlag, Berlin.

Young, Hugh. D., (1992), "University Physics," Eight Edition, Addison Wesley.

# Drilled Shafts

## *Introduction*

Drilled shafts are deep, cylindrical, cast-in-place concrete foundations poured in and formed by a bored (i.e. "drilled") excavation. They can range from 2 to 30 feet in diameter and can be over 300 feet in length. The term *drilled shaft* is synonymous with cast-in-situ piles, bored piles, rotary bored cast-in-situ piles, or simply shafts. Although once considered a specialty foundation for urban settings where vibrations could not be tolerated or where shallow foundations could not develop sufficient capacity, their use as structural support has recently increased due to heightened lateral strength requirements for bridge foundations and the ability of drilled shafts to resist such loads. They are particularly advantageous where enormous lateral loads from extreme event limit states govern bridge foundation design (i.e. vessel impact loads). Further, relatively new developments in design and construction methods of shafts have provided considerably more economy to their use in all settings (discussed in an ensuing section on post grouting drilled shafts). Additional applications include providing foundations for high mast lighting, cantilevered signs, cellular phone and communication towers. In many instances, a single drilled shaft can replace a cluster of piles eliminating the need (and cost) for a pile cap.

With respect to both axial and lateral design procedures for water crossing bridges, all foundation types and their respective designs are additionally impacted by scour depth predictions based on 50 or 100 year storm events. Scour is the removal or erosion of soil from around piles, shafts, or shallow footings caused by high velocity stream flows. It is particularly aggravated by constricted flow caused by the presence of numerous bridge piers. The scour-mandated additional foundation depth dramatically changes driven pile construction where piles can not be driven deep enough without over stressing the piles or without pre-drilling dense surficial layers. Similarly, the increased unsupported length and slenderness ratio associated with the loss of supporting soil can affect the structural stability of the relatively slender pile elements. In contrast, drilled shaft construction is relatively unaffected by scour depth requirements and the tremendous lateral stiffness has won the appeal of many designers.

## *Construction Considerations*

The design methods for drilled shafts presented in this chapter are largely based on empirical correlations developed between soil boring data and measured shaft response to full-scale load tests. In that the database of test cases used to develop these correlations included many different types of construction, these methods can be thought to address construction practices. In reality, most of the design methodologies are extremely conservative for some types of construction and only mildly conservative for others. The construction of drilled shafts is not a trivial procedure. Maintaining the stability of the excavation prior to and during concrete placement is imperative to assure a structurally sound shaft. Various methods of construction have been adopted to address site-specific conditions

(e.g. dry or wet drilling; slurry type; cased or uncased; tremie placed or free fall concrete). All of these approaches as well as the fresh properties of the concrete can affect the load carrying capability of the finished shaft. It is important that the design engineer be familiar with drilled shaft construction methods and can assure that good construction practices are being used.

**Dry / Wet Construction.** *Dry* construction can only be performed in soil formations that are inherently stable when cut (e.g. clay or rock) and where ground water is not present. Any intrusion of ground water into the excavation can degrade the structure of the surrounding soil and hence reduce the capacity of the shaft. In situations where the ground water is present and likely to intrude, some form of wet construction should be used. *Wet* construction implies that a slurry is placed in the excavation that is capable of maintaining a net positive pressure against (or flow into) the walls of the excavation. The slurry can be mineral, synthetic, or natural.

*Mineral* slurries consist of a bentonite or attapulgite clay premixed with water to produce a stable suspension. As mineral slurries are slightly more dense than water, a 4 - 6 ft head differential above the ground water should be maintained at all times during introduction and extraction of the drilling tool. This head differential initially causes a lateral flow into the surrounding soil which is quickly slowed by the formation of a bentonite (or attapulgite) filter cake. Soil particles can be easily suspended in this slurry type for extended periods of time allowing concrete placement to be conducted without significant amounts of debris accumulation. However, no more than 4% slurry sand content is permitted in most States at the time of concreting.

*Synthetic* slurries consist of a mixture of polymers and water that form a syrupy solution. A 6 - 8 ft head differential should be maintained at all times during the introduction and extraction of the drilling tool when using a synthetic slurry. This head differential also causes lateral flow into the surrounding soils, but a filter cake is not formed. Rather, the long strings of the polymer stabilize the excavation walls by clinging to the soil as they flow into the soil matrix. As such, the flow remains relatively uniform and generally will not slow. The soil typically falls out of suspension relatively quickly when using synthetic slurries which permits debris to be removed from the bottom in a timely fashion.

*Natural* slurries are nothing more than readily assessable water (ground water, lake water, or salt water). An 8 - 10 ft head differential should be maintained at all times during introduction and extraction of the drilling tool when using a natural slurry. This head differential causes a lateral flow into the surrounding soil which is fast enough to induce outward lateral stress sufficient to maintain the excavation stability. Although it is possible to use this method in granular soils, it is not recommended nor is it permitted by most State agencies. Slight pressure differentials induced by tool extraction can cause local excavation wall instabilities. As such, this method is most commonly used when excavating clay or rock where the ground water is likely to be present. The above slurry types and the time the slurry is left in an excavation can affect the capacity of the finished shaft (Brown, 2000). To minimize these effects, local specifications have been imposed largely based on past performance in similar soils (FDOT, 2002).

**Casing.** Wall stability can also be maintained by using either partial or full length casing. A casing is a relatively thin walled steel pipe that is slightly larger in diameter than the drilling tool. It can be driven, vibrated, jetted, or oscillated (rotated) into position prior to excavation. The purpose of the casing is to provide stability to weak soils where slurries are ineffective or to bring the top of shaft

elevation to a level higher than the surface of free standing bodies of water. When stabilizing weak soils the casing is often temporary being removed after concreting. Shafts constructed over water must use permanent casing that can be removed after the concrete has fully cured. The method of installing and removing temporary casings can also affect the capacity of the finished shaft. Oscillation removal can increase side shear over vibrated or direct extraction methods. Quickly extracted casings can induce necking due to low pressure developed at the base of the extracted casing.

With the exception of full length temporary casing methods, the practical upper limit of shaft length is on the order of 30D (i.e. 90 ft for 3ft diameter shafts) but can be as much as 50D in extraordinary circumstances using special excavation methods.

**Concreting and Mix Design.** Drilled shaft concrete is relatively fluid concrete that should be tremie placed (or pumped to the base of the excavation) when using any form of wet construction to eliminate the possibility of segregation of fine and coarse aggregate and/or mixing with the insitu slurry. A tremie is a long pipe typically 8 - 12 inches in diameter used to take the concrete to the bottom of the excavation without being altered by the slurry (i.e. mixing or aggregate segregation). Prior to concreting, some form of isolation plug should be placed in-line or at the tip of the tremie to prevent contamination of the concrete flow as it passes through the initially empty tremie. During concrete placement, the tremie tip elevation should be maintained below the surface of the rising concrete (typically 5 - 10 ft). However, until a concrete head develops at the base of the excavation, the potential for initial mixing (and segregation) will always exist. In dry construction, free-fall concrete placement can be used although it is restricted by some State agencies. The velocity produced by the falling concrete can induce higher lateral pressure on the excavation walls, increase concrete density, and decrease porosity/permeability. However, velocity-induced impacts on reinforcing steel may mis-align tied steel stirrups and the air content (if specified) of the concrete can be reduced.

The concrete mix design for drilled shafts should produce a sufficient slump (typically between 6 and 9 inches) to ensure that lateral fluid concrete pressure will develop against the excavation walls. Further, the concrete should maintain a slump no less than 4 inches (slump loss limit) for several hours. This typically allows enough time to remove the tremie and any temporary casing while the concrete is still fluid enough to replace the volume of the tremie or casing and minimize suction forces (net negative lateral pressure) during extraction. However, recent studies suggest that a final slump in the range of 3.5 to 4 inches (or less) at the time of temporary casing extraction can drastically reduce the side shear capacity of the shaft (Garbin, 2003). As drilled shaft concrete is not vibrated during placement, the maximum aggregate size should be small enough to permit unrestricted flow through the steel reinforcing cage. The ratio of minimum rebar spacing to maximum aggregate diameter should be no less than 3 to 5 (FHWA, 1999).



## *Design Capacity of Drilled Shafts*

The capacity of drilled shafts is developed from a combination of side shear and end bearing. The side shear is related to the shear strength of the soil and in sands can be thought of as the lesser of the friction ( $F_r = \mu N$ ) that develops between the shaft concrete and the surrounding soil or the internal friction within the surrounding soil itself. Although a coefficient of friction ( $\mu$ ) can be reasonably approximated, the determination of the normal force ( $N$ ) is more difficult due to lateral stress relaxation during excavation. In clayey soils or rock side shear is most closely related to the unconfined compressive strength,  $q_u$ . The end bearing is analogous to shallow foundation bearing capacity with a very large depth of footing. However, it too is affected by construction induced disturbances and like the side shear has been empirically incorporated into the design methods discussed in the ensuing sections.

The design approach for drilled shafts can be either allowable stress design (ASD) or load and resistance factor design (LRFD) as dictated by the client, local municipality, or State agency. In either case, the concept of usable capacity as a function of ultimate capacity must be addressed. This requires the designer to have some understanding of the capacity versus displacement characteristics of the shaft. Likewise, a permissible displacement limit must be established to determine the usable capacity rather than the ultimate capacity which may be unattainable within a reasonable displacement. The permissible displacement (or differential displacement) is typically set by a structural engineer on the basis of the proposed structure's sensitivity to such movement. To this end, design of drilled shafts (as well as other foundation types) must superimpose displacement criteria onto load carrying capability even when using a LRFD approach. This is divergent from other non-geotechnical LRFD approaches that incorporate design limit states independently (discussed later).

The designer must be aware of the difference in the required displacements to develop significant capacity from side shear and end bearing. For instance, in sand the side shear component can develop 50% of ultimate capacity at a displacement of approximately 0.2% of the shaft diameter ( $D$ ) (AASHTO, 1997), and develops fully in the range of 0.5 to 1.0 %  $D$  (Bruce, 1986). In contrast, the end bearing component requires a displacement of 2.0%  $D$  to develop 50% of its capacity (AASHTO, 1997), and fully develops in the range of 10 to 15%  $D$  (Bruce, 1986). Therefore, a 4 ft diameter shaft in sand can require up to 0.5 inches displacement to develop ultimate side shear and 7.2 inches to develop ultimate end bearing. Other sources designate the displacement for ultimate end bearing to be 5%  $D$  but recognize the increase in capacity at larger displacements (Reese and Wright, 1977; Reese and O'Neill, 1988).

In most instances, the side shear can be assumed to be 100% usable within most permissible displacement criteria but the end bearing may not. This gives rise to the concept of mobilized capacity. The mobilized end bearing is the capacity that can be developed at a given displacement. Upon determining the permissible displacement, a proportional capacity can then be established based on a capacity versus displacement relationship as determined by either load testing or past experience. A general relationship will be discussed in the section discussing end bearing determination methods.

**ASD vs. LRFD.** In geotechnical designs, both ASD and LRFD methods must determine an ultimate capacity from which a usable capacity is then extracted based on displacement criteria. As such the

ultimate capacity is never used, but rather a displacement-restricted usable capacity is established as the *effective ultimate capacity*. For drilled shafts, this capacity typically incorporates 100% of ultimate side shear and the fraction of end bearing mobilized at that displacement. Once this value has been determined, the following generalized equations represent the equality that must be satisfied when using either an Allowable Stress Design or a Load and Resistance Factor Design approach, respectively.

$$\text{Service Load} \leq \frac{\text{Effective Ultimate Strength}}{S.F.} N \quad (\text{ASD})$$

or

$$P_u = \sum \gamma_i P_i \leq \phi P_n N \quad (\text{LRFD})$$

where,  $P_u$  represents the sum of factored or inflated service loads based on the type of loads,  $P_n$  represents the effective ultimate shaft capacity,  $N$  is the number of shafts, and  $\phi$  (the resistance factor) reduces the effective ultimate capacity based on the reliability of the capacity determination method. The use of LRFD in geotechnical designs is relatively new and as such present methods have not yet completely separated the various limit states.

Typically there are four LRFD limit states: strength, service, fatigue, and extreme event. These limit states treat each area as mutually exclusive issues. Strength limit states determine if there is sufficient capacity for a wide range of loading conditions. Service limit states address displacement and concrete crack control. Fatigue addresses the usable life span of steel in cyclic or stress reversal regions. Extreme event limit states introduce less probable but more catastrophic occurrences such as earthquakes or large vessel impacts. Any of the four limit states can control the final design. The ASD method lumps all load types into a single service load and assumes the same probability for all occurrences.

Although LRFD strength limit states should be evaluated without regard to the amount of displacement required to develop full ultimate capacity ( $P_n$ ), present LRFD methods establish geotechnical ultimate capacity based on some displacement criteria. As a result, LRFD geotechnical service limits states are relatively unused. To this end, this chapter will emphasize the design methods used to determine ultimate capacity and will denote (where applicable) the displacement required to develop that capacity. The following design methods are either the most up to date or the most widely accepted for the respective soil type and/or soil exploration data.

### SPT Data in Sand

Standard penetration test results are most commonly used for estimating a drilled shaft capacity in sandy soils. For some design methods direct capacity correlations to the SPT blow count ( $N$ ) have been developed; in other cases correlations to soil properties such as unit weight or internal angle of friction are necessary. Where the unit weight or the internal friction angle (sands) of a soil is required the relationships shown in Figure 1 can be used.

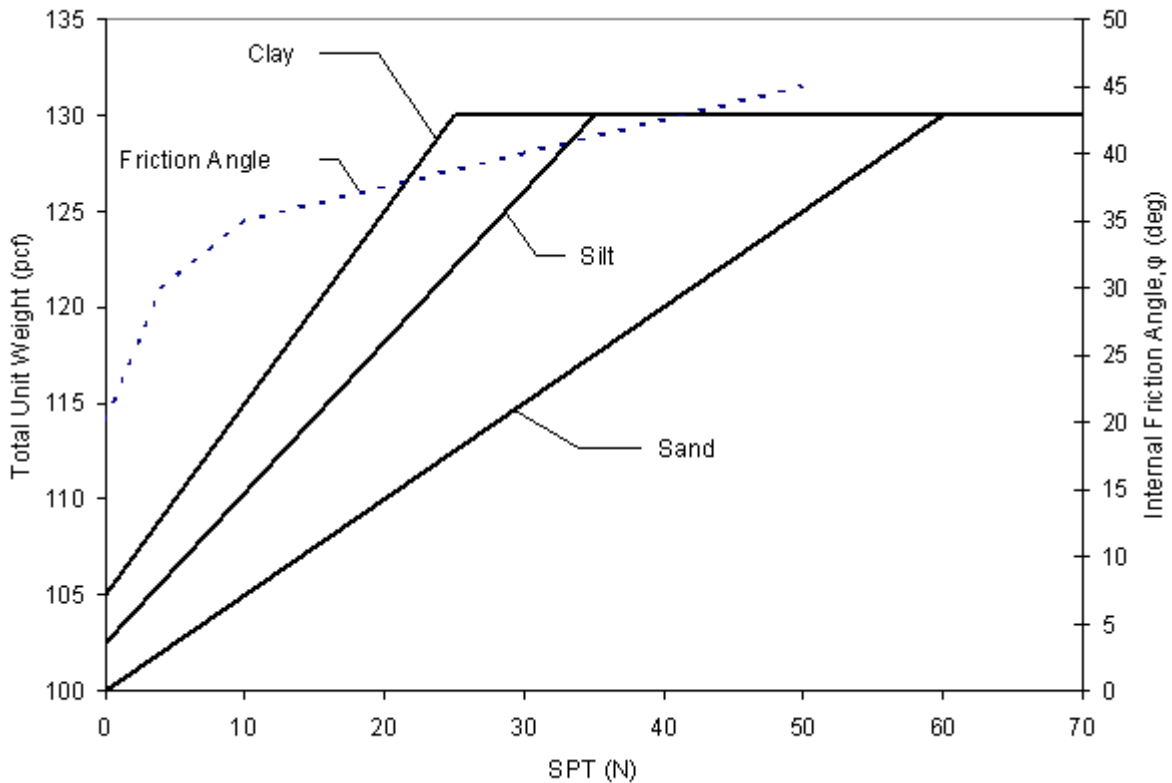


**Figure 1** Estimated soil properties from SPT blow count.

**Side Shear.** The side shear developed between a shaft and surrounding sandy soils can be estimated using the following methods in Table 1. The ultimate load carrying capacity from side shear ( $Q_s$ ) can be expressed as the summation of side shear developed in layers of soil to a given depth containing  $n$  layers:

$$Q_s = \pi \sum_{i=1}^n f_{si} L_i D_i$$

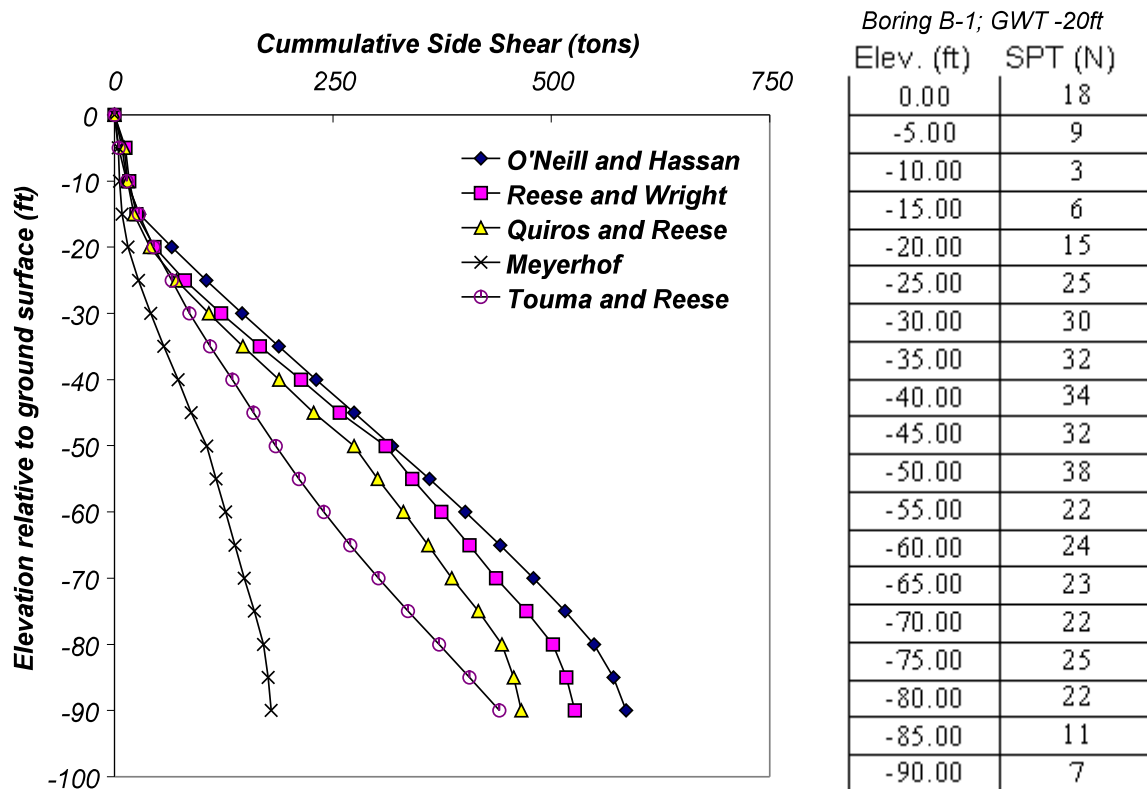
where  $f_{si}$  is the estimated unit side shear for the  $i^{\text{th}}$  soil layer  
 $L_i$  is the thickness of (or length of shaft in) the  $i^{\text{th}}$  soil layer  
 $D_i$  is the diameter of the shaft in the  $i^{\text{th}}$  soil layer

Table 1. Drilled Shaft Side Shear Design Methods for Sand (adapted from AASHTO, 1998)

Source	Side Shear Resistance, $f_s$ (in tsf)
Touma and Reese (1974)	$f_s = K\sigma_v' \tan\phi < 2.5 \text{ tsf}$ where $K = 0.7$ for $D_b \leq 25 \text{ ft}$ $K = 0.6$ for $25 \text{ ft} < D_b \leq 40 \text{ ft}$ $K = 0.5$ for $D_b > 40 \text{ ft}$
Meyerhof (1976)	$f_s = N / 100$

Quiros and Reese (1977)	$f_s = 0.026 N < 2.0 \text{ tsf}$
Reese and Wright (1977)	$f_s = N / 34$ , for $N \leq 53$ $f_s = (N - 53) / 450 + 1.6$ , for $53 < N \leq 100$ $f_s \leq 1.7$
Reese and O'Neill (1988) <i>Beta Method</i>	$f_s = \beta \sigma_v' < 2.0 \text{ tsf}$ , for $0.25 \leq \beta \leq 1.2$  where $\beta = 1.5 - 0.135 z^{0.5}$ , $z$ in ft
O'Neill and Hassan (1994) <i>Modified Beta Method</i>	$f_s = \beta \sigma_v' < 2.0 \text{ tsf}$ , for $0.25 \leq \beta \leq 1.2$  where $\beta = 1.5 - 0.135 z^{0.5}$ for $N > 15$ $\beta = N/15 (1.5 - 0.135 z^{0.5})$ for $N \leq 15$

Using the above methods, the variation in estimated side shear capacity is illustrated for a 3 ft diameter shaft and the given SPT boring log in sandy soil in Figure 2. Although any of these methods may correlate closely to a given site or local experience, the author recommends the O'Neill and Hassan approach in spite of its less conservative appearance.



**Figure 2** Comparison of estimated side shear capacities in sandy soil (3 ft diam).

**End Bearing.** Recalling the importance of the mobilized end bearing capacity concept, a parameter termed the tip capacity multiplier (TCM) will be used to quantify the relationship between ultimate and usable end bearing capacity. Four design methods using two different approaches to mobilized capacity are discussed. The first and second assume ultimate end bearing occurs at 1.0 inch displacement (Touma and Reese, 1974; Meyerhoff, 1976). The others assume ultimate end bearing occurs at a 5% displacement as shown in Figure 3 (Reese and Wright, 1977; Reese and O'Neill, 1988). This figure shows the latter relationship in terms of the permissible displacement expressed as a percentage of the shaft diameter. Therein, the TCM for convention shafts tipped in sand is linearly proportional to the displacement where the TCM = 1 at 5% displacement. This concept can be extended to the first two design methods as well where TCM = 1 at 1.0 inches displacement. Table 2 lists the four methods used to estimate the ultimate end bearing to which a TCM should be applied.

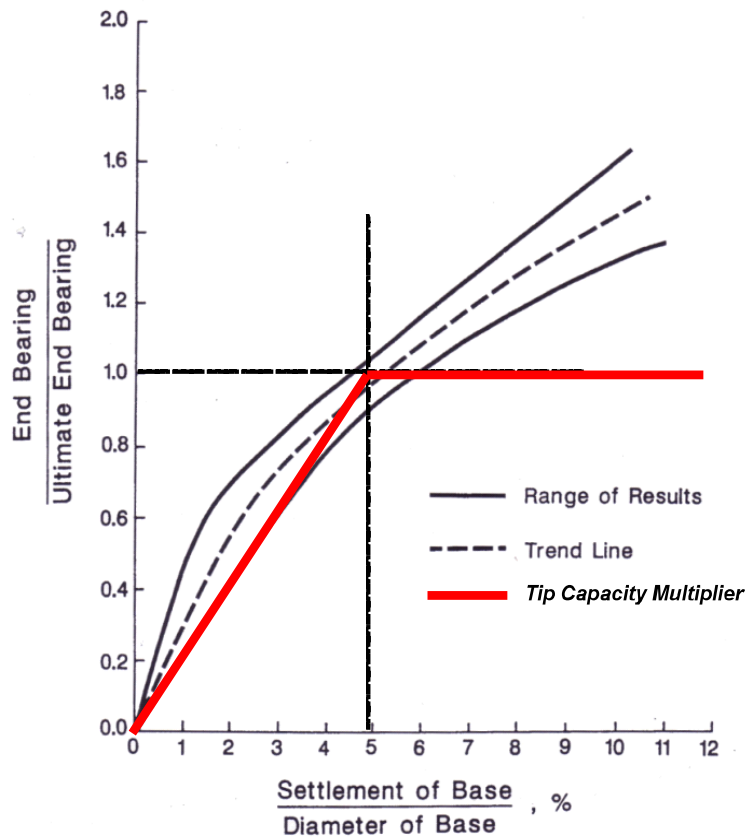


**Figure 3** End bearing response of sands as a function of displacement (based on Reese and O'Neill, 1988).

Figure 4 shows the calculated ultimate end bearing using each of the four methods in Table 2. The Reese and Wright or Reese and O'Neill methods are recommended by the author for end bearing analysis. Using the combined capacity from 100% side shear and  $TCM \cdot q_p$  using O'Neill and Hassan and Reese and O'Neill methods, respectively, the effective ultimate capacity of a 3 ft diameter drilled shaft can be estimated as a function of depth, Figure 5. This type of curve is convenient for design as it is a general capacity curve independent of a specific design load. However, when using a LRFD approach, the factored load ( $P_u$ ) should be divided by the appropriate resistance factor before going to this curve.

Table 2. Drilled Shaft End Bearing Design Methods for Sands (AASHTO, 1998)

Source	End Bearing Resistance, $q_p$ (in tsf)**
Touma and Reese (1974)	Loose Sand, $q_p = 0.0$ Medium Dense Sand, $q_p = 16 / k$ Very Dense Sand, $q_p = 40 / k$  where $k = 1$ for $D_p = 1.67$ ft $k = 0.6 D_p$ for $D_p \geq 1.67$ ft only for shaft depths $> 10 D$
Meyerhof (1976)	$q_p = (2N_{corr}D_b) / (15 D_p)$ $q_p < 4/3 N_{corr}$ for sand $q_p < N_{corr}$ for non-plastic silts
Reese and Wright (1977)	$q_p = 2/3 N$ for $N \leq 60$ $q_p = 40$ for $N > 60$
Reese and O'Neill (1988)	$q_p = 0.6 N$ for $N \leq 75$ $q_p = 45$ for $N > 75$

\*\* For  $D > 4.17$  ft, the end bearing resistance should be reduced to  $q_{pr} = 4.17q_p / D$ .

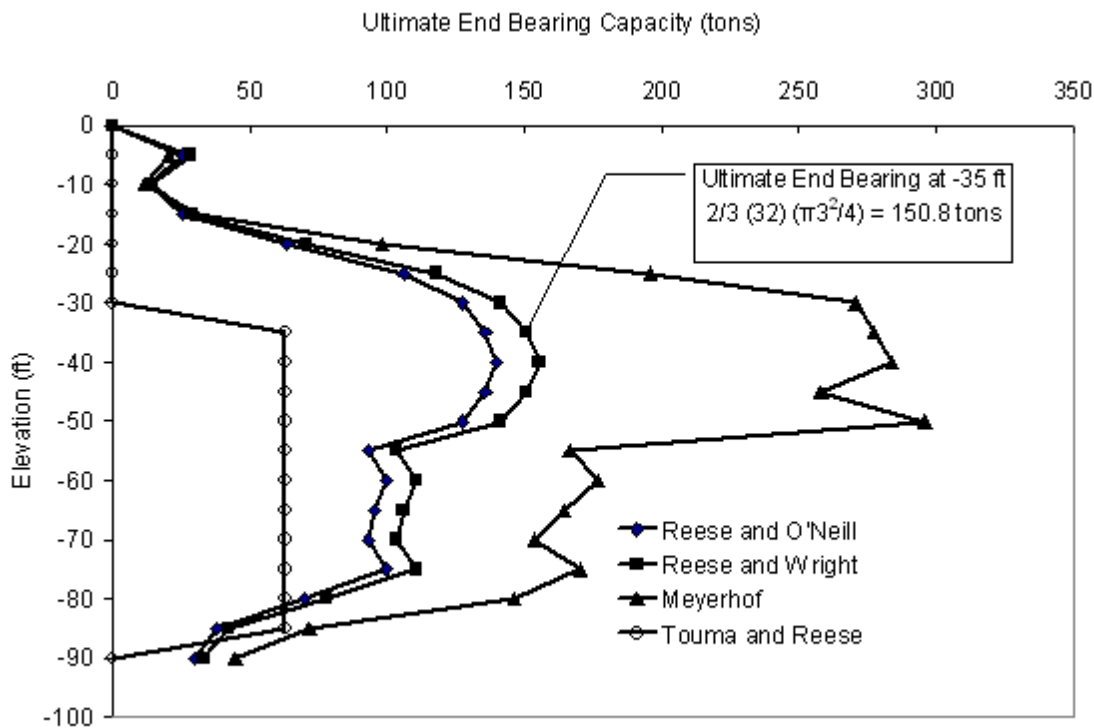
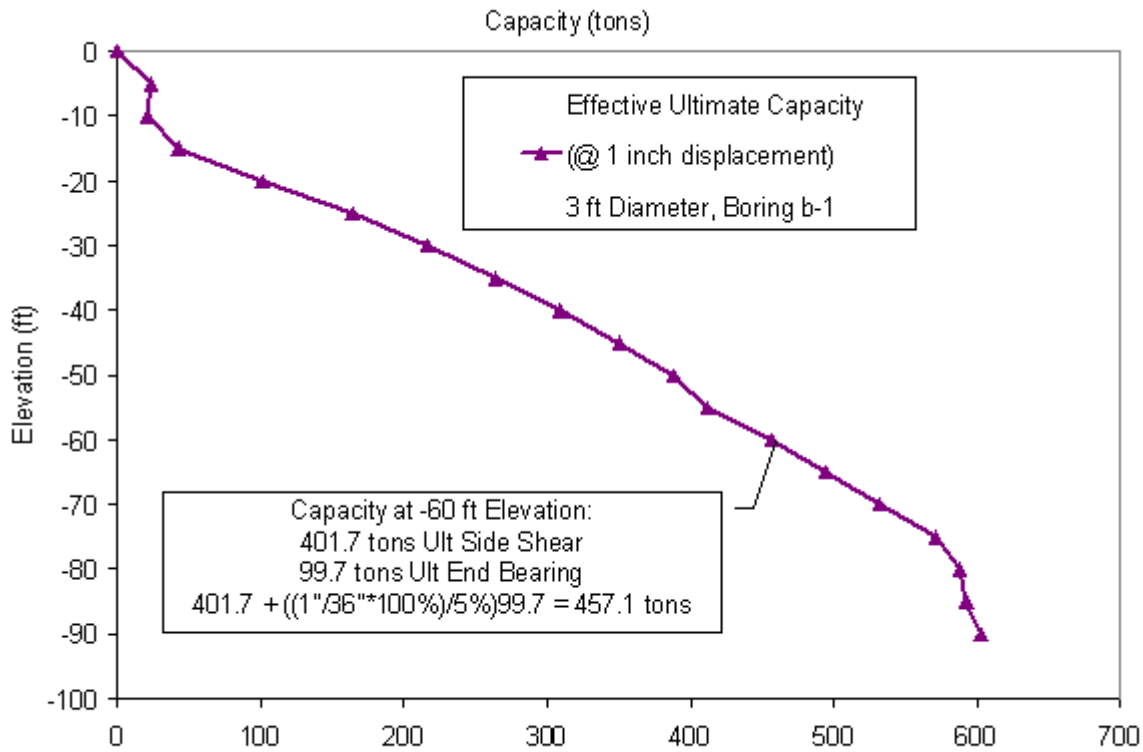


Figure 4 Comparison of end bearing methods in sand (3 ft diam, Boring B-1).





**Figure 5** Example design curve using Boring B-1 from Figure 1.

### Triaxial or SPT Data in Clay

Unconsolidated, undrained (UU) triaxial test results are preferred when estimating the side shear or end bearing capacity of drilled shafts in clayey soil. The mean undrained shear strength ( $S_u$ ) is derived from a number of tests conducted on Shelby tube specimens where  $S_u = 1/2 \sigma_{1 \text{ Max}}$ . In many instances, both UU and SPT data can be obtained from which local SPT(N) correlations with  $S_u$  can be established. In the absence of any UU test results, a general correlation from Kulhawy and Mayne (1990) can be used

$$S_u = 0.0625 N, \text{ in units of tsf}$$

**Side Shear (*alpha method*).** The alpha method of side shear estimation is based on correlations between measured side shear from full-scale load tests and the clay shear strength as determined by UU test results. Therein, the unit side shear  $f_s$  is directly proportional to the product of the adhesion factor ( $\alpha$ ) and  $S_u$ .

$$f_s = \alpha S_u$$

Table 3. Adhesion factor for drilled shafts in clayey soils.

Adhesion Factor, $\alpha$ (dimensionless)	Undrained Shear Strength, $S_u$ (tsf)
0.55	< 2.0
0.49	2.0 - 3.0
0.42	3.0 - 4.0
0.38	4.0 - 5.0
0.35	5.0 - 6.0
0.33	6.0 - 7.0
0.32	7.0 - 8.0
0.31	8.0 - 9.0
Treat as Rock	> 9.0

The side shear developed around drilled shafts in clayey soil has several limitations that were not applied previously applied to shafts cast in sand. Specifically, the top 5 feet of the shaft sides are considered non contributing due to cyclic lateral movements that separate the shaft from the soil as well as potential dessication separation of the surficial soil. Additionally, the bottom 1D of the shaft side shear is disregarded to account for lateral stresses that develop radially as the end bearing mobilizes.

Although rarely used today, belled ends also affect the side shear near the shaft base. In such cases, the side shear surface area of the bell as well as that area 1D above the bell should not be expected to contribute capacity.

**End Bearing.** The end bearing capacity of shafts tipped in clay is also dependent on the mean undrained shear strength of the clay within two diameters below the tip,  $S_u$ . As discussed with shafts tipped in sands, a TCM should be applied to estimated end bearing capacities using the relationship shown in Figure 6. At displacements of 2.5% of the shaft diameter, shafts in clay mobilize 75 to 95% of ultimate capacity. Unlike sands, however, there is little reserve bearing capacity beyond this displacement. Therefore, a maximum TCM of 0.9 is recommended for conventional shafts at displacements of 2.5%D and proportionally less for smaller permissible displacements.

Similar to shallow foundation analyses, the following expressions may be used to estimate the ultimate end bearing for shafts with diameters less than 75 inches (AASHTO, 1998):

$$q_p = N_c S_u \leq 40 \text{ tsf}$$

where

$$N_c = 6 [ 1 + 0.2(Z/D) ] \leq 9 \text{ for } S_u > 0.25 \text{ tsf}$$

$$N_c = 4 [ 1 + 0.2(Z/D) ] \leq 9 \text{ for } S_u < 0.25 \text{ tsf}$$

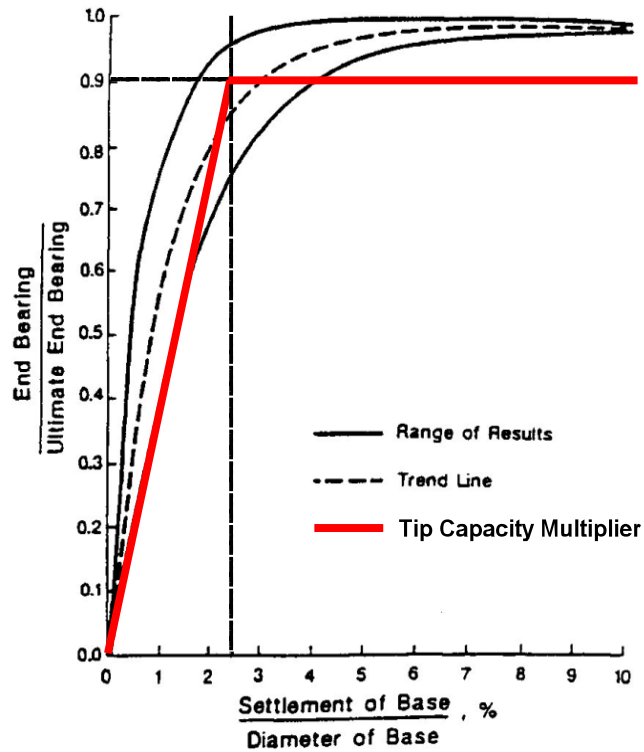


**Figure 6** End bearing response of shafts tipped in clays (Reese and O'Neill, 1988).

and  $Z/D$  is the ratio of the shaft diameter to depth of penetration. For shafts greater than 75 inches in diameter a reduction factor should be used as follows:

$$q_{pr} = q_p F_r$$

$$F_r = \frac{2.5}{12aD_p + 2.5b} \leq 1.0 \text{ where:}$$

and

$$a = 0.0071 + 0.0021 Z/P \leq 0.015$$

$$b = 0.45 (2 S_v)^{0.5}$$

for

$$0.5 \leq b \leq 1.5$$

## Designing Drilled Shafts from CPT Data

Cone penetration test data is considered to be more reproducible than SPT data and can be used for shaft designs in cohesionless and cohesive soils using correlations developed by Alsamman (1995). Although that study provided design values for both mechanical and electric cone data, a single approach is presented below that can conservatively be used for either based on that work.

**Side Shear.** This method for determining side shear resistance in cohesionless soils is divided into two soil categories: gravelly sand/gravel or sand/silty sand. In each case below in Table 4, the side shear is correlated to the cone tip resistance,  $q_c$ , instead of the sleeve friction due to the absence of that data from some case studies at the time of the study. In cohesive soils, a single expression is given which is also dependent on the total vertical stress,  $\sigma_{vo}$ . The same regions of the shaft should be discounted (top 5 ft and bottom 1D) when in cohesive soils as discussed earlier.

Table 4. Side Shear Resistance from CPT data

Soil Type	Ultimate Side Shear Resistance, $q_s$ (tsf)
Gravelly Sand / Gravel	$f_s = 0.02 q_c$ for $q_c \leq 50$ tsf $f_s = 0.0019 q_c + 0.9 \leq 1.4$ for $q_c > 50$ tsf
Sand / Silty Sand	$f_s = 0.015 q_c$ for $q_c \leq 50$ tsf $f_s = 0.0012 q_c + 0.7 \leq 1.0$ for $q_c > 50$ tsf
Clay	$f_s = 0.023 (q_c - \sigma_{vo}) \leq 0.9$

The upper limits for side shear recommended by Alsamman are somewhat less than those cited from AASHTO (e.g. 2.0 tsf for sands using the *Beta Method*). However, CPT data can also be used to estimate the internal friction and soil density necessary for the Touma and Reese or Beta methods.

**End Bearing.** Expressions for estimating the end bearing using CPT data were also recommended by the same study (Alsamman, 1995). Therein, the end bearing categories were limited to cohesionless and cohesive soils. Table 5 provides correlations based on those findings.

Table 5. End Bearing Resistance from CPT data

Soil Type	Ultimate End Bearing Resistance, $q_p$ (tsf)
Cohesionless Soils	$q_p = 0.15 q_c$ for $q_c \leq 100$ tsf $q_p = 0.05 q_c + 10 \leq 30$ for $q_c > 100$ tsf
Cohesive Soils	$q_p = 0.25 (q_c - \sigma_{vo}) \leq 25$

The capacities estimated from Table 5 expressions are ultimate values that should be assigned a proportionally less usable capacity using the general relationships shown in Figures X and Y for sands and clays, respectively.

## Designing from Rock Core Data

A common application for drilled shaft is to be socketed in a rock formation some distance,  $H_s$ . In these cases, the side shear of softer overlying materials is disregarded due to the mismatch in the displacement required to mobilize both material types. Rock sockets require relatively small movements to develop full capacity when compared to sand or clay strata. Further, although the end bearing strength of a rock socket can be quite considerable, it too is often discounted for the same reason. Alternately, a rock socket may be designed for all end bearing instead of side shear knowing that some side shear capacity will always be available in reserve.

**Side Shear.** The side shear strength of rock-socketed drilled shafts is similar to that of clayey soils in that it is dependent on the insitu shear strength of the bearing strata. In this case rock cores are taken from the field and tested in various methods. Specifically, mean failure stress from two tests are commonly used: the unconfined compression test,  $q_u$ ; and the splitting tensile test,  $q_s$ . The test results from these tests can be used to estimate the side shear of a rock socket using the expressions in Table 6. The estimated side shear capacity can be reduced by multiply  $q_s$  by either the rock quality index, RQD, or the percent sample recovered from the rock core. Local experience and results from load tests can provide the best insight into the most appropriate approach.

Table 6. Drilled Shaft Side Shear Design Methods for Rock Sockets

Source	Side Shear Resistance, $f_s$ (tsf)
Carter and Kulhawy (1988)	$f_s = 0.15 q_u$ for $q_u \leq 20$ tsf
Horvath and Kenney (1979)	$f_s = 0.67 q_u^{0.5}$ for $q_u > 20$ tsf
McVay and Townsend (1990)	$f_s = 0.5 q_u^{0.5} q_s^{0.5}$

**End Bearing.** When determining the end bearing resistance (as well as side shear) of drilled shafts in rock, the quality of rock and type of rock can greatly affect the capacity. In competent rock the structural capacity of the concrete will control the design. In fractured, weathered rock or limestone, the quality of the formation as denoted by the RQD or %recovery should be incorporated into the capacity estimate. However, these parameters are influenced by drilling equipment, driller experience and the type of core barrel used to retrieve the samples. The designer should make some attempt to correlate the rock quality to load test data where possible. The Federal Highway Administration recommends the following expression for estimating the end bearing resistance in rock (FHWA, 1988):

$$q_b = 2.5 q_u \%Rec \leq 40 \text{ tsf}$$

The value of 40 tsf is undoubtedly conservative with respect to ultimate capacity, but when used in conjunction with a rock socket side shear it may be reasonable. Under any circumstances, load testing can verify much higher capacities even though they are near impossible to fail in competent rock.

## Designing from Load Test Data

The use of an instrumented load test data for design is thought to be the most reliable approach and is given the highest resistance factor (LRFD) or lowest safety factor (ASD) as a result. This method involves estimating the shaft capacity using one of the previously discussed method (or similar) and verifying the estimated capacity using a full-scale prototype shaft loaded to ultimate capacity. These tests can be conducted prior to construction or during construction (denoted as design phase or construction phase load testing, respectively). In either event, the shaft should be loaded well in excess of the design load while monitoring the response (i.e. axial displacement, lateral displacement and/or internal strains).

An instrumented load test is one that incorporates strain gages along the length of the foundation to delineate load carrying contributions from various soil strata. The test can merely distinguish side shear from end bearing or additional information from discrete shaft segments / soil strata can also be obtained. Any test method capable of applying the ultimate load can provide useful feedback to the designer. Tests conducted to lesser loads are still useful but provide only a “proof test” to the magnitude of the maximum load and can only provide a lower bound of the actual capacity. As such, the designer should realize that a test shaft that fails geotechnically, thus providing the ultimate capacity, is desirable in such a program so that the upper limit of capacity can be realized. The challenge then is to design a shaft that fails at a load reasonably close to the desired ultimate without being too conservative. However, the loading apparatus should have sufficient reserve to account for a slightly conservative capacity estimate.

**Side Shear.** The ultimate side shear can be determine from load testing by evaluating the response from embedded strain gages at various elevations in the shaft. It is desirable to delineate bearing strata by placing these gages at the interface between significantly different soil strata (e.g. clay / sand interface). At a minimum, one level of gages should be placed at the tip of the shaft to separate the load carrying contributions from the side shear and end bearing. By monitoring the strain at a given level, the corresponding load and difference in load between levels can be determined. It is further desirable to use four gages per level to help indicate eccentricities in the loading as well as provide redundancy.

The load at a particular level can be evaluated using strain gage data using the following expression:

$$P_i = \epsilon_i E_i A_i$$

where

- $P_i$  is the load at the  $i^{\text{th}}$  level
- $\epsilon_i$  is the strain measured at the  $i^{\text{th}}$  level
- $E_i$  is the composite modulus of the  $i^{\text{th}}$  level, and
- $A_i$  is the cross sectional area of the  $i^{\text{th}}$  level.

The side shear from a given shaft segment can then be calculated from the difference in measured load from the two levels bounding that segment.

$$f_s = (P_i - P_{i+1}) / (L \pi D)$$



where  $L$  and  $D$  are the length and diameter of the shaft segment, respectively. If only using a single gage level at the toe of the shaft,  $P_i$  is the applied load to the top of the shaft and  $P_{i+1}$  is the load calculated from strain at the toe.

**End Bearing.** The end bearing can be similarly determined from strain data. However, the ultimate end bearing is not necessarily established. Rather, the effective ultimate capacity (usable capacity) is determined on the basis of permissible displacement. Although several approaches do exist that attempt to extract a single capacity value from test data, the entire load versus displacement response should be noted. Figure 7 shows the end bearing response as measured from a load test. A comparison between the measured and predicted values should be prepared so that the original design approach can be calibrated. The end bearing strength is determined from strain gage data using the following expression:

$$q_b = P_{toe} / A = \epsilon_{toe} E_{toe}$$

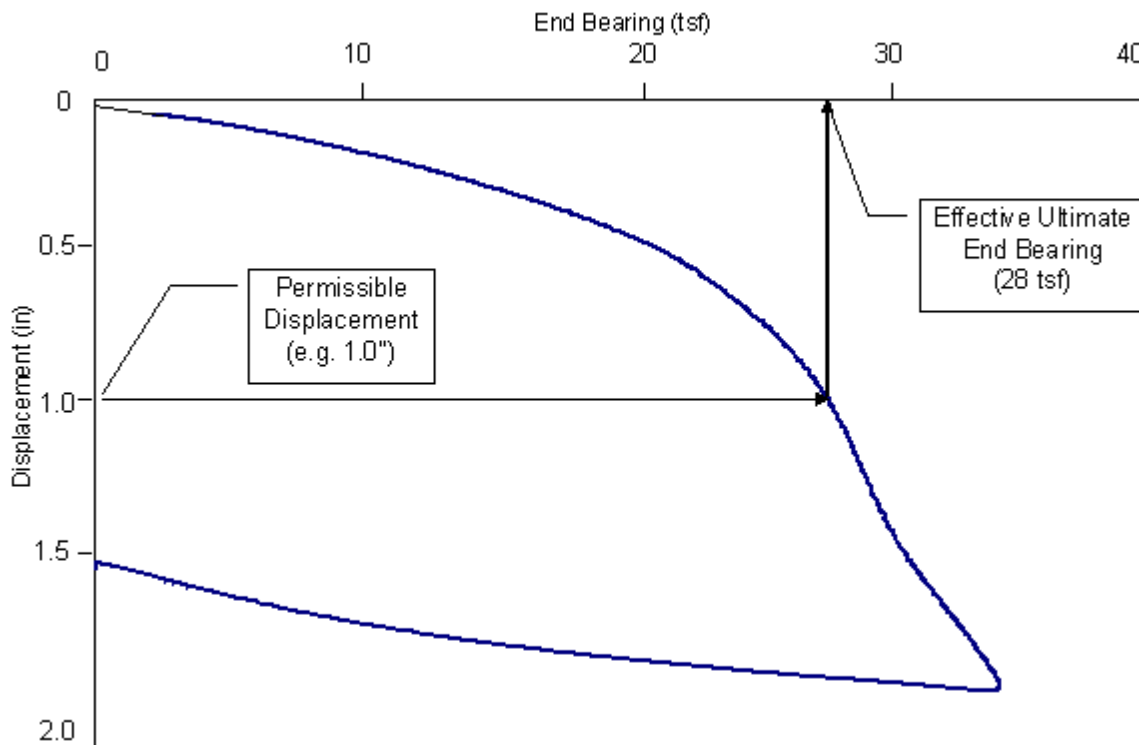


**Figure 7** End Bearing Load Test Results.

## Designing Post Grouted Shafts

The end bearing component of drilled shafts is only fractionally utilized in virtually all design methods ( $TCM < 1.0$ ) due to the large displacement required to mobilize ultimate capacity. Consequently, a large portion of the ultimate capacity necessarily goes unused. In an effort to regain some of this unusable capacity, mechanistic procedures to integrate its contribution have been developed using pressure grouting beneath the shaft tip (also called post grouting or base grouting). Pressure grouting the tips of drilled shafts has been successfully used worldwide to precompress soft debris or loose soil relaxed by excavation (Bolognesi and Moretto, 1973; Stoker, 1983; Bruce, 1986; Fleming, 1993; Mullins et al., 2000; Dapp and Mullins, 2002). The post-grouting process entails: (1) installation of a grout distribution system during conventional cage preparation that provides grout tube-access to the bottom of the shaft reinforcement cage, and (2) after the shaft concrete has cured, injection of high pressure grout beneath the tip of the shaft which both densifies the in-situ soil and compresses any debris left by the drilling process. By essentially preloading the soil beneath the tip, higher end bearing capacities can be realized within the service displacement limits.

Although post grouting along the sides of the shaft has been reported to be effective, this section will only address the design of post grouted shaft tips. The overall capacity of the shaft is still derived from both side shear and end bearing where the available side shear is calculated using one or a combination of the methods discussed earlier. Further, the calculation of the available side shear is an important step in determining the pressure to which the grout can be pumped.

**Post Grouting in Sand.** The design approach for post grouted drilled shaft tips makes use of common parameters used for a conventional (un-grouted) drilled shaft design. This methodology includes the following seven steps:

- (1) Determine the ungrouted end bearing capacity in units of stress.
- (2) Determine the permissible displacement as a percentage of shaft diameter (e.g.  $1"/48" * 100\% \approx 2\%$ ).
- (3) Evaluate the ultimate side shear resistance for the desired shaft length and diameter (in units of force).
- (4) Establish a maximum grout pressure that can be resisted by the side shear (ultimate side shear divided by the tip cross sectional area).
- (5) Calculate the Grout Pressure Index, GPI, defined as the ratio of grout pressure to the ungrouted end bearing capacity (*Step 3 / Step 1*).
- (6) Using design curves from Figure 8, determine the Tip Capacity Multiplier, TCM, using the GPI calculated in *Step 5*.
- (7) Calculate the grouted end bearing capacity (effective ultimate) by multiplying the TCM by the ungrouted end bearing ( $TCM * Step 1$ ).

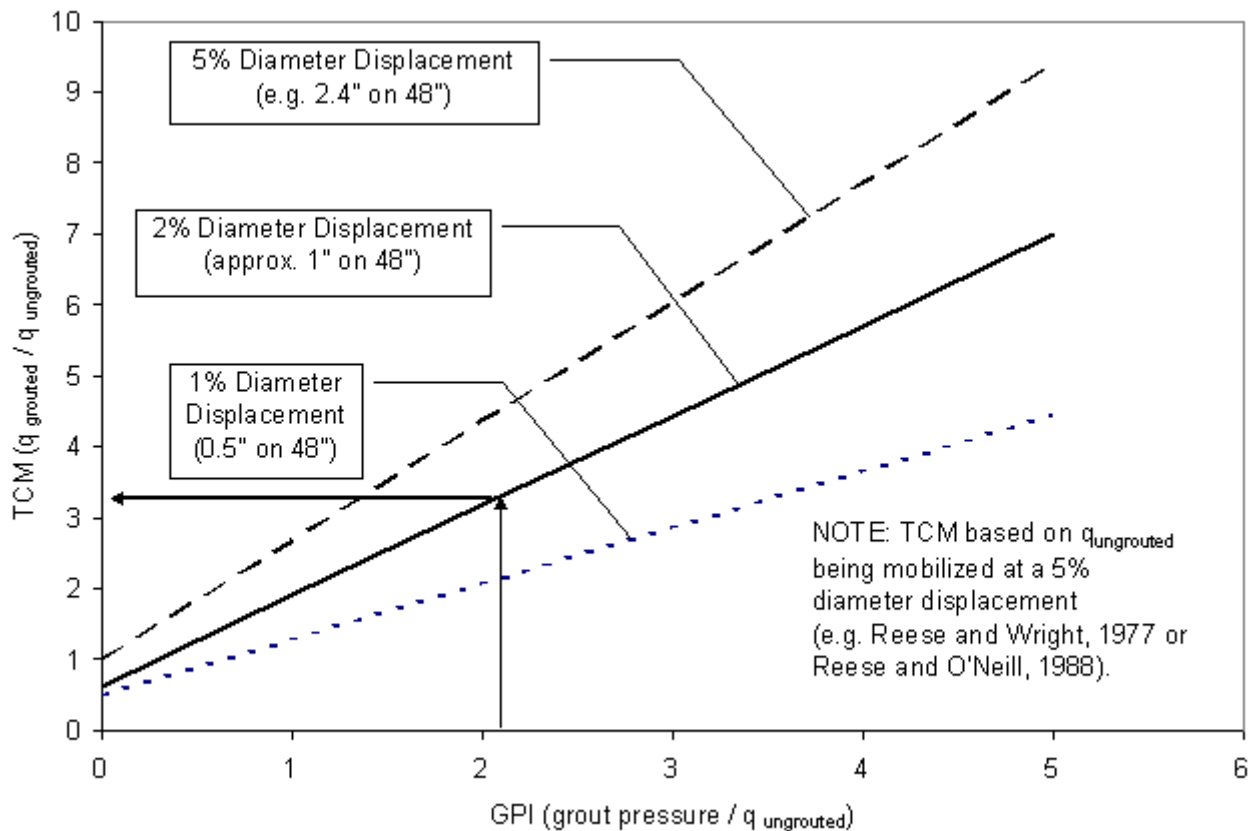


**Figure 8** Correlations used in *Step 6* to establish TCM (Mullins, et al., 2001).

The ungrouted capacity ( $GPI = 0$ ) is represented by these curves at the y-intercept where  $TCM = 1$  for a 5% displacement (no improvement). The 1% and 2% intercepts reduce the end bearing according to the normal behavior of partially mobilized end bearing. Interestingly, the grouted end bearing capacity is strongly dependent on available side shear capacity (grout pressure) as well as the permissible displacement. However, it is relatively independent of the ungrouted end bearing capacity when in sandy soils. As such, the end bearing in loose sand deposits can be greatly improved in both stiffness and ultimate capacity given sufficient side shear against which to develop grout pressure. In dense sands and clays significant improvement in stiffness can be realized with more modest effects on ultimate capacity. Figure 9 shows the effective ultimate capacity that can be expected from a grouted shaft similar to that from Example 1.

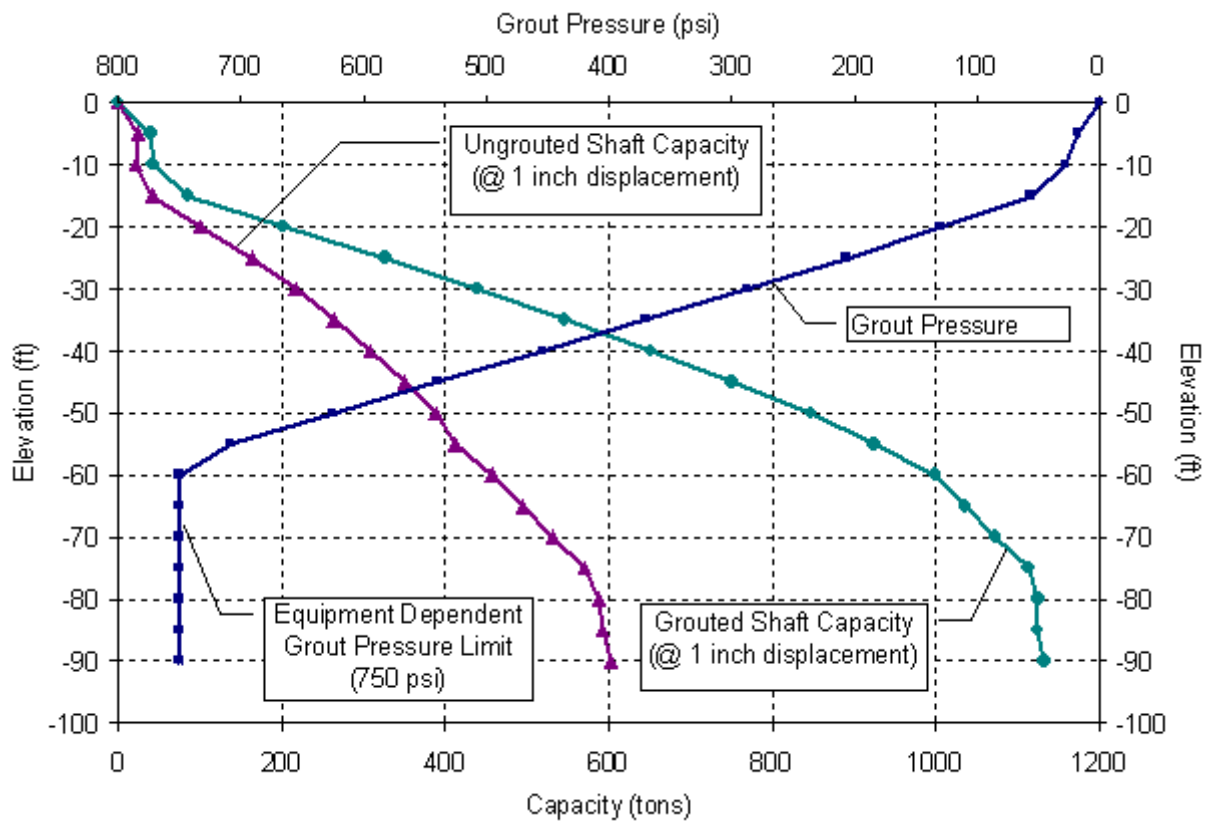


Figure 9 Post grouted shaft capacity extended from Example 1.

**Post Grouting in Other Formations.** Post grouting shaft tips in other formations such as clays, silts, and rock can be advantageous for the same reasons as in sand. However, the degree of improvement may be more modest. In clays and plastic silts, the TCM can be assumed to be 1.0 although studies have shown it to be as high as 1.5 if sufficient side shear can be developed (Mullins and O'Neill, 2003). In non plastic silts, the TCM can be assumed to be 1.0 for initial designs but a verification load test program is recommend as much higher values may be reasonable. In rock, post grouted shafts have the potential to engage both the side shear and end bearing simultaneously. In all soil types the achieved grout pressure can be used as a lower bound for usable end bearing and the attainable grout pressure is always dependent on the available side shear against which to react. In contrast, sufficient side shear capacity does not assure that grout pressure can be developed without excessive volumes of grout.

Post grouting shaft tips provides a capacity verification for every shaft grouted. To optimize its use and design, a full load test program should be scheduled at the onset to confirm the TCM most appropriate for a given site and soil type.

## *Economy of Load Testing*

Although the cost of foundations is most closely linked to the presence of an adequate bearing strata and the applied load, it is also directly affected by the design approach and the diameter of the shaft selected. As such, a designer may employ a range of safety factors (or resistance factors) given the level of confidence that can be assigned to a particular scenario. The most common method of establishing a particular level of certainty is via some form of testing. This testing can range from applying the full anticipated load (static or statnamic tests) to a minimum of a subsurface investigation to estimate insitu soil properties. Load tests result in the highest increase in designer confidence and can be incorporated into the design in the form of adjusted/calibrated unit strengths, reduced safety factors, or increased resistance factors. The effects of design uncertainty can be illustrated by the AASHTO (1998) specifications for driven piles where the designer must select from nine different resistance factors ranging from 0.35 to 0.80 based on the design methodology. Four of these conditions are selected based on the level/quality of testing that is anticipated. Therein, the highest resistance factor (0.8) and confidence is associated with a load test. The next highest (0.65) is assigned to test methods related to installation monitoring. In contrast, the lowest confidence and resistance factor (0.35 - 0.45) is assigned when a design is based solely on capacity correlations with SPT data. Although some resistance factors for drilled shafts are not given by AASHTO, the resistance factors most commonly range from 0.5 to 0.8 for no testing to load testing, respectively.

The following two examples will use estimated costs to illustrate the impact of shaft size (diameter) and design approach ( $\phi$  factor) on cost effectiveness. The cost of shaft construction and testing can vary significantly based on the number of shafts and type of material excavated as well as the physical conditions and location of the site. Even though a typical unit price of a drilled shaft includes each of these parameters, this approach can be used for comparisons using updated site-specific values.

Given:

3 ft diameter shaft	\$100 / lineal foot	excavation and concreting
4 ft diameter shaft	\$200 / lineal foot	excavation and concreting
6 ft diameter shaft	\$400 / lineal foot	excavation and concreting
Static load test	\$125 / ton of test	1% of shafts tested (1 min.)
Statnamic load test	\$35 / ton of test	1% of shafts tested (1 min.)

Use: Boring log and effective ultimate capacity calculations from Example 1, as well as the following resistance values (slightly update from most recent AASHTO)

Static load test	$\phi = 0.75$
Statnamic load test	$\phi = 0.73$
No testing (SPT only)	$\phi = 0.55$

Assume a maximum excavation depth of 30D

**Selecting the Most Economical Shaft Diameter.** Many options are available to the designer when selecting the diameter of shaft to be used for a specific foundation. For instance, a long, small diameter shaft can provide equivalent axial capacity to a shorter, larger diameter shaft. Figure 10

shows the result of re-evaluating Example 1 for 3, 4, and 6 ft diameter shafts while incorporating the cost per ton of capacity using \$100, \$200, and \$400 per ft of shaft, respectively. These curves are based on axial capacity and the cost may further vary given significant lateral loading and the associated bending moment requirements. In this case, the 3 ft diameter shaft is the most cost effective at all depths.

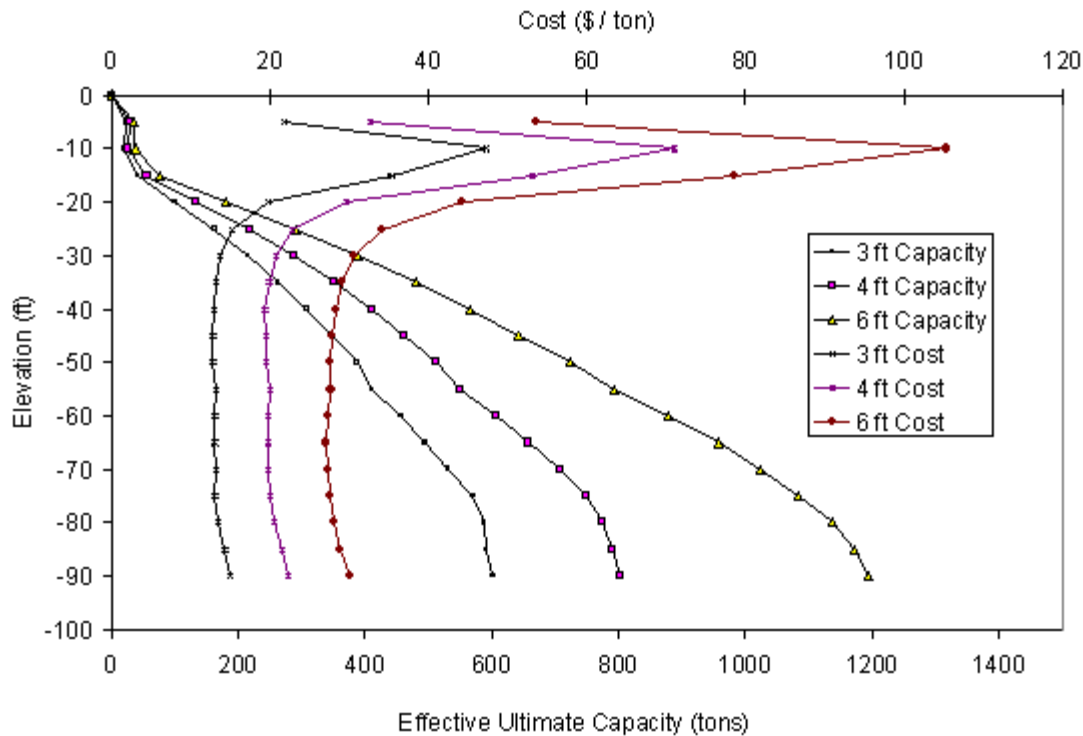


**Figure 10** The effect of shaft size selection on cost.

**Selecting the Most Economical Design Method.** The next comparison that can be made is that which evaluates the cost effectiveness of various design/testing methods. As additional testing (beyond soil exploration) incurs extra expense, a break even analysis should be performed to justify its use. In this case, a 3 ft diameter shaft will be used due to the results shown in Figure 10 where it was consistently less costly. The maximum capacity that can be reasonable provided by a 3 ft diameter shaft will be calculated to be 602 tons at a depth of 90 ft (30D)\*. The effective ultimate capacity is then reduced based on the presumption of testing (or no testing) and the appropriate resistance factor. Using these values a 3500 ton factored pier load ( $P_u$ ) would require more or fewer shafts given various resistance factors as shown in Table 7.

\* NOTE: As deeper excavations are possible, the ultimate structural capacity based on concrete strength should not be exceeded.



Table 7. The effect of various design approaches on required number of shafts.

Design Method or Test Scheme	Resistance Factor	Eff. Ult. Capacity @ 90' $P_n$ (tons)	Usable Capacity $\phi P_n$ (tons)	Number of Shafts Required ( $P_u = 3500$ tons)	Total Shaft Costs
Static	0.75	602	451.5	7.75 (8)	\$69,750
Statnamic	0.73	602	439.5	7.96 (8)	\$71,640
No testing	0.55	602	331.1	10.57 (11)	\$116,640

The above shaft costs will also have to incorporate the cost of testing as well. As such, larger projects can justify more extensive testing, whereas very small projects may not warrant the expense. Figure 11 incorporates the cost of testing while extending the above example to a wide range of project sizes (expressed in terms of total structure load and not the number of shafts). The individual curves representing the various design approaches exhibit different slopes based on the permissible load carrying capability per unit length of shaft.

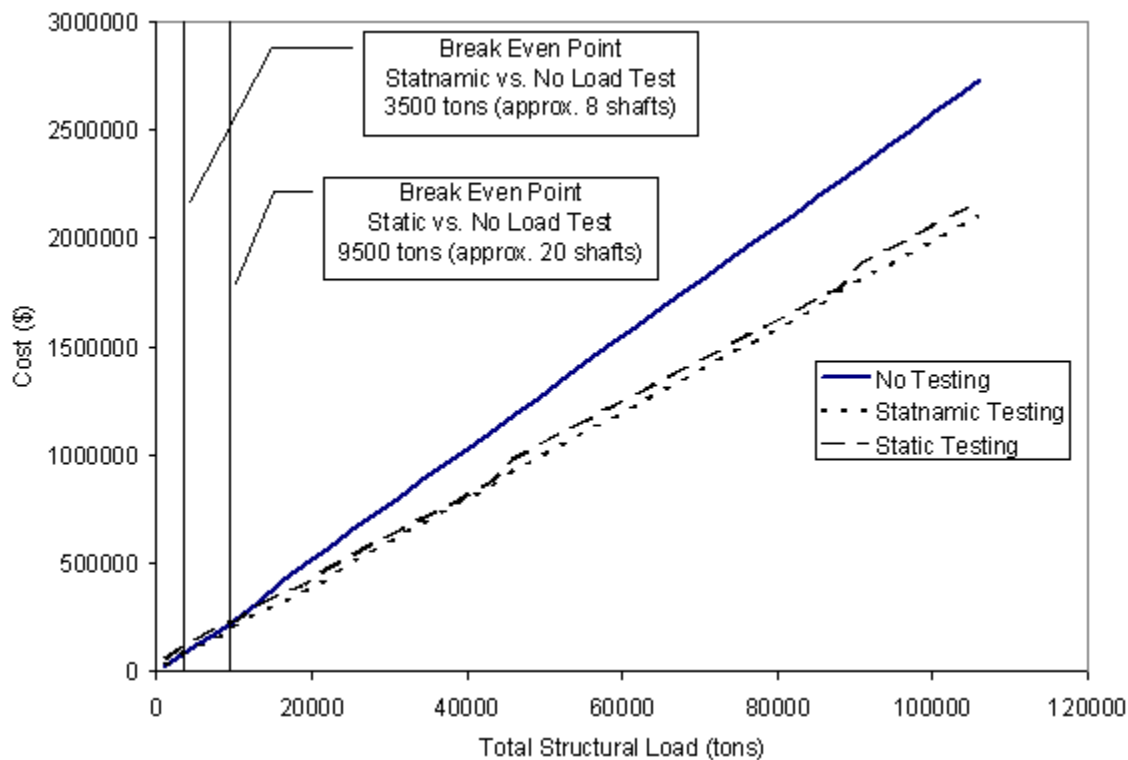


Figure 11 Break even analysis of various design / testing methods.

Comparing the costs for each design and test approach it can be seen that for smaller projects up to 8 shafts (less than 3500 tons total), no testing (over and above SPT) is most cost effective. Above 3500 tons, the cost savings produced by static or static load testing become significant with static costs being slightly less in all cases. The selection of load test method and the associated cost is often based on the availability of test equipment capable of producing the ultimate geotechnical capacity.

Further, the disparity between testing and no testing can be even more drastic when design phase testing can be implemented. Therein, the estimated ultimate capacity based on empirical design methods is often conservative and can be raised using the results of a test program which further widens the range of shaft numbers (testing versus no testing) required for a given pier.

In general, load test results typically show that predictions of ultimate capacity are conservative. This form of verification can be helpful in all instances: when under-predictions are severe, the design capacity of the foundations can be adjusted to provide cost savings; when over-predictions are encountered, more moderate design values can be incorporated to circumvent possible failures.

#### List of Abbreviations

%R	=	percent recovery of rock coring (%)
	=	adhesion factor applied to $S_u$ (DIM)
	=	coefficient relating the vertical stress and the unit skin friction of a drilled shaft (DIM)
$\alpha$	=	SPT N corrected coefficient relating the vertical stress and the unit skin friction of a drilled shaft (DIM)
D	=	diameter of drilled shaft (FT)
$D_b$	=	depth of embedment of drilled shaft into a bearing stratum (FT)
$D_p$	=	diameter of the tip of a drilled shaft (FT)
$\alpha_f$	=	angle of internal friction of soil (DEG)
$f_s$	=	nominal unit side shear resistance (TSF)
	=	unit weight (pcf)
k	=	empirical bearing capacity coefficient (DIM)
K	=	load transfer factor
N	=	average (uncorrected) Standard Penetration Test blow count, SPT N (Blows/FT)
$N_c$	=	bearing capacity factor (DIM)
$N_{corr}$	=	corrected SPT blow count
$q_b$	=	end bearing resistance (units of stress)
$q_c$	=	cone penetration tip resistance (units of stress)
$q_s$	=	average splitting tensile strength of the rock core (TSF)
$Q_s$	=	side shear capacity (units of force)
$q_u$	=	average unconfined compressive strength of the rock core (TSF)
$\sigma'_v$	=	vertical effective stress (TSF)
$S_u$	=	undrained shear strength (TSF)
$\epsilon$	=	measured strain from embedded strain gage

## General References

AASHTO, LRFD Bridge Design Specifications, Customary U.S. Units (2<sup>nd</sup> Edition), American Association of State Highway and Transportation Officials, Washington, D.C., 1998, *w/1999 interim revisions*.

AASHTO, LRFD Bridge Design Specifications, SI (1<sup>st</sup> Edition), American Association of State Highway and Transportation Officials, Washington, D.C., 1994, *w/1996 and 1997 interim revisions*.

ASTM D 0000-99, (submission 2000), "Standard Test Method for Piles Under Rapid Axial Compressive Load." under review at American Society for Testing and Materials, Philadelphia, PA.

ASTM D 1194-94, "Standard Test Method for Bearing Capacity of Soil for Static Load and Spread Footings." American Society for Testing and Materials, Philadelphia, PA.

ASTM D 1586-84, "Standard Method for Penetration Test and Split-Barrel Sampling of Soils." American Society for Testing and Materials, Philadelphia, PA.

ASTM D-1143-98, (1998), "Standard Test Method For Piles Under Static Axial Compressive Load," *Annual Book of ASTM Standards*, Part 20, Philadelphia, PA.

Azizi, Fethi, (2000), "Applied Analyses In Geotechnics," E & FN Spon, New York, NY.

Baker, A. C., and Broadrick, R. L. (1997), "Ground Improvement, Reinforcement, and Treatment: A Twenty Year Update and a Vision for the 21<sup>st</sup> Century," Earth Tech, Clear Water, Florida.

Bolognesi, A. J. L. and Moretto, O. (1973) "Stage Grouting Preloading of Large Piles on Sand" Proceedings of 8<sup>th</sup> ICSMFE, Moscow.

Brown, D. (2001), "Drilled Foundations in Piedmont Residual Soils: Effect of Construction on Axial Capacity," ASCE Journal of Geotechnical and Geoenvironmental Engineering,

Bruce, D.A. (1986), "Enhancing the performance of large diameter piles by grouting," Parts 1 and 2, *Ground Engineering*, May and July, respectively.

Bruce, D. A., Nufer, P. J., and Triplett, R. E. (1995) "Enhancement of Caisson Capacity by Micro-Fine Cement Grouting - a Recent Case History" ASCE Special Publication 57, Verification of Geotechnical Grouting.

Carter, J.P. and Kulhawy, F.H., 1987. "Analysis and Design of Foundations Socketed into Rock." Research Report 1493-4, Geotechnical Engineering Group, Cornell University, Ithaca, New York.

Dapp, S., and Mullins, G., (2002). "Pressure-Grouting Drilled Shaft Tips: Full-Scale Research Investigation for Silty and Shelly Sands," *Deep Foundations 2002: An International Perspective on Theory, Design, Construction, and Performance*, ASCE Geo Institute, GSP No. 116, Vol. I, pp. 335-350.

FHWA, 1998. "Load and Resistance Factor Design (LRFD) for Highway Bridge Substructures." U.S. Department of Transportation, Publication No. FHWA HI-98-032.

Flemming, W. G. K. (1993) "The Improvement of Pile Performance by Base Grouting" Proceedings of the Institution of Civil Engineers, London.

Kulhawy, F.H. and Mayne, P.W., 1990. "Manual on Estimating Soil Properties for Foundation Design." Electric Power Research Institute, Palo Alto, California.

Littlejohn, G. S., Ingle, J., Dadasbilge, K. (1983) "Improvement in Base Resistance of Large Diameter Piles Founded in Silty Sand" Proceedings, *Eighth European Conference on Soil Mechanics and Foundation Engineering*, Helsinki, May.

McVay, M.C. and Townsend, F.C., 1990. "Design of Socketed Drilled Shafts in Limestone." Meyerhof, G.G., 1976. "Bearing capacity and settlement of piled foundations." Proceedings of the

Mullins, G. and O'Neill, M. (2003), "Pressure Grouting Drilled Shaft Tips," Research Report submitted to A.H. Beck Foundation, Inc. May, pp. 198.

Mullins, G., Dapp, S., and Lai, P. (2000), "New Technological and Design Developments in Deep Foundations, Pressure-Grouting Drilled Shaft Tips in Sand," American Society of Civil Engineers, Denver, Colorado.

Mullins, A.G., Dapp, S., Fredrick, E. and Wagner, R., 2000. "Pressure Grouting Drilled Shaft Tips." Final Report submitted Florida Department of Transportation, April, pp.357.

Mullins, G., Dapp, S., Frederick, E. and Wagner, R. (2001), "Pressure Grouting Drilled Shaft Tips," *Final Report* submitted to Florida Department of Transportation, April, pp. 257.

O'Neill, M. W. (1998). "Project 89 Revisited," Proceedings of the ADSC Drilled Shaft Foundation Symposium Held to Honor Dr. Lymon C. Reese, ADSC, Dallas, Texas, January, pp. 7 – 47.

O'Neill, M. W. (2002). Discussion of "Side Resistance in Piles and Drilled Shafts," *Journal of Geotechnical and Geoenvironmental Engineering*, Vol. 127, No. 1, pp. 3-16.

O'Neill, M. W., and Reese, L. C. (1970). "Behavior of Axially Loaded Drilled Shafts in Beaumont Clay," *Research Report No. 89-8*, Center for Highway Research, University of Texas at Austin, December.

O'Neill, M.W. and Hassan, K.M., 1994. "Drilled Shafts: Effects of Construction on Performance and Design Criteria." Proceedings of the International Conference on Design and Construction of Deep Foundations, December 1994, Vol. 1, pp. 137-187.

Reese, L.C. and O'Neill, M.W., 1988. "Drilled Shafts: Construction and Design." FHWA, Publication No. HI-88-042.

Stocker, M.F. (1983), "The influence of post grouting on the load bearing capacity of bored piles,"

Proceedings, *Eighth European Conference on Soil Mechanics and Foundation Engineering*, Helsinki, May.

Touma, F.T. and Reese, L.C., 1974. "Behavior of Bored Piles in Sand." *Journal of the Geotechnical Engineering Division, American Society of Civil Engineers*, Vol. 100, No. GT7, pp. 749-761.

Touma, F. T. (1972). *The Behavior of Axially Loaded Drilled Shafts in Sand*, doctoral dissertation, Department of Civil Engineering, The University of Texas at Austin, December.

TxDOT (1993). *Standard Specifications for Construction of Highways, Streets and Bridges*, Texas Department of Transportation, Austin, March.

# Predicting End Bearing Capacity of Post-Grouted Drilled Shaft in Cohesionless Soils

Gray Mullins, M.ASCE<sup>1</sup>; Danny Winters<sup>2</sup>; and Steven Dapp<sup>3</sup>

**Abstract:** Although pressure grouting beneath the tips of drilled shafts had been used successfully worldwide for close to 4 decades, it has remained relatively unused in the United States in part due to the absence of a rational design procedure. Previous international usage relied predominantly upon experience and unpublished proprietary approaches. More recently, research aimed at quantifying the improvement that could be derived from postgrouting drilled shaft tips has resulted in a design methodology. This paper briefly discusses the postgrouting process and outlines the full scale test programs used to identify parameters affecting postgrouting performance. Correlations developed between applied grout pressure and end bearing improvement are presented along with a numerical example illustrating the design procedure.

**DOI:** 10.1061/(ASCE)1090-0241(2006)132:4(478)

**CE Database subject headings:** Drilled shafts; Bearing capacity; Cohesionless soils; Grouting; Design criteria; Predictions.

## Introduction

The unit ultimate end bearing of drilled shafts tipped in cohesionless soil can be on the order of 20 times the unit ultimate side shear. However, this enormous capacity is rendered virtually unusable due to multiple mechanisms associated with construction techniques and soil mechanics. The two primary construction-related mechanisms that hamper end bearing development include: (1) soil relaxation beneath the shaft tip due to excavation and (2) debris remaining after cleanout. Furthermore, even under ideal shaft construction conditions, ultimate side shear is developed in only a fraction of the displacement required to develop the ultimate end bearing. The side shear fully develops at a displacement between 0.5 and 1.0% of the shaft diameter ( $D$ ); whereas, the end bearing is fully mobilized at displacements of 10–15%  $D$  (Bruce 1986; Mullins et al. 2000). Therefore, the end bearing requires 10–30 times more displacement than side shear in order to mobilize the same percentage of its ultimate value. As a result, engineers typically must discount or significantly reduce the end bearing contribution to the capacity of drilled shafts to accommodate service/displacement limits.

In 1999, a 4 year study was initiated to quantify the effects of pressure grouting beneath the base of drilled shafts and show its

potential to mitigate the above mechanisms plaguing end bearing capacity. This method was expected to be applicable to projects with deep cohesionless deposits where the soil strata would require excessively long drilled shaft lengths without considerable end bearing contribution and in urban areas where vibrations associated with pile driving are not well tolerated. This paper briefly discusses the results from this study and introduces a new design procedure for predicting end bearing capacity in postgrouted drilled shafts tipped in cohesionless soils.

## Background

In the early 1960s, efforts to improve the end bearing of drilled shafts began outside the United States using high pressure grout injected beneath the shaft tip (Bolognesi and Moretto 1973; Gouvenot and Gabiax 1975; Sliwinski and Flemming 1984). Thereafter, numerous case studies have been documented stating its effectiveness. This end bearing modification technique, also called postgrouting or base grouting, has been used worldwide, yet literature on its use lacks a rational design approach. As a consequence, there has been little use in the United States. As this paper focuses on the design of the end bearing capacity, a thorough overview of postgrouting processes can be found elsewhere (Bruce 1986; Mullins et al. 2000).

In general, the postgrouting technique involves casting drilled shafts with a grout delivery system incorporated into the reinforcing cage capable of placing high pressure grout at the base of the shaft (after the shaft concrete has cured). This both densifies the in situ soils and compresses any debris left by the drilling process. Moreover, by preloading the soil beneath the tip, end bearing capacity can be developed within service/displacement limits. In previous studies, it was suggested that pressure-grouted shafts tipped in loose to medium dense sand provided the most benefit, but improvement was observed in all soil types cited. Specifically, end bearing could be improved in sands and clays with ultimate capacities as much as two to three times conventional ungrouted shafts (Bruce 1986). The same sources purported end bearing improvement to be dependent on the volume of grout injected.

<sup>1</sup>Associate Professor, Dept. of Civil and Environmental Engineering, Univ. of South Florida, 4202 E. Fowler Ave., ENB 118, Tampa, FL 33620 (corresponding author). E-mail: gmullins@eng.usf.edu

<sup>2</sup>Research Associate, Dept. of Civil and Environmental Engineering, Univ. of South Florida, 4202 E. Fowler Ave., ENB 118, Tampa, FL 33620. E-mail: dwinters@eng.usf.edu

<sup>3</sup>Principal, Dan Brown & Associates, 300 Woodland Rd., Sequatchie, TN 37374. E-mail: sdapp@danbrownandassociates.com

Note. Discussion open until September 1, 2006. Separate discussions must be submitted for individual papers. To extend the closing date by one month, a written request must be filed with the ASCE Managing Editor. The manuscript for this paper was submitted for review and possible publication on March 16, 2005; approved on August 11, 2005. This paper is part of the *Journal of Geotechnical and Geoenvironmental Engineering*, Vol. 132, No. 4, April 1, 2006. ©ASCE, ISSN 1090-0241/2006/4-478-487/\$25.00.



$$GP_{\max} = 4q_s L/D \quad (3)$$

where  $GP_{\max}$  = maximum predicted grout pressure;  $q_s$  = unit side shear; and  $L/D$  = shaft length to diameter ratio.

From a more practical perspective, several ranges are also identified in Fig. 2 that denote applicable limits on grout pressure. The lines denoting unit side shear values present upper bounds on grout pressure for shafts constructed in soils with average unit side shear values of 0.05, 0.1, and 0.2 MPa (0.5, 1.0, and 2.0 tsf). For all soils and  $L/D$  ratios, an upper limit on grout pressure is typically applied that considers the construction limitations of the grout pump, grout tubes, or the working life of the neat cement grout. Although pressures as high as 11 MPa (1,600 psi) are attainable, a 6.9 MPa (1,000 psi) upper limit is more realistic without having to use specialized equipment.

An example lower limit is also presented that represents the hydrostatic pressure of wet concrete for a 1 m diameter shaft. Assigning a grout pressure at or below this level does not provide a benefit worthy of the effort. Although in some instances the process of merely flushing grout through the tubes and grouting cell has shown grout volume taken into soft areas or unexpected voids, far more can be derived from a pressure grouting protocol that takes full benefit from an optimized design.

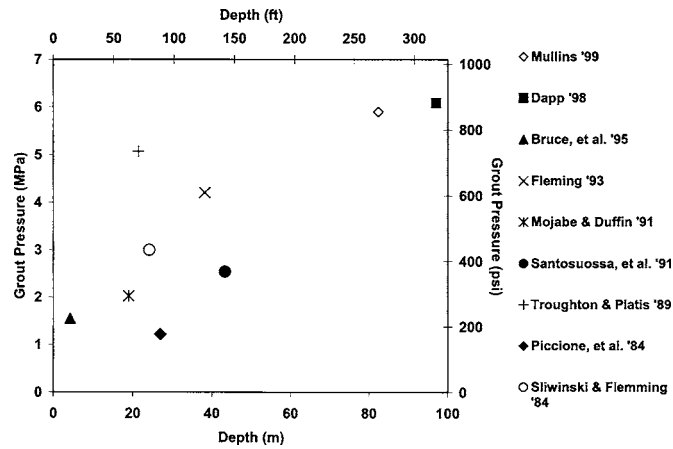


**Fig. 1.** Published grout pressure versus depth prior to this research program [Mullins (1999); Dapp (1998); Bruce et al. (1995); Fleming (1993); Mojabe and Duffin (1991); Santosuosso et al. (1991); Troughton and Platis (1989); Piccione et al. (1984); Sliwinski and Flemming (1984)]

However, the improvement was shown to be more directly related to grout pressure by the authors and forms the basis of the new design method.

During base grouting, the grout pressure produces a bidirectional force at the shaft tip, wherein the development of the end bearing is resisted by the skin friction of the shaft. Hence, longer shafts or shafts that develop more side shear can resist higher grout pressure. Previous studies that cited both the applied grout pressure and shaft length (or depth) show an increasing trend of grout pressure with depth (Fig. 1). This is in keeping with the understanding that the maximum grout pressure is dependent on the available side shear on which the grout pressure can react.

In concept, the anticipated grout pressure for a given site can be generalized with respect to the shaft length, diameter, and the average unit side shear (Fig. 2). As the grout pressure is a function of tip area, unit side shear, and shaft length, the expression for anticipated grout pressure can be simplified as follows:

$$GP_{\max} = \text{side shear force}/\text{tip area} \quad (1)$$

$$GP_{\max} = (q_s \pi DL)/(\pi D^2/4) \quad (2)$$

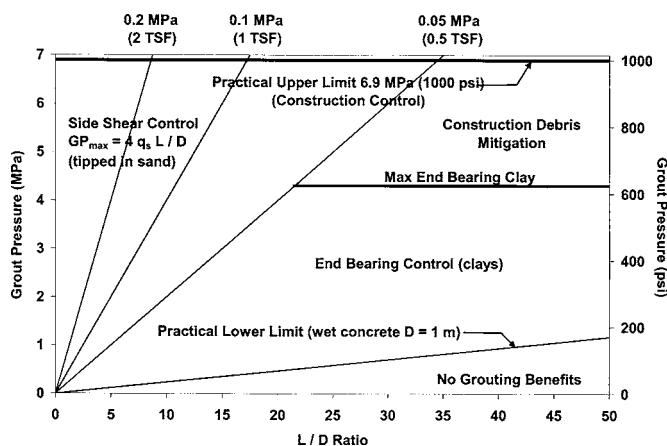


**Fig. 2.** Concept graph of pressure versus depth

## End Bearing Development

Reese and O'Neill (1988) showed that the end bearing capacity of conventional ungrouted shafts could be expressed as a function of shaft diameter and the permissible settlement (Fig. 3). Therein, the ultimate design capacity based on 5% displacement was given by

$$q_b = 0.057N \quad (4)$$

where  $q_b$  = ultimate unit end bearing capacity (MPa); and  $N$  = uncorrected standard penetration test (SPT) blow count.

At displacements less than 5%  $D$ , a reduced capacity should be assigned using a tip capacity multiplier (TCM < 1) based on the above relationship and the permissible displacement; at larger

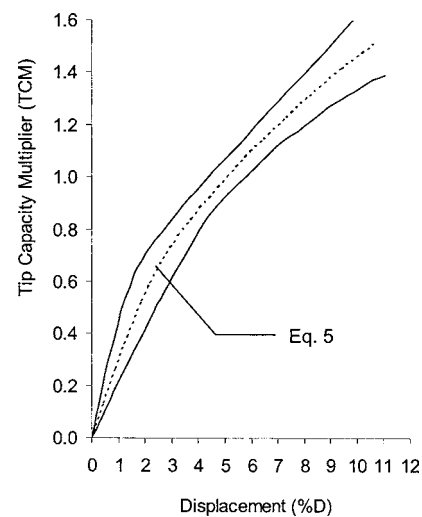


**Fig. 3.** Usable end bearing as function of permissible displacement (adapted from Reese and O'Neill 1988)

displacements beyond 5% *D* even more end bearing can be developed (TCM > 1). Eq. (5) provides a convenient curve fit for the TCM trend shown in Fig. 3

$$TCM = \frac{\%D}{0.4(\%D) + 3.0} \quad (5)$$

TCM values greater than 1.0 corroborate Bruce's (1986) statement that shafts tipped in sand could continue to develop capacity up to 15% *D*. Unfortunately, large displacements such as these are rarely permissible due to service limits. For example, a 1.2 m (4 ft) diameter shaft would have to displace 61 mm (2.4 in.) in order to achieve ultimate capacity; whereas the side shear would develop in 6–12 mm (0.24–0.48 in.), shown in Fig. 4. At full side shear development, only about a third of the design end bearing has been developed. As an alternate, postgrouting beneath the shaft tip provides a method to avail higher usable end bearing at more reasonable displacements.

### Effects of Side Shear Capacity on Grout Pressure

The grout pressure required to affect end bearing improvement in cohesionless soil is dependent on the available side shear. As such, uplift of the shaft is possible as the force from the applied grout pressure over the area of the toe approaches the ultimate side shear capacity. At this point, the grout pressure has both displaced/compressed the soil beneath the toe and strained the side shear in uplift. Depending on whether the grout pressure is maintained or released during the curing of the grout, two stress states may exist. Figs. 5 and 6 conceptually show the load history of the side shear and soil beneath the toe during the grouting and structural loading phases for maintained and released grout pressure, respectively. Four points are highlighted on each graph showing pertinent phases: Point (1), the initial unstressed state; Point (2), the maximum applied grout pressure; Point (3), the grout cured, prior to structural loading; and Point (4), after structural loading assuming a 1% *D* settlement. Although the mechanism by which the load is transferred into the soil is significantly different for the two approaches, the net effect is virtually identical with regards to load carrying capabilities.

When the grout pressure is maintained or locked-in during curing (Fig. 5), the toe load required to hold the shaft in negative

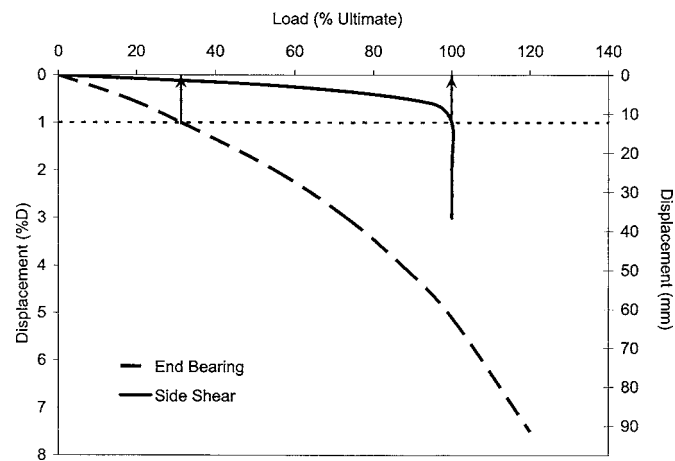


Fig. 4. Typical displacement mismatch between end bearing and side shear

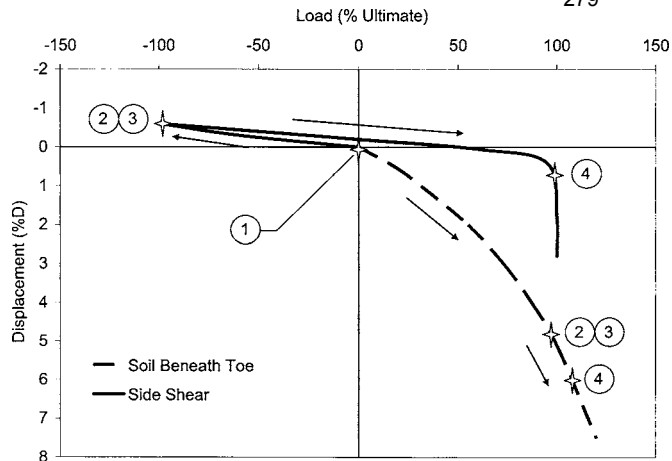


Fig. 5. Conceptual load/displacement history for locked-in grout pressure

side shear increases slightly as applied structural loads overcome the negative side shear (small displacements). In effect, the side shear load required to hold the soil beneath the toe in compression is replaced by the structural loading until the negative side shear is completely overcome, after which, additional load can be developed by positive side shear and a further increase in end bearing. The load carrying mechanism from precompressing the toe soils is analogous to pretensioning bolts used for tensile loading. Therein, bolts are commonly pretensioned during installation to over 90% of the usable capacity. This causes a clamping force that equals the sum of the bolt group pretensioning. The tensile loads in the bolts remain the same throughout the life of the connection but are ultimately resisted by a combination of structural loads and clamping forces. If the structural loads exceed the initial clamping force, plate separation occurs and the remaining 10% of the bolt capacity can be mobilized as needed up to the ultimate load. Fig. 7 shows the similarities between postgrouted shaft tips and a bolted tension connection (the bolt analogy is explained in italics).

When the grout pressure is released before curing or unlocked (Fig. 6), the soil beneath the toe is loaded normally during grouting, allowing large precompressing displacements to occur followed by a relatively stiff unloading. The side shear is stressed

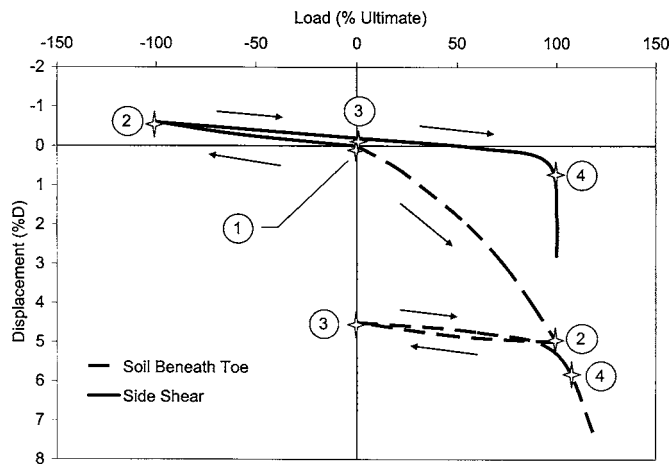


Fig. 6. Conceptual load/displacement history for unlocked grout pressure

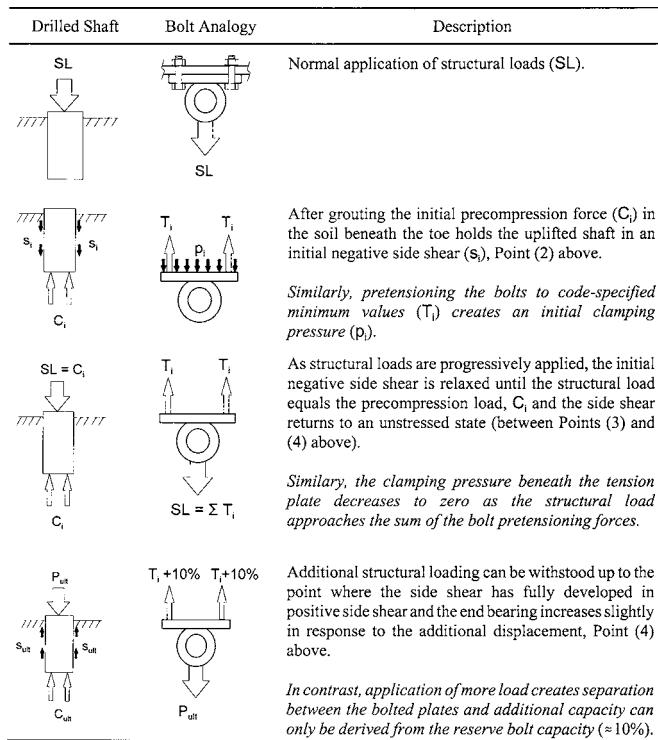


Fig. 7. Comparison of bolt pretensioning to shaft tip precompression

upward and returned to its unstressed state. Upon application of structural loading, the side shear develops normally (acting upward) while the end bearing is reloaded along a much stiffer path where the displacement required to fully develop the end bearing is commensurate with that of the side shear.

Minimal differences have been observed in the resultant capacity from these two mechanisms (Frederick 2001; Mullins and Winters 2004). In reality, some relaxation occurs in the soil beneath the toe even when the pressure is locked in. Consequently, the actual response in these cases reflects a combination of both scenarios.

The design method presented herein stems from a database of 26 grouted and ungrouted test shafts tipped in sand, silt, and clay at eight different sites which incorporated both locked-in and unlocked approaches. Five of these sites had shafts tipped in sand,

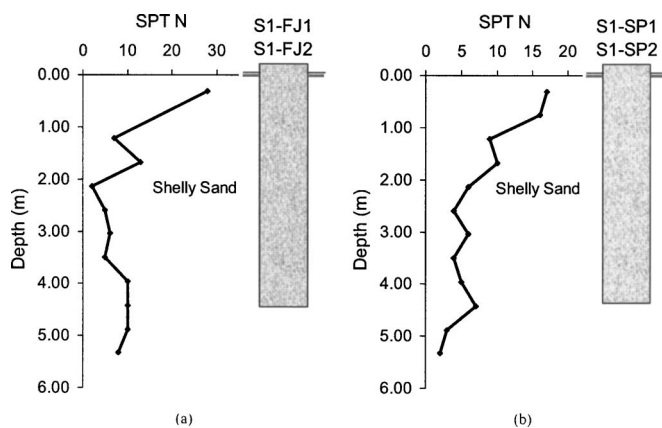


Fig. 8. Soil boring logs for site I (a) flat-jack and (b) sleeve-port test shafts

silty sand, shelly sand, or slightly cemented sand. This paper focuses on the improvement in cohesionless soils. Therefore, a discussion of the sites in cohesive soils is not presented within this paper.

## Full-Scale Field Study

The research program consisted of both model-scale and full-scale testing. Model-scale testing was carried out within a frustum confining vessel and explored parameters affecting postgrouting performance and cavity expansion where the shafts could be easily exhumed (Frederick 2001; Mullins et al. 2001; Dapp 2002; Mullins and Winters 2004). The objective of the field studies were threefold: (1) to quantify the improvement that could be developed by pressure grouting the tip of the shaft; (2) to develop design recommendations for the use of pressure grouting drilled shaft tips; and (3) to establish criteria/guidelines for effective grouting. Although, the majority of sites included a control shaft (conventional, with no postgrouting), the response of the grouted shafts was also compared to end bearing design capacity predictions from soil boring logs (i.e., AASHTO 1999).

Two different grout distribution systems were used throughout the study: the flat jack and the sleeve port (also known as tube-a-manchette). Each system has associated advantages, but both provided similar end bearing improvement. A full discussion of these systems can be found elsewhere (Mullins et al. 2001; and Dapp 2002). The ensuing sections outline the site conditions and load test results for each of the sites where shafts were tipped in sandy soils.

### Sites I and II: Clearwater, Fla.

A total of eight shafts were constructed and tested within two adjacent sites located in Clearwater, Fla. These shafts each had a diameter of 0.61 m (2.0 ft) and were 4.57 m (15 ft) in length. Five shafts, including one control shaft, were tested in Site I (loose to medium dense shelly sand); while three shafts, including one control shaft, were tested in Site II (loose silty sand). Soil exploration involved minicone ( $2.5 \text{ cm}^2$ ) and full-size ( $10 \text{ cm}^2$ ) cone penetration soundings as well as standard penetration testing. The minicone was used to quickly delineate site variability, the  $10 \text{ cm}^2$  cone was used at each shaft location, and the SPT borings were conducted between the shaft locations. Excavation was conducted using polymer slurry for stabilization. Full details

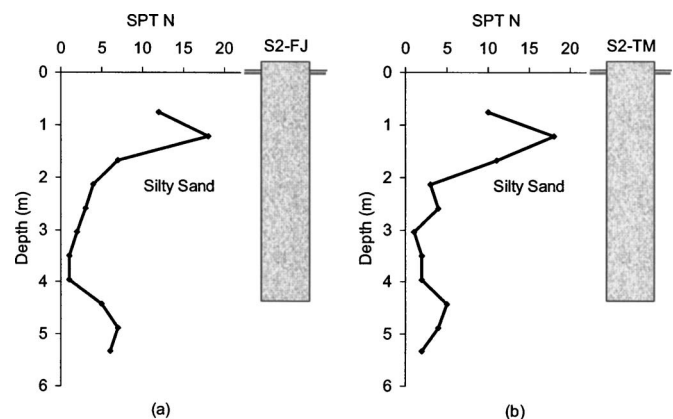


Fig. 9. Site II soil boring logs for test shafts (a) S2-FJ and (b) S2-TM

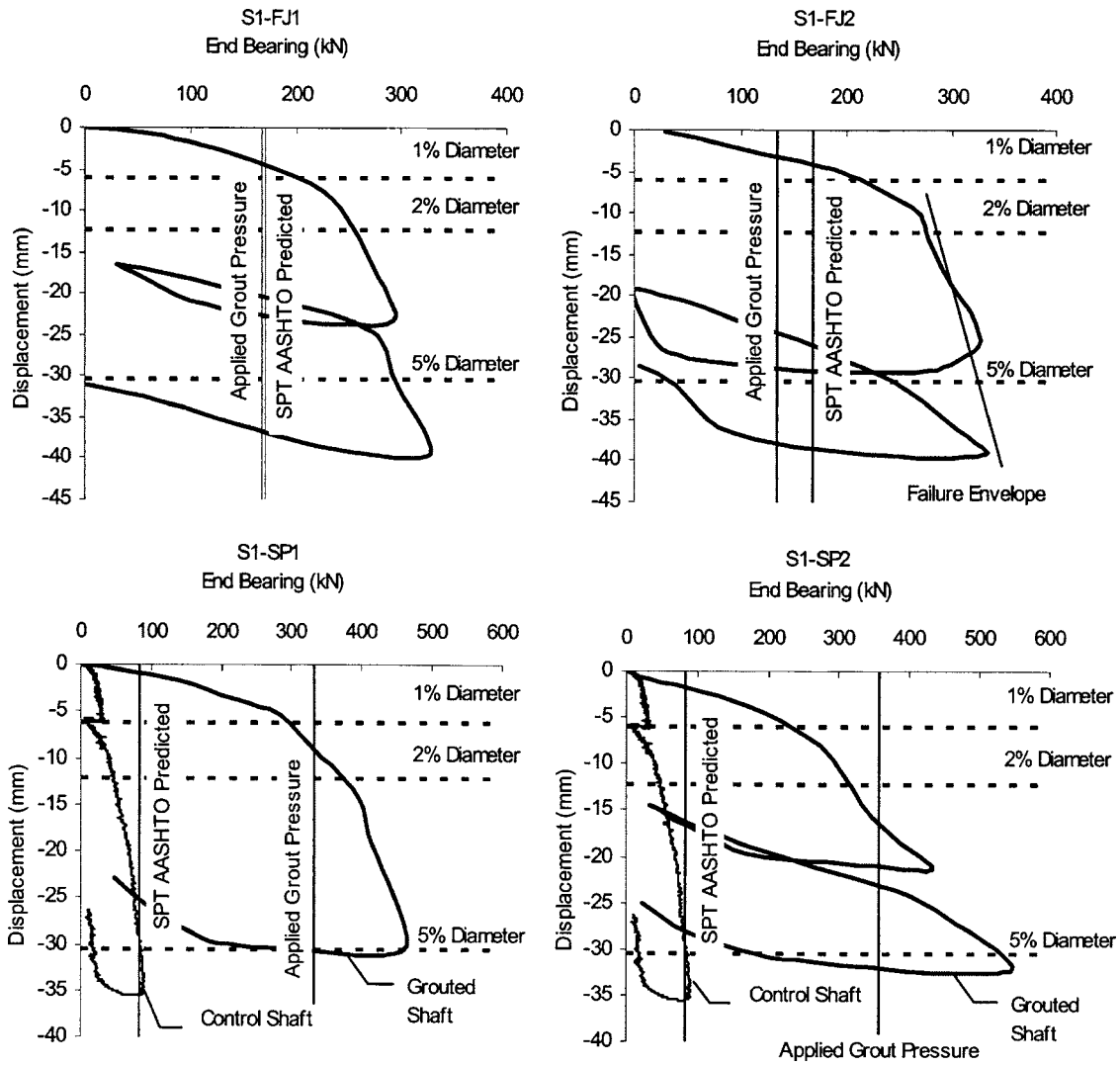


Fig. 10. Load test results for site I

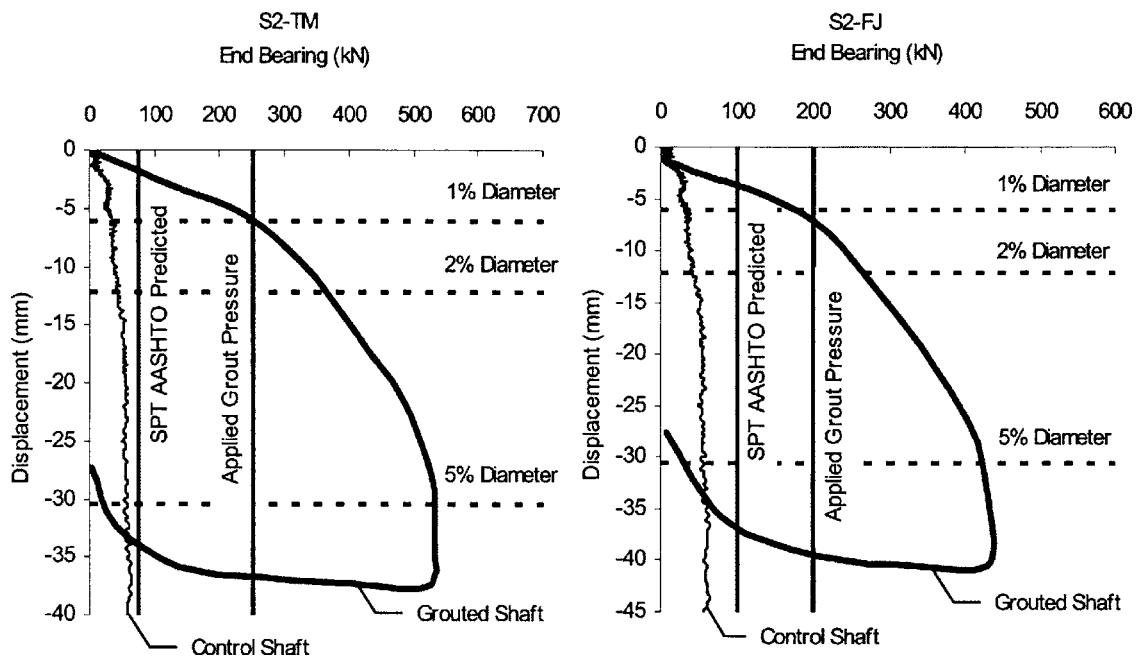


Fig. 11. Load test results for site II

**Table 1.** Full-Scale Field Study Results

Shaft I.D.	$q_p$ Ultimate <sup>a</sup> (kPa)	Grouted capacity TCM			Applied grout pressure (kPa)	GPI
		1% <i>D</i>	2% <i>D</i>	5% <i>D</i>		
S1-FJ1	574	1.22	1.50	1.79	586	1.02
S1-FJ2	574	1.21	1.67	1.91	462	0.80
S1-SP1	287	3.48	4.44	5.51	1,138	3.96
S1-SP2	287	3.09	4.06	6.18	1,220	4.25
S2-FJ	344	1.69	2.58	4.18	683	1.98
S2-TM	258	3.33	4.72	7.09	862	3.34
S3-LT3	2,178	0.60	N/A <sup>b</sup>	N/A <sup>b</sup>	3,447	1.58
S4-LT2	630	3.15	4.40	5.84	5,240	4.68
S5-S2	3,969	1.05	1.30	1.63	1,157	0.69

<sup>a</sup>Reese and O'Neill (1988) [Eq. (4)].

<sup>b</sup>Unable to fully mobilize test shaft during testing (see Fig. 12).

can be found elsewhere (Mullins et al. 2000; 2001; Dapp and Mullins 2002). Figs. 8 and 9 show the soil profiles for Sites I and II, respectively. Likewise, Figs. 10 and 11 show the load-displacement responses for each test shaft for the two sites as well as the applied grout pressure load and AASHTO predicted end bearing values. In each graph the capacities at displacements of 1, 2, and 5% *D* are indicated for future reference (also provided in Table 1).

#### Site III: Palm Beach, Fla.

Three test shafts, grouted and ungrouted, were constructed and tested in slightly cemented coquina sand located at the Royal Park Bridge crossing the Intracoastal waterway in Palm Beach, Fla. One of these shafts, LT-3, was a 1.22 m (4.0 ft) diameter, 34.80 m (114.2 ft) long grouted shaft. A combination of temporary and permanent casing was used with a sea water drill slurry. Fig. 12

shows the SPT soil boring and the end bearing results for LT-3. Additional information for Site III can be found in Dapp and Mullins (2002).

#### Site IV: West Palm Beach, Fla.

Two test shafts, grouted and ungrouted, were constructed and load tested as part of the PGA Blvd Grade Separation Bridge Project in West Palm Beach, Fla. The load test program for this site revolved around the relative end bearing performance of two 0.91 m (3 ft) diameter, 18.3 m (60 ft) long test shafts constructed in loose to medium dense shelly sand. Test shaft LT-1 served as the ungrouted control while LT-2 was grouted. Each shaft was constructed with a mineral slurry. A SPT boring was performed at the centerline of each test shaft. The SPT soil boring and end bearing results for LT-2 are shown in Fig. 13.

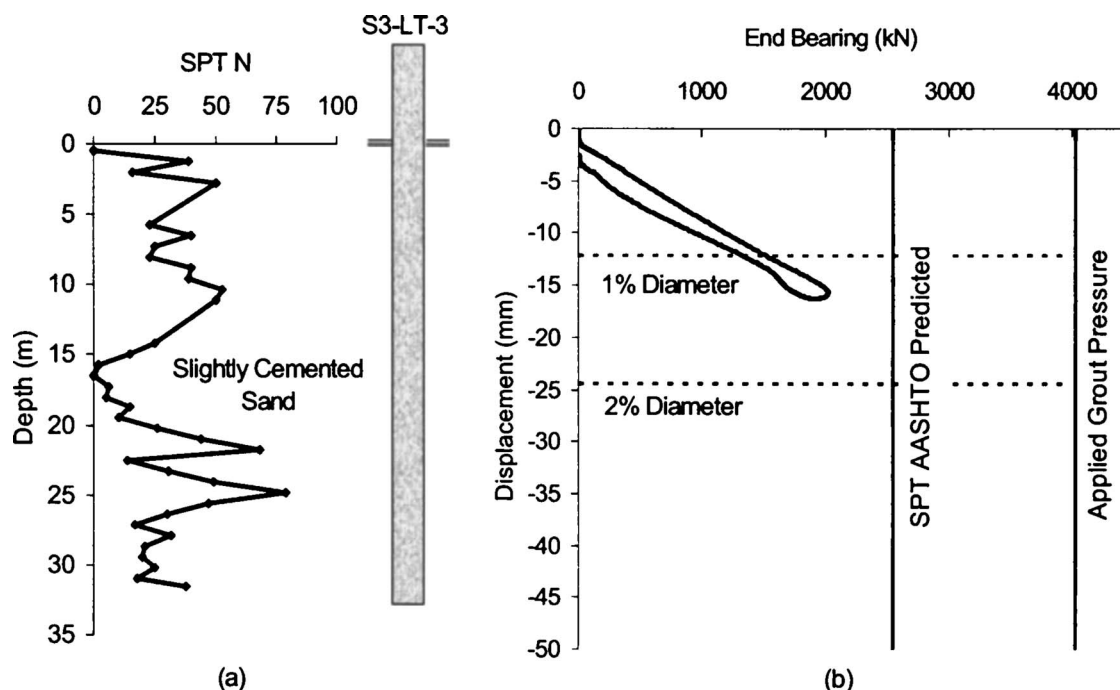


**Fig. 12.** Site III (a) soil boring log and (b) end bearing load test results for test shaft LT-3



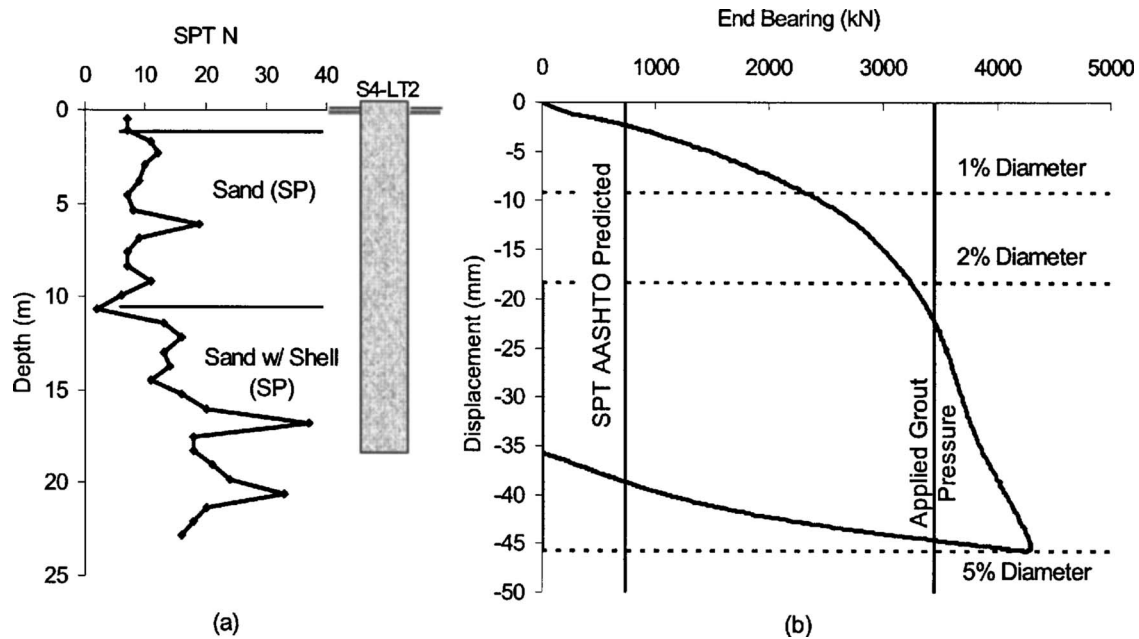


Fig. 13. Site IV (a) soil boring log and (b) end bearing load test results for test shaft LT-2

#### Site V: Houston, Tex.

Testing at Site V (dense sand) was a collaboration between the Univ. of Houston (UH) and the Univ. of South Florida (USF) to demonstrate to the Texas Department of Transportation the effectiveness of post grouting drilled shafts in soils native to the Houston region. A total of four 1.22 m (4.0 ft) diameter drilled shafts were constructed. A target load of 17.8 MN (2,000 t) was used in determining the shaft lengths. Two shafts were tipped in sandy soil while the other two shafts were tipped in clayey soil. Each pair of test shafts included a control shaft and a grouted shaft. The subsurface investigation of the test site was performed using three primary methods of exploration: standard penetration

tests (SPT); Texas cone penetration tests (TCP); and cone penetration tests (CPT). All shafts were constructed using mineral slurry. Fig. 14 shows the SPT soil boring and load test results for test shaft S-2 (tipped in sand and grouted). A full geological and load test discussion for this site can be found in Mullins and O'Neill (2003).

#### End Bearing Results

Many design methodologies exist for the calculation of drilled shaft tip capacities in sandy soils. For example, AASHTO (1999) presents four methods from which this determination can be

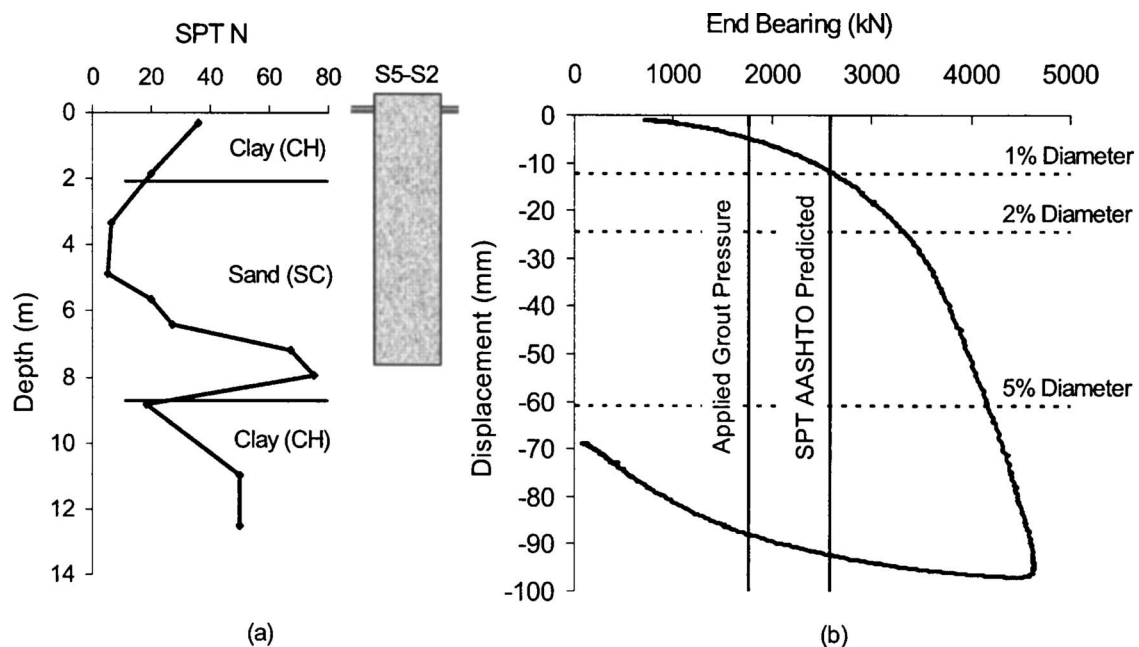


Fig. 14. Site V (a) soil boring log and (b) end bearing load test results for test shaft S-2



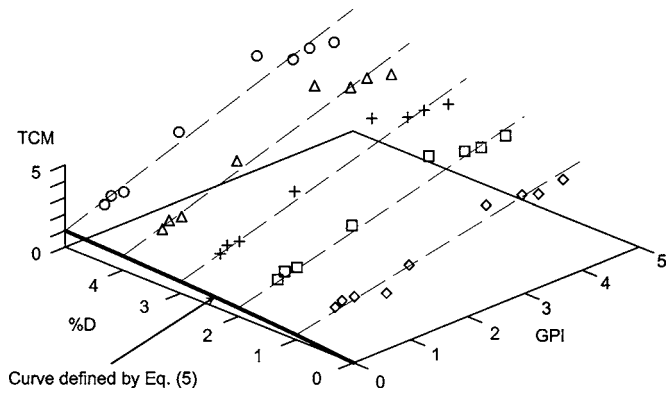


Fig. 15. Full-scale field study results

made. These methods vary in the required parameters but use either SPT  $N$  values, the relative density state, and/or the depth of embedment expressed as a multiple of the diameter to calculate the end bearing capacity. An important aspect of this capacity determination is the displacement at which the capacity will be developed. Some methods clearly state this criterion as a percentage of the shaft diameter or as some service limit displacement (e.g., 5% of  $D$ , or 1 in.), while other methods do not.

This research project used the Reese and O'Neill (1988) method [Eq. (4)] to predict the ultimate end bearing capacity from SPT values as well as load test data. Table 1 provides details from each of the full-scale grouted test shafts expressed as a multiple of the Reese and O'Neill predicted capacity. The end bearing improvement is given in terms of the tip capacity multiplier (TCM), for the measured end bearing at 1, 2, and 5%  $D$  displacements. As the end bearing improvement is dependent on the applied grout pressure, the grout pressure is also listed both dimensionally (in kPa) and nondimensionally [as the grout pressure index (GPI)]. The GPI is defined as a nondimensional ratio of the applied grout pressure to the ungrouted end bearing at a displacement of 5%  $D$  [Eq. (4)]. The applied grout pressure was taken as the maximum sustained grout pressure and not a short duration pressure spike.

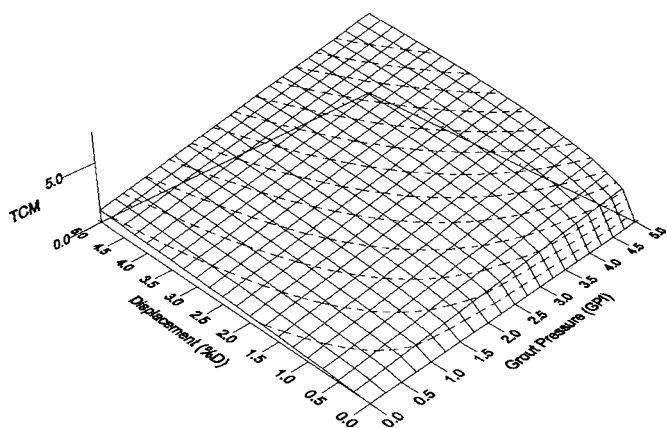


Fig. 16. Surface defined by TCMs derived from load test data dependent on grout pressure and displacement

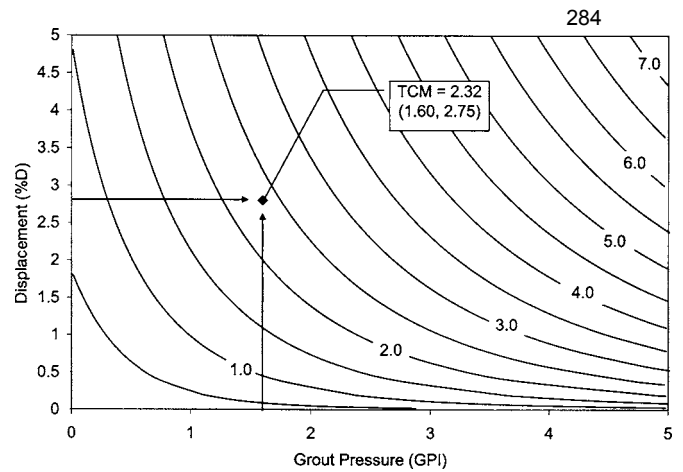


Fig. 17. TCM contours easily adapted for design applications

### Design of Postgrouted Tip Capacity

To quantify the improvement with respect to standard design practice, a predictive approach was established on the basis of the TCM and the GPI. The TCM was defined as a function of displacement and grout pressure. By plotting the results from Table 1 (Fig. 15), a surface can be defined that incorporates both the effects of grout pressure and permissible displacement (Fig. 16). Dashed lines in Fig. 16 show lines of constant TCM while solid lines show lines of constant displacement and grout pressure.

The plane defined by the displacement and TCM axes intersects the surface forming a hyperbolic relationship identical to the centerline trend that Reese and O'Neill published in 1988 shown in Figs. 3 and 15. Therein, when the GPI=0 no improvement is expected and it therefore predicts the same capacity as an ungrouted shaft. Likewise, when the permissible displacement approaches zero, so does the predicted mobilized capacity. A more usable form of this surface is given in Fig. 17 which shows the TCM contours. Given the GPI and displacement, the TCM can be estimated using Fig. 17 or with the following empirical relationship:

$$\text{TCM} = 0.713(\text{GPI})(\%D)^{0.364} + \frac{\%D}{0.4(\%D) + 3.0} \quad (6)$$

The surface defined by Fig. 16 is nonlinear with respect to  $\%D$  but linear with respect to variations in GPI. As the GPI and the TCM are both ratios based on the ungrouted end bearing, both the TCM and GPI increase or decrease similarly dependent on the ungrouted end bearing selected. Therefore, the TCM is only mildly affected by the method of determining the ungrouted end bearing. At high GPI values and low  $\%D$  values, the TCM is insensitive to the ungrouted prediction method. As GPI approaches zero, the grouted end bearing approaches the ungrouted capacity and therefore is subject to the conservatism or unconservatism associated with whatever method was used to estimate the ungrouted capacity.

### Design Procedure

For a given shaft diameter and embedment length, the method for estimating the unit end bearing of grouted shafts involves the following steps:

1. Calculate the ungrouted end bearing capacity at 5%  $D$  displacement,  $q_{p\_Ultimate}$ .
2. Calculate the ultimate side shear resistance,  $F_s$ , for the total length of embedded shaft.
3. Divide the ultimate side shear resistance by the cross-sectional area,  $A$ , of the shaft to determine the maximum anticipated grout pressure,  $GP_{max}$

$$GP_{max} = \frac{F_s}{A} \quad (7)$$

4. Calculate the GPI as the ratio of the maximum anticipated grout pressure (Step 3) to the ungrouted unit tip resistance (Step 1)

$$GPI = \frac{GP_{max}}{q_{p\_Ultimate}} \quad (8)$$

5. Establish the maximum permissible service displacement as a ratio of the shaft diameter, % $D$ .
6. Determine the tip capacity multiplier given the grout pressure index (Step 4) and the permissible displacement (Step 5) using Fig. 17 or Eq. (6).
7. Estimate the grouted unit tip resistance as the product of the tip capacity multiplier (Step 6) and the ultimate ungrouted end bearing capacity (Step 1)

$$q_{grouted} = (TCM)(q_{p\_Ultimate}) \quad (9)$$

For example, a 0.91 m (3 ft) diameter drilled shaft with an ultimate side shear resistance of 1,780 kN (200 t) will have a grouted end bearing capacity of 3.97 MPa (41.8 tsf). This is with a permissible shaft displacement of 25 mm (1 in.) and an ungrouted end bearing capacity of 1.71 MPa (18 tsf) using Eq. (4) ( $N=30$ ).

## Summary and Conclusions

A rational method of predicting the end bearing capacity of post-grouted shafts tipped in cohesionless soils has been developed based on the performance of full scale grouted shaft load tests. The new approach incorporates input parameters such as the service displacement criteria, the attainable grout pressure, and the estimated conventional ungrouted shaft end bearing. Unlike conventional shaft construction and the associated quality assurance methodologies, each and every shaft is tested via the grouting process. Inherently, the grouting then provides quantitative data on the skin friction and end bearing capacity of each shaft. Therefore, grouting verifies a lower limit of total shaft capacity that equals two times the grout pressure acting over the entire tip area. The actual capacity, which is predicted using Eq. (9), is somewhat higher due to an increase in the mobilized end bearing during downward structural loading and the ~30% increase in side shear from downward instead of upward movement (O'Neill 2002).

As the attainable GPI relies on the side shear capacity on which the grout pressure can react, the aspect ratio (embedment length/diameter) of the drilled shafts should be carefully considered in order to provide the most cost efficient design. Note that potentially stringent lateral loading conditions may govern the foundation design, and may further define the shaft geometry that best supplies the capacities required (both axial and lateral). The methodology presented herein only addresses axial capacity.

The use of grouted shafts has long reaching implications with regards to the state of drilled shaft construction and design. This stems from the unparalleled quality assurance that accompanies

the process. Shaft lengths can be reduced and an associated cost savings realized. Further, by statically grout testing each shaft, an increased resistance factor (or lower safety factor) may likely result for shafts constructed in this fashion. Such an increase in the resistance factor can lead to additional economy.

## Acknowledgments

The writers would like to acknowledge the Florida Department of Transportation for funding this study with specific thanks extended to Mr. Peter Lai, the project monitor. Likewise, Auburn University and University of Houston as well as Applied Foundation Testing, Beck Foundation, Coastal Caisson, Driggers Engineering Services, EarthTech, and TreviIcos South are gratefully recognized for their contributions. Therein, Dr. Dan Brown, Dr. Michael O'Neill, Mr. Michael Muchard, Mr. Keith Anderson, Mr. Bud Khouri, Mr. Jaime Driggers, Mr. Ron Broderick, and Mr. Michael Rossie are extended the writers' deepest thanks as well as Rudy, Ltd.

## References

- American Association of State Highway and Transportation Officials (AASHTO). (1999). *LRFD bridge design specifications*, SI, 1st Ed., Washington, D.C.
- Bolognesi, A. J. L., and Moretto, O. (1973). "Stage grouting preloading of large piles on sand." *Proc., 8th ICSMFE Cont.*, Moscow.
- Bruce, D. A. (1986). "Enhancing the performance of large diameter piles by grouting." Parts 1 and 2, *Ground Eng.*, May and June.
- Bruce, D. A., Nufer, P. J., and Triplett, R. E. (1995). "Enhancement of caisson capacity by microfine cement grouting—A recent case history." *Verification of geotechnical grouting*, M. J. Byle and Roy H. Borden, eds., ASCE, New York, 142–152.
- Dapp, S. D. (1998). "Interviews with engineers during load testing on the My Thuan Bridge." Mekong Delta, Vietnam.
- Dapp, S. D. (2002). "Pressure grouting of drilled shafts in sands," PhD dissertation, Univ. of South Florida, Tampa, Fla.
- Dapp, S., and Mullins, G. (2002). "Pressure grouting drilled shaft tips: Full-scale research investigation for silty and shelly sands." *Deep Foundations 2002: An international perspective on theory, design, construction, and performance, Geotechnical Special Publication No. 116*, M. W. O'Neill and F. C. Townsend, eds., Vol. 1, ASCE, Reston, Va., 335–350.
- Flemming, W. G. K. (1993). "The improvement of pile performance by base grouting." *Proc., Institution of Civil Engineers*, London.
- Frederick, E. M. (2001). "Pressure grouting drilled shaft tips: Laboratory scale study in a frustum confining vessel." Master's thesis, Univ. of South Florida, Tampa, Fla.
- Gouvenot, D., and Gabiax, F. D. (1975). "A new foundation technique using piles sealed by concrete under high pressure." *Proc., 7th Annual Offshore Technical Conf.*
- Mojabe, M. S., and Duffin, M. J. (1991). "Large diameter, rock socket, base grouted piles in bristol." *Proc., 4th Int. Conf. on Piling and Deep Foundations*, Stresa, Italy.
- Mullins, G. (1999). "Interviews with engineers during load testing on the Taipei Financial Center." Taipei, Taiwan.
- Mullins, G., Dapp, S., Frederick, E., and Wagner, R. (2001). "Pressure grouting drilled shaft tips—Phase I final report." *Final Rep. Submitted Florida Department of Transportation*, Fla.
- Mullins, G., Dapp, S., and Lai, P. (2000). "Pressure-grouting drilled shaft tips in sand." *New technological and design developments in deep foundations*, N. D. Dennis, R. Castelli, and M. W. O'Neill, eds., ASCE, Reston, Va.

- Mullins, G., and O'Neill, M. (2003). "Pressure grouting drilled shaft tips—A full-scale load test program." *Research Rep.*, Univ. of South Florida, Tampa, Fla.
- Mullins, G., and Winters, D. (2004). "Post grouting drilled shaft tips—Phase II final report." *Final Rep. Submitted Florida Department of Transportation*, Fla.
- O'Neill, M. W. (2002). "Discussion of Side resistance in piles and drilled shafts," *J. Geotech. Geoenviron. Eng.*, 127(1), 3–16.
- Piccione, M., Carletti, G., and Diamanti, L. (1984). "The piled foundations of the Al Gazira Hotel in Cairo." *Proc., Int. Conf. on Advances in Piling and Ground Treatment for Foundations*, Institution of Civil Engineers, London.
- Reese, L. C., and O'Neill, M. W. (1988). "Drilled shafts: Construction and design." *FHWA, Publication No. HI-88-042*.
- Santosuossa, M., Rizzi, G., and Diamanti, L. (1991). "Construction of pile foundation of the postal citadel in the direction center of Naples." *Proc., 4th Int. Conf. on Piling and Deep Foundations*, Stresa, Italy.
- Sliwinski, Z. J., and Flemming, W. G. K. (1984). "The integrity and performance of bored piles." *Proc., Int. Conf. on Advances in Piling and Ground Treatment for Foundations*, Institution of Civil Engineers, London.
- Troughton, V. M., and Platis, A. (1989). "The effects of changes in effective stress on a base grouted pile in sand." *Proc., Int. Conf. on Piling and Deep Foundations*, London.

# A Demonstration of Underwater FRP Repair

A water-activated resin matrix is used to repair piles

BY GRAY MULLINS, RAJAN SEN, KWANG SUK SUH, AND DANNY WINTERS

In the tropical climates of the Southeastern United States, concrete piles exposed to tidal waters are highly prone to corrosion-induced damage. Chlorides from seawater penetrate the concrete cover and destroy the passive layer that normally protects steel from corrosion. The high temperatures and high humidity in this region accelerate the corrosion process, leading, in some cases, to signs of visible damage within as little as 18 months.

Jacketing, in which concrete is cast around the damaged pile, is the most common method of pile repair (Fig. 1). Typically, stay-in-place fiberglass forms are used, and the annular concrete inside the form is reinforced if damage is severe. Unfortunately, such repairs have proven ineffective, as the corrosion process is not stopped, and the opaque jacket and form prevent inspectors from detecting corrosion activity during routine biennial inspections. As a result, corrosion is detected only when it reaches an advanced stage. Since the mid-1990s, a new type of pile jacket, incorporating a cathodic protection system,<sup>1</sup> has been introduced. In this system, a sacrificial zinc anode corrodes preferentially, thereby protecting the steel.

The cost of corrosion damage can be high, especially when frequent re-repairs are needed. This has led highway authorities to explore alternate repairs using fiber-reinforced polymers (FRPs). In 1994, the Vermont Agency for Transportation<sup>2</sup> opted to repair corrosion-damaged columns using FRP, and several other highway agencies have since experimented with this technique in demonstration projects. These repairs show little distress after several years of service.<sup>3</sup> However, this practice remains controversial and is not recommended by ACI Committee 440.<sup>4</sup>

In this article, we describe a field demonstration study in which corroding reinforced concrete piles in tidal waters were wrapped using a unique FRP system. This is part of an ongoing research program conducted by the University of South Florida to evaluate the feasibility of using FRP for repairing corrosion-damaged piles.<sup>5</sup>

## DESCRIPTION

The Gandy Boulevard bridges comprise three side-by-side structures over Tampa Bay, between St. Petersburg and Tampa, FL. The bridges are approximately 2.6 miles (4.2 km) long, with the oldest dating from 1956. Although this bridge was slated for demolition in 1997, the community rallied to have it refurbished. In 1999, it was reopened as the "Friendship Trail Bridge," the longest over-water recreational (pedestrian) trail in the world. The bridge has 275 spans supported by 254 reinforced concrete pile bents and 22 column-type piers located at the main channel crossing.

The salinity of Tampa Bay fluctuates with the seasons, but normally exceeds 30 parts per thousand, thus creating a highly corrosive environment. In fact, our inspection showed that 77% of the 254 pile bents had been jacketed or otherwise repaired.

The main goal of our study was to evaluate the feasibility of making underwater pile repairs without using cofferdams. For simplicity and to avoid remnants and effects of previous repair efforts, only pile bents with no repair history were considered for this demonstration. Further preference was given to adjacent bents in similar condition. This reduced the potential for spatial variation of geotechnical effects (differences in stresses imposed during pile driving) and also minimized mobilization efforts.



## DEMONSTRATION

The bents and piers are numbered 1 through 276, starting on the St. Petersburg side. Piles in Bent 99 were selected as control piles, and those in Bents 100 and 101 were wrapped (Fig. 2). These bents were close to the piers of the new Gandy Bridge, which provided a convenient staging area. The four piles in Bent 100 were wrapped using glass or carbon fibers in a unique, water-activated resin matrix. Two piles in Bent 101 were wrapped using a different epoxy system also developed for underwater use. In this article, we discuss the installation of the wraps in Bent 100 only.

The 20 x 20-in. (510 x 510-mm) piles were originally reinforced with eight No. 8 (25 mm) Grade 60 bars. Using an assumed uniform 20% steel loss, we determined the amount of carbon or glass required to restore full capacity.

For carbon fibers, this translated into one unidirectional (longitudinal) layer, rated at 3400 lb/in. (600 kN/m) capacity, followed by two bidirectional wrapped layers, rated at 2400 lb/in. (420 kN/m) per layer in each direction. Equivalent strengthening using glass fibers required almost double this amount. That is, we used two unidirectional, longitudinal layers, each rated at 2400 lb/in. (420 kN/m), and four bidirectional wrapped layers, rated at 1200 lb/in. (210 kN/m) per layer in each direction.

### Pre-wrap measurements

The chloride content was estimated by taking four concrete cores at two different elevations: the high water line and 18 in. (460 mm) above. The total chloride content was measured every 1 in. (25 mm) down to the level of the steel. The chloride content at the level of the steel



Fig. 1: Piles of the Friendship Trail Bridge that have been previously repaired using concrete jackets



Fig. 2: The four piles of Bent 100 selected for FRP repair



Fig. 3: Corrosion assessment using surface potential measurements per ASTM C 876 prior to repair



Fig. 4: Installation of scaffold around the four piles in Bent 100. Wood railing was subsequently bolted to the steel angles to delineate the extent of the underwater platform



Fig. 5: Pressure-washing of repair zone using fresh water



Fig. 6: Installation of unidirectional wrap on primed surface



Fig. 7: Installation of bidirectional wrap to provide transverse reinforcement



Fig. 8: Placement of glass fiber veil over bidirectional wrap



Fig. 9: Placement of plastic shrink-wrap over glass fiber veil

exceeded the threshold value<sup>6,7</sup> of 1 to 2 lb/yd<sup>3</sup> (0.6 to 1.2 kg/m<sup>3</sup>) in two of the four measurements. Likewise, measurements of surface potential taken using a copper-copper sulfate reference electrode registered values more negative than -350 mV, indicating there was a 90% probability of active corrosion<sup>7</sup> in regions more than 2 ft (610 mm) below the pile cap (Fig. 3).

### Scaffold construction

In an earlier demonstration study on the Allen Creek Bridge,<sup>8</sup> piles could be wrapped by standing on ladders in the shallow water. In Tampa Bay, however, the water is much deeper (about 16 ft [4.9 m]) and the tidal currents are relatively strong. Ladders were therefore not practical, so we devised a simple, inexpensive, and lightweight scaffolding system that was both easy to assemble and sufficiently rigid to support personnel during wrapping.

The scaffold comprised expanded steel grating and steel angles and was configured in four sections with appropriate cutouts for the piles. When assembled, the platform was 33 ft (10 m) long by 7 ft (2.1 m) wide and was suspended 9 ft (2.7 m) from the top of the pile cap. This meant the work

platform was 2 ft (0.6 m) below the nominal low tide elevation and 0.5 ft (150 mm) below the lowest point of the wrap, allowing workers to wrap the piles over a 5.5-ft-long (1.7 m) zone, starting from the underside of the cap. Figure 4 shows the scaffolding being installed around the piles.

### Surface preparation

To prepare the surfaces for wrapping, we removed marine growth and loose concrete and then filled undulations with a quick-setting hydraulic-cement mortar to provide a smooth surface. We used an air grinder to round each of the chamfers at the pile corners to a 3/4-in. (19-mm) radius. Just before wrapping, the surfaces were pressure-washed using fresh water to remove dust, debris, and marine growth (Fig.5).

### Underwater wrapping

Because the repairs were made using a water-activated resin, the fiber mats were cut to manageable lengths, impregnated with the resin, and packed in hermetically sealed pouches to prevent ambient water vapor from initiating curing of the resin. Sealed pouches containing the various resin-impregnated pieces of mat were brought to the site and opened just before wrapping. On-site adjustments to material lengths were made as necessary.

Similar procedures were used for applying the carbon fiber and glass fiber wraps. A primer was first applied over the surface of the pile. For the carbon fiber system, this was followed by the positioning of a longitudinally-oriented, unidirectional layer (Fig. 6). Next, two bidirectional wrap layers (Fig. 7) were spirally wrapped with no overlap from top to bottom for Layer 1, and from bottom to top for Layer 2. The same sequence was used for the glass fiber system, but it was carried out twice for both the unidirectional and wrap layers. Following placement of the structural FRP, a single spirally-wrapped layer of a finely-woven glass veil was applied starting from the bottom with a 2-in. (50-mm) overlap to consolidate the structural fibers (Fig. 8). This was followed by application of plastic shrink-wrap to secure the wrap in place while curing (Fig. 9).


In regions above the water line, water was sprayed on the wrap as it was being placed. Also, because the reaction process during resin curing yields gaseous products, the shrink-wrap was punctured over its entire length to allow these gases to escape. Following a day of curing, the shrink-wrap was removed and the FRP wrap was painted with a UV-resistant coating (Fig. 10). It took a total of 3 hours to complete wrapping of the four piles. Figure 11 shows the pile bent after all four piles had been wrapped.

### SYSTEM POTENTIAL

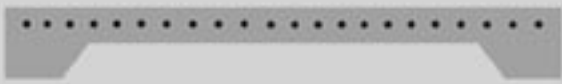
Our pilot study showed that a water-cured resin system makes it possible to install an FRP wrap for the repair of piles, even in open-water conditions. The ease of

## SLAB BRIDGE DESIGNER 2.0


Load and Resistance Factor Design  
software for steel reinforced  
cast-in-place concrete bridges



Easy to input design for  
LRFD analysis



Automatically generates  
analysis reports and graphics



[www.crsi.org](http://www.crsi.org)      See us at WOC  
Booth N2937

CRSI

Concrete Reinforcing Steel Institute  
933 N. Plum Grove Road  
Schaumburg, Illinois 60173-4758  
847-517-1200

©2005 CRSI

CIRCLE READER CARD #22





**Fig. 10: Installation of UV-protective coating (plastic shrink-wrap removed)**



**Fig. 11: FRP wraps installed at Bent 100**

installation of this system, coupled with the previously-observed reduction in corrosion rate<sup>3</sup> made possible by FRP wraps, suggest this approach has tremendous merit. We are continuing to monitor the long-term performance of the system.

## Acknowledgments

This project was carried out with the financial support of Hillsborough County. The authors gratefully acknowledge this support and the cooperation of the State Materials Office of the Florida Department of Transportation. Finally, this study could not have been completed without the assistance of Air Logistics, supplier of the FRP repair material and resin. The support, encouragement, and assistance of Franz Worth, Program Manager, as well as his meticulous planning, enabled this project to be successfully completed.

## References

1. Tarricone, P., "Composite Sketch," *Civil Engineering*, V. 65, No. 5, May 1995, pp. 52-55.
2. Leng, D.L., "Zinc Mesh Cathodic Protection Systems," *Materials Performance*, V. 39, No. 8, Aug. 2000, pp. 28-33.
3. Sen, R., "Advances in the Application of FRP for Repairing Corrosion Damage," *Progress in Structural Engineering and Materials*, V. 5, No. 2, Apr.-June 2003, pp. 99-113.
4. ACI Committee 440, "Guide for the Design and Construction of Externally Bonded FRP Systems for Strengthening Concrete Structures (ACI 440.2R-02)," American Concrete Institute, Farmington Hills, MI, 2002, 45 pp.
5. Suh, K.S.; Mullins, G.; Sen, R.; and Winters, D., "Use of FRP for Corrosion Mitigation Applications in a Marine Environment," Final Report submitted to the Florida Department of Transportation, Oct. 2005, 407 pp.
6. Mindess, S.; Young, J.F.; and Darwin, D., *Concrete*, 2nd Edition, Prentice Hall, Upper Saddle River, NJ, 2003, 644 pp.

7. ASTM C 876-91(1999), "Standard Test Method for Half-Cell Potentials of Uncoated Reinforcing Steel in Concrete," ASTM International, West Conshohocken, PA, 1999, 6 pp.

8. Mullins, G.; Sen, R.; Suh, K.S.; and Winters, D., "Underwater Fiber-Reinforced Polymers Repair of Prestressed Piles in the Allen Creek Bridge," *Journal of Composites for Construction*, V. 9, No. 2, Mar.-Apr. 2005, pp. 136-146.

Received and reviewed under Institute publication policies.



ACI member **Gray Mullins** is an associate professor at the University of South Florida where he teaches substructure and instrumentation of bridge elements. He is a member of ASCE, ADSC, and DFI. Most recently, his research is heavily involved in load testing using Statnamic testing, rehabilitation of corrosion-damaged piles using FRP, and quality assurance of drilled

shafts using thermal integrity methods.



**Rajan Sen**, FACI, is a professor of structural engineering at the University of South Florida. He is a fellow of ASCE and held the Samuel and Julia Flom Chair. He is active in FRP research and serves on ACI Committees 215, Fatigue of Concrete; 440, Fiber Reinforced Polymer Reinforcement; and 444, Experimental Analysis for Concrete Structures. He has authored

numerous research publications and has lectured at forums of professional organizations worldwide.



ACI member **Kwang Suk Suh** is a PhD candidate in civil and environmental engineering at the University of South Florida. His major interest is focused on evaluation and repair methods of corrosion-damaged bridge piles exposed to marine environments. He is a student member of ASCE and SAMPE.



**Danny Winters** is a research associate with the University of South Florida. He received his BSCE and MSCE from the University of South Florida and is currently in the doctoral program. His research interests include underwater FRP repair and corrosion monitoring of bridge pilings in marine environments.

## **FACTORS AFFECTING CONCRETE FLOW IN DRILLED SHAFT CONSTRUCTION**

Gregory G. Deese, M.S.C.E., E.I.<sup>1</sup> and Gray Mullins, Ph.D., P.E.<sup>2</sup>

### **ABSTRACT**

In recent years, it has become apparent that concreting during drilled shaft construction does not necessarily scour the excavation walls as previously thought. In fact, the flow pattern of fluid concrete is highly non-uniform with the preferential path flowing up along the side of the tremie pipe. The primary variable affecting flow was speculated to be concrete slump although other variables such as cage spacing have been hypothesized. This paper discusses several studies conducted by the University of South Florida in conjunction with the Florida Department of Transportation and Auburn University to evaluate construction practices that lead to anomalies. As a result, several parameters that affect concrete flow were identified and are presented herein along with case studies where field measurements documented these effects.

### **INTRODUCTION**

Implementation of drilled shaft foundations has increased significantly since their inception. Their immense lateral stiffness and applicability to geological formations not conducive to pile driving has secured their place as a common, cost-effective type of deep foundation. However, it has become clear that sensitivity to the construction process is paramount for this type of foundation.

The construction process consists of three distinct steps: (1) excavate the borehole, (2) position the reinforcement cage in the shaft, and (3) place concrete into the borehole. There are numerous methods (and numerous problems) for completing each of the three steps, however, the geological environment can govern which is the appropriate course of action to create a reliable structural element.

Due to the host of logistical problem facing the drilled shaft contractor, strict regulations and standards have been imposed on shaft construction by several state DOTs and FHWA. Even so, documented cases of anomalies and/or poorly performing shafts continue to arise. This prompted a deeper look into the mechanics of the construction

<sup>1</sup>Graduate Research Assistant, University of South Florida, 4202 E. Fowler Ave, Tampa, FL 33620 email: [deese@eng.usf.edu](mailto:deese@eng.usf.edu)

<sup>2</sup>Associate Professor, University of South Florida, 4202 E. Fowler Ave, Tampa, FL 33620 email: [gmullins@eng.usf.edu](mailto:gmullins@eng.usf.edu)

process.

Recent research indicates that tremie poured concrete does not flow as commonly thought in a drilled shaft. Instead of evenly rising and scouring of the filter cake on the walls of the borehole (if slurry displaced), a differential between the height of concrete inside and outside of the reinforcement cage has been observed. The development of pressure inside the cage (in the form of concrete head) serves to push the concrete through the cage in concert with a tumbling action flowing over the stirrups. In reality, design values of side shear based on empirical studies have unwittingly incorporated the presence of the filter cake despite the likely misconceived notion of the concrete's perceived flow patterns. The concern, therefore, is not the affect on side shear but rather the potential to encapsulate settled debris, slurry, or other deleterious material that degrades structural performance or durability. This paper quantifies this differential head and relates it to pertinent parameters of the drilled shaft design and/or construction process.

## **BACKGROUND**

Wet concrete flow through steel reinforcement is a behavior dependent on many characteristics. However, the relative size of the coarse aggregate of the concrete and the minimum space between reinforcement bars is one of the most relevant factors. The ACI Code (2002) recommends the maximum coarse aggregate diameter be 3/4 of the clear spacing between rebar. Further, it waives this spacing requirement altogether, if concrete workability is good and consolidation (vibrating) methods may be employed. However, due to the nature of drilled shafts, consolidation methods are often not applicable. Therefore, recommendations call for a minimum cage spacing of 3 to 5 times the coarse aggregate diameter to allow for "free" flow of concrete past the reinforcement into annular area of the shaft FHWA (O'Neill and Reese, 1999).

The first cited occurrence of differential head rising behavior was observed by Fleming and Sliwinski (1977). They briefly described a pour where, due to tight reinforcement spacing, tremie-placed concrete rose up inside the reinforcement cage and only after a critical head differential was reached, "fell" past the cage to the cover area.

Brown (2003) offered a general discussion of this phenomenon and a case study. He suggested two types of problems may result in regard to rebar cages with small clear spacing due to high amounts of steel. The first involves sediment settling out of slurry onto the top of rising concrete. If the concrete does in fact slough off to the side, the sediment will as well. This accumulation may decrease bond that exists between concrete and the bearing formation. He suggests that even with clean slurry, concrete can be impeded enough to create voids outside the cage and likely diminish side shear capacity.

In the case study described by Brown, two shafts were excavated and poured. The first utilized standard Alabama DOT approved concrete which consisted of #57 crushed aggregate (1.9 cm (0.75 in.) maximum diameter) and a slump of 20.3 cm (8 in.). The minimum clear spacing of the reinforcement cage was 12.7 cm (5 in.). He stated the concrete was observed to flow around the tremie pipe and fall out, radially, toward the annular space of the shaft. The concrete was seen to fall through the cage to the cover region at a differential height of about 0.5 m (1.6 ft.). The second shaft, constructed identically, except for the reduction of the 1.9 cm (0.75 in.) aggregate to 1.27 cm (0.5 in.). There was much less falling out observed in this shaft.

A one-tenth scale study to examine the flow of tremie-place concrete in drilled shafts was also recently completed (Mullins et al., 2004). Therein, a device, called a Lateral Pressure Cell (LPC), was developed to study various parameters of concrete flow. The LPC was constructed of clear Lucite pipe and incorporated lateral pressure transducers as well as a total weight load cell. A circular wire mesh of different clear spacings was used to simulate a reinforcing cage inside the lab-scaled drilled shaft. Cement mortar was used to simulate concrete. The primary objective of the LPC was to test the effect of concrete slump on the lateral pressure of the finished shaft, but it was discovered in these small tremie pours that the level of rising concrete inside of the wire mesh was higher than outside the wire mesh. This prompted researchers to run other series of tests to examine this phenomenon more fully.

$$CSD = \frac{\text{Min. ClearSpacing}}{\text{Max. CoarseAggregateDiameter}}$$

The subsequent tests incorporated three different cage spacings. A clear spacing to diameter ratio (CSD) defined the relationship between mortar (concrete) aggregates and reinforcement cage spacings. This ratio served to normalize the size of the rebar spacing to the largest aggregate in the concrete mix.

It was discovered that the mortar in the LPC never rose uniformly as it was assumed. Instead, it would flow up, inside the rebar cage, until a critical point was reached, and fall through the clear spacing to the outside. It was noted that when the cage spacing was small (i.e. smaller CSD) the differential became higher indicating some correlation between CSD and head differential. Further, when the tremie was not perfectly centered (the more common field occurrence), the differential was more drastic with the level outside the cage behind the tremie being the lowest (Figure 1). This was confirmed by full scaled testing done in conjunction with Auburn University at the National Geotechnical Experimentation Site (NGES) in Opelika, Alabama. Figure 2 depicts the relationship found between CSD and head differential in the mortar pours as well as full scale testing completed (Mullins et al., 2004).

This head differential phenomenon causes a flow in the borehole that is completely different from that idealized. The behavior not only brings into question the idea that the

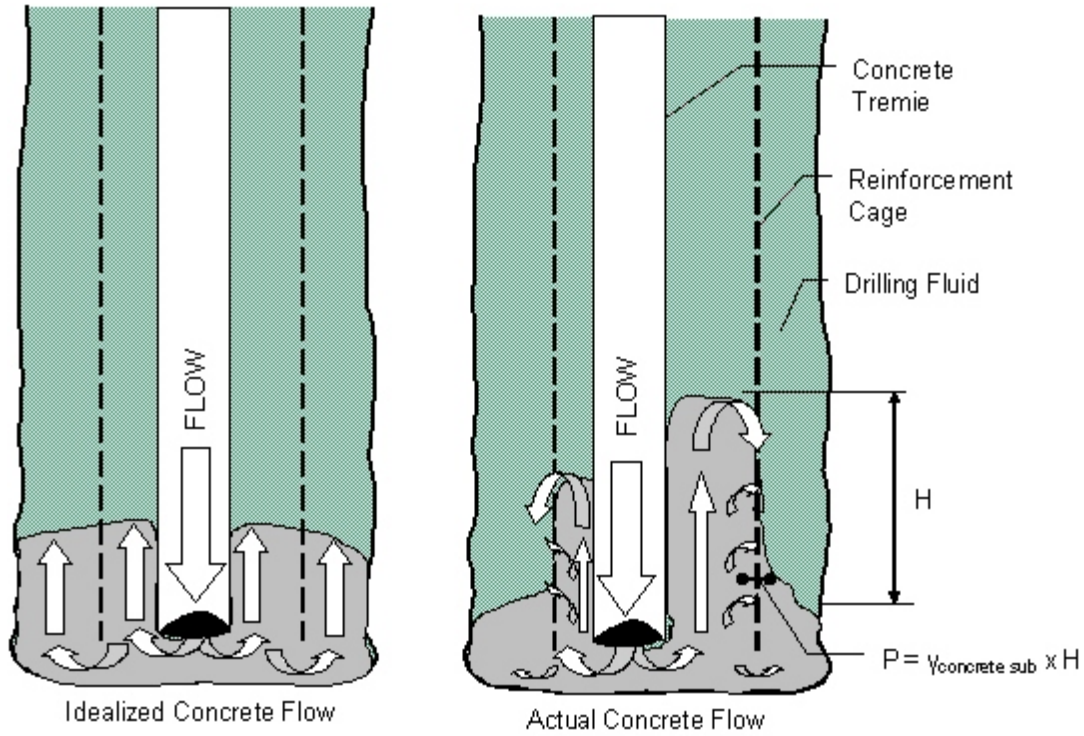


Figure 1 Behavior of Rising Concrete in Tremie Poured Drilled Shaft

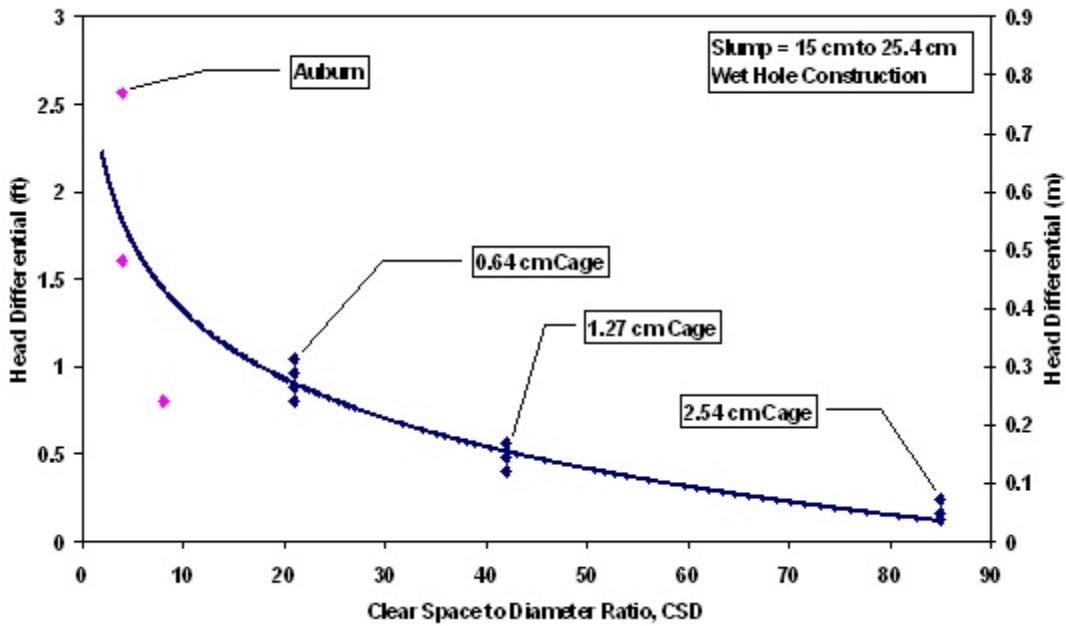


Figure 2 CSD Ratio Versus Head Differential for LPC and NGES Testing

rising concrete scours off the filter cake left by bentonite slurries, but also introduces the possibility of inclusions in the shaft due to concrete falling onto settled material in the borehole outside the cage after longer wait periods between concrete trucks.

## **DATA COLLECTION AND ANALYSIS**

The discovery of a head differential in rising mortar between the inside and outside the reinforcement cage during LPC testing series spawned the desire to better define and understand the phenomenon. To this end, a field testing program was established to survey this behavior in full scale drilled shaft construction of various cage and aggregate combinations. The main objective of this testing was to quantify head differential behavior with variables such as CSD, rising concrete velocity, and fresh concrete properties.

Multiple field visits across several sites were conducted to ascertain the amount of wet concrete head differential in various types of drilled shaft construction. In order to obtain an assortment of data, researchers deliberately chose sites with a large variety of shaft diameters and CSD ratios. The testing sites were: Essex Cement Silos, Crosstown Expressway, and Port Manatee, in addition to data collected from the NGES test site conducted in 2002.

To quantify the head differential, researchers used a weighted tape system, similar to what drilled shaft inspectors use to measure rising concrete between buckets or trucks. Typically, two tapes were dropped before the first concrete was poured, one inside the reinforcement cage and one outside to take initial depths. During the pour, head differential readings (Figure 3) were taken every 30 seconds until the entire truck had been pumped into the shaft, then the final height was measured. In between the 30 second measurements, the weighted tapes were kept slightly above the level of rising concrete during the pour. This process was repeated until the entire shaft had been poured. To ensure precise measurement, the top of the temporary casing was typically used as a datum for both tapes.

### **Essex Cement**

Construction of cement storage silos at Berth 219 in the Port of Tampa for Essex Cement Company called for 177 drilled shafts, 0.9 m (3 ft.) in diameter. The shafts were drilled to a depth of approximately 24 m (79 ft.) and were installed using full length temporary casing with a sidewall thickness of 1.3 cm (0.5 in.). The reinforcing cages were 15.85 m (52 ft.) in length and were designed to terminate at the top of the rock socket. Stirrup spacing and mix specifications yielded at CSD ratio of approximately 27 (minimum clear spacing was 50.8 cm (20 in.) and diameter of coarse aggregate was 1.9 cm (0.75 in.)). The construction site is shown in Figure 4.





Figure 3 Rising Concrete Level Measured Inside and Outside Reinforcing Cage



Figure 4 Shaft Construction at Port of Tampa

The concrete was poured via a pump truck and the tremie remained fully inserted in the shaft during the entire pour. Each shaft had a volumetric requirement equivalent to two concrete trucks (approximately 11.5 m<sup>3</sup> (15 yd<sup>3</sup>), slump was approximately 24 cm (9.5 in.) on all shafts measured. The water table was near the surface.

Successful collection of 4 data sets was completed for this site. It is interesting to note that head differentials varied regardless of a constant CSD ratio. This suggested that another variable, perhaps pour rate, could be key in affecting the wet concrete flow behavior. Upward velocity versus measured head differential trends were examined, although it was difficult to derive any trend from such a small amount of data.

### **Crosstown Expressway Reversible Lanes Bridge**

Construction on the Crosstown Expressway Reversible Lanes Bridge project began in 2003 (Figure 5). The bridge was designed to facilitate three lanes of traffic westward from Interstate 75 into Tampa during morning hours then reverse flow eastward during the afternoon. The bridge utilizes a mono-pier foundation system, meaning that each column rests atop a single large diameter drilled shaft. The design loads for this bridge, which was being built above the existing Crosstown Expressway, required a large amount of reinforcement with tightly-spaced cages to resist overturning moments. Shaft diameters varied from 1.2 to 2.4 m (4 to 8 ft.) with depths of up to 24.4 m (80 ft.). CSD ratios for all shafts were 6 (minimum clear spacing was 15.2 cm (6 in.) and coarse aggregate diameter was 2.5 cm (1 in.)) with slumps ranging from 17.8 cm to 22.9 cm (7 to 9 in.).



Figure 5 Drilled Shaft Construction at the Crosstown Expressway

Three shafts were investigated at two points along the route that offered a significant variation in the construction atmosphere. The first two shafts (piers 167 and 156) were 1.8 and 2.4 m (6 and 8 ft.) in diameter, respectively, and located within close proximity to an already existing roadway. The third shaft (pier 18) was 2.4 m (8 ft.) in diameter and positioned within the Palm River. Construction methods were similar to those used at the Port of Tampa in that a full length temporary casing was vibrated to the top of rock, the reinforcing cages were designed to terminate at the rock socket, and concrete was pumped from ready-mix trucks through a tremie. The larger diameter shafts required upwards of 15 concrete trucks (approximately 92 m<sup>3</sup> (120 yd<sup>3</sup>) and 5 hours to complete which afforded several data sets per shaft.

The CSD ratio versus head differential again clearly demonstrates no direct correlation between these two variables. Plotting the recorded head differential against the upward concrete velocity, however, reveals clear relation for these shafts of constant CSD ratios. This evidence suggested that perhaps a family of curves of head differential versus upward velocity exists for different ranges of CSD ratios. It is evident that another variable may affect the range of head differential fluctuation within a particular shaft. Also observed is the increase in differential range in shaft 167 which was twice as large as the range for shafts 18 and 156.

While waiting between arrival of concrete trucks, differential measurements were taken in the stagnant boreholes. In time periods of up to one hour, it was observed that the wet concrete differential did not decrease appreciably.

### **Port Manatee**

Construction of high mast security lighting at Port Manatee called for 6.1 m (20 ft.) deep, 1.5 m (5 ft.) diameter drilled shafts to support 36.5 m (120 ft.) tall steel poles. Due to height and wind requirements, these shafts had a CSD ratio of 8 (15.2 cm (6 in.) minimum clear spacing and the maximum coarse aggregate diameter of 1.9 cm (0.75 in.). The required concrete volume of these shafts called for two concrete trucks.

As the site is comprised predominantly of dredged clay spoils, a natural slurry was used to maintain hole stability. The concrete was tailgated and a sectional tremie was used. This resulted in relatively low upward velocities at a lower CSD similar to data collected at the NGES site with Auburn University (Mullins et al., 2004).

It can be seen in this series of data that similar head differentials exist for these shafts. Comparing the CSD ratio versus the measured head differentials produces a narrower band of results relative to the other sites, suggesting some correlation. However, the velocity versus head differential shows that a good correlation between increasing velocity and increasing head differential exists for upward velocities between 15.2 - 45.7 cm (0.5-1.5 ft.) per minute.

## Summary

Figure 6 summarizes the head differential data from the Essex Cement, Crosstown, Port Manatee and the NGES sites as a function of the CSD. Clearly, the CSD is not the only parameter affecting the buildup of concrete head inside the reinforcing cage. Figure 7 shows the same data as a function of velocity for each group of common CSDs observed. A second order trend appears to exist for different CSD values, verifying the concept that head pressure is directly proportional to the square of the velocity head. Given a constant upward velocity, a drastic difference in head differential occurs as the CSD increases from 6 to 8; for CSD values above 8, however, the head differential is much less significant for all velocities. It should be noted that the head differential in the Crosstown drilled shafts did not appreciably decrease during wait time between concrete trucks, despite high slump concrete.

Since there are few alternate configurations for a given reinforcement cage, it may be necessary to adjust the coarse aggregate size so as to minimize concrete build-up inside the cage. Therefore, using the results shown in Figure 7, any set of head differential data at a constant velocity will show the CSD limit below which should be avoided. Figure 8 shows that a minimum CSD of 8 is recommended. The FDOT has already taken steps to recommend a minimum CSD in the range of 10 as a result of this project's findings.

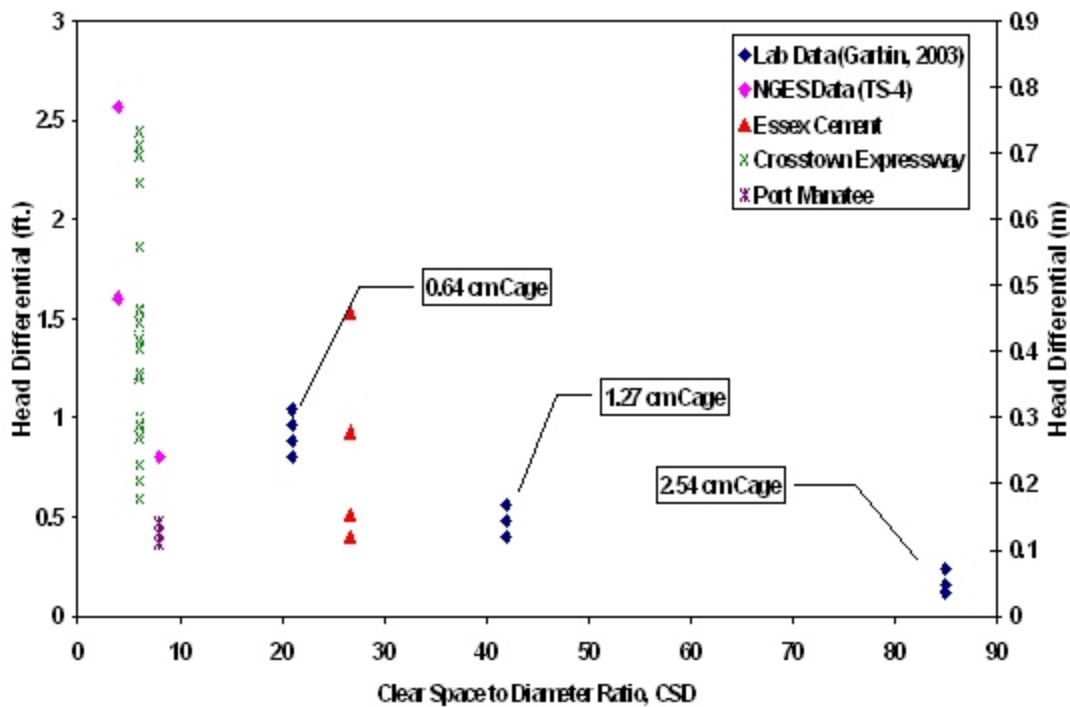


Figure 6 Summary of CSD Ratio Versus Head Differential

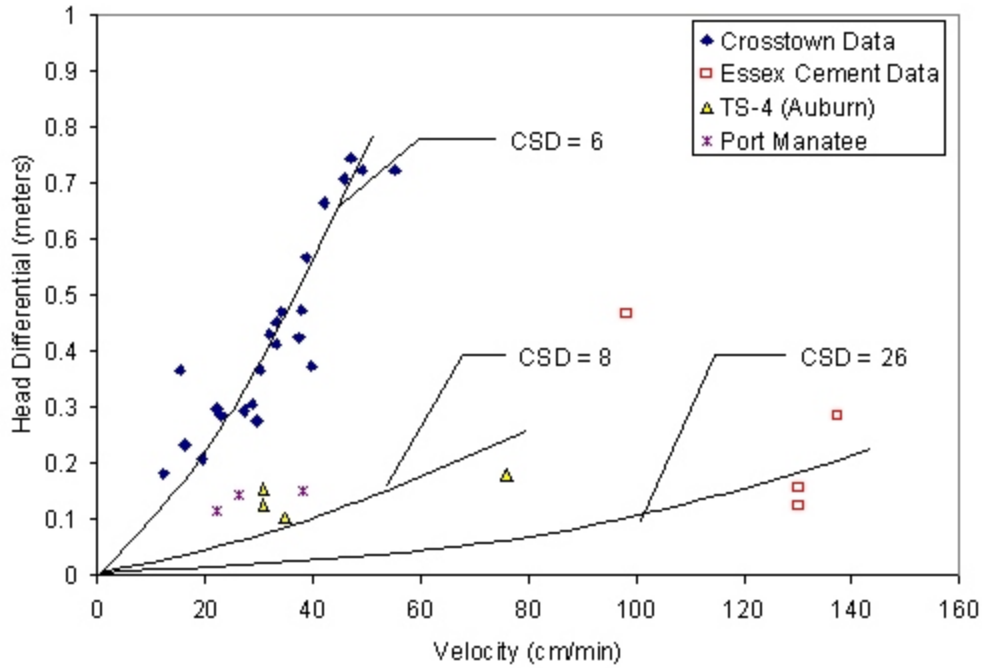


Figure 7 Summary of Velocity Versus Head Differential

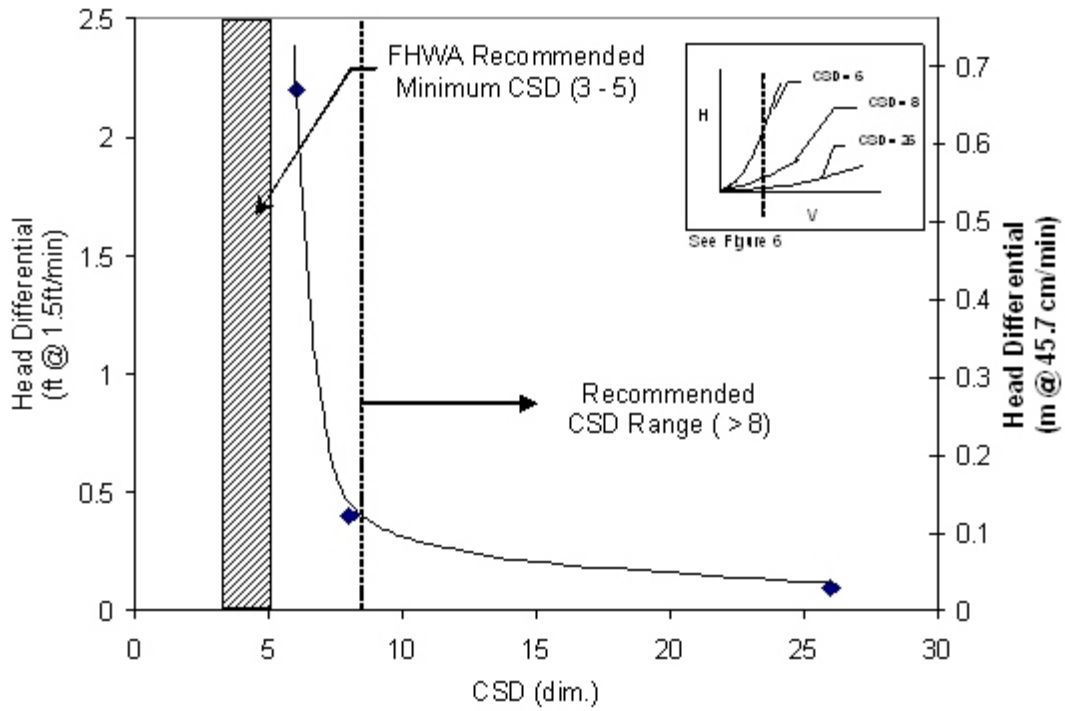


Figure 8 Recommended CSD Range for Drilled Shaft Construction

## CONCLUSION

The original basis for this research stemmed from anomaly formations in drilled shafts (such as soil inclusions) that had been noted to occur in the vicinity of the groundwater table (GWT) elevation. Although not found to be directly correlated to inclusion potential, the GWT does affect wet method construction by influencing the borehole stability. To this end, the project was expanded to observe concrete flow behavior with regards to anomaly formation. As a result, over 40 sets of data were taken in full-scale shafts at four sites. This testing was conducted to quantify head differential as a function of CSD ratio, rising concrete velocity, and wet concrete properties. The full scale testing showed that the CSD ratio was not the sole variable with regard to head differential. Instead, it was found that as upward velocity increased, larger head differentials could be observed. It was also apparent that shafts with similar CSD ratios showed similar head differentials with respect to velocity. The largest head differentials (upwards of 0.75 m) were observed for shafts with CSD ratios of approximately 6. Based on the conclusions derived herein, recommendations for changes in the pertinent sections of drilled shaft construction specifications were as follows:

CSD > 8. Current FHWA recommendations suggest that a CSD ratio as low as 5 is reasonable. However, concrete flow observed (Figure 1) support an increase in this recommended value. This applies to structural, geotechnical, and materials engineers alike. As the size and configuration of rebar in drilled shaft cages cannot always be altered, smaller maximum aggregate diameter may be appropriate. Smaller sized coarse aggregate, such as #7 stone, should be considered for tremie-placed drilled shaft construction. This would help to increase the CSD and thereby lower the potential head differential that could develop. This means less concrete back pressure would be needed to adequately penetrate the cage. Where practical, this limit should be applied to the worst case spacing in the cage, such as spliced cage segments.

Further topics of study include the continued development of a family of curves to correlate upward velocity in shafts with similar CSD ratios to head differential. Also, the potential relationship between radial velocity of concrete in the shaft versus the head differential should be investigated. This would further quantify the phenomenon of head differential and allow designers to create drilled shafts which not only have adequate strength, but also easily construct-able while minimizing the chance of anomaly formation.

## REFERENCES

ACI. (2002). *Building Code Requirements for Structural Concrete (ACI 318-02)*. Farmington Hills, MI: American Concrete Institute.



- Brown, D. (2004). "Zen and the Art of Drilled Shaft Construction: The Pursuit of Quality." *Geosupport Conference: Innovation and Cooperation in the Geo-industry, Drilled Shafts, Micropiling, Deep Mixing, Remedial Methods, and Specialty Foundation System*. American Society of Civil Engineers, Reston, VA.
- Fleming, W.K. and Sliwinski, Z.J. (1977). *The Use and Influence of Bentonite in Bored Pile Construction*. London, England: CIRIA Report PG3.
- Garbin, E.J. (2003). *Construction Related Difficulties in Drilled Shaft Construction*. Doctoral Dissertation, University of South Florida, Tampa, FL.
- Mullins, A.G. and Ashmawy, A.K. (2004). *Factors Affecting Anomaly Formation in Drilled Shafts*. Final Report to the FDOT, University of South Florida, Tampa, FL.
- O'Neill, M.W. and Reese, L.C. (1999). *Drilled Shafts: Construction Procedures and Design Methods Volume 1*. Dallas, TX: ADSC: The International Association of Foundation Drilling.

# Underwater Fiber–Reinforced Polymers Repair of Prestressed Piles in the Allen Creek Bridge

Gray Mullins, M.ASCE<sup>1</sup>; Rajan Sen, F.ASCE<sup>2</sup>; Kwangsuk Suh<sup>3</sup>; and Danny Winters<sup>4</sup>

**Abstract:** This paper presents an overview of a demonstration project in which corroding prestressed piles located in tidal waters were wrapped underwater using carbon and glass fiber-reinforced polymer material. An innovative instrumentation scheme was developed to allow assessment of the prewrap and postwrap corrosion state using linear polarization. This system is simple to install and eliminates the need for wiring or junction boxes. The underwater wrap used a unique water-activated urethane resin system that eliminated the need for cofferdam construction. Linear polarization measurements taken before and after wrapping indicate that the corrosion rate in the wrapped specimens is consistently lower than those in its unwrapped counterpart. These preliminary findings are encouraging and suggest that underwater wrapping without cofferdam construction may provide a cost-effective solution for pile repair.

**DOI:** 10.1061/(ASCE)1090-0268(2005)9:2(136)

**CE Database subject headings:** Fiber reinforced polymers; Corrosion; Rehabilitation; Underwater structures; Bridge foundations.

## Introduction

Concrete's alkaline environment normally prevents steel from corroding by forming a passive oxide layer on its surface that limits access of oxygen and moisture. However, the combination of high humidity and high temperature is lethal even for high quality concrete, as it allows chloride ions to penetrate to the level of the reinforcement. When the chloride concentration reaches a critical threshold value of 0.6–1.2 kg Cl<sup>-</sup>/m<sup>3</sup>, the passive layer is destroyed and corrosion is initiated (Mindess et al. 2003). Such conditions are commonplace in coastal regions of southeastern United States, where concrete piles corrode rapidly.

The requirements for durable repair of corrosion-damage are daunting. All chloride-contaminated concrete must be removed and replaced with low shrinkage, low modulus, high creep, high tensile strength patch material having the same thermal expansion and oxygen permeability (Vaysburd and Emmons 2000). Because the boundaries of the chloride-contaminated region are not known with any precision, such conditions can rarely be met for repairs carried out under dry conditions; they are unrealizable for piles corroding in tidal waters. Cathodic protection provides the only proven (Scheffy 1981) means for ensuring durable repairs. However, the cost of such repairs may not always be affordable.

Fiber-reinforced polymers (FRP) have the potential of being a

lower cost alternative that can match the performance of cathodically protected piles. Cost is critically important and, indeed, lower costs were responsible for the selection of FRP in the first place. In 1994, the Vermont Agency of Transportation opted for FRP to repair corrosion-damaged columns because the fiberglass system led to an estimated cost savings of 35% over conventional repairs (Tarricone 1995). After nine years of service, repairs showed little sign of deterioration (Graham, personal communication, 2003). This can be attributed to FRP's high tensile strength, which can be aligned to withstand forces in any direction, and its excellent durability.

A recent state-of-the-art paper on using FRP for corrosion mitigation (Sen 2003) found that the vast majority of the applications to date are similar to those conducted in Vermont. Typically, bridge columns or bents corroded by salt-water spray from high speed traffic or due to salt water trickling down leaky expansion joints were repaired. Even where repairs were carried out in the tidal zone, they were done under dry conditions (Neale and Labossiere 1998).

Similar FRP repairs of prestressed piles using cofferdam construction were recently completed (Shahawy et al. 2004). However, the high cost of cofferdam construction reduces FRP's competitiveness in the marketplace. As with the initial study conducted in Vermont, FRP systems will only gain widespread acceptance if their use leads to lower costs and improved performance as compared to conventional repairs.

This paper describes a demonstration study in which full-sized, square prestressed piles were wrapped underwater using FRP. The aim of the study was to assess the performance of the wrap and also to determine the ease with which it could be carried out. For this purpose, a robust instrumentation system was developed that was simple to install yet eliminated the need for junction boxes and wiring. The field demonstration was the culmination of a comprehensive laboratory study in which simulated repairs were carried out in a salt-water tank and their performance evaluated through ultimate strength tests. A brief description of the findings from this laboratory study is included for completeness.

<sup>1</sup>Associate Professor, Dept. of Civil and Environmental Engineering, Univ. of South Florida, Tampa, FL 33620.

<sup>2</sup>Professor, Dept. of Civil and Environmental Engineering, Univ. of South Florida, Tampa, FL 33620.

<sup>3</sup>PhD Candidate, Dept. of Civil and Environmental Engineering, Univ. of South Florida, Tampa, FL 33620.

<sup>4</sup>Research Associate, Dept. of Civil and Environmental Engineering, Univ. of South Florida, Tampa, FL 33620.

Note. Discussion open until September 1, 2005. Separate discussions must be submitted for individual papers. To extend the closing date by one month, a written request must be filed with the ASCE Managing Editor. The manuscript for this paper was submitted for review and possible publication on December 2, 2003; approved on March 23, 2004. This paper is part of the *Journal of Composites for Construction*, Vol. 9, No. 2, April 1, 2005. ©ASCE, ISSN 1090-0268/2005/2-136–146/\$25.00.



Fig. 1. Simulated underwater wrap

### Laboratory Study

The FRP repair of corroded piles is a hybrid application in that it is bond-critical in terms of flexural strengthening but contact-critical in terms of resisting expansion forces caused by possible continuing corrosion inside a wrapped specimen. In view of this, laboratory trials were carried out to simulate field repairs and to evaluate their performance.

Eleven one-third scale, 1.8 m long,  $15 \times 15$  cm prestressed specimens were used in the laboratory study. The specimens were prestressed using four 0.8 cm, 1,724 MPa strands and were cast with a 55.9 cm chloride-contaminated region (3% chloride ion by weight of cement). This type of specimen had been used in several previous projects (e.g., Sen et al. 1999; Fischer et al. 2000). Nine of the specimens were subjected to an accelerated corrosion regime using a constant current system to a targeted metal loss of 25% verified by gravimetric testing.

An underwater demonstration was conducted in which five specimens were wrapped with the FRP impregnated with the special water-activated urethane resin; one of the five wrapped specimens was used for the qualitative assessment of bond. The remaining six were used as unwrapped controls tested as eccentrically loaded columns (two uncorroded, two at 25% steel loss, and two at 50% steel loss). A  $3 \times 1.8$  m tank was filled with 3% salt water to a depth of 1.2 m (Fig. 1). Air Logistics of Pasadena, CA, who developed the water-activated resin system, provided the materials and expertise for the demonstration.

Following cure of the FRP material, the wrap was removed from one of the five specimens to evaluate its bond with concrete. It came off relatively easily (Fig. 2) as compared to wraps applied to dry surfaces, indicating that the bond was inferior. However,



Fig. 2. Removal of wrap

eccentric ultimate load tests indicated that the bond was sufficient to restore full capacity when compared with uncorroded controls (Fig. 3). The remaining two wrapped specimens and their controls were subjected to additional accelerated corrosion to a targeted metal loss of 50% and subsequently tested in the same manner. The results from these tests were similar to those obtained earlier. However, full restoration was not realized because of end failure caused by corrosion outside the wrapped region. Nonetheless, the results reaffirmed the satisfactory performance of the wrap. Complete details may be found in the interim final report (Suh et al. 2004).

### Field Demonstration

A field demonstration study was conducted to evaluate the effectiveness of two alternate systems: (1) a “dry” wrap requiring cofferdam construction; and (2) an underwater system. This paper focuses on the latter system. Information on the dry system may be found in Shahawy et al. (2004).

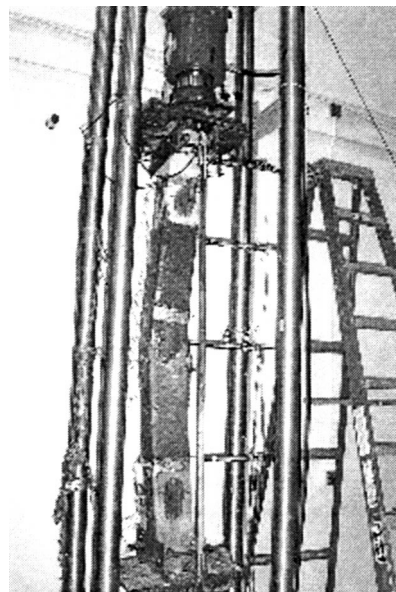


Fig. 3. Ultimate strength test

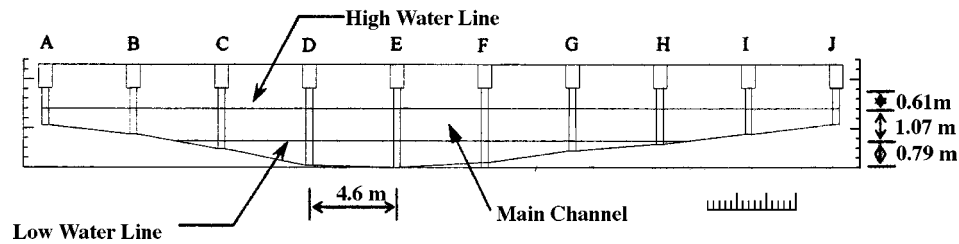


Fig. 4. Allen Creek Bridge looking west

### Allen Creek Bridge Site

The Allen Creek Bridge site used in the demonstration project was recommended by the Florida Department of Transportation. It met critical access requirements, e.g., shallow waters and proximity to the university, yet provided an aggressive environment with a long history of severe substructure corrosion problems in piles.

Allen Creek Bridge is located in the city of Clearwater on the busy U.S. Highway 19, 2.3 km north of SR 686. Originally constructed in 1951, its 4.57 m spans are supported by  $50 \times 50$  cm reinforced concrete piles. In 1982, the bridge was widened to accommodate six lanes of vehicular traffic. The widened section is supported by  $35 \times 35$  cm piles. These are prestressed with eight 1.27 cm 1.86 GPa stress-relieved strands.

An elevation view of the bridge is shown in Fig. 4. The waters from the creek flow east into Old Tampa Bay, which in turn joins the Gulf of Mexico to the south. The environment is very aggressive; all the reinforced concrete piles from the original construction have been rehabilitated several times. At low tide, the water level in the deepest portion of the creek was about 0.8 m. Maximum high tide is about 1.9 m. This shallow depth meant that the underwater wrap would not require divers and could be carried out on a ladder.

### Prewrap Corrosion State

Much of Allen Creek is knee-deep at low tide; therefore, it was possible to access all the piles excepting those forming the main channel. A prewrap inspection was carried out of the entire site to evaluate the corrosion state and also to select the piles that were to be wrapped in the study. None of the piles displayed any visible signs of corrosion. Nor was there any evidence of delamination detectable by tapping the pile gently with a hammer.

Several concrete cores were taken to determine the chloride variation in the cover. The first sample was at the elevation corresponding to high tide. The second was 0.9 m above high tide. The total chloride was determined every 25 mm down to the level of the steel by the Florida Department of Transportation's State Materials Office. Results indicated that the threshold for corrosion was easily exceeded at the high tide location. The chloride level varied between 3.98 and 3.32  $\text{kg}/\text{m}^3$ . Values were much greater 0.9 m above high tide, where it was 7.43  $\text{kg}/\text{m}^3$  in the initial 25 mm cover, reducing to 0.51  $\text{kg}/\text{m}^3$  in the vicinity of the prestressing steel, 75 mm from the surface (Lasa, personal communication, 2003a). This is typical of chloride variation observed in specimens exposed to tidal waters—it is always much higher above the high tide region. This information is useful for deter-

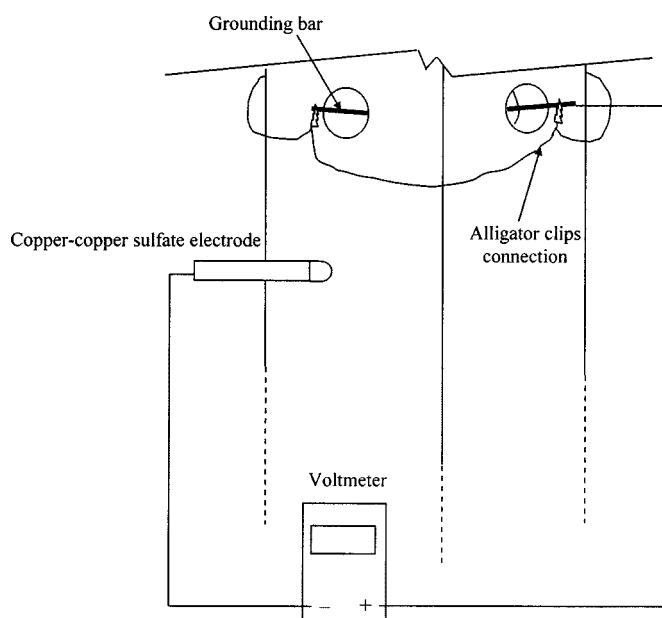


Fig. 5. Schematic of electrical connections



Fig. 6. Template for measuring corrosion potential



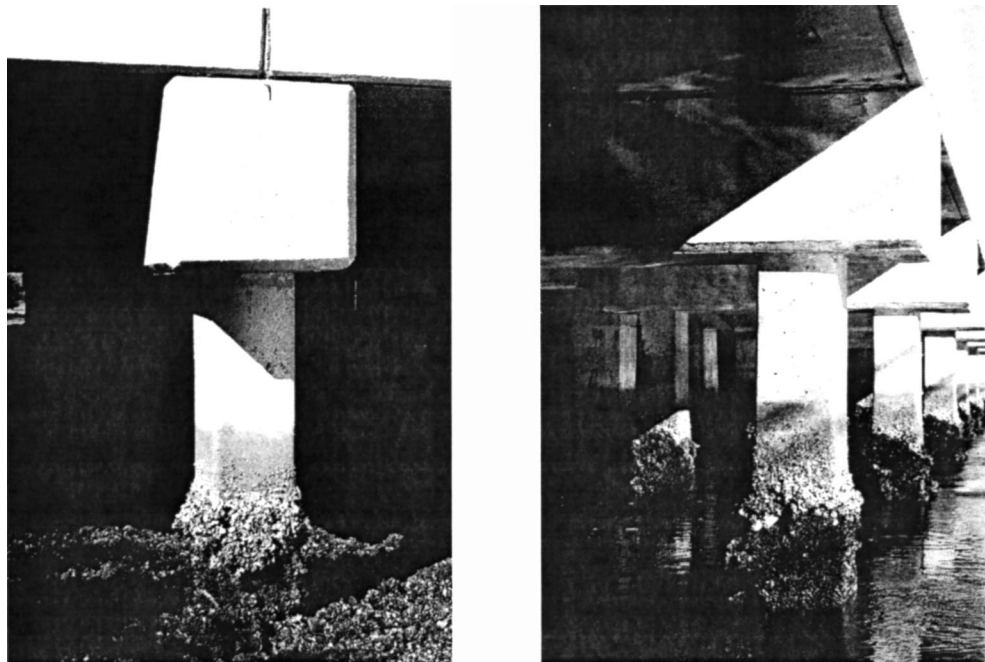


Fig. 7. Marine growth on pile surface

mining the extent of the pile wrap above the high water line. It has been observed that encapsulation of chloride-contaminated regions sometimes leads to an upward shift in the corrosion cells (Lasa, personal communication, 2003b).

### Corrosion Instrumentation

Field instrumentation for long-term monitoring is never a simple task. This is especially so for piles because of accessibility problems at high tide and the aggressive marine environment. Particular attention must be paid to ensure that electrical contacts are not corroded and moisture is not trapped inside junction boxes. More-

over, accessibility of instrumentation ports makes them vulnerable to vandalism. Thus, making instrumentation as unobtrusive as possible is a basic requirement for successful long-term monitoring. In the study, a system suggested by Sagues (personal communication, 2002) was used. It is simple to install and does not require any wiring or corrosion protection.

Four piles—B2, E2, F1, and G1—were instrumented to determine the prewrap corrosion state. The letters signify the position of the bent from the south abutment, and the numbers 1 and 2 signify the row starting from the east. The piles in row 1 are along the outside row visible from the water looking west. Two of the instrumented piles (B2,G1) were retained as unwrapped controls. The remaining piles were used for monitoring the performance of

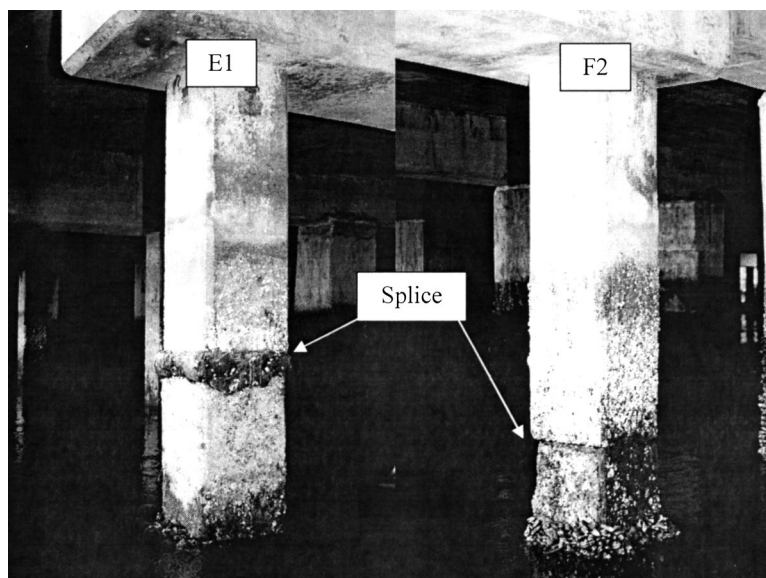


Fig. 8. Discovery of splice in piles E1 and F2

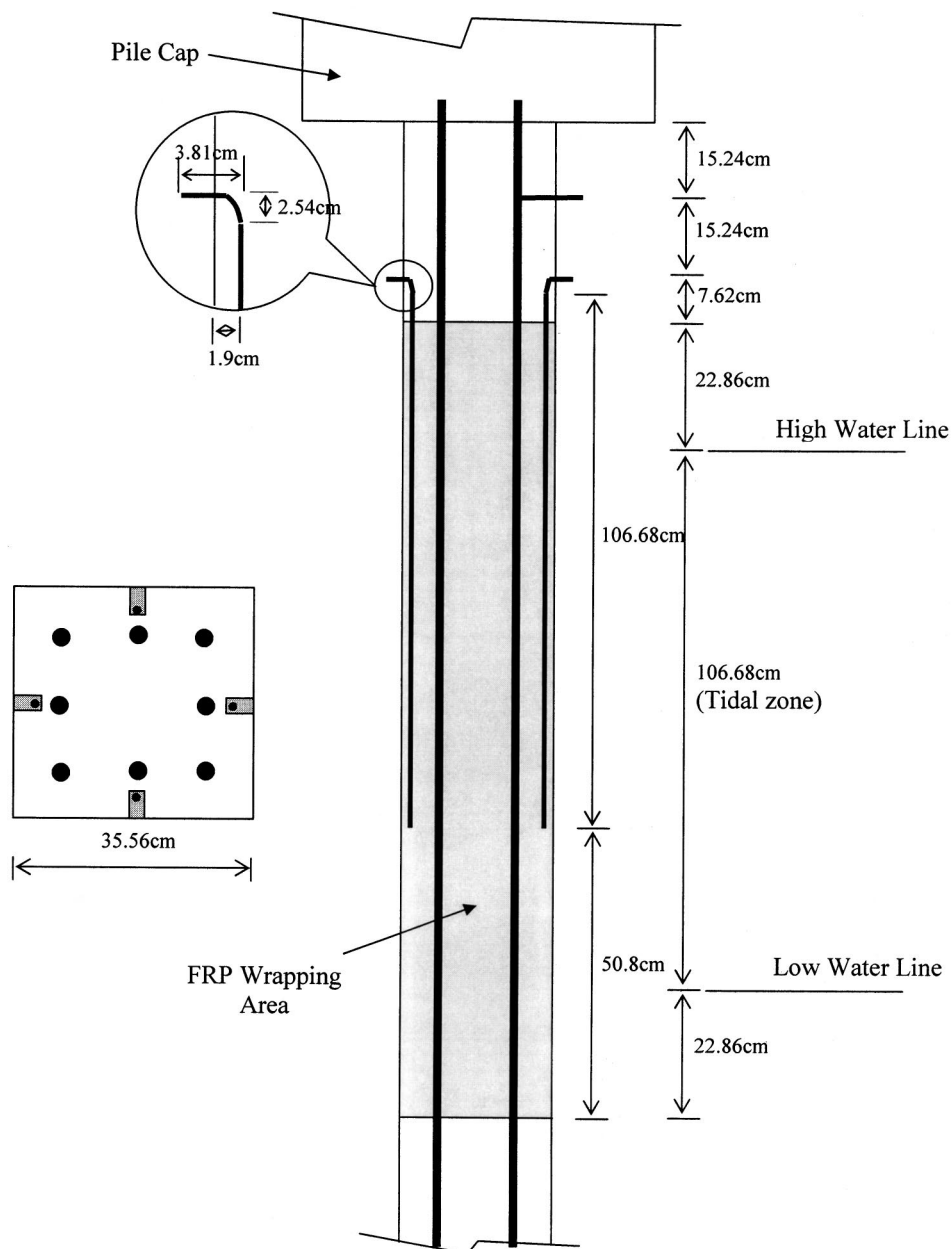


Fig. 9. USF probe

the carbon wrapped (F1) and the fiberglass wrapped (E2) piles. Instrumentation was intended to allow monitoring of both the corrosion potential and the corrosion rate.

### Ground Connection

Before any corrosion measurement can be made, an electrical connection has to be made to the prestressing strands. A 5 cm diameter hole was drilled above the high water line of the pile, about 0.3 m below the underside of the pile cap. The hole was drilled at the center of the pile where a strand was located. A 10 cm long, 0.5 cm diameter 316 stainless steel rod was connected to the strand by brazing. No special preparation was needed, because the strand was in good condition. The 316 stainless steel grade was especially chosen because of its superior corrosion resistance as compared to the less expensive 304 grade.

Although a single connection would have sufficed, four similar holes were drilled, one on each pile face, and identical brazed connections were made to ensure there was continuity between all the strands. The 7.5 cm deep holes were then filled with mortar, leaving a 2.5 cm section of the stainless rod protruding from each face. Potential readings can be taken by connecting a standard copper-copper sulfate half cell to the negative terminal of a high impedance voltmeter while attaching the positive terminal to the steel strand via the stainless steel rods protruding from each face (Fig. 5).

To ensure that potential measurements were consistently taken at the same location, a special template was prepared using a flexible plastic sheeting material. The width of the sheet equaled the pile width, and holes were punched along a 15 cm grid where readings were to be taken. Sponges were attached to one side of



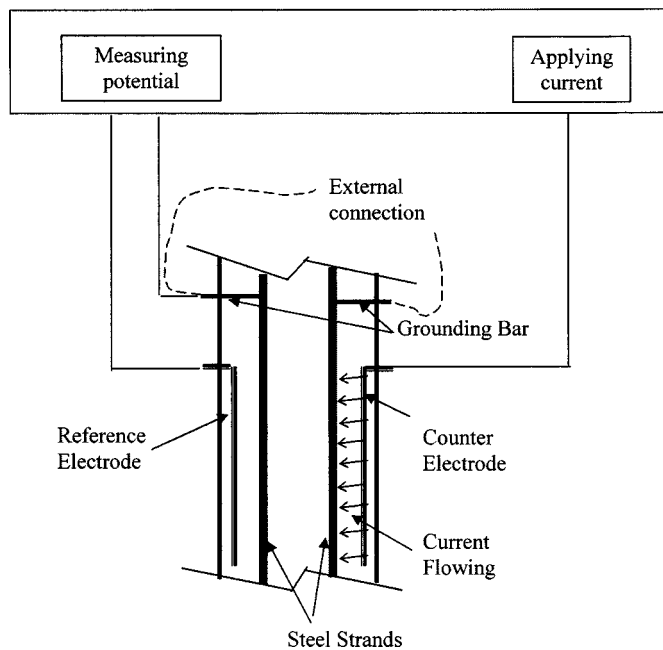


**Fig. 10.** Schematic setup for linear polarization measurements using USF probe

the sheeting. This setup ensured that, once the template was correctly positioned (Fig. 6), all readings could be quickly and accurately taken. This was very important, because measurements took on an average 6 h, during which the tide could come in.

Before readings could be taken, all marine growth covering the pile surface below the high water line (Fig. 7) was scraped off and removed. When this was done, it was found that two of the piles, E1 and F2, were spliced (Fig. 8). In addition, remnants of lifting hooks were detected from unexpectedly high corrosion potential readings on one face of instrumented pile B2 (unwrapped control). However, as there was a second “perfect” control, this was not a problem.

### Corrosion Rate

Corrosion potential can only be measured where the concrete surface is accessible. Thus, it can be used for unwrapped control specimens and for the unwrapped portions of wrapped specimens. Corrosion potential is, however, only indicative of probability of

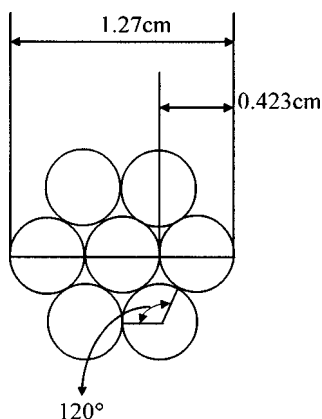


**Fig. 11.** Schematic used for calculation of strand surface area

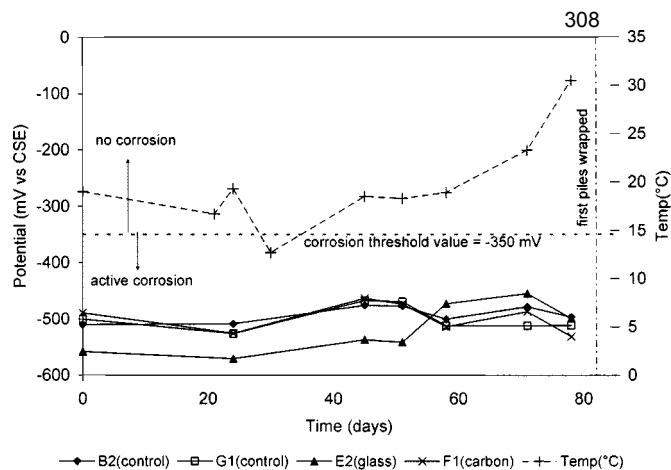


**Fig. 12.** Half-cell potential at 1.22 m from pile cap before wrapping

corrosion. For example, readings more negative than  $-350$  mV have a 90% probability of corrosion. Thus, corrosion monitoring requires measurement of the corrosion rate. This is determined from linear polarization measurement. Linear polarization relies on the linear relationship between the corrosion current and its potential when the equilibrium potential is perturbed by the application of an incremental current (“galvanostatic”) or incremental voltage (“potentiostatic”). Several portable devices are available that can be used to make the measurement. In this study, a PR-Monitor Model 4500, manufactured by Cortest Instrument Systems, Inc., was used.

The measurement of the corrosion rate requires: (1) a working electrode—the element whose corrosion rate is to be determined; (2) a reference electrode to measure the electrical potential of the working electrode; and (3) an auxiliary or counter electrode to apply a current and complete the circuit. The PR-Monitor system has a built-in power supply and its own reference and counter electrodes.

The original plan was to use commercially available probes as had been used in other studies, e.g., Halstead et al. (2000). These probes have a connection cable containing wires from reference, counter, and working electrodes that can be directly connected to a PR-Monitor. However, the installation of such probes in the “splash zone” is problematic, requiring cofferdam construction. Moreover, extensive wiring would have to be run from the piles and multiple junction boxes installed so that the length of the wiring would not exceed 6.1 m to ensure readings were accurate. In view of this, an alternative scheme was developed that eliminated both the need for wiring and potential corrosion problems of electrical connections.

### USF Probe

The corrosion rate is determined from the change in the corrosion potential due to the application of an incremental current or voltage. Therefore, any system that allows this change to be measured can be used as a probe. As mentioned earlier, in this study, a system proposed by Sagues (personal communication, 2002) was used. The system is simple to install and does not require any wiring or corrosion protection.

A schematic of the probe is shown in Fig. 9. It consists of a 0.5 cm diameter 316 stainless steel rod that is embedded relatively close (1.9 cm) to the surface. Four rods were used to allow the corrosion rate of strands on each face to be determined. The rods

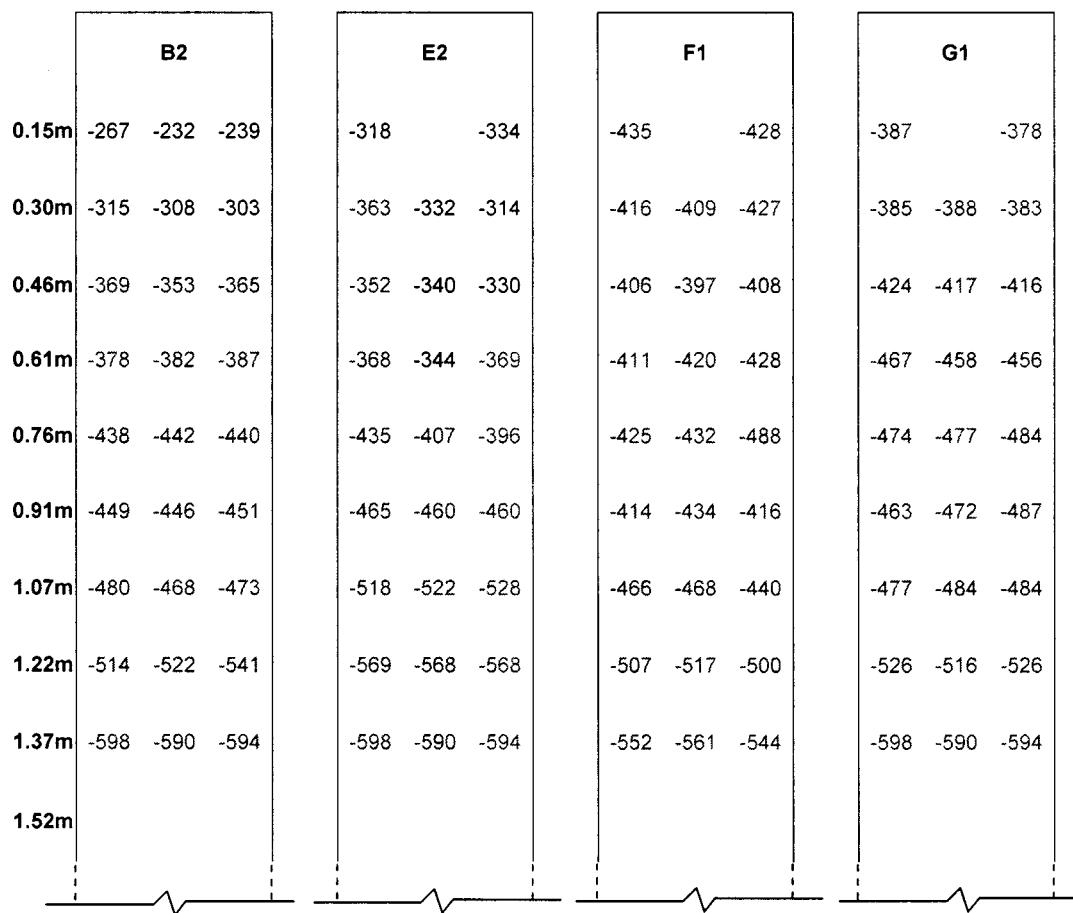


Fig. 13. Initial half-cell potential map for south face (units: mV)

were 1.07 m long and extended 7.5 cm above the top of the wrap, where they terminated in a 90° hook to facilitate electrical connection using alligator clips. Because no cofferdam was used, the length of the rod was limited to 1.07 m, as it was the maximum length that could be installed in the pile at low tide. This is shorter than the 1.52 m wrapped length that extended nearly 0.5 m further. The corrosion rate determined from the testing corresponds to the 1.07 m length of the stainless steel rods.

The probe determines the average corrosion rate, because all the strands are connected to each other (Fig. 10). Usually four sets of measurements were taken and the readings averaged. For each set, the working electrode (strand), the reference electrode (one stainless steel rod) and counter electrodes [the remaining three (or two in the case of pile B2) are connected to each other] were connected to the PR-Monitor. The next reading is taken by alternating the positions of the reference and counter electrodes. Po-

Table 1. Material Properties of Fiberglass and Carbon Used in Allen Creek Bridge

Material	Tensile strength (MPa)	Elastic modulus (MPa)	Load (kN) per layer (per meter)
Glass: unidirectional	586	35,853	420.5
Glass: bidirectional	324	20,684	210.2
Carbon: unidirectional	827	75,842	595.7
Carbon: bidirectional	586	22,063	420.5

tentiostatic testing was used, in which the voltage was incremented in steps from 0 to 15 mV, with the current adjusted accordingly. The slope of the change in potential and applied current gives the polarization resistance,  $R_p$ . Concrete has a high resistance that needs to be considered in the calculation of polarization resistance. Usually,  $R_p$  is corrected by subtracting the concrete resistance from original  $R_p$ .

The corrosion rate is found in the usual manner: the polarization resistance,  $R_p$ , is related to the corrosion rate  $i_{\text{corr}}$  by a proportionality constant given by the well-known Stern-Geary equation. In this study,  $B$  was assumed as 26 mV. The polarized strand length was assumed to be the same as counterelectrode length (1.07 m). The surface area of the strand was calculated assuming that each wire subtended a 240° angle (Fig. 11). This gave a perimeter of 5.3 cm for each strand. Because the assumed polarized steel length was 1.07 m and the pile has eight strands, the total surface area was calculated as 4,534 cm<sup>2</sup>, neglecting the tie area (Suh 2002).

## Prewrap Corrosion Results

Weekly measurements of the corrosion state were planned. However, because of rain, seven sets of measurements were made prior to the wrap.

Fig. 12 shows the variation of the half-cell potential [versus Copper Sulfate Electrode (CSE)] measured 1.22 m below the pile cap before wrapping. All piles showed more negative than

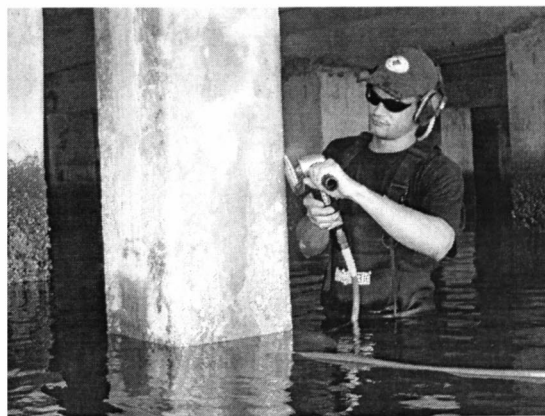
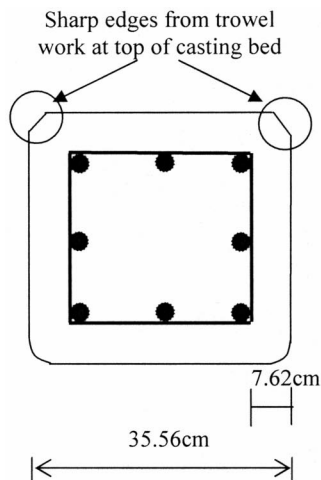


**Fig. 14.** Rounding sharp corners

-350 mV, indicating there was a 90% probability corrosion was occurring (ASTM C-87-91). Fig. 13 shows the distribution of initial half-cell potential value measured on the south face of each pile. Values are lower near the top but increase with depth. These values corroborate the chloride levels discussed earlier.

Prewrap corrosion rates were also determined from linear polarization. Rates were small (less than 0.2 mils per year). They are shown with the postwrap corrosion rate plots later for convenience.

### Wrap Design

The use of FRP for corrosion mitigation is relatively new, and no approved design procedure is currently available. The wrap used for the underwater repair was designed to match an identical

layup requiring cofferdam that was part of this demonstration. For this wrap, a two-step design procedure was developed. In the first step, a strain compatibility analysis was carried out to restore capacity for an assumed 20% metal loss. The fiber layup required for this strength gain was then checked to determine if it could withstand postrepair expansion due to deleterious material trapped inside the wrap. Complete details including numerical examples may be found in Shahawy et al. (2004).

### Underwater Wrap

The underwater wrap was carried out using Aquawrap 22-77 (Air Logistics 2002). This is a water-cured polyurethane resin system that can be used with woven glass fabric, unidirectional glass fabric, woven carbon fabric, and unidirectional carbon fabric. The

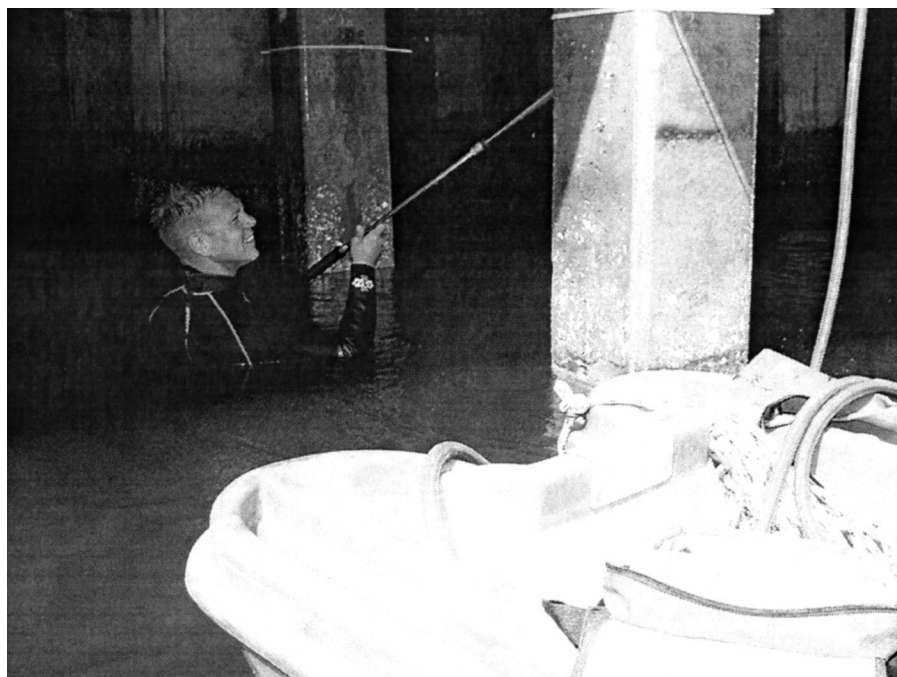


**Fig. 15.** Pressure washing with fresh water



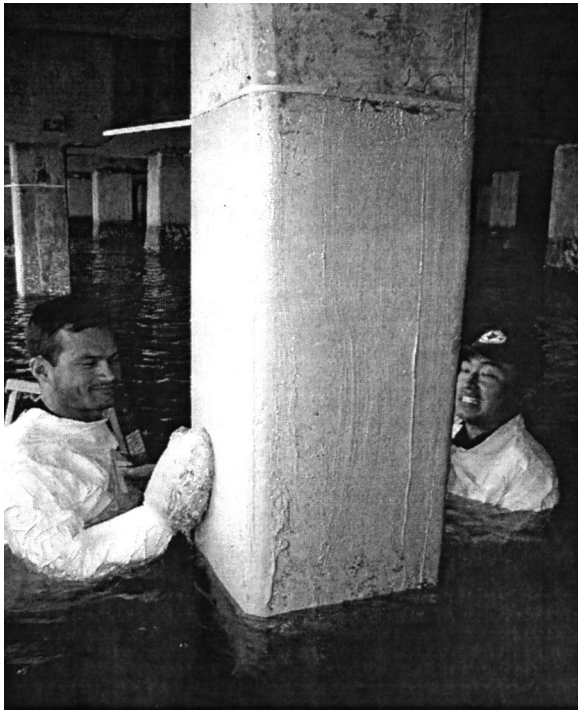


**Fig. 16.** Applying adhesive on pile surface

composite is a prepreg and is delivered in hermetically sealed pouches that are opened at the jobsite as they are applied. The first ever application of this technology was in the wrap of two uninstrumented reinforced concrete piles in North Carolina (Bazin et al. 2003). This was the first application on prestressed piles.

Two different fibers—glass and carbon—were used for the underwater demonstration study. The fiber layout was selected to ensure that they provided comparable strength gain. Material

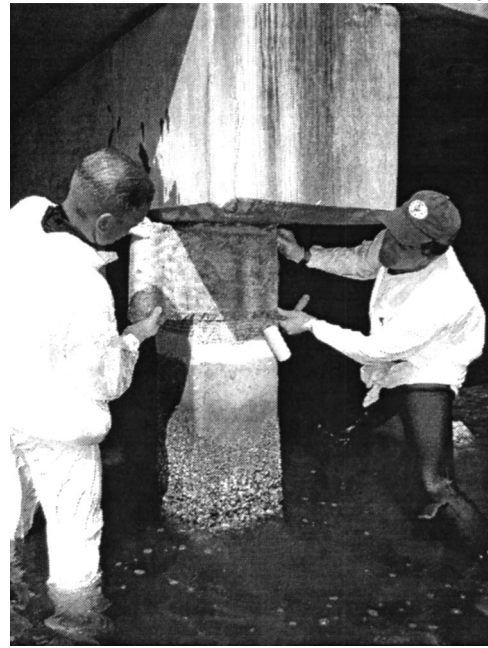


**Fig. 18.** Wrapping witness panel for bond test

properties as provided by the manufacturer are summarized in Table 1 (Air Logistics 2002).

Inspection of Table 1 shows that carbon has a higher tensile strength and modulus as compared to glass. Both unidirectional, i.e., the fibers provided tensile strength in one direction, and bi-directional, i.e., the fibers provided strength in two orthogonal directions, were used. The unidirectional fibers were applied in the longitudinal direction to increase flexural capacity. The bi-directional fibers added capacity in the transverse or hoop direction to provide increased resistance against expansive forces set up due to steel corrosion.

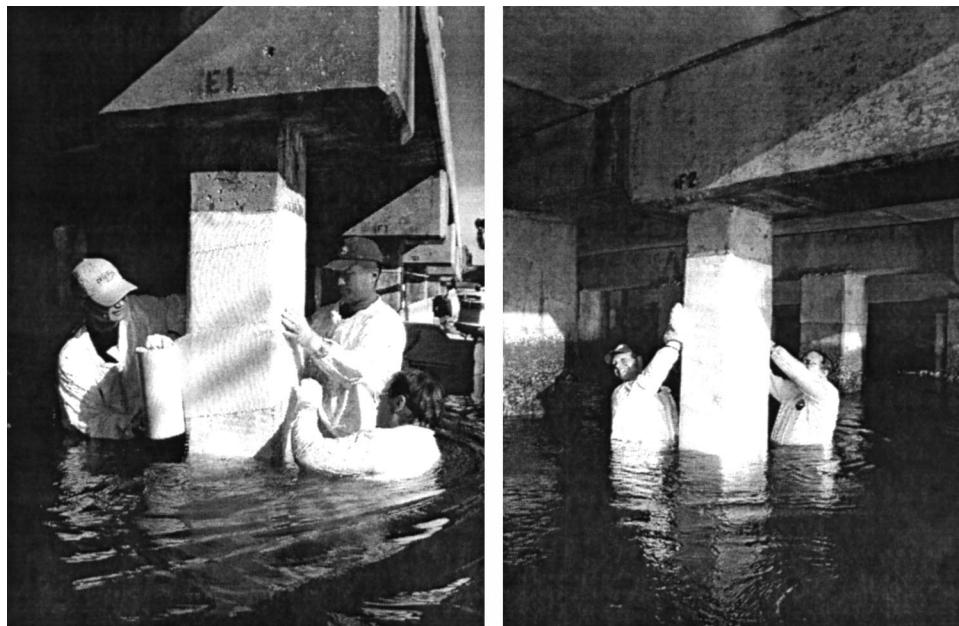


**Fig. 17.** Applying wrap

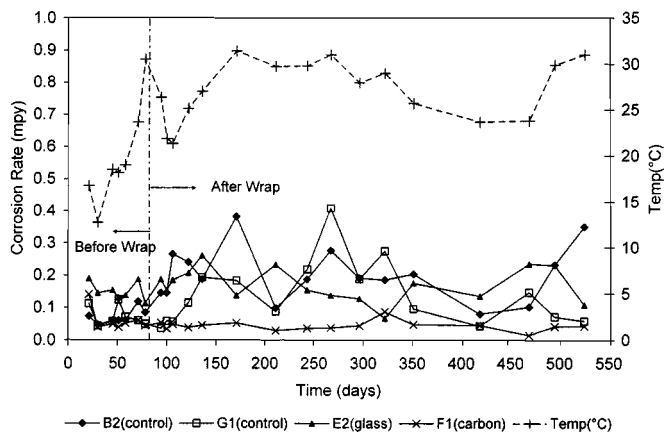


Fig. 19. Corrosion rate measurements of wet wrapped piles

### Aquawrap Carbon Fiber

One layer of unidirectional carbon fiber (tensile strength 595.7 kN/m) using strips that were 30.5 × 152.4 cm long was applied on each face of the 35 cm pile. This was wrapped over spirally in the hoop direction by two continuous layers of bidirectional carbon fiber material (tensile strength 420.5 kN/m × 2 layers = 841 kN/m). One layer of glass fiber veil was applied to cover and protect the carbon.

### Aquawrap Glass Fiber

Two layers of unidirectional glass fiber (tensile strength 420.5 kN/m × 2 layers = 841 kN/m) using the same sized strips as the carbon 30.5 × 152.4 cm were applied on each face of the 35 cm pile. This was wrapped over spirally in the hoop direction by four continuous layers of bidirectional carbon fiber material (tensile strength 210.2 kN/m × 4 layers = 841 kN/m). One layer of glass fiber veil was applied to cover and protect the carbon.

### Surface Preparation

The pile surface had to be smooth and sharp corners rounded to avoid stress concentrations. All marine growth was removed from the region to be wrapped with a scraper. Subsequently, two of the four corners that were not rounded (chamfered during casting) were ground down using an air-powered grinder (Fig. 14). This was a difficult operation, particularly for sections that were below the water line. Quick-setting hydraulic cement was used to fill any depressions, discontinuities, etc., to provide a smooth surface. The entire surface was pressure washed using freshwater to remove all dust and/or marine algae just prior to wrapping (Fig. 15).

### Application

#### Carbon

Pile F1 was wrapped using three layers of carbon fiber (one longitudinal and two lateral). First, an underwater epoxy adhesive was applied to the prepared surface of the pile that was to be wrapped (Fig. 16). The FRP layout required one unidirectional, longitudinal layer that was overlaid by two bidirectional layers. The longitudinally aligned layer (unidirectional) consisted of four 30.5 × 152.4-cm-long strips, one on each face of the pile. These

strips were held in place by the already applied adhesive until the subsequent wrapped layers could secure them. The bidirectional carbon layers were then applied starting at the top. These layers were designed to be wrapped around the pile in a continuous fashion with easily manageable rolls (e.g., 30.5 cm wide × 5–6 m long). After one full horizontal wrap around the pile, subsequent wraps were applied spirally downward with no overlap until the lowest point was reached where the process was reversed and the wrap was applied spirally upward to complete the second layer. No resin was required, because it was a prepreg. However, in regions above the water line, water was sprayed to allow the resin to cure. Upon completion of the structural wrap, a single layer of a 25.4 cm wide prepreg fiberglass cloth (veil) was spirally applied, moving from bottom to top, to consolidate the wrap and provide a better finish. A 5 cm (2 in.) overlap was provided for this layer. The entire wrap was then secured with a plastic stretch film, Stricture Banding.

### Fiberglass

Pile E2 was wrapped using the fiberglass wrap. The procedure for wrapping was identical except that the fiber layout required two unidirectional layers in the longitudinal directions and four bidirectional in the transverse direction. The wrap was allowed to cure for one day, following which the plastic stretch film was removed and the wrap painted over using polyurethane-based paint to provide protection against ultraviolet radiation (Fig. 17).

The entire operation went without a hitch and each pile took less than an hour to wrap.

### Witness Panels

To allow future evaluation of the FRP/concrete bond, witness panels were prepared in which a 0.3 m length of the pile above high tide was wrapped identically to the aforementioned manner for future bond testing (Fig. 18).

### Postwrap Corrosion Monitoring

The wrapping was completed in the second week of March 2003. For the first month after wrapping, corrosion measurements were taken weekly. Subsequently, they were taken every month. These measurements included corrosion potential and linear polarization measurements, from which the corrosion rate was calculated. Temperature readings were also taken regularly.

Results of the postwrap corrosion rate up to April 2004 (413 days after wrapping) are shown in Fig. 19. Rates continue to be small. Fluctuations in the rates may be observed particularly for the unwrapped controls, B2 and G1. This is most probably because of temperature, which affects the corrosion rate. The performance of the carbon fiber originally appeared to be better. However, in the most recent measurement, the performance of carbon and glass were comparable. The performance of both carbon and glass are, however, better than those for the unwrapped controls.

### Conclusions

This paper describes a field demonstration study to evaluate the application of FRP for the underwater repair of corroding pre-

stressed piles. A total of four full-sized 35×35 cm square prestressed piles were wrapped, two with carbon and two with glass. Two of these wrapped piles—one carbon and one glass—were instrumented to allow evaluation of their postwrap performance. Two other unwrapped piles serve as controls. Instrumentation allowed determination of the corrosion potential over the unwrapped surface and the corrosion rate for the wrapped piles. A unique feature of the instrumentation was the use of stainless steel rods with protruding hooks that eliminated the need of wiring and junction boxes. Connections only require alligator clips.

The study showed that underwater wrapping is a viable system. As with most FRP retrofits, surface preparation is of paramount importance. In this case, surface preparation required equipment capable of operating underwater to grind sharp corners. Although initial field tests on the witness panels indicated that the bond between the wet concrete and the FRP was relatively poor, laboratory tests showed the bond was sufficient to restore the full undamaged capacity. Corrosion rate measurements indicate that the performance of the wrapped piles is consistently better than the unwrapped controls.

Underwater FRP repair technology is very new and is under development. The ease and speed with which the repairs were made is very promising. In the study, each pile was wrapped in less than one hour. Corrosion monitoring data suggests that the performance of the underwater wrapped piles is comparable to those wrapped inside a cofferdam in a parallel study being conducted at the same site. All these portend well for the future of this technology.

## Acknowledgments

This study was performed in cooperation and with funding from the State of Florida and U.S. Department of Transportation. This support is gratefully acknowledged. The assistance and guidance of Mr. Jose Garcia and Mr. Steve Womble from the Florida Department of Transportation is gratefully acknowledged. The writers are indebted to Air Logistics, Pasadena, CA, for their assistance throughout this study. They especially thank Mr. Franz Worth and Mr. Steve Bazinet, who participated in the laboratory demonstration and also in the field wrap. The writers thank graduate students Mr. Ivan Gualtero, Mr. Kevin Johnson, Mr. Mike Stokes, and Mr. Kadir Uslu for their contribution.

The opinions, findings, and conclusions expressed in this publication are those of the writers and not necessarily those of the Florida or U.S. Departments of Transportation.

## References

- Air Logistics Corporation. (2002). *Aquawrap repair system*, Pasadena, Calif.
- Bazinet, S., Cercone, L., and Worth, L. (2003). "Innovative FRP piling repair without the use of cofferdams." *Proc., 48th Int. SAMPE J. Conf., Society for the Advancement of Material and Process Engineering, Corvina, Calif.*, 2201–2206.
- Fischer, J., Mullins, G., and Sen, R. (2000). "Strength of repaired piles." *Final Rep.*, Florida Department of Transportation, Tallahassee, Fla.
- Halstead, J., Connor, J., Luu, K., Alampalli, S., and Minser, A. (2000). "Fiber-reinforced polymer wrapping of deteriorated concrete columns." *Transportation Research Record 1696*, Transportation Research Board, Washington, D.C., 124–130.
- Mindess, S., Young, J., and Darwin, D. (2003). *Concrete*, Prentice-Hall, Englewood Cliffs, N.J.
- Neale, K. W., and Labossiere, P. (1998). "Fiber composite sheets in cold climate rehab." *Concr. Int.*, 20(6), 22–24.
- Scheffy, C. F. (1981). "Bridge deck deterioration—a 1981 perspective." FHWA Memorandum, Federal Highway Administration Office of Research, Washington, D.C.
- Sen, R. (2003). "Advances in the application of FRP for repairing corrosion damage." *Progress in Structural Engineering and Materials*, 5(2), 99–113.
- Sen, R., Mullins, G., and Snyder, D. (1999). "Ultimate capacity of corrosion damaged piles." *Final Rep.*, Florida Dept. of Transportation, Tallahassee, Fla.
- Shahawy, M., Mullins, G., and Sen, R. (2004). "CFRP repair and strengthening of structurally deficient piles." *Transp. Res. Rec.*, manuscript under review.
- Suh, K. S. (2002). "Effectiveness of CFRP in reducing corrosion rate of prestressed members." MS thesis, Dept. of Civil and Environmental Engineering, University of South Florida, Tampa, Fla.
- Suh, K. S., Mullins, G., Sen, R., and Winters, D. (2004). "Use of FRP for corrosion strengthening applications in a marine environment." *Interim Rep., Contract No. BC353 RPWO#37*, University of South Florida, Tampa, Fla.
- Tarricone, P. (1995). "Composite sketch." *Civ. Eng. Mag.*, 52–55.
- Vaysburd, A. M., and Emmons, P. H. (2000). "How to make today's repairs durable for tomorrow—corrosion protection in concrete repair." *Constr. Build. Mater.*, 14, 189–197.



## **FRP Application in Underwater Repair of Corroded Piles**

Rajan Sen, Gray Mullins, Kwangsuk Suh and Danny Winters

**Synopsis:** The poor durability of conventional corrosion repairs has led to increased interest for its replacement by fiber reinforced polymers (FRP). Over the past decade, several highway agencies completed demonstration projects in which FRP was used to repair corrosion damage on surfaces that were dry. These repairs have held up well and show little sign of deterioration. The availability of resins that can cure in water has made it possible to explore the application of FRP for the underwater repair of corrosion-damaged piles. This paper presents findings from three demonstration projects in which corroding reinforced and prestressed piles at two contrasting locations were repaired using two different FRP systems. Several piles were instrumented to allow long-term corrosion monitoring. The projects confirm the feasibility of conducting underwater FRP repairs in tidal waters. Preliminary data suggests that the wrap leads to a reduction in the prevailing corrosion rate.

**Keywords:** Corrosion, FRP, Instrumentation, Piles, Repair, Underwater

Rajan Sen is a professor of structural engineering at the University of South Florida, Tampa, FL. He is a fellow of both ACI and ASCE and held the Samuel and Julia Flom Chair. Dr. Sen is active in FRP research and serves on ACI Committees 215, Fatigue of Concrete; 440, Fiber Reinforced Polymer Reinforcement and 444, Experimental Analysis for Concrete Structures.

Gray Mullins is an associate professor in structural engineering at the University of South Florida, Tampa, FL. His primary research interest is in the area of full-scale testing and instrumentation of structures and foundations. Dr. Mullins has authored numerous publications and holds two US patents.

Kwangsook Suh is a Ph.D. candidate in the Department of Civil and Environmental Engineering at the University of South Florida, Tampa, FL. His major interest is on evaluation and repair of corrosion damaged bridge piles exposed to marine environments.

Danny Winters is a research associate and a Ph.D. student in the Department of Civil and Environmental Engineering at the University of South Florida, Tampa, FL. His research interest is in full-scale testing of foundations.

## INTRODUCTION

The high concentration of chloride ion in seawater allows it to penetrate to the level of steel even in high-quality concrete. As a result, the passive layer that normally protects steel is destroyed making corrosion of reinforcing or prestressing steel inevitable. This problem is particularly severe in tidal waters in sub-tropical environments where the combination of wet/dry cycles and high temperature/high humidity can lead to rapid deterioration that necessitate costly repairs.

Corrosion repairs are only durable if the conditions responsible for the original deterioration are removed. This means that all chloride-contaminated concrete including the concrete behind the steel must be removed<sup>1</sup>. Since the boundaries of the chloride contaminated region are not known with any precision this is a daunting task even under dry conditions. For half-submerged piles in salt water this is a near impossibility.

Not surprisingly, corrosion repair of piles is seldom durable with the exception of the Life Jacket system<sup>2-3</sup> developed through the pioneering efforts of the Florida Department of Transportation<sup>4-7</sup>. In this system, corrosion is stopped by integrating a sacrificial cathodic protection system within the repair. Unfortunately, the Life Jacket system may not always be affordable. In such instances there is a need for alternative, cost effective “temporary” repairs that are more durable than conventional ‘chip and patch’ type of repairs.

Fiber reinforced polymers (FRP) offer the prospect of such a cost effective repair. Its lightweight, high strength and resistance to chemicals offer obvious cost advantages. In fabric form, it offers unprecedented flexibility in construction. Moreover, as fibers can be oriented as required they can provide strength in any desired direction. This versatility

has led to several research studies to investigate if FRP's strength and durability can be harnessed to successfully repair corrosion damage.

It should be noted that the use of FRP for corrosion repair is deemed controversial. For example, ACI 440 Committee Guidelines<sup>8</sup> states "*The application of FRP systems will not stop ongoing corrosion ...If steel corrosion is evident ...placement of FRP reinforcement is not recommended without arresting the ongoing corrosion and repairing any degradation to the substrate*".

Economics has been largely responsible for disregarding this valid warning. When faced with the prospect of closing a bridge or a temporary FRP repair, highway authorities have usually opted for the latter. However, the performance of these "temporary repairs", in some cases extending over ten years of service, has been exceptional<sup>9</sup>.

It should be noted that the vast majority of the studies attempted were carried out under dry conditions that are favorable for applying FRP. With the emergence of resin systems that can cure in water it has become possible to conduct corrosion repairs under water<sup>10-11</sup>.

This paper describes three field demonstration studies in which FRP repairs were carried out on corroding, partially submerged piles in tidal waters. An important element in all these applications was that several piles were fully instrumented to allow the corrosion rate to be monitored. Thus, these studies have the potential to yield data on the role FRP plays in slowing down the corrosion rate. Complete descriptions may be found elsewhere<sup>12-15</sup>. This paper provides a brief overview to highlight some of the more important lessons learnt relating to the underwater application of the wrap.

#### RESEARCH SIGNIFICANCE

This paper summarizes information from three separate field demonstration projects relating to an emerging new application of fiber reinforced polymers, namely underwater corrosion repair of piles. Corrosion of piles in tidal waters is a common problem and this information will be helpful in advancing the state of practice.

#### PROBLEM STATEMENT

The application of FRP for corrosion repair of piles serves the dual purpose of enhancing flexural strength and providing confinement to withstand expansive forces set up by corrosion products. Thus, this application is part bond-critical and part contact-critical.

As with any bond-critical application, surface preparation is important; good bond requires the substrate to have an open pore structure to assure capillary suction of the epoxy. In underwater application, however, pores will be saturated with water or small

marine organisms or algae. This is likely to adversely affect bond and alternative measures, e.g. bonding agents, may be required to ensure satisfactory performance.

The logistics of saturating FRP with resin and installing it in underwater applications are more complex given unpredictable environmental conditions. Wind, waves and tides play a critical role and unless they are factored in, wrapping is unlikely to be successful. New techniques have to be established for installation that minimizes the impact of these unfavorable conditions.

As stated earlier, FRPs are only viable for corrosion repair if they are cost effective. Given the high material cost, pile repairs must be properly engineered. Unfortunately, not all relevant information is available, e.g. relationship between corrosion and expansion.

Safety is of paramount important issue and must be factored in all operations. Normal as well as extraordinary measures need to be taken to avoid potentially unfavorable conditions. Meticulous planning and coordination is required to prepare for unexpected situations.

#### DESIGNING CORROSION REPAIR

The role of FRP in pile repair is twofold: first to restore lost flexural capacity due to steel corrosion; second to provide resistance to withstand expansive forces caused by corrosion of steel. The former requires fibers to be oriented parallel to the direction of the reinforcing or prestressing steel, i.e. along the length, while the latter requires fibers in the transverse or hoop direction, i.e. perpendicular to the steel. This can be met either by using two different sets of uni-directional fibers one for each direction or preferably, by using bi-directional FRP material that requires less labor.

An estimate of the required strength in the longitudinal direction may be made based on the steel cross-section that was lost by corrosion. A large body of laboratory test data relating ultimate capacity to metal loss is available in the published literature and this provides a means for developing a rational procedure. Alternatively, a conservative capacity loss may be assumed. This was the case in the demonstration projects where capacity loss was assumed to be 20%.

Currently, there is a lack of reliable information on transverse expansion caused by corrosion. Most available experimental transverse expansion data was obtained from accelerated corrosion tests that resulted in symmetric cracking. In practice, the combined action of wind and waves result in uneven chloride penetration that inevitably results in asymmetric cracking. More importantly, the solubility of corrosion products from accelerated testing may be different. Thus, laboratory data may not be appropriate. In view of this, a simplified procedure was developed<sup>12, 16</sup>. In design, the expansion strain was assumed as 0.1% (approximately 3 times the ultimate concrete tensile strain assumed to be 10% of the ultimate concrete failure strain).

Using the above assumptions, a two step design procedure was developed that was used in all the demonstration projects. In the first step, strain compatibility analysis was used to develop interaction diagrams to determine the number of FRP layers required to make up for the assumed shortfall in flexural capacity due to corrosion. In the second step, the confining lateral strain provided by this strengthening was checked to ensure that this did not exceed an assumed expansion strain of 0.1%. Results obtained using this method were found to be reasonable. For the bi-directional carbon fiber, only two FRP layers were required. Twice as many layers were required for fiberglass because of its lower strength and stiffness.

### DESCRIPTION OF DEMONSTRATION PROJECTS

Three field demonstration studies were conducted at two contrasting sites. The first, Allen Creek Bridge, Clearwater is in shallow, relatively calm waters; the remaining two studies were carried out on piles supporting Gandy Boulevard bridges spanning Tampa Bay. The first of these two bridges is the Friendship Trails Bridge that is now a recreational trail for pedestrians and cyclists. The second is the Gandy Bridge. The waters of the Tampa Bay are much deeper and more turbulent than those of Allen Creek.

These sites were selected because the environment is extremely aggressive. This was confirmed from chloride content analysis of concrete cores taken from the piles. The chloride content at the level of the reinforcement exceeded the threshold required for corrosion to be initiated.

FRP material -- Two differing systems were used in all three demonstration projects. One was a pre-preg, the other a wet lay up. The pre-preg system was from Air Logistics in which all the FRP material was cut to size, resin saturated in the factory and sent to the site in hermetically sealed pouches (Fig. 1). The wet lay up system used for wrapping the piles under wet conditions was from Fyfe. An additional wet lay up system was also used but this was carried out under dry conditions inside a cofferdam. For this reason, it is not discussed in this paper. Both carbon and fiberglass were used. Details of the properties of the fiber and the resin as provided by the suppliers are summarized in Tables 1 to 4.

#### Allen Creek Bridge

Allen Creek Bridge is located on the busy US 19 highway connecting Clearwater and St. Petersburg, FL. The original bridge built in 1950 was supported on reinforced concrete piles driven into Allen Creek. In 1982, the bridge was widened and this new section was supported on 35 cm (14 in.) square prestressed piles.

The waters from Allen Creek flow east into Old Tampa Bay that in turn joins the Gulf of Mexico to the south. The environment is very aggressive; all the reinforced concrete piles from the original construction had been rehabilitated several times. At low tide, the water level in the deepest portion of the creek is about 0.76 m (2.6 ft). Maximum

high tide is about 1.89m (6.2 ft). This shallow depth meant that the underwater wrap could be carried out on a ladder.

Preparatory work -- Pile surfaces were covered with marine growth (Fig. 2) that had to be scraped off. Additionally, two of the four corners that were not rounded but chamfered had to be ground using an air-powered grinder. This was a difficult operation particularly for sections that were below the water line. A quick-setting hydraulic cement was used to fill any depression, discontinuities and provide a smooth surface. Just prior to wrapping the entire surface was pressure washed using freshwater to remove all dust and marine algae.

Instrumentation -- Instrumentation was installed to allow linear polarization and corrosion potential measurements to be made. An innovative instrumentation scheme was developed that eliminated the need for wiring and junction boxes<sup>14</sup>. This was an important consideration since the piles were located in relatively shallow waters that were accessible on foot. Several piles supporting the structure had been defaced and the probability of vandalism was very real.

FRP wrapping -- Two different schemes using two different materials were evaluated. In each scheme four piles were wrapped with two other instrumented piles serving as controls. In the first scheme, cofferdam construction was used and the piles wrapped using a bi-directional FRP in a wet lay up under dry conditions. As this was wrapped under 'perfect' conditions, its performance provided a means for evaluating piles that were directly wrapped in water using a new water activated resin (Fig. 3). The latter scheme was a pre-preg system developed by Air Logistics.

The pre-preg was easy to install since all the material came in labeled hermetically sealed packets. After applying an initial epoxy layer, the packets were opened according to the layout scheme and the FRP material applied. A shrinkage wrap was applied at the end to allow the FRP to cure. On an average, it took between 30 minutes to 45 minutes to wrap a pile over a 1.5 m depth depending on the number of layers of material that had to be applied.

### Friendship Trails Bridge

This is the oldest of the Gandy Boulevard bridges crossing Tampa Bay. It was originally constructed in 1956 and was slated for demolition in 1997. Thanks to community activists, the bridge was saved, refurbished and rehabilitated. In 1999, the bridge was re-opened as a pedestrian bridge and re-christened as the "Friendship Trails Bridge". The 4.2 km (2.6 mile) structure is now the longest over-water recreational trail in the world. The bridge has 275 spans supported by 254 reinforced concrete pile bents and 22 column type piers located at the main channel crossing. Seventy seven percent of the 254 piers supporting this bridge have needed to be repaired indicating that the environment is very aggressive.



Preparatory work -- All piles wrapped were 50.8 cm x 50.6 m (20 in. x 20 in.) reinforced concrete piles and wrapped over a depth of 1.5 m that extended all the way to the underside of the pile cap. The waters are approximately 4.88 m (16 ft) deep. This meant that ladders could no longer be used to apply the FRP in this situation. An innovative scaffolding system was designed and fabricated. It was lightweight, modular yet sufficiently rigid when assembled to support 4-6 people. The scaffolding was suspended from the pile cap and extended 2.74 m (9 ft) below. Its mesh flooring provided a secure platform around the pile that allowed the wrap to be carried out unimpeded in knee deep waters (Fig. 4).

Instrumentation -- Unlike the Allen Creek Bridge where vandalism was a real concern, the piles of the Friendship Trails Bridge are located in deeper and more turbulent waters. Moreover, as the majority of the piles supporting this bridge had been repaired and some were instrumented, the element of novelty was absent making vandalism less likely. In view of this, an instrumentation system developed by the Florida Department of Transportation was selected. This required both wiring and junction boxes. The scheme uses rebar probes (Fig. 5) that are installed at different elevations close to the reinforcing steel. Changes in the direction of the corrosion current between these locations can indicate if the FRP is working as expected. Reductions in the measured current compared to unwrapped controls were also expected to provide an index of the efficacy of the FRP wrap. The drawback with this system is that it takes time for the equilibrium state around the probe to be attained. Until this time, data may not be meaningful.

FRP wrapping -- Two different FRP systems were used. One was the same pre-preg system with a water-activated resin used in the Allen Creek Bridge. The other was Fyfe's system that used resins that cure in water. The pre-preg system was used to wrap four piles – two using carbon and two using glass. The wet-lay up system from Fyfe required on-site saturation of the fibers. Two piles were wrapped with fiberglass using this system. Of the two, one was an experimental FRP system that combined wrapping with a sacrificial cathodic protection system. Two other unwrapped piles in a similar initial state of disrepair were used as controls to evaluate the performance of the wrapped piles. Application was facilitated through the use of a scaffolding system mentioned earlier (Fig. 6).

The pre-preg system was applied as in the Allen Creek Bridge and posed no problems. The Fyfe system was more challenging since the FRP material had to be saturated on-site. Access to foundations of an adjacent bridge provided a convenient staging post for the on-site impregnation (Fig. 7). On an average the operation took 90 minutes to complete.

### Gandy Bridge

The Gandy Bridge built in 1970's connects St. Petersburg to Tampa. The bridge has approximately 300 piers comprising five or eight prestressed concrete piles with 50.8 cm x 50.8 cm (20 in x 20 in.) cross section. The original plan was to just wrap one

heavily corroded pile (Fig. 8). Later, the scheme was revised to include three piles. An additional unwrapped but instrumented pile served as control (Fig. 9).

Preparatory work -- Though the scaffolding system used at the Friendship Trail Bridge provided a safe and stable working space, it required at least four to five people to install and move because of its large size and weight. In view of this, a new scaffolding system was developed that was geared towards wrapping individual piles. This was in two parts that were readily assembled in the field and suspended from the pile cap using steel chains rather than welded angles used earlier. The system could be installed by 2-3 people easily and quickly, and provided a good working space for 3 people (Fig. 10). Prior to applying the wrap, the severely damaged pile (Fig. 8) was repaired. The surface of the exposed concrete and steel was cleaned by sand blasting and the damaged section restored using an underwater patch material, Tyfo® PUWECC, manufactured by FYFE Co. LLC. All procedures recommended by the manufacturer were followed.

Instrumentation -- Since it was expected that FDOT would take over monitoring of the performance of the piles after the project was over, the same rebar probes used in the Friendship Trails Bridge were retained. Additionally, a commercial probe was used. This was relatively bulky in size but could just be accommodated within the cover. The benefit of the new system was it also allowed the corrosion rate to be monitored. Rebar probes were positioned at four different levels for measuring current flow and commercial probes were installed at two levels for performing the linear polarization measurement.

FRP wrapping -- The same two systems used in the Friendship Trails Bridge were also used in the Gandy Bridge. The operation was identical excepting that the system used for saturating the fibers for the Fyfe system was modified. Instead of using the saturating machine, hand methods were used as they were found to be speedier and equally effective. The entire operation went smoothly and the wraps were installed in about an hour each (Fig. 11).

## DISCUSSION

The use of FRP for corrosion repair of piles in tidal waters poses many problems relating to surface preparation, wrapping, instrumentation and monitoring long term performance. In this study the modus operandi was modified to accommodate the contrasting demands of the different sites and also the differing conditions of the piles.

Fig. 12 shows the condition of the wrapped piles in the Allen Creek Bridge after almost two years. The FRP appears to be in reasonable condition although marine growth has formed on the surface of the wrap. This is borne out by corrosion rate measurements shown in Fig. 13. These cover a period of nearly two years from the time the piles were first wrapped in March 2003.

Fig. 13 shows the average corrosion rate measurements in unwrapped controls, and piles wrapped under dry (cofferdam) and wet conditions. The variation in temperature is also shown. Inspection of Fig. 13 shows that the corrosion rate in the wrapped piles is

low and stable while that of the unwrapped piles showed continual fluctuation possibly due to environmental factors such as temperature and tide change. According to criteria proposed by Clear<sup>17</sup>, corrosion is not expected in the wrapped piles and it may occur in 10–15 years in the unwrapped piles.

Fig. 13 also shows that the corrosion rates for the piles wrapped under dry or wet conditions are quite similar. This suggests the underwater epoxies performed well and the piles are being provided comparable protection. Since strengthening is a bond critical application, bond tests are planned before the project ends to evaluate the relative quality of the bond in the two systems.

## CONCLUSIONS

This paper provides a brief overview of three demonstration projects in which instrumented reinforced and prestressed piles were wrapped using different FRP systems. Wrapping was carried out directly under water using ladders and innovative scaffolding systems suspended from the pile cap. The research team was pleasantly surprised at the ease with which the underwater wrapping was carried out.

Procedures that worked best can be summarized as:

1. Transverse wrapping is easiest – longitudinal pieces are awkward to handle and difficult to position. Bi-directional material is best.
2. Scaffolding ensures safety and simplifies installation.
3. Pre-preg is easier to use. On-site FRP saturation can be problematic.
4. High winds and high tides should be avoided.

The instrumentation system used in the Allen Creek Bridge, Clearwater requiring no wiring and junction boxes has proved to be robust and effective. Corrosion rate measurements over 2 years suggest that the performance of piles wrapped under dry conditions, i.e. using cofferdam construction and wet conditions was comparable. This could be because the measured corrosion rates are still low.

Underwater wrap for pile repair is relatively new and many innovations may be expected in the future that will make applications simpler. Should repairs prove durable, highway agencies will have access to another method of pile repair that may be economical in particular situations.

## ACKNOWLEDGEMENTS

The demonstration studies reported were funded by grants from the Florida/US Department of Transportation and Hillsborough County. The support and guidance of Mr. Pepe Garcia and Mr. Steve Womble, both of Florida Department of Transportation are gratefully acknowledged. We thank Ms. Mara Nelson, Hillsborough County for her contribution. FRP materials used were donated by Air Logistics, Corporation and Fyfe Co. LLC. We thank Mr. Franz Worth of Air Logistics and Mr. Ed Fyfe, President, Fyfe

for this support. We are also indebted to SDR Engineering, Tallahassee for their contribution to this research study.

#### REFERENCES

1. Emmons, P.H., 1993, *Concrete Repair and Maintenance Illustrated*, R S Means, Kingston, MA.
2. Leng, D., 2002, "Zinc-Mesh Jacket System Improves Corrosion Control," *Better Bridges*, November.
3. Leng, D., 2002, "Zinc Mesh Cathodic Protection Systems," *Materials Performance*, V. 41, No. 8, Aug., pp. 28-33.
4. Brown, R and Powers, R., 1985, "Update on the Use of Conductive Materials for Cathodic Protection of Steel in Concrete", NACE, Houston, TX, USA, pp. 264.1-264.8.
5. Kessler, R., Powers, R. and Lasa, I., 1991, "Cathodic Protection Using Scrap and Recycled Materials," *Materials Performance*, V. 30, No. 6, Jun, pp. 29-31.
6. Kessler, R., Powers, R. and Lasa, I., 1996, "Zinc Mesh Anodes Cast into Concrete Pile Jackets," *Materials Performance*, V. 35, No. 12, Dec, pp. 11-15.
7. Lasa, I., Powers, R. and Kessler, R., 1997, "Practical Application of Cathodic Protection Systems for Reinforcing Steel Substructure in Marine Environment," *International Seminar and Workshop for the Rehabilitation of Concrete Structures April, Maracaibo, Venezuela*.
8. ACI 440.2R-02, 2002, *Guide for the Design and Construction of Externally Bonded FRP Systems for Strengthening Concrete Structures*, American Concrete Institute, Farmington Hills, MI.
9. Sen, R., 2003, "Advances in the Application of FRP for Repairing Corrosion Damage," *Progress in Structural Engineering and Materials*, Vol. 5, No 2, pp. 99-113.
10. Bazinet, S., Cercone, L. and Worth, L., 2003, "Composite FRP Moves into Underwater Repair Applications," *SAMPE Journal*, V. 39, No. 3, May/June, pp.8-16.
11. Watson, R.J., 2003, "The Use of Composites in the Rehabilitation of Civil Engineering Structures", ACI-SP 215, ed. S. Rizkalla and A. Nanni, American Concrete Institute, Farmington Hills, MI, pp. 291-302.

12. Suh, K., Mullins, G., Sen, R. and Winters, D., 2004, "Use of FRP for Corrosion Strengthening Applications in a Marine Environment," Interim Report, Florida Department of Transportation, April.
13. Mullins, G., Sen, R., Suh, K and Winters, D., 2004, "Underwater Pile Wrap of the Friendship Trails Bridge", Final Report, Hillsborough County, June, 32 p.
14. Mullins, G., Sen, R., Suh, K and Winters, D., 2005, "Underwater FRP Repair of Prestressed Piles in the Allen Creek Bridge," *Journal of Composites for Construction*, Vol. 9, No. 2, Mar-April, pp. 136-146.
15. Mullins, G., Sen, R., Suh, K. and Winters, D., 2005, "Underwater FRP Repair of the Friendship Trails Bridge," To appear in *Concrete International*.
16. Shahawy, M., Mullins, G. and Sen, R., 2004, "CFRP Repair and Strengthening of Structurally Deficient Piles," Paper under review.
17. Clear, K. C., 1989, "Measuring the Rate of Corrosion of Steel in Field Concrete Structures," Transportation Research Board 1211, Transportation Research Board, National Research Council, Washington, DC.

Table 1 -- Properties of Aquawrap® Fabric

<b>Fiber</b>	<b>Material</b>	<b>Tensile Strength (MPa)</b>	<b>Tensile Modulus (GPa)</b>	<b>Load per Ply (kN/m)</b>
Uni-directional	GFRP	590	36	420
Bi-directional	GFRP	320	21	210
Uni-directional	CFRP	830	76	596
Bi-directional	CFRP	590	22	420

Table 2 -- Properties of Aquawrap® Base Primer #4

<b>Properties</b>	<b>Quantities</b>
Compressive Strength	69 MPa
Tensile Strength	33 MPa
Elongation at Break	40%
Flexural Strength	46 MPa
Shore Hardness	91

Table 3 -- Properties of Tyfo® SEH-51 Composite

<b>Properties</b>	<b>Quantities</b>
Tensile Strength	3.24 GPa
Tensile Modulus	72.4 GPa
Ultimate Elongation	4.5 %
Laminate Thickness	0.127 cm
Dry Fiber Weight	915 g/m <sup>2</sup>
Dry Fiber Thickness	0.038 cm

Table 4 -- Properties of Tyfo® SW-1 Epoxy

<b>Properties</b>	<b>Quantities</b>
Mixing Ratio, by wt	100:56
Specific Gravity	1.6
Gel Time, 18 °C, hours	2.5-3.5
7 day Compressive Strength	48-55 MPa





Figure 1 -- Prepreg FRP Material



Figure 2 -- Marine Growth, Allen Creek Bridge, Clearwater



Figure 3 -- Underwater Wrapping, Allen Creek Bridge, Clearwater



Figure 4 -- Scaffolding System, Friendship Trails Bridge, Tampa, FL



Figure 5 -- Rebar Probe Installation



Figure 6 -- Underwater Wrapping, Friendship Trails Bridge, Tampa





Figure 7 -- On-Site Saturation, Friendship Trails Bridge, Tampa



Figure 8 -- Heavily Corroded Pile, Gandy Bridge, Tampa



Figure 9 -- Selected Piles, Gandy Bridge, Tampa



Figure 10 -- Scaffolding System, Gandy Bridge, Tampa



Figure 11 -- Underwater Wrapping, Gandy Bridge, Tampa



Figure 12 -- View of Wrapped Piles, Allen Creek Bridge, Clearwater after Two Years



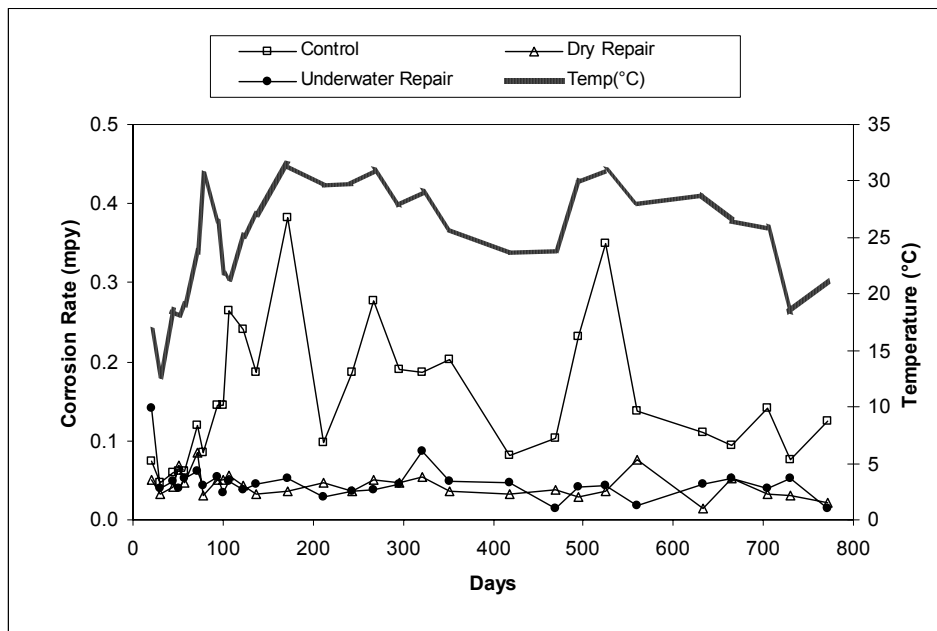


Figure 13 -- Results of Corrosion Rate Measurement at Allen Creek Bridge, Clearwater

# Pore Pressure Measurement in Blast-Induced Liquefaction Experiments

Kyle M. Rollins, J. Dusty Lane, Emily Dibb, Scott A. Ashford, and A. Gray Mullins

**Blast-induced liquefaction experiments have been conducted at a number of test sites to evaluate lateral foundation resistance and soil improvement techniques. Tests can be constructed at full scale without waiting for an earthquake. In this extreme environment, pore pressure transducers must survive transient blast pressures of 41.4 MPa (6,000 psi) yet have enough resolution to measure residual pore pressures of  $\pm 0.69$  kPa (0.1 psi). Three transducer types were evaluated under these demanding conditions, and the piezoresistive transducer was found to be the most robust. These sensors were repeatedly subjected to extreme blast pressures and vibration, but they still provided accurate time histories of residual pore pressure. Although these piezometers are more expensive than other types, installation techniques allowed them to be recovered and reused in subsequent tests and thus reduced overall costs. These pore pressure sensors make it possible to define the extent of the liquefied zone during blast liquefaction experiments and to understand the soil behavior during cyclic loading of deep foundations.**

During the past several years, a procedure has been developed to simulate the earthquake-induced liquefaction process by using controlled blasting. This procedure makes it possible to conduct full-scale testing inside a liquefied soil volume to evaluate foundation behavior and soil improvement techniques without waiting for an earthquake or relying on scale models. This procedure has now been used at a number of sites to evaluate a variety of issues. For example, testing on Treasure Island in California's San Francisco Bay evaluated the lateral resistance of piles and pile groups in liquefied sand (1, 2). Testing in Charleston, South Carolina, evaluated the lateral resistance of an 8.5-ft-diameter drilled shaft in liquefied sand for the Cooper River Bridge and included lateral static loading after blasting (3). Tests in Vancouver, British Columbia, evaluated the ability of prefabricated vertical drains to dissipate pore pressure and prevent liquefaction (4). Testing in Maui, Hawaii, evaluated the liquefaction resistance of coralline sands (5). Testing in Hokaido, Japan, evaluated the lateral resistance of sheet pile walls and pile groups subjected to a blast-induced lateral spread after liquefaction

K. M. Rollins and E. Dibb, Civil and Environmental Engineering Department, Brigham Young University, 368 CB, Provo, UT 84602. J. D. Lane, Lane Engineering, 2550 North Thunderbird Circle, Suite 201, Mesa, AZ 85215. S. A. Ashford, Department of Structural Engineering, 9500 Gilman Drive, University of California-San Diego, La Jolla, CA 92093-0085. A. G. Mullins, Civil and Environmental Engineering Department, University of South Florida, 4202 East Fowler Avenue, ENB 118, Tampa, FL 33620-5350.

*Transportation Research Record: Journal of the Transportation Research Board*, No. 1936, Transportation Research Board of the National Academies, Washington, D.C., 2005, pp. 210–220.

(6). Future studies will evaluate the reduction in axial capacity and the development of downdrag forces on piles after liquefaction.

A critical component in the success of this new field testing approach has been the development of pore pressure sensors that can withstand the high transient blast pressure produced by explosive charges and still record the relatively small residual excess pore pressure with acceptable accuracy and resolution. The piezometers are useful in confirming the development of liquefaction after blasting and in evaluating the pore pressure distribution during foundation testing. A number of sensor types and installation procedures have been used, and successful techniques have been developed through extensive research.

This paper describes the pore pressure sensors and installation procedures that have proven successful in full-scale blast liquefaction experiments. In addition, the results from several experiments will be described to show the value of the pore pressure measurement system in understanding the soil behavior in these experiments.

## PORE PRESSURE SENSORS AND INSTALLATION TECHNIQUES

### Potential Sensors

On the basis of empirical relationships, a pore pressure sensor might be subjected to peak transient pore pressures as high as 41.4 MPa (6,000 psi) at a distance of 5 ft from a 0.45-kg explosive charge. However, it is desirable to be able to measure the residual pore pressure with an accuracy of  $\pm 0.69$  kPa (0.1 psi), because liquefaction is usually a phenomenon that occurs at relatively shallow depths. Although it is possible to obtain a variety of pore pressure sensors that can measure accurately within one of these pressure ranges, it is impossible at present to find a sensor that can measure accurately within both pressure ranges. If a sensor is selected to measure the high pressures, the resolution at low pressures is generally inadequate. Therefore, it is generally necessary to select a sensor that can measure with adequate resolution at the low pressure range and then ensure that the sensor can survive the highest pressures but not necessarily measure them. Although no stock transducer met all these requirements, several possible transducers were evaluated. These transducers included a piezoresistive transducer, a vibrating wire transducer, and an electric resistance transducer.

### Piezoresistive Transducer

The stock transducer that came closest to meeting the various requirements was the P-100MV model produced by Sensotec, Inc.,

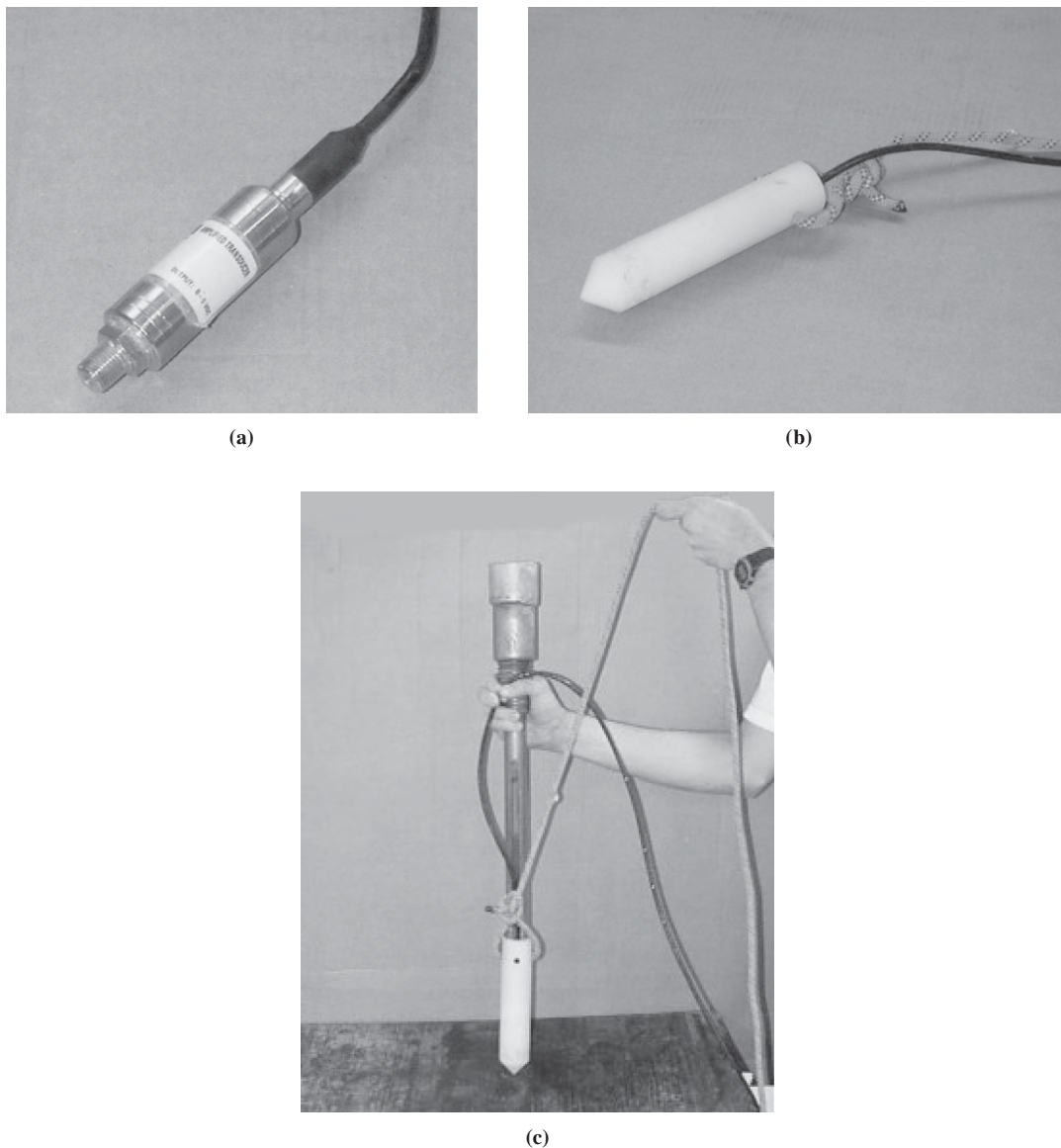


**FIGURE 1** (a) Piezoresistive pressure transducer, (b) transducer inserted into nylon cone tip housing with access holes to water, and (c) nylon cone tip mounted on push rod with electric cable and retrieval rope.

shown in Figure 1a. Design modifications specifically made for these tests produced a model that has a pressure range from 0 to 6.9 MPa (0 to 1,000 psi) with the ability to withstand pressures six times the maximum pressure. The resolution is 0.01% of the full range or 690 Pa (0.1 psi). The transducer is equipped with 30.5 m (100 ft) of waterproof cable that had been hermetically sealed to the instrument.

The sensing element in this transducer is a thin circular silicon diaphragm embedded with four nearly identical piezoresistors. The silicon is an ideal material for the diaphragm, because it is a perfect crystal and has extremely good elasticity. This means that the material can be strained, and it will always return to the original form. The embedding of the piezoresistors in the silicon eliminates problems that have occurred with the bonding of dissimilar materials, such as thermoelastic strain, complex fabrication, and degradation of the bond (7). When a pressure is applied to the diaphragm, it

bends and induces a strain in both the diaphragm and the resistors. This strain causes a change in the resistance, which can then be used to determine the deflection of the diaphragm and the pressure required to cause the change.

The transducer by itself cannot be installed into the ground without significant damage. Therefore, a nylon casing with a conical tip was designed to protect the instrument during installation. A nylon casing also was used to minimize the difference between the unit weight of the soil and the sensor. The casing used for this transducer was developed with the assistance of Professor T. Leslie Youd at Brigham Young University and was patterned after a casing used in measuring liquefaction at the Wildlife site (8). The casing, shown in Figure 1b, consists of two parts: the sleeve and the tip. The sleeve is a solid nylon cylinder with the primary purpose of protecting the transducer. A rope is attached through a hole in the sleeve to help during installation and retrieval of the transducer.

The tip contains 125-mm-diameter holes leading to a central cavity. This allows water to be in contact with the tip of the transducer so that the change in water pressure can be measured. The holes in the tip are stuffed with cotton to prevent sand from entering the tip during installation, allowing water pressure to be transmitted to the transducer.

#### *Vibrating Wire Transducer*

The vibrating wire transducer was a Rocktest, Inc., model PWP piezometer. The transducer has a nominal range of 0 to 690 kPa (0 to 100 psi) with a resolution of 0.1% of full scale or 690 Pa (0.1 psi). Although the transducer was tested at a pressure equal to 150% of full scale by the manufacturer, a vendor indicated that the transducer had withstood pressures of 6.9 MPa at a test site near Mt. St. Helens by orienting the portholes so they faced away from the blast. The pore pressure on the diaphragm is related to the natural frequency of the vibrating wire in the sensor. The natural frequency is obtained by plucking the wire and timing 100 cycles of vibration.

The vibrating wire sensor was inserted into a stainless steel cylinder with a cone tip that could be pushed into the ground using EW drill rods. Three portholes were located just above the tip and contained filters. The sensor was attached to a cable that was hermetically sealed to the instrument.

#### *Electrical Resistance Sensor*

The electrical resistance piezometer was based on a Honeywell/Data Instruments model ABHP-10k strain gauge pressure transducer with two thermally matched strain gauges bonded to the inner face of a stainless-steel diaphragm. The transducer has a nominal range of 0 to 69 MPa (0 to 10,000 psi), a burst pressure of 345 MPa (50,000 psi) or five times the full-scale pressure, and is capable of withstanding a peak shock of 50 *g*, where *g* is the acceleration due to gravity. Therefore, the sensor should be capable of withstanding blast-induced transient pressure and shock. On the downside, the transducer has a manufacturer's reported accuracy of only 0.25% of full scale, which is 172.5 kPa (25 psi). However, when used in conjunction with the MEGADAC data collection system as in this study, the device can indicate pressure to the nearest 6.9 kPa (1 psi). The transducer was housed in a direct burial steel casing affixed to a 150-mm-long nylon porous element that allowed access to the groundwater. Aside from providing a convenient connection, the steel housing also was intended to isolate the edge of the instrumented diaphragm from undesirable lateral soil pressure, which could cause strain in the plain of the diaphragm.

### **Installation and Extraction Procedures**

#### *Piezoresistive Piezometer*

A standardized procedure was used to ensure that accurate pore pressure measurements were made. If an air bubble were present in the tip, errors would occur, and the data would be useless; therefore,

every effort was made to eliminate air bubbles and saturate the probe. After new cotton was inserted into the holes, the tips were boiled to saturate the material and remove the air. The transducer was then submerged in deaired water, and the air bubbles were tapped out. While still submerged, the tips were screwed onto the end of the transducer, and then that unit was screwed onto the sleeve. Before the cone assembly was removed from the deaired water, a rubber membrane was placed around the casing to keep the tip saturated and prevent contamination in the drilling mud until the transducer could be pushed into the ground.

The installation process began by drilling 100- to 125-mm holes at desired locations using rotary mud, drilling to a depth that was approximately 0.3 m short of the desired sensor depth. The drill bit was then replaced by a push rod with the transducer fitted on the end, as shown in Figure 1c. Using the rope to hold the transducer tight against the push rod, the assembly was lowered into the hole. A notch cut along the length of the push rod accommodated the cable, which was fed into the hole. When the bottom of the borehole was reached, the cone tip was pushed into the soil approximately 0.3 m to the design depth, causing the rubber membrane to rupture. This procedure enabled the apparatus to be completely encased in the soil and to remain saturated during installation. The hole was bored to reduce the distance that the transducer needed to be pushed into the ground; however, it also created a large void and provided a drainage path to the surface. Therefore, the borehole was filled with bentonite drilling mud.

Because of the high cost of the piezoresistive transducers, their recovery after the testing was important. After the blast-induced liquefaction, sand typically flowed into the boreholes when thin slurry was used in the borehole. To retrieve the piezometers in this case, water jetting is used to reopen the hole and extract the transducer. When the piezometer was located more than approximately 8 m below the ground surface, it became very difficult to successfully extract the piezometer using the jetting technique. In subsequent tests, a thicker drilling mud (25 lb/100 gal) was used in the boreholes above the sensor. In this case, the sand did not flow into the hole, and the sensors could be successfully extracted simply by pulling the piezometer out of the ground. With the bentonite slurry approach, piezometers were successfully extracted to depths of up to 13.5 m.

#### *Vibrating Wire Piezometer*

The vibrating wire sensors were installed using essentially the same procedure as described for the piezoresistive sensors. However, the EW rod used to push the piezometer into the ground was left attached to the piezometer so that it could be removed after the test blast. The extraction procedure was successful in all cases.

#### *Electrical Resistance Piezometer*

The electrical resistance piezometers were installed by drilling to the desired depth, inserting a polyvinyl chloride (PVC) casing to stabilize the hole, lowering the saturated piezometer to the bottom of the hole, and then extracting the PVC while backfilling the hole with approximately 1.3 m of sand. Because the piezometers were of lower

cost, no effort was made to extract the piezometers from the ground after the blast-induced liquefaction.

**Piezometer Evaluation**

Field evaluations of the vibrating wire and piezoresistive piezometers were conducted at a test site on Treasure Island in San Francisco Bay before the blast liquefaction experiments involving full-scale test foundations were conducted. Because the vibrating wire transducer could be purchased at approximately one-third the cost of a more robust piezoresistive transducer, considerable cost savings could be realized if the vibrating wire transducer proved successful.

*Vibrating Wire Piezometers*

The layout of Test Area A involving vibrating wire piezometers is shown in Figure 2. Three vibrating wire piezometers were installed to a depth of 3.66 m below grade along a line at a spacing of 2.13 m on center. Binary explosive charges (Kinepak), also located at a depth of 3.66 m, were then detonated on a line beyond the outer piezometers, as shown in Figure 2. The soil profile consisted of poorly graded sand ( $D_{50} = 0.2$  mm) with a water table 0.85 m below the ground surface. The unit weights were approximately 19.95 and 19.47 kN/m<sup>3</sup> above and below the water table, respectively. Although the vibrating wire sensors offered the potential for significant cost savings, their performance was unsatisfactory. The first blast (Blast 1), destroyed the transducer at a distance of 2.13 m from the 0.50-kg charge, and the third blast (Blast 3), destroyed the transducer at a distance of 1.98 m from the 0.25-kg charge. These results disqualified the vibrating wire sensor from further use in the testing program. Pressures from both blasts were sufficient to permanently deform the diaphragm.

Despite the failure of the transducers at the higher peak pressures, the sensors that did survive recorded the residual pore pressure during Blast 1, as shown in Figure 3. The peak residual pore pressure at each piezometer location ( $\Delta u$ ) was divided by the initial vertical effective stress ( $\sigma'_v$ ) to obtain the excess pore pressure ratio ( $R_u$ ). An  $R_u$  value of 1.0 indicates full liquefaction. The peak residual  $R_u$  values for Blast 1 were 0.54 and 0.31 at a distance of 4.3 and 6.4 m, respectively from the 0.50-kg blast charge.

*Piezoresistive Piezometers*

The layout of piezoresistive piezometers and blast holes in Test Area B is shown in Figure 4. Three piezoresistive piezometers were installed in a line at a spacing of 2.13, m on center, to a depth of 3.66 m below grade, as was the case in Test Area A. Explosive charges, located at a depth of 3.66 m below grade, were detonated at a distance of 2.13 m on the line beyond the outer piezometer in Blasts 4 and 5. All three piezometers survived the blast and recorded peak residual excess pore pressure ratios of 0.9, 0.57, and 0.28.

Because of the success of the piezometers for the single 0.50 kg blast, an additional test was performed in which two 0.75-kg charges were detonated simultaneously at a distance of 2.13 m from the first piezometer. After approximately 2 min, this blast was followed by the simultaneous detonation of two additional 0.75-kg charges, as shown in Figure 4. Time histories of the residual excess pore pressure ratios ( $R_u = \Delta u / \sigma'_v$ ) measured by the three piezometers during Blast 6, are shown in Figure 5. In all cases, the peak residual excess pore pressure ratio increased to approximately 1.0 immediately after the blast and then gradually dissipated with time. The second detonation once again brought the excess pore pressure ratio to approximately 1.0, after which the ratios dissipated to approximately 0.1 after about 30 min. As expected, the dissipation rate was highest at greater distances from the blast charge where radial drainage was more pronounced. The dissipation rate for Blast 6 (Figure 5) was

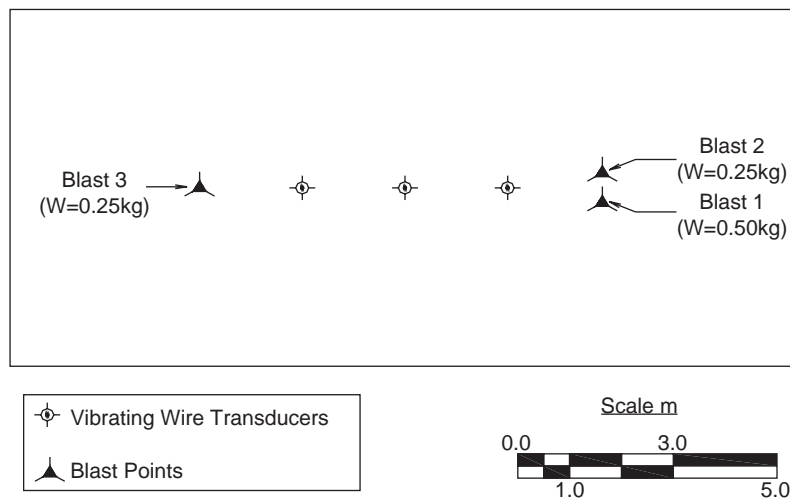


**FIGURE 2** Layout of Test Area A for evaluating vibrating wire piezometers at Treasure Island, San Francisco. Test area, 0.61 m below surrounding grade; blast charge locations, 3.66 m below grade in test area; transducer locations, 3.66 m below grade in test area; water table location, 0.85 m below grade in test area.

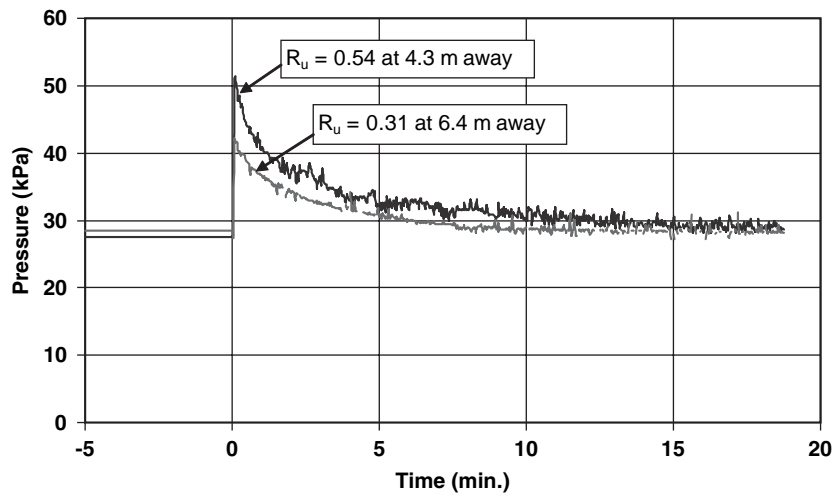


FIGURE 3 Total pore pressure time histories for two surviving vibrating wire transducers at Test Area A during Blast 1.

also much slower than that in Blast 1 (Figure 3), because the radius of the liquefied zone was much larger in Blast 6 (more charges and greater charge weights were used). The noise evident in the plots was traced to a bad board, not the piezometers themselves.

*Electrical Resistance Sensors*

The response of the piezometer was evaluated by installing one electrical resistance piezometer and one piezoresistive piezometer at opposite corners of a 1.83-m square to a depth of approximately

3 m. At the other two corners of the square, 0.52-kg explosive charges were placed at a depth of 3 m and backfilled with sand. Two blast tests were then conducted by detonating each charge individually at the test site in Tampa, Florida, which consisted of silty sand with a water table approximately 0.3 m below the ground surface. During the test blasts, both piezometers appeared to perform with comparable success; however, the noise associated with the electrical resistance piezometer was much larger than that for the piezoresistive piezometer. To minimize this problem, it was recommended that sampling be performed at a minimum rate of 1,000 Hz and that an averaging procedure be used for each data

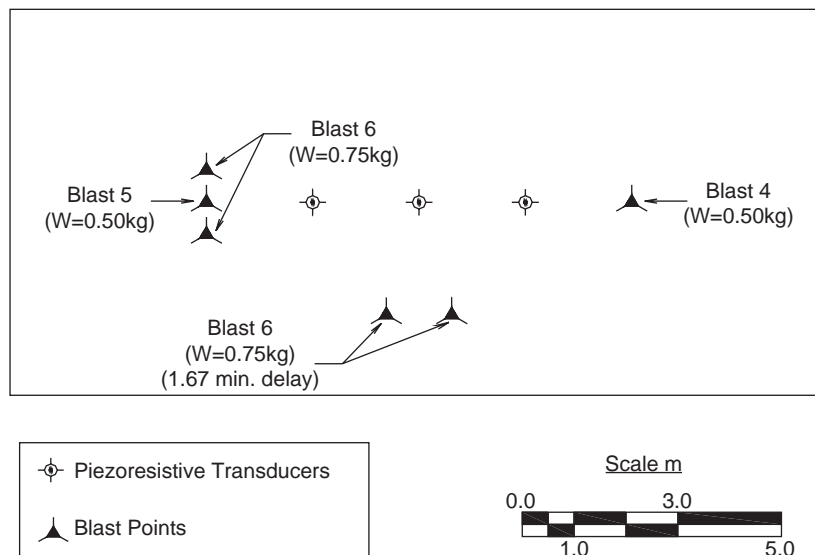


FIGURE 4 Layout of Test Area B for evaluating piezoresistive piezometers at Treasure Island. Test area, 0.61 m below surrounding grade; blast charge locations, 3.66 m below grade in test area; transducer locations, 3.66 m below grade in test area; water table location, 0.85 m below grade in test area.



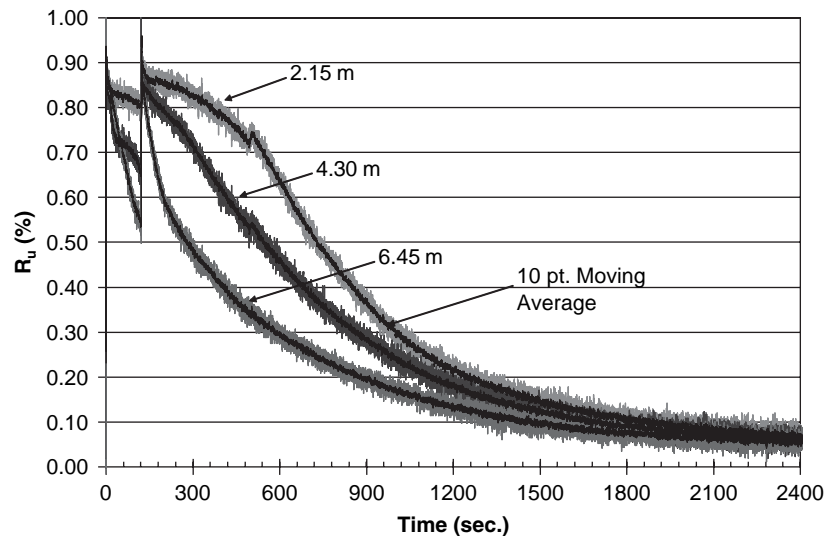


FIGURE 5 Time histories of excess pore pressure ratio ( $R_u = \Delta u/\sigma'$ ) measured at three distances from charge detonation for Blast 6 at Treasure Island.

point. Both piezometers indicated that liquefaction was achieved during the test blast.

Although the electrical resistance piezometers performed well during the test blasts, during subsequent full-scale testing involving repeated blasting and larger charge weights (1 to 2 kg), the electrical resistance piezometers experienced a very high failure rate. In many cases, the transducers underwent a large, but undeterminable, offset in pressure after the test blast and showed only minor pressure dissipation with time. In fewer cases, the piezometer indicated that dissipation was occurring and that the pore pressure would finally stabilize at a new but higher static pressure value. These failures were attributed to insufficient lateral isolation of the instrumented diaphragm, which would therefore indicate a change in lateral soil pressure but of an undetermined magnitude.

## APPLICATIONS FOR BLAST LIQUEFACTION TESTING

### Blast Liquefaction Testing of Pile Group at Treasure Island

Blast liquefaction testing was performed in 1999 at a test site on Treasure Island in San Francisco Bay to evaluate the lateral resistance of pile groups and drilled shafts. The ultimate goal of the research was to develop “ $p$ - $y$ ” curves to define the lateral resistance of the liquefied sand as a function of lateral pile deflection; the development of these curves is described elsewhere (1, 2). The layout of the test foundations, blast holes, and pore pressure transducers is shown in Figure 6. The test foundations consisted of a 0.9-m-diameter cast-in-steel-shell (CISS) pile and a nine-pile group of 0.324-m-diameter steel pipe piles driven open ended. A high-speed hydraulic actuator was placed between the two foundations so they could react against each other. Eight 0.5-kg explosive charges were arranged in a ring around each test foundation and were detonated two at a time with a delay of approximately 250 ms

to produce a volume of liquefied sand around the test foundations. Vertical arrays of piezoresistive pore pressure transducers were installed at locations adjacent to each test foundation and at several distances beyond the foundations in the direction of loading, as shown in Figure 6. These transducer arrays were designed to define the extent of the liquefied zone and to evaluate the variation of the pore pressure as cyclic lateral load was applied by the hydraulic actuator.

Generally, the transducers performed very well during the investigation. Only four of the 30 transducers failed to function properly. Three of the piezometers failed because of cable damage during installation, which allowed water to reach the transducers, whereas the fourth was damaged by the transient blast pressure that apparently exceeded 41.4 MPa (6,000 psi) for this piezometer, which was located only 1.5 m from one of the charges.

Time histories of the excess pore pressure ratio along with the total lateral load are provided in Figure 7 at four depths near the nine-pile group and at four depths approximately 3.2 m in front of the row of piles in the group for the first 10 min after blasting. During this time interval, the average excess pore pressure ratios were typically greater than 95% around the test foundations except at depths of approximately 0.76 and 1.52 m, where the interpolated ratio was approximately 76% and 85%, respectively. These ratios decreased to approximately 85% to 95% at a distance of 3.2 m (9.9 pile diameters) away from the pile group and approximately 40% to 60% at a distance of 5.3 m (16.4 pile diameters). In addition to the evidence of liquefaction provided by the piezometers, a number of large sand boils developed around the test piles a few minutes after the blasting.

Measured pore pressure ratios fluctuated in response to the displacement of the pile group. As shown in Figure 7, pore pressure ratios decreased significantly at shallow depths near the pile group as the lateral load increased. The magnitude of the pressure fluctuations decreased with depth and distance from the pile group. At greater distances from the pile group, the pore pressures tended to increase rather than decrease during loading. The fluctuations can

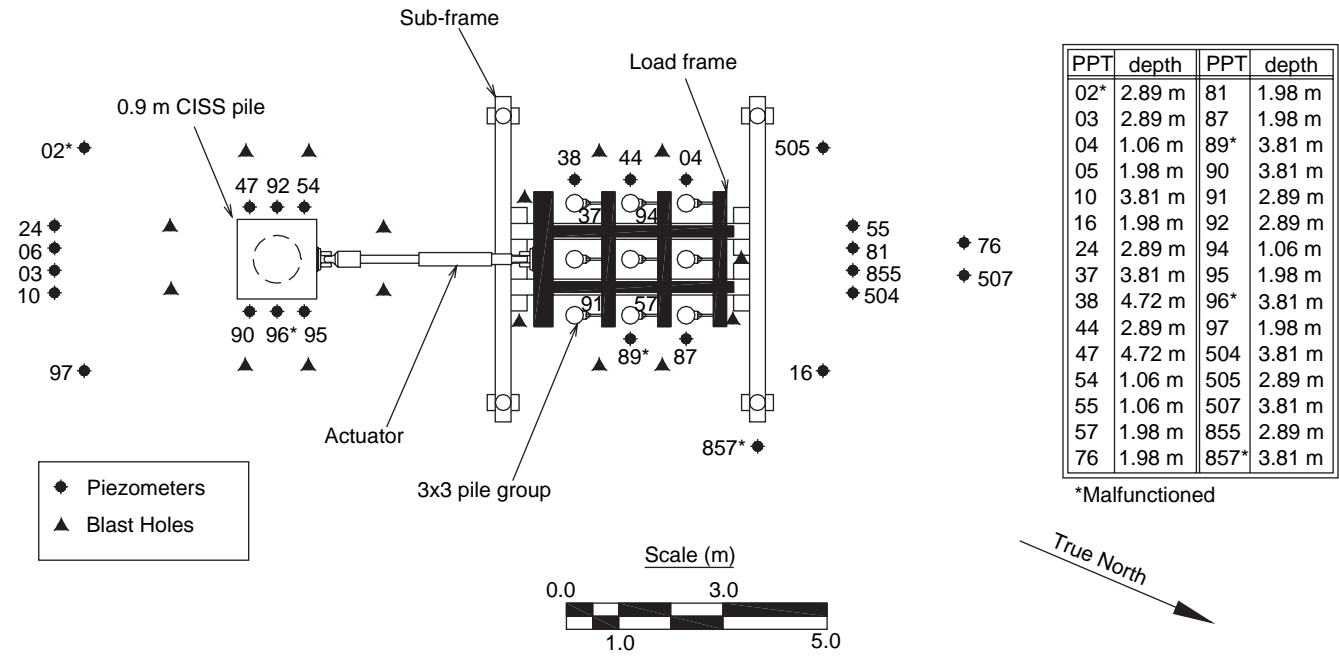


FIGURE 6 Layout of nine pile group and 0.9-m cast-in-steel-shell (CISS) pile along with locations of blast holes and piezoresistive piezometers for Treasure Island testing (PPT = pore pressure transducer).

be attributed to at least two reasons. First, as the pile displaced laterally, sand and water flowed behind the piles, filling the gaps that formed. Second, pile movement strained the soil, resulting in an initial pore pressure increase, and, at large strains, a phase transformation occurred with subsequent pore pressure decrease. At distances close to the pile, where near-field strains were larger, this phase transformation typically led to a decrease in  $R_u$ , which corresponded to the increase in lateral load. At greater distances, strains were smaller and generally insufficient to induce a phase transition except near the ground surface. Therefore, increases in  $R_u$  corresponded to the increase in lateral load at these locations.

Contours showing the distribution of the excess pore pressure ratio on a cross-section through the two foundations are shown in Figure 8 and provide further insight regarding pore pressure response during loading. Figure 8a shows contours at the maximum load and deflection as the two foundations are pushed apart. At this point, the  $R_u$  values in the immediate vicinity of the foundations decrease, particularly at the surface. However, at points in front of the foundations, the excess pore pressure increased. By contrast, Figure 8b shows contours when the foundations have been pulled back to their original starting point, which required a tensile force because sand had flowed behind the pile during loading. At this point, the  $R_u$  values increase near the surface around the test foundations, but decrease at a distance away from the piles.

**Blast Liquefaction Testing of Drilled Shaft at Cooper River Bridge**

Blast liquefaction testing also was performed in 2001 at a test site near the proposed Cooper River Bridge between Mt. Pleasant and Charleston, South Carolina. Liquefaction was expected to develop

to a depth of 12 m in saturated loose silty sand around the foundation during a repeat of the M7.3 1886 Charleston earthquake (9). Liquefaction to this depth could significantly reduce the lateral resistance of the drilled shaft foundations for the bridge. Therefore, full-scale testing was undertaken to evaluate lateral resistance of the bridge foundations after liquefaction.

The layout of the test foundation, blast holes, and pore pressure transducers is shown in Figure 9. The test foundation consisted of a 2.6-m-diameter drilled shaft, 30.5 m long, which extended through the liquefied sand and into a plastic clay known as Cooper Marl below a depth of 12 m (3). A series of three lateral load pulses were produced using the statnamic loading system mounted on a sled. This sled produced lateral forces up to 2,300 kN with a duration of approximately 0.3 s. Before each statnamic test, 1- to 2-kg explosive charges located at three to four depths in each of eight blast holes were detonated to produce a liquefied test volume. The eight blast holes were equally spaced around one of the rings surrounding the test shaft, as shown in Figure 9. Charges in adjacent blast holes were detonated simultaneously from the bottom upward with delays of approximately 200 ms between explosions. Vertical arrays of piezoresistive and electrical resistance pore pressure transducers were installed at radii of 1.83, 7.32, and 10.36 m from the center of the test shaft at depths, as shown in Figure 9. These transducer arrays were designed to define the extent of the liquefied zone and to evaluate the variation of the pore pressure as the statnamic lateral load was applied to the shaft.

On the basis of previous test blast experience at the site, electrical resistance piezometers were used only at relatively large distances from the explosive charges because of very high failure rates. The piezoresistive transducers generally performed very well during this study also; however, there were some cases in

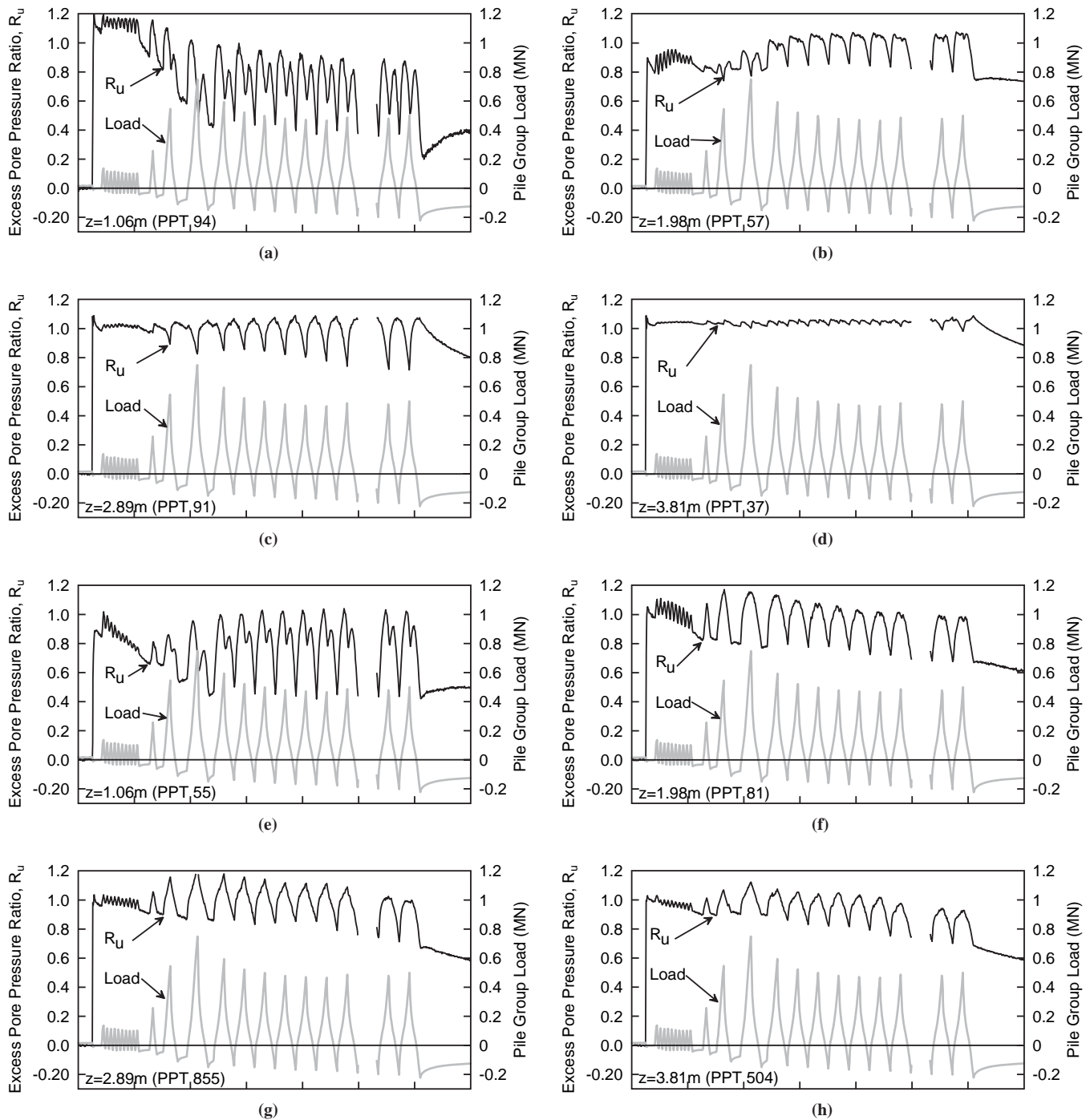


FIGURE 7 Time histories of total load and excess pore pressure ratios at four depths adjacent to nine-pile group, (a) to (d), and four depths 3.2 m in front of group, (e) to (h).

which an offset in the baseline pressure was observed following blasting.

Contours showing the distribution of the excess pore pressure ratio on a cross-section through the test shaft are presented in Figure 10. Figure 10a shows contours approximately 30 s after the detonation of the explosives and immediately before the statnamic test firing. Excess pore pressure ratios near the shaft had dissipated

somewhat from their initial peak values but were still generally above 80% to 90%, which indicates that the sands were essentially liquefied around the test shaft. Figure 10b shows contours for the foundations immediately after the statnamic test firing. In essentially all instances, the  $R_u$  values increased as the statnamic load was applied because the shaft deflection was limited to less than 90 mm.

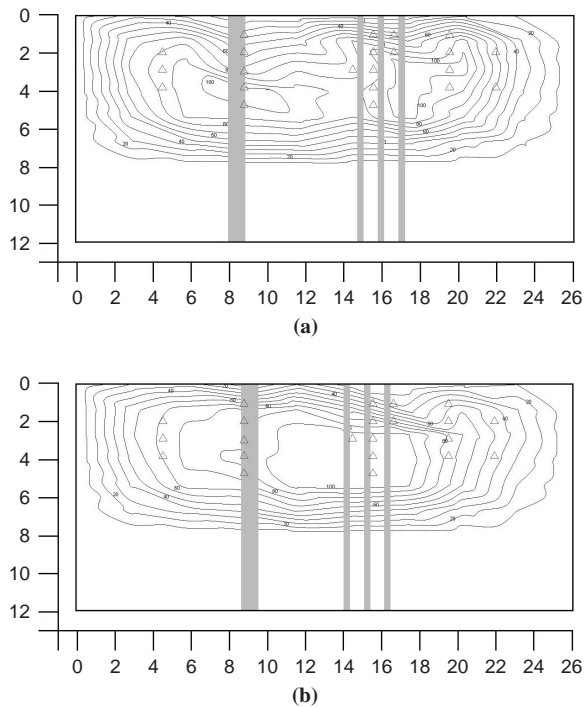


FIGURE 8 Contours of excess pore pressure ratio ( $R_u$ ) on cross section through nine-pile group and CISS pile at Treasure Island (a) while foundations are pushed apart and (b) while foundations are pulled together. (White triangles indicate piezometer locations.  $R_u$  equals 1.0 or 100% at liquefaction.)

**CONCLUSIONS**

On the basis of the test results and analysis performed on this full-scale fixed-head pile group, the following conclusions can be made:

1. The performance piezoresistive transducer was superior to that of the vibrating wire and resistance type strain-gauge piezometers.
2. The piezoresistive piezometer could repeatedly survive a transient blast pressure of up to 41.4 MPa, yet record with a resolution of 690 Pa.
3. Installation and extraction procedures that allowed the piezometers to be reused at other sites, thereby reducing the cost of instrumentation for blast liquefaction testing, were developed.
4. Monitoring of pore pressure response using an array of piezoresistive piezometers made it possible to confirm the development of liquefaction surrounding test foundations and to evaluate the pore pressure response during cyclic loading.

**ACKNOWLEDGMENTS**

Funding for the Treasure Island testing was supported by the state departments of transportation of Alaska, California, Missouri, New York, Oregon, Utah, and Washington through a pooled-fund arrangement. Caltrans served as the lead agency with Tom Shantz as the project manager. Funding for the Cooper River Bridge testing was provided by the South Carolina Department of Transportation, with Modern Continental South as the general contractor, along with the National Science Foundation. This support is gratefully acknowledged. Finally, the authors express appreciation to the U.S. Navy

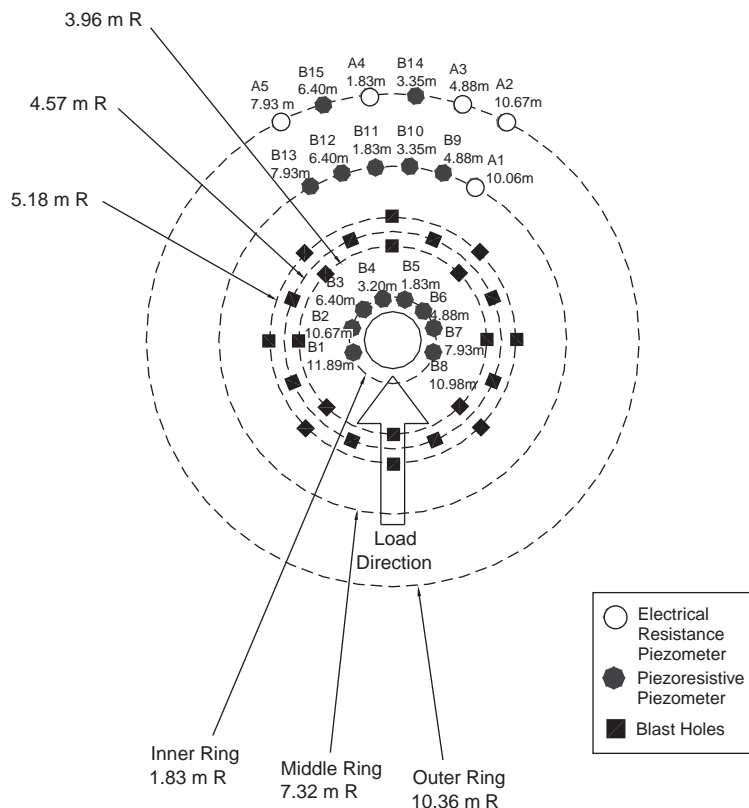
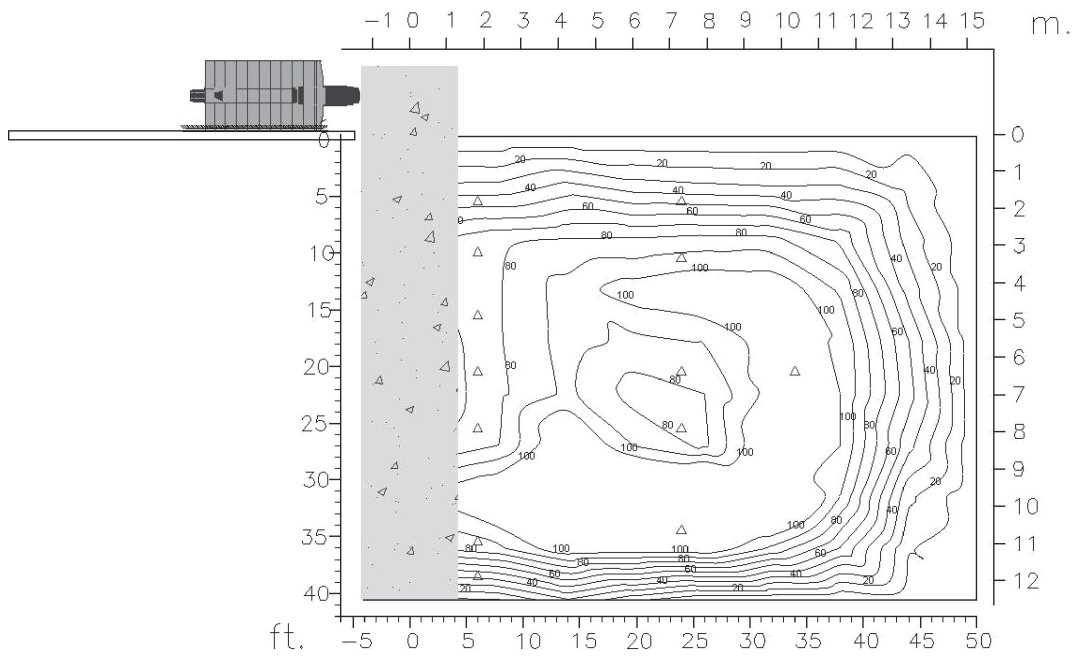
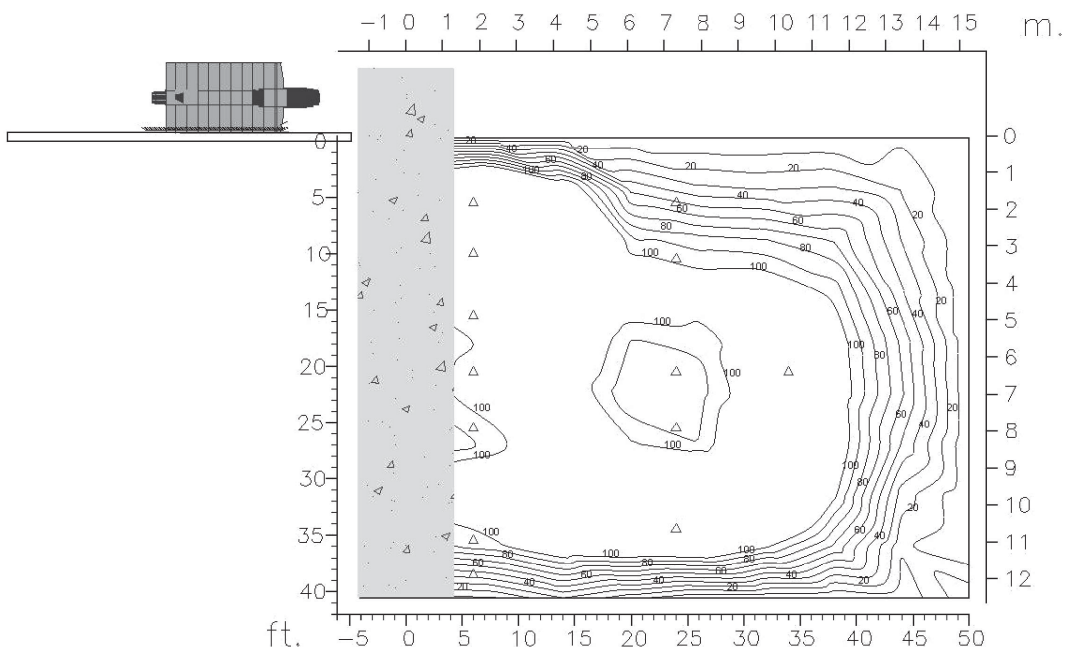


FIGURE 9 Layout of test shaft in relation to blast holes and piezometers at Cooper River Bridge testing.



(a)



(b)

FIGURE 10 Contours of excess pore pressure ratio ( $R_p$ ) on cross section through drilled shaft at Cooper River (a) immediately before and (b) immediately after static test firing.

and the City of San Francisco for allowing the use of the test site on Treasure Island.

## REFERENCES

1. Rollins, K. M., T. M. Gerber, J. D. Lane, and S. A. Ashford. Lateral Resistance of a Full-Scale Pile Group in Liquefied Sand. *Journal of Geotechnical and Geoenvironmental Engineering*, Vol. 131, No. 1, 2005, p. 115–125.
2. Weaver, T. J., S. A. Ashford, and K. M. Rollins. Lateral Resistance of a 0.6 m Drilled Shaft in Liquefied Sand. *Journal of Geotechnical and Geoenvironmental Engineering*, Vol. 131, No. 1, 2005, p. 94–102.
3. Brown, D., and W. M. Camp. Lateral Load Testing Program for the Cooper River Bridge, Charleston, SC. *Proc., Deep Foundations 2002*, American Society of Civil Engineers (ASCE), Reston, Va., 2002, pp. 95–109.
4. Rollins, K. M., J. K. S. Anderson, A. K. McCain, and R. R. Goughnour. Vertical Composite Drains for Mitigating Liquefaction Hazard. Presented at 13th International Conference on Offshore and Polar Engineering, International Society for Offshore and Polar Engineering, Paper 2003-SAK-01, 2003.
5. Rollins, K. M., J. D. Lane, P. G. Nicholson, and R. E. Rollins. Liquefaction Hazard Assessment Using Controlled-Blasting Techniques. *Proc., 11th International Conference on Soil Dynamics and Earthquake Engineering*, Vol. 2, Stallion Press, Singapore, 2004, pp. 630–637.
6. Ashford, S. A. Evaluation of Force Based and Displacement Based Analyses for Responses of Single Piles to Lateral Spreading. *Proc., 11th International Conference on Soil Dynamics and Earthquake Engineering*, Vol. 1, Stallion Press, Singapore, 2004, pp. 752–759.
7. *Pressure, Strain and Force Handbook*, 28. Omega Engineering, Stamford, Conn., 1992, pp. Z-12 and Z-13.
8. Youd, T. L., and T. L. Holzer. Piezometer Performance at Wildlife Liquefaction Site, California. *Journal of Geotechnical Engineering*, Vol. 120, No. 6, 1994, pp. 975–995.
9. Hales, L. J. *Cyclic Lateral Load Testing and Analysis of a CISS Pile in Liquefied Sand*. M.S. thesis. Brigham Young University, Provo, Utah, 2003.

---

*The views expressed in this paper do not necessarily reflect those of the sponsors.*

*The Soils and Rock Instrumentation Committee sponsored publication of this paper.*



# The Statnamic Analysis Workbook: A Tool for Automated Data Analysis and Storage

Edward J. Garbin ■ A. Gray Mullins

## Abstract

*Statnamic load testing, which has been in existence for over a decade, is becoming more widespread as an accepted alternative to large static load tests. Because the test introduces dynamic forces into the system under consideration, these forces must be quantified and removed from the final data so that the static capacity of the foundation is determined properly. The large amount of data collected in a single statnamic test makes this method well suited for computer-based analysis.*

*This paper presents the development of a free software application known as the Statnamic Analysis Workbook, which utilizes Middendorp's Unloading Point Method for determining system damping characteristics. The package is built on a Microsoft Excel platform and extensively enhanced with the Visual Basic for Applications programming language. Statnamic data of virtually any type can be easily imported and regressed, key statistics can be calculated and stored, and final load-displacement curves can be generated. The software can export and save the regressed data, and a special tool links this exporter with the Federal Highway Administration's Deep Foundation Database. The University of South Florida makes the software available via the Internet for engineering consultants as well as foundation engineering educators.*

## Introduction

The importance of accurately determining the load-bearing capacity of a foundation system cannot be overstated. Structures are designed for certain limit state conditions that, when exceeded, could result in catastrophic failure. To ensure such failure does not occur, both the anticipated loading of the structure and the foundation's available resistance to this load must be determined.

Several full-scale load test methods have been devised to establish the load-carrying capacity of a foundation. Generally, these test methods can be grouped into three categories: static, rapid, and dynamic. Static load tests such as those outlined by the American Society for Testing and Materials (ASTM) specifications D1143 and D1194 are considered by industry as highly reliable since they most closely recreate the load duration consistent with the intended use of the foundation.<sup>1</sup> In such tests, the foundation is slowly loaded until it demonstrates sufficient capacity or until it displaces excessively.

Rapid load tests such as statnamic testing, discussed in the 2000 ASTM submission, are becoming more popular because of the economic advantages of their usage.<sup>2</sup> The time required to complete a test, the amount of necessary equipment, and the manpower needed to perform these tests all are substantially less than those required to execute comparable static load tests. Although dynamic effects are introduced due to the rapid rate of loading, the mechanism by which the soil develops capacity is essentially the same as static tests. Thereby, the pile compresses elastically and distributes load to the bearing strata proportional to the displacement and the associated capacity from that soil layer. Regardless, dynamic effects are introduced that must be quantified and removed from the measured data in order to obtain an equivalent static system response profile.

Dynamic tests such as those specified by ASTM D4945 are conducted during pile driving and therefore utilize the least amount of extra equipment and manpower.<sup>3</sup> As this mechanism of loading (installation) differs drastically from the intended structural loads, the analysis for each of the installation blows is necessarily complex. Stress wave considerations become paramount in these tests and serve to complicate the data analysis process. Signal matching is the

preferred technique used to derive static capacity from this type of data, and the engineer's experience becomes a controlling factor in the validity of the results.

Valid results demand extreme care during every stage of the data reduction process, and reproducibility can only manifest itself in scientifically correct, unbiased data interpretation. For statnamic testing, this is addressed by the development of several computer software tools. The focus of this paper is on one such software package developed by the University of South Florida (USF) for the purpose of reducing axial statnamic test data. The Statnamic Analysis Workbook (SAW) is a custom-written, highly automated Microsoft Excel workbook developed as part of a project sponsored by the Federal Highway Administration (FHWA). The goal was to remove user subjectivity from the data reduction process and develop a program that could deliver unbiased, reproducible results.

## Statnamic Background

Developed by Berminghammer Foundation Equipment, the statnamic load test is founded upon the principles of Newton's second and third laws of motion. Newton's second law states that "the acceleration of an object is directly proportional to the resultant force acting on it and inversely proportional to its mass."<sup>4</sup> Newton's third law states "if two bodies interact, the force exerted on body 1 by body 2 is equal to and opposite the force exerted on body 2 by body 1."<sup>4</sup> Whereas dead-weight (Kentledge) static load testing requires the use of large masses whose total force is proportional to the acceleration due to gravity, statnamic load testing uses much smaller reaction masses that are subjected to as much as twenty times the acceleration due to gravity (20 gs). By utilizing the inertial force associated with this accelerated mass, large capacity load tests are possible with comparatively small equipment. A detailed description of the test procedure can be found elsewhere.<sup>5,6,7</sup>

When first introduced in the late 1980s, statnamic testing was performed while monitoring only the applied load and resulting displacement at the top of the foundation. It is commonplace now to also monitor top-of-pile acceleration as well as toe acceleration and strain at various elevations along the pile. This additional information can be used to further describe the reaction of the soil-pile system to the applied statnamic load.<sup>6,8</sup> However, as this paper will show, it is possible to obtain very precise and reproducible system response using only top-of-pile information, provided the pile is not extraordinarily long (<100 feet for concrete piles).<sup>6,9</sup>

The statnamic test is a subset of rapid load tests as described by the 2000 ASTM submission.<sup>2</sup> The implication of this loading classification is that the load duration is long enough that it does not introduce stress waves. Secondly, the pile can be analyzed essentially as a rigid body. As this classification encompasses loadings that may induce acceleration and velocity of the rigid body, any analysis must address the associated resistance to movement.

Figure 1 shows the types of error that can accumulate in the data when these forces are not properly quantified and removed. The left-most curve represents the static load displacement response. Proceeding to the right, increased

dynamic effects tend to cause an overestimation of elastic stiffness and ultimate capacity. Additionally, long-term foundation response to any loading is soil-dependent and may not be reflected by some load tests (static, rapid, or dynamic). In such instances the analysis of foundations may incorporate a rate effect factor to mitigate these discrepancies.

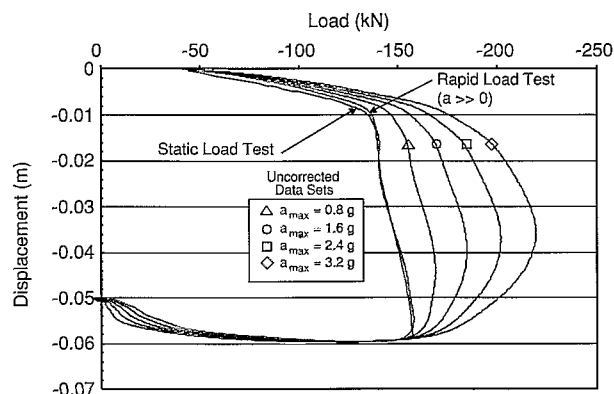


Figure 1. Dynamic force effects on foundation load-displacement response

## Statnamic Data Regression

The data recorded during a basic statnamic test includes elapsed time, magnitude of applied load, top-of-pile acceleration, and top-of-pile displacement. The velocity of the moving pile can therefore be determined by either integration of the acceleration-time data or differentiation of the displacement-time data. Both methods should be incorporated for verification of data quality. Knowing the acceleration, velocity, and displacement of the pile during the test event, there is sufficient information to describe the forces acting on the pile using the general equation of motion. This section provides an explanation of the modeling and numerical analysis process.

A single degree-of-freedom dynamic system can be represented with the Kelvin-Voigt constitutive model shown in Figure 2.<sup>10</sup> Here, the mass represents the mass of the pile that is supported by soil having both static (spring) and viscous (dashpot) resistance components. Excitation of this system is obtained by providing a statnamic load pulse to the top of the pile. The reaction forces that develop in response to this excitation include the acceleration-dependent inertial force of the pile ( $ma$ ), the velocity-dependent viscous resistance of the soil ( $cv$ ), and the displacement-dependent static resistance of the soil ( $kx$ ). At equilibrium, a summation of vertical forces leads to

$$F_{sm}(t) = ma(t) + cv(t) + kx(t) , \quad (1)$$

where

$$\begin{aligned} t &= \text{time} \\ F_{sm}(t) &= \text{applied statnamic force} \\ kx(t) &= \text{static resistance} \\ cv(t) &= \text{damping resistance of the soil} \\ ma(t) &= \text{inertial force} . \end{aligned}$$

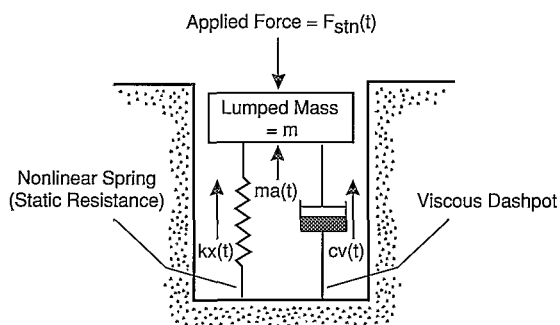


Figure 2. Constitutive model used in data regression

To successfully obtain the static resistance of the pile from a statnamic excitation, equation 1 must be solved for the quantity  $kx(t)$ . Reviewing each of the terms reveals there are two unknowns in this equation: the spring coefficient  $k$  and the damping coefficient  $c$ . The system is underspecified and does not possess a closed-form solution.

Middendorp's Unloading Point Method (UPM) is a numerical procedure developed specifically to solve for the damping coefficient.<sup>5</sup> Several assumptions must be made to apply the UPM. First, it is assumed that the pile behaves as a rigid body, that is, there is no appreciable elastic compression as load is applied. Secondly, once the pile fails, it does so by plunging at a constant static capacity. Finally, the damping coefficient does not change during the test.<sup>5</sup> The validity of these assumptions varies from system to system; however, in noncohesive soils and with piles below the aforementioned critical length, there is good agreement between UPM-based results and those measured during static testing.<sup>11</sup>

Middendorp defines a time window in the statnamic load-displacement data as beginning at the point of maximum force ( $t_1$ ) and ending at the point of maximum displacement ( $t_2$ ). These points are shown as points 1 and 2 in figure 3.

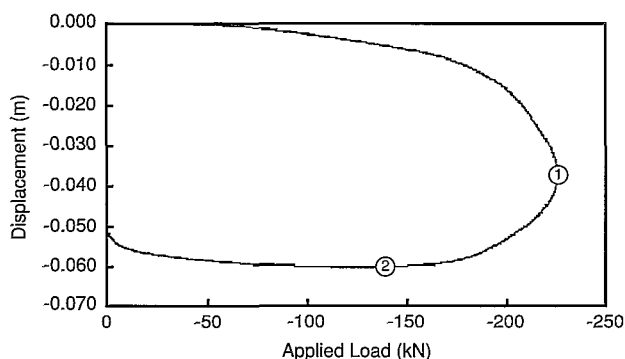


Figure 3. Region in which static capacity is assumed constant

Within this region the static force is assumed constant. This assumption is based on the shear characteristics of a plunging pile and agrees well with actual static load-displacement behavior. Since the velocity becomes zero at

the point of maximum displacement, the static resistance at this point can be determined as

$$kx_2 = F_{stn}(t_2) - ma(t_2), \quad (2)$$

where

$$\begin{aligned} t_2 &= \text{time at which maximum displacement occurs} \\ F_{stn}(t_2) &= \text{applied statnamic force} \\ ma(t_2) &= \text{inertial force} \\ kx_2 &= \text{static resistance at point of maximum displacement.} \end{aligned}$$

Having now solved for the static resistance at this particular time, and assuming that this force remains constant between  $t_1$  and  $t_2$ , the damping coefficient can be calculated for every point in this region as

$$c = \frac{F_{stn}(t) - ma(t) - kx_2}{v(t)} \quad t \rightarrow t_1 \dots t_2. \quad (3)$$

Finally, the median value of all calculated  $c$  terms is computed, and this value is used for the entire test. Having now determined this median value, equation 1 can be solved for the static resistance at each time  $t$  during the test with

$$\begin{aligned} F_{static} &= kx(t) \\ &= F_{stn}(t) - c_{median}v(t) - ma(t). \end{aligned} \quad (4)$$

## The Statnamic Analysis Workbook

The process of completing just one UPM on a typical statnamic data set can be arduous at best. Because the test event is so small, usually 120 ms to 250 ms, high sampling rates are used to collect the data. This process results in thousands of lines of recorded data for each test, further complicating the issue of determining the static capacity of the system.

To address this concern, USF personnel in conjunction with the FHWA developed SAW, a sophisticated data analysis package based on a Visual Basic for Applications (VBA)-enhanced Microsoft Excel spreadsheet. Now in its fourth revision, SAW is a powerful tool that allows for the quick, unbiased determination of the static capacity of a foundation given its statnamic response information. The following sections of this paper explain the development and use of SAW on typical statnamic data.

## Data Import

At the root of any data analysis application is the data itself. Issues such as the type of data file, the number of records within the file, and the arrangement of those records all must be addressed. Statnamic data files typically are tab-delimited, ASCII text files, regardless of the data acquisition system used to record them. However, the arrangement and content of these files varies greatly for different acquisition systems. As a result, analysis programs must be able to distinguish various data file formats and properly import the data from each. Because the final data file format is highly

dependent on the input given during a test, it becomes impossible to provide for every possible arrangement. Therefore, additional functionality must be included in the analysis program to allow data from unknown file formats to be imported.

To meet this demand, SAW is equipped with a strong parsing algorithm that is comprised of a collection of several independent VBA modules. The first is a control module that prompts the user for the name of the data file to be imported, and then transfers this information to the parsing module. The parsing module opens the file, reads a specified section of it, and then transfers the contents of this section to the data type library. The data type library contains entries that are compared to the data that was read in with the parsing module. Once a match is found, a flag is set and then used by the importer module to determine where individual records are located within the data file. If the data is stored in an unrecognized format, another module allows this data to be manually imported. The user simply highlights the data that will be read into SAW and selects a command button to complete the import process, as shown in figure 4.

Figure 4. Primary user interface in SAW

Once the data being imported has been identified, either automatically or manually, the import process commences in two stages. First, the number of records in the data file is determined. Because most of the workbook is generated dynamically depending upon the length of the data file, SAW is equipped with code that allows it to precisely determine the number of records contained in the file, using low-level file manipulation commands embedded in a Do-Until loop. The function of this looped code is to essentially count the number of lines of data in the file. After each line is counted, an integer variable is incremented by one. Once the loop finishes, the value of the integer variable corresponds to the number of lines of data in the file.

Having determined the quantity of data being imported, the second stage of the import process is to actually import the data and write the associated worksheet formulas for zero-correction, units conversion, numerical integration, and numerical differentiation. At this time a number of key values are also determined. The maximum value of applied load is identified and its location within the workbook is specified. The algebraic signs of the imported data are also determined, an important feature because the use of an inconsistent sign convention will lead to erroneous calculations. The algebraic sign of each measured parameter depends upon the instrumentation and acquisition system used. It is standard practice in the study of physics to assign a negative sign to acceleration vectors that are directed toward the center of the earth, and also the standard chosen for data imported into SAW. All values of load and displacement that are directed into the foundation are assigned a negative sign. Similarly, acceleration is assigned an algebraic sign such that when it is integrated twice with respect to time, the resulting displacement is in the same direction as that value measured during the test.

---

“ Rapid load tests such as statnamic testing, discussed in the 2000 ASTM submission, are becoming more popular because of the economic advantages of their usage. ”

---

After the data is imported and the sign convention is verified, the data must be zero-corrected. It is known that there is no initial relative acceleration, velocity, or displacement present in the system. However, the recorded data will not start at zero because the transducers typically measure absolute, not relative, quantities. The origin of the data is therefore adjusted automatically by the VBA code.

### Adapting to Faulty Data

Sometimes there is a problem with one of the transducers that causes it to transmit faulty data. For example, during a statnamic test it is possible to move the foundation beyond the range of the displacement transducer, which is about 50 mm. This condition introduces useless data into the record set. Since the spreadsheet normally includes the laser displacement in calculations and graphs, this erroneous data produces meaningless results. This displacement error is just one example of a problem that can occur in the field. Because all transducers are sensitive electronic devices, any one of them is subject to failure.

SAW is written in a manner that exploits the redundancy in the instrumentation. In addition to numerically integrating accelerometer recordings to obtain velocity and then displacement, the laser displacement is differentiated with respect to time as well. Velocity and acceleration are calcu-

lated again. If either the accelerometer or the displacement transducer fails during a test, the necessary data can be obtained from the remaining transducer. Additionally, it is useful to compare the displacement traces from both the accelerometer and the laser to ensure that they match reasonably well. Results show that the use of the twice-integrated accelerometer data can compensate for noise found in the laser data. As shown in figure 5, SAW offers a customized user form that lets the user select the source of all data for calculations and graphs.

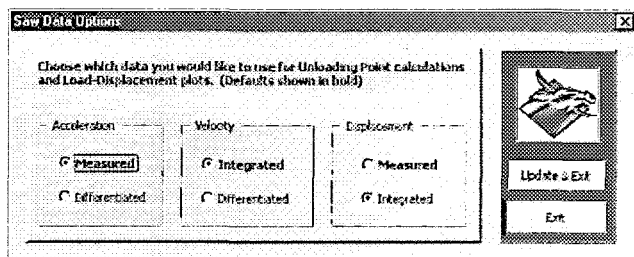


Figure 5. Data Options tool for choosing source data

The custom user form shown in figure 6 allows the user to truncate data as needed. Because both pre- and post-event readings are taken during a statnamic test, it is often desirable to eliminate excess readings from the end of a test to make the results more presentable. One immediate consequence of doing so is that the last recorded load value is lost, thereby nullifying any previous attempt at zero-correcting the load data. In response, the final recorded load value is permanently stored in SAW when the data is first imported. With the custom user form, the analyst then specifies the last desired time value for the test data and the program automatically truncates the file to that point. This process does not affect the zero-correction of the load data and does not change the original data file in any manner.

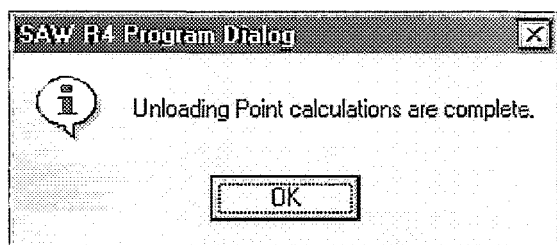


Figure 6. Data Trim tool for removing postevent data

**Data Manipulation**

There are a number of standard calculations that are always performed for each data set imported into SAW, as shown in figure 7. Acceleration is integrated with respect to time to obtain velocity, and then again to obtain displacement. Laser data is differentiated with respect to time to obtain velocity, and then again to obtain acceleration. UPM calculations are performed, in many cases repeatedly for each data set.

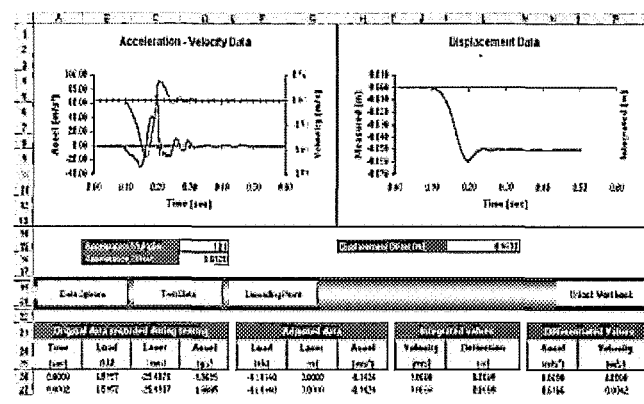


Figure 7. Imported Data screen showing standard calculations and additional controls

Perhaps the greatest advantage offered by SAW is that the time required to complete a UPM analysis of the data is reduced to just a few seconds. All of the steps involved in the UPM analysis are fully automated with VBA code, and the results are presented immediately as shown in figure 8. Changes can be made and a new UPM analysis can be performed quickly and easily. This time savings is particularly helpful when reducing data from several cycles of load tests carried out on multiple foundations.

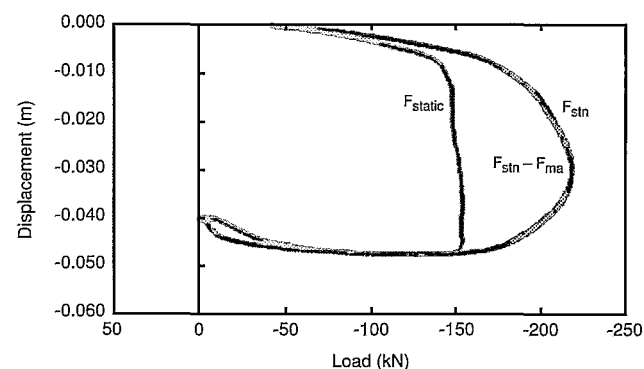


Figure 8. Results screen showing applied load, inertia-corrected load, and static capacity

The flexibility offered by the spreadsheet environment is unparalleled. Not only can standard UPM calculations be performed, but any other desired calculation, manipulation, or presentation of the data can be completed quickly and easily using the spreadsheet's vast resources. Multiple test cycles can be superimposed to create a composite foundation response curve. Static load test data can be inserted and compared directly to the statnamic-derived static response. Even changes in the UPM algorithm can be quickly incorporated by simply altering cell formulas.

**Statistics Database**

Revision 4 of SAW includes several new and useful tools for collecting key statnamic statistics for each processed data set. As stated earlier, the UPM gives a very good initial

estimate of the one key parameter necessary for completing the dynamic force equation: the damping coefficient. Engineering judgement is then employed to adjust this value until a reasonable load-displacement response curve is obtained. Because the damping coefficient is contingent on many variables, it is desirable to keep a database of all values encountered during different statnamic tests. SAW includes a Damping Coefficient Statistics tool that stores the mean, median, and standard deviation of the damping coefficient  $c$  for each test, as shown in figure 9. This information can then be used to develop correlations between the statnamic damping coefficient and parameters such as soil type, load pulse duration, load magnitude, and strain rate. These correlations ultimately could provide engineers with reasonable starting values for new tests. Although not discussed in this paper, correlations between statnamic-determined damping coefficients, unit skin friction, and soil type are being developed.<sup>12</sup>

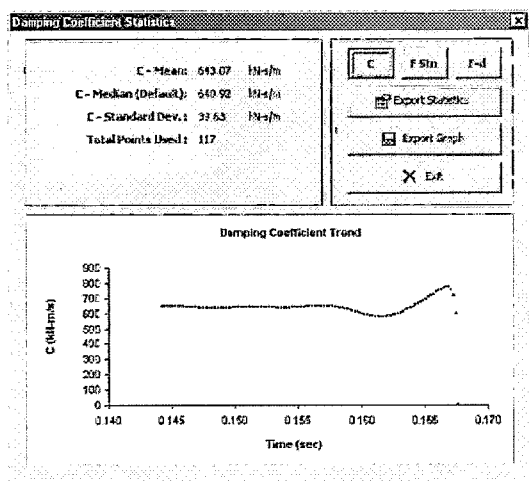


Figure 9. Damping Coefficient Statistics tool

Figure 10 shows SAW's Load-Displacement Statistics tool, which compiles all load-displacement characteristics such as the maximum statnamic force, magnitude of preload, maximum static force, and displacement information such as maximum displacement, displacement at maximum static force, and permanent set of the pile. These values are then displayed along with the response curves for the applied load, inertia-corrected load, and static capacity as a function of displacement. As with the Damping Coefficient Statistics tool, both the data and the graph can be exported separately for future use.

### Data Export

The primary goal of the data export module was to interface with the FHWA's Deep Foundations Database. Currently, this database contains tables into which statnamic data can be uploaded. Before SAW, the only way to enter statnamic data into these tables was to manually input each recorded value of time, displacement, velocity, acceleration, applied load, and derived static resistance for each load test. There is no mystery as to why there is very little statnamic data in the FHWA database.

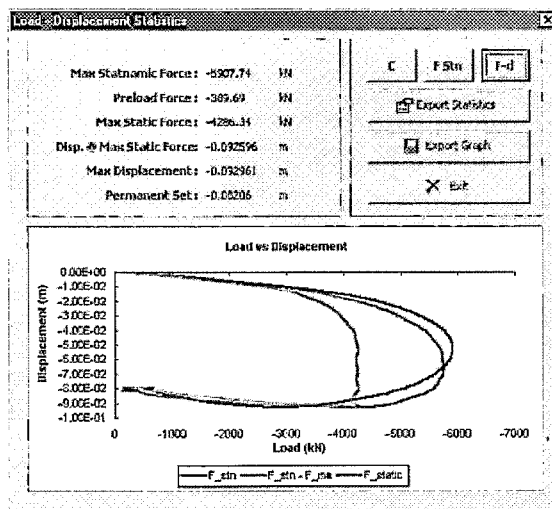


Figure 10. Load-Displacement Statistics tool

Recognizing the need for a better method of integrating statnamic data into the database, USF personnel worked closely with SAW's program designers, Technology & Management Applications, Inc. (TMA) of Maryland. TMA created an automated statnamic Data Import module for the Deep Foundations Database, shown in figure 11, and a corresponding data export module for SAW, shown in figure 12. This export module automatically generates a data file containing all of the reduced values for a statnamic test, formatted so that it is recognized by the Data Import module for loading into the Deep Foundations Database. A typical test containing 1500 lines of reduced data now can be uploaded to the FHWA database in a matter of seconds.

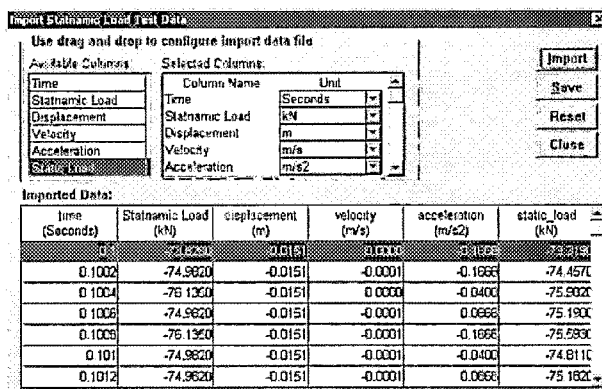


Figure 11. Data Import module for importing formatted data to the FHWA database

A secondary feature of the data exporter is that it can be used to create files containing only reduced data. These files are much smaller in size than a full spreadsheet file, so archiving data from many tests is more efficient. If test results are needed at a later date, the reduced data file can be opened by any spreadsheet program and the charts can be recreated as needed.



Time (s)	P. STN (kN)	S1 (mm)	Vel (m/s)	Accel (m/s <sup>2</sup> )	P. Status (kN)
0.0000	-11.4340	0.000000	-0.000028	-0.142441	-1.4014
0.0002	-11.4340	0.000000	-0.000048	-0.142441	-1.3999
0.0004	-11.5478	0.000000	-0.000070	-0.067523	-1.5378
0.0006	-11.4140	0.000000	-0.000099	-0.142441	-1.2964
0.0008	-11.4596	0.000002	-0.000124	-0.142441	-1.4392
0.0010	-11.3695	0.000003	-0.000152	-0.123707	-1.3498
0.0012	-11.5032	0.000003	-0.000181	-0.142441	-1.4799
0.0014	-11.5032	0.000003	-0.000219	-0.142441	-1.4776
0.0016	-11.5032	0.000000	-0.000245	-0.179609	-1.4724
0.0018	-11.5032	0.000006	-0.000270	-0.142441	-1.4736
0.0020	-11.5478	0.000000	-0.000297	-0.194971	-1.5192
0.0022	-11.5032	-0.000005	-0.000323	-0.161175	-1.4685
0.0024	-11.5924	-0.000011	-0.000350	-0.104971	-1.5600
0.0026	-11.5478	-0.000012	-0.000375	-0.161175	-1.5094
0.0028	-11.5924	-0.000012	-0.000401	-0.104971	-1.5564
0.0030	-11.5032	-0.000005	-0.000430	-0.142441	-1.4625
0.0032	-11.4349	-0.000005	-0.000460	-0.142441	-1.5941
0.0034	-11.5032	-0.000006	-0.000492	-0.161175	-1.4567
0.0036	-11.5478	-0.000006	-0.000523	-0.161175	-1.4991
0.0038	-11.5478	-0.000003	-0.000553	-0.142441	-1.4984
0.0040	-11.5478	-0.000005	-0.000581	-0.161175	-1.4950
0.0042	-11.4596	-0.000003	-0.000608	-0.123707	-1.4060
0.0044	-11.5032	0.000000	-0.000638	-0.142441	-1.4478
0.0046	-11.5478	0.000000	-0.000667	-0.161175	-1.4890
0.0048	-11.5924	0.000002	-0.000694	-0.123707	-1.5243
0.0050	-11.4140	0.000000	-0.000720	-0.142441	-1.2530
0.0052	-11.5924	0.000000	-0.000747	-0.123707	-1.5306
0.0054	-11.5478	0.000000	-0.000770	-0.142441	-1.4632
0.0056	-11.5478	0.000000	-0.000797	-0.094237	-1.4062
0.0058	-11.4349	0.000000	-0.000802	-0.088237	-1.4062
0.0060	-11.5032	0.000003	-0.000821	-0.067523	-1.4404
0.0062	-11.5478	0.000003	-0.000840	-0.123707	-1.4797
0.0064	-11.5478	0.000003	-0.000861	-0.067523	-1.4924
0.0066	-11.4349	0.000000	-0.000882	-0.142441	-1.5665
0.0068	-11.5478	0.000000	-0.000902	-0.067523	-1.4786
0.0070	-11.5478	0.000002	-0.000924	-0.123707	-1.4730

Figure 12. Data Export module for exporting formatted data from SAW

## Summary

Since its introduction in the early 1980s, statnamic testing has become more widespread as a suitable alternative to large-scale static load tests. Utilizing a rapid load pulse and accelerations of as much as 20 gs, the method can be used to measure the static response of a pile to a given load, provided the inertial and viscous forces introduced during testing are quantified and removed from the final data. Although several methods of analyzing this type of data presently exist, the UPM was selected for this application.<sup>5</sup>

The large volume of data collected during a typical statnamic test together with the extensive calculations necessary to fully reduce a single data set begs the use of computer-based analysis. To this end, USF personnel have developed SAW, a Visual Basic-enhanced spreadsheet program that automates much of the data reduction task. Additionally, this software interfaces with the FHWA's Deep Foundation Database and allows for the upload and storage of key load test data in the database. SAW is freely available via the Internet to educational institutions, engineering consultants, or other organizations requiring this type of statnamic data analysis.<sup>13</sup>

## Acknowledgments

The authors would like to express their gratitude to the Federal Highway Administration for funding this project,

as well as to Birmingham Foundation Equipment, Hamilton, Ontario, Canada, and the Florida Department of Transportation for their technical advice.

## References

1. American Society for Testing and Materials. *Annual Book of Standards*. Volume 04.08, Soil and Rock (I): D420-D4914. West Conshohocken, Penn: ASTM, 1996.
2. American Society for Testing and Materials. "Standard Test Method for Piles Under Rapid Axial Compressive Load." Unpublished, 2000.
3. American Society for Testing and Materials. *Annual Book of Standards*. Volume 04.09, Soil and Rock (I): D4943-Latest; Geosynthetics. West Conshohocken, Penn: ASTM, 1998.
4. Serway, R. A. *Physics for Scientists and Engineers*. 3d ed., volume 1. Orlando, Fl.: Harcourt Brace and Company, 1992.
5. Middendorp, P., P. Birmingham, and B. Kuiper. "Statnamic Load Testing of Foundation Piles." *4th International Conference on Stress Waves*, September 21-24, 1992, The Hague, Balkema: 581-88.
6. Lewis, C. "Analysis of Axial Statnamic Testing using the Segmental Unloading Point Method." Master's thesis, University of South Florida, 1999.
7. Garbin, E. "Data Interpretation for Axial Statnamic Testing and the Development of the Statnamic Analysis Workbook." Master's thesis, University of South Florida, 1999.
8. Mullins, G., C. Lewis, and M. Justason. "Advancements in Statnamic Data Regression Techniques." *Proceedings of the ASCE International Deep Foundations Congress*, ASCE Geotechnical Institute GSP No. 116, Vol. II (2002): 915-30.
9. Bielefeld, M. W., and P. Middendorp. "Statnamic Simulation." *Proceedings of the First International Statnamic Seminar*, September 27-30, 1995, Vancouver, British Columbia, Canada: 207-22.
10. Das, B. M. *Principles of Soil Dynamics*. Boston, Mass.: PWS-Kent Publishing Company, 1993.
11. Middendorp, P., and R. J. van Foeken. "When To Apply Dynamic Load Testing And Statnamic Testing." *Proceedings of the 2nd International Statnamic Seminar*, October 28-30, 1998, Tokyo, Japan: 253-61.
12. Winters, D. "Analysis of Statnamic Damping Values using the Segmental Unloading Point Method." Master's thesis, University of South Florida, 2002.
13. Statnamic Analysis Workbook website: <http://www.sawr4.com>.

Edward Garbin earned a doctorate in Civil Engineering from the University of South Florida. His areas of expertise include geotechnical engineering software design, structural and geotechnical instrumentation, and nondestructive testing of deep foundation systems. He is currently a senior project engineer at Universal Engineering Sciences in Tampa, Florida, and also teaches as an adjunct professor at USF.

Gray Mullins holds a doctorate in Civil Engineering from the University of South Florida. A specialist in structural and geotechnical instrumentation and alternative testing methods, he is one of the leading authorities on statnamic testing and has worked closely with manufacturers in developing the technology. He is currently an associate professor of Civil Engineering at USF.

## Consider Submitting Your Paper to the Journal of Engineering Technology!

Papers submitted to the *Journal of Engineering Technology* are reviewed for their contribution to the advancement of the field of engineering technology.

To submit a manuscript, contact Paul Wilder, Manuscript Editor, at (260) 422-5561 or e-mail [PWilder@indianatech.edu](mailto:PWilder@indianatech.edu).

# MOBILIZATION OF CAPACITY DURING RAPID AXIAL LOAD TESTING

P. Bermingham, G. Mullins, M. Stokes

## 1.0 INTRODUCTION:

Rapid axial load testing, the Statnamic load testing method, was first conceived in concept in response to Bengt Fellenius's determination to have at his disposal a means of mobilizing high capacity piles, which at that time, meant 600 tons. Without sufficient force energy, capacity may not be determined accurately by any method. At the time, in 1986, the most common shortcoming of dynamic "PDA" testing was the inability to mobilize the pile after an initial set had been achieved.

This challenge of mobilization became greater when the foundation industry looked for ways to apply existing testing techniques from driven pile practices to the expanding drilled shaft market in the USA. The increased mass of cast in place foundations made the use of hammers impractical, therefore Statnamic was developed to meet the need for a practical and cost effective means of mobilizing high capacity foundations and cast in situ foundations. Today the challenge continues. Design loads continue to move upwards to new levels, while a greater understanding of the factors which limit our ability to mobilize and proof capacity grows. The current research of Mullins et al, provides improved insight into the factors which govern the mobilization of capacity, through a series of very controlled static and rapid load tests. Mullins endeavours to determine the true damping factors which are present during testing and the extent to which they vary with displacement and velocity.

## 2.0 BACKGROUND

Two assumptions are employed when analyzing statnamic test data: (1) the foundation behaves as a rigid body throughout the duration of the test, and (2) the viscous damping associated with rapid movements is linearly related to the velocity via a constant damping coefficient,  $C_v$ . As such, a relatively simple equation of motion can be used to regress the data

$$\Sigma F = kx + ma + C_v$$

where the term  $kx$  represents the static capacity;  $ma$  represents the inertial response from the rapid loading; and  $C_v$  represents the viscous damping.

Several publications (Mullins, et al., 2000; Ealy and Justason, 2000, and Stokes, 2004) have shown a recurring trend in the damping coefficient of rapid load tests. Therein, the damping coefficient was determined by direct comparison of identical foundations that were either statically or statnamicly tested. The findings showed two distinct damping relationships, both linearly related to velocity, but having different constant values. The first was noted in elastically loaded foundations and a second in fully shearing foundations. Elastically loaded foundations exhibited higher damping effects than those plastically displaced. Foundations that fully sheared the surrounding soils (geotechnical failure) underwent an elastic response early on and subsequently failed as would be expected, but were assigned a single value of damping that improperly addressed the elastic region of the test. It should be noted that the present method of analysis can not over predict ultimate capacity, but rather may only over predict the elastic stiffness.

Using present analysis procedures the damping coefficient is determined at the end of the statnamic test via the Unloading Point Method (Middendorp, et al., 1992). In such cases the ultimate capacity is always correctly determined as it occurs at the end of the test coincident with the time period over which the damping coefficient is determined. However, the derived response of a foundation that shears will

appear artificially stiff in the elastic region of the test. Test programs documenting this response are presented below.

## 2.1 PLATE LOAD TESTS

In a series of plate load tests, Statnamic testing was applied to shallow foundations (Mullins, et al., 2000). Three separate yet identical foundations on clean sand were tested in the following manner: (Test 1) incrementally increasing Statnamic load cycles until bearing failure, (Test 2) static load test, and (Test 3) a single Statnamic load cycle well in excess of the bearing capacity. Using the *Unloading Point Method*, a derived static load-displacement response was obtained for each load cycle, and compared with the static load test in which three load/unload cycles were recorded. Figures 1 and 2 illustrate the results of these tests.

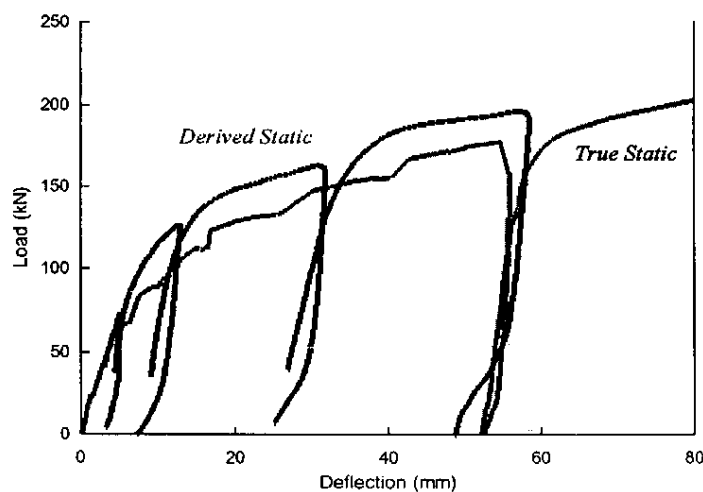


**Figure 1** Comparison of derived static response from four Statnamic load cycles (test 1) with the true static response (test 2).

The derived static load for cycles one through four (Test 1) as well as the static load response (Test 2) are shown in Figure 1. The peak applied Statnamic loads were 74, 128, 196, and 262 kN for cycles one through four, respectively. Damping coefficients ( $C$ ) calculated for each of these cycles using the *Unloading Point Method* (Middendorp, et al., 1992) were 146, 76, 78, and 92 kN-s/m, respectively. The derived static response slightly over estimates the capacity of the foundation when compared to the true static capacity. This is not altogether surprising based on densification of the soils within the initial cycles. This densification can also be seen from Test 3 (Figure 2) which produced a peak load of only 219 kN yet resulted in more displacement than the fourth cycle of Test 1 (262 kN). Figure 2 shows the results of Test 3 superimposed over Test 2 and provides an example of a trend that develops when the Statnamic load fully mobilizes the bearing capacity of the foundation. During the linear loading stage, Statnamic results indicate a stiffer response than that of a static test, but once bearing failure occurs the two test results are similar. Derived static values for shallow foundations are relatively unaffected by inertial forces but a far more sensitive to the damping coefficients. The damping coefficients calculated from the unloading portion

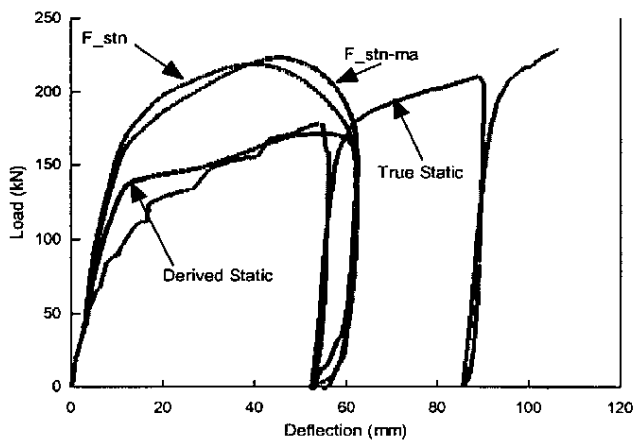


**Figure 2** Static / derived static comparison of Statnamic test performed well above bearing capacity (tests 2 and 3).

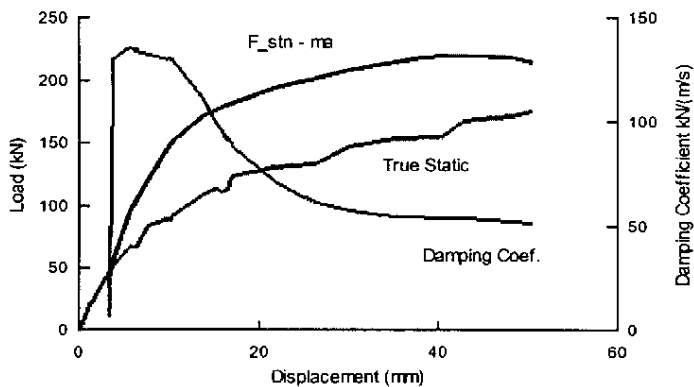


**Figure 3** Values of the variable damping coefficient calculated using the true static response and the inertia corrected Statnamic force.

of the test satisfy the system dynamics in that portion of the loading but fail to do so initially. This implies that  $C$  varies as the soil strains beyond yield and is supported by the difference in the calculated damping coefficient observed in Test 1 (cycle 1) and Test 3, 146 and 58 kN-s/m, respectively. If it is assumed that the difference between the true static and inertia-corrected Statnamic force is due to a variable damping coefficient, then the coefficient at any point can be determined for a specific site using the following expression:

$$C_x = \frac{F_{stn_x} - F_{ma_x} - F_{static_x}}{V_x}$$

where  $C$ ,  $V$ ,  $F_{stn}$ , and  $F_{ma}$  are the dynamic force parameters at displacement  $x$  and  $F_{static}$  corresponds to the true static force at that displacement. Using this expression, Figure 3 illustrates the variation in the damping coefficient as a function of displacement (or degree of shearing). It is interesting to note that  $C$  computed from this side-by-side comparison (Figure 3) is similar to that of determined by the Unloading Point Method at a similar state of shear (or displacement). Therein the  $C$  value in the elastic range is relatively large (like Test 1, Cycle 1) and in the plastic range the  $C$  value is relatively small (like Test 3).

## 2.2 MODEL PILE GROUP TESTING

Research conducted by Justason and Ealy (2000) on model-scale pile groups showed strong agreement between derived static capacity from and the static test results. These tests were conducted at a wide range of loading rates using various static test methods. However, with regards to damping coefficient determination, it was noted that the overall shape of the derived static curve did not follow the static test results exactly. They concluded that the possibility of a more sophisticated strain-dependent damping model may be plausible. Figure 4 shows the computed damping from back substitution like that discussed earlier. The data shows a similar trend of decreased damping at a post yield displacement of 7mm.

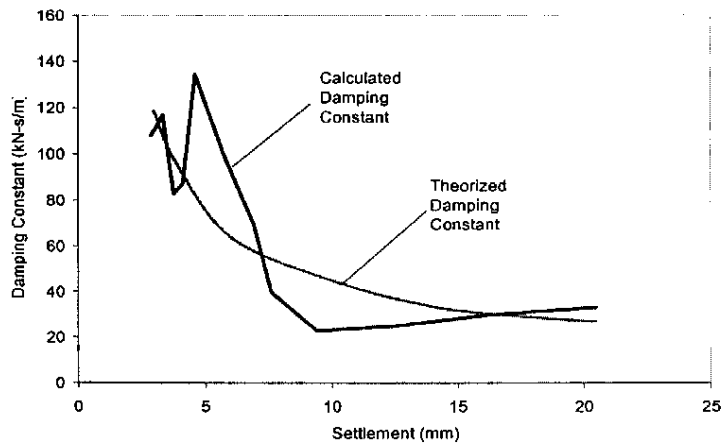


**Figure 4** Damping constant as cited by Justason and Ealy, 2000.

## 2.3 FRUSTUM SHAFT TESTING

Using 1/10th scale drilled shafts constructed in a high stress modeling cell Stokes (2004) conducted alternating cycles of static / statnamic / static tests. This lab-scale device is particularly helpful with modeling a foundation response to statnamic loads when it is used in conjunction with a 0.2 MN statnamic device. This allows consecutive static / statnamic tests on a single foundation without the costs associated with larger-scale devices.

The performance of drilled shafts and driven piles have been explored in the laboratory using the *Frustum Confining Vessel* (FCV) which provides a method of physically modeling pile-type in-situ stresses on small-scale piles without the use of a centrifuge. The device, developed by Berminghammer Foundation Equipment in conjunction with McMaster University (Horvath et al., 1995), is a conical-shaped steel vessel in which sands are placed and stressed as shown in Figure 5.

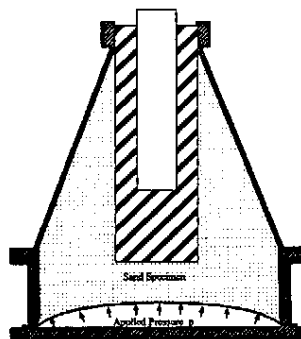


**Figure 5** Frustum Confining Vessel used for physical modeling of pile load tests (after Horvath, 1998).

The resulting vertical and horizontal stress distributions are reasonably similar to those of full-scale prototype piles. Figure 6 shows the control volume portion of the FCV where stresses are similar to those encountered in the field, as well as the vertical and horizontal stress distribution measured along the centerline for different levels of applied pressure. 355

Some significant advantages of the FCV with respect to other physical modeling methods are the

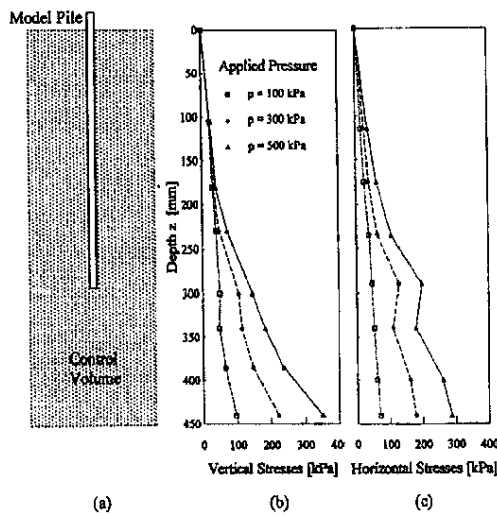


**Figure 6** (a) The control volume (b) vertical stress distribution, and (c) horizontal stress distribution within the FCV (after Horvath, 1998).

simplicity of testing, relatively low cost, and its ability to model relatively large model piles (e.g. 36" long, 4" diameter) thus simplifying instrumentation and relaxing some of the scaling requirements; e.g. Schofield, (1980) and Craig & Sabagh, (1994). Figure 7 shows the USF frustum testing facility used by Stokes (2004).



**Figure 7** Frustum test facility.



**Lab-Scale Statnamic Device.** Reliable lab-scale testing has recently been made available via a new 0.2MN test device at USF. This device is identical in concept and operation to the full-scale prototype devices and is equipped with a mechanical catching mechanism. Figure 8 shows the USF lab-scale statnamic device complete with a static reaction beam. The entire assembly is attached to the FCV preparing to test a 1/10th scale drilled shaft. This type of setup provides quick static / statnamic / static test series without significant delay between tests.

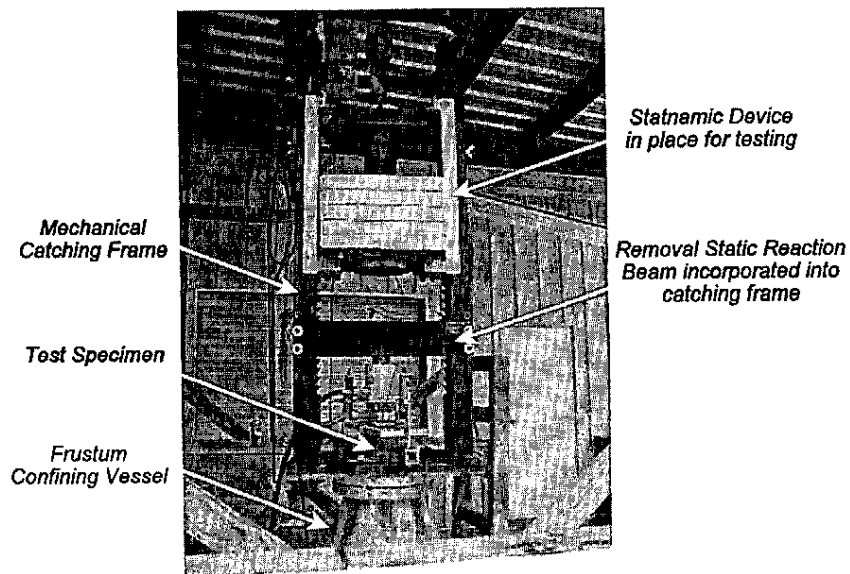


**Figure 8** Static and STN test setup on FCV.

The results of sequential static -statnamic - static tests in the FCV corroborate previous findings with the

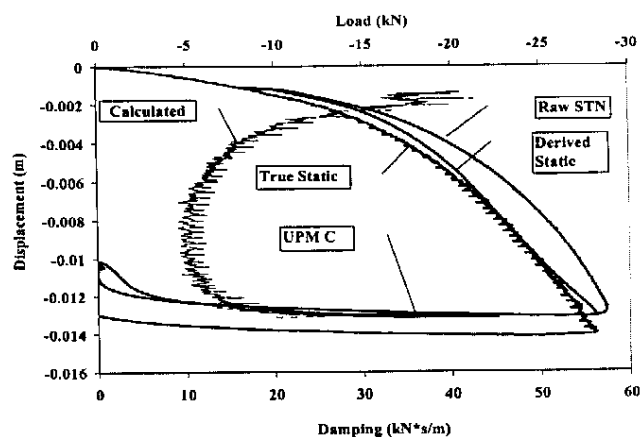


**Figure 9** Exhibited trend in damping coefficient  $C$  values from lab scale testing.

addition of linking the calculated damping coefficient to the determined  $C$ . Figure 9 shows the static as well as both the raw and regressed statnamic test results from a 1/10th scale drilled shaft in the FCV. Additionally, this figure shows the damping coefficient from both back calculation and the similar to the previous studies.

Note the decrease in the back calculated  $C$  with increased displacement once shearing occurred.

Similarly, note the restoration of the damping value as the shaft regained hold of the surrounding soils. This is not altogether surprising given the trends that are often observed from  $C$  values as a function of displacement although not clearly obvious from Figure 9. However, full-scale foundations with greater mass (which develop more significant momentum) also exhibit this trend. Figure 10 shows the results from a single segment of a statnamic loaded prestress piles at the Bayou Chico Bridge Project in Pensacola, FL. Therein, a nearly constant  $C$  value is observed while the pile is shearing and a rapid increase in  $C$  as it regains hold of the surrounding soils (Winters, 2002). This analysis used the Segmental Unloading Point method (Mullins, et al., 2002).

Preliminary results from on-going numerical modeling of the soil surrounding deep foundations show promising correlations with this observed phenomenon. Consistently, higher damping coefficients are assigned to elastically behaving foundations when compared to identical foundations loaded to mobilize full capacity. Although too early in the research to be certain, the elastic damping coefficient is often shown to be on the order of 3 times that computed in the post yield region of the load versus displacement response.

### 3.0 CONCLUSIONS

The results from several studies were discussed where the relationship between computed or derived static capacity from rapid axial load tests were compared to static load tests on nearly identical foundations. This type of comparison provided a glimpse into a trend in the damping coefficient that appeared to be stress state / displacement dependent. It was noted that although present relatively simplistic methods of dealing with viscous damping only consider a single damping coefficient, those methods accurately assess the ultimate capacity. However, a limitation may exist in evaluating the elastic stiffness when the foundation is loaded beyond yield. On the other hand, when a foundation is rapidly loaded within the elastic region, the computed stiffness is commensurate with a static test. Further results are pending the completion of an on-going project funded by the Federal Highway Administration.

### 4.0 REFERENCES

- Ealy, C. and Justason, M.D., 2000. "STATNAMIC and Static Load Testing of a Model Pile Group in Sand." Proceedings fo the Second International Statnamic Seminar, Tokyo, Japan, October 28-30, 1998, pp. 169-177.
- Garbin, E.J., 1999. "Data Interpretation for Axial Statnamic Testing and the Development fo the Statnamic Analysis Workbook." Master's Thesis, University of South Florida, Tampa, Florida.
- Lewis, C., 1999. "Analysis of Axial Statnamic Testing using the Segmental Unloading Point Method." Master's Thesis, University of South Florida, Tampa, Florida.
- Mullins, G., Garbin, E.J., Lewis, C., and Ealy, C., 2000. "STATNAMIC Testing: University of South Florida Research." Proceedings fo the Second International Statnamic Seminar, Tokyo, Japan, October 28-30, 1998, pp. 117-132
- Mullins, G., Lewis, C., and Justason, M., 2002. "Advancements in Statnamic Data Regression Techniques." Deep Foundations 2002: An International Perspective on Theory, Design, Construction, and Performance, ASCE Geo Institute, GSP#116, Vol.II, pp. 915-930.
- Stokes, M., 2004. "Laboratory Statnamic Testing." Master's Thesis, University of South Florida, Tampa, Florida.
- Winters, D., 2002. "SUPERSAW Statnamic Analysis Software." Master's Thesis, University of South Florida, Tampa, Florida.

## **Developments in Underwater FRP Repair**

**Rajan Sen and Gray Mullins**

*Department of Civil and Environmental Engineering  
University of South Florida, Tampa, FL 33620 USA  
sen@eng.usf.edu*

### ***Abstract***

*Fiber reinforced polymers are widely used in structural repair and rehabilitation. Their application for repairing corrosion-damaged structures located in tidal waters is very recent and has become possible because of the development of a new water-activated resin that can cure underwater. This paper discusses some of the issues relating to this new application with particular reference to some recently completed demonstration studies. The experience indicates that this new technology is promising and may be competitive at this time in applications where corrosion damage can be patch repaired so that there is no need for re-forming the cross-section.*

### **INTRODUCTION**

Reinforced or prestressed piles subjected to wet/dry tidal cycles in seawater are very vulnerable to corrosion damage especially in coastal regions of southeastern United States. The combination of high temperature and high humidity allows chloride ions to penetrate high quality concrete destroying the passive layer that normally protects steel by preventing access of oxygen and moisture. The destruction of the passive layer initiates corrosion that leads to cracking, spalling and loss of cross-section that must be repaired. Durable repair of corrosion damage may be achieved by following one of two broad strategies (1) by removing all chloride-contaminated concrete and replacing it by low shrinkage, low modulus, high creep, high tensile strength patch material with the same physical and electrochemical properties and,

(2) by integrating a cathodic protection system within the repair. Since the exact boundaries of the chloride contaminated regions are impossible to locate, corrosion repairs using the first strategy do not necessarily result in durable repairs. The second strategy is proven but can be very costly. As a result, highway authorities in US are showing increasing interest in alternative repairs using fiber reinforced polymers (FRP) because of their potential for a lower cost solution (Sen 2003). While the application of FRP for repair and strengthening structures under dry conditions is well established, its use for underwater repair is at its infancy. This paper presents a brief overview of developments in the underwater repair of piles using FRP.

## **BACKGROUND**

Pile jackets are commonly used for the repair and rehabilitation of corrosion-damaged piles in the United States. They consist of three components (1) a stay-in-place form encapsulating the damaged portion of the pile usually made of fiberglass, (2) an optional reinforcement cage (depending on the severity of the damage) and, (3) cement or epoxy based concrete or grout filler. Fig. 1 shows a photograph of a jacketed pile.

Pile jackets cannot stop corrosion from continuing since deleterious materials such as chlorides, moisture and oxygen are trapped in the repair. As a result, corrosion continues unabated. Unfortunately, the opaque fiberglass jacket obstructs signs of the on-going corrosion until it reaches an advanced state when rust stains and splitting of the jacket becomes visible. In one particular instance it was found that nearly all the prestressing strands in a jacketed pile in Florida had corroded completely. To prevent recurrence of such damage, the Florida Department of Transportation (FDOT), pioneered research into the development of a new jacket that allowed integration of a sacrificial anode cathodic protection system. This system, known as the LifeJacket® system, uses an expanded zinc mesh anode that is placed directly against the inside of the fiberglass jacket and is electrically connected to the steel reinforcement. The annular space between the pile and the jacket is filled with an approved concrete material. In addition to the zinc mesh, a 21.8 kg bulk zinc anode is placed 60 cm below mean low tide to polarize the submerged portion of the pile and prevent excess consumption of the mesh anode during high tide.

Typically, the zinc-mesh system is designed for a 25-30 year service life. Manufacturers claim they can be engineered to have much longer lives. However, estimates of service life are based only on the consumption rate of the zinc and disregard other parameters such as the integrity of the electrical connections and water tightness of the PVC junction boxes. These are equally important since the system relies on galvanic coupling for protection.

## **FRP FOR CORROSION REPAIR**

The Lifejacket® system was first tested in Florida in 1994 and has been found to be effective though costly. FRP offers the prospect of an equally effective repair that is less expensive. Although material costs for FRP are high, overall repair costs may be lower. Their lightweight and high tensile strength means that heavy equipment is not needed and mobilization costs are lower. Moreover, they are aesthetically more pleasing since repairs are indistinguishable once the FRP material is painted.

The first application of FRP for corrosion repair was carried out in Japan in 1977 nearly twenty years after its initial construction (Ohta et al. 1992). The five girder, three-span post-tensioned Masuhoro Bridge located 70 m from the Sea of Japan had developed large cracks that were as much as 7.5 mm wide. A combination of epoxy injection, steel plates and glass fiber reinforced polymer (GFRP) wrapping was used in its repair and rehabilitation. Strengthening was achieved by bonding a 4.5 mm thick steel plate to the bottom flange and by using two GFRP layers to wrap the webs of the most severely cracked beams. In the remaining beams, one GFRP layer was applied to the *entire* surface.

In 1990, thirteen years after the FRP repair, the bridge was replaced and the opportunity was taken to carry out an in-depth investigation of three of the girders that were retrieved. Chloride content analysis indicated that the GFRP applied to the web had prevented further ingress of chlorides. Ultimate load tests indicated that the tensile strength of the GFRP had reduced by 60% and its elastic modulus by 18% from the time of the original rehabilitation.

The performance of this bridge demonstrated that the GFRP material served as an effective barrier for the ingress of chlorides. However, it was unable to prevent on-going corrosion caused by deleterious materials already trapped

inside the post-tensioning duct. This field application showed the potential of FRP in corrosion-repair.

## FIBER REINFORCED POLYMERS

FRPs are made of low cost glass fiber or high cost aramid / carbon fibers embedded in a polymer resin matrix. Fibers can be in the form of sheets or woven fabric oriented in one direction ("*unidirectional*") or in several directions ("*multidirectional*"). They are linear, elastic materials with high tensile strength in the direction of the fibers but low tensile strength in other directions where they are only as strong as the resin matrix.

FRP systems used for corrosion-repair are categorized based on how they are delivered on site and assembled as "*wet lay-up*", "*prepreg*" or "*precured*". In wet lay-up systems, dry FRP sheets or fabrics are saturated with resin on-site and cured in place. Prepregs refer to systems where the FRP material is impregnated with resin at the manufacturer's facility but is cured on site with or without additional resin. Precured laminates are in the form of cured FRP shells or plates that can be directly bonded to the concrete surface.

## WRAP DESIGN

Given the high cost of FRP material, its ability to compete in the market place requires that it be engineered so that it can match the Lifejacket® system in both price and performance. The design of the FRP wrap requires consideration of strengthening in both the longitudinal direction and transverse direction. Longitudinal strengthening makes up for the shortfall in ultimate bending capacity due to metal loss while transverse strengthening is required to withstand potential expansion forces due to corrosion.

Determination of the strengthening required to make up for a shortfall in ultimate axial and bending capacity may be obtained from a simplified strain compatibility analysis. The determination of the transverse strengthening is more problematic since it requires expansion data that relates metal loss to expansion. Unfortunately, corrosion expansion is difficult to measure and published data shows considerable scatter. In part this is because it is obtained from accelerated laboratory tests and measurements reflect the type of corrosion products that were formed. If oxygen is limited, soft, black, water-soluble compounds are formed that result in lower strains for the same mass loss. In most cases strains reported are obtained from crack width that is averaged over the circumference. This provides an upper bound on the



strain since it is based on unrestrained dimensional change that arises following cracking. The strain corresponding to the modulus of rupture stress provides a lower bound on the expansion strain. In any event, how well laboratory strain data compare with that in piles exposed to a marine environment is not known.

### **Transverse Expansion**

CALTRANS 2000 and ISIS 2001 use the familiar hoop stress equation to calculate the number of layers of FRP material to accommodate transverse expansion. This approach was also used in a recent demonstration study (Shahawy et al. 2004). However, in the absence of reliable data, the expansion strain was arbitrarily assumed to be 0.001 that is three times the ultimate tensile strain of concrete. A two step approach was then used; in the first step, strain compatibility analysis was carried out to establish the number of layers required to restore lost axial capacity. A confinement model was then used to verify that this wrap configuration could also accommodate the design lateral strain of 0.001. This approach was found to yield results that were less conservative than CALTRANS or ISIS.

## **FRP SYSTEM FOR UNDERWATER APPLICATION**

Most FRP strengthening systems require the concrete surface to be dry. The development of a specially formulated, water-activated resin has made it possible to conduct underwater wrap economically (AQUAWRAP® 22-77) since it eliminates the need for cofferdam construction (Fig. 2). This greatly reduces costs and makes underwater FRP wrapping economically viable. Divers or a scaffolding system may be used to install the wrap. The width of the FRP material is kept small, e.g. 15 cm to 30 cm to facilitate handling under water.

Since the resin cures in water, the FRP material must be cut to size, pre-impregnated with the same resin in a factory and sent to the site in hermetically sealed packages. Otherwise, it would cure prematurely due to water vapor present in the atmosphere. Thus, the seal is broken just prior to use.

## **SURFACE PREPARATION**

Surface preparation for underwater wrapping is no different than that for above ground applications. Existing cracks must be sealed and concrete

spalls must be restored to their original condition by using appropriate fast setting hydraulic cements. Sharp corners must be ground to remove stress concentrations and all marine growth (Fig. 3) must be removed. Just prior to the application of the wrap, the surfaces have to be pressure washed to remove dust particles or algae that could be adhering to the pile surface.

## **FIELD APPLICATION**

The first application of the new system was on two steel reinforced concrete pilings on a bridge over the North River near Wilmington, NC (Bazinet et al. 2003). Two 30.5 cm square pilings were repaired. The wrap length was 2.44 m and 1.83 m respectively and extended 35 cm below low tide. Fig. 4 shows a photo of the wrapping in progress.

The first application of this new system on prestressed piles was conducted on the Allen Creek Bridge, Clearwater, FL. In this application, four 35 cm x 35 cm prestressed piles driven in an aggressive environment were wrapped over a 1.52m depth, two with fiberglass and two with carbon. Prior to the repair, selected piles were instrumented to assess their initial corrosion state. Instrumentation was designed to allow measurement of the corrosion rate and the corrosion potential of the piles. More recently, four piles on the Friendship Trails Bridge, Tampa, FL were wrapped. In this case, the piles were 50 cm x 50 cm reinforced concrete piles that were wrapped over a depth of 1.83 m. These piles are also instrumented and measurements are being taken to compare the pre- and post-wrap performance.

In all the above applications, the FRP wrap was applied spirally from the top with the layers touching but not overlapping. However, the first and last layer at the top and bottom were kept horizontal. No splices were needed since the FRP material was cut to the exact size. Since water is required for curing, water must be sprayed between each layer above the water line. After the wrap is completed, a single layer of a fiberglass tape is applied to provide a smooth finish. This is followed by the application of a special high tensile strength stretch film that secures the wrap in place. This is removed after the resin cures when the surface is painted over using a protective epoxy adhesive.

## **DISCUSSION**

The development of this new water -activated system makes it possible to

wrap FRP underwater. Manufacturers of the new system have conducted many tests to evaluate bond and found it to be satisfactory. However, whether this is true for field applications where conditions may be different remains to be proven. This especially the case since oily deposits from seawater may form on the pile surface making bonding that much more difficult. USF researchers plan to conduct pullout tests to assess bond in the two demonstration studies described.

Bond with concrete is important from the strengthening standpoint but not from confinement considerations. In piles, strengthening is usually not important since design is dictated by soil conditions, not structural capacity. The more critical concern is the ability of the FRP wrap to withstand expansive forces due to corrosion. Here the interlayer FRP to FRP bond may provide adequate resistance (Harichandran and Baiyasi 2001).

## **SUMMARY AND CONCLUSIONS**

This paper provides a brief overview of underwater pile repair using FRP. Demonstration studies confirm its feasibility; it took less than one hour to wrap a pile in the two Florida bridges. However, the application of this technology is at its infancy and new advances may be anticipated particularly in the area of specialist epoxies and installation techniques that will lead to increased efficiency.

The new FRP system will be attractive to bridge owners only if it can outperform the Lifejacket® system and cost less. At the present time, it would appear that the FRP system will be more economical in situations where there is insufficient section loss to warrant re-forming the cross-section. The Lifejacket® systems may be more suitable where re-forming is necessary since the fiberglass shell serves as formwork for the concrete needed to restore the cross-section. However, this equation may change if the use of FRP gains widespread acceptance and innovative construction practices emerge.

## **ACKNOWLEDGEMENTS**

The authors thank Air Logistics Corporation, Pasadena, CA for their contribution. Funding for the demonstration studies carried out by USF was provided by the Florida Department of Transportation and Hillsborough County. This support is gratefully acknowledged. The authors thank Mr.

Jose Garcia, Mr. Steve Womble (both FDOT) and Ms Mara Nelson (Hillsborough County) for their contribution. However, the opinions, findings and conclusions expressed in this publication are those of the authors and not necessarily those of the Florida Department of Transportation.

## REFERENCES

1. AQUAWRAP 22-77 Resin System, Air Logistics, Pasadena, CA.
2. Bazinet, S., Cercone, L. & Worth, L. (2003), Innovative FRP Piling Repair without the Use of Cofferdams. *Proceedings of the 48<sup>th</sup> International SAMPE Conference*, Vol. 48, Book 2 of 2, pp. 2201-2206.
3. CALTRANS (2000), Memo to Designers 20-4 Attachment B, November.
4. Harichandran, R. & Baiyasi, M., (2000), Repair of corrosion-damaged columns using FRP wraps. *Research Report RC-1386*, submitted to Michigan Department of Transportation, Lansing, MI, 2000.
5. ISIS Canada (2001)., Strengthening Reinforced Concrete Structures With Externally-Bonded Fibre Reinforced Polymers, Design Manual, ISIS-M05-00, Spring.
6. Ohta, T., Sakai, K., Obi, M. & Ono, S., (1992), "Deterioration in a Rehabilitated Prestressed Concrete Bridge". *ACI Materials Journal*, Vol 89, Sen, R., (2003). "Advances in the Application of FRP for Repairing Corrosion Damage", *Progress in Structural Engineering and Materials*, Vol. 5, No 2, pp. 99-113.
7. Shahawy, M., Mullins, G. and Sen, R., (2004), "CFRP Repair and Strengthening of Structurally Deficient Piles". Submitted to 83<sup>rd</sup> Annual Meeting of the Transportation Research Board, Washington, DC.



**Fig.1 Jacketed Pile**

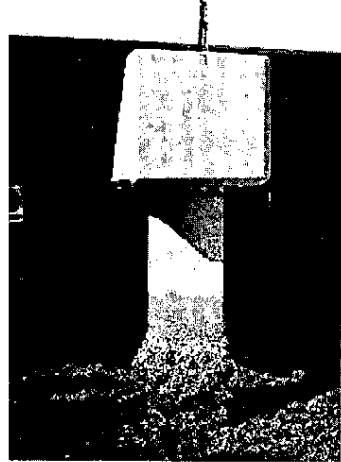


**Fig.2 Marine Growth**

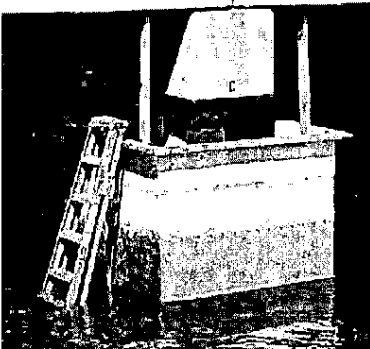


**Fig.3 Cofferdam Construction**



**Fig.4 Underwater Wrap  
(courtesy Air Logistics, CA)**

## Post Grouted Drilled Shafts: A Case History of The PGA Boulevard Bridge Project

Gray Mullins, Ph.D., P.E.

*Associate Professor, University of South Florida, Department of Civil and Environmental Engineering, Tampa, Florida, USA*

Mike Muchard, P.E.

*Principal Geotechnical Engineer, Applied Foundation Testing, Inc., Green Cove Springs, Florida, USA*

Bud Khouri, P.E.

*Vice President, Trevi Icos South Corporation, Clearwater, Florida, USA*

**Abstract:** A post grouted drilled shaft foundation system was successfully used in place of the specified driven pile foundation system as a Value Engineering Cost Proposal (VECP) for the new PGA Boulevard Grade Separation Project. Pressure grouting the cohesionless sandy soils at the drilled shaft base significantly increased the end bearing capacity and stiffness allowing drilled shafts to be the more cost effective foundation system. The post grouted drilled shaft option also provided other benefits including reducing owners risk normally associated with pile driving vibrations and offered a high level of quality assurance for the drilled shafts.

This paper discusses the implementation of post grouted drilled shafts from design to completion of construction. A design procedure for post grouted drilled shafts developed by the University of South Florida was used for initial VECP evaluation. Prior to construction, two instrumented test shafts were installed and load tested, one of which was post grouted. Therein, the design procedure was calibrated, tip elevations for production shafts were refined, drilled shaft construction and grouting procedures were demonstrated, and a grouting criteria was developed for the project.

### **Introduction**

Although technically feasible, drilled shafts are not typically thought of being cost effective in sandy soils. This is mainly because little to no end bearing can be relied upon within service displacement limits. Additional skepticism on the use of end bearing in sand can be attributed to soil disturbance at the shaft base during construction and the ability to effectively cleanout the excavation. End bearing capacity in sand can be significant but large displacements are required to fully benefit from its use. By post construction pressure grouting below the shaft tip,

the base resistance can be mobilized thereby eliminating these problematic issues. In many cases, the available base resistance improvement is bounded only by the skin friction resistance to upward shaft movement.

Post grouting of drilled shafts has been successfully used on many projects in Europe and Asia to precompress soft debris or loose soil relaxed by excavation (Bolognesi and Moretto, 1973; Stoker, 1983; Bruce, 1986; Fleming, 1993; Mullins et. al, 2000). Its use in the USA, while it is only recent, is gaining wide acceptance due in part to a rational design method developed



by the University of South Florida and its heightened quality assurance aspects. This paper only provides a brief description of this design method and is included only to assist in the understanding of a case history where post grouted drilled shafts were used on a major Florida Department of Transportation bridge project. A more detailed description of the design procedure can be found elsewhere (Mullins et. al, 2001). The main focus is on the construction and load testing of the post grouted drilled shafts.

### **Project Information**

The PGA Boulevard Grade Separation Project was located in West Palm Beach, Florida and consisted of improvements to its intersection of Alt A1A. In all, the project had three bridge structures including PGA Boulevard Alt A1A, A1A SW Ramp to I-95 and Alt A1A SW Ramp over FEC Railway.

The project was funded by the Florida Department of Transportation and the Federal Highway Administration. Astaldi Construction Corporation was the General Contractor and TreviIcos South, Inc. the drilled shaft contractor. Inspection was performed by Delta Consulting Engineers, Inc. on behalf of the FDOT. Applied Foundation Testing, Inc. provided instrumentation, Statnamic load testing and performed the pressure grouting services on the project.

The structures foundations were originally designed using a LRFD design approach on 24" square prestressed concrete piles arranged in bents and groups. Factored design loads were 135 to 220 tons with a resistance factor of 0.65. Pile lengths were up to 70 feet. Because nearby structures were sensitive to vibration, pile driving hours were heavily restricted and confined to a four hour work window at night.

To circumvent these problems, drilled shafts were considered as a Value Engineering Cost Proposal (VECP). Pressure grouting of the drilled shaft tips was used to increase their capacity allowing the drilled shaft option to be more economical. Other benefits included reducing the project schedule due to increased work hours, reduction of pier cap size, reducing risks associated with vibrations, and increased drilled shaft quality assurance.

A total of 108 drilled shafts replaced 234 24 inch driven piles. The shafts design diameter was 36 inches (nominal) with lengths of 30 to 50 feet. Factored design loads ranged from 195 to 490 tons. A resistance factor of 0.75 was used due to the added quality assurance from load testing. Although not considered at the design phase, additional confidence could have been incorporated in the form of an increased resistance factor due to post grouting every shaft.

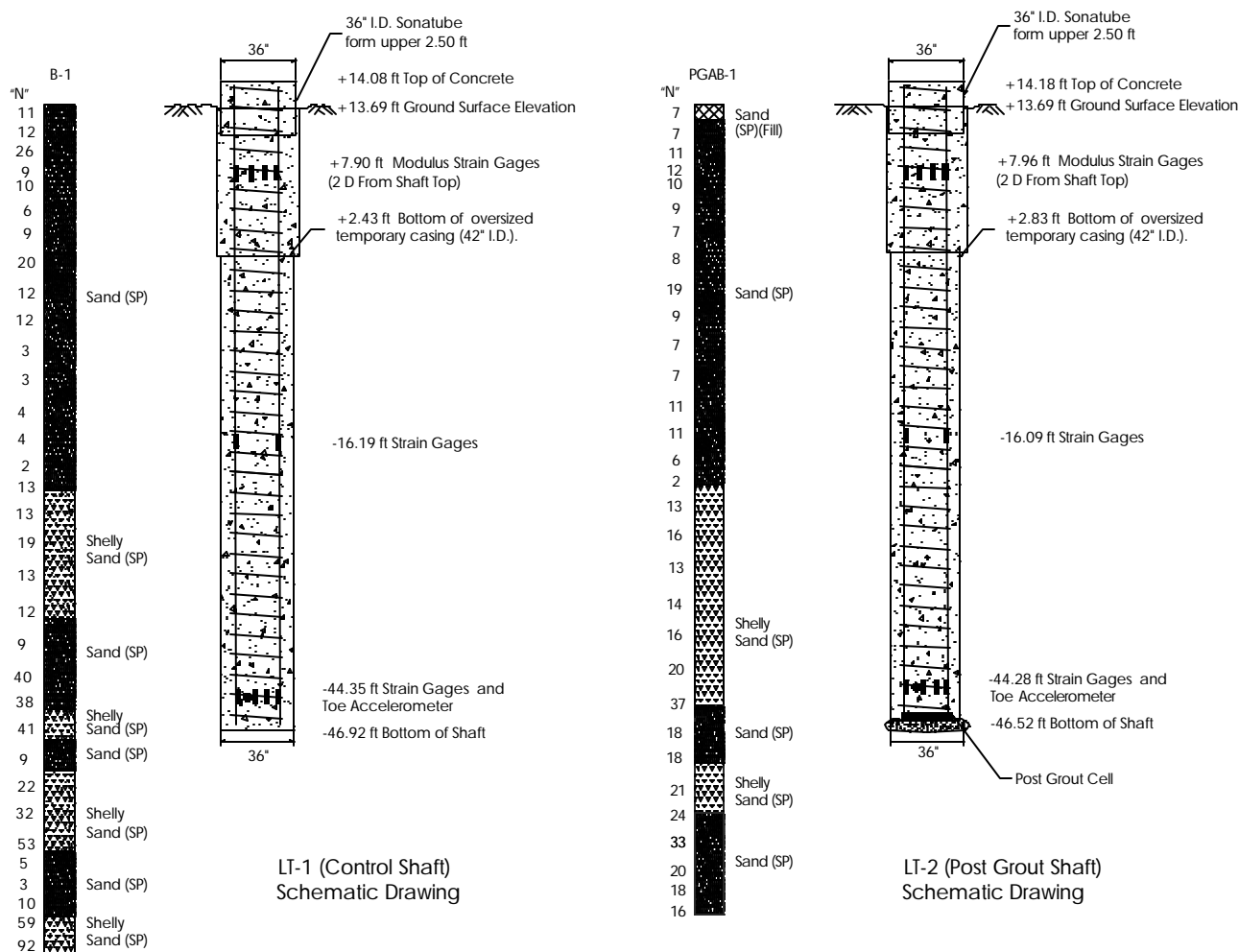
To verify design and demonstrate the construction method, a load test program was undertaken. Two test shafts, designated as LT-1 and LT-2, were constructed with nearly identical geometric properties and subsurface conditions except LT-2 was equipped with a post grout apparatus at the tip. Each shaft was also instrumented with 3 levels of embedded strain gages. LT-2 also included telltales at three different levels.

The test program involved first performing a grouting test of LT-2 then performing downward axial compression Statnamic load tests on each shaft. The instrumentation was monitored during pressure grouting and load testing. Based on the grouting and load test results shaft tip elevations were refined and a grouting criteria was developed for the project.

**Soil Conditions**

A soil boring was drilled at each test shaft location. The as-built location of Test Shaft LT-1 corresponded to Boring B-1. Boring PGAB-1 coincided with the Test Shaft LT-2 location. Test shaft schematic drawings and soil profiles are shown in Figures 1 and 2. The soil profile generally consisted of very loose to dense Sand (SP) with intermittent layers of shelly Sand for the entire depth of the borings.

Generally, the upper 30 feet were very loose to medium dense (N= 2 to 20) and the lower 50 feet were medium dense to very dense sands (N= 9 to 41). Large amounts of rainfall following several years of near drought conditions in Florida produced unusually large fluctuations in groundwater levels between 3 to 10 feet in depth during the course of the project.



Figures 1 and 2. Schematic drawing of test shafts and soil profile.

## Design Approach

As part of an FDOT-funded research program beginning in June 1999, a design methodology and construction guidelines were developed by USF and adopted for FDOT highway bridge projects. The technology was effectively transferred to design and construction where post-grouted drilled shafts have been implemented on several DOT projects in Florida, Mississippi and Texas and is planned for several more upcoming projects. Full details of this study can be found elsewhere (Mullins, et al., 2001). The design approach for post grouted drilled shaft tips makes use of common parameters used for a conventional (un-grouted) drilled shaft design. This methodology includes the following seven steps:

- 1) Determine the ungrouted end bearing capacity in units of stress.
- 2) Determine the permissible displacement as a percentage of shaft diameter (e.g.  $1"/48" * 100\% = 2\%$ ).
- 3) Evaluate the ultimate side shear resistance for the desired shaft length and diameter (in units of force).
- 4) Establish a maximum grout pressure that can be resisted by the side shear (ultimate side shear divided by the tip cross sectional area).
- 5) Calculate the Grout Pressure Index, GPI, defined as the ratio of grout pressure to the ungrouted end bearing capacity (*Step 3 / Step 1*).
- 6) Using design curves from [Figure 3](#), determine the Tip Capacity Multiplier, TCM, using the GPI calculated in *Step 5*.
- 7) Calculate the grouted end bearing capacity by multiplying the TCM with the ungrouted end bearing ( $TCM * Step 1$ ).

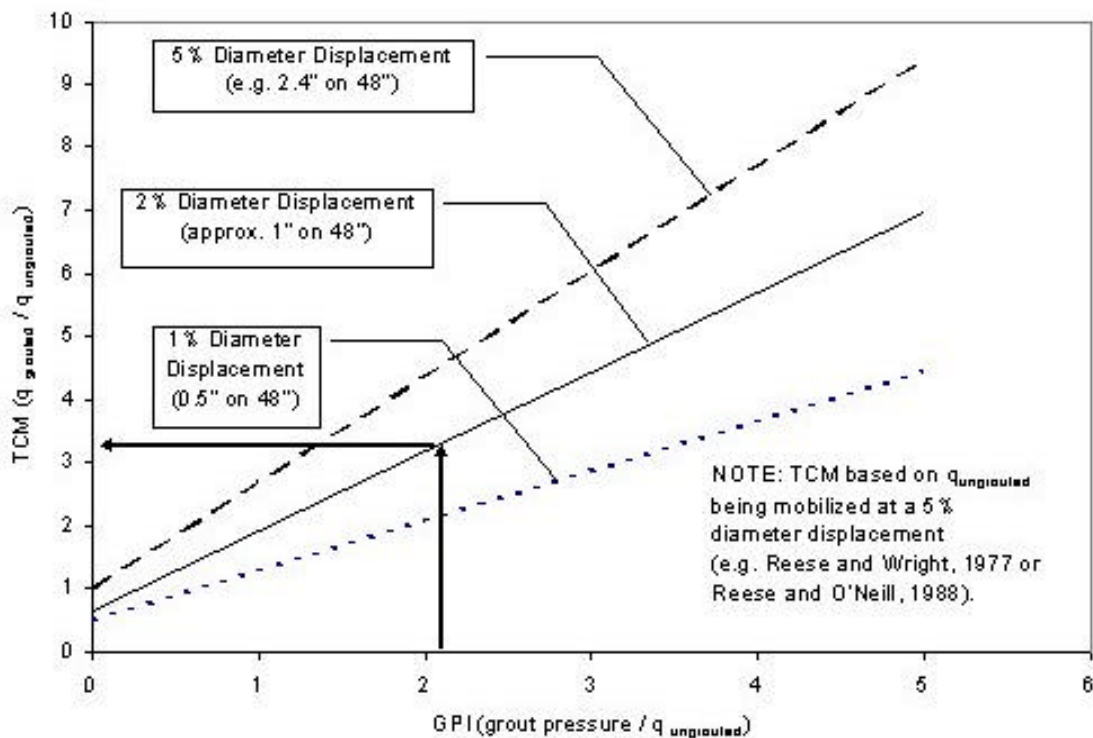


Figure 3. Design curve for shaft tips in sand (Mullins et al., 2001).

The ungrouted capacity ( $GPI = 0$ ) is represented by these curves at the y-intercept where  $TCM = 1$  for a 5% displacement (no improvement). The 1% and 2% intercepts reduce the end bearing according to the normal behavior of partially mobilized end bearing. Interestingly, the grouted end bearing capacity is strongly dependent on available side shear capacity (grout pressure) as well as the permissible displacement. However, it is relatively independent of the ungrouted end

bearing capacity when in sandy soils. As such, the end bearing in loose sand deposits can be greatly improved in both stiffness and ultimate capacity given sufficient side shear against which to develop grout pressure. An example of the ungrouted and grouted capacity analysis as described above is shown in [Figure 4](#). In dense sands and clays significant improvement in stiffness can be realized with more modest effects on ultimate capacity.

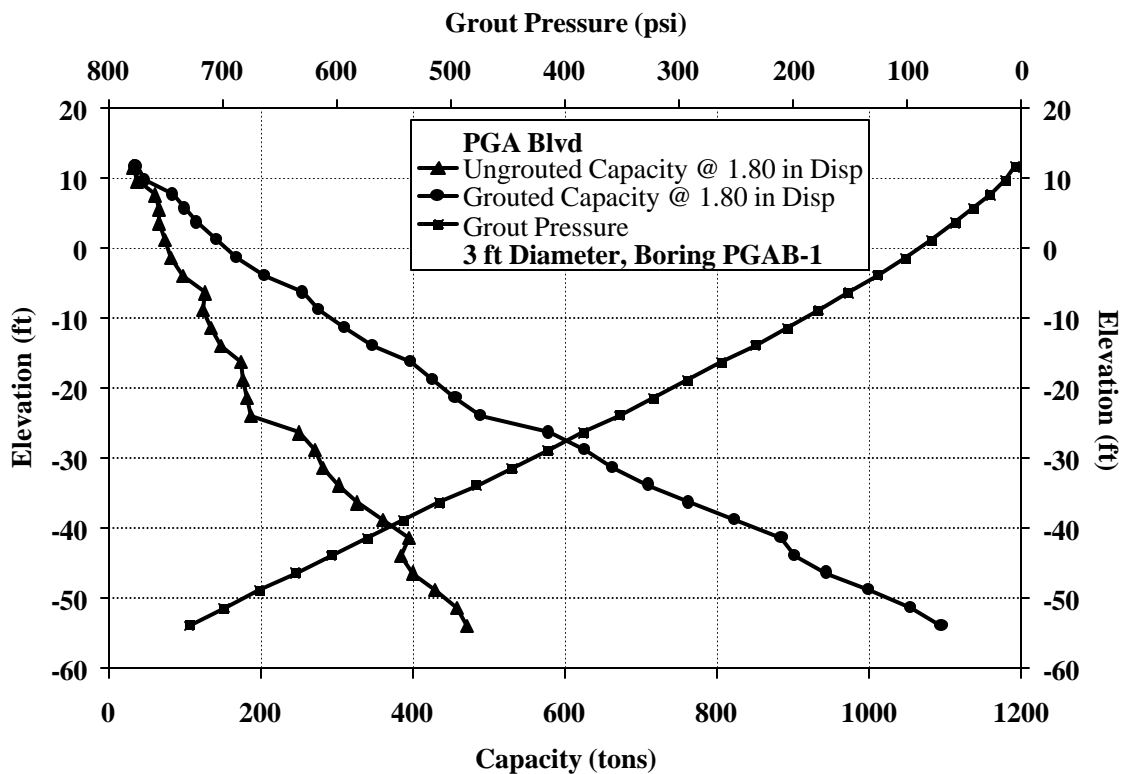


Figure 4. Site-specific design curve

### **Foundation Descriptions**

Shaft LT-1 was an out of position non-production shaft constructed in accordance with the Standard FDOT 455 Drilled Shaft Specifications. An oversized diameter temporary casing was installed to a depth of 13 feet to stabilize the upper soils. This casing which was removed immediately after pouring concrete had an outer diameter of 42 inches and a ½ inch wall thickness. The remaining shaft excavation was drilled under a bentonite slurry with a 34 inch diameter drilling tool. The total

length of LT-1 was 60.8 feet including 1 foot formed and poured above ground. Shaft schematic drawings for both test shafts are shown in Figures 1 and 2.

Shaft LT-2 was an out of position non-production shaft constructed nearly identical to LT-1 but had a Flat Jack type post grout apparatus installed in the tip. Because an oversized diameter upper temporary casing was used, the upper 13 feet of the shaft had a section diameter of 42 inches. The remaining shaft below the temporary casing depth had a diameter of 34 inches. The total length of LT-2 was 60.5 feet including 1 foot formed and poured above



Figure 5. Instrumented test shaft cages.

ground. Figure 5 shows the instrumented test shafts. Figure 6 shows the drill rig used for shaft installation.



Figure 6. Test Shaft Installation.

### **Post Grouting of Test Shaft**

During the base grouting, the bi-directionally acting grout pressure is resisted by the skin friction of the shaft. Thus, the available end bearing improvement is bounded by the shaft friction. Inherently, the grouting process then provides quantifiable data on the skin friction and a lower limit of end bearing capacity of each shaft.

A flat jack type grout delivery system was fastened to the bottom of the rebar cage prior to placing it in the excavation. A flat-jack consists of a steel plate wrapped in a rubber membrane thus providing a debonded pressurizing surface beneath the shaft tip (shown in Figure 7).

Post grouting was performed with a high pressure high efficiency mixing grout plant as shown in Figure 8. The plant included a colloidal mixing tank and an agitated holding tank. The pump was a single stage hydraulic actuated piston type capable of 1500 psi grouting pressure. The grout was Type I/II Portland cement with a water/cement ratio of 0.50.



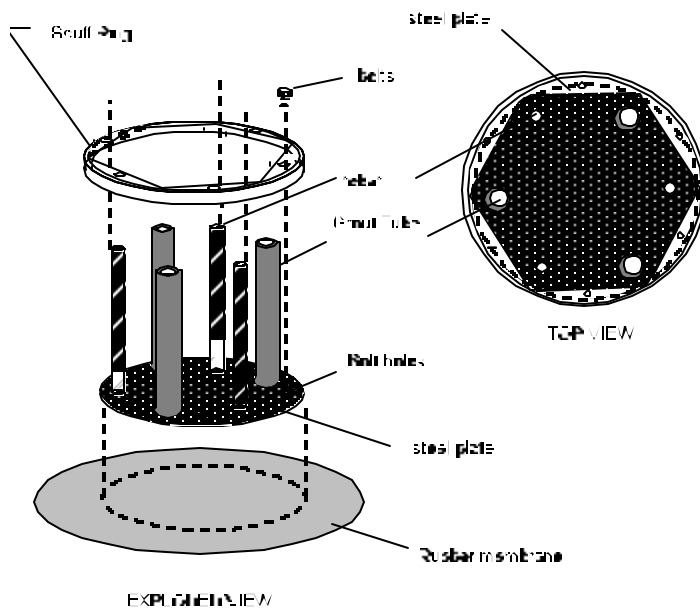


Figure 7. Flat jack grout plate.

For the grouting of the test shaft, a reference beam was set up over the shaft. Note that a reference beam was not used on any of the production shafts but rather a survey level. LVDTs and string potentiometers were mounted



Figure 8. Three part grout plant.

on the reference beam to measure the shaft top upward displacement and the upward displacement from the telltales. An electronic pressure transducer was used to measure grout pressure. The embedded strain gages directly above the shaft tip were used to calibrate the grout pressure to load applied at the shaft base. The upper levels of strain gages provided the side shear distribution. A data acquisition system was used to monitor all instrumentation with a measurement frequency of 1 sample every second. The grouting demonstration set up is shown in Figure 9. Manual measurements were also made during grouting including shaft top upward displacement with a survey level, grout pressure from a dial gage at the pump and grout volume placed. These three measurements were made on each production shaft.

The general procedure consisted of first flushing the grout lines with fresh water until clear water return was observed. Grouting began with the lines open. When grout return was observed, the return line valves were closed and pressurization started. The grout was injected at low flow rates and stopped periodically for various measurements.



Figure 9. Monitoring test shaft during grouting.



## **Load Test Program**

Axial load tests were conducted using a Statnamic device, shown in [Figure 10](#). This device is capable of applying downward load to the top of the shaft of up to 2000 tons. A mechanical catching mechanism allows efficient test set up.



Figure 10. 2000 ton Statnamic load test.

Instrumentation included sister-bar mounted strain gages at the elevations shown on [Figures 1 and 2](#). The strain gages are included to provide determination of base and side shear resistance. The sister bars included full bridge resistance type strain gages. The full bridge (four active gages) provides stable strain measurements to a precision of less than ½ microstrain and inherent temperature compensation. The resistance gages

allow high frequency data logging during the rapid load testing. As is typical with the Statnamic load test setup, load was measured with a calibrated load cell and displacement was measured with a photo-voltaic sensor triggered by a stationary laser reference. Three capacitive type accelerometers provide redundant measurement of displacement and also measure any eccentricity at the shaft head.

A high speed data acquisition system was used to monitor all instrumentation with a measurement frequency of 5000 samples per second. Traditional survey was performed before and after each test to provide a check on permanent displacements.

The derived static capacity from the Statnamic tests was performed using the Segmental Unloading Point Method (SUP) developed at the University of South Florida (Mullins, et. al., 2002). The SUP method, discretizes a foundation into segments. The number of segments and their lengths are defined by the locations of the embedded strain gages. This allows the standard Unloading Point Method (UPM) to be applied to each segment. Then the total derived static response is calculated as the sum of the derived static response from the individual segments.

## **Test Results**

During the grouting demonstration, a total volume of 6.2 cubic feet of grout was placed. The maximum upward shaft displacement was 0.687 inches. [Figure 11](#) shows the grout pressure measured at the pump and the concrete stress measured at the strain gages (based on a calculated concrete modulus of elasticity). The pressure spikes of the single stage grout pump are not as evident in the strain gage readings. This type of figure provides a relationship between

grout pressure measured at the pump and that pressure (stress) achieved at the shaft tip. Good correlation was observed during continuous grouting. However, the divergence shown is due to grout setting up in the lines during prolonged waiting periods indicated by the three unloads. Side shear stiffness is not typically thought to significantly improve through reloading as it did in this case. This information was then used to establish the Production Grouting Criteria (discussed later). The grout volume is superimposed in [Figure 12](#). In [Figure 13](#) the upward load distribution from the strain measurements are depicted in terms of upward shaft top displacement. This figure shows a mobilized upward skin friction capacity of 336 tons at the termination of grouting. In turn, resisted by a minimum of 336 tons of end bearing.

After the shaft was displaced upward during the grouting process, a downward Stanamic test was performed. The maximum static capacity for the grouted shaft, as shown in [Figure 14](#), was 1,170 tons at a top deflection

of 1.80 inches. The maximum capacity of the ungrouted shaft was 878 tons at 1.63 inches of displacement.

[Figure 15](#) shows the end bearing curves calculated from the strain measurements for the ungrouted and grouted shafts. The grouted shaft showed 484 tons of end bearing at 5% diameter displacement, whereas the ungrouted showed 133 tons.

[Figure 16](#) shows the skin friction capacity from the strain measurements for the ungrouted and grouted shafts. The maximum friction capacity of the grouted shaft was 720 tons at a displacement of 1.50 inches. In the early part of this curve, the effect of stress reversal can be seen. It is estimated that 0.2 inches of downward movement was required to redevelop any shear capacity. This only mildly affected the total capacity as shown in [Figure 14](#) up to 500 tons. The maximum side shear capacity of the ungrouted shaft was 777 tons at a displacement of 1.50 inches.

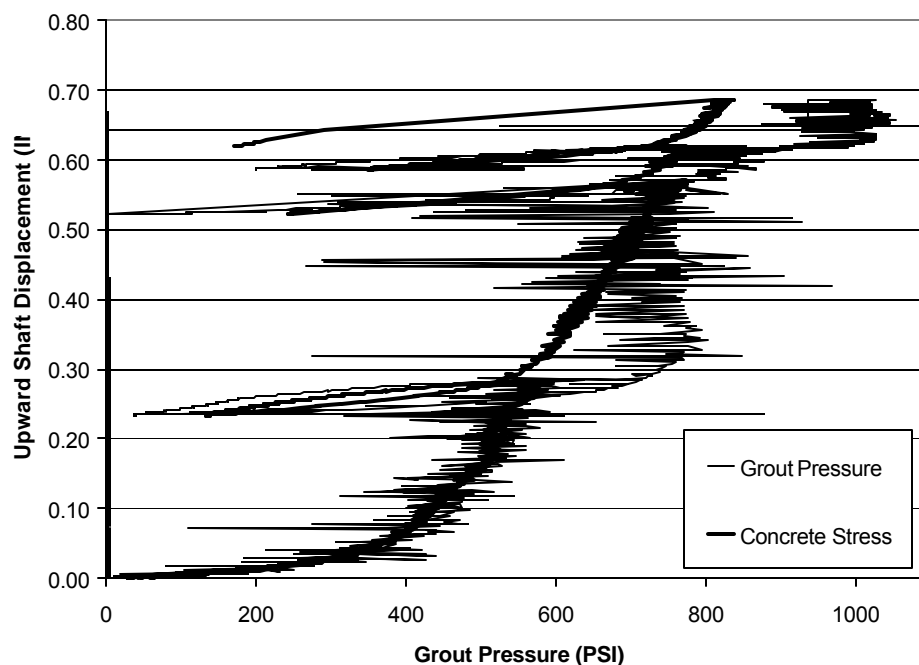


Figure 11 Grout pressure measured at pump and at strain gages in shaft toe.

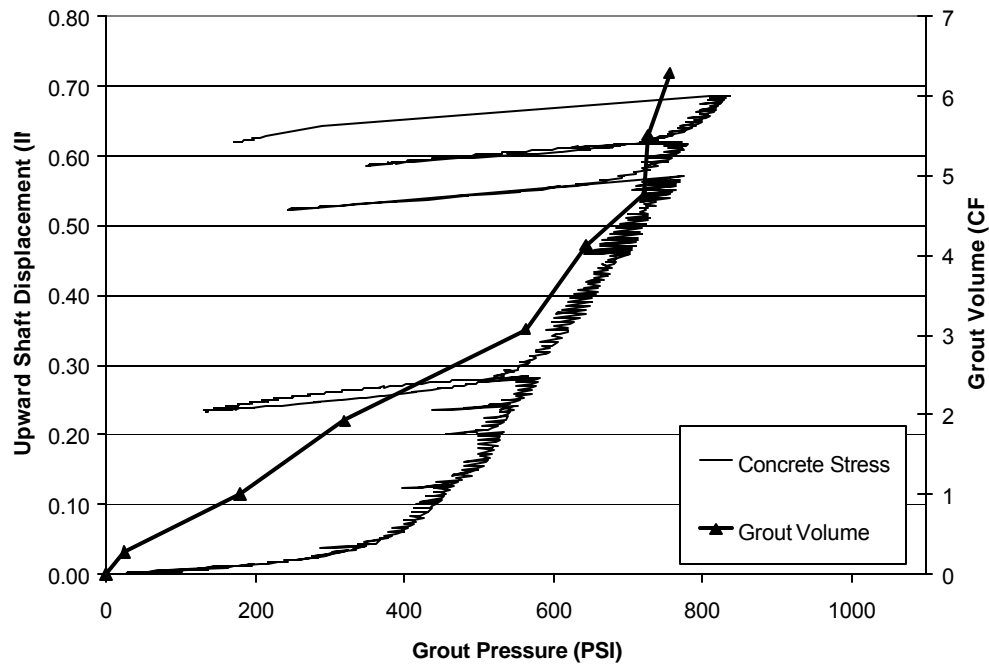


Figure 12. Grout volume and pressure measured at the shaft toe vs displacement.

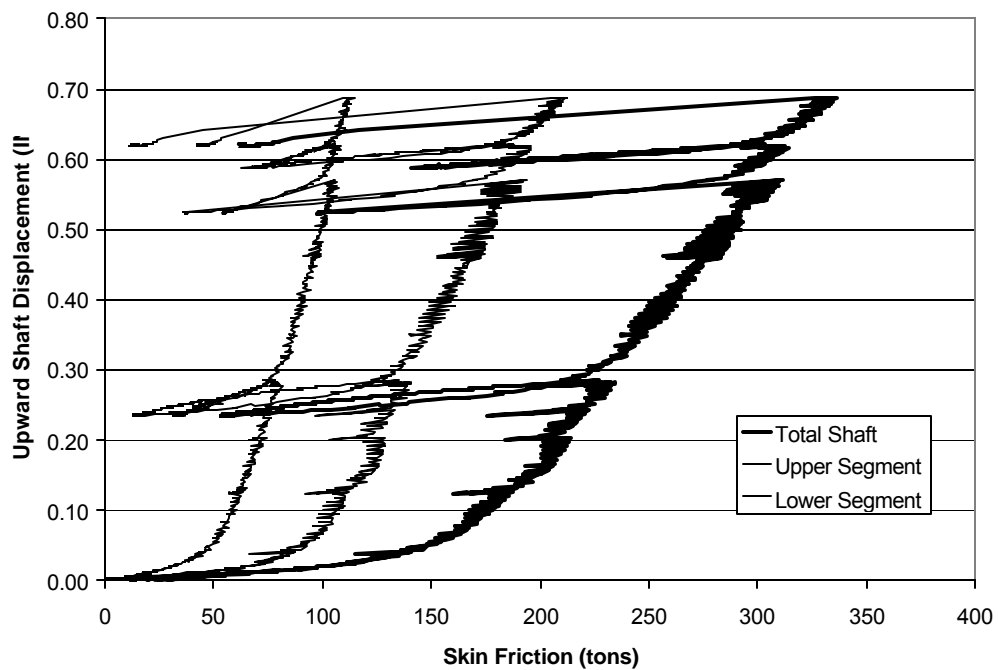


Figure 13. Upward load distribution from strain measurements.

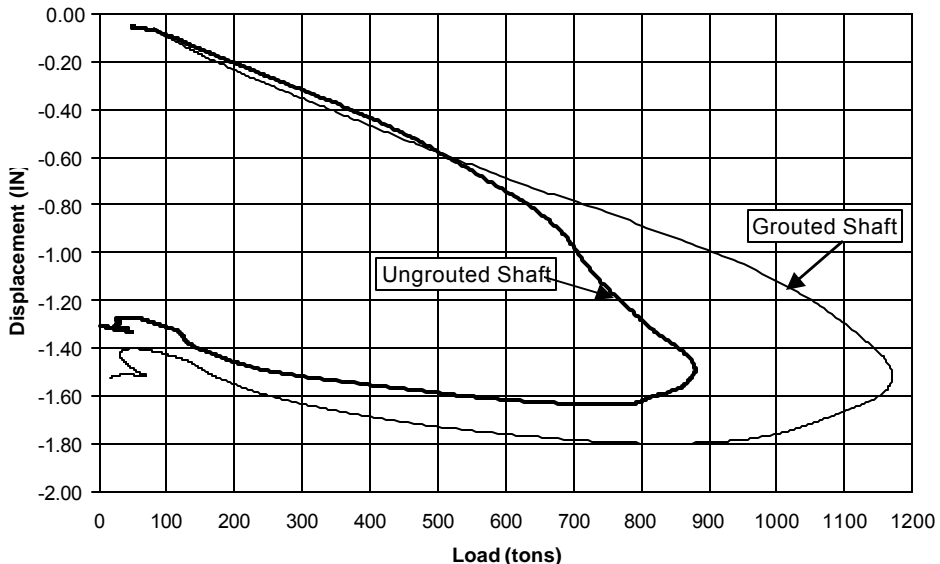


Figure 14. Downward load-displacement for grouted and un-grouted shafts.

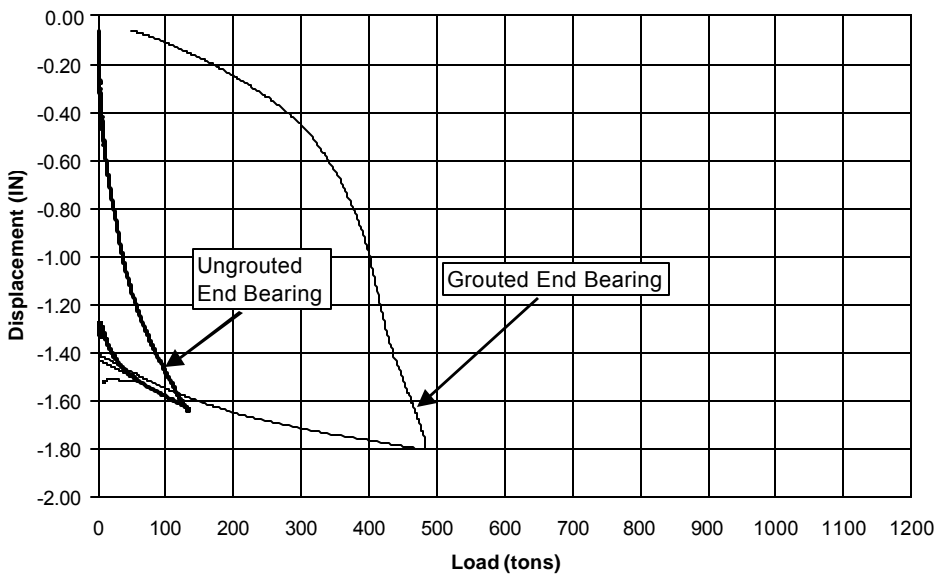


Figure 15. End bearing load-displacement for grouted and un-grouted shafts.

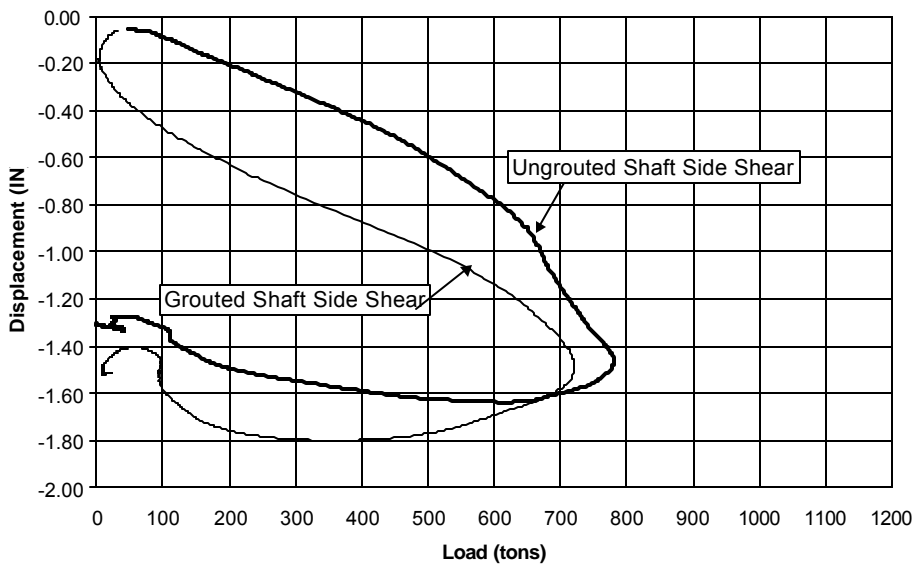


Figure 16. Friction load-displacement for grouted and un-grouted shafts

**Production Grouting**

Upon Completion of the load test program, a grouting criteria was set up for the remaining production shafts. The criteria consisted of three components. Most importantly was the grout pressure, which varied as a function of the required shaft ultimate capacity. Secondly, an upward displacement limit was set based on the T-Z response of the soil. Although not problematic for the strain hardening soils at this site, this type of limit is necessary to minimize degradation of the side shear to a lesser residual strength in more sensitive soils. Lastly, a minimum volume was set to ensure that artificial pressure was not developed due to clogged lines.

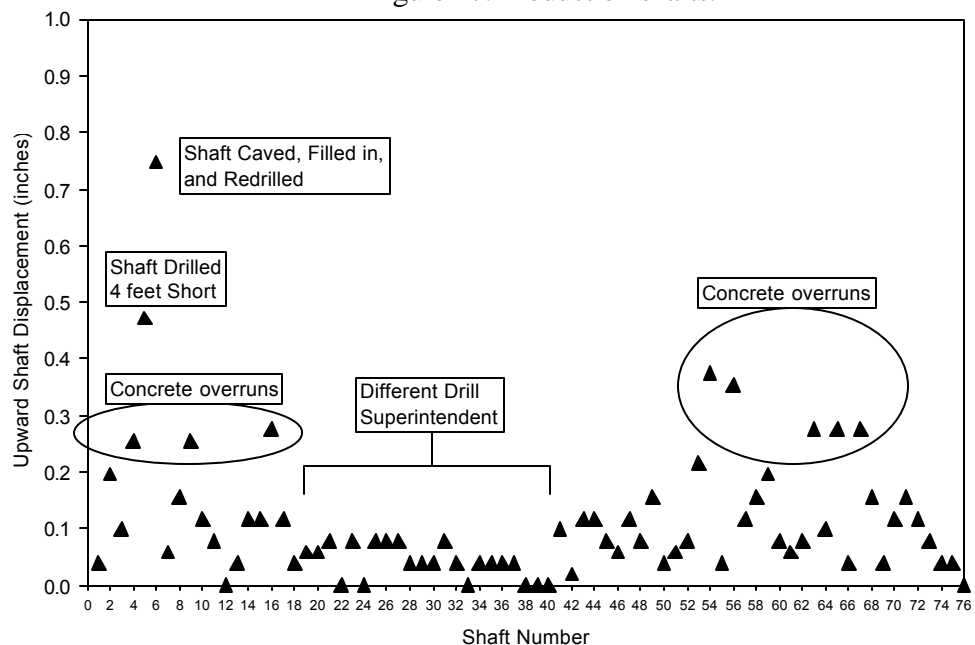
Perhaps the most significant benefit of the post grouted construction method is the quality assurance that is derived. Therein, quantify-able information on the capacity of every shaft on the project was obtained. The upward displacement versus applied pressure relationship was documented for each shaft in addition to confirming a volume of grout was indeed placed beneath each shaft. Plots of upward displacement for the first 76 production shafts (Phase I of the project) are shown in Figure 18. Interestingly, shafts that were constructed with no obvious deviations

from expected performed very well. This is evidenced by small upward displacements during the grouting (excellent side shear capacity). Those with somewhat higher upward displacements could be linked to some form of construction difficulty. Nevertheless, all shafts demonstrated full capacity by developing design grout pressures within the recommended upward displacement limit. However, it is interesting to note that concrete overruns do not equate to higher capacity in spite of the obvious increase in dimension. This can be attributed to the radial disturbance (loosening) caused by excavations that become slightly unstable and subsequently slough soil into the bored hole. Further, each shaft was constructed within State construction and inspection guidelines which obviously played into the ability of each shaft to ultimately develop the required side shear.



Figure 17. Production shafts.

Figure 18. Post-grouted drilled shaft upward displacement summary for phase 1 of the project.



## Conclusions

Post grouted drilled shafts were successfully implemented as a VECP to replace driven piles due to the enhanced end bearing they provide. The additional benefits from heightened quality assurance are unparalleled by other methods of ascertaining shaft integrity. As such, the side shear and end bearing capacity of every shaft can be assured to a level proportional to the applied grout pressure. Although there is no present method of fully deriving the entire benefit of testing every foundation element, it is envisioned that future design codes will encompass the enormous statistical reliability of knowing every shaft's capacity. In this case, a modest resistance factor of 0.75 (present code upper value) was used as the program incorporated load testing.

The outlined design method, developed by USF for FDOT, provided a good overall model for setting shaft tip elevations and predicting capacity in the shelly sand bearing strata. These predictions were additionally used to establish minimum grout pressure for each shaft that was then verified by achievable grout pressure and inspection.

The cost implications of using post grouted drilled shafts are vast. At this site, the VECP was accepted implying that the grouted shaft option was at least as cost effective as the driven pile option. Although the number of shafts grouted and site related factors may sway bid values, the actual cost of grouting a shaft is commensurate with other quality assurance testing such as Mini-SID (shaft inspection device), CSL (cross-hole sonic logging), or sonic echo tests. However, designers can directly estimate the savings associated with post grouted shafts based on shaft length reductions; as shown in [Figure 4](#) a 400 ton load requires an ungrouted shaft to be over 50 ft while a grouted shaft would be under 30 ft.

## References

AASHTO, LRFD Bridge Design Specifications, Customary U.S. Units (2<sup>nd</sup> Edition), American Association of State Highway and Transportation Officials, Washington, D.C., 1998, *w/1999 interim revisions*.

ASTM D 1586-84, "Standard Method for Penetration Test and Split-Barrel Sampling of Soils." American Society for Testing and Materials, Philadelphia, PA.

ASTM D-1143-98, (1998), "Standard Test Method For Piles Under Static Axial Compressive Load," *Annual Book of ASTM Standards*, Part 20, Philadelphia, PA.

Baker, A.C. and Broadrick, R.L., (1997), "Compaction Grouting, a twenty year update and a vision for the 21<sup>st</sup> century," *Proceedings Florida/South Florida Section Annual Meeting*, Clearwater, FL, September.

Baker, W. H., (Ed) (1982), "Proceeding of the Conference on Grouting in Geotechnical Engineering," American Society of Engineers, Denver, Colorado.

Beck, A.H., (2002), "Post Stressed Pier", United States Patent No.: 6,371,698 B1.

Birmingham, P.D., (2000). "STATNAMIC: The first ten years." *Proceedings of the Second International Statnamic Seminar*, Tokyo, Japan, October 28-30, 1998, pp.457-464.

Bolognesi, A. J. L. and Moretto, O. (1973) "Stage Grouting Preloading of Large Piles on Sand" *Proceedings of 8<sup>th</sup> ICSMFE*, Moscow.

Bruce, D.A. (1986), "Enhancing the performance of large diameter piles by grouting," Parts 1 and 2, *Ground Engineering*, May and July, respectively.



- Bruce, D. A., Nufer, P. J., and Triplett, R. E. (1995) "Enhancement of Caisson Capacity by Micro-Fine Cement Grouting - a Recent Case History" ASCE Special Publication 57, Verification of Geotechnical Grouting.
- Dapp, S., and Mullins, G., (2002). "Pressure-Grouting Drilled Shaft Tips: Full-Scale Research Investigation for Silty and Shelly Sands," *Deep Foundations 2002: An International Perspective on Theory, Design, Construction, and Performance*, ASCE Geo Institute, GSP No.116, Vol. I, pp. 335-350.
- Dunnicliff, J. (1988), "Geotechnical Instrumentation for Monitoring Field Performance," Wiley-Interscience, New York.
- Ealy, C. & Justason, M.D., (2000). "STATNAMIC and static load testing of a model pile group in sand." Proceedings of the Second International Statnamic Seminar, Tokyo, Japan, October 28-30, 1998, pp.169-177.
- Flemming, W. G. K. (1993) "The Improvement of Pile Performance by Base Grouting" Proceedings of the Institution of Civil Engineers, London.
- Garbin, E.J., (1999). "Data Interpretation for Axial Statnamic Testing and the Development of the Statnamic Analysis Workbook." Master's Thesis, University of South Florida, Tampa, Florida.
- Gouvenot, D. and Gabiax, F. D. (1975), "A new foundation technique using piles sealed by concrete under high pressure," Proceedings, *Seventh Annual Offshore Technical Conference*.
- Holtz, R. D., and Kovacs, W. D. (1981), "An Introduction to Geotechnical Engineering," Prentice Hall, New Jersey.
- Justason, M.D., Mullins, G., Robertson, D.T., & Knight, W.F., (2000). "A comparison of static and STATNAMIC load tests in sand: A case study of the Bayou Chico bridge in Pensacola, Florida." Proceedings of the Second International Statnamic Seminar, Tokyo, Japan, October 28-30, 1998, pp.43-53.
- Kahn, Y. (1984), "Innovative Cement Grouting," ACI Publication SP-83, American Concrete Institute, Detroit, Michigan.
- Lewis, C., (1999). "Analysis of Axial Statnamic Testing Using The Segmental Unloading Point Method." Master's Thesis, University of South Florida, Tampa, Florida.
- Littlejohn, G. S., Ingle, J., Dadasbilge, K. (1983) "Improvement in Base Resistance of Large Diameter Piles Founded in Silty Sand" Proceedings, *Eighth European Conference on Soil Mechanics and Foundation Engineering*, Helsinki, May.
- Lizzi, F., Viggiani, C., Vinale, F. (1983) "Some Experience with Pre-Loading Cells at the Base of Large Diameter Bored Piles" Proceedings of the 7<sup>th</sup> Asian Regional Conference on Soil Mechanics and Foundation Engineering, Haifa, Israel
- Logie, C. V. (1984) "Drilled Pier Foundation Rehabilitation Using Cement Grouting" ACI Publication SP-83, Innovative Cement Grouting.
- McClelland, M. (1996). "History of Drilled Shaft Construction by the Texas Department of Transportation," Presented to the Annual Meeting of the Transportation Research Board, Washington, DC, January, 1996.
- Middendorp, P. and Bielefeld, M.W., (1995). "Statnamic load testing and the influence of Stress phenomena." Proceedings of the First

International Statnamic Seminar, Vancouver, British Columbia, September 27-30, 1995.

Middendorp, P., Bermingham, P., & Kuiper, B., (1992). "Statnamic load testing of foundation piles." Proceedings of the Fourth International Conference on Application of Stress Wave Theory to Piles. The Hague, Holland, 1992, pp.581-588.

Mojabe, M.S., and Duffin, M. J. (1991) "Large Diameter, Rock Socket, Base Grouted Piles in Bristol" Proceedings of the 4<sup>th</sup> International Conference on Piling and Deep Foundations, Stresa, Italy, April

Mullins, G., Dapp, S., and Lai, P. (2000), "New Technological and Design Developments in Deep Foundations, Pressure-Grouting Drilled Shaft Tips in Sand," American Society of Civil Engineers, Denver, Colorado.

Mullins, G., Garbin, E.J., Lewis, C., & Ealy, C., (2000). "STATNAMIC testing: University of South Florida research." Proceedings of the Second International Statnamic Seminar, Tokyo, Japan, October 28-30, 1998, pp.117-132.

Mullins, G., Dapp, S., Frederick, E. and Wagner, R. (2001), "Pressure Grouting Drilled Shaft Tips," *Final Report* submitted to Florida Department of Transportation, April, pp. 257.

Mullins, G., Lewis, C., and Justason, M., (2002). "Advancements in Statnamic Data Regression Techniques," *Deep Foundations 2002: An International Perspective on Theory, Design, Construction, and Performance*, ASCE Geo Institute, GSP No.116, Vol II, pp. 915-930.

Mullins, G., and O'Neill, M. W., (2003). "Pressure Grouting Shaft Tips, A full Scale Load Test Program in Houston, Texas," Proceedings, *University of Houston, Post Grouted Drilled Shaft Seminar*, May.

O'Neill, M. W., and Reese, L. C. (1970). "Behavior of Axially Loaded Drilled Shafts in Beaumont Clay," *Research Report No. 89-8*, Center for Highway Research, University of Texas at Austin, December.

O'Neill, M. W. (1998). "Project 89 Revisited," Proceedings of the ADSC Drilled Shaft Foundation Symposium Held to Honor Dr. Lymon C. Reese, ADSC, Dallas, Texas, January, pp. 7 – 47.

O'Neill, M. W. (2002). Discussion of "Side Resistance in Piles and Drilled Shafts," *Journal of Geotechnical and Geoenvironmental Engineering*, Vol. 127, No. 1, pp. 3-16.

Poulos, H.G., (2000). "Pile testing - From the designer's viewpoint." Proceedings of the Second International Statnamic Seminar, Tokyo, Japan, October 28-30, 1998, pp.3-21.

Ramachandran, V. S. (1995), "Concrete Admixtures Handbook, Properties, Science, and Technology," Second Edition, Noyes Publication, Park Ridge, New Jersey.

Rixom, R., and Mailvaganam, N. (1999), "Chemical Admixtures for Concrete," Third Edition, Routledge, New York, New York.

Stoker, M.F. (1983), "The influence of post grouting on the load bearing capacity of bored piles," Proceedings, *Eighth European Conference on Soil Mechanics and Foundation Engineering*, Helsinki, May.

Touma, F. T. (1972). *The Behavior of Axially Loaded Drilled Shafts in Sand*, doctoral dissertation, Department of Civil Engineering, The University of Texas at Austin, December.

Troughton, V. M. and Platis, A.(1989) "The Effects of Changes in Effective Stress on a Base Grouted Pile in Sand" Proceedings of the International Conference on Piling and Deep Foundations, London, UK, May.

# New Design Method Gives Drilled Shafts a Boost

By Gray Mullins, Ph.D., P.E., Associate Professor, University of South Florida

Drilled shafts have seldom been cost effective in sandy soils due to the merits of driven piles in such conditions. This is in part due to the relatively poor end bearing performance of shafts caused by the large displacement required to mobilize the ultimate capacity. Recently, a new design method has revitalized a construction method that significantly improves the end bearing capacity of shafts in virtually all scenarios. This article will summarize the design and construction of drilled shafts using this technique.

## INTRODUCTION

The end bearing of drilled shafts (especially in sands) has long been discounted due to a variety of reasons such as borehole cleanliness and the like. However, even in the ideal conditions of perfectly clean excavations, the end bearing in virtually all soil types is only partially available due to the large displacements required to develop that capacity. Simply stated, the side shear and end bearing components of the drilled shafts are analogous to side-by-side spring systems with vastly different characteristics. As such, the side shear is like a series of short-stroke, high stiffness shear springs where more shaft length incorporates more of these springs. The end bearing is more like a single long-stroke, low stiffness spring that can develop enormous loads, but only at very large displacements (Fig. 1). This article addresses a construction method that significantly improves the stiffness of the end bearing “spring.”

## BACKGROUND

As far back as 1961, engineers around the world have targeted improving the end bearing of drilled shafts using post construction, high pressure grouting beneath the shaft tip (also called post grouting or base grouting). The first published citing was much later in 1973 by Bolognesi and Moretto. These early test programs showed that post-grouting large diameter shafts led to increased ultimate load capacity up to three times in both sands and clays. As a result, post-grouting techniques have become a routine construction process in many parts of the world. However, the notable absence of the practice in the United States has been attributed to no recognized design approach.

Post grouting drilled shafts targets the mechanisms intrinsic to drilled shaft construction that make the end bearing only minimally usable. These mechanisms include: (1) soil relaxation beneath the shaft tip due to

excavation, (2) debris remaining after clean out, and (3) strain incompatibility between the side shear and end bearing (mobilizing displacement mismatch). By precompressing the soil after construction, it is clear how the first two mechanisms can be mitigated. However, the third is better understood via illustration. Fig.1 shows four states of a drilled shaft from the perspective of the displacement required to distribute load. It includes: (a) the post construction state where no load is applied, (b) the fully loaded state of a conventional, ungrouted shaft, (c) the conditions just after post grouting, and (d) the loaded state of a grouted shaft.

The conventional, ungrouted shaft (b) shows little end bearing contribution based on the displacement required to obtain ultimate capacity. In this case, the ultimate side shear displacement and/or the permissible service limits are exceeded far before the end bearing can contribute. Consequently, little to no end bearing is typically considered for design. Fig. 1(c) shows two significant features: (1) the end bearing strata can be pre compressed to access more of the ultimate capacity, and (2) the upward movement of the shaft during grouting may lock in negative skin friction that when loaded will increase the permissible downward movement (up to 2% diam.) without exceeding the ultimate side shear displacement. This helps to transfer load to the toe while balancing the displacement at ultimate side shear and end bearing. However, from a “nuts and bolts” perspective, the upward movement should be monitored and limited based on a pilot grouting program at the beginning of construction. Interestingly, Fig. 1(d) depicts the full structural load applied to the foundation while mobilizing significant end bearing and minimizing overall displacement. By engaging a large fraction of the ultimate end bearing, shafts can either be shortened for a given load or can provide higher capacity for a given length.

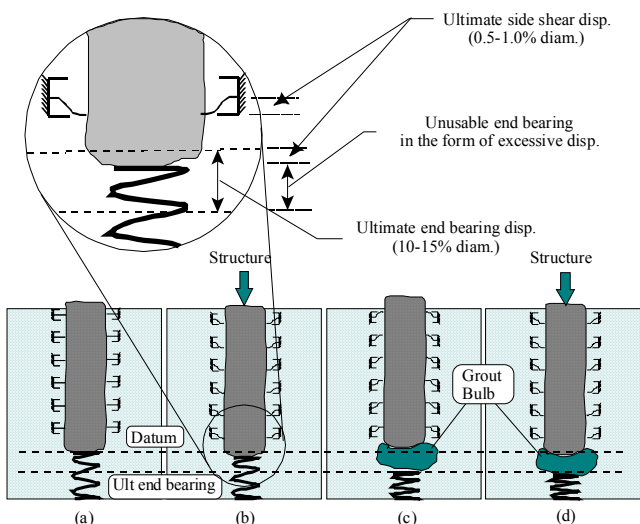


**Fig. 1 Spring analogy of the loading states of drilled shafts (grouted and ungrouted)**

## DESIGN AND CONSTRUCTION PROCEDURE

In 1998, the Florida Department of Transportation (FDOT) requested the University of South Florida to submit a proposal to investigate the use of post grouted drilled shafts. At the conclusion of the first phase of research (in 2001), a viable design and construction procedure was made available to consultants that incorporated these findings. Within the two short years that followed, four bridge projects using post grouted shafts have been undertaken with over twenty general contractors having given it serious consideration. A brief overview of both the design and construction procedures are presented below.

**Design.** The design of post-grouted drilled shaft tips can be easily summarized in the following seven steps:

- (1) Determine the ungrouted end bearing capacity in units of stress.
- (2) Determine the permissible displacement in units of percent shaft diameter ( $\text{disp}/\text{diam} * 100\%$ ).
- (3) Evaluate the ultimate side shear resistance for the desired shaft length in units of force.
- (4) Establish a maximum grout pressure that can be resisted by the side shear in units of stress (*Step 3 / Tip Area*).
- (5) Calculate the Grout Pressure Index, *GPI*, defined as the ratio of grout pressure to the ungrouted end bearing capacity (*Step 4 / Step 1*).
- (6) Using design curves from Fig. 2, determine the Tip Capacity Multiplier, *TCM*, using the *GPI* calculated in *Step 5*.

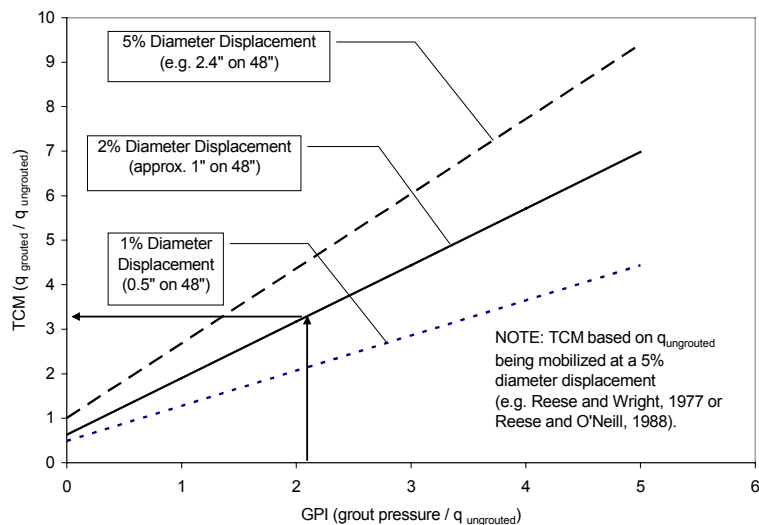


**Fig. 2 Correlations used in Step 6 to establish TCM (Mullins. et al., 2001)**

- (7) Calculate the grouted end bearing capacity (ultimate) by multiplying the *TCM* by the ungrouted end bearing (*TCM \* Step 1*).

The design procedure affords the designer the ability to select the “usable ultimate” capacity as a function of permissible settlement (Fig. 2; larger displacement yields higher *TCM*). Therein, unless using very small diameter shafts (or high % diameter), reserve capacity will exist should more settlement occur.

**Construction.** The construction of grouted drilled shafts varies only slightly from conventional shafts: (1) during cage fabrication a grout distribution cell is installed at the base of cage with grout tubes that extend to the top of shaft, Fig. 3, (2) no spacer feet are required below the cell but rather the cell rests on the bottom of the excavation, and (3) after the shaft concrete has cured to sufficient strength, neat cement grout is pumped to the base of the shaft until the design pressure is achieved, Fig. 4.



**Fig. 3 Installation of grout distribution cell (Courtesy of Applied Foundation Testing, Inc.)**

The grout pressure can be locked in using sacrificial in-line valves, but it is not necessary.



**Fig. 4. Top of shaft receiving grout**

The first shaft grouted on site is usually used to set the grouting/construction criteria for proper shaft design and installation. Aside from verifying a designated grout pressure, a pilot program will provide criteria including the maximum permissible uplift and the minimum acceptable grout volume. These are set on the basis of field data such as that shown in Fig. 5. The maximum uplift criterion should minimize the adverse effects of over-stressing the side shear (in this case 0.1 inches). The minimum grout volume criterion is intended to assure that a reasonable volume is pumped to the base of the shaft as the design pressure is achieved. This prevents a grout line blockage from artificially satisfying the design grout pressure criterion. In the case shown in Fig. 5, a minimum of 2 cubic feet would suffice. This type of information can also

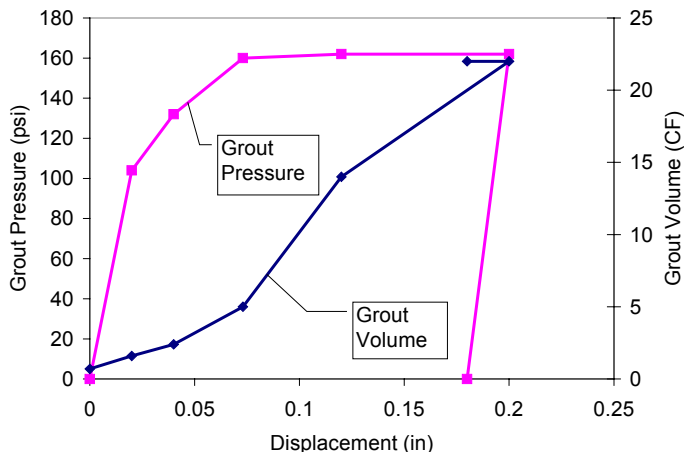


**Fig. 5 Typical field measurements for QA/QC**

be used to estimate the grout volume that the contractor may expect to use per shaft (approximately 10 CF at 0.1 inches).

**Quality Assurance.** Post grouting drilled shafts provides a level of quality assurance that is unparalleled by other shaft integrity methodologies. The information in Fig. 5 can and should be collected for every shaft installed to provide verification of shaft performance. Therein, the side shear and end bearing resistance of the shaft are proven for every shaft up to the level of the applied grout pressure. At a minimum the shaft capacity is therefore capable of resisting 2 times the product of the grout pressure and the end bearing area. This lower limit of the shaft capacity is often more than the service loads thus providing 100% certainty of competence.

**CASE STUDIES OF END BEARING ENHANCEMENT**

Within the two years that this end bearing enhancement procedure has been available, several bridge projects have incorporated post grouting into the drilled shaft design. These include: (1) Royal Park Bridge, Palm Beach, FL; (2) PGA Blvd, West Palm Beach, FL; (3) Natchez Trace Parkway, Natchez, MS; and (4) FM507 Bridge, in Willacy County, TX. Additionally, the post grouted shafts have been tested in sands, silts, and clayey soils with shafts 2', 2.5', 3', 3.5', 4', and 6' in diameter. Figs. 6 - 8 show the results of load tests on both grouted and ungrouted shafts with diameters of 2', 3', and 4', respectively.

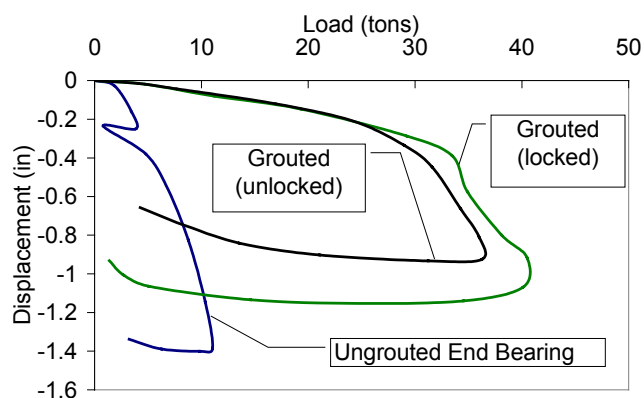


**Fig. 6 End bearing capacity in silty sands (2' diam., Dapp, 2002)**



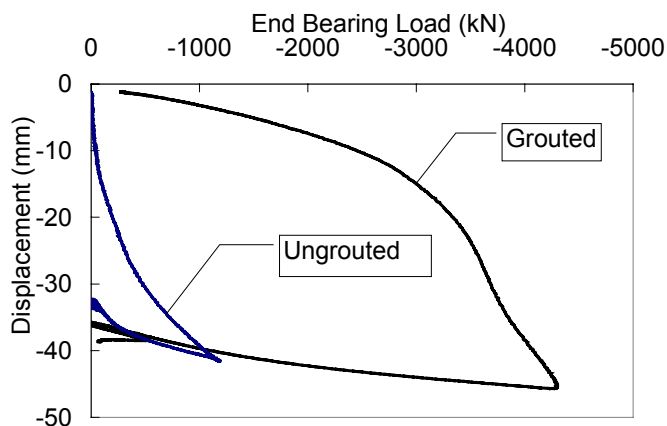


**Fig. 7 End bearing capacity in shelly sands (3' diam., Mullins, et al., 2003)**

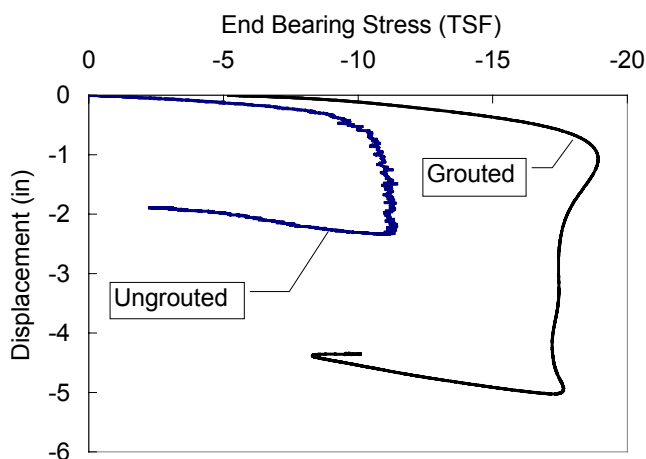


**Fig. 8 End bearing capacity in clay (4' diam., Mullins and O'Neill, 2003)**

Figs. 6 and 7 (in sandy soils) show significant improvement in both ultimate capacity and stiffness. Fig. 6 shows only a moderate difference between locking in the grout pressure and not. In clayey soils (Fig. 8) increased stiffness may be expected with more modest improvement in ultimate end bearing.

## CONCLUSIONS

Although pressure grouting drilled shaft tips has been proven successful worldwide, its use in the U.S. has only recently evolved largely due to the availability of a new rational design approach. Case studies have confirmed the findings of the research that led to this method while also accenting the merits of a tremendous quality assurance mechanism.

## ACKNOWLEDGMENTS

The author would like to gratefully thank FDOT, Applied Foundation Testing, Inc., A. H. Beck Foundation, Inc., Coastal Caisson Corp., Earth Tech, Inc., and Treviicos South for their support of this research.

## GENERAL REFERENCES

Bolognesi, A. J. L. and Moretto, O. (1973) "Stage Grouting Preloading of Large Piles on Sand" Proceedings of 8<sup>th</sup> ICSMFE, Moscow.

Dapp, S. (2002). "Pressure Grouting of Drilled Shaft Tips in Sand," Doctoral Dissertation, University of South Florida, Tampa, pp. 358.

Dapp, S., and Mullins, G., (2002). "Pressure-Grouting Drilled Shaft Tips: Full-Scale Research Investigation for Silty and Shelly Sands," *Deep Foundations 2002: An International Perspective on Theory, Design, Construction, and Performance*, ASCE Geo Institute, GSP No.116, Vol. I, pp. 335-350.

Mullins, G., Dapp, S., and Lai, P. (2000), "New Technological and Design Developments in Deep Foundations, Pressure-Grouting Drilled Shaft Tips in Sand," American Society of Civil Engineers, Denver, Colorado.

Mullins, G. and O'Neill, M. (2003). "Pressure Grouting Drilled Shaft Tips: A Full-Scale Load Test Program," Final Report submitted to Texas Department of Transportation for A.H. Beck, Inc. May, pp.299.

Mullins, G., Muchard, M., and Khouri, B (2003). "Post Grouted Drilled Shafts: A Case History of the PGA Boulevard Bridge Project," Proceedings of the 28<sup>th</sup> Annual Conference on Deep Foundations, Deep Foundations Institute, October 22 - 24.



**Durability of E-Glass/Vinylester Reinforcement in Alkaline Solution.** Paper by Rajan Sen, Gray Mullins, and Tom Salem.

**Discussion by Aftab A. Mufti, Maria Onofrei, Baidar Bakht, and Vaibhav Banthia**

The authors should be congratulated for bringing into focus the question of the durability of glass fiber-reinforced polymer (GFRP) reinforcement in concrete. The results they have presented are startling. Bars in a strong alkaline solution and stressed to 25% of their failure loads failed in 15 to 25 days, and most of the bars stressed to 15% of the failure load failed in 42 to 173 days. If GFRP had similar poor durability in concrete, then many GFRP-reinforced structures built several years ago should have suffered visible damage by now.

The authors have clearly stated that the simulated pore solution does not replicate the conditions in hardened concrete. This disclaimer, however, should not absolve them of the responsibility of allaying the fears that their paper is likely to cause in the engineering community. We invite the authors to respond to the questions raised in the following.

1. As a part of a short-term study on the durability of GFRP tendons in prestressed concrete, we have built six specimens with the E-glass/vinylester tendons stressed to 55% of the fifth percentile tensile strength of their individual ultimate strength. Three of these specimens are already 365 days old and the tendons are holding their strains. Why haven't these specimens failed? Could it be that the oxygen ions necessary for the chemical reaction are more freely available in the alkaline solution than in hardened concrete? It is noted that we are in the process of testing the concrete straps to check both prestress losses and any reduction in the strength of the GFRP bars.<sup>12</sup>

2. The cantilever overhangs,<sup>13</sup> traffic barriers,<sup>14-16</sup> and sidewalks<sup>14,17</sup> of a number of deck slabs of bridges are reinforced with E-glass/vinylester bars; the overhangs, in particular, are subjected to axial stresses induced by live load transverse negative moments in the slab. The oldest deck slab thus reinforced was constructed in 1996<sup>14</sup> and shows no sign of distress that would result from the lack of durability of GFRP in concrete. Could it be that the cumulative effect of transitional live loads is less damaging than that caused by permanent stress?

3. Is it possible that the durability of GFRP is very poor in the alkaline solution, as compared with its durability in hardened concrete, in which an alkaline fluid is not available in abundance to permeate through the matrix? The concrete pore solution (SPS) used by the authors contains  $K^+$ ,  $Na^+$ , and  $Ca^{2+}$  but lacks a series of other ions such as  $Mg^{2+}$ ,  $Al^{3+}$ ,  $Si^{4+}$ , and  $SO_4^{2-}$ . Wouldn't the synergetic effect of all elements present in the fluid be affected by the absence of some?

4. The use of SPS with higher than 12.5 pH (buffered by the solid  $Ca(OH)_2$ ) is debatable. A high value of pH in concrete is expected to exist for only a short period of time. Shouldn't the pH in the pore fluid decrease due to carbonation and/or water penetration?

## REFERENCES

- Banthia, V., "Transverse Confinement of Steel Free Deck Slabs by Prestressed Concrete Straps," 2002, Master's thesis being written. University of Manitoba, Winnipeg, Manitoba, Canada.
- Black, C. J.; Tsai, P. C.; and Ventura, C. E., "Ambient Vibration Measurements of the University Drive/Crowchild Trail Bridge in Calgary, Alberta," *The University of British Columbia Earthquake Engineering Research Report EQ 97-005*, 1997.
- Benmokrane, B.; Chekired, M.; and Nicole, J. F., "Evaluation of the Joffre Concrete Bridge Decks Reinforced with FRP Rebars and Grids," *Progress Technical Report*, 1998, 50 pp.
- Aly, A.; Bakht, B.; and Schaefer, J., "Design and Construction of a Steel-Free Deck Slab in Ontario," *Proceedings, Annual Conference—Canadian Society for Civil Engineering*, V. 6, 1997, also *Structures—Composite Materials, Structural Systems, Telecommunication Towers*, Proceedings of the 1997 Annual Conference of the Canadian Society for Civil Engineering, Part 6, May 27-30, 1997, Sherbrooke, Canada, pp. 81-90.
- Newhook, J. P., and Mufti, A. A., "Reinforcing Steel-Free Concrete Deck Slab for the Salmon River Bridge," *Concrete International*, V. 18, No. 6, June 1996, pp. 30-34.
- Rizkalla, S.; Shehata, E.; Abdelrahman, A.; and Tadros, G., "New Generation (Design and Construction of Highway Bridge)," *Concrete International*, V. 20, No. 6, June 1998, pp. 35-38.

## AUTHORS' CLOSURE

The authors thank the discussers for their comments and especially for including information on laboratory tests and field studies they conducted. The authors offer the following remarks to address their concerns:

The durability of all fiber-reinforced polymers (FRP) including glass fiber-reinforced polymer (GFRP) is strongly dependent on how they are manufactured. Because of the known vulnerability of glass fibers in alkaline environments,<sup>1</sup> the protection afforded by the resin is critically important. The authors tested GFRP bars manufactured before there was a general awareness of this weakness; as such, no special measures were taken to protect the glass fibers. Their results, startling as they are to the discussers, are quite similar to those reported by other researchers in Japan and the U.S. for first generation reinforcement bars summarized in Malar's review paper.<sup>18</sup> In newer-generation GFRP products, special attention was paid to manufacturing to ensure adequate protection of the glass fibers. The discussers' laboratory data is consistent with results reported for tests on such second generation GFRP bars.<sup>19,20</sup> Clearly, results from exposure to alkaline solutions may represent a more severe environment for reasons stated by the discussers, that is, greater ion mobility. Until long-term studies are conducted to find the relationship between degradation observed in laboratory specimens and field specimens, however, no reliable prediction on long-term performance may be made.

Researchers have used a wide range of pH values to evaluate the durability of GFRP bars. The choice of pH selected by the authors was influenced by the measured pH value of

pore solutions extracted from cement paste. It was found that during the first few weeks of curing, the pH of the pore solution is in the 13 to 14<sup>21,22</sup> range primarily due to the presence of sodium and potassium hydroxides. As the time scale for the authors' tests ranged from 4 to 39 weeks, the SPS used in the authors' tests only contained calcium, potassium, and sodium salts to provide a similar high pH environment. In the testing, the pH value was kept higher for the shorter duration (4-week) tests than the longer duration (39-week) tests to reflect the gradual reduction in pH over time.

The discussers have suggested that the maximum pH be limited to 12.5 (that for saturated calcium hydroxide). In the authors' opinion, this value is permissible only for special situations, that is, where no soluble potassium and sodium hydroxides are present in the pore solution or where they are leached out because of continuous exposure to water. The time frame over which this can occur, however, cannot be predicted with any degree of certainty. Moreover, reductions in pH due to carbonation, that is, the reaction of carbon dioxide and sulfur dioxide with alkaline constituents of cement paste, are a very slow process. In their review paper, Page and Treadway<sup>23</sup> stated that the rate of carbonation is less than 1 mm/year. Thus, for a 25 mm cover for a concrete slab, more than 25 years will be needed before the pH drops appreciably at the level of the GFRP reinforcement.

Given the vulnerability of glass fibers in alkalis, the authors believe it is imperative to evaluate their durability under high pH as was done in this study. The more difficult task is to correlate the results of such accelerated tests in SPS to the performance of the same material in demonstration structures. This may be far from simple because synergistic effects not accounted for in laboratory tests may come into play. For example, mismatch in the thermal expansion coefficients between glass fibers and the resin may lead to cracking under diurnal and seasonal temperature unless the matrix has sufficient ductility. Resin cracking can expose

bare fibers to concrete's alkaline environment. In view of this, complete reliance on the resin to provide the necessary protection may not be prudent especially because recent data<sup>24</sup> indicates that exposure of glass fibers even to very low pH levels (around 9) can result in significant tensile capacity reduction over time. Alternative E-Glass fibers that are more alkali resistant, that is, new boron-free glass,<sup>25</sup> should be used in conjunction with the new resin formulations to provide added protection. Such a belt and suspender approach provides the redundancy needed to make glass more suitable for structural applications.

## REFERENCES

18. Malar, L. J., "Durability of Composites in Reinforced Concrete," *CDCC '98, Durability of Fiber-Reinforced Polymer (FRP) Composites for Construction*, B. Benmokrane and H. Rahman, eds., University of Sherbrooke, Sherbrooke, Quebec, Canada, 1998, pp. 361-372.
19. Clarke, J. L., and Sheard, P., "Designing Durable FRP-Reinforced Concrete Structures," *CDCC '98, Durability of Fiber-Reinforced Polymer (FRP) Composites for Construction*, B. Benmokrane and H. Rahman, eds., University of Sherbrooke, Sherbrooke, Quebec, Canada, 1998, pp. 13-24.
20. Alsayed, S. H.; Alhozaimy, A.; Al-Salloum, Y. A.; and Almusallam, T., "Durability of the New Generation of GFRP Rebars under Severe Environments," *CDCC '02, Durability of Fiber-Reinforced Polymer (FCP) Composites for Construction*, B. Benmokrane and E. El-Salakawy, eds., University of Sherbrooke, Sherbrooke, Quebec, Canada, 2002, pp. 651-663.
21. Andersson, K.; Allard, B.; Bengtsson, M.; and Magnusson, B., "Chemical Composition of Cement Pore Solution," *Cement and Concrete Research*, V. 19, 1989, pp. 327-332.
22. Barneyback, R. S., and Diamond, S., "Expression and Analysis of Pore Fluids from Hardened Cement Pastes and Mortars," *Cement and Concrete Research*, V. 11, 1981, pp. 279-285.
23. Page, C. L., and Treadway, K. W. J., "Aspects of the Electrochemistry of Steel in Concrete," *Nature*, V. 297, May 1982, pp. 109-114.
24. Svecova, D.; Rizkalla, S. H.; Vogel, H.; and Jawara, A., "Durability of GFRP Bars in Low-Heat High Performance Concrete," *CCC '02, Durability of Fiber Reinforced Polymer (FRP) Composites for Construction*, B. Benmokrane and E. El-Salakawy, eds., University of Sherbrooke, Sherbrooke, Quebec, Canada, 2002, pp. 75-86.
25. Greenwood, M., "Pultruded GFRP Composite Durability: A Key Value," *Composite 2001*, Composites Fabricators Association, Tampa, Fla., Oct. 3-6, 2001, TE304.

## Full-Scale Testing of Seal Slab / Pile Interface Bond

by G. Mullins, R. Sen, R. Sosa, and M. A. Issa

### Synopsis:

The construction of submerged or partially submerged pile caps often requires the use of a cast-in-place unreinforced slab referred to as a seal slab. This slab is cast underwater around piling and inside sheet pile walls to form the bottom of a cofferdam and withstand upward hydrostatic pressure. As the seal slab is only used for a relatively short period of time during placement of the reinforcing steel and concreting, its design has received little attention in refinement tending toward conservatism. Therein, the magnitude of available bond strength between the seal slab and piling to resist the uplift pressure has been poorly quantified and largely underutilized. This paper presents experimental results from 32 full-scale tests conducted to define the interface bond between cast-in-place concrete seal slabs and piling (sixteen 356 mm square prestressed concrete piles and sixteen 356 mm deep steel H-piles). Three different concrete placement environments—dry, fresh water, and bentonite slurry—were evaluated using the dry environment (where no fluid had to be displaced by the concrete) as the control. The effective seal slab thickness was varied between  $0.5d$  and  $2d$ , where  $d$  was either the width or depth of the pile section. Both “soil-caked” and normal, clean pile surfaces were investigated. Additionally, four of the sixteen concrete piles were cast with embedded gages located at the top, middle and bottom of the interface region to define the shear distribution.

The study showed that: (1) significant bond stresses developed even for the worst placement environment, and (2) the entire embedded surface area should not be used in calculating the pile-to-seal slab bond capacity. Current design values in the Florida Department of Transportation specifications reflect the findings of this study.

Keywords: bond stress; bond values; pile cap; pile walls; seal slab

Gray Mullins is an Associate Professor in Civil and Environmental Engineering at the University of South Florida, Tampa, FL

Rajan Sen is the Samuel and Julia Flom Professor in Civil and Environmental Engineering at the University of South Florida, Tampa, FL. He is a member of ACI 215, 440 and 444.

Ruben Sosa holds BSCE and MSCE degrees from the University of South Florida. He is presently with GeoSyntec Consultants, Tampa, FL.

Moussa Issa is currently the Chief Structural Engineer, T Y Lin International, Chicago, IL. He is a member of ACI E 801, 340 and 444.

## INTRODUCTION

Construction of a submerged or partially submerged pile cap typically requires the use of a cofferdam to provide a dry working environment in which reinforcing steel and structural concrete can be placed. When the bottom of pile cap elevation requires excavation of existing soil, interlocking sheet piles are driven to form the walls of the cofferdam, define the limits of excavation, and stabilize the surrounding submerged soils. The target depth of excavation must consider both the bottom of the pile cap as well as the thickness of a cast-in-place seal slab. The seal slab is an unreinforced concrete slab intended to prevent or seriously impede the intrusion of water, form the bottom of the cap, and provide dry access for the pile cap construction. Placement of the seal slab is typically carried out by displacing water (or natural slurry) using a tremie pipe or a concrete pump hose. Regardless of equipment type, the pipe or hose must be placed near the bottom of the excavation to commence concreting and must remain beneath the level of the newly placed fluid concrete during the entire process to prevent segregation of the concrete mix components (cement and coarse or fine aggregates). As the entire process is conducted underwater, a certain degree of construction expertise and quality control is required to minimize variations in the top of seal slab elevation. Low regions can lead to slab failures, whereas high regions require chipping the excess before pile cap construction can continue. A series of tremie pipes should be used to limit the flow of concrete in the horizontal direction and to prevent the build-up of excessive laitance<sup>1</sup>.

As the seal slab is only used for a relatively short period of time during reinforcing steel and concrete placement, its design has received little attention in

refinement tending toward conservatism. The slab thickness is selected so that its weight balances the hydrostatic uplift forces. Thus, a 5 m unbalanced head would require a 2 m thick seal slab since concrete density is approximately two and a half times that of water. This methodology neglects the bond resistance that develops at the interfaces between the seal slab and foundation elements such as driven piles or drilled shafts.

After seal slab placement, the Florida Department of Transportation (FDOT)<sup>2</sup> requires the seal slab to cure for at least 72 hours before the standing water (or slurry) inside the cofferdam can be pumped out. At that time, the seal slab experiences full uplift pressure due to the imbalance in hydrostatic pressure inside and outside of the cofferdam. To incorporate the contribution of the pile to seal slab bond, information on the interface shear strength corresponding to the 72-hour concrete strength is necessary. Prior to this study, no published data was available even though the earliest work on interface shear between two concrete surfaces was reported as far back as 1914<sup>3</sup>.

Specifications that provide interface shear values are necessarily conservative to reflect the lack of experimental data in this area. Shear values from the AASHTO<sup>4</sup> and FDOT<sup>5</sup> specifications are listed in Table 1. Therein AASHTO provides a blanket value for all pile types (concrete, steel, or timber) of 69 kPa (10 psi); the FDOT 1998 Florida Design Guidelines allows the interface bond between the seal slab and piles to be appreciably larger for concrete, 276 kPa (40 psi) but is more restrictive for steel piles, 36 kPa (10 psi).

In January 1998, the FDOT contracted the University of South Florida to commence in a two-year research program to investigate this problem. The goal of the study was to evaluate the bond using full-scale tests and provide recommended pile/seal slab bond values. To aide in the design of the full-scale test program, a pilot study using 36 - 1/3rd scale pullout tests and numerical modeling were initially carried out to evaluate critical parameters. Following the pilot study evaluations, 32 full-scale tests were conducted to assess the interface seal slab/pile bond characteristics for prestressed concrete and steel piles. Although the pilot study is briefly discussed, this paper focuses on the results of the full scale tests and the associated design recommendations. Results of the pilot studies for the 1/3 scale concrete and steel H-piles are available in separate papers<sup>6, 7</sup>. The complete experimental results as well as the comparative finite element modeling may be found elsewhere<sup>8,9</sup>.

#### RESEARCH SIGNIFICANCE

As this study provides the first experimental data from full-scale tests to evaluate the seal slab/pile interface bond, the results have readily been incorporated

into the latest FDOT design specifications<sup>10</sup>. Therein, the allowable bond stresses are greater permitting thinner seal slabs and providing significant savings in construction costs.

## OBJECTIVES

The overall goal of the study was to recommend bond values for the interface between seal slabs and piles that could be directly used in the FDOT design specifications. These values were to be based on full-scale tests on specimens prepared in accordance with current FDOT specifications for commonly encountered conditions. Variables examined were the pile embedment depth, pile surface, pile material (steel or concrete), and the type of fluid displaced by the concrete.

## EXPERIMENTAL PROGRAM

A seal slab is subject to uplift pressures that are resisted partly by dead weight and partly by shear resistance that develops at the pile and seal slab interfaces (Fig. 1a). The same loading can be simulated by applying a tensile load to the pile and a uniformly distributed compressive load to the seal slab (Fig 1b). Hence, pullout tests could be used to simulate the bond stresses imposed on the seal slab/pile interface by upward hydrostatic pressure. Further, preliminary numerical modeling showed that a 2.4 cm thick distribution pad at the base of a pullout device could minimize stress concentrations imposed by the test apparatus at the level of the interface bond under investigation.

The pullout device required to extract the piles from a seal slab had to meet multiple requirements of geometry, capacity, economy and portability. An adaptable design was also required to accommodate the differing connections for the steel and concrete pile specimens. Additionally, it needed to integrate measuring devices capable of monitoring the applied load and the resulting displacement.

A key parameter in the design of the test equipment was capacity. An upper limit could be determined on the basis of the ultimate tensile capacity of the pile. This depended on the pile size, material strength and the effective prestress (concrete only). The greater the capacity, the larger and heavier the equipment making testing that much more difficult (and expensive).

Uncertainties associated with bond strength predictions were addressed with a comprehensive pilot study using small-sized piles. A scale model study was carried out to develop an efficient testing method and to identify critical parameters for the subsequent full-scale program. Brief details from the 1/3 scale pilot study and the results used to formulate the full-scale test program are presented.



## 1/3-SCALE PILOT STUDY

The intent of the pilot study was to provide realistic bond values for the design of a full-scale pullout device, identify trends associated with fluid types, and streamline the seal slab placement procedures. This program simulated three different seal slab fluid types: (1) salt water (2) fresh water and (3) mineral drilling fluid. Results were compared against a fourth environment where no fluid was displaced by the concrete (control specimens). One-third scale specimens were selected since this allowed standard 45 cm square prestressed piles to be exactly modeled using smaller commercially available prestressing strands.<sup>11</sup> Scaling the steel piles was not as difficult due to the abundance of available steel sections, but the same 1/3 scale was selected for convenience. Additionally, a soil-caked specimen was introduced each of the four concrete placement environments. Fig. 2 shows the four simulated cofferdams in which the seal concrete was cast around the pullout pile specimens.

Based on results of preliminary trials leading into the pilot study, the maximum interface bond between the two concrete surfaces was estimated to be 1.7 MPa. This value was used to determine the maximum embedment depth that would not cause tension failure of a prestressed concrete pile. The steel piles were hypothesized to exhibit lower bond strengths and tension failure would not be problematic. As a result, three different concrete embedment depths ( $d$ ,  $1.5d$  and  $2d$ ) and two different steel embedment depths ( $1.5d$  and  $2d$ ) were investigated. Depending on whether the specimen was concrete or steel,  $d$  was the width or depth of the pile section, respectively. For each embedment depth, two concrete specimens and one steel specimen were tested. Therefore, the test matrix included 24 concrete piles (4 conditions  $\times$  3 embedment depths  $\times$  2 specimens) and 8 steel piles (4 conditions  $\times$  2 embedment depths). Including an additional four soil-caked concrete specimens which were embedded  $2d$  (based on an assumed poorer bond), a total of 36, 1/3rd scale pullout tests were conducted.

The prestressed concrete piles (1.22 m long, 15 cm wide) were fabricated at a commercial prestressing facility. During fabrication, 3.2 cm threaded Dywidag bars were embedded centroidally in the specimens to provide a convenient attachment for pulling the specimens. Further, as the actual bond strength was uncertain, the Dywidag bar provided a larger tensile capacity than the combined capacity of the prestressing strands. The steel pile specimens were fabricated using W 6  $\times$  15, A36 structural steel sections. Each steel pile was 0.91 m (36 inches) in length. On each pile, a line of three, 23.8 mm (15/16 inch) diameter holes were drilled into each flange to facilitate the twelve, 22 mm (7/8 inch) bolts provided to form the connection with the pullout apparatus. Rather than casting different seal slab thicknesses to simulate varied embedment depths, the piles were coated with a bituminous debonding material in certain regions leaving a predetermined bond length. Complete fabrication details may be found in the final report<sup>8</sup>.

At the conclusion of the pullout tests, each of the seal slabs were dismantled to examine the modes of bond failure between the piles and the cast-in-place slabs. Figs. 3 and 4 show the typical failure modes for the concrete and steel piles, respectively. In most cases (excluding bentonite or soil caked), the concrete pile exhibited tensile cracking as well as slippage. Each of the steel piles specimens simply slipped at the steel/concrete interface leaving an H-pile shaped void in its previous location. All specimens were pulled out at least 25 mm to assess residual capacity. In general, concrete piles maintained a near constant residual capacity while steel piles exhibited a reduction in pullout resistance after the initial debond<sup>6,7</sup>.

The pilot study test results are graphically presented in Figs. 5 and 6 for the concrete and steel piles, respectively. Fig. 5 shows the average of two concrete specimens per condition with a single data point, whereas the data points in Fig. 6 indicate only a single test specimen. A trend of increased pullout capacity with greater bonded surface was noted for all pile types up to a limiting embedment depth of 1.5d. Likewise, the failure bond stress remained relatively uniform up to the same limiting embedment; beyond which a noticeable decrease was observed. With the exception of the bentonite specimens, the bond strength was relatively uniform regardless of the placement environment. The trends associated with the bentonite specimens are shown with dashed lines; the trends for all other conditions are grouped and denoted with the solid lines (Figs. 5 and 6).

The following observations were incorporated into the full-scale testing programs.

1. Significantly higher than expected bond stresses were developed; the highest value obtained for the prestressed concrete piles was 4.4 MPa (salt water/1.5d) and the lowest 0.2 MPa soil-caked control (not shown); for the steel piles, 3.66 MPa (salt water/1.5d) was the highest observed bond strength with the lowest being 1.27 MPa (bentonite/2d). The highest values were from the salt water environment, followed closely by controls and fresh water.
2. Results for salt water and fresh water cofferdam conditions did not differ significantly.
3. Embedment depths above 1.5d led to lower average values. This suggests that the bond stress distribution is non-uniform and instrumentation should be incorporated to delineate the load transfer.
4. The soil-caked condition did not affect interface bond except in the case of controls and bentonite slurry. For the salt water or fresh water condition, the soil caking was washed off by the water prior to the installation of the seal slab.
5. For the larger embedment depths, the prestressed concrete specimens

cracked (see Fig. 3). This suggested that depths in excess of 1.5d may not be feasible for the full-scale tests.

### FULL SCALE STUDY

The results of the pilot study were used to develop the program for full-scale tests. In general the procedure outlined in the pilot study was duplicated on a larger scale with the exception of these primary changes: (1) the salt water environment was discontinued (2) a limited number of concrete piles were instrumented with internal strain gages to allow the evaluation of the bond stress distribution with respect to embedment depth and (3) the soil-caked surface condition was restricted to the bentonite slurry environment where it had shown the most effect. In view of the very high bond stresses that were obtained, the depth of embedment was limited to 1.5d with the exception of bentonite where the maximum depth was increased to 2d. In addition, embedment depths of 0.5d were investigated for the control and fresh water placement conditions where the interface bond was expected to be very high.

Both the concrete and steel piles had the same test matrix consisting of three different placement conditions (control, fresh water and bentonite), two different embedment depths (d and 1.5d or 2d) and two specimens per test, a total of 24 (12 concrete and 12 steel) specimens were required. Eight additional specimens (4 concrete and 4 steel) were tested - one each for embedment depth of 0.5d (for the control and fresh water condition) and two for investigating the effect of soil caking for the bentonite slurry for an embedment depth of 1d. Thus, the controls and the fresh water condition each had five specimens with six specimens in the bentonite slurry for each pile material type.

#### Specimen Fabrication

The bond stresses obtained from the pilot study ranged from a low of 1.1 MPa (concrete/bentonite/2d) to a high of 4.3 MPa (concrete/control/1.5d). In light of the high bond values observed for concrete piles, 36 cm wide square prestressed piles were selected for the full-scale tests in lieu of the envisaged 45 cm section after which the 1/3 scale specimens were modeled. The length of each specimen was limited to 1.5 m. The ends of the strands protruding from the non-pulling end were clinched (flattened) to provide increased anchorage. This would not be required in practice where the pile lengths are much greater and extend beyond the upper surface of the seal slab. The depth (35 cm) and length of the steel piles was kept the same as that for the prestressed piles. As a result, 1.5 m long W14 x 90 sections made from A36 steel were used. Holes for 28.6 mm (1-1/8 inch) diameter bolts were drilled in each flange to connect the pile specimens to the tension assembly frame (Fig. 7).

A central threaded bar, like that used in the smaller concrete piles, was not a viable option to provide the pullout attachment for the larger piles. Further, the

tensile capacity and its axial stiffness needed to be incorporated into the experimental pullout capacity as well as serving as an upper limit design value. However, to ensure that the piles would have a somewhat greater capacity, larger 15mm strands were used instead of the standard 12.5 mm strands though they were stressed to provide the same effective prestress. The eight 15 mm strands gave an ultimate pulling capacity of  $260 \times 8 = 2.1$  MN which exceeded the expected pullout load of the pile. This provided a margin of safety against sudden, dangerous tensile failure of the strands.

A total of eighteen 36 cm specimens were cast at the same commercial prestressing yard as the smaller 15 cm piles. The spacing of the specimens inside the prestressing bed was adjusted so that each specimen had a 0.6 m length of strand extending from the pulling end that served as a connection point to the pull-out frame.

Additionally, four prestress concrete specimens were instrumented with embedded sister bar-type strain gages to allow the distribution of bond stresses to be assessed. With this type of gage, an instrumented steel bar is positioned along side a strand at designated depths. This type of strain gage is widely used in foundation testing to determine the load shedding associated with the side shear resistance of surrounding soil strata. This is not unlike the side shear anticipated from the seal slab with the exception that the full tensile capacity of the pile would be developed over a much shorter length.

Fig. 7 shows the layout of the three sister-bar strain gages which consist of a resistive foil strain gage bonded to a short length of 13 mm rebar. The gages were located at the bottom, middle and top of the bonded length of  $1d$  (three specimens) or  $2d$  (1 specimen) (Fig. 7). The bottom most sister bar was necessarily bent (forming a 28 cm hook) to assure the detection region of the gage would align with the bottom of the bond region without extending beyond the end of the pile. This aided in providing sufficient development as the gages require the 13mm rebar to have sufficient development length to properly register strain in the bar. The surface of the steel piles was thought to be too sensitive to strain gage type inclusions (surface bonded gages and the associated protective coatings) to instrument for load transfer measurements. Therefore, no attempt was made to similarly instrument the steel sections. Complete fabrication details may be found in the final report<sup>8</sup>.

#### Cofferdam Preparation

Three cofferdams were constructed for the three conditions deemed suitable for full scale testing (control, fresh water, and bentonite). The dimensions of the cofferdams were determined by the number of piles and a  $3d$  pile spacing (1.07 m) as in the pilot study. Thus, two of the cofferdams - fresh water and control - were identical in size, but the bentonite slurry-filled cofferdam was larger as it had more specimens.

The cofferdams were constructed using rented steel reinforced plywood box forms made by Symons Corporation, Des Plaines, IL. The forms were connected to form each cofferdam using wedge pins provided by the manufacturer. They were also externally braced using wooden stakes and internally braced with a wooden template that maintained the pile positions. Additionally, each cofferdam was lined with 0.15 mm plastic sheeting. This made the forms watertight, preventing the loss of any construction fluid (water or bentonite slurry).

Following the construction of the cofferdam, the specimens were accurately positioned on plywood pads to prevent damage to the plastic lining. Additionally, a polystyrene seal was placed between each concrete pile specimen and the wooden pad to prevent possible bonding between the cast-in-place seal concrete and the bottom of the pile. The specimens were vertically supported by a wooden framework that was secured to the Symons forms (Fig. 8).

As in the pilot study, differing lengths (0.5d, 1d, 1.5d and 2d) of the pile surface were bonded or debonded. Debonding was achieved in the identical manner. The bonded concrete surfaces were left in their natural state excepting for the two specimens that were tested in a soil-caked condition. For this case, a more plastic clay soil, similar to that used by artists was used because it bonded better than the kaolinite paste tested in the pilot study.

The debonded length extended from the boundary of the bonded region to approximately 15 cm above the intended elevation of the finished surface of the seal slab. This included an additional 36 cm depth determined from finite element analysis to ensure uniform distribution of compressive loads to the seal slab (Fig. 2b).

#### Slurry Preparation and Seal Slab Placement

Two slurry types were prepared and placed in their respective simulated cofferdams: fresh water and bentonite. The water was obtained from a nearby potable water source. The bentonite slurry was made by mixing dry, high yield bentonite and fresh water. The mixing was accomplished through the use of a shear pump. Enough bentonite clay was added to achieve slurry properties similar to FDOT specifications. The final density achieved was 10.2 kN/m<sup>3</sup> with a viscosity of 40 seconds (Marsh Cone Method) and a pH of 8.

Seal concrete was placed using a concrete pump truck. The concrete was pumped through a 15 cm diameter hose. It was placed from the bottom upwards keeping the hose tip below the rising level of concrete. This procedure is identical to the tremie method commonly used in construction practice. Fig. 9 shows the filling and completion of the bentonite slurry filled simulated cofferdam.

#### Testing Apparatus

Similar considerations of capacity, economy and portability dictated the

design of the pullout frame. This design incorporated a double-acting, 3 MN hydraulic jack, a 69 MPa hydraulic pump system, and could accommodate connections to both concrete and steel pile types. Additionally, it provided sufficient clearance for a 4MN loadcell as well as means to record pile displacement.

As with the pilot test, the reaction frame consisted of a tension and compression assembly. The tension assembly was connected directly to the pile using prestressing chucks and supported by the hydraulic jack and load cell. A stiffened beam was integrated directly into the compression assembly which applied compressive loads to the seal slab. Fully assembled the device weighed 16 kN and was placed over each specimen with a straight mast industrial forklift. Fig. 10 shows a diagram of the load frame constituents and the basic assembly. Additional information on the design and fabrication may be found elsewhere.<sup>8</sup>

### Test Setup

The test setup was similar to the pilot study and involved placement of a grout layer, assembly and connection of the hydraulic testing apparatus, attachment of the data acquisition system, and application of loading until failure. Given the requirement that testing be completed quickly following the 72 hour curing period, appropriate adjustments were made to expedite testing.

### Leveling Grout Pad

Since concrete vibration is not used in seal slab construction due to possible aggregate segregation in the submerged environment, various degrees of surface roughness developed depending on the pour condition. The bentonite pour condition had the greatest degree of unevenness; the control had the least. The uneven surfaces were leveled using a thin layer of high strength grout that was placed directly over the seal slab. The grout was poured and finished two days after the placement of the CIP seal slab. Since the debonded portion of each pile specimen extended well above the CIP slab, there were no difficulties with possible bonding of the grout to the piles.

### Frame Assembly

Although much heavier than the pilot study device, the full-scale pullout device was easier to use in that it could be left fully assembled between tests. This reduced the number of heavy lifts and expedited testing.

As the entire frame was lowered over the test specimen, the exposed prestressing strands were threaded through the holes in the base of the tension assembly. Standard prestressing chucks which incorporate wedge-type grips were secured on each strand. A 76 mm gap was maintained between the tension assembly and the top of the pile to permit removal of the prestressing chucks after testing.



With the chucks in place, the frame was centered and the concrete pile tested. Figs. 11a and 11b show the pullout device connection to both the prestressed concrete and steel piles, respectively.

#### Data Acquisition

A Megadac data acquisition system by the Optim Electronics Corporation was used for collecting and recording the test data generated by the pull-out testing. Along with the Megadac, a load cell and two electronic displacement gages (LVDTs) were used to monitor each pile specimen as it was tested. The load cell had a capacity of 4 MN. The electronic displacement gages had a 50 mm range. Additionally, strains were monitored in selected piles that had been cast with embedded resistance-type sister bar strain gages (Fig. 7). For the concrete specimens, one LVDT was magnetically attached to the bottom of the tension assembly and positioned to register displacement with respect to an external reference beam. The other LVDT recorded relative displacement between the tension assembly and the top of the pile specimen. This accounted for any possible slippage of the prestressing chucks.

#### Test Procedure

Testing commenced as soon as the load frame assembly was positioned, the pile connection completed, displacement transducers attached, and the data acquisition system was recording. The tensile load was increased slowly using a manually operated toggle switch which intermittently engaged the power to the hydraulic pump. The load rate of 4-5 kN/sec ( $1\pm 0.1$  kips/sec) was maintained throughout all tests for consistency and to reduce any possible dynamic stiffening of the system. Each specimen was displaced upward at least 25 mm to ensure that the bond interface had sheared and to determine the residual capacity.

### RESULTS

A summary of the test results is presented in Table 2. This provides information from all 32 tests and contains details of the compressive strength, failure load, and the computed average bond stress. Inspection of Table 2 shows that the concrete bond stresses were quite high ranging between 4.5 MPa for 0.5d embedment in the controls to the lowest value of 1.1 MPa for one of the soil-caked bentonite specimens. The corresponding stresses for the steel specimens were not as high with the largest shear value being 1.63 MPa (control/0.5d) and the lowest 0.50 MPa (bentonite/2d). Trends observed in the pilot tests were repeated: the average bond stresses decreased with increased embedment depth. For example, the average bond stress reduces from 2.7 MPa to 2.0 MPa for concrete specimens in fresh water embedded 1.0d and 1.5d, respectively.

Variations in concrete strength over the duration of the test may also be noted. The lowest compressive strength was for the bentonite series ( $f'_c = 23$  MPa) and the highest for the controls (32 MPa). This was in part due to increase in strength over the seven day period it took to complete the testing. This effect was addressed by normalizing the measured shear values with respect to lowest observed seal concrete strength.

A typical load vs slip variation plot is shown for both the prestressed concrete and steel piles in Figs. 12 and 13. Each graph shows typical results for a bond length (simulated seal slab thickness) of 0.5d, 1d, and 1.5d. The plots show continuous displacement with increasing load; initially somewhat linear and then nonlinear. Concrete piles with embedment lengths greater than 0.5d mobilized enough bond resistance to crack the pile ( $\approx 1100$ kN) regardless of the fluid displaced during construction. Further, both the concrete and steel piles showed noticeable increased pullout resistance with increase in embedment up to 1d. Embedment lengths of 1.5d consistently provided marginal increases in ultimate pullout strength; in some cases exhibiting less capacity. In general the prestressed concrete piles continued to gain capacity with displacement, whereas the steel piles showed marked reductions in capacity after initial slip. Therein, seal slabs using steel piles could experience sudden catastrophic failure whereas, those constructed around prestressed concrete piles would demonstrate more visible signs of distress.

The trend of decreasing load carrying efficiency with increased bond area was further evidenced by the reduced average bond strength with deeper embedment. Figs. 14 and 15 show typical average stress measurements throughout the pullout tests for 0.5d, 1d, and 1.5d embedment. Therein, the developed bond strength (peak measured stress) was consistently higher for shorter embedment lengths.

Although the bentonite placement condition adversely affected the bond strength, the magnitude of this reduction was generally rather insignificant (with the exception of soil caked conditions). Fig. 16 graphically depicts the bond strength as a function of embedment for both the prestressed concrete and steel piles. The average of all conditions is plotted as a line whereas each data point represents the average of two specimens at that embedment. The trend shows significant reductions in bond with higher embedment for concrete to concrete interfaces but more modest reductions for the steel to concrete interfaces.

### Bond Stress Distribution

The bond stress distribution within the bonded region of the pile was evaluated using embedded strain gages in four of the prestressed concrete specimens. Within this region gages were located at the top, middle, and bottom (Fig 7 and 17). Fig. 17 shows the axial strain measured at three points along the bond interface during testing of one instrumented pile specimen. The strain gage locations define the boundaries for two bonded layers (upper and lower) separated by the middle

gage. When the strain is converted to axial load, the difference between the top and middle gage indicates the load carried by the upper layer. Likewise, the difference between the middle and bottom gage indicates the load carried by the lower bonded layer. The top gage reading linearly relates to the loadcell as there is no alternate load path between them; the gage at the bottom of the bond area registers near zero strains as no additional bond resistance can be developed below that level due intentional bituminous debonding. The non-linear response of the middle gage indicates the upper layer bond failing and transferring load to the lower layer.

The load distribution as measured by the strain gages indicates that the full bond length contributed to its capacity initially. However, as the peak bond capacity is exceeded the associated slippage transfers a larger proportion to lower layers. As such the entire pile/seal slab interface does not mobilize full capacity simultaneously. This can also be deduced by inspecting the load versus displacement response (Figs. 12 and 13) where the initial stiffness was almost identical for the different embedment lengths.

#### Pilot versus Full Scale

Comparing the results from both the 1/3 scale and full scale tests several observations can be noted: (1) seal slab concrete strengths varied for all tests both scaled and full size, (2) the smaller specimens exhibited higher bond strengths for similar non dimensional embedment depths (with respect to  $d$ ), (3) placement environment had little effect on capacity (excluding soil caked), and (4) bond strengths overall decreased as embedment was increased. In an attempt to isolate these effects, the results from both test programs were normalized with respect to concrete shear strength and all data for a given embedment was averaged regardless of environment and plotted versus actual embedment (in cm). Fig. 18 shows a strong correlation between bond strength and embedment where the concrete/concrete bond strength approaches an upper limit related to the seal concrete shear strength<sup>12</sup> as embedment decreases. The steel/concrete bond strength is considerably less as the mode of failure involves loss of adhesion and dimensional reduction due to Poisson's ratio effects. The trend for the concrete/concrete interface is quite strong. The small scale steel piles were noted to have well developed surface rust prior to construction, whereas the full scale specimens were still coated with a smooth mill scale. This would account for the slightly higher values for those specimens and could affect field performance.

### CONCLUSIONS

This study presents results from an experimental study that investigated the interface bond stress that developed between seal concrete and prestressed piles as well as steel H-piles in cofferdams. Two series of tests were conducted. In the first series, one-third scale models were fabricated and tested. Three variables were investigated (1) displacement of fresh water, salt water and bentonite slurry, (2)

regular and soil caked pile surface conditions, and (3) embedment depths expressed as multiples of the pile width ( $d$ ). In the second series, full-scale tests were conducted for only two conditions (fresh water and bentonite slurry) and varied embedment depths. In all cases, results were compared against controls where no fluid was displaced. Seal slabs were cast using concrete delivered by ready-mix plants that conformed to Class III concrete in current FDOT specifications<sup>2</sup>. The concrete was allowed to cure for 72 hours prior to testing as permitted by existing specifications. The following conclusions may be drawn:

1. Bond stresses determined experimentally were significantly higher than set in current specifications. Values obtained from the full-scale tests varied from 4.5 MPa for prestressed concrete control specimens embedded 18 cm to 0.5 MPa for steel piles embedded 86 cm in the bentonite slurry displaced cofferdam.
2. Bond stress values from the full-scale tests were generally smaller than those for the model tests leading to the strong correlation shown in Fig. 18.
3. Strain data indicated that regardless of the embedment depth, loads were transferred to the pile up to a limiting depth. For the specimens tested, this depth was the same as the size of the pile ( $d$ ).
4. The bond between seal slab and piles caked with mud was largely unaffected when fresh water or salt water was displaced. These effects became important in concrete controls or when bentonite slurry was displaced. The smoother steel surface showed no discernible effect.
5. Prestressed piles and seal slabs developed cracks before the full pullout load was developed. Thus, structural failure of the seal slab and/or the piles themselves should be considered in any rational design process and may well control such designs.

## RECOMMENDATIONS

The buoyancy force generated at the base of a seal slab can be withstood using a combination of both the bond strength formed between the pile and the cast-in-place concrete as well as its self weight. While using this bond to offset a portion of the upward load, the tensile force developed in the pile cannot be permitted to exceed its cracking strength. The bond capacity developed by an individual pile may be determined using the allowable bond stress,  $f_b$ , listed in Table 3.

This stress ( $f_b$ ) may be assumed to act uniformly over an effective surface area,  $A_c$  (in  $m^2$ ) given by:

$$\begin{aligned} A_c &= pD & \text{if } D < 0.045 \text{ m, or} \\ A_c &= 0.045p & \text{if } D > 0.045 \text{ m} \end{aligned}$$

given the pile perimeter  $p$  (in m), and the seal slab thickness  $D$  (in m). This limits the effective bond length to 45 cm of the pile. Hence, the uplift capacity of the pile ( $P$ ) is the lesser of the allowable bond capacity ( $P_u = f_b A_c$ ), or the pile tensile strength (e.g. AASHTO (5.6.3.4.1-1)). Fig. 19 shows three predictions of seal slab to concrete pile bond capacity (in MN) for two different sized piles: 356 mm (14") and 610 mm (24"). The solid line represents the capacity as predicted by the trends shown in Fig. 18. The dashed line represents the design capacity recommended by the authors above. The dotted line represents the design capacity as stated by FDOT specifications.

In the latest Florida Design Guidelines<sup>9</sup>, allowable bond stress values have been increased from 40 psi (0.3 MPa) to 250 psi (1.7 MPa) based on the results of this study. However, this assumes the bond capacity can be developed over the entire bond area simultaneously. When using this value, the authors recommend limiting the usable bond area to a depth of 60 cm else it becomes un-conservative (Fig.19). A similar evaluation can be made for steel piles.

#### ACKNOWLEDGMENTS

This investigation was carried out with the financial support of the Florida Department of Transportation. The authors especially acknowledge the contribution of Hayward Baker Inc. Tampa, FL in the full-scale testing as well as Rudy. The opinions, findings and conclusions expressed in this publication are those of the writers and not necessarily those of the Florida Department of Transportation.

#### REFERENCES

1. Tomlinson, M.J., Foundation Design and Construction, 5<sup>th</sup> ed., Longman Scientific and Technical, Essex, England, 1986.
2. FDOT, Standard Specifications for Road and Bridge Construction, Florida Department of Transportation, State Specifications Office, Tallahassee, FL, 1999.
3. Johnson, L.J. and Nichols, J.R., "Shearing Strength of Construction Joints in Stems of Reinforced Concrete T-Beams as Shown by Tests," Transactions of the American Society of Civil Engineers, Dec., 1914, pp. 1499-1522.

4. Standard Specifications for Highway Bridges 13<sup>th</sup> Edition, American Association of State Highway and Transportation Officials, Washington, D.C., 1983, Section 4.3.4.6.2.
5. Structural Design Guidelines, Florida Department of Transportation, Section 4.18, Topic No: 625-020-150c, July, Tallahassee, FL, 1998, pp. 4-12.
6. Mullins, G., Sosa, R., Sen, R. and Issa, M., "Seal Slab/Steel Pile Interface Bond from Full-Scale Tests," ACI Structural Journal, Vol 99, No.6, Nov.- Dec., 2002, pp.757-763.
7. Mullins, G., Sosa, R., Sen, R. and Issa, M., "Seal Slab Prestressed Pile Interface Bond from Full-Scale Tests." ACI Structural Journal, Vol 98, No.5, Sept.- Oct., 2001, pp.743-751.
8. Mullins, G., Sosa, R. and Sen, R., "Seal Slab/Pile Interface Bond", *Final Report* submitted to Florida Department of Transportation, June, 2000, pp. 151.
9. Wu, Z, "Studies of Bond of Cast-in-Place Concrete to Other Surfaces." MSCE Thesis, Department of Civil and Environmental Engineering, University of South Florida, Tampa, FL, August, 1999.
10. Structural Design Guidelines, Florida Department of Transportation, Table 5.3, Tallahassee, FL, 2000.
11. Fischer, J., Mullins, G. and Sen, R., "Strength of Repaired Piles. " *Final Report* submitted to Florida Department of Transportation, March, 2000.
12. Mindess, S, and Young, J., Concrete, Prentice-Hall, Inc., Englewood, NJ, 1981, p. 401.

Table 1. Design Values Prior to Study.

Pile Material	Seal Slab / Pile Bond Values	
	AASHTO	FDOT
Concrete	69 kPa (10 psi)	276 kPa (40 psi)
Steel	69 kPa (10 psi)	34 kPa (5 psi)
Timber	69 kPa (10 psi)	no listing



Table 2. Summary of Full Scale Test Results.

Type	Specimen	$f_c$ (MPa)	Bond Length	Pullout Load (kN)	Bond Stress (MPa)	Average (MPa)
CONCRETE PILES IN CONTROL ENVIRONMENT	C0.5	27	0.5d	1151	4.5	3.2
	C1.0A	32	1d	1656	3.2	
	C1.0B	32	1d	1580	3.1	
	C1.5A	32	1.5d	1584	2.1	2.4
	C.15B	32	1.5d	2020	2.6	
CONCRETE PILES IN FRESH WATER ENVIRONMENT	W0.5	27	0.5d	892	3.5	2.7
	W1.0A	27	1d	1358	2.7	
	W1.0B	27	1d	1336	2.6	
	W1.5A	27	1.5d	1591	2.1	2.0
	W1.5B	27	1.5d	1527	2.0	
CONCRETE PILES BENTONITE ENVIRONMENT	B1B	23	1d	1338	2.6	2.5
	B1D	23	1d	1274	2.5	
	B2A	23	2d	1625	1.6	1.5
	B2B	23	2d	1438	1.4	
BENTONITE (SOIL CAKED)	B1A	23	1d	931	1.8	1.5
	B1C	23	1d	570	1.1	
STEEL PILES IN CONTROL ENVIRONMENT	SC0.5	32	0.5d	618	1.63	1.40
	SC1.0A	32	1d	1018	1.34	
	SC1.0B	32	1d	1100	1.45	
	SC1.5A	32	1.5d	1140	1.00	1.02
	SC.15B	32	1.5d	1187	1.04	
STEEL PILES IN FRESH WATER ENVIRONMENT	SW0.5	27.5	0.5d	438	1.15	1.31
	SW1.0A	27.5	1d	1105	1.33	
	SW1.0B	27.5	1d	975	1.29	
	SW1.5A	27.5	1.5d	1317	1.16	1.07
	SW1.5B	27.5	1.5d	1116	0.98	
STEEL PILES IN BENTONITE ENVIRONMENT	SB1B	23.5	1d	874	1.15	0.88
	SB1D	23.5	1d	466	0.62	
	SB2A	23.5	2d	827	0.55	0.52
	SB2B	23.5	2d	767	0.50	
STEEL-BENT. (SOIL-CAKED)	SB1A	23.5	1d	629	0.83	0.91
	SB1C	23.5	1d	753	0.99	

Table 3. Allowable Bond Stresses for Square Concrete or H-Piles.

Material	Condition	$f_b$ (MPa)
Concrete	Salt or Fresh Water	2.1
	Bentonite	1.5
Steel	Salt or Fresh Water	1.0
	Bentonite	0.5

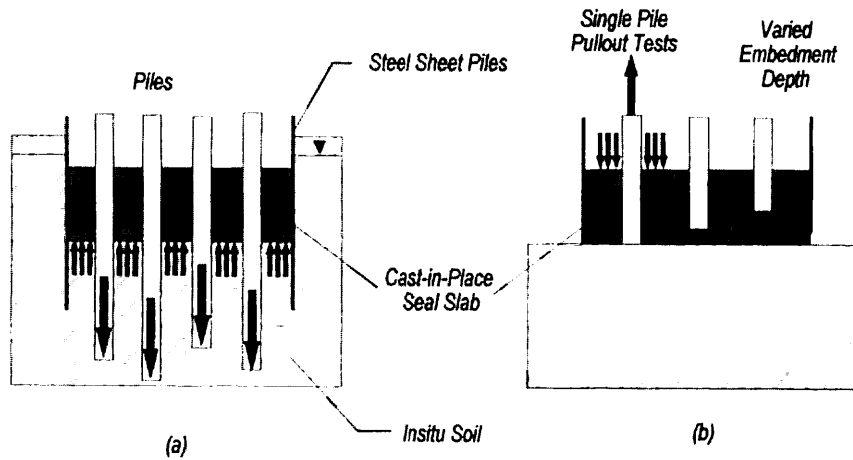


Fig.1. (a) Hydrostatic Uplift Load, (b) Experimental Load Simulation

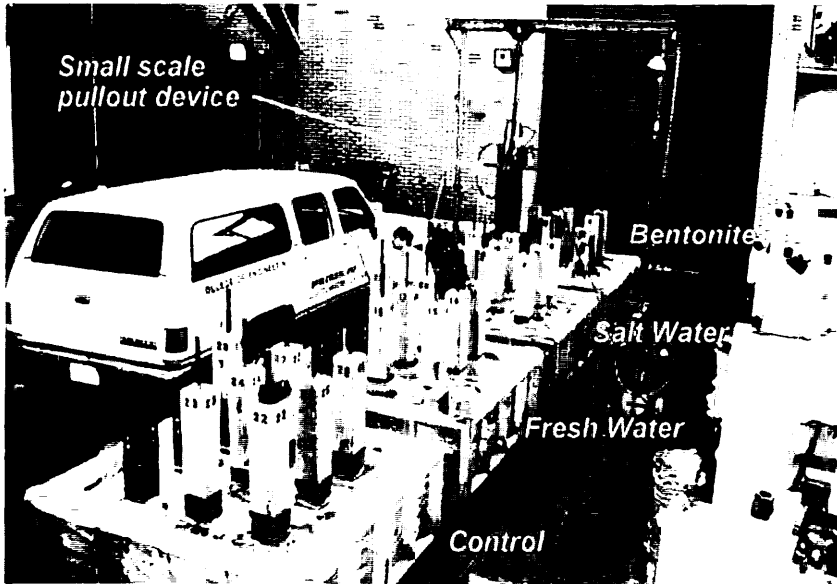


Fig.2. Small-Scale Coffier Cells.

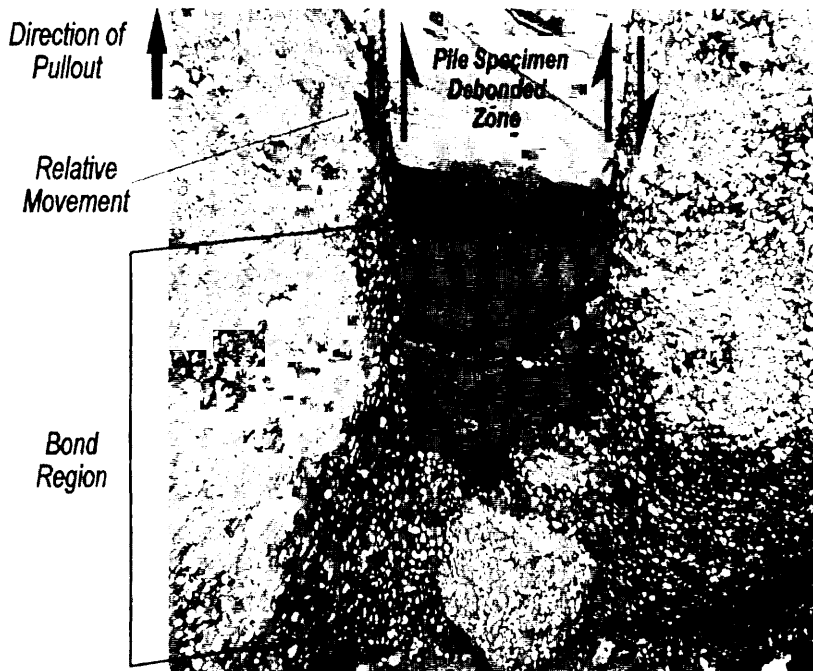


Fig.3. Cut-a-way Side View of Concrete Specimen Failure Modes.

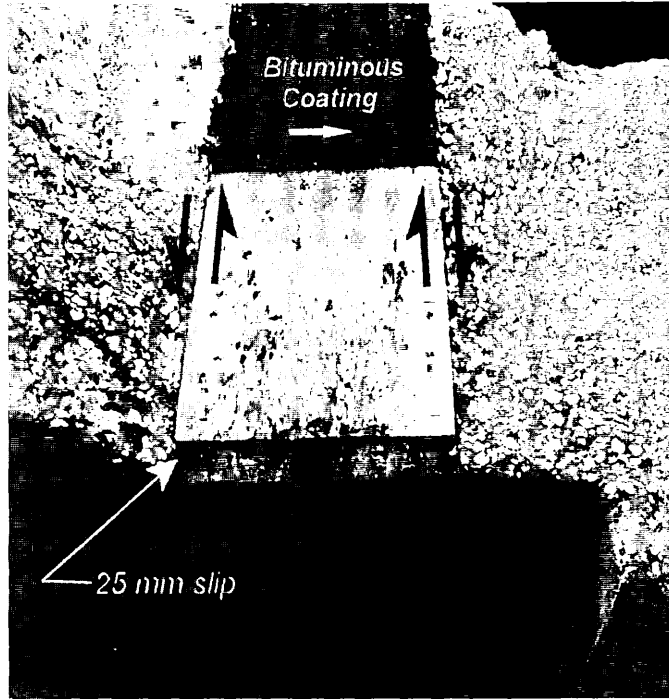


Fig.4. Cut-a-way Side View Showing H-Pile Failure Mode.

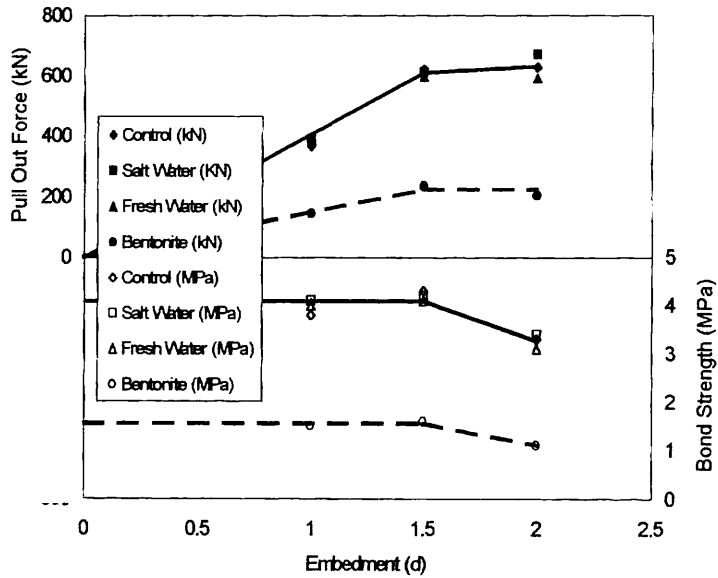


Fig.5. Results of 1/3 Scale Prestress Concrete Pile Pullout Tests.

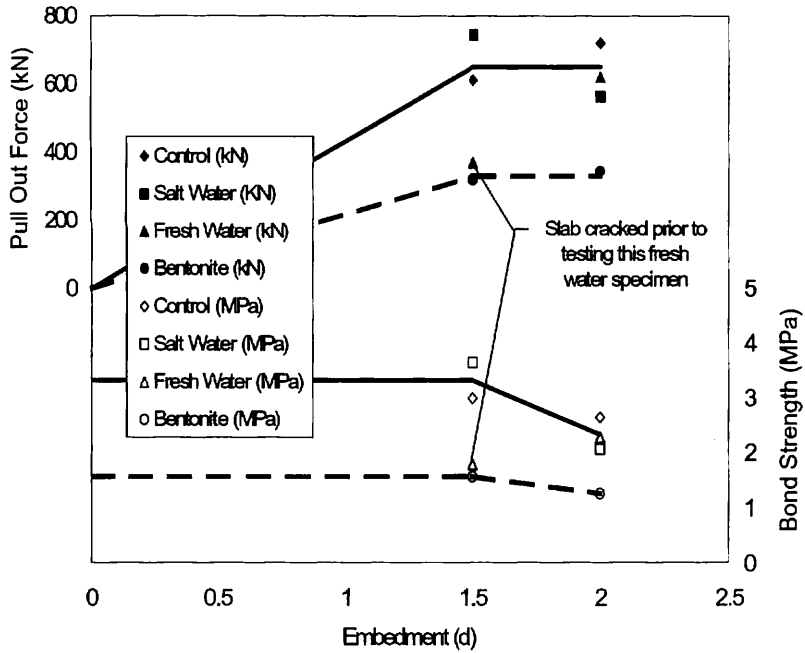


Fig. 6. Results of 1/3 Scale Steel Pullout Tests.

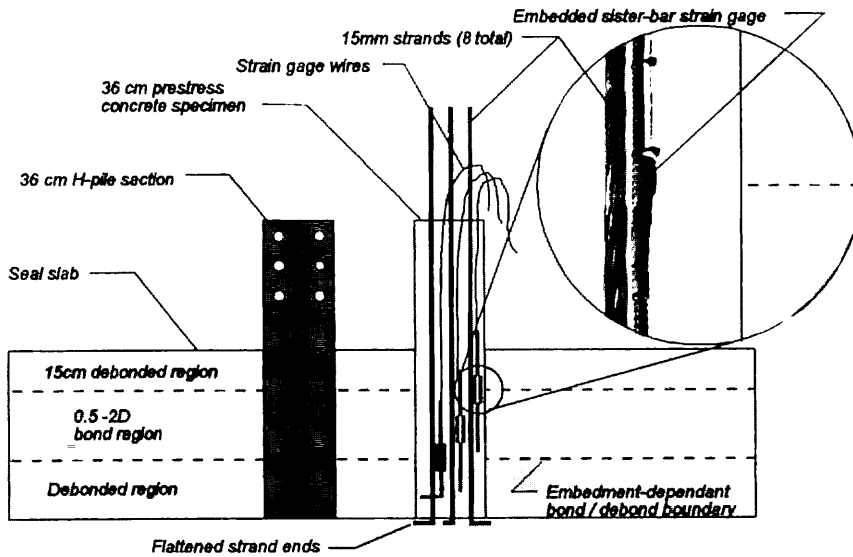


Fig.7. Test Specimen / Seal Slab Schematic.

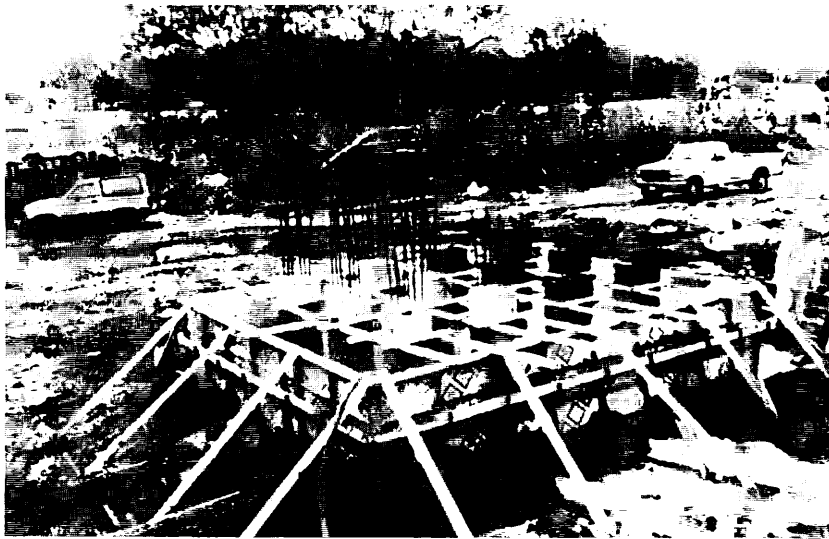


Fig.8. Piles Supported by Template in Simulated Cofferdam (bentonite).

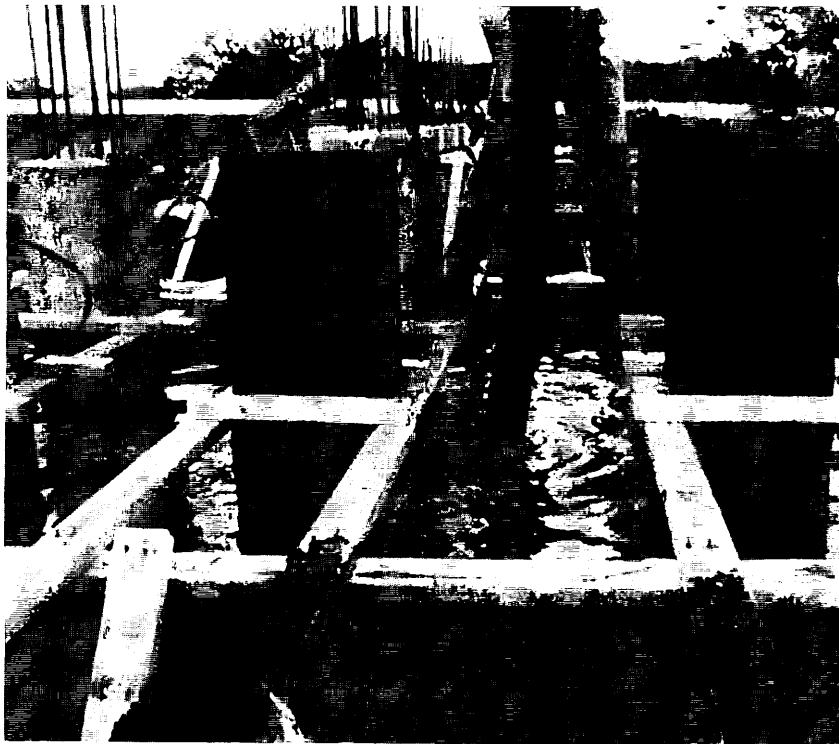


Fig.9. Tremie Placing CIP Seal Slab in Simulated Cofferdam (water).



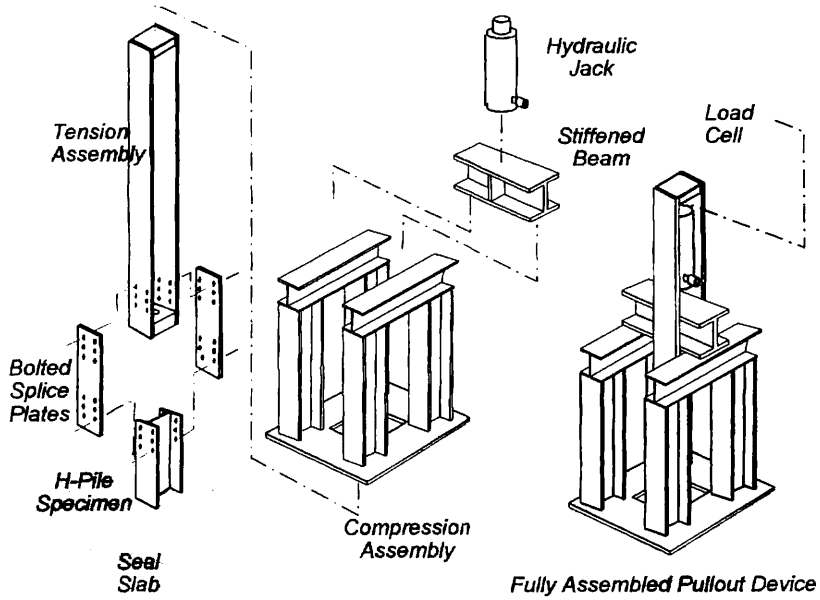


Fig.10. Full-Scale Pullout Device.

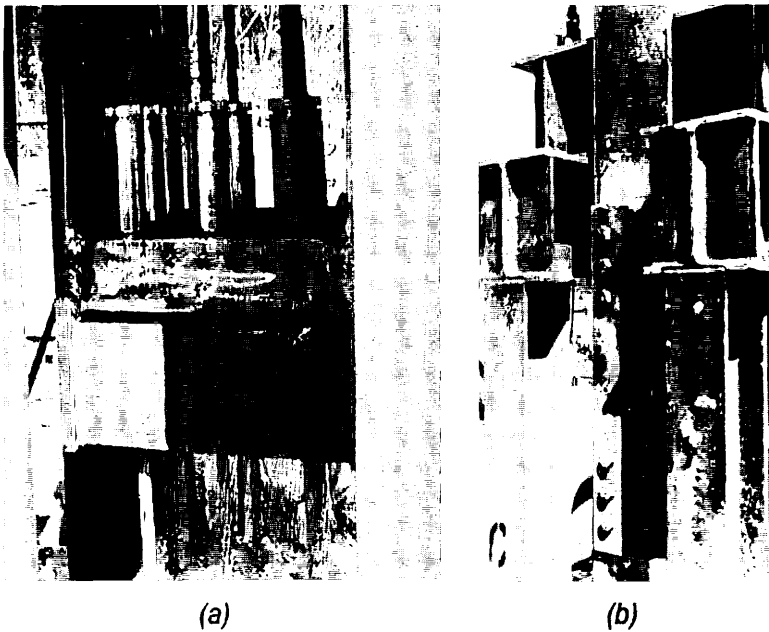


Fig.11. Connection to Prestressed Concrete (a) and Steel H-Piles (b).

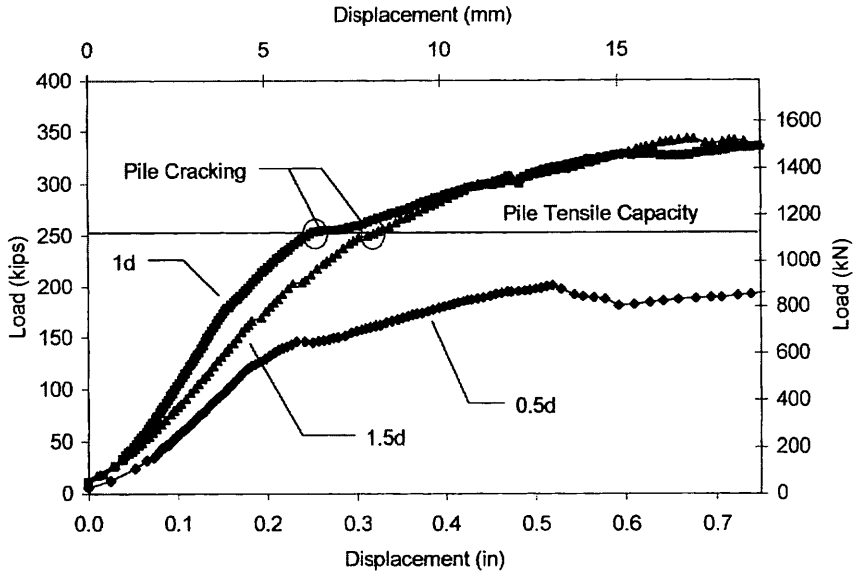


Fig.12. Concrete Pile Pullout Load versus Displacement.

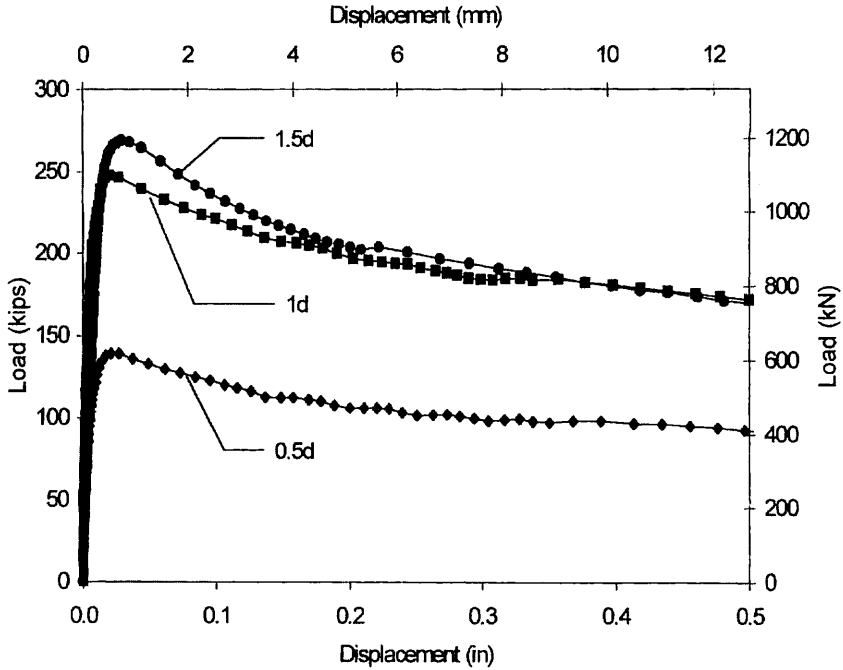


Fig.13. Steel Pile Pullout Load versus Displacement.

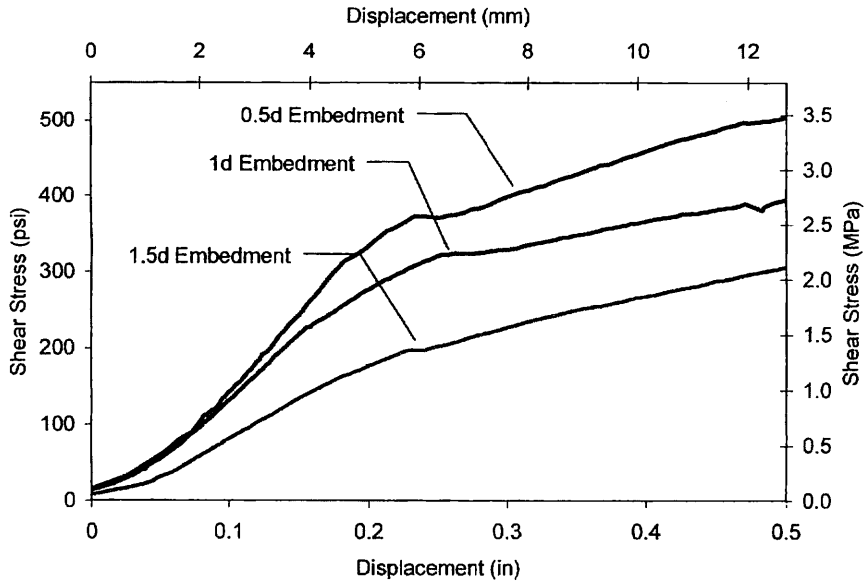


Fig.14. Concrete Pile Interface Shear Stress versus Displacement

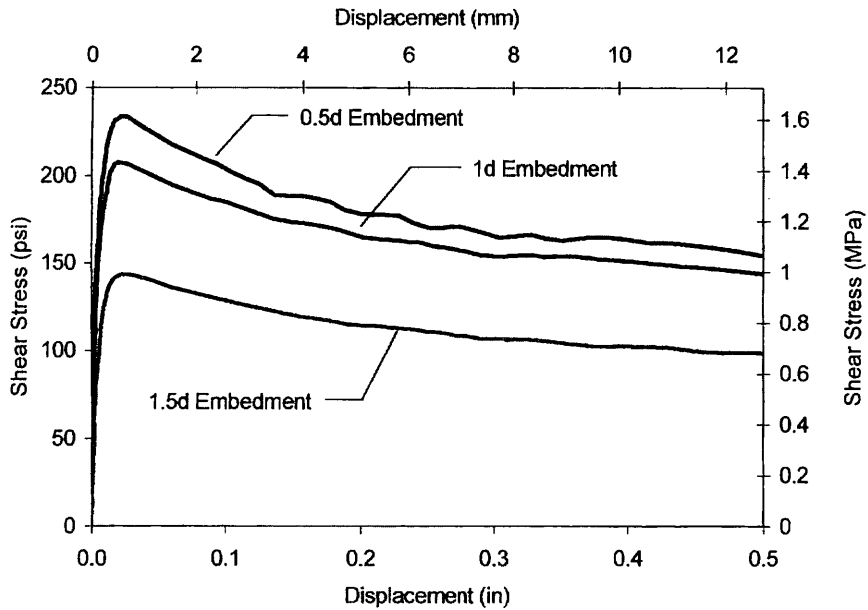


Fig.15. Steel Pile Interface Shear Stress versus Displacement.

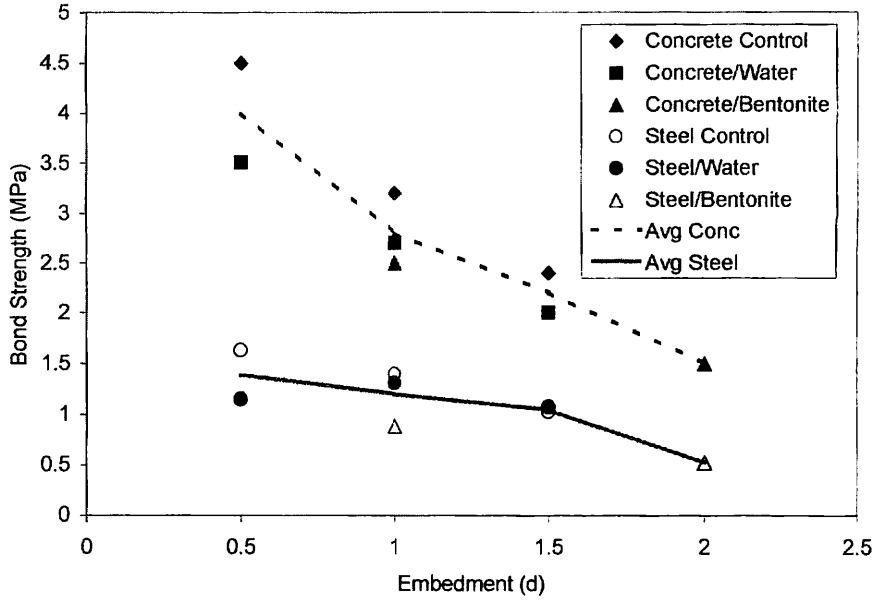


Fig. 16. Bond Strength from Full Scale Pullout Tests.

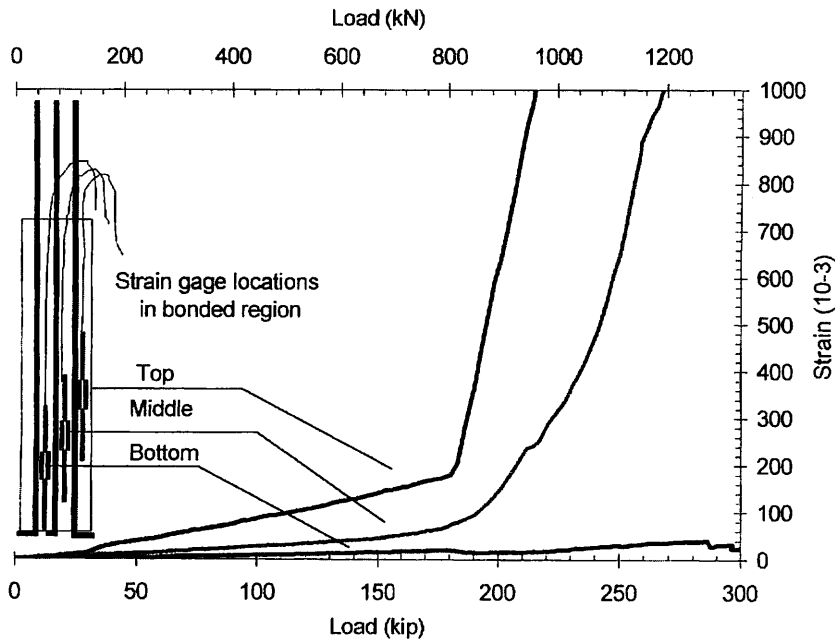


Fig. 17. Strain Distribution in Bonded Region.

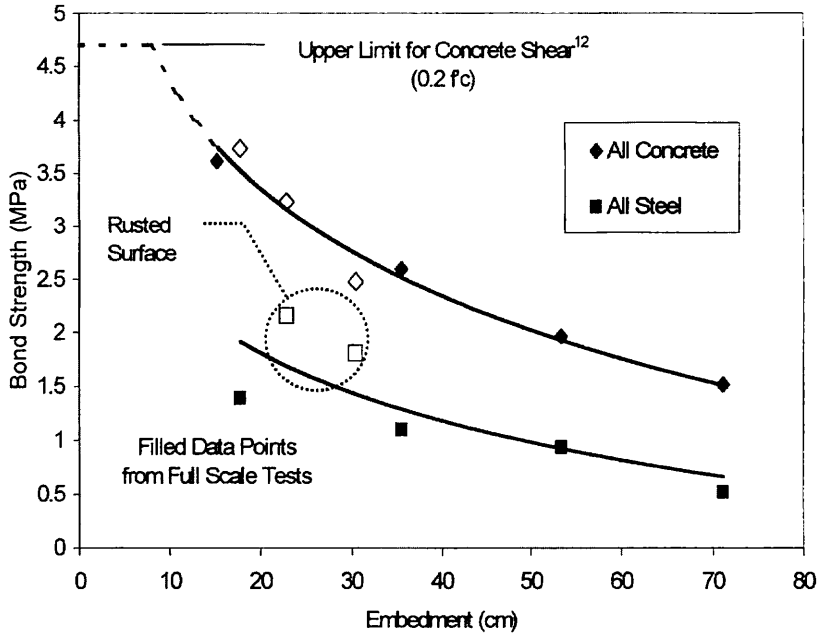


Fig.18. Bond Strength from 1/3 Scale and Full Scale Tests.

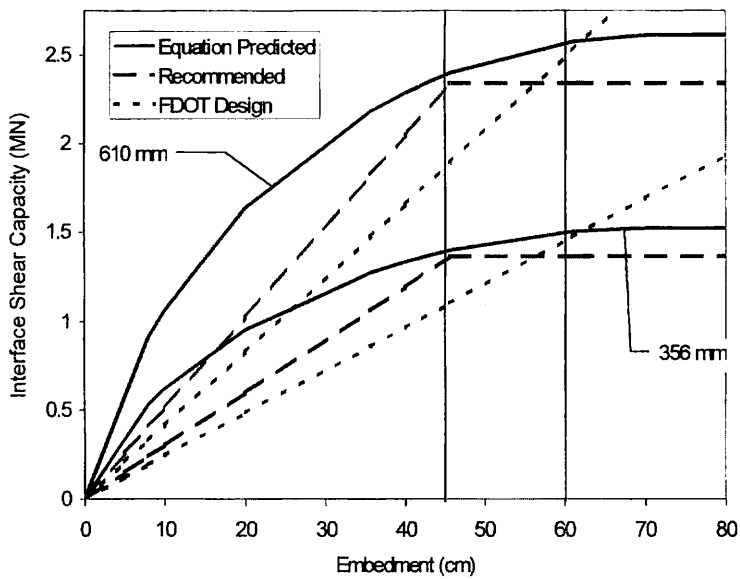


Fig.19. Comparison of Design Capacities.

Title no. 99-S76

# Seal Slab/Steel Pile Interface Bond from Full-Scale Testing

by Gray Mullins, Ruben Sosa, Rajan Sen, and Moussa Issa

This paper presents results from model and full-scale tests to assess the interface bond between a cast-in-place concrete seal slab and steel H-piles in cofferdams. Three different seal slab placement conditions—fresh water, salt water, and bentonite slurry—were evaluated and the results were compared against controls where no fluid was displaced by the concrete. Normal pile surfaces were investigated. Additionally, the situation of soil-caked piles was also tested.

In the model tests, eight 15 cm deep, W6 x 15 sections were used for two different embedment depths of 1.5d and 2d, with d being the depth of the section. In the full-scale tests, 16 specimens 35 cm deep (W14 x 90 sections) were tested with the embedment varied between 0.5d and 2d. The results show that significant bond stresses developed even in the worst placement condition. Recommendations made for revising current values in specifications have already been implemented by the Florida Department of Transportation.

**Keywords:** bond; pile; slab; steel.

## INTRODUCTION

Cofferdams are usually required in the construction of bridge foundations over waterways. Typically, a sheet pile enclosure is constructed in water and piles are driven as shown in Fig. 1. A tremie concrete seal is then placed. When the seal has sufficiently cured, the cofferdam is dewatered and internal bracing is installed. Thus, the seal allows the construction of the pier to be carried out under dry conditions.

Because the function of the unreinforced seal slab is primarily to provide dry working conditions, its design is quite simple. The seal thickness is essentially determined so that its weight balances the maximum uplift pressure since the allowable interface shear stresses are very small. Previous AASHTO specifications<sup>1</sup> permitted interface shear stress values of 69 kPa (10 psi). These values, however, were reduced to 34.5 kPa (5 psi) for steel interfaces in the Florida Design Guidelines.<sup>2</sup> Neither values are based on test data.

In 1997, the Florida Department of Transportation (FDOT) funded a study to evaluate interface bond from full-scale tests. This paper presents results relating to the seal slab/steel pile interface bond. A companion paper provides the corresponding results for prestressed piles.<sup>3</sup> The complete results from this study including finite element modeling may be found elsewhere.<sup>4,5</sup>

## RESEARCH SIGNIFICANCE

This study provides the first set of experimental results on the interface shear between steel piles and seal concrete slabs cast in accordance with construction specifications.<sup>6</sup> The results obtained have already led to increased allowable interface shear in the latest specifications.<sup>7</sup> This should result in reduced construction costs.

## OBJECTIVES

The overall goal of the study was to recommend interface shear stress values for seal slab and piles that could be directly



Fig. 1—Sheet pile cofferdam with pile-driving template. (Photo courtesy of Applied Foundation Testing.)

used in FDOT's design specifications. These values were to be based on full-scale tests conducted on specimens that had been prepared in accordance with current FDOT specifications<sup>6</sup> for conditions that were commonly encountered. Variables examined were the pile embedment depth, effect of pile surface, effect of the pile material (steel or concrete), and the type of fluid that was displaced by the concrete.

## EXPERIMENTAL PROGRAM

The load transfer characteristics in seal slabs can be simulated by conducting pullout tests, illustrated in Fig. 2, in which compressive loads are applied to the seal slab and tensile loads to the steel piles. Careful attention had to be paid to the experimental setup so that tests could be carried out under field conditions. Small-scale bond tests were conducted to identify the maximum pullout lengths for a 1/3 scale pilot study. Results of the pilot study were used to subsequently refine the apparatus and procedures for the full-scale testing.

## PILOT STUDY

The pilot study simulated three different seal slab placement conditions involving: 1) salt water; 2) fresh water; and 3) drilling fluid. These results were compared against controls where no fluid had to be displaced by the concrete. The 15 cm-deep, wide flange sections were tested for two different embedment depths, 1.5d and 2d (d is the nominal pile size). A total of eight model scale tests were conducted (four conditions and two embedment depths).

The steel pile specimens were fabricated using a W6 x 15 beam section made from A36 structural steel. Each steel pile

ACI Structural Journal, V. 99, No. 6, November-December 2002.

MS No. 01-267 received August 18, 2001, and reviewed under Institute publication policies. Copyright © 2002, American Concrete Institute. All rights reserved, including the making of copies unless permission is obtained from the copyright proprietors. Pertinent discussion will be published in the September-October 2003 ACI Structural Journal if received by May 1, 2003.



**Gray Mullins** is an assistant professor in the Department of Civil and Environmental Engineering at the University of South Florida, Tampa, Fla. He received his BSCE, MSCE, and PhD from the University of South Florida. His research interests include full-scale instrumentation and testing in geotechnical structures and the application of advanced composite materials.

**Ruben Sosa** received his BSCE and MSCE from the University of South Florida. He is with GeoSyntec Consultants, Tampa, Fla.

ACI member **Rajan Sen** is the Samuel and Julia Flom Professor in the Department of Civil and Environmental Engineering at the University of South Florida. He is a member of ACI Committees 215, Fatigue of Concrete; 440, Fiber Reinforced Polymer Reinforcement; and 444, Experimental Analysis for Concrete Structures. His research interests include masonry, prestressed concrete, steel, and the application of advanced composite materials.

ACI member **Moussa Issa** is Chief Structural Engineer, T. Y. Lin International, Chicago, Ill. He is a member of ACI Committees E 801, Student Activities; 340, Design Aids for ACI Building Codes; and 444, Experimental Analysis for Concrete Structures.

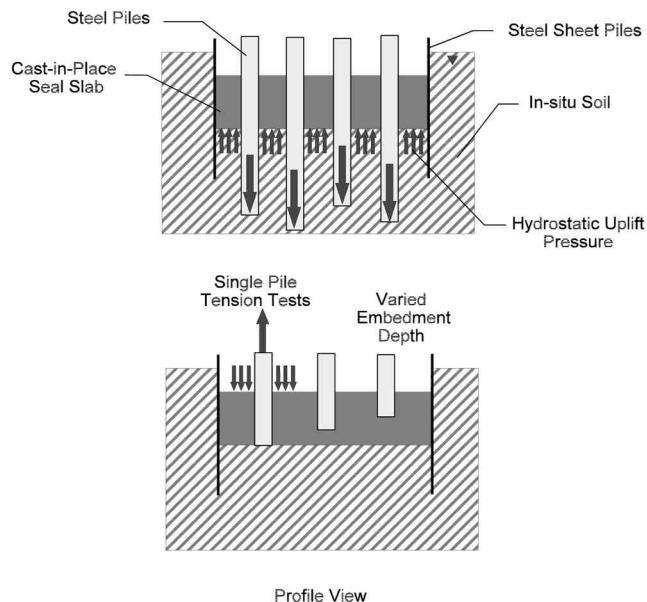


Fig. 2—Simulation of loads.

was 0.91 m (36 in.) in length. On each pile, a line of three 23.8 mm (15/16 in.) diameter holes were drilled into each flange to facilitate the twelve 22 mm (7/8 in.) bolts required to provide the connection to a pullout apparatus.

### Cofferdam simulation

Four 0.76 m-high wood boxes with inside dimensions of 1.4 x 1.4 m were fabricated to simulate the four placement conditions. Plastic sheeting was used to line and seal the boxes. Wood templates were used to properly position each pile within the simulated cofferdams. The piles were spaced at three times the pile size, that is, the center to center distance was 45 cm. The edge spacing from the center line to the box edge was  $1.5d$  or 22.5 cm.

All piles were identical in length and tip elevation; however, the two different embedment depths of  $1.5d$  and  $2d$  were accommodated by varying the bonded and debonded lengths within the concrete. The bonded region (steel to seal slab) was provided at the bottom of the simulated cofferdam in all the specimens. For the 15 cm piles, the bonded length was either 22.5 cm ( $1.5d$ ) or 30 cm ( $2d$ ). Above this bonded length, the piles were debonded using a thick layer of bitumen (Fig. 3) applied up to a height sufficiently above the anticipated upper surface of the seal slab. The overall slab thickness and debonded region was set such that the bitumen extended at least

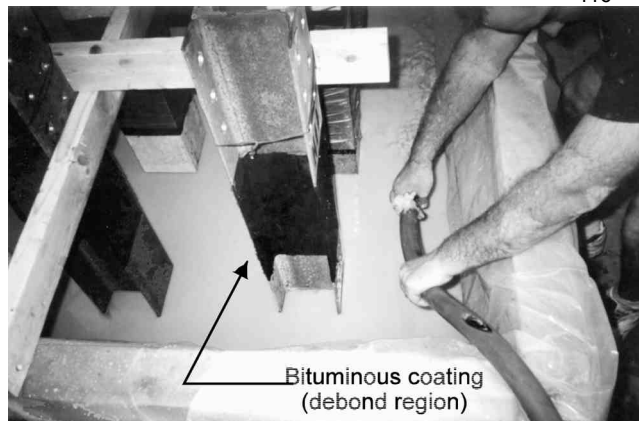


Fig. 3—Drilling fluid pumped into simulated cofferdam.

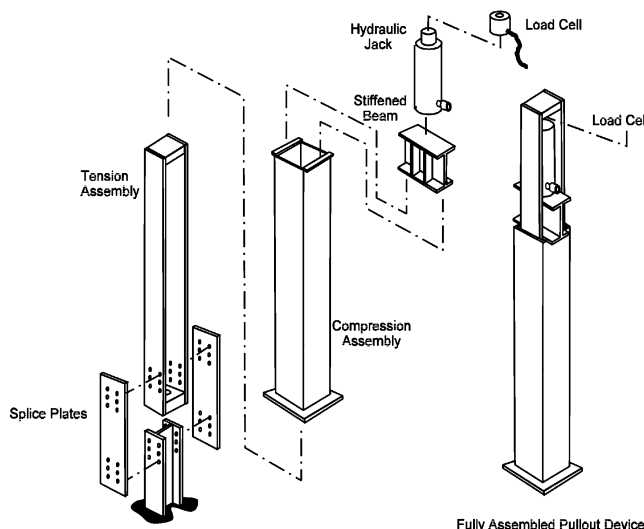


Fig. 4—Model scale pullout equipment.

1d below the upper seal slab surface for all specimens. This minimum debond length was intended to eliminate bearing stress concentrations based on finite element modeling.

Three of the four boxes were filled with either fresh water, 3% salt water, or bentonite slurry (Fig. 3). The latter was made by mixing dry, high-yield bentonite and fresh water to achieve slurry properties similar to those in the FDOT specifications.<sup>6</sup> The final density achieved was 10 kN/m<sup>3</sup> (64 pcf) with a pH of 8 and a viscosity of 37 s (Marsh Cone method). The fourth box served as a control and was therefore not filled.

### Seal slab placement

Class III seal concrete specified by FDOT<sup>6</sup> was used. The specified 28-day strength of the seal slab was 21 MPa (3000 psi). This mixture has 330 kg of cement/m<sup>3</sup> (560 lb of cement/yd<sup>3</sup>) and a water-cement ratio ( $w/c$ ) of 0.51. The concrete was purchased from a local concrete plant and was pumped through a 76 mm (3 in.) diameter hose. The concrete was placed from the bottom upwards keeping the hose tip below the rising level of concrete. This is similar in placement and identical in effect to using a tremie pipe.

### Pullout frame

The pullout frame used is shown in Fig. 4. It consists of two telescopic sections that react against each other via a

**Table 1—Summary of pilot test results**

Type	Specimen	$f'_c$ , MPa	Bond length	Bond area, m <sup>2</sup>	Pullout load, kN	Bond stress, MPa
Control	H41	31	1.5 <i>d</i>	0.206	611	3.01
	H42	31	2 <i>d</i>	0.274	720	2.66
Salt water	H21	31	1.5 <i>d</i>	0.206	744	3.66
	H22	31	2 <i>d</i>	0.274	563	2.08
Fresh water	H31	31	1.5 <i>d</i>	0.206	336	1.66*
	H32	31	2 <i>d</i>	0.274	620	2.29
Bentonite	H11	31	1.5 <i>d</i>	0.206	320	1.58
	H12	31	2 <i>d</i>	0.274	344	1.27

\* Seal slab was cracked prior to testing due to earlier testing of adjacent pile.

stiffened beam and a hydraulic jack. The pile specimen was bolted to the tension assembly. The pullout frame weighed 2.2 kN fully assembled and required an overhead chain hoist to assemble and/or move. Tension loads were measured using a load cell positioned between the top of the jack and the tension assembly. The stiffened beam transferred load from the base of the jack to a built-up column section that in turn applied uniform compressive stress to the seal slab.

### Leveling

Before the pullout frame was installed, a grout pad was placed around each pile specimen using a high-strength, fast-curing, self-leveling grout. To further assist in this alignment process, a steel bearing plate was placed in the fresh grout and squared with respect to the longitudinal axis of the pile.

### Instrumentation

A data acquisition system was used for monitoring and recording the test data generated. Loads were measured using a load cell and slip was monitored by two displacement transducers. One of the displacement transducers was magnetically attached to the compression assembly and positioned to record displacement with respect to an external reference beam. This registered any possible seal slab surface crushing or settlement that might occur during testing. The other displacement transducer was attached to the tension assembly and referenced to the top of the compression assembly. This recorded specimen movement as well as the compliance of the frame that was later accounted for in the data reduction.

### Test procedure

Pullout tests began after the seal slab had been cured for 72 h in accordance with FDOT requirements. Concrete cylinders were tested at periodic intervals to monitor the change in compressive strength. The tension assembly was bolted to the piles using 22 mm (7/8 in.) diameter bolts. Once the grout had time to cure (approximately 15 min), the compression assembly was lowered onto the bearing plate. The stiffened beam along with the hydraulic jack were then positioned between the compression section and the upper end of the tension assembly as shown in Fig. 4.

With the specimens set up, the pullout test commenced. The tensile load was increased slowly using a manually operated toggle switch that intermittently engaged the power to the hydraulic pump. The load was increased slowly to reduce any possible dynamic stiffening of the system. Each specimen was displaced at least 25 mm.

## RESULTS

A summary of the test results is presented in Table 1. This provides information from the eight tests and contains details

of the compressive strength, the failure load, and the average bond stress. Over the duration of the tests, there was no change in the compressive strength.

The following observations may be made:

1. Significant bond stresses were developed; the highest value obtained was 3.66 MPa (salt water/1.5*d*), and the lowest was 1.27 MPa (bentonite/2*d*). The highest values varied with embedment depth. For 1.5*d* embedment, the highest was for salt water followed by controls and fresh water. For 2*d*, control values were highest followed by fresh water then salt water;
2. The magnitude of the bond stress decreased with an increase in embedment depth. This suggests that the distribution of bond stress is nonuniform;
3. The results for bentonite slurry were surprisingly good. Indeed, for embedment depth of 1.5*d*, values obtained were comparable to that for fresh water; and
4. Values for salt and fresh water are similar.

## FULL-SCALE STUDY

The pilot study provided important information on the magnitude of the interface steel/seal bond that could develop. The significant scatter in the results indicated the need to conduct additional tests. These findings led to refinements in the full-scale test program. The principal changes were: 1) elimination of the salt water condition—this was based on the results of more extensive tests carried out on prestressed piles;<sup>3</sup> 2) consideration of the effect of soil-caked surface; and 3) increase in the number of specimens.

In view of the very high bond stresses that were obtained, the depth of embedment was limited to 1.5*d* except for bentonite, where the maximum depth was increased to 2*d*. In addition, embedment depths of 0.5*d* were investigated for the control and fresh water placement conditions.

With three different placement conditions (control, fresh water, and bentonite), two different embedment depths (*d*, 1.5*d*, or 2*d*), and two specimens per test, a total of 12 specimens were required. Four additional specimens were tested—one each for embedment depth of 0.5*d* (for the control and fresh water condition) and two for investigating the effect of soil caking for the bentonite slurry for an embedment depth of 1*d*. Thus, the controls and the fresh water condition each had five specimens, and the bentonite slurry condition had six specimens. These were identical to the conditions investigated for prestressed piles.<sup>3</sup>

The depth (35 cm) and length of the steel piles was kept the same as that for the prestressed piles. As a result, 1.52 m-long W14 x 90 sections made from A36 steel were used. Holes for 28.6 mm (1-1/8 in.) diameter bolts were drilled in each flange to connect the pile specimens to the tension assembly frame (Fig. 5).

### Simulated cofferdam

Three cofferdams had to be constructed for the three conditions that were investigated. Two of these—fresh water and control—were identical in size. The bentonite slurry condition with the larger number of specimens was larger. The dimensions of the cofferdam were determined by specimens and edge distances that were kept the same  $3d$  (1.06 m) as in the pilot study.

The cofferdams were constructed using rented steel reinforced plywood box forms connected to each other using wedge pins provided by the manufacturer. They were also externally braced using wooden stakes and a 2 x 4 framework. Additionally, each cofferdam was lined with 0.2 mm (6 mil) plastic sheeting. This provided a water-tight barrier, preventing the loss of any construction fluid (water or bentonite slurry). Figure 5 shows one of the cofferdams just prior to filling with fluid.

### Specimen support

Following the construction of the cofferdam, the specimens were accurately positioned on plywood pads to prevent damage to the plastic lining. The specimens were vertically

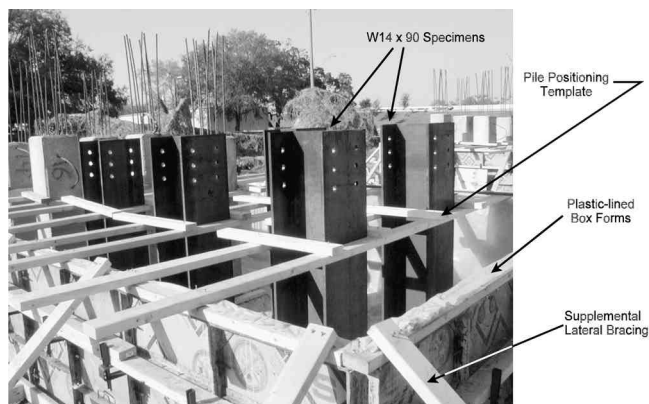


Fig. 5—Steel piles in simulated cofferdam. (Prestressed piles were also tested in the same bed.)

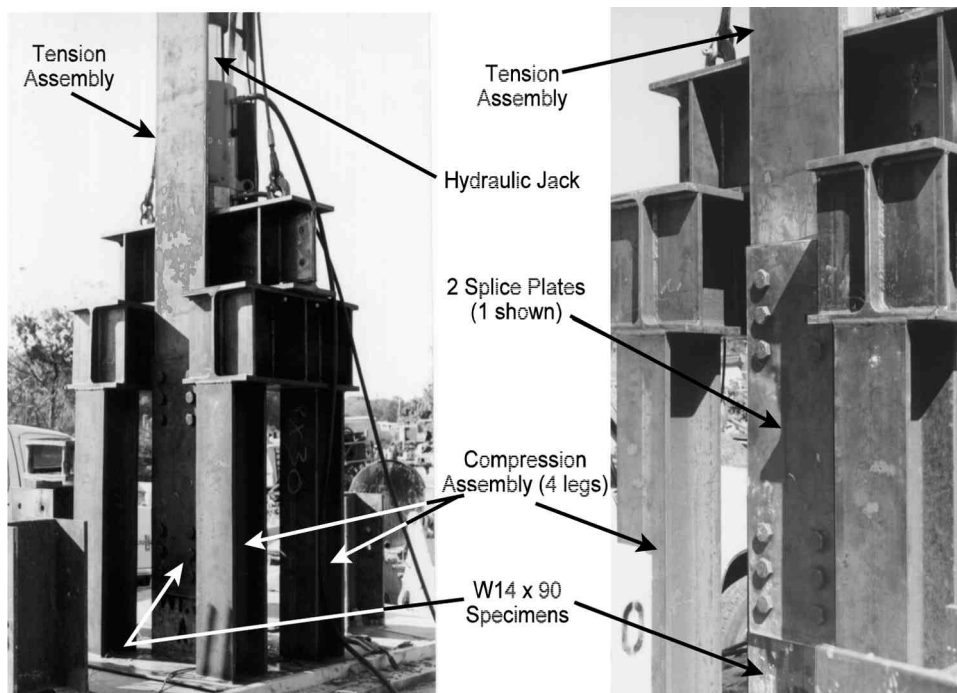


Fig. 6—Full-scale test apparatus.

supported with a wooden 2 x 4 framework that was secured to the box forms (Fig. 5).

### Debonded surface

As in the pilot study, differing lengths ( $0.5d$ ,  $1d$ ,  $1.5d$ , and  $2d$ ) of the pile surface were bonded or debonded. Debonding was achieved in the identical manner as in the pilot study. The bonded steel surfaces were left in their natural state except for the two specimens that were tested for the soil-caked condition. For this case, an adhesive clay soil, typically used for clay models by artists, was used because it bonded better than the kaolinite paste tested in the pilot study.<sup>3</sup> The debonded length extended from the boundary of the bonded region to approximately 15 cm above the intended elevation of the finished surface of the seal slab. This included an additional 35 cm length determined as needed by finite element analysis to ensure uniform distribution of compressive loads to the seal slab surrounding the bonded region.

### Placement conditions

One cofferdam was left dry prior to concrete placement (control); the second was filled with fresh water from a nearby potable source. The third was filled with bentonite slurry that was made by mixing dry, high-yield bentonite and fresh water. The mixing was accomplished through the use of a shear pump. Enough bentonite clay was added to achieve slurry properties similar to FDOT specifications. The final density achieved was  $10 \text{ kN/m}^3$  ( $65 \text{ lb/ft}^3$ ) with a viscosity of 40 s (Marsh Cone method) and a pH of 8.

### Seal slab placement

Seal concrete was placed using a concrete pump truck. The concrete was pumped through a 15 cm (6 in.) diameter hose and was placed from the bottom upwards keeping the hose tip below the rising level of concrete. This is similar in placement and identical in effect to the tremie method.

## Testing apparatus

Identical considerations of capacity, economy, and portability dictated the design of the pullout equipment. A steel reaction frame was designed to take advantage of an available double-acting, 2670 kN (300 ton) hydraulic jack that would be operated with a portable 69 MPa (10 ksi) hydraulic pump system. The frame required connection designs for both concrete and steel pile types. Additionally, the frame would need to be integrated with electronic devices to measure load and displacement.

As for the pilot test, the reaction frame consisted of a tension and compression assembly. The tension assembly was connected directly to the pile with two splice plates and housed the hydraulic jack and load cell. The compression assembly applied compressive loads to the seal slab. Figure 6 shows a photograph of the complete assembly being placed over a pile specimen. Additional information on the design and fabrication may be found elsewhere.<sup>4</sup>

## Test procedure

The test setup and procedure was similar to the pilot study involving placing a grout layer, connecting the tension assembly to the pile, lowering the compression assembly onto the leveled grout surface, attaching the appropriate instrumentation, and extracting the specimens. Some variations, however, were adopted to expedite the testing procedure so less variation in concrete strength would be observed after the 72-h FDOT curing period.

Because no concrete vibration or finishing is used in seal slab construction, various degrees of surface roughness developed in the submerged conditions. Instead of leveling the base of each pile individually, all cofferdams were leveled at the same time with a skim coat of grout batched from a single truck. The grout was placed and finished 2 days after the placement of the cast-in-place (CIP) seal slab without adding significant delay before testing could commence. The bentonite placement condition had the greatest degree of unevenness, whereas the control was more uniformly placed due to the visual input during its placement (although unfinished). Because the debonded portion of each pile specimen extended well above the CIP slab, there were no difficulties with possible bonding of the grout to the piles (Fig. 7).

Although much larger than the model scale device, the pullout apparatus could be attached more quickly due to easy

access of the splice plate bolts. It was also left fully assembled between tests. Instrumentation and data acquisition attached to the device was again similar to the model scale tests with the exception of the load cell capacity (2670 kN) that was sized to accommodate the increased loads. One of two displacement gages was magnetically attached to the pile and referenced to the top of the slab. The other gage was magnetically attached to the pile and referenced to an external reference beam to monitor global movements.

The tensile load was increased slowly using a manually operated toggle switch that intermittently engaged the power to the hydraulic pump. The load was increased slowly to reduce any possible dynamic stiffening of the system. Each specimen was displaced upward at least 25 mm to ensure that the bond capacity had been fully developed.

## RESULTS

A summary of the test results is presented in Table 2. This provides information from all 16 tests and contains details of

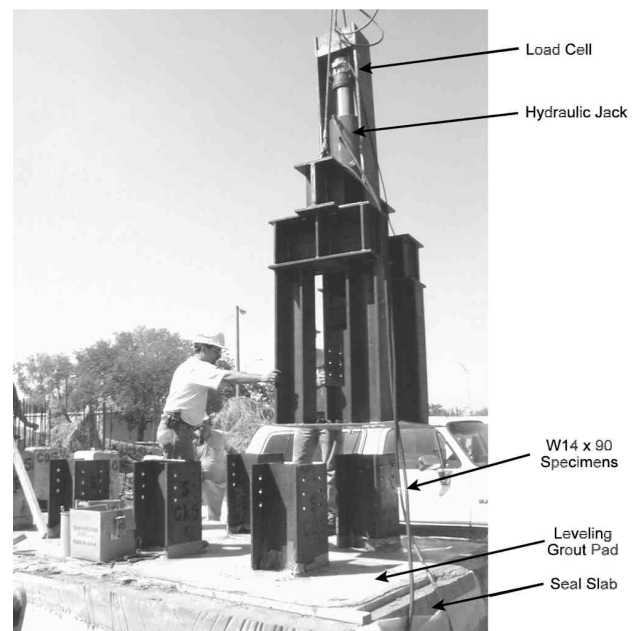


Fig. 7—Full-scale pullout device suspended over test specimen.

Table 2—Summary of full-scale test results

Type	Specimen	$f'_c$ , MPa	Bond length	Pullout load, kN	Bond stress, MPa	Average, MPa	Normalized, MPa
Control	SC0.5	32	0.5d	618	1.63	—	—
	SC1.0A	32	1d	1018	1.34	1.40	1.20
	SC1.0B	32	1d	1100	1.45		
	SC1.5A	32	1.5d	1140	1.00	1.02	0.88
	SC.15B	32	1.5d	1187	1.04		
Fresh water	SW0.5	27.5	0.5d	438	1.15	—	—
	SW1.0A	27.5	1d	1105	1.33	1.31	1.21
	SW1.0B	27.5	1d	975	1.29		
	SW1.5A	27.5	1.5d	1317	1.16	1.07	0.99
	SW1.5B	27.5	1.5d	1116	0.98		
Bentonite	SB1B	23.5	1d	874	1.15	0.88	0.88
	SB1D	23.5	1d	466	0.62		
	SB2A	23.5	2d	827	0.55	0.52	0.52
	SB2B	23.5	2d	767	0.50		
Bentonite (soil-caked)	SB1A	23.5	1d	629	0.83	0.91	0.91
	SB1C	23.5	1d	753	0.99		

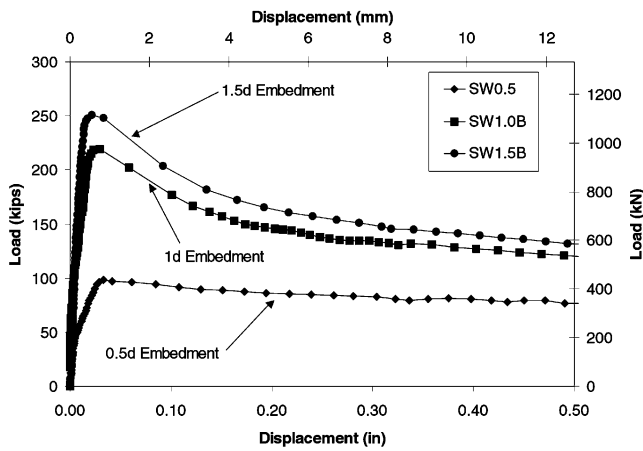


Fig. 8—Water-filled cofferdam test results.

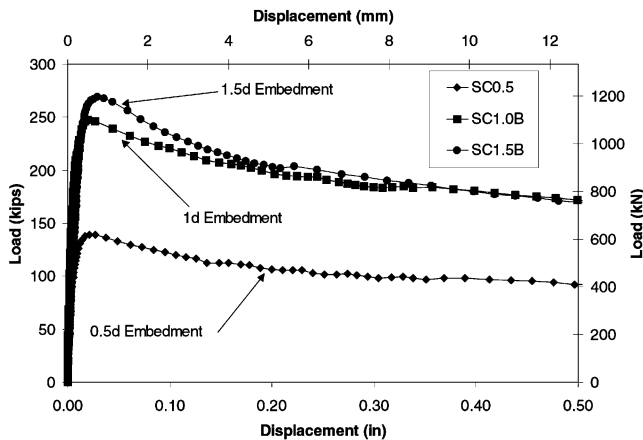


Fig. 9—Control cofferdam test results.

the compressive strength, the failure load, and the average bond stress. Inspection of Table 2 shows that the bond stresses were quite low compared with the pilot study. The highest value was 1.63 MPa (control/0.5d) and the lowest was 0.50 MPa (bentonite/2d). Trends observed in the pilot tests were repeated, however; the average bond stresses declined with increased embedment depth. For example, the average bond stress reduces from 1.31 to 1.07 MPa for a fresh water embedment depth increase from  $d$  to 1.5d.

Variations in concrete strength over the duration of the test may also be noted. The lowest compressive strength was for the bentonite series ( $f'_c = 23.5$  MPa) and the highest for the controls (32 MPa). The bond strength is normalized to a 23.5 MPa concrete strength in Table 2 by dividing the measured values by the percent increase in the square root of the concrete strength. For example, the control values were normalized as follows

$$1.20 \text{ MPa} = 1.40 \text{ MPa} \frac{\sqrt{23.5}}{\sqrt{32}}$$

Representative load versus displacement plots are shown for each of the simulated cofferdam conditions in Fig. 8 to 10. Each graph also shows the effect of embedment depth on the pullout response for the various conditions. The control and fresh water environments showed similar results for normalized bond values of 1.20 and 1.21 MPa, respectively. Likewise, the trends associated with the effects of embedment were comparable (Fig. 8 and 9). The pullout capacity increased

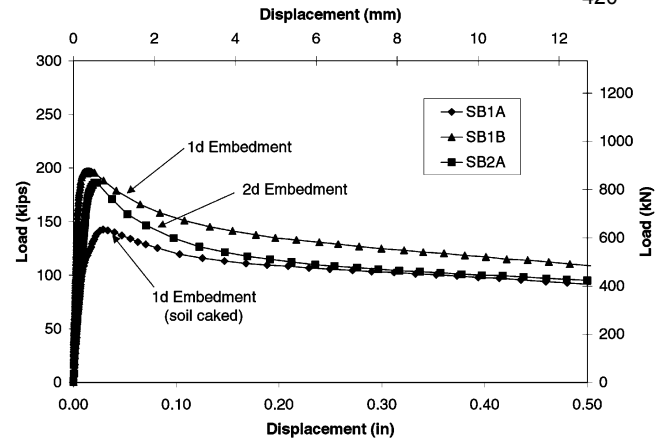


Fig. 10—Bentonite slurry-filled cofferdam test results.

somewhat linearly with embedment depth up to 1d. This can be noted in both peak and residual values when comparing the 0.5d and 1d test results. With longer embedment depths (1.5d), little increase in average capacity was observed (10% in controls and 17% in water). This was also noted in Table 2 where average bond strengths decreased 18% (1.31 to 1.07 MPa) and 27% (1.40 to 1.02 MPa) in the water and control specimens, respectively, for the same increased embedment depths.

Figure 10 shows the pullout response of the piles cast in the bentonite slurry-filled cofferdam. Therein, several differences were introduced due to anticipated decreases in bond strength: 1) 0.5d embedment was not used; 2) the 1.5d was increased to 2d; and 3) soil caking was applied to some 1d specimens. The effects of embedment were similar in this set of tests as no significant additional pullout capacity was realized with the additional bond area from 1d to 2d embedment. This is supported by the moderate 19% average increase in pullout with a 100% increase in embedment (670 to 797 kN). This decreased bond efficiency is further illustrated by the 41% decrease in the average bond strength in Table 2 (0.88 to 0.52 MPa). The effect of soil caking was less significant than that of the embedment depth most probably due to the scouring action during the seal slab placement. In general, the bentonite condition produced larger variations in the measured bond values. The overall findings, however, indicate that the bond between steel and seal slabs is significantly higher than specified in design codes.

## DISCUSSION

The goal of the study was to determine the interface bond between steel piles and seal slabs that had been cast in accordance with existing construction specifications (concrete piles were also tested). As the FDOT specifications allow a 72 h cure period for the seal slab, the need to develop a scheme that met the requirement for rapid testing without compromising the results was of critical importance. Pullout testing was used and several innovative measures adopted to expedite the testing process.

In the model study, 36 tests (28 concrete and eight steel) were completed within 8 h following the 72 h cure period. During this time, no changes in concrete strength were observed. In the full-scale tests, greater time was required to complete the testing. An important constraint was access to heavy lifting equipment (and an operator) to move the pull-out frame after every test. All 32 tests (16 concrete and 16

**Table 3—Allowable bond stresses**

Material	Condition	$F_b$ , kPa
Steel	Salt/fresh water	1000
	Bentonite	350

steel), however, were completed within 10 days of the casting of the seal slab. As concrete strengths were evaluated throughout the test period, the relationship between the interface bond and concrete strength was used to normalize the bond values. Taking into consideration the totality of the study, the model and full-scale results provide a good indication of the magnitude of the interface bond that develops between the seal concrete and piles.

The results from the model tests gave higher bond values than those from the full-scale tests (Table 1 and 2). Similar trends were observed in the tests on the prestressed piles,<sup>3</sup> though the differences were much smaller. This is most likely because the surfaces of the steel piles in the full-scale tests were smoother compared with those used in the model tests. In contrast, the concrete surfaces in both model and full-scale tests were similar.

As with prestressed piles, the results clearly indicate that the variation in the interface bond is nonlinear since the pullout load was not proportional to the embedment depth. Unfortunately, this distribution could not be measured without introducing surficial anomalies due to instrumentation. In the concrete piles where strain gages could be embedded during casting, however, this relationship could be ascertained.<sup>3</sup> The nonlinearity in the interface shear distribution was indirectly incorporated in the proposed recommendation by defining an effective embedment depth. Embedment in excess of this effective depth did not contribute significantly towards the total resistance (Fig. 8 to 10).

### CONCLUSIONS

This study presents results from an experimental study that attempted to determine the interface bond stress that developed between seal concrete and steel piles. Two series of tests were conducted. In the first series, a 1/3-scale model was fabricated and tested. Three different placement conditions were investigated: displacement of fresh water, salt water, and bentonite slurry for two different embedment depths. In the second series, full-scale tests were conducted for two different conditions: fresh water and bentonite slurry. In all cases, results were compared against controls where no fluid was displaced. Seal slabs were cast using concrete delivered by ready-mix plants and conformed to Class III concrete in current FDOT specifications. The concrete was allowed to cure for at least 72 h prior to testing as permitted by existing specifications. The following conclusions may be drawn:

1. Bond stresses determined experimentally were significantly higher than set in current specifications. Average values obtained from the full-scale tests varied between 1.1 and 1.3 MPa for fresh water displacement and 0.5 and 0.9 MPa for bentonite displacement. The lowest value obtained was for piles embedded in bentonite cofferdam at depth  $2d$ ;
2. Bond strength varied with embedment depth as indicated by both the model and full-scale test results. This implies that

thicker seal slabs cannot develop full bond capacity simultaneously along the entire bonded area beyond a maximum length. Instead, they develop full capacity over shorter bonded lengths dependent on the concrete shear strain limit value with respect to the elongation of the pile. In this case it was shown that embedment depths in excess of  $1d$  were ineffective in supplying additional pullout capacity;

3. The results of the study confirm the poorer interface bond for steel surfaces compared with concrete, where  $1d$  average values for water and bentonite conditions were 2.7 and 2.5 MPa, respectively;<sup>4</sup> and

4. Variations between the model-scale and full-scale test results can be in part attributed to the surface roughness of the as-delivered steel piles. The model piles were partially oxidized, whereas the full-scale piles had never been exposed to an outdoor environment prior to placement. The recommended values are based on the full-scale test results that are therefore conservative.

### RECOMMENDATIONS

Loads supported by the bond between seal concrete and steel piles (section depth  $d$ , perimeter  $p$ , embedded depth  $D$  in seal slab) may be determined from the allowable bond stress  $F_b$  listed in Table 3. This stress may be assumed to be uniform over an effective area  $A_e$  given by

$$A_e = pD \text{ if } D < d$$

$$A_e = pd \text{ if } D > d$$

In the latest Florida "Design Guidelines,"<sup>7</sup> allowable interface shear values have been greatly increased based on the findings presented in this paper.

### ACKNOWLEDGMENTS

This investigation was carried out with the financial support of the Florida Department of Transportation. The authors especially acknowledge the contribution of Hayward Baker, Inc. in Tampa, Fla., in the full-scale testing as well as Rudy. However, the opinions, findings, and conclusions expressed in this publication are those of the writers and not necessarily those of the Florida Department of Transportation.

### REFERENCES

1. "Standard Specifications for Highway Bridges 13th Edition," American Association of State Highway and Transportation Officials, Washington, D.C., 1983.
2. "Structural Design Guidelines," Section 4.18, Topic No: 625-020-150c, Florida Department of Transportation, Tallahassee, Fla., July 1998, pp. 4-12.
3. Mullins, G.; Sosa, R.; Sen, R.; and Issa, M., "Seal Slab Prestressed Pile Interface Bond from Full-Scale Tests," *ACI Structural Journal*, V. 98, No. 5, Sept.-Oct. 2001, pp. 743-751.
4. Mullins, G.; Sosa, R.; and Sen, R., "Seal Slab/Pile Interface Bond," *Final Report* submitted to Florida Department of Transportation, June 2000, 151 pp.
5. Wu, Z., "Studies of Bond of Cast-in-Place Concrete to Other Surfaces," Masters' thesis, Department of Civil and Environmental Engineering, University of South Florida, Tampa, Fla., Aug. 1999.
6. "Standard Specifications for Road and Bridge Construction," Florida Department of Transportation, State Specifications Office, Tallahassee, Fla., 1999.
7. "Structural Design Guidelines," Florida Department of Transportation, Table 5.3, Tallahassee, Fla., 2000.



## **Pressure Grouting Drilled Shaft Tips: Full-Scale Research Investigation for Silty and Shelly Sands**

Steven D. Dapp\* and Gray Mullins\*\*

\*Graduate Researcher, University of South Florida, Department of Civil and Environmental Engineering, 4202 East Fowler Ave. ENB 118, Tampa, FL 33620-5350; PH 813-974-2275;

\*\*Assistant Professor, University of South Florida, Department of Civil and Environmental Engineering, 4202 East Fowler Ave. ENB 118, Tampa, FL 33620-5350; PH 813-974-5845; gmullins@eng.usf.edu

### **Abstract**

The tip (toe) capacity of drilled shafts in sands can often be many times greater than the side shear component; however, the tip capacity is often discounted from the total shaft capacity due to the relatively large displacements required to mobilize this end bearing component. Concerns of soil disturbance at the shaft tip (i.e. insitu stress relief) and cleanliness also discourage the use of end bearing as available capacity within any reasonable service load displacement criteria. Pressure grouting the shaft tip has been successfully employed throughout the world as a method of mitigating these conditions. However, there is an apparent lack of ration design procedures and construction guidelines for its use. In cooperation with the Florida Department of Transportation, the University of South Florida is researching the effects of post-grouting on shaft capacity. This paper describes two sites at which full scale shafts have been tested: (1) five shafts, including one control shaft, tipped in a shelly sand, and (2) three shafts, including one control shaft, tipped in a silty sand. The results of these tests show that significant tip capacity improvement can be realized through the use of pressure grouting drilled shaft tips.

### **Introduction**

When designing for drilled shaft capacities in sandy soils, engineers typically must significantly reduce end bearing capacity or even discount it altogether to account for potential soft toe conditions. Even in ideal conditions, end bearing is typically not mobilized before service load displacement criteria are exceeded. The bulk of the capacity is therefore derived from side friction which can be developed with relatively small displacements. This is particularly a problem for larger shafts in cohesionless soils which must displace even further to fully develop tip capacity (e.g. AASHTO tip capacities are based on top of shaft displacements of 5% of the shaft diameter). Consequently, the end bearing strength component, which may be on the order of up to twenty times the side friction component, is unavailable to the shafts useful capacity.

As the end bearing component of drilled shafts is highly under-utilized, mechanistic procedures to integrate its contribution have been developed using pressure grouting. Pressure grouting the tips of drilled shafts has been successfully used world wide to precompress soft debris or loose soil relaxed by excavation (Bolognesi and Moretto, 1973; Stoker, 1983; Bruce, 1986; Fleming, 1993; Mullins et. al, 2000). However, the absence of its use in the United States is probably due to associated uncertainties and the lack of a rational design method. Recognizing this shortfall, the Florida Department of Transportation issued a request for proposals (RFP) to assess the effect of pressure grouting on drilled shaft tip capacity. In June 1999, the University of South Florida commenced a two-year research program to investigate this technique.

The overall objectives of this study were to quantify the improvement that could be developed by pressure grouting the tip of drilled shafts and to develop design guidelines for its use. This paper discusses the results relating to the first objective, the pressure grouting and load testing of drilled shafts in sandy soils. A full discussion of the results of the entire research can be found elsewhere (Mullins, et. al, 2001).

### **Research Program**

The research program outlined below is only a portion of a larger project which also included small scale (1:10) laboratory testing in a frustum confining vessel, computer modeling of pressure grouted drilled shaft tips, and two 1.22 m (4.0 ft.) diameter shafts tipped in cemented coquina. This portion discusses the field results from six 0.61 m (2.0 ft.) diameter drilled shafts cast, pressure grouted, and subsequently load tested. The performance of the pressure grouting is based on comparisons with two additional ungrouted control shafts.

A total of eight shafts were constructed, pressure grouted, and load tested at two sites located on a large property (20 acres) in Clearwater, Florida. Shafts at Site I were tipped in a shelly sand. A dimensioned layout of Site I showing the shaft positions, CPT soundings, and SPT borings conducted within the Site are provided in Figure 1; typical CPT and SPT data are shown in Figure 2. Shafts at Site II were tipped in a silty silica sand. The layout of Site II is shown in Figure 3, while typical CPT and SPT data are shown as Figure 4.

The shafts were each 0.61 m (2.0 ft) diameter and were all approximately 4.57 m (15.0 ft.) long. Five shafts, including one control, were tested at Site I; three shafts, including one control, were tested at Site II. All pressure grouting was conducted using an auger style grout pump. All of the shafts were then load tested using a 4 MN Statnamic device with a hydraulic catch mechanism. The results from the grouted shafts have been compared their respective control shafts to assess the load capacity improvement obtained from the tip grouting process.

### **Site Investigation**

These sites were chosen and the tip elevations set, based upon an exploratory investigation program which looked for the types of soil most likely to be improved with tip grouting (Mullins et. al, 2000), loose to medium dense sands. The sand particles at these two sites span the diverse range that can be encountered in cohesionless soils (shelly to silty). The shelly of Site I was very angular and flat, while the silty silica sand was very smooth and round.

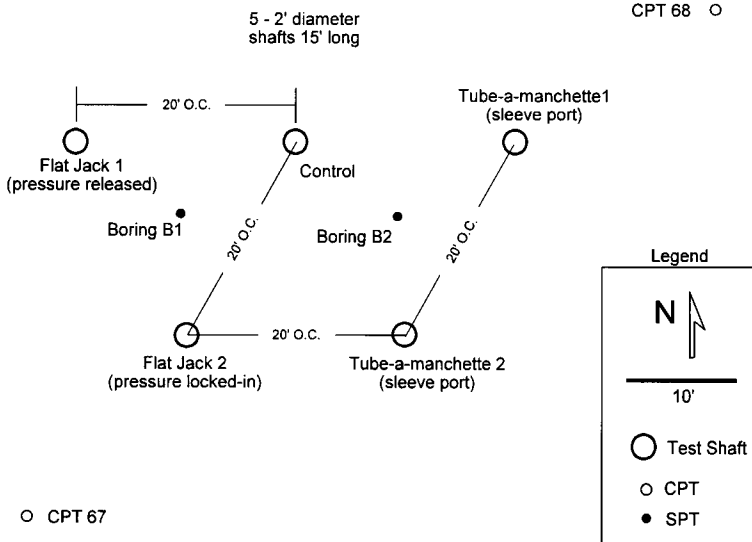


Figure 1. Site I (Shelly Sand) Layout

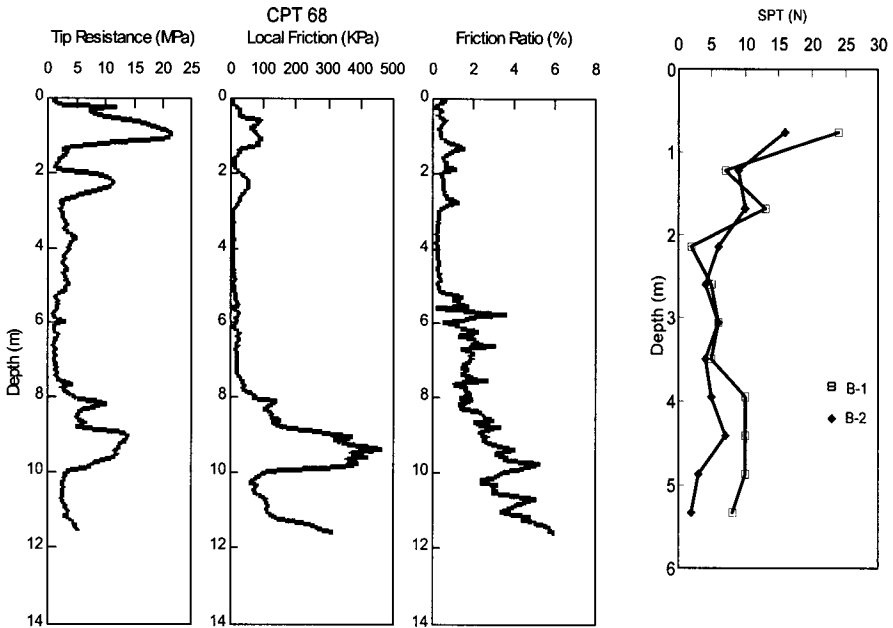


Figure 2. Site I (Shelly Sand), CPT and SPT Data.

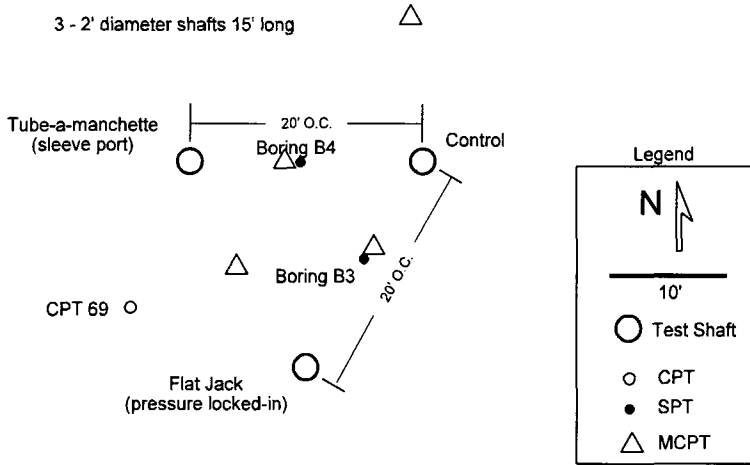


Figure 3. Site II (Silty sand) Layout

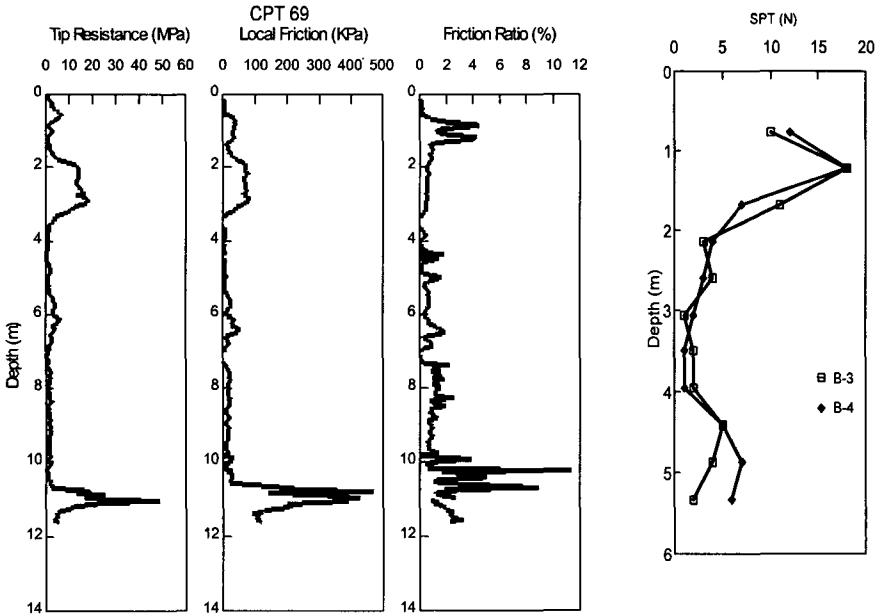


Figure 4. Site II (Silty Sand), CPT and SPT Data.

### Grout Distribution Systems

Both flat-jack and sleeve-port type grouting apparatus were tested. A flat-jack consists of a steel plate wrapped in a rubber membrane thus providing a debonded pressurizing surface beneath the shaft tip. Sleeve-port systems use a rubber tube over a perforated pipe section which provides a smaller grouting area, but more flexibility in staged grouting applications. A summary of the grout distribution systems used is contained in Table 1. Two flat-jack devices had the grout pressure locked in during the grout cure, while one did not. Two sleeve-port devices had a steel plate above them, while one did not.

Table 1. Grouting Apparatus.

		Site I (Shelly Sand)	Site II * (Silty Sand)
Control Shaft (no Grouting)		1	1
Flat - Jack	Release Grout Pressure	1	
	Hold Grout Pressure	1	1
Sleeve-Port	With Steel Plate Above	1	1
	No Plate	1	
Total Shafts		5	3

\* The two tip grouted shafts of Site II (only), were also skin grouted.

**Flat-Jacks.** All flat-jacks were identical in construction; however, one in Site I was allowed to release grout pressure immediately after grouting. The remaining two, one in Site I and one in Site II, had the grout pressure locked in with the use of a ball valve in the grout supply lines during the grout cure. Figure 5 illustrates the flat-jack tip grouting apparatus.

A scuff ring was incorporated into the design of the flat-jacks, which protected the 0.8 mm ( $1/32$  in.) thick natural gum rubber membrane where it wraps around the edge of the plate. This was to ensure durability in the event that the cage was improperly handled during placement. Further, the scuff ring had tabs attached to the top which allowed for the ring to be bolted to the steel plate, therefore providing a better seal between the rubber membrane and the top plate (rather than just relying on the rubber cement contact adhesive alone). The flat-jack apparatus was tied into the reinforcing cage, and securely fixed in place.

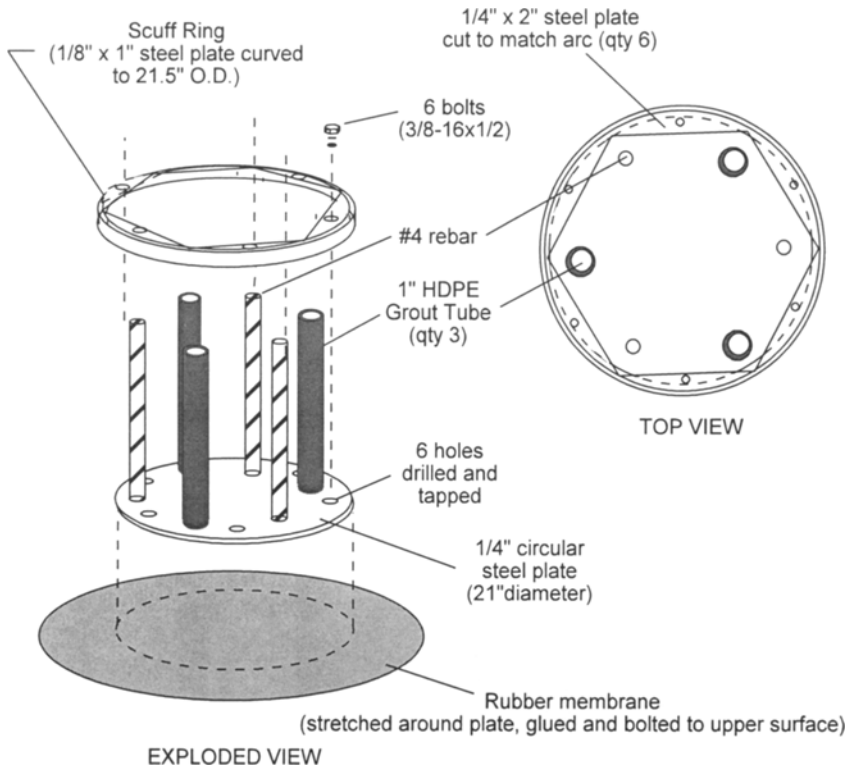


Figure 5. Flat-Jack Grouting Apparatus.

**Sleeve-Ports.** Sleeve-port systems were identical in construction with the exception that one in Site I did not have a steel plate above it, as is shown in Figure 6. Note that all the sleeve ports locked in the grout pressure due to the nature of their design. The two tip grouted shafts in Site II were also skin grouted, while their respective control shaft was not. The skin grouting of Site II shafts provided more reaction during tip grouting that would not have otherwise been available. Discussion of skin grouting will otherwise not be addressed here.

The grout delivery pipe consisted of a 254 mm (10 in.) section of 19mm ( $\frac{3}{4}$  in.) galvanized steel pipe with 7 pairs of diametrically opposed 6mm ( $\frac{1}{4}$  in.) grout delivery ports drilled through both pipe walls at any location along the pipe. These 7 sets of ports alternated in circumferential position by  $90^\circ$ , and were equally spaced along the length of the pipe. A natural gum rubber tube (the sleeve) with an initial inside diameter of approximately 24mm ( $\frac{15}{16}$  in.), and a wall thickness of 6mm ( $\frac{1}{4}$  in.) was then pulled over the grout delivery pipe,



with the use of soapy water as a lubricant. Alternately, baby powder and compressed air can be used to install the sleeve. The elastic stretch in the rubber tube was needed to seal the grout delivery system during shaft construction, and acts as a one way valve to allow for staged grouting. Often in industry, electrical tape will be wrapped around the edges of the rubber tube to ensure that the pipe is not infiltrated by concrete/cement during shaft construction.

When the option of a steel plate above the sleeve-port apparatus was utilized, each plate had four 38mm (1-1/2 in.) diameter holes drilled through. The male fitting from the grout pipe would then simply fit through the hole in the plate and screw into the female 90° elbow ends of the sleeve-port. The system was constructed in this way such that the plate assembly could be tied into the cage via its reinforcing bar tie attachments, and thus its weight (or any forces experienced during placement) would not be supported by the pressure fittings to the sleeve-port.

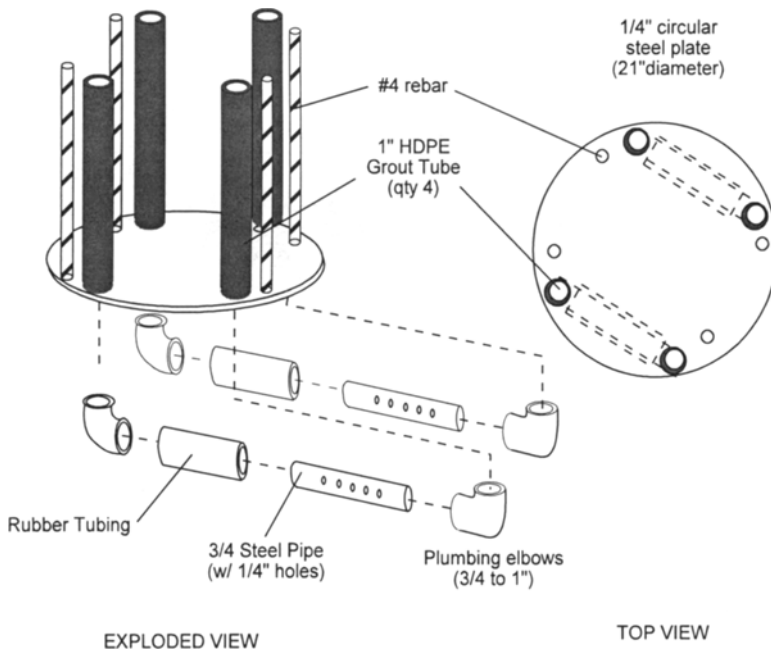


Figure 6. Sleeve-Port Grouting Apparatus (with Optional Steel Plate).

### Data Acquisition and Instrumentation

Two separate data acquisition systems were utilized simultaneously during the test, and both uploaded their respective data to a common laptop computer. The two systems used during the test were a MEGADAC manufactured by Optim Electronics, and the Foundation Pile Diagnostic System (FPDS) made by The Netherlands Organization (TNO). A variety of transducers were utilized, in both the grouting and load testing operations. Table 2 shows this system arrangement, and the transducers that were monitored during grouting and load testing operations.

Table 2. Data Acquisition and Instrumentation.

	GROUTING	LOAD TESTING
Data Acquisition System	laptop, Megadac	laptop, FPDS, Megadac
Top of Shaft	LVDT, grout pressure transducer	load cell, accelerometer, laser displacement sensor
Along Shaft Length	strain gages	strain gages
Shaft Tip	strain gages, tension tell-tales	strain gages,

The total load imparted to the top of shaft by the Statnamic device is directly measured by a load cell built into the Statnamic piston mounted to the top of shaft. A laser sensor is also built into this piston which provides a direct measurement of displacement during load testing. Accelerometers are used to confirm displacement and provide direct measurements of acceleration.

Top of shaft displacement during grouting operations was directly measured utilizing linear voltage differential transformers (LVDT's), while bottom of shaft displacements were made with linear cable potentiometers attached to tension tell-tales. Grout pressure was monitored by a pressure gage in-line with the grout supply hose. A rubber membrane and grease pocket within the fitting protected the instrument from the grout.

Strain gages in groups of three were embedded at two levels within the shaft at approximately 0.46 m (1.5 ft.) and 3.2 m (10.5 ft.) from the shaft tip. These strain measurements yield the force at these levels using a composite shaft modulus determined by concrete strengths (concrete cylinder breaks), and the area fraction of steel reinforcement.

The tension tell-tales consisted of a 12mm casing ( $\frac{1}{2}$  in. schedule 40 PVC pipe), capped at the bottom end, and a stainless steel braided cable strung through the center of the casing. The steel braided cable was secured to the bottom end of the casing through the end cap, clamped,

and sealed. Ample length was left outside the end cap and looped to provide development length for tension that would be put upon it during their use in grouting. Significant elastic shaft shortening was not expected during grouting at these sites, nor did it occur.

### Shaft Construction

The vertical reinforcement consisted of six 25 mm (# 8) reinforcement bars equally spaced about the perimeter. The stirrup reinforcement consisted of 16 mm (# 5) reinforcement bars, equally spaced every 0.46 m (1.5 ft.). All reinforcing bars used were Grade 60. The finished cages were 4.42 m (14.5 ft.) in length, and had an outside diameter at the stirrups of 0.46m (1.5 ft.).

The grout pipes were made from 25mm (1 in.) high density polyethylene (HDPE) tubing (CTS SDR-9). A 25mm (1 in.) male pipe thread fitting was secured at either end of the grout pipe made of brass (C84-44 1" CTS Compression MIPT Adapter) and had thin stainless steel inserts (#52 Stainless Insert) to keep the tubing from being crushed by the pipe fitting. These materials are common and readily available. This male fitting could suitably connection to either type of grouting apparatus used. This system has a working pressure rating of 1000-1400 kPa (150-200 psi), and was more than adequate for the grouting pressures experienced on this site. This system of continuous rolled tubing was easy to install, and would be especially convenient with long multi-section reinforcing cages. Figure 7 shows completed cages with the various types of grouting apparatus tied in.

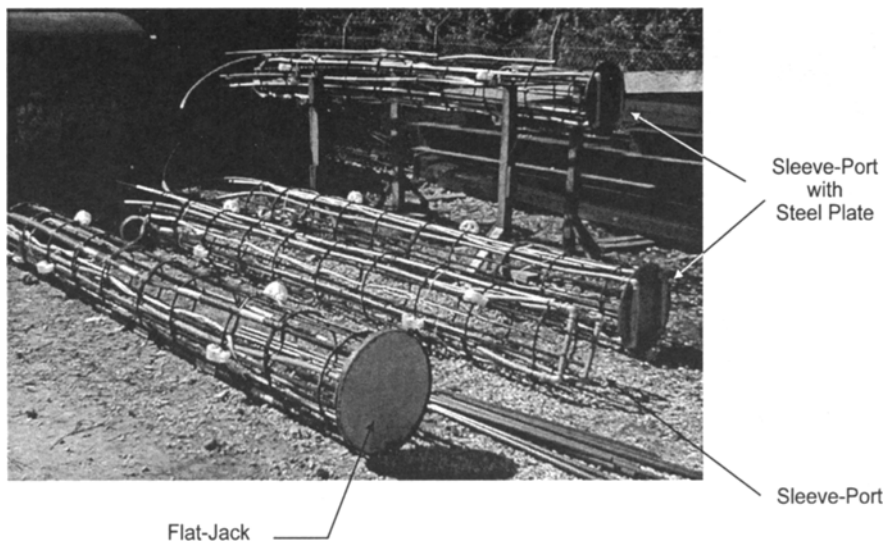


Figure 7. Reinforcing Cages Complete with Instrumentation and Grouting Apparatus.

A truck mounted Texoma 700 drill rig was utilized to excavate the shafts of Site I, while a track mounted BG-7 drill rig was used to excavate Site II. Both were excavated using a synthetic slurry. Both Site I and II utilized the same drill auger in construction. A clean-out bucket was not used during construction as it would not produce a significant improvement in tip condition, nor would the use of standard down-hole or air-lift pumps. Even under ideal conditions it is essentially impossible to thoroughly "clean out" any shaft excavation at the tip, as is customary with rock socketed tips, as any action taken simply tends to further upset the excavation. A benefit of tip grouting is that this condition is mitigated, and is a point that this study confirmed. A Hitachi 60 ton track mounted hydraulic crane was used to pick and set the cages.

Site I Flat-Jack 2 (locked-in pressure) was set nearly 0.3 m (1.0 ft.) too high due to a tight tolerance between the plate and borehole. Careful observations of the grouting of this shaft confirmed that 51 liters (1.8 ft.<sup>3</sup>) of grout was needed to fill the void under the flat-jack plate before any grout pressure above that required to pump the grout through the lines could be detected. This represents a volume that would be equivalent to a column the same diameter as the flat-jack by 0.22m (0.7 ft.) high. As a direct result, an unanticipated variable was tested between the two flat-Jacks of Site I; the effect of varying amounts of soft debris and/or voids below the flat-jack grouting apparatus. Results show that this condition was mitigated by the tip grouting procedure, this grout volume of 51 liters (1.8 ft.<sup>3</sup>) is not included in the subsequent analysis.

### **Grouting and Load Testing**

The grouting at these sites was then accomplished using a helical style grout pump and paddle type mixer, as shown in Figure 8. The pump was adequate, as shaft uplift or grout volume proved to be the limitation at all test shafts. In all cases the shaft concrete was allowed to gain sufficient strength before grouting operations commenced. The grout mix utilized was a water-cement slurry (Type I and II cement) with a water to cement ratio of 0.5. The grouting lines of both sleeve-port and flat-jack apparatus were gently flushed with grout before the return lines were capped and grout pressure was applied.

Prior to any grouting work, the sleeve-port apparatus on these sites were "burst" open using water pressure. This was done the day following concrete placement, as is common practice, such that the concrete had set up, yet had not gained significant strength. The intent of this action is to open a path for subsequent grouting, which may be performed at a later date when the shaft has reached acceptable strength. The volumetric flow during this process should be minimal to reduce the soil disturbance. The helical style grout pump was first used; however a small widely available pressure washer was better suited for this task.

The load testing was carried out with the use of a 4 MN Statnamic device after the grout was given time to obtain sufficient strength. A minimum of three load cycles were performed on each test shaft. The hydraulic catch mechanism made reloading of the shaft proceed rapidly, as all three load cycles would typically occur within a 30 minute time span. In all cases the test shafts were displaced many times more than the ultimate capacity displacement, such that the load vs. displacement response would be fully defined. Figure 9 shows a test in progress.

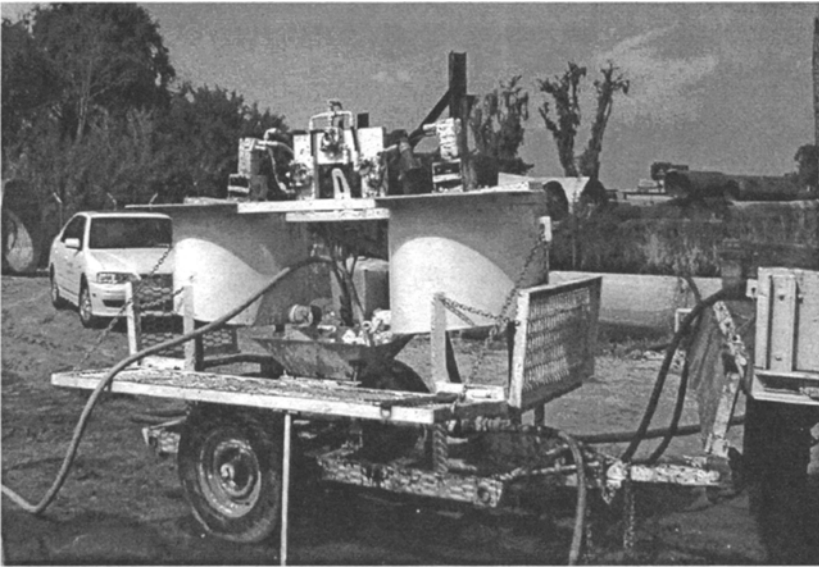


Figure 8. Trailer Mounted Grout Mixing and Pumping System.



Figure 9. Statnamic Load Test in Progress.

## Results

Grout pressure and shaft displacement were directly measure as previously described. The grouting rate should be slow enough to build pressure, and not simply hydrofracture the soil. The grout consistency can be adjusted to control this aspect. The maximum sustained grout pressure, peak upward displacement, and total grout volume for each of the grouted shafts are listed in Table 3. In general, the flat-jacks have a lower grout take than the sleeve-ports due to the flat-jacks acting as a confined pressure cell. Conversely, the grout from the sleeve-ports is in intimate contact with the surrounding soil matrix, and thus has a greater potential to migrate away from the immediate tip area.

Table 3. Pressure Grouting Data Summary.

Site	Grout Delivery Mechanism	Shaft Designation	Grout Volume liters (ft. <sup>3</sup> )	Grout Pressure kPa (psi)	Shaft Uplift mm (in)
Site I (Shelly Sand)	Flat-Jack	S1-FJ1 (release press.)	50 (1.75)	586 (85)	3.78 (0.149)
		S1-FJ2 (hold press.)	107 * (3.79)	462 (67)	4.83 (0.190)
	Sleeve-Port	S2-SP1 (with plate)	165 (5.82)	1138 (165)	2.74 (0.108)
		S2-SP2 (no plate)	86 (3.05)	1220 (177)	1.42 (0.056)
Site II (Silty Sand)	Flat-Jack	S2-FJ (hold press.)	217 (7.65)	683 (99)	3.81 (0.150)
	Sleeve-Port	S2-SP (with plate)	180 (6.34)	862 (125)	1.23 (0.043)

\* Does NOT include grout volume to fill void left under this flat-jack apparatus.

The “bottom-up” load displacement response of a shaft is obtained when combining these time traces with the load based upon strain gage data, as is consistent with bi-directional load testing procedures. The measured displacement is the shaft uplift, and the load is the side friction component, which is equal but opposite to that of the end bearing component. In order to compare the grout pressure readings to this curve, a shaft tip load is also calculated by multiplying the pressure reading by the shaft tip cross-sectional area.

Typical shaft response during grouting utilizing flat-jack apparatus is presented as Figure 10. The shaft tip loads calculated by means of both the strain gage and grout pressure data correspond extremely well to each other, even at the beginning of the grouting cycle. This is attributed to the flat-jack apparatus design allowing the grout to disperse rapidly across the



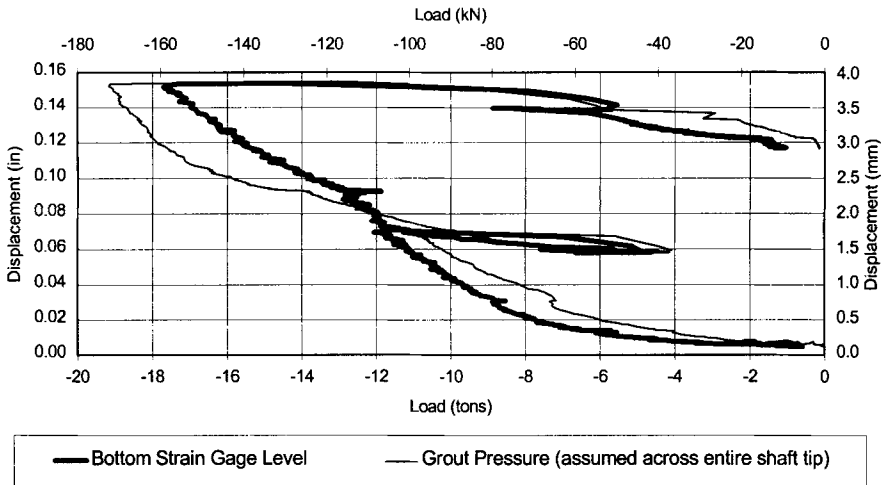


Figure 10. Typical Flat-Jack Tip Grouting Load vs. Displacement.

entire shaft tip between the top plate and rubber membrane. This illustrates the strong advantage of a flat-jack apparatus in a production setting providing a “proof test” of the shaft capacity. The load displacement response of every grouted shaft can be obtained by simply utilizing top of shaft displacements and grout pressure. If the shafts are significant in length, the elastic shortening must be considered.

An ungrouted control shaft, was constructed and load tested at both Sites I and II, such that the improvement in load capacity due to pressure grouting could be assessed by direct comparison to its respective control shaft. Figure 11 presents a typical shaft load comparison. Both the top and tip of shaft response is shown for both a grouted and ungrouted control shaft. As most tip resistance designs are based on an assumed displacement of 5% of the shaft diameter, (e.g. Reese and O’Neill, 1988), the improvement in shaft tip and total capacity is evaluated at displacements of 5% of the shaft diameter for all the test shafts, as summarized in Table 4. The grouted improvement is defined by the following:

$$\% \text{ Improvement} = \frac{(\text{Capacity}_{\text{grouted pile}} - \text{Capacity}_{\text{control}})}{\text{Capacity}_{\text{control}}} * 100\%$$

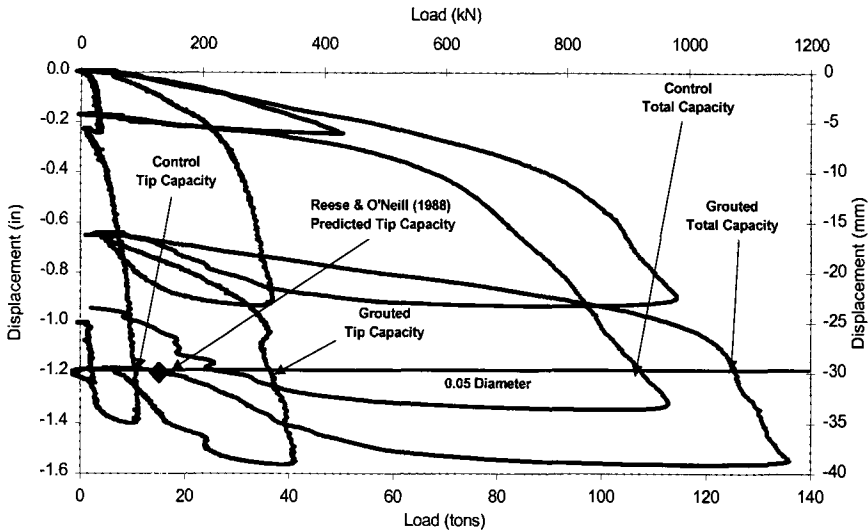


Figure 11. Load Test Comparison of Typical Grouted Shaft to Control Shaft.

Table 4. Load Performance at a Displacement of 5% Shaft Diameter.

Site	Grout Delivery Mech.	Shaft Desig.	Total Load kN /(tons)	Tip Load kN /(tons)	Tip Contrib. (%)	Tip Improve. (%)	Total Improve. (%)
Site I (Shelly Sand)	Control	S1-CON (no grout)	961 (108)	98 (11)	10	N/A	N/A
	Flat-Jack	S1-FJ1 (release press.)	1094 (123)	347 (39)	32	255	14
		S1-FJ2 (hold press.)	1210 (136)	365 (41)	30	273	26
	Sleeve-Port	S2-SP1 (with plate)	1379 (155)	507 (57)	37	418	44
		S2-SP2 (no plate)	1450 (163)	569 (64)	39	482	51
Site II (Silty Sand)	Control	S2-CON (no grout)	890 (100)	62 (7)	7	N/A	N/A
	Flat-Jack	S2-FJ (hold press.)	1290 (145)	463 (52)	36	643	45
	Sleeve-Port	S2-SP (with plate)	1397 (157)	587 (66)	42	843	57

The improvement for the shaft tip capacity is further evaluated in Figure 12 where it is plotted for all measured displacements until ultimate capacity is reached. The greatest amount of tip improvement occurred in Site I at a displacement of only 2% of the shaft diameter, 12 mm (0.48 in.), and in Site II at a displacement of 4% to 5% of the shaft diameter, 24 mm (0.96 in.) to 30 mm (1.20 in.). Undoubtedly, this was due to the tip grouting locking in some amount of negative side shear, and thus more readily transferring the subsequent load to the shaft tip which was also prestressed in compression. Although the total shaft improvement is more modest, the increased stiffness of the grouted shaft aides in meeting service limit displacements.

### Summary

The field results of a two year, full-scale load testing program have been presented identifying the magnitude of improvement that can be obtained by pressure grouting drilled shaft tips. Three grout distribution systems were used: (1) flat-jack, (2) sleeve-port, and (3) sleeve-port and plate. A total of eight test shafts were constructed and tested at two sites, Site I (shelly sand) and Site II (silty sand). All grouted shafts showed increased tip capacity, *regardless of distribution system*, when compared to ungrouted control shafts. Sleeve-port systems developed higher grout pressures, while flat-jack systems produced more uniform tip loading and higher uplift displacements. The tip improvement (at 0.05 shaft diameters of displacement) for sleeve-port systems was 455% and 843% for Sites I and II, respectively. Flat-jack systems produced 264% and 643% improvement, similarly. Although not presented herein, a design procedure has been developed based on the results of this research which is being incorporated into the FDOT design guidelines.

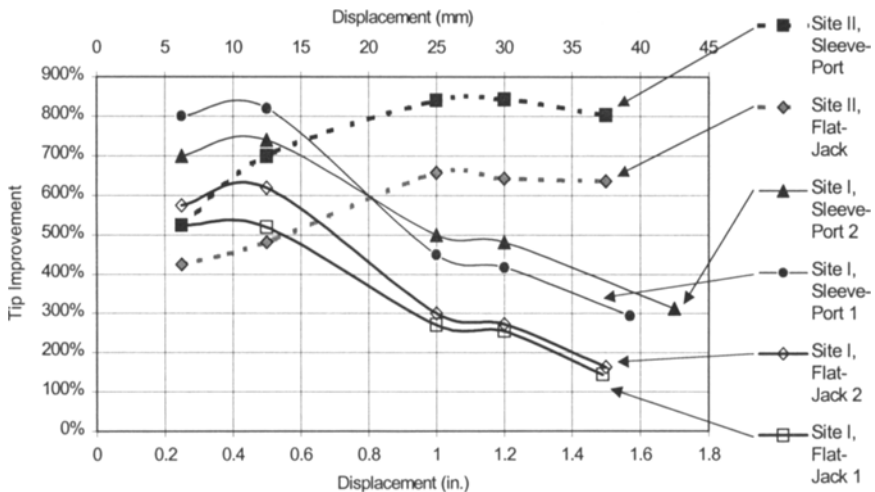


Figure 12. Grouted Tip Capacity Improvement vs. Shaft Displacement.

### Acknowledgments

The authors would like to acknowledge and thank the following groups for the materials and services that they provided. The Florida Department of Transportation funding and awarding this research contract to the University of South Florida, and providing much of the CPT and SPT investigation. Coastal Caisson Corp. provided the site and made available lifting, moving, and excavation equipment that was essential for this study. Earth Tech, Inc. provided the grouting equipment and supplies. Applied foundation Testing, Inc. supplied the Statnamic test fuel and trucking required to transport the University of South Florida's 4MN hydraulic-catching Statnamic device.

### References

- Bolognesi, A. J. L. and Moretto, O. (1973) "Stage Grouting Preloading of Large Piles on Sand" Proceedings of 8<sup>th</sup> ICSMFE, Moscow.
- Bruce, D.A. (1986), "Enhancing the performance of large diameter piles by grouting," Parts 1 and 2, *Ground Engineering*, May and July, respectively.
- Bruce, D. A., Nufer, P. J., and Triplett, R. E. (1995) " Enhancement of Caisson Capacity by Micro-Fine Cement Grouting - a Recent Case History" ASCE Special Publication 57, Verification of Geotechnical Grouting.
- Dapp, S. (2001) Pressure Grouting of Drilled Shaft Tips in Sand. Doctoral dissertation submitted to the University of South Florida, May 2001.
- Fleming, W. G. K. (1993) "The Improvement of Pile Performance by Base Grouting" Proceedings of the Institution of Civil Engineers, London.
- Mullins, G., Dapp, S., and Lai, P., (2000) "Pressure grouting Drilled Shaft Tips in Sand". *New Technological and Design Developments in Deep Foundations*, Dennis, N. D., et al. (ed.), ASCE, Geo Institute, Vol. 100, pp 1-17.
- Mullins, G., Dapp, S. Frederick, E. and Wagner, R. (2001). "Pressure Grout Drilled Shaft Tips", *Draft Report* submitted to Florida Department of Transportation, April, pp. 257.
- Stocker, M.F. (1983), "The influence of post grouting on the load bearing capacity of bored piles," Proceedings, *Eighth European Conference on Soil Mechanics and Foundation Engineering*, Helsinki, May.

## **Advancements In Statnamic Data Regression Techniques**

Gray Mullins\*, Christopher L. Lewis\*\*, and Michael D. Justason\*\*\*

*\*Assistant Professor, University of South Florida, Department of Civil and Environmental Engineering, Tampa, FL 33620, [gmullins@eng.usf.edu](mailto:gmullins@eng.usf.edu)*

*\*\*Geotechnical Engineer, Applied Foundation Testing, Green Cove Springs / Tampa, FL 33610, [clewis@testpile.com](mailto:clewis@testpile.com)*

*\*\*\*Senior Engineer, Berminghammer Foundation Equipment, Hamilton, ON., LBL4Z9, [mjustason@berminghammer.com](mailto:mjustason@berminghammer.com)*

### **Abstract**

Until recently, the analysis of Statnamic test data has typically incorporated the “Unloading Point Method” (Middendorp et. al, 1992) to determine an equivalent static capacity. The Unloading Point (UP) method requires that the foundation move as a rigid body, thus excluding stress wave phenomenon from the analysis. If this requirement is met the foundation capacity can be determined using this simplified method. However, many foundations do not meet the UP criteria (e.g. fixed end or relatively long piles) and have proven difficult to analyze without more complex techniques. This paper presents a new analysis method that uses measured strain data as well as the standard Statnamic test data to determine foundation capacity. This new method discretizes the foundation into smaller segments that each meet the rigid body criteria of the UP method. Thereby, a more refined inertia and viscous damping evaluation can be implemented that individually determines the contributions from the various segments. This approach, termed the “Segmental Unloading Point” (SUP) method, is developed herein and then demonstrated with results from full-scale Statnamic test data.

### **Introduction**

Since its inception in 1988, Statnamic testing of deep foundations has gained popularity with many designers largely due to its time efficiency, cost effectiveness, data quality, and flexibility in testing existing foundations. Where large capacity static tests may take up to a week to set up and conduct, the largest of Statnamic tests typically takes no more than a few days. Further, multiple smaller-capacity tests can easily be completed within a day. The direct benefit of this time efficiency is the cost savings to the client and the ability to conduct more tests within a given budget. Additionally, this test method has boosted quality assurance by giving the contractor the ability to test foundations thought to have been compromised by construction difficulties without significantly affecting production.

Statnamic testing is designated as a rapid load test that uses the inertia of a relatively small reaction mass instead of a reaction structure to produce large forces. Rapid load tests are differentiated from static and dynamic load tests by comparing the duration of the loading

event with respect to the axial natural period of the foundation ( $2L/C$ ), where  $L$  represents the foundation length and  $C$  represents the strain wave velocity. Test durations longer than  $1000 L/C$  are considered static loadings and those shorter than  $10 L/C$  are considered dynamic (Janes et al., 2000; Kusakabe et al., 2000). Tests with a duration between  $10L/C$  and  $1000 L/C$  are denoted as rapid load tests. The duration of the Statnamic test is typically 100 to 120 milliseconds, but is dependant on the ratio of the applied force to the weight of the reaction mass. Longer duration tests of up to 500 milliseconds are possible but require a larger reaction mass.

The Statnamic force is produced by quickly-formed high pressure gases that in turn launch a reaction mass upward at up to twenty times the acceleration of gravity. The equal and opposite force exerted on the foundation is simply the product of the mass and acceleration of the reaction mass. It should be noted that the acceleration of the reaction mass is not significant in the analysis of the foundation; it is simply a by-product of the test. Secondly, the load produced is not an impact in that the mass is in contact prior to the test. Further, the test is over long before the masses reach the top of their flight. The parameters of interest are only those associated with the movement of the foundation (i.e. force, displacement, and acceleration).

Typical analysis of Statnamic data relies on measured values of force, displacement and acceleration. A soil model is not required, hence, the results are not highly user dependent. A new method of analysis is introduced that extends present methods by incorporating additional measured values of strain at discrete points along the length of the foundation. In the ensuing sections a discussion of analysis methods and their applicability will be presented. Full details on the development of this method can be found elsewhere (Lewis, 1999).

### Present Analysis Procedures

The Statnamic forcing event induces foundation motion in a relatively short period of time and hence acceleration and velocities will be present. The accelerations are typically small ( $1-2 g$ 's), however the enormous mass of the foundation when accelerated resists movement due to inertia and as such the fundamental equation of motion applies, Equation 1.

$$F = ma + cv + kx \quad (1)$$

where,

- $F$  = forcing event
- $m$  = mass of the foundation
- $a$  = acceleration of the displacing body
- $v$  = velocity of the displacing body
- $c$  = viscous damping coefficient
- $k$  = spring constant of the displacing system
- $x$  = displacement of the body

The equation of motion is generally described using four terms: forcing, inertial, viscous damping, and stiffness. The forcing term ( $F$ ) denotes the load application which varies with time and is equated to the sum of remaining three terms. The inertial term ( $ma$ ) is the force which is generated from the tendency of a body to resist motion, or to keep moving once



it is set in motion (Young, 1992). The viscous damping term ( $cv$ ) is best described as the velocity dependant resistance to movement. The final term ( $kx$ ), represents the classic system stiffness, which is the static soil resistance.

When this equation is applied to a pile/soil system the terms can be redefined to more accurately describe the system. This is done by including both measured and calculated terms. The revised equation is displayed below:

$$F_{Statnamic} = (ma)_{Foundation} + (cv)_{Foundation} + F_{Static} \quad (2)$$

where,  $F_{Statnamic}$  is the measured Statnamic force,  $m$  is the calculated mass of the foundation,  $a$  is the measured acceleration of the foundation,  $c$  is the viscous damping coefficient,  $v$  is the calculated velocity, and  $F_{Static}$  is the derived pile/soil static response.

There are two unknowns in the revised equation  $F_{Static}$  and  $c$ , thus the equation is under specified.  $F_{Static}$  is the desired value, so the variable  $c$  must be obtained to solve the equation. Middendorp (1992) presented a method to calculate the damping coefficient referred to as the Unloading Point Method (UP). With the value of  $c$  known, the static force can be calculated. This force, termed "Derived Static," represents an equivalent soil response similar to that produced by a traditional static load test.

### UP Description

The UP is a simple method which allows the equivalent static resistance to be derived from the measured Statnamic quantities. It uses a simple single degree of freedom model to represent the foundation/soil system as a rigid body supported by a non-linear spring and a linear dashpot in parallel (see Figure 1). The spring represents the static soil response ( $F_{Static}$ ) which includes the elastic response of the foundation as well as the foundation/soil interface and surrounding soil response. The dashpot is used to represent the dynamic resistance which depends on the rate of pile penetration (Nishimura, 1995).

The UP makes two primary assumptions in its determination of "c." The first is the static capacity of the pile is constant when it plunges as a rigid body. The second is that the damping coefficient is constant throughout the test. By doing so a time window is defined in which to calculate the damping coefficient as shown in Figure 2. This figure shows a typical Statnamic load-displacement curve which denotes points (1) and (2). The first point of interest (1) is that of maximum Statnamic Force. At this point the static resistance is assumed to have become steady state, for the purpose of calculating "c". Thus, any extra resistance is attributed to that of the dynamic forces ( $ma$  and  $cv$ ). The next point of interest (2) is that of zero velocity which has been termed the "Unloading Point." At this point the foundation is no longer moving and the resistance due to damping is zero. The static resistance, used to calculate "c" from point (1) to (2), can then be calculated by the following equation:

$$F_{Static_{UP}} = F_{Statnamic} - (ma)_{Foundation} \quad (3)$$

where,  $F_{Statnamic}$ ,  $m$ , and  $a$  are all known parameters;  $F_{Static_{UP}}$  is the static force calculated at (2) and assumed constant from (1) to (2).

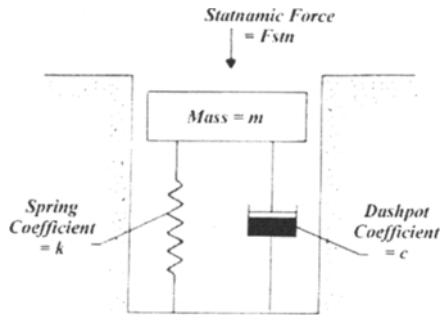
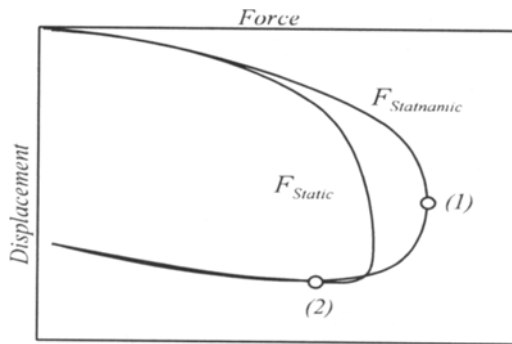


Figure 1. Single D.O.F. Model

Figure 2. UP time window for  $c$  determination.

Next, the damping coefficient can be calculated throughout this range, from maximum force (1) to zero velocity (2). The following equation is used to calculate  $c$ :

$$c = \frac{F_{Static} - F_{Static_{UP}} - (ma)_{Foundation}}{v_{Foundation}} \quad (4)$$

Damping values over this range should be fairly constant. Often the average value is taken as the damping constant, but if a constant value occurs over a long period of time it should be used (see Figure 3). Note that as  $v$  approaches zero at point (2), values of  $c$  can be different from that of the most representative value and therefore the entire trend should be reviewed. Finally the derived static response can be calculated as follows:

$$F_{Static} = F_{Statamic} - (ma)_{Foundation} - (cv)_{Foundation} \quad (5)$$

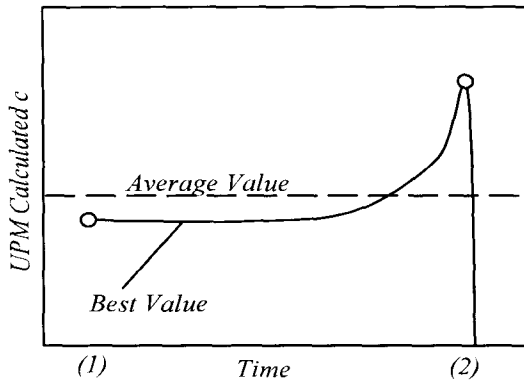


Figure 3. Variation in  $c$  between times (1) and (2).

Currently software is available to the public that can be used in conjunction with Statamic test data to calculate the derived static pile capacity using the UP Method (Garbin, 1999). This software was developed by the University of South Florida and the Federal Highway Administration and can be downloaded from [www.eng.usf.edu/~gmullins](http://www.eng.usf.edu/~gmullins) under the Statamic Analysis Workbook (SAW™) heading.

### UP Shortcomings

The UP has proven to be a valuable tool in predicting damping values when the foundation acts as a rigid body. However, as the pile length increases an appreciable delay can be introduced between the movement of the pile top and toe, hence negating the rigid body assumption. This occurrence also becomes prevalent when an end bearing condition exists; in this case the lower portion of the foundation is prevented from moving jointly with the top of the foundation.

Middendorp (1995) defines the “Wave Number” ( $N_w$ ) to quantify the applicability of the UP. The wave number is calculated by dividing the wave length ( $D$ ) by the foundation depth ( $L$ ).  $D$  is obtained by multiplying the wave speed  $c$  in length per second by the load duration ( $T$ ) in seconds. Thus, the wave number is calculated by the following equation:

$$N_w = \frac{D}{L} = \frac{cT}{L} \quad (6)$$

Through empirical studies Middendorp determined that the UP would accurately predict static capacity, from Statamic data, if the wave number is greater than 12. Nishimura (1995) established a similar threshold at a wave number of 10. Using wave speeds of 5000 m/s and 4000 m/s for steel and concrete respectively and a typical Statamic load duration, the UP is limited to piles shorter than 50 m (steel) and 40 m (concrete). Wave number analysis

can be used to determine if stress waves will develop in the pile. However, this does not necessarily satisfy the rigid body requirement of the UP.

Statnamic tests cannot always produce wave numbers greater than 10, and as such there have been several methods suggested to accommodate stress wave phenomena in Statnamicly tested long piles (Middendorp, 1995). Due to limitations on paper length these methods are not presented.

### **Modified Unloading Point Method**

Given the shortcomings of the UP, users of Statnamic testing have developed a remedy for the problematic condition that arises most commonly. The scenario involves relatively short piles ( $N_w > 10$ ) that do not exhibit rigid body motion, but rather elastically shorten within the same magnitude as the permanent set. This is typical of rock-socketed drilled shafts or piles driven to dense bearing strata that are not fully mobilized during testing. The consequence is that the top of pile response (i.e. acceleration, velocity, and displacement) is significantly different from that of the toe. The most drastic subset of these test results show zero movement at the toe while the top of pile elastically displaces in excess of the surficial yield limit (e.g. upwards of 25 mm). Whereas with plunging piles (rigid body motion) the difference in movement (top to toe) is minimal and the average acceleration is essentially the same as the top of pile acceleration; tip restrained piles will exhibit an inertial term that is twice as large when using top of pile movement measurements to represent the entire pile.

The Modified Unloading Point Method (MUP), developed by Justason (1997), makes use of an additional toe accelerometer that measures the toe response. The entire pile is still assumed to be a single mass,  $m$ , but the acceleration of the mass is now defined by the average of the top and toe movements. A standard UP is then conducted using the applied top of pile Statnamic force and the average accelerations and velocities. The derived static force is then plotted versus the top of pile displacement as before. This simple extension of the UP has successfully overcome most problematic data sets. Plunging piles instrumented with both top and toe accelerometers have shown little analytical difference between the UP and the MUP. However, MUP analyses are now recommended whenever both top and toe information is available.

### **Need For Advancement**

Although the MUP provided a more refined approach to some of the problems associated with UP conditions, there still exists a scenario where it is difficult to interpret Statnamic data with present methods. This is when the wave number is less than ten (relatively long piles). In these cases the pile may still only experience compression (no tension waves) but the delay between top and toe movements causes a phase lag. Hence an average of top and toe movements does not adequately represent the pile.

### SUP Method Description And General Procedure

The fundamental concept of the SUP is that the acceleration, velocity, displacement, and force on each segment can be determined using strain gage measurements along the length of the pile. Individual pile segment displacements are determined using the relative displacement as calculated from strain gage measurements and an upper or lower measured displacement. The velocity and acceleration of each segment are then determined by numerically differentiating displacement then velocity with respect to time. The segmental forces are determined by calculating the difference in force from two strain gage levels.

Typically the maximum number of segments is dependent on the available number of strain gage layers. However, strain gage placement does not necessitate assignment of segmental boundaries; as long as the wave number of a given segment is greater than 10, the segment can include several strain gage levels within its boundaries. The number and the elevation of strain gage levels are usually determined based on soil stratification; as such, it can be useful to conduct an individual segmental analysis to produce the shear strength parameters for each soil strata. A reasonable upper limit on the number of segments should be adopted because of the large number of mathematical computations required to complete each analysis. Figure 4 is a sketch of the SUP pile discretization.

The notation used for the general SUP case defines the pile as having  $m$  levels of strain gages and  $m+1$  segments. Strain gage locations are labeled using positive integers starting from 1 and continuing through  $m$ . The first gage level below the top of the foundation is denoted as  $GL^1$  where the superscript defines the gage level. Although there are no strain gages at the top of foundation, this elevation is denoted as  $GL^0$ . Segments are numbered using positive integers from 1 to  $m+1$ , where segment 1 is bounded by the top of foundation ( $GL^0$ ) and  $GL^1$ . Any general segment is denoted as segment  $n$  and lies between  $GL^{n-1}$  and  $GL^n$ . Finally, the bottom segment is denoted as segment  $m+1$  and lies between  $GL^m$  and the foundation toe.

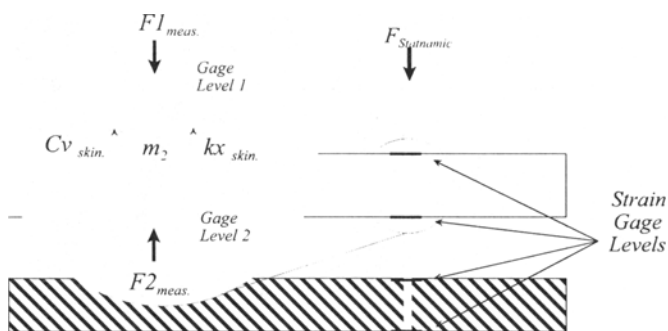


Figure 4. Segmental Free Body Diagram

### Calculation Of Segmental Motion Parameters

The SUP analysis defines average acceleration, velocity, and displacement traces that are specific to each segment. In doing so, strain measurements from the top and bottom of each segment and a boundary displacement are required. Boundary displacement may come from the Statnamic laser reference system (top), top of pile acceleration data, or from embedded toe accelerometer data.

The displacement is calculated at each gage level using the change in recorded strain with respect to an initial time zero using Equation 7. Because a linearly-varying strain distribution is assumed between gage levels, the average strain is used to calculate the elastic shortening in each segment.

Level displacements

$$x_n = x_{n-1} - \Delta\epsilon_{\text{average seg } n} L_{\text{seg } n} \quad (7)$$

where

$$\begin{aligned} x_n &= \text{the displacement at the } n\text{th gage level} \\ \Delta\epsilon_{\text{average seg } n} &= \text{the average change in strain in segment } n \\ L_{\text{seg } n} &= \text{the length of the } n\text{th segment} \end{aligned}$$

To perform an unloading point analysis, only the top-of-segment motion needs to be defined. However, the MUP analysis, which is now recommended, requires both top and bottom parameters. The SUP lends itself naturally to providing this information. Therefore, the average segment movement is used rather than the top-of-segment; hence, the SUP actually performs multiple MUP analyses rather than standard UP. The segmental displacement is then determined using the average of the gage level displacements from each end of the segment as shown in the following equation:

$$x_{\text{seg } n} = \frac{x_{n-1} + x_n}{2} \quad (8)$$

where  $x_{\text{seg } n}$  is the average displacement consistent with that of the segment centroid.

The velocity and acceleration, as required for MUP, are then determined from the average displacement trace through numerical differentiation using Equations 9 and 10, respectively:

$$v_n = \frac{x_{n_i} - x_{n_{i+1}}}{\Delta t} \quad (9)$$

$$a_n = \frac{v_{n_i} - v_{n_{i+1}}}{\Delta t} \quad (10)$$

where

$$\begin{aligned} v_n &= \text{the velocity of segment } n \\ a_n &= \text{the acceleration of segment } n \\ \Delta t &= \text{the time step from time } t \text{ to } t+1 \end{aligned}$$



It should be noted that all measured values of laser displacement, strain, and force are time dependent parameters that are field recorded using high speed data acquisition computers. Hence the time step,  $\Delta t$ , used to calculate velocity and acceleration is a uniform value that can be as small as 0.0002 seconds. Therefore, some consideration should be given when selecting the time step to be used for numerical differentiation.

The average motion parameters ( $x$ ,  $v$ , and  $a$ ) for segment  $m+1$  can not be ascertained from measured data, but the displacement at  $GL^m$  can be differentiated directly providing the velocity and acceleration. Therefore, the toe segment is evaluated using the standard UP. These segments typically are extremely short (1 - 2 m) producing little to no differential movement along its length.

### Calculation Of Segmental Statnamic And Derived Static Forces

Each segment in the shaft is subjected to a forcing event which causes movement and reaction forces. This segmental force is calculated by subtracting the force at the top of the segment from the force at the bottom. The difference is due to side friction, inertia, and damping for all segments except the bottom segment. This segment has only one forcing function from  $GL^m$  and the side friction is coupled with the tip bearing component. The force on segment  $n$  is defined as:

$$S_n = A_{(n-1)} E_{(n-1)} \epsilon_{(n-1)} - A_n E_n \epsilon_n \quad (11)$$

where

$S_n$	=	the applied segment force from strain measurements
$E_n$	=	the composite elastic modulus at level $n$
$A_n$	=	the cross sectional area at level $n$
$\epsilon_n$	=	the measured strain at level $n$

Once the motion and forces are defined along the length of the pile, an unloading point analysis on each segment is conducted. The segment force defined above is now used in place of the Statnamic force in Equation 2. Equation 12 redefines the fundamental equation of motion for a segment analysis:

$$S_n = m_n a_n + c_n v_n + S_{n \text{ Static}} \quad (12)$$

where,

$S_{n \text{ Static}}$	=	the derive static response of segment $n$
$m_n$	=	the calculated mass of segment $n$
$c_n$	=	the damping constant of segment $n$

The damping constant (in Equation 13) and the derived static response (Equation 14) of the segment are computed consistent with standard UP analyses:

$$c_n = \frac{S_n - S_{n \text{ Static}}}{v_n} \quad (13)$$

$$S_{n \text{ Static}} = S_n - m_n a_n - c_n v_n \quad (14)$$

Finally the top-of-foundation derived static response can be calculated by summing the derived static response of the individual segments as displayed in the following equation:

$$F_{Static} = \sum_{n=1}^{m+1} S_{n Static} \quad (15)$$

Software capable of performing SUP analyses (SUPERSAW™) is currently being developed at the University of South Florida in cooperation with the Federal Highway Administration.

### Site Characteristics And SUP Application

Prepared in this section are examples of the motion parameters, segment forces, and load displacement trends as analyzed by SUP. The foundation was instrumented with four strain gage levels ( $m = 4$ ) which produced five segments. Data was obtained at the 17<sup>th</sup> Street Causeway Replacement Bridge project as part of an extensive load test program implemented by the Florida Department of Transportation (FDOT), which included Statnamic load tests. Statnamic load testing was performed using a 30MN Statnamic device equipped with a gravel catch structure. Shaft instrumentation consisted of standard Statnamic equipment as well as, resistive type strain gages, and a toe accelerometer. Instrumentation elevations are presented in Table 1.

Table 1 Instrumentation Schedule

Instrumentation Elevation (m)	Number of Transducers	Type of Transducer
3.0	4	Calibrated Load Cell, 2 Accelerometers, and Laser Reference System
-1.8	3	Strain Gage
-4.2	3	Strain Gage
-17.0	3	Strain Gage
-18.3	3	Strain Gage
-19.0	1	Accelerometer

The test shaft had a planned diameter of 1.22 m and was 22 m in length. It was constructed using a temporary casing method and sea water as the drilling fluid. The 1.22 m O.D. steel casing (1 cm wall thickness) was installed to elevation -18.96 m using a vibratory hammer. The concrete was placed using a tremie method, then the casing tip was pulled to elevation -0.9 m, using a vibratory hammer.

A soil boring performed at the test shaft location indicated that the natural ground elevation was approximately 1.5 m. The water table was reported to exist at elevation 0.3 m. SPT testing was initiated at the ground surface (elevation +3 m) and extended to elevation -

28.15 m. The upper two meters of soil consisted of compacted limestone fill with SPT "N" values ranging from 16 to 27.

The following strata was reported as fine sand with fragments of limestone and shell. This strata extended to elevation -14.7 m, "N" values ranged from 9 to 57. From elevation -14.7 m throughout, the rock socket length averaged 34% RQD at 80% recovery. RQD values ranged from 18% to 73% in the limestone below the shaft tip. Recovery values in this strata were generally greater than 70%.

Figure 5 shows the measured change in strain with respect to time  $t = 0$  for each gage level. Figures 6 through 8 illustrate the motion parameters determined for each of the five segments. Figure 9 shows the forces calculated at each gage level with the true measured strain. Figure 10 shows the dynamic forces on each of the segments as calculated by Equation 11.

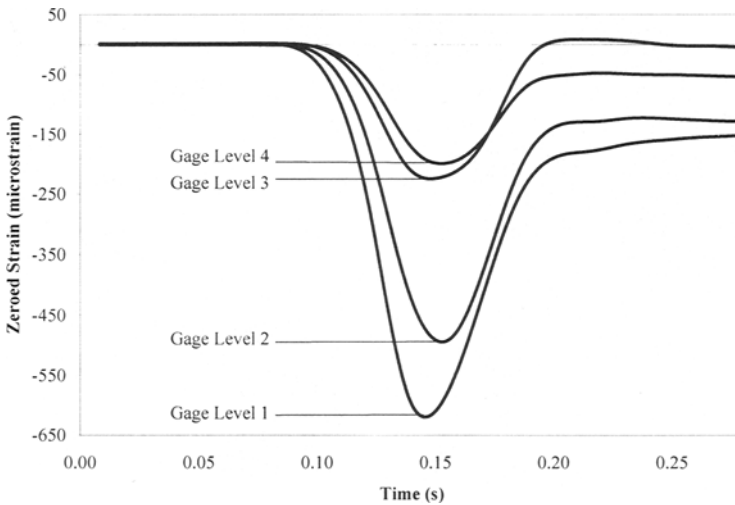


Figure 5. Strain versus Time

Using the segmental forces, the derived static soil resistance is determined for each of the segments. Figure 11 shows a typical segment load versus segment displacement curve. By simply dividing the segment force by circumferential surface area this curve can be converted in to a shear stress versus displacement (T-Z) curve for that specific soil strata.

It can be seen in Figure 10 that the peak of each segment force may occur at different times and therefore at different top-of-pile displacements. This can effect the pile capacity in that the ultimate shear strengths of the strata should not be simply summed. This is most probably not a significant concern with this pile due to the plunging nature of the failure. This is evidenced by the similar top and toe movements shown in Figure 6. However, to be technically correct, SUP uses the summation of segment forces as they were developed. This accounts for upper soil layers that may fully mobilize and become residual in nature while

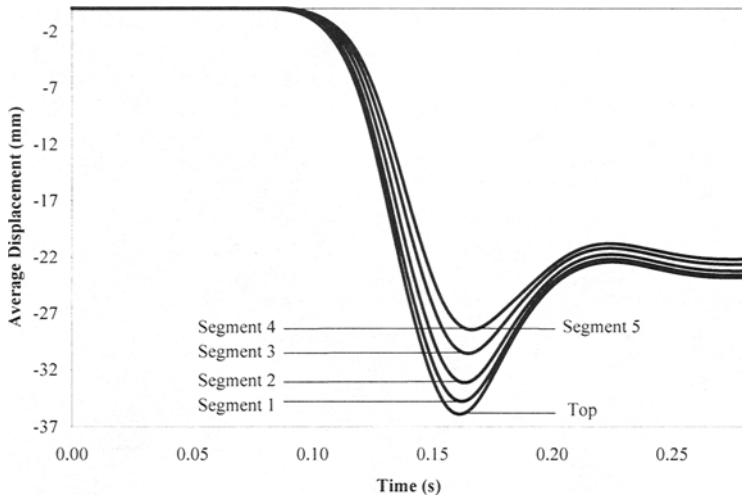


Figure 6. Segmental Average Displacements

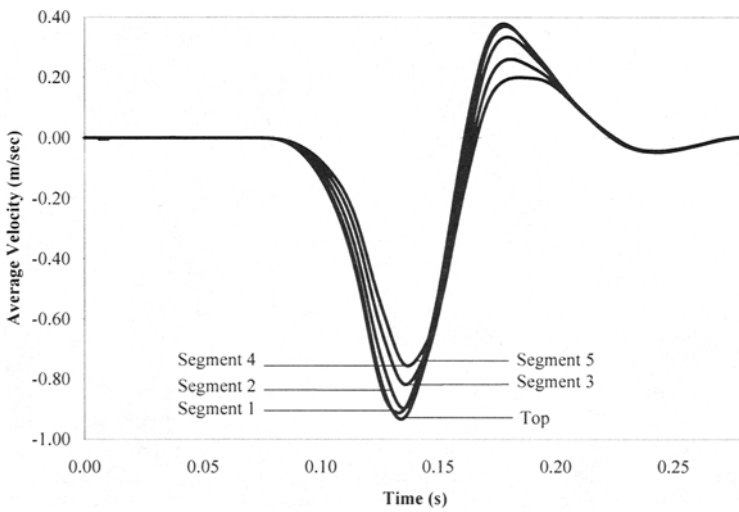


Figure 7. Segmental Average Velocity

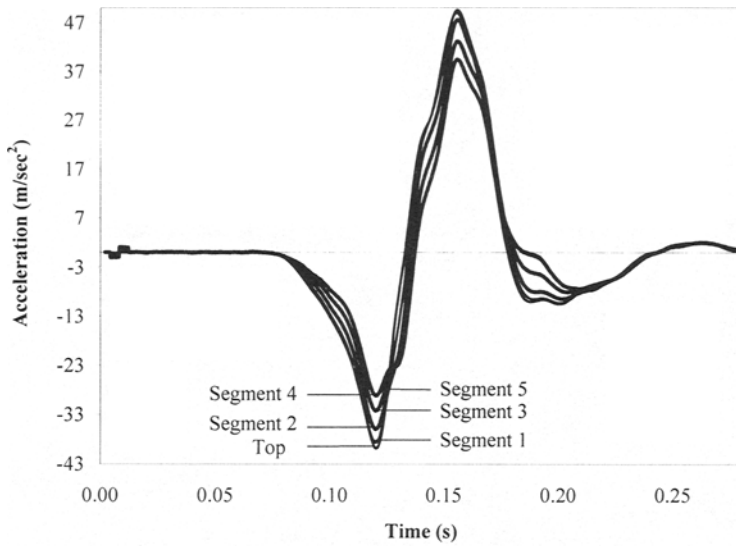


Figure 8. Segmental Average Acceleration

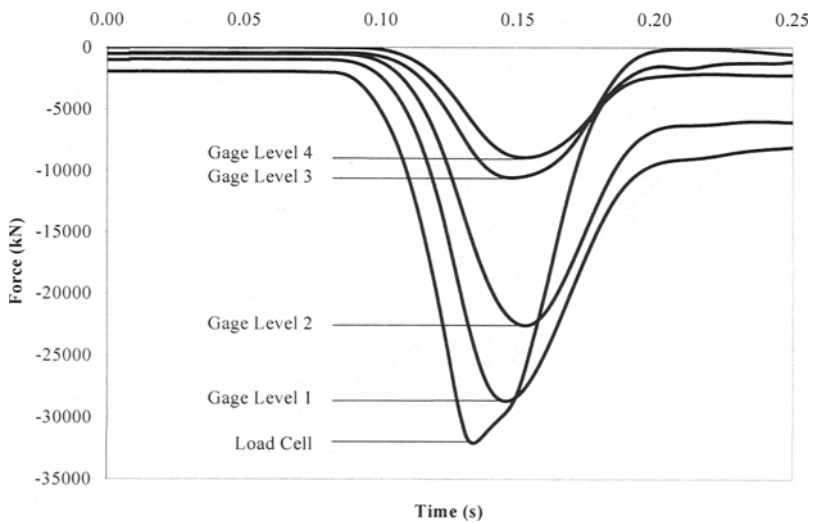


Figure 9. Force at Gage Levels

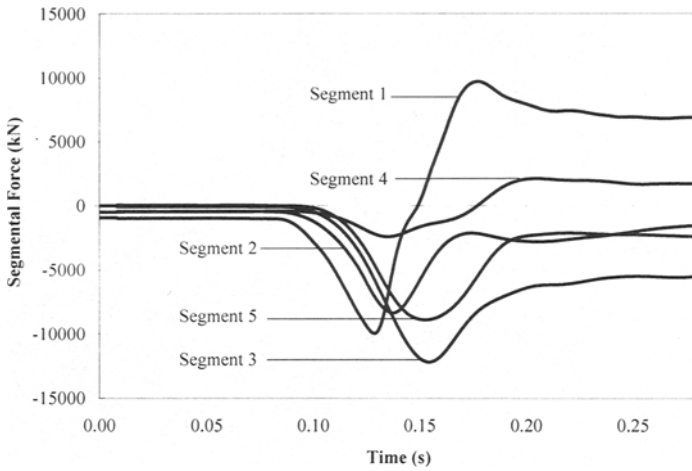


Figure 10. Segmental Statnamic Forces

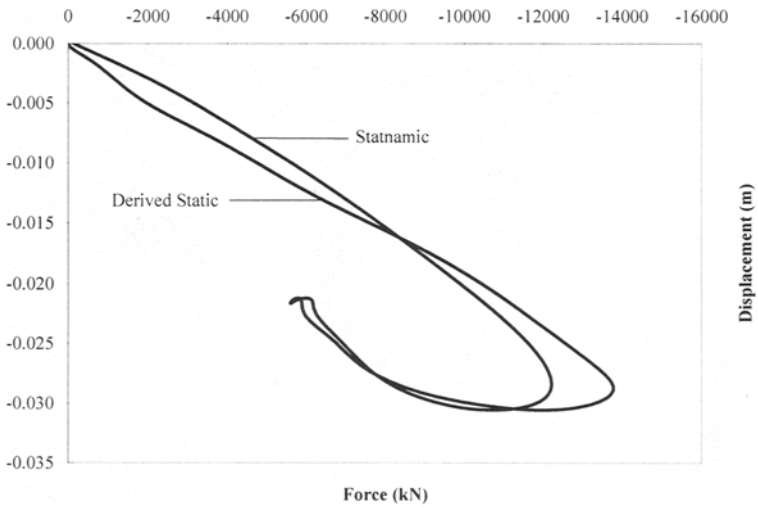


Figure 11. Segment Load Displacement Curves

lower soil layers begin to develop ultimate strengths. Figure 12 shows the raw Statnamic load displacement curve as well as SUP, MUP, and UP derived static capacity versus the top-of-pile displacement.

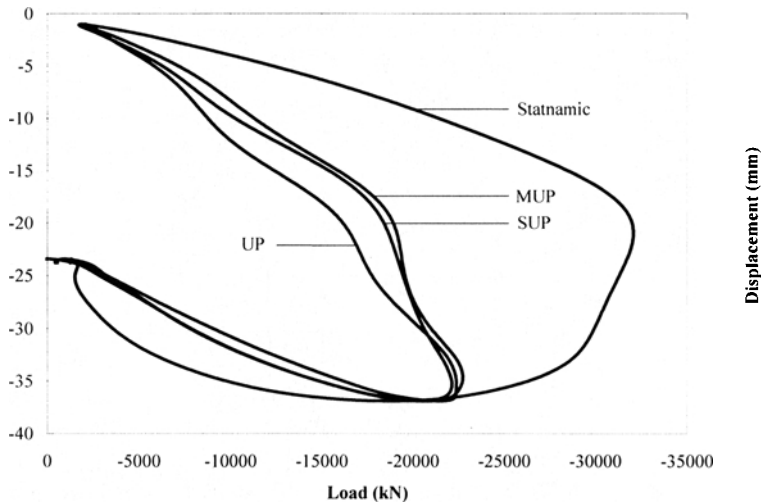


Figure 12. Top of Pile Load versus Displacement

### Summary

A new method of analysis called the Segmental Unloading Point Method (SUP) was presented that evaluates Statnamic loaded foundations as segments whose lengths are defined by embedded strain gage elevations. The recorded strain measurements are used to determine both the segmental motion parameters as well as the segmental force traces. Each segment is then treated as an individual foundation whose static response is derived using either the UP or MUP methods. The summation of each segment contribution with respect to time provides a top of foundation response that more closely incorporates the actual distribution of inertial and damping forces throughout the foundation. This is most important in the analysis of relatively long or fixed-ended piles. Although the UP and MUP methods of analysis are sufficient for most loading conditions, SUP provides information for soil strata T-Z curves as well as cut-off elevation load-displacement curves.

### References

Bermingham, P., and White, J., (1995), "Pyrotechnics and the Accurate of Prediction of Statnamic Peak Loading and Fuel Charge Size", First International Statnamic Seminar, 1995, Vancouver, British Columbia Canada



Garbin, E. J., (1999), "Data Interpretation for Axial Statnamic Testing and the Development of the Statnamic Analysis Workbook," Master's Thesis, University of South Florida, Tampa, FL.

Kusakabe, Kuwabara, and Matsumoto (eds), (2000), "Statnamic Load Test," Draft of 'method for rapid load test of single piles (JGS 1815-2000),' *Proceedings of the Second International Statnamic Seminar*, Tokyo, October 1998 pp. 237-242.

Janes, M.C., Justason, M.D., Brown, D.A., (2000), "Long period dynamic load testing ASTM standard draft," *Proceedings of the Second International Statnamic Seminar*, Tokyo, October, 1998, pp. 199-218.

Justason, M.D., (1997), "Report of Load Testing at the Taipei Municipal Incinerator Expansion Project," Taipei City, Taipei.

Lewis, C.L., (1999), "Analysis of Axial Statnamic Testing by the Segmental Unloading Point Method," Master's Thesis, University of South Florida, Tampa, FL.

Middendorp, P., Bermingham, P., and Kuiper, B. , (1992), "Statnamic Load Testing Of Foundation Pile." *Proceedings, 4<sup>th</sup> International Conference On Application Of Stress-Wave Theory To Piles*, The Hague, pp. 581-588.

Middendorp, P. and Bielefeld, M.W., (1995), "Statnamic Load Testing and the Influence of Stress Wave Phenomena," *Proceedings of the First International Statnamic Seminar*, Vancouver, Canada, pp. 207-220.

Nishimura, S., and Matsumoto, T., (1995), "Wave Propagation Analysis During Statnamic Loading of a Steel Pipe Pile," *Proceedings of the First International Statnamic Seminar*, Vancouver, Canada, September.

Young, Hugh. D., (1992), "University Physics," Eight Edition, Addison Wesley.

Title no. 99-S39

# Durability of E-Glass/Vinylester Reinforcement in Alkaline Solution

by Rajan Sen, Gray Mullins, and Tom Salem

*This paper presents results from a 9-month experimental study to evaluate the durability of E-glass/vinylester reinforcement used by the U.S. Navy in the construction of the MRI Pier in San Diego, Calif. A total of 36 specimens were tested. These were split into four groups of 9 specimens each that were exposed to simulated pore solution (SPS) with a pH ranging between 13.35 to 13.5 for periods of 1, 3, 6, and 9 months. Of the nine specimens in each group, a third were unstressed, a third stressed to 10%, while the remaining third were stressed to either 15 or 25% of their ultimate short-term tensile strength. At the end of the designated exposure periods, surviving specimens were tested to failure to determine their residual tensile strength.*

*The results showed that the E-glass/vinylester bars tested had very limited durability in this environment, especially at stress levels of 15% or higher. All six specimens stressed to 25% failed within 25 days of exposure. Five of six specimens stressed to 15% failed within 180 days. Specimens stressed to 10% lost 70% of their original strength after 9 months of exposure. Even unstressed specimens lost 63% of their original strength after 9 months, indicating that diffusion of the alkaline solution through the resin matrix was largely responsible for their degradation. The faster deterioration of the stressed specimens indicated that resin cracking also played a significant role in the degradation.*

*Prediction of remaining life for the test specimens based on a Fickian (diffusion) model was between 1.6 to 4.6 years (unstressed) and between 0.5 to 1.7 years for the specimens stressed to 10%. Overall, the results confirm the unsuitability of first-generation glass fiber-reinforced polymer bars as structural reinforcement in concrete members.*

**Keywords:** alkali; concrete; durability; polymer; reinforcement.

## INTRODUCTION

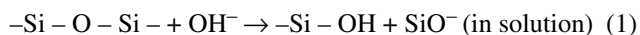
The U.S. Navy used E-glass/vinylester reinforcing bars in the construction of the MRI Pier, San Diego, Calif., in 1993. Glass fiber-reinforced polymer (GFRP) bars ranging in size from No. 3 to No. 5 bars were used as the main reinforcement for pile caps and the concrete deck.

A legitimate concern regarding the use of GFRP reinforcing bars in concrete is their long-term durability. This arises because of glass fibers' well-known vulnerability in alkalis.<sup>1</sup> Because the resin matrix protects glass fibers from direct contact in the GFRP composite, this vulnerability is believed to be reduced. However, reliable data substantiating this was unavailable at that time. Given the uncertainty, the U.S. Navy arbitrarily limited stresses to 10% of the maximum short-term tensile strength.<sup>2</sup>

This paper summarizes the results of a 9-month experimental investigation to evaluate the validity of this limit. In the tests, E-glass/vinylester reinforcing bars identical to those used in the construction of the MRI Pier were exposed to simulated pore solution. The study was completed in 1996 and additional information may be found in the final report.<sup>3</sup>

## BACKGROUND

Silica constitutes 55% of E-glass fibers.<sup>4</sup> In alkalis, silica reacts chemically with the hydroxyl ions that dissolve its basic silicon-oxygen-silicon structure as



This dissolution of silica results in rapid and severe strength loss.

Because concrete has billions of microscopic voids distributed throughout its mass, for example, due to the use of air-entraining admixtures to improve freezing-and-thawing resistance and other factors, any capillary water present in these voids due to exposure to wet/dry conditions has a pH value ranging from 12.5 to 13.5. This represents a caustic or highly alkaline solution.<sup>5</sup> If this alkaline solution can cross the resin barrier, the durability of the GFRP composite will be in jeopardy.

Two mechanisms that allow passage of the alkaline pore solution in concrete to attack glass fibers in GFRP composites are (a) resin cracking under load, and (b) diffusion through the resin. Tests on E-glass/polyester pultruded rods conducted by Canadian researchers<sup>6</sup> indicate that even at stress levels as low as 10% of the ultimate short-term tensile strength of GFRP, the resin matrix can crack at locations where the fibers are not aligned. Misalignment may occur during fabrication and may also be present due to the use of helical wrap for improving bond with concrete. Diffusion is always present and was identified as the mechanism by which alkaline pore solution attacked S-2 glass fibers.<sup>7</sup>

## OBJECTIVES

The primary aims of the study were:

- to determine the performance of the E-glass/vinylester reinforcing bars in simulated concrete pore solution at the arbitrarily imposed 10% stress level;
- to assess whether the 10% stress limit was unduly conservative or if it could be increased; and
- to quantify durability in terms of residual strength following exposure in simulated concrete pore solution.

## RESEARCH SIGNIFICANCE

Information on the laboratory performance of GFRP used in a demonstration project is important for future calibration. Many innovative features developed in the exposure setup and the testing are presented. Data on the performance of

*ACI Structural Journal*, V. 99, No. 3, May-June 2002.

MS No. 01-234 received August 7, 2001, and reviewed under Institute publication policies. Copyright © 2002, American Concrete Institute. All rights reserved, including the making of copies unless permission is obtained from the copyright proprietors. Pertinent discussion will be published in the March-April 2003 *ACI Structural Journal* if received by November 1, 2002.

ACI member **Rajan Sen** is the Samuel and Julia Flom Professor in the Department of Civil and Environmental Engineering at the University of South Florida, Tampa, Fla. He is a member of ACI Committees 215, Fatigue of Concrete; 440, Fiber Reinforced Polymer Reinforcement; and 444, Experimental Analysis for Concrete Structures. His research interests include masonry, prestressed concrete, steel, and the application of advanced composite materials.

**Gray Mullins** is an assistant professor in the Department of Civil and Environmental Engineering at the University of South Florida. He received his BSCE, MSCE, and PhD from the University of South Florida. His research interests include full-scale instrumentation and testing in geotechnical structures and the application of advanced composite materials.

**Tom Salem** received his BSCE and MSCE from the University of South Florida.

GFRP bars subjected to high pH levels at different stress levels is useful for evaluation of structures constructed using this material.

### EXPERIMENTAL PROGRAM

The aim of the durability study was to evaluate the appropriateness of the 10% stress limit for the E-glass/vinylester bar used in the construction of the MRI Pier, San Diego, Calif. In view of this, test specimens were investigated at stress levels both above and below this 10% limit to allow for possible increases (or decreases) in the allowable stress.

Four series of tests were carried out in which specimens were tested to determine residual strength after exposure periods of 1, 3, 6, and 9 months. In each series, a total of nine specimens was tested—three each at stress levels of 0, 10, and 25%. The upper limit was later reduced to 15% for the 6- and 9-month series—possible because these tests commenced only after the 1- and 3-month series had been concluded. In all, a total of 36 specimens was tested.

### Specimen details

Thirty 3.05 m (10 ft) long No. 3 E-glass/vinylester bars were used in the experimental investigation. Because each test specimen was approximately 1.12 m (44 in.) long, each reinforcing bar provided two specimens and a remnant that was approximately 0.81 m (32 in.) in length. The two specimens were identified by the reinforcing bar number from which it was cut followed by the letter (a) or (b); for example, Specimen 21(b) indicated it was the second bar cut from the reinforcing bar labeled as No. 21. The remnant was similarly identified by the reinforcing bar number followed by the letter (c); for example, 10(c) is the remnant from reinforcing bar No. 10. The remnants were used to evaluate the short-term mechanical properties, that is, tensile strength and elastic modulus as summarized in Table 1.

### University of South Florida (USF) anchor

A resin sleeve-type anchor using a steel pipe and a low viscosity epoxy was developed for this study (Fig. 1). This used readily available, inexpensive pipes used in plumbing. The resin used was a high-modulus, low-viscosity epoxy. A polyvinyl chloride (PVC) plug was used to seal the open end.

Three sizes: 0.5, 0.75, and 1.0 in. (12.7, 19.05, and 25.4 mm) diameter, respectively, galvanized steel nipples were evaluated. The length of the anchor was based on the typical dimension of commercially available pipe. Couplers were provided at each end to extend its length. The threaded inside provided greater contact area with the epoxy and improved performance.

The 0.75 in. (19.05 mm) diameter pipe was selected based on the 0.1875 in. (4.7625 mm) clearance on each side between

**Table 1—Average properties of No. 3 E-glass/vinylester bars tested**

Properties	U.S. units	SI units
Effective area*	0.078 in. <sup>2</sup>	50.3 mm <sup>2</sup>
Ultimate load	9260 lb	41.1 kN
Failure stress	119 ksi	821 MPa
Tensile modulus	6440 ksi	44.4 GPa
Failure strain, %	1.84	1.84

\*Manufacturer's data.

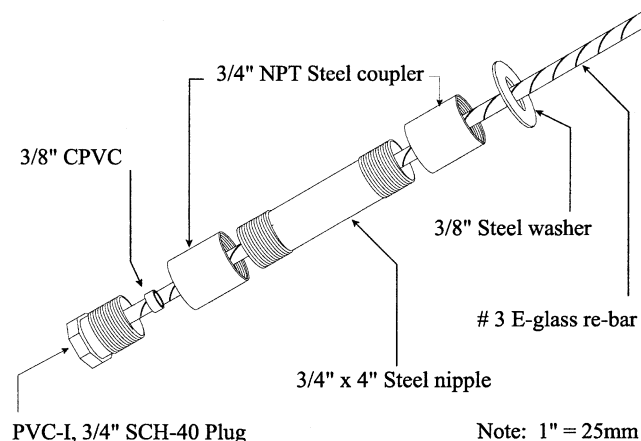


Fig. 1—USF anchor assembly.

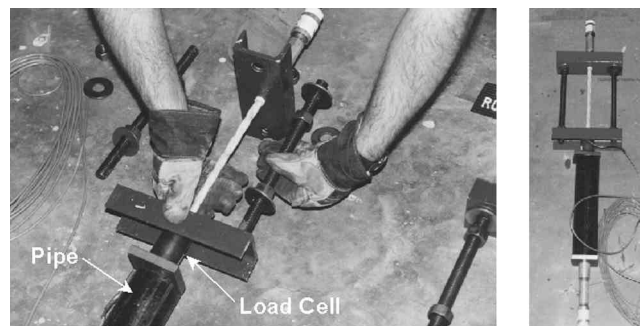


Fig. 2—Assembly of exposure unit (left); assembled unit with stress GFRP bar (right).

the reinforcing bar and the pipe. The 0.5 in. (12.7 mm) diameter pipe was found to be too narrow. The 1.0 in. (25.4 mm) diameter pipe, although successfully tested, was discarded because of its extra cost and also concerns of possible shrinkage separation between the epoxy and the pipe wall.

### Exposure setup

The exposure setup was designed so that it met three key requirements: 1) the method for monitoring and controlling load levels in each specimen was simple; 2) the procedure for determining residual tensile strength was in-built; and 3) it had the facility to circulate (and replace, if necessary) the simulated pore solution (SPS). More importantly, the system devised had to be very inexpensive because of the limited funding available.

A self-straining, portable setup was developed. Its essential components are shown in Fig. 2. A 1.12 m (44 in.) long E-glass/vinylester No. 3 bar provided with a permanent USF anchor at one end was inserted through openings in two

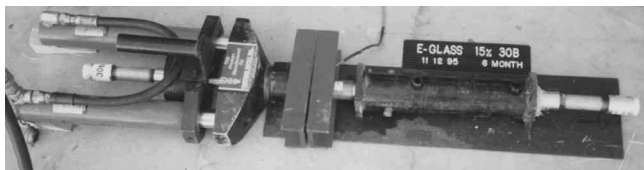


Fig. 3—Residual strength test setup.

channel sections, a load cell, spacer plates, and a steel pipe. A second anchor was subsequently provided at the free end.

The threaded rods were bolted to the channel sections and were tightened against the steel pipe to provide the required preload. The force in the GFRP bar was measured by a load cell sandwiched between the lower channel section and the steel pipe. Removal of the threaded rod released the preload and also freed up space that was utilized by a prestressing jack to determine the residual tensile strength (Fig. 3). The pipe was used as a receptacle for the simulated concrete pore solution (SPS) but also served as part of the reaction frame in resisting the force applied by the prestressing jack.

As the pipe housed the SPS, its bottom was sealed to prevent leakage. Two sets of holes were drilled 200 mm (8 in.) apart along the sides of the steel pipe to serve as an inlet and an outlet to facilitate circulation and replacement of the pore solution. This meant that in the absence of wicking, failure of the GFRP bar would be confined to this 200 mm (8 in.) region.

A total of 18 units were built. As there were 36 specimens, this required the tests to be carried out in sequence. Thus, the 6- and 9-month exposure series commenced after the 1- and 3-month series had been concluded. The 18 units were placed vertically in a rack shown in Fig. 4. Plastic tubing connected the 18 pipes to each other and to a pump that constantly circulated the SPS. As a result, all specimens were exposed to the same solution. The top plastic tube connecting all 18 specimens fed into an upright cylindrical plastic container with a screw-on lid. This was used for daily monitoring of the pH of the circulating solution.

A plexiglass tank was provided below the specimens to capture any SPS that spilled over when the specimens failed or had to be removed for testing. Special solid piping of the same diameter was used to seal the pipes in this case. Thus, the system was flexible enough to permit draining or replacing the SPS as needed.

Considerable attention was paid to the pH of the SPS used. Several alternative pore solutions proposed in the literature were reviewed. In the end, an SPS developed by Sagüés<sup>8</sup> was selected because of its high pH. This solution consisted of 8.33 g of sodium hydroxide, 23.3 g of potassium hydroxide, and 10 g of calcium hydroxide (saturated) in 1 L of distilled water. The pH was monitored daily and average measured values were 13.55, 13.52, 13.35, and 13.41 for the 1-, 3-, 6-, and 9-month studies, respectively. It is important to note that a pH of 13.5 is five times ( $10^{0.7} = 5$ ) higher than the final pH of 12.8 used to test newer GFRP bars.<sup>9</sup>

The applied load was monitored daily throughout the study. A wrench was used to make appropriate adjustments so that constant loads were maintained. The 18 load cells from the specimens were hooked to a strain indicator box through two switch-and-balance units. The channel sections were color-coded for convenience to identify the three different stress levels investigated. Blue corresponded to the lowest limit (0%) and red to the highest limit (25%—later reduced to 15%). Green was used for the intermediate stress limit of 10%.



Fig. 4—Durability setup.

### Residual tensile strength

Following completion of the predesignated periods of 1, 3, 6, or 9 months, specimens were removed from the exposure setup for residual tensile strength testing. Because a maximum of nine of the 18 specimens was removed, it was important that the circulating SPS solution was not drained. For this reason, as the specimens were individually detached from the plastic tubing (Fig. 4), the free ends were replaced by identical solid sections that sealed the openings.

The pre-existing tensile force was released by loosening and removing the threaded rods completely. The resulting space was taken up by a twin-cylinder, 20-ton prestressing jack. Tension force was applied by jacking against the pipe (Fig. 3). The applied load was increased at an approximately constant stress rate of 175 MPa/min. The same load cell that monitored the load during exposure was hooked to a strain indicator box to provide the failure load. Following completion of the testing, the load cells were recalibrated against a computer-controlled material testing machine. These results confirmed the accuracy of the strain indicator box readings.

## RESULTS

### One-month exposure

Table 2 summarizes the test results. The 9 specimens tested were 1(a) to 3(a), all unstressed; 7(a) to 9(a), all stressed to 10%; and 13(a) to 15(a), all stressed to 25%. Only the unstressed specimens and those stressed to 10% of their ultimate short-term tensile strength survived the exposure period. All three specimens stressed to 25% ruptured within 25 days of exposure (Fig. 5). The earliest specimen to fail (15(a)) failed after 15 days; the last to fail (14(a)) failed at 25 days. The average time-to-failure of all three specimens was only 19 days. All failures occurred within the part of the specimen constantly exposed to the alkaline solution, indicating that alkali attack of the glass fibers was primarily responsible for the failure. The six surviving specimens, that is, the unstressed specimens and the ones stressed to 10% of their short-term tensile strength, were tested to failure to determine their residual strength as described previously. The results of these tests indicated very substantial strength losses that averaged from 50% for the three unstressed specimens (Specimens 1(a) to 3(a)), to 60% for those stressed to 10% (Specimens 7(a) to 9(a)).

The reduction in capacity of the unstressed specimens clearly indicated that diffusion of the hydroxyl ion through

**Table 2—Percent strength reduction with exposure (1 month)**

Specimen no.	Load, %	Time to failure, days	Residual strength		Strength reduction, %	
			kN	lb	Nominal	Average
1(a)	0	—	23.6	5310	41	50
2(a)	0	—	19.3	4315	52	50
3(a)	0	—	16.9	3807	58	50
7(a)	10	—	17.9	4006	56	60
8(a)	10	—	12.1	2724	70	60
9(a)	10	—	18.4	4130	55	60
13(a)	25	17	—	—	100	100
14(a)	25	25	—	—	100	100
15(a)	25	15	—	—	100	100

**Table 3—Percent strength reduction with exposure (3 months)**

Specimen no.	Load, %	Time to failure, days	Residual strength		Strength reduction, %	
			kN	lb	Nominal	Average
4(a)	0	—	15.5	3474	61	63
5(a)	0	—	14.1	3160	65	63
6(a)	0	—	14.6	3280	63	63
10(a)	10	—	10.7	2407	73	72
11(a)	10	—	10.6	2380	73	72
12(a)	10	—	11.5	2589	71	72
16(a)	25	20	—	—	100	100
17(a)	25	14	—	—	100	100
18(a)	25	19	—	—	100	100

the vinylester resin was primarily responsible for the degradation of the E-glass/vinylester bars. The greater reduction in load capacity of the stressed bars is indicative of the added contribution due to resin cracking.

Since the applied load was 10 and 25% of the short-term tensile strength, the strain in the E-glass/vinylester bars varied between 0.18 to 0.45% obtained from values for effective area and tensile modulus in Table 1. The results indicate that even at such low strains resin can crack, possibly because of misalignment of fibers.

### Three-month exposure

Table 3 summarizes the test results for this series. The nine specimens tested were 4(a) to 6(a), all unstressed; 10(a) to 12(a), all stressed to 10%; and 16(a) to 18(a), all stressed to 25%. As for the 1-month series, all unstressed specimens and those stressed to 10% survived the exposure period, whereas all the specimens stressed to 25% failed within 20 days of exposure—Specimen 17(a) was the first to fail after 14 days. As before, all failures occurred within the part of the bar that was constantly exposed to the alkali solution, indicating that failure was due to alkali attack.

The six surviving specimens were tested in the manner described previously to determine their residual strength. The results of these tests indicated strength losses averaging 63% for the three unstressed specimens, and 72% for those stressed to 10% of their short-term tensile strength. As stated in the previous section, this difference is indicative of resin cracking in the stressed specimens that provided an additional pathway for the hydroxyl ion to attack the E-glass fibers. The overall reduction in capacity after two additional months of exposure,

**Table 4—Percent strength reduction with exposure (6 months)**

Specimen no.	Load, %	Time to failure, days	Residual strength		Strength reduction, %	
			kN	lb	Nominal	Average
4(b)	0	—	17.5	3874	57	64
5(b)	0	—	12.7	2895	68	64
6(b)	0	—	13.5	3080	66	64
25(b)	10	—	13.7	3254	64	69
26(b)	10	—	10.6	2391	73	69
27(b)	10	—	13.1	2779	69	69
28(b)	15	108	—	—	100	92
29(b)	15	173	—	—	100	92
30(b)	15	—	10.1	2240	75	92

**Table 5—Percent strength reduction with exposure (9 months)**

Specimen no.	Load, %	Time to failure, days	Residual strength,		Strength reduction, %	
			kN	lb	Nominal	Average
1(b)	0	—	—	4314	52	63
2(b)	0	—	—	2396	74	63
3(b)	0	—	—	3216	64	63
19(a)	10	—	—	3673	59	70
20(a)	10	—	—	1788	80	70
21(a)	10	—	—	2507	72	70
22(a)	15	42	—	—	100	100
23(a)	15	80	—	—	100	100
24(a)	15	100	—	—	100	100

however, was relatively modest—13% for the unstressed specimens, and 12% for the specimens stressed to 10%.

### Six-month exposure

Table 4 summarizes the test results for specimens tested in this series. Because all six specimens loaded to 25% of their short-term tensile strength failed within 25 days in the two earlier series, the maximum load was reduced to 15% for the remaining series. The nine specimens tested in this series were 4(b) to 6(b), all unstressed; 25(b) to 27(b), all stressed to 10%; and 28(b) to 30(b), all stressed to 15%. As in the two previous series, all unstressed and specimens stressed to 10% of their short-term tensile strength survived the exposure period. Of the three specimens stressed to 15%, only one survived. The remaining two failed within 173 days of exposure, with 28(b) being the first to fail after 108 days. As with previous failures, they occurred within the part of the specimen constantly exposed to the alkali solution, confirming the vulnerability of glass fibers in this environment.

The seven surviving specimens were tested to determine their residual strength. The results of these tests indicated strength losses that averaged 64% for the three unstressed specimens, and 69% for those stressed to 10% of their short-term tensile strength. The relatively small difference suggests that resin cracking plays a limited role, especially at low strain levels.

### Nine-month exposure

Table 5 summarizes the test results the nine specimen tested in this series. These were 1(b) to 3(b), all unstressed; 19(a) to 21(a), all stressed to 10%; and 22(a) to 24(a), all stressed to

**Table 6—Strength reduction prediction<sup>10</sup>**

Test series	Load, %	Diffusion coefficient $k$ mm <sup>2</sup> /h	Three month percent reduction		Six month percent reduction		Nine month percent reduction		Predicted life, years
			Experimental	Theoretical	Experimental	Theoretical	Experimental	Theoretical	
One month	0	1.80E-3	63	75	64	91	63	—	—
	10	2.80E-3	60	87	69	99	70	—	—
	25	34.7E-3	100	—	—	—	—	—	—
Three months	0	1.06E-3	—	—	69	80	70	89	1.60
	10	1.54E-3	—	—	69	88	70	96	0.50
	25	34.0E-3	100	—	100	—	—	—	—
Six months	0	0.55E-3	—	—	—	—	70	74	2.36
	10	0.73E-3	—	—	—	—	70	80	1.17
	15	3.04E-3	—	—	92	—	—	—	—
Nine months	0	0.320E-3	—	—	—	—	—	—	4.60
	10	0.38E-3	—	—	—	—	—	—	1.70
	15	7.07E-3	—	—	—	—	100	—	—

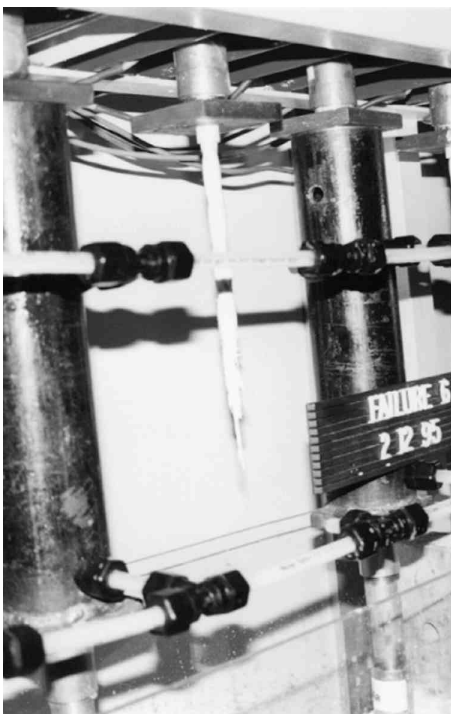


Fig. 5—Failed GFRP bar.

15%. As in all the preceding series, the unstressed specimens, and those stressed to 10% of their short-term tensile strength, survived the exposure period. All three specimens stressed to 15% of their short-term tensile strength failed, however, within 100 days of exposure, with 22(a) being the first to fail after 42 days. This contrasts with similarly loaded specimens in the previous series where specimens lasted much longer and one survived 180 days of exposure. As before, all failures occurred within the part of the specimen that was constantly exposed to the alkali solution.

The six surviving specimens were tested in the manner described previously to determine their residual strength. The results of these tests indicated strength reductions averaged 63% for the three unstressed specimens, and 70% for those stressed to 10%. These results confirm the trend observed in the previous series where the rate of reduction in strength dropped off with time for specimens stressed to relatively low levels.

### RESIDUAL LIFE PREDICTION

Katsuki and Uomoto<sup>10</sup> have proposed a simplified procedure to predict the deterioration of GFRP rods immersed in alkali solution that is based on Fick's First Law of Diffusion. The model allows the residual tensile stress  $\sigma_r$ , to be predicted from four parameters: a) diffusion coefficient  $k$  (mm<sup>2</sup>/h); b) the alkaline concentration  $C$  (mol/L); c) exposure time  $t$  in hours; and d) initial conditions, that is, radius,  $R_0$ , and initial tensile strength  $\sigma_0$ .

To utilize this model, experimental results of strength reduction over a given time frame were used to evaluate an average diffusion coefficient. This value was then used to predict the strength retained after different exposure times, that is, the 3-month diffusion coefficient was used for predicting strength retained after 6 months' exposure. In the case of stressed specimens, the predicted life was obtained by setting the strength retained to just below that needed to sustain the applied stress.

The results from the 1-month study were used to predict the residual strength after 3, 6, and 9 months, and also the remaining life. Similar calculations were carried out using results from the 3-, 6-, and 9-month series.

The results obtained are summarized in Table 6. This table also lists the calculated diffusion coefficients for each of the cases. Because strength reductions in the unstressed bars were smaller, the calculated average diffusion coefficients were also smaller.

Inspection of Table 6 shows that the use of results from the 1-month study for predicting the remaining life of both stressed and unstressed bars is unduly pessimistic, that is, failure is predicted much earlier. This is probably because resin cracking leads to a higher average initial diffusion value. The agreement gets better where results of later tests—for example, those done at 3 months—are used.

Because the model was calibrated for unstressed bars, predictions for these bars is of particular interest. The agreement is fair, however, except for predictions using the 6-month diffusion coefficient where the predicted reduction of 74% compares very favorably with the observed reduction of 70% after 9 months of exposure.

The predicted remaining life for the unstressed specimens ranges from 1.6 to 4.6 years. For the specimen stressed to 10%, it ranges from 0.5 to 1.7 years. The lower limit is based on results from the 3-month tests and the upper limit from the results of the 9-month tests. These predictions, of course,

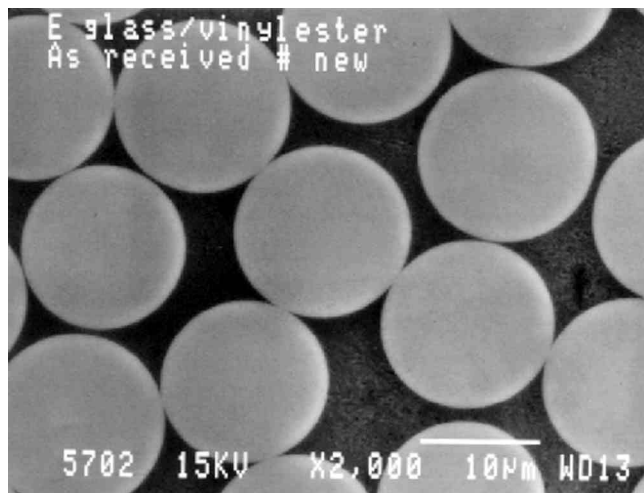


Fig. 6—As-received micrograph.

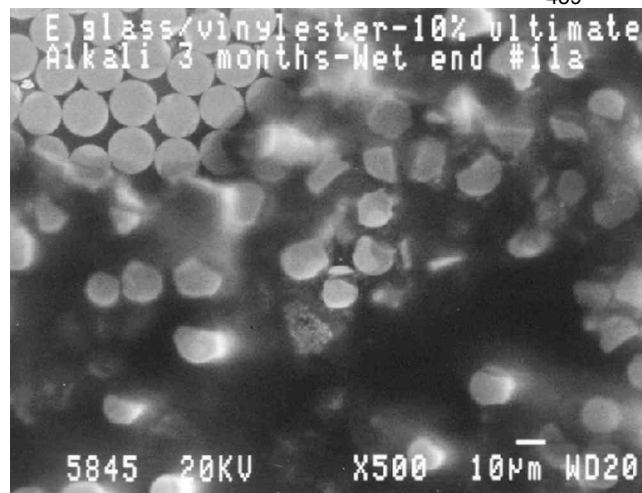


Fig. 9—10% stress after 3 months.

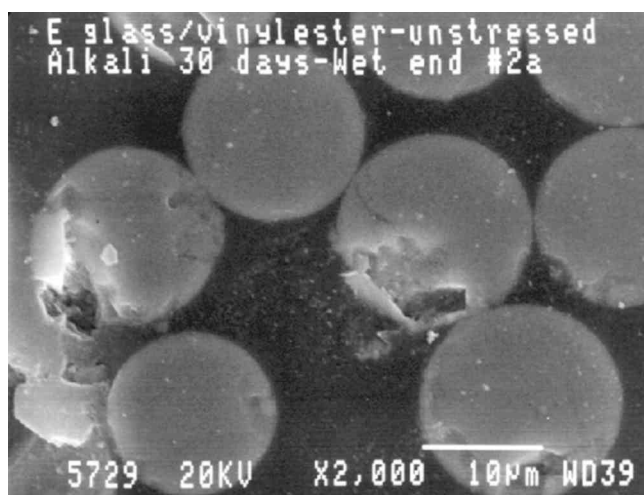


Fig. 7—Unstressed after 30 days.

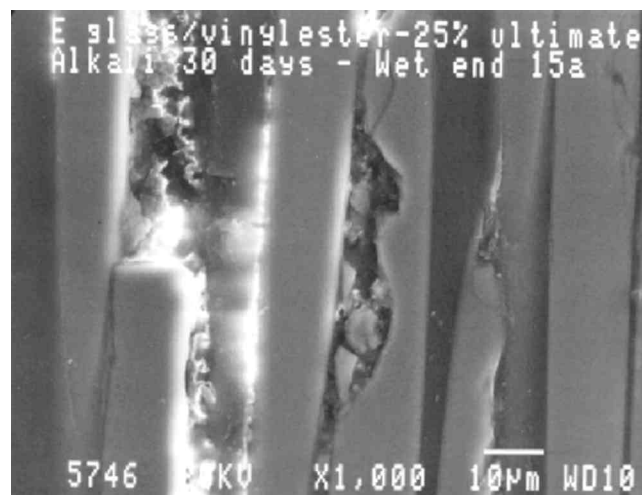


Fig. 10—Longitudinal failed section, 25% load.

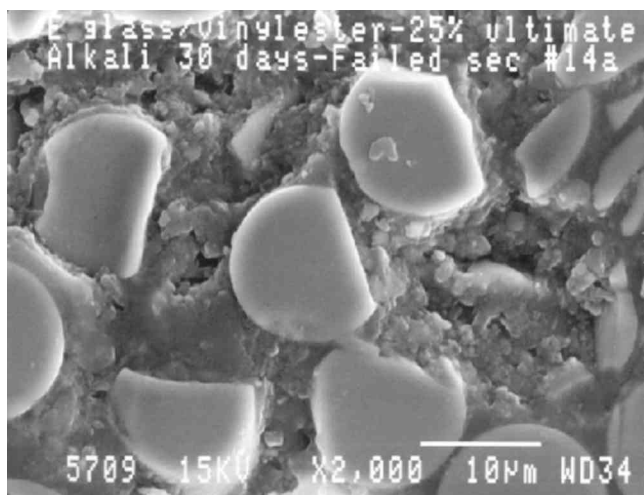


Fig. 8—25% stress after 30 days.

relate to the experimental conditions where the pH concentration remains the same throughout this time frame.

### DISCUSSION

The aim of this investigation was to assess the durability of the E-glass/vinylester bars used in the construction of the

MRI Pier, San Diego, Calif., at a sustained stress of 10% of its short-term tensile strength. In the study, an accelerated test was carried out in which these reinforcing bars were exposed to a highly alkaline solution that served to simulate concrete pore solution.

The results from the study convincingly demonstrate the lack of durability of the E-glass/vinylester bars tested. All specimens stressed to 25% failed within 25 days of exposure (Table 2). Five of the six specimens stressed to 15% failed within 180 days, and only one survived (Table 4 and 5). Only the unstressed specimens and the ones stressed to 10% survived the entire duration of the study. Even these specimens sustained substantial strength reductions. For unstressed specimens exposed for 9 months, the reduction averaged 63%, while for those stressed to 10%, the reduction was 70%.

Confirmation of alkali attack may be found from the scanning electron micrographs taken from the as-received specimen (Fig. 6) and from the failed sections of some of the exposed specimens (Fig. 7 to 9). For unstressed specimens, the process of dissolution may be seen in Fig. 7.

For specimens stressed to greater levels, missing cross sections, indicative of fibers that have dissolved, may be seen in Fig. 8 and 9 (the sharp edges of the surviving fibers in this plate are probably the result of cuts made to obtain a



sample and should be disregarded). The degradation can also be seen in the longitudinal section shown in Fig. 10.

The reduction in strength of the unstressed specimens shows that the alkali solution could readily diffuse through the vinyl ester resin that was used in the pultrusion process. The greater reduction in stressed specimens compared to the unstressed ones is indicative of the role played by resin cracking that provides a passage for additional hydroxyl ions from the alkali solution to attack the E-glass fibers. For specimens stressed to 10%, however, cracking is relatively minor given the small difference in residual strength compared with the unstressed specimens. Clearly, cracking plays a much more significant role for specimens stressed to higher limits, that is, 25% where failure occurred within 25 days, or 15% where failure occurred in five of six specimens within 180 days.

The results relate, of course, to the durability of the E-glass/vinyl ester bars tested in simulated pore solution. While this does not replicate the conditions the E-glass/vinyl ester reinforcing bars are exposed to in hardened concrete, they do, however, indicate extremely poor durability. In view of this, the bars tested are considered unsuitable for applications involving fresh concrete where diffusion is likely to be prevalent.

## CONCLUSIONS

This study presents results from a focused experimental investigation that evaluated the durability of E-glass/vinyl ester bars in an alkaline environment. The specimens tested were identical to those used in the construction of the MRI Pier, San Diego, Calif. Four stress levels: 0, 10, 15, and 25% of the ultimate short-term tensile strength were investigated. The pH of the simulated concrete pore solution varied between 13.35 to 13.5 over the duration of the study.

The following conclusions may be drawn:

1. The USF anchor (Fig. 1) provides a very reliable and inexpensive method of gripping the ends of GFRP polymer bars;

2. The exposure setup developed was quite versatile—it successfully allowed maintenance of the stresses in the GFRP bars, the pH level of the simulated pore solution, and permitted determination of the ultimate residual strength (Fig. 2 to 4);

3. The E-glass/vinyl ester bars tested showed limited durability in simulated concrete pore solution at stress limits above 15% of its short-term tensile strength. All six bars stressed to 25% failed within 25 days of exposure. Of the six bars stressed to 15%, five failed within 180 days. Unstressed specimens, and those stressed to 10% of the ultimate short-term tensile strength, survived the entire 9-month exposure duration. However, the specimens lost strengths ranging from 63% (unstressed) to 70% (10%) of their original strength. The loss in strength of the unstressed specimens indicates that diffusion of the simulated concrete pore solution through the vinyl ester resin was primarily responsible for the alkali attack of the glass fibers. The difference in the durability of stressed and unstressed specimens indicates that resin

cracking played an important role in the degradation process, particularly at higher stress levels;

4. The predicted life of the bars stressed to 10%, based on a model that only considers diffusion and disregards the effect of resin cracking, is between 0.5 to 1.7 years. The same model predicted a remaining life of between 1.6 to 4.6 years for the unstressed bars (Table 6); and

5. Given the experimental findings, the U.S. Navy's decision to select a 10% limit in a demonstration structure appears to be a judicious one, especially if conditions in the hardened concrete are less severe. The bar tested, however, is not durable and should not be used to reinforce concrete.

It is important to recognize that the above conclusions are only valid for the E-glass/vinyl ester bar tested. Newer GFRP bars developed are reputed to have much better alkaline resistance, though testing was carried out at lower pH levels, that is, 12.8<sup>9</sup> versus the 13.35 to 13.5 pH levels used in this study. Note that a pH of 12.8 is only 20% as strong as a pH of 13.5. Recent pH measurements<sup>11</sup> appear to validate the higher range used in this study because a pH of 13.5 is not uncommon. The profession needs to pay careful attention to the pH level specified in tests if GFRP is to be used as the primary structural reinforcement with confidence.

## ACKNOWLEDGMENTS

This investigation was carried out with the financial support of the U.S. Army Corps of Engineers. The authors wish to thank Edward O'Neil, program manager, and M. Chawla, of the Materials Engineering Naval Facilities Engineering Service Center, for their contribution. However, the opinions, findings, and conclusions expressed in this publication are those of the authors and not necessarily those of the U.S. Army Corps of Engineers.

## REFERENCES

1. Bentur, A., and Mindess, S., *Fiber Reinforced Cementitious Composites*, Elsevier Science Publishers, New York, N.Y., 1990.
2. Chawla, M. S., personal communication with R. Sen, 1993.
3. Sen, R.; Mullins, G.; and Salem, T., "Durability of E-Glass/Vinyl ester Bars in Alkali Solution," *Final Report* submitted to U.S. Army Corps of Engineers, Aug. 1996.
4. Hartman, D. R.; Greenwood, M. E.; and Miller, D. M., "High Strength Glass Fibers," *39th International SAMPE Symposium*, V. 39, Bk 1, 1994, pp. 521-533.
5. Mehta, P. K., and Monteiro, P., *Concrete: Structure, Properties and Materials*, Prentice-Hall, N.J., Second Edition, 1993, 154 pp.
6. Plumtree, A., and Jessen, S. M., "Damage Development in Composite under Stress in Composite Structures and Materials," *Composite Structures & Materials*, S. V. Hoa and R. Gauvin, eds., Elsevier Applied Science, Barking, England, 1990, pp. 68-75.
7. Sen, R.; Mariscal, D.; and Shahawy, M., "Durability of Fiberglass Pretensioned Beams," *ACI Structural Journal*, V. 90, No. 5, Sept.-Oct., 1993, pp. 525-533.
8. Sagüés, A., "Corrosion of Epoxy Coated Rebar in Florida Bridges," *Final Report* to Florida Department of Transportation, 1994.
9. Benmokrane, B.; Rahman, H.; Minh-Tan Ton-That; and Robert, J., "Improvement of the Durability of FRP Reinforcements for Concrete Structures," *Durability of Fibre Reinforced Polymer (FRP) Composites for Construction*, Montreal, Canada, 1998, pp. 571-585.
10. Katsuki, F., and Uomoto, T., "Prediction of Deterioration of FRP Rods to Alkali Attack," *Proceedings of the Second International RILEM Symposium (FRPRCS-2), Non-Metallic (FRP) Reinforcement for Concrete Structures*, L. Taerwe, ed., E&FN Spon, London, 1995, pp. 83-89.
11. Li, L.; Sagues, A. A.; and Poor, N. D., "In Situ Leaching Investigation of pH and Nitrite Concentration in Concrete Pore Solution," *Cement and Concrete Research*, V. 29, No. 3, 1999, pp. 315-321.

Title no. 98-S72

## Seal-Slab Prestressed Pile Interface Bond from Full-Scale Testing

by Gray Mullins, Ruben Sosa, Rajan Sen, and Moussa Issa

This paper presents experimental results from a study to assess the interface bond between a cast-in-place concrete seal slab and prestressed concrete piles in cofferdams. Three different seal slab placement conditions—fresh water, salt water, and bentonite slurry—were evaluated and the results compared against controls where no fluid had to be displaced by the concrete. Normal pile surfaces were investigated. Additionally, the situation of soil-caked piles was also investigated. Both model and full-scale tests were conducted. In the model tests, twenty-eight 15 cm square prestressed sections were used with the embedment depth varied between  $d$  and  $2d$ , where  $d$  is the width of the pile. In the full-scale tests, 16 specimens were tested. The prestressed piles were 36 cm square with the embedment varied between 0.5 and  $2d$ . Four of the 16 piles were cast with embedded gages located at the top, middle, and bottom of the interface region. The results showed that loads were transferred to the piles over an effective area, not the entire embedded depth. Significant bond stresses developed even for the worst placement condition. Recommendations are made for revising current values in specifications.

**Keywords:** concrete; foundation; pile; prestressed; salt water; slab.

### INTRODUCTION

Seal slabs are unreinforced concrete slabs cast inside cofferdams to prevent the intrusion of water and provide a dry working surface for subsequent construction (Fig. 1). Concreting is typically carried out by displacing water (or natural slurry in cases where the cofferdam supports the sides of an excavation) using a tremie. A tremie is essentially a funnel with a long pipe that places concrete directly on the bottom of the cofferdam. Because the concrete does not fall through the water, cement is not washed away and there is no segregation of coarse and fine aggregates. A series of tremie pipes is used to limit the flow of concrete in the horizontal direction to prevent the build-up of excessive laitance.<sup>1</sup>

As the function of the seal slab is primarily to provide a dry working surface, its design is relatively unsophisticated. The slab depth is selected so that its weight balances the maximum uplift forces. Thus, a 10 m unbalanced head would require a 4 m thick seal slab because concrete density is approximately 2-1/2 times that of water. Such a calculation neglects the frictional resistance that develops at the interfaces between the seal slab and foundation elements such as piles or drilled shafts.

The Florida Department of Transportation (FDOT) requires<sup>2</sup> the seal slab to cure for at least 72 h before the standing water (or slurry) inside the cofferdam can be pumped out. At that time, the seal slab experiences full uplift pressure due to imbalance in hydrostatic pressure inside and outside of the cofferdam. Rational design therefore requires information on the interface shear corresponding to the 72 h concrete strength. Unfortunately, no published data are available, even though the earliest work on interface

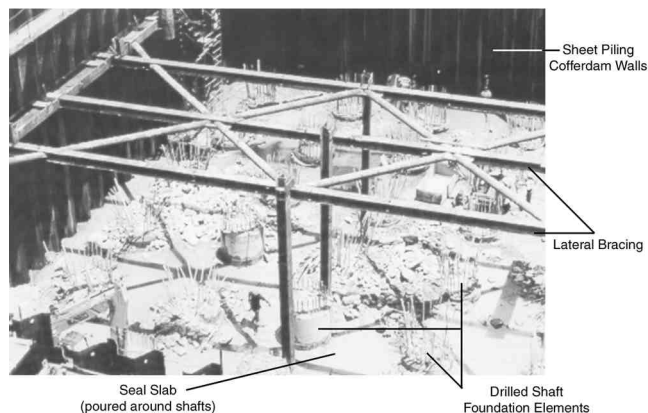


Fig. 1—Seal slab in cofferdam construction (Courtesy Georgia Department of Transportation).

shear between two concrete surfaces was reported as early as 1914.<sup>3</sup>

In the absence of experimental data, specifications provide interface shear values that are, by necessity, conservative. For example, AASHTO<sup>4</sup> states that “in seals, the bond between timber, steel, or concrete piles and surrounding concrete may be assumed to be 10 psi (69 kPa).” The 1998 Florida Design Guidelines<sup>5</sup> limited the interface bond between the seal slab and concrete piles to 276 kPa, though it was only set at 34 kPa for steel piles. The larger values permitted in Florida may be due to the local experience associated with the large number of bridges crossing waterways, a relatively high water table, and the predominance of highly pervious cohesionless (sandy) soils that result in excavations quickly filling with inflowing ground water.

In January 1998, the University of South Florida commenced a two-year research program to investigate this problem. Although the goal of the study was to evaluate bond on the basis of full-scale tests, a one-third-scale pilot study was initially carried out to evaluate critical parameters and to develop an efficient method of testing. Following completion of this study, a limited number of full-scale tests were conducted to assess the interface seal slab/pile bond characteristics for prestressed concrete and steel piles, and to recommend suitable values for design. This paper presents results relating to the seal slab/concrete interface bond. A companion paper provides the corresponding results for steel piles.<sup>6</sup> The

*ACI Structural Journal*, V. 98, No. 5, September-October 2001.

MS No. 00-266 received October 31, 2000, and reviewed under Institute publication policies. Copyright © 2001, American Concrete Institute. All rights reserved, including the making of copies unless permission is obtained from the copyright proprietors. Pertinent discussion will be published in the July-August 2002 *ACI Structural Journal* if received by March 1, 2002.

**Gray Mullins** is an assistant professor in civil and environmental engineering at the University of South Florida, Tampa, Fla.

**Ruben Sosa** received his BSCE and MSCE from the University of South Florida. He is with GeoSyntec Consultants, Tampa, Fla.

ACI member **Rajan Sen** is the Samuel and Julia Flom Professor in Civil and Environmental Engineering at the University of South Florida. He is a member of ACI Committees 215, Fatigue of Concrete; 440, Fiber Reinforced Polymer Reinforcement; and 444, Experimental Analysis for Concrete Structures.

**Moussa Issa** is currently the Chief Structural Engineer, T Y Lin International, Chicago, Ill. He is a member of ACI Committees E 801, Student Activities; 340, Design Aids for ACI Building Codes; and 444, Experimental Analysis for Concrete Structures.

complete experimental results, as well as the comparative finite element modeling, may be found elsewhere.<sup>7,8</sup>

## RESEARCH SIGNIFICANCE

No studies have previously been carried out to evaluate the seal slab/concrete interface bond for conditions that may be directly used in design specifications. This study provides the first such experimental data from full-scale tests. Results of the study have already led to changes in the latest specifications.<sup>9</sup> Therein, the allowable stresses are greater, permitting thinner seal slabs and bringing about significant savings in construction costs.

## OBJECTIVES

The overall goal of the study was to recommend interface bond values for seal slab and piles that could be directly used in FDOT's design specifications. These values were to be based on full-scale tests on specimens prepared in accordance with current FDOT specifications for commonly encountered conditions. Variables examined were the pile embedment depth, pile surface, pile material (steel or concrete), and the type of fluid displaced by the concrete.

## EXPERIMENTAL PROGRAM

A seal slab is subject to uplift pressures that are resisted in part by its weight and in part by shear resistance that develops at the pile/slab and sheetpile/slab interfaces, as shown in Fig. 2(a). The same load transfer characteristics can be simulated by applying tensile loads to the pile and compressive loads to the seal slab (Fig. 2[b]). In essence, the determination of the interface bond translated into conducting pullout tests on individual piles embedded in the seal slab; such an equivalent system was used in this study.

The reaction frame required to remove the piles from a seal slab had to meet multiple requirements of capacity, economy, and portability. An adaptable design was also required to accommodate the differing connections for the steel and concrete pile specimens. Additionally, it needed to be integrated with electronic devices that permitted measurement of load and displacement.

A key parameter in the design of the test equipment was capacity. An upper limit could be determined on the basis of the ultimate tensile capacity of the prestressed pile. This depended on the pile size, concrete strength, and the effective prestress. The greater the capacity, the larger and heavier the equipment, which made testing that much more difficult (and expensive).

Uncertainties associated with bond strength predictions were addressed using a comprehensive pilot study with small-sized piles. A scale model study was carried out to develop an efficient testing method and also to identify critical

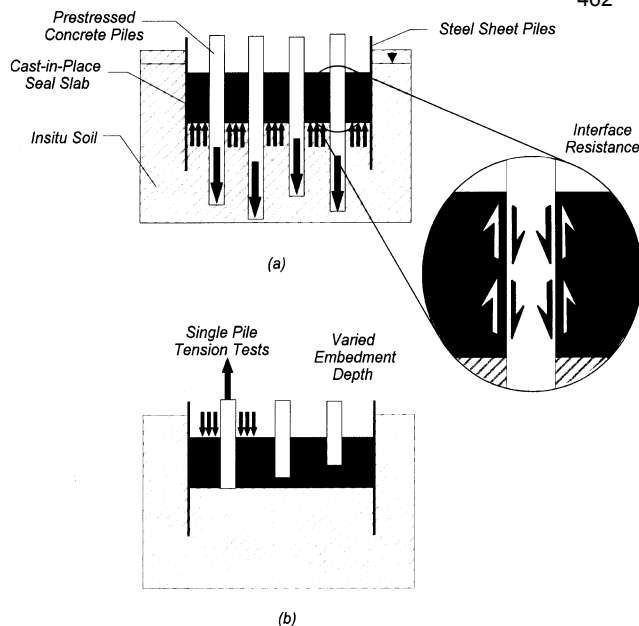


Fig. 2—(a) Field loading; and (b) uplift load simulation.

parameters for the subsequent full-scale program. Brief details from both studies, a complete set of results, and their analysis are presented.

## PILOT STUDY

The pilot study simulated three different seal slab placement conditions involving: 1) salt water; 2) fresh water; and 3) drilling fluid. Results were compared against the controls where no fluid was displaced by the concrete. One-third scale was selected since this allowed standard 45 cm prestressed piles to be exactly modeled.<sup>10</sup> Two different surface conditions—natural and soil-caked—were investigated.

Based on results of preliminary trials, the maximum interface bond between the two concrete surfaces was estimated to be approximately 1.7 MPa. This value was used to determine the maximum embedment depth that would not cause tension failure of the prestressed pile. As a result, three different embedment depths— $d$ ,  $1.5d$ , and  $2d$  ( $d$  is the side of the pile)—were investigated. For each embedment depth, two specimens were tested, that is, 24 tests were conducted (4 conditions  $\times$  3 embedment depths  $\times$  2 specimens). In addition, four soil-caked specimens were tested—one for each placement condition, and for an embedment depth of  $2d$ .

A total of 28 prestressed piles were tested. Square prestressed piles (1.22 m long, 15 cm wide) were fabricated at a commercial prestressing facility. During fabrication, 3.2 cm threaded bars were embedded centroidally in the specimens to provide a convenient attachment for pulling the specimens (Fig. 3 and 4). Complete details may be found in the final report.<sup>7</sup>

## Cofferdam simulation

Four 0.76 m high wood boxes with inside dimensions of 1.4  $\times$  1.4 m were fabricated to simulate the four excavation conditions. Plastic sheeting was used to make the boxes watertight. Wood templates were prepared so that the piles could be accurately positioned inside the form. The piles were spaced at  $3 \times$  pile size, that is, the center-to-center distance was 0.45 m ( $3 \times 0.15$ ). The edge distance from the center line was  $1.5d$  or 0.23 m.

As all the specimens were the same length and the seal slab the same thickness, the three different embedment depths of  $d$ ,  $1.5d$ , and  $2d$  were accommodated by varying the bonded and debonded lengths. For the 15 cm piles, this length varied between 15 cm ( $d$ ) and 30 cm ( $2d$ ). All bonded regions were at the bottom of the pile/seal slab. The debonded area was achieved by using bitumen covered with felt paper wrapped in duct tape (Fig. 3). A soil-caked surface was simulated by applying (with a trowel) a paste consisting of a viscous mixture of the clay mineral kaolinite and water. The clay had to be kept moist to prevent it from flaking off when it dried.

Three of the four simulated cofferdams were initially filled with one of the following items

1. Fresh water;
2. 3% salt water; or
3. Drilling fluid.

The latter was made by mixing dry, high-yield bentonite and fresh water to achieve slurry properties similar to those in the FDOT specifications. The final density achieved was  $10 \text{ kN/m}^3$  with a pH of 8 and a viscosity of 37 s (Marsh Cone method). The fourth cofferdam was the control and was therefore not filled.

### Seal slab placement

Class III seal concrete specified by FDOT<sup>2</sup> was used. This mixture has 332 kg of cement/ $\text{m}^3$ , a water-cement ratio ( $w/c$ ) of 0.51, and a specified 28-day strength of 21 MPa. The concrete was purchased from a ready-mix plant and was pumped through a 7.6 cm diameter hose. It was placed from the bottom upwards, keeping the hose tip below the rising level of concrete. This is similar in placement and identical in effect to the tremie method. Figure 3 shows the fresh water cofferdam just after concreting with several inches of free water still present.

### Pullout frame

The frame designed for the one-third-scale pilot study is shown in Fig. 4. It consists of two telescopic sections that react against each other via a stiffened beam and a hydraulic jack as shown. A standard nut was used to connect the free end of the threaded rod in the prestressed pile to the base of the tension assembly. Although Fig. 4 conceptually depicts the device assembly, the test procedure was streamlined by leaving it partially assembled between tests. The entire device weighed over 2.2 kN fully assembled and required an overhead chain hoist to assemble and/or move.

Tension loads were measured using a load cell inserted between the top of the jack and the tension assembly. The stiffened beam transferred the load from the base of the jack to a built-up column section which, in turn, applied a uniform compressive stress to the seal slab.

### Leveling

As the exposed surface of the seal slab was left uneven from the tremie placement method, a self-leveling grout pad had to be poured around each pile before testing. To further assist in the leveling process, a 12 mm steel bearing plate was placed on the grout immediately afterward. Once the grout had time to cure (approximately 15 min), the tension assembly was connected to the pile and the compression assembly supported on the bearing plate.

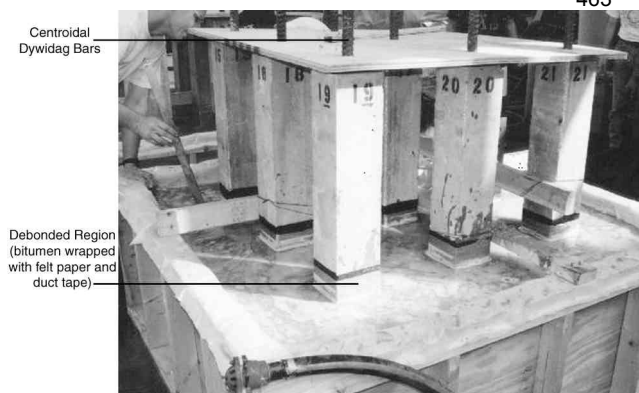


Fig. 3—Pilot study simulated cofferdam.

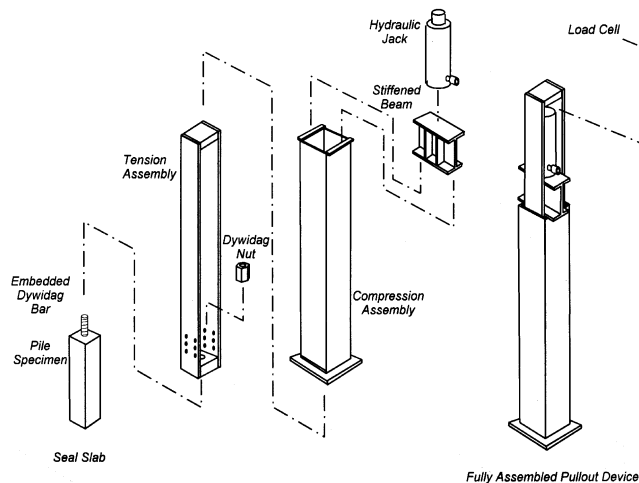


Fig. 4—Pullout equipment in pilot tests.

### Instrumentation

A data acquisition system was used for collecting and recording the test data generated. Loads were measured using a 100 tonne load cell and movement was monitored by two linear variable displacement transducers (LVDTs). One of the LVDTs was magnetically attached to the compression assembly and positioned to record displacement with respect to an external reference beam. This registered any possible seal slab surface crushing or settlement occurring during testing. The other LVDT was attached to the tension assembly and referenced to the top of the compression assembly. This accounted for specimen movement, along with elastic deformation of the frame which was later accounted for in the data reduction.

### Test procedure

Tests were initiated after the seal slab had been cured for 72 h. Concrete cylinders were periodically tested to monitor changes in compressive strength during the time it took to complete the tests. The frame was set in position and the pullout test commenced. The tensile load was increased slowly using a manually operated toggle switch, which intermittently engaged the power to a hydraulic pump. The load was increased slowly to reduce any possible dynamic stiffening of the system. Each specimen was displaced upward at least 2.5 cm.

**Table 1—Summary of pilot test results**

Type	Specimen	$f'_c$ , MPa	Bond length	Pullout load, kN	Bond stress, MPa	Average, MPa
Control	C22	27	1d	377	3.9	3.8
	C23	27	1d	358	3.8	
	C24	27	1.5d	610	4.2	4.3
	C25	27	1.5d	632	4.3	
	C26	27	2d	630	3.3	3.3
	C27	27	2d	625	3.3	
Salt water	C8	29	1d	398	4.1	4.1
	C9	29	1d	378	4.1	
	C10	29	1.5d	631	4.4	4.2
	C11	29	1.5d	591	4.1	
	C12	29	2d	651	3.3	3.4
	C13	29	2d	689	3.6	
Fresh water	C15	29	1d	354	3.7	4.0
	C16	29	1d	417	4.3	
	C17	29	1.5d	620	4.3	4.1
	C18	29	1.5d	573	3.9	
	C19	29	2d	560	2.9	3.1
	C20	29	2d	622	3.2	
Bentonite	C1	29	1d	141	1.5	1.5
	C2	29	1d	149	1.5	
	C3	29	1.5d	557*	3.9	2.8
	C4	29	1.5d	237	1.6	
	C5	29	2d	206	1.1	1.9
	C6	29	2d	543*	2.8	
Soil-caked	Control	27	2d	39	0.2	—
	Salt water	31	2d	521	2.7	—
	Fresh water	31	2d	397	2.0	—
	Bentonite	31	2d	49	0.3	—

\*Higher values are attributed to scouring action of pumped concrete on piles closest to inflow.



Fig. 5—Postmortem profile view of pilot study specimen during dismantling.

### PILOT STUDY RESULTS

A summary of the test results is presented in Table 1. This provides information from all 28 tests and contains details of the compressive strength, the failure load and the computed average bond stress. This was determined as the quotient of the measured failure load and the calculated surface area of the pile in contact with the seal slab. The following observations may be made:

1. Concrete strengths varied between 27 and 31 MPa over the duration of testing;

2. Significant bond stresses developed; the highest value obtained was 4.4 MPa (salt water/1.5d), and the lowest was 0.2 MPa soil-caked control. Highest values were for salt water, followed closely by controls and fresh water;

3. Embedment depths above 1.5d led to lower average values (Table 1). This suggests that the bond stress distribution is nonuniform and instrumentation would be required to gain an understanding on the stress transfer;

4. Results for salt water and fresh water cofferdam conditions did not differ significantly; and

5. The soil-caked condition did not affect interface bond except in the case of controls and bentonite slurry. For the salt water or fresh water condition, the soil caking was washed off by the water before the installation of the seal slab.

For the larger embedment depths, the prestressed concrete specimens cracked (Fig. 5). This suggested that depths in excess of 1.5d may be inappropriate for the full-scale tests. Cracking of the seal slab was also observed during dismantling of the test setup when the sides of the simulated cofferdam were removed. Figure 6 shows a load-slip plot obtained from the pilot study where the pullout capacity did not exceed the tensile capacity. Inspection of this plot indicates that there was continuous slip although minimal up to 50 kN (the elongation of the member was very small).

### FULL-SCALE STUDY

The results of the pilot study were used to develop a program for full-scale tests. The principal changes were: 1) elimination of the salt water condition; 2) instrumentation of selected piles to allow evaluation of bond stress distribution with embedment depth; and 3) restriction of the soil-caked surface to bentonite slurry placement. In view of the very high bond stresses that were obtained, the depth of embedment was limited to 1.5d, except for bentonite, where the maximum depth was increased to 2d. In addition, embedment depths of 0.5d were investigated for the control and fresh water placement conditions where the interface bond was expected to be very high.

With three different placement conditions (control, fresh water, and bentonite), two different embedment depths (d, 1.5d, or 2d) and two specimens per test, a total of 12 specimens, were required. Four additional specimens were tested—one each for embedment depth of 0.5d (for the control and fresh water condition) and two for investigating the effect of soil caking for the bentonite slurry for an embedment depth of 1d. Thus, the controls and the fresh water condition each had five specimens, with six specimens in the bentonite slurry condition.

The bond stresses obtained from the pilot study (Table 1) ranged from a low of 1.1 MPa (bentonite/2d) to a high of 4.3 MPa (control/1.5d). Because of these large values, 36 cm wide square prestressed piles were used in the full-scale tests. The length of each specimen was limited to 1.5 m. The ends of the strands protruding from the nonpulling end were clinched (flattened) to provide increased anchorage. This would not be required in practice where the pile lengths are much greater and extend beyond the upper surface of the seal slab.

Unlike the pilot tests where a central threaded rod was integrally cast with the specimens, for the full-scale tests the strands were directly attached to the tension frame with prestressing chucks. To ensure that the piles would have a somewhat greater capacity, larger 15 mm strands were used

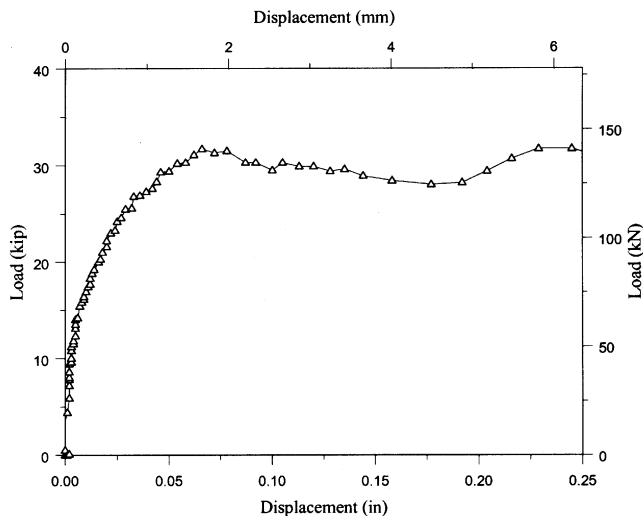


Fig. 6—Load versus displacement: Specimen C1 (1d, bentonite).

instead of the standard 12.5 mm strands, though they were stressed to provide the same effective prestress. The eight 15 mm strands gave an ultimate pulling capacity of  $260 \times 8 = 2.1$  MN that exceeded the expected pullout load of the pile. This provided a margin of safety against sudden, dangerous tensile failure of the strands.

A total of 18 specimens were cast at the same commercial prestressing yard. The spacing of the specimens inside the prestressing bed was adjusted so that each specimen had a 0.6 m length of strand projecting from the pulling end that served as a connection point to the pullout frame. Additionally, four specimens were instrumented with embedded sister bar-type strain gages to allow the distribution of bond stresses to be assessed. Figure 7 shows three sister-bar strain gages that consist of a resistive foil strain gage bonded to a short length of 13 mm reinforcing bar. These were located at the bottom, middle, and top of the bonded length of  $1d$  (three specimens) or  $2d$  (one specimen) (Fig. 7). Complete fabrication details may be found in the final report.<sup>7</sup>

### Simulated cofferdam

Three cofferdams had to be constructed for the three conditions investigated. The dimensions of the cofferdams were determined by the number of piles and a  $3d$  pile spacing (1.07 m) as in the pilot study. Thus, two of the cofferdams—fresh water and control—were identical in size, but the bentonite slurry-filled cofferdam was larger as it had more specimens.

The cofferdams were constructed using rented steel-reinforced plywood box forms. The forms were connected to form each cofferdam using wedge pins provided by the manufacturer. They were also externally braced using wooden stakes and internally braced with a wooden template that maintained the pile positions. Additionally, each cofferdam was lined with 0.15 mm plastic sheeting. This allowed for the forms to be watertight, preventing the loss of any construction fluid (water or bentonite slurry).

### Specimen support

Following the construction of the cofferdam, the specimens were accurately positioned on plywood pads to prevent damage to the plastic lining. Additionally, a polystyrene seal was placed between each concrete pile specimen and the wooden pad to prevent possible bonding between the cast-in-

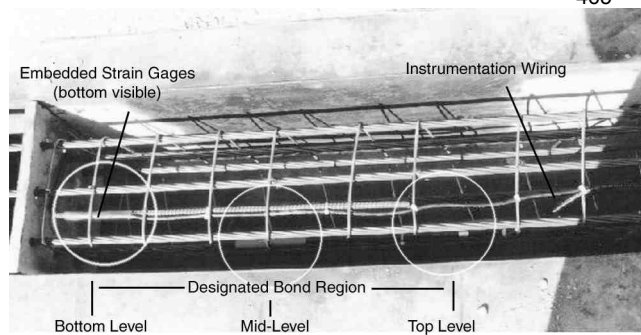


Fig. 7—Prestressing bed for casting 36 cm instrumented piles.



Fig. 8—Overview of cofferdam during concreting.

place seal concrete and the bottom of the pile. The specimens were vertically supported by a wooden framework that was secured to the forms (Fig. 8).

### Debonded surface

As in the pilot study, differing lengths ( $0.5d$ ,  $1d$ ,  $1.5d$  and  $2d$ ) of the pile surface were bonded or debonded. Debonding was achieved in the identical manner. The bonded concrete surfaces were left in their natural state except for the two specimens that were tested for the soil-caked condition. For this case, an adhesive clay soil, typically used for clay models by artists, was used because it bonded better than the kaolinite paste tested in the pilot study.

The debonded length extended from the boundary of the bonded region to approximately 15 cm above the intended elevation of the finished surface of the seal slab. This included an additional 36 cm depth determined from finite element analysis to ensure uniform distribution of compressive loads to the seal slab (Fig. 2[b]).

### Bentonite

The bentonite slurry was made by mixing dry, high-yield bentonite and fresh water. The mixing was accomplished through the use of a shear pump. Enough bentonite clay was added to achieve slurry properties similar to FDOT specifications. The final density achieved was  $10.2 \text{ kN/m}^3$  with a viscosity of 40 s (Marsh Cone Method) and a pH of 8. Fig 8 shows the filling and completion of the bentonite slurry filled simulated cofferdam.

the 72 h cure period, appropriate adjustments were made to expedite testing.



Fig. 9—Full-scale pullout device.

### Seal slab placement

Seal concrete was placed using a concrete pump truck. The concrete was pumped through a 15 cm diameter hose. It was placed from the bottom upward keeping the hose tip below the rising level of concrete. This procedure is identical to the tremie method commonly used in construction practice.

### Testing apparatus

Similar considerations of capacity, economy, and portability dictated the design of the pullout frame. This design incorporated an available double-acting, 3 MN hydraulic jack, a 69 MPa hydraulic pump system, and could accommodate connections for both concrete and steel pile types. Additionally, it provided sufficient clearance for a 4 MN load cell as well as means to record pile displacement.

As with the pilot test, the reaction frame consisted of a tension and compression assembly. The tension assembly was connected directly to the pile using prestress chucks and supported by the hydraulic jack and load cell. The stiffened beam was integrated directly into the compression assembly which applied compressive loads to the seal slab. Fully assembled, the device weighed 16 kN and was placed over each specimen with a straight mast industrial forklift (Fig. 9). Additional information on the design and fabrication may be found elsewhere.<sup>7</sup>

### Test setup

The test setup was similar to the pilot study and involved placement of a grout layer, assembly and connection of the hydraulic testing apparatus, attachment of the data acquisition system, and application of loading until failure. Given the requirement that testing be completed quickly following

### Leveling grout pad

Because concrete vibration is not used in seal slab construction due to possible aggregate segregation in the submerged environment, various degrees of surface roughness developed depending on the placing condition. The bentonite placing condition had the greatest degree of unevenness; the control had the least. The uneven surfaces were leveled using a thin layer of high-strength grout that was placed directly over the seal slab (Fig. 9). The grout was placed and finished two days after the placement of the CIP seal slab. Since the debonded portion of each pile specimen extended well above the CIP slab, there were no difficulties with possible bonding of the grout to the piles.

### Frame assembly

Although much heavier than the pilot study device, the full-scale pullout device was easier to use in that it could be left fully assembled between tests. This reduced the number of heavy lifts and expedited testing.

As the entire frame was lowered over the test specimen, the exposed prestressing strands were threaded through the holes in the base of the tension assembly. Standard prestressing chucks that incorporate wedge-type grips were secured on each strand. A 76 mm gap was maintained between the tension assembly and the top of the pile to permit removal of the prestressing chucks after testing. With the chucks in place, the frame was centered and the concrete pile tested.

### Data acquisition

As with the pilot study, the data acquisition system was used for collecting and recording the test data generated by the pullout testing. Along with the system, a load cell and two electronic displacement gages (LVDTs) were used to monitor each pile specimen as it was tested. The load cell had a capacity of 4 MN. The electronic displacement gages had a 50 mm range. Additionally, strains were monitored in selected piles that had been cast with embedded resistance-type sister bar strain gages (Fig. 7). For the concrete specimens, one LVDT was magnetically attached to the bottom of the tension assembly and positioned to register displacement with respect to an external reference beam. The other LVDT recorded relative displacement between the tension assembly and the top of the pile specimen. This accounted for any possible slippage of the prestressing chucks.

### Test procedure

Once the setup procedure was completed, the pullout testing could be conducted. The tensile load was increased slowly using a manually operated toggle switch which intermittently engaged the power to the hydraulic pump. The load was increased slowly to reduce any possible dynamic stiffening of the system. Each specimen was displaced upward at least 25 mm to ensure that the bond interface had been displaced.

## RESULTS

A summary of the test results is presented in Table 2. This provides information from all 16 tests and contains details of the compressive strength, failure load, and the computed average bond stress. Inspection of Table 2 shows that the bond stresses were quite high, ranging between 4.5 MPa for 0.5*d* embedment in the controls to the lowest value of 1.1



**Table 2—Summary of full-scale test results**

Type	Specimen	$f'_c$ , MPa	Bond length	Pullout load, kN	Bond stress, MPa	Average, MPa
Control	C0.5	27	0.5d	1151	4.5	—
	C1.0A	32	1d	1656	3.2	3.2
	C1.0B	32	1d	1580	3.1	
	C1.5A	32	1.5d	1584	2.1	2.4
	C1.5B	32	1.5d	2020	2.6	
Fresh water	W0.5	27	0.5d	892	3.5	—
	W1.0A	27	1d	1358	2.7	2.7
	W1.0B	27	1d	1336	2.6	
	W1.5A	27	1.5d	1591	2.1	2.0
	W1.5B	27	1.5d	1527	2.0	
Bentonite	B1B	23	1d	1338	2.6	2.5
	B1D	23	1d	1274	2.5	
	B2A	23	2d	1625	1.6	1.5
	B2B	23	2d	1438	1.4	
Bentonite (soil-caked)	B1A	23	1d	931	1.8	1.5
	B1c	23	1d	570	1.1	

MPa for one of the soil-caked bentonite specimens. Trends observed in the pilot tests were repeated: the average bond stresses decreased with increased embedment depth. For example, the average bond stress reduces from 2.7 MPa to 2.0 MPa for fresh water specimens embedded 1.0d and 1.5d, respectively.

Variations in concrete strength over the duration of the test may also be noted. The lowest compressive strength was for the bentonite series ( $f'_c = 23$  MPa) and the highest for the controls (32 MPa). This was due in part to an increase in strength over the seven-day period it took to complete the testing. A typical load-versus-slip variation plot is shown for each cofferdam condition in Fig. 10 to 12. As previously noted, the plots show continuous displacement with increasing load, initially elastic and then plastic. While measurements included the effect of elongation of the 1.5 m long prestressed pile, calculations show that length increases were minimal even after the pile had cracked. Figure 10 shows no evidence of cracking (bentonite) whereas Fig. 11 and 12 indicate pile cracking at 1044 and 955 kN, respectively. The cracking load was consistently smaller than expected due to the shortened transfer length near the end of the pile and the associated inability to develop effective prestress in the concrete. This was due to the relatively short length of the test piles. In actual construction where longer piles are used, this would not be the case. Additionally, variations in cracking force in nearly identical specimens were attributed to indiscernible alignment errors during testing.

### Strain variation

The shear stress distribution within the bonded region of the pile was evaluated using embedded strain gages in four of the specimens: fresh water (1); control (1); and bentonite (2). The bond length was 1d for three of the specimens (one in each bed) and 2d for an additional specimen in the bentonite. The gages were located at the top, middle, and bottom of the bonded region. Figure 13 shows the axial strain measured at three points along the bond interface during testing of one instrumented pile specimen. Additional results may be found in the final report.<sup>7</sup> The strains recorded at three levels (top, middle, and bottom of the bond interface) define two bonded layers

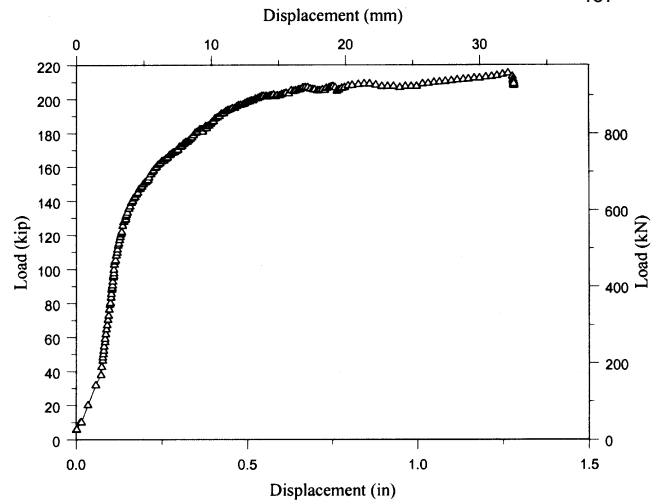


Fig. 10—Load versus displacement—Specimen B1A (1d, bentonite, soil-caked).

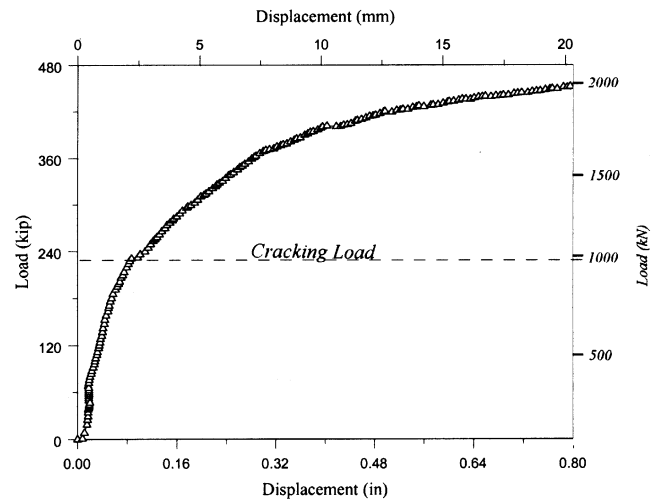


Fig. 11—Load versus displacement—Specimen W1.5B (1.5d, water).

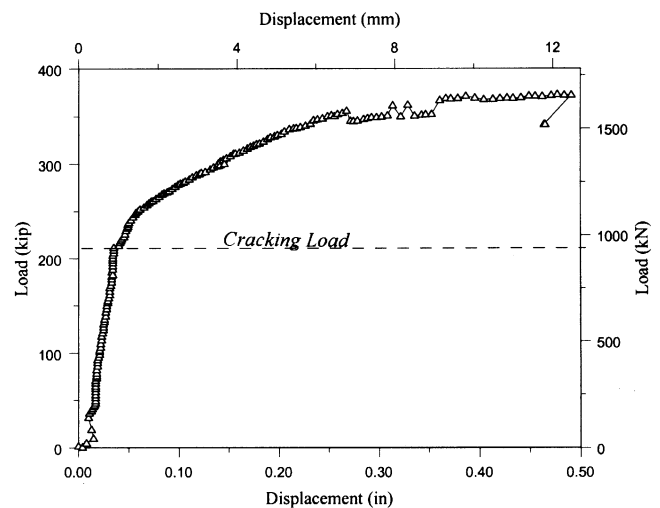


Fig. 12—Load versus displacement—Specimen C1.0A (1d, control).

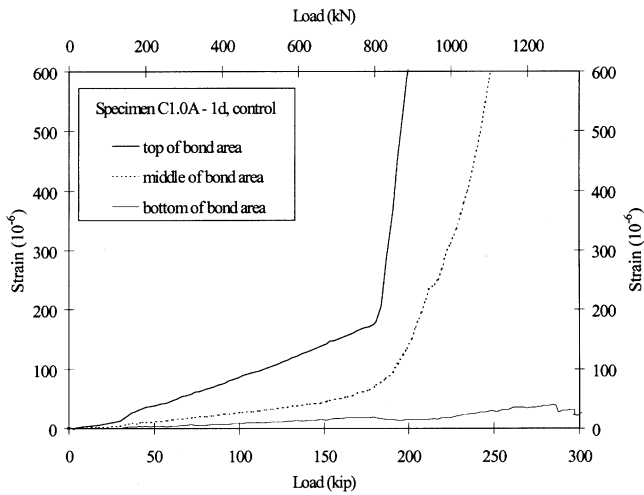


Fig. 13—Change in strain with respect to load for Specimen C1.0A (control, 1d embedment).

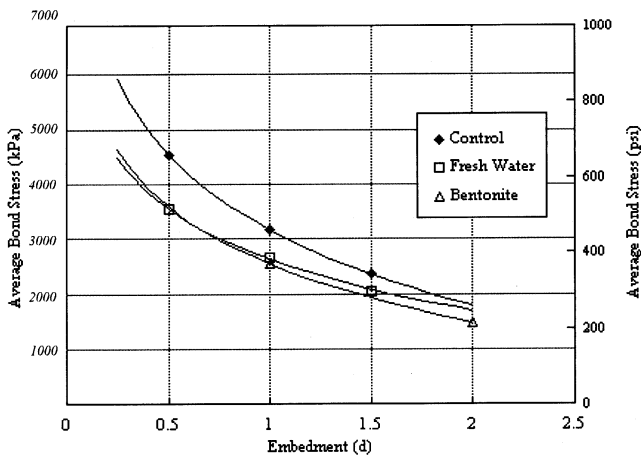


Fig. 14—Average bond stress variation with embedment from full-scale testing.

Table 3—Allowable bond stresses for square piles

Material	Condition	$f_b$ , MPa
Concrete	Salt or fresh water	2.1
	Bentonite	0.7

(upper and lower) separated by the middle gage. The difference between the top and middle gage indicates the load carried by the upper layer. Likewise, the difference between the middle and bottom gage indicates the load carried by the lower bond layer. Inspection of this plot shows the load distribution stayed relatively constant up to the elastic limit of the upper bonded layer (2 MPa); at which time the load was gradually transferred to a lower layer. The top gage reading should linearly relate to the load cell as there is no alternate load path between them. As expected, the gage at the bottom of the bond area registers near zero strains as no additional capacity can be developed below that level. The nonlinear portion of the middle gage indicates the upper layer bond failing and transferring load to the lower layer. Sharp discontinuities are observed in the upper gages due to sudden cracking; whereas less severe strain changes are noticed in the middle gages as the cracked sections reach further into the seal slab.



Fig. 15—Pile cracks during loading.



Fig. 16—Seal slab cracks during testing.

The load distribution as measured by the strain gages indicates that the full bond length contributed to its capacity. However, peak bond capacities occurred at different locations and times from top to bottom in that the amount of slippage required to develop peak shear strength is small with respect to elastic elongation. This can also be deduced by evaluating the average bond strengths from Table 2 with respect to embedment (for example, average control values: 0.5d, 4.5 MPa; 1.0d, 3.2 MPa; and 1.5d, 2.4 MPa). As embedment decreases, bond strength approaches an upper limit proportional to the concrete strength as shown in Fig. 14.

As in the pilot study, cracking was observed in both the prestressed piles and in the seal slab. Figure 15 shows a transverse tension crack just above the seal slab. Figure 16 shows a crack that formed in the seal slab originating from the corner of a pullout specimen. These conditions need to be addressed in design.

### CONCLUSIONS

This paper presents results from an experimental study that investigated the interface bond stress that developed between seal concrete and prestressed piles in cofferdams. Two series of tests were conducted. In the first series, one-third-scale models were fabricated and tested. Three variables were investigated: 1) displacement of fresh water, salt water, and bentonite slurry; 2) different pile surface conditions; and 3) varied embedment depths expressed as multiples of the pile width  $d$ . In the second series, full-scale tests were conducted for only two conditions (fresh water and bentonite slurry) as well as varied embedment depths. In all cases, results were compared against controls where no fluid was displaced. Seal slabs were cast using concrete delivered by ready-mix plants that conformed to Class III concrete in current FDOT specifications.<sup>2</sup> The concrete was allowed to cure for 72 h before testing as permitted by existing specifications. The following conclusions may be drawn:

1. Bond stresses determined experimentally were significantly higher than set in current specifications. Average values obtained from the full-scale tests varied between 2.0 to 2.7 MPa for fresh water displacement and from 1.5 to 2.5 MPa for bentonite displacement. The lowest value obtained was 1.1 MPa for piles caked in soil and embedded in bentonite to a depth  $d$ ;

2. Bond stress values from the full-scale tests were generally smaller than those for the model tests excepting for bentonite slurry (Table 1 and 2);

3. Strain data indicated that regardless of the embedment depth, loads were transferred to the pile over an effective depth. For the specimens tested, this depth was the same as the size of the pile  $d$ ;

4. The bond between seal slab and piles caked with mud was largely unaffected when fresh water or salt water was displaced. These effects became important in controls or when bentonite slurry was displaced. This was because the caked soil was washed away by water currents that developed during concreting; and

5. Prestressed piles and seal slabs developed cracks before the full pullout load was developed. Thus, structural failure of the seal slab and/or the piles themselves should be considered in any rational design process.

### RECOMMENDATIONS

The buoyancy force generated at the base of a seal slab can be withstood using a combination of both the bond strength formed between the pile and the cast-in-place concrete as

well as its self-weight. While using this bond to offset a portion of the upward load, the tensile force developed in the pile cannot be permitted to exceed its cracking strength. The bond capacity developed by an individual pile may be determined using the allowable bond stress  $f_b$  listed in Table 3.

This stress  $f_b$  may be assumed to act uniformly over an effective surface area  $A_e$ , given by

$$A_e = pD \quad \text{if } D < d$$

or

$$A_e = pd \quad \text{if } D > d$$

given the pile width  $d$ , pile perimeter  $p$ , and the seal slab thickness  $D$ . This limits the effective bond length to  $1.0d$  of the pile. Hence, the uplift capacity of the pile  $P$  is the lesser of the allowable bond capacity ( $P_a = f_b A_e$ ), or the pile tensile strength (for example, AASHTO [5.6.3.4.1-1]).

In the latest Florida Design Guidelines,<sup>9</sup> allowable bond stress values have been increased from 40 to 250 psi (0.3 to 1.7 MPa) based on the results that are presented in this paper.

### ACKNOWLEDGMENTS

This investigation was carried out with the financial support of the Florida Department of Transportation. The authors especially acknowledge the contribution of Hayward Baker, Inc., Tampa, Fla., as well as Rudy in the full-scale testing. Additional thanks are extended to P. V. Liles, Jr. and the Georgia Department of Transportation for providing Fig. 1. The opinions, findings, and conclusions expressed in this publication are those of the authors and not necessarily those of the Florida Department of Transportation.

### REFERENCES

- Tomlinson, M. J., *Foundation Design and Construction*, 5th Edition, Longman Scientific and Technical, Essex, England, 1986.
- "Standard Specifications for Road and Bridge Construction," Florida Department of Transportation, State Specifications Office, Tallahassee, Fla., 1999.
- Johnson, L. J., and Nichols, J. R., "Shearing Strength of Construction Joints in Stems of Reinforced Concrete T-Beams as Shown by Tests," *Transactions of the American Society of Civil Engineers*, Dec. 1914, pp. 1499-1522.
- "Standard Specifications for Highway Bridges," 13th Edition, American Association of State Highway and Transportation Officials, Washington, D.C., 1983.
- "Structural Design Guidelines," Florida Department of Transportation, Tallahassee, Fla., July 1998, pp. 4-12.
- Mullins, G.; Sosa, R.; Sen, R.; and Issa, M., "Seal Slab/Steel Pile Interface Bond from Full-Scale Tests," 2001. (in preparation)
- Mullins, G.; Sosa, R.; and Sen, R., "A Seal Slab/Pile Interface Bond," *Final Report* submitted to Florida Department of Transportation, June 2000, 151 pp.
- Wu, Z., "Studies of Bond of Cast-in-Place Concrete to Other Surfaces," MSCE thesis, Department of Civil and Environmental Engineering, University of South Florida, Tampa, Fla., Aug. 1999.
- "Structural Design Guidelines," Florida Department of Transportation, Tallahassee, Fla., 2000.
- Fischer, J.; Mullins, G.; and Sen, R., "Strength of Repaired Piles," *Final Report* submitted to Florida Department of Transportation, Mar. 2000.

## Studies on the Use of Powder Actuated Nails in Pile Repair

Jeff Fischer<sup>1</sup>, Gray Mullins<sup>1</sup>, Rajan Sen<sup>1</sup> and Moussa Issa<sup>2</sup>

### Abstract

The bond between original and new material is of critical importance in any repair. In an effort to improve bond, the Florida Department of Transportation recently proposed the use of powder actuated nails as shear connectors in the repair of corrosion-damaged prestressed piles. This paper presents results from an experimental study that investigated the efficacy of such repairs. In the study, six one-third scale repaired prestressed columns were tested under concentric axial loads. The repairs were carried out in accordance with current specifications on sections where damage had been simulated during fabrication. Two different shear connector arrangements were investigated. The results indicated that improvement in performance was relatively modest. However, damage caused by the installation of the powder-actuated nails could be problematic.

### Introduction

Corrosion damaged piles are commonly repaired by pile jacketing. In this method, jackets consisting of removable or stay-in-place forms are installed around a pile and subsequently filled with concrete, mortar or epoxy. This type of repair is referred to as *non-structural* and is carried out where damage is minor. In case of extreme damage, *structural* repairs are carried out in which a reinforcement cage is incorporated inside the jacket to provide increased capacity.

---

<sup>1</sup> Department of Civil and Environmental Engineering, University of South Florida  
Tampa, FL 33620

<sup>2</sup> T Y Lin International, Chicago, IL

The efficiency of a repair may be improved by achieving better bond between the pile core and the repair material. Shear connectors are widely used in bridge decks to ensure composite action. The idea of using the same concept in piling applications was first recommended by one of Florida Department of Transportation's districts who proposed the use of powder actuated nails as shear connectors. These are simple to install and have a proven track record for applications involving concrete and steel. In their proposed scheme, the powder actuated nails are fastened to the pile surface in a rectangular grid pattern at 75 mm (3 in.) on centers in the top region of the jacket above the high water level. This arrangement was based on an intuitive understanding of the structural response.

In 1998 the University of South Florida embarked on a study to assess the efficiency of jacketed repairs. As part of this investigation, they chose to conduct experimental studies to assess the effect of using powder actuated nails on the ultimate axial capacity. The repairs were carried out on one-third scale prestressed piles and results evaluated against the ultimate capacity of undamaged controls. This paper presents a brief description of the experimental program and a summary of the test results. Complete test results may be found elsewhere (Fischer et al., 2000).

## Experimental Program

### Specimen Detail

The test specimens were each 2.44 m long and 15 cm x 15 cm in cross-section. This was established on the basis of a survey of damage in corroded prestressed piles observed statewide. They were prestressed by four 7.9 mm Grade 250 prestressing strands each jacked to 51.5 kN. This provided a jacking stress of 8.9 MPa that is consistent with values of 8.3-9.5 MPa in prototype piles.

To ensure uniformity, accelerated corrosion methods were not used for simulating damage. Instead, damage was artificially formed during fabrication with the help of plywood cutouts. The damage zone had a constant cross-section of 11.4 cm x 11.4 cm that extended over a 45 cm length corresponding to 1.35 m in the prototype. A 3:1 transition slope was provided at each end of the uniformly damaged surfaces to the 15 cm by 15 cm section. As 19 mm plywood was used, this meant the damage length was an additional 11.4 cm. The resulting *formed* surface provided the texture that was used in all the repairs that are reported.

### Powder Actuated Nails

In addition to FDOT's scheme in which powder actuated shear connectors are provided in the upper region of the pile jacket above the waterline, an alternate scheme was investigated in which shear connectors extended over the *entire* repair region. The latter scheme is referred to as the *modified* scheme. These two schemes were used in both the non-structural and structural repairs.

Because a limited number of specimens were available, the majority of the specimens tested were non-structural as is generally the case in actual repairs. Thus, only two of the six specimens tested were structural, the remaining four being non-structural. As the modified scheme was anticipated to provide better results, four of the test specimens employed this scheme. These included both structural and non-structural repairs. The original FDOT scheme was limited to non-structural repairs.

Powder actuated nails come in a limited number of sizes and therefore their use in the one-third scale model presented particular problems especially since spacings had to comply with limitations imposed by the manufacturer. As a result, only a single line of 5 cm long fasteners could be used. These had a 7.5 mm head diameter with a shank diameter of 3.6 mm. They were installed with a low velocity, semi-automatic .27 caliber tool. These nails were selected specifically because they were appropriate for the concrete strength of the prestressed piles.

Fig.1 shows the layout of the nails. The first nail was driven along the centerline of the pile 5 cm above mid height. The remaining fasteners were spaced at 7.5 cm intervals. These nails were placed on each of the four faces. In the first (original) scheme, a total of 20 nails were used. In the modified scheme, 40 nails were used since they extended below the waterline.

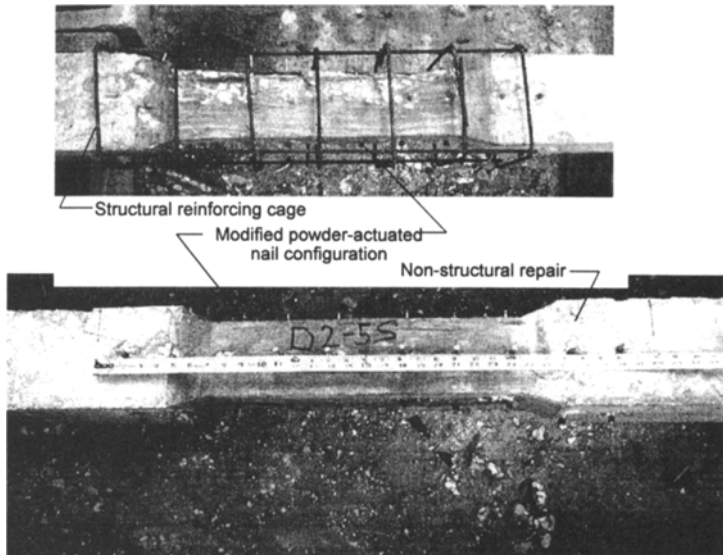


**Figure 1.** Structural and non-structural repair.

## Repair Procedure

Field repairs are carried out on loaded bridges where piles support both service dead and vehicular loads. A special service load simulator was fabricated that permitted sustained loads to be applied to the pile prior to jacketing. This maintained increased stress in the reduced section typical of damaged piles prior to the application of the repair material. In essence it consisted of a pair of steel angles that were clamped in place by high strength bolts (Fig. 2). Two threaded rods were connected to these angles and tensioned to provide the requisite compressive stress in the pile. A calibrated torque wrench was used to maintain desired sustained compressive stress.

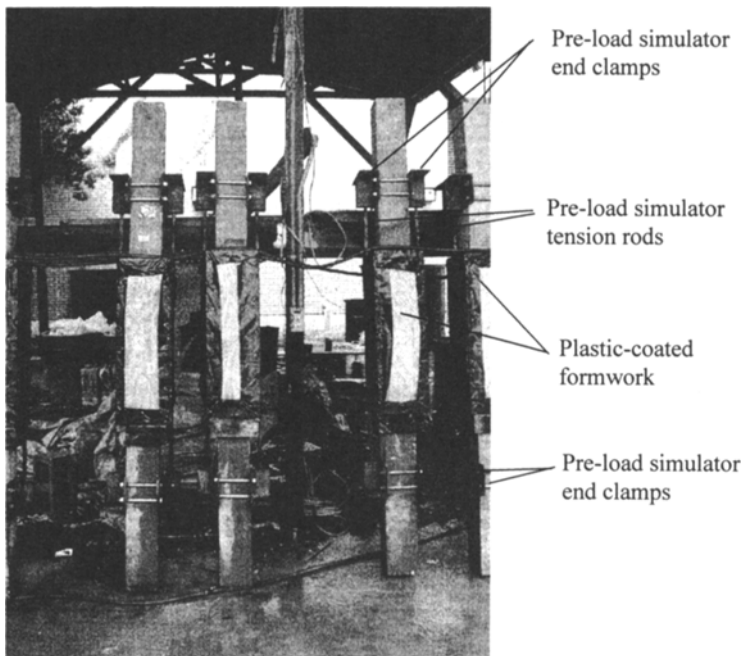


**Figure 2.** Piles with jackets and pre-load simulator prior to concreting.



A jacket was formed around the pile and filled with water. The forms were drained just prior to the placement of Class IV concrete (FDOT, 1996). The repaired piles were cured at least 28 days with the plastic lined plywood forms in place.

## Results

An earlier phase of the study indicated that axial load tests were better at identifying improvements in interface bond between the repair material and the pile core. In view of this, testing of the repaired piles was limited to concentric load tests that were conducted on all six specimens. The results of these tests were compared against those for undamaged controls.

Prior to the test, specimens were instrumented by a number of strain gages that were bonded to the outside surface of the jacket. Additional gages were also attached to the prestressed pile surface. Readings from these gages enabled an assessment to be made of the load transfer characteristics in the jacketed region.

Table 1 provides a summary of the average failure loads from the three series of tests carried out on the six specimens. It also includes information on the debonding load and presents it as a percentile of the ultimate load and that of the undamaged control. Inspection of Table 1 shows that the performance of the structural repair was the best as it reached 73.9% of the capacity of the undamaged control. The performance of the non-structural repairs was surprising; the capacity of the modified repair was lower than that of the original repair in which powder actuated shear connectors were limited only to the top region. This result is believed to be caused by damage that resulted during the installation of the fasteners. As damage was greater, with the installation of more nails, there was greater reduction in capacity.

**Table 1** Summary of results from axial load tests.

Test Series	Average Debond Load kN	Average Ultimate Load kN	Debond Percent kN	Percent of Undamaged Control kN
Undamaged controls	n/a	1064	n/a	100%
Structural repairs	774	786	98.3	73.9
Non-Structural <i>nails at top</i>	632	674	93.9	63.4
Non-Structural <i>nails top and bottom</i>	574	620	92.7	58.3

Inspection of Table 1 also shows that there was little capacity beyond debonding. This was also reflected in the failure modes. In the case of structural repairs where there was a modest 1.7% increase, there was some cracking in the jacket but no separation. In the case of the non-structural repair, the jacket was completely separated where nails were only provided at the top. In the remaining case, the jacket was still held to the pile at the bottom.

Measurement of strain variation across the depth of the pile jacket indicated that the strains were lower at the top than at the bottom. This suggests that bond is poorer at the top than at the bottom. This is probably because of water from the concrete mix rising to the top. It may be noted that ACI 318 imposes a 30% penalty on rebars that have 12 in of concrete below it.

### **Conclusions**

This paper presents results of a study conducted to evaluate the effect of using powder actuated nails to improve composite action in piles. In the testing, repairs were carried out under sustained load that simulated service dead and live loads on a bridge. This meant that additional applied load had to be transferred across the repaired region.

The results of the study showed that improvements in the efficiency of the repairs were quite modest and even declined where powder actuated nails were driven over the entire depth of the repair zone. This was attributed to damage to the concrete core during their installation. As a result, the capacity of original core that was sustaining the service dead and live loads was reduced.

The findings of the study are based on tests on model-scale piles. Given the small size of the piles it was not possible to exactly simulate the layout of powder actuated nails recommended by the Florida Department of Transportation. Thus, whether the same conditions apply to prototype piles is debatable. Nonetheless, it will be prudent to ensure that fasteners chosen do not damage the concrete. Also, as powder actuated nails rely on compression bond for their holding capacity, the bond may deteriorate under eccentric loading that was not tested in this study.

### **Acknowledgments**

The opinions and findings reported in this study are those of the authors and not necessarily those of the Florida Department of Transportation

### **References**

Fischer, J., Mullins, G. and Sen, R. (2000). Strength of Repaired Piles. Final Report submitted to Florida Department of Transportation, Tallahassee, FL.

Florida Department of Transportation (1996). Standard Specifications for Road and Bridge Construction, Tallahassee, FL

## Effect of Environment on the Integrity of CFRP/Concrete Bond

*Rajan Sen and Gray Mullins*

University of South Florida, Tampa, FL, USA

*Mohsen Shahawy*

SDR Engineering, Tallahassee, FL, USA

*John Spain*

PSI Environmental Geotechnical Construction, New Haven, CT, USA

### ABSTRACT

The Florida Department of Transportation (FDOT) is one of the leaders in the US on the application of CFRP material for the repair of bridges damaged by vehicular collision or corrosion. As part of an integrated research effort, FDOT sponsored a multi-year experimental study to investigate the long term integrity of the bond between CFRP/epoxy adhesive and concrete. In the study, five competing epoxy systems were evaluated for three disparate exposure conditions representative of Florida's sub-tropical climate. Results were compared with identically prepared specimens kept in a controlled environment. Following completion of exposure, bond integrity was evaluated visually and through destructive testing. The results reaffirmed that bond deterioration was a function of workmanship and surface preparation. It also indicated that visual inspection was limited in its ability to identify degradation. Despite the severity of the exposure, all systems performed satisfactorily.

**KEY WORDS:** bond; carbon; concrete; durability; tension; torsion; epoxy; FRP.

### INTRODUCTION

Carbon fiber reinforced polymers (CFRP) are increasingly used for repair and strengthening of structural elements made of reinforced or prestressed concrete. As the performance of the repaired element depends on the integrity of the epoxy bond between the CFRP and the concrete surface, evaluation of its likely long-term performance is of critical importance.

Bond integrity of particular interest is that encountered under *service* conditions. This varies from application to application depending on the *post-repair* environment. For this reason, satisfactory service performance of CFRP bridge column retrofit in temperate California cannot necessarily be assumed to apply, for instance, to similar repairs carried out in New Hampshire where freeze-thaw cycles are encountered. Consequently, there is a need to evaluate performance for specific service conditions.

This paper is an overview of studies carried out over several years to investigate the likely long-term performance of CFRP repairs carried out by the Florida Department of Transportation (Sen 1997; Sen et al. 1999; 2000). In the experimental investigation, long-term performance was assessed both qualitatively and quantitatively. Qualitative assessment refers to visual and tactile examination while quantitative assessment refers

to destructive tests carried out to measure the residual interface bond. This required the development of specialist equipment, Mullins et al. 1998, 1999.

### BACKGROUND

In the 1990s the Florida Department of Transportation used CFRP material to repair several busy highway bridges. Such repairs fell into two broad categories (1) emergency repair of bridge superstructures damaged by vehicular collision and (2) repair of corrosion-damaged structural elements. In either case, time and cost considerations led to the selection of the CFRP repair system.

Typical examples of both categories of repair are illustrated in Figs 1-2. Fig. 1 shows a prestressed concrete AASHTO girder bridge on I-75 near Naples, FL that was hit by a construction vehicle carrying a large crane whose boom had not been lowered. This caused severe damage to several of the girders. The need to keep the main highway connecting New York and Miami open necessitated rapid repairs that were carried out using CFRP. Fig. 2 shows corrosion damage in a reinforced concrete bridge on State Road 24 over Indian River, Melbourne FL. As before, speedy repairs were carried out using CFRP.

The service environment for the two repairs is completely different. In the first structure, Fig.1, environmental effects are due to changes in ambient conditions. Thus, the integrity of the bond would have to resist the detrimental effects of a mis-match in the coefficient of thermal expansion between the concrete and the CFRP material (Hancox and Mayer, 1994). In the second structure, Fig. 2, the repaired element is located within tidal waters and therefore subjected to repeated wet/dry cycles in salt water. The water temperature also changes, so it will be subject to combined wet/dry and thermal cycles.

### Objectives

The overall goal of the study was to conduct accelerated tests to assess the integrity of the CFRP bond for the disparate conditions repaired structures were exposed to. No formal accelerated tests have yet been developed though methods for evaluating adhesion were recently proposed (ACI Committee 440, 2000). Consequently, acceleration was simulated using exposure conditions more severe than normally encountered in service.

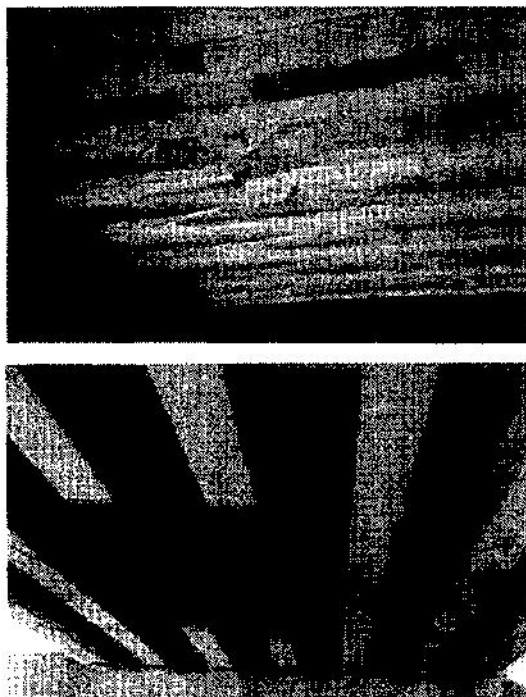


Figure 1. CFRP repair of vehicular damage.



Figure 2. CFRP repair of corrosion damage.

Two factors make the integrity of the bond potentially problematic: *first*, the relatively large temperature range in Florida (see Table 1); *second*, moisture absorption by the epoxy under conditions of high humidity that are characteristic of Florida (Hancox and Mayer 1994). Both effects lead to swelling and potential separation of the CFRP material from concrete.

Table 1. Temperature range and average humidity for Florida cities (1961-90).

City	Maximum, C	Minimum, C	Range, C	Relative Humidity, %
Jacksonville	39	-14	53	81
Key West	34	5	29	76
Miami	37	-1	38	78
Orlando	38	-7	45	79
Pensacola	41	-14	55	78
Tampa	37	-8	45	78

## EXPERIMENTAL PROGRAM

### Specimens

A total of 24 specimens (19 for exposure and 5 controls) were prepared by the Structural Research Center in Tallahassee, FL and shipped to the University of South Florida campus where the study was conducted. The specimens, each 455 mm square in plan, used uni-directional or bi-directional carbon fibers that were directly bonded to concrete slabs in single or double layers (Table 2). Five different epoxy systems were investigated and these are identified by the roman numerals I-V. The bi-directional carbon fibers used in systems I-III were identical; two different manufacturers made the uni-directional carbon fibers in systems IV and V.

### Initial Inspection

All specimens were carefully inspected to identify and catalogue any defects prior to exposure. No evidence of debonding could be detected; however, minor defects were found at the CFRP/concrete corners and edges in four specimens from Systems II and III.

Table 2. Specimen details.

System	Number of Specimens	Fiber Type	Layers
I	6	bi-direct	1 or 2
II	4	bi-direct	2
III	6	bi-direct	1
IV	4	uni-direct	1 or 2
V	4	uni-direct	1 or 2

### Exposure

Specimens were exposed to three different environments and the performance compared to that of controls kept in an air-conditioned laboratory. These were (a) outdoor exposure referred to as *ambient*, (b) wet/dry cycles in 15% salt water referred to as *tidal*, and (c) combined wet/dry cycles and hot/cold cycles in 5% salt water referred to as *tidal+thermal*.

Exposure (a) was representative of the environment encountered in vehicular damage repair (Fig. 1). Exposure (b) and (c) simulated conditions representative of the repair of the corrosion-damaged bridge

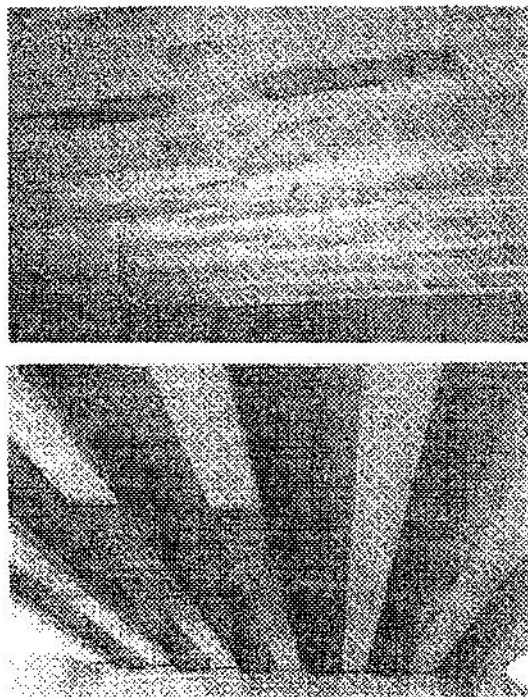


Figure 1. CFRP repair of vehicular damage.

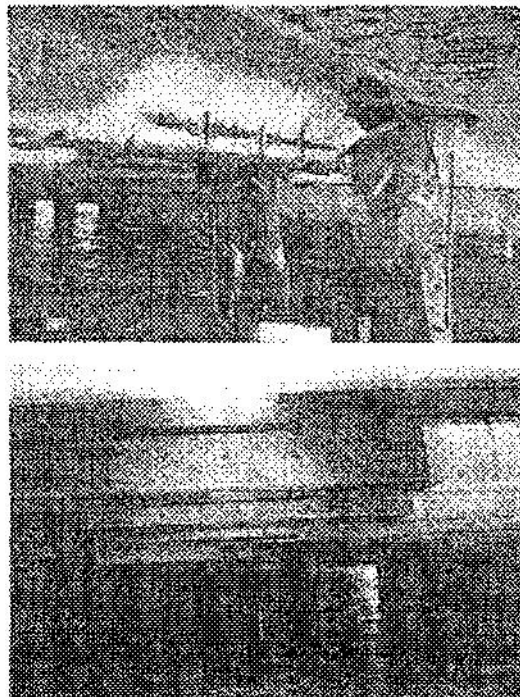


Figure 2. CFRP repair of corrosion damage.

Two factors make the integrity of the bond potentially problematic: *first*, the relatively large temperature range in Florida (see Table 1); *second*, moisture absorption by the epoxy under conditions of high humidity that are characteristic of Florida (Hancock and Mayer 1994). Both effects lead to swelling and potential separation of the CFRP material from concrete.

Table 1. Temperature range and average humidity for Florida cities (1961-90).

City	Maximum, C	Minimum, C	Range, C	Relative Humidity, %
Jacksonville	39	-14	53	81
Key West	34	5	29	76
Miami	37	-1	38	78
Orlando	38	-7	45	79
Pensacola	41	-14	55	78
Tampa	37	-8	45	78

## EXPERIMENTAL PROGRAM

### Specimens

A total of 24 specimens (19 for exposure and 5 controls) were prepared by the Structural Research Center in Tallahassee, FL and shipped to the University of South Florida campus where the study was conducted. The specimens, each 455 mm square in plan, used uni-directional or bi-directional carbon fibers that were directly bonded to concrete slabs in single or double layers (Table 2). Five different epoxy systems were investigated and these are identified by the roman numerals I-V. The bi-directional carbon fibers used in systems I-III were identical; two different manufacturers made the uni-directional carbon fibers in systems IV and V.

### Initial Inspection

All specimens were carefully inspected to identify and catalogue any defects prior to exposure. No evidence of debonding could be detected; however, minor defects were found at the CFRP/concrete corners and edges in four specimens from Systems II and III.

Table 2. Specimen details.

System	Number of Specimens	Fiber Type	Layers
I	6	bi-direct	1 or 2
II	4	bi-direct	2
III	6	bi-direct	1
IV	4	uni-direct	1 or 2
V	4	uni-direct	1 or 2

### Exposure

Specimens were exposed to three different environments and the performance compared to that of controls kept in an air-conditioned laboratory. These were (a) outdoor exposure referred to as *ambient*, (b) wet/dry cycles in 15% salt water referred to as *tidal*, and (c) combined wet/dry cycles and hot/cold cycles in 5% salt water referred to as *tidal+thermal*.

Exposure (a) was representative of the environment encountered in vehicular damage repair (Fig. 1). Exposure (b) and (c) simulated conditions representative of the repair of the corrosion-damaged bridge



(Fig. 2). In both cases, test conditions were more severe than likely to be encountered under service conditions. In the tidal exposure, specimens were placed in a tank in which the water level was raised or lowered every two weeks. In the first week, they were completely submerged simulating high tide; in the following week the water level was lowered below the bond line to simulate low tide. The tanks were covered with a plastic sheet that served to increase humidity. The tanks themselves were placed outdoors to ensure that temperature changes were comparable to those in highway structures.

An identical arrangement was used for the tidal-thermal exposure excepting that the fully-submerged specimens were placed inside a covered, insulated tank in which the water was heated to 60°C. At low tide, the heating was stopped and the specimens allowed to cool without the cover. This led to rapid reductions in humidity and temperature that were deemed more critical for degradation of epoxy bond. The hot/cold cycles were repeated every week and as for the tidal exposure, the tanks were kept outdoors. The water temperature inside the tanks was monitored, as was the ambient temperature. During winter when ambient temperatures were low the temperature range was maximized. The temperature range recorded was comparable to that in Table 1 (Sen et al. 1997).

## RESULTS

### Visual Inspection

After 17 months of exposure the experiment was stopped because of technical problems associated with maintaining the thermal cycles. Visual and tactile inspection of all 24 specimens was then carried out to identify degradation in bond. A thorough examination revealed deterioration in only four of the 24 specimens. These were the very same specimens that had previously been identified as having flaws (System II and III) and were evenly divided between the tidal and tidal+thermal exposures. With the exception of a single specimen shown in Fig. 3 only minor increases in the extent of debonding were observed.

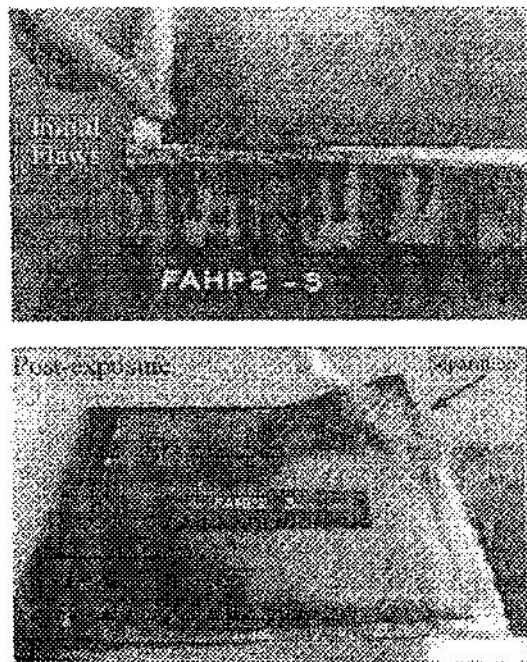


Figure 3. Visual inspection.

The results of the visual inspection were useful in that they provided a measure of the role of workmanship on the integrity of the CFRP-concrete

bond. However, it was unable to provide information on the changes in the interface epoxy-concrete bond due to exposure.

### Destructive Tests

Three devices were developed - one to measure the interface tensile bond and two others to measure the shear bond. Complete details may be found elsewhere (Mullins et al. 1998). The tension test apparatus was similar to commercially available equipment. The shear devices measured the integrity of the bond between CFRP and concrete under *direct* and *torsional* shear. All these devices used a 50 mm diameter metal disk (called a dolly) that was bonded to the CFRP surface using epoxy. A water-flashed, diamond-tipped core barrel was used to score around the metal disk through the CFRP for the tensile and the torsional shear test. For the direct shear test, a 50 mm diameter core was extracted from the specimen. This cylindrical specimen was inserted inside a special shear box that ensured the failure plane coincided with the location of the CFRP/epoxy bond. Because of the need to extract a core, this test was more time consuming. Moreover, results were inconsistent because of surface defects in the core that led to the introduction of bending stresses along the failure plane. In view of this, only tensile and torsional shear tests were conducted.

Under the action of tensile or shear loads, five different failure modes can occur. These are (1) debonding of the dolly - this means that the strength of the epoxy bond between the dolly and the CFRP material was too low (2) complete debonding of the CFRP from the concrete - this provides a baseline for the bond strength (3) partial debonding of the CFRP/concrete bond (4) separation of the CFRP layers - this indicates that bond between the two CFRP layers was weaker than the epoxy/concrete bond - only possible for Systems I, II, IV or V (see Table 2) where two layers were present and (5) failure in the concrete - this only indicates that the epoxy bond was at least as strong as the concrete.

The tension and torsion tests were conducted on all 24 specimens including the five controls. As the specimens were 455 mm square in plan, several tests could be conducted on the same specimen. On an average, two tension and two torsional shear tests were carried out on each specimen. A total of one hundred tests were carried out altogether.

### Tension Tests

Fig. 4 summarizes the results of the 58 tension tests for the four different exposures. The numeric integers in the three segments in this figure specify the numbers of tests relating to a particular mode. It may be seen that a total of 13 (1+5+7) (24%) debonded completely and 18 others (33%) debonded partially. The remaining 24 (43%) did not debond and failure occurred in the concrete.

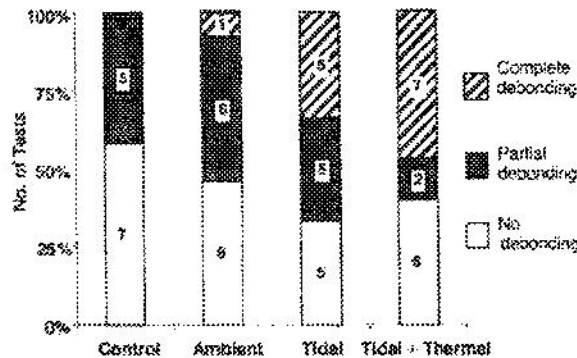


Figure 4. Summary of tensile bond results.

Inspection of Fig. 4 shows that debonding was largely limited to exposure in the wet/dry environment. None of the controls debonded

(Fig. 2). In both cases, test conditions were more severe than likely to be encountered under service conditions. In the tidal exposure, specimens were placed in a tank in which the water level was raised or lowered every two weeks. In the first week, they were completely submerged simulating high tide; in the following week the water level was lowered below the bond line to simulate low tide. The tanks were covered with a plastic sheet that served to increase humidity. The tanks themselves were placed outdoors to ensure that temperature changes were comparable to those in highway structures.

An identical arrangement was used for the tidal+thermal exposure excepting that the fully-submerged specimens were placed inside a covered, insulated tank in which the water was heated to 60C. At low tide, the heating was stopped and the specimens allowed to cool without the cover. This led to rapid reductions in humidity and temperature that were deemed more critical for degradation of epoxy bond. The hot/cold cycles were repeated every week and as for the tidal exposure, the tanks were kept outdoors. The water temperature inside the tanks was monitored, as was the ambient temperature. During winter when ambient temperatures were low the temperature range was maximized. The temperature range recorded was comparable to that in Table 1 (Sen et al. 1997).

## RESULTS

### Visual Inspection

After 17 months of exposure the experiment was stopped because of technical problems associated with maintaining the thermal cycles. Visual and tactile inspection of all 24 specimens was then carried out to identify degradation in bond. A thorough examination revealed deterioration in only four of the 24 specimens. These were the very same specimens that had previously been identified as having flaws (System II and III) and were evenly divided between the tidal and tidal+thermal exposures. With the exception of a single specimen shown in Fig. 3 only minor increases in the extent of debonding were observed.

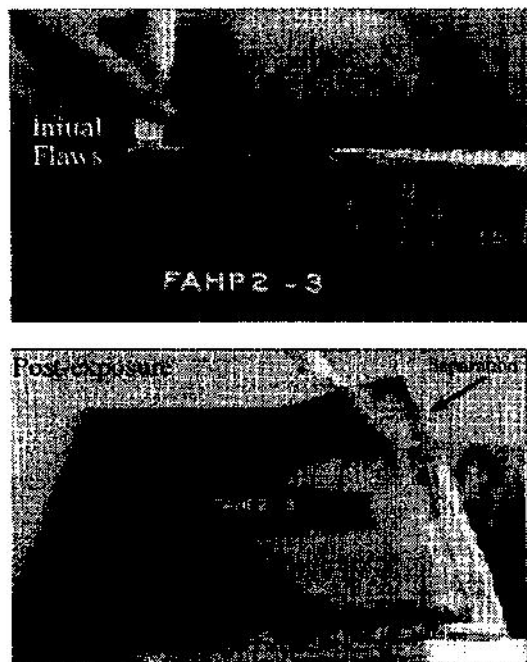


Figure 3. Visual inspection.

The results of the visual inspection were useful in that they provided a measure of the role of workmanship on the integrity of the CFRP concrete

bond. However, it was unable to provide information on the changes in the interface epoxy/concrete bond due to exposure.

### Destructive Tests

Three devices were developed – one to measure the interface tensile bond and two others to measure the shear bond. Complete details may be found elsewhere (Mullins et al. 1998). The tension test apparatus was similar to commercially available equipment. The shear devices measured the integrity of the bond between CFRP and concrete under *direct* and *torsional* shear. All these devices used a 50 mm diameter metal disk (called a dolly) that was bonded to the CFRP surface using epoxy. A water-flushed, diamond-tipped core barrel was used to score around the metal disk through the CFRP for the tensile and the torsional shear test. For the direct shear test, a 50 mm diameter core was extracted from the specimen. This cylindrical specimen was inserted inside a special shear box that ensured the failure plane coincided with the location of the CFRP/epoxy bond. Because of the need to extract a core, this test was more time consuming. Moreover, results were inconsistent because of surface defects in the core that led to the introduction of bending stresses along the failure plane. In view of this, only tensile and torsional shear tests were conducted.

Under the action of tensile or shear loads, five different failure modes can occur. These are (1) debonding of the dolly - this means that the strength of the epoxy bond between the dolly and the CFRP material was too low (2) complete debonding of the CFRP from the concrete - this provides a baseline for the bond strength (3) partial debonding of the CFRP/concrete bond (4) separation of the CFRP layers - this indicates that bond between the two CFRP layers was weaker than the epoxy/concrete bond - only possible for Systems I, II, IV or V (see Table 2) where two layers were present and (5) failure in the concrete - this only indicates that the epoxy bond was at least as strong as the concrete.

The tension and torsion tests were conducted on all 24 specimens including the five controls. As the specimens were 455 mm square in plan, several tests could be conducted on the same specimen. On an average, two tension and two torsional shear tests were carried out on each specimen. A total of one hundred tests were carried out altogether.

### Tension Tests

Fig. 4 summarizes the results of the 55 tension tests for the four different exposures. The numeric integers in the three segments in this figure specify the numbers of tests relating to a particular mode. It may be seen that a total of 13 (1+5+7) (24%) debonded completely and 18 others (33%) debonded partially. The remaining 24 (43%) did not debond and failure occurred in the concrete.

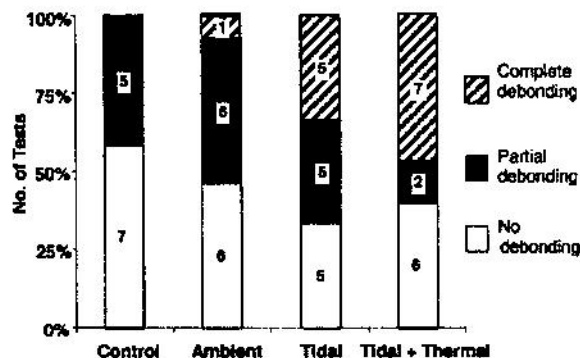


Figure 4. Summary of tensile bond results.

Inspection of Fig. 4 shows that debonding was largely limited to exposure in the wet/dry environment. None of the controls debonded



completely; only one exposed to ambient conditions debonded completely. Thus, constant exposure to wet/dry cycles is more detrimental to the long term CFRP/ concrete bond.

**Shear Tests**

Fig. 5 summarizes the results from the 45 torsional shear tests. Of these 9 (20%) debonded completely, 12 (27%) partially. Thus, nearly, half the specimens tested debonded partially or completely. The remaining 24 (53%) did not debond. As before, exposure to the wet/dry or a combination of wet/dry and thermal cycles led to the greatest degradation. None of the controls debonded completely; partial debonding was observed in one test.

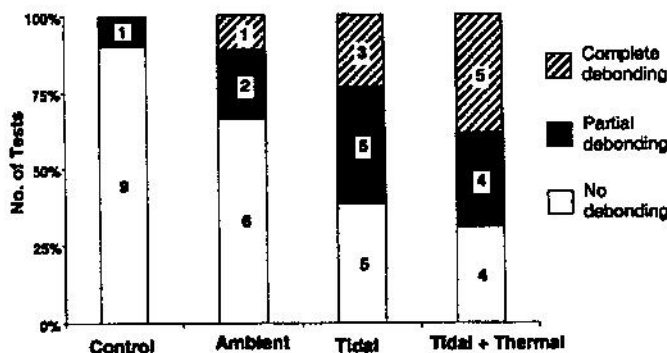


Figure 5. Summary of torsional shear bond results.

The average bond stress from the tensile and torsional shear tests are shown in Fig. 6. The stresses shown in this figure relate only to those tests that led to complete debonding, i.e. 13 tension tests (Fig. 4) and 9 torsional shear tests (Fig. 5).

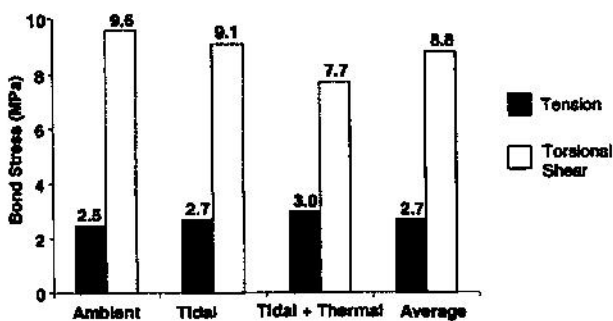


Figure 6. Failure bond stresses in tension and shear.

The tensile debonding stress values range from 2.5-3.0 MPa with an average value of 2.7 MPa. In contrast, the corresponding values for torsional shear are much higher and range between 7.7-9.6 MPa with an average value of 8.8 MPa. These results are consistent with results for plain concrete (Mindess and Young, 1981) where the shear strength is about three times the tensile strength.

When failure occurred in the concrete, no estimate can be made of the extent of degradation in the epoxy/concrete bond. However, where there was partial or complete debonding, a measure of degradation may be obtained by comparing the relative failure loads of the exposed and control specimens. Such an assessment makes the important assumption that all specimens belonging to the same series were identically prepared and were bonded to identical concrete slabs having the same tensile and shear strengths.

**Critical Exposure**

The residual bond strength may be used to identify the exposure that is most critical for the CFRP/concrete bond. Fig. 7 is a plot of the average residual bond stress from all the 100 tests that were carried out. Exposure to wet/dry cycles or combined wet/dry and thermal cycles led to the greatest degradation in bond while exposure to ambient conditions has relatively minor effect. Surprisingly, the effect of tidal and tidal+thermal were comparable. The researchers had anticipated the latter environment to be more detrimental.

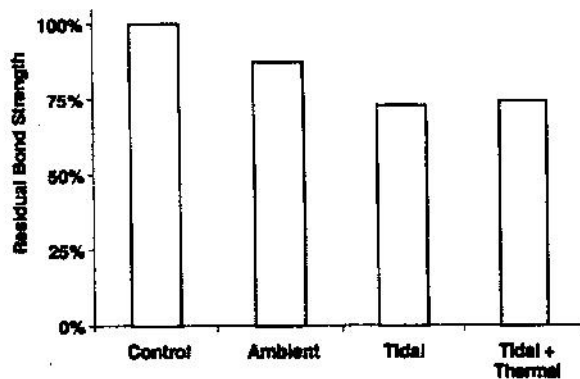


Figure 7. Critical exposures.

**System Performance**

The relative performance of the five different systems based on the residual bond strength is shown in Fig. 8. For ambient conditions, systems II and IV performed the best and System V the worst. For tidal exposure, System IV was the best but System II was the worst. For tidal plus thermal, System IV was the best and System II the worst. Overall, System IV performed the best showing no deterioration. Systems I and III also performed satisfactorily in all the environments. System II did not perform well in wet/dry environments. System V generally did not perform well in any of the outdoor environments.

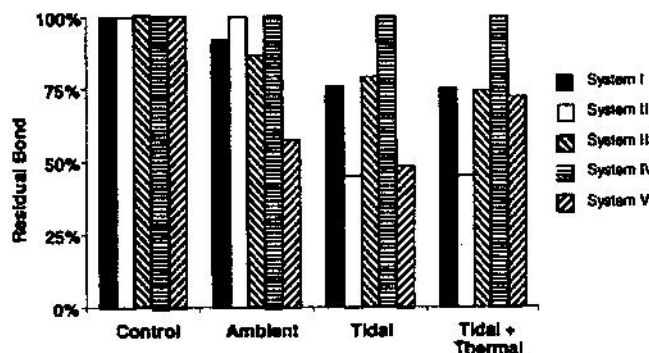


Figure 8. Relative performance.

The relative performance of the five epoxy systems for the exposures are shown in Fig. 9. Tidal exposure shown is the average of tidal and tidal+thermal. It may be seen that the epoxy systems performed better in the ambient rather than the more severe tidal exposure.

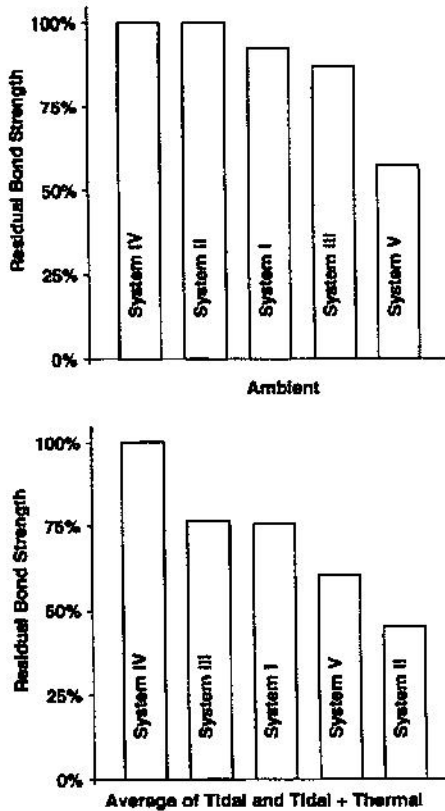


Figure 9. Ranking of systems.

## DISCUSSION

The goal of this study was to assess the long-term performance of CFRP/epoxy concrete bond in the disparate environments encountered in Florida. Both qualitative and quantitative measures were used. Visual examination detected degradation in the four specimens that had been initially identified as containing minor defects at the corners and edges. Destructive tension and torsional shear tests detected degradation in an additional 14 of the 24 specimens including controls and those exposed outdoors. Thus, only 6 of the 24 specimens did not degrade. In these six specimens, all failures, i.e. tensile and torsional shear, occurred in the concrete. Visual examination is therefore not very reliable in detecting bond degradation.

The results showed that the average debonding tensile stress was 2.7 MPa, much lower than the corresponding torsional shear bond value of 8.8 MPa. These values were calculated for the 22 tests (9 shear, 13 tensile) in which complete debonding occurred. Partial debonding was observed in 18 tensile tests (Fig. 4) but only 12 torsional shear tests (Fig. 5). As both tests were carried out on the same specimen, it is apparent that the tensile test results provide a lower bound on available strength. Tensile bond failure therefore does not necessarily indicate that the repair will be unable to transfer flexural loads.

## CONCLUSIONS

The following conclusions may be drawn:

1. Visual examination alone cannot identify degradation in the epoxy/concrete bond due to exposure. It detected degradation in only 4 of the 24 specimens (19 exposed and 5 controls) instead of the 18 specimens identified by destructive testing.

2. Severe degradation may be expected where CFRP is not properly bonded to concrete at the time of repair (Fig. 3).
3. Tension tests provide a lower bound on the integrity of the bond. Average computed tensile bond for specimens that completely debonded was approximately a third of that obtained from torsional shear (Fig. 6).
4. Exposure to wet/dry cycles was the most critical environment. The addition of thermal cycles did not prove detrimental (Fig. 7)
5. Some epoxy systems performed well in all the environments. Others performed well in selected environments (Fig. 8).

Overall, the results are quite encouraging given the severity of the exposure investigated. The extreme temperature range and humidity exposure greatly exceed conditions that could be reasonably expected under normal service conditions. In spite of this, bond degradation was minimal especially in specimens that had been prepared properly.

## ACKNOWLEDGMENTS

This study was funded in part by the Florida Department of Transportation. Additional support was provided by the Department of Civil and Environmental Engineering, University of South Florida, Tampa, FL. This support is gratefully acknowledged. The opinions findings and conclusions expressed in this publication are those of the writers and not necessarily those of the Florida Department of Transportation.

## REFERENCES

- ACI Committee 440 (2000). "Guidelines for the Selection, Design and Installation of Fiber Reinforced Polymer (FRP) Systems for Externally Strengthening Concrete Structures", Draft Report.
- Hancox, N. and Mayer, R. (1994). *Design Data for Reinforced Plastics*, Chapman and Hall, New York, New York.
- Mindess, S. and Young, J. (1981). *Concrete*, Prentice-Hall, Englewood Cliffs, NJ, pp. 400-401.
- Mullins, G., Sen, R. and Spain, J. (1998). "Testing of CFRP/Concrete Bond," in *Fiber Composites in Infrastructure* (Ed. H. Saadatmanesh and M. Ehsani), Vol II, University of Arizona, Tucson, pp. 211-218.
- Mullins, G., Race, R. and Sen, R. (1999). "A New Device for In-Situ Testing of FRP/Concrete Adhesion". *Fourth International Symposium, ACI SP-188* (Ed. C. Dolan, S. Rizkalla and A. Nanni), Farmington Hills, MI, pp. 383-391.
- Sen, R. (1997). "Durability of Epoxy/Carbon/Concrete Bond in a Marine Environment," *Final Report submitted to Florida Department of Transportation*, January, pp. 67.
- Sen, R., Shahawy, M., Mullins, G. and Spain, J. (1999). Durability of CFRP/Epoxy/Concrete Bond in Marine Environment, *ACI Structural Journal*, Vol. 96, No. 6, pp. 906-915.
- Sen, R., Shahawy, M., Mullins, G. and Spain, J. (2000). Durability of CFRP/Epoxy Concrete Bond". *Proceedings of the ACUN-2, International Composites Conference Composites in the Transportation Industry* (Ed. S. Bandyopadhyay, N. Gowripalan, N. Drayton and Rik Heslehurst), University of New South Wales, Vol 1, pp. 259-265.



# Strengthening steel bridge sections using CFRP laminates

Rajan Sen<sup>a,\*</sup>, Larry Liby<sup>b</sup>, Gray Mullins<sup>c</sup>

<sup>a</sup>Samuel and Julia Flom Professor, Department of Civil and Environmental Engineering University of South Florida, Tampa, FL 33620, USA

<sup>b</sup>Formerly graduate student, Department of Civil and Environmental Engineering, University of South Florida, Tampa, FL 33620, USA

<sup>c</sup>Assistant Professor, Department of Civil and Environmental Engineering, University of South Florida, Tampa, FL 32620, USA

Received 17 December 2000; accepted 15 February 2001

---

## Abstract

This paper presents results from an experimental investigation to determine the feasibility of using carbon fiber reinforced polymer (CFRP) epoxy laminates to repair steel composite bridge members. Six specimens, each consisting of a 6.1 m long W8 × 24 wide flange A36 steel beam acting compositely with a 0.114 m thick by 0.71 m wide reinforced concrete slab, were first loaded past yield of the tension flange to simulate severe service distress. The damaged specimens were then repaired using 3.65 m lengths of 2 or 5 mm thick CFRP laminates bonded to the tension flange and tested to failure. The results indicated significant ultimate strength gains but more modest improvement in the elastic response. Non-linear finite element analyses were in good agreement with the experimental results. The study suggests that it is feasible to strengthen steel composite members using CFRP laminates. © 2001 Elsevier Science Ltd. All rights reserved.

*Keywords:* A. Laminates; Carbon fiber reinforced polymer

---

## 1. Introduction

Fiber reinforced polymers have been successfully used to strengthen structural elements made of concrete, masonry and wood. Numerous applications have been cited for bridge structures (e.g. repair of prestressed concrete and wood bridges in Switzerland [10], multi-span hollow box girder bridge in Germany [11], slab bridges in Japan [12], and reinforced/prestressed concrete bridges in the United States [13]).

Although there have been some studies which involved strengthening steel members (e.g. Refs. [3,4]), this extension has not been so widespread since it poses a different set of problems. First, the likelihood of lateral buckling makes it necessary to fabricate composite steel sections where the compression flange is continuously supported by a reinforced concrete slab. These sections are much more difficult to fabricate and test in comparison with rectangular concrete or wood sections. Second, steel's high strength and stiffness make it a more difficult material to strengthen especially since carbon fiber reinforced polymers (CFRP) that are commonly used have a smaller modulus. This means that substantial load transfer can only take place *after* the steel

has yielded. Finally, for this system, the CFRP/adhesive bond is the weakest link and will always control the mode of failure. Thus, consideration of surface preparation alone will not suffice. Instead, more attention must be paid to augment the capacity of the adhesive through the use of appropriate fasteners.

Successful strengthening of steel bridge sections with CFRP would be particularly useful as steel stringer bridges constitute a large segment of aging bridges in the United States that are nearing the end of their useful service life. If service life could be extended, highway authorities would have access to a lightweight, speedy and therefore economical strengthening method that would minimally disrupt traffic.

The opportunity to use CFRP laminates to strengthen steel came unexpectedly. In 1992, the University of South Florida, Tampa, FL were developing a steel composite bridge model to evaluate the restraint effect of elastomeric bridge bearings [7]. For this study, the girder spacing, slab thickness or the number of shear connectors was not critically important. Consequently, advantage was taken to alter these parameters to boost the ultimate capacity of the slab and to ensure that if the concrete slab were cut longitudinally, three identical steel composite beams would result. In addition, an identical second bridge was fabricated to provide additional specimens.

---

\* Corresponding author. Fax: +1-813-974-2957.

E-mail address: sen@eng.usf.edu (R. Sen).

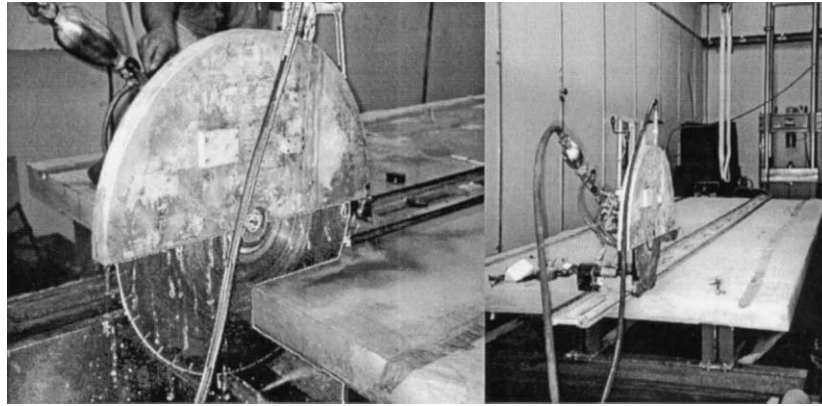


Fig. 1. Cutting bridge into three composite beam sections.

Following completion of the experimental phase of the bearing restraint study, the concrete slabs of the two bridges were cut (Fig. 1) to obtain the six test specimens used in this study. This paper presents a brief summary of the technical problems that were overcome and highlights some of the principal findings. A comprehensive report describing all aspects of the research is available [6].

## 2. Objectives

The overall goal of the study was to assess the feasibility of using CFRP laminates for strengthening steel composite bridge members. Since only distressed sections would be strengthened it was necessary to simulate such damage prior to any strengthening. The main objectives of the study may be summarized as follows:

1. To develop a procedure that could be used for strengthening steel composite members using CFRP laminates.
2. To evaluate the potential benefit of strengthening damaged steel composite specimens using CFRP laminates.
3. To assess the extent to which experimental results may be predicted using available non-linear finite element computer programs.

## 3. Specimen details

As mentioned already, the six specimens used in the study were obtained by cutting each of two concrete/steel composite bridge models into three parts (Fig. 1). The resulting cross-section is shown in Fig. 2. It consisted of a 114 mm thick, 710 mm wide reinforced concrete slab that was attached to a  $W8 \times 24$  steel section by 36 shear connectors. The spacing of the 50 mm long, 19 mm diameter stud-type shear connectors was varied — they were more closely spaced near the supports than at mid-span. The concrete slab deck was reinforced top and bottom in the longitudinal and transverse directions by 20M (#6 bars). These were spaced at 230 mm in the transverse direction and 280 mm in the longitudinal direction.

The specimens were identified as *North*, *Center* or *South* depending on their location in the original bridge deck. Although the six specimens were geometrically identical, test coupons provided by the fabricator indicated that the yield strength of the A36 steel in the two bridge models were 310 and 370 MPa. Thus, three of the specimens had wide flange beams with a yield stress of 310 MPa and three others had a yield stress of 370 MPa. In the following, specimens are identified by their position in the original bridge deck and the yield stress that is used as a suffix, e.g. *North-310 MPa*, *Center-370 MPa*, etc.

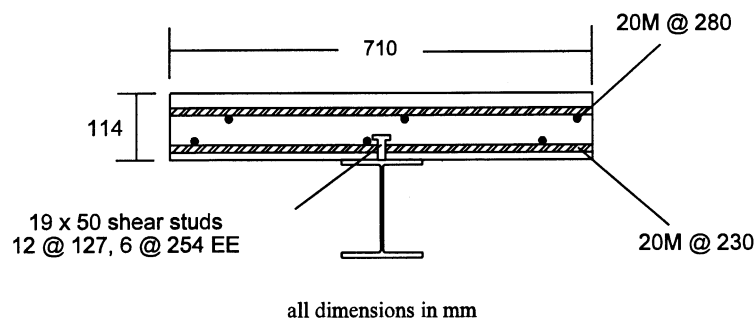


Fig. 2. Slab reinforcement details.

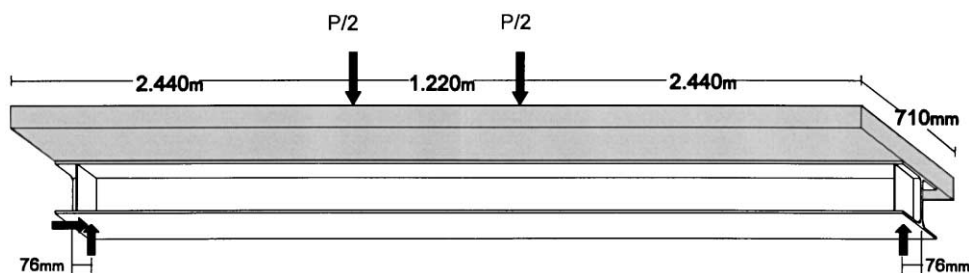


Fig. 3. Loading of simply supported steel composite bridge section.

## 4. Materials

### 4.1. Concrete

Normal weight concrete used in casting the bridge deck was supplied locally and was selected to satisfy Florida Department of Transportation's specifications for Class II concrete. Specialist help was used for pouring, screeding and finishing. The 28 day compressive strength of 43.6 MPa was 40% higher than the 31 MPa design strength. An additional 18% compressive strength gain was realized at the time of testing, which resulted in a compressive strength range of 48.5–52.6 MPa.

### 4.2. CFRP laminates

The CFRP laminates used were fabricated by Composite Horizons, Covina, CA using a simple hand layup process. Widely available T300 carbon fibers and an epoxy matrix were used. The laminate had a uni-directional elastic modulus of 114 GPa and an average unidirectional tensile strength of 1840 MPa. A linear stress-strain relationship gave an ultimate failure strain of 1.6%. Three of the six laminates were 2 mm thick, the remaining three were 5 mm thick. These thicknesses are considerably greater than those used for strengthening concrete or wood and were established from non-linear finite element analyses to ensure comparable strengthening [9]. The width of the laminate was 0.165 m to match the width of the flange of the W8 × 24 beam but its length was only 3.65 m, being limited by fabrication considerations of the CFRP laminate.

### 4.3. Adhesive

The two-part epoxy adhesive FR1272 was selected based on the recommendation of the CFRP laminate fabricator. It is relatively inexpensive and is widely available. However, it has a pot life of 10–15 min at 24°C making its field applicability limited.

## 5. Simulation of damage

In order to meet the objectives of this study, it was first necessary to simulate severe service distress in the

specimens. This was achieved by pre-loading each specimen (see Fig. 3 for schematic arrangement) past yield of the tension flange, a much higher stress level than the maximum stress of 55% of yield permitted by the AASHTO Bridge Specifications [1]. As a result of this loading, there was permanent deformation in each member prior to strengthening. A summary of the applied loads, deflections and maximum recorded steel strains for all the specimens appears in Table 1. The applied loads averaged 142 and 187 kN for the 310 and 370 MPa girders, respectively.

## 6. Repair of damaged specimens

### 6.1. Beam/CFRP combination

Since there were two different sets of yield strengths (310 and 370 MPa) and two different CFRP laminate thicknesses (2 and 5 mm), several beam/laminate combinations were considered. However, to obtain the most data, each steel type was strengthened using each of the two different CFRP laminate thicknesses.

Two of the three lower capacity 310 MPa steel composite beams were strengthened using thicker 5 mm CFRP laminate since this would provide a measure of the maximum strength gain that was attainable. The remaining specimen was strengthened using the 2 mm laminate. This meant that two of the three 370 MPa specimens were strengthened using 2 mm CFRP laminates (providing a lower bound on strength gain) and one by the 5 mm laminate.

### 6.2. Adequacy of adhesive

Because the epoxy adhesive is so much weaker than steel, non-linear finite element analyses were carried out to evaluate its adequacy under ultimate conditions. The results of the analyses indicated that the epoxy would fail at the ends of the CFRP laminate due to high peeling stresses. To prevent this type of failure, a three-piece steel clamp was designed so that it could be positioned precisely where needed to withstand the predicted peeling stresses. The clamps were attached to the bottom flange of the W8 × 24 section using two, 19 mm A490 bolts and two smaller 8 mm hardened steel bolts. Only two sets of clamps were needed since they could be re-used. Brief details on the analysis and

Table 1  
Summary of results

Specimen ID (CFRP thickness)	Mid-span values							Plain section ultimate capacity (kN)	Strength gain (%)	Comments
	Simulating service damage			Repaired specimen						
	Load (kN)	Deflection (mm)	Tensile strain ( $\mu\epsilon$ )	Ult. load (kN)	Deflection (mm)	Concrete strain ( $\mu\epsilon$ )	CFRP strain ( $\mu\epsilon$ )			
North 310 (2-mm)	142	40.90	1524	237	102.9	2258	6646	196	21.0	No failure bolts
Center 370 (2-mm)	186	44.96	1744	271	> 100.0	2267	8164	249 <sup>a</sup>	8.7	No failure no bolts
South 370 (2-mm)	187	44.96	1717	272	> 100.0	2284	7811	249 <sup>a</sup>	9.1	No failure no bolts
Center 310 (5-mm)	142	39.69	1239 <sup>b</sup>	298	96.0	1918	5099	196	52.2	CFRP rupture along bolts
South 310 (5-mm)	142	30.23	1275 <sup>b</sup>	169	32.3	786	1538	196	–13.7	Adhesive failure no bolts
North 370 (5-mm)	187	45.72	1695	329	87.9	1778	4859	249 <sup>a</sup>	32.0	CFRP rupture along bolts

<sup>a</sup> Predicted value.

<sup>b</sup> indicates gage failure at specified strain (after value).

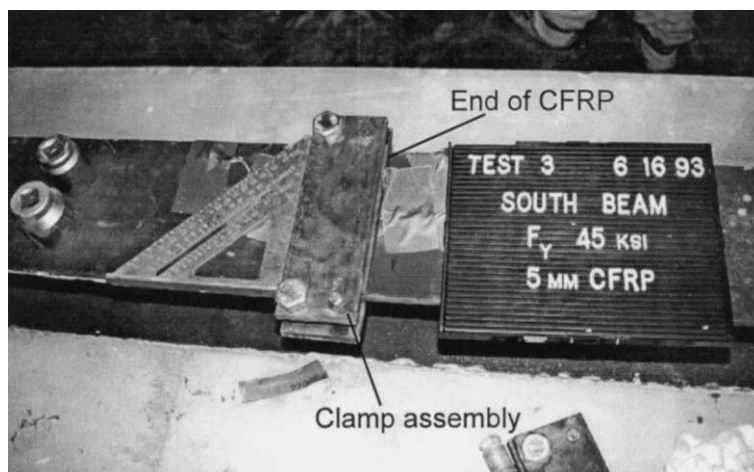


Fig. 4. Clamp assembly used to withstand peeling stresses.

design of the clamps may be found elsewhere [8]. Complete details of the study are presented in Ref. [6].

### 6.3. Bonding CFRP to steel

Surface preparation is important for ensuring a successful bond between CFRP laminate and steel. Since the steel girders used in the bridges were provided with a protective coat of paint, it was necessary to remove this paint. The specimens were turned over to provide access to the bottom flange where the CFRP was to be bonded and a portable sandblaster was used to obtain the necessary etched surface. The CFRP laminate was bonded to the steel surface using the epoxy adhesive in accordance with the manufacturer's recommendations. After the adhesive cured for 48 h, the specially designed clamps resisting peeling stresses were positioned over the ends of the laminate and secured in place using bolts as shown in Fig. 4.

## 7. Testing of repaired specimens

### 7.1. Instrumentation

The test specimens were most heavily instrumented at the quarter and mid-span locations. Strain gages were embedded inside the deck slab during casting and were also attached to the top concrete surface and to the underside of the steel flanges. Strain gages were also affixed to the CFRP laminate at mid-span and at 50 mm from each end of the 3.65 m long CFRP laminate, i.e. 1.27 m from the end of the beam. Additionally, gages were also attached to the bottom flange of the steel beam just beyond the CFRP laminate (1.14 m from the end of the beam). Comparison of strains in the steel beam and that in the CFRP laminate in close proximity allowed slip to be readily detected.

LVDTs were used to measure deflections at the mid-span and quarter-span locations. Load cells were used to measure applied loads and support reactions. All data were auto-

matically recorded by a SYSTEM 4000 data acquisition system.

### 7.2. Loading

The same four-point loading scheme used for simulating service damage (see Fig. 3) was used for testing the repaired specimens. The applied load was transmitted through two 0.71 m long stiffened spreader beams that were welded to a 1.22 m long stiffened cross beam. The length of the spreader beams was the same as the width of the concrete slab. This meant that the test specimens were subjected to two uniform, transverse line loads spaced 1.22 m apart.

The crossbeam was directly connected to the ram of a 45 ton hydraulic jack using a swivel head that was attached by custom-designed connectors. This ensured that the loads were transferred equally to the two spreader beams. Four 150 mm × 200 mm fabric pads were placed under both spreader beams to ensure uniform distribution.

### 7.3. Adhesive failure

The first two specimens tested were the *Center-* and *South-*370 MPa steel composite beams strengthened using 2 mm CFRP laminates. The test was stopped when no additional load could be applied (271 and 272 kN) and the deflection exceeded the 100 mm limit of the LVDT (see Table 1). There was no adhesive failure, as was predicted by non-linear analysis.

The third specimen tested was *South-*310 MPa steel composite beam strengthened using 5 mm CFRP laminate. This test ended suddenly with the separation of the CFRP laminate from the steel flange. The clean separation was believed to be adhesive failure due in part to a manufacturing defect that left a small depression on the bonded face of the 5 mm thick CFRP laminate.

To prevent a recurrence of this failure, bolts were used to augment the load transfer capacity of the epoxy adhesive. The configuration and arrangement of bolts was based on



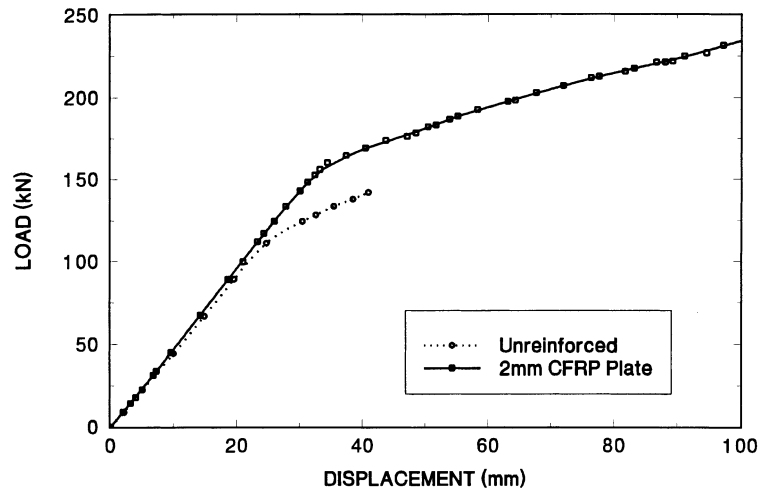


Fig. 5. Load-displacement *North-310 MPa-2 mm* (epoxy + bolted).

non-linear finite element analysis and consisted of two lines of three, 19 mm A490 bolts spaced at 41.9 cm, starting 8.9 cm from the edge of the laminate [6]. In all, a total of 12 steel bolts were used (six at each end) in the two remaining tests involving 5 mm thick CFRP laminates. Although no bolts were needed for the 2 mm CFRP laminate, they were provided nonetheless to assess the effect of load transfer in the presence of bolts. A pair of bolts was provided 8.9 cm from each end of the CFRP in the last specimen strengthened using 2 mm, (for details refer to Ref. [8]).

## 8. Results for repaired beams

### 8.1. Strengthening

Load vs displacement plots comparing the responses of the six repaired and plain specimens are presented in Figs. 5–10. The results for specimens repaired with 2 mm CFRP laminates appear in Figs. 5–7, and those for the 5 mm CFRP

laminates in Figs. 8–10. A summary of the maximum loads and mid-span deflections and strains in both concrete and the CFRP laminate is presented in Table 1. This table also contains information on the load applied to simulate damage referred to earlier.

Table 1 shows that with one exception *South-310 MPa*, increases in the ultimate strength were substantial. For example, *Center-310 MPa* realized an increase in strength from 142 to 298 kN, a strength gage of 110%. Inspection of Figs. 5–10 shows that the strengthening effect is largely confined to the post-yield region. This is not altogether surprising since the CFRP laminate has a lower elastic modulus –56% that of steel. This meant that prior to yielding, stresses in the composite laminate were lower than those in the bottom steel flange.

The premature local adhesive failure of *South-310 MPa*, enabled it to be re-tested to determine the ultimate capacity of the steel section (see Fig. 9). The results of this test were used to fine-tune the non-linear finite element model to predict the ultimate capacities of all the specimens that

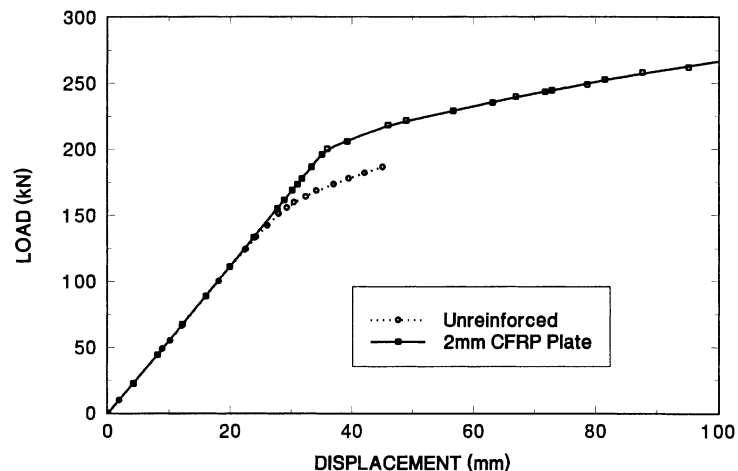


Fig. 6. Load displacement *Center-370 MPa-2 mm* (epoxy only).

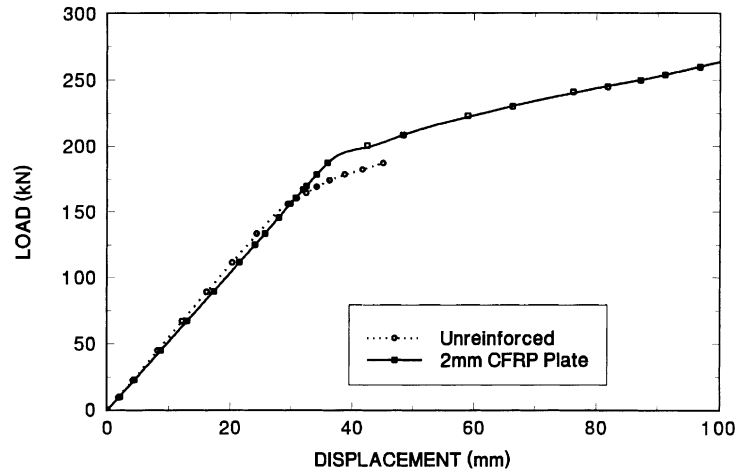


Fig. 7. Load displacement *South-370 MPa-2 mm* (epoxy only).

were tested. The predicted value was found to be 249 kN for the 370 MPa girders. Using the measured and the predicted failure loads, the *absolute* increases in ultimate strength of the strengthened steel beams were found to range between 9 and 52% (Table 1). The smaller increases correspond to the 2 mm laminate and the larger increases to the 5 mm ones.

In addition to increases in ultimate load, the elastic region of the plain section was considerably extended in the repaired specimen. The increases ranged from about 20% for *South-370 MPa/2 mm* (Fig. 7), where the elastic range was extended from 156 to 187 kN, to over 67% in the case of *North-370 MPa/5 mm* (Fig. 10). This increase is particularly encouraging since it suggests that service loads of repaired specimens could be increased using this technique.

## 8.2. Stiffening

The load vs deflection response of the strengthened and unstrengthened beams also provide a measure of the stiffen-

ing effect in the elastic region. This is an important consideration particularly for bridge application where live load deflection limits are very stringent.

Figs. 5–10 show that there is very little stiffening in the elastic region except for specimens strengthened with the 5 mm CFRP laminates (Figs. 8–10). Even for this case, there was practically no stiffening for *Center-310 MPa* specimen (Fig. 8) due to cracking in the slab from the initial loading. For specimens strengthened using 2 mm laminates there is even a reduction in stiffness in the elastic region (Fig. 7). This is probably because the concrete damage in this beam could not be fully offset by repairs and the stiffness lost as a result was not regained by bonding the CFRP laminate.

The lack of increase of stiffness in the elastic range is due to CFRP's smaller elastic modulus compared with steel. The increase in stiffness resulting by bonding a CFRP laminate to the steel surface farthest from the neutral axis is partially offset by this lower modulus. However, with thicker

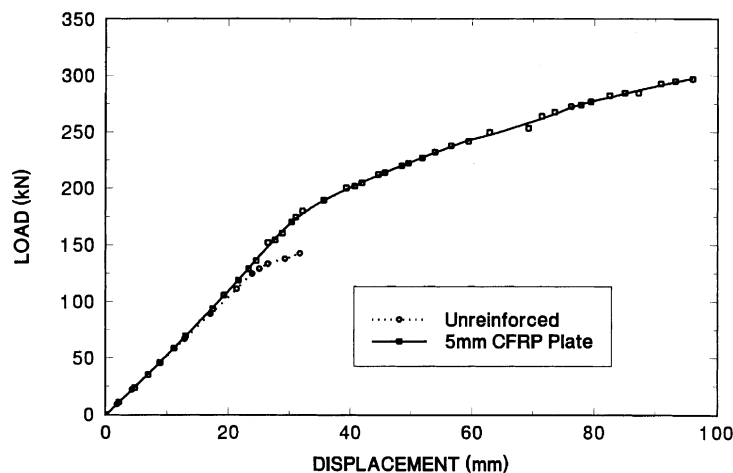


Fig. 8. Load displacement *Center-310 MPa-5 mm* (epoxy + bolted).

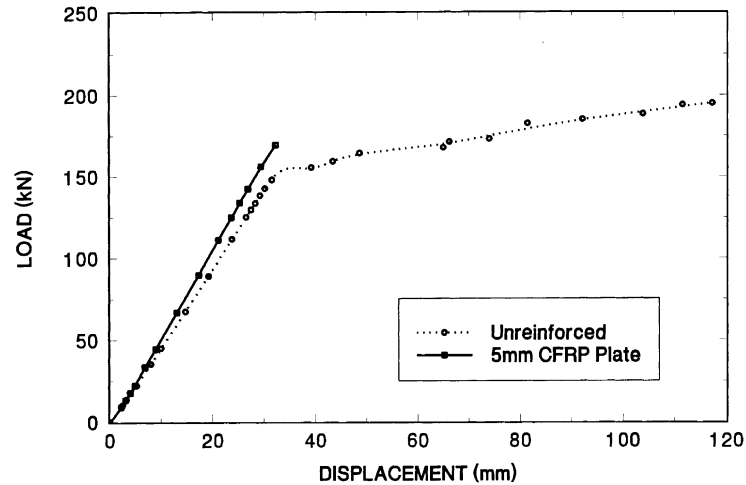


Fig. 9. Load displacement *South*-310 MPa-5 mm (epoxy only).

laminates, increases are larger provided there is no adhesive failure (Fig. 10). If local adhesive failures occur, strengthening cannot be expected (e.g. Fig. 9).

### 8.3. Failure mode

The load deflection plots in Figs. 5–10 indicate that, in general, there was a considerable amount of deflection when the maximum load was reached (Fig. 11). For the beams strengthened using 2 mm CFRP the test was stopped when no additional load could be applied. As such, there was no failure of the CFRP laminate or its bond with the steel surface. With the beams strengthened using 5 mm CFRP, however, failure occurred due to shearing off the CFRP laminate by the bolts (see Fig. 12).

### 8.4. Bolted vs bonded

In order to assess the relative performance of bonded and bolted specimens, the strain variations with depth at the critical mid-span locations for different cases are shown in

Figs. 13–16. The results for the 2 mm CFRP laminates are shown in Figs. 13 and 14 while those for the 5 mm laminates in Figs. 15 and 16.

Inspection of Figs. 13 and 14 showing the strain variation for the 2 mm CFRP laminate indicate their similarity. This is not surprising since there was no separation of the 2 mm laminates, whether bonded or bolted. In each of these cases, the load was transferred primarily by the adhesive.

The comparison of strain variation along the depth of the specimen strengthened with 5 mm CFRP laminate shown in Figs. 15 and 16 indicate obvious dissimilarities. For the bonded specimen (Fig. 15) there is load transfer to the laminate by the epoxy until adhesive failure. The bolted specimen (Fig. 16) transfers load in the same manner until the CFRP delaminates from the steel at about the same load. The loads hitherto being carried by the epoxy were now transferred to the bolts with commensurate strain relaxation in the CFRP laminate. Failure finally occurred when excessive strain (and therefore deformation) around the bolts led to rupture of the CFRP laminate (Fig. 12). This

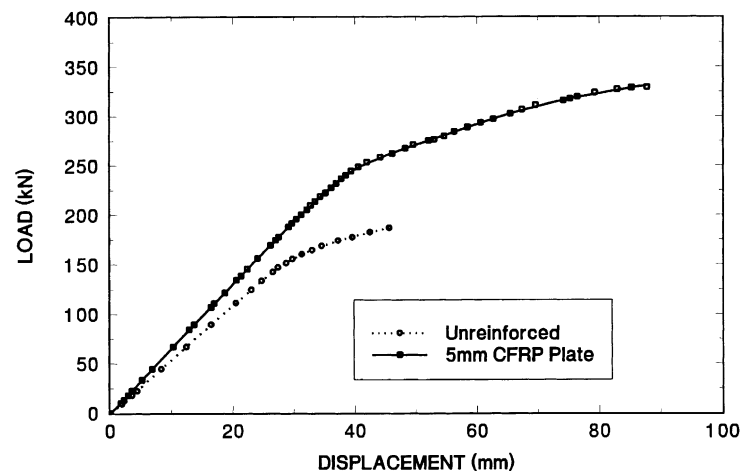


Fig. 10. Load displacement *North*-310 Mpa-5 mm (epoxy + bolted).

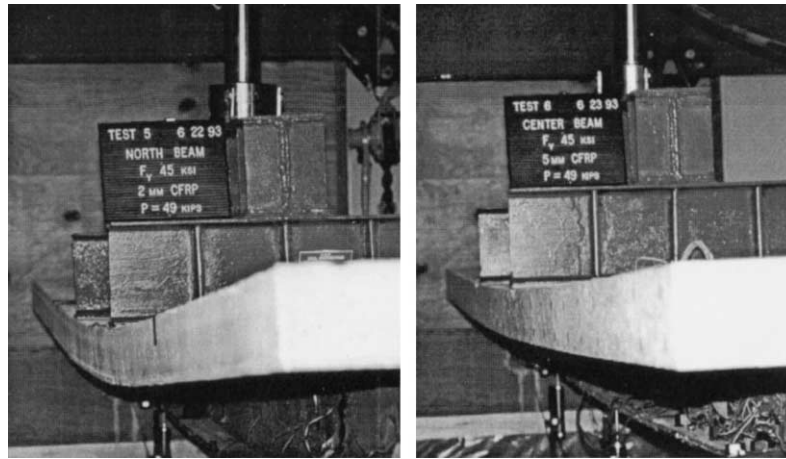


Fig. 11. Deflected shape of repaired 310 MPa beams at 218 kN.

problem may be avoided by using a greater number of bolts, thereby limiting their maximum strain and by using CFRP laminates manufactured with bolt holes and multi-directional carbon fiber reinforcement around such holes.

## 9. Discussion

The results from the study indicate clearly that it is possible to strengthen steel composite bridge sections using CFRP laminates. Because of the high strength and stiffness of steel the operation is somewhat more complicated than that used for concrete or wood. In this study, a combination of adhesive, fasteners, and clamps were used.

Because T300 carbon fibers were used for cost reasons, strengthening was more pronounced in the post-yield region than in the elastic region. However, if CFRP laminates with higher stiffness are used, an increase in the elastic region may be expected. With the prices of carbon fiber dropping, this may be realizable earlier than previously thought possible.

Since the epoxy adhesive is very weak in comparison with steel, bolting was required especially to assist in the load transfer for the thicker laminates. In configurations that

dictate transferring shear using bolts, the use of adhesives would still be recommended to help distribute the load and provide transfer of shear until the bolts become fully loaded in bearing. In this case, the use of adhesives served to secure the CFRP laminate while the bolt holes were drilled. It would be preferable to use a larger quantity of smaller bolts to minimize the magnitude of localized stress concentrations at the bolts and to reduce the tendency for transverse CFRP laminate fractures. The magnitude of the localized stress concentrations may also be reduced by implementing high quality drilling techniques, and by utilizing CFRP laminates which have more plies with varying fiber orientation in the bolt hole regions, or by using CFRP laminates specially manufactured to include reinforced holes for bolting. Installation would be facilitated by such manufactured holes or by pre-drilling the abrasive, drill-resistant CFRP laminates prior to transport to a field site.

Although bolts and clamps were successfully designed, sized, and positioned to aid in shear transfer and to resist peeling stresses at the laminate ends, the use of bolts somewhat negates the time efficiency of CFRP repairs. To ensure effective repairs the bond interface of the CFRP must be free from defects at the onset to maintain uniform adhesive thickness and reduce incidence of local adhesive failures.

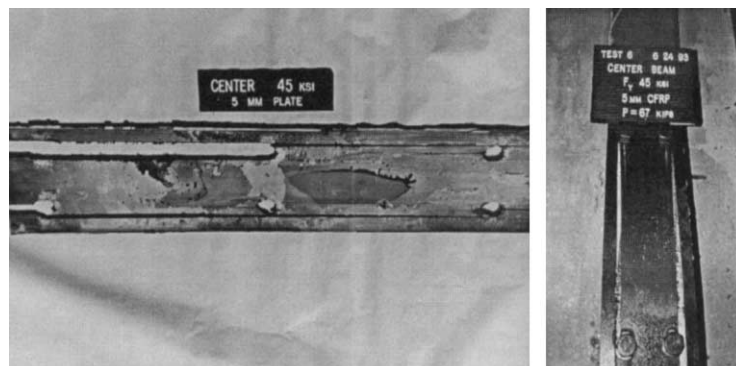


Fig. 12. Rupture of 5 mm CFRP plate (*Center-310 Mpa*).

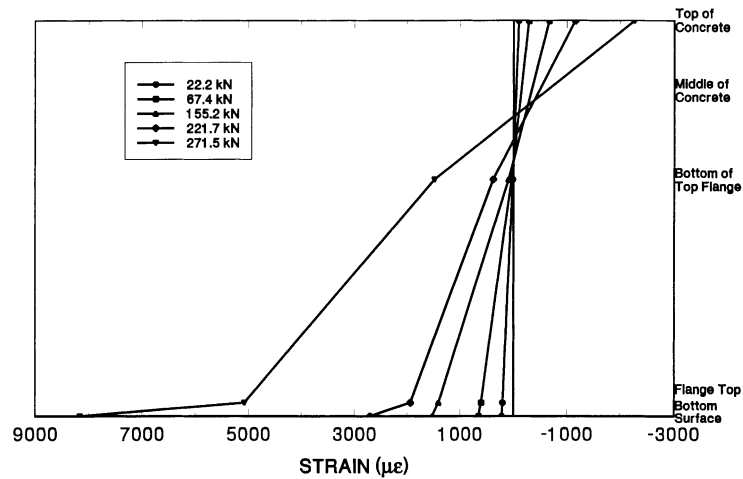


Fig. 13. Strain variation at mid-span *Center*-370 MPa-2 mm (epoxy).

Additionally, tapered laminates in both width and thickness accompanied by a scheme of adhered tapering with an adhesive fillet can reduce the stress concentrations leading to high peeling stresses.

## 10. Non-linear finite element analysis

The non-linear finite element analysis program PCFRAME [5] was used to predict the response of the six steel composite bridge sections tested. The concrete slab was discretized into 20 layers and the steel reinforcement by two. The wide flange section was modeled as eight steel layers with the CFRP laminate and the adhesive represented by single layers (see Fig. 17). Along the length, each beam was discretized using 41 members.

Figs. 18–20 show comparisons of predictions from the non-linear finite element analysis with test results. The strain variation in the CFRP laminate and concrete strain

are shown in these figures. Additional results, including a complete set of comparisons for load vs deflection and steel strains for the unreinforced and strengthened beams tested, may be found elsewhere [2].

Inspection of Figs. 18–20 show excellent correlation between the experimentally measured strains and predictions from the finite element analysis. This is especially true with the 2 mm laminate. The correlation is somewhat poorer for the 5 mm laminate at higher loads. This is not altogether surprising since some of the load taken by the bolts could not be modeled. Use of bolts in the 2 mm specimens proved to have no effect as the adhesive sufficiently transferred the shear forces without causing bearing in the bolts.

Agreement for load vs displacement was not as close with the finite element analysis predicting a stiffer post-yield response. This was because the effect of pre-damage was only approximated in the analysis. The overall agreement between experiment and finite element analysis was generally quite satisfactory.

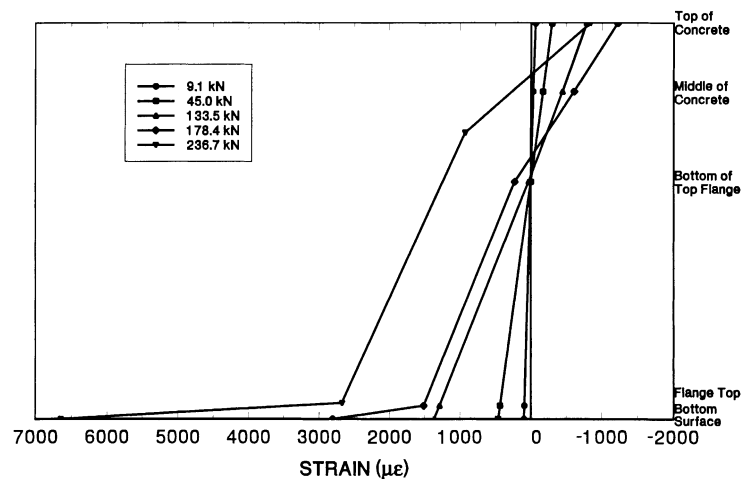


Fig. 14. Strain variation at mid-span *North*-310 MPa-2 mm (epoxy + bolted).

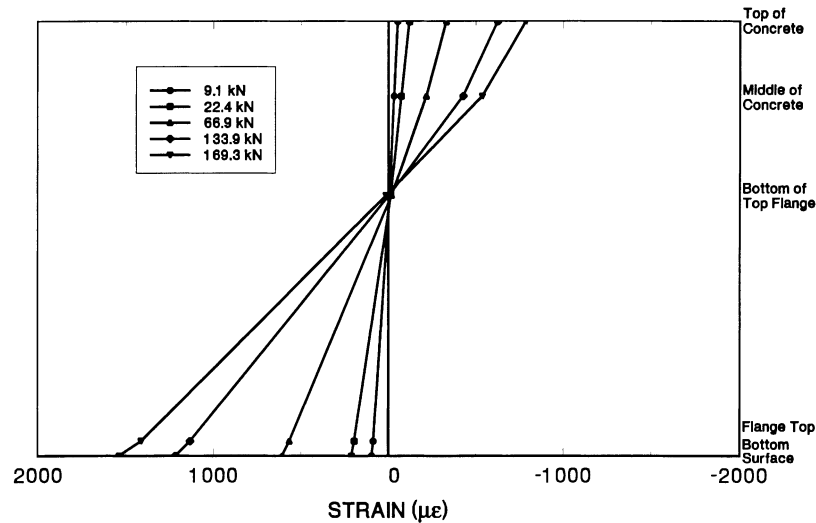


Fig. 15. Strain variation at mid-span *South-310 MPa-5 mm* (epoxy only).

## 11. Conclusions

On the basis of the experimental and numerical studies presented, the following conclusions may be drawn:

1. Steel composite members may be strengthened by bonding CFRP laminates. However, much thicker laminates are needed to achieve comparable strength and stiffness gains typically obtained in strengthened concrete or wood members. Additionally, the capacity of the epoxy adhesive to transfer loads to the CFRP laminates may need to be augmented, e.g. by clamps or fasteners, to ensure load transfer past yielding of steel.
2. Test results showed significant increases in ultimate capacity of steel composite bridge members strengthened by CFRP laminates. Strength gains for the bridge sections containing 310 MPa wide flange shapes were 21 and 52% for the 2 and 5 mm CFRP laminates, respec-

tively. Corresponding increases for the bridge sections containing 370 MPa wide flange shapes were 9 and 32%, respectively.

3. Increases in the elastic stiffness were relatively modest (see Figs. 5–10) particularly when thinner 2 mm CFRP laminates were used. However, increases in the elastic region of strengthened members were substantial indicating the potential for increases in service loading.
4. The failure mode of the strengthened sections was generally ductile and accompanied by considerable deformation (see Fig. 11). However, where only epoxy adhesive was used for bonding a 5 mm CFRP laminate, adhesive failure led to separation of the CFRP laminate and sudden failure (*South-310 MPa*). No similar separation was observed with 2 mm CFRP laminates bonded using epoxy alone in that smaller tensile forces developed in the thinner CFRP and the associated shear stresses never exceeded the epoxy's shear strength.

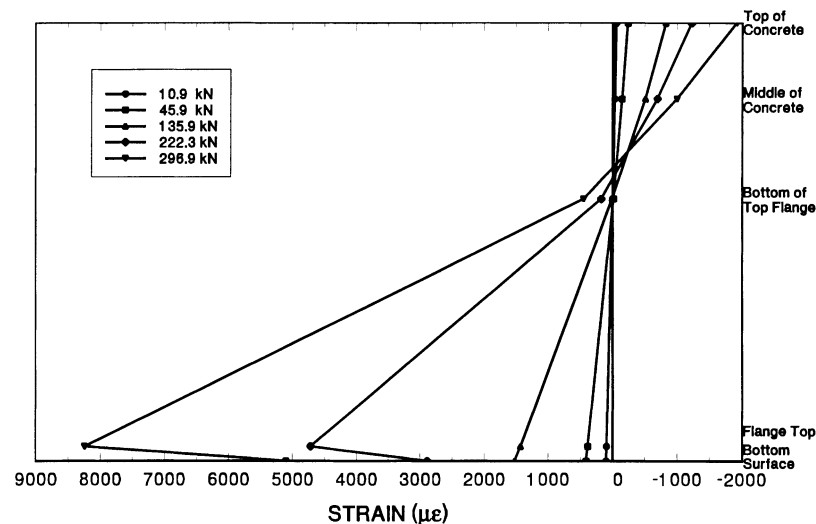


Fig. 16. Strain variation at mid-span *Center-310 MPa-5 mm* (epoxy + bolted).

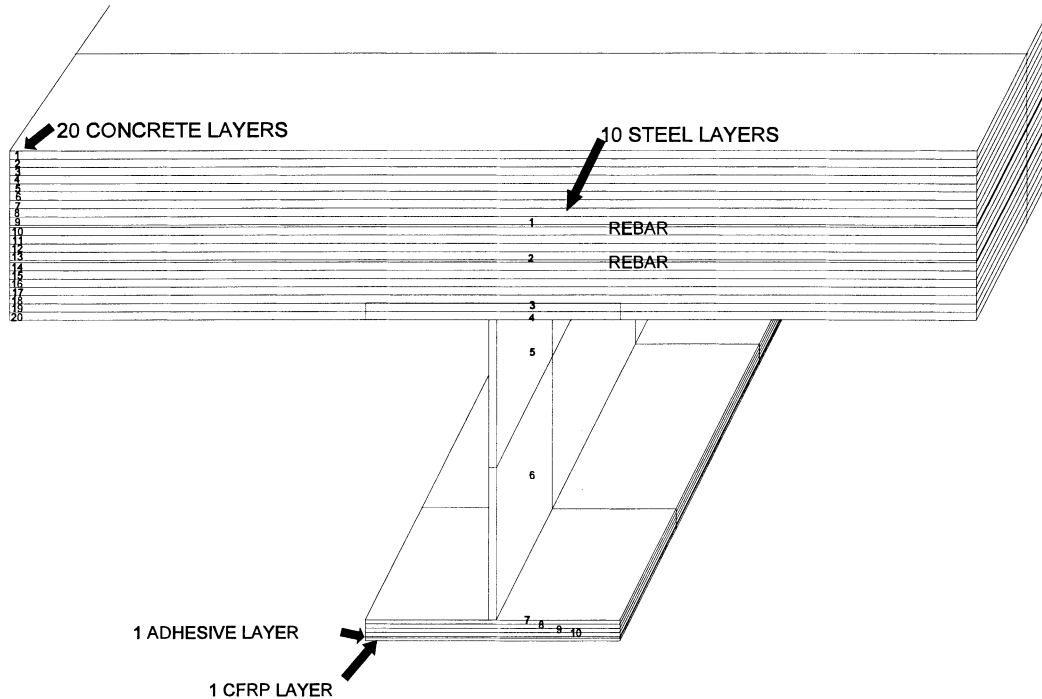


Fig. 17. Discretization of cross-section for finite element analysis.

5. The CFRP laminate must be adequately anchored to the steel flange to prevent peeling failure at the ends. In this study, a re-usable clamp system (see Fig. 4) was developed from non-linear finite element analysis that proved to be simple, efficient and inexpensive. These peeling forces could be minimized by sculpting the ends of the laminates and adhesive to reduce stress concentrations in this region. However, this would probably require ordering the laminates to case-specific lengths and would reduce field installation flexibility.
6. The response of the strengthened specimens was

predicted with reasonable accuracy by non-linear finite element analyses.

The study demonstrated the feasibility of using CFRP laminates for strengthening steel composite bridge members. If the intent of the installation is to increase the service load capacity and not to simply restore lost capacity due to damage, both the slab and shear connectors attaching it to the upper steel flange must have the reserve capacity needed for supporting the additional compressive and shear forces.

While clamps and fasteners were both used in the study,

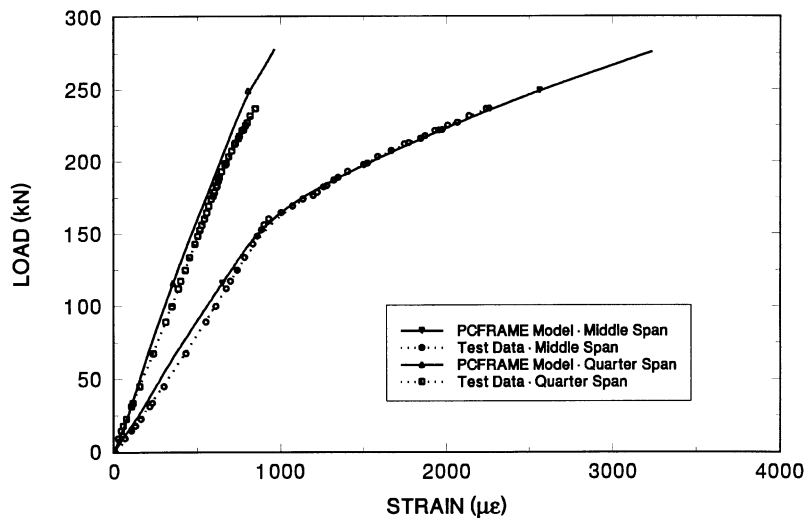


Fig. 18. Comparisons: load vs concrete strain (North-310 Mpa-2 mm).



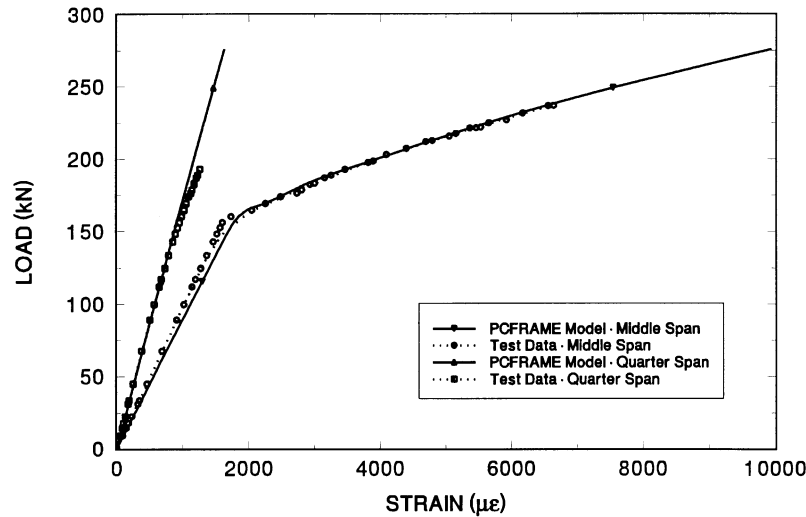


Fig. 19. Comparisons: load vs CFRP strain (*North-310 Mpa-2 mm*).

ideally clamps alone will be more desirable for field installation as it eliminates the need for heavy magnetic drills that will otherwise be needed to secure the CFRP laminates. This will greatly facilitate the speed with which repairs can be carried out particularly in congested urban areas — a very important consideration for using the light-weight CFRP laminates in the first place.

The effects of moisture and humidity on the long-term performance of the adhesive must be evaluated before field applications. However, this issue was not included within the scope of this study. In addition, appropriate measures developed by the aerospace industry should be used to prevent possible galvanic action due to the direct contact of the CFRP laminate with steel in the presence of moisture.

### Acknowledgements

The investigations reported were carried out with the financial support of the Florida Department of Transportation and the US Department of Transportation. The authors gratefully acknowledge the contribution of Dr Mohsen Shahawy, Director, Structural Research Center, Florida Department of Transportation and Mr Ken Spillett, formerly a graduate student in the Department of Civil and Environmental Engineering, University of South Florida, currently a Professional Associate, Parsons Brinckerhoff Construction Services, Tampa, FL. They also wish to express their sincerest appreciation to Composite Horizons, Covina, CA for their invaluable advice and assistance. However, the opinions,

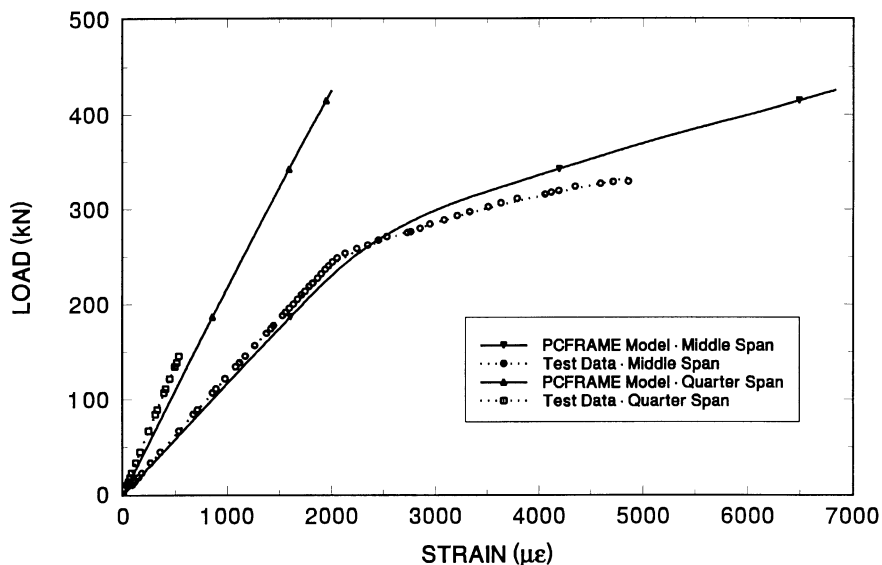


Fig. 20. Comparisons: load vs CFRP strain (*North-370 Mpa-2 mm*).

findings and conclusions expressed in this publication are those of the writers and not necessarily those of the Florida or US Department of Transportation.

## References

- [1] American Association of State Highway and Transportation Officials. Standard specifications for highway bridges. Washington, DC., 15th ed., 1994.
- [2] Liby L. Steel composite bridge sections strengthened by carbon fiber reinforced plastic laminates, MSCE Thesis submitted to Dept. of Civil Engng and Mechanics, University of South Florida, Tampa, FL, November, 1993. 353 p.
- [3] Mertz DR, Gillespie JW. Rehabilitation of steel bridge members through the application of advanced composites. Final Report, NCHRP-93-ID01, 1996.
- [4] Mosallam AS, Chakrabarti PR. Making the connection, Civil Engineering, ASCE, April, 1999. p. 56–9.
- [5] PCFRAME. Computer program for non-linear analysis of reinforced and prestressed concrete frames. Developed by Y. Kang, Ph.D dissertation, University of California, Berkeley, 1977.
- [6] Sen R, Liby L. Repair of steel composite sections using CFRP laminates. Final report submitted to Florida and US Department of Transportation, August, National Technical Information Service, VA, 1994.
- [7] Sen R, Spillett K. Restraint effect of bridge bearings. Final Report submitted to Florida and US Department of Transportation, January, National Technical Information Service, VA, 1994.
- [8] Sen R, Liby L, Spillett K, Mullins G. Strengthening steel composite bridge members using CFRP laminates. In: Taerwe L, editor. Non-metallic (FRP) reinforcement for concrete structures. London, England: E and FN Spon, 1995. p. 551–8.
- [9] Wang Y. Bridge strengthening using advanced composites, MSCE thesis submitted to the Department of Civil Engineering and Mechanics, University of South Florida, Tampa, FL, December, 1992.
- [10] Meier U, Deuring M, Meier H, Schwegler G. Strengthening of structures with CFRP laminates: research and applications in Switzerland. In: Neale KW, Labossiere P, editors. Advanced Composite Materials in Bridges and Structures. CSCE, Montreal, P.Q., 1992. p. 243–51.
- [11] Rostasy FS, Hankers C, Ranisch E-H. Strengthening of R/C and P/C structures with bonded FRP plates. In: Neale KW, Labossiere P, editors. Advanced Composite Materials in Bridges and Structures. CSCE, Montreal, P.Q., 1992. p. 253–63.
- [12] Uemura M, Aoyama K, Kligler H. A new reinforcing fiber sheet material and its application in the repair of concrete structures. In: 39th International SAMPE Symposium, April, Vol. 39, 1994. p. 347–54.
- [13] Shahawy M. Strengthening highway bridges with carbon fiber materials. In: 74th Annual Meeting of the Transportation Research Board, Washington, D.C., January, 1995.

# IMPLEMENTATION AID FOR DYNAMIC REPLACEMENT OF ORGANIC SOILS WITH SAND

By H. S. Thilakasiri,<sup>1</sup> M. Gunaratne,<sup>2</sup> G. Mullins,<sup>3</sup> P. Stinnette,<sup>4</sup> and C. Kuo<sup>5</sup>

**ABSTRACT:** The objective of this research was to understand the mechanism of dynamic replacement (DR) with the view of identifying the attributes needed to effectively implement it. This was achieved by analytically modeling DR of organic soils with sand using the finite-element method. First, this paper describes briefly the finite-element formulation and the calibration of the finite-element model using common laboratory soil tests. Then, model predictions are compared with observations made during a fully instrumented field DR trial. The respective laboratory tests utilized to extract the model parameters certainly confirmed the applicability of the chosen constitutive models for the relevant geomaterials involved in the field DR test. Furthermore, the analytical predictions of the drop hammer displacement and acceleration, as well as pore pressures and lateral displacements in the drop hammer vicinity, agree reasonably well with those observed during the full-scale field DR. Finally, a parametric study is performed to demonstrate the usefulness of the analytical model in predicting the optimum thickness of the initial sand blanket that would produce the maximum treatment benefits.

## INTRODUCTION

Recent research has led to the recognition of relatively new dynamic replacement (DR) as a viable method of weak soil improvement. The literature reports at least two case histories (Kruger et al. 1980; Lo et al. 1990) in which weak soils have been improved by DR. This is essentially an extension of dynamic compaction where the craters formed after each impact are continuously filled with sand to form strong pervious granular columns that penetrate the weak parent soil as shown in Fig. 1. Kruger et al. (1980) and Lo et al. (1990) discovered that when pounding and filling are carried out in an appropriate sequence, it was possible to create a network of such granular columns throughout the weak soil thereby improving not only its consolidation properties but also the shear strength. The optimum sand column depth that can be achieved with a given energy level under specific geological conditions and the spacing of the column grid to achieve the maximum treatment benefits are the major issues associated with effective field implementation of DR. Currently, parameters such as the column depth and spacing are established based on preliminary laboratory or field tests specific to given site conditions (Lo et al. 1990; Stinnette et al. 1996). However, this practice becomes time consuming and even impractical when a wide variation of geological conditions is observed at the same site. Therefore, in the planning stages of a given treatment project, it is invaluable to have a less expensive alternative to ascertain the viability of this technique for the available site.

Hence, the objective of this research is to formulate an analytical methodology that yields the above-mentioned DR parameters based on geology and soil properties of a given site and compare the model predictions with full-scale field DR data. In this paper, the finite-element modeling of the DR process will be described and the applicability of the finite-element

model to DR also will be investigated based on laboratory soil tests and a field DR study. The laboratory testing program consisted of the tests necessary to calibrate the material constitutive models, whereas observations from an instrumented full-scale field DR test program were compared with the theoretical predictions of the finite-element model. Parameters involved in the comparative study were the predicted and measured drop hammer acceleration, pore pressure response of the foundation material, and the lateral deformation in the vicinity of the drop hammer. A sensitivity analysis was also carried out to scrutinize the variation of the drop hammer penetration with the mesh size and the time step size in an effort to explore the suitability of the selected mesh configuration and time step size. Finally, to demonstrate the usefulness of the program, a parametric study was conducted to obtain the optimum initial sand blanket thickness required for effective implementation of dynamic replacement.

## NUMERICAL SIMULATION

### Finite-Element Formulation

As seen in Fig. 1, one realizes that any realistic solution to the dynamic replacement problem must account for such complexities as pore water flow, improvement of soil properties associated with treatment, and, above all, the excessive axial and lateral deformations induced by high energy impact. Hence, consequent to preliminary analysis based on a 1D analytical model (Thilakasiri et al. 1996b), it was seen that the 3D finite-element method had to be adopted in order to appropriately address all of the above issues.

At the first impact point, dynamic replacement is axisymmetric, and, accordingly, a cylindrical coordinate system with updated Lagrangian coordinates will be utilized for the ensuing formulation. Formulation proposed by Kleiber (1989) and Fung (1965) is used to take into account the finite strains in the vicinity of the drop hammer. The equations of motion of

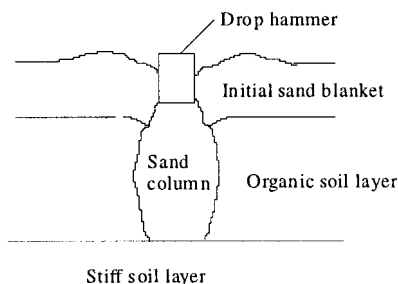


FIG. 1. Dynamic Replacement

<sup>1</sup>Sr. Lect., Dept. of Civ. Engrg., Univ. of Moratuwa, Moratuwa, Sri Lanka.

<sup>2</sup>Assoc. Prof., Dept. of Civ. and Envir. Engrg., Univ. of South Florida, Tampa, FL 33620.

<sup>3</sup>Asst. Prof., Dept. of Civ. and Envir. Engrg., Univ. of South Florida, Tampa, FL.

<sup>4</sup>Asst. Prof., Dept. of Civ. and Envir. Engrg., Hillsboro Community Coll., Plant City, FL 33566.

<sup>5</sup>Chf. Engr., Professional Services Industries, Tampa, FL 33634.

Note. Discussion open until June 1, 2001. To extend the closing date one month, a written request must be filed with the ASCE Manager of Journals. The manuscript for this paper was submitted for review and possible publication on January 9, 1997. This paper is part of the *Journal of Geotechnical and Geoenvironmental Engineering*, Vol. 127, No. 1, January, 2001. ©ASCE, ISSN 1090-0241/01/0001-0025-0035/\$8.00 + \$.50 per page. Paper No. 14920.

the solid skeleton and the fluid phase are considered separately while maintaining volume compatibility between the two phases (Zienkiewicz et al. 1988). Subsequently, the finite-element method with four-node, axisymmetric, isoparametric elements is used to spatially discretize the system of equations, and then direct time integration is utilized to integrate the equations of motion in the time domain.

For the explicit form of equilibrium equations, a diagonal mass matrix must be obtained by lumping the element mass at discrete points. However, the numerical convenience of lumping is generally paid off by some loss of accuracy in the solution. For some cases it has been shown that lumping can improve the accuracy by error cancellation, and, in transient approximations, the lumping process introduces additional dissipation of the “stiffness matrix” form, thus canceling out numerical oscillation (Zienkiewicz and Taylor 1991). The solution scheme is progressed in the time domain using the direct time integration in which the solution is obtained at discrete time intervals. Of the many time integration schemes available, Newmark’s explicit scheme, a popular algorithm for dynamic analysis, is used in the present study. Then, together with a diagonal mass matrix, the algorithm becomes explicit. With Newmark’s explicit time integration, the algorithm becomes conditionally stable whereby the size of the time step governs the stability of the solution. It can be shown (Hallquist 1983) that the critical time step size is related to the time taken to propagate an elastic wave across the shortest dimension of the element.

### Constitutive Relations

It is a well-known fact that soils exhibit nonlinear behavior even at low strain levels. Therefore, the traditional assumption of linear elasticity is inapplicable for soil at the vicinity of the drop hammer. Considering the implementation ease and their ability to represent most of the soil properties, two constitutive relations are adopted in the present formulation, namely, the elliptical cap model (DiMaggio and Sandler 1971) for granular soil cover (replacement material) and the modified Cam-clay model (Chen and Mizuno 1990) for weak soft organic soil. The cap model consists of a strain hardening elliptical cap and an elastic perfectly plastic Drucker-Prager failure surface that, in the octahedral plane (or  $\pi$  plane), touches the irregular hexagon formed by the Mohr-Coulomb failure surface at its outermost three nodes. Then, following the classical plasticity theory proposed by Zienkiewicz and Taylor (1991), the elastoplastic stress-strain tensor  $\mathbf{C}_{ijmn}^{ep}$  can be obtained [(1)] considering a strain hardening yield function  $f = f(\boldsymbol{\sigma}_{ij}, \chi(\boldsymbol{\varepsilon}_{ij}))$ , where  $\boldsymbol{\sigma}_{ij}$  and  $\chi(\boldsymbol{\varepsilon}_{ij})$  are, respectively, the stress tensor and the hardening parameter, which is a function of plastic strain tensor  $\boldsymbol{\varepsilon}_{ij}^p$

$$\mathbf{C}_{ijmn}^{ep} = \left[ \mathbf{C}_{ijmn} - \frac{\frac{\partial g}{\partial \sigma_{rs}} C_{ijrs} C_{klmn} \frac{\partial f}{\partial \sigma_{kl}}}{H' - \frac{\partial f}{\partial \sigma_{ab}} C_{abcd} \frac{\partial g}{\partial \sigma_{cd}}} \right] \quad (1)$$

where

$$H' = - \frac{\partial f}{\partial \chi} \frac{\partial \chi}{\partial \boldsymbol{\varepsilon}_{ij}} \frac{\partial g}{\partial \sigma_{ij}} \quad (2)$$

and  $\mathbf{C}_{ijmn}$  = elastic constitutive matrix.

At each time step, a trial elastic second Piola-Kirchhoff stress increment  $d\boldsymbol{\sigma}^e$  is calculated for that time step (Kleiber 1989). Then,  $d\boldsymbol{\sigma}^e$  is transformed to the Cauchy stress increment at the end of that time step. Similarly, after the stress at the beginning of the  $n$ th time step  $\boldsymbol{\sigma}_n$  is also transformed to the corresponding Cauchy stress at the end of  $n$ th time step,

the final trial stress  $\boldsymbol{\sigma}_{n+1}$  on the current configuration referring to the rotated coordinates at the end of the time step is estimated by adding the stress increment to  $\boldsymbol{\sigma}_n$  (Kleiber 1989). If the trial stress tensor  $\boldsymbol{\sigma}_{n+1}$  is outside the current yield surface, then the stress increment is elastoplastic and (3) is used to estimate the stress increment

$$d\boldsymbol{\sigma}_{ij} = \mathbf{C}_{ijmn}^{ep} d\boldsymbol{\varepsilon}_{mn} \quad (3)$$

The validity of the approximation in (3) depends on the magnitude of the strain increment. If the strain increment is excessive, it should be divided into smaller increments and passed through the constitutive relations subroutine several times. However, it is possible for such approximations to deviate the stress point from the yield surface even for small strain increments, and such small deviations can become cumulative during several steps, thereby inducing significant errors in the final results. There are a number of methods to relocate the stress point back on the yield surface after each strain increment. The method adopted in the present formulation is known as the radial return method (Chen and Mizuno 1990) where it is assumed that the relocation is done along the direction of the normal to the current yield surface.

### Slideline Algorithm

An obvious complexity involved in finite-element modeling of dynamic replacement (or dynamic compaction) procedures is the simulation of the soil punching mechanism. Hence, a unique feature of the current analysis is the development of a specific sideline algorithm to account for the relative displacement between adjacent nodes. In accordance with previous theoretical developments by Thilakasiri et al. (1996b) and Chow et al. (1992) as well as experimental observations, in the present analysis it is assumed that the soil column immediately underneath the hammer punches through the surrounding soil together with the hammer. This punching causes relative displacement between the adjacent nodes on either side of the punching soil column. It is also assumed that whether or not sliding develops between adjacent nodes is determined by the limiting Coulomb friction between them. There is a number of sideline algorithms available to account for various mesh discontinuities in the finite-element or finite-difference formulations (Hallquist et al. 1985). Of those, the model constraints, the penalty, and the distributed parameter methods are widely used; in this formulation the penalty method is adopted.

For all of the sideline algorithms, it is customary to identify one side as the slave side and the other side as the master side. The sideline algorithm employed in this formulation considers the forces transferred from solid to solid and fluid to fluid across the sideline discontinuity. Each slave node is considered in turn, and the effective area for the  $n$ th slave node is defined between the center of the  $n - 1$ th slave segment and the center of the  $n$ th slave segment. This effective area is indicated for node  $c$  in Fig. 2. If the master segment is in contact with the slave side, integrated quantities related to forces corresponding to each slave node are prorated according to the relevant area of contact and transferred to the master node(s) within the effective area.

In the penalty formulation, the nodes are allowed to penetrate the opposite side. Such a situation is shown in Fig. 3, where node  $\mathbf{q}$  has penetrated segment  $rs$  of the adjacent element. In this situation, as the node is inside the segment (such as node  $\mathbf{q}$  in  $rs$ ), a new contact point  $y$  (on segment  $rs$ ) and the amount of penetration  $l_q$  are found using the relationships given by (4) and (5), respectively.

$$\frac{\partial y(\eta_c)}{\partial \eta} \cdot [\mathbf{q} - \mathbf{y}(\eta_c)] = 0 \quad (4)$$

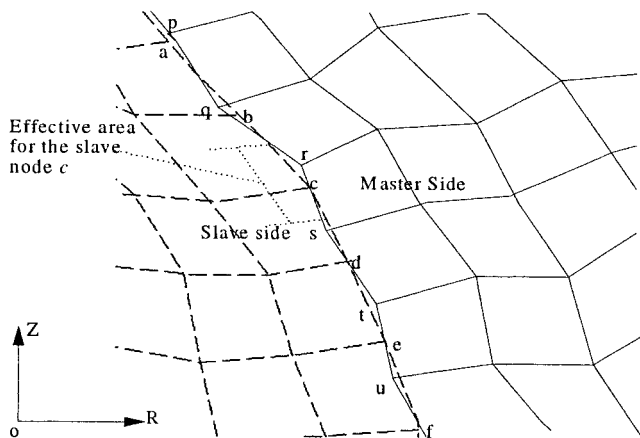


FIG. 2. Typical Mesh Discontinuity with Dotted Lines Showing Slave Side and Solid Lines Showing Master Side

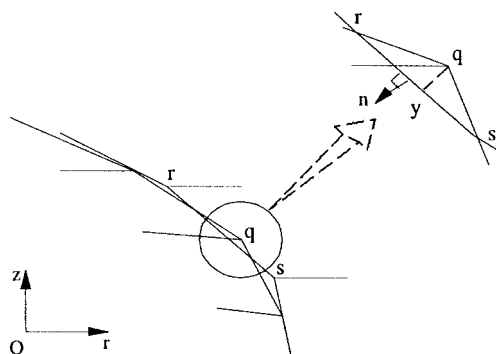


FIG. 3. Penetration of Node  $q$  through Opposite Side

$$l_q = \mathbf{n} \cdot [\mathbf{q} - \mathbf{y}(\eta_c)] < 0 \quad (5)$$

where  $\mathbf{n}$  = normal vector to segment  $rs$ ;  $\mathbf{y}$  = vector  $oy$ ;  $\mathbf{q}$  = vector  $oq$ ; and  $\eta_c$  = local coordinate of the contact point with respect to points  $r$  and  $s$ . Then, a penalty force  $f_q$  [(6)] proportional to the amount of penetration  $l_q$  is applied to get the node back onto segment  $rs$

$$f_q = -l_q K_q \eta \quad (6)$$

$$K_q = \frac{f_{si} K_b A_i^2}{V_i} \quad (7)$$

where  $A_i$  = face area of the element containing segment  $rs$ ;  $V_i$  = volume of the element containing segment  $rs$ ;  $K_b$  = bulk modulus of the material of the element containing  $rs$ ; and  $f_{si}$  = scale factor. The value of the coefficient  $K_b$  is generally kept constant, but if excessive penetration is noticed it should be increased to reflect the gradual densification. Then, the master side acceleration is updated for the next time step using the new integrated quantities. As illustrated in (8) and (9), the estimated acceleration is used to determine the respective forces acting on each slave node tangential and normal to the master segment

$$f_m = (a_m \cos \theta + a_{zn} \sin \theta) m_n - f_m \cos \theta - f_{zn} \sin \theta \quad (8)$$

$$f_m = (-a_m \sin \theta + a_{zn} \cos \theta) m_n + f_m \sin \theta - f_{zn} \cos \theta \quad (9)$$

where  $a_m$  = acceleration of the  $n$ th node in the  $r$ -direction;  $a_{zn}$  = acceleration of the  $n$ th node in the  $z$ -direction;  $f_m$  = internal force at the  $n$ th node in the  $r$ -direction;  $f_{zn}$  = internal force at the  $n$ th node in the  $z$ -direction;  $m_n$  = lumped mass at the  $n$ th node; and  $\theta$  = inclination of the normal vector  $\mathbf{n}$  to the  $r$ -direction.

For any node, if the normal force is found to be tensile, then

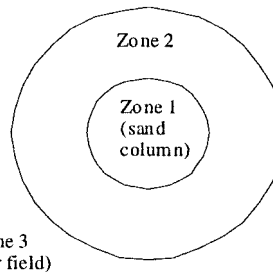


FIG. 4. Vicinity of Impact Location

the slave node is released, and it is no longer considered to be in contact with the master side. The normal force determined above is used to estimate the shear strength based on Coulomb limiting friction expressed by (10). Then, when the tangential force  $f_m$  exceeds the frictional shear strength  $f_m^s$ , the slave node slides relative to the master segment

$$f_m^s = f_m \tan \delta + c \quad (10)$$

where  $f_m^s$  = shear strength at the  $n$ th node tangential to the interface;  $\delta$  = angle of friction between master and slave sides; and  $c$  = cohesion between master and slave sides.

When  $f_m \geq f_m^s$ , a frictional resistive force  $f_m^f$  equal to  $f_m^s$  is applied on  $q$  in the tangential direction, and the node is allowed to slide. Then, the direction of the limiting Coulomb frictional force  $f_m^f$  applied on the sliding node is determined based on the relative velocity  $\mathbf{v}$  in the tangential direction between the contact node  $q$  and the point of contact  $y$  (Fig. 3) as given in (10).

It was observed by Nagger et al. (1994) and Thilakasiri et al. (1996b) that the impact vicinity can be divided into three zones, namely, Zone 1, Zone 2, Zone 3 (Fig. 4) based on the magnitude of the accumulated plastic strains. Furthermore, it was also emphasized that the strains developed in Zone 3 are essentially elastic. Therefore, the boundary traction force vector in the equilibrium equations is determined based on linear elastic material behavior.

## CALIBRATION OF CONSTITUTIVE RELATIONS

### Estimation of Material Parameters

Calibration of the constitutive models to accurately represent the material behavior is vital to obtaining reliable predictions from finite-element analysis. The bulk modulus  $K$  and the shear modulus  $G$  can be constants or stress or strain level dependent elastic material properties. After analyzing the results of a test series carried out on the replacement material (sandy soils), it was concluded that the assumption of constant bulk modulus  $G$  and shear modulus  $K$  is reasonable for this material type for the relevant range of pressures. As for the foundation material (organic soil), the bulk modulus is assumed to be a function of the first invariant of the stress tensor (Cam-clay assumption), and the shear modulus is assumed to be constant.

The Cam-clay model requires five material parameters for a complete description of the material (Chen and Mizuno 1990), and the elliptical cap model needs seven independent parameters (Chen and Mizuno 1990). In addition to the material parameters required for the constitutive relations, there are other properties such as density, permeability, and porosity that must be evaluated as well.

The material used for the initial layer and subsequent crater fillings were sandy in nature, and hence they were modeled in the finite-element formulation using the elliptical cap model. In the calibration of the elliptical cap model, isotropic consolidation, consolidated drained, and consolidated undrained triaxial test results were used.

The material parameters obtained during the calibration phase were subsequently used for the prediction of stress-strain and pore pressure-strain response of the respective material during an independent test series, in order to verify the applicability of selected material models, for each material type. The predicted and observed variations are shown in Figs. 5 and 6.

In addition to the volumetric compressibility due to dissipation of pore water pressure (primary consolidation), the long-term settlement due to creep (secondary consolidation) is also excessive for organic soil and persists for a long period under prolonged loading. However, the duration of the impact of a single hammer blow during dynamic replacement is relatively short making it impossible for secondary consolidation to take place. Hollingshead et al. (1971) carried out two 1D consolidation test series on a similar type of material (Canadian muskeg), one with 4-h load increments and the other with 24-h load increments. The results show that the difference in the slope of the  $e$  versus  $\log P$  curve is essentially the same for both test series. Furthermore, another consolidated undrained test series carried out by Hollingshead et al. (1971) showed that the general shapes of the stress-strain curves of these tests are similar to those of insensitive unbound clays. They also showed that the pore pressure response during undrained shearing was similar to what might be expected from an insensitive clayey soil. Hence, a 1D consolidation test series was carried out on the organic material at the study site to estimate the primary consolidation parameters, and these tests were terminated after the primary consolidation phase with the aid of the data acquisition system, which displays the specimen displacement on screen while the test progresses.

The general behavior of Florida organic material under con-

solidated undrained triaxial conditions resembled the previously mentioned observations of Hollingshead et al. (1972). The stress path plot during one undrained triaxial test is reproduced in Fig. 7. The evaluated material parameters were then utilized in the Cam-clay model to predict the experimental stress path shown in Fig. 7. It is seen that the model predictions agree reasonably well with the experimental results.

1D consolidation test results were also used to investigate the variation of permeability of organic material with the void ratio. Fig. 8 shows permeability versus void ratio trend, and, within the range of values relevant to this study, the following linear fit can be made:

$$\log(k) = 1.9322e - 14.04 \quad (11)$$

where  $k$  is measured in centimeters per second. Since it is the direct shear test condition that closely represents the mechanics of shearing taking place at the slideline, the angle of internal friction obtained from a direct shear test is used in the Mohr-Coulomb shear strength expression to get the limiting frictional force.

The compressibility of pore water  $k_f$  has a prominent effect on the predicted pore pressure results. It is an accepted fact that the natural pore fluid contains microbubbles and tiny air pockets entrapped in the voids between soil particles (Menard and Broise 1975). When treated as a single substance under a dynamic load, the presence of these air pockets and microbubbles give rise to a high compressibility compared to pure water. The effective elastic bulk modulus of the air-water mixture can be defined as

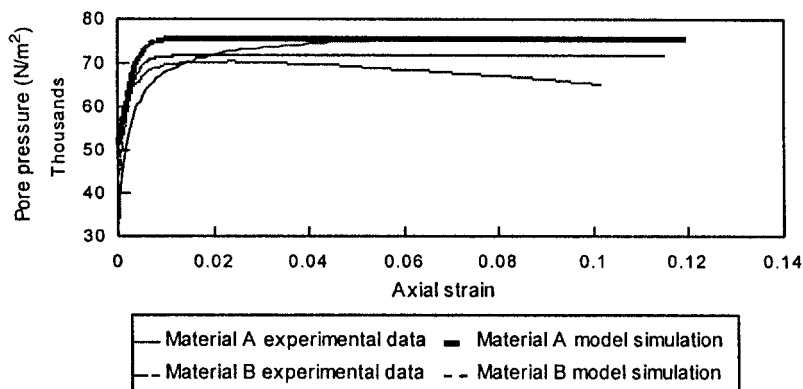


FIG. 5. Experimental Pore Water Pressure versus Strain Variation and Corresponding Elliptical Cap Model Predictions

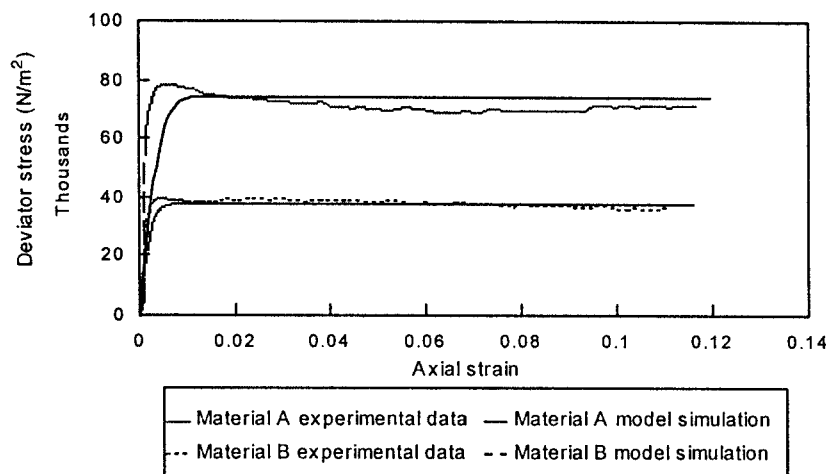


FIG. 6. Experimental Stress versus Strain Curve and Elliptic Cap Model Predictions

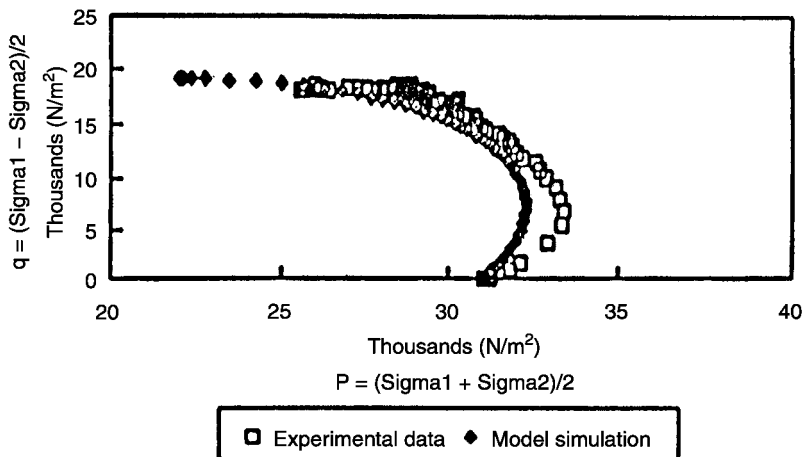


FIG. 7. Experimental and Predicted Stress Paths for Undrained Triaxial Tests on Florida Soils

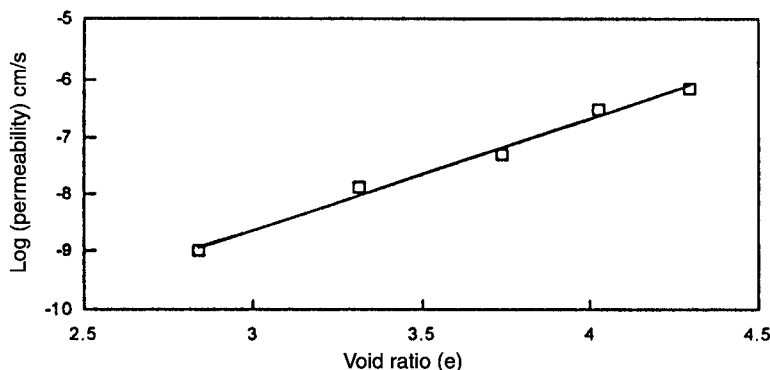


FIG. 8. Variation of Permeability with Void Ratio for Organic Soil

$$\frac{d\rho_w}{\rho_w} = \frac{dp}{K_f} \quad (12)$$

where  $\rho_w$ ,  $dp$ , and  $K_f$  are density, pressure change, and bulk modulus of the mixture, respectively. On the other hand,  $K_f$  can be related to the bulk modulus of pure water  $K_{fo}$  by (Mei and Fonda 1982)

$$\frac{1}{K_f} = \frac{1}{K_{fo}} + \frac{1-s}{p} \quad (13)$$

in which  $s$  = degree of saturation of the soil; and  $p$  = absolute pore pressure. The effect of entrapped air on the bulk modulus of the mixture can be illustrated by the following example. Assume that  $K_{fo} = 2 \times 10^9$  N/m<sup>2</sup>,  $S = 95\%$ , and  $p = 1$  atm =  $10^5$  N/m<sup>2</sup>. Thus,  $K_f$  is estimated to be  $2 \times 10^6$  N/m<sup>2</sup> from (13) clearly showing a magnitude reduction of three orders from  $K_{fo}$  due to 5% air. As the order of magnitude of pore pressure  $p$  is much less than that of  $K_{fo}$ , a constant value of  $K_f$  was used assuming the degree of saturation of 95% for air-water mixture.

### Computer Program for Finite-Element Formulation

The computer program DYCOM was developed to execute the theoretical procedure outlined above. This program is capable of modeling single or multiple impacts during the dynamic replacement procedure and generating output files of mesh deformation as well as time history data.

Once the main finite-element program was developed, the accuracy of the written subroutines (except the constitutive relations subroutine, the slideline subroutine, and the pore pressure subroutine) were checked against the commercially available dynamic finite-element program DYNA2D. For this

purpose, a simple impact load case involving linear elastic material behavior without pore water was analyzed using both DYNA2D and the DYCOM programs. Despite the difference in the number of integration points employed for these two programs (four point integration for DYCOM and one point integration for DYNA2D), excellent agreement was obtained in their predictions. Flowcharts illustrating the organization of the main finite-element program and the constitutive subroutine for the Cam-clay model are shown in Thilakasiri (1996a).

## MODELING OF FULL-SCALE FIELD TEST

### Field Testing Program

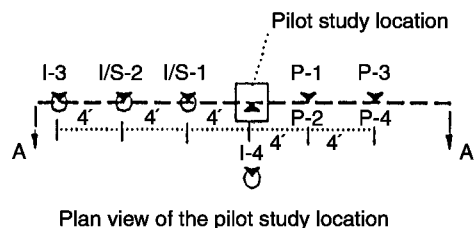
A field testing program was devised to investigate the feasibility of dynamic replacement of Florida organic soil during one phase of the comprehensive research project. The test site is located in Plant City, Florida, adjacent to Interstate 4 (I-4). The subsurface profile at the test consisted of 1.2- to 1.8-m-thick organic soil layer underlain by a dense silty sand deposit. After investigating the thickness of the organic soil layer based on "muck" probes, an area of  $26 \times 18$  m was cleared. Then, the cleared area was covered with sand with a layer thickness varying from 1.2 to 2.1 m. The time duration between placing of the surcharge and the beginning of actual dynamic replacement testing was approximately 1 month. Considering the consolidation characteristics of organic soil, it can be reasonably assumed that during that period, the organic soil layer had reached the end of the primary consolidation phase, thus leaving a hydrostatic pressure distribution at the beginning of dynamic replacement. One impact location was selected for the pilot study and instrumented with inclinometers and resistivity type piezometers as shown in Fig. 9.



ified by the crater prediction method proposed by Mullins et al. (1996).

The soil layer dimensions for the finite-element mesh were selected based on the previously carried out cone penetration test and borehole log results. The mesh boundaries were selected well outside the influence area of the drop hammer. The final mesh configuration was determined after carrying out a sensitivity analysis of the predicted results with respect to the number of elements in the mesh. The ground-water table was observed to be at the top of the organic soil layer. The actual impact velocity of the hammer was estimated by multiplying the free fall velocity by an efficiency factor. Based on the velocity measurement using the laser beam method and videotaping of the free-fall, the efficiency factor was found to be 90%.

The mesh output data were obtained at 20-ms intervals. Fig. 10 shows the initial finite-element mesh, and Figs. 11(a and



Plan view of the pilot study location

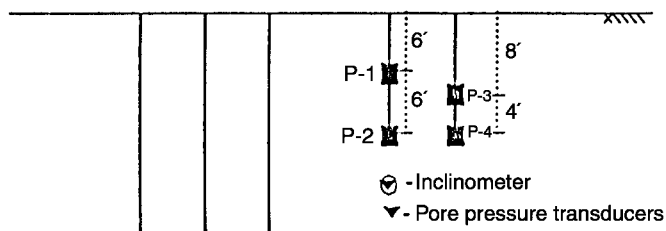


FIG. 9. Instrumentation of Pilot Study

### Instrumentation

The instrumentation included inclinometers, resistivity-type electronic piezometers, and an accelerometer. The pressure transducers (6,897 kPa capacity) were first encapsulated in a PVC porous material and then attached to a 19.1 mm schedule 40, PVC standpipe to physically protect the electrical connection to the computer.

The inclinometers were used to measure the lateral deformation of the soil in the vicinity of the drop hammer. Attached to the inclinometers were magnetic rings to measure the vertical settlements. A magnet sensitive probe could descend to facilitate the settlement monitoring. The inclinometer/settlement monitoring system consisted of the inner inclinometer casing surrounded by a flexible corrugated plastic hose to which the magnetic rings were attached. The spacing of the magnetic rings along the casing was kept at 0.61 m.

Fig. 9 shows the plan view and a sectional view of the instrumentation relative to the impact location. In Fig. 9, *I/S* denotes the inclinometer-settlement monitoring system, and *I* denotes only the inclinometer. The typical inclinometer probe, which consists of spring-loaded wheels mounted to an approximately 2-ft-long, 1-in.-diameter rod, was used to measure the position of the inclinometer after the impact.

Apart from the above-mentioned instruments, laser pointers with laser detectors were used to measure the impact velocity of the hammer and trigger the data acquisition system. A drop hammer was also fabricated from 49-mm-thick,  $0.61 \times 0.61$  m square steel plates to a total height of 1.22 m, producing a total weight of 4 tons. Then, an accelerometer was mounted on the top plate of the hammer coinciding with the center of the hammer. A terminal box with receptacles for each of the eight transducers was fabricated to expedite data acquisition during testing.

### Comparison of Model Predictions and Field Data

#### First Blow of Drop Hammer

The aforementioned finite-element program DYCOM was used to model the drop hammer impacts during the field testing program. Then, the predicted displacement and pore pressure fields in the neighborhood of the hammer were compared with the corresponding quantities measured in the field. After conducting a few trials in the area (under similar subsurface conditions) well away from the pilot study location, an initial drop height of 6.1 m was selected. This drop height was ver-

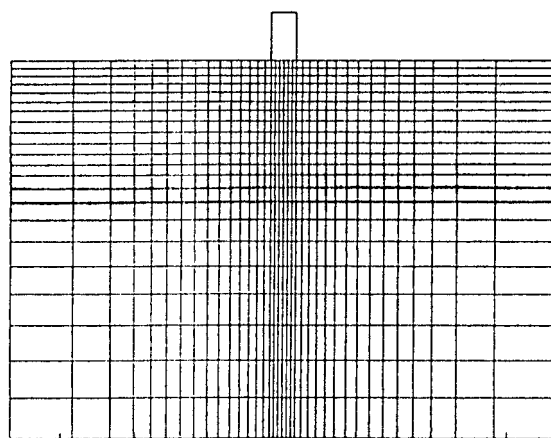


FIG. 10. Initial Mesh

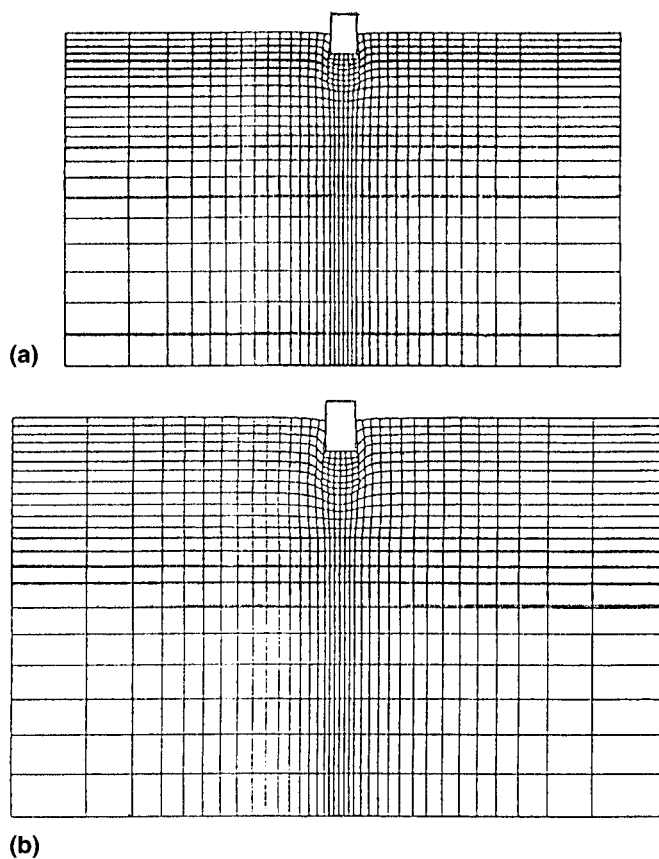


FIG. 11. Hammer Displacement after: (a) 160 ms; (b) 200 ms

b) show the time history of the deformation of the finite-element mesh as predicted by the finite-element model, at 160 and 200 ms after the impact.

The crater depth measured after the first blow was 0.87 m, whereas the theoretical prediction from the model was 0.78 m. In Fig. 12, the rebound portion of the predicted acceleration curve of the drop hammer was of a higher magnitude than the measured negative acceleration, indicating that the rebound velocity of the hammer is less than the rebound velocity predicted by the model. This is probably the reason for the dis-

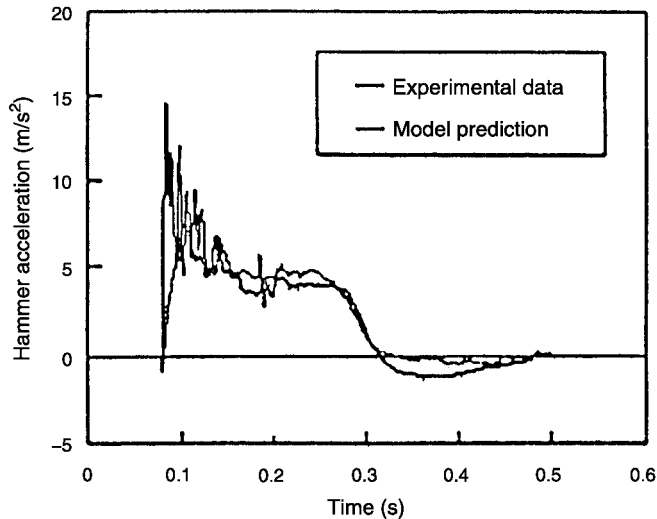


FIG. 12. Acceleration Time History of Drop Hammer

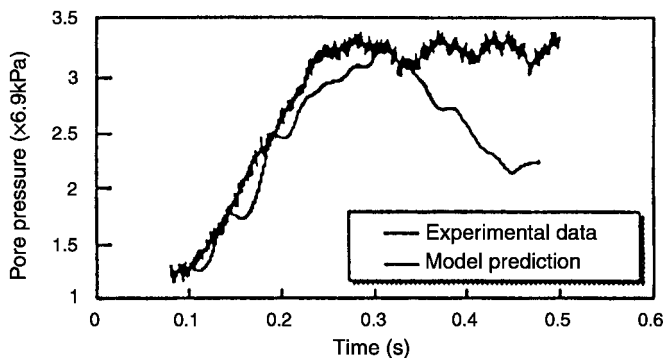


FIG. 13. Measured and Predicted Pore Pressure at Location P-1 of Fig. 9

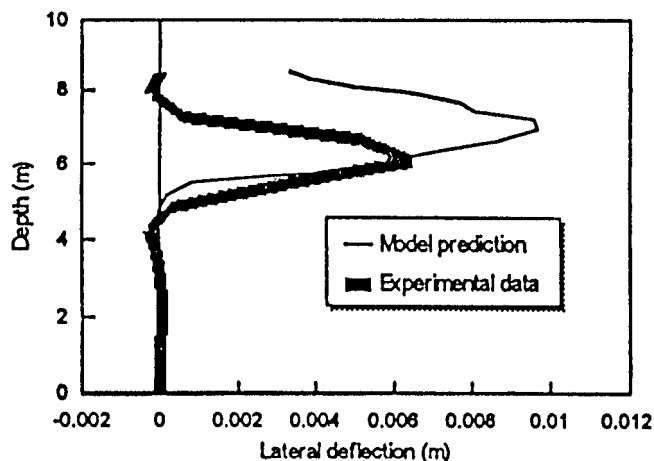


FIG. 14. Measured and Predicted Lateral Displacement at Location I/S-1 of Fig. 9

crepancy between the predicted and the measured crater depths.

The model was also utilized to predict the pore pressure responses of the installed piezometers. The results of the comparison of the model and the measured pore pressure response at location P-1 of Fig. 9 is shown in Fig. 13. The comparison of the lateral deformation of the inclinometer I/S-1 with the corresponding model prediction is shown in Fig. 14. Similar comparisons made with other piezometer and inclinometer readings are found in Thilakasiri (1996a).

As mentioned earlier, a convergence study was carried out to select the best mesh configuration and the time step size. For this study, the final hammer penetration was selected as the control parameter. The variations of the control parameter with respect to the number of elements and the time step size are shown in Figs. 15 and 16. In varying the number of elements in the mesh, both the far-field configurations were changed. Accordingly, a time step size of 0.00002 s and a mesh with 464 elements were selected for the field test simulation.

### Multiple Blows

The program DYCOM is also capable of modeling multiple blows during dynamic replacement. At the end of a particular hammer blow, the program automatically creates an output file containing the current geometry of the mesh, updated material properties, slip surface information, and other parameters specified by the user in the initial input file. The output file, thus created, acts as the input file for the simulation of the next hammer blow. In addition, the user has to specify the refill material properties together with the re-meshing dimensions for the next hammer blow. For subsequent hammer blows, the program re-meshes only the refilled crater created by the preceding hammer blow and the slave side of the slideline of the previous mesh. On the other hand, the master side of the slideline of the previous mesh is kept unaltered.

Once the re-meshing dimensions and the refill material properties are provided, re-meshing is automatically carried out by taking into account the refilled area and the user specified dimensions. In the process of re-meshing, the updated soil properties at the integration points are determined by linear interpolation of the corresponding quantities from the mesh configuration at the end of the preceding hammer blow. The computational procedure is repeated for the new mesh with the updated material properties.

The first four hammer blows imparted during the field testing program were numerically simulated using the above procedure. Since the hammer acceleration and pore pressure data were not available for comparison, only the lateral displacement measured using the inclinometers are shown in Figs. 17–20 along with predicted values. In addition, the vertical displacement of the top of the organic soil layer predicted and measured with the progression of the treatment process are shown in Fig. 21. Both the predicted and the measured vertical displacement of the bottom of the organic layer was insignificantly small.

If one assumes that the measured displacements are accurate, then it is evident from the comparison of the measured and the predicted lateral displacements (Figs. 17–20) that the model overpredicts the lateral deformation of the organic soil layer. For precise measurement of the lateral deformation, the stiffness of the measuring device should be of the same order of magnitude as that of the surrounding soil. However, the inclinometer pipes were grouted after installation, thus increasing the lateral stiffness of the inclinometer setup. Therefore, it is possible that the inclinometer pipe surrounded by hardened grout may have been stiffer than the weak organic soil, resulting in lower lateral displacement of the inclinometer in the

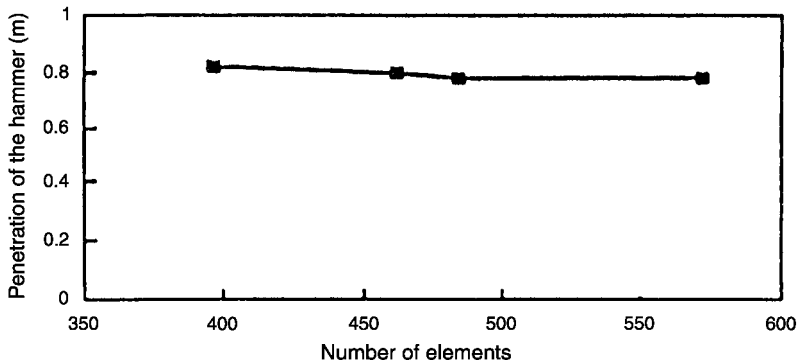


FIG. 15. Variation of Final Hammer Penetration with Number of Elements

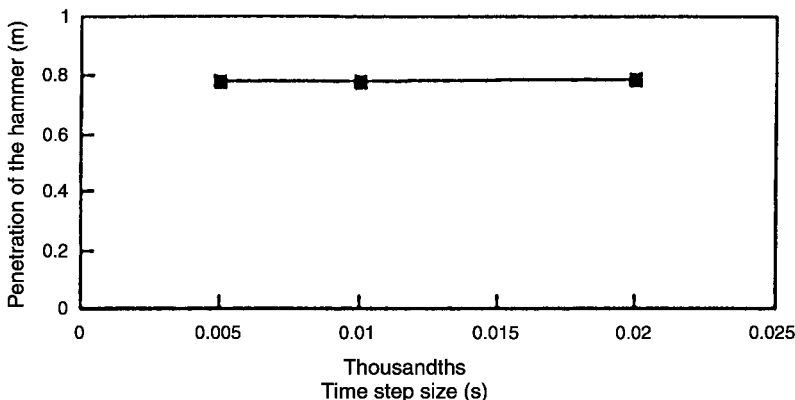


FIG. 16. Variation of Final Hammer Penetration with Time Step Size

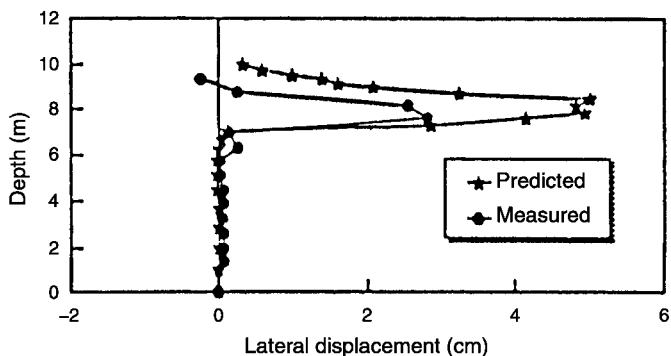


FIG. 17. Lateral Displacement of Inclinometer I/S-1 after Second Blow

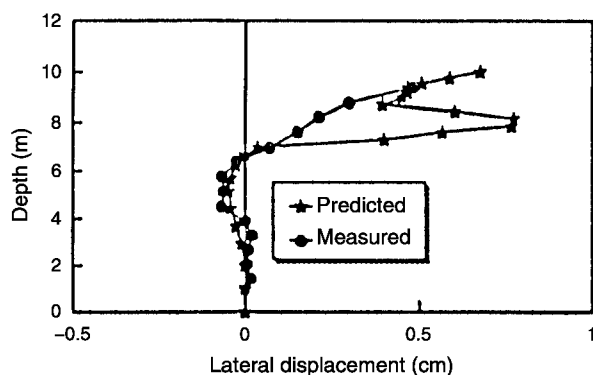


FIG. 19. Lateral Displacement of Inclinometer I/S-2 after Second Blow

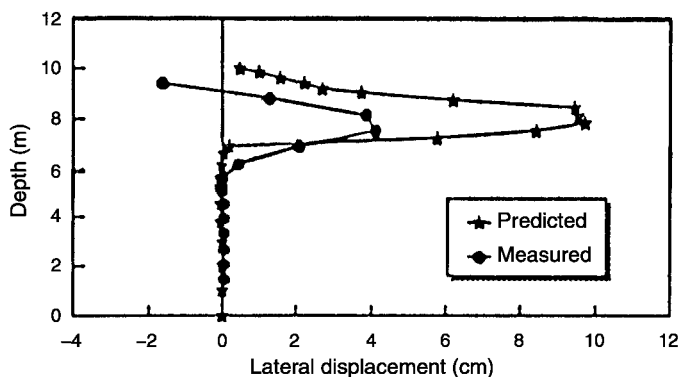


FIG. 18. Lateral Displacement of Inclinometer I/S-1 after Fourth Blow

organic soil layer. Hence one can also view the results in Figs. 17–20 as indicating a significant limitation of inclinometer measurements rather than an overprediction by the analytical method. This deficiency of the inclinometer systems is hard to overcome when using them in very weak soils.

**Parametric Study**

The finite-element methodology developed in this study can be effectively utilized in predicting the optimum values of energy level, initial sand blanket thickness, and other significant attributes of dynamic replacement. This would certainly aid in curtailing needless labor and expenses required for field trials needed to assess the impact of each individual attribute. To illustrate this facility, a parametric study was performed using DYCOM to observe the effect of changing the initial sand blanket thickness. The depth of the sand column formation and

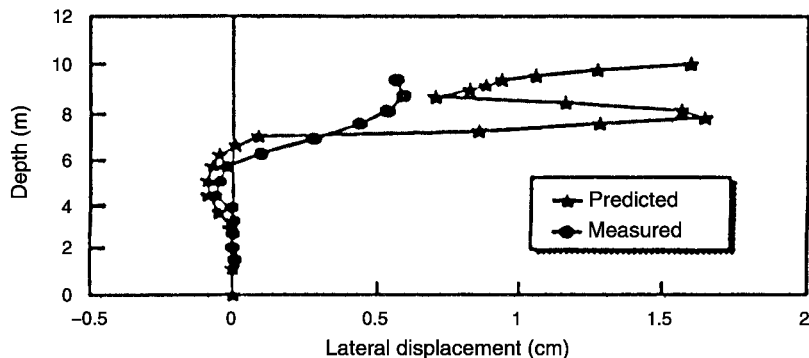


FIG. 20. Lateral Displacement of Inclinometer I/S-2 after 4th Blow

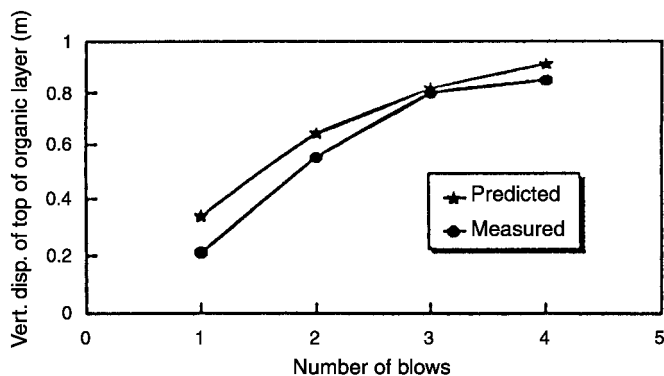


FIG. 21. Vertical Displacement of Top of Organic Layer

the lateral extent of the improvement zone can be regarded as fitting indicators of the effectiveness of dynamic replacement. Hence the parametric study was performed for the test site using three values of the initial sand layer thickness (0.91, 1.22, and 1.53 m), in order to investigate the effect of the initial sand layer thickness on the extent of the column formation and the hammer penetration. The variation of the lateral deformation at a location 1.22 m away from the impact location (I/S-1 of Fig. 9) and the hammer penetration predicted by DYCOM for the first three blows are shown in Figs. 22–25.

As one might expect, the sand column depth and the extent of the lateral influence zone increase with the decrease in the thickness of the initial sand layer thickness. However, thin sand layers create other practical problems such as excessive hammer penetration accompanied by problems of hammer recovery and irregular column formation with intermittent organic soil layers. The latter phenomenon can result from caving-in of organic soil during and after the hammer retrieval, if a significant thickness of the organic soil has been exposed

due to a single penetration. The values of hammer penetration after the first blow for each of the layer thicknesses are given in Table 1. If the organic soil layer should not be exposed after the first blow, the maximum hammer penetration must be limited to the thickness of the covering sand layer. Hence, based on the values given in Table 1, a 1.22-m-thick sand layer was selected for the field study.

#### APPLICABILITY OF STRESS-STRAIN RELATIONS

The main aims of the technique described in this paper are to predict the depth of poulder penetration, depth of compaction influence in organic soil, and the extent of sand column formation. It is apparent that, in terms of these phenomena, the more important deformation behavior is that of the organic soil, which is described adequately by the Cam-clay model. The encouraging computer predictions bear testimony to this statement.

Bishop (1966) stated that the extended von Mises criterion (on which Drucker and Prager failure surface is based) fails to predict meaningful results for cohesionless soils with  $\phi'$  larger than  $36.9^\circ$  in both extension and compression. Bishop (1966) also stated that experimental results strongly support the Mohr-Coulomb failure criterion. In the case of the sand overburden that provides the compaction blanket and refill material for sand columns, the mode of deformation that directly impacts the poulder penetration and vertical influence zone of compaction is compression. Since the triaxial compression tests conducted on the tested sand yielded  $\phi'$  values  $<36.5^\circ$  ( $34^\circ$  for blanket sand, and  $32^\circ$  for refill sand), the above limitations of the von Mises failure criterion would not have significant implications on the results of this study, especially in the initial stages of dynamic compaction. However, on repeated pounding of the sand columns, as the sand columns become saturated and begin to expand laterally, it is quite possible for the sand in the columns to approach a density that would correspond to the limiting  $\phi'$  value of  $36.5^\circ$ . Under

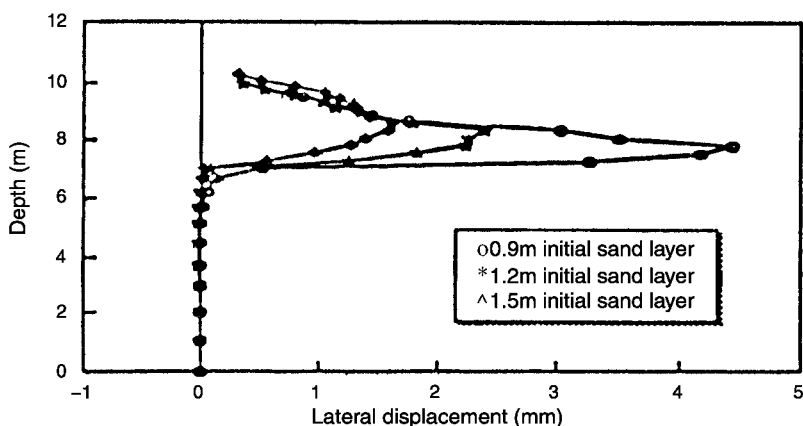


FIG. 22. Lateral Displacement at 1.2 m away from Impact Location after the First Blow

TABLE 1. Hammer Penetration after First Blow

Initial sand layer thickness (m)	Penetration of hammer after first blow (m)
(1)	(2)
0.91	0.91
1.22	0.73
1.53	0.55

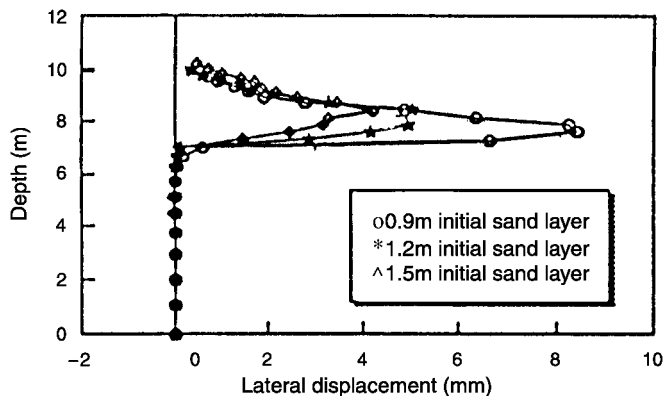


FIG. 23. Lateral Displacement at 1.2 m away from Impact Location after Second Blow

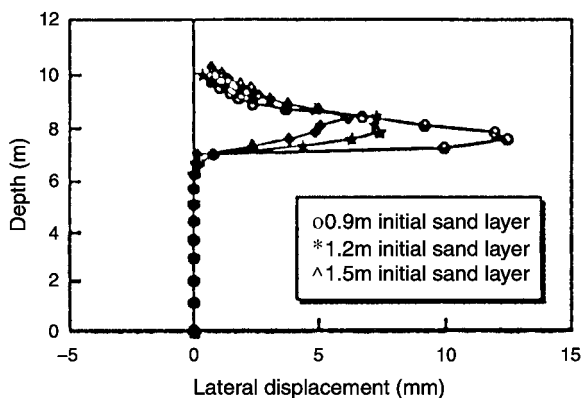


FIG. 24. Lateral Displacement at 1.2 m away from Impact Location after Third Blow

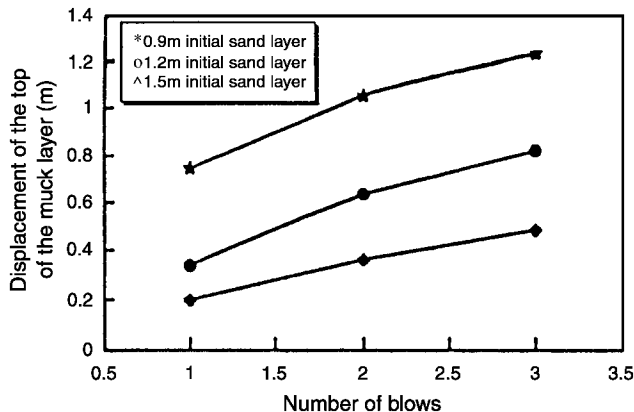


FIG. 25. Variation of Displacement of Top of Organic Layer with Sand Layer Thickness

these conditions, the rates of lateral and even the vertical progression of the sand predicted by the model could be questionable. However, this will not apply to the deformation behavior of the relatively loose refill sand.

## CONCLUSIONS

The objective of this study was to develop a finite-element model to explore the significant attributes of the ground modification technique of dynamic replacement and compare model predictions with a full-scale instrumented dynamic replacement test program. As one would anticipate, dynamic impacts produce relatively large strains during dynamic replacement, leading to excessive deformation in the vicinity of the drop hammer. Moreover, at high strain levels, soil exhibits

nonlinear characteristics making the linear elastic stress-strain relations unrealistic. Most of the currently available analytical methods used for dynamic compaction analysis assume linear stiffness and damping properties in simulating the dynamic response of the ground. In the current formulation on the other hand, two constitutive relations are used to model the two material types involved: (1) The elliptical cap model for sand; and (2) the modified Cam-clay model for organic soil. The stress is increased in a stepwise manner according to the updated Lagrangian method, and the geometrical nonlinearity is considered in the stress incremental process. Hence this analytical methodology can be considered as a significant improvement in the analysis of dynamic stabilization methods. Kinematics of both the solid phase and the pore fluid are considered separately, whereas volumetric compatibility is maintained to ensure the integrity of the two phases. In addition, the complex punching mechanism is also successfully modeled by formulating a comprehensive slideline algorithm. Laboratory drained and undrained triaxial, and isotropic consolidation tests were used to extract the material parameters for the finite-element model. Subsequently, the chosen material parameters were utilized to numerically model the pore pressure and the stress-strain behavior of separate triaxial tests in order to verify the applicability of the selected material models. The agreement between the predicted and the experimental data was reasonable. Then, the hammer acceleration, lateral deformation, and pore pressure generation in the neighborhood of the impact location measured during the test program were compared with the corresponding model predictions. Reasonably good agreement between the measured and the predicted results was observed thereby verifying the applicability of the proposed finite-element methodology for field dynamic replacement. Furthermore, the usefulness of the finite-element program in determining the optimum sand layer thickness was also demonstrated by a parametric study. Hence in field construction situations where field pilot DR studies are impractical due to highly variable site geology or when a preliminary DR viability study is needed, this analytical tool can be expediently employed to determine the optimum DR depth and spacing of the DR column grid to achieve maximum treatment benefits.

## ACKNOWLEDGMENT

Funding provided by Florida Department of Transportation is gratefully acknowledged.

## APPENDIX. REFERENCES

- Bishop, A. W. (1966). "The strength of soils as engineering materials." *Sixth Rankine Lecture, Géotechnique*, London, 16, 91–130.
- Chen, W. F., and Mizuno, E. (1990). *Nonlinear analysis in soil mechanics—Theory and implementation*, Elsevier Science Publishing Company Inc., New York.
- Chow, Y. K., Yong, D. M., Yong, K. Y., and Lee, S. L. (1992). "Dynamic compaction analysis." *J. Biotech. Engrg.*, ASCE, 118(8), 1141–1157.
- DiMaggio, F. L., and Sandler, I. S. (1971). "Material model for granular soils." *J. Engrg. Mech.*, ASCE, 97(3), 935–950.
- Fung, Y. C. (1965). *Foundations of solid mechanics*, Prentice-Hall, Englewood Cliffs, N.J.
- Hallquist, J. O. (1983). *Theoretical manual for DYNA3D*, Lawrence Livermore National Laboratory, University of California, Calif.

- Hallquist, J. O., Goudreau, G. L., and Benson, D. J. (1985). "Sliding interface with contact-impact in large scale Lagrangian computations." *J. Comp. Meth. Appl. Mech. and Engrg.*, South Africa, 51, 107–137.
- Hollingshead, G. W., and Raymond, G. P. (1971). "Field loading tests on muskeg." *Civ. Engrg. Res. Rep. 71-7*, Royal Military College of Canada, Kingston, Ontario, Canada.
- Kleiber, M. (1989). *Incremental finite element modelling in non linear solid mechanics*, Ellis Horwood Ltd., Chichester, England.
- Kruger, J. J., Guyot, C., and Morizot, J. C. (1980). "The dynamic substitution method." *Proc., Int. Conf. on Compaction*, Ecole Nationale des Ponts et Chaussées and the Laboratoire Central des Ponts et Chaussées, Editions Anciens ENPC, 339–343.
- Lo, K. W., Ooi, P. L., and Lee, S. L. (1990). "Unified approach to ground improvement by heavy tamping." *J. Geotech. Engrg. Div.*, ASCE, 116(3).
- Mei, C. C., and Fonda, M. A. (1982). "Boundary layer theory of waves in a poro-elastic sea bed." *Soil mechanics—Transient and cyclic loads*, G. N. Pande and O. C. Zienkiewicz, eds., Wiley, New York, 573.
- Menard, L., and Broise, Y. (1975). "Theoretical and practical aspects of dynamic consolidation." *Géotechnique*, London, 25(1), 3–18.
- Mullins, G., Gunaratne, M., Stinnette, P., and Thilakasiri, H. S. (1996). "Prediction of dynamic compaction pounder penetration." *Soils and Found.*, 40(5), 91–97.
- Nagger, M. H. El, and Novak, M. (1994). "Non-linear model for dynamic axial pile response." *J. Soil Mech. and Found. Div.*, ASCE, 120(2).
- Thilakasiri, H. S. (1996a). "Analytical simulation of dynamic replacement of Florida organic soil." PhD dissertation, University of South Florida, Tampa, Fla.
- Thilakasiri, H. S., Gunaratne, M., Mullins, G., Stinnette, P., and Jory, B. (1996b). "Analytical and experimental investigation of dynamic compaction induced stresses." *Int. J. Numer. and Analytical Methods in Geomech.*, 20, 753–767.
- Zienkiewicz, O. C., Humpheson, C., and Lewis, R. W. (1977). "A unified approach to soil mechanics problems (including plasticity and viscoplasticity)." *Finite element in geomechanics*, G. Gudehus, ed., Wiley, New York, 573.
- Zienkiewicz, O. C., Leung, K. H., Hinton, E., and Chang, C. T. (1982). "Liquefaction and permanent deformation under dynamic condition—numerical solution and constitutive relations." *Soil mechanics—Transient and cyclic loads*, G. N. Pande and O. C. Zienkiewicz, eds., Wiley, New York, 627.
- Zienkiewicz, O. C., and Taylor, R. L. (1988). *The finite element method*, Vol. 1, McGraw-Hill, New York.
- Zienkiewicz, O. C., and Taylor, R. L. (1991). *The finite element method*, Vol. 2, McGraw-Hill, New York.

## Pressure-Grouting Drilled Shaft Tips in Sand

Gray Mullins<sup>1</sup>, Steven D. Dapp<sup>2</sup>, and Peter Lai<sup>3</sup>

### *Abstract*

Considering the strain incompatibility between end bearing and side friction of drilled shafts, tip capacity is often discounted from total shaft capacity. This is due to the relatively large displacements required to mobilize the tip which often exceed service load displacement criteria. Additionally, concerns regarding shaft tip soil disturbance (i.e. insitu stress relief) and toe cleanliness further discourage designers from using end bearing as available capacity. As a method of mitigating these conditions, pressure-grouting the shaft tip after its construction has been successfully employed throughout the world. With very few exceptions, the benefits of tip-grouting have been disregarded in the United States. Sources of skepticism arise from the uncertainty of the grout formation beneath the tip and the lack of rational design procedures for its use. In cooperation with the Florida Department of Transportation, the University of South Florida is researching the effects of post-grouting on shaft capacity in loose to medium dense sands. This paper presents a review of past and present base-grouting methods used throughout the world and the scope of on-going full-scale load test programs.

### *Introduction*

The use of drilled shafts as structural support has recently increased due to heightened lateral strength requirements for bridge foundations and the ability of drilled shafts to resist such loads. They are particularly advantageous where enormous lateral loads from extreme event limit states govern bridge foundation design (i.e. vessel impact

---

<sup>1</sup>Assistant Professor, Department of Civil and Environmental Engineering, University of South Florida, Tampa, FL 33620

<sup>2</sup>Graduate Researcher, University of South Florida, Tampa, FL 33620

<sup>3</sup>State Geotechnical Engineer, Florida Department of Transportation, Tallahassee, FL



loads). Additional applications include high mast lighting, cantilevered signs, and most recently, cellular phone and communication towers. With respect to bridge construction, design procedures, both axial and lateral, have been additionally impacted where increased unsupported pile lengths are mandated by scour depth predictions based on 100 year storm events. This dramatically changes driven pile construction where piles cannot be driven deep enough without overstressing the concrete or without pre-drilling dense surficial layers. In contrast, drilled shaft construction is relatively unaffected by scour depth requirements and the tremendous lateral stiffness has won the appeal of many designers. However, drilled shaft design and construction is plagued with quality control issues (e.g. shaft bottom cleanliness or open excavation time) not experienced during pile driving.

Typically, designers have chosen to significantly reduce end bearing capacity or even discount it altogether to account for soft toe conditions. Even in ideal conditions, full end bearing is typically not mobilized before service load displacement criteria are exceeded. The bulk of the capacity is therefore derived from side friction which can be developed with relatively small displacements. This is especially problematic for larger shafts which must displace even further to fully develop tip capacity in loose to medium dense cohesionless soils where unit side friction values are comparably low with respect to competing foundation systems. Consequently, the end bearing strength component, which may be on the order of up to twenty times the unit side friction, is unavailable to the useful capacity of the shaft (AASHTO, 1997). In an effort to mitigate shaft toe cleanliness and also balance the useful capacity between end bearing and side friction, projects throughout the world have implemented pressure grouted shaft tips after normal shaft construction (sometimes termed "post-grouting"). An overview of pressure grouting considerations will be presented herein as well as efforts underway to develop recommendations for its use by the Florida Department of Transportation (FDOT).

### *Background*

In the early 1960's, efforts began to obtain more usable tip capacity of drilled shafts using pressure grouting below the shaft tip. In 1975, Gouvenot and Gabiax presented results of a test program where post-grouting large diameter piles led to increased ultimate load capacities up to three times in sands and clays. As a result, post-grouting techniques have become a routine construction process in many parts of the world (Bruce, 1986). The post-grouting process entails: (1) installation of grout pipes during conventional cage preparation that run to the bottom of the shaft reinforcement cage, and (2) after the concrete in the shaft has cured, injection of high pressure grout beneath the tip of the shaft which both densifies the insitu soil and compresses any debris left by the drilling process. By essentially preloading the soil beneath the tip, end bearing capacities can be realized within the service displacement limits.

Although the performance of a drilled shaft is bounded by the maximum contribution of end bearing and skin friction components, these values are not fully realized due to flaws introduced by full scale construction techniques. Three

mechanisms, or combinations thereof, are responsible for the excessively large shaft displacements required to develop bearing capacity:

- Strain incompatibilities typically exist between the end-bearing and side friction components in relation to service displacement criteria. The ultimate side frictional component develops with relatively small shaft displacements compared to the displacements required to mobilize ultimate end bearing. Development of the side friction component can be 50% of ultimate at displacements of approximately 0.2% of the shaft diameter ( $D$ ) (AASHTO, 1997), and fully developed in the range of 0.5 to 1.0 %  $D$  (Bruce, 1986). In contrast, mobilization of the end bearing component can be 50% mobilized at 2.0%  $D$  (AASHTO, 1997), and fully mobilized in the range of 10 to 15 %  $D$  (Bruce, 1986). The end bearing component therefore requires 10 to 30 times more shaft displacement in order to mobilize the same percentage of its ultimate value as the side shear component. This means that the side friction is strained beyond its ultimate strength and into a residual state by the time the end bearing capacity is realized. In addition, the service load deflection criteria is often exceeded long before any significant amount of end bearing can be developed.
- The pile toe zone is often disturbed by normal construction procedures. This disturbance can occur by soil stress relaxation due to excavation of the overburden, inflow of groundwater due to insufficient hydrostatic head or rapid removal of the excavation tool during the construction process. This soil disturbance of the pile toe zone by normal construction procedures is often difficult or nearly impossible to eliminate. Displacements necessary to overcome this disturbance and mobilize end bearing are usually in excess of allowable service limits. In instances of less competent soil, this problem is further compounded.
- Construction methods and processes may leave soft debris/deposits at the bottom of the excavation. Primary contributing factors are: overall shaft bottom cleanliness, a non-uniform distribution of toe debris causing an initially reduced shaft area bearing on the soil, excessive sand content in the drilling fluid, prolonged time for cage and concrete placement, and deposits of drilling fluid itself at the bottom. These construction related factors may then also be the cause of excessive deflections required to mobilize end bearing due to toe inclusions not evident in an otherwise clean excavation.

Depending on soil type and drilling method, any or all of the above mechanisms may occur at a given excavation. However, each scenario can be mitigated by a procedure, relatively unused in the United States, where post-grouting is performed beneath the shaft tips. This grouting concept accommodates the trend towards large diameter drilled shafts due to lateral load considerations, while allowing for the end bearing component to contribute to the useful capacity of the shaft.

### *Soil Type Applicability*

End bearing strata may be grouped into three broad categories in relation to the

process of post-grouting pile tips. These categories are cohesionless soils (sands to silts), cohesive soils (clays), and soft or fractured rock formations. Although all soils can be improved to some degree by grouting techniques, the applicability and effectiveness of grouting, primarily compaction grouting, is many times more effective in cohesionless soils than other soil types (Baker and Broadrick, 1997). Historically, nearly all of the studies and construction projects involving grouting of the pile tips to increase end bearing have been in cohesionless soils.

*Sand and Silt.* The first effective large scale grouting of pile tips was performed in sandy soils in 1961 at the Maracaibo Bridge (Sliwinski, 1984). Since then many studies and construction projects have proven the extreme benefits of post-grouting the pile tips in cohesionless soils (Piccione in Cairo, 1984; Sliwinski and Fleming, 1984; Logie in Jakarta, 1984; Stocker in Jedda-Mecca Expressway, 1983; and Bauer in Brooklyn, NY, 1988). In general, results have shown that post-grouting the pile tips in cohesionless soils has significantly increased end bearing capacities. Figures 1, 2 and 3 show the effectiveness of post-grouted shafts.

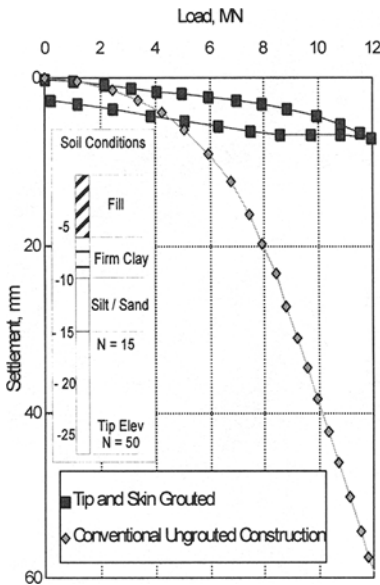


Figure 1. Comparison of two 1.5m diameter drilled shafts (Sliwinski, et al., 1984).

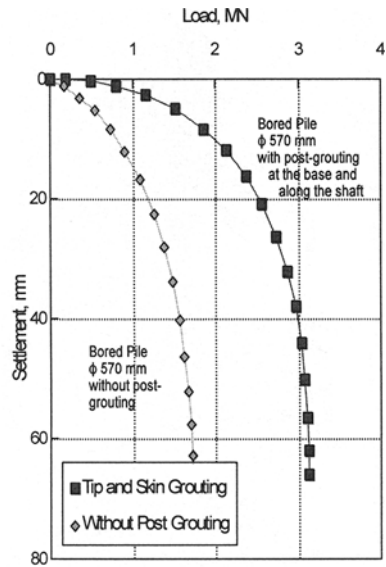


Figure 2. Load-displacement of 570 mm bored piles (Stocker, 1983).

Loose to medium dense sands hold the highest potential for increase in useable shaft end bearing. This is due to this soil profile being the most susceptible to the three mechanisms contributing to lack of pile end bearing as outlined in the previous section.

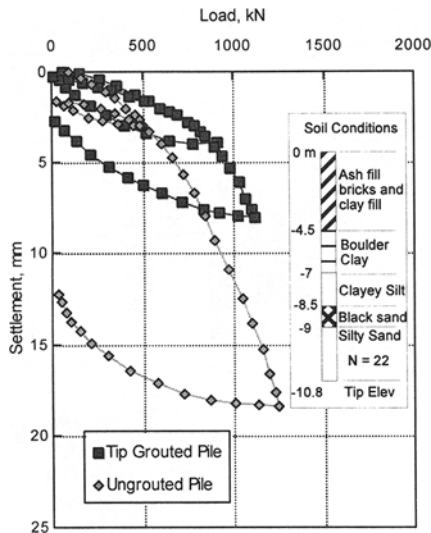


Figure 3. Results from 450 mm shaft load tests (Sliwinski, et al., 1984).

Two different grouting methods, permeation grouting and compaction grouting, are applicable to these soils. The permeation grouting can easily create a very large grout bulb, and compaction grouting can dramatically improve the soil stiffness. Both processes can be done with the use of ordinary cementitious grout.

Dense sands can be both permeation and compaction grouted with cementitious grout in the same manner as loose sands. However, a micro-fine cement may become necessary for permeation grouting, and may not yield significant improvement over compaction grouting alone. The grout volume used in dense sands would be significantly less. Bruce (1986) reviewed many cases to state that there is a direct relationship between ultimate load increase and volume of cement grout injected for all sands; when grouting dense sands the grout volume simply corresponded to the void volume of the gravel pack (discussed later, Figure 8).

Sandy silts can be densified by means of applying effective stresses during compaction grouting with ordinary cementitious grouts, although it is less effective than compaction grouting of clean sands. Permeation grouting in silty soil, however, would involve the use of chemical grouts, such as a silica gel, and is beyond the scope of this paper.

Although disturbance to the shaft toe area during construction is of little practical importance in soft rocks and clays (Sliwinski and Philpot, 1980), Sliwinski and Fleming (1984) concluded that in sands the end bearing contribution to the total load capacity is

extremely sensitive to construction induced soil disturbances. Therein, full scale load testing was used to verify the effectiveness of pressure grouting for mitigating these conditions.

*Clay.* Post-grouting in clay produces only a minimal gain in end bearing governed by the amount of consolidation that can occur within the set time of the grout. The high pressures introduced by this method may only result in hydrofracture of the soil matrix. Careful consideration would be needed so that the allowable end bearing contribution, even after grouting, would not exceed the creep limit of the clay at the grout bulb/soil interface. The most effective way of grouting in clay material would be to jet-grout, or deep-soil-mix under the shaft tip. While these are certainly viable options for remediating deep foundations in this soil type, it is not the focus of this paper.

*Rock.* Grouting of fractured and soft rock formations with low strength grout in order to fill voids, fractures, seams, and solution channels is sometimes conducted to alleviate drilling problems associated with karst topography. However, this is usually accomplished prior to drilling, and is not the grouting technique that is discussed herein. These formations typically are incapable of consolidation or densification by effective stresses induced by compaction grouting. Further, permeation grouting of the macro inclusions is effectively accomplished by the concrete head during normal construction, as is evidenced by high concrete over-runs in such cavernous strata.

Although grouting can effectively mitigate soft toe conditions caused by excessive construction debris/deposits at an excavation bottom for all soils, current quality control procedures for drilled shaft production already effectively address shaft bottom cleanliness for clay and rock during normal construction. Thus, only a marginal benefit would be realized in these conditions through the use of post-grouting. An exception may be where shaft bottom cleanliness is problematic due to extreme depths and time requirements such as the My Thuan Bridge Project, Vietnam (Dapp, 1998) or for cases where the capacity of shafts already constructed fall short of adequate (Logie, 1984).

Post-grouting can be effective in all soil types; however, research shows the greatest performance gain in cohesionless soils. As such, an ongoing study at the University of South Florida, Tampa is concentrating on the effectiveness of post-grouting in cohesionless soils (both sands and silt) with an emphasis on identifying the most effective grouting techniques. Effectiveness is evaluated by: (1) the final strain compatibility of the tip and skin friction components, (2) constructability, and (3) overall capacity gain.

### *Uplift Considerations*

In general, upward movement of shafts during compaction grouting should be limited such that the frictional strength of the shaft is not developed beyond its ultimate value and into a lesser residual value. This is most critical in dense sand where there is

a pronounced loss of frictional resistance with large strains (Figure 4). Historically, uplift criteria have been limited to ranges from 2 mm (Stoker, 1983) to 20 mm (Bolognesi and Moretto 1973). Presently, in Taipei, a 3mm uplift criterion is in effect (Mullins, 1999). It is unclear, however, if these criteria were placed only on top-of-shaft movement or if the tip movement associated with elastic compression was also given a maximum permissible movement. Long shafts such as those in Taipei (80 m) can exhibit relatively large displacements at the tip without being detected at the top (and vice versa).

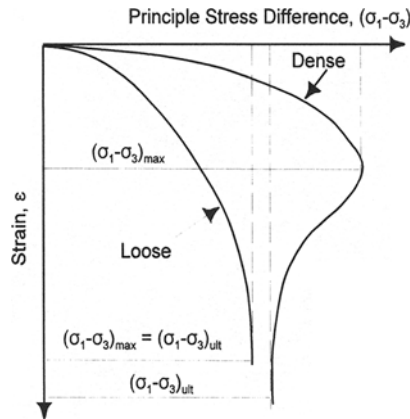


Figure 4. Stress / strain curves for typical loose and dense sands (Holtz and Kovacs, 1981).

Essentially, the maximum amount of end bearing improvement is dependent on how much downward resistance the side friction component of the shaft can provide. As such, post-grouting can also be applied to the sides of the shaft to improve unit side friction values. This aids in providing downward restraint during the tip-grouting process (resisting uplift). This is of particular importance for shorter shafts, and as a consequence skin grouting has been employed to aid in providing reaction (e.g. Bauer system of pile grouting). Additional criteria of maximum grout volume (per stage) and minimum grout pressure are established based on reasonable cavity expansion and the anticipated tip performance, respectively. Figure 5 shows grout pressures that have been used on various sites throughout the world in relation to the shaft tip depth.

### *Grouting Types*

Standard grouting techniques can be divided into two basic categories: permeation grouting and compaction grouting. Staged grouting procedures are often designed which have a combination of these two, first permeation and then compaction. There are also state-of-the-art techniques available for cohesive soils, such as jet grouting or deep soil mixing, which alter the soil type and structure without inducing significant effective stresses.

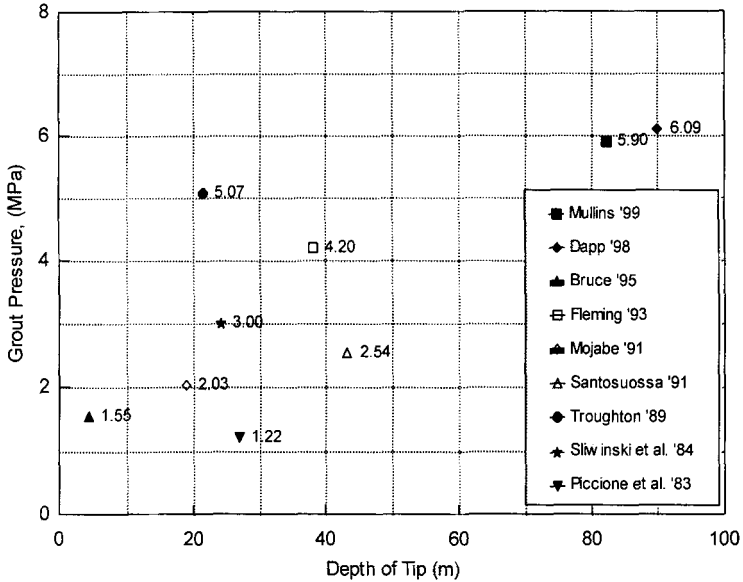


Figure 5. Tip grouting pressures used at various sites worldwide.

*Permeation Grouting.* Permeation grouting uses a fluid grout which is highly mobile within the soil formation, and therefore travels through the void spaces without providing any significant compaction or densification of the surrounding soils. In this manner a very large zone of improved soil below the pile tip is developed. Careful adjustment of the water-to-cement ratio is used to control the mobility of the grout. The type of grout mix design is also crucial to achieve this mobility. For example Littlejohn (1983), at the Jeddah - Corniche Centre, first tried remediating substandard piles with the use of a cement grout in a dense sand profile interbedded with hard sandy silt. However, grout takes were very low, and the remediation technique failed. Subsequently, a low viscosity resorcinol formaldehyde grout was successfully used.

*Compaction Grouting.* In contrast to permeation grouting, compaction grouting utilizes a thick, viscous, homogeneous, typically cementitious mass designed to remain together within the soil matrix. Generally there is a distinct interface between the soil and grout material, thus the insitu soil is consolidated and densified by cavity expansion of the grout bulb (Baker and Broderick, 1997). A typical compaction grouting mix design is shown in Table 1. However, this mix is recommended for minimum grout pipe diameters of 100mm.



Table 1. Typical Compaction Grout Mix (Baker and Broderick, 1997)

Description	Quantity	Standard	Comment/Effect
Sand	800-1000 kg	ASTM C-33	Well graded, rounded edge, min. 15% passing 0.075 mm sieve
Cement	110-225 kg	ASTM C-150	Control strength of mix, increase density of mix
Flyash *	90-310 kg	ASTM C-618	Improve pumpability, increase density, reduce cement content required for mix, Class F or Class C
Water	60-160 L		Control slump
Admixtures (optional)	1%-2% of cement		Control set time, control shrinkage

\* Depending on the fines available from the sand.

Compaction grouting develops its own "filter cake" at the soil/grout interface which differs from the Bauer system of grouting where a mechanical grouting system uses steel plates and an impermeable cover or a liner embedded between the plates (discussed later). In either case, the mechanism of soil improvement is the same; the grout applies an effective stress to the soil, thus densifying it. A notable difference is that the simple compaction grouting (i.e., with a filter cake) is a uniform stress case at the pile tip, whereas the mechanical compaction system of steel plates provides a uniform strain condition. A potential benefit of compaction grouting the shaft tip is that this procedure could provide a means of proof testing shaft tip capacity during the compaction grouting procedure.

Presently, a testing program is underway to quantify the effectiveness of pile tip grouting to improve end bearing in loose to medium dense sand. Therein, simple compaction grouting will be compared to compaction grouting with a mechanical compaction cell, and a combination of permeation and compaction grouting.

### *Injection Techniques*

Grouting techniques vary in the mechanism by which the grout is dispensed beneath the shaft tip. Variations include whether to use:

- stem, orifice, tube-a-manchette, or mechanical distribution system
- a gravel pack beneath the tip to aide in distribution of grout
- fixed or floating distribution system
- permeation, compaction, or a staged combination.

Two basic distribution systems are mainly used: (1) *simple compaction grouting* in which

the tube-a-manchette system employs a network of exposed grout tips, and (2) the *mechanical grouting system* in which the Bauer-type system of one or two steel plates with an impermeable membrane is used. Although both systems can be used in a wide variety of soils, the membrane-type mechanisms minimize hydro-fracture grout losses more common with tube-a-manchettes used in weakly layered soils.

The tube-a-manchette has several variations, but is primarily a simple pipe network across the bottom of the shaft pre-drilled along its length on the bottom face and connected to grout tubes to the top of shaft. The pipes are wrapped in a rubber membrane at the location of the holes to prevent blockage of grout passage during normal shaft construction where the tubes become completely encased in concrete. A problem with fixed tube-a-manchette systems is that the grouting must be accomplished immediately after the concrete has set (24 to 48 hours), while its strength is still low enough to burst the encapsulation. A simple tube-a-manchette system fixed to the cage and resting on the bottom of the excavation was used in the shafts supporting a major cable stay bridge in Thailand in 1985, as shown in Figure 6. A similar configuration has recently been used for the foundations supporting the cable-stay bridge over the Mekong River in Vietnam (Dapp, 1998). Presently, at the Taipei Financial Center project in Taiwan, an adaptation is being employed that closely contours the pipe network to the shaft bottom (Figure 7). The shape resembles the reverse circulation cutting tool and minimizes the concrete cover between the grout pipes and the shaft bottom.

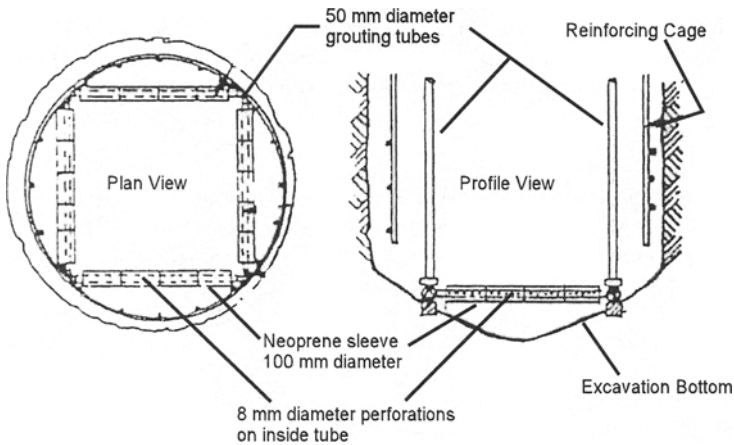


Figure 6. Simple tube-a-manchette compaction grout apparatus (after Bruce, 1986).

Complications can arise if the excavation depth is lower than the tube-a-manchette elevation. In such instances, the grout pressure is unable to break the

encapsulation and modify the soil. Such was the case when the first 90 m deep excavation in Vietnam was inadvertently over-excavated by 0.5m by way of extensive clean out procedures. This caused the tube-a-manchette to be embedded in an extra 0.5m of concrete. To avoid this problem, floating tube-a-manchettes were used for subsequent shafts which used slip joints allowing the distribution system to adjust to the actual bottom of excavation elevation. Other systems have used flexible grout hoses to overcome this problem. It is thus recommended that suspending the tube-a-manchette, by either method, should be considered necessary for proper steel placement of extremely long shafts where cage length and excavation depths may not be consistent.

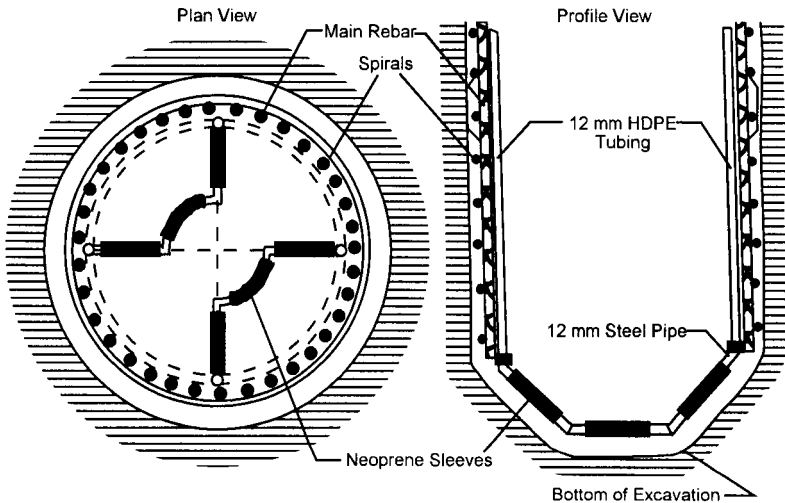


Figure 7. Tube-a-manchette system used in Taipei, Taiwan (Mullins, 1999).

Sliwinski and Fleming (1984) described first placing a gravel plug in the excavation, then the tube-a-manchette with a steel plate above (both suspended from the cage). This configuration is shown in Figure 8. The steel plate has the benefits of isolating the tube-a-manchette and gravel plug from the concrete so that the post-grouting process can take place after the concrete has gained design strength, the tube-a-manchette is protected from the tremie during concreting operations, and the steel plate gravel interface provides a consistent bearing surface for the compaction grouting pressure to act against (important for proof testing aspects). The gravel is beneficial for both permeation and compaction grouting by exposing more soil interface to the grout, as well as providing aggregate to knit the soil bulb together directly below the shaft tip.

Lizzi (1981) discussed a mechanism consisting of two steel plates separated by mechanical spacers (to allow grout pressure to initially act upon the full face of the

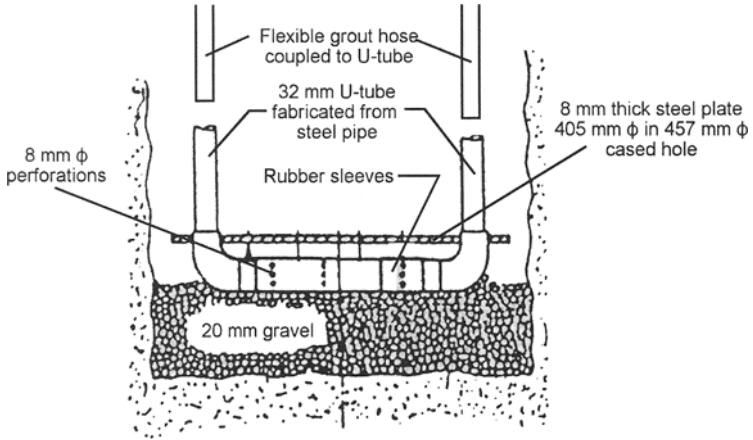


Figure 8. U-shaped grouting cell positioned at bottom of excavation (after Sliwinski and Fleming, 1984).

plates). This technique is similar to the Bauer system of tip grouting used on the Jeddah-Mecca Expressway (Bruce, 1983) and the Brooklyn Queen's Expressway (1988). The

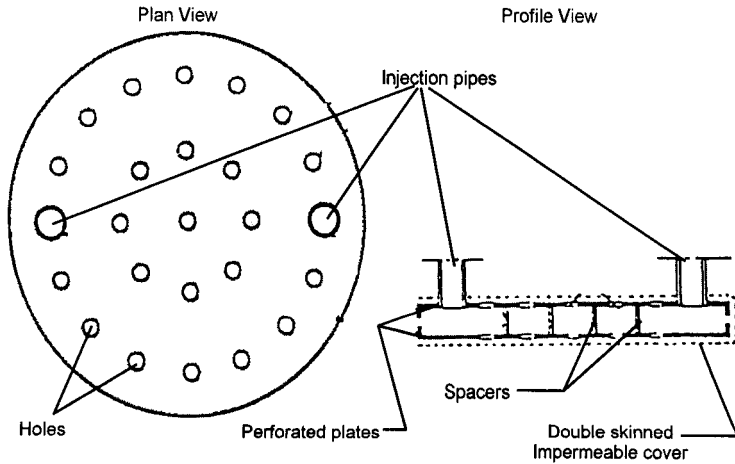


Figure 9. Mechanical compaction grout apparatus (from Lizzi, 1981)

difference is that Lizzi had the plates covered with an impermeable liner to ensure that separation of grout injection ports and concrete was maintained (see Figure 9). The impermeable liner ensured that no permeation into the surrounding soil occurred. Consideration can also be given as to whether a gravel pack should be included between the two plates, as was discussed in the early work by Bolognesi and Moretto in Paranah River (1973), shown in Figure 10. The benefit of the gravel pack again is as stated

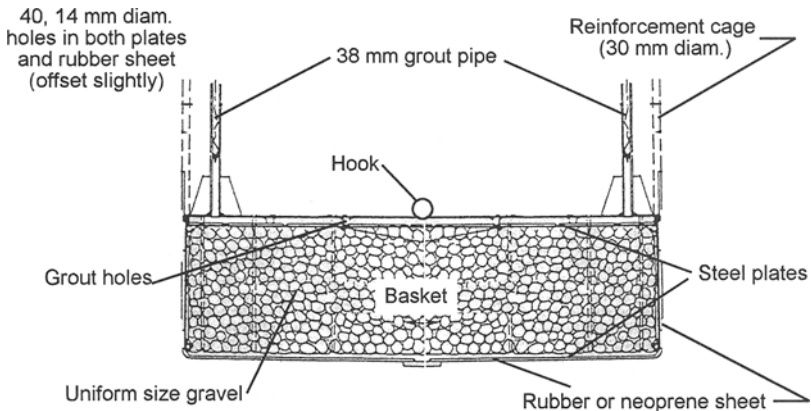


Figure 10. Gravel pack between two steel plates (after Bolognesi and Moretto, 1973).

above; however, this configuration must be suspended from, and lowered into the excavation with the cage which could become extremely cumbersome in a production-oriented setting.

#### *Scope of Testing and Research*

To investigate the various mechanisms of post-grouting and evaluate their effects on shaft performance, the University of South Florida, Tampa is presently conducting concurrent laboratory and full-scale testing on post-grouted drilled shafts. The laboratory component is looking at parameters such as: grout bulb formation, strength gains, grout mechanisms, and residual stress states after grouting; whereas the field component is addressing issues such as constructability, applicable mechanisms, mechanism durability, maintaining production, as well as strength gain and design recommendations.

The laboratory testing is being conducted using a relatively new device called a Frustum Confining Vessel (FCV) which provides a method of physically modeling pile-type insitu stresses on small-scale piles without the use of a centrifuge. The device, developed by Birmingham Foundation Equipment in conjunction with McMaster University (Sedran, 1999), is a conical-shaped steel vessel in which sands are placed and

stressed as shown in Figure 11. The resulting vertical and horizontal stress distributions are reasonably similar to those of full-scale prototype piles. In the control volume portion of the FCV stresses are distributed similar to those encountered in the field. Some significant advantages of the FCV with respect to other physical modeling methods are the simplicity of testing, relatively low cost, and its ability to model relatively large model piles (e.g. 1 m long, 100 mm diameter).

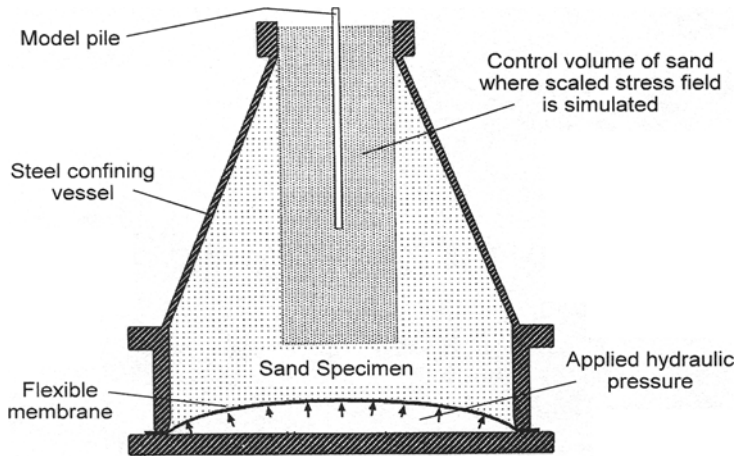


Figure 11. Frustum Confining Vessel used for physical modeling of pile load tests (after Sedran, 1999).

Specifically, post-grouting model piles/shafts requires overburden pressures that provide adequate reaction to pre-load the soil beneath the tip. Furthermore, the effects of scaling the size of the shaft will require additional foundation mass to restrain the upward movement of the shaft. Although scaling parameters require close attention to conduct meaningful load testing, the initial goal is merely to show the formation of the grout bulb at various relative densities for the sand. Subsequent load testing of post-grouted model shafts in the FCV is an added benefit that will afford interesting results.

The performance of post-grouted shafts is largely dependant on the strain compatibility of the tip and skin resistance. Additionally, for post-grouting to be fully beneficial, the soil must be returned to an unstressed state at the completion of the grouting process to remove locked-in stresses from negative skin friction. The benefit from post-grouting is therefore derived from the improved stiffness associated with reloading. The effects of residual stress are being investigated by maintaining various grout pressures during the curing of the grout and then testing the capacity of these model shafts. Instrumentation is included within the model shafts to confirm the state of stress locked into the soil.

The full scale portion of the program presently involves two sites where drilled shafts are being installed with post-grouting mechanisms. The first site has eight relatively short shafts, 5 meters long, installed in loose to medium dense silty sand that will be used to investigate both the effects of tip grouting as well as skin grouting. Four shafts will be installed with only tip grout mechanisms (similar to those in Figures 6, 8, and 9), two with tip and skin grouting, and two with no grouting systems as a controls. Figure 12 shows three variations of grouting mechanisms currently in use at the University of South Florida test site.

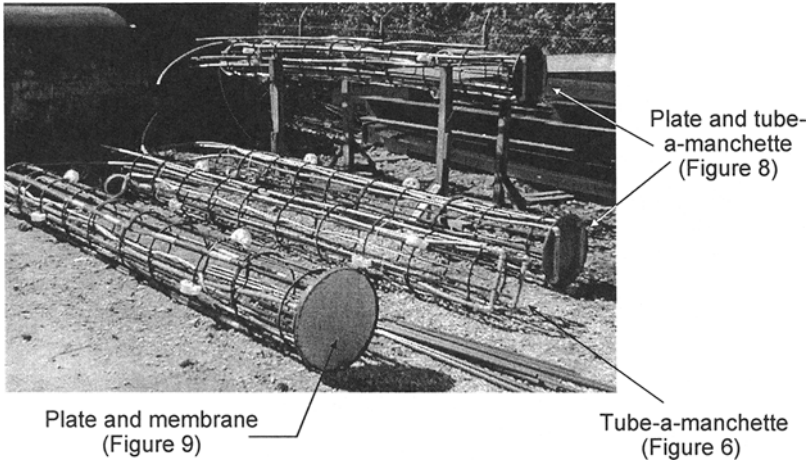


Figure 12. Post grouting mechanism used at the first site.

The second site has three proposed test shafts in sand and limestone involving five 30MN load tests. Due to the variable nature of the site, post-grouting has been selected for shafts tipped in sand to reduce their length. Two of the shafts will be tested prior to post-grouting and then subsequently after post-grouting for direct comparison. The third shaft will only be tested without grout effects. The tip grout mechanism will be selected based on the performance evaluation of the previous site. All shafts from both sites will be fully strain instrumented and continuously monitored to determine the distribution of load and the presence of residual stresses throughout the load test/post-grout/load test procedures.

### Summary

Pressure grouting drilled shaft tips (post-grouting) has been successfully employed throughout the world for over thirty years with surprisingly little use within the



United States. Recently, the FDOT has contracted research to investigate the parameters affecting its performance and to develop recommendations and guidelines for its use on Florida roadway projects. The method provides a means by which to mitigate many of the factors that presently exclude the contribution of the end bearing from the useful shaft capacity (e.g. toe cleanliness). Presently, researchers at the University of South Florida are examining many of the considerations designers will need to address for its eventual use. By including significant end bearing contributions into the useful capacity, the design of drilled shafts can be drastically improved. Moreover, this inexpensive procedure could directly provide test results for every shaft installed.

### *References*

AASHTO, LRFD Bridge Design Specifications, SI (1<sup>st</sup> Edition), American Association of State Highway and Transportation Officials, Washington, D.C., 1994, w/1996 and 1997 interim revisions.

Baker, A.C. and Broadrick, R.L., (1997), "Compaction Grouting, a twenty year update and a vision for the 21<sup>st</sup> century," Proceedings *Florida/South Florida Section Annual Meeting*, Clearwater, FL, September.

Bauer in Brooklyn Queen's Expressway, NY (1988) Bauer inner office Tech Note.

Bolognesi, A. J. L. and Moretto, O. (1973) "Stage Grouting Preloading of Large Piles on Sand" Proceedings of 8<sup>th</sup> ICSMFE, Moscow.

Bruce, D.A. (1986), "Enhancing the performance of large diameter piles by grouting," Parts 1 and 2, *Ground Engineering*, May and July, respectively.

Bruce, D. A., Nufer, P. J., and Triplett, R. E. (1995) "Enhancement of Caisson Capacity by Micro-Fine Cement Grouting - a Recent Case History" ASCE Special Publication 57, Verification of Geotechnical Grouting.

Dapp, S.D. (1998) "Interviews with engineers during load testing on the My Thuan Bridge" Mekong Delta, Vietnam."

Dhir, V. K., (1984) "Grouting to save money," *Gulf Construction*, July.

Flemming, W. G. K. (1993) "The Improvement of Pile Performance by Base Grouting" Proceedings of the Institution of Civil Engineers, London.

Gouvenot, D. and Gabiax, F. D. (1975), "A new foundation technique using piles sealed by concrete under high pressure," Proceedings, *Seventh Annual Offshore Technical Conference*.

Holtz, R. D., and Kovacs, W. D. (1981), "An Introduction to Geotechnical Engineering," Prentice Hall, New Jersey.

Littlejohn, G. S., Ingle, J., Dadasbilge, K. (1983) "Improvement in Base Resistance of Large Diameter Piles Founded in Silty Sand" Proceedings, *Eighth European Conference on Soil Mechanics and Foundation Engineering*, Helsinki, May.

Lizzi, F., Viggiani, C., Vinale, F. (1983) "Some Experience with Pre-Loading Cells at the Base of Large Diameter Bored Piles" Proceedings of the 7<sup>th</sup> Asian Regional Conference on Soil Mechanics and Foundation Engineering, Haifa, Israel

Logie, C. V. (1984) "Drilled Pier Foundation Rehabilitation Using Cement Grouting" ACI Publication SP-83, Innovative Cement Grouting.

Mojabe, M.S., and Duffin, M. J. (1991) "Large Diameter, Rock Socket, Base Grouted Piles in Bristol" Proceedings of the 4<sup>th</sup> International Conference on Piling and Deep Foundations, Stresa, Italy, April

Mullins, A. G. (1999) "Interviews with engineers during load testing on the Taipei Financial Center" Taipei, Taiwan.

Piccione, M., Carletti, G., and Diamanti, L. (1984) "the Piled Foundations of the Al Gazira Hotel in Cairo" Proceedings of the International Conference on Advances in Piling and Ground Treatment for Foundations, Institution of Civil Engineers, London, UK.

Santosuossa, M., Rizzi, G., Diamanti, L. (1991) "Construction of Pile Foundation of the Postal Cittadel in the Direction Center of Naples" Proceedings of the 4<sup>th</sup> International Conference on Piling and Deep Foundations, Stresa, Italy, April

Sedran, G. (1999) "Experimental and Analytical Study of a Frustum Confining Vessel," Doctoral Dissertation, McMaster University, Hamilton, ON, September.

Sliwinski, Z. J., and Philpot, T. A. (1980) "Conditions for Effective End Bearing of bored Cast in Situ Piles" Proceedings of Recent Developments in the Design and Construction of Piles, Institute of Civil Engineers, London, UK

Sliwinski, Z. J., and Flemming, W. G. K. (1984) "the Integrity and Performance of Bored Piles" Proceedings of the International Conference on Advances in Piling and Ground Treatment for Foundations, Institution of Civil Engineers, London, UK.

Stocker, M.F. (1983), "The influence of post grouting on the load bearing capacity of bored piles," Proceedings, *Eighth European Conference on Soil Mechanics and Foundation Engineering*, Helsinki, May.

Troughton, V. M. and Platis, A. (1989) "The Effects of Changes in Effective Stress on a Base Grouted Pile in Sand" Proceedings of the International Conference on Piling and Deep Foundations, London, UK, May.

## PREDICTION OF DYNAMIC COMPACTION POUNDER PENETRATION

GRAY MULLINS<sup>i)</sup>, MANJRIKER GUNARATNE<sup>i)</sup>, PAMELA STINETTE<sup>ii)</sup>  
and SAMAN THILAKASIRI<sup>iii)</sup>

## ABSTRACT

A semi-empirical computational technique is presented for predicting the depth of craters formed by dynamic compaction (DC) pounders after the first impact. This technique utilizes a correlation developed between the initial shear strength of the soil beneath the pounder, determined by a CPT profile, and the impact energy per unit area (*specific impact energy*). First, the correlation is established by a series of model impact tests involving different drop heights, drop weights and impact areas. Then, the correlation is verified by the results from a full-scale field test performed by the authors. Further, data from a DC project performed elsewhere is also shown to support the predictive technique. An illustrative example is provided to demonstrate how typical CPT data can be adapted to predict the crater depths during DC projects for a given level of applied impact energy. On the other hand, this method can be used to determine the maximum impact energy that can be applied without causing excessive *initial* penetration of pounders and thus preclude the need for trial impacts. Hence well in advance of heavy equipment mobilization, this technique can certainly aid in effective planning of DC projects on particularly weak ground where penetration predominates heave.

**Key words:** CPT, crater, dynamic compaction, dynamic replacement, organic soil, pounder, specific impact energy (IGC: K3/K5)

## INTRODUCTION

Dynamic Compaction (DC) is a ground modification technique used to densify loose soil deposits as deep as 10 meters below the surface. The DC process entails dropping a large weight or pounder onto the ground to be compacted. Although dynamic compaction is reported to be effective both above and below the ground water table, certain construction difficulties arise if the water table is not maintained at least 2 m below the ground surface. This is achieved by dewatering or raising the grade (Lukas, 1986). Raising the grade by the addition of a sand layer can aid the ensuing construction by providing a working mat. Moreover, when unusually soft soils are to be modified, the sand furnishes a replacement material that is driven into the underlying soft layer. The latter process, Dynamic Replacement (DR), has been shown effective in stabilizing weak compressible soils that have poor consolidation properties (Ramaswamy et al., 1979; Lo et al., 1990; Chow et al., 1992; Mullins, 1996).

During DC or DR, the first penetration of the pounder is an uncertain parameter that can cause considerable construction difficulties especially in the case of softer soils. A pounder that penetrates too deeply can develop such high suction forces during withdrawal that it cannot be recovered without additional equipment. To prevent

this, the common practice is to limit the crater depth to "the height of the pounder plus a few feet" (Lukas, 1986). Because of the uncertainties involved Lukas (1986) states that it is not possible to predict precisely the crater depth, prior to impact and suggests that the information obtained during the first pass be used as a guide to establish a criterion for subsequent passes. However, this exercise involves mobilization of heavy equipment and thus it cannot be utilized for preliminary project surveys.

Typically, the energy application for the first impact on soft soils is governed by experience or general guidelines formulated on the basis of the drop energy (WH). As an example, the National University of Singapore's experience suggests limiting the first impact drop energy to 150 tonne-meter (Chow, 1995). It is evident therefore, that accurate predictions of the crater depths are useful for efficient implementation of DC or DR processes. Chow et al. (1992) proposed a model to predict the penetration depth based on the one-dimensional wave equation. However, since its application involves determining a number of soil parameters from additional laboratory tests, its field applications may be limited. The new method presented herein predicts crater depths on the basis of impact energy per unit contact area and the soil strength obtained from the routinely conducted Cone Penetration Tests. The new technique has been de-

<sup>i)</sup> Department of Civil and Environmental Engineering, University of South Florida, Tampa, FL 33620, USA.

<sup>ii)</sup> Hillsborough Community College, Plant City, FL 33620, USA.

<sup>iii)</sup> Department of Civil Engineering, University of Moratuwa, Moratuwa, Sri Lanka.

Manuscript was received for review on January 28, 1999.

Written discussions on this paper should be submitted before May 1, 2001 to the Japanese Geotechnical Society, Sugayama Bldg. 4F, Kanda Awaji-cho 2-23, Chiyoda-ku, Tokyo 101-0063, Japan. Upon request the closing date may be extended one month.

veloped based on laboratory impact tests and validated by full-scale field studies.

### EFFECT OF SPECIFIC IMPACT ENERGY

The effect of the impact area of a pounder has not been adequately addressed in the literature when considering the depth of improvement. Despite Lukas' (1986) realization that contact pressure ( $W/A$ ) must affect the depth of improvement, the following relationship presented by Menard et al. (1975) is used most commonly:

$$D = n\sqrt{WH} \quad (1)$$

where:  $D$ =depth of improvement, m  
 $W$ =weight of pounder, tonnes  
 $H$ =drop height, m  
 $n$ =an empirical coefficient (less than 1)

The empirical coefficient,  $n$ , accounts for variability in soil types and layers, contact area of the pounder, and the efficiency of the drop mechanism. The strong correlations that evolved into this relationship exist possibly due to the uniformity of contact pressures for DC pounders (generally 40 to 75 kN/m<sup>2</sup>). Lukas (1986) proceeds to advise that pounders with lower contact pressures create a shallow densified crust of soil and are generally used for the ironing pass. Pounders with higher contact pressures can cause excessive penetration or punching failure of the soil surface. However, these considerations qualitatively address drop energy as well as contact pressure and fail to quantitatively incorporate the effects of all pertinent parameters, pounder weight, drop height, contact area, and pounder base width. Another drawback of the current guidelines for determining the crater depths is the absence of soil strength criteria since it is obvious that the crater depth must depend on the soil strength properties. The proposed method addresses these issues by introducing specific impact energy and the soil strength as the key parameters controlling pounder penetration.

### PROPOSED METHODOLOGY

In terms of quantifying the soil strength, the Cone Penetration Test (CPT) is preferred over Standard Penetration Test (SPT) especially in soft soils. This is primarily for two reasons: (1) the high sensitivity of an electronic cone penetrometer, and (2) the test provides a continuous record of soil resistance with respect to depth. The proposed approach utilizes the sensitivity and continuity of CPT data and incorporates the *specific impact energy* of the pounder to predict initial impact penetrations.

The *specific impact energy*,  $E$ , is defined as the impact energy per unit area as shown in Eq. (2).

$$E = \eta \frac{WH}{A} \quad (2)$$

where  $E$ =specific impact energy  
 $A$ =contact area

$\eta$ =drop energy reduction factor  $= (V_0/V_t)^2$

$V_0$ =observed impact velocity

$V_t$ =theoretical impact velocity  $(\sqrt{2gH})$

The energy reduction factor ( $\eta$ ) accounts for the amount of energy lost to cable drag and the spool inertia. For a given soil profile and drop energy (pounder weight and drop height), one would expect deeper crater depths for smaller contact areas and *vice-versa*. Further, the depth of penetration is dependent on the variable soil strength profile as evidenced by different crater depths observed in essentially the same soil profile. Hence the depth of penetration must be a function of the *specific impact energy* (energy per unit area) and the shear strength characteristics of the soil profile. In this regard, one can assume that the cone resistance,  $q_c$ , at a given depth, indicates soil shear strength at that elevation. The validity of this assumption is further discussed in the next section.

In an attempt to formulate the above speculated relationship, the authors semi-empirically correlated the *specific impact energy* and the cumulative shear resistance encountered by the pounder up to the depth of penetration. The technical basis for the existence of such a correlation is described below.

If the initial ground heave is insignificant, the *specific impact energy* can be equated to the work done to overcome the shear resistance of the penetrated soil per unit pounder base area as expressed in Eq. (3).

$$E = \int_0^{z_p} q_c dz + \epsilon \quad (3)$$

where:  $E$ =specific impact energy  
 $q_c$ =cone resistance at any depth  $z$   
 $z_p$ =effective depth of penetration  
 $\epsilon$ =error term due to losses.

It has been assumed that the local shearing resistance encountered by the DC pounder at any penetrated point can be expressed by its  $q_c$  value. However, since the mechanisms of ground penetration are different in DC and CPT, there are limitations to the applicability of this method. In light of the discussion on penetration resistance of soils offered by Schmertmann (1978), one can visualize two basic differences between these two penetration mechanisms. They differ in (1) the shape of the penetrating object and (2) the rate of penetration. In this newly introduced practical correlation between impact energy and penetration resistance, the authors compute the total penetration resistance encountered by the pounder by integrating the CPT profile from the ground surface to the depth penetrated by the pounder. Hence the shape difference will be insignificant if one assumes that the cone tip is small enough to present data representative of any-point under the pounder base, at any depth.

On the other hand, there is a marked difference in the penetration rates especially when the pounder first touches the ground with a free fall penetration rate much higher than the 2 cm/s advancing rate of the cone. Rapidly penetrating objects can impede pore pressure dissipa-

tion thereby lowering the effective stresses and the penetration resistance, in turn. However, this phenomenon is certainly limited to saturated soils with low hydraulic conductivity ( $k$ ) values. According to Schmertmann (1978), this “ $k$ ” threshold is around  $10^{-5}$  cm/s. Therefore, the above assumption would be reasonable for dynamic compaction of granular and silty soil deposits as well as unsaturated clays. Unrelated laboratory hydraulic conductivity tests on the tested organic soils revealed  $k$  values in the range of  $10^{-4}$ – $10^{-5}$  cm/s. Thus, no significant pore pressure effects were expected in this particular study. Further support for this assumption is offered in the section on Correlation of Results.

Equations (2) and (3) verify common experience that larger-width pounders penetrate less than smaller-width pounders in the same soil for a given impact energy. The integration term in Eq. (3) can be graphically illustrated in Fig. 1 as the area under the  $q_c$  profile. However,  $z_p$  (in Eq. (3)) cannot be simply the crater depth, but rather the effective depth of the active soil wedge advancing with the poulder as shown in Fig. 2. This is because a part of the impact energy is also utilized in mobilizing some shear resistance in the soil wedge beneath the poulder. If it is assumed that the active soil wedge resembles one that is formed during typical bearing capacity failures, one can approximately determine the effective depth  $z_p$  as follows.

Due to the variable cross-sectional area of the active soil wedge and possible variations in cone resistance over the entire depth of the wedge, Eq. (3) can be expanded to differentiate two separate zones: (1) the zone penetrated by the full area of the poulder ( $A_p$ ), and (2) the zone affected by the varying area of the failure wedge,  $A(z)$ .

$$E = \int_0^{z_c} q_c dz + \int_{z_c}^{z_c+h} q_c \frac{A(z)}{A_p} dz + \epsilon \quad (4)$$

where  $z_c$  = crater depth  
 $h$  = height of the wedge  
 $A(z)$  = cross sectional wedge area at depth  $z$   
 $A_p$  = projected area of the poulder base

The first integral term expresses the energy required to overcome the shear strength of the crater per unit area of the poulder. The second term on the other hand expresses the energy required to mobilize shear strength in the failure wedge per unit area of the poulder.

The depth of the failure wedge will be relatively small for small pounders such as the one used in the model study herein. Hence,  $q_c$  will be essentially constant over the entire depth of the failure wedge reducing Eq. (4) to:

$$E = \int_0^{z_c} q_c dz + q_c \int_{z_c}^{z_c+h} \frac{A(z)}{A_p} dz + \epsilon \quad (5)$$

It can be shown that the second integrand in Eq. (5) is mathematically reduced to  $h/3$ . Then,

$$E = \int_0^{z_c} q_c dz + q_c(z_p) \frac{h}{3} + \epsilon \quad (6)$$

where

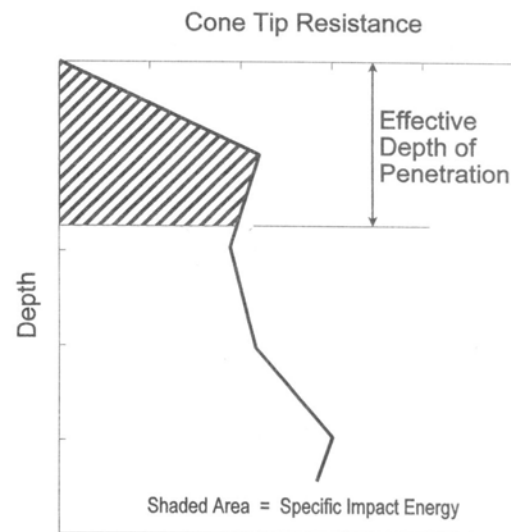


Fig. 1. Penetration calculated from a given specific impact energy

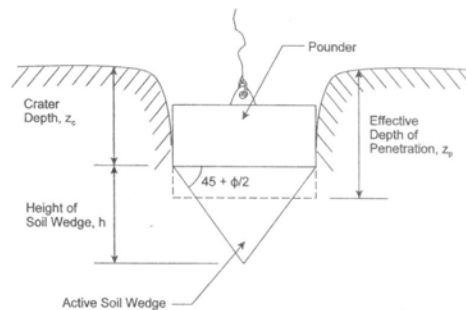


Fig. 2. Effective depth of penetration in advancing soil wedge

$$z_p = z_c + \frac{h}{3} \quad (7)$$

given that from Fig. 2,  $h$  can be approximated by

$$h = \frac{B}{2} \tan \left( 45 + \frac{\phi}{2} \right) \quad (8)$$

and

$B$  = poulder base width  
 $\phi$  = angle of internal friction

Therein, the crater depth can be estimated by finding the appropriate  $z_p$  to satisfy Eq. (3) and then combining Eqs. (7) and (8) in the following form:

$$z_c \cong z_p - \frac{B}{6} \tan \left( 45 + \frac{\phi}{2} \right) \quad (9)$$

The angle of internal friction can be approximated by employing any one of the common correlations that are available between  $q_c$  and  $\phi$  (Robertson and Campanella, 1983).

For relatively large pounders, the depth of the failure wedge will be significant, possibly penetrating a number

of variable layers. In such situations, one must use Eq. (4) for varying  $q_c$  values beneath the pounder. This requires an iterative approach in that  $z_c$  depends on  $A(z)$ ,  $h$ , and the average  $\phi$  beneath the pounder, and  $\phi$  depends on the depth to which the pounder penetrates,  $z_c$ .

Based on Eqs. (3) and (9) and data from a number of model tests, the investigators developed a correlation between the specific impact energy  $E$  and the area under the  $q_c$  profile as shown in Fig. 1.

**MODEL TESTING**

A series of DR tests was conducted in order to investigate the effects of pounder weight, drop height, impact area, number of impacts and initial soil strength on the pounder penetration. Although the primary objective was to develop guidelines for efficient implementation of DR in weak soils, the results were used to develop the correlation between impact energy and the pounder penetration.

The tests were conducted in a 2.44 m square, 1.22 m deep test pit. The test pit was equipped with a sand-gravel drain and a 3.5 m high, steel lifting frame shown in Fig. 3. The frame was supported by four rollers which rested on two parallel steel angles serving as guides on opposite sides of the pit. A drop mechanism was attached to the upper I-beam of the frame via a trolley and pulley system. The rollers and trolley provided 2 degrees of freedom allowing the drop mechanism to impact soil at any desired location in the pit. The drop mechanism could deliver free-fall impacts from a maximum height of 3 m. A 1 m deep bed of organic rich soil was prepared in 15 cm lifts and compacted with a WACKER BS-45-Y vibratory rammer. In order to prevent excessive compaction of the soil, the rammer was modified with a larger base. The soil was obtained from a site in Central Florida with an organic content ranging from 50 to 90%. Since organ-

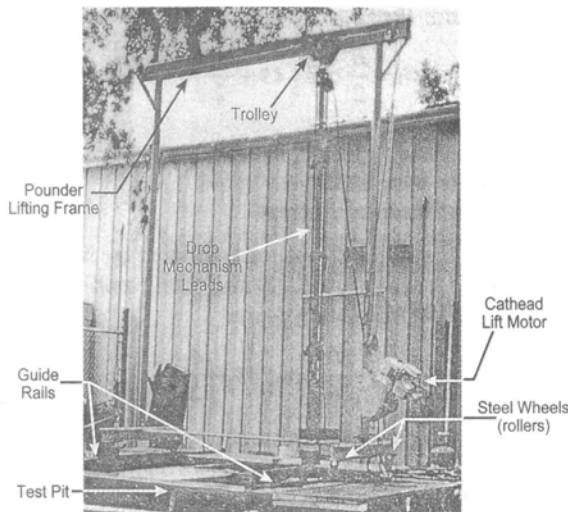


Fig. 3. Frame assembly used to lift and release the pounder over the test pit

ic soils are generally classified based on organic content or the moisture content, the consistency limits were not determined. However, further classification revealed the soil to be silty sands mixed with amorphous organic matter. Although care was taken to prepare a homogeneous bed of soil, a cone penetrometer was used to establish the soil strength profile at 24 locations within the bed to detect local variations. The penetrometer was specifically designed to register low stresses (2200 kPa capacity) such as those typically encountered in organic soils.

Four 177.56 N square pounders were fabricated with base areas ranging from 58 to 232 cm<sup>2</sup>. Each of the pounders was dropped from five different heights ( $H=0.9, 1.2, 1.5, 1.8$  and 2.1 m). As a result, 20 specific impact energy levels were analyzed. Figure 4 shows the plan view of the test bed which includes the 20 impact locations, contact areas ( $A$ ), and the impact energies ( $WH$ ).

**CORRELATION OF RESULTS**

The effective depth of penetration for each initial impact was used as the upper limit of numerical integration (Eq. (3)) of the CPT profile from its respective print location. The area estimated from the CPT curve from  $z=0$  to  $z=z_p$  is shown in Fig. 5 for a typical initial impact (a numerical example of the prediction methodology is presented in Appendix II). The computed areas for each test were then compared to the specific impact energy ( $E$ ) of the corresponding pounder. Figure 6 shows the plot of  $E$  versus 'Area under CPT curve' for impact tests on the organic soil used in the model test. A sandy soil was used in the test pit to provide a blanket for dynamic compaction of the organic soil. As one would expect, punching through the sand blanket with the pounders produced sand columns in the organic soil at the impact locations. Linear regression with a coefficient of correlation of 0.93 confirms the relationship in Eq. (3) with an efficiency of energy transfer ( $\eta$ ) of 98%. It is also seen from Fig. 6 that the energy loss term ( $\epsilon$ ) appears to be negligible for the model tests.

The results from impact tests on both the organic and sandy soil were re-evaluated to *predict*  $z_c$  based on the pounder drop energy and the  $q_c$  profile. Equations (3) and (9) were used in this exercise by assuming zero energy

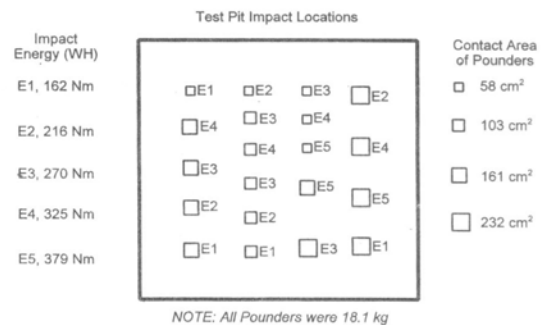


Fig. 4. Layout of test pit showing print locations, contact area, and applied impact energy

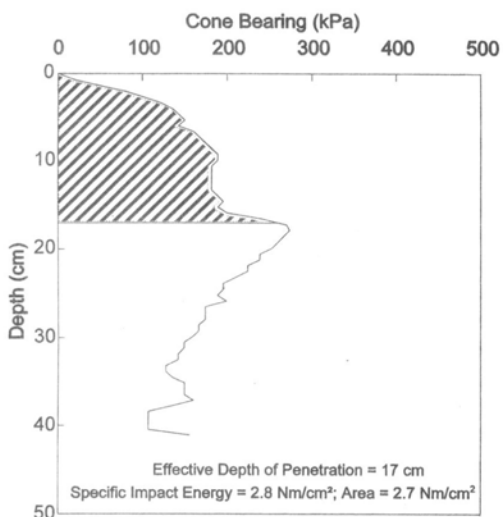


Fig. 5. Typical numerical integration results

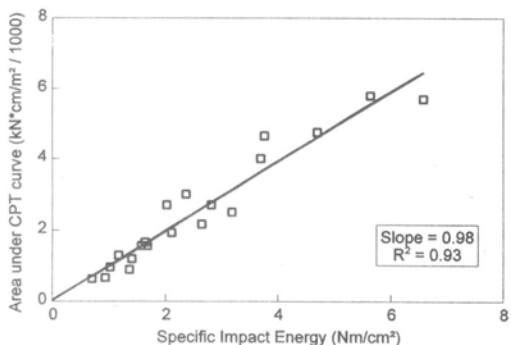


Fig. 6. Comparison of specific impact energy with area under CPT curve

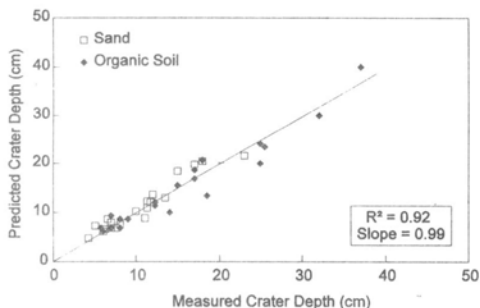


Fig. 7. Crater depth predictions for model test impacts

losses. Figure 7 shows the comparison of predicted penetrations and measured penetrations for all of the model tests. The linear correlation along a slope of 0.99 with a coefficient of correlation of 0.92 indicates the potential of this new method in accurately predicting crater depths.

It is recalled that the crater depth prediction technique advanced in this study stems from the assumption that  $q_c$

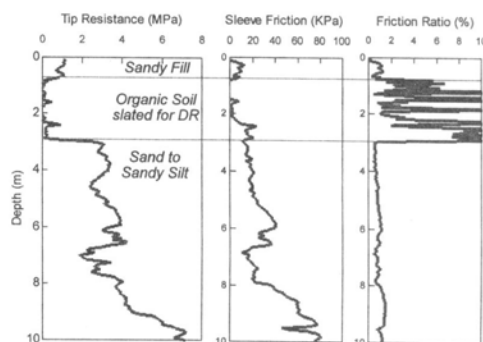


Fig. 8. Cone penetration sounding prior to DR process in Plant City, Florida

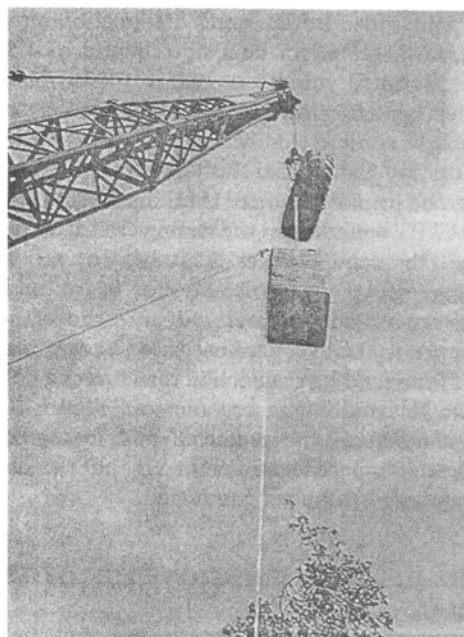


Fig. 9. Pounding (36 kN) designed for DR

values represent the shear resistance encountered by the dynamic pounder at every depth. A clear affirmation of the validity of this assumption for many field situations is seen in the results of this study itself. In this respect, Figs. 6 and 7 show that, for the tested organic soil and sand, the difference in the penetration resistance manifested for the cone and the pounder is insignificant for all practical purposes.

**FIELD VERIFICATION**

The results of the model study predictions were verified during a full-scale Dynamic Replacement project conducted as part of the I-4 expansion project in Plant City, Florida. Therein, a portion of the Exit 13 westbound on-ramp was set aside for experimental ground modification using DR as an alternative to replac-



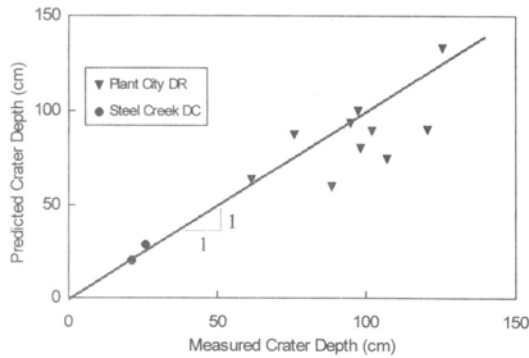


Fig. 10. Comparison of predicted and field measured crater depths

ing organic soils. Initial muck delineation probes revealed a surficial organic deposit to depths of 4.5 meters with an estimated volume exceeding 1000 cubic meters. After clearing and grubbing the site, an 18 meter by 45 meter area was blanketed with approximately one meter of clean sandy fill material. Full details of the entire program can be found elsewhere (Mullins, 1996). Figure 8 is a typical CPT sounding in the testing area after the application of the sand blanket. This type of soil strength profile is particularly problematic for the initial impacts due to excessively deep craters. Figure 9 shows the 36 kN pounder with a 0.6 m square base used to cause punching failure of the sand layer which in turn drives a column of sand into the underlying organic soil. Figure 10 shows the comparison of the predicted and measured crater depths at ten impact locations throughout the site where CPT soundings had been conducted.

#### CRATER DEPTH PREDICTIONS FOR OTHER DC PROGRAM

Crater depth predictions were also made using CPT data supplied by GKN Hayward Baker, Inc. from the Steel Creek Dam project on the Savannah River south of Augusta, Georgia, USA. This project entailed the construction of a 600 meter-long earthen dam up to 25 meters above the original stream elevation. To alleviate the problem of excessive penetration during DC with a 266.7 kN pounder dropping from a 30 m height, a 168.6 kN pounder dropping from a 15 meter height was used for the first pass in order to densify upper layers enough to withstand blows from the heavier pounder. The two pounders were of cross-sections of approximately 2 m  $\times$  1.3 m and 1.3 m  $\times$  1.3 m, respectively. The compacted soil was predominantly sandy with a clay layer appearing from about 1 to 3 meters. The entire DC process was performed in four passes totaling over 1300 impact locations (prints). The print pattern and spacing was based on a 15 m square configuration and the crater depths were typically recorded after 5 to 10 drops. In a few locations where initial impacts were recorded and CPT data were available, the predicted crater depths matched reasonably with those recorded in the field (Fig. 10).

#### CONCLUSIONS

An empirical-mechanistic method is presented for predicting the initial crater depth created by a dynamic compaction pounder after the first impact on a soil. This computational technique will be particularly useful for dynamic compaction projects on weak soil types where the ground heave is expected to be negligible. In this approach, the *specific impact energy* (impact energy per unit area) of dynamic compaction is equated to the cumulative area under the CPT curve between the ground surface and the effective depth of penetration. Hence it certainly addresses shortcomings of the current methods of evaluating the depth of pounder penetration which account for neither the soil strength nor the pounder surface area.

Although the correlations leading to the prediction technique are based on a large number of model tests, full-scale dynamic replacement results are used to verify it. Further, field data obtained from dynamic compaction tests performed elsewhere have been used to corroborate the new technique. Although the methodology is intended for use in uniform soft soils, its application also can be extended to non-uniform soils. A numerical example (Appendix) illustrates how typical CPT data can be adapted to predict the effective depth of penetration and subsequently, the crater depth. The newly developed method is expected to enable engineers to determine approximately the optimum impact energy that can be used in dynamic compaction without causing excessive initial penetrations, based only on cone penetration test results. Furthermore, since the ensuing impacts carried out on refilled craters do not generally cause deeper penetrations than the initial one, the initial crater depth can provide an approximate idea of the influence zone. Hence the predictive technique will furnish an effective planning tool for dynamic compaction programs on sites with weak soils, well before the mobilization of heavy equipment.

#### ACKNOWLEDGMENTS

The writers would like to thank the following: Hayward Baker, Inc. of Tampa for their collaboration in the Plant City, DR project and for providing the field information from the Steel Creek Dam program; Bob Lukas for clarifying some points concerning crater depths measurements found in Lukas (1986); Rudy; and the Florida Department of Transportation, District I Geotechnical Engineering Group for their extended support in conjunction with ongoing USF research.

#### REFERENCES

- 1) Chow, Y. K. et al. (1992): "Dynamic compaction analysis," J. of the Geotech. Engrg. Div., ASCE, Vol. 118, No. 8, pp. 1141-1157.
- 2) Chow, Y. K. (1995): Personal communication with the second author.
- 3) Lo, K. W. et al. (1990): "Unified approach to ground improvement

- by heavy tamping," J. of the Geotech. Engrg. Div., ASCE, Vol. 116, No. 3, pp. 514-527.
- 4) Lo, K. W. et al. (1990): "Dynamic replacement and mixing of organic soils with sand charges," J. of the Geotech. Engrg. Div., ASCE, Vol. 116, No. 10, pp. 1463-1482.
  - 5) Lukas, R. G. (1986): "Dynamic compaction for highway construction, Design and construction guidelines, Volume I," Federal Highway Administration Report FHWA-RD-86-133.
  - 6) Menard, L. and Broise, Y. (1975): "Theoretical and practical aspects of dynamic consolidation," Géotechnique, pp. 3-18.
  - 7) Mullins, A. G. (1996): "Field characterization of the dynamic replacement of Florida organic soils," Doctoral Dissertation, Univ. of South Florida, Tampa, FL.
  - 8) Ramaswamy et al. (1979): "Treatment of peaty clay by high energy impact," J. of the Geotech. Engrg. Div., ASCE, Vol. 105, No. GT8, pp. 957-967.
  - 9) Robertson, P. K. and Campanella, R. G. (1989): "Guidelines for use and interpretation of the electronic cone penetration test," UBC, Civil Engrg. Dept., Vancouver, British Columbia; also available from Hogentogler & Company, PO Drawer 2219, Columbia, Maryland 21045, (4th Ed.).
  - 10) Schmertmann, J. H. (1978): "Guidelines for cone penetration test, Performance and design," Federal Highway Administration, Report FHWA-TS-78-209.

## APPENDIX

### Numerical Example

To illustrate the new method of predicting crater depths, Eq. (3) is rewritten for discrete CPT values in Eq.

(10). Assuming the typical depth recording interval of a mechanized cone to be  $\Delta z$  and the average cone resistance  $q_c$  over each interval as a discrete value, a cumulative  $q_c \Delta z$  is computed as a function of depth ( $z$ ). Then  $z_p$  can be determined as the depth at which the cumulative  $q_c \Delta z$  equals the specific impact energy for the given drop configuration.

$$\sum_0^{z_p} q_c \Delta z = \eta E \quad (10)$$

where:  $q_c$  = average CPT value over that depth interval  
 $\Delta z$  = depth recording interval (typically 5 cm)  
 $\eta$  = drop efficiency ( $\eta \approx 1$ , for free-fall)  
 $E = WH/A$

Assume that CPT data from a site in Central Florida where predictions of crater depths due to free-fall impacts are needed are shown in CPT data below:

Given:  $W = 6$  tonnes (58.9 kN)  
 $H = 20$  meters  
 $B = 1$  m square ( $A = 1$  m<sup>2</sup>)  
 $\phi = 35$  degrees,

predict the initial crater depth.

### Cone Penetration Test Data for Numerical Example

SOUNDING DATA IN FILE 6

ENGINEER: W. R. MCLAUGHLIN

CONE ID: 271

FLORIDA DEPARTMENT OF TRANSPORTATION

BARTOW DISTRICT

02/05/95 14:42

LOCATION: 6

JOB #: 99901 1521

Depth (meters)	TIP resistance (kPa)	Local friction (kPa)	Friction Ratio (%)	Inclination (deg)	Cumulative area under CPT ( $z$ )
0.00	0.01	0.00	0.00	-0.1	0
0.05	512.68	1.08	0.21	-0.2	12.82
0.1	769.01	1.92	0.25	-0.2	44.86
0.15	1412.11	4.24	0.3	-0.2	99.39
0.2	2202.11	8.37	0.38	-0.2	189.74
0.25	2784.74	9.75	0.35	-0.2	314.41
0.3	3356.32	12.08	0.36	-0.2	467.94
0.35	3432.11	11.67	0.34	-0.2	637.65
0.4	3920.21	9.80	0.25	-0.2	821.45
0.45	4052.11	13.37	0.33	-0.2	1020.76
0.5	3927.37	18.46	0.47	-0.2	1220.24
0.55	3905.26	31.24	0.80	-0.2	1416.06
0.6	3773.68	40.38	1.07	-0.2	1608.03
0.65	3695.79	32.15	0.87	-0.2	1794.77
0.7	3737.37	16.44	0.44	-0.2	1980.6
0.75	2001.05	8.80	0.44	-0.2	2124.06
0.8	2511.05	14.06	0.56	-0.2	2236.86

The prediction process involves three steps:

1. Estimate the cumulative area under the CPT curve at different depths.

This is recorded at each depth in the last column of Table 1.

2. Determine the *specific impact energy* ( $E$ ) for the given drop mechanism, assuming a free fall.

The specific impact energy =  $58.9 * 20 / 1.0 = 1177.2$  kN/m.

3. Estimate the effective penetration depth where the cumulative area equals the *specific impact energy*.

Thus,  $z_p$  can be estimated to be 49 cm. Then, by using Eq. (9) the crater depth is predicted to be 17 cm.

# Settlement Repair of Lightly Reinforced Concrete Block Walls Using CFRP

---

G. MULLINS, A. HARTLEY, D. ENGBRETSON and R. SEN

## ABSTRACT

This paper presents the results of an experimental study to assess the feasibility of using uni-directional carbon fiber reinforced polymer sheets for repairing lightly reinforced concrete masonry walls that have cracked due to foundation settlement. In the study, two full-sized 8 in. block walls, 8 ft high and 20 ft long were first damaged under simulated settlement loading and then re-tested after being repaired using carbon fiber sheets bonded to one side of the wall. Strength gains of over 50% were recorded. This suggests that carbon fiber reinforced polymers may be suitable for repairing concrete block walls damaged by foundation settlement.

## INTRODUCTION

Un-grouted, lightly reinforced concrete block walls are widely used in residential construction in southeastern United States where wind, not earthquake loading, is critical. Until as recently as the early 1990's, walls were vertically reinforced by #5 bars at the corners or every 240 sq. ft. (i.e. every 30 ft, for typical 8 ft high walls) and by a horizontal #5 bar in 8-in. bond beams. This is in stark contrast to masonry construction in seismic regions that are fully grouted with significant reinforcement in both the vertical and horizontal directions.

The vast majority of masonry homes are fortunately not subjected to hurricanes (or even earthquakes) in their lifetime. Instead, they stand a greater chance of being damaged by foundation settlement. Nationwide, foundation subsidence affects an estimated quarter-million homeowners *annually* [1]. Conventional repair of settlement damage can be both time consuming and costly. In contrast, fiber reinforced polymer (FRP) materials offer the prospect of speedy, unobtrusive and inexpensive repairs. This paper describes the results from a pilot study to investigate the feasibility of using FRP material to repair foundation settlement problems in lightly reinforced masonry walls.

---

Gray Mullins and Rajan Sen, Department of Civil and Environmental Engineering, University of South Florida, Tampa, FL 33620  
Alfred Hartley, Carian Killam Consulting Group Inc., Tampa, FL 33619  
Dan Engbretson, Walter P. Moore and Associates, Inc., Tampa, FL 33602

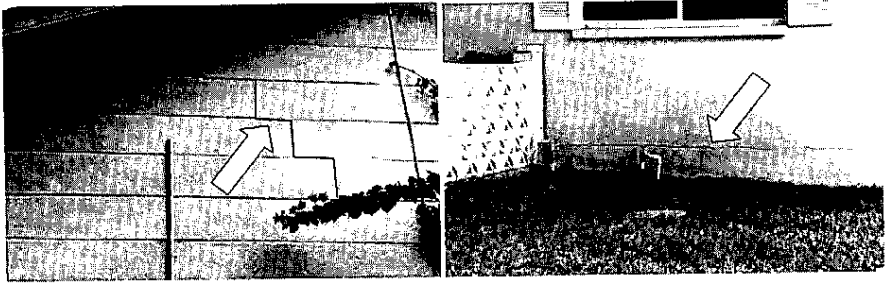


Figure 1. Characteristic Settlement Cracking.

## BACKGROUND

Foundations for masonry walls (in the southeast) are commonly reinforced longitudinally by two #5 bars to allow the footing to bridge over soft nonuniform soil. However, improper compaction or the presence of buried compressible material such as tree roots or construction debris can nonetheless lead to excessive settlement. As unreinforced masonry is brittle it has a greater propensity to crack even when the movement is within the allowable limit for the concrete footing.

Characteristic settlement cracks observed in block homes are stair-step mortar cracking or horizontal mortar cracks between the concrete floor slab and the first course of blocks as shown in Fig. 1. The failure is the result of un-grouted masonry's very low tensile strength - allowable values vary between 25-50 psi [2] - compared to modulus of rupture values of over 400 psi for 3000 psi concrete [3].

Typically, repairs involve two steps. *First*, the movement of the foundation is stabilized either through the use of grade beams or a combination of both grade beams and pin piles. *Second*, the wall is transformed to a 'wall-beam' by the introduction of vertical steel reinforcement (Fig. 2) or fully grouting all the cells. The latter option provides a nearly eightfold increase in shear capacity. The cost of repairing an average home with 140 ft length of masonry wall is in the range of \$40-45,000 [4].

## OBJECTIVES

The primary goal of this study was to investigate the feasibility of using uni-direction fiber-reinforced polymer material to repair walls damaged by foundation settlement. An important element was to examine the performance of as-built walls that conformed to construction standards since the 1960's so that the results of the study would be more widely applicable.

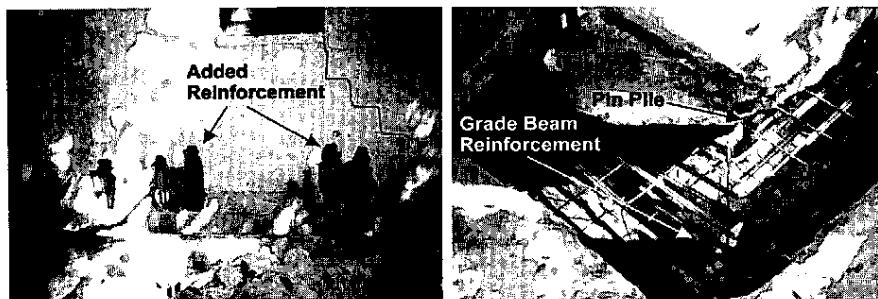


Figure 2. Conventional Repair of Settlement Damage.

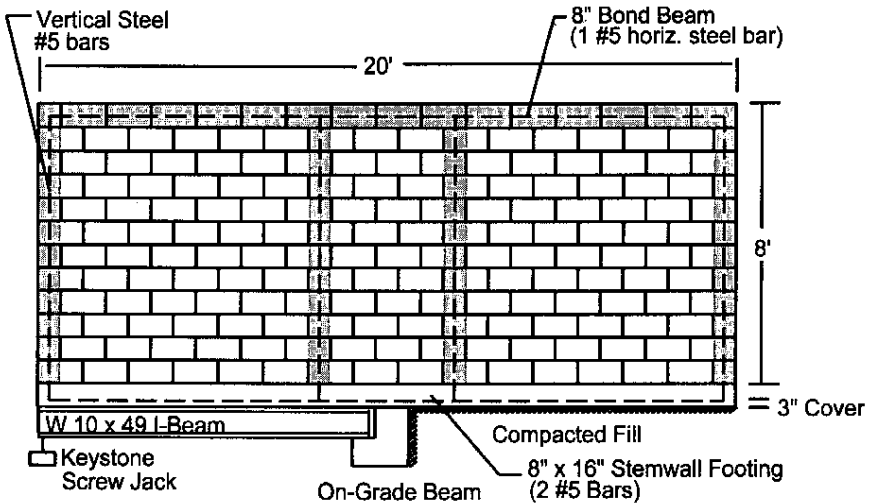
## SBC PROVISIONS

The governing design code for the southeast is the Standard Building Code (SBC) [5]. As part of this study, a detailed historical review of the relevant masonry and wind provisions of SBC was carried out to identify construction practice since the first edition of the code was published in 1946. The findings may be summarized as follows: (1) no vertical reinforcement - 1940's through 1950's construction; (2) vertical reinforcement only at the corners - 1960's through early 1990's; and (3) intermediate reinforcement required - 1993 to present.

Intermediate reinforcement was actually required starting with the 1969 edition where masonry could "... not exceed 240 square feet without approved vertical and horizontal support..." for walls which were 8 in. thick. However, this revision specifically excluded "one and two family residences". By the 1988 SBC Edition, this exemption was removed but the fact that most single-story masonry walls were only eight feet high meant that intermediate reinforcement was still only required every 30 feet. At best, a continuous masonry wall may have required one intermediate rebar; and this revision had little impact on single-story residential walls. The deemed to comply "Standard for Hurricane Resistant Residential Construction (SSTD 10)," first published in 1993 [6], further reduced the spacing for vertical reinforcement. For example, SSTD 10-93 required that a 44 ft x 8 ft x 8 in masonry wall have intermediate reinforcement at a maximum spacing of four feet and a rebar aside every opening to withstand 110 mph wind velocities.

## TEST PROGRAM

A careful survey was made of subsidence damage to masonry block homes in the Tampa Bay area prior to the design of the test specimens. Based on this inspection and interviews with consulting engineers, the representative wall length in testing was determined to be 20 ft. The wall height was taken as 8 ft which is typical for residential construction.



NOTE: Intermediate Vertical Reinforcement Omitted in Wall 3

Figure 3. Reinforcement Details - Wall 2.

A total of four walls were constructed by experienced local masonry contractors to represent the prevailing building standards from the 1960's to the present. Walls 2 and 3 represent construction practice prior to the 1990's that provided vertical reinforcement only at the corners and optionally at intermediate locations; Walls 1 and 4 represent current practice with vertical reinforcement at 4 ft spacing. Wall 2 had intermediate reinforcement spaced at 8 ft from the ends (see Fig. 3) while Wall 3 had no intermediate reinforcement (ends only).

Past and current building practices were represented by two different methods of forming the bond beam. In the older style of construction, a 6 in. wide felt strip was applied to the last course of the masonry unit just prior to the bond beam course. The felt strip covers the open cells of the masonry units and prevents grout from falling through while the bond beam is poured. The felt cap, however, reduces the face shell bedding for the typical 8 in. block from 1.25 in. to only 13/16 in. width for each shell. Current practice is to cover each cell with a thin metal pan. Walls 1 and 4 were constructed with metal fill caps while Walls 2 and 3 were built with a felt cap.

The four walls were built such that they shared a common support wall that was perpendicular to each wall. All of the walls were built on top of a 8 in x 16 in concrete footing reinforced with two #5 bars. Dowels with 90° hooks were provided at the location of the vertical steel to connect wall to the foundation. Each footing was cantilevered approximately 10 ft. 6 in. past a concrete grade beam. This beam served mainly to retain the soil and support the steel beam - the footing did not bear upon the grade beam.

The interface between the test walls and the support wall was a butt rather than an interlocking joint that is typical of actual construction. An interlocking joint would have provided greater support to the test walls at the interface and prevented rotation of the wall panel as a whole. However, the bond beam was poured continuously such that the common grout core shared by all of the walls provided some degree of support. The grouting of the reinforced cells and pouring of the bond beam was performed in one operation.

## **Test Setup**

Differential settlement cracking has been observed to occur only over a portion of a masonry wall. This suggests that part of the wall is continuously supported while the rest is free to subside. This condition was simulated in the test setup by constructing about half the length of the wall on compacted fill. The remainder was supported on a W10x49 steel beam that cantilevered off a grade beam. This steel beam was supported at its free end on a keystone screw jack (see Fig. 3). Plastic sheeting was used to separate the footing from the steel beam and prevent composite action.

Three complete turns of the hex-nut in the screw jack provided 3/8 in. settlement which was sufficient to allow a 10 ft, 6 in. length of the wall to act as a cantilever under its own weight. Additional settlement was induced by applying loading at the top of the wall using a 50-ton ENERPAC hydraulic jack. A steel reaction frame made of W12 x 22 steel beams provided the reaction to the jack. The frame was held down by chains connected to "Chance" anchors bored into the soil. Each was drilled to a depth of 12 ft to 15 ft and was located on both sides of each wall. The reaction frame geometry and the location of the ground anchors permitted loads of up to 15 tons to be applied to the cantilevered end of each wall (see Fig. 4).

## **Instrumentation**

The test specimens were instrumented using load cells, LVDT's, and strain gages. Two load cells were used - one at the free end to measure the self weight when the screw jack was released and the second to measure the magnitude of the simulated roof load. LVDT's measured deflections in both the vertical and horizontal directions; strain gages were used to record strains in both the wall and the footing. A battery powered MEGADAC 3108 DC data acquisition system was used for recording data.

## **Test Procedure**

Two series of tests were carried out. In the first series, the settlement loads consisting of the self weight of the cantilevered wall and simulated roof loads were applied that led to the development of stair-step cracks. Subsequently, the loads were removed and the hex nuts of the screw jack returned to their original position. The



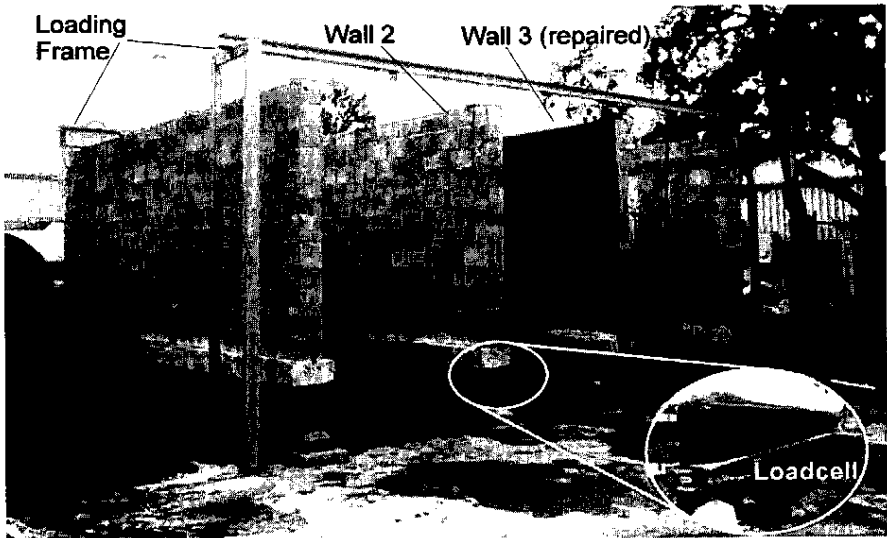


Figure 4. View of Wall Set-Up.

wall was then repaired using carbon fiber reinforced polymer sheeting. As the surface of the walls was smooth, no special surface preparation was deemed necessary and manufacturer's recommendations were generally followed. The ends of the CFRP were secured to the wall with 3 in. steel plates using Tapcon anchors.

Since the uni-directional carbon fiber sheeting (FTS-C1-120) was only intended to increase bending resistance, it was oriented parallel to the length of the wall. Three sheets, each 20 in. wide, were attached *only to one face* as shown in Fig. 4. The intent was to provide additional bending and shear capacity in the zone of the wall that was expected to be in tension. Strain gages were mounted on the CFRP surface and the strengthened wall tested in the same manner as the plain wall. As the specimens were constructed outdoors, all tests were carried out in the pre-dawn hours to ensure constant thermal conditions during the testing.

## RESULTS

Two of the four walls constructed have been tested. These were the two weakest walls (#3 with vertical reinforcement at the ends) and (#2 with vertical reinforcement 8 ft from the ends). The results obtained included crack patterns, load deflection and strain variation with depth. Because of space limitations only results relating crack pattern and load deflection are presented.

The crack pattern from the two walls are shown in Figs. 5 and 6. Note the stair step cracking in the supported section of the wall caused by the rotation of the cantilevered

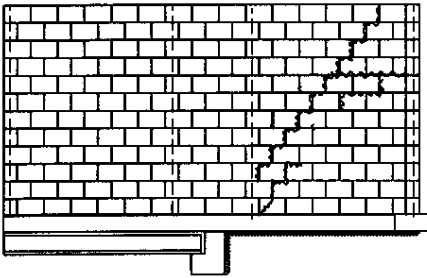


Figure 5. Crack Pattern, Wall 2.

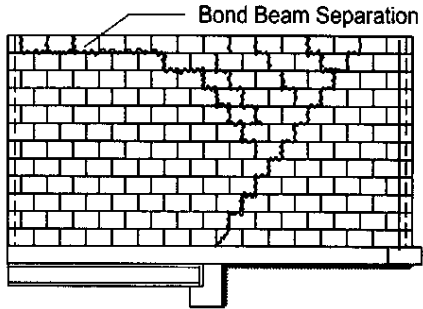


Figure 6. Crack Pattern, Wall 3.

section. The cracking was more pronounced in the weaker wall (#3) as there was no intermediate vertical steel. In contrast, cracking in the stronger wall was confined to the supported region. This is not surprising given that the cantilevered portion of the structure was somewhat longer.

The effect of repair on the capacity of the walls is shown in Figs 7 and 8. Each figure displays the response of plain and strengthened walls. As the weaker wall cracked at a proportionately smaller load, its strength gain was greater (72% vs 57%). Inspection of Figs. 7 and 8 also show improvement in the stiffness of the repaired wall. This was evident in the load vs strain plot. The highest strains were in the bond beam and in the footing. Strains in the remainder of the wall were relatively modest [7].

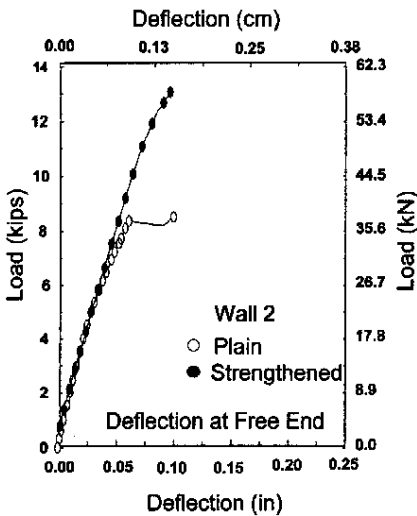


Figure 7. Load-deflection for Wall 2.

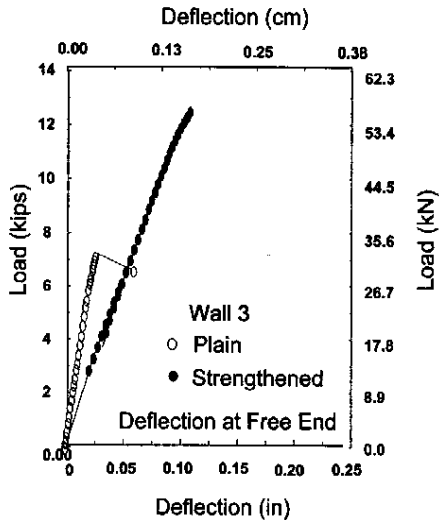


Figure 8. Load-deflection for Wall 3.

## DISCUSSION

Masonry walls are subjected to in-plane bending moments and shears due to settlement loading. The bending moment is resisted by a couple formed by the tension steel in the bond beam and compression concrete in the foundation. Due to the very large lever arm, substantial, bending resistance can be realized even by lightly reinforced members. However, the absence of vertical steel, acting as shear reinforcement, causes the wall to crack. In the study, carbon fiber sheets were aligned along the length of the wall to increase the tension capacity of the bond beam. This continuous bonding also improved shear capacity of the wall since resin has a much higher shear capacity than mortar. As a result, significant strength gains were realized and indeed the second specimen, Wall 2 could not be tested to failure.

In the study, three 20 in. wide strips of carbon fiber were used and no attempt was made at material optimization. Finite element analysis carried out [8] indicated that for the walls tested, much narrower strips could be used to provide the same bending resistance. Strips as little as 8 in. or 20 in. would be adequate for most residential repairs though stiffness improvement would be poorer.

The settlement forces that develop in a wall are of course identical regardless of whether it is constructed in a seismic or non-seismic region. However, the repair scheme used in this study will need to be modified to reinforce the wall in both horizontally and vertically and provide greater ductility in seismic regions. It may be convenient to use bi-directional CFRP material for this purpose.

The repair was completed in 1995. After over four years of exposure in Florida's sub-tropical climate there was no discernible deterioration in the CFRP epoxy bond.

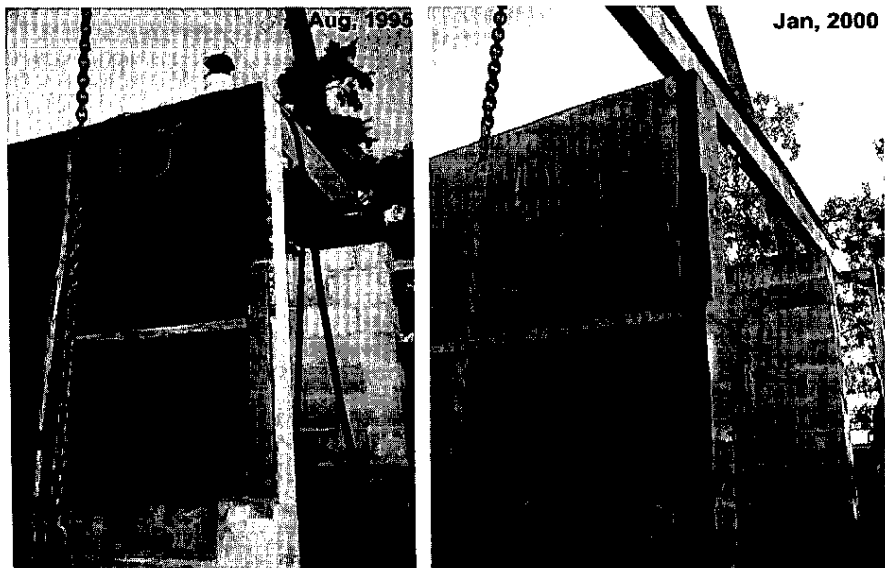


Figure 9. Effect of Exposure on Wall 3.

Fig. 9 compares the wall in its original to its current state. Note the corrosion in the steel that was used to anchor the ends of the CFRP sheeting, and the original sheen in the epoxy coating has lost its luster.

## **CONCLUSIONS**

FRP material has been widely considered for the seismic retrofit of unreinforced masonry. Though devastating, earthquakes are relatively rare. In contrast, damage due to foundation settlement is much more common and affects homes nationwide. This paper presents results from an experimental study to investigate the feasibility of using uni-directional carbon fiber sheets for the repair and rehabilitation of lightly reinforced masonry walls damaged by foundation settlement.

The full-sized test walls were built by experienced masonry contractors in the same manner in which homes have been constructed over the past thirty years. Two of the walls, representative of earlier construction, were tested under simulated foundation settlement before and after strengthening. The CFRP material was applied to one surface to accommodate homeowner preference for minimizing disruption. The results of the tests are very encouraging and suggest that FRP material may be appropriate for repairing some types of foundation damage. Where damage is very severe, it may be also used in conjunction with traditional repairs for strengthening the wall after the foundation settlement has been stabilized using other means (Fig. 3). Moreover, it may be possible to optimize the repair so as to minimize costs.

The study was directed towards applications in southeastern United States where wind loading is more critical. In seismic regions, additional strengthening will be required in the horizontal and vertical directions to comply with ductility requirements for lateral-force resisting systems. In addition, the connections between the masonry walls/ roof framing /foundations will need to be appropriately strengthened. Inadequate anchorage is one of the chief causes of failure of masonry construction during earthquakes. Detailed information on the seismic retrofit of unreinforced masonry may be found elsewhere [9].

## **ACKNOWLEDGMENTS**

The authors gratefully acknowledge the support and contribution of the Tampa Bay Chapter of the Masonry Contractors Association of Florida who donated their services and all materials needed for the fabrication of the walls. We thank Mr. Jack Harrington, P.E. for his contribution in the design of the test setup to simulate settlement. We also wish to thank Dr. Howard Kliger for technical advice and Tonen Corporation, Japan for donating materials used in the testing.

**REFERENCES**

1. A. B. Chance Company (1995). "Chance Helical Pier System". Bulletin 01-9501, Revised 4/95, Centralia, MO.
2. ACI 530-99 (1999). Building Code Requirements for Masonry Structures, American Concrete Institute, Farmington Hills, MI 48333.
3. ACI 318-99 (1999). Building Code Requirements for Structural Concrete, American Concrete Institute, Farmington Hills, MI 48333.
4. Hungerford, L. (1997). Brown Testing Services, Tampa, FL. Private Communication, March 27.
5. Southern Building Code Congress International (1997). Standard Building Code 1997 Edition, Birmingham, AL.
6. Southern Building Code Congress International (1993). Standard for Hurricane Resistant Residential Construction (SSTD 10-93), Birmingham, AL.
7. Hartley, A., Mullins, G. and Sen, R. (1996). "Repair of Concrete Masonry Block Walls using Carbon Fiber", *Advanced Composite Materials in Bridges and Structures* (Editor M.El-Badry), Canadian Society of Civil Engineers, Montreal, P.Q. pp. 795-802.
8. Engebretson, D., Sen, R., Mullins, G. and Hartley, A. (1996). "Strengthening Concrete Block Walls with Carbon Fiber". *Materials for the New Millennium, Proceedings of the Materials Engineering Conference Volume 2*, ASCE, New York, NY, pp. 1592-1600.
9. Federal Emergency Management Agency (1997). "NEHRP Guidelines for the Seismic Rehabilitation of Buildings", FEMA 273, and "Commentary", FEMA 274, Washington, DC, October.

# Durability of Carbon Fiber-Reinforced Polymer/Epoxy/Concrete Bond in Marine Environment

by Rajan Sen, Mohsen Shahawy, Gray Mullins, and John Spain

*This paper presents results from a two-year exposure study to evaluate the durability of the epoxy bond formed with concrete and carbon fiber-reinforced polymers (CFRP) in a marine environment. Twenty-four unstressed slab specimens were used to investigate five different epoxy systems exposed to four different environments. Five of the 24 specimens—one for each epoxy system—were controls kept in an air-conditioned laboratory. The remaining 19 slabs were exposed to one of three environments: a) wet/dry cycles in salt water; b) combined wet/dry and thermal cycles in salt water; and c) outdoor. Long-term performance was evaluated both qualitatively, that is, visual inspection, and quantitatively from destructive shear and tension tests conducted at the end of the exposure period. The results showed there was some deterioration in bond, particularly in specimens exposed to wet/dry cycles. This could be more readily detected by destructive testing rather than visual inspection. Overall, the results are promising and suggest that several competing epoxy systems are likely to be durable in Florida's harsh marine environment.*

**Keywords:** bond; carbon; concretes; durability; tension; torsion.

## INTRODUCTION

Carbon fiber-reinforced polymer (CFRP) material is increasingly being used for the repair and rehabilitation of flexural concrete elements in buildings and bridges.<sup>1,2</sup> In this method, the CFRP material is bonded to the concrete surface using epoxy adhesives. As the load is transferred to the CFRP material by epoxy, the durability of its bond with concrete is critically important for the integrity and safety of the repaired structure.

Information on the long-term durability of CFRP/epoxy/concrete bond is relatively scarce. Product literature sometimes contains data that purports to provide evidence of satisfactory performance, although testing details are seldom included.<sup>3</sup> Recently, results of exposure tests on CFRP sheeting material were reported at ICCI '98.<sup>4,5</sup> In one of the two studies presented, CFRP sheeting material was exposed to 300 wet/dry cycles (completed in 150 days) and 50 freezing-thawing cycles (completed over 50 days). Tensile tests conducted at the end of the exposure period indicated that there was no degradation in one type of CFRP material tested. The second CFRP type, however, registered a 10% reduction in tensile strength under wet/dry cycles.<sup>4</sup>

The second study provided interim results from a more elaborate on-going investigation.<sup>5</sup> In the study, 12 composite overwrap systems intended for seismic retrofitting were being examined for durability qualification. Of the 12, nine were carbon and three were glass fiber composites. Exposure consisted of several different environments including 100% humidity, salt water, alkali solution, diesel fuel, ultra-violet light, elevated temperature (60 C), and cyclic freezing-thawing conditions. Results presented following 3000 h of a 10,000 h exposure program showed that the majority of the systems tested had excellent du-

rability, although minor reduction in CFRP tensile strength (< 10%) was observed due to saltwater exposure.

Although the two studies provide useful data, their focus was primarily on the effects of exposure on the degradation in material properties, not the bond between concrete, epoxy, and the CFRP sheet material. Indeed, the authors of the second study remarked that "a strong adhesive bond between the composite and the concrete is probably not required" because the wrapping encases the column and its function is largely to provide confinement in the event of an earthquake.<sup>5</sup> Thus, these results are of limited value in flexural applications where the durability of CFRP/epoxy/concrete bond is much more critical.

In 1995, the University of South Florida commenced a 24 month exposure study to evaluate the long-term durability of the CFRP/epoxy bond system in a marine environment. In the study, five different epoxy systems were investigated with specimens exposed to four different environments. At the end of the exposure phase, all specimens were carefully inspected for evidence of bond deterioration. Subsequently, destructive tests were conducted to evaluate the bond under tension and shear. This paper summarizes the principal findings from this study.

## PROBLEM STATEMENT

An essential requirement for successful performance of CFRP strengthened structures is the physical and chemical compatibility between concrete and the adhesive material used for bonding. If incompatibilities exist, internal stresses develop that can lead to a weakening of the long-term CFRP/epoxy/concrete bond.

When epoxy is used to bond CFRP material to concrete, both physical and chemical incompatibilities are introduced. Physical incompatibility stems from a mismatch in the coefficient of thermal expansion between epoxy, CFRP, and concrete; for example, the coefficient of thermal expansion for epoxy, reported as  $44-120 \times 10^{-6}$  per C,<sup>6</sup> is several times greater than concrete that varies between  $6-13 \times 10^{-6}$  per C depending on aggregate.<sup>7</sup> This suggests that if a CFRP-strengthened structure is subjected to large temperature variations, its performance may be impaired. Records from the National Climatic Data Center, Asheville, N. C., show that over the past 50 years several regions in Florida have experienced a significant temperature change, such as Pensacola, Fla., recorded a temperature range in excess of 55 C.<sup>8</sup> Thus, temperature variation encountered under normal service conditions can adversely affect the CFRP/epoxy/concrete bond.

Chemical incompatibility can stem from permeability differences between concrete and epoxy. The permeability of concrete depends on a number of factors, most notably its wa-

*ACI Structural Journal*, V. 96, No. 6, November-December 1999.

Received March 10, 1998, and reviewed under Institute publication policies. Copyright © 1999, American Concrete Institute. All rights reserved, including the making of copies unless permission is obtained from the copyright proprietors. Pertinent discussion will be published in the September-October 2000 *ACI Structural Journal* if received by May 1, 2000.

**Rajan Sen** is the Samuel and Julia Flom Professor in Civil and Environmental Engineering at the University of South Florida, Tampa, Fla. He is a member of ACI Committee 440, Fiber-Reinforced Polymer Reinforcement.

**Mohsen Shahawy** is the director of the Structural Research Center of the Florida Department of Transportation, Tallahassee, Fla. He is a member of ACI Committee 440, Fiber-Reinforced Polymer Reinforcement.

**Gray Mullins** is an assistant professor in the Department of Civil and Environmental Engineering at the University of South Florida.

**John Spain** is with PSI Environmental Geotechnical Construction, New Haven, Conn. He received his MSCE in civil engineering at the University of South Florida, in 1997.

ter/cement ratio ( $w/c$ ).<sup>9</sup> In applications involving flexural members, permeabilities are likely to be much higher because of cracking. Mismatches in permeabilities result in accelerated corrosion of steel in chloride-contaminated concrete. The resulting volume increase can set up internal stresses that can lead to debonding of the CFRP sheet material.

Information on long-term moisture absorption characteristics of CFRP/epoxy/concrete systems in harsh marine environments is very limited. What is known, however, is that moisture absorption increases under wet/dry cycles because of progressive microstructure damage.<sup>10</sup> A measure of absorption levels can be obtained from recently published test results that showed that CFRP/epoxy composites absorbed 1% moisture by weight after 9 years of exposure in outdoor tropical environments.<sup>11</sup>

It is evident that both temperature increase and moisture absorption lead to volume increases at the epoxy/concrete interface. More importantly, under normal service conditions both effects act simultaneously. Therefore, the combined effect of wet/dry cycles and thermal cycles on the CFRP/epoxy/concrete bond is of critical importance and needs to be carefully evaluated. This was an important objective of the study.

### OBJECTIVES

The objective of the study was to assess the likely long-term performance of epoxy systems that had actually been used to repair bridge elements in the State of Florida. An equally important objective was to quantify bond deterioration in terms of residual

strength so as to provide a measure of the degradation caused by exposure.

The primary objectives of the study can be summarized as follows:

1. To investigate the performance of five different epoxy systems used for bonding CFRP to concrete in conditions characteristic of marine environments.

2. To quantify the degradation in bond strength in terms of changes in tensile and shear resistance relative to that of unexposed controls.

As surface preparation and workmanship are critical parameters for bond integrity, their role in the performance of the CFRP/epoxy/concrete bond was also examined.

### RESEARCH SIGNIFICANCE

This paper provides unique results relating to the exposure of five different epoxy systems to different environments characteristic of the application of CFRP for the external repair of highway structures in subtropical environments. The study is believed to be the first to quantify bond degradation in terms of changes in tension/shear strength at the bond line.

### EXPERIMENTAL PROGRAM

#### Specimens

Two different carbon fibers—bidirectional woven fabric and unidirectional carbon fiber prepreg sheets—were investigated in the study. A total of 24 specimens were prepared by bonding the two carbon-fiber types to concrete slabs using five different epoxy systems (Table 1). These systems identified by the Roman numerals I-V comprised commercially developed systems as well as others that were under development.

Although there are subtle differences in the manufacturer's installation procedures, the basic steps are as follows:

1. Grind/abrade the concrete surface to remove debris or coatings, to level the surface, and to form a radius on corners when wrapping CFRP around sharp edges.
2. Coat the dry clean surface with the respective manufacturer-supplied epoxy-based primer.
3. Fill voids with an epoxy-based putty (optional).
4. Roll on an undercoating of epoxy resin to all bond surfaces.



(a) Minor defects at edges of CFRP.



(b) Frayed corner from poor top coat.



(c) Loose edge of CFRP.



(d) Loose corner of CFRP.

Fig. 1—Defects in as-received specimens.



5. Cut-to-size, align, and install the carbon fiber sheets rolling out any entrapped air bubbles (note: keep sheet sizes manageable).

6. Roll on a generous topcoat of epoxy resin to seal in and fully saturate the carbon fiber sheets.

All specimens were prepared by the Florida Department of Transportation in Tallahassee and shipped to the University of South Florida where the testing was carried out. The concrete slabs were each 455 x 455 mm in plan with the thickness varying between 75 and 95 mm. Details of the specimens are summarized in Table 1. Inspection of Table 1 shows that both single-layer and double-layer applications were considered for each type of carbon fiber.

**Table 1—Specimen details**

Epoxy system	Identifier	No. of specimens	Carbon fiber type	No. of carbon layers
I	FA2	6	Bidirectional	1 or 2
II	FAHP2	4	Bidirectional	2
III	FAH2	6	Bidirectional	1
IV	T2	4	Unidirectional	1 or 2
V	MP2	4	Unidirectional	1 or 2

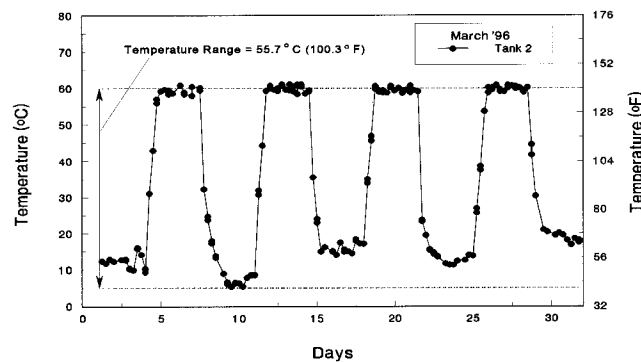


Fig. 2—Typical temperature time history of bond exposure spec-

## Initial inspection

Before exposure, all specimens were carefully inspected to identify and catalogue any existing defects. No evidence of debonding could be detected; however, minor defects were found at the CFRP/concrete corners and edges in four specimens from the FAH2 and FAHP2 series. These are shown in Fig. 1.

## Exposure

Four different exposures were investigated. These were: a) combined wet/dry cycles and hot/cold cycles in 5% salt-water termed bond; b) wet/dry cycles in 15% salt water termed durability; c) outdoor conditions, termed outdoor; and d) air-conditioned laboratory termed control.

Exposures (a) and (b) were identical to that used recently to investigate the durability of CFRP pretensioned beam elements.<sup>12-13</sup> Unlike the beam specimens, however, there was no splash-zone and the slab specimens were either completely submerged or completely dry during the wet/dry cycles.

In the bond exposure, saltwater in the tanks containing the slab specimens was heated to 60°C at high tide. At low tide, the tank was left uncovered to allow for rapid humidity and temperature change. Figure 2 shows the variation in the saltwater temperature with time. Inspection of Fig. 2 shows that during a cold spell around March 10, the temperature range was at its most extreme. Much smaller ranges were recorded towards the end of the month when ambient temperatures were higher.

## RESULTS

The durability and bond exposures had to be terminated after 17 months because of technical problems associated with the hot/cold cycles. At this time, all 24 specimens were reinspected for signs of deterioration of the CFRP/epoxy/concrete bond. This provided a qualitative in-place measure of the state of bond after exposure.

To provide a quantitative measure of degradation, two devices were developed to measure the tensile and shear capacity of the CFRP/epoxy/concrete bond.<sup>14</sup> These devices took six months to perfect, during which time the outdoor and laboratory exposures continued. At the end of this period, all 24 specimens were tested to determine their tensile and shear bond strength. Thus, the qual-

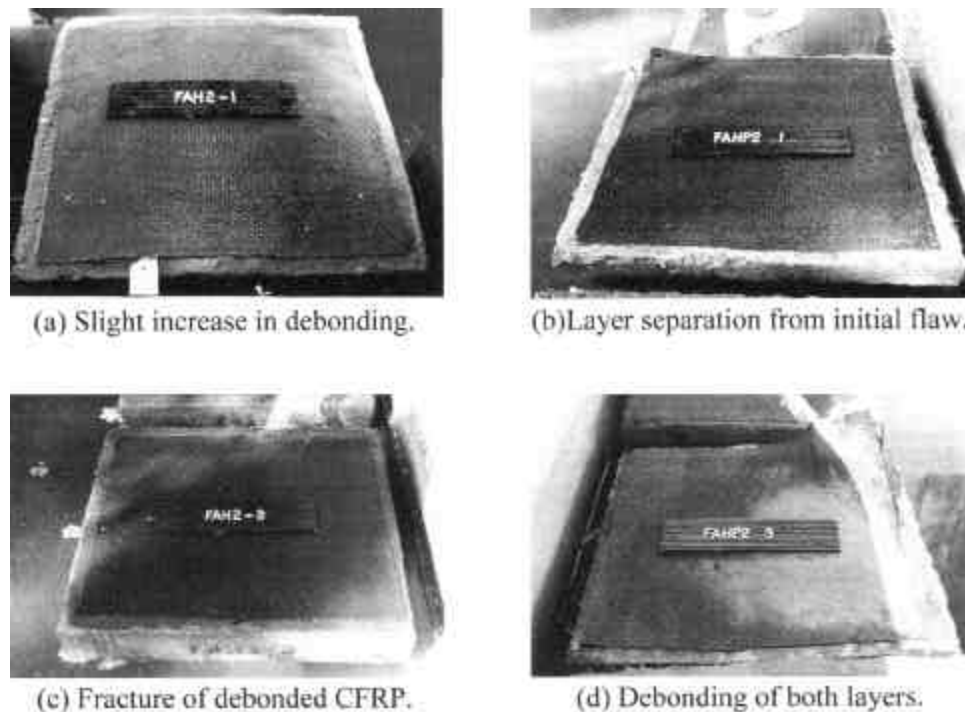


Fig. 3—Deterioration in epoxy bond due to 17 months exposure.

itative results relate to 17 months of exposure for all specimens. The quantitative results, however, relate to 17 months exposure for the durability and bond specimens (with an additional six-month outdoor exposure before testing), and 23 months of continuous exposure for the outdoor and control specimens.

**Qualitative observations**

Deterioration in bond was only observed in the four specimens identified as having initial defects. Exposure generally resulted in increases in the extent of the initial defect. The most extensive increase was recorded for specimen FAHP2-3 exposed to wet/dry cycles. Only the specimens having bidirectional CFRP fabric experienced deterioration. Details are in Table 2 and Fig. 3.

**Quantitative results**

To obtain a quantitative measure of bond degradation, destructive torsion and tension tests were conducted on all 24 specimens. In the tests, a 50 mm metal disk called a dolly was

bonded to the CFRP surface using epoxy and a water-flushed, diamond-tipped core barrel was used to score around the metal disk through the CFRP (Fig. 4 through 6). Each dolly was either subjected to tension or torsion. Center-drilled and tapped dollies were used for tension tests; all others were equipped with a hexagonal upper surface for torsional shear tests. Figure 4 shows nine dollies bonded to the CFRP-covered concrete. Five of the nine were prepared for tension testing, the other four for torsion testing (hexagonal upper surface).

The tests were conducted using specialized devices developed at the University of South Florida (Fig. 7 and 8). Torsional shear stresses were induced at the bond line by applying a torque to the dolly via a 25 mm diameter instrumented shaft that was in turn connected to a hydraulically activated lever arm. The torque was continuously monitored with a MEGADAC Series 5100 computerized data acquisition system. The failure torque ( $T$ ) was then used to determine the maximum torsional shear stress ( $\tau$ ) at the outer radius ( $r$ ) of the dolly (where  $\tau = Tr/J$  and  $J$  is the polar moment of inertia of the dolly). Uniaxial tension tests were also monitored in a similar fashion, but used an axial load cell, LVDT, and a portable hand-operated tension frame; the peak axial stress was determined by calculating the quotient of the peak load and the dolly surface area. Complete details on these devices and procedures used may be found elsewhere.<sup>14,15</sup>

Under the action of tensile or shear loads, five different failure modes can occur (see Fig. 9). These are: 1) debonding of the dolly—this means that the strength of the epoxy bond between the dolly and the CFRP material was too low; 2) complete deb-

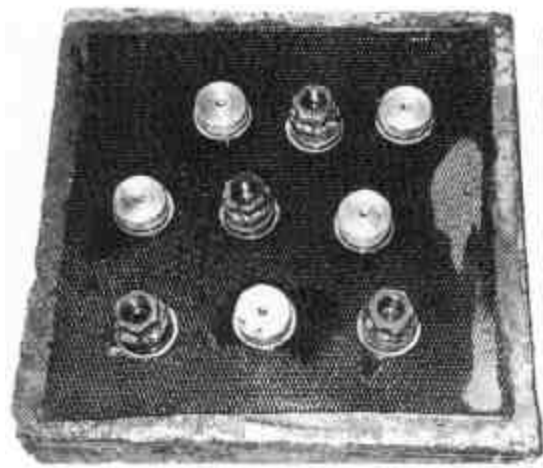


Fig. 4—Tension and torsion dollies bonded to CFRP.

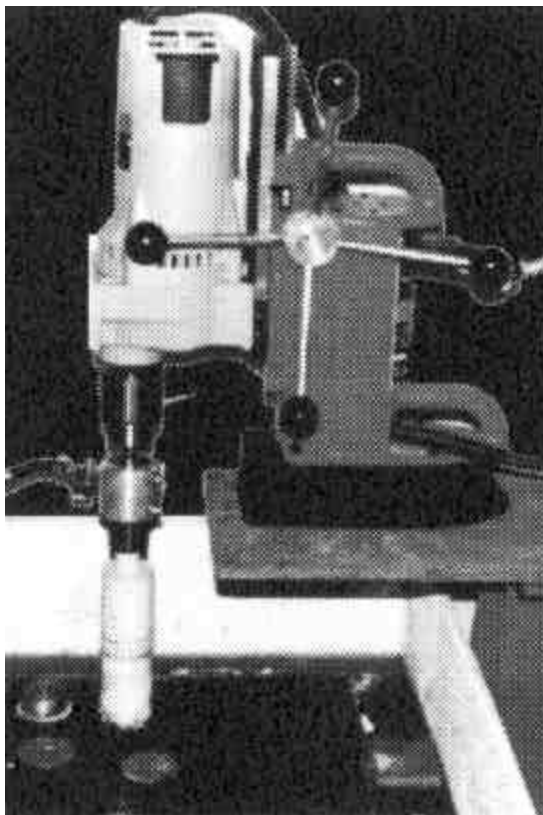


Fig. 5—Scoring CFRP.

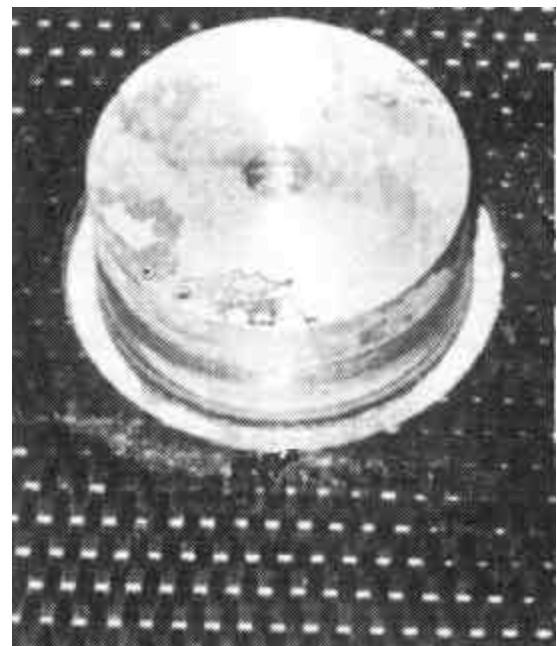


Fig. 6—Bonded dolly and scored CFRP.

**Table 2—Summary of 17 months qualitative results**

Identifier	Exposure	Epoxy	Defective	Comments
FAH2-1	Durability (Fig. 3(a))	III	Yes	Slight increase in extent of debonding
FAHP2-1	Bond (Fig. 3(b))	II	Yes	Separation of layers from location of initial flaw
FAH2-3	Bond (Fig. 3(c))	III	Yes	Propagation of debonding and fracture of CFRP from location of original defect
FAHP2-3	Durability (Fig. 3(d))	II	Yes	Greatest increase in extent of separation between two layers from location of initial flaw

onding of the CFRP from the concrete—this gives the bond strength; 3) partial debonding of the CFRP/concrete bond; 4) separation of the CFRP layers—this indicates that bond between the two CFRP layers was weaker than the epoxy/concrete bond—only possible for FA2, FAHP2, T2, and MP2 series (see Table 1) where two layers were present; and (5) failure in the concrete—this only indicates that the epoxy bond was at least as strong as the concrete.

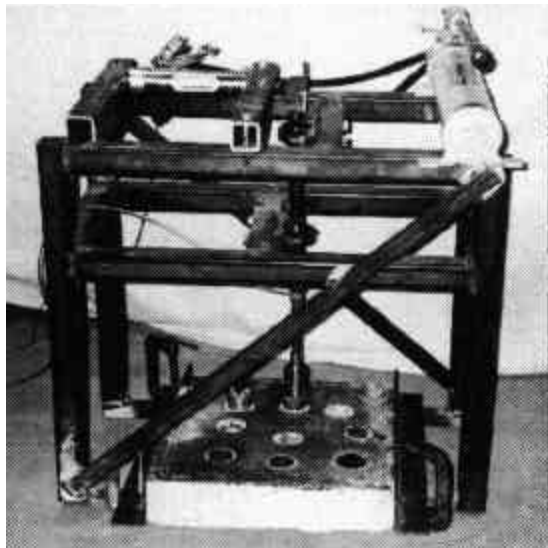


Fig. 7—Torsional shear apparatus.

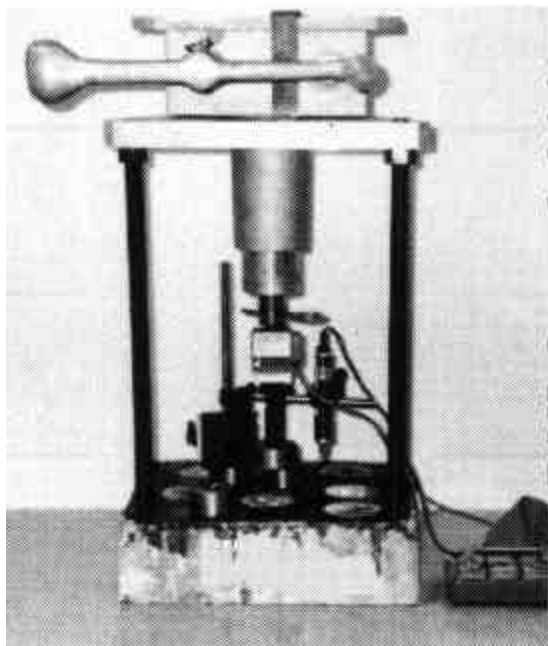


Fig. 8—Tension test apparatus.

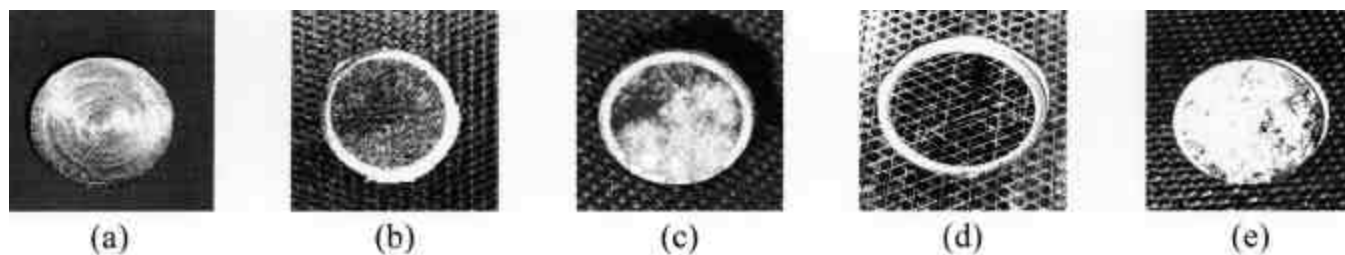


Fig. 9—Possible failure modes: (a) dolly bonded; (b) epoxy bonded; (c) partial debonded; (d) sheet separation; and (e) concrete fail-

Tension and torsion tests were conducted on all 24 specimens including the five controls. On an average, two tension and two torsion tests were carried out on each specimen. Altogether, a total of over 100 tests were carried out. The test results for all the specimens are summarized in Table 3. For each specimen, an estimate of the extent of debonding where partial debonding was observed is provided (see Fig. 9[c]). Additionally, the tensile load, the torsional moment, the corresponding computed stresses at the bond line, and average tensile and shear stress values are also included.

Compared to the qualitative results where degradation was only observed in specimens that were blemished before exposure (see Table 2), the quantitative results provided evidence of deterioration in an additional fourteen specimens. Several specimens from the bond (FA2-1, FA2-3, FAHP2-1) and durability (FAH2-4) exposures debonded completely under both tensile loads and torsional moments. Durability specimen FAHP2-3 completely debonded in tension and would most likely have debonded in torsion; however, the sheets were too badly separated to prepare a torsion sample (see Fig. 3). In addition, one specimen exposed outdoors (FA2-4) also debonded completely under torsion.

None of the five controls debonded completely under shear or torsion. Three control specimens experienced only partial debonding under tension loads (FA2-6, FAHP2-2, MP2-1) and one (FA2-6) under torsional moment. In cases of partial debonding, the surface of the concrete was found to be uneven and the epoxy remained in the debonded locations (Fig. 10). This indicated that partial debonding may have been the result of the CFRP not being bonded to the concrete surface in the first place. In contrast, the exposed concrete surface in cases of complete debonding was found to be smooth (see Fig. 11).

It is evident that where failure occurred in the concrete, no estimate can be made of the extent of degradation in the epoxy/concrete bond. Where there was partial or complete debonding, however, a measure of degradation can be obtained by comparing the relative failure loads of the exposed and control specimens. Such an assessment makes the important assumption that all specimens belonging to the same series were identically prepared and were bonded to identical slabs having the same tensile and shear strengths.

The average results of the tension and torsion tests in Table 3 have been replotted in Fig. 12 through 16 to provide an assessment of the extent of degradation in the epoxy/CFRP bond due to exposure. In these plots, the residual bond strength of the exposed specimens is the ratio of its failure load to that of the control when there was some evidence of debonding, for example, FA2-1 had a residual strength of 86% in tension because it failed at a load of 6.7 kN compared with 7.8 kN for the control. Similarly, its residual torsional resistance is 60% (ratio of 176 N-m to 294 N-m for the control). Where there was no debonding, however, the residual strength was taken as unity, that is, T2-4. In this case, the test results simply showed that the bond strength still exceeded the concrete strength.

Inspection of Fig. 12 through 16 indicates that, compared with the controls, there was some degradation in the epoxy/concrete bond in all exposures with the exception of specimen FAHP2-4

(Fig. 13) and all the T2 specimens (Fig. 15). This is in marked contrast to the results from visual inspection where similar degradation could not be discerned.

The overall trend in bond degradation for all the specimens relative to that of the controls is shown in Fig. 17. Inspection of Fig. 17 shows that exposure to wet/dry cycles (in the bond or durability exposures) tended to lead to greater degradation than outdoor exposure. This suggests that moisture absorption, not the mismatch in the thermal expansion coefficients between the CFRP, epoxy, and concrete, was more critical for long-term performance. A similar finding was also made in the exposure tests carried out on CFRP pretensioned beam specimens.<sup>12-13</sup>

**DISCUSSION**

This paper presents results from a study that attempted to evaluate the extent of degradation in the CFRP/epoxy/concrete bond in five epoxy systems that had been exposed to four different environments simulating a range of indoor and outdoor applications. In the investigation, bond degradation was evaluated on the basis of both visual inspection and destructive testing.

Visual examination led to the detection of degradation in only four specimens—two each from the bond and durability exposures that had been identified as blemished before exposure (Fig. 1). No deterioration was found in any of the controls or the outdoor specimens that had been exposed for a longer period. In contrast, destructive tension and shear tests detected degradation in an additional fourteen specimens including 60% of control and outdoor specimens (Table 3). Bond degradation could

not be determined in six of the 24 specimens as the residual bond strength exceeded the concrete strength. It is evident, therefore, that visual examination may not be reliable in identifying bond degradation.

It can be tempting to rank the performance of the various epoxy systems on the basis of the results obtained from the study. Such a ranking would be valid if all specimens tested had been prepared exactly in accordance with the manufacturer's recommendations. Examination of the failure interface obtained from tension and shear tests showing partial debonding and fiber separation provide compelling evidence to the contrary. This indicated that despite laboratory conditions, surface preparation had been improper in some cases; partial debonding was generally the result of an uneven concrete surface and was a di-



Fig. 10—Partial debonding.

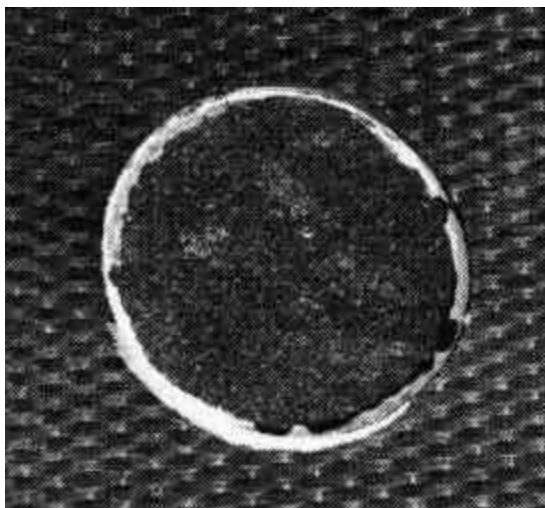


Fig. 11—Complete debonding.

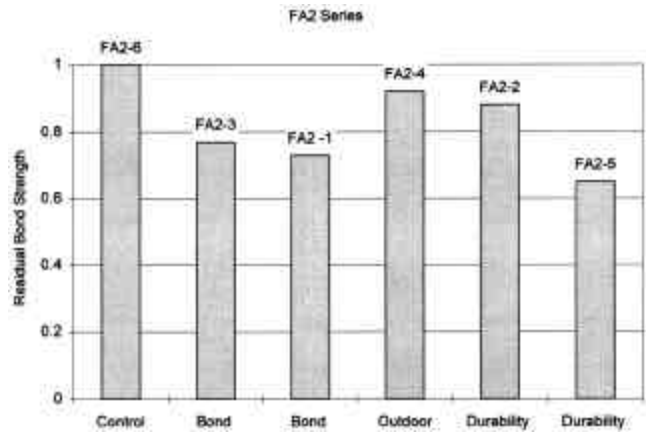


Fig. 12—Performance of epoxy System I.

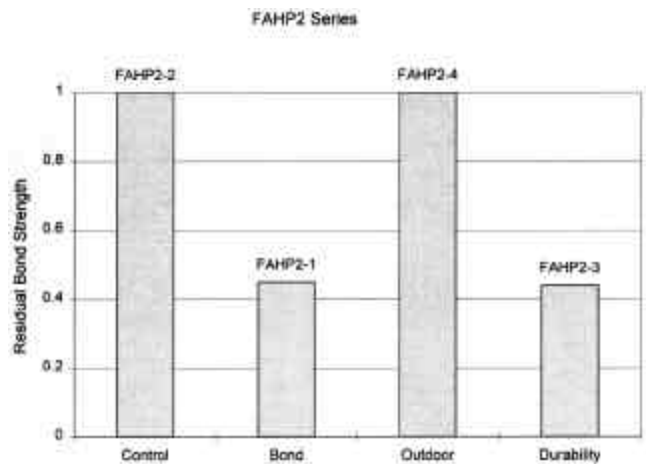


Fig. 13—Performance of epoxy System II.

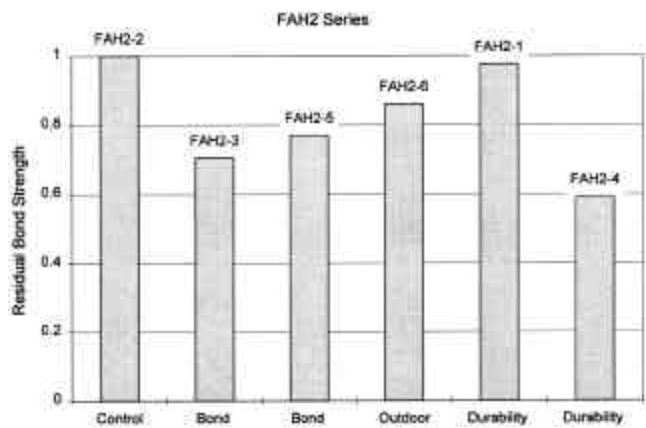


Fig. 14—Performance of epoxy System III.

Table 3—Summary of results

Identifier	Epoxy	Exposure	Tension					Torsion				
			kN	$\sigma^*$ (MPa)	$\sigma_{avg}$ (MPa)	% debond	Average % debond	N-m	$\tau^*$ (MPa)	$\tau_{avg}$ (MPa)	% debond	Average % debond
FA2-6	I	Control	7.7	3.8	3.9	40	33	369	14.3	11.4	0	25
			7.0	3.4		30		220	8.5		50	
			8.8	4.3		30						
FA2-1	I	Bond	5.3	2.6	3.3	100	100	172	6.7	6.8	100	100
			8.2	4.0		100		179	6.9		100	
FA2-3	I	Bond	5.5	2.7	2.8	100	100	248	9.6	9.1	100	100
			6.0	3.0		100		222	8.6		100	
FA2-2	I	Durability	9.1	4.5	4.3	20	30	271	10.5	8.6	70	55
			8.3	4.1		40		174	6.7		40	
FA2-5	I	Durability	1.9	0.9	1.8	100	80	153	6.0	6.8	30	35
			5.5	2.7		60		195	7.6		40	
FA2-4	I	Outdoor	8.9	4.4	3.8	90	77	270	10.5	9.6	100	100
			5.1	2.5		100		222	8.6		100	
			9.2	4.5		40						
FAHP2-2	II	Control	11.8	5.8	5.4	0	25	339	13.2	13.0	0	0
			9.8	4.9		50		331	12.9		0	
FAHP2-1	II	Bond	3.0	1.5	2.1 (4.3)	100	100	168	6.5	6.5	100	100
			5.6	2.8		100						
FAHP2-3	II	Durability	4.2	2.1	2.4	100	100	No sample left to be tested				
			5.3	2.6		100						
FAHP2-4	II	Outdoor	4.9	2.4	3.2	50	17	248	9.6	9.6	0	0
			8.2	4.1		0						
			7.2	3.5		0						
FAH2-2	III	Control	8.6	4.2	3.5	0	0	232	9.0	9.8	0	0
			5.6	2.8		0		274	10.6		0	
FAH2-3	III	Bond	6.8	3.4	3.4	40	13	277	10.7	10.8	50	45
			6.7	3.3		0		281	10.9		40	
			7.4	3.6		0						
FAH2-5	III	Bond	9.3	4.6	4.4	100	95	346	13.4	13.3	60	60
			8.7	4.3		90		340	13.2		60	
FAH2-1	III	Durability	13.2	6.5	6.2	10	5	359	14.0	16.2	0	0
			11.9	5.9		0		475	18.4		0	
FAH2-4	III	Durability	7.2	3.6	3.8	100	100	153	6.0	9.1	100	100
			8.3	4.1		100		226	8.8		100	
								323	12.5		100	
FAH2-6	III	Outdoor	9.2	4.6	4.4	70	60	353	13.7	14.0	0	0
			8.5	4.2		50		370	14.4		0	
T2-2	IV	Control	12.2	6.0	5.8	0	0	452	17.5	16.5	0	0
			11.5	5.7		0		400	15.5		0	
T2-4	IV	Bond	11.4	5.6	6.0	0	0	416	16.2	15.6	0	0
			12.9	6.4		0		388	15.1		0	
T2-3	IV	Durability	13.0	6.5	5.6	0	0	410	15.9	16.3	0	0
			9.6	4.7		0		430	16.7		0	
T2-1	IV	Outdoor	8.3	4.1	4.5	0	0	401	15.6	15.5	0	0
			9.7	4.8		0		397	15.4		0	
MP2-1	V	Control	4.2	2.1	2.4	0	10	258	10.0	9.9	0	0
			6.3	3.1		0		251	9.8		0	
			4.3	2.1		30						
MP2-2	V	Bond	10.2	5.0	3.3	0	0	85	3.3	6.1	0	0
			3.2	1.6		0		231	9.0		0	
MP2-3	V	Durability	3.7	1.8	2.6	0	10	144	5.6	5.9	0	30
			9.2	4.5		30		161	6.3		60	
			3.1	1.5		0						
MP2-4	V	Outdoor	3.5	1.7	2.4	0	0	400	15.5	9.6	0	30
			9.7	4.8		0		94	3.6		60	
			1.4	0.7		0						

\*Note:  $\sigma = P/A$ , where  $A = 0.001963 \text{ m}^2$ ; and  $t = Tr/J$ , where  $r = 0.025 \text{ m}$ ,  $J = 6.14\text{E-}7 \text{ m}^4$ .

rect consequence of only partial contact between the CFRP and epoxy. It is believed that had a filler material been used to smooth the surface, results would have been better. Similarly, in cases of sheet separation (Fig. 9) observed particularly in the MP2 specimens (Epoxy System V), the carbon fibers in the first layer were dry and had not been properly impregnated with resin.

In the testing, the specimens belonging to the T2 series fared the best with no evidence of bond degradation from any of the exposure schemes (Fig. 15). This, however, was attributed to the visually apparent high quality of workmanship. It is conceivable, however, that longer exposure times could eventually degrade this bond to a detectable level, even though none could be shown herein.

Although both tension and shear tests were conducted, the latter are more representative of stresses that typically need to be transferred by the epoxy to the CFRP. The results indicated that the computed failure stresses under shear were significantly higher than those in tension (see Table 3), a trend observed in similar tests on repaired concrete.<sup>16</sup> As a result, whereas there was partial or complete loss of bond in 18 tension test specimens, only 12 of the same specimens failed in a similar manner in shear (Table 3).

The disparity in failure stresses is not surprising given that concrete's shear strength exceeds its tensile strength. While the tensile strength varies between 8 to 15% of concrete's compressive strength,<sup>17</sup> the shear strength is estimated to be about 20 percent of the same value.<sup>18</sup> Thus, the results of tensile bond tests provide only a lower bound of the available bond strength for flexural applications. For this reason, tensile bond failures do not necessarily imply that bond is impaired for transferring shear.

Although the tension and shear tests carried out are destructive, only a small area of the slab is affected. By reapplying the CFRP to the location where it was removed and providing adequate lap length, the original capacity can be restored.

**CONCLUSIONS**

This paper presents results from an exposure study in which five different epoxy systems bonding CFRP to concrete were evaluated. Exposure comprised four different environments simulating indoor and outdoor conditions in tropical coastal regions for a period ranging between 17 and 23 months. Both qualitative and quantitative measures were used to evaluate the CFRP/epoxy/concrete bond.

The following conclusions may be drawn:

1. Visual examination cannot recognize the full extent of bond degradation. In the study, only four cases of bond degradation were detected by visual examination, which were limited to specimens that were blemished before exposure. This amounted to only 22% (four out of 18) of the all specimens that were found to have developed bond degradation. With respect

to workmanship, visual examination is a primary mechanism for detecting flaws; postmortem inspection of partially and completely debonded test specimens suggested that departures from recommended installation procedures accounted for these failures.

2. Destructive tension and torsion tests provide a more reliable measure of bond degradation not detectable from visual inspection. Tension testing caused debonding in more specimens at lower failure stresses than torsion testing and consequently provided more pessimistic measures of bond degradation. Therefore, torsional shear testing that consistently produced higher stresses at the bond line is more appropriate for detecting bond degradation in flexural applications.

3. Bond degradation was least for outdoor exposure and greatest under wet/dry cycles. This suggests that moisture absorption by the epoxy is potentially more detrimental to bond durability where CFRP is used for repair.

4. Surface preparation and proper application of epoxy following recommended procedures is essential for the long-term integrity of the CFRP/epoxy/concrete bond. In the tests, bond deterioration was compounded at locations where there were initial blemishes. Such damage can be readily detected from careful visual and tactile inspection that should be routinely carried out during repair.

Overall, the results are quite encouraging given the severity of the exposure conditions investigated. The extreme temperature range and humidity the specimens were subjected to are far more severe than could be reasonably expected under normal service conditions. In spite of this, bond degradation was minimal, especially in specimens that had been prepared properly. What is particularly gratifying is the satisfactory performance of all the five disparate epoxy systems that were tested. This indi-

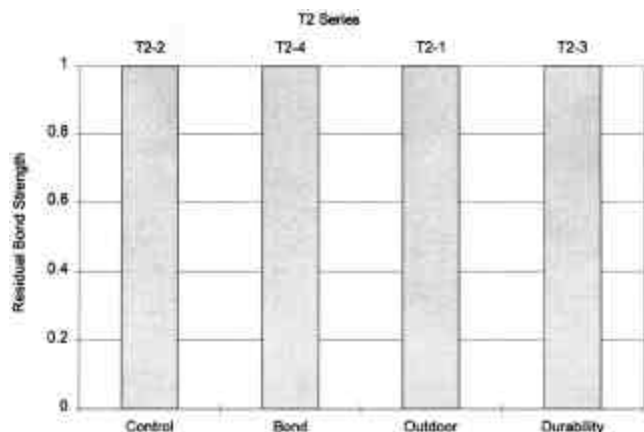


Fig. 15—Performance of epoxy system IV.

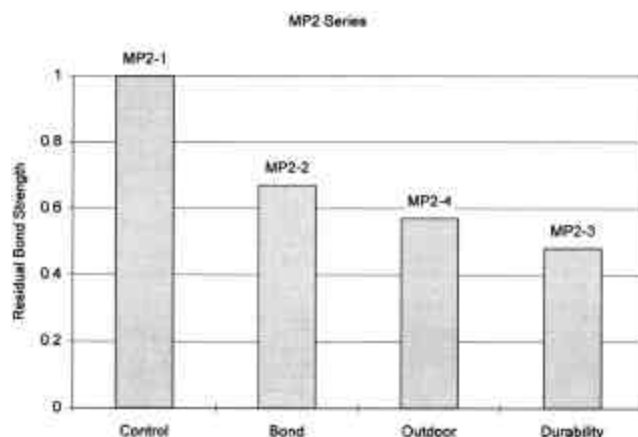


Fig. 16—Performance of epoxy System V.

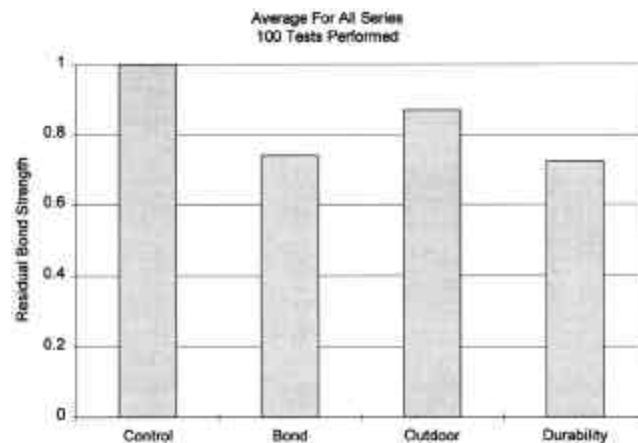


Fig. 17—Results summary.

cates the availability of competing epoxy systems that can lead to equally durable repairs under very harsh environments. Such availability is likely to have a positive long-term effect on the economy of repairs.

The durability of epoxy systems observed in this investigation is not altogether surprising. Epoxy's crosslink structure ensures high chemical resistance and makes it durable in aggressive environments. In bridge applications, epoxy-bonded steel plates have a long history of successful performance.<sup>19</sup>

## ACKNOWLEDGMENTS

This study was funded in part by the Florida Department of Transportation. The opinions, findings, and conclusions expressed in this publication are those of the writers and not necessarily those of the Florida Department of Transportation. Additional support was provided by the Department of Civil Engineering, University of South Florida. This support is gratefully acknowledged. The writers acknowledge the contribution of graduate students Al Hartley, Jose Rosas, Hasan Shaffee, and Steve Johnson.

## REFERENCES

1. "Non-Metallic Reinforcement for Concrete Structures," *Proceedings of the Third International Symposium on Non-Metallic (CFRP) Reinforcement for Concrete Structures*, Sapporo, Japan, Oct. 1997, Japan Concrete Institute, V. 1, Strengthening Applications, pp. 587-646.
2. "Fiber Composites in Infrastructure," *Second International Conference on Composites in Infrastructure ICCI '98*, V. 1, H. Saadatmanesh and M. Ehsani, eds., Tucson, Ariz., Jan. 1998, Part II, Repair and Retrofit, pp. 113-340.
3. *Revitalizing Concrete Structures*, Replark, Mitsubishi Chemical Corp., Tokyo, Japan, 4 pp.
4. Toutanji, H., and El-Korchi, T., "Tensile Durability Performance of Cementitious Composites Externally Wrapped with FRP Sheets," *Second International Conference on Composites in Infrastructure, ICCI '98*, H. Saadatmanesh and M. Ehsani, eds., Tucson, Ariz., Jan. 1998, V. 2, pp. 410-422.
5. Steckel, G.; Hawkins, G.; and Bauer, J., "Environmental Durability of Composites for Seismic Retrofit of Bridge Columns," *Second International Conference on Composites in Infrastructure, ICCI '98*, H. Saadatmanesh and M. Ehsani, eds., Tucson, Ariz., Jan. 1998, V. 2, pp. 460-475.
6. Hancox, N. L., and Mayer, R. M., *Design Data for Reinforced Plastics*, Chapman and Hall, 1994, London.
7. Priestley, M. J. N., "Thermal Response of Concrete Bridges," *Concrete Bridge Engineering: Performance and Advanced*, R. J. Cope, ed., Elsevier Applied Science, London, 1987, pp. 143-188.
8. National Climatic Data Center, "Climatic Averages and Extreme Temperatures for US Cities," Asheville, 1991.
9. Mindess, S., and Young, J., *Concrete*, Prentice-Hall, Englewood Cliffs, N.J., 1981.
10. Delasi, R. J.; Whiteside, J. B.; and Wolter, W., "Effects of Varying Hygrothermal Environments on Moisture Absorption in Epoxy Composites," *Fibrous Composites in Structural Design*, E. M. Lenoe; D. W. Oplinger; and J. J. Burke, eds., Plenum Press, New York, 1980, pp. 809-818.
11. Chester, R. J., and Baker, A. A., "Environmental Durability of F/A-18 Graphite Epoxy Composite," *Polymers and Polymer Composites*, V. 4, No. 5, 1996, pp. 312-323.
12. Sen, R.; Shahawy, M.; Rosas, J. and Sukumar, S., "Durability of CFRP Pretensioned Elements in Marine Environment," *ACI Structural Journal*, V. 95, No. 5, Sept.-Oct. 1998, pp. 578-587.
13. Sen, R.; Shahawy, M.; Sukumar, S.; and Rosas, J. "Durability of CFRP Pretensioned Elements under Tidal/Thermal Cycles," *ACI Structural Journal*, V. 96, No. 3, May-June 1999, pp. 450-457.
14. Mullins, A. G.; Sen, R.; and Spain, J., "Testing of CFRP/Concrete Bond," *ICCI '98, Second International Conference on Composites in Infrastructure*, H. Saadatmanesh and M. Ehsani, eds., Tucson, Ariz., Jan. 1998, pp. 211-218.
15. Spain, J., "CFRP/Concrete Bond under Shear and Tension," MSCE thesis, University of South Florida, Tampa, Fla., Dec. 1997.
16. Emmons, P. H., *Concrete Repair and Maintenance Illustrated*, R. S. Means, Mass., 1993, 158 pp.
17. MacGregor, J. G., *Reinforced Concrete*, 3rd Edition, Prentice-Hall, Englewood Cliffs, N.J., 1997.
18. Mindess, S., and Young, J., *Concrete*, Prentice-Hall, Englewood Cliffs, N.J., 1981.
19. Meier, U., "Strengthening of Structures with CFRP Laminates," *Advanced Composite Materials in Civil Engineering Structures*, S. Iyer and R. Sen, eds., ASCE, New York, pp. 224-232.



SP 188-35

## **New Device for In Situ Testing of Fiber Reinforced Polymer/Concrete Adhesion**

**by G. Mullins, R. K. Race, R. Sen, and J. From**

### **Synopsis:**

Fiber reinforced polymer (FRP) is proving to be increasingly cost-effective as a solution for the repair and rehabilitation of substandard concrete structures. As the integrity of the repair is dependent on the FRP/concrete bond, its evaluation for both acceptance and long-term maintenance purposes is of obvious importance.

FRP/concrete adhesion is currently evaluated from the more common tension test or the less used shear test. In either test, a metal disk called a dolly is bonded to the FRP surface. The force needed to separate the dolly under tensile or shear loads is used to determine the FRP-concrete interface adhesion. The similarity of the procedures for the two tests suggests it would be logical to develop a single device that could be used to conduct both in-situ tension and shear tests.

This paper describes the basis and development of a new device that allows both tension and shear tests to be carried out in-situ. The device is simple to use and only requires an instrumented socket wrench to apply the separation load. Preliminary results from tests carried out to assess the role of different surface finishes on the FRP/concrete bond are presented to demonstrate the application of the device.

**Keywords: adhesion; bond; carbon; concrete; repair; shear; tension**

**Gray Mullins** is an Assistant Professor in the Department of Civil and Environmental Engineering, University of South Florida, Tampa, FL

**Rob Race** is a Graduate Student in the Department of Civil and Environmental Engineering, University of South Florida, Tampa, FL

**Rajan Sen** is the Samuel and **Julia Flom** Professor in the Department of Civil and Environmental Engineering, University of South Florida, Tampa, FL

## INTRODUCTION

The increased use of fiber reinforced polymer (FRP) sheets in rehabilitation and retrofit of concrete *flexural* components has made the evaluation of the FRP/concrete bond an important consideration for design. The simplicity of the uniaxial tension test accounts for its widespread use for this purpose (1). In this test, a metal disk (*referred to as a 'dolly'*) is bonded to the FRP surface and the tensile force required for separation measured. The quotient of the separation load and the area of the dolly give the tensile bond stress. Despite its popularity, the results from this test may not be very meaningful since flexural load transfer relies on shear rather than tensile bond (2). More importantly, the low tensile strength of concrete generally leads to failure in the concrete so that the test only provides a *lower bound* on the true FRP/concrete interface bond value.

In 1996, the University of South Florida embarked on a program to develop equipment that would allow the FRP/concrete adhesion to be evaluated under shear loading. In the study, two devices were developed to permit evaluation under both direct and torsional shear. For the direct shear test, a core of the concrete specimen with the FRP material bonded to it was taken and tested in the laboratory using a specially developed direct shear box (3,4). This elaborate procedure made the direct shear test unsuitable for in-situ testing. In the torsional shear test, no coring was required and torque was directly applied to the dolly bonded to the FRP surface. This test was found to give good results. However, the equipment developed required an unwieldy reaction frame that made it less than ideal for in-situ testing.

In view of the similarity in the procedure for conducting tension and torsional shear tests, the possibility of developing a more manageable device to conduct in-situ tests appeared to be a logical extension of the earlier study. This paper describes the development of a simple device that utilizes two dollies and a socket wrench to determine the in-situ FRP/concrete tensile and shear bond. The basis for the equipment developed and the preliminary results are presented herein.

## TEST APPARATUS

Typically, devices for evaluating FRP/concrete adhesion consist of several essential components: (a) dollies, (b) a reaction frame, (c) a loading mechanism,

and (d) a load cell. In developing a device that could be used for in-situ shear and tension testing, radical changes were needed to earlier designs to minimize equipment mobilization and the affected testing area. The most significant of these changes was the introduction of an annular tension dolly that served as an alignment frame for the torsion test as well as fulfilling the requirement for the simple tension test. This not only made the device compact but more importantly permitted the use of an instrumented socket wrench for applying both shear and tension loads.

Shear and tension tests require separate dollies and therefore a device that conducts both tests also requires *two* dollies. The shape and dimensions of the dollies must be sized such that excessive force is not required to initiate separation. The choices of shapes conceptually entertained were (a) an inner circular disk, and outer annular disk or (b) two concentric annular disks. The first option was selected in part due to the availability of 50-mm diameter circular dollies (*with a welded hexagonal nut*) from the earlier study, but also it required one less step in scoring the FRP.

Since the concrete shear capacity is almost double its tensile capacity, the 50-mm diameter inner circular dolly was selected for the torsional shear test so that a single operator could manually produce the required separation torque. Due to the enormous mechanical advantage of the tension apparatus, virtually any size annular dolly could have been used. Hence, a commercially available 75-mm diameter, schedule 80 pipe nipple was selected which when cut in half, produced two tension dollies economically. The finished tension dolly had an external radius of 45-mm and an internal radius of 37-mm resulting in an adhesive surface area of 20.2 cm<sup>2</sup>. The use of this dolly configuration limited the area affected by destructive testing to less than 85 cm<sup>2</sup>.

As noted earlier, the annular tension dolly also serves as an alignment frame for the torsional shear test. To this end, two separate steel caps - one for torsion and one for tension - were fashioned from 75-mm end caps forming the nucleus of each testing device (see Figure 1). Both caps have openings for bolts that incorporate either a bushing to provide alignment during torsion, or threads to apply the required force during tension. For the shear test, a 22-mm bolt is inserted through the adjustable steel bushing of the shear cap and secured in the torsion dolly. Subsequent tightening of this bolt directly transmits torque into the shear dolly.

Once the shear dolly (inner) has failed, the shear cap and dolly are removed and a thrust bearing is seated in the position now vacated by the shear dolly (see Figure 2). The tension cap is then screwed onto the tension dolly. At this point in the testing procedure, the role of the tension dolly is transformed from a torsion alignment frame to a tension test specimen. Tension can now be applied to the outer dolly with a bolt threaded through the tension cap that bears on the thrust bearing assembly. As the bolt is turned, the applied rotation is translated into

linear motion placing the dolly in tension. Hence, the applied force on the tension dolly is indirectly determined from torque measurements. The entire time of testing requires less than five minutes. Figure 1 shows the actual equipment, whereas Figure 2 shows a schematic drawing of its components.

A critical requirement prior to tension testing was the calibration of the socket wrench to correlate applied torque on the bolt with equivalent tensile force on the dolly. For this purpose, strain gages - mounted in a full bridge configuration - were attached to a standard 150-mm long socket extension (see Figure 3). With the tension cap mounted on a reaction frame, the applied torque and corresponding tensile force was measured using the instrumented extension and load cell (see Figure 4). All data was automatically recorded with a MEGADAC computerized data acquisition system during calibration.

For machine design purposes, the tensile forces on the dolly were calculated using Eq. 1 from known values of torque, bolt and thread characteristics and the coefficient of friction of the bolt threads (4).

$$F = M / [r \tan(\theta + \alpha)] \quad (1)$$

In Eq. 1,  $F$  is the axial force developed in the bolt,  $M$  is the moment needed to impend motion or sustain uniform motion,  $R$  is the average of minimum and maximum bolt radii,  $\theta$  is  $\tan^{-1}(\mu)$  where  $\mu$  is the coefficient of static or kinetic friction and  $\alpha$  is the slope of bolt thread.

Several different thread conditions from oxidized, non-lubricated threads to clean, well-lubricated threads were tested. A new, non-lubricated bolt yielded a coefficient of friction value of approximately 0.27 in the first trial. As the threads became conditioned with each trial the coefficient of friction decreased. Lubricating the bolt yielded a coefficient of friction of approximately 0.19 after several trials. Therefore, the importance of using a properly conditioned and lubricated bolt should not be underestimated. Ultimately, the measured torque vs. force function (1.0 N-m torque corresponds to a 447 N tensile force) was regressed from data obtained from numerous calibration cycles.

### TEST PROGRAM

A systematic test program was completed to evaluate the effectiveness of the new device in measuring the FRP/concrete bond in shear and tension. Over a hundred tests were conducted during the development of this test mechanism/procedure. Forty-seven of these tests reflect the final testing procedure adopted herein.

#### Specimen Preparation

Before the dollies can be bonded to the FRP surface, their outline had to be scored. This was carried out in a jig using a laminate trimmer (see Figure 5) fitted

with an 8-mm (5/16-inch) carbide bit. When scoring was complete, the adhesive surface of the CFRP and the dollies were lightly sanded and cleaned with acetone. The dollies were then positioned on the CFRP using Sikadur 32 Hi-Mod epoxy adhesive. All adhesives were cured for a minimum of 7 days prior to testing.

### Test Procedure

After the dollies have fully bonded to the FRP surface, the shear device is assembled (Figure 2). A 22-mm bolt is then inserted through the shear cap bolt guide (bushing) and threaded into the shear dolly. Once the bolt is securely threaded into the shear dolly, the bolt guide is tightened in-place to prevent lateral movement or bending during testing. A socket attached to a 13-mm socket wrench via the instrumented extension is placed over the head of the bolt. Using the tension dolly as an alignment anchor, torque is increased on the bolt head smoothly and continuously until shear failure occurs. The output of the instrumented extension is continuously monitored to detect the peak torque applied. Figure 6 shows typical results from the shear testing portion of the procedure.

Upon completion of the torsion test the shear cap, dolly and any debris are removed from the center of the annular tension dolly. The thrust bearing is then inserted as previously described and the tension cap installed. A 19-mm fully-threaded bolt is advanced by hand until it contacts a recess on the top of the thrust bearing assembly. Using the instrumented wrench previously described, a tension force is now applied and recorded by way of torque measurements. As the bolt is tightened, the tension dolly is axially stressed and separates; the tension cap and thrust bearing are removed and the failure mode noted. Curves similar to Figure 6 are also obtained from tensile tests; they differ only in that must be converted from torque to tensile load as previously described.

## RESULTS

Table 1 summarizes results obtained from 25 shear and 22 tension tests conducted on a total of 26 specimens. Values reported are *average* from each of the six series reported. Specimen labels identify surface treatment, substrate material, and CFRP type. N denotes no treatment, M - mechanically abraded, and W - water blasted. The two substrate identifiers indicate their nominal strength in ksi for masonry (3) and concrete (5). The CFRP types were either balanced or unbalanced weaves, denoted by B and U, respectively. Water blasted surfaces were prepared using a portable pressure washer while the mechanically abraded surfaces were prepared with a belt sander.

As no instances of complete debonding were recorded, definite pronouncements relating to the magnitude of the CFRP/concrete adhesion cannot be made. However, the results indicate that surface preparation had varied effects dependent on the substrate type. For the masonry substrate, water blasting

consistently produced lower shear values and mechanical abrasion higher values or no effect when compared to the controls with no treatment. Alternately, water blasting produced higher shear values on the concrete substrate whereas mechanical abrasion resulted in lower values.

### CONCLUSIONS

This paper describes the basis and development of a new device that may be used to conduct in-situ shear and tension tests to evaluate the integrity of the FRP/concrete bond. The device is compact, inexpensive and light-weight. The prototype only weighed 31 N (7 lbs) making it suitable for outdoor use. Moreover, a single conventional socket wrench is used to apply *both* shear and torsion loads.

Application of the device to shear and tension testing proved to be fairly straightforward. The device was used to investigate the effect of surface preparation on the bond between CFRP and concrete. Both balanced and uni-directional CFRP materials were tested.

Preliminary results suggest that water blasting of the substrate prior to application of the CFRP led to greater bond strength for concrete when compared to mechanical abrading or no treatment. The reverse was true for masonry. These results imply that an optimal surface roughness produces the best bonding condition. This was also noted in the development of the dolly surfaces where surfaces too rough or too smooth would not effectively transfer stress to the FRP.

### ACKNOWLEDGEMENTS

The authors gratefully acknowledge the advice and support of Dr. Howard Kliger. Tonen Corporation of Japan donated materials tested. This support is gratefully acknowledged.

### REFERENCES

1. Steele, J. 1994. "Testing Adhesion of Concrete Coatings Applied to Concrete," *Materials Performance*, Vol. 33, No. 11, 33-36.
2. Karbhari, V. M. and M Engineer, 1996. "Investigation of Bond Between Concrete and Composites: Use of a Peel Test," *Journal of Reinforced Plastics and Composites*, Vol. 15, Feb. 1996, 208-227.
3. Mullins, G., Sen, R. and Spain, J. 1998. "Testing of CFRP/Concrete Bond," in *Fiber Composites in Infrastructure Vol 2* (Edited H. Saadatmanesh and M.R. Ehsani), Second International Conference on Composites in Infrastructure, ICCI '98, University of Arizona, Tucson, AZ, pp. 211-218.

4. Spain, J., 1997. "Evaluation of CFRP/Concrete Bond Under Shear and Tension," Master's Thesis, University of South Florida, Tampa, FL.
5. Bedford, A. and Wallace L. Fowler, 1995. "Statics-Engineering Mechanics" Addison-Wesley Publishing, Reading, MA.

TABLE 1—SUMMARY OF TEST RESULTS.

Label	Number Of Specimens	Shear Stress from Tr/J		Percent Debond	Tension Stress from P/A		Percent Debond
		ksi	MPa		ksi	MPa	
N3U	4	1.86	12.8	40	0.49	3.4	7.5
N3B	4	1.52	10.5	0.0	0.49	3.4	6.7
M3U	4	1.86	12.8	6.3	0.52	3.6	16.5
W3U	4	1.65	11.4	20.0	0.57	3.9	7.5
M5U	4	1.32	9.1	1.3	0.38	2.6	0.0
W5U	6	1.47	10.1	3.0	0.55	3.8	0.0

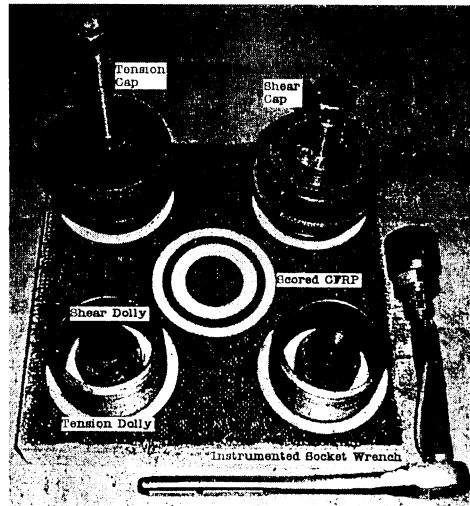


Fig. 1—Tension/shear setup.



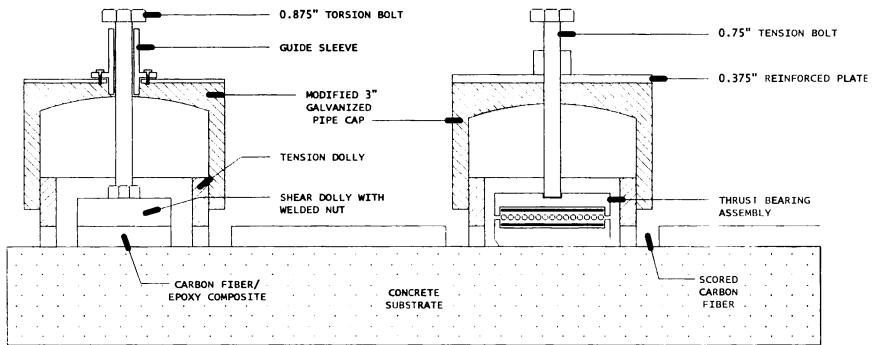


Fig. 2—Schematic drawing of shear (left) and tension (right) test apparatus.

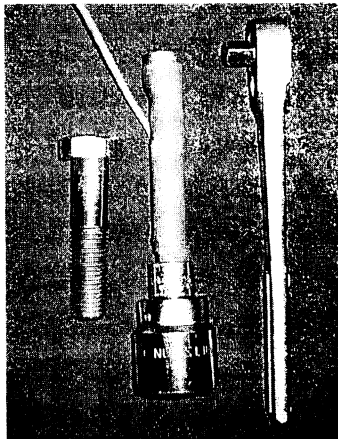


Fig. 3—Instrumented wrench.

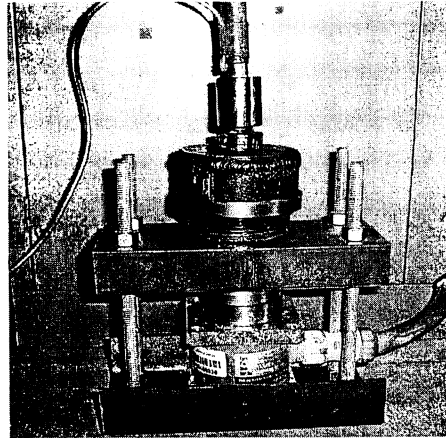


Fig. 4—Tension device calibration.



Fig. 5—CFRP scoring.

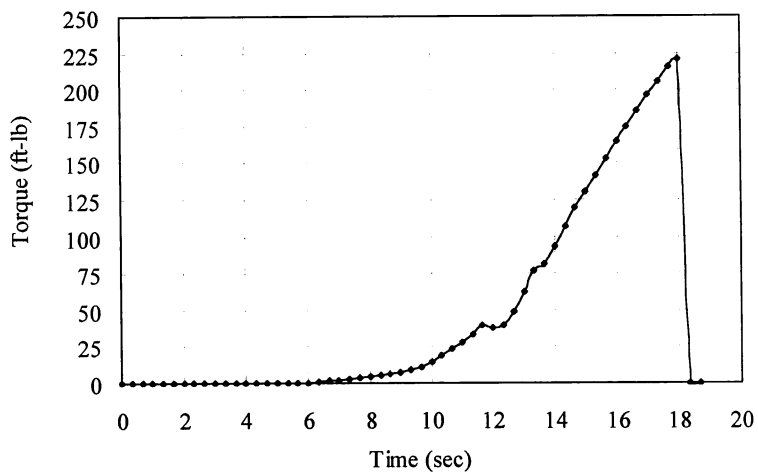


Fig. 6—Torque versus time during shear test.

# STATNAMIC and dynamic load testing of an instrumented drilled shaft at an I-35/I-80 bridge in Des Moines, Iowa

M. Muchard & D.T. Robertson

*Applied Foundation Testing Incorporated, Green Cove Springs, Fla., USA*

G. Mullins

*University of South Florida, Tampa, Fla., USA*

B. Stanley

*Iowa Department of Transportation, Ames, Iowa, USA*

**ABSTRACT:** The Iowa Department of Transportation in conjunction with the Federal Highway Administration performed a design phase Statnamic load test program on a drilled shaft foundation for a series of four new bridges along I-35/I-80 in Des Moines, Iowa. For research purposes, high strain dynamic testing via a drop hammer was also performed. This paper presents the results of Statnamic and high strain dynamic tests conducted at a drilled shaft test site adjacent to the new 2<sup>nd</sup> Avenue Bridge. Load testing was performed on a single instrumented 1.07 meter diameter drilled shaft 27.3 meters in length. The test shaft was designed predominately for side shear in "Glacial Till", gravelly sands and weathered shale. End bearing in the weathered shale was also considered in the design. Internal instrumentation consisted of 12 resistance strain gages and a toe accelerometer which were monitored during Statnamic and dynamic load testing. The paper discusses the results of each test method and their applicability to drilled shaft load testing.

## 1 INTRODUCTION

### 1.1 *Project Background*

A several mile corridor of I-35/I-80 in Des Moines, Iowa is being widened. This construction includes five existing structures that will be replaced with new larger structures four of which will be founded on drilled shafts. The Iowa Department of Transportation in conjunction with the Federal Highway Administration took an approach to this design which incorporated the most contemporary design and construction technics. Recent drilled shaft designs in the area by Iowa Department of Transportation were based on side shear and end bearing in the shale formation. This design was to include side shear in the overburden soils locally termed "Glacial Till" as well as the shale for two of the bridges. Shaft designs for the other two bridges will rely on side shear in the glacial till and will not extend into the shale. The local database of drilled shaft design parameters for glacial till was not specific enough to the construction methods anticipated for this site. Therefore, a full scale load test program was organized and implemented. To take full advantage of the load test program results, it was carried out early in the design phase of the new structures. The test site was selected adjacent to the existing 2<sup>nd</sup> Avenue Bridge on the north side of Des Moines, Iowa shown Figure 1. The load test program also allowed evaluation of site specific drilled shaft construction intricacies using the "wet hole" method involving polymer slurry admixture. The paper is limited to discussions of the load test methods.

Statnamic load testing was selected for this project for several technical and economical reasons as follows: (1) It requires no special shaft construction procedures so installation is more representative of production shaft construction, (2) The shaft is loaded entirely in downward compression as will occur when the structure is placed on the foundation, thus load and deflection of the shaft top is measured directly, (3) Load distribution within the shaft was directly measured via strain gages mounted on the reinforcement cage, (4) Displacement of the shaft toe was obtainable by casting an accelerometer in the shaft bottom, (5) Statnamic load testing is non destructive, (6) It is set up faster and more economically than static load testing, and (7) To compare this method to the cast in place bi-directional jack method used on an adjacent drilled shaft site. There is an interesting irony to this project in that it was the first Statnamic load test program performed by the Iowa Department of Transportation and it also incorporated many firsts for Statnamic and high and low strain dynamic testing.

The Federal Highway Administration also saw this project as an excellent opportunity for gaining data involving high strain dynamic testing, a testing technique widely used on driven piles, on a fully instrumented drilled shaft. Drop weight testing was monitored concurrently with a PDA/DLT<sup>®</sup> manufactured by The Netherlands Organization for Building and Construction Research (TNO) and a PDA<sup>®</sup> manufactured by Pile Dynamics, Inc (PDI). The internal strain and acceleration instrumentation was also measured during the drop weight testing with a MEGADAC<sup>®</sup> 5100 data acquisition system manufactured by Optim, Inc.

Shaft integrity was evaluated before and after all load testing sequences using several methods including Crosshole Sonic Logging (CSL), Sonic Integrity Testing (SIT) and Pile Integrity Testing (PIT). These test methods will not be discussed in this paper. The results will only be used to backup some of the analysis and conclusions presented in this paper.

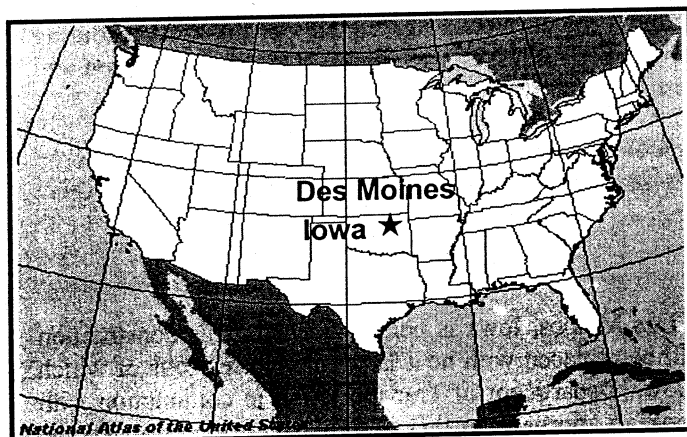


Figure 1. Site Location Map.

## 1.2 Soil Conditions

A comprehensive geotechnical exploration was performed at this site by the Iowa Department of Transportation, part of which included an SPT boring drilled at the precise location of the test shaft. This boring is shown in Figure 2. Soils at this test site generally consist of a surficial layer of silty clay, 5 meters in thickness. The upper 5 meters of silty clay will not be considered as foundation supporting material in the design. Below this, a mottled silty, sandy, clayey soil with intermittent gravel seams and boulders, locally termed glacial till, is present from a depth of 5 meters extending to 19 meters below ground surface. Fine sands, coarse gravely sands and bouldery gravel was present to 25.75 meters in depth where the top of the shale formation was. SPT "N" values in the shale were 100 blows per 0.27 meters and 72 blows per 0.30 meters. SPT "N" values in the glacial till generally ranged from 10 to 20 blows per 0.30 meters.

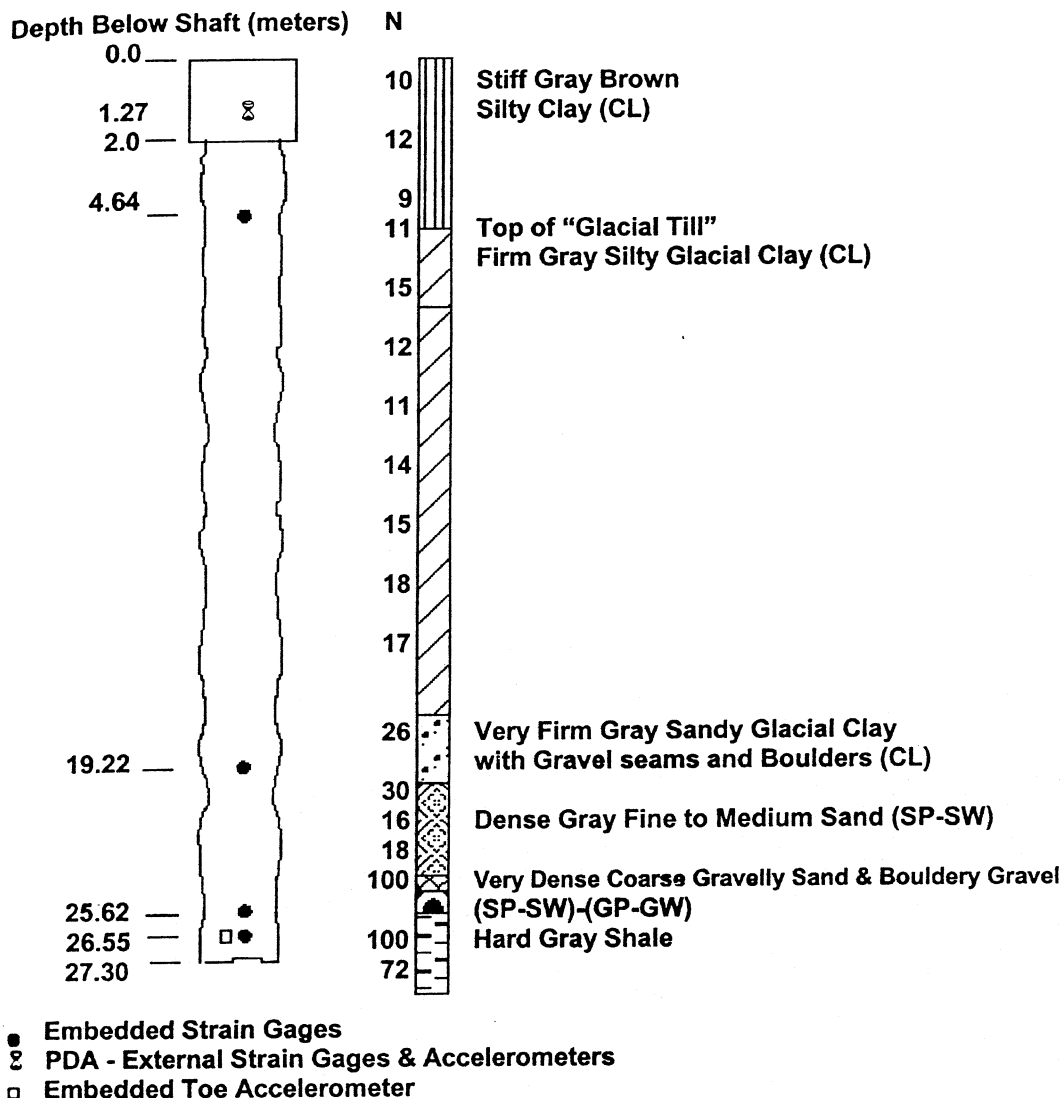


Figure 2. Soil Test Boring.

### 1.3 Test Foundation Description

The test shaft diameter is 1.2 meters for the upper 2 meters as a result of surface casing and assumed to be 1.07 meters in diameter for the remaining length. The overall length is 27.3 meters. Drilled shafts were constructed using the "Wet Hole" technique with polymer slurry admixture to stabilize the hole walls. Longfellow Drilling, Inc. used a Watson crane mounted drill rig to power the cutting tools. Drilling tools with a 1.04 meter diameter were used to excavate the shaft. Several drilling tools were used to excavate the hole consisting of a single flight auger for the glacial overburden soils, a core barrel for penetrating the bouldery material and the single flight auger to excavate the shale material. A clean out bucket with scraper teeth on the bottom was used to clean the shaft bottom prior to placement of the reinforcement cage. Soundings of the shaft bottom were made with a weighted tape for depth determination and estimate cleanliness of the hole bottom. The clean out bucket was used several times until a reasonably sound bottom was felt with the weighted tape. The Contractor decided to install the cage in two parts to closely simulate the methods anticipated for tight space constraints on the upcoming bridge work. Cage placement took approximately 4 hours. Weighted tape soundings

after cage placement (prior to concrete placement) indicated sedimentation on the order of 100 mm in depth on the shaft bottom. Subsequent CSL test results support a soft bottom condition. Load testing results also indicate poor end bearing resistance as a result of not cleaning the bottom. It should be noted that a bottom cleanout procedure such as air lifting or a submersible pump will be implemented for production shafts. Concrete was tremie placed with a pump truck. The tremie pipe was lowered to the shaft bottom and plugged with a "nurf ball". During concreting, the tremie was raised slowly maintaining at least 3 meters below the top level of the concrete. The shaft was over poured until clean concrete was observed at the shaft top. The top of shaft was troweled smooth at the desired top elevation.

The instrumentation scheme consisted of four vertical levels of resistance strain instrumentation installed on the test shaft reinforcement cage with three gages on each plane, 120 degrees apart for a total of 12 strain gages in the shaft. An accelerometer was mounted on the cage adjacent to the lowest level of strain gages (0.6 meters above the shaft toe). The instrumentation locations are shown in Figure 2.

#### 1.4 *Statnamic Test Procedure*

The Statnamic load test system provides a fast and economical method of achieving large downward loads to foundations by "launching" a reaction mass upwards with the test shaft used as a base for the system. During the launching of the mass upwards, an equal and opposite force acts downward on the foundation according to Newton's third law, which states that: "For every action there is an equal and opposite reaction". A mass "m" of 72,398 kg (5 percent of the desired downward load) was used in this case. Upward acceleration "a" of the mass was approximately 20 g's. The theoretical downward load is 20 times the mass. The actual load is measured directly with a calibrated load cell mounted on the shaft top. Shaft top displacements are measured via a photovoltaic sensor mounted to the shaft top, excited with a laser reference beam. Standard instrumentation also includes a shaft top accelerometer. Thus load, displacement, acceleration, and velocity are directly measured at the shaft top. All of these devices are a part of the patented Statnamic testing system and are monitored during a 0.4 to 0.6 second window encompassing the test duration using a high speed data acquisition system sampling at 4000 Hz. A more detailed description of the test methodology and analysis method is provided in references such as Brown (1994) and Middendorp (1992) as well as others.

In this case, as with most, standard Statnamic instrumentation was augmented with strain and accelerometer instrumentation cast inside the foundation for determination of load distribution and shaft toe displacement. The additional instrumentation as well as the Statnamic instruments were monitored with the MEGADAC, which was interfaced with the FPDS Statnamic module. This configuration provides very important redundancy in the measurements and also links the strain gage and toe accelerometer data in time with the other measurements.

The Statnamic load testing was applied in two cycles, first to 5 MN (anticipated design load) and then to 14 MN. This paper only focuses on the larger 14 MN Statnamic test because a greater shaft capacity was mobilized in this test.

#### 1.5 *High Strain Dynamic Test Procedure*

High strain dynamic testing is a method used to quickly and economically evaluate many aspects of a pile driving process including: pile hammer performance, tension and compression driving stresses, pile capacity, and pile integrity. On occasion, the system has been used to test drilled shafts. The test is accomplished by attaching sets of strain gages and accelerometers on opposite sides of the pile near the head using concrete anchors and bolts. During pile driving, measurements of strain and acceleration are made in the region of the pile head for each hammer impact using one of the commercially available data acquisition systems specifically designed for this type of testing. Strain and acceleration signals processed in the field between

each hammer blow are referred to as direct calculations. These calculations are based on simplistic models to perform the calculations in the short time between each hammer impact. Direct calculations of pile capacity are most commonly evaluated using the Case Method approach. The field signals are stored and later subjected to rigorous post processing using commercially available software packages such as TNODLT Signal Matching (TNODLT) and CAse Pile Wave Analysis Program (CAPWAP). In this process, pile and soil data are modeled and a calculation is carried out using the wave equation. The models describe the pile and soil in terms of acceleration, velocity and displacement functions, using empirical parameters which depend on soil properties. Using iterative methods in which the results of each analysis are compared to the actual measured pile behavior, appropriate dynamic parameters are refined and the shaft and toe resistance estimated. The success of this procedure for predicting static capacity is user dependent and the solution is not unique. The margin of error in testing drilled shafts has a potential to be much greater than in driven piles due to the many unknown properties of a cast in place foundation element.

The drop hammer used in this study consisted of two air hammer rams fastened together having a total mass of 9050 kg's (6787 kg's and 2263 kg's). The falling mass was guided by a 0.66 meter width, free swinging box lead section. No provisions for a fixed hammer to shaft alignment were made. A cushion was used to protect the shaft from damaging stresses derived from impact. The cushion was made of three steel disks 50 mm in thickness each over three sheets of plywood 19 mm in thickness for a total thickness of 207 mm. A friction crane with free fall capabilities was used to lift and drop the ram.

The upper 2 meters of the shaft (cased portion) was excavated to allow placement of external strain gages and accelerometers. Eight square holes were cut in the casing to expose the concrete for gage placement. Drop in anchors were installed in the concrete to allow fastening of a total of 6 strain gages and 6 accelerometers from two separate PDA systems. The gages were 1.27 meters below the shaft top.

A total of 7 impacts were monitored varying the drop height from 0.5 meters to 3 meters. The paper focuses on blow number six since this was the highest energy blow.

## 2 TEST RESULTS

### 2.1 *Static Results*

The derived static load versus displacement curve shown in Figure 3 was calculated using a variation of the Unloading Point Method (UPM) (Middendorp et. al., 1992) involving the average shaft acceleration and average shaft velocity rather than only the top values typically used. The results indicate a mobilized static capacity of 14.25 MN with a maximum shaft top deflection of 8.8 mm and a permanent set of only 3 mm. In this test case, the load/displacement response is within the elastic realm of the pile/soil system similar to that which would be observed from a static test not run to failure. Because the load/displacement response was within the elastic range and shaft movement was very small, dynamic effects were minimal on the maximum capacity. Correction for the dynamic effects, however, better describes the slope of the elastic region of the pile/soil system.

The shaft bottom load/displacement is also shown in Figure 3 based on toe strain and toe accelerometer measurements. The dynamic effects of inertia are insignificant at the shaft bottom. A maximum load of 1.2 MN is estimated at the shaft toe with a maximum displacement of 3 mm and a permanent displacement of 2.2 mm. The results also indicate residual load and displacement after the test.

Shaft loads at each of the strain gage levels are presented in Figures 4 and 5 and were calculated by the equation:

$$P = \epsilon AE \quad (1)$$



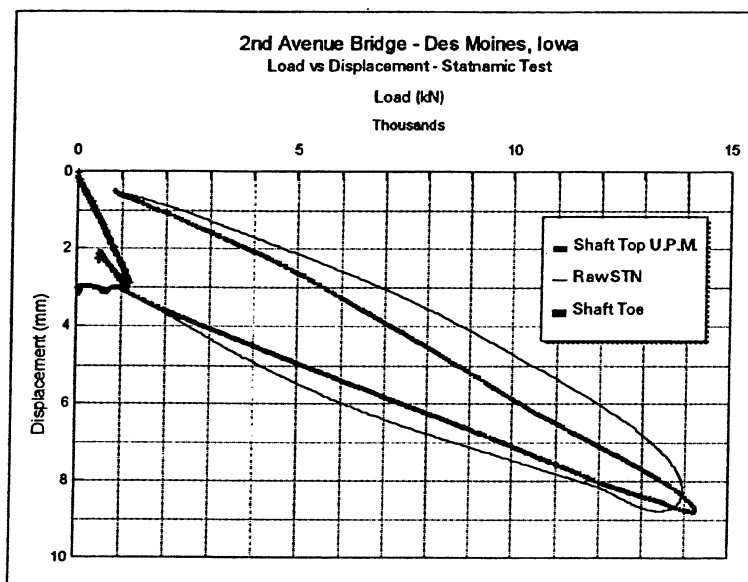


Figure 3. Load vs Displacement.

where  $P$  is the load at strain gage location;  $\epsilon$  is the average strain of the three gages at each level;  $A$  is the assumed shaft cross sectional area; and  $E$  is assumed shaft equivalent elastic modulus

This calculation is highly influenced by the shaft diameter and elastic modulus, which must be estimated from as-built information and commonly accepted formula. Shaft top load and displacement are direct measurements thus, not influenced by any of these factors.

Equivalent modulus values for these calculations were based on concrete cylinder break strengths and the weighted average concrete and steel area. The concrete modulus was calculated using the American Concrete Institute (ACI) method:

$$E = 5000(f'c)^{1/2} \quad (2)$$

where  $E$  is concrete elastic modulus; and  $f'c$  is concrete compressive strength in MPa.

The  $f'c$  values were obtained from concrete compressive strength tests performed within two hours of Statnamic testing. An average  $f'c$  value of 27.03 MPa was used based on two cylinder tests. The shaft diameter was assumed to be 1.07 meters at the strain gage locations based on the diameter of the drilling tools. The upper 2.0 meters of the shaft was cased and has a diameter of 1.22 meters. The steel area was calculated based on a cage made of ten 25mm vertical reinforcing bars and four 50 mm diameter Schedule 40 steel tubes. A steel modulus of 200 GPa was used. A shaft equivalent modulus of elasticity of 25.91 GPa was calculated for each strain gage location.

The forces from the strain measurements in Figures 4 and 5 were also corrected for dynamic effects by performing a U.P.M. analysis at each level. The load distribution curve in Figure 4 was created by plotting values at various slices in time from Figure 5.

The Statnamic load test produced a compressive load lasting 120 milliseconds as shown in Figure 5 (sign convention is compression negative). The load is applied in a linearly increasing manner then a controlled unloading takes place. Dividing the shaft length of 27.3 meters by an assumed wave speed of 4000 m/s indicates a wave travel time (natural period) of 6.8 milliseconds. For this case, the duration of loading was around 17 to 18 times longer than the natural period of the shaft. This long period dynamic loading has several interesting results. One is that tensile stresses are non-existent in a shaft of this length as shown in Figure 5. Tensile

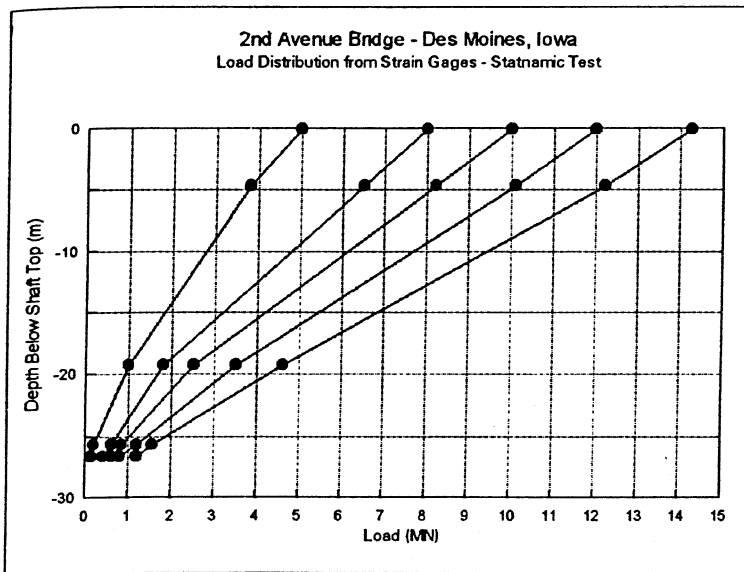


Figure 4. Load Distribution vs Depth.

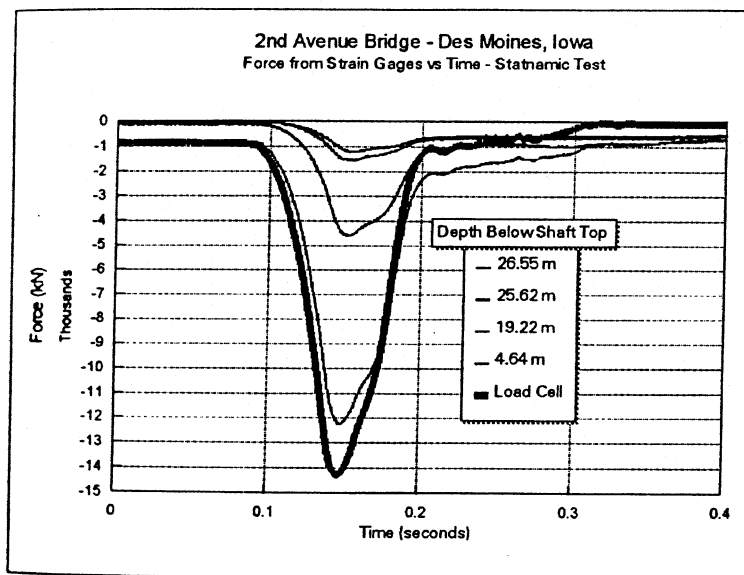


Figure 5. Forces From Load Cell and Strain Gages vs Time.

stress waves are not present with a load duration of more than 12 times the natural period of the shaft (Middendorp, 1995). Secondly, the entire shaft is in compression during the test and moves as a rigid body, like in a conventional static load test. Lastly, the shaft as a whole undergoes translation during the compressive loading, thus minimal shaft accelerations and velocities are present. The measurements of shaft top and bottom accelerations, velocities, and displacements are shown in Figures 6, 7, and 8. Figures 7 and 8 show that the top and bottom accelerations and velocities are relatively small. They are also generally in phase. The slight shift noted is due to the elastic compression of the shaft. The difference in magnitude of the accelerations, and velocities at the top and bottom are due to the soil not being loaded to full plastic deformation. The difference in displacement between top and bottom in Figure 8 is due to the elastic compression of the shaft soil/system. These measurements provide additional support that in evaluation of Statnamic test data, it is correct to consider the mechanics of the pile moving as a rigid body.

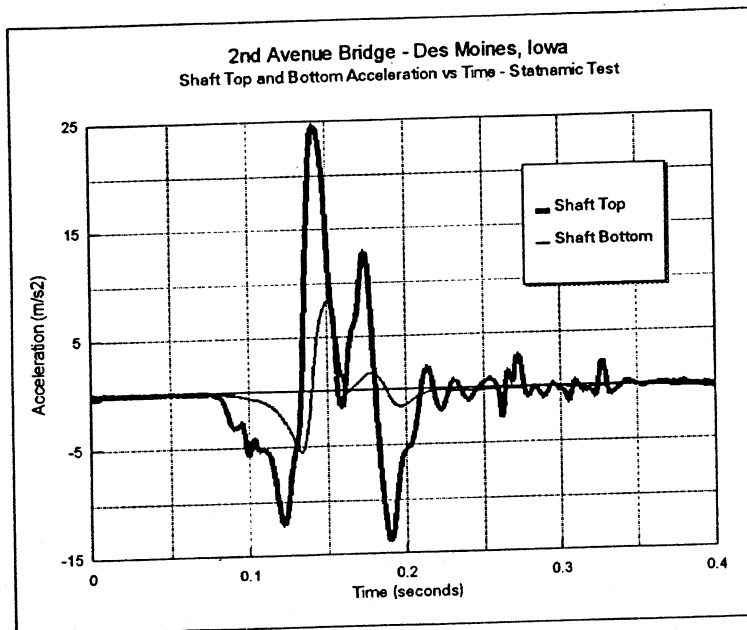


Figure 6. Shaft Top and Bottom Acceleration vs Time.

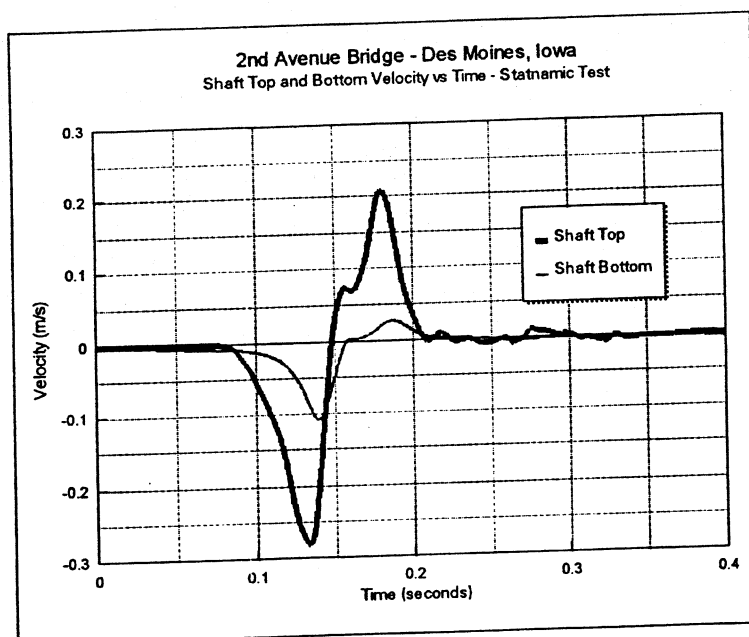


Figure 7. Shaft Top and Bottom Velocity vs Time.

## 2.2 High Strain Dynamic Test Results

### 2.2.1 Applicability to Cast in-Situ Piles

Interpretation of test results in this case is much more difficult for high strain dynamic testing because the element tested was a drilled shaft. For driven piles, results have been shown to be reliable because key pile properties can be determined in a controlled manner. For cast in place foundations like drilled shafts there are several uncertainties for high strain dynamic testing which can lead to considerable error in pile capacity prediction. These include properties such as modulus of elasticity, density, stress wave speed, pile shape and cross section. Further

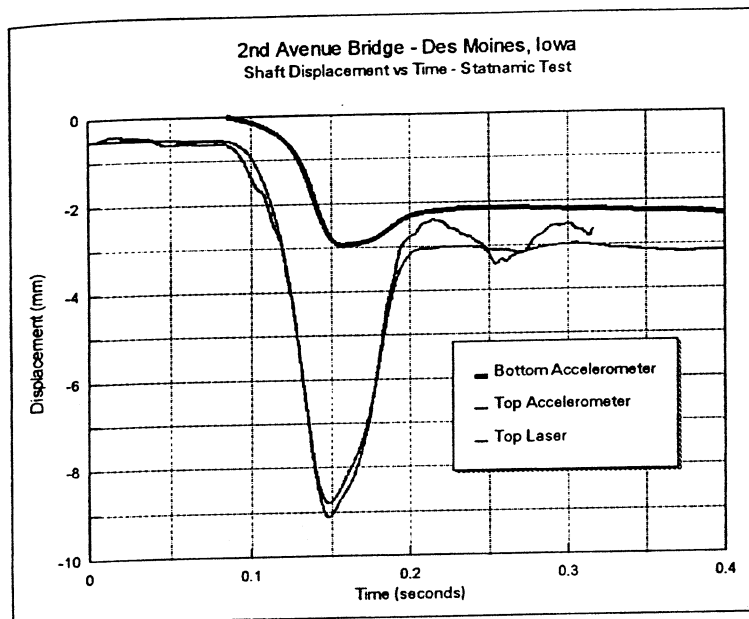


Figure 8. Shaft Top and Bottom Displacement vs Time.

difficulties arise in high strain dynamic testing of cast in-situ piles because tension waves are easily generated. Drilled shafts may become damaged since they are only conventionally reinforced opposed to prestressed concrete piles which are designed to handle tension stresses from driving. Thus, to prevent damage, testing must be stopped prior to mobilizing the large displacements required to fail a drilled shaft. Additionally, the ram to pile alignment is very difficult to control and bending stresses result from eccentric loading. Bending stresses can cause damage and also complicate the analysis method.

With respect to capacity prediction, the only derivation assumption in the Case Method equation is a linearly elastic uniform pile with constant cross section along its length. Therefore, this method alone is not reliable for cast in place foundations. Complex models must be made using TNODLT or CAPWAP to attempt any prediction. These models are also plagued by the same unknown pile properties. The perplexities in assuming pile properties are compounded in these models by unknown dynamic soil parameters such as damping and quakes. Results produced by independent parties do not compare within the same margin of error for driven piles because of these unknowns and the inherent non-unique solution.

### 2.2.2 Wave Speed Determination

The wave speed is one of the most pivotal pile properties and must be correctly determined or large errors may result. A 10 percent error in wave speed results in a 20 percent error in modulus and subsequent pile capacity and stress calculations (Likins, 1996). Wave speed is a function of the following material properties of the pile, elastic modulus and mass density and are related through the equation:

$$c = (E/\rho)^{1/2} \quad (3)$$

where  $c$  equals wave speed;  $E$  is the elastic modulus; and  $\rho$  is the mass density of the concrete.

Several methods of wave speed determination were evaluated for use in the analysis of this data which are: (1) Free Pile Test, (2) Wave Up and Wave Down Method in early driving, (3) Published "standard" values, (4) Inspection of wave up and wave down from current data, (5)

Calculated from laboratory tests, (6) Low strain Sonic Integrity Testing, and (7) Measured from embedded instrumentation.

The two preferred methods to find wave speed are impossible with respect to drilled shafts because they rely on a pile with no shaft resistance from the soil i.e. before driving (Free Pile Test) or during the first blows before the pile significantly penetrates into the ground (Wave Up and Wave Down Method). The free pile test is obviously impossible for cast in-situ piles. In the case of a drilled shaft, which by design and construction method, has large side friction, wave speed determination by WU/WD inspection may be erroneously slow due to high shaft friction. Impact diagrams showing pile top force and velocity times impedance and the resistance wave down and wave up are shown for Blow 6 in Figures 9 and 10. The very soft pile/soil response shown makes wave speed determination difficult. The resistance wave down and wave up shown in Figure 10 illustrates the very rounded area where the toe reflection should be. The best estimates of wave speed from this procedure range from 3962 m/s to 3567 m/s which is as much as 10 percent less than standard published values of 4000 m/s for concrete. Under normal high strain dynamic test circumstances, this would be the only way to determine the shaft wave speed.

Supplementary low strain Sonic Integrity Test (SIT) or Pile Integrity Test (PIT) methods may be used to shed additional light on which wave speed to use. It may also help determine large cross section variations for subsequent signal matching models. But there is also a margin of error associated with low strain test methods which may just confuse matters. The wave speeds reported from the SIT and PIT results are 3600 m/s and 3650 m/s.

The wave speed was also calculated based on laboratory tests. The modulus was calculated by the ACI equation (2) based on concrete cylinder breaks made within 2 hours of the drop hammer test. The concrete compressive strength based on a 10 micro-strain per second loading rate is 27.79 Mpa and the modulus is 26.3 GPa. Loading rate during the drop hammer test was on the order of 200,000 micro-strain per second. It is suggested that the compressive strength is 15 percent greater at a loading rate of 8000 micro-strain per second (Metha, 1986). Therefore, this modulus calculation corrected for loading rate should be somewhat larger, perhaps by 3 to 5 percent. In the laboratory, the unit weight of the cylinder was also determined to be 2195 kg/m<sup>3</sup>. The wave speed calculated by (3) is 3465 m/s. If loading rate and reinforcing steel add 5 percent, the wave speed is 3638 m/s.

For this test, internal measurements of strain at four levels and acceleration at the shaft toe were made during the drop hammer test. Using these data is probably the most accurate way to determine the wave speed and pile/soil response. Inspection of the acceleration versus time plot in Figure 12 or any one of Figures 11 through 14 implies a wave travel time of 8 milliseconds over a length of 25.28 meters between the top and bottom accelerometers. Data in Figure 11 also indicates that variations in the wave speed occur over the length of the shaft. The composite wave speed of the shaft from these measurements is 3160 m/s.

So there seems to be an irresolution in the best determination of the wave speed for drilled shaft testing. Values are shown to range from 3962 m/s to 3160 m/s in this case. Capacity variation with wave speed is shown in Table 1.

### 2.2.3 Accuracy in Load Measurement

The elastic modulus also directly influences the accuracy of load measurement, since the load is calculated via strain gages near the pile top by equation (1). Essentially, the shaft cross section at the gage locations is a load cell. Load cells used in static and Statnamic testing are required to be calibrated and traceable back to the National Institute of Standards and Technology (NIST). The shaft concrete curing process near the shaft top is the most unrepresentative of the shaft as a whole. Moreover, the modulus is linearly dependent on the mass density of the pile. What's more, the elastic modulus is variable over the length of the shaft and over the cross section. Accuracy in load measurement is also influenced by the cross sectional area. In this case, the shaft top was slightly elliptical and the gages were placed 0.7 meters above a transition zone from permanent casing to a smaller diameter uncased shaft.

Table 1. Case Method Capacity Prediction Variation with Wave Speed Value TNO FPDS-5.

Blow Number	c=3963 m/s	c=3638 m/s	c=3600 m/s*	c=3160 m/s
	Static Resistance (MN)	Static Resistance (MN)	Static Resistance (MN)	Static Resistance (MN)
1	3.1	3.0	2.9	2.5
2	6.5	5.7	5.4	4.9
3	7.2	6.3	6.1	5.3
4	8.7	7.5	7.1	6.5
5	9.1	7.7	7.3	7.4
6	9.3	7.6	7.1	7.5
7	8.4	7.0	6.7	7.4

Table based on a damping constant of JC=0.5.

Table 2. High Strain Dynamic Testing Summary Table (Direct Calculations) from TNO/PDI.

Blow Number	Static Resistance* (MN)	Maximum Compression Stress (MPa)	Maximum Tension Stress (Mpa)	Energy Transferred (kJ)	Drop Height (m)
1	2.9 / 2.3 3 / 3	1 / 1	4 / 4	0.5	
2	5.4 / 4.7 6 / 6	3 / 2	18 / 20	1.3	
3	6.1 / 5.8 8 / 7	2 / 2	27 / 28	1.8	
4	7.1 / 6.5 9 / 9	2 / 2	40 / 41	2.1	
5	7.3 / 6.9 10 / 10	1 / 2	48 / 50	2.5	
6	7.1 / 7.1 11 / 11	2 / 2	55 / 59	2.7	
7	6.7 / 6.7 10 / 10	1 / 2	43 / 47	3.0	

\* Maximum Case Method with JC=0.5 & a wave speed of 3600 m/s.

\* TNO/PDI data.

### 2.2.4 Discussion of Results

The data contained in Table 2 summarize the results of the high strain dynamic testing. The values shown are direct calculations based on the maximum CASE Method (closed form solution) approach. Since the only derivation assumption in the Case Method equation is a linearly elastic uniform pile with constant cross section along its length, this method is not totally reliable for cast in place foundations. This is a simplistic approach compared to signal matching, but may very well be the best, just because of its simplicity and repeatability. The maximum Case Method capacity independently reported from the TNO and PDI systems were nearly identical in Table 2. Supplemental information such as driving stresses and energy are also reported in Table 2.

Independent evaluations on blow number 6 made by GRL researchers with CAPWAP show a capacity prediction of 10.2 MN with 3.8 MN of end bearing and 6.4 MN of skin friction. GRL researchers performing the CAPWAP analysis were not provide the embedded strain gage and toe accelerometer data. Their analysis was based on shaft top data only.

Signal matching analysis TNODLT of blow 6 performed by the authors produced variable results depending on various permutations of pile properties. Predicted capacities from TNODLT ranged from 6.1 MN to 8.85 MN. A common denominator in these variations was the very low predicted end bearing of only 0.1 MN.

If the embedded strain and accelerometer data was used to back fit a TNODLT model to these internal measurements, a total mobilized pile capacity of 7.8 MN with 7.7 MN in skin friction and 0.1 MN in end bearing was estimated.

Statnamic load test results shown in Figure 38 indicates 0.5 MN to 0.8 MN of end bearing at comparable loads. CAPWAP using only shaft top data over estimated end bearing by 375%.

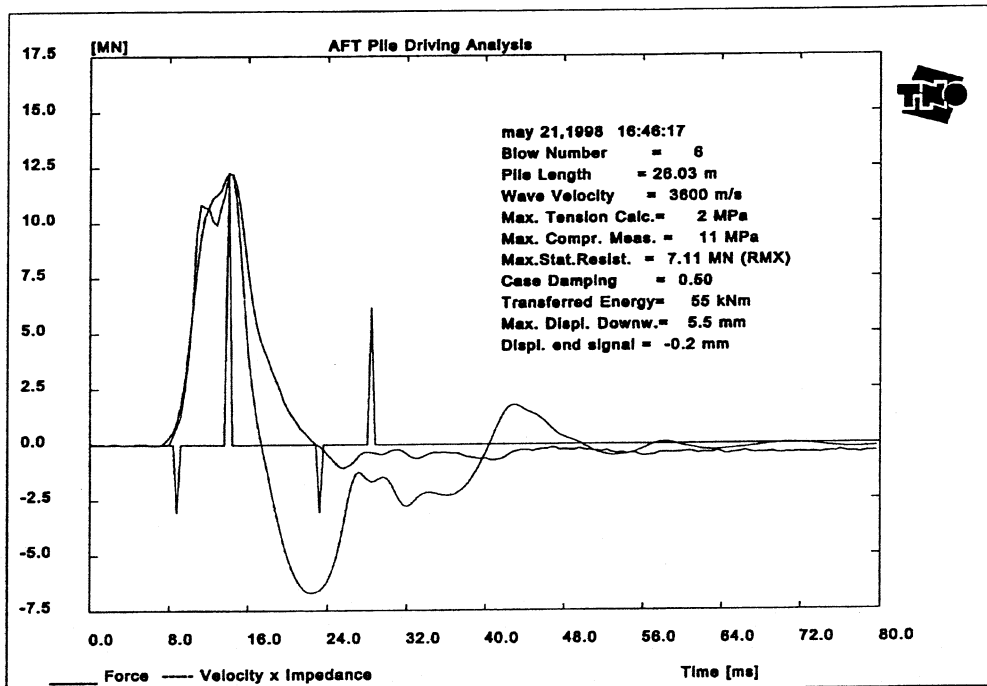


Figure 9. Shaft top force and velocity times impedance - Blow 6.

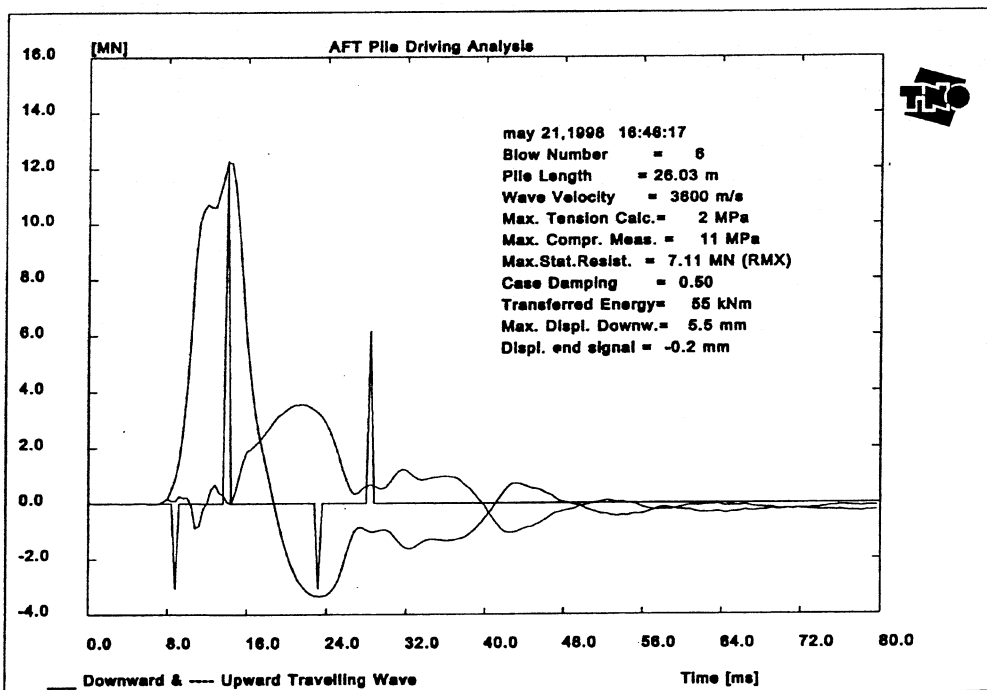


Figure 10. Resistance wave down and wave up - Blow 6.

TNODLT under estimated end bearing by 88 %. Poor end bearing resistance is supported by weighted tape soundings of the shaft bottom prior to concrete placement and subsequent Cross Hole Sonic Logging.

It appears that the more detailed the signal match model becomes, by using measured quantities, the more difficult the match becomes. This is largely due to the uncertainties associated with pile properties previously discussed. Variations in cross section cause stress



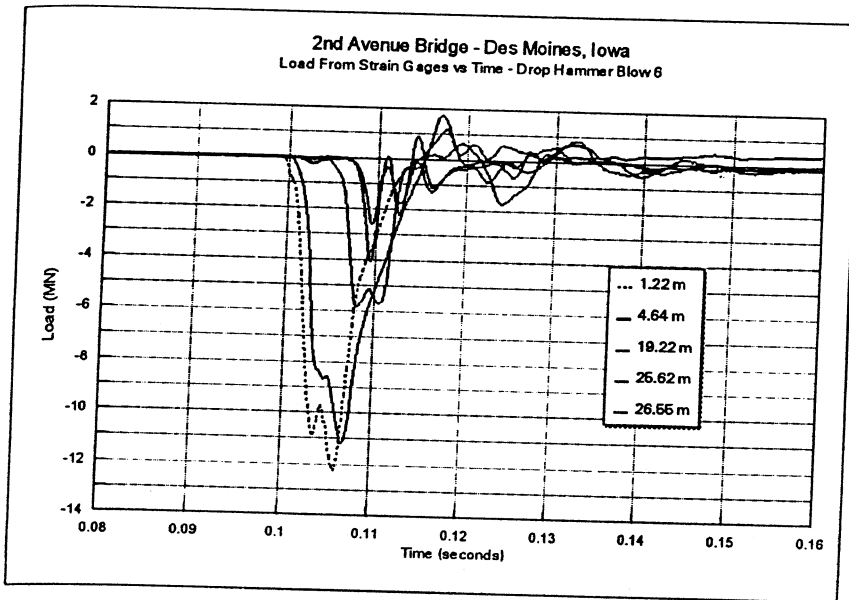


Figure 11. Force from Strain Gages - Blow 6.

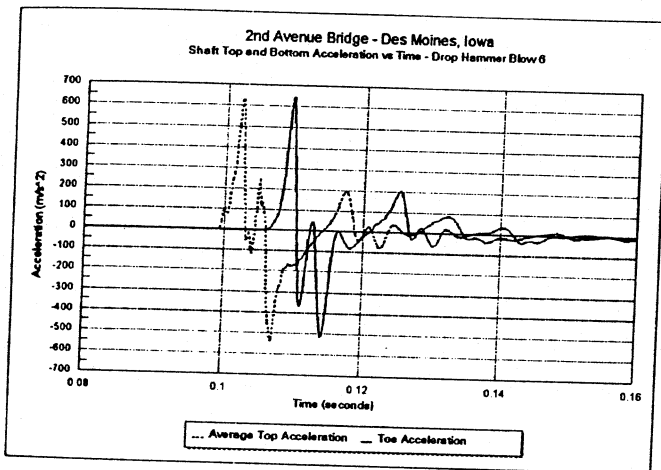


Figure 12. Average shaft top acceleration and shaft toe acceleration.

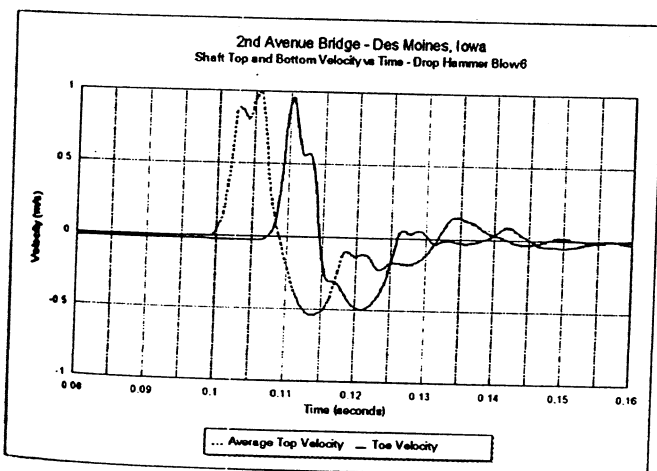


Figure 13. Average shaft top velocity and shaft toe velocity.

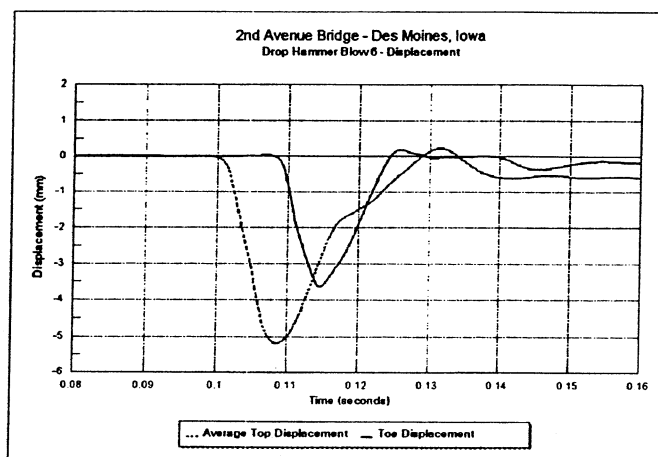


Figure 14. Average shaft top displacement and shaft toe displacement.

wave reflections that can easily be mistaken for soil resistance reflections. A bulge in the shaft can be characterized as high soil resistance and a neck can be taken as low soil resistance. Models cannot adequately describe these complex field conditions. Unknown properties have been shown to seriously influence capacity predictions.

Embedded strain measurements shown in Figure 11 were converted to load via equation (1). The internal measurements clearly indicate the effects of stress wave propagation. Due to this wave propagation, drilled shaft side shear values can not be directly interpreted from these data. The data also shows the presence of tension waves with the maximum tension force of 1.8 MN at 4.64 meters below the shaft top. This corresponds precisely to the maximum calculated tension from the FPDS and PDA. This tension was approaching the maximum allowable value for a non prestressed concrete element. Integrity testing schemes before any load testing indicated an impedance change around 21 to 22 meters below shaft top. This impedance change appeared more prevalent after each test method but was still not a major defect. Figure 11 also shows variation of wave speed over the shaft based on wave arrival times from gage to gage.

The measured acceleration presented in Figure 12 was integrated to velocity in Figure 13 and then to displacement shown in Figure 14. The measurements in these figures are out of phase by the magnitude of the wave travel time. The maximum displacement of the shaft top is shown to be 5.3 mm with a final set of 0.6 mm. The shaft top displacement was also checked with standard survey equipment and reported to have a permanent set of 1.4 mm for this blow. Note that displacement recorded with the survey equipment was a total of 6 mm for the 7 blows. The accuracy of the survey equipment was  $\pm 2$  mm. As shown in Figure 14, the shaft toe had a maximum displacement of 3.6 mm and a final set of 0.2 mm indicating some residual stress. With displacements of this magnitude, only a fraction of the full shaft capacity was mobilized.

### 3 LOAD TEST PROGRAM REMARKS

The short coming to the program was that the test shaft was over designed so its ultimate capacity was not measured with the 14 MN Statnamic device. The test shaft at the adjacent site was not loaded to failure either using the bi-directional jack method. Conditions were quite different for that site although it was only a few miles away. The jack was placed in the shaft bottom and loading was from the bottom up. The substantial strength of the shale socket was not overcome and the shaft was permanently cased through the overlying soils. It was just the opposite for the Statnamic test which did not fail the shale. Thus, the two methods complimented each other.

Drilled shaft foundation designs on two of the four bridges will rely entirely on side shear in the glacial till and will not be extended into the shale. Zero end bearing will be used in this

scenario. Larger structural loads will be required for the other two bridges therefore, design criteria includes side shear and end bearing in the shale as well as side shear in the glacial till.

Load test results indicate poor end bearing resistance as a result of not cleaning the shaft bottom. The subsequent construction specifications will require a bottom clean out procedure such as an airlift or submersible pump. A nominal end bearing value in the shale will be used in light of the bottom clean out specification.

Design values for the new structures were based on a combination of both test methods. Statnamic load test results were used for the glacial till and upper soils. Design values in shale were used from the cast in place bi-directional jack method results as well as local data base shale values. The design team felt that a safety factor of 2.5 on the ultimate side shear was appropriate for sizing shafts to match the required structural service loads.

The load test program performed during the design phase is a very innovative approach since the information may be directly incorporated into these designs.

## 4 CONCLUSIONS

### 4.1 *Statnamic*

- Statnamic is not effected by uncertainties in pile properties because top load and displacement are measured directly with a calibrated load cell and displacement sensor.
- Embedded strain and accelerometer instrumentation allows direct interpretation of load distribution and toe displacement in Statnamic testing.
- Embedded toe accelerometer instrumentation verified rigid body motion in Statnamic and improved the Unloading Point Method in the elastic range by using average shaft acceleration.
- The duration of the Statnamic load is 10 times longer than high strain dynamic testing, therefore no tensile forces exist in the shaft and the soil is loaded as a rigid body like in a static test.
- Statnamic can safely mobilize greater capacity than dynamic testing.
- It requires no special shaft construction procedures so installation is more representative of actual production shaft construction.
- Comparisons between Statnamic and bi-directional cast in place jack results could not be made since neither test was run to failure.
- Poor end bearing resistance resulted from not cleaning the shaft bottom.

### 4.2 *High Strain Dynamic Testing*

- High strain dynamic testing has inaccuracy in load measurement on drilled shafts because of unknown pile properties.
- Displacement is not measured directly.
- Capacity prediction from high strain dynamic testing depends on wave speed which has been shown to vary from 3962 to 3160 m/s in this case resulting in considerable variation in capacity estimates.
- High strain dynamic testing is also effected by non-uniform shaft cross section. Unknown cross section variations cause stress wave reflections which can be easily mistaken for soil resistance.
- The Case method is based on a linearly elastic uniform pile with constant cross section along its length, this assumption is not totally reliable for cast in place foundations. This is a simplistic approach compared to signal matching, but may very well be the best, just because of its simplicity and repeatability.
- Capacity estimated from complex signal match models had variations of over 4 MN due to unknown soil properties. Independent CAPWAP analysis based on pile top measurements only indicated a capacity of 10.2 MN while analysis back fit to match embedded strain gages

- and toe accelerometer data showed a capacity of 7.8 MN.
- Measurements from internal strain gages may not be directly interpreted in high strain dynamic testing. A signal match must be back fit for prediction of side shear and end bearing.
  - To prevent damage, high strain dynamic testing must be stopped prior to mobilizing the large displacements required to fail a drilled shaft. Additionally, the ram to pile alignment is very difficult to control and bending stresses result from eccentric loading. Bending stresses can cause damage and also complicate the analysis method.
  - High strain dynamic testing is an excellent tool for driven piles because key pile properties can be determined in a controlled manner.

#### ACKNOWLEDGMENTS

The authors wish to thank all parties involved including Mr. Carl Ealy of the Federal Highway Administration, the Iowa Department of Transportation, Mr. Dick Longfellow of Longfellow Drilling, Inc., Mr. Scott Webster and Mr. Frank Rauche of GRL/PDI for performing independent field measurements and data analysis.

#### REFERENCES

- Applied Foundation Testing, Inc. 1997. *Report of Statnamic Load Testing - I-35/I-80 Bridge over Second Avenue*. For Soil and Land Use Technology, Inc. on behalf of the Iowa Department of Transportation and Federal Highway Administration.
- Brown, D.A. 1994. Evaluation of Static Capacity of Deep Foundations from Statnamic Testing. *Geotechnical Testing Journal*, December, 1994.
- GRL & Associates, Inc. 1997. *Summary Report for Dynamic Testing and Analysis - Second Avenue Bridge Test Shaft Project*. For Soil and Land Use Technology, Inc. on behalf of the Iowa Department of Transportation and Federal Highway Administration.
- Likins, G. 1996. Helpful Hints for Field Testing and Data Interpretation using the Pile Driving Analyzer. *PDA Users Day*, Orlando, Florida, 1996.
- Metha. 1986. *Concrete Materials and Properties*. McGraw Hill.
- Middendorp, P. 1995. Statnamic Load Testing and the Influence of Stress Wave Phenomena. *Proceedings of the First International Statnamic Seminar*, Vancouver, September 1995.

## STATNAMIC testing: University of South Florida research

G. Mullins, E.J. Garbin, Jr. & C. Lewis  
*University of South Florida, Tampa, Fla., USA*

C. Ealy  
*Federal Highway Administration, McLean, Va., USA*

**ABSTRACT:** Over the past two years researchers at the University of South Florida in Tampa, Florida have conducted over 150 Statnamic tests in conjunction with privately and federally funded test programs. In this time a research program has been developed exploring further applications for its use. This paper will describe some of the areas of research presently under investigation, developments in instrumentation and testing procedures, and preliminary findings.

### 1. INTRODUCTION

Since its inception in 1988, Statnamic testing has gained acceptance in more than 15 countries and in 6 continents, and it is estimated that over 500 tests have been conducted worldwide. With its growth has come the exploration of new avenues for its application. Although typically considered an axial deep foundation test procedure, it was expanded into lateral load testing in North Carolina (1994) and most notably, in Mississippi (1998), where lateral loads exceeded 7 MN. Additionally, developments such as the hydraulic catching mechanisms, shallow foundation applications, and under water reaction masses continue to emerge. Although some of the most recent developments have yet to be released for production, they promise to be equally beneficial to the full-scale testing arena.

Over the past two years researchers at the University of South Florida have conducted over 150 Statnamic tests on both deep and shallow foundations. These tests were performed in conjunction with production and research oriented projects in cooperation with *Applied Foundation Testing Inc., Auburn University, Birmingham Foundation Equipment, the Federal Highway Administration, Hayward Baker Inc., University of Massachusetts*, and eight different state departments of transportation. The Statnamic test programs have included: (1) axial load tests on piles and shafts in sands, clays, or rock-sockets, (2) lateral load tests on pile groups and shafts, and (3) plate load tests on sands and full-scale spread footings on sands and vibro-compacted soils (stone columns). This paper will describe some of the research areas presently under investigation, developments in instrumentation and testing procedures, and preliminary findings.

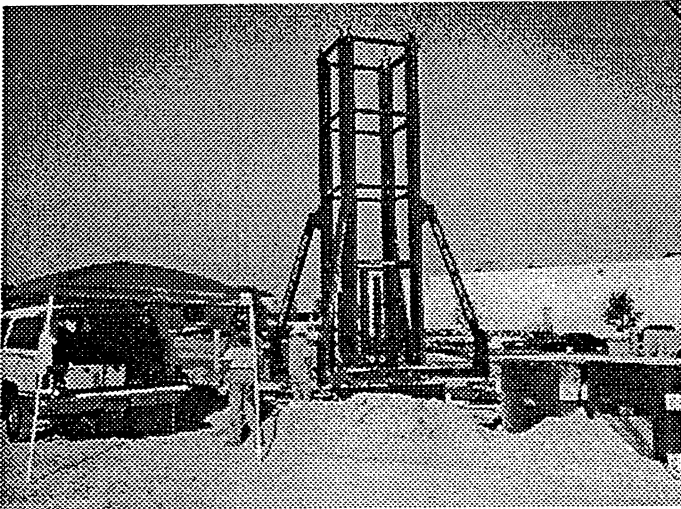


**Figure 2.1** Level frame using hydraulic legs.

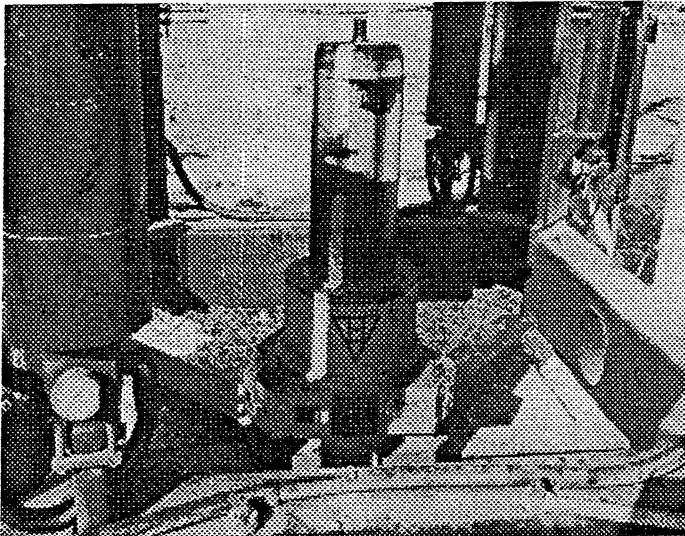


**Figure 2.2** Secure piston to foundation.

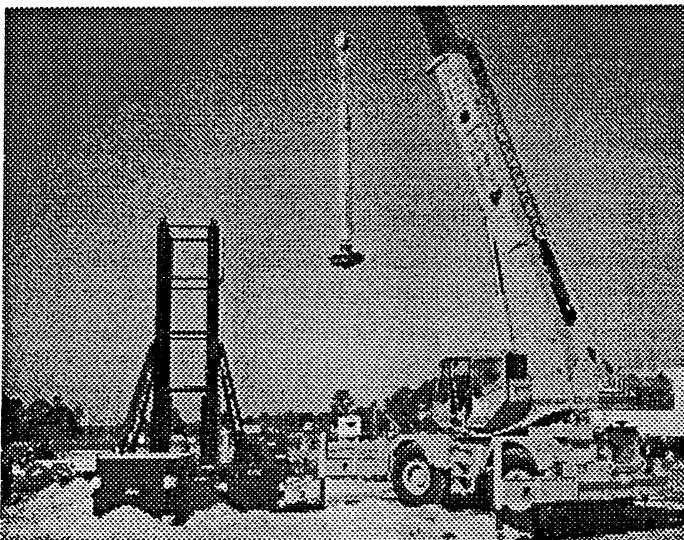


**Figure 2.3** Install silencer. *NOTE: fuel basket can be installed after assembly is complete.*

## 2. HYDRAULIC CATCHING MECHANISM

By means of a grant with the Federal Highway Administration, USF purchased a 4 MN hydraulic catching mechanism (HCM), the largest-capacity hydraulic catching mechanism to date. Although not used exclusively, this device serves as the primary core of the university's Statnamic research program. This catch mechanism provides the luxury of multiple load cycles within a matter of minutes, the ability to inspect the ignition circuit without disassembly, the benefit of single-truck mobilization, and it avoids the environmental problems with gravel retrieval when testing over water.

Hydraulic catching systems eliminate the need for gravel and gravel structure since the upward moving reaction masses are caught at the top of their flight by four hydraulic actuators (or rams). These 3.2 m stroke rams are activated by four low pressure (1500 psi) nitrogen accumulators which store compressed nitrogen gas over hydraulic oil. As the weight on the rams is released during a test, the compressed nitrogen quickly expands to force hydraulic oil into the rams causing them to chase the reaction masses to the apex of their flight. The hydraulic oil is routed (in series) through one-way valves at the base of each ram which restricts reverse flow and thus the downward movement of the masses. Each of the four rams is independent of the others providing redundancy and safety. The masses remain at this position until the user redirects the additional fluid in the rams back into the accumulators. At which time, a subsequent load cycle can be performed.

By transferring the initial weight of the masses to the rams at the onset of the test it is possible to perform Statnamic testing without a pre-load condition. Additionally, hydraulic catching systems have no minimum required jump-height for the silencer/reaction mass assembly which is a concern for gravel catching systems. By removing this restriction, low load tests can be performed with much greater than 5% reaction mass. Such tests can produce long duration load pulses greater than 0.5 seconds, thus reducing inertial and damping forces for large portions of the test.

Although the set-up time for a 4MN gravel or hydraulic catching systems is comparable, multiple cycles can be performed in a matter of minutes when using the latter. Further, the break-down typically takes less time. In using gravel catching systems, great care is exercised in the preparation of the ignition circuitry. An inadequate ignitor connection could cost a project as much as a day of delay time. This is of little concern when using the hydraulic catching system due to the ability to raise the entire stack of reaction masses with the hydraulic rams so as to access the fuel basket.

A substantial portion of all Statnamic testing costs stems from the mobilization of equipment. Typically, a 4 MN test requires two tractor-trailers to ship the combined weight of the equipment and reaction masses (27,000 kg total) where only 20,000 kg is permitted per truck. The USF device is equipped with two reaction mass options: (1) an entire set of six concrete-filled steel masses which requires two trucks to ship, or (2) an optional set of two empty, structurally-reinforced steel cans that replace five of the concrete-filled steel masses. The empty can option allows single truck mobilization to distant sites with a total shipped mass of 19,000 kg. Once at the site the cans can be filled with sand, gravel, water or any combination to attain the required mass. Lower loads (up to 2.3 MN) can be attained by using just the empty cans without any fill material. Option 2 has the added advantage of using only three reaction masses which translates into time savings in crane usage. Figures 2.1 - 2.10 illustrate typical assembly of the device.



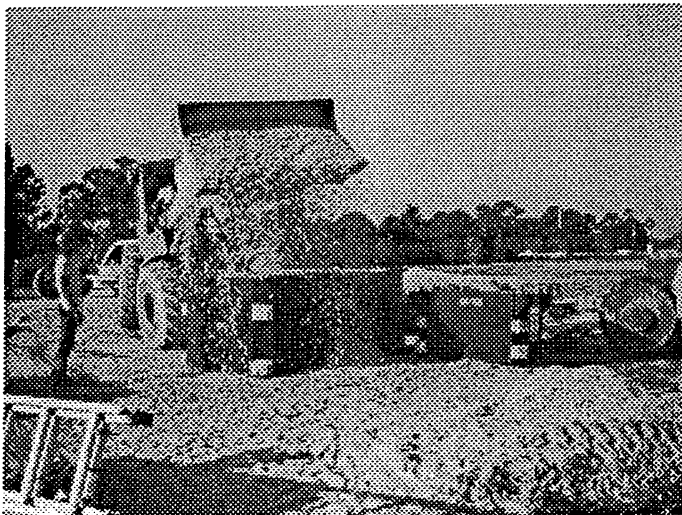


**Figure 2.4** Filling cans with gravel (Option 2).

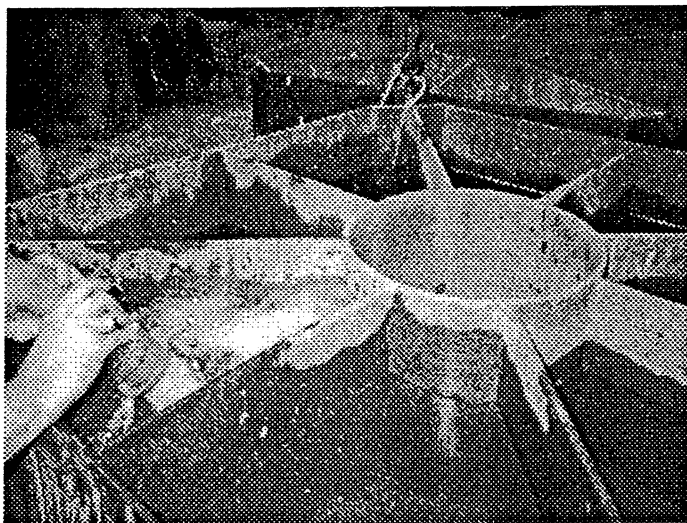


**Figure 2.5** Alternatively, cans are filled with water.

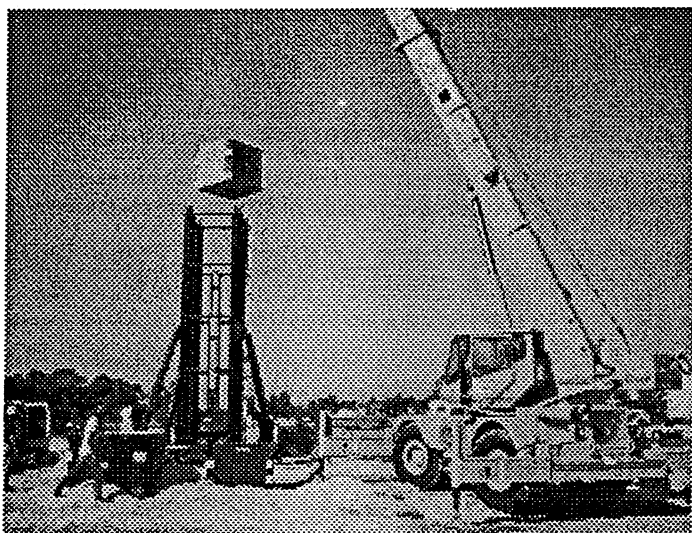


**Figure 2.6** Assemble reaction masses (either Option 1 or 2)

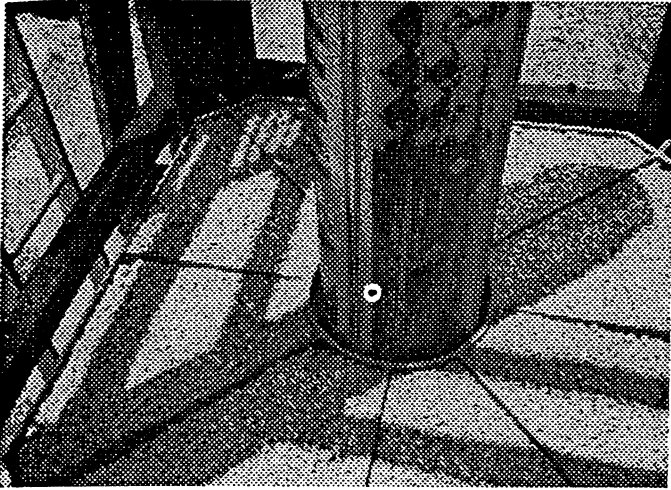


**Figure 2.7** Gravel-filled can installed.



**Figure 2.8** Fully assembled mechanism.



**Figure 2.9** Statnamic test.

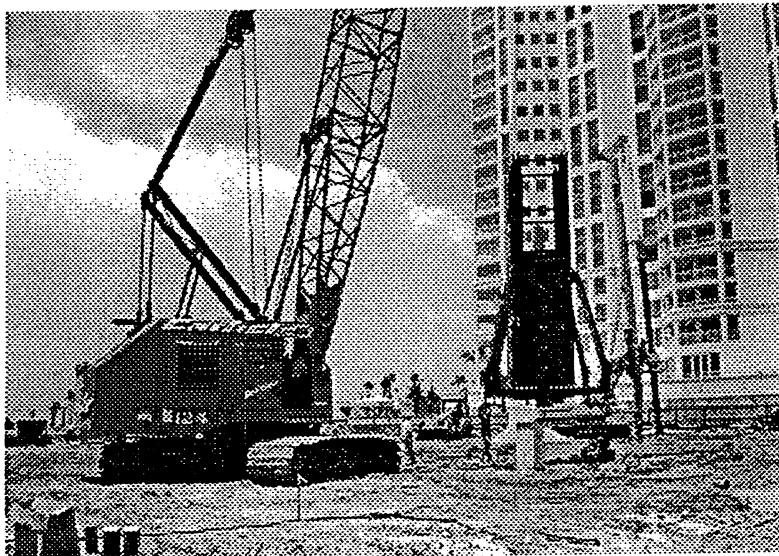


**Figure 2.10** Entire mechanism can be placed on the next test pile without disassembly.

### 3. SHALLOW FOUNDATION TESTING

Researchers at the University of South Florida are currently exploring the correlations between Statnamic and static load testing of shallow foundations. Statnamic testing of shallow foundations has the potential to provide a cost effective alternative to static load testing, and the initial findings have been favorable.

#### 3.1 Federal Highway Administration Collaboration

In a series of plate load tests performed in conjunction with the Federal Highway Administration, Statnamic testing was applied to shallow foundations. Three separate yet identical foundations on clean sand were tested in the following manner: (Test 1) incrementally increasing Statnamic load cycles until bearing failure, (Test 2) static load test, and (Test 3) a single Statnamic load test well in excess of the bearing capacity. Using the *Unloading Point Method* (Middendorp et al., 1992), a derived static load-displacement response was obtained for each load cycle, and compared with the static load test in which three load/unload cycles were recorded. Figures 3.1 and 3.2 illustrate the results of these tests.

Shown in Figure 3.1 are the results from the incrementally increasing Statnamic tests (test 1) and the static load test (test 2). The derived static load is shown for each of the four cycles where the peak Statnamic loads were 74, 128, 196, and 262 KN, respectively. Damping coefficients ( $C$ ) calculated for each cycle were 146, 76, 78, and 92 KN-s/m, respectively. The derived static response slightly over estimates the capacity of the foundation when compared to the true static capacity. This is not altogether surprising based on the probable densification of the soils within the initial cycles. This can be seen from Test 3 (Figure 3.2) which produced a peak load of 219 KN and resulted in more displacement than the fourth cycle of Test 1 (262 KN).

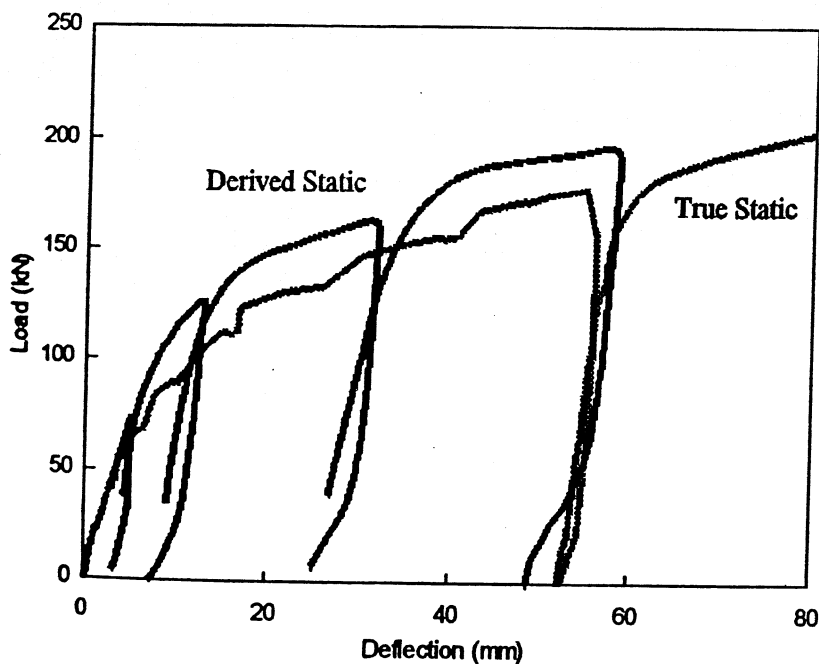


Figure 3.1 Comparison of derived static response from four Statnamic load cycles (test 1) with the true static response (test 2).

Figure 3.2 shows the results of Test 3 and provides an example of a trend that develops when Statnamic load grossly exceeds the bearing capacity of the foundation. During the linear elastic stage, Statnamic results indicate a much stiffer system than that of a static test, but once bearing failure occurs the two test results are similar. Derived static values for shallow foundations are relatively unaffected by inertial forces but seem sensitive to the damping coefficients. The damping coefficients calculated from the unloading portion of the

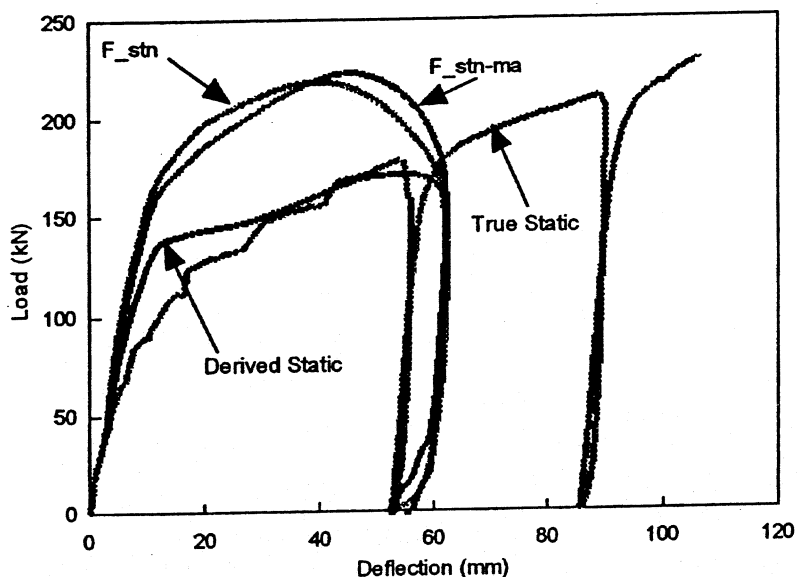


Figure 3.2 Static / derived static comparison of Statnamic test performed well above bearing capacity (tests 2 and 3).

test satisfy the system dynamics in that portion of the loading but fail to do so initially. This indicates that  $C$  varies as the soil strains and is supported by the difference in the calculated damping coefficient observed in Test 1 (cycle 1) and Test 3, 146 and 58 KN-s/m, respectively. It is assumed that the difference between the true static and inertia-corrected Statnamic force is due to a variable damping coefficient, then the coefficient at any point could be determined for this site using the following expression:

$$C_x = \frac{F_{stn_x} - F_{ma_x} - F_{static_x}}{V_x} \quad (3.1)$$

where  $C$ ,  $V$ ,  $F_{stn}$ , and  $F_{ma}$  are the dynamic force parameters at displacement  $x$  and  $F_{static}$  corresponds to the true static force at that displacement. Using this expression, Figure 3.3 illustrates the variation in the damping coefficient as a function of displacement. It is interesting to note that  $C$ , at small displacements, is similar to that of Test 1 (cycle 1) and at large displacements similar to Test 3.

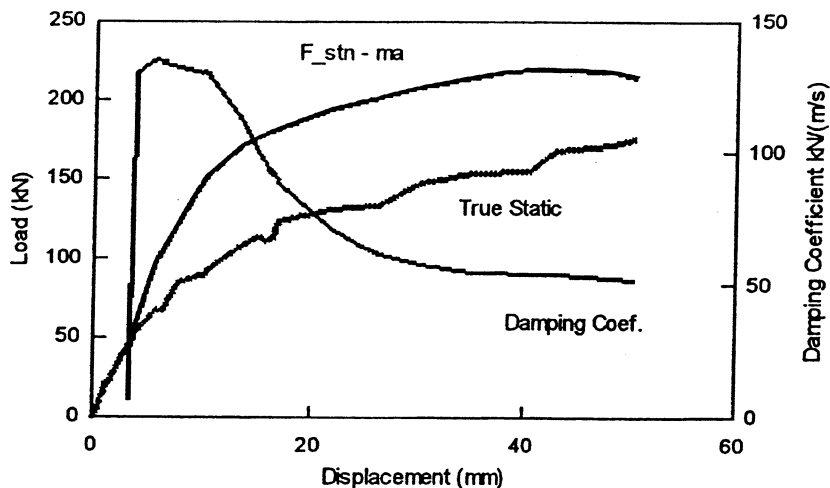


Figure 3.3 Values of the variable damping coefficient calculated using the true static response and the inertia corrected Statnamic force.

### 3.2 Testing Foundations on Stone Columns

Tests performed in conjunction with Hayward Baker using the 4 MN hydraulic catching system provided the opportunity to investigate the Statnamic response of shallow foundations on stone columns. This program consisted of side by side comparisons of full-scale Statnamic and static load tests on a 2 m square steel footing. Figures 3.4 and 3.5 show the two test configurations.

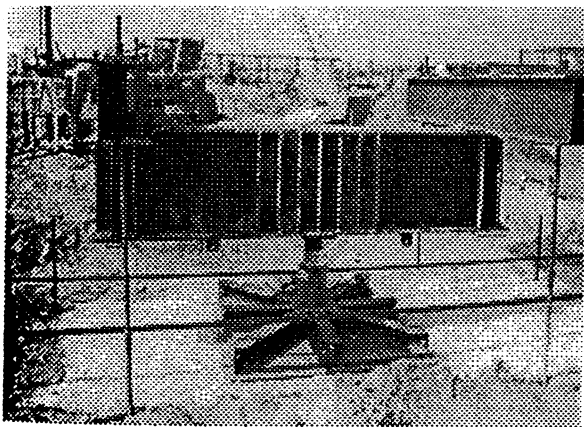


Figure 3.4 Static load test assembly on stone column-reinforced soil.

Shown in Figure 3.6 are the results of the Statnamic testing of the stone column shallow foundations, and the comparison of derived static and true static response of the footing.

As indicated in Figure 3.6, the Statnamic response of the stone column foundation was very similar to the true static response. Because neither test was conducted beyond the bearing capacity of the foundation, the response for both was highly linear. After what appears to be some initial device seating, the Statnamic-derived static load curve has a slope that is nearly identical to the true static. The apparent strain hardening observed in both methods was most likely due to the flexibility

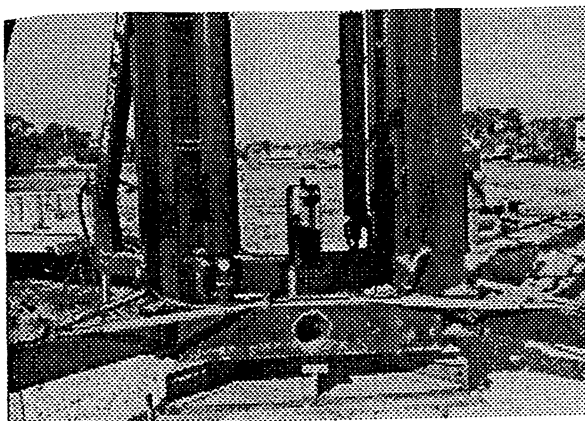


Figure 3.5 4 MN Statnamic piston and HCM frame installed on test plate.

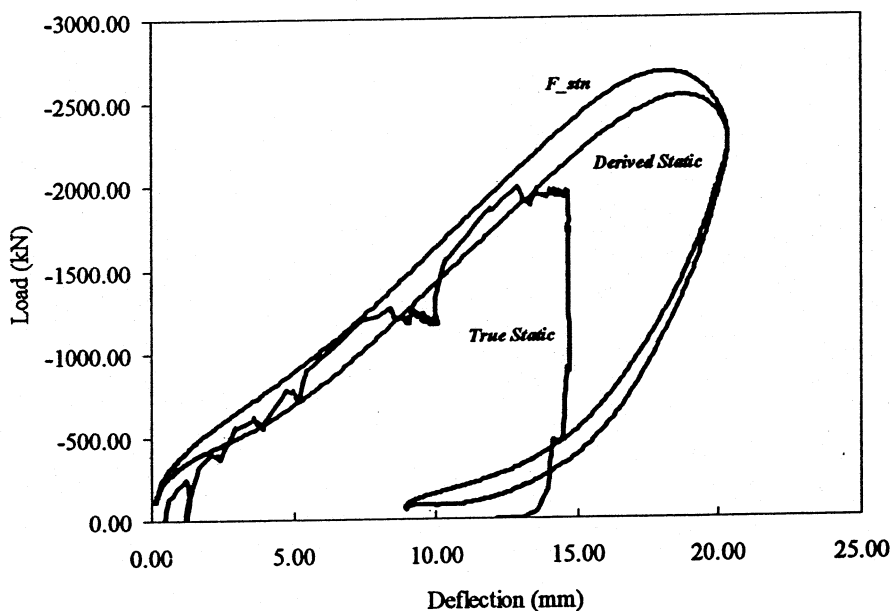


Figure 3.6 Comparison of static and Statnamic test results for shallow foundations on stone columns.

of the plate. Recognizing this as a potential problem, Hayward Baker has agreed to test stiffer, production-type concrete footings in an upcoming test program.

## 4. DEEP FOUNDATIONS

### 4.1 *Soft Toe-Constructed Shafts*

In an effort to minimize testing expenses associated with full-scale load testing, drilled shafts with soft toes can be constructed. Such shafts can be tested at loads below that of their ultimate



capacities. Hence, smaller test equipment can be used as a means of measuring the ultimate skin friction provided by the soil, without having to overcome tip resistance.

Drilled shafts can be constructed with soft toes by welding a flat plate to the bottom of the reinforcement cage and then attaching a Styrofoam plug to the bottom of the plate. Figure 4.1 shows a typical soft toe-prepared cage. The plug at the tip of the shaft provides virtually no toe resistance when loaded and allows the foundation to fail purely in shear. Strain gauges placed at selected levels can be used to determine unit skin friction for specific soil layers.

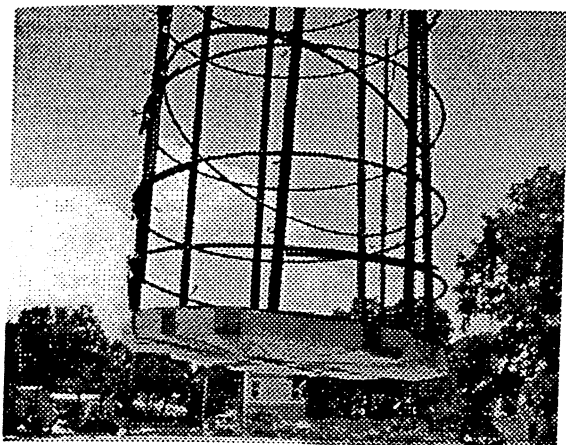


Figure 4.1 Styrofoam soft-toe assembly.

This type of testing requires that load cycling be used to ensure the toe capacity is regained. Because of the need for load cycling the HCM is the perfect device to use in association with soft toes. The initial cycles define the ultimate skin capacity and subsequent cycles develop the toe capacity. Once the plug completely compresses, the toe is seated and the designer can be assured of its capacity.

Figure 4.2 displays the load cycling effects on a 0.9 meter diameter, 7.4 meter long drilled shaft with a soft toe. The shaft was constructed in sand for the upper 3 meters, which was underlain by a 1.5 meter sandy clay layer, and finally tipped in Florida limestone. Foundation testing was completed using USF's 4 MN HCM.

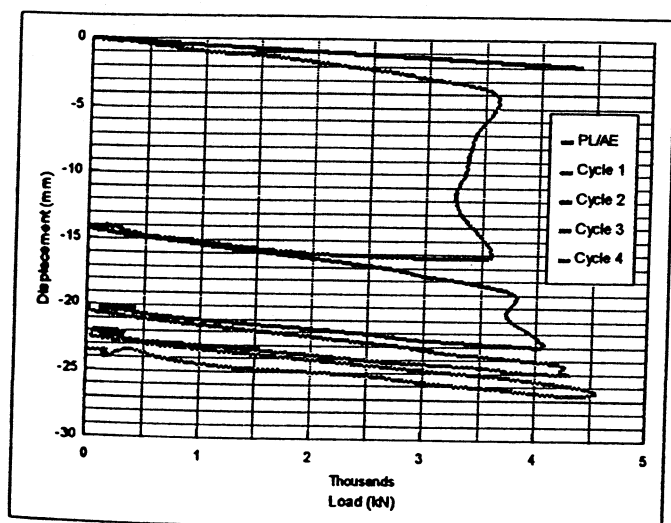


Figure 4.2 Results of load-cycling on a soft-toed drilled shaft.

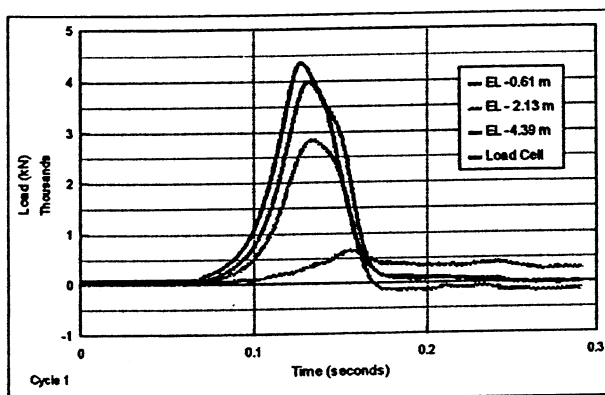


Figure 4.3 Cycle 1: toe load increases late in the test after significant displacement

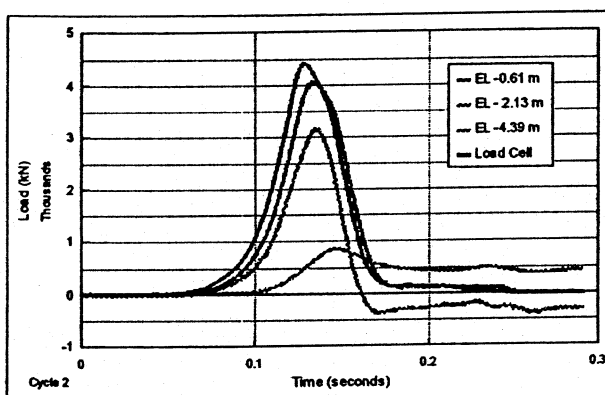


Figure 4.4 Cycle 2: toe load increases, and bottom rock layer fully mobilizes

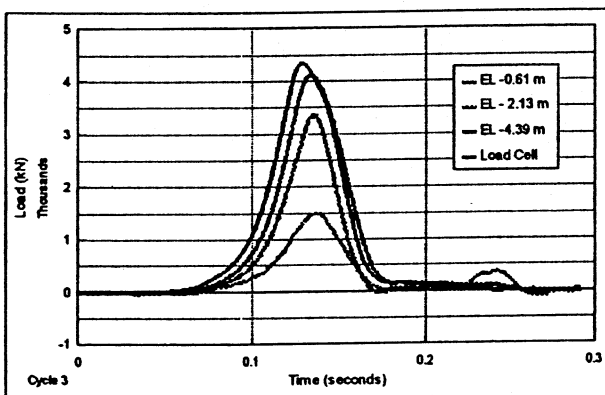
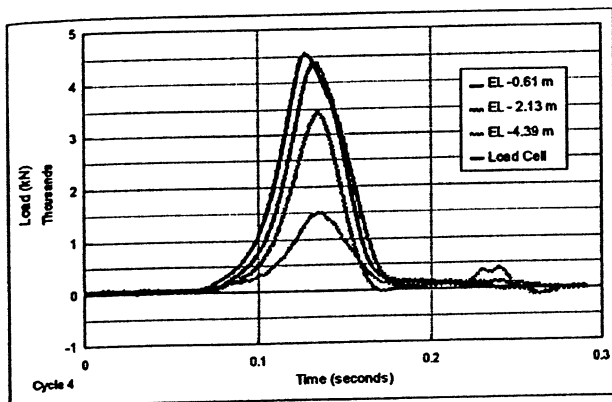


Figure 4.5 Cycle 3: toe load maximizes given the size of the equipment

Shown are four derived static load cycles along with the elastic compression curve. The first load cycle fails the shaft and fully mobilizes the skin friction. In subsequent cycles the toe capacity begins to develop until the third cycle when it has developed enough to exceed the device capabilities. This is confirmed by identical tow response in the fourth cycle. Figures 4.3 through 4.6 display the distribution of load throughout the shaft for cycles 1 through 4 respectively. Shown are the load traces from the Statnamic load cell (upper most) and the embedded strain gauges (lower most being the toe gauge).



**Figure 4.6** Cycle 4: no significant change in load distribution

Soft-toe test shafts allow the engineer to gain an understanding of in-situ soil strengths with smaller, more cost-effective devices.

#### 4.2 Post-Grouted Drilled Shaft Tips

Although post-grouting of drilled shaft tips has been adopted in many countries, it is only now being considered for use in the southeastern United States. A program is presently developing to evaluate its effectiveness using Statnamic testing as the primary mechanism of loading. Statnamic testing is ideal for this effort because it is cost-effective and can be implemented without affecting normal construction techniques. Further, the HCM-equipped Statnamic device will allow for multiple staged load cycles that may be required, especially for ungrouted control piles, to fully define the shaft's ultimate end-bearing characteristics.

As a potential side benefit, post-grouting may provide a proof test for all shafts on a project, once the initial Statnamic load testing is completed. This can be accomplished by comparing the pile strain distribution from post-grouting with that of the Statnamic test.

### 5. DOWN-HOLE LATERAL MOTION SENSOR

#### 5.1 Background

Recently, starting in 1996, lateral Statnamic load tests have been performed in addition to static tests to simulate more closely the lateral loads from ship impacts or seismic events. The duration of this test excludes the use of conventional inclinometers which are typically used to measure down-hole lateral displacements for static lateral load tests. Therefore, a dynamic device analogous to the inclinometer has been developed to measure lateral motions beneath the ground surface during a transient lateral load.

#### 5.2 Concept, Design and Development

The laterally deflected shape of a steel pile can be estimated from bending strain measurements by double integrating a fitted moment equation. However, the deflected shape of a drilled shaft cannot usually be generated from embedded strain gages due to the changing moment of inertia after tension cracks form in the concrete. The need for displacement measurements during lateral Statnamic tests

gave rise to the *down-hole lateral motion sensor (DLMS)*. This device has been designed with several significant features: (1) it can be preset to monitor motion in line with the applied load, (2) it is compatible with standard inclinometer casings, (3) it can be lowered to any desired depth in the casing, and (4) it is retrievable. Additionally, by using several devices in a string, the deflected shape of the casing can be defined.

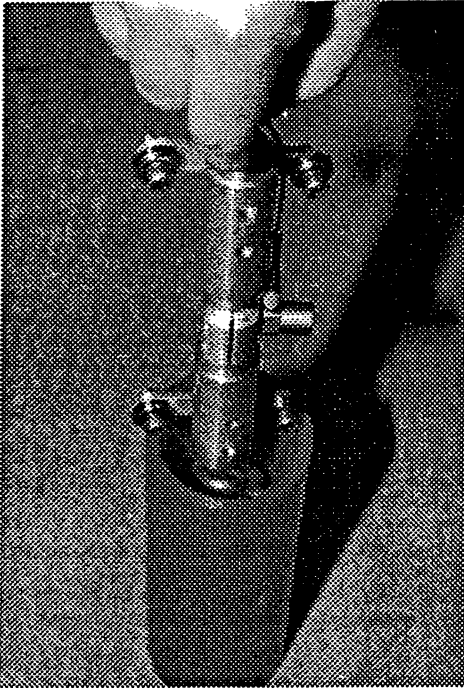


Figure 5.1 Down-hole lateral motion sensor (DLMS) assembly.



Figure 5.2 Prototype DLMS in Opelika, Alabama.

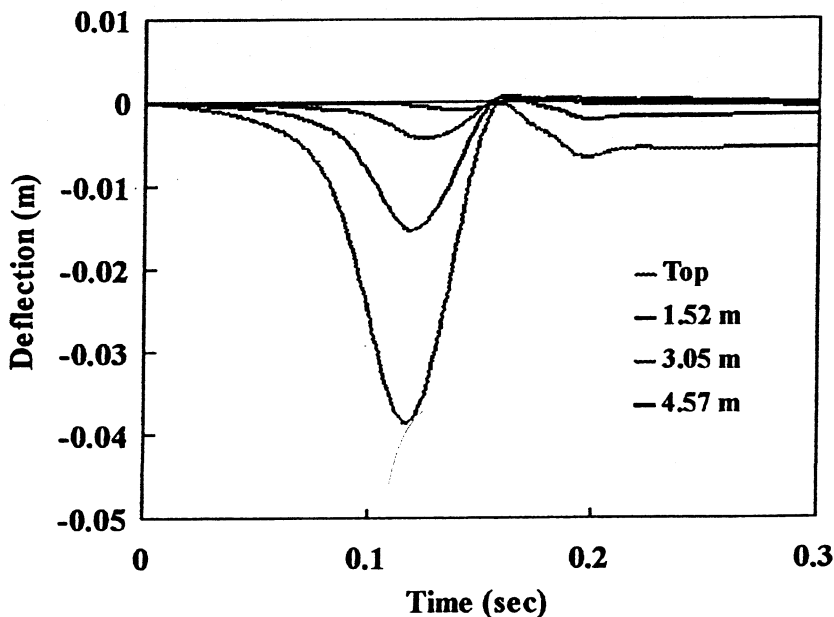


Figure 5.3 Displacement response from four locations along the shaft.

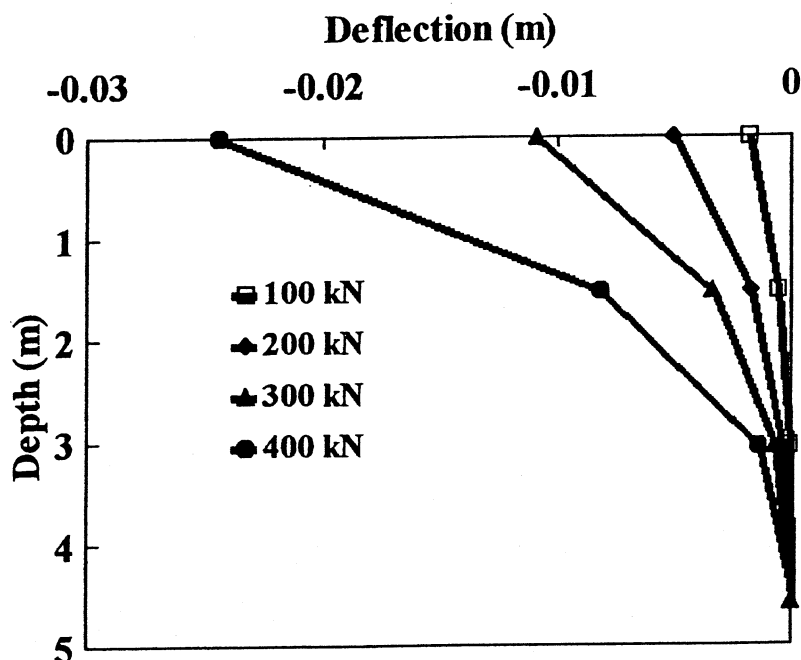


Figure 5.4 Deflected shape of the shaft at 100, 200, 300, and 400 kN.

The device basically uses an accelerometer aligned with the direction of loading. Because the grooves of the inclinometer casing are typically oriented other than that desired, the accelerometer is mounted on an adjustable collar which can be secured in a prescribed direction of loading. This orientation is maintained during installation using spring loaded wheels that snap into the grooves of the inclinometer casing (similar to that of the inclinometer). Figures 5.1 and 5.2 show the DLMS sensor prior to installation.

Several Statnamic load tests have been conducted on drilled shafts where the deflected shape was determined from the down-hole lateral motion sensor data. Each program compared the foundation response of static and Statnamic lateral loads. Full details of these results can be found elsewhere (Brown et al., 1998). Results from data obtained from a string of three devices (1.52, 3.05, and 4.57 meters below the ground surface) are shown in Figure 5.3. This figure shows the displacement trace of a 10 meter, single-shaft lateral load test at the Auburn University site in Opelika, Alabama. Figure 5.5 shows the deflected shape of the shaft from four instances during the Statnamic loading.

## 6. SUMMARY

In the past two years, the University of South Florida has performed numerous Statnamic tests due to the support received from state and federal agencies, and private industry. As a direct result, an extensive research program has been developed in each of these areas: shallow foundations, deep foundations, lateral testing, and instrumentation. With the purchase of a hydraulic catch mechanism, USF researchers have been able to explore new applications and refine existing procedures. The objective of this paper is to encourage further discussion of these topics. Comments or questions, addressed to [gnullins@eng.usf.edu](mailto:gnullins@eng.usf.edu), would be appreciated.

## REFERENCES

- Bermingham, P. & Janes, M. 1989. An innovative approach to load testing of high capacity piles. *Proc. Int. Conf. On Piling and Deep Foundations*, London, 1: 409-413.
- Brown, D., Chakraborty, S., and Mullins, G. 1998. Dynamic measurements and data analysis of statnamic lateral loading. *Second International Statnamic Seminar*, Tokyo, Japan.
- Middendorp, P., Bermingham, P., and Kuiper, B. 1992. Statnamic load testing of foundation piles. *Proc. Of the 4<sup>th</sup> Int. Conf. On the Application of Stress-Wave Theory to Piles*, The Hague, The Netherlands, A.A. Balkema Publishers, 581-588.

# The behavior of piles in clay during Statnamic and different static load testing procedures

E.L. Hajduk & S.G. Paikowsky  
*University of Massachusetts, United States*

G. Mullins & C. Lewis  
*University of South Florida, United States*

C.D. Ealy  
*Federal Highway Administration, McLean, VA, United States*

N.M. Hourani  
*Massachusetts Highway Department, Boston, MA, United States*

**ABSTRACT:** A long-term investigation of pile capacity in the Boston Area was carried out in predominately fine-grained soils at a bridge reconstruction site in Newbury, Massachusetts. This investigation included heavily instrumented piles subjected over a lengthy period of time to different static load and dynamic measurements during driving and restrikes. Staged Statnamic load tests were conducted on two of the test piles following the completion of the capacity gain investigation. A comparison is presented between the final static load tests and the Statnamic testing. Conclusions are drawn regarding (i) the accuracy of the testing, (ii) the Statnamic measurements versus dynamic measurements during testing and (iii) the effect of the testing procedure on the surrounding soil behavior.

## 1. INTRODUCTION

An investigation of pile capacity gain with time was conducted by the Geotechnical Engineering Research Laboratory of the University of Massachusetts - Lowell (UML). Three full-scale instrumented piles were installed at a bridge reconstruction site along Route 1 in Newbury, MA. Static and dynamic testing were conducted over a period of one year and two of the test piles were subjected to Statnamic testing after the capacity gain investigation had been completed. The presented Statnamic tests are the first to be conducted on deep foundations in the New England area. The Newbury Testing program provided the conditions to examine Statnamic testing in the region (1) the soil profile at the Newbury Site is typical of the Boston, Massachusetts area and a detailed subsurface investigation was carried out at the site and extensive testing was conducted on the test pile cluster and (2) the piles and the soil were well instrumented.

A series of static load tests were performed on each test pile at the end of the pile capacity investigation. The purpose of these tests was to evaluate the final pile capacity as well as to compare various procedures of static load testing. Measurements of the pore pressure along the piles and in the ground piezometer field showed that all excess pore pressure due to driving of the test pile itself or an adjacent pile had completely dissipated at that stage. In addition, a significant amount of time (minimum 4 months) had passed since the last adjacent test pile had been driven, allowing for all pile capacity gain to be completed. Based on this information, it was concluded that these final static load tests would determine the final pile capacity.

The final static load tests are classified as slow maintained, short duration, and static-cyclic, based on the pile loading increments, length of time each load increment was held constant, or loading rate. The slow maintained and short duration tests were conducted according to the of the Massachusetts Highway Department (1995). The static-cyclic tests were conducted according to criteria developed in a concurrent research that is beyond the scope of the present paper (Paikowsky and Operstein, 1999). To minimize the effects of each static load test on each subsequent test, the testing was conducted in the following order: slow maintained, short duration, and static-cyclic. This schedule allowed for the maximum possible time between



loading cycles while allowing the tests to be performed over a short period. Furthermore, the pore pressure measurements along the pile were allowed at or near hydrostatic conditions before the next static load test was conducted. Based on this information, it was assumed that any effect each test may have on another would be negligible.

The results from the various load tests conducted on the two test piles showed that each had reached final capacity. Pore pressure measurements along the piles and in the ground piezometer field before the Statnamic testing indicated that they were at or near hydrostatic conditions. This suggested that the test piles had gained no further capacity.

The Statnamic testing was conducted 6 and 4 months after the completion of static load testing for Test Piles #2 and #3, respectively. A summary of the static and Statnamic testing performed on the two test piles is listed in Tables 1 and 2 for Test Pile #2 and #3, respectively. Each pile was subjected to several Statnamic tests at increasing loads until approximately twice the final static failure load was reached. A total of 10 Statnamic tests were conducted on the two test piles. Six Statnamic tests at increasing capacities were conducted on TP#3, with the tests being labeled TP#3-1 through 6. After completion of these tests, the Statnamic device was positioned over Test Pile #2. Four Statnamic tests were completed on TP#2 at various capacities. These tests were labeled TP#2-1 through 4. All Statnamic testing for both piles was conducted on the same day within a 10-hour period.

Table 1 Timetable of testing for test pile #2

	TP#2 SLT7	TP#2 SLT8	TP#2 SLT9	TP#2-1 – 4
Type of Test	Slow Maintained	Short Duration	Static-Cyclic	Statnamic
Date of Test	10/22/97 to 10/24/97	10/27/98	10/28/98	4/23/98
Time from End Of Driving (EOD)	8 Months	8 Months	8 Months	14 Months

Table 2 Timetable of testing for test pile #3

	TP#3 SLT3	TP#3 SLT4	TP#3 SLT5	TP#3-1 – 6
Type of Test	Slow Maintained	Short Duration	Static-Cyclic	Statnamic
Date of Test	12/2/97 to 12/4/97	12/4/98	12/5/98	4/23/98
Time from End Of Driving (EOD)	12 Months	12 Months	12 Months	16 Months

## 2. THE NEWBURY TEST SITE

The Newbury bridge reconstruction site is located along Route 1 on the Newbury - Newburyport border, north of Boston, Massachusetts. The test pile program consisted of three-instrumented test piles laid out in a triangular formation near the north abutment of the bridge. In addition to the test piles, a ground piezometer field consisting of ten vibrating wire piezometers was installed to monitor the piezometric pressures at various elevations and distances away from the test piles. Seven piezometers were located near the center of the clay layer, with an average depth of 11m (36ft). The remaining three ground piezometers were located in a silty sand layer, with an average depth of 29m (69ft). A report describing the test pile cluster, the ground piezometer field, and the testing program is currently being prepared for the Massachusetts Highway Department (Paikowsky and Hajduk, 1998). Figure 1 shows the test pile layout and the ground piezometer field.

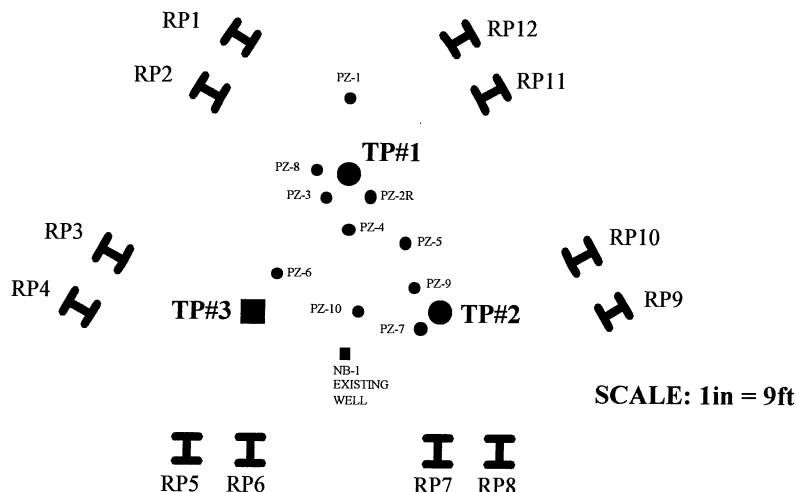


Figure 1. Newbury test site layout (after Paikowsky and Hajduk, 1998).

The soil stratigraphy of the site is typical of the conditions found in the Boston area. The general soil profile at the pile testing location (from ground surface downward) consists of the following soil strata: 8 feet (2.44 meters) of granular fill composed of very dense, brown sand and gravel intermixed with frequent concrete fragments, overlies a thin layer (approximately 1 foot (0.3 meters)) of highly compressible organic silt and peat. In order to protect the test piles, these layers were excavated and cased with steel pipe sections. Below the fill and organics is an approximately 45 feet (13.7 meters) thick deposit of a marine clay, known as Boston Blue Clay. The clay consists of approximately 9 feet (2.7 meters) of very stiff to medium stiff, over-consolidated layer (crust), over 20 feet (6.1 meters) of soft normally consolidated clay and 16 feet (4.9 meters) normally consolidated clay. An interbedded deposit of silt, sand, and clay approximately 9.5 feet (2.9 meters) thick underlies the clay. Below this interbedded deposit is a layer of silty sand approximately 8 feet (2.4 meters) thick. Another interbedded deposit of silt, sand, and clay approximately 7.5 feet (2.3 meters) thick underlies the silty sand. Below this interbedded deposit is a layer approximately 8 feet (2.4 meters) thick of medium dense to dense, fine to medium sand. Underlying the fine to medium sand is a dense glacial till consisting of medium dense to dense, fine to coarse sand and gravel, with traces of silt and rock fragments. Good quality, unweathered bedrock was encountered at approximately 100 feet below the ground level (elevation 81.7 feet) (Paikowsky and Chen, 1998). A detailed characterization of the subsurface at the site is provided by Paikowsky and Chen, (1998). The typical soil profile of the site and results from a CPT test conducted alongside the configuration of Test Piles #2 and #3 are shown in Figure 2.

### 3. INSTRUMENTED TEST PILES

Three full-scale instrumented test piles, two friction and one end bearing, were installed at the Newbury test site. Only the two friction piles were selected for additional Statnamic testing. These two piles consisted of a steel pipe pile and a square, pre-stressed concrete pile, designated Test Pile #2 and #3 respectively. A report is currently under preparation detailing the design and construction of these test piles (Paikowsky and Hajduk, 1998).

Test Pile #2 (TP#2) is a 324mm diameter x 13mm x 24.4m long (12.75in diameter x 0.5in thick x 80ft) steel pipe pile. This pile is instrumented with electrical resistance piezometers, vibrating wire piezometers, and strain gages at various depths below the pile top. The piezometers were installed in such a manner that they lie halfway between sets of strain gages. This arrangement allowed for pore pressure measurements to be taken and compared with an

average skin resistance during static load testing. Additional electrical resistance strain gages and piezo-resistive accelerometers were located at the middle and tip of the pile to record dynamic measurements. Over the course of pile capacity gain investigation, an interior water leak damaged the electrical resistance gages of TP#2. These instruments were therefore not available during the Statnamic testing. Pile Driving Analyzer™ (PDA) load transducers and piezo-electric accelerometers were also mounted near the pile top during dynamic and Statnamic testing. A instrumentation layout of TP#2 is shown in Figure 2 relative to the soil profile.

Test Pile #3 is a 356mm square x 23.9m long (14in square x 78.5ft) pre-stressed concrete pile. This pile is instrumented with four vibrating wire piezometers and six vibrating wire strain gages located at various distances from the pile top. As with TP#2, PDA load transducers and piezo-electric accelerometers were also mounted near the pile top during dynamic and Statnamic testing. Figure 2 shows the instrumentation layout of TP#3 in relation to the typical soil profile.

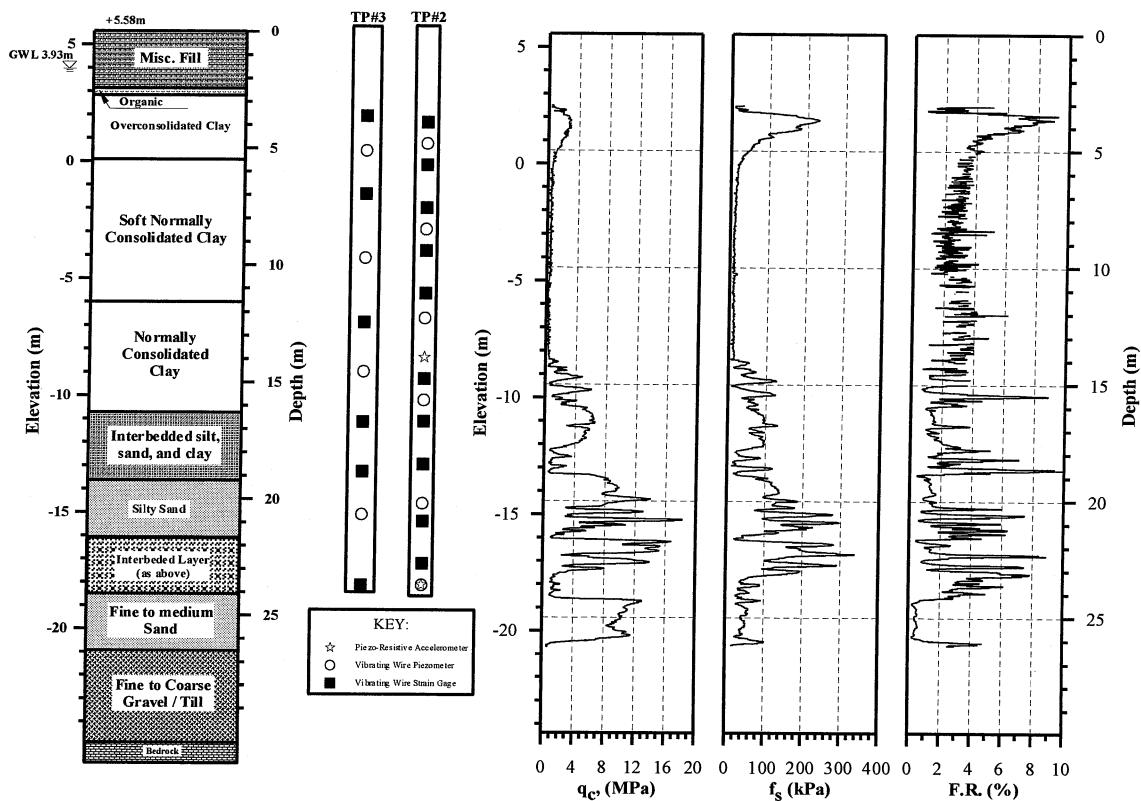


Figure 2. Newbury site soil profile with test piles #2 and #3 layouts and typical CPT test results.

## 4. LOAD TESTING METHODS

### 4.1 Static load tests

Four HP14x89 reaction piles were driven along each side of the test pile triangle before the installation of the test piles. Each reaction pile was driven to a minimum depth of 18.3m (60ft) and was located a minimum of 2.1m (7ft) from any test pile. This distance was deemed sufficient enough to not disturb the soil at the test pile locations. The triangular layout of the reaction frame allowed for a reaction beam (two W33x201 steel beams) to be placed over any test pile at any time to conduct a static load test. Load was transferred from the reaction beam to the reaction piles with HP14x89 transfer beams. The configuration over each test pile was

identical and produced a 4.4MN (500 ton) test frame. Figure 1 shows the reaction pile layout relative to the test piles. Paikowsky and Hajduk (1998) describe in detail the static load test instrumentation used for TP #2 and #3. All the reaction piles were removed from the site on 1/29/98 to 1/30/98, four months before the Statnamic testing.

#### 4.2 Statnamic load tests

A Statnamic load test involves the application of a short duration load (approximately 120ms) to a pile or caisson. Burning a solid fuel inside the Statnamic device produces a high-pressure gas. The attendant force associated with this gas accelerates a reaction mass upward at 20 g's, producing an equal force on the pile. Typically, the reaction mass weighs 5% of the desired load (Justason et al., 1998).

The Statnamic device consists of a reaction mass, a fuel chamber, piston, and silencer. In addition, a gravel chamber or a hydraulic mechanism is used to catch the reaction mass after it is propelled upward. A load cell is placed between the piston and pile to record the load placed on the pile. Displacement is measured by use of a laser sensor. Acceleration is recorded via a servo accelerometer near the load cell. In addition to this instrumentation, Pile Dynamics' load transducers and piezo-electric accelerometers were also attached to the pile to record force and acceleration similar to conventional dynamic pile monitoring during driving. More information on Statnamic testing is provided by the test system manufacturer (Birmingham, 1997).

A 8MN Statnamic device, owned jointly by the University of South Florida and the Federal Highway Administration, was used at the Newbury Test Site. This device is equipped with a hydraulic catch mechanism, which allows for rapid consecutive testing on one pile. Figure 3 shows the Statnamic testing apparatus on Test Pile #2.



Figure 3. View of Statnamic load test apparatus over test pile #2

### 4.3 Pile capacity determination

In order to standardize the pile capacity determination, Davisson's Failure Criteria was used to determine the pile capacity for the maintained, short duration, and Statnamic load tests. This procedure is consistent with Massachusetts Highway Department specifications and is typically used as the standard method of pile capacity determination. For the static-cyclic tests pile capacity is determined from the points formed by the intersection of the loading and unloading curves. Paikowsky and Operstein (1999) provide details regarding the pile capacity determination under static cyclic test procedures.

## 5. TEST RESULTS

### 5.1 Static load test results

For the maintained and short duration load tests conducted on Test Pile #2, each test showed a pile capacity of 750kN (84 tons), near a displacement of 14mm (0.55in). The static-cyclic tests showed that a capacity of 670kN (75 tons) was achieved through the recommended analysis procedure. A summary of the results of static load testing conducted on Test Pile #2 is listed in Table 3. The load - displacement curves for all three tests are shown in Figure 4.

Table 3 Summary of static load test results for test pile #2.

	TP#2 SLT7	TP#2 SLT8	TP#2 SLT9
Type of Test	Slow Maintained	Short Duration	Static-Cyclic
Failure Load	750 kN (84 tons)	750 kN (84 tons)	670 kN (75 tons)
Maximum Displacement	33.9 mm (1.333 in)	25.9 mm (1.020 in)	26.8 mm (1.055 in)
Permanent Set	28.5 mm (1.121 in)	20.7 mm (0.815 in)	21.4 mm (0.841 in)

The analysis of the maintained and short duration tests on TP#3 showed a pile capacity of 1150kN (130 tons), near a displacement of 12.3mm (0.48in). The static-cyclic tests showed that a capacity of 1025kN (115 tons) was achieved through the recommended analysis procedure. Table 4 presents the results of the static load tests conducted on Test Pile #3. The load - displacement curves for all three tests are shown in Figure 5.

Table 4 Summary of static load test results for test pile #3.

	TP#3 SLT3	TP#3 SLT4	TP#3 SLT5A
Type of Test	Slow Maintained	Short Duration	Static-Cyclic
Failure Load	1150 kN (130 tons)	1150 kN (130 tons)	1025 kN (115 tons)
Maximum Displacement	34.8 mm (1.371 in)	26.8 mm (1.056 in)	23.7 mm (0.933 in)
Permanent Set	26.9 mm (1.059 in)	21.0 mm (0.828 in)	18.2 mm (0.716 in)

The near identical load-displacement curves of all three static load tests as well as the identical Davisson's failure load for the maintained and short duration load tests for both Test Piles #2 and #3 showed that each pile had achieved its maximum capacity. In addition, this information showed that the repeated loading cycles did not substantially affect each subsequent test.

## 5.2 Statnamic test results

The Statnamic test results conducted on Test Piles #2 and #3 are presented in Figures 4 and 5, respectively. In both figures, the Statnamic load vs. displacement is shown in section (a), while the derived static load vs. displacement is shown in section (b). A summary of the Statnamic test results for Test Pile #2 and #3 are presented in Tables 5 and 6, respectively.

The Unloading Point Method was used to calculate the derived static force, which is the common method of analyzing Statnamic tests. This method determines the static resistance by assuming that the long duration of the Statnamic load allows for modeling of the pile as a concentrated mass and a series of springs (Middendorp and Bielefeld, 1995). The derived static curve shows the load-displacement relationship with the inertia and damping forces removed from the measured Statnamic force (Justason et al., 1997). The mathematical procedure for Unloading Point Method is described by Middendorp et al. (1992).

For the first test conducted on Test Pile #2, the pile experienced small displacements that could not be distinguished from the noise of the data. Data for the third test conducted on Test Pile #3 was not properly collected. These two test results are therefore not presented.

Examination of the Statnamic force - displacement curves (refer to Figures 4(a) and 5(a)) show that the pile load - displacement relations during all tests conducted on both piles was primarily elastic. Each test follows the elastic compression curve of the pile and has little or none permanent set at the end of each Statnamic test. Both piles behave in a similar manner with the elastic behavior being more pronounced in Test Pile #2. Several Statnamic tests were conducted at loads greater than the static failure load on both piles. No trend that could indicate a clear failure of the pile was observed.

The derived static - displacement curves followed the same trend as the Statnamic force - displacement curves (see Figures 4(b) and 5(b) for Test Piles #2 and #3, respectively). The results of the derived static analysis show no indication of failure based on load - displacement relations or as defined by Davisson's criteria, for all the load tests.

In addition to the analysis above, a comparison was conducted between the force measured by the Statnamic load cell and the Pile Dynamic load transducers attached directly to the pile top. The primary purpose of this comparison was to observe if there was any stress wave phenomena present that would affect the measurement of the Statnamic load cell, such as the presence of tension waves. Figures 6 and 7 show the comparison between the average force measured by the load transducers and the Statnamic load cell readings during the Statnamic tests TP#2-2 through 4 and tests TP#3-4 through 6, respectively. The Statnamic force is shifted in time and magnitude (zeroed) to allow for a comparison with the average dynamic load transducer measurements. Both shifts between the two measured force signals is due to the difference in the data acquisition system operations. The Pile Dynamics PDA responds to dynamic forces only (all stationary forces are zeroed) and was triggered based on an increase in the measured force. The Statnamic data acquisition system measures absolute forces and presents an entire time span before and after the event. The time and magnitude shifts are therefore justified and the Statnamic force was adjusted. For each test, an excellent agreement exists between both measurements (see Tables 5 and 6).

Pore water pressure measured along Test Pile #3 during the Statnamic testing are presented in Figure 8. Measurements of the pore water pressure for the ground piezometer field are presented in Figure 9. The decrease in pore water pressure during shearing suggests that the clay along the pile is under over-consolidated clay conditions. A similar behavior was also displayed for the majority of the ground piezometer measurements in the clay layer. An exception was ground piezometer number 7 (Gnd PZ-7), which showed an increase in pore pressure during the testing of Test Pile #2. The proximity of this piezometer to the test pile (less than 3 pile radii) could explain this measurement. For the ground piezometers located in the silty sand layer, any buildup of pore pressure was quickly dissipated.

Table 5 Summary of Statnamic test results for test pile #2.

	TP#2 - 2	TP#2 - 3	TP#2 - 4
Maximum Statnamic Force	572 kN (64 tons)	976 kN (110 tons)	1186 kN (133 tons)
Duration of Test	0.24 sec	0.19 sec	0.18 sec
Maximum PDA Force	531 kN (60 tons)	890 kN (100 tons)	1047 kN (118 tons)
Maximum Displacement	2.6 mm (0.102 in)	10.2 mm (0.402 in)	12.1 mm (0.476 in)
Permanent Set	0.3 mm (0.012 in)	3.0 mm (0.118 in)	3.0 mm (0.118 in)

Table 6 Summary of Statnamic test results for test pile #3.

	TP#3-1	TP#3-2	TP#3-4	TP#3-5	TP#3-6
Maximum Statnamic Force	538 kN (60 tons)	1115 kN (125 tons)	1689 kN (190 tons)	1943 kN (218 tons)	1186 kN (250 tons)
Duration of Test	0.23 sec	0.17 sec	0.15 sec	0.14 sec	0.13 sec
Maximum PDA Force	NA	1257 kN (141 tons)	1869 kN (210 tons)	2010 kN (226 tons)	2303 kN (259 tons)
Maximum Displacement	2.1 mm (0.083 in)	6.1 mm (0.240 in)	11.1 mm (0.437 in)	13.5 mm (0.531 in)	16.1 mm (0.634 in)
Permanent Set	0.1 mm (0.004 in)	1.1 mm (0.043 in)	3.3 mm (0.130 in)	3.3 mm (0.130 in)	3.3 mm (0.130 in)

## 6. CONCLUSIONS

The Statnamic test produces a compression force wave of a much longer duration (in the order of one order of magnitude) when compared to the typical dynamic impact during driving. This force application cannot however be considered pseudo-static and resulted in a significantly higher response even when compared to a very fast static load test. The static-cyclic tests presented in Figures 4 and 5 were conducted in about 15 minutes per cycle. Their good match to the slow maintained and short duration tests suggest that the impact of the Statnamic test requires dynamic interpretation. The procedures suggested by Middendorp and Bielefeld (1995) seemed to produce excellent results in stiff and/or granular soils. The unfavorable results obtained in the presented tests suggest an influence of soil viscosity alongside buildup of pore pressure in fine-grained soils. These results may require the development of additional analysis tools and experience before the reliable application of the Statnamic test under similar soil conditions.



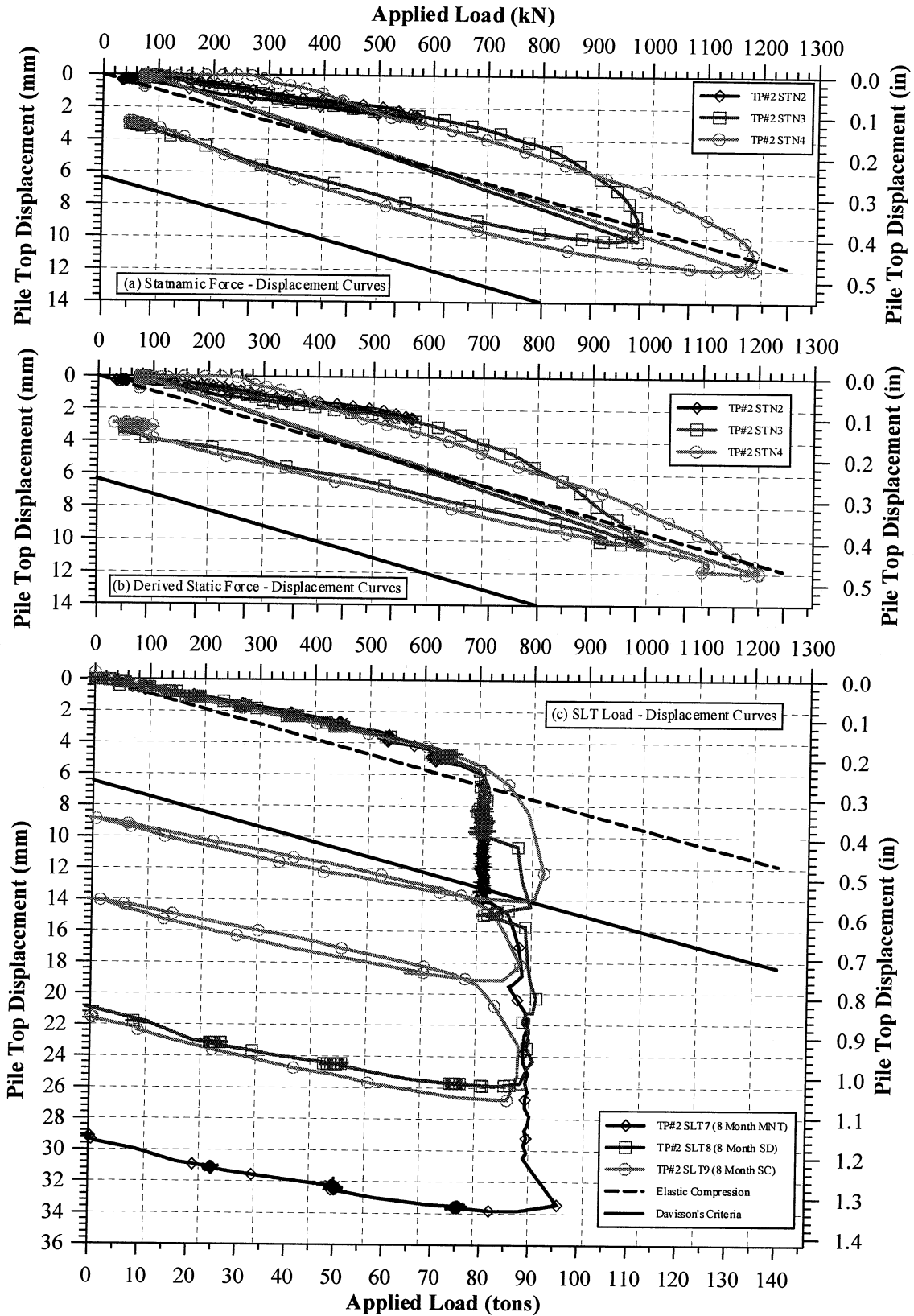


Figure 4. Static and Statnamic test results for test pile #2.

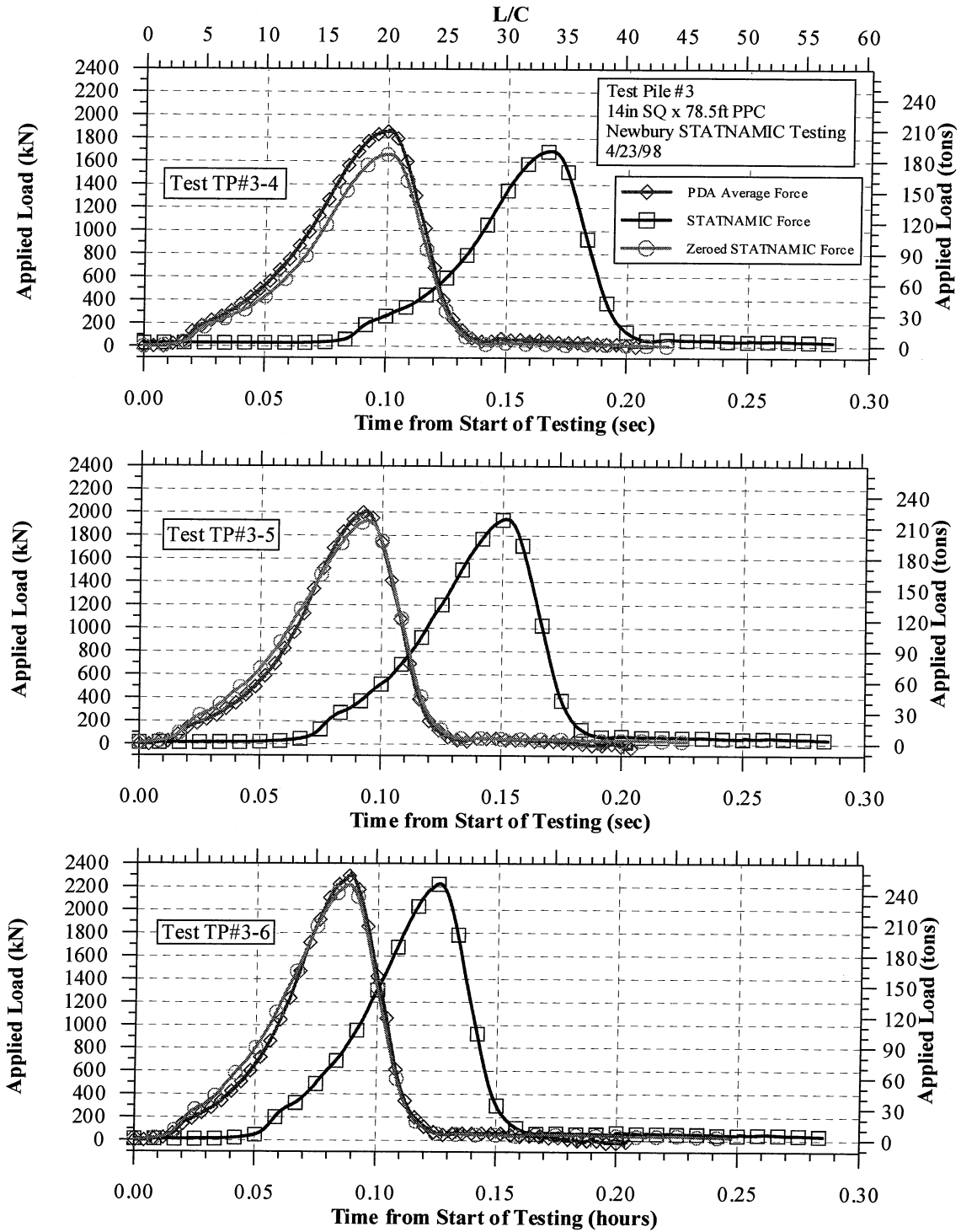


Figure 5. Static and Statnamic test results for test pile #3.

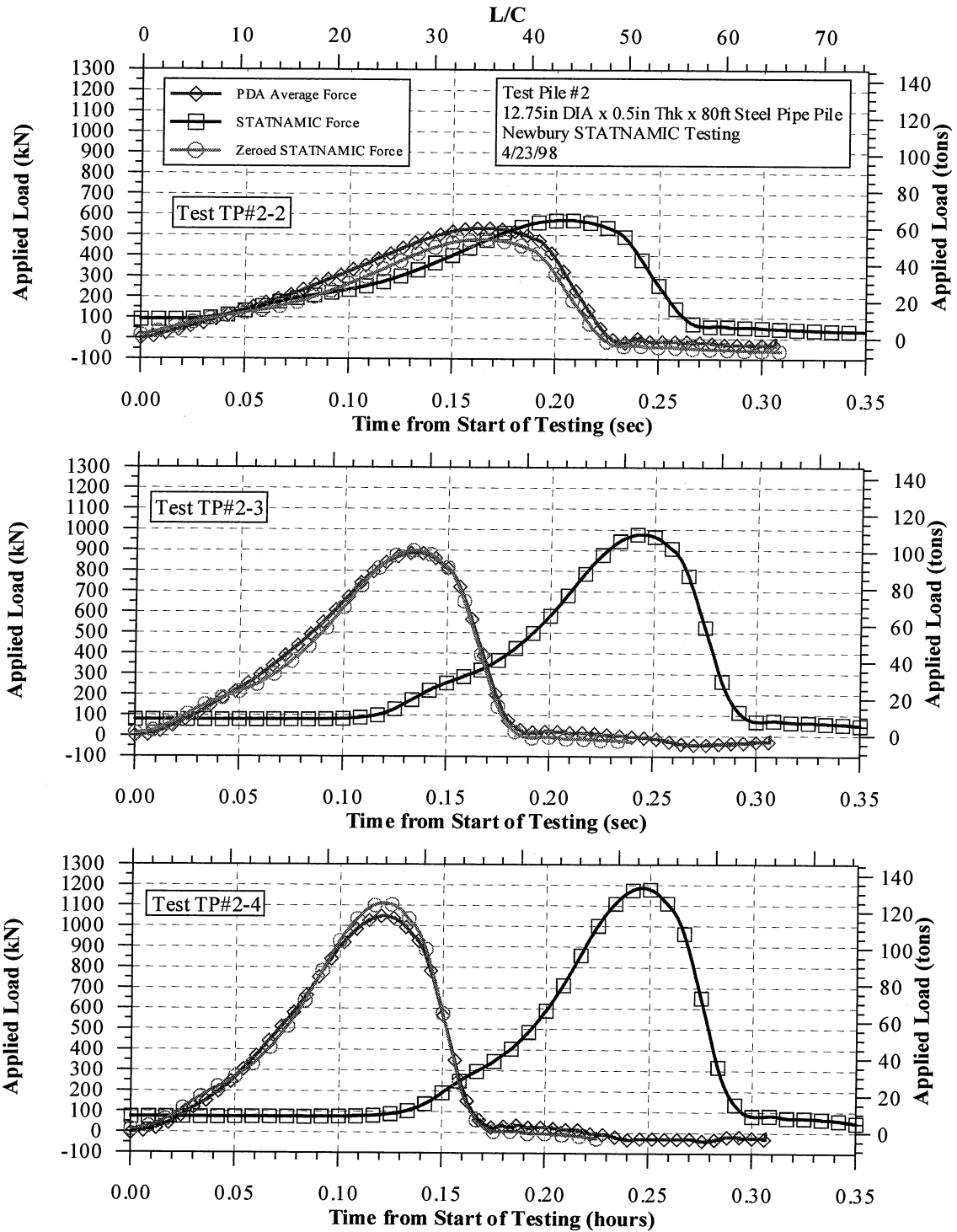


Figure 6. Statnamic and pile dynamic force measurements for test pile #2.

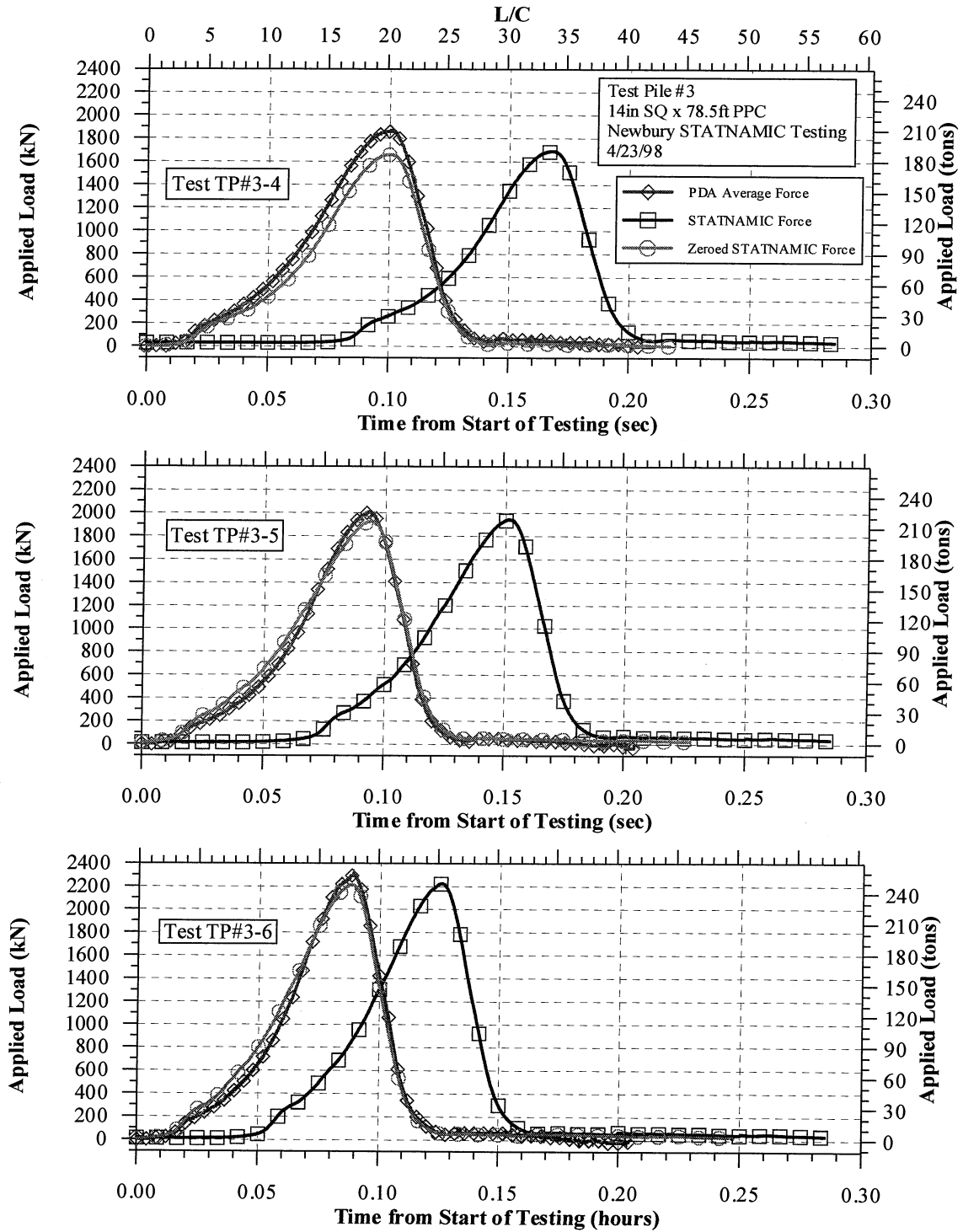


Figure 7. Statnamic and pile dynamic force measurements for test pile #3.

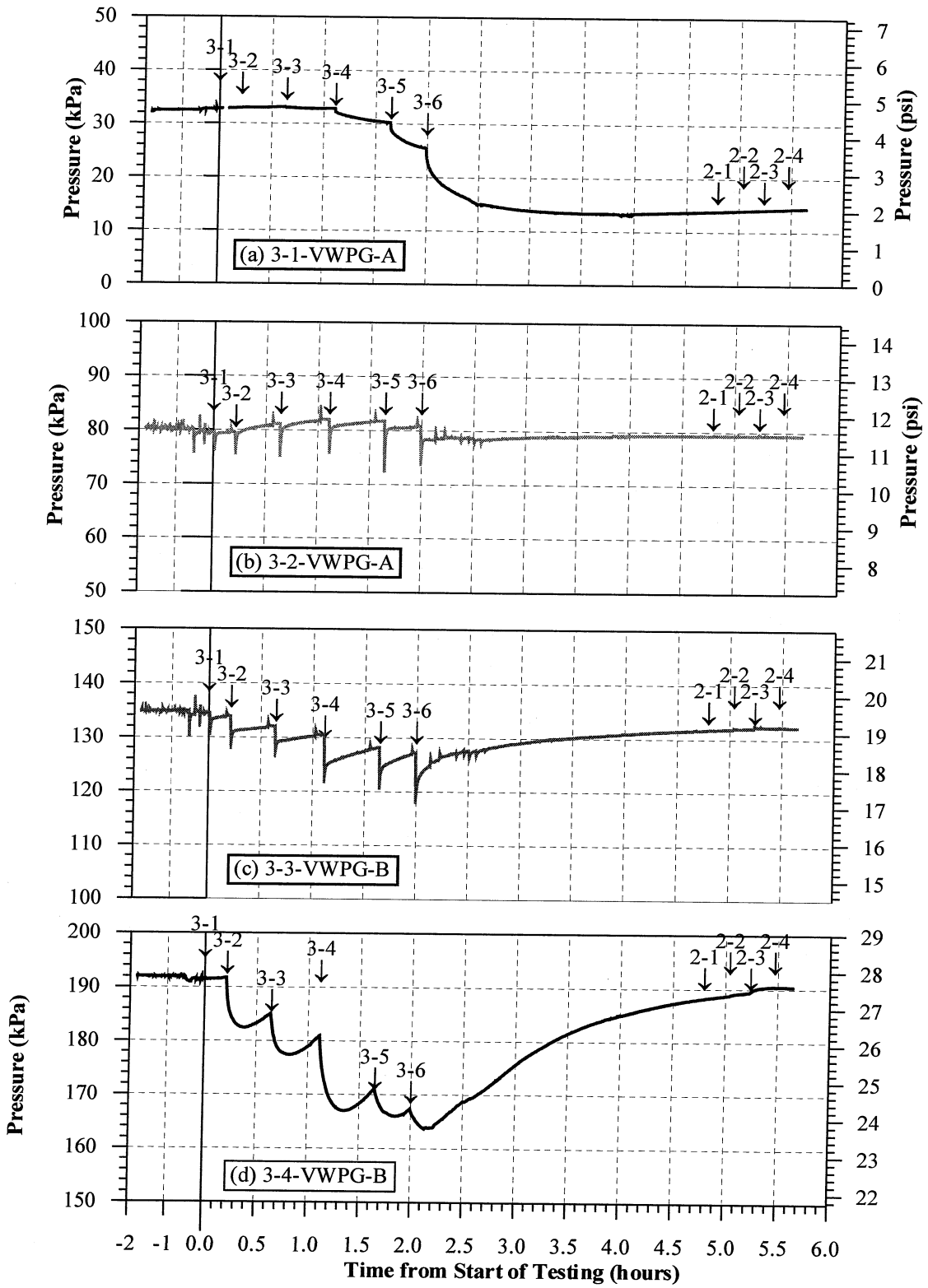
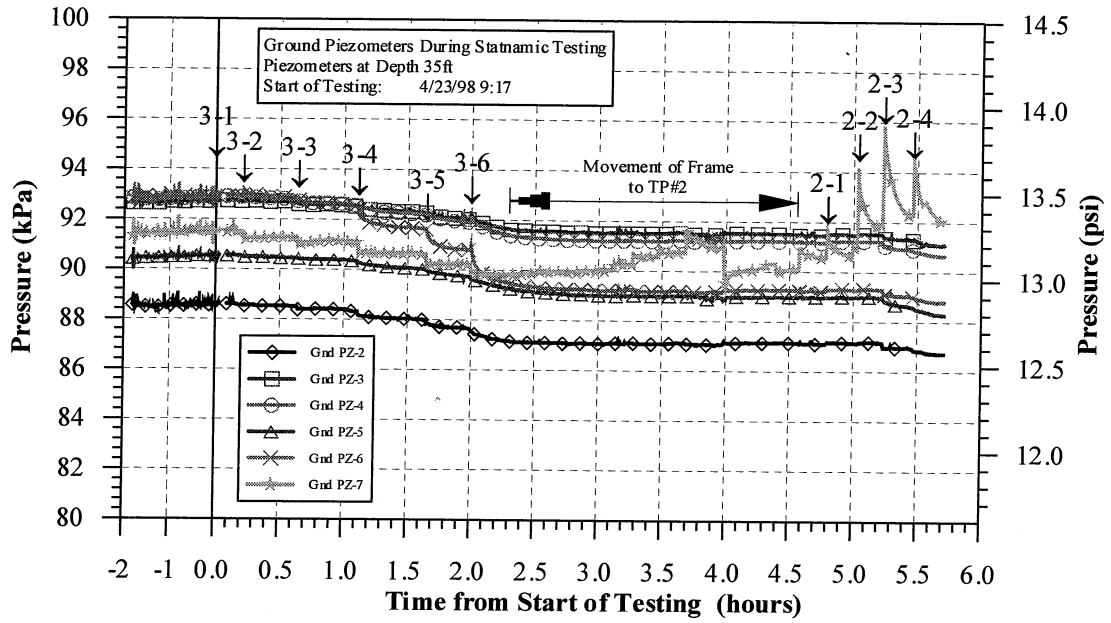
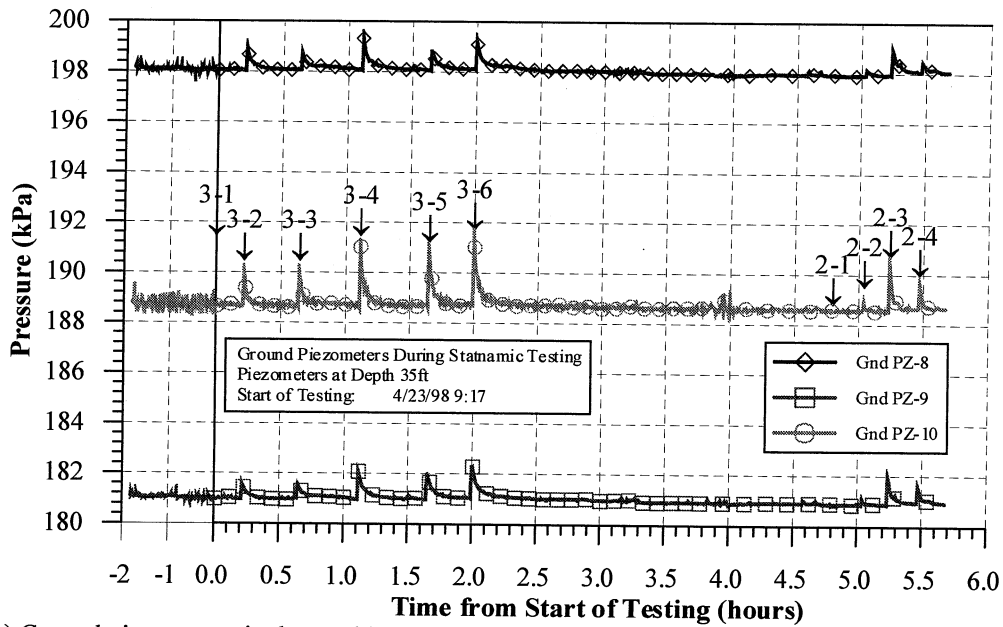


Figure 8. Vibrating wire piezometer measurements during Statnamic testing for test pile #3.



(a) Ground piezometers in the clay layer.



(b) Ground piezometers in the sand layer.

Figure 9. Ground piezometer measurements during Statnamic testing.

## ACKNOWLEDGEMENTS

The presented results are a part of a long-term research project supported by the Massachusetts Highway Department (MHD) and assisted by the Federal Highway Administration (FHWA).

The authors would like to acknowledge the assistance of Mr. Al DiMillio of the FHWA and John Pettis of the MHD. Also acknowledged are all the individual and companies associated with this research project, in particular the Graduate Research Students of the Geotechnical Engineering Research Laboratory under the direction of Samuel Paikowsky: Leo Hart, Chris Palmer, John Chen, and Mike Bachand.

The static load testing was conducted by personal from the University of Massachusetts - Lowell Geotechnical Engineering Research Laboratory (UML). The Statnamic testing was conducted by personal from the University of South Florida (USF) in conjunction with the Federal Highway Administration.

## REFERENCES

- Birmingham Foundation Equipment. 1997. *Statnamic Load Testing Proposal Notes*.
- Janes, M., Birmingham, P., & White, J. 1995. Work, Velocity, and the Relationship of Shaft Stiffness in Statnamic Load Testing. *Proceedings, First International Statnamic Seminar*, Vancouver, British Columbia, Canada.
- Justason, M. D., Mullins, A. G., Robertson, D. T., & Knight, W. F. 1997. A Comparison of Static and Statnamic Load Tests in Sand: A Case Study of the Bayou Chico Bridge in Pensacola, Florida. *Proceedings, Twenty Second Annual Deep Foundations Institute Members Conference*, Toronto, Ontario, Canada.
- Massachusetts Highway Department. 1995. *Standard Specifications for Highways and Bridges*.
- Middendorp, P., & Bielefeld, M. W. 1995. Statnamic Load Testing and the Influence of Stress Wave Phenomena. *Proceedings, First International Statnamic Seminar*, Vancouver, British Columbia, Canada.
- Paikowsky, S. G., & Chen, Y. U. 1998. *Field and Laboratory Study of the Physical Characteristics and Engineering Parameters of the Subsurface at the Newbury Site*. Report submitted to the Massachusetts Highway Department, University of Massachusetts Lowell.
- Paikowsky, S. G., & Hajduk, E. L. 1998. *Design and Construction of an Instrumented Test Pile Cluster*. Research report to be submitted to the Massachusetts Highway Department.
- Paikowsky, S. G., & Hart, L. J. 1998. *Development and Field Testing of Multiple Deployment Model Pile (MDMP)*. Research report submitted to the Massachusetts Highway Department, University of Massachusetts Lowell.
- Paikowsky, S. G., & Operstein, V. 1999. *Express Method of Pile Testing by Static-Cyclic Load*. Research report to be submitted to the Massachusetts Highway Department, Geotechnical Research Laboratory, University of Massachusetts Lowell.
- Paikowsky, S. G., & Weeks, K. 1997. *Design and Construction of a Pressure Chamber*. Research report under REU submitted to the National Science Foundation.



# A comparison of static and Statnamic load tests in sand: a case study of the Bayou Chico bridge in Pensacola, Florida

M.D. Justason

*Birmingham Foundation Equipment, Canada*

G. Mullins

*University of South Florida, US*

D.T. Robertson

*Applied Foundation Testing, US*

W.F. Knight

*Florida Department of Transportation, US*

**ABSTRACT:** This paper details the static and Statnamic load testing on a 600 mm square prestressed concrete pile. The pile was located at Pier 15 on the 20 million-dollar Bayou Chico Bridge Project in Pensacola, Florida. The pile was 10.5 meters long and had a design load of 1.3 MN. Three static load test cycles were performed in November, 1996. The Statnamic load test was performed in January, 1997. The Davisson failure load of the first cycle of the static test was 3.7 MN, and the Davisson failure load of the Statnamic test was 3.2 MN. The load-displacement curves for the two types of tests were similar, indicating that the Statnamic load test performed well in the sandy soils. Strain gauges embedded in the pile showed 35% skin friction and 65% end bearing for both test methods. Strain gauges were located at equal spacing at five elevations in the pile. A toe accelerometer verified the rigid body assumption of the Unloading Point Method currently used in the analysis of Statnamic load tests. The data collected from the pile instrumentation was of excellent quality and represents some of the best research to date comparing static and Statnamic load tests.

## 1 INTRODUCTION

As part of the 20 million-dollar Bayou Chico Bridge Project, State Road 292, in Pensacola, Florida, the Florida Department of Transportation (FDOT) implemented an extensive load testing program. It included static, Statnamic, and dynamic load tests. The geotechnical consultants for the load testing were Williams Earth Sciences and Applied Foundation Testing, Inc. Birmingham Foundation Equipment performed the Statnamic load tests. Metric and Beiswenger, Hoch & Associates supplied the design for the bridge structure in cooperation with FDOT. Figg Construction Services provided the construction engineering and inspection, and the contractor was PCL Civil Constructors.

The goal of the test program was firstly, to confirm the design capacity of the piles and secondly, to compare the results obtained by the three test methods. Of the three comparisons made at this site, the results of the static and Statnamic load tests at Pier 15 form the basis of this paper. Testing at two additional locations will be studied in future papers.

Statnamic load testing has been used extensively in Florida for large diameter bored piles. In each case, the Statnamic testing was performed as an alternative to static load testing, or as the only possible testing method. This was due to the high capacity of the shafts and the difficulties associated with static testing. Consequently, previous tests programs were unable to provide static/Statnamic comparisons. The Bayou Chico Project provided an excellent opportunity for a detailed static/Statnamic comparison and also provided the first Statnamic testing on driven piles in Florida.

The test piles were 600 mm concrete piles with lengths between 10.5 and 14.0 meters. Static load tests were performed using a 10.7 MN capacity test frame and eight steel reaction piles (H-piles). The Statnamic tests were performed using a 14MN Statnamic device with a conventional gravel catching system. The design capacity of the piles was 1.3 MN.

The test program recognized the effects of multiple loading cycles on pile capacity and thus alternated the order of static and Statnamic tests for each pile. Three piles were tested, with a total of three static tests and four Statnamic tests. Three static load cycles were performed at Pier 15 on November 26, 1996. The Statnamic test was performed on January 17, 1997.

Each test pile was instrumented with vibrating wire and resistance strain gauges as well as an embedded toe accelerometer. The data obtained at this site was of excellent quality, and is perhaps some of the most revealing data obtained during a Statnamic load test in recent years. The importance of this data is largely due to the presence of the embedded toe accelerometer which provided an opportunity to conduct a detailed investigation of pile top and toe behavior during Statnamic load testing.

The following table summarizes the Bayou Chico test program.

Table 1. Outline of load test program (static and Statnamic)

Location	Test Method
Pier 15	Static, November 26, 1996
	Statnamic, January 17, 1997
Pier 5*	Statnamic, February, 1997
	Static, March, 1997
Pier 10*	Statnamic, April, 1997
	Static, July, 1997
	Statnamic, August, 1997

\*Piers 5 and 10 will be discussed in future papers

## 2 FOUNDATIONS

### 2.1 Soil profile and properties

The soils at the Bayou Chico Bridge were comprised of medium to dense, poorly graded sand with some silty sand. Each of the three test pile locations was investigated using a cone penetrometer and standard boreholes were performed in the immediate area. The results of a typical cone sounding are shown in Figure 1. The Bayou Chico Bridge site was generally uniform in its soil profile.

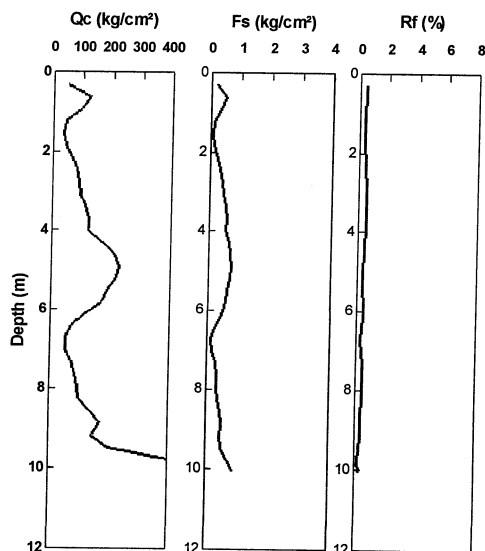


Figure 1 Typical cone sounding

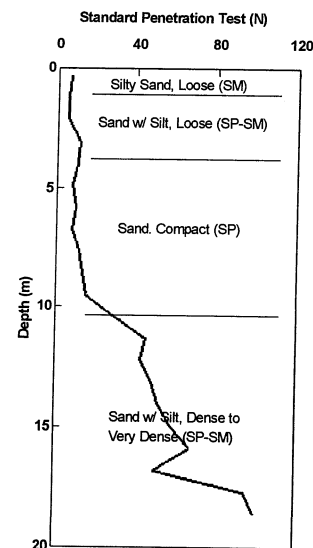


Figure 2 Typical borehole and SPT results

Dense sand layers were present at depths of 10–15 meters, with SPT values in the range of 80–100. A typical borehole log is presented in Figure 2, with SPT values.

## 2.2 Pile details

The piles used at the Bayou Chico Bridge were 600 mm square pre-stressed concrete piles, typical of piles used on FDOT projects. The three test piles ranged from 10.5–14.0 meters in length. The test pile at Pier 15 was 10.5 meters long. A cross-section of the piles is shown in Figure 3. Figure 4 shows a picture of a 5 × 5 pile group.

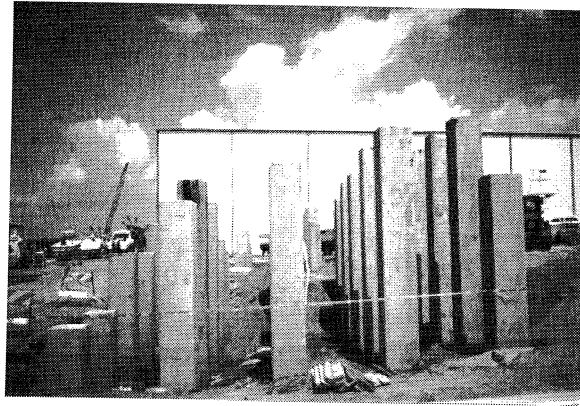
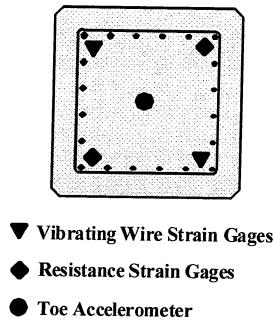


Figure 3 Pile cross-section

Figure 4 Typical 5 × 5 pile group

## 2.3 Instrumentation

Each of the three test piles was instrumented with 10 resistance and 10 vibrating wire strain gauges, a total of 20 gauges. The vibrating wire gauges were intended as the primary measurement for the static load tests and the resistance gauges were intended for the Statnamic load tests. The pile cross-section in Figure 3 shows the positions of the strain gauges. The strain gauge depths are shown in Figure 5.

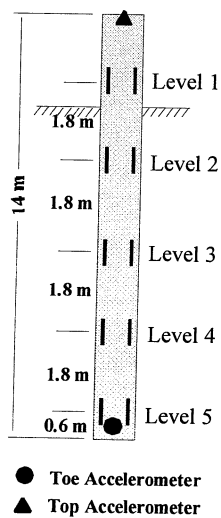


Figure 5 Strain gauge depths

The test data was recorded using a MEGADAC data acquisition and signal-conditioning unit which recorded the load cell, 3 LVDTs, 10 resistance strain gauges, and the hydraulic jack

pressure. An independent recording system was also used to record the vibrating wire gauge response.

Each test pile was equipped with an embedded toe accelerometer (see Figure 3), which was monitored during the Statnamic test by the MEGADAC. A TNO FPDS-5 was used to monitor the Statnamic load cell and laser-activated photo-voltaic displacement transducer. An accelerometer was used as a backup to the laser sensor, in the event that the displacement exceeded the sensor capabilities.

### 3 LOAD TEST METHODS

#### 3.1 *Static load test*

The static load tests were conducted using a 10.7 MN test frame supplied by FDOT. For each test pile, eight reaction piles were installed around the test pile at a distance of approximately five pile diameters (3 meters). Figure 6 shows the static load test configuration.

The reaction piles at Pier 15 were 350 mm steel H-piles which were installed using a diesel pile hammer. The piles were driven to a depth of approximately 20 meters.

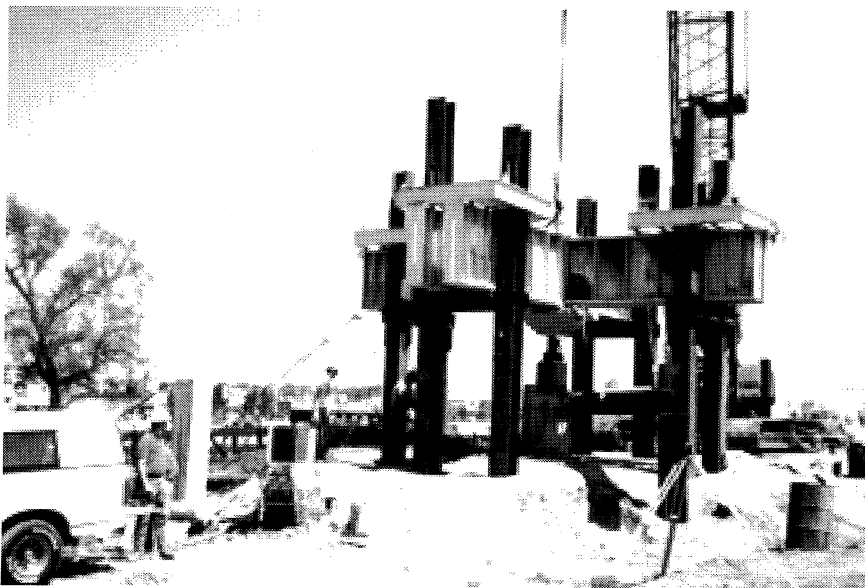


Figure 6 Photo of static load test at Pier 5

#### 3.2 *Statnamic load test*

The Statnamic load test involved the application of a short duration load (about 120 ms). Burning a solid fuel inside the Statnamic device produced high-pressure gas. The attendant force accelerated a reaction mass upwards at 20g. An equal force was applied to the pile. The reaction mass weighed 5% of the desired load.

A schematic diagram of a Statnamic device is shown in Figure 7. The device used at the Bayou Chico Bridge was a 14 MN Statnamic device (see photo in Figure 8). A more detailed description of Statnamic load testing is available in Bermingham, 1989.

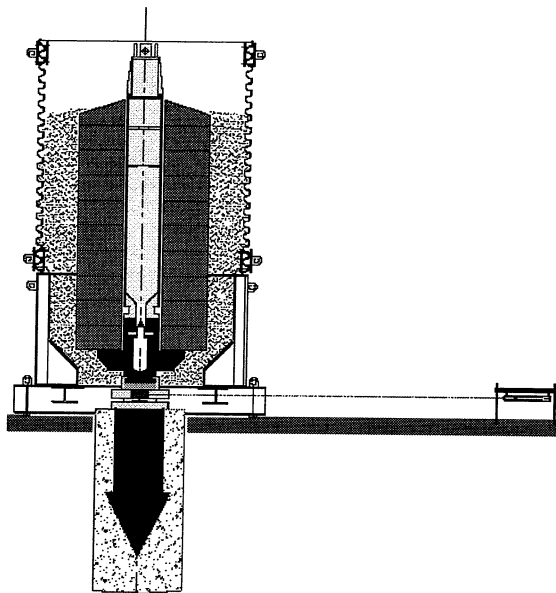


Figure 7 Schematic of a Statnamic load test

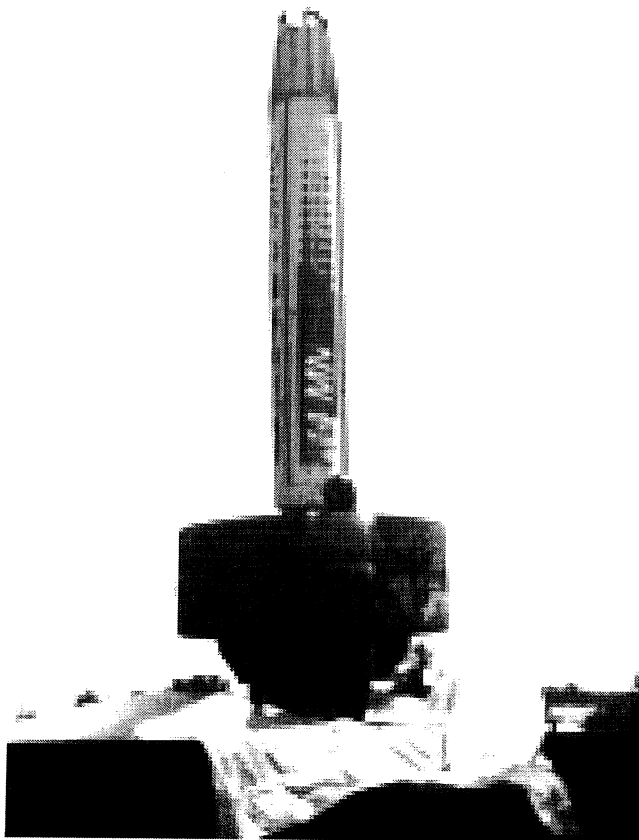


Figure 8 Photograph of the 14 MN Statnamic device

## 4 TEST RESULTS AND DISCUSSION

### 4.1 Static load test at pier 15

Figure 9 shows the results of the static load test performed on the test pile at Pier 15. The test was performed on November 26, 1996.

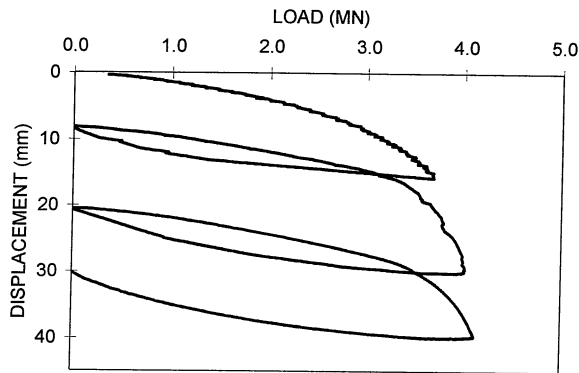


Figure 9 Static load test results

The three static load cycles showed a stiffening trend. The Davisson failure load was 3.7 MN for the first cycle, and increased for subsequent load cycles (3.8 MN and 3.8 MN respectively). The peak load for the three cycles ranged from 3.8 to 4.1 MN, and the peak displacement ranged from 10.2 to 16.0 mm. After the third load cycle, the pile had accumulated 30.0 mm of permanent displacement. None of the three load cycles exhibited a dramatic plunging failure, but rather a gradual softening.

Figure 10 shows the results of the resistance strain gauges vs. time for the 3rd cycle. The vibrating wire gauges yielded similar results for the 1st cycle. The results shown are the average strain values of the gauges at each depth.

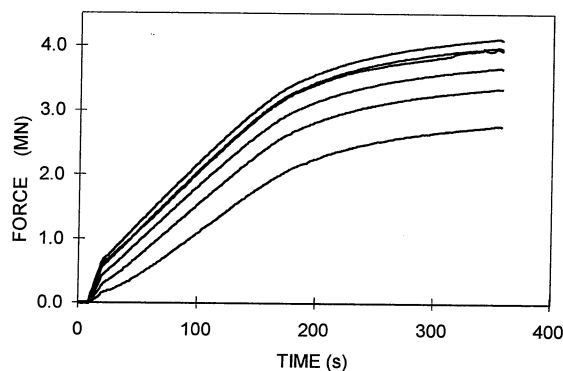


Figure 10 Force vs. time from resistance strain gauges for Pier 15

Near the peak load, approximately 35% of the pile capacity was attributable to skin friction and 65% to end bearing.

### 4.2 Statnamic load test at pier 15 and comparison with static test

Figure 11 shows the results of the Statnamic load test performed on January 17, 1997. The load test was performed by Berminghammer Foundation Equipment with no prior knowledge of the

static load test results. A load of 7.0 MN was targeted. As Figure 11 shows, the actual peak load achieved was 6.3 MN; much more load than was required to achieve the Davisson failure load. The shortfall from the target load was due to the very large pile displacement.

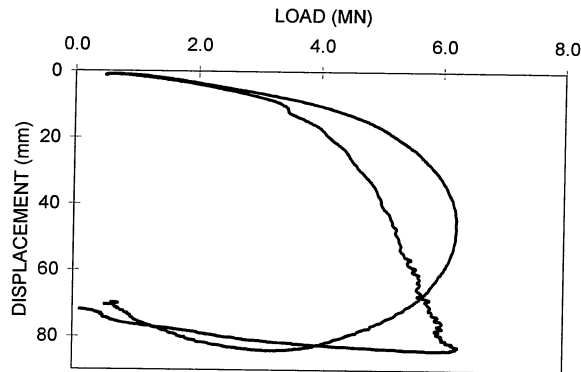


Figure 11 Statnamic and derived static load-displacement

The measured Statnamic curve is the more rounded curve in Figure 11, while the other curve is the calculated static behavior of the pile using the Unloading Point Method (3). Sometimes called the 'derived static' curve, this graph shows the load-displacement relationship with the inertia and damping forces removed from the measured Statnamic force.

Figure 12 shows force vs. time as measured by the load cell, as well as the inertia and damping forces vs. time.

Figures 19 and 20 shown later in this section, depict the acceleration and velocity of the pile. Note that these figures are the same shape as the inertia and damping forces shown in Figure 12.

The inertial forces were calculated by multiplying the pile mass by the measured pile acceleration. The damping forces were calculated by multiplying a damping constant by the velocity. The damping constant was derived using the Unloading Point Method (4). A linear relationship between velocity and damping was assumed. The peak inertial force was  $-2.8$  MN, and the peak damping force was  $0.5$  MN. These peak values alone are not sufficient to understand the Statnamic loading event. As Figure 12 shows, the full inertial and damping time histories are necessary. This Statnamic load test has unusually high inertia and damping forces due to the large displacement.

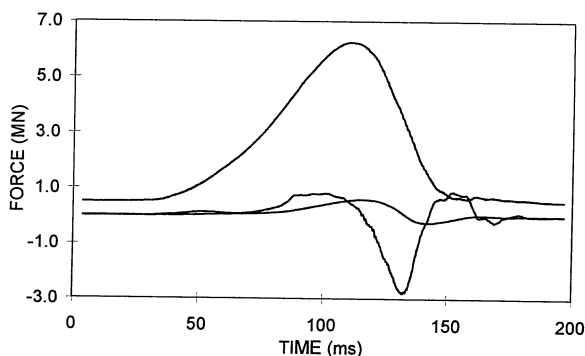


Figure 12 Measured force, inertial force, and damping force vs. time

To find the static soil resistance (or 'derived static') force curve, the damping and inertial forces were subtracted from the measured force. The resulting curve is shown in Figure 13, along with the measured force. This force curve was used to produce the 'derived static' load-



displacement, shown in Figure 11. The 'derived static' curve shows a loading rate that is slower than the measured load, and an unloading rate that is faster.

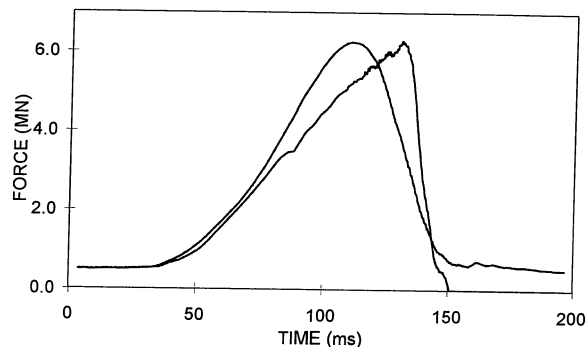


Figure 13 Measured force and derived static force vs. time

When plotted on the same graph the derived static curve and the three static load tests show very similar behavior, as shown in Figure 14.

The static and Statnamic curves appear different due to the large movement of the pile during the Statnamic load test. The loading and unloading portions of the curves are similar.

Figure 15 shows the results from the strain gauges for the Statnamic test at Pier 15. The results shown represent the average strain values of the two gauges at each elevation in the pile.

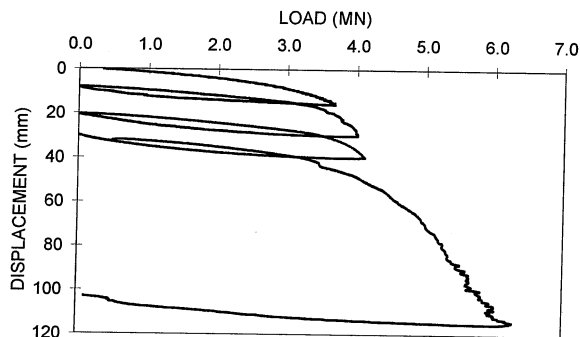


Figure 14 Static and Statnamic derived static

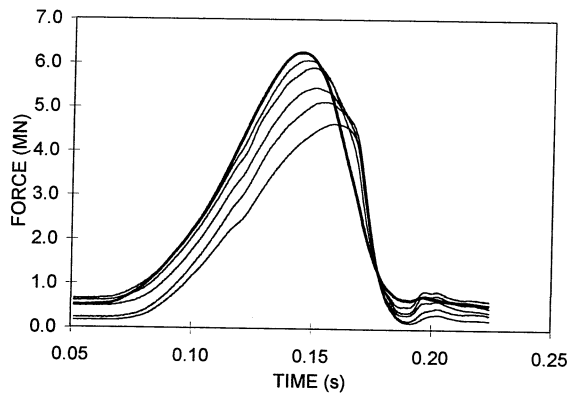


Figure 15 Statnamic force and strain gauge results

The curve showing the highest force in Figure 15 is the force measured by the load cell. The other curves represent the calculated force at each level of strain gauges. To calculate force, the measured voltage signals were converted to micro-strain using the manufacturer-supplied calibration factors, and introducing an elastic modulus of 34.5 GPa and a cross sectional area of  $0.37 \text{ m}^2$ .

The data displayed in Figure 15 was of interest for many reasons. Firstly, having strain gauges embedded in a pre-cast pile meant that no assumptions were needed for the cross-sectional area. For bored piles, strain gauge results must be interpreted more carefully for this reason. Also, the elastic modulus for the concrete could be checked against the force measured in the load cell. In this case, the first level of strain gauges was only 2.7 m from the load cell, allowing for an accurate 'calibration' of the elastic modulus. The value of 34.5 GPa, may seem higher than expected but is not unreasonable. The rate of loading might also serve to increase the observed elastic modulus, as does the reinforcing steel. In Figure 10, an elastic modulus of only 31 GPa was used. The age of the concrete combined with the faster loading rate of the Statnamic test could have accounted for this difference.

A notable aspect of Figure 15 is the lag between the peak force at the top of the pile and the bottom of the pile. In previous studies, this time lag has been associated with the compressive wave speed in the pile material (2). For this pile, it became apparent that the compressive wave speed was not the cause of the lag.

Assuming a wave speed of 4000 m/s, and given a pile length of 10.5 meters, the time for a compressive wave to travel from the top to the bottom of the pile is only 0.002–3 s. The observed time lag ( $\sim 0.025 \text{ s}$ ) is obviously greater so an alternate explanation was necessary.

It is proposed that the time lag was indirectly caused by the large displacement of the pile. Just as a force applied at the top of the pile caused a force distribution downward, the pile penetrating the soil and increasing in capacity caused a force distribution up the pile. This should not be confused with stress wave phenomena, as both the downward and upward forces were distributed at a speed well below the compressive wave speed in the pile material. The resulting superposition of these two force distributions causes the time lag in the strain signals. It has been shown in previous studies that Statnamic tests with smaller displacements do not have time lags as large as those seen in Figure 15 (2).

The displacement at the top of the pile would have normally been measured using the laser sensor, but due to the large displacement, the maximum travel of the sensor was exceeded at approximately 55 mm. The back-up accelerometer was used to derive the displacement at the top of the pile.

The embedded toe accelerometer performed well, and the signal produced a high quality displacement curve. Figure 16 shows both the top and toe displacement curve as well as the force vs. time.

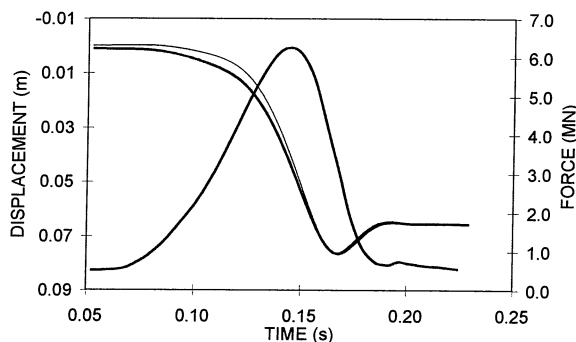


Figure 16 Top and toe displacement and measured force vs. time

Figure 16 shows the time lag between the peak force and the peak displacement. Notice that the peak displacement occurs at nearly the same time as the peak force at the toe of the pile (see Figure 15).

Figure 17 shows the load-displacement curve for the top of the pile, as well as the load-displacement using the toe accelerometer (from Figure 16) and the bottom level of strain gauges (from Figure 15).

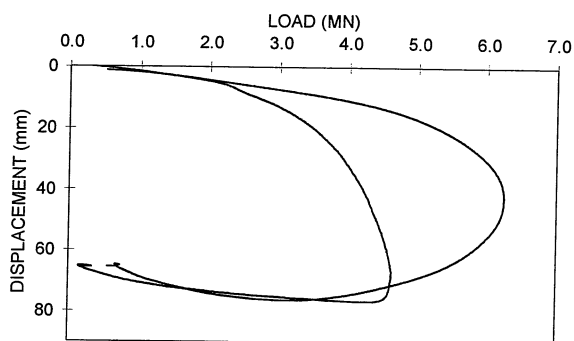


Figure 17 Load-displacement at the top and toe of the pile

Note that the load-displacement at the toe of the pile is very similar in shape to a static load test. This is due to the minimal effects of pile damping and inertia at the pile toe. The load-displacement at the pile toe can also be compared to the 'derived static' load-displacement (see Figure 18).

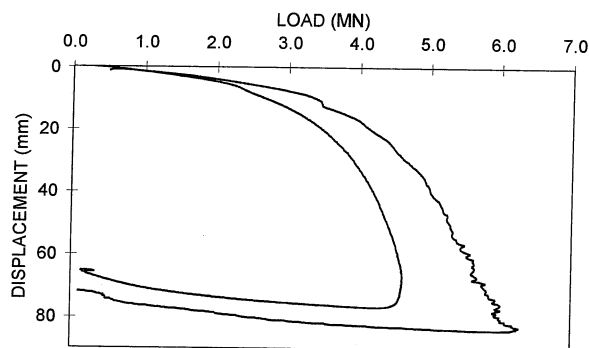


Figure 18 Load-displacement at the pile toe and derived static load displacement

Figures 19 and 20 show the velocity vs. time and the acceleration vs. time at the top and toe of the pile. In each figure, the slightly larger peak values belong to the pile top. Note the similarities between the pile top and pile toe behaviors.

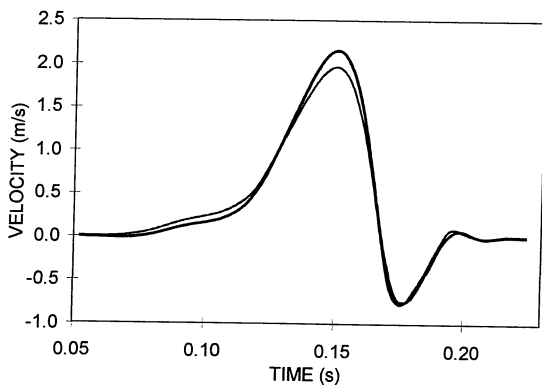


Figure 19 Pile top and toe velocity vs. time

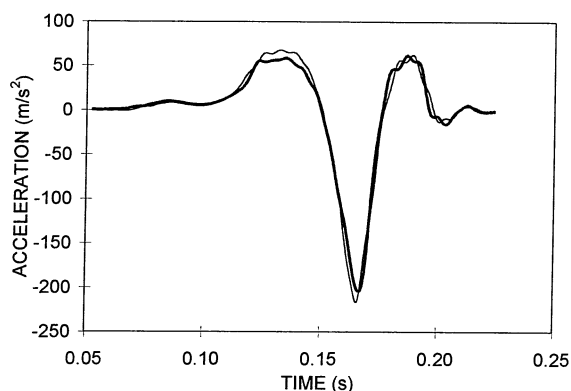


Figure 20 Pile top and toe acceleration vs. time

Figures 19 and 20 support the rigid body assumption of the Unloading Point Method. It also proves the absence of stress wave effects. This assertion may not be true for piles with lengths greater than approximately 50 m (4).

## 5 CONCLUSIONS

Firstly, it should be concluded that the test pile at Pier 15 achieved the required capacity based on the Davisson failure load of both the static and Statnamic load tests. The required capacity of 2.6 MN (2 times design) was below the capacity determined by the first cycle of the static load test (3.7 MN). The Davisson failure load of the Statnamic test was 3.2 MN.

Secondly, it can be concluded that the static and Statnamic load tests produce similar results. The Statnamic test was taken to a load far exceeding the Davisson failure load and subsequently produced a large permanent displacement (80 mm). The static tests were taken to lesser loads, but the load-displacement behaviors were similar. The first cycle of the static load test produced a somewhat softer response than the subsequent cycles, indicating some increase in capacity due to the testing. The 'derived static' curve from the Statnamic test suggested that the pile was gaining capacity as more load was applied.

Both the static and Statnamic strain gauge results showed that approximately 35% of the pile capacity was skin friction and 65% was end bearing. This indicated that the load distribution in the pile was not affected by the loading rate.

In addition to the above conclusions, the testing on Pier 15 showed that the Unloading Point Method used in the analysis of the Statnamic test was a valid method. The similarity between the movement at the pile top and the pile toe (provided by the toe accelerometer) indicated that the pile essentially moved as a rigid body.

The agreement between the static load test and the 'derived static' curve from the Statnamic test indicated that the effects of loading rate are not significant in this soil.

The testing at Pier 15 of the Bayou Chico Bridge Project supports the use of Statnamic testing for driven piles in sand. Further testing on this site will be explored in future papers.

## ACKNOWLEDGMENTS

The authors wish to thank PCL for their work in setting up the static and Statnamic load tests, and Gray Mullins' dog Rudy for his patience and understanding.

## REFERENCES

- Birmingham, P., & Janes, M., 1989. An Innovative Approach to Load Testing of High Capacity Piles. *Proceedings of the International Conference on Piling and Deep Foundations*, London, May 15-18, 1989, pp.409-413.
- Janes, M., 1995. Statnamic Load Testing of Strain Instrumented Large Diameter Bored Shafts. *Proceedings of the First International Statnamic Seminar*, Vancouver, September 27-30, 1995, pp.65-74.
- Middendorp, P., Birmingham, P., & Kuiper, B., 1992. Statnamic Load Testing of Foundation Piles. *Proceedings of the 4th International Conference on Application of Stress Wave Theory to Piles*. The Hague, Holland, 1992, pp.581-588.
- Middendorp, P., & Bielefeld, M.W., 1995. Statnamic Load Testing and the Influence of Stress Wave Phenomena. *Proceedings of the First International Statnamic Seminar*, Vancouver, September 27-30, 1995, pp.207-221.

# Lateral Statnamic load testing: A new method for evaluating lateral load capacity

D. T. Robertson & M. K. Muchard

*Applied Foundation Testing, Green Cove Springs, Florida, USA*

A. G. Mullins

*University of South Florida, Tampa, Florida, USA*

**ABSTRACT:** The Statnamic test method was originally developed as a method for evaluating axial capacity; however, in the last 3 years a new application for the device has been developed. In October 1994, the North Carolina Department of Transportation became the first to perform lateral Statnamic load testing of drilled shafts. Brigham Young University, the Utah DOT and the FHWA followed in 1996 with lateral load tests performed on a group of pipe piles. This testing was done to evaluate foundations under ship impact and earthquake type loading since the force-time pulse generated by the Statnamic device is on the same order of magnitude and frequency. Since that time, the lateral Statnamic test and associated data acquisition systems have been refined and improved. These improvements allow the collection of data in zones of influence while maintaining cost savings over more traditional methods. Tests using these improvements have been most recently performed in Pascagoula, Mississippi as part of a design phase load test program for the Mississippi Department of Transportation.

The paper will describe the test method, describe the equipment utilized to generate the lateral load, describe the data acquisition equipment and present an overview of the results from the most recent test site.

## 1 INTRODUCTION

Static lateral tests are commonly used to assist in the design of foundations subjected to lateral loads. However, lateral loads are typically generated by various events, which include high wind, earthquakes, impacts from various types of vehicles and numerous other static and dynamic sources. Traditionally, geotechnical and structural engineers have used static lateral test as a guide to the structural response for a dynamic event. Static tests provide data which is used to fine tune computer models such as COM624P, LPILE and Florida PIER. These computer programs estimate the static response of a foundation or structure based on the static properties of the soil and neglect the additional capacity available from the dynamic soil strength and structure response.

Recently, more attention has been placed on the dynamic properties of both soil and the structure. The high costs associated with the construction of foundations and structures to withstand lateral forces have justified more in depth testing and analysis. The Statnamic test method is considered a viable method for generating dynamic lateral loads because of its ability to impart relatively high loads over a time frame similar to that generated by ship impacts, earthquakes and transient wind loads. Load pulses can last up to 200 milliseconds and are capable of generating lateral forces of 2000 tons. Figure 1 shows a typical force time history for a lateral Statnamic test.

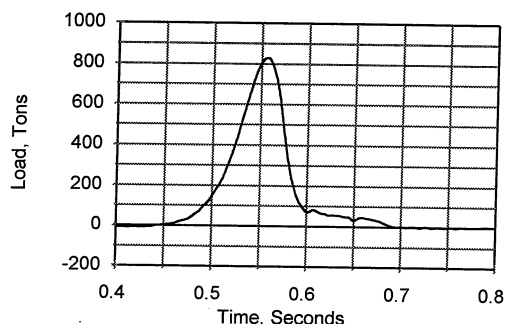


Figure 1. Force-time trace, lateral Statnamic test.

In 1994, the North Carolina Department of Transportation performed the first Statnamic lateral testing. Several tests were performed using a 67-ton Statnamic device on a single drilled shaft during a design phase load test program for the Neuse River Bridge in New Bern, North Carolina. In 1996, Brigham Young University, the Utah Department of Transportation and the FHWA performed lateral Statnamic tests on a group of instrumented pipe piles. This test utilized a 1600-ton device without reaction masses and generated lateral loads of up to 250 tons. Both test programs were performed on land. In 1996, the Mississippi Department of Transportation began planning for a design phase load test program for the US 90 Bridge over the East Pascagoula River. Large lateral load requirements were imposed on this bridge mainly due to vessel impact. Statnamic lateral load testing was specified to better model these conditions. This program included 15 Statnamic tests with loads of up to 823 tons. To the authors knowledge this is the largest lateral test program to date.

Dan Brown, Ph.D., P.E. under a contract with the FHWA and the Alabama Department of Transportation also began investigating the dynamic response of foundations. In April 1997, lateral Statnamic tests were performed at the Auburn University test site located in Opelika, Alabama. Four tests were performed on 36-inch diameter drilled shafts. The tests were performed using a 450-ton Statnamic device on shafts, previously, tested using static methods. The Statnamic tests were performed in the opposite direction of the static test to minimize soil disturbance. During the static tests, care was taken not to induce large permanent plastic deformations, which may have affected the results of the Statnamic tests. Figure 2 shows an example of the 450-ton Statnamic test setup at the 1997 GEOLOGAN conference.

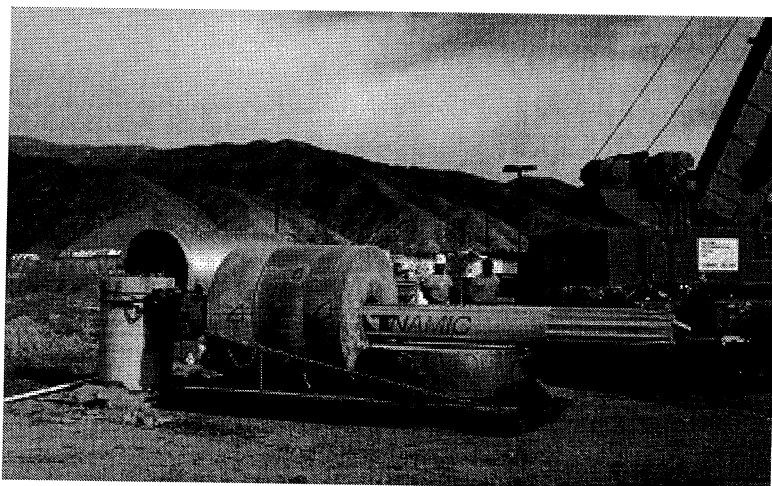


Figure 2. Lateral Statnamic test- 1997 GEOLOGAN conference.



## 2 STATNAMIC EQUIPMENT

The Statnamic test equipment consists of three essential parts, the piston, the cylinder/silencer assembly, and the reaction masses. Before the test method can be described, the reader must understand the function of each piece.

### 2.1 *The piston*

The Statnamic piston is the most important part of the system. The piston includes a fuel chamber, where the fuel is ignited and burns, generating a gas, which accelerates the cylinder/silencer assembly away from the piston. The piston also contains a load cell and laser displacement sensor which provide the load and displacement signals. Figure 3 shows a picture of the 1600 ton piston used for the Utah and Mississippi test programs being loaded with fuel.

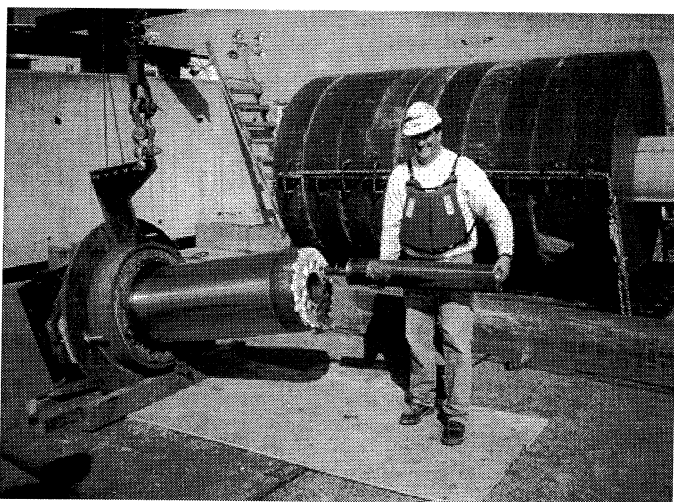


Figure 3. 1600 ton Statnamic piston.

### 2.2 *The cylinder/silencer assembly*

The cylinder/silencer assembly fits over the piston and forms a pressure chamber. Gas generated in the chamber moves the cylinder off the piston. The base of the cylinder has a large flange, which serves as the support for reaction masses. The silencer portion of this assembly acts as a large muffler. This portion of the device allows the gas to expand and vent in a controlled manner. The silencer reduces the report of the device. Figure 4 shows the 1600-ton cylinder/silencer assembly.

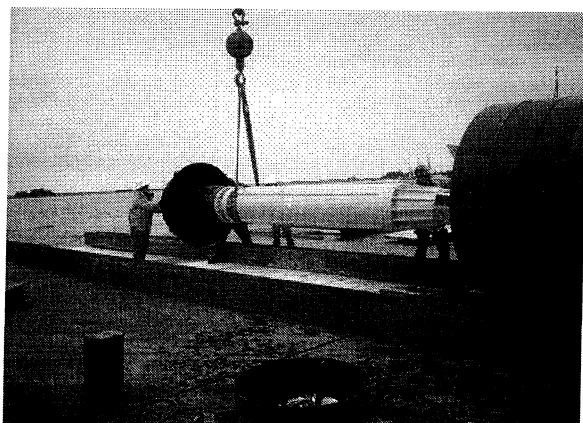


Figure 4. Cylinder/silencer assembly being inserted into masses for lateral testing.

### 2.3 *The reaction masses*

The “doughnut” shaped rings are constructed of concrete and steel. They typically have a mass equal to 5 to 8 percent of the target maximum load for an axial test. For lateral testing, this ratio can be much greater. Figure 4 shows the cylinder/silencer assembly being inserted into the reaction masses.

## 3 THE TEST METHOD

### 3.1 *Basic Statnamic principles*

The Statnamic test method uses two basic principles. The first is that for every action there is an equal and opposite reaction. The second is that force is equal to mass times acceleration. Currently Statnamic equipment can generate test loads of up to 3400 tons.

Fuel is burned inside the piston to generate a gas. The quickly forming gas pressure forces the cylinder/silencer assembly with the reaction masses to accelerate up to twenty times the acceleration of gravity, in turn producing a equal and opposite force acting downward on the foundation. The downward force can be defined as:

$$F = ma \tag{1}$$

where  $m$  = the reaction mass and  $a$  = the upward acceleration of the reaction masses.

The load cell measures the forces acting on the foundation. As the piston and foundation move, the laser sensor measures this movement relative to a stationary laser beam. A laser projector positioned forty to sixty feet away from the test area generates this laser beam.

An accelerometer is also mounted on the piston or foundation to measure acceleration and to act as a backup to displacement measurement system. During the test, the load cell, laser displacement sensor and accelerometer signals are measured by a data acquisition system interfaced with a laptop computer.

### 3.2 *The lateral Statnamic test*

The lateral Statnamic test uses these basic principles to generate lateral loads. The only difference between the axial test and the lateral test is working on a horizontal plane instead of a vertical plane. This means that additional reaction mass must be used to make up for the loss of the gravity induced forces (19 g's vs. 20 g's).

To overcome working on a horizontal plane a sled was constructed. This sled supports the reaction masses and cylinder/silencer assembly. The sled is allowed to slide in a runway, which runs on the same axis as the test. Rollers are used under the sled to eliminate soil disturbance near the test shaft due to friction generated between the sled and runway surface. For over water tests the runway can be constructed on a barge. For safety, rails are placed on either side of the sled. However, the large inertia of the sled produces a relatively straight travel path. Figure 5 shows the sled and barge track.

The Statnamic load is transferred to the foundation through a hemispherical bearing. The spherical bearing reduces eccentric loading and corresponding moments. Figure 6, shows the base of the piston and the spherical bearing configured for a lateral Statnamic test at the Pascagoula, Mississippi site.

### 3.3 *Instrumentation*

Additional instrumentation is necessary to monitor the lateral displacement at points of interest. This instrumentation can include potentiometers, accelerometers and resistance type strain gauges. To allow the monitoring of displacement of a shaft or pile at various levels, a down hole linear motion sensor was developed by Gray Mullins, Ph.D., P.E. of the University of South Florida. This string of sensors uses traditional slope inclinometer casing. The accelerometers are mounted on specially constructed carriers, which can be tied together and placed at various locations.

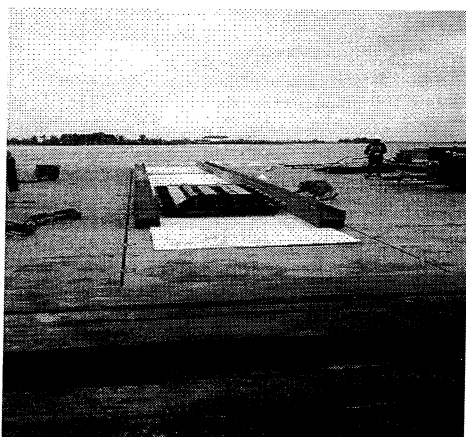


Figure 5. Statnamic sled and runway barge.

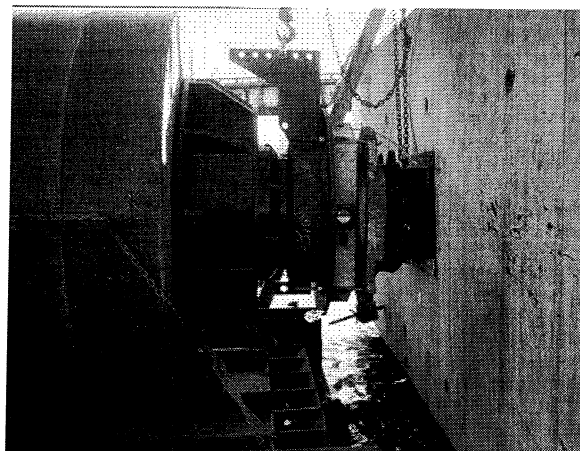


Figure 6. Spherical bearing.

Data from the various sensors is recorded using a high-speed data acquisition system. This system can monitor at rates of 250,000 samples per second. For Statnamic testing, data is normally acquired at rates of 2,000 to 5,000 samples per second. This acquisition rate can vary depending on the numbers of channels that are monitored and the length of sampling.

#### 4 THE US-90 BRIDGE OVER THE PASCAGOULA RIVER LOAD TEST PROGRAM

The lateral Statnamic tests done at this site were part of a design phase test program. The load test program was performed to provide better design information for the foundation of the new US 90 over the Pascagoula River Bridge. The program consisted of the construction and testing of two concrete piers. The first pier was founded on a 2 X 3 pile group. The piles were 30-inch, square, pre-stressed concrete. The second pier was founded on two 84-inch diameter drilled shafts. The piers were constructed to allow a jack system to be placed in between for lateral static testing. Sufficient space was left outside the piers to allow barge access for the lateral Statnamic testing.

In addition to the lateral testing, static tests were performed on one drilled shaft and one 30-inch concrete pile. A 54-inch diameter, post-tensioned, concrete pipe pile was also driven and dynamically tested.

Statnamic testing was performed after all other testing was completed. During static testing, loads were controlled to prevent large permanent plastic deformations. Measurements taken after the completion of static testing show a permanent lateral displacement of  $\frac{1}{4}$  inch for the driven pile group and  $\frac{3}{4}$  inch for the drilled shaft group.

Fifteen lateral Statnamic tests were performed at the Pascagoula site on both the strong and weak axis of each group. Instrumentation for each pier included strain gauges embedded within the piles and shafts, accelerometers mounted at various points of interest around the piers, potentiometers mounted on a fixed reference beam and two strings of down hole linear motion sensors. Applied force was measured using the load cell contained within the Statnamic piston.

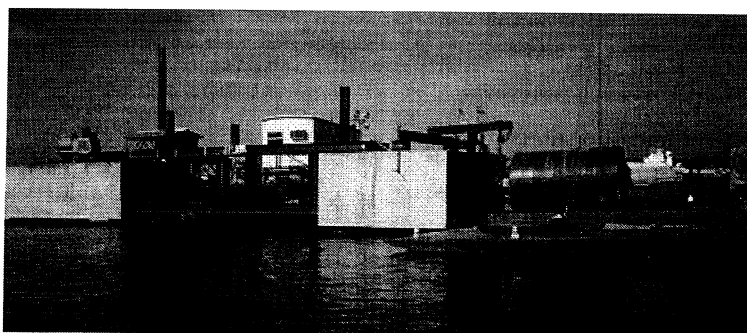


Figure 7. Mississippi set up.

#### 4.1 Test results

Analysis of the data obtained during the lateral Statnamic testing is being performed by the Auburn University Highway Research Center under the direction of Dan Brown, Ph.D., P.E. This paper will present some of his initial analysis. The full results are being presented to Mississippi Department of Transportation and should be available in the future.

Figure 8 shows a time history plot of the applied Statnamic load, lateral translation and acceleration for a typical lateral Statnamic test on the strong axis of the drilled shaft pier. The results show a damped harmonic response, which dissipates relatively quickly due to the large damping in the system. This also shows the pier cap was subjected to a maximum force of 823 tons and accelerated to a maximum acceleration of 1.3 g's during the loading. The cap had a maximum displacement of 2.25 inches.

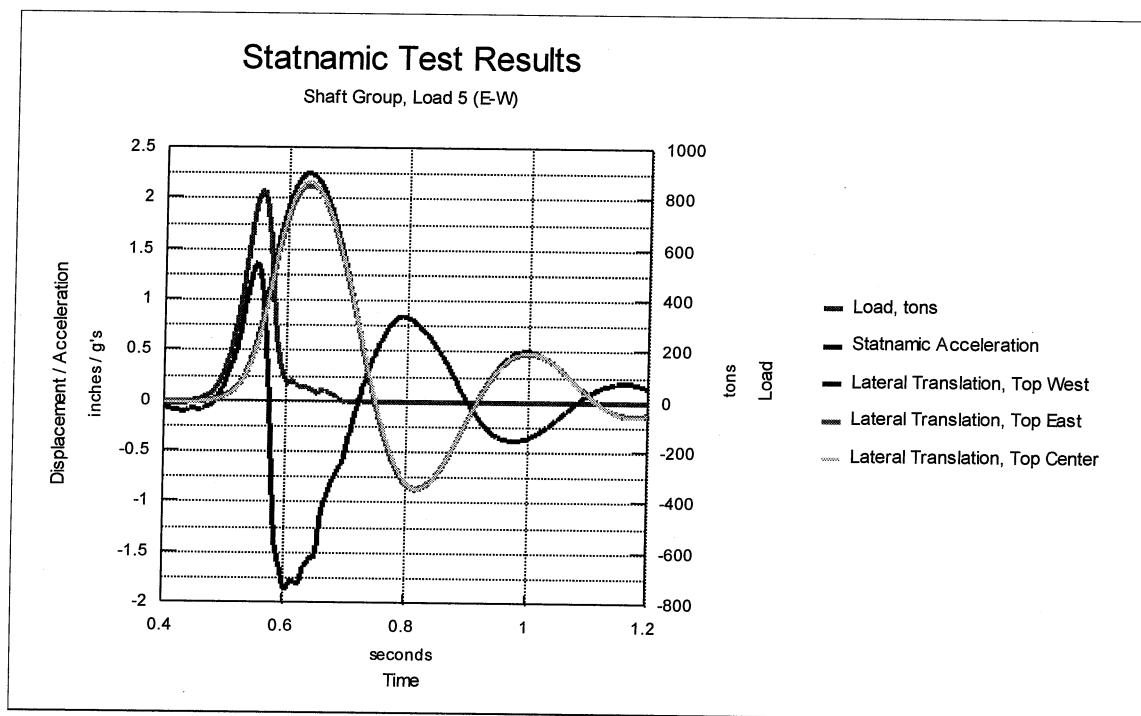


Figure 8. Lateral translation & acceleration.

The resistance to the Statnamic load has three components, which can be modeled as a single degree of freedom system.

The equation of motion is defined as:

$$F = ma + F_d + F_s \quad (2)$$

where,  $F$  = applied force, tons;  $m$  = mass of the foundation;  $a$  = acceleration in g's;  $F_d$  = damping force,  $Cv$ , tons;  $F_s$  = static soil resistance,  $Ku$ , tons;  $C$  = damping coefficient, ton/ft./sec;  $v$  = velocity, ft./sec.;  $K$  = static stiffness, tons/in; and  $u$  = displacement, in.

Using this model,  $C$  and  $K$  can be adjusted until a modeled displacement and acceleration response matches the measured response similar to other signal matching techniques. Figure 9, shows the modeled acceleration and displacement response compared to the measured.

Once  $C$  and  $K$  are calculated, the damping force and static soil resistance can be calculated. Figure 10 shows the Statnamic load, the calculated static soil resistance, the calculated damping force and the calculated inertia force.

The pier translation for the calculated and measured static soil resistance should be similar. Figure 11 shows the peak calculated static soil resistance for the 5 tests done on the shaft group vs. pier translation measured during the static test. This match quality suggests that it is possible to use Statnamic lateral tests to derive static lateral response. The derived static lateral response model is sensitive to the mass used in the computation as well as the subjective fitting of the  $K$  and  $C$  parameters by the engineer.

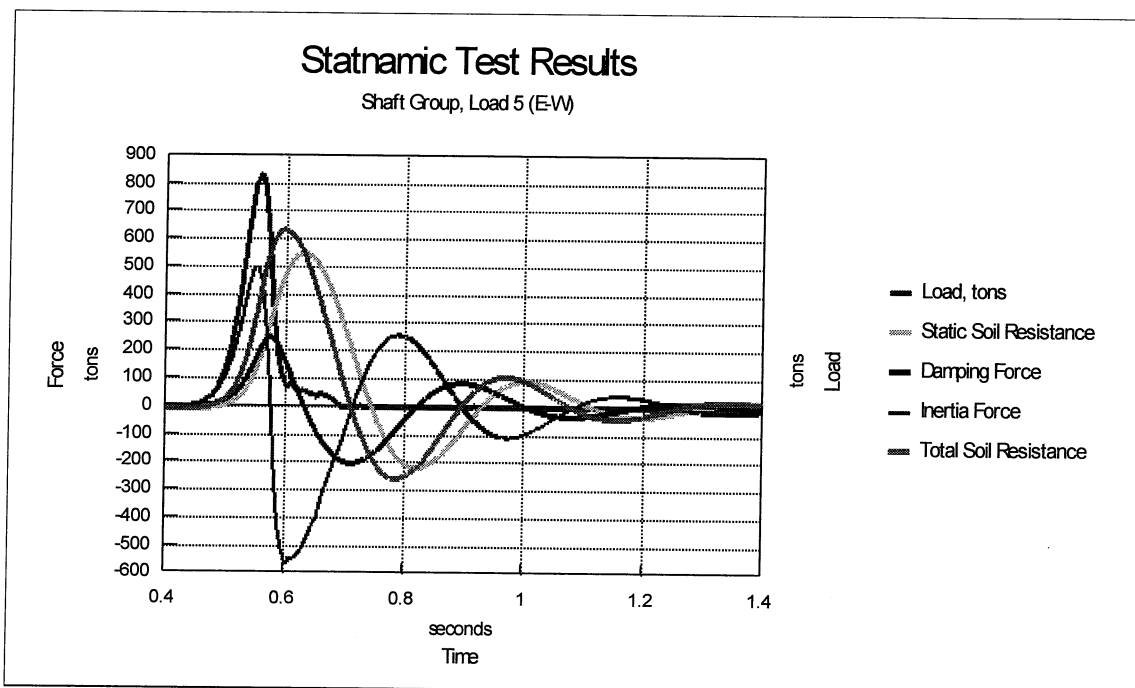


Figure 9. Actual versus model translation & acceleration.

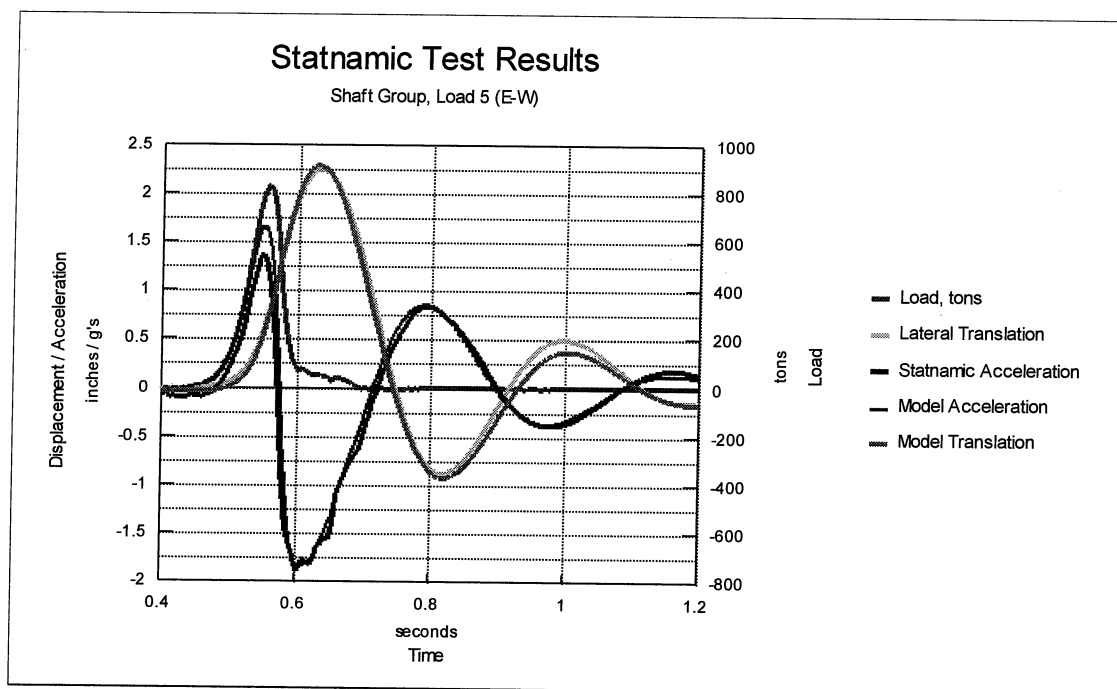


Figure 10. Statnamic forces.

Figure 12 shows a plot of the strain gauge data obtained from an instrumented pile. The Statnamic strain response is taken from a moment in time corresponding to the peak strain. For this loading the maximum total calculated static resistance plus the soil damping was 500 tons. The static strain data shown is taken from the maximum loading of 440 tons. The strain data is of opposite sign because the tests were performed in opposing directions.

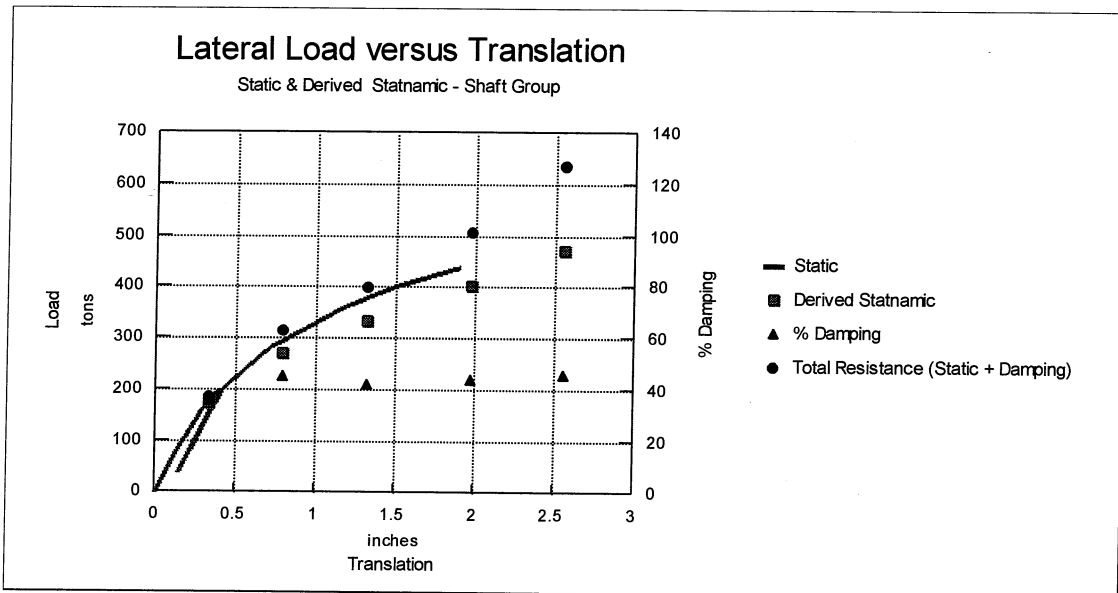


Figure 11. Derived Statnamic & static translation versus lateral load.

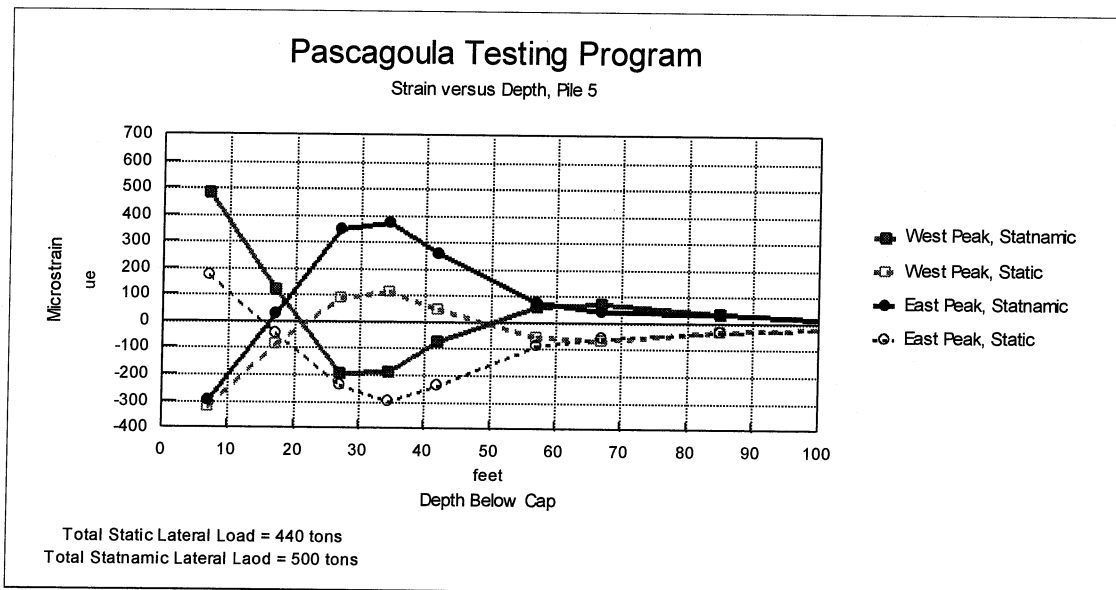


Figure 12. Strain versus depth, Pile 5.

The axial forces in the pile can be derived from the strain gage data. Figure 13 shows the derived axial force in the pile. Once again, the results are similar except for the opposite signs. The bending moment can also be derived as shown in Figure 14. Here the pattern is again similar, but with opposite signs.

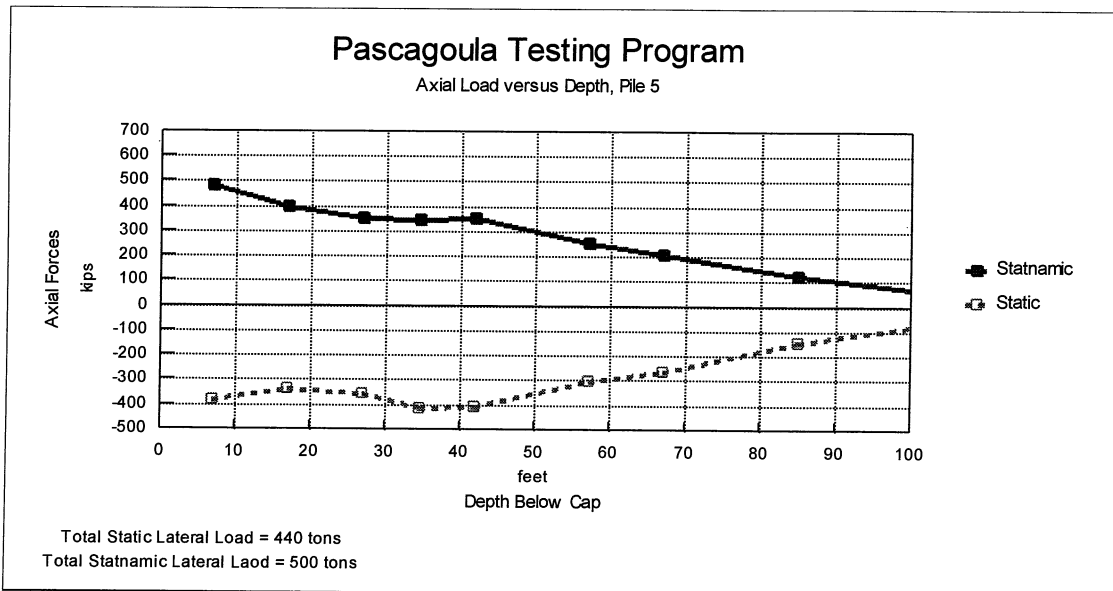


Figure 13. Axial load versus depth, Pile 5.

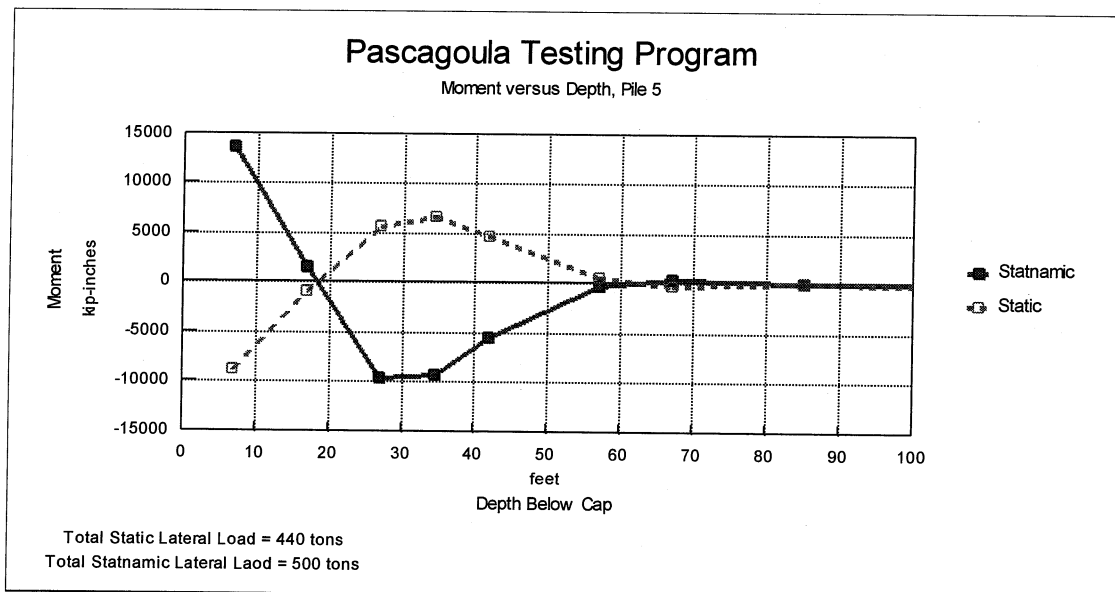


Figure 14. Moment versus depth, Pile 5.

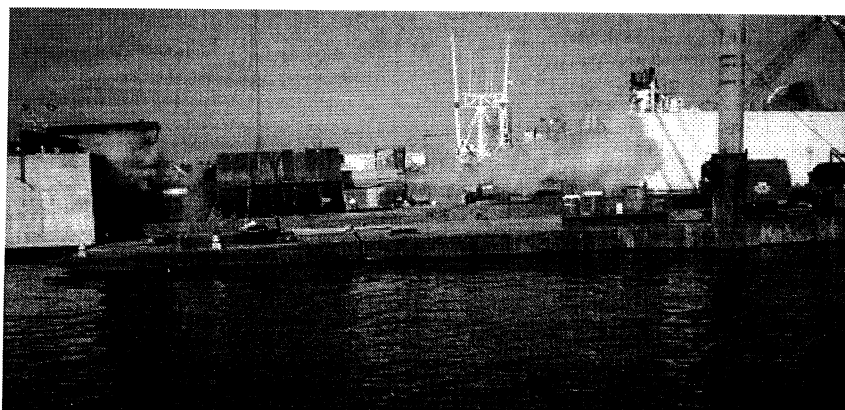


Figure 15. Lateral Statnamic test in progress.



## 5 CONCLUSIONS

The lateral Statnamic test method has been developed into a viable design and testing tool. The developments of both the loading and data acquisition equipment have progressed beyond the experimental stage. Figure 15 shows a lateral Statnamic test in progress.

Since the lateral Statnamic test method does not require a second foundation on which to react, it is more economical and can be performed in less time than the traditional lateral static method. The lateral Statnamic method can also provide much higher loads than the traditional static load test. The test also provides damping values, which are not provided by a traditional static test.

The calculated static soil resistance appears to provide good agreement with the measured static soil resistance. The lateral Statnamic test also provides dynamic soil response which, to date, has not been examined.



Figure 16. Load testing team.

## ACKNOWLEDGEMENTS

The authors wish to thank Dan Brown for supplying the preliminary graphs shown in the report; David Crapps and Dan Brown for designing and implementing this challenging load test program; Bob Hodges and the crew of Warren Paving for providing the strong backs and good equipment; Mike Justason and the personnel at Berminghammer for their technical assistance; and Mike Wright and the staff of the Mississippi Department of Transportation, Geotechnical Branch for allowing us the opportunity to do this project.

## REFERENCES

- Brown, D.A. 1998. Report of Statnamic Load Testing, US 90 Over the Pascagoula River, Mississippi Department of Transportation.
- Berkovitz, B. C. & Hahn, M. 1995. A Review of Statnamic Experiences for Transportation Applications. *Proceedings of the First International Statnamic Seminar*: 243-254. Vancouver.



## Testing of CFRP/Concrete Bond

G. Mullins, R. Sen, and J. Spain

University of South Florida, Tampa, Florida, U.S.A.

The University of South Florida has investigated the use of two new devices that test the bond between concrete and fiber reinforced plastic (FRP) material under (1) direct and (2) torsional shear stress. Results of tests carried out using these devices on two different unidirectional carbon fiber materials, Tonen Corporation's Forca Tow Sheets (FTS-C1-20) and Fyfe's SCH-41/TYFO™ S, are presented and compared against those on the *same* specimen from a uniaxial tensile test. The tensile tests led to failures in the concrete, implying that the bond was excellent. However, shear tests led to *partial or complete* debonding failures at the concrete/carbon fiber interface. The results of the study suggest that torsional shear testing provides the most accurate assessment of bond strength.

### INTRODUCTION

Epoxy bonding of fiber reinforced plastic (FRP) material is increasingly being used for strengthening reinforced or prestressed concrete highway structures. As structural performance is reliant on the bond between FRP and concrete, its long term integrity is of critical importance. Tests for measuring bond between concrete and FRP are needed as *acceptance criteria* when the repair is initially carried out. They may also be required during scheduled maintenance to evaluate possible degradation in bond due to prolonged exposure in a hostile environment.

The most common test for measuring bond between FRP and concrete is the *uniaxial tension* test [1]. In this test, a metal disk is epoxied to the FRP surface bonded to concrete. After the epoxy has cured, the force required to pull the metal disk and the bonded material from the concrete surface is measured. The quotient of the applied tensile force ( $P$ ) and the area of the metal disk ( $A$ ) bonded to the FRP surface gives the uniaxial tensile bond stress.

The uniaxial tension test is undoubtedly a very simple test that can be performed *in situ* or in a laboratory. However, as the bond line is subjected to tensile stresses, the results obtained may not be very meaningful especially for flexural members where load transfer to the FRP material is primarily through shear. Moreover, as the tensile bond strength of the epoxy adhesive is generally greater than the tensile strength of concrete, failures inevitably occur in the concrete. Thus, while the results are very useful in evaluating initial repairs and making appropriate adjustments they maybe less useful in assessing long term performance.

In 1996, the University of South Florida initiated a test program to assess the bond between FRP material and concrete. As part of this program, two new test devices were designed and fabricated to allow measurement of the shear bond stress between FRP material and concrete. This paper provides a description of the test program and a summary of the results obtained.

### OBJECTIVES

The principal objectives of the study were: (1) to develop suitable equipment and evaluate test procedures for measuring the bond line shear strength between FRP material and concrete, (2) to determine if the widely used uniaxial tension test is appropriate for testing the bond between FRP and concrete, and (3) to compare the results of three types of tests on identical specimens.

### EXPERIMENTAL PROGRAM

To meet the objectives of the study it was necessary to prepare sets of identical specimens whose bond could be measured under both tensile and shear loads. The quality of bond was varied for each set of specimens. The equipment used for the tensile bond testing was based on a design developed by the Virginia Transportation Research Council [2]. Shear bond was evaluated using two new devices that were designed to produce shear stress from either direct shear or torsion.

#### CFRP Material

Two different types of uni-directional CFRP sheets were tested, FTS-C1-20 provided by the Tonen Corporation of Japan and SCH-41/TYFO<sup>™</sup>S provided by the Fyfe corporation.

#### Specimen Preparation

Forca Tow sheets and Fyfe SCH-41/TYFO<sup>™</sup>S sheets were bonded to 300 x 300 x 88 mm concrete slabs. Five sets of slab specimens were prepared: **F1**, **F2**, **F3** and **F4** from Forca Tow sheets, and the **H1** series from Fyfe SCH-41/TYFO<sup>™</sup>S. Each specimen set varied in its surface preparation: (1) in the **F1** series surface preparation consisted of priming as per manufacturers specifications, (2) slabs **F2**, **F4**, and **H1** were ground smooth and then primed, and (3) slab **F3** was ground smooth and no primer applied. Following surface preparation, the CFRP sheets were bonded to each slab using the respective manufacturer-supplied proprietary epoxy products.

## Test Fixtures

Metal disk test fixtures, also called dollies, were fabricated for each type of test (tension, torsion, and direct shear). These fixtures were 50 mm diameter cold-rolled steel disks drilled and tapped on the upper face with appropriate adaptations for the specific test requirements [3]. Each dolly was bonded to the CFRP surface using a high modulus, low viscosity epoxy, Sikadur 32 (Figure 1).

## Scoring

For the uniaxial tension and torsion tests, a water-flushed, diamond-tipped core barrel with an inner diameter of 50-mm was used to score around the metal disk and through the CFRP. This scoring technique was used to minimize micro-cracking damage to the concrete [1]. Direct shear specimens were obtained using the same core barrel by fully coring through the slab. Figures 2 and 3 show the scoring procedure and the test-ready dolly, respectively.

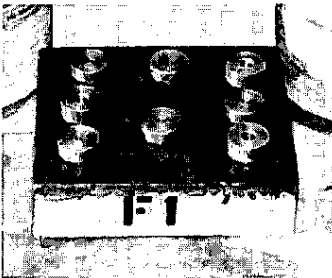


**Figure 1.** Bonded Test Fixtures (dollies)

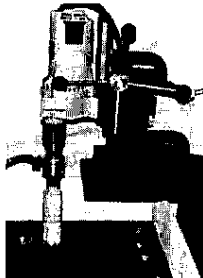


**Figure 2.** Scoring and Coring Slabs



**Figure 3.** Bonded Dolly and Scored CFRP

## TENSILE BOND APPARATUS

The uniaxial tension test apparatus used in the study is shown in Figure 4. It was comprised of a hand operated screw jack mounted to a reaction frame supported by three adjustable legs. The screw jack was used to apply a tensile force to the test dolly via an electronic load cell and a universal joint. The universal joint minimized loading irregularities associated with eccentricities. The load cell and a LVDT were monitored by a MEGADAC data acquisition system. Typical test results are shown in Figure 5.

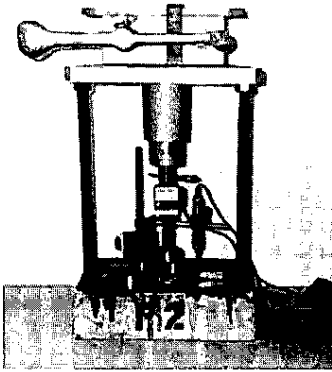


Figure 4. Tension Apparatus

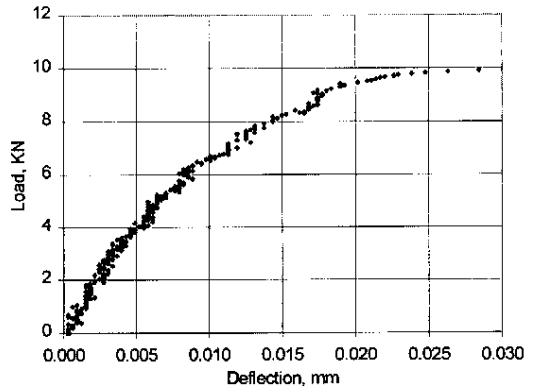


Figure 5. Typical Tension Test Results

### DIRECT SHEAR TEST APPARATUS

The direct shear test apparatus was designed to cause shear failure along the CFRP/concrete interface. An average applied shear stress was determined by dividing the peak load ( $H$ ) by the surface area ( $A$ ) of the metal disk in contact with the CFRP material.

The essential features of the direct shear apparatus are shown in Figure 6. It consisted of a shear box made in three sections - the main box (top left), a sliding plate with a circular opening to accommodate the metal disk attached to the CFRP specimen (right), and a clamp to secure the specimen inside the box (front left). A 3 mm gap exists between the main section and the sliding plate that forms a predetermined failure plane. The box has appropriate fittings at its top and bottom so that it can be installed in a tension testing machine.

In contrast to the tensile bond test, the direct shear tests involved considerably more setup time and effort. Where tension tests only required the CFRP to be scored, the direct shear test required a cored slab sample be completely removed. Additionally, more precautions were required to eliminate the introduction of bending stresses. Therefore, the slide plate was supported by six sets of linear bearings that prevented out-of-plane rotation of the dolly. Each cored specimen was carefully aligned with the sliding plate and then cast into the direct shear apparatus with quick curing "pour rock" to eliminate stress concentrations on the uneven core surface. The entire assembly was then mounted in an Instron/MTI universal testing machine and a shear force applied to the plane containing the CFRP/concrete bond. Measurements of force vs vertical displacement were recorded throughout the testing. Typical results are shown in Figure 7.

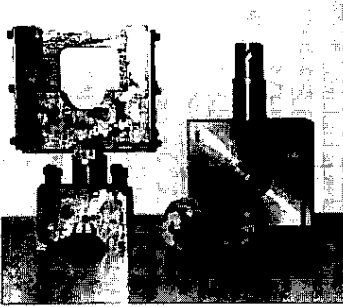


Figure 6. Direct Shear Apparatus

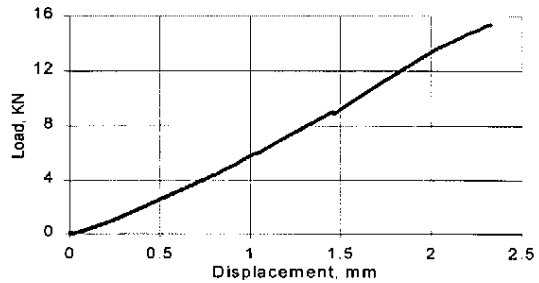


Figure 7. Typical Direct Shear Test Results

### TORSION TEST

Apart from direct shear, specimens were also subjected to shear stress as a result of an applied torque. Due to the distribution of shear stresses induced by torsional loading, the failure stress was determined from the maximum measured torque.

Originally, a calibrated torque wrench was used in the testing as in a recent study [5]. However, it was evident that compound stresses were being induced by the manual application of the torque. Therefore, a reaction frame was designed and fabricated that allowed only pure torque to be applied to the specimen (Figure 8). Typical torsion test results are shown in Figure 9 from which peak torque was determined.

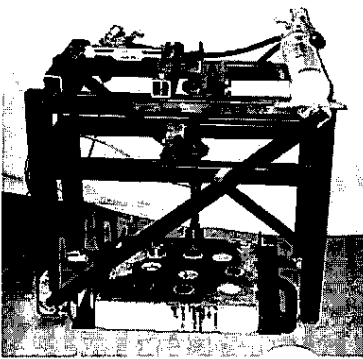


Figure 8. Torsion Test Frame

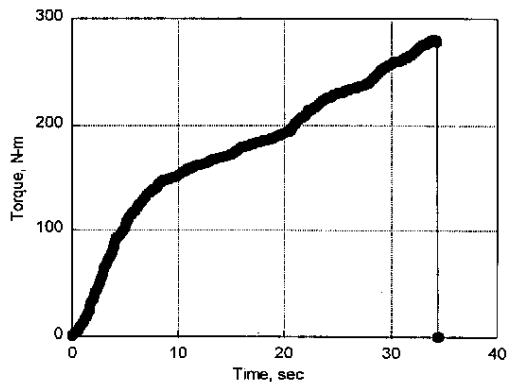


Figure 9. Typical Torsion Test Results

The torsion test frame was fabricated from 50 x 50 x 9.5 mm square tubing. A 25 mm diameter vertical shaft passes through the center of the frame, aligned by two pillow block bearings. At its lower extremity, the shaft is attached to a torque cell. At its upper extremity, the shaft is welded to a lever which pivots about the bearings. The ram of a hydraulic jack (mounted at the top of the frame), presses against the lever arm to apply the torque.

The torque cell was a calibrated shaft instrumented with four strain gages in a full bridge configuration aligned to detect torsional shear stresses. It was calibrated prior to the test to directly convert strains into torques.

The slab specimen is immobilized below the shaft in the reaction frame. A 19 mm hardened steel bolt was threaded and seated into the top of the torsion dolly. A socket placed on the head of the bolt completed the connection from the torque cell to the specimen. During testing, the torque cell was connected to a data acquisition system that recorded the peak applied torque (T). The maximum shear stress was calculated using the outer fiber radius (r) and the polar moment of inertia ( $J = \pi r^4/2$ ).

### TEST RESULTS

Results from uniaxial tension, direct shear and torsional shear tests are summarized for all five slab specimens in Table 1. The table lists the average failure stresses for each of the five slabs and the percentage of dolly area that debonded (*italicized*). This data was compiled from 45 tension, torsion and direct shear tests.

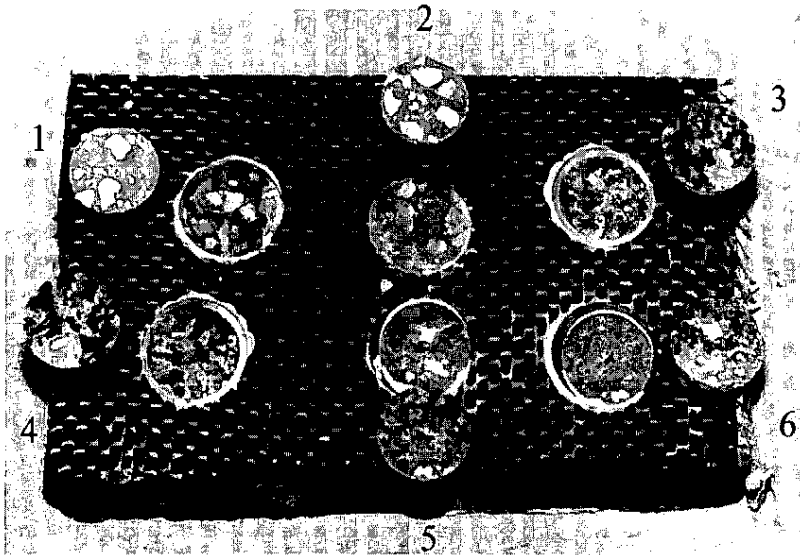
**Table 1.** Summary of Average Failure Stresses and Percent of Area Debonded

Slab ID	Average Failure Stress, MPa (ksi) and <i>Percent of Area Debonded %</i>					
	Tension (P/A)		Torsion (Tr/J)		Direct Shear (H/A)	
F1	5.2 (0.76)	0%	7.2 (1.04)	0%	7.2 (1.04)	0%
F2	5.1 (0.74)	0%	8.0 (1.27)	33%	6.6 (0.95)	0%
F3	5.1 (0.73)	0%	6.1 (0.89)	85%	5.8 (0.84)	50%
F4	4.3 (0.63)	0%	7.3 (1.06)	20%	6.2 (0.90)	3%
H1	4.3 (0.62)	0%	8.1 (1.27)	65%	6.0 (0.87)	50%
<b>Average of All Slabs</b>						
All	4.8 (0.70)	0%	7.3 (1.11)	41%	6.4 (0.92)	20.6%



Inspection of Table 1 shows tension failures occurred in the concrete in all five slabs even in series F3 (specimen prepared with poor bond). In contrast, when defective specimens were tested in direct shear or torsion, partial debonding occurred in some tests (Figure 10). This suggests that in situations where bond is suspect, tensile tests may provide a misleading picture. The results also indicate that tensile bond stress values are about 30-40% lower than those from the shear bond tests. This trend is consistent with observations from similar tests carried out on repaired concrete [6].

In the torsional tests, only perfectly prepared specimens (F1) developed the full shear strength of the concrete. Although the direct shear tests exhibited less debonding than torsion, the failure stress was consistently lower than that produced on similar torsion samples. This implies that the torsion test can more effectively stress the bond line without affecting the base concrete.



Legend: 1, 2 Tension  
3, 4 Torsion  
5, 6 Direct Shear

**Figure 10.** Failure Surfaces from Tension, Torsion, and Direct Shear Tests

## CONCLUSIONS

The uniaxial tension test is widely used for assessing the bond between FRP and concrete. Unfortunately, in most applications the bond line is subjected to shear not tension making the uniaxial tension results of limited value. Moreover, as concrete has a very low tensile strength compared to the epoxy, failures generally occur in the concrete making it impossible to assess degradation in bond under service conditions unless the bond is disastrously weak. The alternative shear tests described in the paper lead to higher induced bond line stresses that do not necessarily lead to failure in concrete. Of these tests, the torsion test is the easiest to conduct, produces the highest bond line stresses, and better assesses the bond quality. However, when FRP is bonded correctly, none of the tests truly test the full strength of the epoxy bond due to the relatively lower strength of concrete.

## ACKNOWLEDGMENTS

The authors gratefully acknowledge the advice and support of Dr. Howard Kliger. Materials tested were donated by Tonen Corporation of Japan and by Mr. Duane J. Gee of Fyfe Co. LLC. This support is gratefully acknowledged.

## REFERENCES

1. Steele, J. (1994). "Testing Adhesion of Coatings Applied to Concrete", *Materials Performance*, Vol 33, No 11, pp. 33-36.
2. Sprinkel, M. (1995). Private Communication with R. Sen, August 11.
3. American Concrete Institute (1995). "Manual of Concrete Practice", Section 503R-95, Use of Epoxy Compounds with Concrete, Farmington Hills, MI.
4. Gere, J.M. and Timoshenko, S.P. (1984). *Mechanics of Materials*, Second Edition, PWS Publisher, Boston, MA.
5. Vaysburd, A.(1996). "External Carbonfiber Reinforcement Bond to Concrete". Presentation, ACI Fall Convention, New Orleans, November.
6. Knab, L.I., Sprinkel, M.M. and Lane, O.J. (1989). "Preliminary Performance Criteria for the Bond of Portland Cement and Latex Modified Concrete Overlays", NISTIR 89-4156, National Institute of Standards and Technology, MD.

Manjriker Gunaratne,<sup>1</sup> Pamela Stinnette,<sup>1</sup> A. Gray Mullins,<sup>1</sup> Ching L. Kuo,<sup>2</sup> and Wayne F. Echelberger, Jr.<sup>1</sup>

## Compressibility Relations for Peat and Organic Soil

**REFERENCE:** Gunaratne, M., Stinnette, P., Mullins, A. G., Kuo, C. L., and Echelberger, W. F., Jr., "Compressibility Relations for Peat and Organic Soil," *Journal of Testing and Evaluation*, JTEVA, Vol. 26, No. 1, January 1998, pp. 1-9.

**ABSTRACT:** A new technique is formulated to predict the ultimate settlement (primary and secondary) of normally consolidated organic soils on the basis of the organic content. Data from a large number of oedometer tests on samples collected from organic soil deposits in Central Florida exhibit a definitive relationship of ultimate settlement versus organic content. These laboratory test results are analyzed using the Gibson and Lo rheological model to develop expressions for primary and secondary compressibilities in terms of organic content and consolidation pressure. It is shown how the compressibility relations predicted by the authors' approach concur with extensive data collected by other researchers. The usefulness of the authors' analytical relations is displayed by showing how the expected ultimate settlement of an organic soil subjected to a given pressure increase can be computed readily by using them.

**KEYWORDS:** consolidation, organic soil, peat, ultimate settlement

Of the total area of organic soils in North America, an area of two million acres is in a single deposit in Florida known as the Everglades (Thomas 1965). These organic-rich soils are generally referred to as "muck," and when they contain more than 75% organics, as "peat." When this organic material is encountered within proposed roadway alignments, it is often regarded as an undesirable foundation material for highways because of its high compressibility and poor strength. Surcharging is one technique used to preconsolidate and stabilize such material. When surcharging is impractical, complete excavation or "demucking" is sought. However, in some situations, such costly construction practices can be avoided if the ensuing ultimate settlement can be estimated accurately and determined to be tolerable for the intended structure. Thus, analytical expressions for settlement estimation based on laboratory test results are invaluable for highway construction operations on natural organic soil deposits.

Although research findings on compressibility of peats are commonplace in the literature, data for natural amorphous organic deposits are scarce. Moreover, in spite of the recent application of rheological models to explain the settlement behavior of organic soils [1,2], definitive expressions for evaluating the model parameters have not been developed in terms of basic organic soil proper-

ties. Hence, the objective of this research is to present simple expressions to predict the ultimate, one-dimensional (1-D) settlement of natural organic soils with reasonable accuracy, using their basic index properties. Researchers have shown that the most significant basic index property of a normally consolidated organic soil is its organic content. Consistency limits such as the plasticity index and liquid limit are not practically meaningful when dealing with fibrous organic soils with a granular mineral soil component. Even in the case of amorphous organic samples in which a liquid limit can be experimentally found, a plasticity index may be difficult to obtain, a fact clearly seen by the position of organic soils in the Casagrande plasticity chart.

A number of consolidation tests run on normally consolidated Florida organic soil samples show definitive trends of ultimate settlement variations with organic content and with consolidation pressure. The ultimate laboratory settlements also agree reasonably well with the predictions of the Gibson and Lo [8] long-term solution for Merchant and Taylor's (1940) consolidation theory. Hence, using this theory, analytical relations are generated for primary and secondary compressibilities in terms of the organic content and the consolidation pressure. These relations enable one to determine simply the ultimate 1-D compression of an organic soil, precluding the need to differentiate the primary and the secondary settlements on a time scale.

### Sample Classification and Consolidation Testing

Classification of the organic rich soils is generally done based on two classification systems. They are the Von Post System and the Kearns and Davison [5] System (Table 1). In the latter, the chemical and physical properties of organic soils at organic contents greater than 35% are dominated by the organics; therefore, the IT is placed in parentheses after the organic term. The appropriate IT term will depend on the dominant inorganic component (sand, silt or clay) of the soil. This method of classification agrees

TABLE 1—Kearns and Davison [5] classification of organic rich soils.

Organic Content, %	Classification
<5	IT
5-15	mucky IT
15-35	IT muck
35-55	muck (IT)
55-75	peaty muck (IT)
>75	peat (IT)

Manuscript submitted 11/30/95; accepted for publication 4/12/97.

<sup>1</sup>Department of Civil Engineering, University of South Florida, Tampa, FL.

<sup>2</sup>Senior engineer, Professional Services Industries (PSI), Tampa, FL.

with that of the American Society for Testing and Materials (ASTM) which defines true peat as containing more than 75% organic material.

Table 2 shows the classification and index properties of a number of Shelby tube organic soil samples recovered from various districts in South Central Florida, at depths of 0.3 to 0.5 m. These are identified by the designation of highways closest to the site where they were retrieved such as US 27, SR 597, etc. The inorganic portion of the samples was predominantly coarse grained or silty and the fiber contents were very low, making them mostly amorphous material. Furthermore, none of the samples indicated any appreciable overconsolidation during conventional consolidation testing performed on them [6]. Thus, all the samples were adjudged to be normally consolidated (NC) for all practical purposes, which can be attributed to the shallow depths where they were retrieved. This assertion is further verified by the compressibility relations formulated in this study, which portray all of the samples tested as being in the same family (NC) of soils, as far as the ultimate settlement behavior is concerned. Since there is no traceable stress history, such as reported previous loadings, there was no need to include that factor, except to emphasize that the developed relations are valid for NC organic soils. Retrieval of significantly overconsolidated samples and modifying the relations with the overconsolidation ratio (OCR) parameter can be an extension to this project.

### Analysis of Laboratory Consolidation Tests

In Florida organic soil deposits, which are often completely saturated, the main causes of settlement due to a stress increase are expulsion of pore fluids and simultaneous compression of the organic soil structure. These causes, classically separated into primary and secondary compression, respectively, have been postulated to occur concurrently. Researchers [1] have often sought rheological models to predict the settlement behavior of organic soils.

A commonly adopted parameter to express the secondary settlement behavior of organic soils is the coefficient of secondary consolidation ( $C_{\alpha}$ ), which is defined as the slope of the linear portion of a vertical strain versus logarithm-of-time plot. Although convenient for settlement rate predictions, such a linear plot does not adequately explain any termination in secondary compression. Berry and Poskitt (1972) used a rheological model to provide an analytical base to the above approach and validate the  $C_{\alpha}$  concept for both amorphous and fibrous peats. Their theoretical formulation is based on linking the primary and secondary compression to discrete void ratio changes in the soil skeleton, a concept that

is utilized in the current work as well. More recently, Fox et al. [7] showed that  $C_{\alpha}/C_c$  concept does not apply to peat. This empirical concept also suffers from its inability to predict the ultimate settlement.

Out of all the above-mentioned techniques, the Gibson and Lo [8] model based on Merchant and Taylor's theory was found to be more applicable for the organic soils tested in this project. The main attractiveness of the Merchant and Taylor theory lies in its generalization of Terzaghi's 1-D primary consolidation theory to include creep effects, as seen in Eq 1.

$$C_v \frac{\partial^2 u}{\partial z^2} = \frac{\partial u}{\partial t} - \frac{\lambda}{ab} \left[ (a + b)(u_o - u) + \frac{e - e_o}{1 + e_o} \right] \quad (1)$$

where

- $a$  = primary compressibility =  $\delta \epsilon_p / \delta \sigma$
- $b$  = secondary compressibility =  $\delta \epsilon_s / \delta \sigma$
- $\lambda/b$  = secondary compression rate factor
- $\epsilon_p$  = primary component of strain
- $\epsilon_s$  = secondary component of strain
- $e_o, u_o$  = initial void ratio and pore pressure
- $C_v$  = conventional coefficient of consolidation

The above theory simulates the reality where both pore pressure dissipation and creep take place simultaneously. Hence, although the theory acknowledges different mechanisms as causing the two types of settlement and treats them accordingly, the following solutions derived for Eq 1 by Gibson and Lo [8] do not differentiate the two phenomena on a time scale.

For small time periods,

$$\epsilon = 2 \sqrt{\frac{kt}{\pi a \gamma_w}} \frac{\Delta \sigma}{a} \left[ 1 + \frac{\lambda t}{3a} + \text{Order} \left( \frac{\lambda t}{a} \right)^2 \right] \quad (2)$$

For large time periods,

$$\epsilon = \Delta \sigma \left[ a + b \left( 1 - e^{-\frac{\lambda t}{b}} \right) \right] \quad (3)$$

where

- $\Delta \sigma$  = effective stress increment
- $k$  = coefficient of permeability

It should be noted that  $a$ ,  $k$ , and  $C_v$  are considered constants. Equation 3 predicts the settlement at  $t \rightarrow \infty$  as  $(a + b)\Delta \sigma$ . This would be the settlement after both primary and secondary settlements are completed. From the original Merchant and Taylor's solution it can be shown that  $a$  is the commonly used coefficient of primary compressibility,  $m_v$ .

The Gibson and Lo model has been used successfully to represent the laboratory and field compression curves for organic soils that exhibit significant secondary compression behavior [1]. However, the model does not take into account certain nonlinearities that may result from finite strains, stress level, and strain rate. In spite of these drawbacks, this model yields reasonable results in predicting the rate and magnitude of settlement when compared to field measurements [1]. However in a latter study, Edil and Simon-Gilles [2] report limitations of the above model in predicting field settlement. The authors address this issue in a section of this paper where their model predictions are compared with published laboratory results.

TABLE 2—Classification of Florida organic soil samples.

Location	Water Content, (%)	Organic Content, (%)	Wet Density, (kN/m <sup>3</sup> )	Specific Gravity	Initial Void Ratio	Classification
SR 951B	116	8.6	13.5	2.40	2.8	mucky sand
SR 951A	97	10.8	13.1	2.63	2.9	mucky sand
SR 597A	61	12.4	14.9	2.40	1.5	mucky silt
S 951B	165	15.8	13.3	2.41	3.7	muck
S 951A	292	37.0	11.0	2.13	6.5	muck
S 951C	326	43.5	10.6	1.95	6.7	clayey muck
SR 597B	291	57.4	10.8	2.09	6.4	peaty muck
US 27B	686	81.7	9.9	1.58	11.3	silty peat
US 27A	726	88.9	9.8	1.34	10.1	silty peat
SR 46E	654	92.1	10.1	1.45	9.6	sandy peat

### Comparison of Laboratory Results with the Gibson and Lo Model Predictions

Since Eq 3 expresses the combined 1-D strain of a soil undergoing concurrent pore pressure dissipation and creep during large time intervals, the authors applied it for predicting the combined (ultimate) settlement of Florida organic soil. Hence, although the pore pressures were monitored, the more common approach of indicating the EOP on the settlement plots was unnecessary for development of this model. In evaluating the parameters  $a$ ,  $b$ , and  $\lambda$  for each consolidation test, the technique developed by Edil and Dhowian [9] was used. This technique employs a plot of the logarithm of strain rate versus time  $[(\log(\Delta\epsilon/\Delta t)) \text{ versus } t]$ . By simple manipulation of Eq 3, it can be shown to be linear for the time range corresponding to secondary compression if the soil agrees with the basic assumptions made in the model. The slope and intercept of the best-fit line yield the values of  $a$ ,  $b$ , and  $\lambda$  as follows:

$$\text{Slope} = -0.434(\lambda/b) \quad (4)$$

$$\text{Intercept} = \log_{10}(\Delta\sigma\lambda) \quad (5)$$

$$a = \frac{\epsilon(t_k)}{\Delta\sigma} - b + be^{-(\lambda/b)t_k} \quad (6)$$

where  $t_k$  is equal to the last time a reading of compression was taken [1].

Edil et al. [2] also state that long-term compression tests performed on fibrous peats do not show a linear  $\ln \epsilon$  versus  $t$  tendency when the load increments are permitted to remain on a specimen for up to six months. This further supports the Gibson and Lo model for large time intervals (Eq 3), which predicts a nonlinear relationship between  $\ln \epsilon$  and time.

Figure 1 shows the logarithm of strain rate versus time plots obtained from a sample taken from US 27B for six different consolidation stages. A pronounced departure from linearity is seen in the initial stages. This is because Eq 3 is a specific solution valid only for relatively large time periods. On the other hand, the perfect matching of Eq 3 with actual data for large time periods is remarkable, as indicated by Fig. 1. Similar results were obtained for all the samples tested [6].

Moreover, the predicted ultimate settlement also agreed very well with the asymptotic value established by tracing the deflection versus time curves for each test [6]. Thus, it was concluded that the above rheological approach is suitable for modeling the ultimate compression of Florida organics. As the model also offers the added advantage of yielding primary and secondary compressibilities, it was determined to be ideal for the development of compressibility relations.

### Compressibility Relations

The  $a$  and  $b$  coefficients found using Eqs 4–6 from plots (such as Fig. 1) corresponding to all of the samples are seen in Table 3.  $a$  and  $b$  are seen to vary with consolidation pressure ( $\sigma$ ) and the organic content ( $oc$ ). The following formulation describes the derivation of explicit relationships for  $a$  and  $b$ , based on the experimental data in Table 3.

To decouple the discrete void ratio changes due to primary and secondary compressions, the authors assumed the void ratio to constitute primary compression and secondary compression components of the soil skeleton. For each consolidation load step, these

components correspond to the void volumes that can be separately closed by exhaustive primary and secondary compressions, respectively. In this paper, they will be referred to as  $(\Delta e)_p$  and  $(\Delta e)_s$ , which correspond to one-dimensional strains  $\Delta\epsilon_p$  and  $\Delta\epsilon_s$  identified in relation to Eq 3.

When the initial void ratios ( $e_0$ ) of the samples are plotted against their organic contents (Table 2), the following linear relation is obtained (Fig. 2):

$$e_0 = 1.79 + 9.72(oc) \quad (7)$$

Equation 7 is in concurrence with the Andersland et al. [3] conclusion for fibrous organic samples.

Next, the authors expressed basic compressibility relationships in terms of  $e_p$  and  $e_s$ , which are the equilibrium (final) void ratios for a given loading under purely primary and purely secondary compressions, respectively:

$$e_p = e_0 - (\Delta e)_p = f_1(oc, \sigma) \quad (8)$$

$$e_s = e_0 - (\Delta e)_s = f_2(oc, \sigma) \quad (9)$$

Thus, the actual equilibrium void ratio under any loading is given by:

$$e = e_0 - (\Delta e)_p - (\Delta e)_s \quad (10)$$

It should be noted that the primary and secondary compressibilities are separated in Eq 10 on a magnitude basis and not on a time scale. The combination of Eqs 8–10 produces the useful relationship,

$$e = e_p + e_s - e_0 \quad (11)$$

The authors then employed the following methodology to synthesize the functions  $f_1$  and  $f_2$  utilizing the data in Table 3. During the  $j$ th loading step of 1-D consolidation of a given organic soil sample:

$$a_j = -\frac{1}{1 + e_j} \frac{(\Delta e)_{j,p}}{\Delta\sigma_j} \quad (12)$$

where  $(\Delta e)_{j,p}$  is the change in primary void ratio of the sample and  $e_j$  is the initial void ratio during that step.

Therefore, at the end of a consolidation test with  $n - 1$  load increments, the final void ratio due to primary compression alone is:

$$e_{n,p} = e_0 - \sum_{j=1}^{j=n-1} a_j(\Delta\sigma)_j(1 + e_j) \quad (13)$$

which is the equilibrium void ratio due solely to primary compression (Eq 8) of the particular sample at a consolidation pressure  $\sigma$  given by:

$$\sigma = \sum_1^{n-1} \Delta\sigma_j \quad (14)$$

Using similar reasoning, the equilibrium void ratio due to secondary compression (Eq 9) of a sample with a specified organic content,  $oc$ , at a consolidation pressure,  $\sigma$ , (Eq 14) is given by

$$e_{n,s} = e_0 - \sum_{j=1}^{j=n-1} b_j(\Delta\sigma)_j(1 + e_j) \quad (15)$$

The above steps illustrate how  $e_p$  and  $e_s$  can be evaluated using  $a$ ,  $b$ , and  $e_0$  values in Tables 2 and 3 as well as Eq 10, which

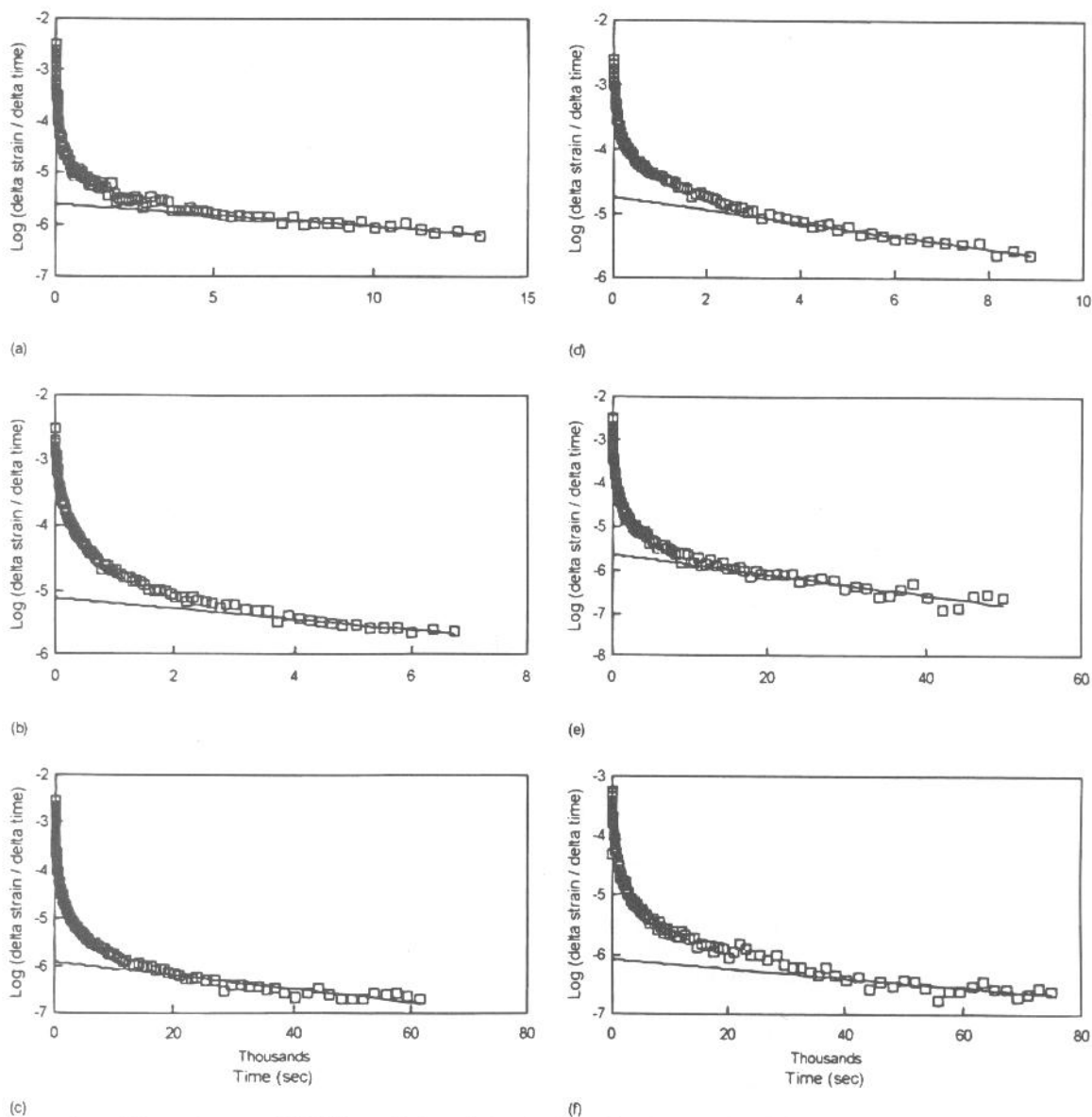


FIG. 1—Comparison of the settlement of US 27 sample B with the rheological predictions. Applied pressures are (a) 31.9 kPa, (b) 63.79 kPa, (c) 127.59 kPa, (d) 255.18 kPa, (e) 510.35 kPa, (f) 1020 kPa.

computes the actual void ratio  $e_j$  in each loading step. At this stage of the formulation, functions  $f_1$  and  $f_2$  in Eqs 8 and 9 can be illustrated graphically by plotting  $e_p$  and  $e_s$  values for each sample against its organic content at different consolidation pressures  $\sigma$ . As seen in Figs. 3 and 4, these individual plots are linear with respect to the organic content. It is realized that  $e_p$  and  $e_s$  are imaginary void ratios back-calculated based on the  $a$  and  $b$  values in Table 3 that relate to the final void ratio,  $e$ , through Eq 1. It can be deduced from the above linear relations that the resultant equilibrium void ratio due to both primary and secondary compressions should also be linear with respect to the organic content, which confirms Andersland et al. [3] observations.

Now, following the Andersland et al. [3] approach, expressions 8 and 9 can be rewritten as:

$$e_p = I_p(\sigma) + M_p(\sigma).oc \quad (16)$$

$$e_s = I_s(\sigma) + M_s(\sigma).oc \quad (17)$$

where  $I(\sigma)$  and  $M(\sigma)$  are intercepts and slopes corresponding to any given consolidation pressure  $\sigma$  of Figs. 3 and 4. Derivation of expressions for  $I(\sigma)$  and  $M(\sigma)$  values will be discussed in the following section. Since the expressions must accommodate the lower and the upper boundaries of  $\sigma$  which are (1)  $\sigma = 0$ —the unloaded condition and (2)  $\sigma \rightarrow \infty$ —the infinite pressure condition, the following 3-parameter rectangular hyperbolic equation  $F(\sigma)$  was fitted for all four  $I$  and  $M$  expressions in Eqs 16 and 17:

$$F(\sigma) = A - \frac{\sigma}{B\sigma + C} \quad (18)$$

It is obvious from Eq 18 that when  $\sigma = 0$ ,  $F(\sigma)$  should provide the value of  $A$ . Hence, inspection of Eq 7 and comparison with Eqs 16 and 17 reveal that the  $A$  term for both  $I$  and  $M$  functions will be 1.79 and 9.72, respectively.

With the  $A$  parameter known, the following rearranged linear



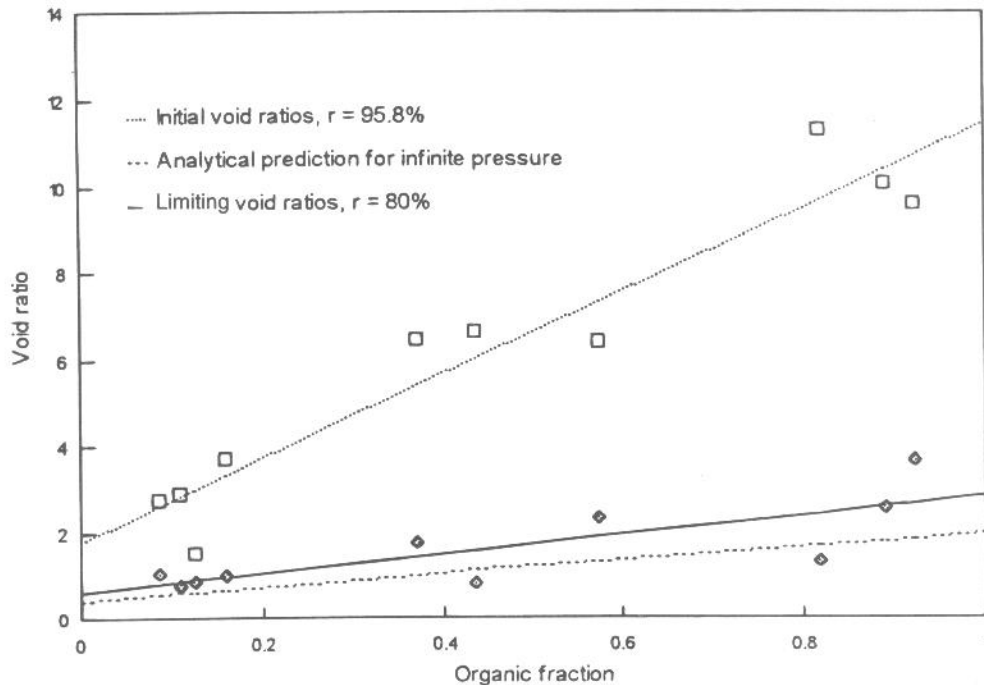


FIG. 2—Initial and ultimate void ratio versus organic content correlations for all samples tested.

form of Eq 18 was used to find *B* and *C* using linear regression analysis:

$$\frac{\sigma}{A - F(\sigma)} = B\sigma + C \quad (19)$$

It is realized that *F*( $\sigma$ ) values are obtained from the slopes or intercepts of Fig. 3 (for primary compression) and Fig. 4 (for secondary compression), depending on whether *F* represents *M* or *I*. The resulting expressions and the corresponding correlation coefficients (*r*) are given in Eqs 20–23, in which the pressure is measured in kPa.

$$I_p(\sigma) = 1.79 - \frac{\sigma}{1.27\sigma + 97.79} \quad r = 99.95\% \quad (20)$$

$$M_p(\sigma) = 9.72 - \frac{\sigma}{0.16\sigma + 23.13} \quad r = 99.95\% \quad (21)$$

$$I_s(\sigma) = 1.79 - \frac{\sigma}{1.86\sigma + 360.17} \quad r = 96.2\% \quad (22)$$

$$M_s(\sigma) = 9.72 - \frac{\sigma}{0.52\sigma + 40.61} \quad r = 99.95\% \quad (23)$$

When the ultimate deflection of all the samples was plotted against the consolidation pressure over the entire range of pressures (Fig. 5), the ultimate settlement tends to diminish gradually with increasing pressure as one would anticipate, until what appears to be a limiting settlement is reached at very high pressures. Based on the

TABLE 3—Experimental compressibility values *a* and *b* (in parentheses) in  $10^{-5} \text{ m}^2/\text{kN}$ .

Organic Content, (%)	Stress (kPa)					
	31.9	63.8	127.6	255.2	510.4	1020.8
8.6	170 (23)	96 (32)	89 (13)	25 (10)	19 (4)	7 (1)
10.8	303 (59)	106 (52)	99 (22)	28 (13)	24 (4)	9 (2)
12.4	144 (16)	34 (8)	32 (6)	14 (3)	11 (2)	5 (1)
15.8	416 (118)	116 (74)	79 (28)	41 (14)	15 (4)	8 (2)
37.0	456 (172)	116 (142)	69 (86)	33 (25)	15 (6)	3 (4)
43.5	276 (169)	146 (163)	138 (63)	68 (28)	27 (22)	9 (7)
57.4	97 (93)	81 (36)	82 (21)	30 (16)	28 (6)	12 (3)
81.7	548 (81)	219 (63)	163 (29)	52 (31)	46 (8)	23 (5)
88.9	366 (94)	53 (63)	153 (26)	52 (21)	36 (6)	11 (3)
92.1	160 (235)	78 (52)	64 (38)	59 (12)	21 (4)	8 (2)

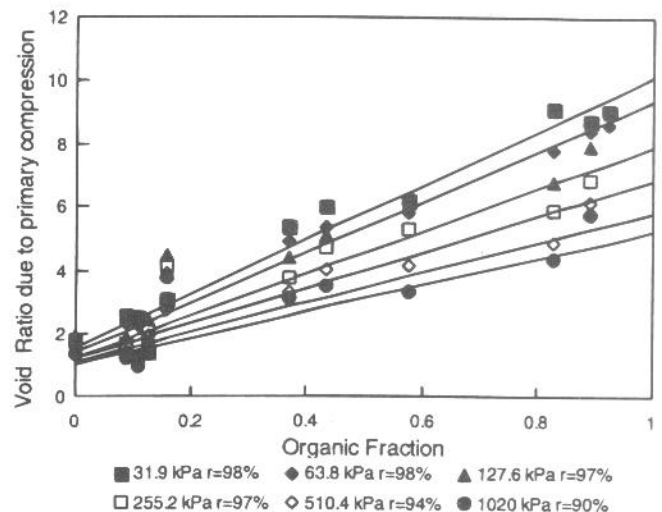


FIG. 3—Void ratio due to primary compression versus organic content correlation for all of the samples.



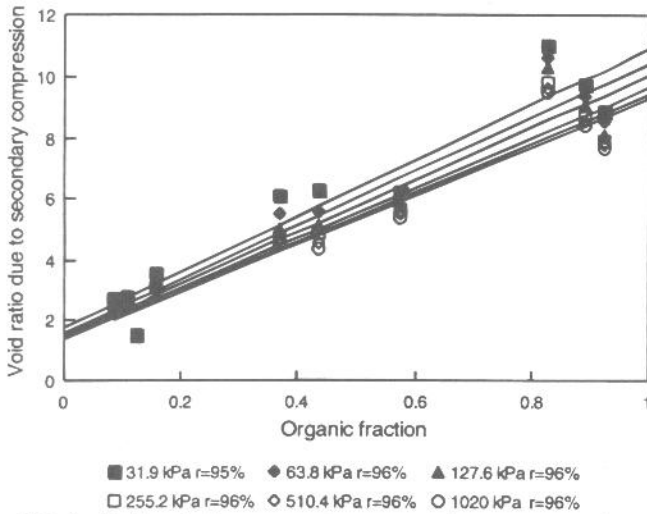


FIG. 4—Void ratio due to secondary compression versus organic content correlations for all of the samples.

limiting settlement value for each sample in Fig. 5, the authors estimated the corresponding limiting void ratios (for  $\sigma \rightarrow \infty$ ) for each sample and extracted the ultimate void ratio versus organic content curve, which is the upper pressure boundary of the family of  $e$  versus  $oc$  plots in Fig. 2.

The above limiting void ratio versus organic content curve can also be obtained by using the authors' analytical relation by setting  $\sigma \rightarrow \infty$  in Eqs 20–23 and substituting in Eqs 16, 17 and 11 as

$$e_{\infty} = 0.46 + 1.55(oc) \tag{24}$$

When plotted on Fig. 2, Eq 24 matches well with its experimental counterpart, thus further confirming the validity of the relationships in the entire range of pressure values from zero to infinity.

**Determination of  $a$  and  $b$  Compressibility Parameters**

It is known that  $a$  can be determined by the continuous form of Eq 12 as

$$a = -\frac{1}{(1 + e)} \frac{\partial e_p}{\partial \sigma} \tag{25}$$

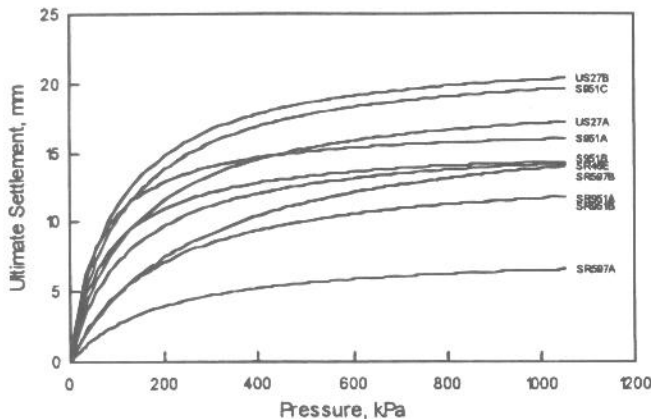


FIG. 5—Ultimate settlement versus consolidation pressure curves for all of the samples.

Then, by substitution for  $e_p$  from Eq 16:

$$a = -\frac{1}{(1 + e)} \left[ \frac{d}{d\sigma} \overline{I_p(\sigma)} + oc \frac{d}{d\sigma} \overline{M_p(\sigma)} \right] \tag{26}$$

The actual equilibrium void ratio  $e$  in the denominator in Eq 6 can also be represented with a hyperbolic relation on its own as in the cases of  $e_p$  and  $e_s$ . Finally, by introducing the first derivatives of Eqs 20 and 21 in Eq 26, the expression for  $a$  can be obtained as ( $\sigma$  in kPa)

$$a = \frac{97.79}{(1.27\sigma + 97.79)^2} + \frac{23.13 \cdot oc}{(0.16\sigma + 23.13)^2} \tag{27}$$

Similarly for  $b$ , one can deduce

$$b = \frac{360.17}{(1.86\sigma + 360.17)^2} + \frac{40.61 \cdot oc}{(0.52\sigma + 40.61)^2} \tag{28}$$

where

$$F(oc, \sigma) = \left[ 2.79 - \frac{\sigma}{(0.78\sigma + 74.28)} \right] + oc \left[ 9.72 - \frac{\sigma}{(0.12\sigma + 15.33)} \right]$$

The above primary and secondary compressibility expressions can be used to evaluate the 1-D ultimate strain from Eq 3 as:

$$\epsilon_{ult} = \Delta\sigma[a + b] \tag{29}$$

Sometimes it is common practice to characterize an organic soil deposit based on its moisture content rather than the organic content. Hence, a useful relationship was developed between the initial moisture content,  $w_o$  (%), and the organic content,  $oc$  (%), [6] as:

$$oc = w_o * 0.136 + 2.031 \quad r = 93\% \tag{30}$$

Equation 30 can be used to estimate the ultimate strain from Eqs 27–29 when the organic content is not available.

**Verification of the Compressibility Relation**

Figure 6 shows a plot of the predictions of  $a$  and  $b$  from the above expressions compared with the experimental values for the

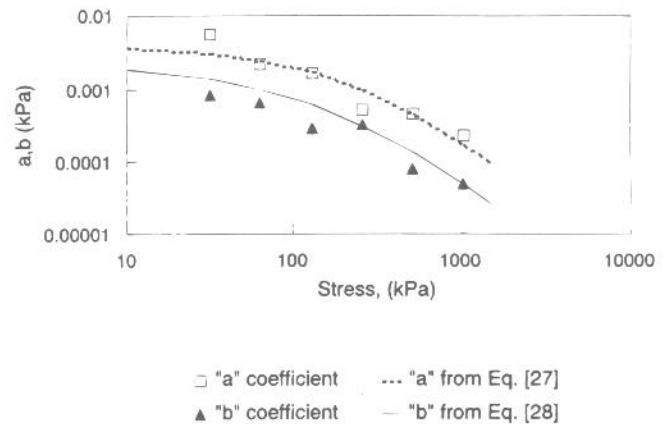


FIG. 6—Comparison of analytical predictions of  $a$  and  $b$  with experimental values for US 27 sample B.

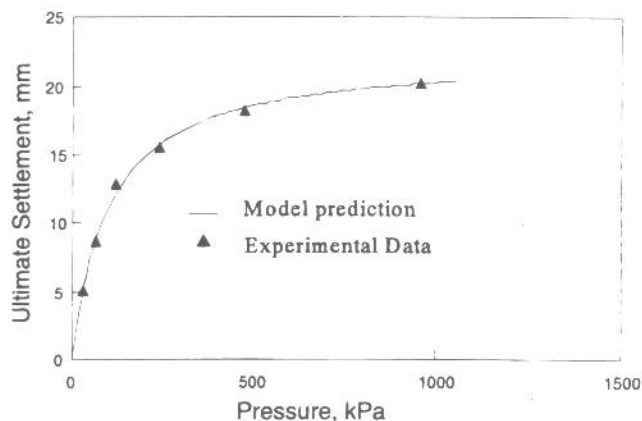


FIG. 7—Comparison of the model predictions and experimental data for US 27 sample B.

US 27 sample B found in Table 3. For the same sample (US 27 sample B) in Fig. 7, the authors also plotted the ultimate settlement obtained from the above expressions against the experimental values shown in Fig. 5. Reasonable agreement is observed in both Figs. 6 and 7. An additional consolidation test on a similar sample of organic soil ( $oc = 95\%$ ) was also performed for a much longer period of time. Figure 8 shows the settlement versus time plot for the new test up to a period of 18 days. It is seen how the secondary settlement continued at the end of the observation period, at a reduced rate. Figure 8 also shows the model prediction of the ultimate settlement and one can observe the agreement between the extrapolated (extended) settlement curve and the model prediction.

### Comparison with Published Laboratory Results

The authors scrutinized the validity of their model for laboratory tests conducted by independent sources [1]. Figures 9 and 10 are plots of  $a$  and  $b$  values obtained by Eqs 27 and 28 against the pressure for different organic contents. A proposed average experimental correlation suggested by Edil and Mochtar [1] based on a large base of laboratory data is plotted on Figs. 9 and 10 as well. The agreement between the authors' predictions for organic contents in the range of 50% to 90% and Edil's laboratory results is encouraging. Furthermore, when comparing the authors' predictions with Edil and Mochtar's [1] plots, one realizes that the scatter in the latter group of data can be due predominantly to the variability

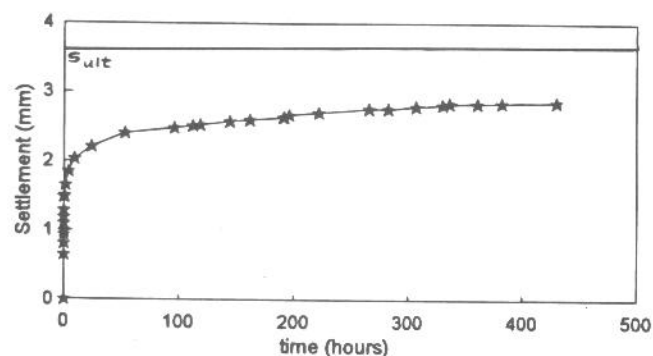


FIG. 8—Comparison of the model prediction and experimental data for the I-4 sample.

ity of organic contents of the peats and the OCRs in the case of OC peat samples.

### Application to Field Organic Soil Deposits

The Edil and Mochtar [1] field database for peat shown in Fig. 10 shows a deviation from the laboratory results. Edil and Mochtar [1] attribute this departure in the field results to differences in strain rates.

One can attribute part of the above deviation to lateral strains that can occur in the field as well. Gruen and Lovell [10] also state that settlement resulting from lateral movement under load have been found to be relatively large and report that in the field, lateral strains can contribute up to 30% of the total settlement. The authors' 1-D model can be modified by incorporating 3-D field effects arising from lateral strains to show that magnitudes of measured  $a$  and  $b$  values can vary between laboratory and field conditions [6]. Therefore, Eqs 27 and 28 may also be applied to predict the settlement behavior of organic soil deposits where the lateral strains are insignificant. These conditions can typically occur in the middle of loads, such as roadway fills, covering an extensive area. It should also be noted that field primary consolidation is usually estimated based on 1-D consolidation tests.

### Numerical Example

The following numerical example illustrates the significance and the use of Eqs 27 and 28. Assume that based on the laboratory consolidation test results, one wishes to predict the ultimate 1-D settlement expected in a 1 m thick organic soil layer ( $oc = 50\%$  and current overburden stress 50 kPa) due to an extensively placed surcharge of 50 kPa.

Since there is no significant stress attenuation within 1 m due to an extensive surcharge, the final pressure will be 100 kPa throughout the layer. Then, by applying Eq 29, one obtains

$$\epsilon_{ult} = \int_{50}^{100} [a(\sigma) + b(\sigma)] d\sigma \quad (31)$$

where  $a(\sigma)$  and  $b(\sigma)$  are obtained from Eqs 27 and 28 using an  $oc$  value of 0.5.

Finally, when Eqs 27 and 28 are substituted in Eq 31 and numerically integrated, primary and secondary compressions of 0.107 m and 0.041 m are predicted. Hence, an ultimate settlement of 0.148 m can be anticipated. The numerical integration can be easily performed using *Mathcad* or a similar package.

### Conclusion

Results of laboratory tests conducted on Florida's natural normally consolidated organic soils indicate that the ultimate settlement can be predicted accurately by the Gibson and Lo [8] rheological model. Using laboratory correlations, closed-form expressions useful for predicting analytically the ultimate 1-D settlement of normally consolidated organic soils have been developed and experimentally verified for a wide range of organic contents. The close agreement between the authors' analytical predictions and the results collected elsewhere [1] suggests a possible extension of these relations to other natural organic soils with coarse-grained inorganic components.

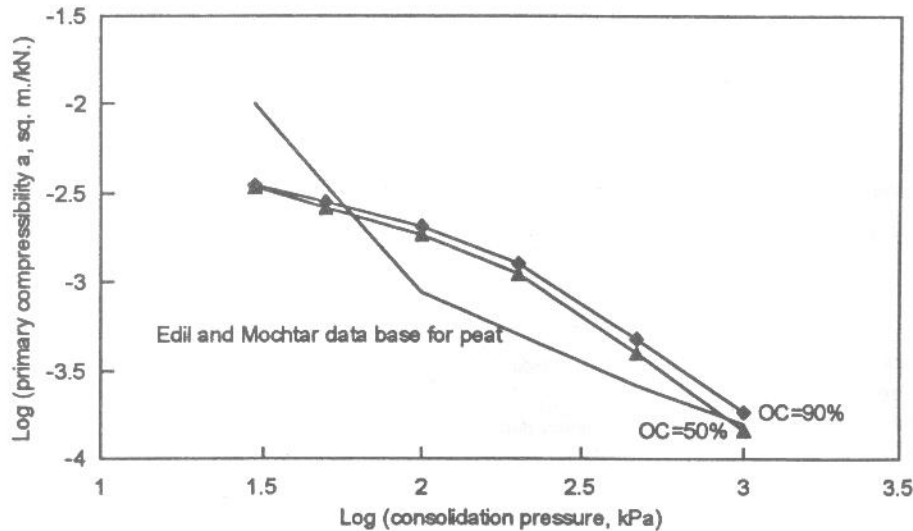


FIG. 9—Variation of primary compressibility with consolidation pressure and organic content compared with Edil and Mochtar's [1] database for peat.

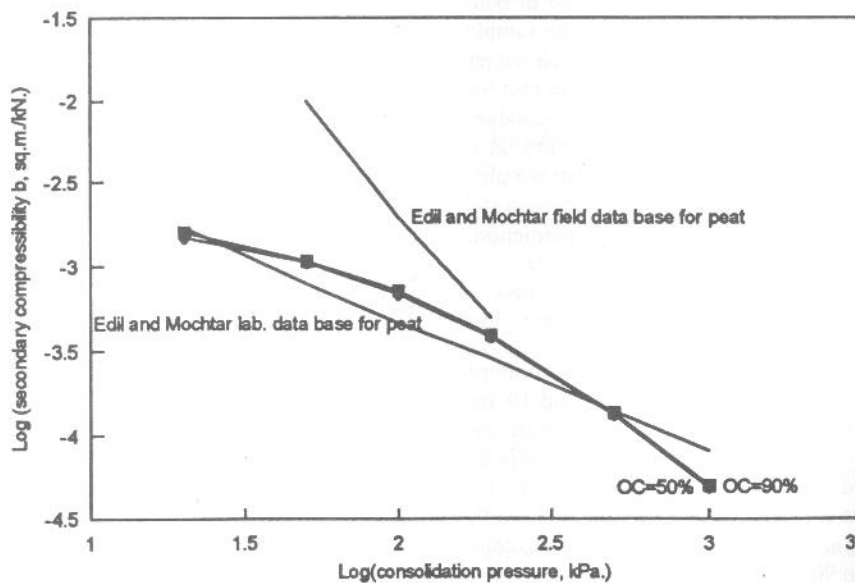


FIG. 10—Variation of secondary compressibility with consolidation pressure and organic content compared with Edil and Mochtar's [1] database for peat.

The inclusion of zero pressure and infinite pressure boundary conditions in formulating  $e$  versus  $\sigma$  plots allows these relations to be applicable for a wide consolidation pressure range. This feature makes it a unique model compared to existing consolidation models that do not accommodate extreme pressure conditions, leading to undefined void ratios at extremely low and extremely high pressures. Another significant outcome of this study is that the frequently observed nonlinearity of  $e$  versus  $\log \sigma$  curves for most organic soils is explained by the hyperbolic nature of the newly-developed  $e$  versus  $\sigma$  curves.

#### Acknowledgments

The authors wish to thank Dr. Rajaram Janardhanam, professor of civil engineering at the University of North Carolina, Charlotte, for review of this manuscript.

#### References

- [1] Edil, T. B. and Mochtar, N. E., "Prediction of Peat Settlement," *Sedimentation Consolidation Models Predictions and Validation*, Proceedings of a symposium sponsored by the ASCE Geotechnical Engineering Division in conjunction with the ASCE Convention in San Francisco, CA, October 1, 1984, R. N. Young and F. C. Townsend, Eds., American Society of Civil Engineers, New York, 1984, pp. 411-424.
- [2] Edil, T. B. and Simon-Gilles, D. A., "Settlement of Embankments on Peat: Two Case Histories," *Proceedings, Conference on Advances in Peatlands Engineering*, National Research Council of Canada, 1986.
- [3] Andersland, O. B. and Al-Khafaji, A. A. W. N., "Organic Material and Soil Compressibility," *ASCE Journal of the Geotechnical Engineering Division*, Vol. GT7, July 1980, p. 749.
- [4] Holtz, R. D. and Kovacs, W. D., *An Introduction to Geotechnical Engineering*, Prentice-Hall, Inc., 1981.
- [5] Kearns, F. L. and Davison, A. T., "Field Classification of Organic Rich Soils," *Proceedings, Mineral Matter in Peat: Its Occurrence, Form and*

- Distribution, R. Raymond, Jr. and M. J. Andrejko, Eds., Los Alamos National Laboratory, Los Alamos, NM, 1983, pp. 147–157.
- [6] Stinnette, P., "Engineering Properties of Florida Organic Material," Masters thesis, University of South Florida, Tampa, FL, 1992.
- [7] Fox, P. J., Edil, T. B., and Li-Tus, L., " $C_{\alpha}/C_c$  Concept Applied to Compression of Peat," *Journal of Geotechnical Engineering*, Vol. 118, No. 8, 1992.
- [8] Gibson, R. E. and Lo, K. Y., "A Theory of Consolidation of Soils Exhibiting Secondary Compression," *Acta Polytechnical Scandinavia*, Ci 10 296: Scandinavian Academy of Science, 1961.
- [9] Edil, T. B. and Dhowian, A. W., "Analysis of Long-Term Compression of Peats," *Journal of Geotechnical Engineering*, Vol. 10, 1979, pp. 159–178.
- [10] Gruen, H. A. and Lovell, C. W., "Use of Peats as Embankment Foundations," Joint Highway Research Project IN/JHRP-83/3, 1983, p. 43.

# A quality control programme for performance evaluation of dynamic replacement of organic soil deposits

P. STINNETTE\*, M. GUNARATNE, G. MULLINS and S. THILAKASIRI

*Department of Civil and Environmental Engineering, University of South Florida, 4202 E. Fowler Avenue, Tampa, FL 33620, USA*

Received: 18 March 1996

Accepted: 19 August 1997

## Summary

Dynamic replacement (DR) is a relatively new ground-modification technique that has been used successfully to stabilize organic soil deposits by replacing the organic soil with sand columns. A full-scale DR field study was conducted in order to assess its effectiveness on Florida organic soils. A computer-based quality control system was developed using data-acquisition-management techniques to evaluate the degree of improvement of the organic soil layer at a given stage of treatment. One of the DR drop locations was instrumented in order to select technical criteria such as the print spacing and the number of blows per print for effective DR implementation, and to facilitate monitoring of the improvement of soil properties. The new quality control system evaluates the effects of treatment by computing the dynamic settlement modulus (DSM) from the impact acceleration data collected during the treatment period. This paper presents the results obtained from the pilot study and their subsequent use in establishing evaluation criteria for the test programme. It is also shown how the DSM-based treatment criteria are in agreement with those obtained from conventional methods. Hence, it is concluded that with the use of the quality control system presented, the implementation of any DR programme can be effectively monitored.

*Keywords:* Dynamic replacement; organic soil; data acquisition; data management.

## Introduction

Organic soils are abundant in Florida, with two million acres existing in a single deposit known as the Everglades (Thomas, 1965). These organic-rich soils are generally referred to as 'muck', and when high in organic levels (> 75%) as 'peat'. When this organic material is encountered within proposed roadway alignments, it is often regarded as an

\* To whom correspondence should be addressed at: Hillsborough Community College, 1206 N. Park Road, Plant City, FL 33566, USA.

undesirable foundation material for highways due to its high compressibility and poor strength. Surcharging is one technique used to preconsolidate and stabilize such material. However, when surcharging is deemed impractical, complete excavation or 'demucking' is sought. Clearly, a timely and cost-effective treatment alternative is desirable.

The commonly used dynamic compaction is typically confined to loose natural soil deposits and miscellaneous fill materials (Lukas, 1992). However, several dynamic replacement (DR) case studies have been reported that involve the application of low- and high-energy impacts onto organic soil deposits that are overlain with sand surcharges. Lo *et al.* (1990) report that, by using a combination of low-energy impacts followed by high-energy ones, a peaty clay deposit can be transformed into an upper sand raft with pockets of peaty sand underlain by a fairly uniform layer of mixed sand and peat. They further report that both layers exhibit relatively insignificant secondary compression characteristics. In an earlier study on peaty clay, Ramaswamy *et al.* (1979) report improvements in both strength and consolidation characteristics of the site studied as a result of high-energy impacts. Ramaswamy *et al.* (1979) also note the procedure's cost effectiveness over other alternatives and estimate potential savings of 30%.

### Field study site

The DR field study site selected is located in Plant City, Florida, USA. The site, owned by the Florida Department of Transportation (FDOT), is adjacent to Interstate I-4 in Eastern Hillsborough County. In order to conduct the study, an area of the site of 0.2 ha was cleared and filled with approximately 1–1.5 m of sandy fill material (approximately 7% fines). This material acted as a foundation for the crane and cone truck and as initial replacement material for the dynamic replacement process. The cleared study site with the fill material placed is shown in Fig. 1. The extent of the organic deposit at the site satisfied the requirements of the project, being representative of what is typically encountered in highway construction alignments. In fact, the site itself is expected to become a part of a scheduled I-4 on-ramp (slip road) to be constructed in the summer of 1996.

The thickness of the surficial organic deposit at the site varied from approximately 0.91 m to 1.83 m. The site was characterized as primarily amorphous in nature having an organic content of 95%.

### Dynamic replacement programme

The dynamic replacement testing programme was conducted using two drop weights. One – specifically designed for the DR process – was fabricated out of 25 square steel plates 4.93 cm high; its total height was 1.26 m with a square base of width ( $b$ ) 0.61 m and it weighed 3.64 tonnes. The other weight which was used for the final smoothing pass was 1.22 m in diameter and weighed 5.09 tonnes. Hayward-Baker, Inc. acted as technical advisor and provided the contractorial services for this project, including the second weight, crane and crane operator. The crane used to lift the weights was a model 50 manufactured by Northwest Engineering; it had a 23.5 m boom and a lifting capacity of

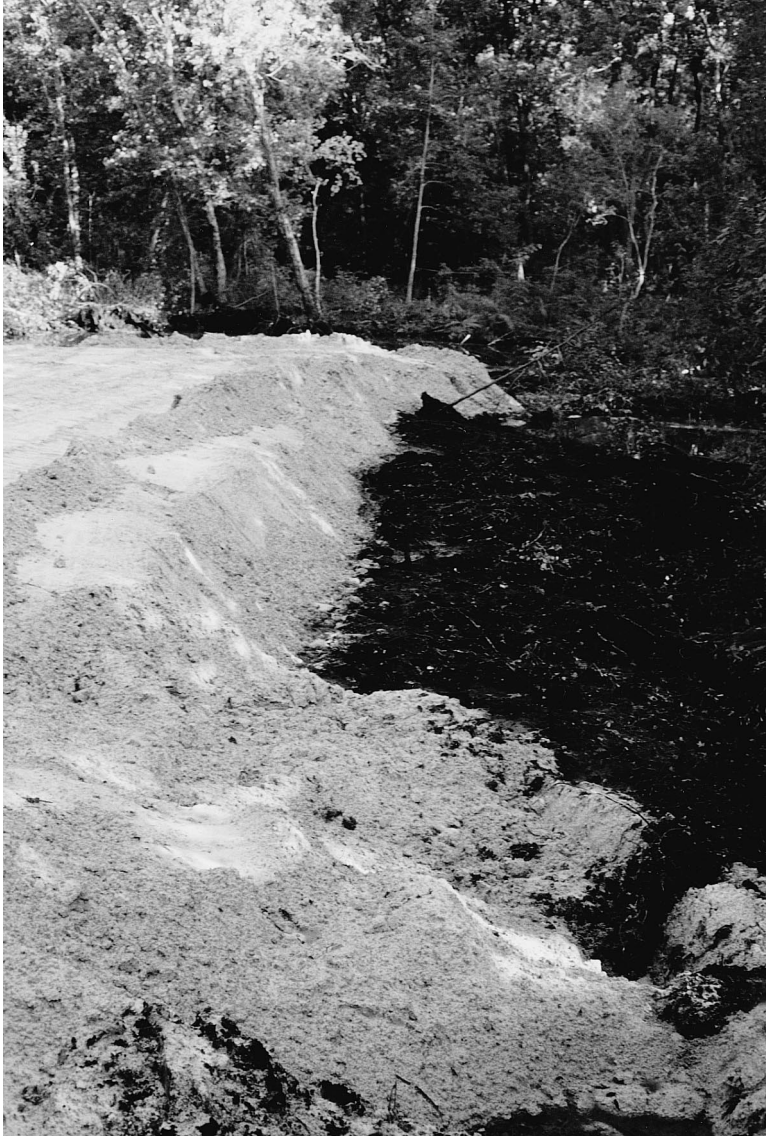


Fig. 1. Cleared and filled study site in Plant City, Florida.

90.91 tonnes. The drop location pattern was hexagonal so as to maintain a constant spacing between the drop locations. The centreline spacing between the drop locations was determined to be 2.44 m, which corresponds to 4 times the hammer base ( $4 \times b$ ). The rationale for the selection of this spacing will be addressed later in the paper. The pattern consisted of 19 drop locations identified by coordinates, (0,0), (0,1), set with respect to two sides as shown in Fig. 2. Drop location (1,3) was selected as the point to be fully instrumented. The instruments included: (1) an accelerometer attached to the falling drop weight, (2) three laser diode photoelectric cells to determine velocity and drop hammer



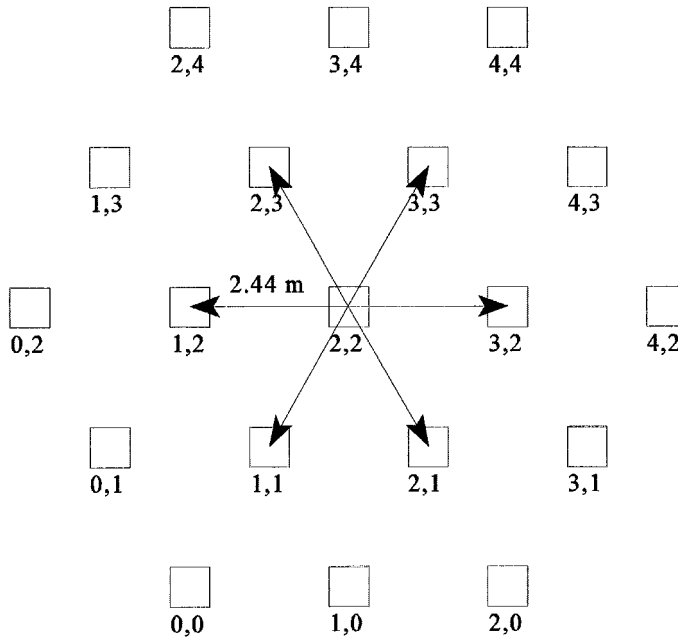


Fig. 2. Hexagonal test pattern with the drop locations identified by coordinates.

efficiency, and (3) five inclinometers to show lateral deflection and provide guidelines for spacing criteria. Additionally, cone penetration tests were performed before and after each impact. Figure 3 shows a boring log, typical of the site, taken at the pilot study location (1,3) after the fill was placed. The pilot study testing programme, instrumentation and monitoring schemes employed will be discussed in the following section.

### Pilot study instrumentation and monitoring programme

#### *Test programme*

Dynamic replacement of the pilot study location consisted of two passes – the first with a relatively low energy and the second pass with a higher energy. However, in order to ensure that the drop weight would not be irrecoverable due to excessive penetration and the subsequent development of suction forces, it was decided to employ a lower drop height during the first pass, the result of which is a low applied energy. The initial drop height selected for the first series of drops was 6.1 m. This choice was based on a new approach that predicts the crater depth of a dynamic replacement drop hammer after the first impact (Mullins *et al.*, 1996).

After each impact, clean sandy fill was used to fill the resulting crater. After five drops it was seen that the drop weight was easily recoverable, and the drop height was raised to 12.2 m. The drops were continued until the energy (number of blows) required to reach the

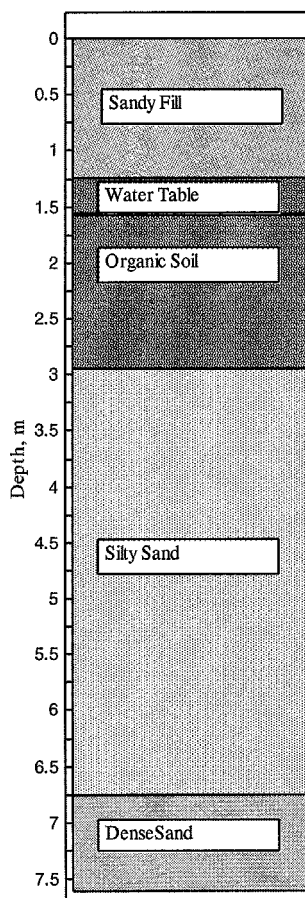


Fig. 3. Boring log taken at pilot study location (1,3).

desired level of improvement was identified. The analytical techniques used to monitor the improvement and the associated computer data acquisition system are discussed below.

#### *Computer interface and programming*

The data acquisition and analysis system used includes a 486–33 MHz microcomputer with 20 megabytes of random access memory (RAM). The computer interface with the transducers was by a AT-MIO-16F-5 multifunction interface board. It contains a 12-bit analogue to digital converter (ADC) which can sample up to 16 separate single-ended (SE) analogue inputs or eight channels of differential input (DI) at 200 kilo-samples per second.

*Visual Basic 3.0* Windows-based programming software was used to interface the data acquisition board to the microcomputer. Visual Basic communicates with the selected data acquisition board through the use of NI-DAQ Windows. NI-DAQ Windows is a *Windows 3.1* Dynamic Link Library (DLL) that includes functions for controlling the data

**Dynamic Replacement**

Filename	Baseline Stress	Corrected Max Stress	Residual Static Stress	
d:\wb\data\DR.prn	<input type="text"/>	<input type="text"/>	<input type="text"/>	Acceleration
32000 Data points	<input type="text"/>	<input type="text"/>	<input type="text"/>	Laser Switch #1
8 Number of Channels	<input type="text"/>	<input type="text"/>	<input type="text"/>	Laser Switch #2
Dynamic Compaction to be monitored? Yes = 1, No = 2	<input type="text"/>	<input type="text"/>	<input type="text"/>	Laser Switch #3
Residual Pore Pressure and Stress to be monitored? Yes = 1, No = 2	<input type="text"/>	<input type="text"/>	<input type="text"/>	Baseline Pore Pressure
Total Residual monitoring time (hours)	<input type="text"/>	<input type="text"/>	<input type="text"/>	Corrected Max Pore Pressure
Print time interval to file (seconds) (Screen will update residual pressures)	<input type="text"/>	<input type="text"/>	<input type="text"/>	Residual Static Pore Pressure
	<input type="text"/>	<input type="text"/>	<input type="text"/>	Pore #1
	<input type="text"/>	<input type="text"/>	<input type="text"/>	Pore #2
	<input type="text"/>	<input type="text"/>	<input type="text"/>	Pore #3
	<input type="text"/>	<input type="text"/>	<input type="text"/>	Pore #4

START STOP

Acceleration (g's)

0 Time, sec 1

Fig. 4. Dynamic replacement data acquisition screen.

acquisition board for the AT microcomputer. Through the use of this DLL, executable programs were developed using *Visual Basic* for the field DR tests performed.

A data-management system for organic soil (DMSOS) was developed to enable the acquisition, management and analysis of organic soil data as well as the presentation of results to be conducted effectively through a common interface. It is through this interface that data acquisition is initiated. The interface was also written in Visual Basic and incorporates data management through interaction with ACCESS, a relational data base (RDB), and analysis and presentation through Excel, a programmable spreadsheet. Details of the DMSOS structure and its operation are found in Stinnette (1996). Figure 4 shows the data-acquisition-user interface. It is on this screen that the user provides pertinent test information such as an output filename and sets the test options desired for the specific test.

All test results obtained at the study site, by manual observation or by manipulating the stored digital data file, are stored in the ACCESS database where they can be easily retrieved, analysed and graphically presented through the combined interactive use of Visual Basic programming and Excel macro programming.

The computer containing the outlined data acquisition and monitoring system was operated from a truck on the site. All of the instruments were battery operated. The computer was powered by a gas generator and was also equipped with a back-up battery power supply.



Fig. 5. Weight positioned between poles with mounted laser photocells.

#### *Instrumentation of pilot study location*

*Drop hammer velocity determination.* To determine the velocity of the drop hammer at impact, three laser diode photoelectric cells were used, mounted along two vertical poles at predetermined heights. This configuration is shown in Fig. 5. The drop weight obstructs the photocell beams at these predetermined heights and since the photocell beams are located at a known distance apart and the time interval between the breaks are recorded by the data-acquisition system, the instant velocity,  $V$ , can be determined.

The efficiency factor,  $\eta$ , for the crane can be defined as the ratio of the present kinetic energy to the original potential energy as follows:

$$\eta = \frac{E_k}{E_p} = \frac{V^2}{2gh} \quad (1)$$

where  $\eta$  = efficiency factor,  $E_k$  = kinetic energy at impact,  $E_p$  = potential energy at start,  $g$  = acceleration due to gravity ( $\text{m s}^{-2}$ ),  $h$  = drop height (m), and  $V$  = velocity at impact ( $\text{m s}^{-1}$ ).

Then  $\eta$  can be computed from Equation 1, knowing  $V$ . The average efficiency factor for the crane was determined to be 81%. The reduction of efficiency may be attributed to cable drag, drum resistance and sheave resistance. However, the above value agrees with reported values of 80–90% for that of typical production cranes (McMullin, 1994).

Impact velocity was also determined by video-recording the impact. Standard video cameras capture frames at the rate of 30 per second. Once the video footage was taken, the measured velocity can be ascertained by determining the number of video frames required to capture the complete impact process. Then, with the drop height ( $h$ ) known, and letting each frame represent 1/30th of a second, the velocity,  $V$ , can be calculated as:

$$V = \frac{2h}{t} \quad (2)$$

where  $h$  = drop height (m) and  $t$  = drop time interval (s). The efficiency (Equation 1) was determined to be 83% by this method. This is in strong agreement with the value previously determined through the use of the laser diode photoelectric cells.

*Acceleration determination.* The 3.64 tonne drop weight had a piezoelectric accelerometer attached to its top. The transducer was connected by wire to the data-acquisition system described previously. When the first photoelectric cell beam sensed the falling drop weight, the data-acquisition system was initiated. Measurements were recorded during the impact for 1 s and were then stored in the computer. During testing, the acceleration *versus* time graph was automatically plotted on the screen (Fig. 4). The values of acceleration, velocity and displacement *versus* time were calculated and plotted using an Excel spreadsheet. Figure 6 shows those graphs for a typical high-energy impact (12.1 m drop height).

As seen in Fig. 6, there are irregularities in the deceleration record. These irregularities have been previously reported during dynamic compaction and most probably reflect the reverberation of seismic waves bouncing through the drop weight (Mayne and Jones, 1983). This phenomenon was probably amplified due to the fact that the drop weight was composed of 25 separate plates which, although welded along the edges, had their own degrees of freedom.

*Shear-resistance by cone penetration tests (CPTs).* The FDOT provided use of their cone truck for the cone resistance comparisons for the pilot study location. CPT's were taken to a maximum depth of 7.6 m, initially and after each impact for the pilot study location. The first profile, CPT-0, represents the initial conditions at the pilot study location. Values for CPT-1 to CPT-5 were obtained after a total of five low-energy blows, and for CPT-6 to CPT-20 after 15 high-energy ones. For ease of comparison, Fig. 7 shows the resulting plots

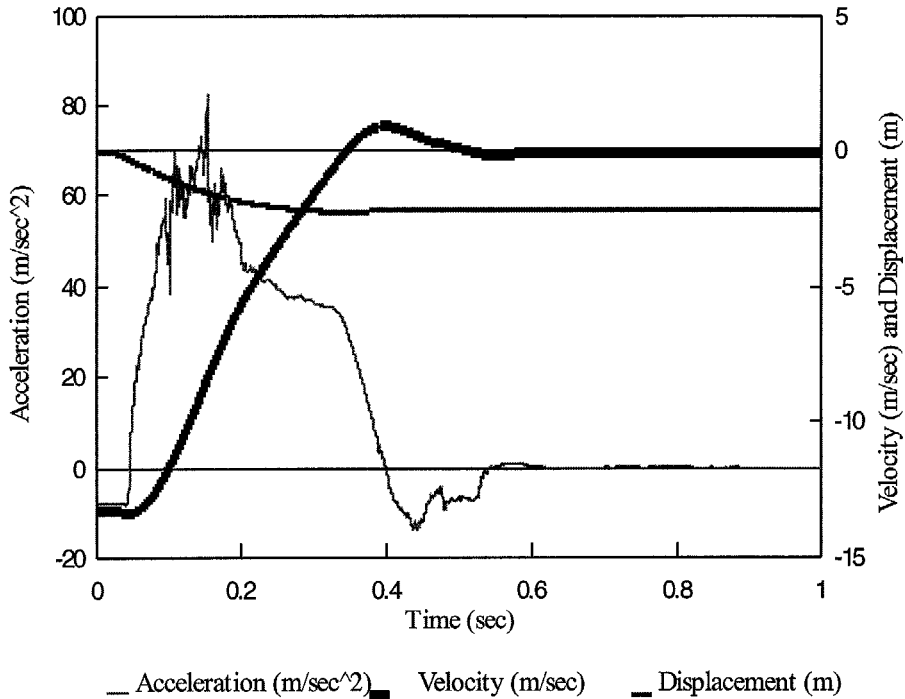


Fig. 6. Acceleration, velocity and displacement graphs for a typical high-energy impact (12.1 m drop height).

when CPT-0 to CPT-20 are plotted on a single graph. Only the first 3.0 m of the cone profiles are shown in the graph so as to emphasize the position of the organic layer. The top horizontal line on the graph represents the measured crater depth before each CPT. The second and third horizontal lines delineate the limits of the organic layer. As can be seen in Fig. 7, the organic layer was initially 1.7 m deep, but by the 20th blow it had diminished to 0.12 m deep. This is attributable to (1) the vertical compression of the organic layer, and (2) the lateral expulsion and compression of organic material into the area surrounding the impact zone. Lateral compression of the organic layer can be more clearly observed by means of the inclinometer data taken at the test site.

*Inclinometer/settlement monitoring systems.* Four inclinometer casings, I/S-1, I-4, I/S-2, and I-4 were installed at radial centreline distances of 1.22 m, 1.83 m, 2.44 m and 3.66 m, respectively, from the pilot study location (1,3). Figure 8 shows the position of each of these systems around the pilot study location. Each of these casings were installed to a depth of 9.14 m. Two of these systems, I/S-1 and I/S-2, were also instrumented with magnetic settlement monitoring systems.

The inclinometers were read initially and after each of the 20 impacts. Figure 9 shows the final inclinometer results for each of the four inclinometers. Figure 9 demonstrates the amount of lateral ground compression and hence the extent of overall improvement as a result of the 20 applied impacts. Inclinometer I-1, located at a distance of twice the hammer base (*b*) from the centreline of the pilot study location, is seen to have deflected

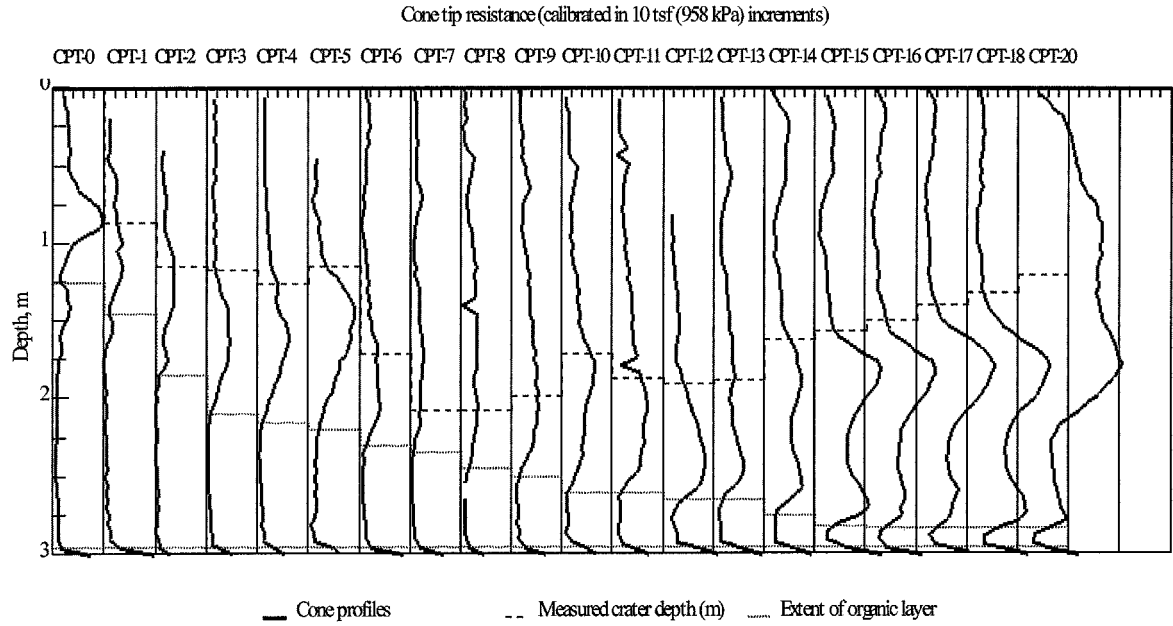


Fig. 7. All cone penetration tests taken at pilot study location (1,3) (initially and after each blow).



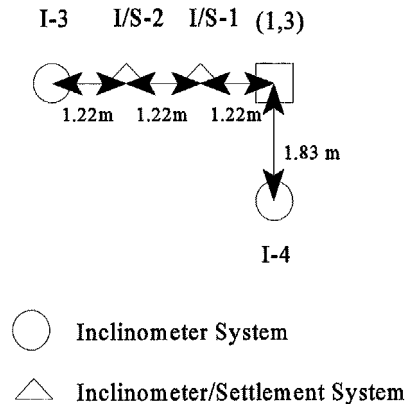


Fig. 8. Plan view of positions of instrumentation systems around the pilot study location.

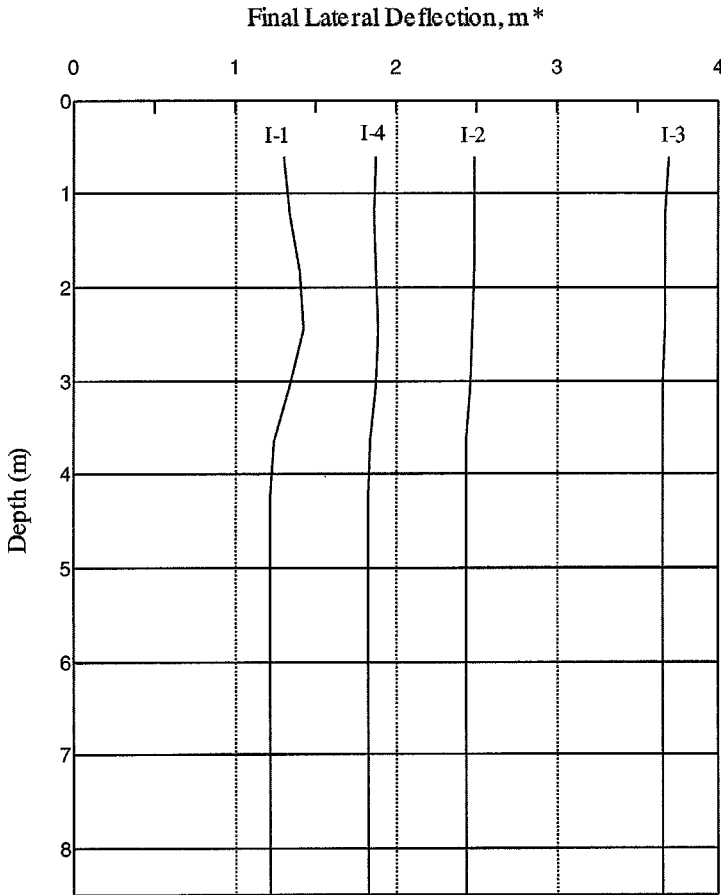
0.20 m. Hence, the test pattern spacing criterion of four times the hammer base (or 2.44 m) was selected to allow for the development of an interference zone of laterally compressed organic soil of approximately 0.4 m at the midpoints between successive print positions. This magnitude of an interference zone will ensure substantial treatment of the intermediate ground as well.

### Analysis of pilot study results

As mentioned in the preceding text, a spacing of  $4 \times b$  or 2.44 m was selected. It was also determined that an initial low-energy pass was required to avoid excessive penetrations and alleviate the development of suction forces, which could make the drop weight potentially unrecoverable. However, a more in-depth analysis and comparison of the pilot study results led to the decision to use a minimum of 10 high-energy impacts. The primary quality-control criterion used to evaluate the improvement of the organic soil layer was the computation of the dynamic stiffness of the soil based on the dynamic settlement modulus (DSM). Concurrent inspection of the change in measured crater depth per blow also provides insight as to when the desired level of improvement has been reached. These criteria were independently verified by examining the gradual compression of the organic soil layer as indicated by the CPT profiles. The method of analysis used for determining the DSM and a comparison of the various test results obtained for the pilot study location follows.

#### *Dynamic settlement modulus (DSM) approach*

As described in the subsection 'Acceleration determination', by employing data acquisition techniques and the DMSOS, magnitudes of velocity and displacement can be calculated from the digitally stored acceleration impact record. This procedure is processed by the EXCEL spreadsheet as follows. First, the acceleration record is integrated once with respect to time to obtain the impact velocity record,  $V$ , as



\* Distance measured from centerline of test location #1,3.

Fig. 9. Final lateral deflections at depth measured with inclinometers at 1.22 m, 1.83 m, 2.44 m, and 3.66 m from the pilot study location.

$$V = \int_0^t a \, dt + \sqrt{\eta} V_{th} \quad (3)$$

where  $a$  = acceleration,  $V_{th}$  = theoretical velocity at moment of impact ( $t = 0$ ) and  $\eta$  = system efficiency (Equation 1).

The impact velocity record is then integrated to obtain the displacement record. The record of impact stress,  $\sigma$ , is then calculated from the acceleration record,  $a$ , as

$$\sigma = \frac{ma}{A} \quad (4)$$

where  $m$  = mass of the drop weight, and  $A$  = base area of the drop weight.

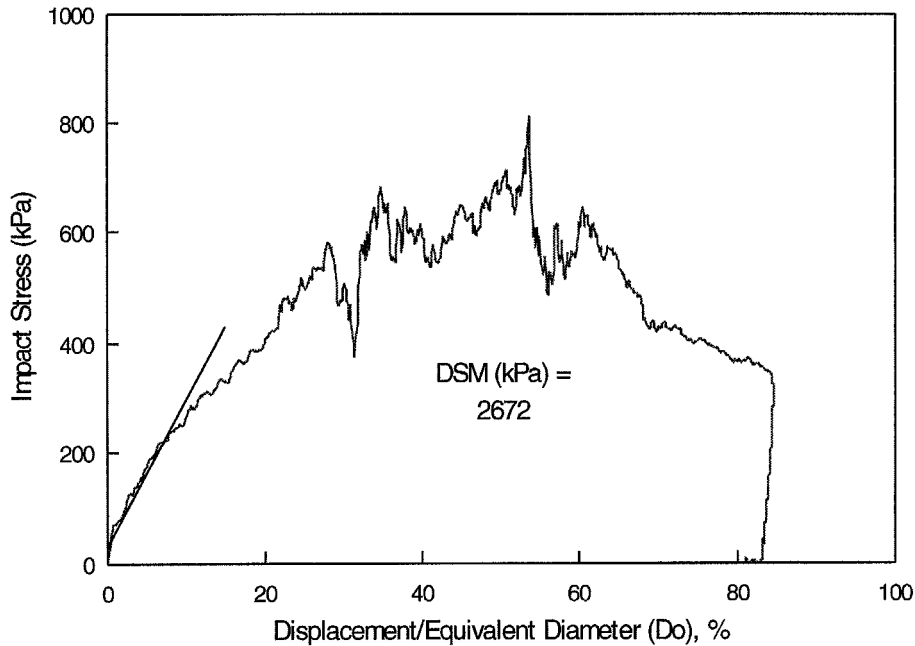


Fig. 10. Impact stress *versus* relative displacement.

The ratio of the instant displacement to the drop weight's equivalent diameter,  $D_o$ , (relative displacement) was then plotted against impact stress,  $\sigma$ . The dynamic settlement modulus, DSM, is defined as the slope of the tangent of the loading portion of the impact-stress–relative-displacement curve and is given by

$$DSM = \frac{\Delta\sigma}{\Delta\left(\frac{d}{D_o}\right)} \quad (5)$$

Figure 10 shows the resulting impact stress versus relative displacement plot and the value of the DSM for a typical high energy impact.

Poran *et al.* (1992a) outlined the use of this technique for the quality control of dynamic compaction on dry sand, and report that the DSM values obtained from experimental tests conducted in the laboratory have shown good correlation to soil densities and that the relative change in DSM values was found to be proportional to the rate of densification (density increase as a function of number of drops).

The values of the DSM versus blow number are plotted for the pilot study location in Fig. 11. As can be seen from the Figure, the DR was more effective in the first 15 drops, while after that there is a small relative increase in the DSM, corresponding to little additional improvement. The same trend was seen by Poran *et al.* (1992a).

In order to correlate the DSM results to the improvement of the organic layer, the organic layer thickness obtained from the CPT profiles and measured crater depth were plotted against the blow number (Fig. 12). It can be seen that the thickness of the organic layer, initially 1.70 m, is reduced to only 12 cm after 15 blows. No additional compression

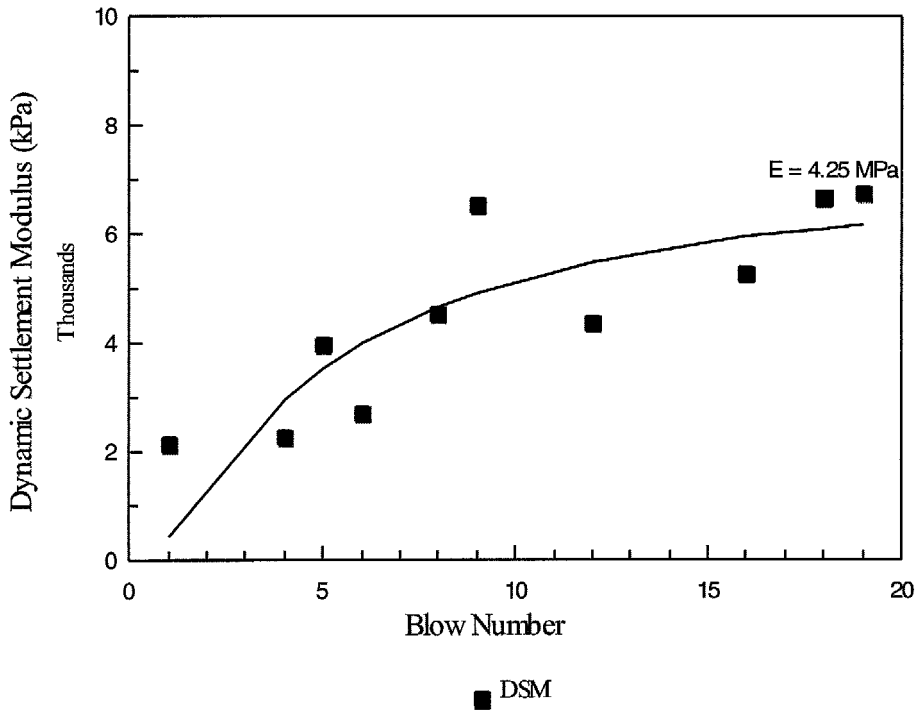


Fig. 11. DSM *versus* blow number for the pilot study location.

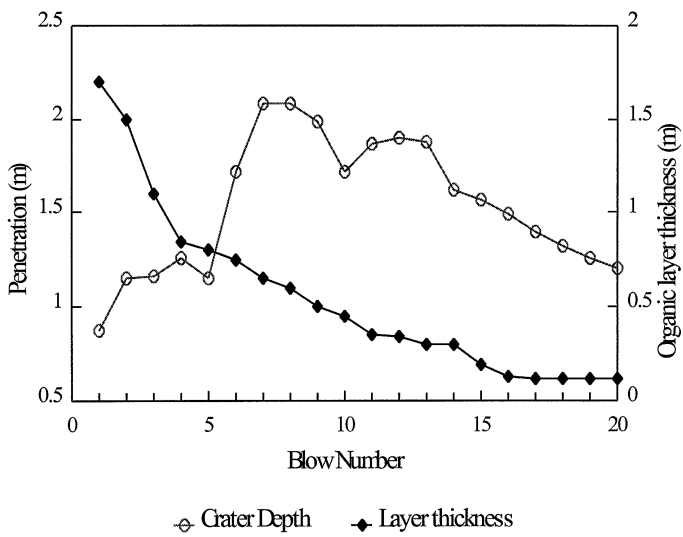


Fig. 12. Measured crater depth and depth of organic layer *versus* blow number.

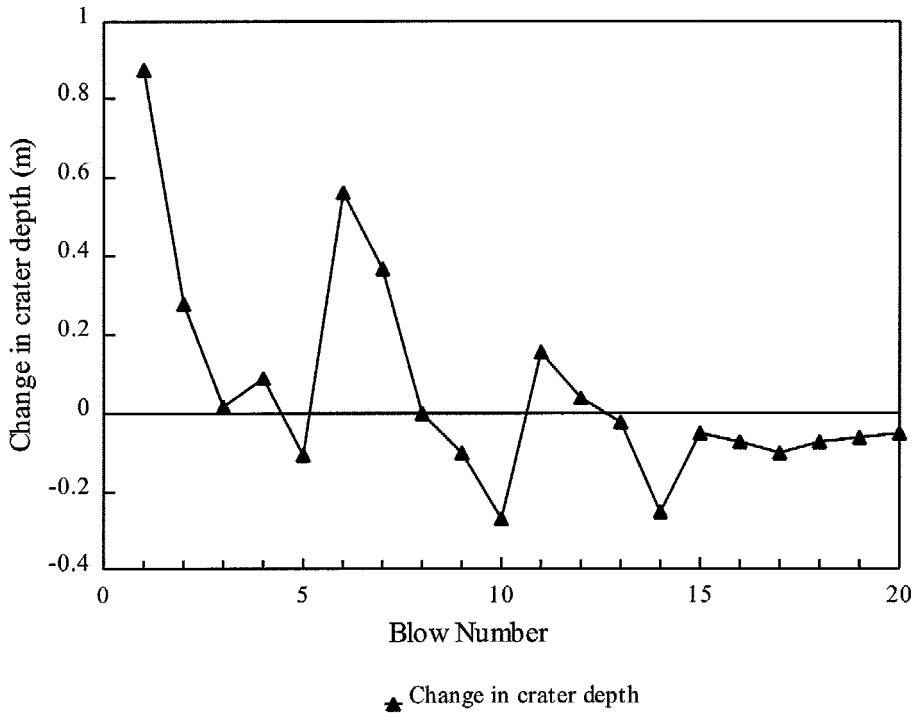


Fig. 13. Change in crater depth *versus* blow number for the pilot study location.

of the organic layer is seen to occur as a result of the last five blows. This observation is in agreement with the improvement shown by the DSM approach where there is very little improvement after the 15th blow (Fig. 11).

The measured crater depth is seen to increase initially during both the low-energy impacts (blows 1–5) and the high-energy ones (blows 6–20). However, after reaching a peak value, the crater depth decreases with each additional blow. This behaviour corresponds to a gain in the density of the sand column and is shown by the soil resistance to penetration (Fig. 12). In order to observe this trend more clearly, a plot of the change in crater depth per blow is shown in Fig. 13. The soil density is seen to increase as the change in crater depth approaches an asymptotic value near zero around the 15th blow. This trend is also in agreement with the DSM results.

Hence, by comparing Figs 11, 12 and 13 it can be seen that the DSM in fact provides an alternative parameter for DR quality control. Another advantage of using the DSM approach is that DSM can be used to monitor the improvement of soil properties by means of available correlations.

#### *Correlation of DSM to elastic modulus*

Poran *et al.* (1992a) report correlations of DSM to elastic properties. The dynamic stiffness of the soil at impact,  $K'$  (in  $\text{kN m}^{-1}$ ) may be related to the DSM as

$$K' = \frac{\pi(D_o)}{4} \text{ DSM} \quad (6)$$

Then, by examining the stiffness of a circularly loaded area with diameter  $D_o$  on an elastic half space,  $K'$ , was expressed by Gazetas (1991) as

$$K' = \frac{1.135E D_o}{(1 - \nu^2)} k(\omega) \quad (7)$$

where  $K'$  = dynamic system stiffness ( $\text{kN m}^{-1}$ ),  $K(\omega)$  = dynamic stiffness coefficient,  $\nu$  = Poisson's ratio,  $E$  = elastic modulus ( $\text{kN m}^{-2}$ ), and  $D_o$  = equivalent diameter of the loaded area (m).

The dynamic system stiffness,  $K'$ , computed from experimental data in Equation 6 should be the same as that in Equation 7. By equating Equation 6 to Equation 7,  $E$  may be expressed in terms of the DSM and  $k(\omega)$  as

$$E = 0.692 (1 - \nu^2) k(\omega) \text{ DSM} \quad (8)$$

Poran *et al.* (1992a) report that, based on the frequency content of the dynamic pulses found in the laboratory, a  $k(\omega)$  value of approximately 1.0 may be assumed for loose and medium-dense sandy soils with  $\nu < 0.4$ . Poran *et al.* (1992a) conclude that the dynamic stiffness coefficient,  $k(\omega)$ , is practically equal to the static value.

If a Poisson's ratio of 0.25 is assumed for the fill material used to build the sand columns in the current test, and a value of 1 is assumed for  $k(\omega)$ , then the final asymptotic value of  $E$  for the last impact was calculated to be 4.25 MPa (Fig. 11) – a low value that can be attributed to the loosened soil state after the high-energy blows. However, after the high-energy pass was completed, four additional low-energy blows (two 3.048 m drops and two 1.524 m drops) were applied to densify this loosened top stratum of soil. Although acceleration data was not taken for these four blows, plate load tests conducted afterwards indicate a secant subgrade modulus,  $k_s$ , for the pilot study location of  $12\,818 \text{ kN m}^{-3}$ . The elastic modulus,  $E$ , may be estimated from a plate load test by

$$E = k_s B (1 - \nu^2) \quad (9)$$

where  $k_s$  = subgrade modulus ( $\text{kN m}^{-3}$ ), and  $B$  = footing width (equivalent plate width, 0.675 m).

Knowing the subgrade modulus and assuming the same Poisson's ratio of 0.25 for the fill material, the elastic modulus is calculated to be 8 MPa. On the other hand, the DSM correlation predicts the elastic modulus to be approximately 4 MPa prior to the upper layer being densified by the additional low-energy drops. This discrepancy may also arise from the fact that the DSM reflects the properties of a larger volume of material than that of the plate load test.

Based on the results obtained by the DMSOS, a decision was made to apply a minimum of five low-energy blows and 10 high-energy blows to each of the remaining 18 print positions in the study pattern. Thus, the DMSOS was effectively utilized in the field implementation of dynamic replacement.

### Energy considerations

It was determined by means of the DSM approach, and verified by CPTs, that the sand columns were sufficiently developed in the organic layer after five low-energy drops ( $h = 6.1$  m) and 10 high-energy drops ( $h = 12.2$  m). However, this same level of improvement could have been obtained by using a different combination of low and high energy, including the use of a different drop weight – provided that the drop weight satisfies the slenderness ratio (height/diameter) of approximately 1.83:1.

The different combinations of applied energy needed to achieve the desired level of improvement can be addressed by the following analysis. The cumulative specific energy ( $WH/Ad_c$ ) versus  $d_c/D_o$  for the pilot study are plotted in Fig. 14, where  $A$  is the contact area of the drop weight,  $W$  is its weight and  $d_c$  is the sand-column depth in the organic soil stratum determined from the CPTs. It is noted that a unique linear relationship is obtained in Fig. 14. Linear regression of the above data yields the best fit line of:

$$\sum_1^n \frac{WH}{Ad_c} = 4423.18 \frac{d_c}{D_o} \quad r^2 = 0.94 \quad (10)$$

It should be noted that Equation 10 depends on soil properties and is therefore site specific.

Hence, Equation 10 can conveniently be used to select the energy requirements for forming a sand column by DR at this site. The following example will illustrate the application of this concept. First, determine the required cumulative specific energy to build a sand column through the 1.7 m organic layer using the previous drop weight. In this case  $d_c = 1.7$  m and  $D_o = 0.6879$  m, so  $d_c/D_o = 2.47$ . Then, from Fig. 14 (or Equation 10), the required cumulative specific energy is determined to be  $10\,932$  kN-m m<sup>-3</sup>. The

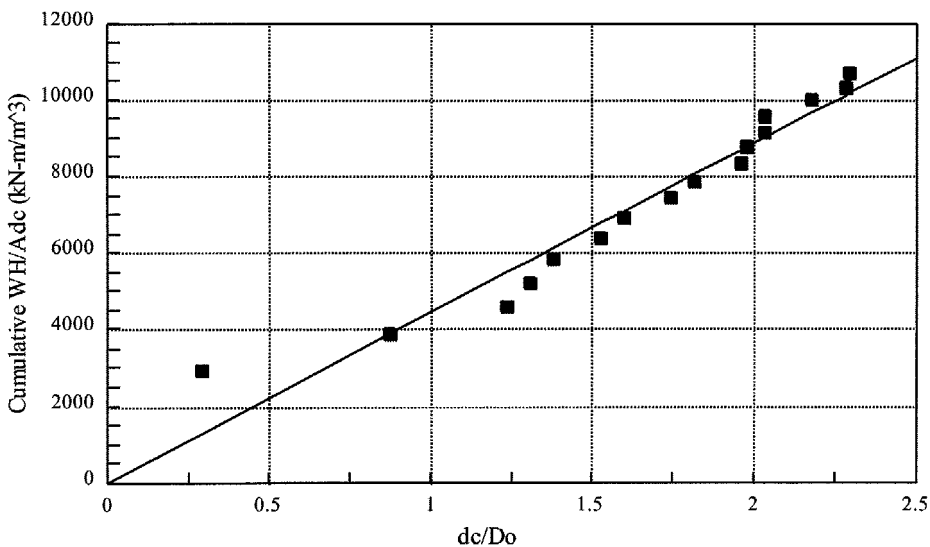


Fig. 14. Cumulative specific energy per blow versus normalized strain.



unit energy,  $\Sigma WH/A$ , independent of  $d_c$ , is then computed to be 18 583.71 kN m<sup>-1</sup>. Since it is desired to use a low initial energy to alleviate excessive penetration problems at the beginning, the following initial low-energy pass is assumed; No. of blows ( $n$ ) = 5,  $h = 4.57$  m,  $W = 35.59$  kN,  $A = 0.3716$  m<sup>2</sup>,  $D_o = 0.6879$  m. Then, solving for  $d_c$  in Equation 10 yields  $d_c = 0.58$  m. Therefore, the portion of total unit energy exhausted for these five low-energy blows is

$$\frac{nWh}{A} = 2188.46 \text{ kN m}^{-1} \quad (11)$$

The required cumulative unit energy for the high-energy drops is then determined as the difference between the total cumulative required unit energy and the total unit energy for the low-energy blows as 16 395.25 kN m<sup>-1</sup>.

Selecting a high-energy drop height,  $h$ , of 9.144 m, the unit energy per blow is:

$$\frac{Wh}{A} = 875.75 \text{ kN m}^{-1} \quad (12)$$

Hence, the number of high-energy blows required will be approximately 19.

It is seen how different combinations of low and high drop energies may be selected to achieve a given column depth by using this approach. Thus, this approach will be useful when multiple cranes or drop weights are in use at a single site or if a relatively low 'high' energy level is desirable due to the proximity of adjacent structures. Moreover, the approach would be invaluable if a variation in depth of the organic layer is noted on different boring logs at the same site. Then by simply adjusting  $d_c$  in the preceding analysis to reflect the height of the organic layer at a specific location, one can select a combination of appropriate energy levels for that location.

Poran *et al.* (1992b) outlined a similar rational design method for dynamic compaction (DC) of dry sand based on correlations between the normalized impact energy and the resulting densification measured in terms of normalized volumetric strain.

## Discussion

The goal of this research was to achieve a desired degree of improvement in an organic soil stratum by introducing sand columns. The study site consisted of 19 drop locations, one of which was fully instrumented. The optimum print spacing, drop height and the number of blows required to yield the desired level of improvement was determined based on the test results of this location. The DSM method stands out among the several criteria used to identify the level of improvement. These results were then used as a guide for treating the remaining locations, as a similar soil profile was seen to exist at the entire study site. However, in larger projects, the ground profile may vary significantly, in which case representative boring logs for the site to be modified should be obtained at many locations. Thus, potential pilot-study locations can then readily be identified from the soil profiles. Depending on the necessity, acceleration data may be obtained for some or all of the drop locations. However, if only a few of the drop locations are instrumented, then the trend in the change in crater depth can be used as an indicator of densification at the non-instrumented drop locations.

Field implementation of the computerized data-acquisition system proved to be very reliable in general. However, in several instances, the acceleration record registered by the data acquisition system was unusable. This can be attributed to the delayed actuation of data acquisition due to the late response of the laser diode photoelectric cells. This problem can be easily overcome by using an additional laser diode photoelectric cell as a backup, to initiate data acquisition.

The cost of setting up such a system which includes the computer, associated software, data acquisition board, and instruments (accelerometer and laser diode photocells) is in the range of US\$8000, which makes it cost-effective.

## Conclusion

A quality-control system has been developed for evaluation of dynamic replacement (DR) of organic soils. It is incorporated in an existing database management system for organic soils (DMSOS) that stores and retrieves all acquired test data from both field and laboratory tests. The system also facilitates analysis and graphical presentation of the test results. These include the plots of acceleration, velocity and displacement of the drop weight for each impact. The dynamic settlement modulus (DSM) parameter was computed and plotted for each impact. From this plot, the optimum energy level can be obtained when the change in the DSM per blow becomes relatively insignificant. Once the final DSM value is available, the elastic modulus,  $E$ , may also be computed to identify the level of improvement achieved. Furthermore, the plot of the change in crater depth *versus* blow number provides yet another way of observing maximum improvement. Post-DR ground testing using CPTs and plate load tests further verified the DSM prediction of the level of improvement achieved. Based on the findings of this field study, it appears feasible to use the DSM-based quality-control system to evaluate the degree of improvement and select the optimum DR technical criteria such as the number of blows and drop print spacing.

## Acknowledgements

We thank Mr Brian Jory and Ms Terry Puckett of the Florida Department of Transportation for their support during the study. The FDOT grant funding this research under contract No. 99700-7572-119 is gratefully acknowledged.

## References

- Gazetas, G. (1991) Foundation vibrations, in *Foundation Engineering Handbook*, Fang, H.Y. (ed.) Van Nostrand Reinhold, pp. 571-5.
- Lo, H.W., Ooi, P.L. and Lee, S.L. (1990) Dynamic replacement and mixing of organic soils with sand charges, *ASCE Journal of Geotechnical Engineering*, **116**, 1463-82.
- Lukas, R.G. (1992) Dynamic compaction engineering considerations, in *Grouting, Soil Improvement and Geosynthetics*, Geotechnical Special Publication No. 30, ASCE, New York, pp. 940-53.
- Mayne, P.W. and Jones, J.S. (1983) Impact stresses during dynamic compaction, *ASCE Journal of Geotechnical Engineering*, **109**, 1342-6.
- McMullin, S.R. (1994) Evaluation of dynamic compaction of low level waste burial trenches containing B-25 boxes, in *In-Situ Deep Soil Improvement*, Geotechnical Special Publication No. 45, ASCE, New York, pp. 44-54.

- Mullins, A.G., Gunaratne, M., Stinnette, P. and Thilakasiri, S. (1996) Prediction of crater depth from dynamic compaction using CPT, submitted to *ASCE Journal of Geotechnical Engineering*.
- Poran, C.J., Heh, K.S. and Rodriguez, J.A. (1992a) A new technique for quality control of dynamic compaction, in *Grouting, Soil Improvement and Geosynthetics*, Geotechnical Special Publication No. 30, ASCE, New York, pp. 915–26.
- Poran, C.J., Heh, K.S. and Rodriguez, F.A. (1992b) Impact behavior of Sand, *Soils and Foundations*, **32** (4), 81–92.
- Ramaswamy, S.D., Aziz, M.A., Subrahmanyam, R.V., Khader, M.H. and Lee, S.L. (1979) Treatment of peaty clay by high energy impact, *ASCE Journal of the Geotechnical Engineering Division*, **105** (No. GT8), 957–67.
- Stinnette, P. (1996) Geotechnical Data Management and Analysis System for Organic Soil, PhD Thesis, University of South Florida.
- Thomas, F.H. (1965) Subsidence of peat and muck soils in Florida and other parts of the United States – A review, *Proc. of the Soil and Crop Society*, **25**, 153–160.

# INVESTIGATION OF IMPACT STRESSES INDUCED IN LABORATORY DYNAMIC COMPACTION OF SOFT SOILS

H. S. THILAKASIRI, M. GUNARATNE, G. MULLINS, P. STINNETTE AND B. JORY<sup>†</sup>

*Department of Civil and Environmental Engineering, University of South Florida, Tampa, FL 33647, U.S.A.*

## SUMMARY

The majority of currently available analytical tools to predict ground stresses due to impact are based on linear spring-dashpot dynamic models. Although these simple models adequately represent stiff ground possessing linear visco-elastic behaviour, they suffer from two striking limitations when applied to relatively softer ground; (1) the inability to account for the permanent deformation resulting from impact, (2) failure to incorporate stiffness changes of softer soil within the impact duration. In this paper, the authors present an improved analytical approach formulated on the basis of a series of laboratory impact tests, to address the shortcomings of the current dynamic models in relation to soft soils. In this procedure, the impact zone is modelled as three distinct zones; (1) a zone beneath the falling weight undergoing non-linear axial deformation while being in vertical motion, (2) an inner zone immediately surrounding zone 1 with non-linear shear deformation, and (3) an outer zone undergoing a relatively lower degree of (linear) shear deformation. The soil constitutive parameters pertinent to the model are obtained from a modified dynamic compression test that simulates the impact conditions. It is shown that analytical predictions of the impact stress history and penetration are in agreement with test results. The findings are useful in the exploration of dynamic compaction techniques that will be effective in soft soil improvement.

KEY WORDS: dynamic; compaction; soil; damping; non-linear stressing

## 1. INTRODUCTION

A number of analytical models have been proposed by several researchers<sup>1-4</sup> in recent years to estimate surface stresses during dynamic compaction. In these models, it is assumed that the soil behaviour is linear elastic, isotropic and hence can be modelled by a linear spring and a linear dashpot. However, it is a common observation made during dynamic compaction of soft soil that the soil mass close to the surface is subjected to a very high strain level resulting in permanent deformation. Obviously a model that employs a linear spring and a linear dashpot is unable to simulate these observations because non-linearity is clearly exhibited by soils at high strain levels. Apart from the above-mentioned simplified models, Chow *et al.*<sup>3</sup> proposed a different analytical approach where the one-dimensional wave equation model for pile-driving analysis is modified by replacing the pile with a soil column extending to at least the anticipated depth of improvement. In this method, the soil surrounding the soil column is represented by linear elastic springs and linear dashpots. Furthermore, they adopted an implicit finite element method to solve the equation of motion of the soil column.

<sup>†</sup>Present address: Florida Department of transportation, Bartow, FL, U.S.A.

An improved analytical model is proposed in this paper to estimate the surface stress and the surface deformation, accounting for non-linearity of soil immediately below the drop hammer as well as that of the immediate neighbourhood of the hammer. In this procedure, equations of motion are separately written for three zones distinguished by their mode and degree of deformation while satisfying compatibility. A numerical procedure is adopted to solve these equations of motion because of complexity arising from the constitutive model that accounts for non-linearity. The solution procedure uses an explicit direct time integration together with lumped mass formulation for computational efficiency. Finally, analytical predictions of the impact surface stress history and penetration are compared with laboratory measurements.

## 2. EXPERIMENTAL OBSERVATIONS

Figure 1 shows a typical plot of the impact surface stress history recorded during the authors' experiments on a wet organic soil by employing a falling hammer instrumented with sensitive pressure transducers. The sensitivity of the data acquisition system is discussed in the ensuing Section 4 on the experimental set-up. The stress-time plot such as that shown in Figure 1 obtained from a series of tests consistently demonstrate the existence of two distinct regions:

- (1) An immediate peak followed by rapidly diminishing stress. This phase of the stress history usually lasts only an extremely small time (1–2 ms) thus possibly eluding detection without a sensitive data acquisition system. This could be one reason why such an instantaneous peak has not been documented in previous experimental studies.
- (2) A subsequent oscillatory stress pattern. This phase of the stress pulse on the other hand has been the subject of most previous experimental and analytical investigations.

## 3. MATHEMATICAL IDEALIZATION

From the perspective of deformation, the soil mass in the impact vicinity can be considered as being comprised of three distinct zones (Figure 2):

- Zone 1: soil under the falling hammer in the zone of influence undergoing significant vertical deformation that permits it to be considered as a moving or participating soil mass,  
 Zone 2: soil in the immediate neighbourhood undergoing excessive shear deformations that can only be characterized by non-linear models,

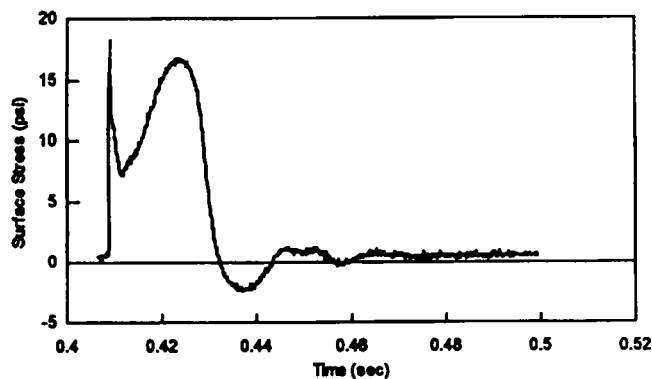


Figure 1. Typical experimental impact stress history

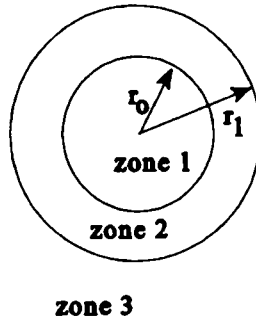


Figure 2. Plan view of the impact vicinity

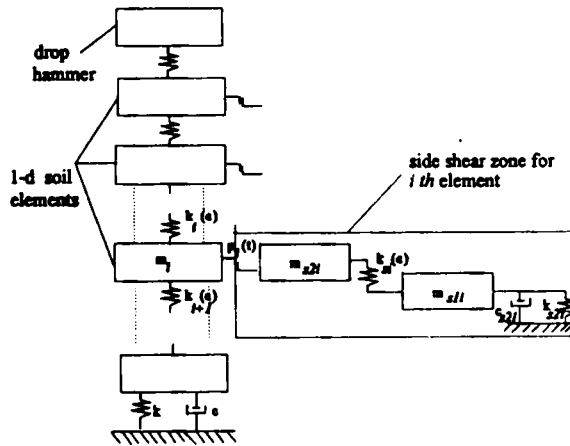


Figure 3. Dynamic model (shear zone is shown only for the *i*th element)

Zone 3: soil in the outer region undergoing limited shear deformations within linear elastic limits.

The authors' analytical formulation discussed here is founded on consideration of the mechanics of these three zones. The analytical formulation is kept simple by replacing the soil in the above zones with equivalent lumped masses. Researchers have observed that the depth of the zone of influence ( $z$ ) during dynamic compaction varies in the range of  $\sqrt{(W_1 h)} \geq z \geq 1/2 \sqrt{W_1 h}$ ,<sup>6,7</sup> where  $W_1$  and  $h$  are drop weight in tonnes and drop height in meters, respectively. Hence, in their formulations the authors suggest that the vertical depth ( $z$ ) of the above non-linear zones should at least extend to a depth of  $\sqrt{(W_1 h)}$ . In the mathematical discretization, zones 1 and 2 up to the depth of influence are divided into elements of equal thickness as shown in Figure 3. Since the vertical strain within each element is assumed to be uniform, their thickness should be decided by a sensitivity analysis.

Since the strains in zone 1 are large, it is logical to expect non-linear behaviour. Thus, the soil elements in that zone are replaced in the current model by moving solid lumped masses ( $m_i$ ) having the same cross-sectional area as that of the drop weight and are connected by non-linear

springs of stiffness  $k_i(\epsilon)$  as shown in Figure 3.  $k_i(\epsilon)$  can be expressed by  $M_i(\epsilon)A/L$  where  $M_i(\epsilon)$ ,  $A$  and  $L$  are the constrained modulus corresponding to the current strain ( $\epsilon$ ) (Section 3.1), cross-sectional area of the element and the current length of the element, respectively. The soil half-space beneath the immediate vicinity of the non-linear soil column is modelled by a linear spring ( $k$ ) and a linear dashpot in parallel having a spring stiffness of  $4G_s r_0/(1 - \nu)$  and a dashpot coefficient of  $3.4G_s r_0^2/(1 - \nu)$  as proposed by Lysmer and Richart<sup>8</sup> in which  $r_0$ ,  $G$  and  $\nu$  are the radius of the soil column, initial shear modulus and the Poisson ratio, respectively. In the case where there is a stiff layer present within the zone of influence, the displacement of the last element is set to zero to account for it. In such a situation, the spring and the dashpot are not required.

On the other hand, the elements in annular zone 2, represented by two masses ( $m_{s,1i}$  and  $m_{s,2i}$ ) of radius ( $r_1$ ) surrounding zone 1 are also subjected to high strain levels. Therefore, its effect on the impact zone must also be modelled by non-linear shear stiffness properties ( $k_{si}$ ). In this regard, the stiffness expression developed by El Naggar and Novak<sup>9</sup> would be appropriate. The expression for  $k_{si}$  is derived in the Appendix. The mass of the  $i$ th element in zone 2 is equally distributed to lumped masses  $m_{s,1i}$  and  $m_{s,2i}$  as shown in Figure 3. The elements in zone 2 interact with the corresponding elements in zone 1 through rigid plastic sliders  $p_i(t)$  as shown in Figure 3.

Outside zone 2, the shear strains are small enough to permit the application of linear elastic constitutive relations. Thus, the shearing resistance of zone 3 is simulated by a linear spring ( $k_{s2i}$ ) and a dashpot ( $c_{s2i}$ ) having a stiffness of  $2.75G_s dz_i$  and a damping constant of  $2\pi r_1 \sqrt{\rho_s G_s dz_i}$ , respectively, as proposed by Novak et al.<sup>10</sup> in which  $G_s$ ,  $\rho_s$  and  $dz_i$  are the initial shear modulus, initial density and vertical thickness of elements in zone 2, respectively. Hence, zone 3 provides shear resistance to the vertical movement of elements in zone 2 through the parallel combination of spring  $k_{s2i}$  and  $c_{s2i}$ .

It is assumed that slipping can occur at the interface between the deforming soil elements in zone 1 and the elements in the surrounding zone 2 when the shear stress in the rigid plastic sliders  $p_i(t)$  exceeds the maximum static resistance which is taken to be  $k_0 \sigma'_v \tan \Phi$ ; where,  $k_0$ ,  $\sigma'_v$  and  $\Phi$  are coefficient of lateral earth pressure at rest, current vertical effective stress and angle of internal friction of the soil, respectively. It is accepted that the coefficient of lateral earth pressure depends on the over consolidation ratio (OCR) of the soil. Hence, in the proposed model  $k_0$  is taken to be equal to  $(1 - \sin \phi) \sqrt{\text{OCR}}$ . Except for fully saturated low permeable soils with multiple impacts, the generation of pore water pressure in zone 1 is comparatively small<sup>6</sup> resulting in increased vertical effective stress in zone 1 during an impact. Therefore, it is important to note here that the maximum shear resistance changes during an impact even for a normally consolidated soil as the effective vertical stress changes with deformation of the soil column.

Finally, Newmark's explicit time step integration is employed to solve the equations of motion of the soil elements. The impacting hammer is disconnected from the numerical solution when the contact stress becomes less than zero.

If the depth of the non-linear zone is insignificant such as in the case of a small amplitude vibration, it is clear that the present model approaches the already accepted visco-elastic models, in which linear spring and a dashpot are in parallel (Figure 3). Further, the thickness of the influence zone can decrease with decrease in the drop weight and the drop height according to the aforementioned effective zone criterion ( $\sqrt{Wh}$ ).

### 3.1. Determination of non-linear stiffness values

Figure 4 shows a typical axial stress–strain curve obtained for loading and unloading during a dynamic impact. The experimental procedure used to obtain Figure 4 is highlighted in Section 4. A unique feature of the stress–strain curve is a distinct yielding stage as shown in Figure 4 after



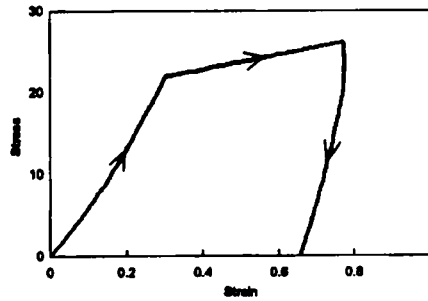


Figure 4. Experimental stress–strain curve

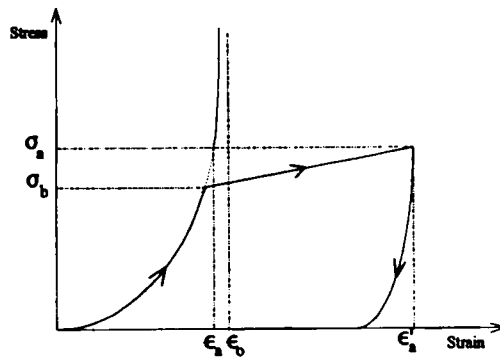


Figure 5. Typical theoretical stress–strain graph with symbols used in mathematical expressions

which a major portion of the axial strain is irrecoverable. This sudden change of the stiffness can be attributed to plastic flow resulting from shear failure. It was found that the pre-bearing capacity region of the curve can be conveniently expressed by the mathematical expression given by Ginsberg<sup>11</sup> for one-dimensional dynamic loading (equations (1) and (2)). Moreover, Ginsberg's<sup>11</sup> expression for the unloading phase correctly represented the unloading curve obtained by the authors as well (equations (5)–(6)). However, it should be noted that the post bearing capacity failure portion of the curve is linear with a small slope instead of being flat, indicating some strain hardening. Hence, based on Figure 4, the axial force in zone 1 can be determined by employing a constitutive relationship similar to that proposed by Ginsburg<sup>11</sup> for non-linear uniaxial dynamic compression. During each time step, the incremental strain in a given element is calculated based on the shortening of the element during the period and the current length of the element. Then, those incremental strains are summed up to estimate the total strain in the element and the corresponding axial stress from Figure 4. While the shape of the stress–strain curve proposed for loading and unloading is shown in Figure 5, the related mathematical relationships modified from the original Ginsburg model to include plastic flow, are expressed below.

For the loading stage

Up to the bearing capacity

$$\sigma = \frac{M_0 \varepsilon \varepsilon_0}{\{\varepsilon_0 - \varepsilon\}} \quad (1)$$

$$M(\varepsilon) = \frac{M_0 \varepsilon_0^2}{\{\varepsilon_0 - \varepsilon\}^2} \quad (2)$$

Beyond the bearing capacity

$$\sigma = k\{\varepsilon - \varepsilon_b\} + \sigma_b \quad (3)$$

$$M(\varepsilon) = k \quad (4)$$

For the unloading state

$$\sigma = M_0 \varepsilon_* \varepsilon_0 / \{\varepsilon_0 - \varepsilon_*\} \quad (5)$$

$$\varepsilon_* = (\varepsilon - (\varepsilon'_a - \varepsilon_a) - \varepsilon_a \eta / 1 - \eta) \quad (6)$$

$$M(\varepsilon) = M_0 \varepsilon_0^2 / \{1 - \eta\} \{\varepsilon_0 - \varepsilon_*\}^2 \quad (7)$$

$$\varepsilon_a = \varepsilon_0 \sigma_a / (\sigma_a + M_0 \varepsilon_0) \quad (8)$$

where

$M_0$  = initial constrained modulus,

$M(\varepsilon)$  = constrained modulus at strain  $\varepsilon$ ,

$\varepsilon_0$  = asymptotic value of strain corresponding to the pre-bearing failure portion,

$\eta$  = a material constant,

$\varepsilon'_a$  = strain at the beginning of the unloading phase,

$\sigma_a$  = stress at the beginning of the unloading phase,

$\sigma_b$  = bearing capacity,

$k$  = modulus after the bearing capacity failure.

As mentioned in the mathematical idealization, the following expression for stiffness developed by E1 Nagggar and Novak<sup>9</sup> assuming a plane strain condition are used for zone 2.

For loading

$$k_{sji} = \frac{2\pi G_s}{\ln \frac{r_1/r_2 - \eta_0}{1 - \eta_0}} \quad (9)$$

For unloading

$$k_{sji} = \frac{2\pi G_s}{\ln(r_1/r_0)} \quad (10)$$

where

$r_1$  = outer radius of the inner zone,

$r_0$  = radius of the soil column,

$G_s$  = initial shear modulus,

$\tau_0$  = shear stress at the axial element and shear element interface,

$\tau_f$  = ultimate shear strength,

$\eta_0 = \tau_0/\tau_f$ .

3.2. Kinematic equations of the system

Using the notation indicated in Figure 6, the following equations of motion can be written for various components of the system:

For the drop hammer

$$w_1 - q_1(t) = \frac{w_1}{g} d_1''(t) \tag{11}$$

For the *i*th axial element (in Figure 6)

$$q_i(t) - q_{i+1}(t) - p_i(t) = m_i d_i''(t) \tag{12}$$

For *i*th shear element (in Figure 6)

$$p_i(t) - q_{si}(t) = m_{s1i} d_{s1i}''(t) \tag{13}$$

$$q_{si}(t) - k_{s2i} d_{s2i}(t) - c_{s2i} d_{s2i}'(t) = m_{s2i} d_{s2i}''(t) \tag{14}$$

where

$$k_{s2i} = 2.75 G_s dz_i, \tag{15}$$

$$c_{s2i} = 2\pi r_1 \sqrt{(\rho_s G_s)} dz_i, \tag{16}$$

$dz_i$  = thickness of the *i*th element in zone 2.

Newmark's explicit time step integration can be used to solve the equations (11)–(14) in combination with equations (17) and (18) as previously mentioned. For an element with a displacement  $d(t)$  at any time  $t$ , Newmark's classical explicit time step integration algorithm (14) involves following recurrence relationships:

$$d_{n+1}(t) = d_n(t - \Delta t) + \Delta t d_n'(t - \Delta t) + \frac{\Delta t^2}{2} d_n''(t - \Delta t) \tag{17}$$

$$d_{n+1}'(t) = d_n'(t - \Delta t) + \Delta t(1 - \beta_1)d_n''(t - \Delta t) + \Delta t\beta_1 d_{n+1}''(t) \tag{18}$$

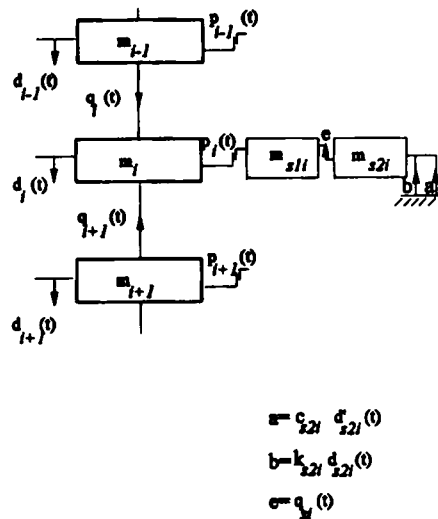


Figure 6. Free body diagrams for the *i*th axial and shear elements

where  $\beta_1$  is Newmark's parameter, the value of which can be chosen for effective implementation of the particular algorithm.

Equation (17) can be used to explicitly obtain the current displacement  $d_{n+1}(t)$  knowing the displacement, velocity and the acceleration of the element during the previous time step, while equation (18) enables one to express the current velocity of the element in terms of the current acceleration.

Thus, when equations (17) and (18) are separately applied to the elements in motion in Figure 3, it will facilitate the solution of equations (11)–(14) by evaluating the current displacement and the acceleration of each element based on the state of motion of the entire system at the preceding time step. Furthermore, at the end of each time step, element thicknesses and soil properties are upgraded according to the current strains, using the non-linear constitutive model described in the previous section. By repeating this procedure for a number of time steps, the numerical solution procedure can be successfully implemented. The explicit direct time integration algorithm is conditionally stable and the stability is governed by the magnitude of the time step size. It is found from the literature that the maximum size of the time step for a stable solution is related to the time required for an elastic wave to propagate across the shortest element of the mesh. In contrast to implicit algorithms, explicit algorithms require a large number of small time steps to avoid the solution of a large matrix equation which is typical of implicit methods at each time step.

#### 4. EXPERIMENTAL SET-UP

The experimental set-up shown in Figure 7 was used to determine the dynamic impact stress due to a drop weight and the related stress–strain behaviour of an organic soil in the laboratory. The organic soil had a water content of 378 per cent, a we density of  $1064 \text{ kg/m}^3$  (66 pcf) and an

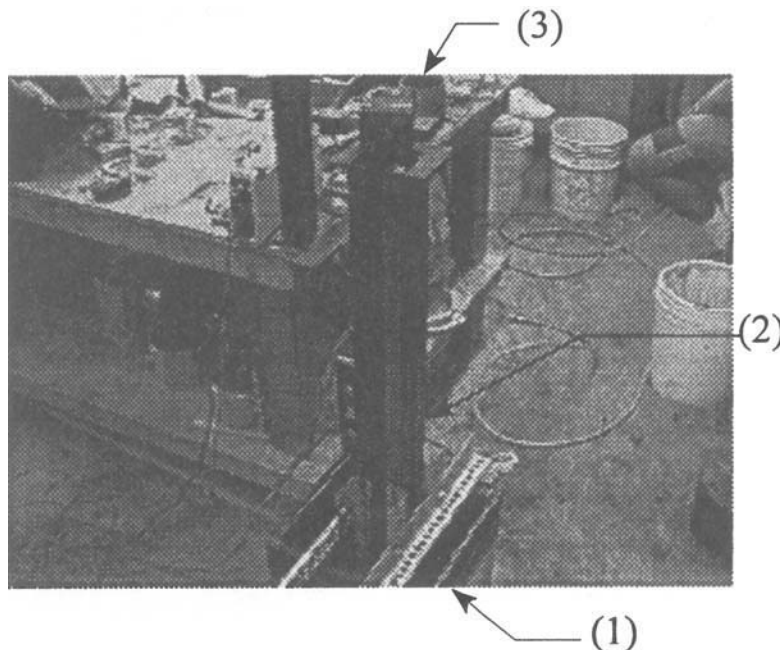


Figure 7. Experimental set-up

organic content of 80 per cent. The soil was compacted in a PVC lined 0.03 m<sup>3</sup> (one cubic foot-1' x 1' x 1') container to a final bed depth of 10.16 cm (4 in) for the test used to get the surface stress history while a reduced depth of 2.6cm (1 in) was used for the test to determine the stress-strain relationship. A 0.923 m (3 ft) tall guide rail system (2) was placed on top of the box. A 2.27 kg (5 lb) steel weight with a 7.62 cm (3 in) square base (3) was held by an electro-magnet at the top of the guide rail. The weight was instrumented with five pressure transducers that were installed in such a manner that they were flush with the surface of the bottom of the weight. An accelerometer was also attached to the top of the weight so that its position was in line with the centre of gravity of the weight. The pressure transducers and the accelerometer were interfaced to a 486-33 MHz microcomputer through the use of a AT-MIO-16F-5 interface board.

Programs are written in Visual Basic to facilitate multiple channel data acquisition. A remote relay was used to simultaneously release the weight from the electro-magnet and initiate data acquisition. The impact stress was sampled at a rate 10 000 samples/s for each of the five

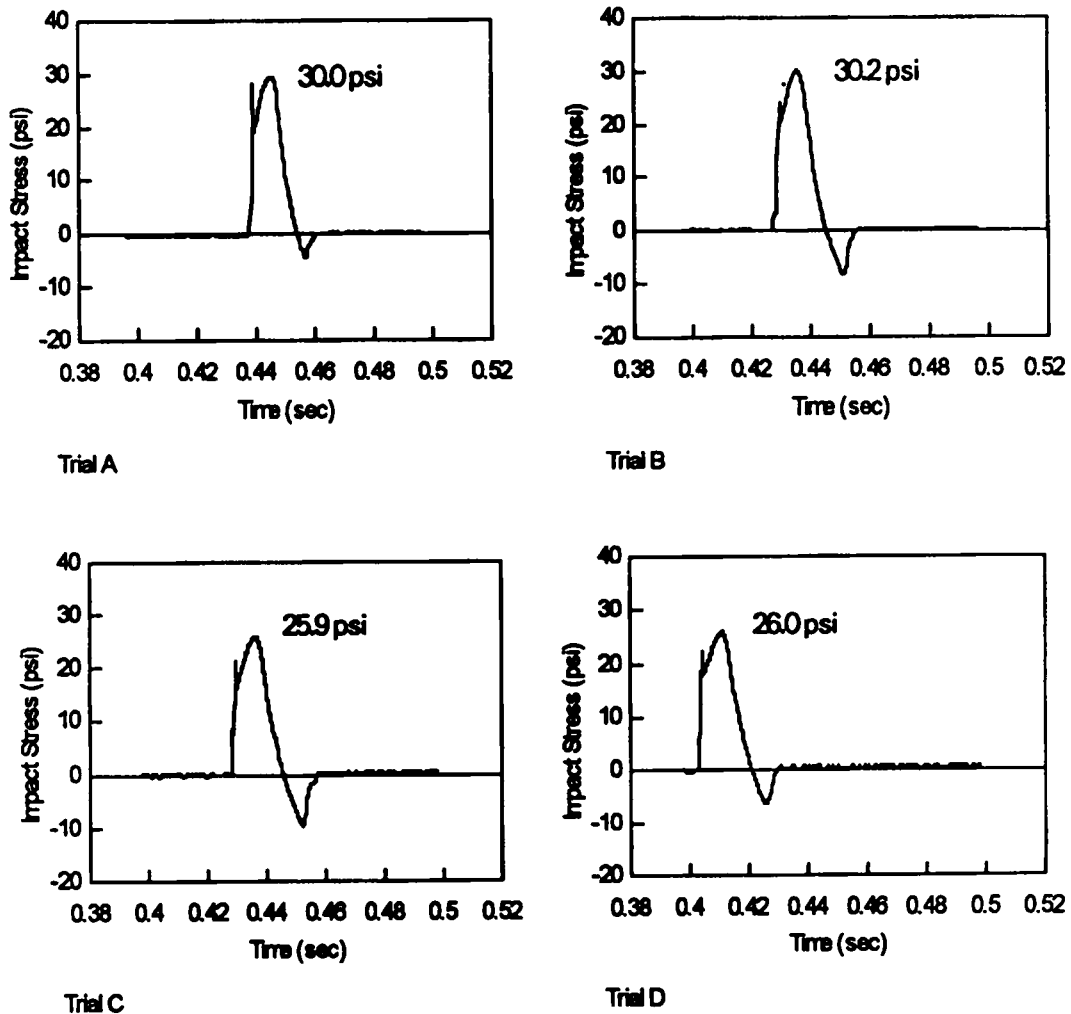


Figure 8. Impact stress versus time graphs for trials A-D

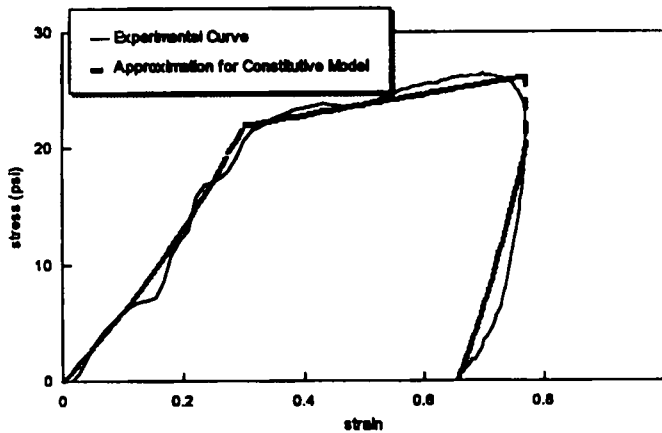


Figure 9. Experimental and simulated stress–strain curves

Table I. Model parameters for organic soil

Parameter	Assigned value
Outer radius of zone 2 ( $r_1$ )	8.56 cm ( $2r_0$ )
Initial modulus ( $M_0$ )	379 572 N/m <sup>2</sup>
Poisson ratio	0.37
Angle of internal friction	35°
$\epsilon_0$ (equations (1)–(8))	1.25
$\eta$ (equations (6) and (7))	0.06
$K_0 = (1 - \sin \Phi) \sqrt{(\text{OCR})}$	0.4264
$k$ (equations (3) and (4))	7.0 N/m <sup>2</sup>

transducer channels in order to register the initial stress peak. Acceleration data was also sampled at a rate of 10 000 samples/s. Once data had been acquired and stored on the computer, data analysis was performed using LOTUS-123.

In order to verify reproducibility, four separate trials (A–D) were conducted using the same experimental set-up described above. Figure 8 shows the resulting impact stress versus time plot for each trial and the magnitude of the peak average impact stress. As seen from Figure 8, the peak average impact stress as well as the duration of impact are in agreement for all the trials.

By employing the accelerometer readings, the authors used the same test set-up with a thin soil layer to establish a non-linear stress–strain relationship for soil in zone 1 in the following manner. The vertical strain history can be deduced by converting the accelerometer results to displacements and then to corresponding strains assuming uniform strain throughout the thin layer of soil (2.5 cm) used in that test. Then, by comparing the average stress and strain histories at different stages of time in the soil layer, the dynamic stress–strain plot shown in Figure 9 was created. The constitutive parameters extracted from Figure 9 are shown in Table I.

## 5. EXPERIMENTAL VERIFICATION

In order to compare the analytical predictions with the experimental results, the authors discretized the 10 cm thick peat layer used in the experiment into 10 elements of equal thickness.

The steel bottom of the container was assumed to be infinitely stiff. Hence, the displacement and the velocity of the 10th element were set to zero. In addition, the outer radius of zone 2 was assumed to be  $2 \times r_0$  (8.56 cm) where  $r_0$  is the radius of the soil column (zone 1) (Table I). In order to scrutinize the sensitivity of the selected number of elements and the radius of zone 2 on the analysis, variation of the final penetration with the above parameters were plotted as shown in Figures 10 and 11. It is seen that the values of the above parameters can be determined based on Figures 10 and 11 so that a computationally efficient analysis could be performed.

Figure 11 shows that the hammer penetration responds significantly to the change of the radii ratio (zone 2 to zone 1) up to a value of 3.5. It also shows that under the present impact conditions, introduction of the non-linear zone changes the final penetration by only a factor of 0.97. This is mainly due to the fact that during the small-scale laboratory impact considered here, the *in situ* shear strength of the elements in zone 1 is inadequate to enforce the formation of a non-linear zone that provides a transition between the participating soil mass (zone 1) and the stationary zone 3. In case of field dynamic compaction where the influence zone extends to deeper layers with higher lateral stresses, the presence of the non-linear zone will be more significant. Hence Figure 11 by no means indicates an insignificant role of the non-linear transition zone.

In a trial run of the numerical algorithm with  $\beta_1 = 0.5$ , it was found that the results were insensitive to the selected time interval, at time intervals smaller than 0.00005 s for the parameters indicated in Table I. The corresponding analytical prediction of the stress history is plotted against the experimental results in Figure 12, where the agreement between them with respect to the magnitude and time seems to be reasonable.

Furthermore, the penetration predicted from the ultimate value of  $d_1$  was 12 mm while experimentally it was observed to be 7 mm.

Figures 12 and 8 show the eventual introduction of tension at the bottom of the weight mainly due to the suction created by pore water. Although the current analytical technique can predict tensile stresses, due to its inability to incorporate the pore pressure behaviour and tensile soil

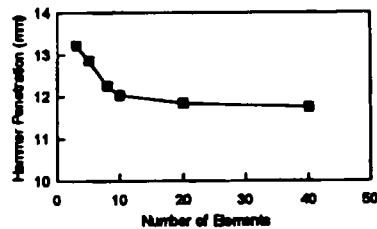


Figure 10. Variation of penetration with element thickness

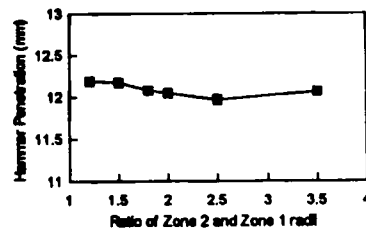


Figure 11. Variation of penetration with the ratio of zone 2 to zone 1 radii



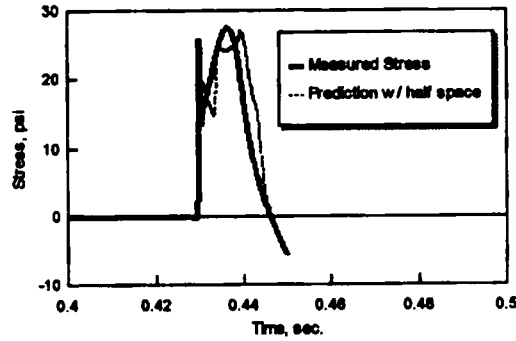


Figure 12. Comparison of measured and predicted stress pulses

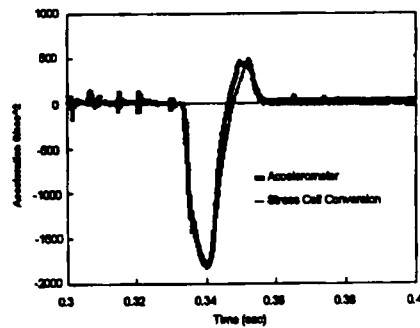


Figure 13. Comparison of the accelerometer and converted stress cell readings

properties, the predicted stress pulse was truncated after the compression wave. It is apparent that a major portion of the penetration discrepancy could be attributed to the rebound of soil during the tension stress pulse.

The authors further verified the accuracy of the measured stresses by comparing the accelerometer reading with the converted average stress cell readings according to the following equation, for another trial impact in the same experimental set-up.

$$a = \frac{[-\sigma_{\text{avg}}A + mg]}{m}$$

where

$A$  = base area of the drop weight,

$a$  = acceleration,

$m$  = mass of drop weight,

$\sigma_{\text{avg}}$  = average of stress cell readings.

Figure 13 shows excellent agreement between the accelerometer and converted stress cell readings verifying the accuracy of the above measurements.

## 6. GUIDELINES FOR USE OF THE MODEL

Reliability of any analytical model depends upon appropriate mathematical idealization of a given engineering problem and accurate determination of the model parameters. Estimation of the zone of influence, element thickness and the radius of the inner zone are the main tasks in the idealization phase of this specific problem. On the other hand, the parameters needed for this specific model are those associated with the constitutive relationship. As previously mentioned, the  $\sqrt{Wh}$  criterion can be used to estimate the zone of influence while the thickness of individual elements should be decided after a sensitivity analysis using different trial element thicknesses. The outer radius of the non-linear shear zone (zone 1) is usually considered as a multiple of the inner soil column radius and should be based on past experience of the extent of deformation around the hammer. Moreover, in the case of a rectangular or a square hammer, the use of an equivalent radius is advocated.

The parameters needed for the constitutive relationship include initial constrained modulus ( $M_0$ ), asymptotic strain ( $\epsilon_0$ ) and the material dependent constant ( $\eta$ ). The constrained modulus ( $M$ ) and the shear modulus ( $G$ ) are related to the Young's modulus ( $E$ ) and the Poisson's ratio ( $\nu$ ) by the following expressions:

$$M = \frac{E(1 - \nu)}{(1 - 2\nu)(1 + \nu)}$$

$$G = \frac{M(1 - 2\nu)}{2(1 - \nu)}$$

Phillips and Baladi<sup>12</sup> and Nelson<sup>13</sup> suggested that, for loose granular soil,  $\eta$  takes values between 0.80 and 0.90 while  $\epsilon_0$  is between 0.40 and 0.50 for ideal one-dimensional dynamic compression. On the other hand, in loose soils like peat, the authors observed that  $\epsilon_0$  goes up to 1.25 and  $\eta$  takes the value of 0.06 under simulated dynamic compaction. Thus, especially for soft soils, it is advisable to find the parameters using laboratory tests where soils are subjected to similar conditions as that of dynamic compaction. The yield point ( $\sigma_b$ ) in the stress-strain curve can be found from the standard bearing capacity equations.

## CONCLUSIONS

The stress history of impact loading of soft soils has been studied using analytical and experimental techniques. When the falling weight was instrumented with pressure transducers and an accelerometer, two distinct stress peaks were consistently observed during the dynamic compaction of soft materials like organic soils. Furthermore, as one would anticipate, these impact produce relatively large strains during dynamic compaction leading to permanent deformations.

The above observations cannot be explained by any of the currently available analytical models for impact loading since they incorporate linear stiffness and damping properties. In the improved methodology advanced in this work, the stiffness and damping properties of the entire impact vicinity are modelled using spring and dashpot elements which appropriately represent the deformation modes of the individual zones. Moreover, the different degrees of deformation of the distinct zones are also considered in the model by utilizing nonlinear stiffness properties wherever necessary. On the other hand, when the impact is relatively mild, the non-linear zone becomes insignificant, thus appropriately reducing the model to currently available linear models.

Finally, it was displayed that the current technique possesses the capability of predicting the entire surface stress history including the two distinct peak stresses to a reasonable accuracy. In

addition, its ability to predict the approximate permanent penetration is indeed another advantage of the model.

## APPENDIX

### A.1. Derivation of the stiffness expression<sup>9</sup> of zone 2

The following stress-strain relationship is used for zone 2:

$$\gamma/\gamma_r = \beta/(1 - \beta)$$

$$\beta = \tau/\tau_f$$

$$\gamma_r = \tau_f/G_s \text{ where}$$

$\tau_0$  = shear stress at the soil column interface,

$\tau_f$  = ultimate shear strength,

$G_s$  = initial tangent shear modulus,

$\tau$  = shear stress at radius  $r$  from the centre of the impact area.

By assuming plane strain conditions, the displacement at soil column surface ( $w_0$ ) is obtained by direct integration of the angular distortion from the radius of the zone 1 ( $r_0$  to the radius of the zone 2  $r_1$ ).

$$w_0 = \int_{r_0}^{r_1} \gamma dr$$

$$w_0 = \int_{r_0}^{r_1} \frac{dr}{\frac{1}{\beta\gamma_r} - \frac{1}{\gamma_r}}$$

But for the equilibrium of zone 2

$$2\pi r_0 \tau_0 dx = 2\pi r \tau dx$$

By substituting the above condition and simplifying

$$w_0 = \int_{r_0}^{r_1} \frac{dr}{\left\{ \frac{G_s r}{\tau_0 r_0} - \frac{1}{\gamma_r} \right\}}$$

Then by integrating and simplifying the above equation, it can be proved that  $k_3 = \tau_0/w_0$

$$k_{sli} = \frac{2\pi G_s}{\ln \left[ \frac{(r_1/r_0) - (\tau_0/\tau_f)}{1 - (\tau_0/\tau_f)} \right]}$$

## REFERENCES

1. P. Mayne and J. Jones, 'Impact stresses during dynamic compaction, *J. of Geotechnical Engineering, ASCE* **109**, 1342-1346 (October 1983).
2. R. A. Scott and R. W. Pearce, 'Soil compaction by impact', *Geotechnique*, **25**(1), 19-30 (1975).
3. J. H. Qian, 'Dynamic consolidation from practice to theory', *Proc 8th Asian Regional Conf. on Soil Mechanics and Found. Engrg.*, Vol. 2 Japanese Society for Soil Mechanics and Foundation Engineering, 1986, pp. 213-217.

4. J. W. Roesset, E. Kausel, V. Cuellar, J. L. Monte and Valerio, 'Impact of weight falling onto the ground', *J. Geotech. Eng. Div., ASCE*, **120**, 1395–1412 (1994).
5. Y. K. Chow, D. M. Yong, K. Y. Yong, and S. L. Lee, 'Dynamic compaction analysis', *J. Soil Mech. Found. Div. ASCE*, **118**(8), (1992).
6. L. Menard and Y. Broise, 'Theoretical and practical aspects of dynamic consolidation', *Geotechnique*, London, **25**(1), 3–18 (1975).
7. G. A. Leonards, W. A. Cutter and R. D. Holtz, 'Dynamic compaction of granular soil', *J. Geotech. Eng. Div. ASCE*, **106**(1), 35–44 (1980).
8. J. Lysmer and F. E. Ricart, 'Dynamic response of footings to vertical loading', *J. Soil Mech. Found. Div. ASCE* **92**(1), 65–91 (1966).
9. M. H. E. I. Naggari and M. Novak, 'Non-linear model for dynamic axial pile response', *J. Soil Mech. Found. Div. ASCE*, **120**(2), 308–329 (1994).
10. M. Novak, T. Nogami and F. Aboul-Ella, 'Dynamic soil reactions for plane strain case', *J. Eng. Mech. Div. ASCE* **104**, EM4 953–959 (1978).
11. T. Ginsburg, 'Propagation of shock waves in the ground', *J. Soil Mech. Found. Div. ASCE*, **90**(1), 125–163 (1964).
12. B. R. Phillips and G. Y. Baladi, 'Results of two free-field code calculations versus field measurements for the distant plain 1A event', Misc. Paper S-73-21, U.S. Army Engr. Waterways Experiment Station, Vicksburg, Ms, 1973.
13. I. Nelson, 'Numerical solution of problems involving explosive loading, in 'Proc. Dynamic Methods in Soil and Rock Mechanics, Vol. 2: Plastic and Long Term Effects in Soils, A. A. Balkema, Rotterdam, The Netherlands, 1977.
14. O. C. Zienkiewicz, 'The Finite Element Method Vol. 2, McGraw-Hill New York.

# INVESTIGATION OF IMPACT STRESSES INDUCED IN LABORATORY DYNAMIC COMPACTION OF SOFT SOILS

H. S. THILAKASIRI, M. GUNARATNE, G. MULLINS, P. STINNETTE AND B. JORY<sup>†</sup>

*Department of Civil and Environmental Engineering, University of South Florida, Tampa, FL 33647, U.S.A.*

## SUMMARY

The majority of currently available analytical tools to predict ground stresses due to impact are based on linear spring-dashpot dynamic models. Although these simple models adequately represent stiff ground possessing linear visco-elastic behaviour, they suffer from two striking limitations when applied to relatively softer ground; (1) the inability to account for the permanent deformation resulting from impact, (2) failure to incorporate stiffness changes of softer soil within the impact duration. In this paper, the authors present an improved analytical approach formulated on the basis of a series of laboratory impact tests, to address the shortcomings of the current dynamic models in relation to soft soils. In this procedure, the impact zone is modelled as three distinct zones; (1) a zone beneath the falling weight undergoing non-linear axial deformation while being in vertical motion, (2) an inner zone immediately surrounding zone 1 with non-linear shear deformation, and (3) an outer zone undergoing a relatively lower degree of (linear) shear deformation. The soil constitutive parameters pertinent to the model are obtained from a modified dynamic compression test that simulates the impact conditions. It is shown that analytical predictions of the impact stress history and penetration are in agreement with test results. The findings are useful in the exploration of dynamic compaction techniques that will be effective in soft soil improvement.

KEY WORDS: dynamic; compaction; soil; damping; non-linear stressing

## 1. INTRODUCTION

A number of analytical models have been proposed by several researchers<sup>1-4</sup> in recent years to estimate surface stresses during dynamic compaction. In these models, it is assumed that the soil behaviour is linear elastic, isotropic and hence can be modelled by a linear spring and a linear dashpot. However, it is a common observation made during dynamic compaction of soft soil that the soil mass close to the surface is subjected to a very high strain level resulting in permanent deformation. Obviously a model that employs a linear spring and a linear dashpot is unable to simulate these observations because non-linearity is clearly exhibited by soils at high strain levels. Apart from the above-mentioned simplified models, Chow *et al.*<sup>3</sup> proposed a different analytical approach where the one-dimensional wave equation model for pile-driving analysis is modified by replacing the pile with a soil column extending to at least the anticipated depth of improvement. In this method, the soil surrounding the soil column is represented by linear elastic springs and linear dashpots. Furthermore, they adopted an implicit finite element method to solve the equation of motion of the soil column.

<sup>†</sup>Present address: Florida Department of transportation, Bartow, FL, U.S.A.

An improved analytical model is proposed in this paper to estimate the surface stress and the surface deformation, accounting for non-linearity of soil immediately below the drop hammer as well as that of the immediate neighbourhood of the hammer. In this procedure, equations of motion are separately written for three zones distinguished by their mode and degree of deformation while satisfying compatibility. A numerical procedure is adopted to solve these equations of motion because of complexity arising from the constitutive model that accounts for non-linearity. The solution procedure uses an explicit direct time integration together with lumped mass formulation for computational efficiency. Finally, analytical predictions of the impact surface stress history and penetration are compared with laboratory measurements.

## 2. EXPERIMENTAL OBSERVATIONS

Figure 1 shows a typical plot of the impact surface stress history recorded during the authors' experiments on a wet organic soil by employing a falling hammer instrumented with sensitive pressure transducers. The sensitivity of the data acquisition system is discussed in the ensuing Section 4 on the experimental set-up. The stress-time plot such as that shown in Figure 1 obtained from a series of tests consistently demonstrate the existence of two distinct regions:

- (1) An immediate peak followed by rapidly diminishing stress. This phase of the stress history usually lasts only an extremely small time (1–2 ms) thus possibly eluding detection without a sensitive data acquisition system. This could be one reason why such an instantaneous peak has not been documented in previous experimental studies.
- (2) A subsequent oscillatory stress pattern. This phase of the stress pulse on the other hand has been the subject of most previous experimental and analytical investigations.

## 3. MATHEMATICAL IDEALIZATION

From the perspective of deformation, the soil mass in the impact vicinity can be considered as being comprised of three distinct zones (Figure 2):

- Zone 1: soil under the falling hammer in the zone of influence undergoing significant vertical deformation that permits it to be considered as a moving or participating soil mass,  
 Zone 2: soil in the immediate neighbourhood undergoing excessive shear deformations that can only be characterized by non-linear models,

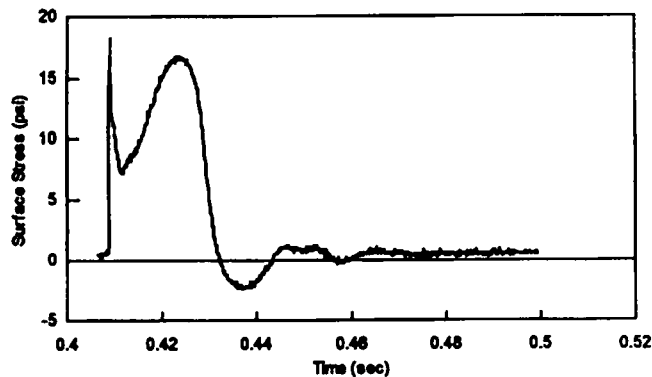


Figure 1. Typical experimental impact stress history

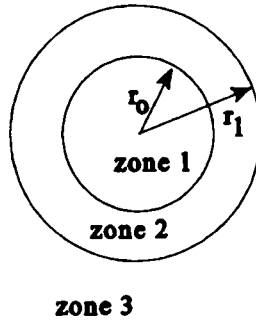


Figure 2. Plan view of the impact vicinity

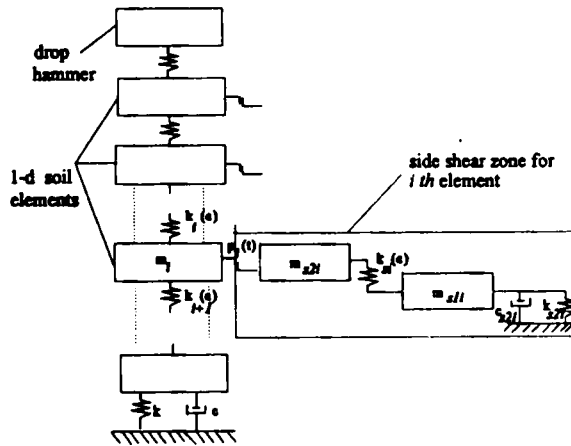


Figure 3. Dynamic model (shear zone is shown only for the *i*th element)

**Zone 3:** soil in the outer region undergoing limited shear deformations within linear elastic limits.

The authors' analytical formulation discussed here is founded on consideration of the mechanics of these three zones. The analytical formulation is kept simple by replacing the soil in the above zones with equivalent lumped masses. Researchers have observed that the depth of the zone of influence ( $z$ ) during dynamic compaction varies in the range of  $\sqrt{(W_1 h)} \geq z \geq 1/2\sqrt{W_1 h}$ ,<sup>6,7</sup> where  $W_1$  and  $h$  are drop weight in tonnes and drop height in meters, respectively. Hence, in their formulations the authors suggest that the vertical depth ( $z$ ) of the above non-linear zones should at least extend to a depth of  $\sqrt{(W_1 h)}$ . In the mathematical discretization, zones 1 and 2 up to the depth of influence are divided into elements of equal thickness as shown in Figure 3. Since the vertical strain within each element is assumed to be uniform, their thickness should be decided by a sensitivity analysis.

Since the strains in zone 1 are large, it is logical to expect non-linear behaviour. Thus, the soil elements in that zone are replaced in the current model by moving solid lumped masses ( $m_i$ ) having the same cross-sectional area as that of the drop weight and are connected by non-linear

springs of stiffness  $k_i(\epsilon)$  as shown in Figure 3.  $k_i(\epsilon)$  can be expressed by  $M_i(\epsilon)A/L$  where  $M_i(\epsilon)$ ,  $A$  and  $L$  are the constrained modulus corresponding to the current strain ( $\epsilon$ ) (Section 3.1), cross-sectional area of the element and the current length of the element, respectively. The soil half-space beneath the immediate vicinity of the non-linear soil column is modelled by a linear spring ( $k$ ) and a linear dashpot in parallel having a spring stiffness of  $4G_s r_0/(1 - \nu)$  and a dashpot coefficient of  $3.4G_s r_0^2/(1 - \nu)$  as proposed by Lysmer and Richart<sup>8</sup> in which  $r_0$ ,  $G$  and  $\nu$  are the radius of the soil column, initial shear modulus and the Poisson ratio, respectively. In the case where there is a stiff layer present within the zone of influence, the displacement of the last element is set to zero to account for it. In such a situation, the spring and the dashpot are not required.

On the other hand, the elements in annular zone 2, represented by two masses ( $m_{s,1i}$  and  $m_{s,2i}$ ) of radius ( $r_1$ ) surrounding zone 1 are also subjected to high strain levels. Therefore, its effect on the impact zone must also be modelled by non-linear shear stiffness properties ( $k_{si}$ ). In this regard, the stiffness expression developed by El Naggar and Novak<sup>9</sup> would be appropriate. The expression for  $k_{si}$  is derived in the Appendix. The mass of the  $i$ th element in zone 2 is equally distributed to lumped masses  $m_{s,1i}$  and  $m_{s,2i}$  as shown in Figure 3. The elements in zone 2 interact with the corresponding elements in zone 1 through rigid plastic sliders  $p_i(t)$  as shown in Figure 3.

Outside zone 2, the shear strains are small enough to permit the application of linear elastic constitutive relations. Thus, the shearing resistance of zone 3 is simulated by a linear spring ( $k_{s2i}$ ) and a dashpot ( $c_{s2i}$ ) having a stiffness of  $2.75G_s dz_i$  and a damping constant of  $2\pi r_1 \sqrt{\rho_s G_s dz_i}$ , respectively, as proposed by Novak et al.<sup>10</sup> in which  $G_s$ ,  $\rho_s$  and  $dz_i$  are the initial shear modulus, initial density and vertical thickness of elements in zone 2, respectively. Hence, zone 3 provides shear resistance to the vertical movement of elements in zone 2 through the parallel combination of spring  $k_{s2i}$  and  $c_{s2i}$ .

It is assumed that slipping can occur at the interface between the deforming soil elements in zone 1 and the elements in the surrounding zone 2 when the shear stress in the rigid plastic sliders  $p_i(t)$  exceeds the maximum static resistance which is taken to be  $k_0 \sigma'_v \tan \Phi$ ; where,  $k_0$ ,  $\sigma'_v$  and  $\Phi$  are coefficient of lateral earth pressure at rest, current vertical effective stress and angle of internal friction of the soil, respectively. It is accepted that the coefficient of lateral earth pressure depends on the over consolidation ratio (OCR) of the soil. Hence, in the proposed model  $k_0$  is taken to be equal to  $(1 - \sin \phi) \sqrt{\text{OCR}}$ . Except for fully saturated low permeable soils with multiple impacts, the generation of pore water pressure in zone 1 is comparatively small<sup>6</sup> resulting in increased vertical effective stress in zone 1 during an impact. Therefore, it is important to note here that the maximum shear resistance changes during an impact even for a normally consolidated soil as the effective vertical stress changes with deformation of the soil column.

Finally, Newmark's explicit time step integration is employed to solve the equations of motion of the soil elements. The impacting hammer is disconnected from the numerical solution when the contact stress becomes less than zero.

If the depth of the non-linear zone is insignificant such as in the case of a small amplitude vibration, it is clear that the present model approaches the already accepted visco-elastic models, in which linear spring and a dashpot are in parallel (Figure 3). Further, the thickness of the influence zone can decrease with decrease in the drop weight and the drop height according to the aforementioned effective zone criterion ( $\sqrt{Wh}$ ).

### 3.1. Determination of non-linear stiffness values

Figure 4 shows a typical axial stress-strain curve obtained for loading and unloading during a dynamic impact. The experimental procedure used to obtain Figure 4 is highlighted in Section 4. A unique feature of the stress-strain curve is a distinct yielding stage as shown in Figure 4 after



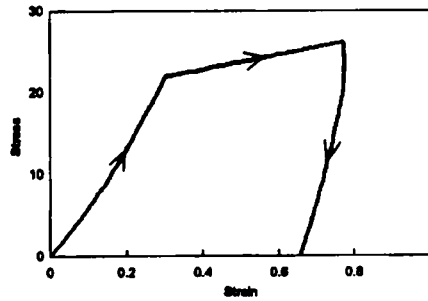


Figure 4. Experimental stress–strain curve

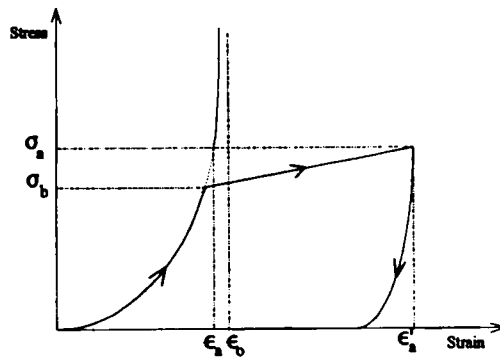


Figure 5. Typical theoretical stress–strain graph with symbols used in mathematical expressions

which a major portion of the axial strain is irrecoverable. This sudden change of the stiffness can be attributed to plastic flow resulting from shear failure. It was found that the pre-bearing capacity region of the curve can be conveniently expressed by the mathematical expression given by Ginsberg<sup>11</sup> for one-dimensional dynamic loading (equations (1) and (2)). Moreover, Ginsberg's<sup>11</sup> expression for the unloading phase correctly represented the unloading curve obtained by the authors as well (equations (5)–(6)). However, it should be noted that the post bearing capacity failure portion of the curve is linear with a small slope instead of being flat, indicating some strain hardening. Hence, based on Figure 4, the axial force in zone 1 can be determined by employing a constitutive relationship similar to that proposed by Ginsburg<sup>11</sup> for non-linear uniaxial dynamic compression. During each time step, the incremental strain in a given element is calculated based on the shortening of the element during the period and the current length of the element. Then, those incremental strains are summed up to estimate the total strain in the element and the corresponding axial stress from Figure 4. While the shape of the stress–strain curve proposed for loading and unloading is shown in Figure 5, the related mathematical relationships modified from the original Ginsburg model to include plastic flow, are expressed below.

For the loading stage

Up to the bearing capacity

$$\sigma = \frac{M_0 \varepsilon \varepsilon_0}{\{\varepsilon_0 - \varepsilon\}} \quad (1)$$

$$M(\varepsilon) = \frac{M_0 \varepsilon_0^2}{\{\varepsilon_0 - \varepsilon\}^2} \quad (2)$$

Beyond the bearing capacity

$$\sigma = k\{\varepsilon - \varepsilon_b\} + \sigma_b \quad (3)$$

$$M(\varepsilon) = k \quad (4)$$

For the unloading state

$$\sigma = M_0 \varepsilon_* \varepsilon_0 / \{\varepsilon_0 - \varepsilon_*\} \quad (5)$$

$$\varepsilon_* = (\varepsilon - (\varepsilon'_a - \varepsilon_a) - \varepsilon_a \eta / 1 - \eta) \quad (6)$$

$$M(\varepsilon) = M_0 \varepsilon_0^2 / \{1 - \eta\} \{\varepsilon_0 - \varepsilon_*\}^2 \quad (7)$$

$$\varepsilon_a = \varepsilon_0 \sigma_a / (\sigma_a + M_0 \varepsilon_0) \quad (8)$$

where

$M_0$  = initial constrained modulus,

$M(\varepsilon)$  = constrained modulus at strain  $\varepsilon$ ,

$\varepsilon_0$  = asymptotic value of strain corresponding to the pre-bearing failure portion,

$\eta$  = a material constant,

$\varepsilon'_a$  = strain at the beginning of the unloading phase,

$\sigma_a$  = stress at the beginning of the unloading phase,

$\sigma_b$  = bearing capacity,

$k$  = modulus after the bearing capacity failure.

As mentioned in the mathematical idealization, the following expression for stiffness developed by E1 Nagggar and Novak<sup>9</sup> assuming a plane strain condition are used for zone 2.

For loading

$$k_{s,li} = \frac{2\pi G_s}{\ln \frac{r_1/r_2 - \eta_0}{1 - \eta_0}} \quad (9)$$

For unloading

$$k_{s,li} = \frac{2\pi G_s}{\ln(r_1/r_0)} \quad (10)$$

where

$r_1$  = outer radius of the inner zone,

$r_0$  = radius of the soil column,

$G_s$  = initial shear modulus,

$\tau_0$  = shear stress at the axial element and shear element interface,

$\tau_f$  = ultimate shear strength,

$\eta_0 = \tau_0/\tau_f$ .

3.2. Kinematic equations of the system

Using the notation indicated in Figure 6, the following equations of motion can be written for various components of the system:

For the drop hammer

$$w_1 - q_1(t) = \frac{w_1}{g} d_1''(t) \tag{11}$$

For the *i*th axial element (in Figure 6)

$$q_i(t) - q_{i+1}(t) - p_i(t) = m_i d_i''(t) \tag{12}$$

For *i*th shear element (in Figure 6)

$$p_i(t) - q_{si}(t) = m_{s1i} d_{si}''(t) \tag{13}$$

$$q_{si}(t) - k_{s2i} d_{s2i}(t) - c_{s2i} d_{s2i}'(t) = m_{s2i} d_{s2i}''(t) \tag{14}$$

where

$$k_{s2i} = 2.75 G_s dz_i, \tag{15}$$

$$c_{s2i} = 2\pi r_1 \sqrt{(\rho_s G_s)} dz_i, \tag{16}$$

$dz_i$  = thickness of the *i*th element in zone 2.

Newmark's explicit time step integration can be used to solve the equations (11)–(14) in combination with equations (17) and (18) as previously mentioned. For an element with a displacement  $d(t)$  at any time  $t$ , Newmark's classical explicit time step integration algorithm (14) involves following recurrence relationships:

$$d_{n+1}(t) = d_n(t - \Delta t) + \Delta t d_n'(t - \Delta t) + \frac{\Delta t^2}{2} d_n''(t - \Delta t) \tag{17}$$

$$d_{n+1}'(t) = d_n'(t - \Delta t) + \Delta t(1 - \beta_1) d_n''(t - \Delta t) + \Delta t \beta_1 d_{n+1}''(t) \tag{18}$$

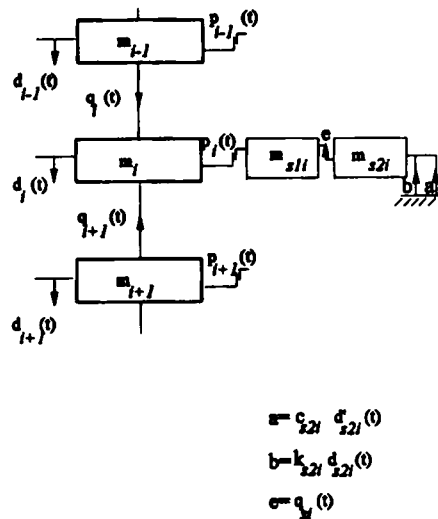


Figure 6. Free body diagrams for the *i*th axial and shear elements

where  $\beta_1$  is Newmark's parameter, the value of which can be chosen for effective implementation of the particular algorithm.

Equation (17) can be used to explicitly obtain the current displacement  $d_{n+1}(t)$  knowing the displacement, velocity and the acceleration of the element during the previous time step, while equation (18) enables one to express the current velocity of the element in terms of the current acceleration.

Thus, when equations (17) and (18) are separately applied to the elements in motion in Figure 3, it will facilitate the solution of equations (11)–(14) by evaluating the current displacement and the acceleration of each element based on the state of motion of the entire system at the preceding time step. Furthermore, at the end of each time step, element thicknesses and soil properties are upgraded according to the current strains, using the non-linear constitutive model described in the previous section. By repeating this procedure for a number of time steps, the numerical solution procedure can be successfully implemented. The explicit direct time integration algorithm is conditionally stable and the stability is governed by the magnitude of the time step size. It is found from the literature that the maximum size of the time step for a stable solution is related to the time required for an elastic wave to propagate across the shortest element of the mesh. In contrast to implicit algorithms, explicit algorithms require a large number of small time steps to avoid the solution of a large matrix equation which is typical of implicit methods at each time step.

#### 4. EXPERIMENTAL SET-UP

The experimental set-up shown in Figure 7 was used to determine the dynamic impact stress due to a drop weight and the related stress–strain behaviour of an organic soil in the laboratory. The organic soil had a water content of 378 per cent, a we density of  $1064 \text{ kg/m}^3$  (66 pcf) and an

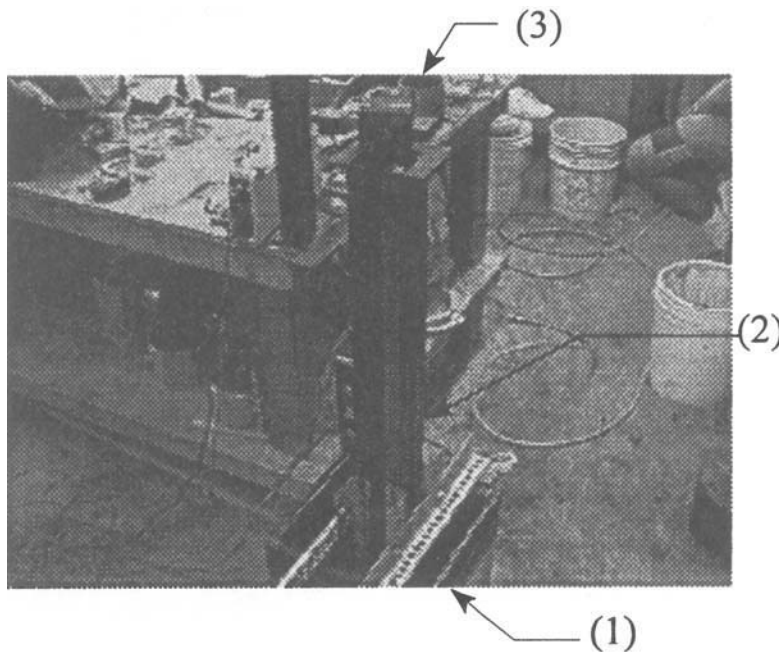


Figure 7. Experimental set-up

organic content of 80 per cent. The soil was compacted in a PVC lined 0.03 m<sup>3</sup> (one cubic foot-1' x 1' x 1') container to a final bed depth of 10.16 cm (4 in) for the test used to get the surface stress history while a reduced depth of 2.6cm (1 in) was used for the test to determine the stress-strain relationship. A 0.923 m (3 ft) tall guide rail system (2) was placed on top of the box. A 2.27 kg (5 lb) steel weight with a 7.62 cm (3 in) square base (3) was held by an electro-magnet at the top of the guide rail. The weight was instrumented with five pressure transducers that were installed in such a manner that they were flush with the surface of the bottom of the weight. An accelerometer was also attached to the top of the weight so that its position was in line with the centre of gravity of the weight. The pressure transducers and the accelerometer were interfaced to a 486-33 MHz microcomputer through the use of a AT-MIO-16F-5 interface board.

Programs are written in Visual Basic to facilitate multiple channel data acquisition. A remote relay was used to simultaneously release the weight from the electro-magnet and initiate data acquisition. The impact stress was sampled at a rate 10 000 samples/s for each of the five

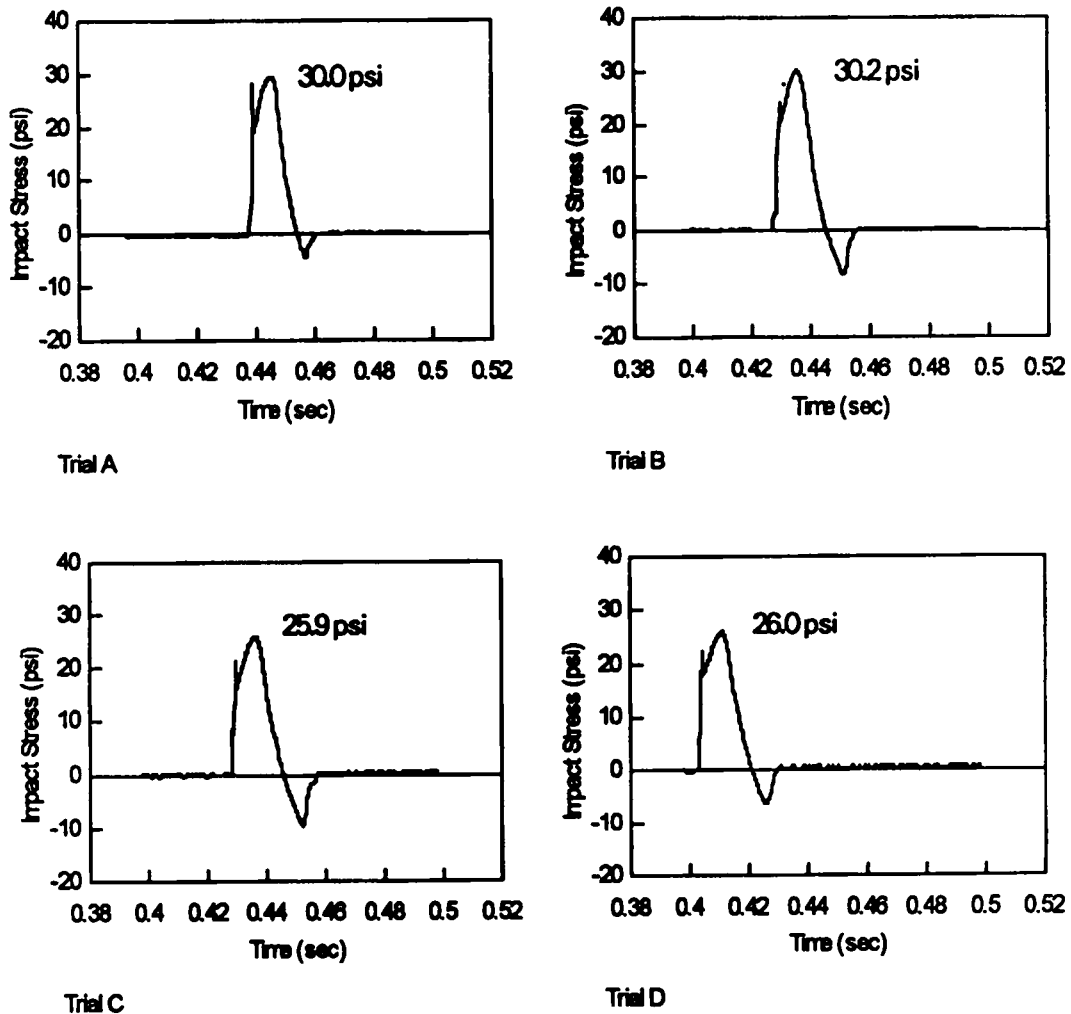


Figure 8. Impact stress versus time graphs for trials A-D

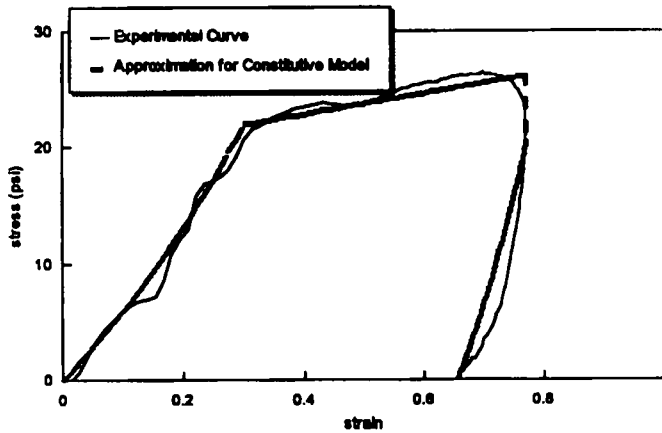


Figure 9. Experimental and simulated stress–strain curves

Table I. Model parameters for organic soil

Parameter	Assigned value
Outer radius of zone 2 ( $r_1$ )	8.56 cm ( $2r_0$ )
Initial modulus ( $M_0$ )	379 572 N/m <sup>2</sup>
Poisson ratio	0.37
Angle of internal friction	35°
$\epsilon_0$ (equations (1)–(8))	1.25
$\eta$ (equations (6) and (7))	0.06
$K_0 = (1 - \sin \Phi) \sqrt{(\text{OCR})}$	0.4264
$k$ (equations (3) and (4))	7.0 N/m <sup>2</sup>

transducer channels in order to register the initial stress peak. Acceleration data was also sampled at a rate of 10 000 samples/s. Once data had been acquired and stored on the computer, data analysis was performed using LOTUS-123.

In order to verify reproducibility, four separate trials (A–D) were conducted using the same experimental set-up described above. Figure 8 shows the resulting impact stress versus time plot for each trial and the magnitude of the peak average impact stress. As seen from Figure 8, the peak average impact stress as well as the duration of impact are in agreement for all the trials.

By employing the accelerometer readings, the authors used the same test set-up with a thin soil layer to establish a non-linear stress–strain relationship for soil in zone 1 in the following manner. The vertical strain history can be deduced by converting the accelerometer results to displacements and then to corresponding strains assuming uniform strain throughout the thin layer of soil (2.5 cm) used in that test. Then, by comparing the average stress and strain histories at different stages of time in the soil layer, the dynamic stress–strain plot shown in Figure 9 was created. The constitutive parameters extracted from Figure 9 are shown in Table I.

## 5. EXPERIMENTAL VERIFICATION

In order to compare the analytical predictions with the experimental results, the authors discretized the 10 cm thick peat layer used in the experiment into 10 elements of equal thickness.

The steel bottom of the container was assumed to be infinitely stiff. Hence, the displacement and the velocity of the 10th element were set to zero. In addition, the outer radius of zone 2 was assumed to be  $2 \times r_0$  (8.56 cm) where  $r_0$  is the radius of the soil column (zone 1) (Table I). In order to scrutinize the sensitivity of the selected number of elements and the radius of zone 2 on the analysis, variation of the final penetration with the above parameters were plotted as shown in Figures 10 and 11. It is seen that the values of the above parameters can be determined based on Figures 10 and 11 so that a computationally efficient analysis could be performed.

Figure 11 shows that the hammer penetration responds significantly to the change of the radii ratio (zone 2 to zone 1) up to a value of 3.5. It also shows that under the present impact conditions, introduction of the non-linear zone changes the final penetration by only a factor of 0.97. This is mainly due to the fact that during the small-scale laboratory impact considered here, the *in situ* shear strength of the elements in zone 1 is inadequate to enforce the formation of a non-linear zone that provides a transition between the participating soil mass (zone 1) and the stationary zone 3. In case of field dynamic compaction where the influence zone extends to deeper layers with higher lateral stresses, the presence of the non-linear zone will be more significant. Hence Figure 11 by no means indicates an insignificant role of the non-linear transition zone.

In a trial run of the numerical algorithm with  $\beta_1 = 0.5$ , it was found that the results were insensitive to the selected time interval, at time intervals smaller than 0.00005 s for the parameters indicated in Table I. The corresponding analytical prediction of the stress history is plotted against the experimental results in Figure 12, where the agreement between them with respect to the magnitude and time seems to be reasonable.

Furthermore, the penetration predicted from the ultimate value of  $d_1$  was 12 mm while experimentally it was observed to be 7 mm.

Figures 12 and 8 show the eventual introduction of tension at the bottom of the weight mainly due to the suction created by pore water. Although the current analytical technique can predict tensile stresses, due to its inability to incorporate the pore pressure behaviour and tensile soil

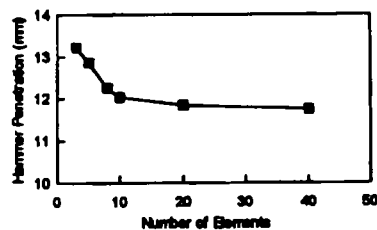


Figure 10. Variation of penetration with element thickness

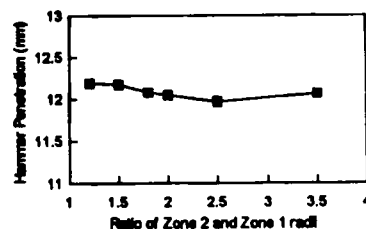


Figure 11. Variation of penetration with the ratio of zone 2 to zone 1 radii

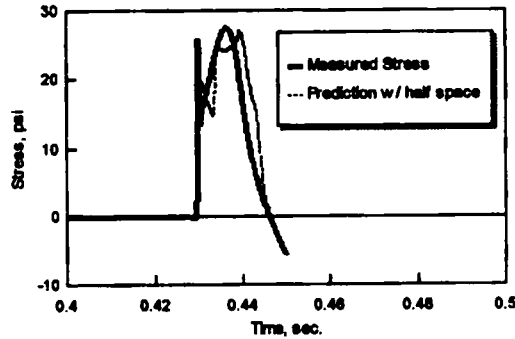


Figure 12. Comparison of measured and predicted stress pulses

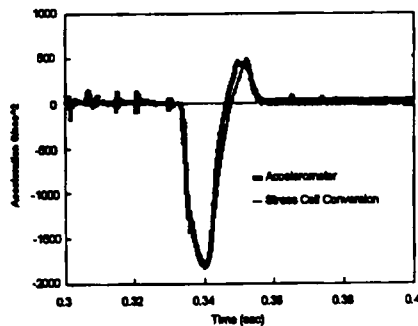


Figure 13. Comparison of the accelerometer and converted stress cell readings

properties, the predicted stress pulse was truncated after the compression wave. It is apparent that a major portion of the penetration discrepancy could be attributed to the rebound of soil during the tension stress pulse.

The authors further verified the accuracy of the measured stresses by comparing the accelerometer reading with the converted average stress cell readings according to the following equation, for another trial impact in the same experimental set-up.

$$a = \frac{[-\sigma_{\text{avg}}A + mg]}{m}$$

where

$A$  = base area of the drop weight,

$a$  = acceleration,

$m$  = mass of drop weight,

$\sigma_{\text{avg}}$  = average of stress cell readings.

Figure 13 shows excellent agreement between the accelerometer and converted stress cell readings verifying the accuracy of the above measurements.



## 6. GUIDELINES FOR USE OF THE MODEL

Reliability of any analytical model depends upon appropriate mathematical idealization of a given engineering problem and accurate determination of the model parameters. Estimation of the zone of influence, element thickness and the radius of the inner zone are the main tasks in the idealization phase of this specific problem. On the other hand, the parameters needed for this specific model are those associated with the constitutive relationship. As previously mentioned, the  $\sqrt{Wh}$  criterion can be used to estimate the zone of influence while the thickness of individual elements should be decided after a sensitivity analysis using different trial element thicknesses. The outer radius of the non-linear shear zone (zone 1) is usually considered as a multiple of the inner soil column radius and should be based on past experience of the extent of deformation around the hammer. Moreover, in the case of a rectangular or a square hammer, the use of an equivalent radius is advocated.

The parameters needed for the constitutive relationship include initial constrained modulus ( $M_0$ ), asymptotic strain ( $\epsilon_0$ ) and the material dependent constant ( $\eta$ ). The constrained modulus ( $M$ ) and the shear modulus ( $G$ ) are related to the Young's modulus ( $E$ ) and the Poisson's ratio ( $\nu$ ) by the following expressions:

$$M = \frac{E(1 - \nu)}{(1 - 2\nu)(1 + \nu)}$$

$$G = \frac{M(1 - 2\nu)}{2(1 - \nu)}$$

Phillips and Baladi<sup>12</sup> and Nelson<sup>13</sup> suggested that, for loose granular soil,  $\eta$  takes values between 0.80 and 0.90 while  $\epsilon_0$  is between 0.40 and 0.50 for ideal one-dimensional dynamic compression. On the other hand, in loose soils like peat, the authors observed that  $\epsilon_0$  goes up to 1.25 and  $\eta$  takes the value of 0.06 under simulated dynamic compaction. Thus, especially for soft soils, it is advisable to find the parameters using laboratory tests where soils are subjected to similar conditions as that of dynamic compaction. The yield point ( $\sigma_b$ ) in the stress-strain curve can be found from the standard bearing capacity equations.

## CONCLUSIONS

The stress history of impact loading of soft soils has been studied using analytical and experimental techniques. When the falling weight was instrumented with pressure transducers and an accelerometer, two distinct stress peaks were consistently observed during the dynamic compaction of soft materials like organic soils. Furthermore, as one would anticipate, these impact produce relatively large strains during dynamic compaction leading to permanent deformations.

The above observations cannot be explained by any of the currently available analytical models for impact loading since they incorporate linear stiffness and damping properties. In the improved methodology advanced in this work, the stiffness and damping properties of the entire impact vicinity are modelled using spring and dashpot elements which appropriately represent the deformation modes of the individual zones. Moreover, the different degrees of deformation of the distinct zones are also considered in the model by utilizing nonlinear stiffness properties wherever necessary. On the other hand, when the impact is relatively mild, the non-linear zone becomes insignificant, thus appropriately reducing the model to currently available linear models.

Finally, it was displayed that the current technique possesses the capability of predicting the entire surface stress history including the two distinct peak stresses to a reasonable accuracy. In

addition, its ability to predict the approximate permanent penetration is indeed another advantage of the model.

## APPENDIX

### A.1. Derivation of the stiffness expression<sup>9</sup> of zone 2

The following stress-strain relationship is used for zone 2:

$$\gamma/\gamma_r = \beta/(1 - \beta)$$

$$\beta = \tau/\tau_f$$

$$\gamma_r = \tau_f/G_s \text{ where}$$

$\tau_0$  = shear stress at the soil column interface,

$\tau_f$  = ultimate shear strength,

$G_s$  = initial tangent shear modulus,

$\tau$  = shear stress at radius  $r$  from the centre of the impact area.

By assuming plane strain conditions, the displacement at soil column surface ( $w_0$ ) is obtained by direct integration of the angular distortion from the radius of the zone 1 ( $r_0$  to the radius of the zone 2  $r_1$ ).

$$w_0 = \int_{r_0}^{r_1} \gamma dr$$

$$w_0 = \int_{r_0}^{r_1} \frac{dr}{\frac{1}{\beta\gamma_r} - \frac{1}{\gamma_r}}$$

But for the equilibrium of zone 2

$$2\pi r_0 \tau_0 dx = 2\pi r \tau dx$$

By substituting the above condition and simplifying

$$w_0 = \int_{r_0}^{r_1} \frac{dr}{\left\{ \frac{G_s r}{\tau_0 r_0} - \frac{1}{\gamma_r} \right\}}$$

Then by integrating and simplifying the above equation, it can be proved that  $k_3 = \tau_0/w_0$

$$k_{3li} = \frac{2\pi G_s}{\ln \left[ \frac{(r_1/r_0) - (\tau_0/\tau_f)}{1 - (\tau_0/\tau_f)} \right]}$$

## REFERENCES

1. P. Mayne and J. Jones, 'Impact stresses during dynamic compaction, *J. of Geotechnical Engineering, ASCE* **109**, 1342-1346 (October 1983).
2. R. A. Scott and R. W. Pearce, 'Soil compaction by impact', *Geotechnique*, **25**(1), 19-30 (1975).
3. J. H. Qian, 'Dynamic consolidation from practice to theory', *Proc 8th Asian Regional Conf. on Soil Mechanics and Found. Engrg.*, Vol. 2 Japanese Society for Soil Mechanics and Foundation Engineering, 1986, pp. 213-217.

4. J. W. Roesset, E. Kausel, V. Cuellar, J. L. Monte and Valerio, 'Impact of weight falling onto the ground', *J. Geotech. Eng. Div., ASCE*, **120**, 1395–1412 (1994).
5. Y. K. Chow, D. M. Yong, K. Y. Yong, and S. L. Lee, 'Dynamic compaction analysis', *J. Soil Mech. Found. Div. ASCE*, **118**(8), (1992).
6. L. Menard and Y. Broise, 'Theoretical and practical aspects of dynamic consolidation', *Geotechnique*, London, **25**(1), 3–18 (1975).
7. G. A. Leonards, W. A. Cutter and R. D. Holtz, 'Dynamic compaction of granular soil', *J. Geotech. Eng. Div. ASCE*, **106**(1), 35–44 (1980).
8. J. Lysmer and F. E. Ricart, 'Dynamic response of footings to vertical loading', *J. Soil Mech. Found. Div. ASCE* **92**(1), 65–91 (1966).
9. M. H. E. I. Naggar and M. Novak, 'Non-linear model for dynamic axial pile response', *J. Soil Mech. Found. Div. ASCE*, **120**(2), 308–329 (1994).
10. M. Novak, T. Nogami and F. Aboul-Ella, 'Dynamic soil reactions for plane strain case', *J. Eng. Mech. Div. ASCE* **104**, EM4 953–959 (1978).
11. T. Ginsburg, 'Propagation of shock waves in the ground', *J. Soil Mech. Found. Div. ASCE*, **90**(1), 125–163 (1964).
12. B. R. Phillips and G. Y. Baladi, 'Results of two free-field code calculations versus field measurements for the distant plain 1A event', Misc. Paper S-73-21, U.S. Army Engr. Waterways Experiment Station, Vicksburg, Ms, 1973.
13. I. Nelson, 'Numerical solution of problems involving explosive loading, in 'Proc. Dynamic Methods in Soil and Rock Mechanics, Vol. 2: Plastic and Long Term Effects in Soils, A. A. Balkema, Rotterdam, The Netherlands, 1977.
14. O. C. Zienkiewicz, 'The Finite Element Method Vol. 2, McGraw-Hill New York.

**Discussion by S. Thilakasiri,<sup>7</sup> G. Mullins,<sup>8</sup>  
P. Stinnette,<sup>9</sup> and M. Gunaratne<sup>10</sup>**

The authors present a closed-form solution to predict impact stress in soil due to a falling weight using a linear-elastic

---

<sup>7</sup>Dept. of Civ. Engrg. and Mech., Univ. of South Florida, Tampa, FL 33620.

<sup>8</sup>Dept. of Civ. Engrg. and Mech., Univ. of South Florida, Tampa, FL.

<sup>9</sup>Dept. of Civ. Engrg. and Mech., Univ. of South Florida, Tampa, FL.

<sup>10</sup>Dept. of Civ. Engrg. and Mech., Univ. of South Florida, Tampa, FL.

spring and dashpot model. It should be noted that very similar models, such as those proposed by Scott and Pearce (1975) and Qian (1982), have previously been used to predict impact stresses in soil. However, the authors have advanced the mass-spring-dashpot model further by not overlooking the significance of overdamped and critically damped conditions, as opposed to Scott and Pearce (1975) and Qian (1982).

The discussers have also investigated the same problem, both analytically and experimentally. Accordingly, impact tests on soil were designed by the discussers to understand the effects of drop height, drop weight, and impact area on the contact stress. One series of tests in this experimentation involved dropping a 2.27 kg, 7.62 cm square drop hammer on compacted sandy soil from various drop heights. Stress measurements, recorded at a sampling rate of 10,000 Hz, were obtained using stress cells embedded in the surface of the hammer at the corners and center. The input parameters required to execute the authors' model, such as the shear wave velocity and Poisson's ratio, were back-calculated from the experimentally observed peak stress and contact time from the first trial of a previous test series on compacted sand. This prevented possible uncertainties in the precise measurement of the shear wave velocity, which is an important parameter in the authors' model. The values of shear wave velocity and Poisson's ratio were suitable for the compacted sand tested. These parameters were then utilized to predict the impact stresses and contact times for the consequent drops.

Fig. 19 shows the comparison of predicted peak stresses and those measured from experimentation, while Fig. 20 shows the stress-time history for the predicted and experimental stress for the 0.61 m drop. Although the peak stress and the contact time are predicted reasonably well, the shape of the curve, and hence the area under the curve vary significantly from the experimental results. This deviation, which invariably affects the prediction of the impulse applied to the ground, may be attributed to the deformations in the participating soil mass and the nonlinearity of soil even at low strains. As the authors

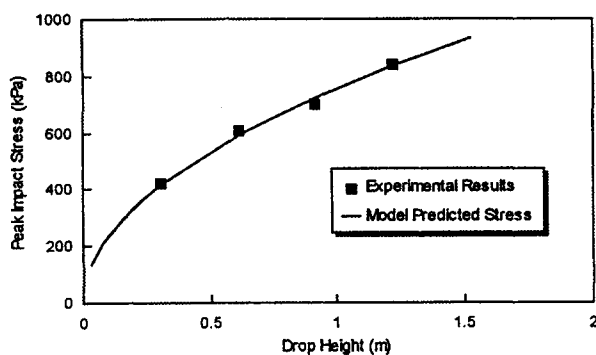


FIG. 19. Peak Stress versus Drop Height for 2.27 kg Drop Weight

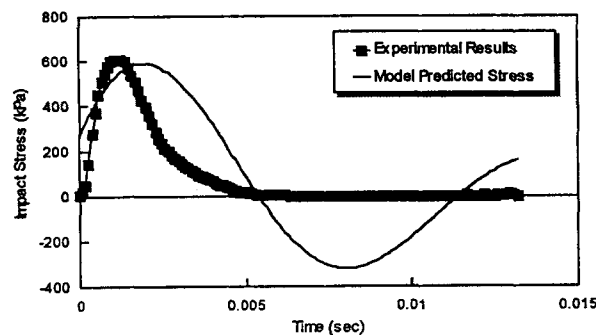


FIG. 20. Stress-Time History for 2.27 kg Drop Weight with 0.61 m Drop Height

point out, the contact time is comparable to the travel time of waves within the participating soil mass; however, the extent of the participating soil mass changes during the contact time thereby changing the parameters related to the soil half-space during that time period. Fig. 20 also indicates that the initial damping stress predicted by the authors' model is not observed in the tested soil. Similar discrepancies were reported by Scott and Pearce (1975) and Qian (1982).

The writers, on the other hand, had to formulate a nonlinear spring and dashpot model to explain the experimental observations (Thilakasiri et al. 1994). However, the complexity involved in a more realistic model certainly prohibits a closed-form solution such as that presented by the authors.

Furthermore, in most cases, drop weights permanently deform the ground surface. Nonlinear models such as the one formulated by the writers are needed to predict the permanent ground indentation. This limits the applicability of the authors' model to situations involving a low energy impact on a relatively stiff soil, which is certainly not illustrated by the example provided in the paper where a 125.7 kg weight is dropped from 5 m on a stiff soil. Moreover, the contact stress of 6,000 kPa produced in the authors' example is likely to induce a bearing capacity failure in the soil, thus invariably exceeding the limiting strain levels for elastic behavior.

Generally, elastic total stress techniques are also inadequate for saturated or partially saturated soils where pore pressure generation and dissipation govern the soil behavior under dynamic conditions. Within the limitations described previously, the authors' analytical model does provide an accurate closed-form prediction of the magnitude of peak stress induced by a rigid mass dropped on soil.

## APPENDIX. REFERENCES

- Qian, J. H. (1982). "Dynamic consolidation from practice to theory." *8th Asian Regional Conf. on Soil Mech. and Found. Engrg.*, Japanese Soc. for Soil Mech. and Found. Engrg., 2, 213-217.
- Scott, R. A., and Pearce, R. W. (1975). "Soil compaction by impact." *Géotechnique*, London, England, 25(1), 19-30.
- Thilakasiri, S., Mullins, G., Stinnette, P., Gunaratne, M., and Jory, B. (1994). "Investigation of impact stresses induced in laboratory dynamic compaction of soft soil." Under rev. by the *Int. J. for Analytical and Numer. Methods in Geomech.*

Closure by Jose M. Roesset,<sup>11</sup>  
Member, ASCE, Eduardo Kausel,<sup>12</sup>  
Member, ASCE, Vicente Cuellar,<sup>13</sup>  
Jose L. Monte,<sup>14</sup> and Julian Valerio<sup>15</sup>.

The writers wish to thank the discussers for bringing to their attention some earlier works containing additional material relevant to the topic at hand, of which they were not aware. Of these, only the paper by Scott and Pearce (1975) is readily available to us for immediate consultation. We are also indebted to the discussers for presenting some actual test results for drop masses, which they used to highlight aspects where simple models fall short.

We are impressed by Thilakasiri et al.'s excellent agreement

<sup>11</sup>Prof., Dept. of Civ. Engrg., Univ. of Texas, Austin, TX 78712.

<sup>12</sup>Prof., Dept. of Civ. Engrg., Massachusetts Inst. of Technol., Cambridge, MA 01239.

<sup>13</sup>Head, Geotech. Engrg. and Testing Div., CEDEX, Alfonso XII-3, 28014 Madrid, Spain.

<sup>14</sup>Head, Special Testing Program, CEDEX, Alfonso XII-3, Madrid, Spain.

<sup>15</sup>Head, Dynamic Methods Program, CEDEX, Alfonso XII-3, Madrid, Spain.



## Study of Pore Pressures Induced in Laboratory Dynamic Consolidation

M. Gunaratne, M. Ranganath, S. Thilakasiri, G. Mullins,  
P. Stinnette & C. Kuo<sup>†</sup>

Department of Civil and Environmental Engineering, University of South Florida, Tampa,  
FL 33620, U.S.A.

(Received 28 July 1994; revised version received 8 December 1994; accepted 14 February 1995)

### ABSTRACT

*Knowledge of the pore pressure behavior during dynamic impacts on moderately low permeability soils is essential in averting possible liquefaction and effective field implementation of dynamic consolidation. Although field observations of dynamically induced pore pressures are abundant in the literature, analytical or numerical approaches for pore pressure prediction are scarce. Herein, the authors advance a simple technique to analytically model the laboratory dynamic consolidation by modifying the classical Terzaghi's static consolidation theory. Since the analytical prediction of dynamic surface stress and experimental verification are performed in a companion paper, the surface stress due to a dynamic impact is assumed to be known in this work. Then, the time dependent stress pulse is de-synthesized into a number of constant load steps to predict the subsequent pore pressure behavior. Since this methodology accounts for even the dynamic stress attenuation within the soil sample, a rigorous closed form solution has to be replaced by a numerical solution. It is shown how this solution rapidly converges when the load steps are made sufficiently small. Finally, the analytical predictions of dynamic pore pressure are verified by well controlled laboratory experiments performed on a special apparatus set up at the University of South Florida.*

### INTRODUCTION

Since its first introduction by Menard, dynamic consolidation has been successfully applied in stabilizing soils with poor drainage and consolidation properties. In spite of the extensive field application, analytical or numerical

<sup>†</sup>Formerly District Geotechnical Engineer, Florida Department of Transportation, Bartow, FL.

methods to predict the rate of pore pressure dissipation are scarce in the literature. One reason for this may be the inability to adequately address the dynamically induced stress problem in its entirety.

In a companion paper [1], the authors describe their analytical model to predict the dynamic surface stresses observed in laboratory dynamic consolidation. Therefore, in the work presented here, the investigation is extended to explore the pore pressure behavior due to such dynamic impacts on relatively impervious soil. The authors also experimentally show that the dynamic stress attenuation with depth is in close agreement with the static elastic stress distribution. Due to the analytical complexity involved in predictions at off-centerline positions, the current investigation is limited to the locations on the load centerline where the most severe condition of pore pressure is registered on any horizontal plane. It is also theoretically shown that drainage can be expected to be vertical under the centerline of the impact especially close to the impact region. Hence, a modified version of Terzaghi's 1-D consolidation equation is utilized to predict the induced pore pressure behavior based on a load step method.

It is also shown how the numerical solution can be made to rapidly converge by considering sufficiently small load steps. Finally, the numerical predictions are compared to the results of an experimental setup developed at the University of South Florida.

## DYNAMIC SURFACE STRESS

Several researchers have attempted to analytically examine the surface stresses induced during dynamic compaction. Scott and Pierce's [2] approach using basic stiffness and damping properties of the soil and Mayne and Jones' [3] technique based on the deceleration of the hammer during penetration are some of them. The former researchers predict a dynamic stress pulse producing a significant initial stress value due to the instantaneous damping. However, early experimental observations within the soil mass have revealed no such initial instantaneous stress value [2,3]. On the other hand, Mayne and Jones [2] introduced an analytical approach which complies with the experimental observation of a zero initial stress.

One drawback of the latter approach is that it does not model the continued but less severe stress pulses observed in more recent laboratory studies conducted by the authors utilizing stress cells placed at different locations in the sample. Moreover, the authors' tests indicate very high initial instantaneous stresses close to the surface especially under saturated conditions. In the companion paper [1], the authors address the shortcomings of the aforementioned theories by advancing a new analytical approach that can explain

the observed dynamic stress history and the vibration behavior of the soil upon dynamic impact, addressing the shortcomings of the aforementioned theories. Hence, in this paper, the discussion is limited to the pore pressure predictions using the dynamic stresses observed in the authors' experiments (Fig. 1).

### DISTRIBUTION OF STRESSES BELOW THE IMPACT SURFACE

During their experimental program, the authors conducted a series of experiments to investigate the dynamic stress attenuation. Both the vertical and horizontal stress distributions below the impact center were seen to be in agreement with the elastic theory. Figure 2 exhibits a comparison of stress distributions from the authors' results and other experimental evidence, with the elastic theory.

Thus, if  $\Delta\sigma_0$  is the contact dynamic stress developed under a falling weight of radius  $r_0$ , then the vertical stress at any depth  $z$  vertically below the center of the weight can be expressed using elastic theory as:

$$\Delta\sigma_v = \Delta\sigma_0 \left[ 1 - \frac{1}{[1 + (r_0/z)^2]^{3/2}} \right] \quad (1)$$

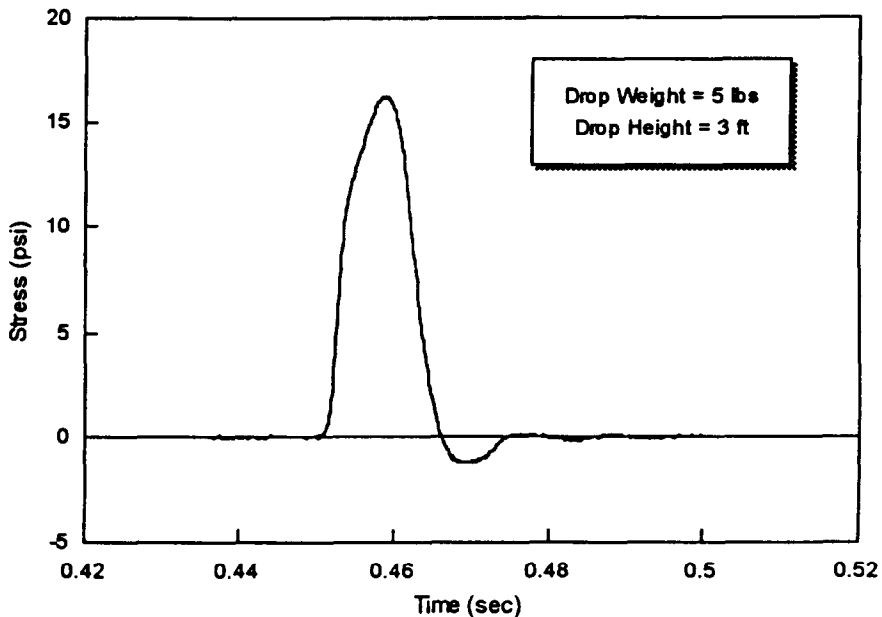


Fig. 1. Impact stress measured at a depth of three (3) inches.



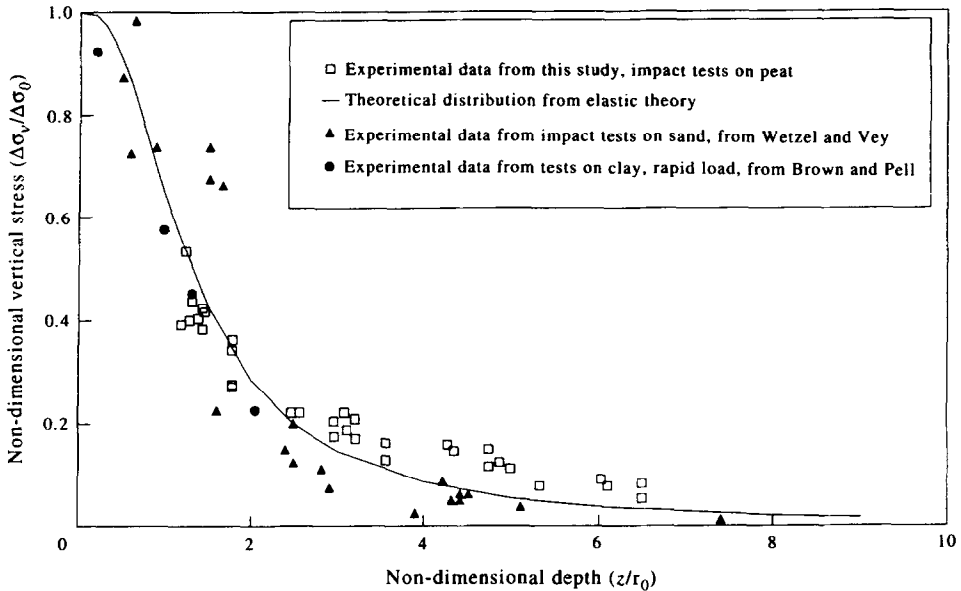


Fig. 2. Comparison of dynamic vertical stress distribution with elastic predictions.

## DRAINAGE CONDITIONS

On impact, the pore pressure will increase instantaneously under the hammer inducing drainage in the radial and vertical directions. However, if a water particle is considered at any depth beneath the center of the weight, under isotropic soil conditions, clearly it cannot acquire a velocity in any preferential radial direction due to symmetry. Hence, the pore pressure variation contributing to the response of a transducer placed at any location under the centerline of the impact is theoretically a result of the vertical drainage only. This is especially the case when the observation point is located in the vicinity of the surface. This fact can be mathematically illustrated as follows.

Consider the volumetric changes induced by the drainage conditions due to a centerline radial velocity of  $v$  and a vertical velocity of  $u$  as shown in Fig. 3. If the net flow out of the element having a radius of  $dr$  is equated to the volume reduction in the element, one would obtain the following expression:

$$\pi(dr)^2 \left[ \frac{\partial u}{\partial z} dz + u - u \right] + 2\pi(dr)(dz) \left[ v + \frac{\partial v}{\partial r} dr \right] = -\frac{1}{1+e} \frac{\partial e}{\partial t} [\pi(dr)^2 dz]$$

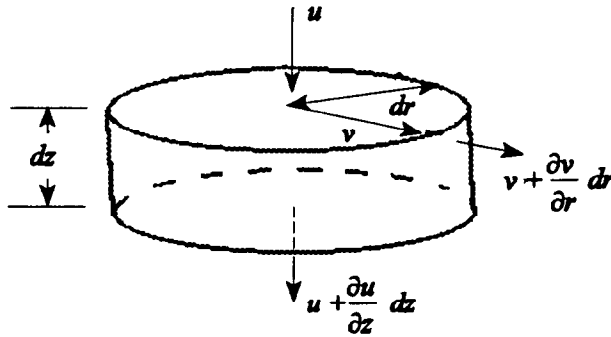


Fig. 3. Consolidation of a small cylindrical element.

which when simplified produces

$$\frac{\partial u}{\partial z} dr + 2v + 2 \frac{\partial v}{\partial r} dr = - \frac{1}{1-e} \frac{\partial e}{\partial t} dr$$

It is seen that as the radius  $dr$  becomes smaller, the centerline radial velocity  $v$  approaches zero.

The above conclusion can be further verified by theoretically illustrating that there is no radial pore pressure gradient on the centerline. As it will be shown later [eqn (13)], the instantaneous pore pressure generated at any depth  $z$  ( $u_z$ ) is proportional to the total vertical stress induced at that depth ( $\Delta\sigma_z$ ). On the other hand, the authors extended their dynamic stress monitoring program to obtain the radial distribution of  $\Delta\sigma_z$  as well, as shown in Fig. 4. Hence, the radial distribution of pore pressure ( $u_z$ ) will also be a similar distribution. It is obvious from Fig. 4 that:

$$\left[ \frac{\partial(\Delta\sigma_z)}{\partial r} \right]_{r=0} = 0$$

thus it follows that:

$$\left[ \frac{\partial u_z}{\partial r} \right]_{r=0} = 0$$

which supports the assumption of no radial drainage conditions on the centerline. Furthermore, since the radial pore pressure gradient increases only gradually as  $r$  increases (Fig. 4), it is also reasonable to assume that the radial flow is insignificant even in the immediate neighborhood of the centerline. Accordingly, in the testing program, the authors utilized a very fine

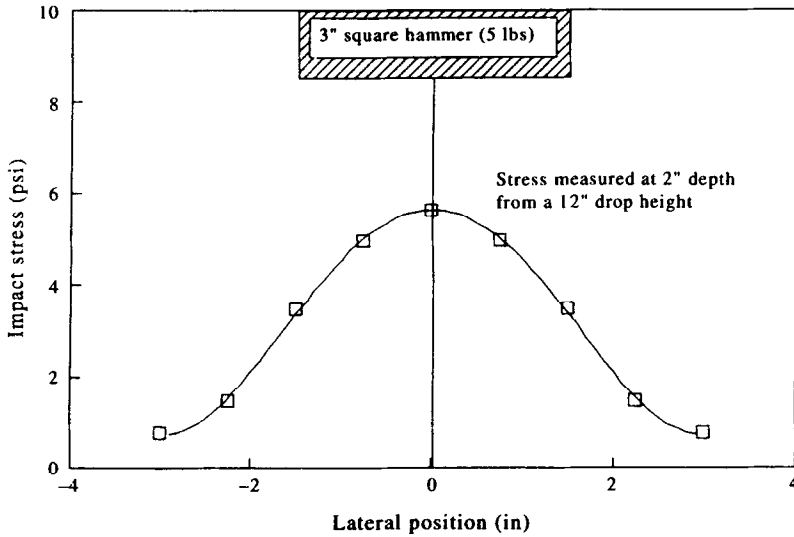


Fig. 4. Vertical stress variation with lateral ( $r$ ) position.

pore pressure probe with a negligible diameter compared to the base width of the drop weight, to monitor the pore pressure at the centerline.

As for the boundary conditions, a free draining boundary is assumed at the top of the compacting soil layer while the bottom of the soil layer or the transducer soil interface is assumed to be perfectly impervious.

### PORE PRESSURE MODEL

Under 1-D drainage conditions, the pore pressure dissipation in a saturated medium at any depth  $z$  due to a constant load can be analyzed starting from the following initial step of Terzaghi's formulation [4]:

$$\frac{a_v}{(1+e)} \frac{\partial \sigma'}{\partial t} = -\frac{k}{\gamma_w} \frac{\partial^2 u}{\partial z^2} \quad (2)$$

where  $a_v$ ,  $k$  and  $e$  are the compressibility of the soil skeleton, the hydraulic conductivity and the void ratio of the soil, respectively.

If the water compressibility is assumed to be  $C_w$ , unlike in Terzaghi's formulation where it is neglected, the water pressure and the total stress can be introduced to the above equation as:

$$\frac{a_v}{(1+e)} \left[ \frac{\partial \sigma}{\partial t} - \frac{\partial u}{\partial t} \right] - \frac{e}{1+e} C_w \frac{\partial u}{\partial t} = -\frac{k}{\gamma_w} \frac{\partial^2 u}{\partial z^2} \quad (3)$$

The above expression can be simplified to

$$\frac{\partial u}{\partial t} \left( 1 + \frac{eC_w}{a_v} \right) - \frac{\partial \sigma}{\partial t} = C_v \frac{\partial^2 u}{\partial z^2} \quad (4)$$

which is a general 1-D consolidation equation, applicable for static as well as dynamic loading, and  $C_v$  is the coefficient of consolidation of the soil. Under a static total stress (no variation of total stress with time) and negligible water compressibility, eqn (4) simplifies to the classical Terzaghi's 1-D consolidation equation which expresses solely the dissipation behavior of pore pressure with no generation.

$$\frac{\partial u}{\partial t} = C_v \frac{\partial^2 u}{\partial z^2} \quad (5)$$

On the other hand, for undrained loading or unloading conditions which can be simulated by setting the hydraulic conductivity  $k$  or  $C_v$  to zero, eqn (4) reduces to:

$$\frac{\partial u}{\partial t} \left( 1 + \frac{eC_w}{a_v} \right) = \frac{\partial \sigma}{\partial t}$$

which can be rearranged in the more common form as

$$\frac{\partial u}{\partial t} = B \frac{\partial \sigma}{\partial t} \quad (6)$$

where  $B$  is the Skempton's pore pressure parameter relevant to isotropic stress increments as expressed below.

$$B = \frac{1}{(1 + eC_w/a_v)} \quad (7)$$

In fact, it can be shown using the generalized Hooke's law that the stress condition is isotropic for 1-D undrained loading which induces zero strains in all directions. It is noted that eqn (6) is applicable to generation of pore pressure without any dissipation.

By blending  $B$  with  $C_v$ , eqn (4) can be rewritten as:

$$\frac{\partial u}{\partial t} = B \frac{\partial \sigma}{\partial t} + C_v \frac{\partial^2 u}{\partial z^2} \quad (8)$$

From the above discussion, it is obvious that eqn (8) encompasses both pore pressure generation and dissipation components during dynamic loading.

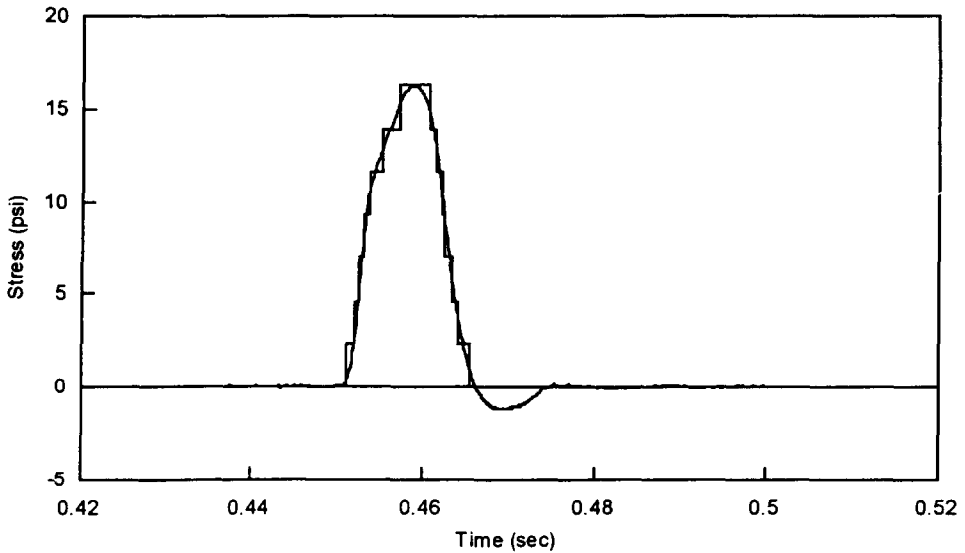


Fig. 5. Approximation of dynamic loading with constant stress increments.

This can be further illustrated by applying eqn (8) during a time interval  $\Delta t$  to depict the individual magnitudes of the pore pressure components at any depth  $z$  as:

$$\Delta u = B\Delta\sigma + \left( C_v \frac{\partial^2 u}{\partial z^2} \right) \Delta t \quad (9)$$

The above concept is utilized in the ensuing formulation to isolate the generation and dissipation components of pore pressure during sufficiently small time intervals (Fig. 5). In summary, the pore pressure generation is treated as a boundary condition by utilizing eqn (6) and the dissipation during the same time is expressed by Terzaghi's expression in eqn (5).

### SOLUTION OF PORE PRESSURE EQUATION

Since the vertical stress has been experimentally verified to be distributed according to elastic theory, the classical Terzaghi solution which is valid for uniform or linear vertical stress distributions has to be replaced by a fresh solution. A solution of the following general form is possible for eqn (5).

$$u = (P \cos Az + Q \sin Az) e^{Dt} \quad (10)$$

By substitution in eqn (5), one finds that,

$$D = -A^2 C_v$$

Hence eqn (10) can be modified to,

$$u = (P \cos Az + Q \sin Az) e^{-A^2 C_v t} \quad (11)$$

At this stage, the previously discussed spatial boundary conditions can be utilized as follows:

*Free draining surface at the top*

$$u = 0 \quad \text{at} \quad z = 0 \quad \text{for} \quad t > 0^+$$

*Rigid boundary at the bottom*

$$\frac{\partial u}{\partial z} = 0 \quad \text{at} \quad z = H$$

to find expressions for  $P$  and  $A$  as:

$$P = 0$$

and

$$A = (2n - 1) \frac{\pi}{2H}$$

where  $n$  is any integer. This modifies the solution in eqn (11) to

$$u_{z,t} = \sum_{n=1}^{\infty} Q_n \sin \left[ (2n - 1) \frac{\pi}{2H} z \right] e^{-[(2n-1)\pi/2]^2 T} \quad (12)$$

where

$$T = \frac{C_v t}{H^2}$$

If the soil medium is saturated, the initial pore pressure  $u_z$  at any point below the impact center due to a total stress increase  $\Delta\sigma_z$  can be expressed using eqn (6) as:

$$u_z = B \Delta\sigma_z \quad (13)$$

Substituting from eqn (1) in the above equation, a third boundary condition for  $t = 0$  can be written as:

$$u_{z,0} = \Delta\sigma_0 B \left[ 1 - \frac{1}{[1 + (r_0/z)^2]^{3/2}} \right] \quad (14)$$

At  $t = 0^+$ , eqn (12) becomes

$$u_{z,0} = \sum_{n=1}^{\infty} Q_n \sin\left[(2n-1)\frac{\pi}{2H}z\right] \quad (15)$$

By comparing eqns (14) and (15),  $Q_n$  can be found using the Fourier half-range expansion as:

$$Q_n = \frac{2}{H} \int_0^H u_{z,0} \sin\left[(2n-1)\frac{\pi z}{2H}\right] dz \quad (16)$$

In order to extend the above concepts to the dynamic stress increment shown in Fig. 1, the latter was considered as being composed of a series of equal positive stress increments  $i$  ( $i = 1, m_1$ ) of magnitude  $\Delta\sigma_0$  (or  $Q_{\max}/m_1$ ) imposed at time  $t_i$  followed by a similar series of negative stress increments  $i$  ( $i = m_1 + 1, m_2$ ) of the same magnitude (Fig. 5). It is realized that this approximation should yield the exact dynamic solution at the limit where the stress increment,  $\Delta\sigma_0$ , approaches zero. However, one limitation of this approach is that it does not account for the time lag between the actual impact and the arrival of the consequent stress wave at the considered depth  $z$ , as stress and pore pressure increments at that depth [eqn (14)] are considered to be static.

According to eqns (12), (14) and (16), the pore pressure variation in space and time due to the first total stress increment  $\Delta\sigma_0$  imposed at the time  $t_1$ , can be expressed as,

$$u_{z,t} = \frac{2B\Delta\sigma_0}{H} \sum_{n=1}^{n=\infty} \left[ \int_0^H k(z) \sin \frac{Nz}{H} dz \right] \sin \frac{Nz}{H} e^{-\frac{c_v N^2}{H^2}(t-t_1)} \quad (17)$$

where

$$k(z) = \left[ 1 - \frac{1}{[1 + (r_0/z)^2]^{3/2}} \right]$$

and

$$N = (2n-1)\pi/2$$

Therefore, the pore pressure distribution at a subsequent time  $t$  due to all of the increments up to  $t_{m1}$  can be expressed as

$$u_{z,t} = \frac{2B \cdot \Delta\sigma_0}{H} \sum_{n=1}^{n=\infty} \left[ \int_0^H k(z) \sin \frac{Nz}{H} dz \right] \sin \frac{Nz}{H} \sum_{i=1}^{m_1} e^{-\frac{C_v N^2}{H^2}(t-t_i)} \quad (18)$$

Similarly, the pore pressure distribution at any time  $t$  due to a load removal of equal magnitude at a time  $t_j$  ( $> t_{m1+1}$ ) will be:

$$u_{z,t} = \frac{B^* \cdot 2 \cdot \Delta\sigma_0}{H} \sum_{n=1}^{n=\infty} \left[ \int_0^H k(z) \sin \frac{Nz}{H} dz \right] \sin \frac{Nz}{H} e^{-\frac{C_v^* N^2}{H^2}(t-t_j)} \quad (19)$$

where  $C_v^*$  represents the coefficient of swelling (reverse consolidation) and  $B^*$  is the isotropic pore pressure parameter [eqn (7)] relevant to unloading. From the basic definition of the coefficient of consolidation, it can be shown that

$$\frac{C_v}{C_v^*} = \frac{a_v^*}{a_v} = r$$

where

$$\begin{aligned} a_v^* &= \text{coefficient of recompression} \\ a_v &= \text{coefficient of compression} \end{aligned}$$

and thus  $r$  is a factor representing the ratio of the soil compressibilities ( $a_v$ ) under unloading and loading.

Since eqn (7) exhibits that a difference in  $a_v$  values in loading and unloading should reflect a corresponding difference in the  $B$  parameter as well, another factor  $R$  can be defined to account for the difference in the pore pressure parameter during loading and unloading as

$$R = \frac{B^*}{B}$$

Finally, the pore pressure variation for the combination of the loading and unloading sequence (Fig. 5) is determined by the following equation:

$$u(z, t) = \frac{2B \cdot R \cdot \Delta\sigma_0}{H} \sum_{n=1}^{n=\infty} \left[ \int_0^H k(z) \sin \frac{Nz}{H} dz \right] \sin \frac{Nz}{H} \sum_{i=1}^{m_2} e^{-\frac{r C_v N^2}{H^2}(t-t_i)} \quad (20)$$

under conditions stated below:



*Positive stress increase*

$$\text{If } i \leq m_1, \text{ then } R = 1, r = 1$$

*Negative stress increase*

$$\text{If } i > m_1, \text{ then } \Delta\sigma_0 = -\Delta\sigma_0$$

A computer program was written to execute eqn (20) and determine the variation of pore pressure with time due to a single impact. In order to illustrate that the numerical solution rapidly converges to what can be assumed to be the exact dynamic solution when  $\Delta\sigma$  approaches zero, a hypothetical pore pressure distribution due to the stress history in Fig. 1 is predicted and plotted for different magnitudes of stress increments ( $\Delta\sigma_0 = 2.11, 4.23$  and  $8.46$ ) in Fig. 6.

The following data have been used in the example:

Coefficient of consolidation	=	0.002 in. <sup>2</sup> /s
Depth of soil sample	=	3 in.
Base diameter of weight	=	3.4 in.
$R$	=	0.95
$r$	=	1.3
$B$	=	0.95

Moreover, the authors utilized the above computer program to perform a parametric study of the impact of  $C_v$  on the dissipation of pore pressure

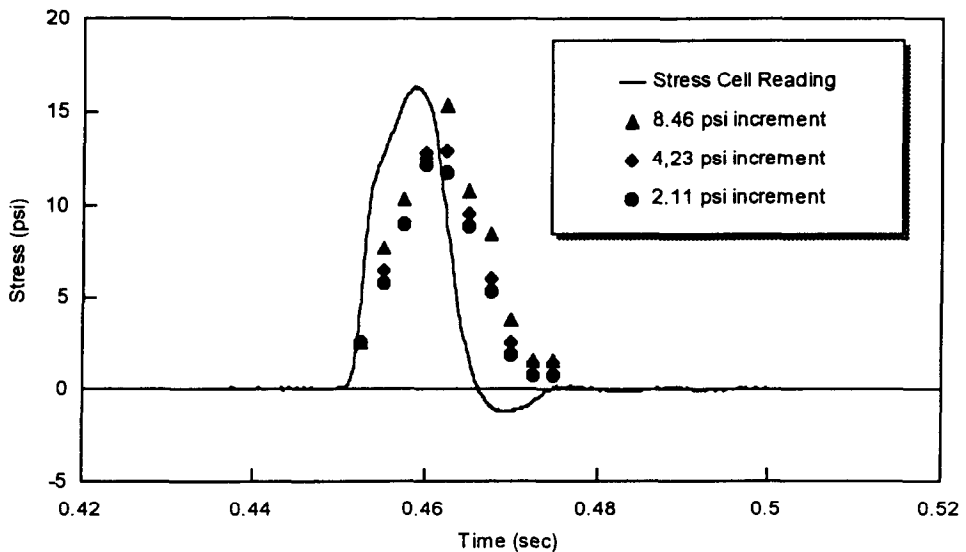


Fig. 6. Convergence of numerical solution with small stress increments.

during the short impulse stress duration. From the results, it was concluded that the need for “coupled analysis” [eqn (9)] clearly depends on the magnitude of the coefficient of consolidation,  $C_v$  and hence indirectly on the hydraulic conductivity,  $k$ . As one would expect, the authors also found that  $C_v$  values corresponding to coarse grained soils do not allow significant pore pressure generation, whereas  $C_v$  values that represent clayey soils typically exhibit undrained behavior during impact loading. Hence, consideration of pore pressure dissipation during the impact stress is unnecessary for the above soil types. However, the numerical values revealed that modeling of dissipation is essential for moderately pervious soils (with approximately  $10^{-2} > C_v > 10^{-4}$  in.<sup>2</sup>/s).

As illustrated in the following section on experimental verification,  $C_v$  value for the organic soil tested in this research was approximately 0.002 in.<sup>2</sup>/s. This value yields an equivalent hydraulic conductivity of  $10^{-5}$  cm/s from the following basic relationship:

$$C_v = \frac{k(1 + e)}{a_v \gamma_w}$$

The coefficient of compressibility ( $a_v$ ) and void ratio ( $e$ ) values were obtained from the authors' previous work on this organic soil [5]. Although the above  $k$  value indicates a “moderately” low permeability, it does not fall in the range of much more impervious clayey soils ( $k < 10^{-6}$ – $10^{-7}$  cm/s) which are known to exhibit typical undrained behavior. Classification tests on the tested organic soil also supported the above determination, since it was found to consist of a coarse grained mineral fraction mixed with 50–80% mostly amorphous organic matter. Even experimentally, all of the monitored impacts on this organic soil revealed partially drained behavior under impact loading. Hence, it can be concluded from the computational and experimental results that the assumption of “undrained” behavior is too idealistic for moderately low permeability soils.

## EXPERIMENTAL VERIFICATION

The experimental set-up shown in Fig. 7 was used to simulate dynamic consolidation in the laboratory. A 5 lb weight having a 3 in. square base was held by an electro-magnet the height of which was adjustable along the length of a support. A switching relay was used to simultaneously release the weight from the electro-magnet and initiate a computerized data acquisition system. The impact stress history was registered by means of a stress cell attached to the base of the drop weight.

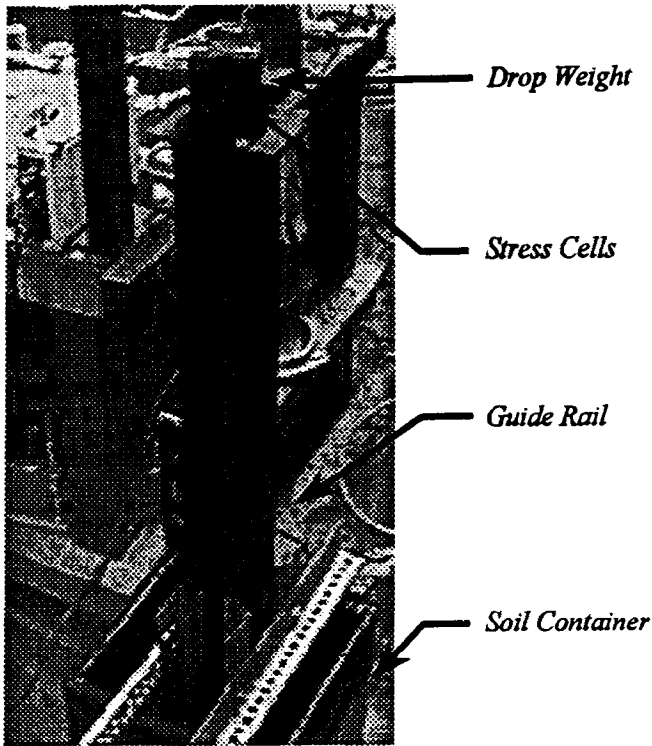


Fig. 7. Dynamic impact apparatus.

The soil sample was prepared in a one cubic foot container. The container (Fig. 7) was placed below the weight so that the weight would impact the soil directly above the pore pressure transducer. Before performing each test, the position of the container was clearly marked on the ground to achieve this condition. Then, the box was filled with an organic soil having a relatively low hydraulic conductivity up to the required height and compacted using a vibratory process which also insured higher saturation. After the pore pressure transducer connections were saturated with water, the surface stress and the pore pressure variation at the bottom of the sample were monitored by the data acquisition system.

The most commonly used values for  $A$  and  $B$  parameters in organic soils are 0.65 and 1.0, respectively [6]. The authors verified the above values using conventional triaxial testing. The stress cell reading indicating the dynamic surface stress and the pore pressure variation at the bottom plate initially placed one (1.0) inch below the impact is plotted in Fig. 8. The final clearance between the weight and the bottom plate after the impact induced penetration was 0.69 in. as indicated. The corresponding pore pressure variation

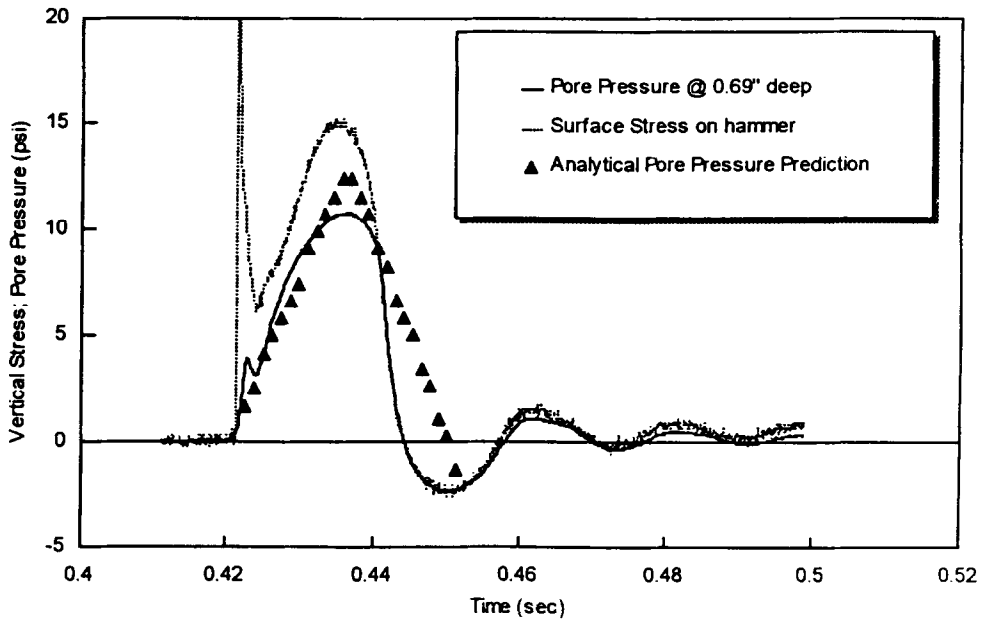


Fig. 8. Comparison of predicted and measured pore pressure variation.

predicted from the stress cell reading using the authors' theoretical formulation is also depicted in Fig. 8 for comparison. An initial depth of 1 in. was selected to obtain a significant pore pressure response in the transducer and to ensure that the centerline drainage is mostly vertical as stipulated in the analysis. The average  $C_v$  value of the organic soil was determined from separate laboratory consolidation tests to be approximately  $0.002 \text{ in.}^2/\text{s}$  using the Casagrande's fitting method.

The slight deviation of the predictions from the measurement can be attributed to two main reasons. A number of consolidation tests performed on the same organic material yielded a range of  $C_v$  values indicating the sensitivity of this parameter to sample preparation, natural texture and the stress level. Thus, the average  $C_v$  value used in the prediction may not have accurately represented that of the sample tested. Secondly, the measurement depth varied from an initial value of 1 in. to a final value of 0.69 in. thereby introducing some uncertainty in the actual depth to be used in eqn (1). The authors chose to use an average depth of 0.85 in. for this prediction.

## CONCLUSIONS

A procedure was developed to predict the variation of pore pressure directly beneath the impact location during laboratory dynamic consolidation,

using a known dynamic contact stress. The technique was based on substituting a step-wise varying function for the dynamic stress history. When the stress steps are made sufficiently small, the numerical solution is shown to converge rapidly. An important feature of this formulation is that it can accommodate the possible differences in the soil compressibility under loading and unloading conditions. Furthermore, the vertical distribution of dynamic stress within an organic soil is experimentally shown to follow the predictions of the elastic theory thus confirming the same conclusion reached by previous researchers for other soil types.

As anticipated, a computational parametric study resulting from the developed numerical model clearly exhibited that the time variation of induced pore pressure is predominantly dependent on the coefficient of consolidation or the hydraulic conductivity of the treated soil. Within the short duration of the impact load, free draining soils with relatively high  $C_v$  values show no significant pore pressure development while impervious soils with much lower  $C_v$  values behave in an undrained fashion. Thus, the presented theoretical model is useful for moderately impervious soils such as this amorphous organic soil which induce partial drainage under dynamic loading. The authors also found other published research on field dynamic consolidation [7] in which the *in situ* soil types have been distinctly characterized as pervious, semi-pervious and impervious, depending on the monitored pore pressure behavior.

Finally, the authors demonstrated that the laboratory pore pressure measurements reasonably corroborate the analytical procedure in terms of the pore pressure magnitude and the dissipation time. Hence, it is concluded that the pore-pressure model presented in this paper is adequate to predict the dynamic pore pressure behavior of semi-pervious (moderately low permeability) soils.

## REFERENCES

1. Thilakasiri, S., Mullins, G., Stinnette, P., Gunaratne, M. & Jory, B., Analytical and experimental investigation of dynamic compaction induced stresses. To be published in *Int. J. Numer. Anal. Meth. Geomech.*
2. Scott, R. A. & Pearce, R. W., Soil compaction by impact. *Geotechnique*, **25**(1), (1975) 19–30.
3. Mayne, P. W. & Jones, J. S. Jr, Impact stresses during dynamic compaction. *J. Geotech. Engng Div.*, **109**(10), (1983) 1342–1346.
4. Holtz, R. & Kovacs, R., *An Introduction to Geotechnical Engineering*. Prentice-Hall, Englewood Cliffs, NJ, 1981.
5. Gunaratne, M., Stinnette, P., Mullins, G., Kuo, C. & Echelberger, W., Compressibility relations for Florida organic soils. Submitted to *Can. Geotech. J.*
6. Andersland, O. B., Khattak, A. S. & Al-Khafaji, A. W. N., Effect of organic material on soil shear strength. *Laboratory Shear Strength of Soil*, ASTM STP 740, 1981.

7. FHWA, *Dynamic Compaction for Highway Construction, Vol. I, Design and Construction Guidelines*. FHWA/RD 86-/133, 1986.
8. Wetzel, R. A. & Vey, E., Axisymmetric stress wave propagation sand. *J. Soil Mech. Foundation Div., ASCE*, **96**(SM5), (1970) 1763–1786.
9. Brown, S. F. & Pell, P. S., Subgrade stress and deformation under dynamic load. *J. Soil Mech. Foundation Div., ASCE*, **93**(SM1), Proc. Paper 5057 (1967) 17–46.

## FIELD MEASUREMENT OF TRANSFER LENGTH

Rajan Sen<sup>1</sup>, Jose Rosas<sup>2</sup>, Gray Mullins<sup>1</sup>, Larry Liby<sup>3</sup>, Satya Sukumar<sup>4</sup> and Ken Spillet<sup>5</sup>

<sup>1</sup> Department of Civil & Environmental Engineering, University of South Florida, Tampa, FL

<sup>2</sup> David Volkert & Associates, Tampa, FL, formerly graduate student, University of South Florida, Tampa, FL

<sup>3</sup> Department of Civil Engineering, University of Texas, Austin, TX, formerly graduate student, University of South Florida, Tampa, FL

<sup>4</sup> American Consulting Engineers PLC, Land O'Lakes, FL, formerly graduate student, University of South Florida, Tampa, FL

<sup>5</sup> Parsons Brinckerhoff Construction Services, Atlanta, GA, formerly graduate student, University of South Florida, Tampa, FL

**Abstract:** Five aramid fiber reinforced plastic (AFRP) and five carbon fiber reinforced plastic (CFRP) beams, cast in adjacent 122 m beds in a commercial pretensioning facility, were field instrumented to determine their transfer length. The rods were jacked to 55% and 60% of the characteristic strength of the AFRP and CFRP material respectively. A total of twelve strain gages - five at each end and two in the middle - were attached to the top surface of the beams. The prestressing force in the rods was monitored using load cells located at the live and dead ends. Following release, concrete strains were recorded by a computerized data acquisition system. Reconciliation of test results with finite element analysis indicated that the transfer lengths for the sand coated AFRP rod and the grit coated CFRP rod were very similar - equal to about 30 times the rod diameter - in broad agreement with results reported previously.

**Keywords:** Aramid, ARAPREE, AFRP, beam, carbon, CFRP, field, finite element analysis, FRP, grit coated, kevlar, pretensioned, sand coated, transfer length

### Introduction

Transfer length is the length at the end of pretensioned members over which the prestressing force is transferred to the concrete. Because large eccentricities are the norm in prestressing, high tensile stresses develop at release. Since the transfer length determines the location where these stresses must be checked, knowledge of its magnitude is of obvious importance.

In 1992, the University of South Florida, Tampa, FL utilized commercial prestressing facilities to cast a total of 33 aramid fiber reinforced plastic (AFRP) and 33 carbon fiber reinforced plastic (CFRP) beams that were used in a long term durability study. The beams were cast side-by-side in adjacent 122 m prestressing beds normally used for fabricating 25 cm x 25 cm piles, by inserting appropriately sized wood forms. The opportunity was also taken to instrument five AFRP and five CFRP beams to determine their transfer length. This paper presents the results obtained from this study.

## Experimental program

### Materials

Circular AFRP and CFRP rods were used for pretensioning the test specimens. The material properties of these rods and the target jacking force, as given by their manufacturers, are listed in Table 1.

Table 1. Short term properties of AFRP and CFRP rods.

Property	AFRP	CFRP
Diameter, mm	5.7	5.8
Breaking Load, kN	33.7	43.0
Ultimate Tensile Stress, MPa	3,000 <sup>†</sup>	2,250
Elastic Modulus, GPa	125-130 <sup>†</sup>	121
Failure Strain, %	2.3	1.5
Jacking Force (% of ultimate)	55	60

<sup>†</sup> Values relate to the effective fiber cross-section

The surface of the AFRP rods, tradename ARAPREE, had sand particles impregnated to improve its bond with concrete. The surface of the CFRP rod (manufactured by NDI, the Netherlands) was similarly provided with a special grit finish.

### Fabrication

The beams fabricated were 114 mm x 150 mm in cross-section. Each beam was pretensioned with two AFRP or two CFRP rods at an eccentricity of 50 mm. The length of the beam was 2.44 m to match the size of available plywood sheeting. A complete description of the fabrication is presented elsewhere [1].



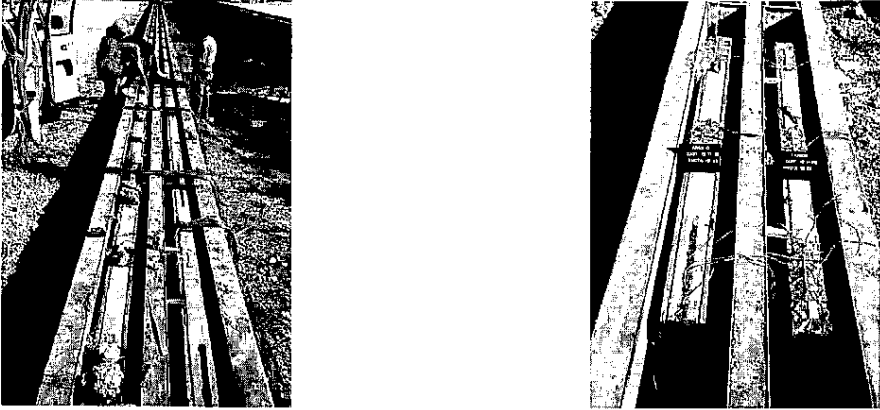


Figure 1. (Left) Overview of field instrumentation for transfer length. (Right) Instrumentation of adjacent AFRP and CFRP beams.

### Instrumentation

The logistics involved in outdoor experimentation limited the number of beams that could be instrumented. The two most important constraints were the number of strain gage channels available in the data acquisition system and the length of wiring needed. Based on these considerations, only five of the thirty three AFRP and CFRP specimens cast could be instrumented.

The *location* of the AFRP and CFRP specimens in the prestressing bed was the primary basis for selecting specimens for instrumentation. *Adjacent* AFRP and CFRP specimens were selected (see Figure 1) to allow the same wires to be used for measuring strains in either beam.

Since load cells were mounted at both the live and dead ends, the AFRP or CFRP specimens closest to these locations were instrumented. These were specimens AR-1 or CA-1 (nearest to the live end) and AR-33 or CA-33 (closest to the dead end). Their selection enabled the accuracy of the strain measurements to be assessed relative to that of the load cell readings. Moreover, it also provided an index of the instantaneous elastic shortening losses. The three remaining specimens selected were located near the middle of the bed where uniform conditions were expected. These were AR-16 or CA-16, AR-17 or CA-17 and AR-18 or CA-18. More importantly, their proximity to the data acquisition system, (housed in the van in Figure 1) greatly reduced the length of wiring needed.

To capture the strain variation, five gages were attached to the concrete surface at each end spaced 5 cm apart. This meant that strains were measured at 2.5 cm, 7.5 cm, 12.5 cm, 17.5 cm and 22.5 cm (from each end). In addition, two further gages were placed symmetrically 119.4 cm from each end.

### Test procedure

Just prior to release, the prestressing force was estimated by averaging readings of the four load cells connected to each prestressing rod at both the dead and live ends. An electric grinding wheel (see Figure 2) was then used to cut the prestressing rod and release the prestressing force.

After each rod was cut, strain readings were taken using the computerized data acquisition system that was located in a van near the middle of the prestressing bed. This operation was repeated until the prestressing force had been released in all 33 beams.

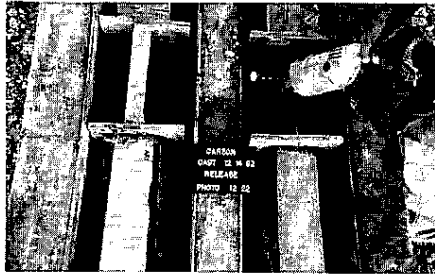


Figure 2. Release of prestressing force.

Since the instrumentation for the AFRP and CFRP beams was identical and they were cast in adjacent beds (see Figure 1), it was possible to conduct the testing expeditiously even though it had to be carried out sequentially.

After all measurements for the CFRP beams had been concluded, the wires leading from the (CFRP) beams to the data acquisition system were dis-connected at the beam site and immediately re-hooked to the corresponding locations in the AFRP beams. The procedure for determining transfer length outlined before was then repeated.

## Results

The target jacking force was 55% and 60% of the reported ultimate tensile capacities of the AFRP and CFRP rods respectively (see Table 1). Based on load cell measurements just prior to release, the average prestressing force was 50.6% of ultimate in the AFRP beams [2] and 51% of ultimate in the CFRP beams [3].

Since the strain gages were attached to the top surface of the beams, the concrete strain,  $\epsilon$  (tension positive), should reach a terminal value approximately given by Eq. 1

$$\epsilon = -\frac{P}{AE} + \frac{Pe}{SE} - \frac{M}{SE} \quad (1)$$

In Eq. 1,  $P$  is the prestressing force,  $M$  the self weight bending moment,  $A$  the beam cross-section,  $S$  its section modulus and  $E$  the Young's Modulus for concrete.

By substituting appropriate values for all the variables in Eq. 1, the expected strain variations for the AFRP and CFRP beams may be calculated. At the ends, where the effects of self weight bending moments are minimal, the concrete strains were  $64\mu\epsilon$  (tension) and  $81\mu\epsilon$  (tension) in the AFRP and CFRP beams respectively. The corresponding strains at mid-span, where bending moment effects are important, were  $42\mu\epsilon$  (tension) and  $59\mu\epsilon$  (tension). The strain variation between these locations is parabolic to match the variation in strains due to self weight bending moments.

Typical results for the representative beams are shown in Figures 3-4. These show the strain variation in AFRP and CFRP beams located near the live end (AR-1 and CA-1 in Figure 3) and those located near the middle of the prestressing bed (AR-17 and CA-18 in Figure 4). Tensile strains are assumed positive in these figures.

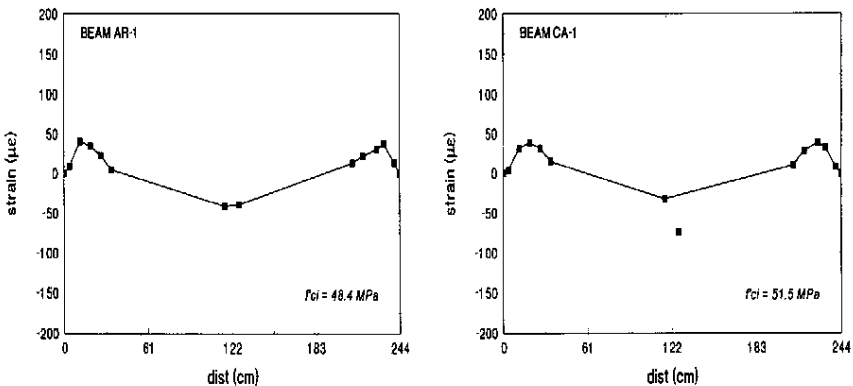


Figure 3. Strain variation in AFRP and CFRP beams located near live end.

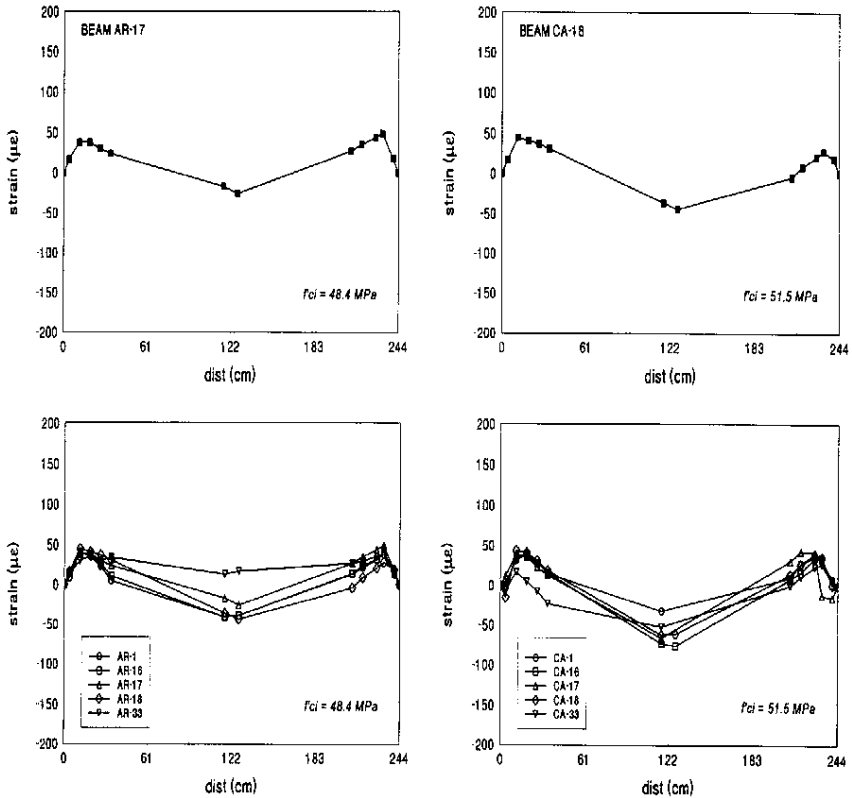


Figure 4. Strain variation in AFRP and CFRP beams.

Inspection of Figures 3-4 shows that while the distribution of strains is more or less symmetrical, the magnitudes of the maximum and minimum strains depart significantly from that predicted by Eq. 1. While minor variations could be attributed to inaccuracies in the estimate of the prestressing force or in the assumed modulus of concrete, this cannot be used to explain why mid-span strains were compressive rather than tensile.

Since this pattern was observed in all the beams tested (see Figure 4), instrumentation error was ruled out. Instead, it was hypothesized that when the prestressing force was released, the upward movement of the beams was impeded by frictional type forces that developed between the wood forms and the concrete. This was believed to be due to the presence of concrete that had been inadvertently placed in the narrow space between the sides of the steel form and the wood insert (see Figure 5).

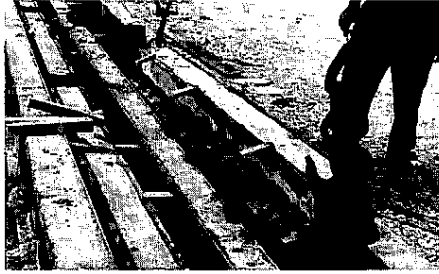


Figure 5. Concrete sticking to sides of wood form.

Normal forces required for the frictional force to develop were due in part to bending about the weak axis caused by the unsymmetric placement of the prestressing rods in the beam and the unequal magnitude of the forces in the two rods [2,3]. Consequently, finite element analyses were carried out to determine the theoretical transfer length and also to establish the kind of frictional force needed to match the test results.

#### Finite element analysis

Three dimensional finite element analyses were carried out using ANSYS 5.0. The beams were modeled using SOLID95 type elements. These are 3-D structural elements defined by twenty nodes - eight at each face and four intermediate nodes. Each node had three translation degrees of freedom. Two separate analyses were carried out. The first attempted to determine the theoretical transfer length; the second, to re-produce the results that were obtained from the testing.

To determine the theoretical transfer length, the idealization assumed perfect symmetry. Thus, the location of the AFRP and CFRP rods was assumed to be symmetrical with respect to *both axes* with the force in each prestressing rod assumed to be *identical*. In the second analysis, the actual locations of the prestressing rods in the cross-section and the actual forces obtained from load cell readings were used to reconcile the results obtained from the testing. For the former case, symmetry allowed the problem size to be greatly reduced. Because the results for transfer length were found to be insensitive to the exact location of the AFRP or CFRP rods, only one representative mesh was used for analyzing all the beams in the latter analysis. The finite element mesh for the cross-section for both analyses is shown in Figure 6a, b.

The discretization along the length was kept the same for the two analyses (Figure 6c). Since the prestressing force was assumed to be unchanged over the length of the specimen it was only necessary to model half the length. To obtain agreement with the theoretical transfer strain (see Eq. 1), a very fine discretization was needed. A total of 48 elements each 2.5 cm long were used to model half the length. Because of the discretization of the cross-section this meant that six layers of 48 elements were provided along the length. A total of 2,592 elements and 12,817 nodes were used in the discretization. In the cross-section, 193 nodes were present.

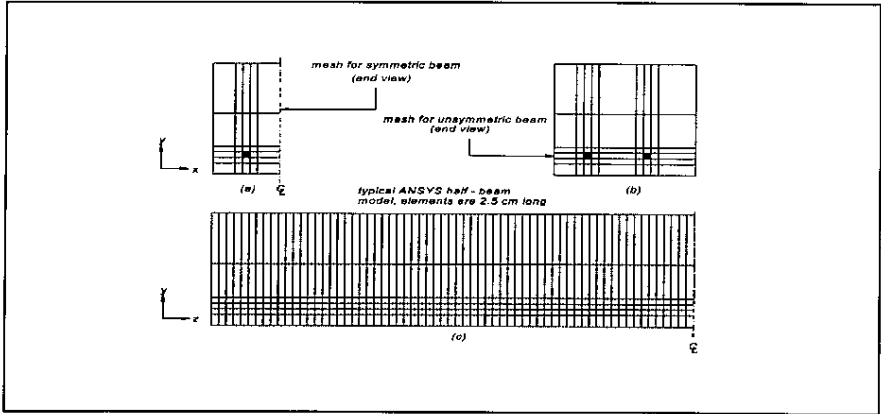


Figure 6. Finite element mesh for transfer length analysis.

Since prestress forces are transferred to the concrete by the *Hoyer* effect, the Poisson's ratio of the two materials is an important variable. For concrete, a value of 0.2 given in design specifications was used. For the AFRP and the CFRP material, values were different in the axial and radial directions. In the axial direction, the AFRP used a value of 0.36. For CFRP it was taken as 0.28. In the radial directions, the resin value of 0.35 was used for both materials.

To determine the theoretical transfer length ideal conditions were assumed. Thus, the beam was assumed to be free to move longitudinally because of elastic shortening ( $z$ ) and upward ( $y$ ) because of eccentricity of the prestressing force. However, the ends were assumed to be simply supported and restrained to prevent out of plane movement ( $x$  direction). The prestressing force was equally distributed among each of the corners of the element(s) representing the AFRP and CFRP rods (see darkened element(s) in Figure 6a, b).

The results from the finite element analyses for the theoretical transfer length for AFRP and CFRP are shown in Figure 7. As stated earlier, the transfer length (also referred to as the *transmission length* [7]) is the distance measured from the end face over which

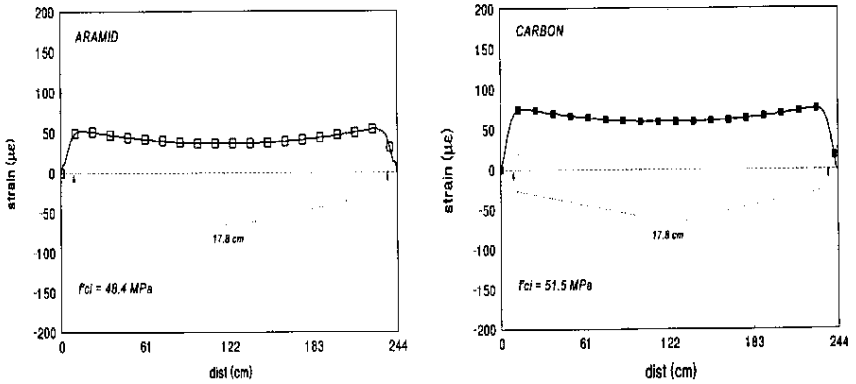


Figure 7. Transfer length prediction from finite element analysis.

the full initial stress is developed. The transfer length predicted is about 17.8 cm for both AFRP and CFRP. The corresponding concrete strains are  $59\mu\epsilon$  for AFRP and  $81\mu\epsilon$  for CFRP. These compare favorably with strains of  $64\mu\epsilon$  (AFRP) and  $81\mu\epsilon$  (CFRP) obtained by appropriate substitutions in Eq. 1. This suggests that the finite element discretization was satisfactory.

The transfer length of 17.8 cm predicted by the finite element analyses corresponds to about 30 diameters for both AFRP and CFRP. This falls broadly within the range reported by other researchers [4-6], though it is somewhat larger for the aramid rods in comparison to results reported recently by Belgian researchers [7].

### Friction forces

As noted earlier, the discrepancy between the field results (Figures 3-4) and expected results (Figure 7) was attributed to friction forces that impeded the upward movement of the beam at transfer. The normal forces needed for these friction forces developed at the locations along the length where spacers had been provided (see Figure 1) and also where hardened concrete prevented movement of the beam (see Figure 5).

The assumptions made in the finite element analysis for modeling the frictional force are illustrated in Figure 8. The eccentricity of the prestressing force ( $e_1$  and  $e_2$ ), and their unequal magnitude ( $P_1$  and  $P_2$ ), gave rise to bending moments ( $M$ ) about the weak axis. This moment caused only a part of the tensile surface to press against the wood forms, described as the *contact surface* in Figure 8. The compression face moved away from the form and was therefore not subject to any friction force.

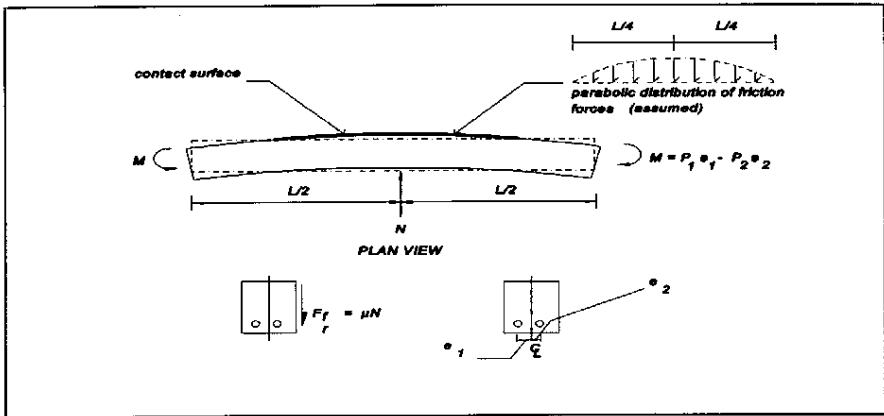


Figure 8. Idealization of frictional force in finite element analysis.

The frictional force was assumed to have a parabolic distribution that extended from quarter point to quarter point. This is consistent with the upward movement which is greater in the middle and smaller near the ends. This force was additionally assumed to act only on the tension face as shown in Figure 8.

Trial and error was used to obtain correlation between test results and predictions from ANSYS. Since the frictional forces were not identical in each beam, the magnitude of this force varied from beam to beam. These ranged from 0.9 kN to 1.9 kN for the AFRP specimens and from 2.3 to 3.2 kN for the CFRP beams. Using a very simplified model, this suggests a large friction coefficient [2,3].

Figure 9 compares the predictions from finite element analysis incorporating frictional forces and test results. The overall agreement is close and appears to confirm the validity of the hypothesis.

## Conclusions

This paper presents results of field measurements carried out to determine the transfer length of beams pretensioned using AFRP and CFRP rods. The surfaces of these rods were provided with sand or grit to improve bond with concrete. A total of ten 2.44 m long beams were instrumented by strain gages that were bonded to the top surface of the beam at both ends and also at the middle.

The strain distributions obtained from the tests were consistent yet inexplicable (see



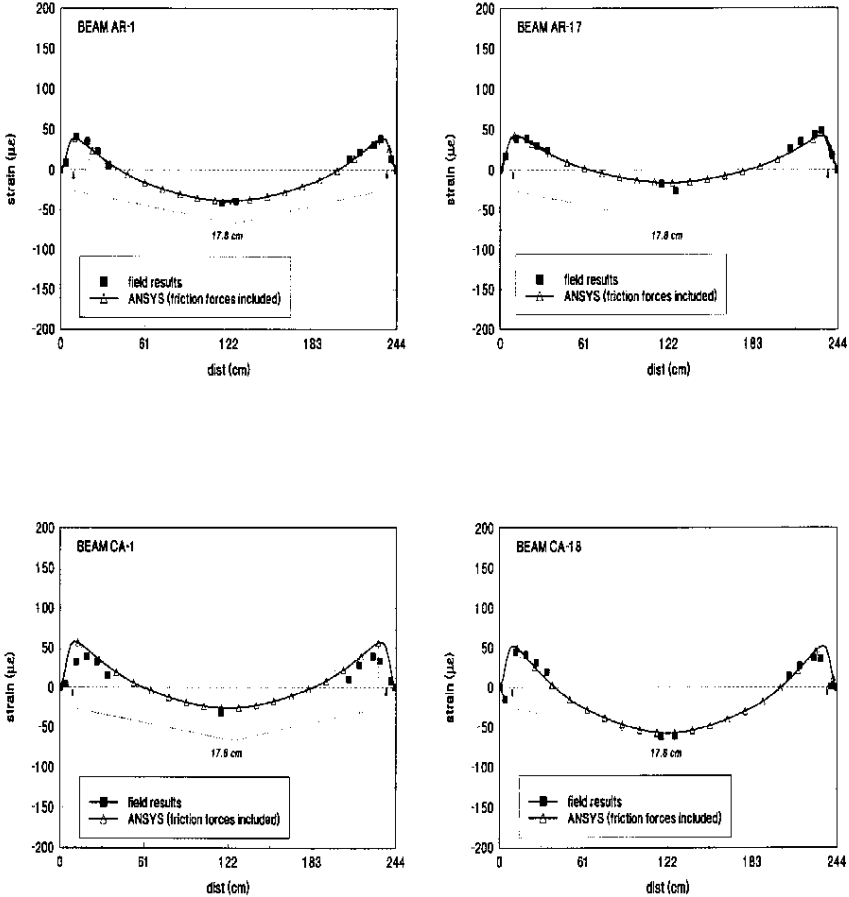


Figure 9. Comparison of test results and predictions from finite element analysis.

Figures 3-4). Finite element analysis appeared to confirm the hypothesis that frictional forces impeding movement along the length were responsible for this variation. The results of the finite element analysis incorporating frictional forces provided close correlation with the test results. The analysis also indicated that the transfer length for the beams tested was about 30 diameters, in broad agreement with results reported previously [4-6].

## Acknowledgments

The investigation reported in this paper was carried out with the financial support of a research contract from the US and Florida Department of Transportation. The authors gratefully acknowledge the many contributions of Dr. Mohsen Shahawy, Director, Florida Department of Transportation in this study. However, the opinions, findings and conclusions expressed in this paper are those of the writers and not necessarily those of the Florida or US Department of Transportation.

## References

1. Sen, R., Spillett, K. and Shahawy, M. (1994). "Fabrication of aramid and carbon fiber reinforced plastic pretensioned beams." *Concrete International, Vol 16, No. 6, pp. 45-47.*
2. Rosas, J. (1995). "Studies in durability of AFRP pretensioned piles." MSCE Thesis submitted to Department of Civil Engineering & Mechanics, University of South Florida, Tampa, FL, May.
3. Sukumar, S. (1995). "Studies in durability of CFRP pretensioned piles." MSCE Thesis submitted to Department of Civil Engineering & Mechanics, University of South Florida, Tampa, FL, May.
4. Machida, A. (1993). Editor, "State-of-the-art-report on continuous fiber reinforcing materials." *Japanese Society of Civil Engineers*, Tokyo, Japan, October.
5. McKay, K.S. and Erki, M.A. (1993). "Flexural behaviour of concrete beams pretensioned with aramid fiber reinforced plastic tendons", *Canadian Journal of Civil Engineering*, Volume 20, Number 4, August, pp. 688-695.
6. Arockiasamy, M. and Sandepudi, K.S. (1994). "Active deformation of bridges prestressed with aramid FRP cables." Final report submitted to Florida Department of Transportation, August.
7. Taerwe, L. and Pallemans, I. (1995). "Force transfer of AFRP bars in concrete prisms." *Non-Metallic (FRP) Reinforcement for Concrete Structures*, Proceedings of the Second International RILEM Symposium (FRPRCS-2) Edited by L. Taerwe, F & FN Spon, London, UK, pp. 154-163.

## STRENGTHENING CONCRETE BLOCK WALLS USING CARBON FIBER

Dan Engebretson<sup>1</sup>, Rajan Sen<sup>2</sup>, Gray Mullins<sup>3</sup>, and Alfred Hartley<sup>4</sup>

### Abstract

The University of South Florida is conducting full scale tests to assess the feasibility of using uni-directional carbon fiber sheet material in repairing damaged concrete masonry walls. The damage under investigation was from in-plane loads resulting from soil subsidence—a common problem in the Southeastern United States. A finite element study was undertaken as part of this research. This paper presents the results obtained using the finite element program FEM/I developed under the joint U.S.-Japan Coordinated Program for Masonry Research. The predictions from the finite element analysis show reasonable agreement with the test results for both plain and strengthened walls. Interestingly, the analysis also suggests that comparable strengthening could have been achieved with narrower strips than those evaluated in the tests.

### Introduction

Concrete blocks are used predominantly in the Southeastern United States where wind rather than seismic forces govern design. Historically, residential masonry structures in this region are only partially reinforced because the design loads are relatively small and ductility is less important. Vertical reinforcement has typically been provided only at the corners in conjunction with horizontal reinforcement in the bond beam. While such construction has adequately resisted out-of-plane bending due

<sup>1</sup> Graduate Research Assistant, Department of Civil & Environmental Engineering, University of South Florida, Tampa, FL 33620

<sup>2</sup> Professor, Department of Civil & Environmental Engineering, University of South Florida, Tampa, FL 33620

<sup>3</sup> Assistant Professor, Department of Civil & Environmental Engineering, University of South Florida, Tampa, FL 33620

<sup>4</sup> Structural Engineer, Ayres & Associates, Tampa, FL 33619

to hurricane force winds, it is incapable of withstanding in-plane bending resulting from settlement loads.

In 1995, the University of South Florida commenced a systematic study to investigate the feasibility of using carbon fiber sheets to repair concrete block walls damaged by foundation settlement. Four full-sized test walls representative of the practices stipulated by the prevailing Standard Building Code over the past thirty years were built. Two of the walls were damaged under simulated subsidence loads and then repaired using Forca Tow sheets from Tonen Corporation of Japan (Hartley et al. 1996). The second phase of the research involves numerical analyses which will be used to validate the available finite element programs.

The analysis of unreinforced masonry walls is complicated by the presence of horizontal and vertical mortar joints which are significant planes of weakness. Specialist programs for unreinforced masonry that use interface elements to model the joints (e.g., Manzouri et al. 1995) are still in development. In view of this, the program FEM/L, a finite element program developed under the joint U.S.-Japan Coordinated Program for Masonry Research (Ewing et al. 1990), was used for the preliminary analysis. It was developed to analyze *reinforced* masonry building components but surprisingly provided reasonable agreement for both the plain and strengthened partially reinforced test walls.

#### Test program

Four 5.9 m (232 in.) x 2.4 m (96 in.) test walls were constructed using 194 mm (7.63 in.) nominal blocks atop a 203 mm (8 in.) x 406 mm (16 in.) concrete footer. The steel reinforcement consisted of two 15M (#5) rebars in the footer and one vertical 15M (#5) rebar at the following spacings: 1.2 m (4 ft.), 2.4 m (8 ft.), or rebars only at the corners. All specimens included a reinforced bond beam at roof level. The walls were cantilevered over half their length, fully supported over the rest, and a concentrated load was placed on the end to simulate severe ground settlement. The plain walls were loaded to failure and repaired with a unidirectional carbon fiber tow sheet. Three horizontal oriented strips, each 51 cm (20 in.) wide, were applied to one side of each specimen. The strips were bonded from the top down and overlapped such that each wall was repaired with an approximately 152 cm (60 in.) wide strip across the full 5.9 m length of the wall. Each repaired wall was tested in the same manner as the plain walls



*Figure 1. - One of Four Repaired Test Specimens*

and the increase in strength was determined. Two of the four specimens (Wall #1 and Wall #2) have been tested (Hartley 1995).

### Finite Element Analysis

The PC based finite element program, FEM/I, was used to analyze the test specimens. This program models the reinforcement and the underlying masonry matrix separately using appropriate stress-strain relationships. The two elements are assumed to share the same nodes and remain fully bonded. The resulting smeared hybrid element is an overlay, or layered, model where the computed strains are assigned to both materials. This approach lends itself well to carbon fiber sheets but, as discussed above, the program has a major drawback: it was designed for the analysis of fully grouted, reinforced masonry structures. It therefore employs stress-strain relationships where the effects of the masonry joints are averaged rather than modeled specifically. Grouting provides continuity across the mortar joints and reduces the degree of anisotropy in the masonry. It has been found to significantly increase the tensile and shear strengths relative to the bed joint (Drysdale et al. 1994). The program only allows one value for tensile strength which implies that the masonry is considered as isotropic. The mortar joints are a significant area of weakness for unreinforced masonry, and the tensile strength of masonry normal to the bed joint is typically half of that normal to the head joint. To compound the potential inaccuracies the program includes several models which are based on concrete research. A before-cracking constitutive model based on the Darwin-Peckhold model is used, and the modeling of strength enhancements due to lateral confinement and decreases due to compression softening are also derived from concrete research.

A program that perhaps better addresses the effects of the mortar joints on the overall strength of unreinforced or partially reinforced masonry was developed by Manzouri et al. (1995). It also uses a smeared-crack approach for the concrete blocks but uses the interface element developed by Lotfi and Shing (1994) to model the mortar joints. This interface element better represents the shear dominated behavior of the masonry joints.

Unfortunately, the program developed by Manzouri et al. was not readily available at the time of the initial analysis. The researchers decided to use the FEM/I program for the following reasons: i) to provide generalized results; ii) the test specimens were full-sized walls rather than masonry assemblages and the approach utilized by FEM/I may be suitable; and iii) the cracking pattern, which FEM/I cannot accurately predict, is not as important for this study.

Idealization of Test SpecimensMasonry Properties

The masonry is modeled as a material with bimodular orthotropy, and with tensile cracking modeled using a non-coaxial rotating smeared crack approach. The secant moduli  $E_1$  and  $E_2$  are determined from the compressive stress-strain relationships specified by six parameters:  $f'_m$ ,  $\epsilon_0$  (at peak uniaxial stress),  $A_1$ ,  $A_2$ ,  $A_3$ , and  $A_4$ . The parameters  $A_1$  through  $A_4$  specify the shape and attachment points of the three functions which define the stress-strain curve. The tensile stress-strain curve is assumed to be linear up to cracking and is defined by four parameters:  $F_{cr}$ ,  $E_m$ ,  $B_1$ , and  $\alpha$ . The tensile cracking strain is derived from the cracking stress ( $F_{cr}$ ) and Young's Modulus ( $E_m$ ) for masonry which is assumed to be equal to the initial linear portion of the compression stress-strain curve. Debonding of the reinforcement from the masonry is modeled as a material property and is reflected in the tensile stress-strain curve. Table 1 summarizes the parameters used to model the compressive stress-strain curves for unreinforced masonry, reinforced masonry (i.e., grouted cells), and concrete (i.e., footer). The properties were determined via actual materials testing when economically feasible or from the literature (Drysdale et al. 1979; Guo 1991; Hamid and Drysdale 1988) when it was reasonable to do so. These and all other parameter values were validated using an extensive parametric study and sensitivity analysis. It was found that the parameters  $F_{cr}$ ,  $f'_m$ ,  $\epsilon_0$ , and  $E_m$  had the greatest impact on the predicted results while the others had little or no impact.

Parameter	Unreinforced Masonry	Reinforced Masonry	Concrete Footer
$f'_m$ or $f'_c$ (MPa) (psi)	11.43 (1657)	9.3 (1341)	30.6 (4442)
$\epsilon_0$	0.0018	0.0016	0.0019
$A_1$	2.0	2.0	2.0
$A_2$	1.2	1.4	2.3
$A_3$	0.1	0.1	0.1
$A_4$	0.6	0.6	0.6
$F_{cr}$ (kPa) (psi)	517.1 (75.0)	827.4 (120.0)	2937.3 (426.0)
$E_m$ or $E_c$ (GPa) (psi x $10^{-6}$ )	11.99 (1.74)	10.83 (1.57)	30.54 (4.43)
$B_1$	n/a	0.50	n/a
$\alpha$	n/a	0.18	n/a
$\nu$	0.175	0.175	0.190

Table 1. - Summary of Material Parameters

(Hollow masonry is based on net area; reinf. masonry on gross area)

### Steel Properties

The program uses a bilinear model for the reinforcement stress-strain curve and is determined by three parameters:  $F_y$ ,  $E_s$ , and  $\zeta$ . The plastic modulus is derived by multiplying the elastic modulus ( $E_s$ ) by the parameter,  $\zeta$ , which estimates the effects of strain hardening. Its value had no impact on the results since the steel did not reach yielding. The reinforcement may be specified in both horizontal or vertical orientations. It is also considered smeared over the element but is uni-directional per the orientation specified.

### CFRP Properties

The carbon fiber sheet used was Tonen's FORCA Tow Sheet (FTS-C1-20). It is uni-directional providing high tensile strength in the longitudinal fiber direction, and is almost perfectly linear elastic up to the ultimate stress. For a 152 cm (60 in.) wide sheet, the Forca Tow sheet displays an ultimate stress of 3.48 GPa (504,825 psi) and a tensile modulus of 231.0 GPa ( $33.5 \times 10^6$  psi) (Tonen 1995).

### Results

Preliminary analyses have been completed for Wall #1 and Wall #2. FEM/ provided promising results when compared with actual test results. Figures 2 and 3 show the comparisons of horizontal strains measured from Wall #1 without the Forca Tow sheet (plain) and after being repaired with a 152 cm (60 in.) wide strip across the top (repaired). The strains were measured along two vertically aligned gage positions: one at 193 cm (76 in.) from the cantilevered end and the other at 335 cm (132 in.) from the end. With the exception of the uppermost bond beam gages in Figure 3, the predicted results yielded reasonable values and similar strain variation patterns. The large disparity in the top gages was due to the program's assumption of compatibility of strains between nodes at the joint interface (in absence of a discretized joint element) and its inability to model shear behavior along the joint. The bond beam of Wall #1 was formed by using a 152 mm (6 in.) wide felt cap applied along the length of the wall before the last course of bond beam units were mortared in place. The felt cap prevented the grout from falling through the cells below and was typical of older style construction. Unfortunately, it reduced the effective width of the mortar bed from 32 mm (1.25 in.) to 21 mm (0.813 in.) for each face shell. A separation was observed along this weaker interface for almost the full length of the wall. In addition, it was suspected that a separation occurred along the interfaces between the face shells and grout core of the bond beam. This resulted in the grout core being able to strain relatively independently to the rest of the wall. The uppermost strain gage was attached to the bond beam's grout core while the Forca Tow sheet was bonded to one of the face shells of the bond beam. The lack of connectivity would result in the actual recorded strains being significantly less than the predicted values.

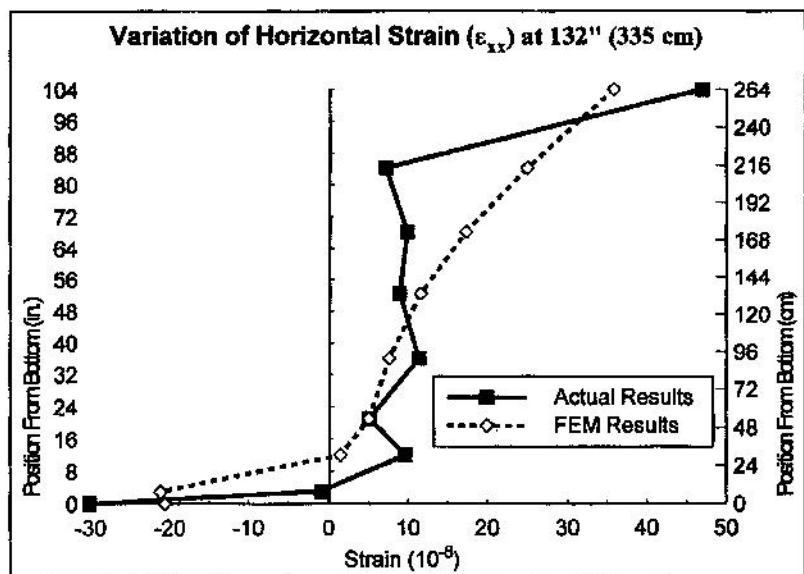
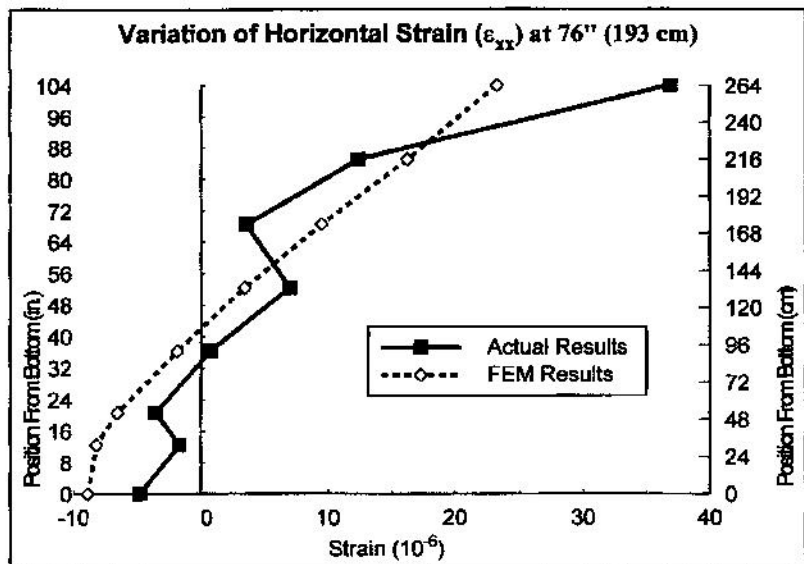


**Figure 2. - Variation of Horizontal Strain ( $\epsilon_{xx}$ ) for Wall #1 (Plain)**



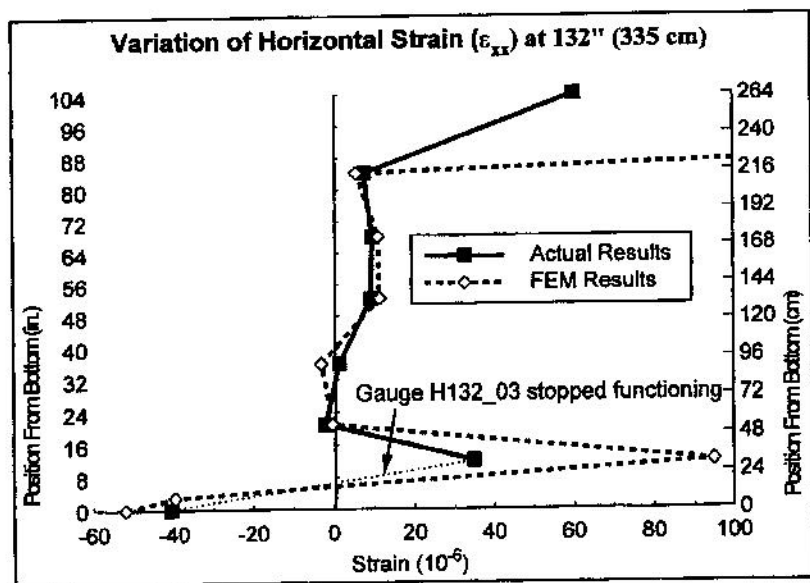
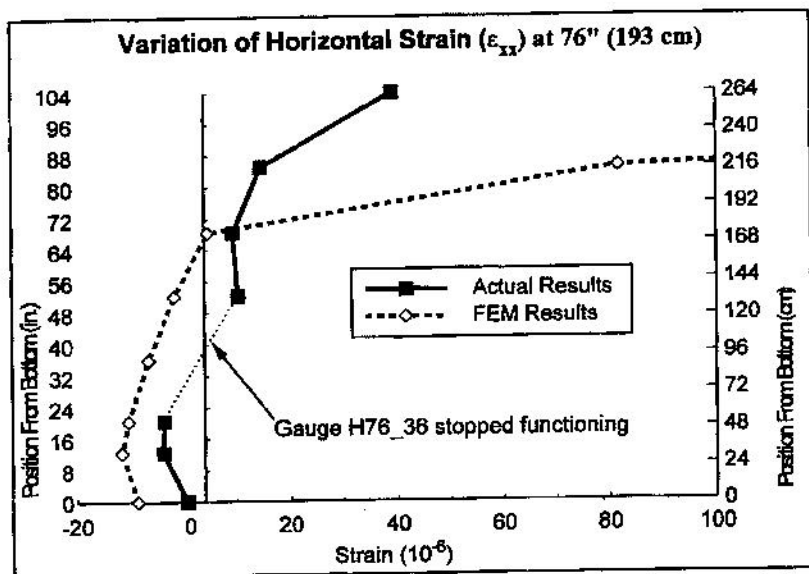


**Figure 3. - Variation of Horz. Strain ( $\epsilon_{xx}$ ) for Wall #1 (Repaired)**

FEM/I did not accurately predict the crack pattern as was expected. Such disparities are not uncommon because smeared crack models are unable to accurately model the type of shear dominated behavior apparent during testing. Although the predicted deflections at the peak recorded load were reasonable, especially for the plain Wall #1, the program yielded a predicted load-deflection curve which took a significantly different path from the actual curve.

Because the agreement between predicted and actual results were satisfactory, FEM/I was used to examine the correlation of tow sheet width and strength gains. Additional analyses were conducted for repairs of Wall #1 using 31 cm (12 in.), 51 cm (20 in.), and 102 cm (40 in.) wide tow sheet strips. The respective predicted deflections were 549.7  $\mu\text{m}$  (0.02164 in.), 507.0  $\mu\text{m}$  (0.01996 in.), and 530.6  $\mu\text{m}$  (0.02089 in.) versus an actual deflection of 697.5  $\mu\text{m}$  (0.02167 in.) for 152 cm (60 in.) at an arbitrary load of 32.2 kN (7232 lbs.). This arbitrary load was the peak load for Wall #1 (plain) and was chosen in order to provide a basis of comparison between the plain and strengthened configurations. In addition to the deflections, the analyses yielded similar plots of stress trajectories for the different tow sheet strip widths. The plots indicated that the carbon fiber applied along the bond beam consistently provided the greatest tensile strength while the portions of the tow sheet applied below the bond beam had little impact. The implications are that narrower, less costly strips could have been used with no commensurate strength reduction.

### Conclusions

This paper presents comparisons of results obtained from the finite element program FEM/I with data from full-scale tests on walls which were damaged by foundation settlement. The walls used different reinforcement configurations and were subsequently repaired with carbon fiber Forca Tow sheets to assess strengthening capabilities.

Obvious problems arise when analyzing unreinforced or partially reinforced masonry structures with programs that are based on fully grouted masonry. Although FEM/I is intended for analyzing fully grouted walls, the correlation between the test results and the predictions of strain and deflections was surprisingly good—despite an inability to accurately predict the cracking pattern.

The analysis indicates that similar strength enhancements could be achieved with overall narrower tow sheet strips rather than the 152 cm (60 in.) width originally evaluated in this study. The ability to strengthen damaged masonry walls, and to do so with narrower strips, would be a significant cost savings to the home owner.

This study is on-going and the next phase will include analyses with finite element programs that better model the shear dominated behavior of the mortar joints.

### Acknowledgments

The authors gratefully acknowledge the contributions of Mr. Bob Ewing, Mr. Howard Kliger, and the Tonen Corporation of Japan to this study.

### References

- Drysdale, R., Hamid, A., and Heidebrecht, A. (1979). "Tensile strength of concrete masonry." *Journal of the Structural Division, ASCE*, 105(ST7), 1261-1275.
- Drysdale, R., Hamid, A., and Baker, L. (1994). *Masonry structures: behavior and design*. Prentice-Hall, Englewood Cliffs, N.J.
- Ewing, R., El-Mustapha, A., Kariotis, J. (1990). "A finite element computer program for the nonlinear static analysis of reinforced masonry building components." *Report No. 2.2-1*, Ewing and Associates, Rancho Palos Verdes, CA.
- Guo, P. (1991). "Investigation and modeling of the mechanical properties of masonry." Ph.D. thesis, McMaster University, Hamilton, Ontario.
- Hamid, A. and Drysdale, R. (1988). "Flexural tensile strength of concrete block masonry." *Journal of Structural Engineering, ASCE*, 114(1), 50-66.
- Hartley, A. (1995). "Strengthening of concrete masonry walls using CFRP material," Masters Thesis, University of South Florida, Tampa, FL.
- Hartley, A., Mullins, G., and Sen, R. (1996). "Repair of concrete masonry block walls using carbon fiber," *Second International Conference on Advanced Composite Materials in Bridges and Structures*, Montreal, P.Q., Canada.
- Lotfi, H., and Shing, P.B. (1994). "Interface model applied to fracture of masonry structures," *Journal of Structural Engineering, ASCE*, 120 (1), 63-80.
- Manzouri, T., Shing, P.B., Amadei, B., Schuller, M., and Atkinson, R. (1995). "Repair and retrofit of unreinforced masonry walls: experimental evaluation and finite element analysis," University of Colorado at Boulder, CO.
- "FORCA Tow sheet technical notes." (1995). Tonen Corp., Japan.



**ADVANCED COMPOSITE MATERIALS IN BRIDGES AND STRUCTURES**  
M.M. El-Badry, Editor; Canadian Society for Civil Engineering, Montreal, Quebec, 1996

**MATÉRIAUX COMPOSITES D'AVANT-GARDE POUR PONTS ET CHARPENTES**  
M.M. El-Badry, éditeur; Société canadienne de génie civil, Montréal, Québec, 1996

## REPAIR OF CONCRETE MASONRY BLOCK WALLS USING CARBON FIBER

**Alfred Hartley, Gray Mullins and Rajan Sen**  
University of South Florida  
Tampa, Florida, USA

### ABSTRACT

The University of South Florida has embarked on an outdoor test program to investigate the feasibility of using uni-directional carbon fiber sheets for repairing settlement damaged block walls used in home construction. For the initial phase of the study, four 200 mm (8 in.) thick concrete block walls each 2.44 m (8 ft) high and 6.1 m (20 ft) long have been designed and built. Vertical steel reinforcement has been varied to meet past and present requirements of the Standard Building Code. In the testing, the walls are subjected to simulated foundation settlement to replicate observed cracking and then repaired by bonding carbon fiber tow sheets *on only one wall face*. The repaired walls are then loaded identically to assess the efficacy of the repair. Preliminary results are very encouraging and suggest that this technique may be economically viable for repairing damaged homes.

### INTRODUCTION

Sixty-five percent of all residential structures in the state of Florida are constructed from concrete masonry units, making Florida the biggest user of concrete blocks in the United States. Because loads on single family dwellings are small, such structures were not required to be engineered; however, damage by successive hurricanes has led to new requirements currently enshrined in "*deemed to comply*" rules (SBC 1993). For typical 200 mm (8 in.) walls, these rules require (a) one 15M (#5) vertical rebar at the corners and every 9.14 m (30 ft), and (b) 200 mm (8 in.) deep bond beam reinforced (horizontally) by one 15M (#5) bar. Construction must also ensure continuity of the horizontal and vertical steel so that the entire structure acts in concert to resist hurricane force winds.

Apart from high winds and their attendant uplift problems, external masonry walls in homes may also be subjected to foundation movement. This is a common problem that affects large numbers of homeowners nationwide. Since foundation subsidence subjects walls to *in-plane* loading, vertical reinforcing steel provided to resist out-of-plane bending is largely ineffective; the resulting damage, calls for expensive repairs. Unfortunately, relatively little is known about the response of such lightly reinforced walls under settlement loading. As such, repair methods, e.g. use of micro-piles combined with grouting of cells, may be both inappropriate and costly. Instead, more effective repairs may be achieved through the use of advanced composites.

## OBJECTIVES

The overall objectives of the study are twofold: (1) to determine the response of typical concrete block walls built for residential construction in accordance to the Standard Building Code (*the prevailing code in the Southeastern United States and parts of Texas*) under settlement loading (2) to repair the damaged walls using advanced composites and to assess the extent of the strengthening. Although the focus of the study is largely experimental, numerical analyses will also be conducted. These will be directed towards calibrating finite element models developed for masonry construction in seismic zones, e.g. Ewing 1993, and also to identify simplified idealizations that can be used by consulting engineers to obtain reasonably accurate predictions.

## TEST PROGRAM

A careful survey was made of subsidence damage to masonry block homes in the Tampa Bay area prior to the design of the test specimens. Based on this inspection, and interviews with consulting engineers, the representative wall length was determined to be 6.1 m (20 ft). The wall height was taken as 2.4 m (8 ft) as this is typical for residential construction.

For the initial phase, four 200 mm (8 in) concrete block walls each 2.4 m (8 ft) x 6.1 m (20 ft) were designed and built. The spacing of vertical reinforcement was varied from 6.1 m (20 ft) to 1.22 m (4 ft) to reflect changing provisions in code specifications. A typical wall elevation is shown in Fig. 1.

### Settlement Simulation

Each wall is supported by 200 mm (8 in.) x 400 mm (16 in.) concrete footings reinforced by two 15M (#5) rebars - typical of residential construction as shown in Fig. 1. It may be seen that over half its length, the footing is supported on compacted fill 0.91 m (3 ft) above grade; in the remaining half it is supported on a W10 x 49 steel beam. The steel beam is simply supported above grade between a keystone screw jack at the free end of the wall and on an on-

grade beam at the center of the wall. During construction, a plastic sheet was used to completely separate the footing from the steel beam to prevent any composite action. By unscrewing the jack with a wrench the wall can be made to settle.

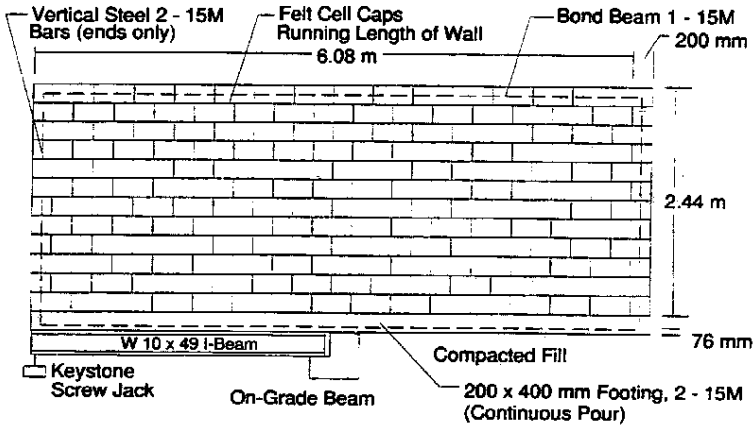


Fig. 1. Concrete block details, Wall #1

The settlement loads are equivalent to the cantilevered weight of the wall. Additional loads, simulating the weight of other materials that bear on the wall and actual roof loads, can also be applied at the top of the wall by a 27 tonne ENERPAC hydraulic jack. This is jacked against a steel beam that is chained to ground anchors bored into the ground. The reaction frame geometry and the location of the ground anchors permit loads of up to 9 tonnes to be applied to any location along each wall (see Fig. 2a).

### Instrumentation

The test specimens were instrumented using load cells, LVDT's, and strain gages. Two load cells placed at the free end measure the self weight during subsidence and the magnitude of the simulated roof load. LVDT's measure deflections in both the vertical and horizontal directions; strain gages are used to record strains in both the wall and the footing.

Strain gages were provided along three vertical lines across the subsiding portion of the wall: at the support, at mid-span in the cantilevered section, and at the free end. A battery powered MEGADAC 3108 DC data acquisition system is used for recording data.

## Test Procedure

The wall is initially subjected to several load-unload cycles in the elastic range to verify its stiffness. Following completion of these tests, it is loaded past its cracking load. The wall is then repaired using advanced composites and tested as before. All data is automatically recorded during testing using the data acquisition system.

## Repair of Wall

In the initial phase, walls damaged due to subsidence will be repaired using uni-directional carbon fiber Force Tow Sheets (FTS-C1-120) developed by Tonen Corporation of Japan. This is a lightweight, high strength material that is epoxy bonded to the wall surface. The Forca Tow Sheet was designed and developed for structural rehabilitation and has been primarily used for repairing concrete structures (Kobayashi et al. 1995).

The application of the tow sheets generally involves six steps (1) surface preparation, (2) application of a primer coating, (3) application of epoxy adhesive after the primer surface has dried, (4) placement of the tow sheet (5) removal of excess resin and air bubbles with a putty knife, and (6) application of a second epoxy coating. Because of the nature of the intended application, surface preparation was kept to a minimum and essentially consisted of only removing any mortar that was protruding from the wall surface. No attempt was made to grind the mortar joints.

To expedite placement, the Forca Tow Sheets were cut to lengths of approximately 6.1 m (20 ft) to match the wall length. More importantly, the sheets were then *re-rolled* inside out. This greatly simplified placement since the tow sheet could then be unrolled directly onto the wall as epoxy was being applied. Since the carbon fiber was only intended to increase bending resistance, it was oriented parallel to the length of the wall. Three sheets, each 500 mm (20 in.) wide, were attached *only to one face* as shown in Fig. 2b.

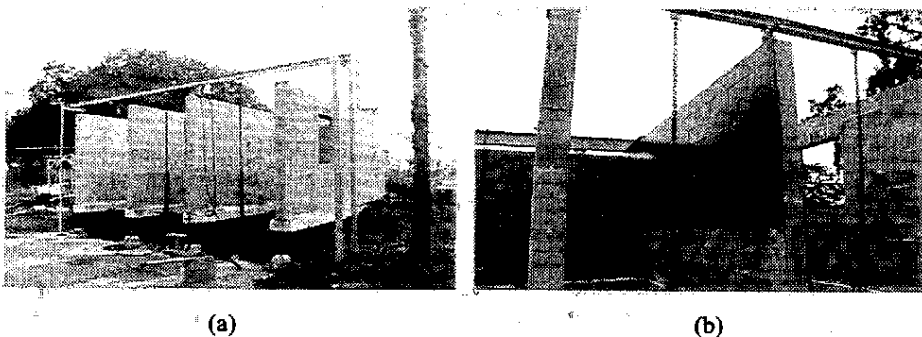


Fig. 2. (a) View of walls and reaction frame (b) Repaired wall.

## RESULTS

The study is on-going and only preliminary results from two of the walls are available, Hartley 1995. However, many additional tests are planned. Since the aim of the investigation is also to assess long term performance, the repaired walls were not loaded to failure. Because the specimens are outdoors, all testing is restricted to pre-dawn hours when constant conditions prevail.

In the tests, the original wall referred to here as the '*plain wall*' was loaded and unloaded several times to verify its elastic response prior to the application of the final cracking load. Under this load, the wall developed step cracks along horizontal and vertical mortar joints as was observed in actual buildings. It was then repaired using carbon fiber Forca Tow sheets (see Fig. 2b).

Tests results obtained from Wall #1 (for wall details see Fig. 1) appear in Figs. 3-6. Similar trends were observed from Wall #2, Hartley 1995. Fig. 3 compares the vertical load versus vertical displacement for the plain and repaired walls. The loads shown exclude the self-weight of the wall. Under the applied vertical load, the plain wall cracked at a load of 30.2 kN (6.78 kips). The repaired wall was then tested in the identical manner. The test on this wall was stopped when the load reached 55.6 kN (12.5 kips), an increase of over 80% of the original load. No evidence of cracking could be detected in this wall.

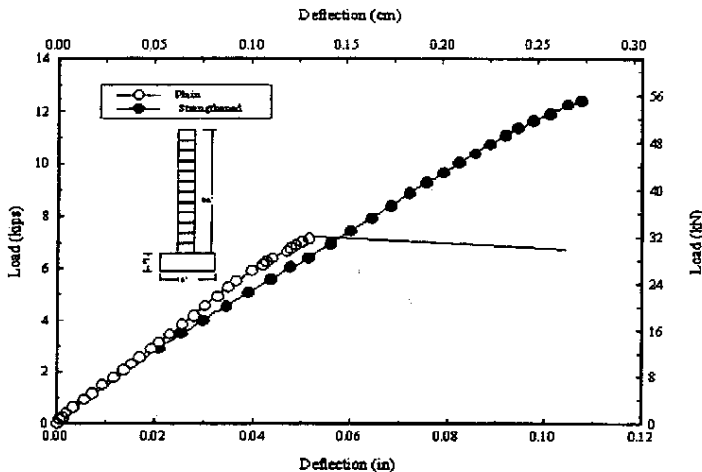


Fig. 3. Wall #1: Load vs. Deflection



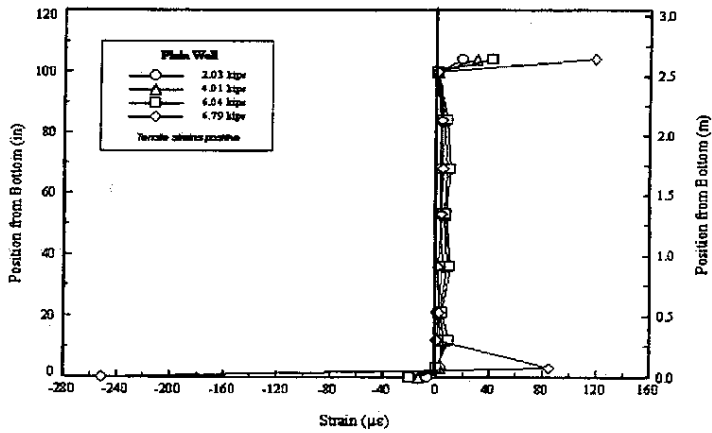


Fig. 4. Wall #1 (Plain): Variation of strain down wall

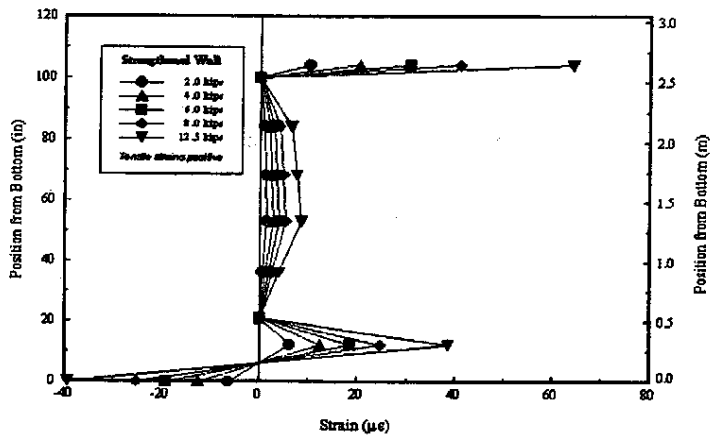


Fig. 5. Wall #1 (strengthened): Variation of strain down wall

Fig. 4 shows the strain variation with load in the plain wall. No strains were recorded on gages that were positioned at mid-height of the bond beam when the load was varied. This suggests that the grout is not bonded to the sides of the masonry unit forming the bond beam. Inspection of Fig. 4 also shows that the overall strains are relatively small until cracking. The strain variation with depth for the strengthened wall is shown in Fig. 5. The larger strains recorded show the effect of the carbon fiber. A comparative plot of strains in the plain and strengthened walls under selected loads is shown in Fig. 6.

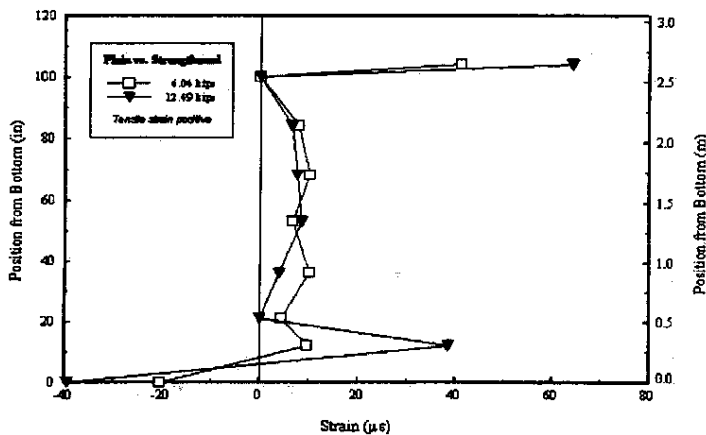


Fig. 6. Wall #1: Comparison of strain for both plain and strengthened

## CONCLUSIONS

Homes damaged by foundation settlement are traditionally repaired by preventing further movement through the use of micro-piles/grade beams followed by repair of the damaged walls. While these solutions are undoubtedly effective, they are costly, time consuming and very disruptive. The alternative examined in this paper is the use of carbon fiber sheets to *only* strengthen damaged walls so as to make them capable of sustaining additional loads or movement without further deterioration. While this technique may not be suitable for all situations, e.g. sinkholes, the results from preliminary tests reported clearly show that the strength of damaged walls can be significantly increased. Moreover, since the repairs need only be carried out on the outside of the home, disruptions are minimized. This study is still in the preliminary stage; however, the results obtained are encouraging and suggest that carbon fiber sheets may offer a viable and economical alternative for repairing concrete block walls damaged by ground subsidence.

### ACKNOWLEDGMENTS

The authors gratefully acknowledge the support and contribution of the Tampa Bay Chapter of the Masonry Contractors Association of Florida. We also wish to thank Howard Kliger for much useful technical advice and for providing the carbon fiber Forca Tow Sheets and resin used in the testing.

### REFERENCES

- Ewing, R. (1993). "Nonlinear Static Finite Element Analysis of Reinforced Masonry Walls in Tall Buildings," *The Structural Design of Tall Buildings*, Vol. 2, pp. 133-152.
- Hartley, A. (1995). "Strengthening of Concrete Masonry Walls using CFRP Material," Thesis submitted in partial fulfillment of MSCE degree, Department of Civil and Environmental Engineering, University of South Florida, Tampa, FL, December, pp. 215.
- Kobayashi, A., Ohori, N. and Kuroda, H. (1995). "Repair and Reinforcement of Concrete Structure with Carbon Fiber Tow Sheet," *Non-metallic (FRP) Reinforcement for Concrete Structures (Editor L. Taerwe)*, E & FN Spon, London, England, pp. 688-695.
- Southern Building Code Congress International, Inc. (1993). "*Standard for Hurricane Resistant Residential Construction SSTD 10-93*," Birmingham, AL.

## STRENGTHENING STEEL COMPOSITE BEAMS WITH CFRP LAMINATES

Rajan Sen<sup>1</sup>, Larry Liby<sup>2</sup>, Gray Mullins<sup>3</sup> and Ken Spillet<sup>4</sup>

### Abstract

The University of South Florida completed an experimental and numerical study in which wide flange steel beams acting compositely with concrete slabs, were strengthened using carbon fiber reinforced plastic (CFRP) laminates. This paper presents an overview of the research project and also compares the material cost of providing equivalent strengthening using conventional means, i.e. by welding steel plates.

### Introduction

Steel stringer bridges are very common in the United States and make up almost a third of all bridges with spans exceeding 6.1 m. Since many were constructed just prior to World War II, they are nearing the end of the average 65-70 year useful service life. Strengthening steel members in these bridges using bonded CFRP laminates offers the prospect of speedy and economical repair with minimal disruption to traffic.

---

<sup>1</sup>Professor, Dept. of Civil & Environmental Engineering, University of South Florida, Tampa, FL 33620

<sup>2</sup>Graduate Student, Texas A&M University, College Station, TX 77843

<sup>3</sup>Assistant Professor, Dept. of Civil & Environmental Engineering, University of South Florida, Tampa, FL 33620

<sup>4</sup>Operations Manager & Professional Associate, Parsons Brinckerhoff Construction Services, Tampa, FL 33607

In 1993, the University of South Florida completed an experimental and numerical study to examine the feasibility of using CFRP laminates for strengthening steel composite beams typically used in highway construction. This paper presents a brief overview of the study. Additional information may be found elsewhere Sen et al 1994a, 1995.

### Test Specimens

The specimens tested were obtained from two composite bridge models from a separate study, Sen et al 1994b. The concrete deck slab was reinforced longitudinally and transversely and stud shear connectors were welded to the top flange of the steel beams to ensure composite action. The yield stresses of the steel in the two bridge models were 310 MPa and 370 MPa.

The test specimens were obtained by cutting the 6.1 m long by 2.13 m wide concrete deck slab longitudinally. Since each bridge had three equi-spaced steel beams, each bridge provided three specimens so that a total of six specimens were tested. Each test section comprised a W8 x 24 steel section attached to a 0.71 m wide, 0.114 m thick reinforced concrete slab.

CFRP laminates were used to strengthen the composite sections. The 0.165 m width of the 3.65 m long CFRP laminates was the same as the steel flange. The average tensile strength parallel to the unidirectional laminates' fiber orientation was reported as 1839 MPa and the tensile modulus, 114 GPa. Fiber Resin Corporation's two part epoxy adhesive, FR-1272, was used to bond the CFRP laminate to the steel surface, augmented by bolts for some tests.

### Test Results

A total of 13 tests were carried out in three series of tests. In the initial series, plain composite beams were loaded past yield of the tension flange to simulate severe distress under service loading. In the next series, the damaged specimens were strengthened by bonding the CFRP laminate to the tension flange and loaded to failure. In the final series, a plain composite beam was loaded to failure to assess its actual strength. Comparison of the relative performance of the unreinforced and strengthened beams provided a measure of the efficacy of the CFRP laminate.

Typical results obtained from the testing are shown in Figs 1 and 2. Fig. 1 shows the comparison of the load displacement response of a beam strengthened using 2 mm thick CFRP laminate with that of a plain composite beam.

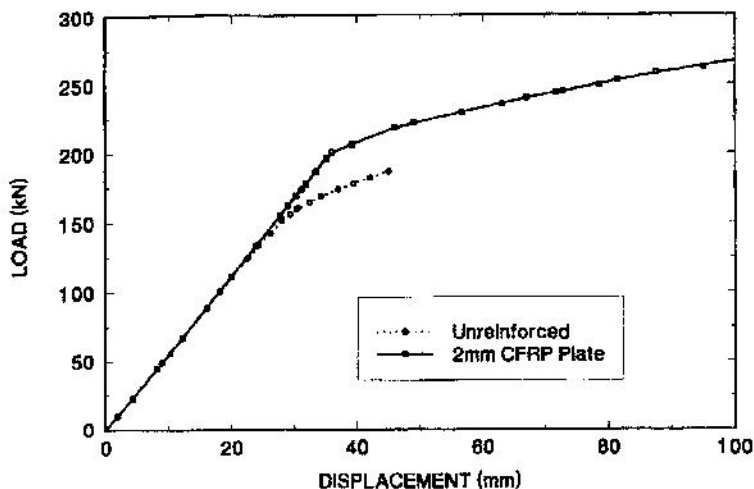


Fig. 1. Load Displacement 370 MPa - 2mm (epoxy only).

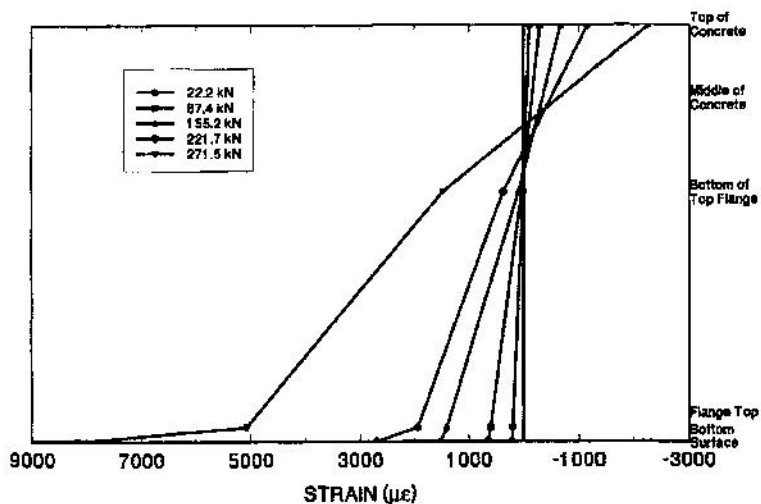


Fig. 2. Strain Variation at Mid-Span 370 MPa - 2-mm (epoxy only).

Inspection of Fig. 1. shows that the use of the CFRP laminate leads to an increase in both the elastic and ultimate capacity though there is practically no increase in stiffness. However, in other tests using 5 mm thick CFRP laminates, substantial stiffness increases were realized.

The strain variation with depth for the same strengthened beam is shown in Fig. 2. It may be seen that until the steel yields, there is relatively little load transfer to the CFRP laminate.

Table 1 summarizes the test results. The percentage increases in this table are relative to the load at which the tension flange yielded and range from 19% to 109% depending on the yield stress of the steel and the thickness of the CFRP laminates. The larger increases correspond to the thicker CFRP laminate and the weaker steel.

Table 1. Summary of Strengthening Results.

Steel (MPa)	Test	Yield Load (kN)	2-mm CFRP		5-mm CFRP	
			Load (kN)	% Gain	Load (kN)	% Gain
310	1	141.9	236.6	66.7	-	-
	2	142.3	-	-	298.0	109.4
	3	141.9	-	-	169.0	19.1
370	1	186.4	271.3	45.5	-	-
	2	186.8	271.3	44.8	-	-
	3	187.3	-	-	329.1	76.2

The opposite combination, i.e. thinner CFRP laminate and stronger steel, gave smaller increases as can be anticipated. Since these increases are relative to the yield load, they are somewhat misleading. Absolute increases, i.e. relative to the failure strength of the unstrengthened were smaller for the one beam that was tested in this manner. The increase for this beam was substantial and compared favorably with average strength increases of 22% reported from tests on reinforced concrete members, Meier et. al 1992.

### Prototype Bridge Section

The bridge sections tested were not however, representative of prototype sections since the deck slab was deliberately kept larger to ensure that concrete failure would not occur prior to yielding of the steel wide flange shapes. A quarter scale model bridge called for a 50 mm concrete slab reinforced with No. 6 gage wire placed 150 mm on center instead of the 114 mm slab reinforced by 20M (#6) bars that was tested.

To determine if the more typical bridge section would also benefit from strengthening using CFRP laminates, non-linear finite element analyses were carried out. The predicted response of the bridge sections with 310 MPa steel wide flange beams showed strength gains of 40% and 75% when strengthened by 2-mm and 5-mm CFRP laminates, respectively. The corresponding gains for the prototype model bridge section with 370 MPa steel were 30% and 60%. These strength gains are in line with those obtained from the ultimate load capacity tests of the model bridge sections.

### Equivalent Steel Plate

In order to compare costs, bridge sections based on a prototype bridge were analyzed to determine the thickness of steel cover plates that would provide strengthening that was equivalent to that provided by 2-mm and 5-mm CFRP laminates.

The non-linear finite element analyses revealed that to provide the same strengthening, the 2-mm CFRP laminate would need to be replaced by 6.3 mm thick steel plates and the 5-mm CFRP laminate by 11.1 mm thick steel plates. At \$0.20/N, the 6.3 mm steel plate would cost \$58.70 and the 11.1 mm plate, \$103.20. This compares with the CFRP laminate cost of \$560 for the 2-mm CFRP laminate and \$780 for the 5-mm CFRP laminate. Thus, the CFRP laminate is roughly 8-10 times more expensive than the steel plate for this configuration. Complete results may be found in Liby 1993.

### Conclusions

This paper provides a brief summary of a study conducted to investigate the feasibility of strengthening steel composite bridge members using CFRP laminates. Although the CFRP laminates are less stiff than the steel flange to which it was attached and the shear strength of the epoxy adhesive orders of



magnitude smaller than steel, substantial strength gains were realized. Moreover, since the majority of the load transfer to the CFRP laminate occurred only after the steel flange had yielded, failures were preceded by large deflections.

Cost comparisons are presented which compare the actual cost of the CFRP laminates used in the study with that of steel plates required to provide the same strengthening. This shows that the CFRP material costs were between 8-10 times that of steel. Since the CFRP laminates are much lighter than the equivalent steel plates, the repair can be carried out speedily with minimal disruption to traffic. Thus, the overall cost differential will be lower especially in busy urban areas.

The study indicates that it is feasible to use CFRP laminates to strengthen steel composite bridges provided durability of the adhesive is assured and measures are taken to ensure that there is no galvanic action due to the direct contact between the CFRP laminate and steel. At the present time, however, such repairs are likely to be more costly though this may change in the future.

#### Acknowledgements

This investigation was carried out with the financial support of the Florida Department of Transportation and the US Department of Transportation. The authors thank Dr. Mohsen Shahawy for this support. They also wish to express their appreciation to Composite Horizons, Covington, CA for their many contributions to the study. However, the opinions, findings and conclusions expressed in this publication are those of the writers and not necessarily those of the Florida Department of Transportation or the US Department of Transportation.

#### References

- Liby, L. (1993) Steel Composite Bridge Sections Strengthened by CFRP Laminates. Master's Thesis submitted to Department of Civil Engineering & Mechanics, University of South Florida, Tampa, FL, November, pp.353.
- Meier, U., Dearing, M., Meier, H. and Schwegler, G. (1992) Strengthening of Structures with CFRP laminates: Research and Applications in Switzerland, *Advanced Composite Materials in Bridges and Structures* (Ed. K.W. Neale and P. Labossiere), CSCE, Montreal, P.Q., pp. 243-251.

Sen, R. and Liby, L. (1994a) Repair of Steel Composite Bridge Sections using CFRP Laminates. Final Report submitted to the US and Florida Department of Transportation, National Technical Information Service, VA, August, pp. 95.

Sen, R. and Spillett, K. (1994b) Restraint Effect of Bridge Bearings. Final Report submitted to the US and Florida Department of Transportation, National Technical Information Service, VA, January, pp. 118.

Sen, R., Liby, L., Spillett, K. and Mullins, G. (1995) Strengthening Steel Composite Bridge Members using CFRP Laminates. *Non-metallic (FRP) Reinforcement for Concrete Structures* (Editor L. Taerwe), E & FN Spon, London, England, pp. 551-558.